

A 226 815



Sixth International Conference on
Modulated Semiconductor Structures

94-08508

RECEIVED
MAR 17 1994
S B

August 23 - 27, 1993
Garmisch-Partenkirchen
Germany

Workbook

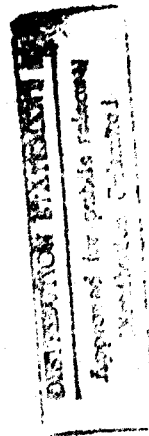


PHOTO COPY FORWARDED 1

24 3 16 012

Best Available Copy

**Best
Available
Copy**

Preface

This workbook contains refereed manuscripts of papers which will be presented at the 6th International Conference on Modulated Semiconductor Structures to be held in Garmisch-Partenkirchen, Germany from August 23 to August 27, 1993. Abstracts are included for those manuscripts not received in time. The papers will be refereed and accepted papers will be published in a special issue of *Solid State Electronics*. We expect roughly 300 participants from 20 countries, presenting approximately 180 papers. More than 200 papers had to be rejected in order to keep the conference reasonably small with no parallel sessions. This was not an easy task for the program committee but we believe nevertheless that the papers chosen are representative of some of the best current work in the area of Modulated Semiconductor Structures.

The organization of the conference was made possible by the financial support of

Deutsche Forschungsgemeinschaft
Bayerisches Staatsministerium für Unterricht, Kultus, Wissenschaft und Kunst
Commission of the European Communities
European Research Office United States Army
AUXTRON Semiconductor Technologies
Alcatel Hochvakuumtechnik
Balzers Hochvakuum

Bruker
Coherent
Cryovac
Daimler Benz
DILOR
FIZONS Instruments
IBM Deutschland
Instruments S.A.
Intervac
Leybold
L.O.T.
Oxford Instruments
Siemens

On behalf of the organizing committee I would like to express my gratitude to all sponsors.

The conference was organized at the Walter Schottky Institut, Technische Universität München, Garching with telephone and fax-numbers familiar to many participants now. I want to mention especially the many contributions to the local organization by the secretaries Veronika Entler, Claudia Färstel and Sirku Pimmininen as well as Ulrich Beckelmann, Max Bichler, Sepp Brunner, Werner Donndl, Christoph Engelhardt, Joachim Nützel, Dirk Többen, Robert Strenz, Adi Ziegler and others. In addition we had the pleasure of working with very capable and cooperative staff at the conference center in Garmisch-Partenkirchen.

Gerhard Abstreiter
Chairman of MSS6
July 1993

Organizing Committee

G. Abstreiter (TUM, Garching) Chairman
E. Gornik (TUM, Garching) Program
K. von Klitzing (MPI, Stuttgart) Finances
P. Vogl (TUM, Garching) Arrangements
A. Zrenner (TUM, Garching)

Program Committee

G. Bastard (ENS, Paris)
G. Bauer (Universität Linz)
S. J. Bending (University of Bath)
H. Dambkes (TUM, Garching)
A. Fenchel (Universität Würzburg)
E. Göbel (Universität Marburg)
E. Gornik (TU München, Garching)
J. P. Kotthaus (LMU, München)
E. Molinari (CNR, Rome)
H. Oppolzer (Siemens, München)
K. Ploog (PDI, Berlin)

Advisory Committee

Z. J. Alferov (Ioffe Inst., St. Petersburg)
F. Briones (CSIC, Madrid)
L. L. Chang (IBM, Yorktown Heights)
G. H. Dohler (Univ. Erlangen)
L. Esaki (Univ. Tsukuba)
A. Fasolino (SISSA, Trieste)
T. Foxon (Univ. of Nottingham)
A. C. Gossard (Univ. of California)
D. Heimann (Univ. Hamburg)
S. Hiyamizu (Univ. of Osaka)
E. Kasper (Daimler, Ulm)
M. J. Kelly (Univ. of Surrey)
F. Koch (TUM, Garching)
D. J. Lockwood (NRC, Ottawa)
P. Lugli (Univ. of Roma)
J. C. Maan (Katholieke Univ. Nijmegen)
B.D. McCombe (SUNY at Buffalo)
H. Ohno (Hokkaido Univ.)
H. Okamoto (Chiba Univ.)
J. F. Palmier (CNET, Bagneux)
A. Pinczuk (AT&T Bell Labs, Murray Hill)
F. H. Pollak (CUNY, Brooklyn)
J. Robert (USTL, Montpellier)
H. Sakaki (RCAT, Univ. of Tokyo)
S. C. Shen (Shanghai Inst. of Tech. Physics)
Y. Shiraki (RCAT, Univ. of Tokyo)
C. Tejedor (Univ. Autònoma de Madrid)
D. C. Taul (Univ. of Princeton)
B. Vinter (Thomson, Orsay)
M. Vons (ENS, Paris)
G. Weimann (TUM, Garching)
C. Weisbuch (Thomson, Orsay)
J. M. Worlock (Univ. of Utah)
Xie Xide (Fudan Univ., Shanghai)
W. Zawadzki (Polish Academy of Sci., Warsaw)

MSSS PROGRAM

Monday, August 23, 1993

Conference Opening 8:30 - 8:50

MoA Growth of GaAs and Dots 8:50 - 10:20

MoA1 Fabrication of Quantum Wires and Dots by MOCVD Selective Area Growth Y. Arakawa (Invited) 8:50

MoA2 Polarization Spectroscopy of Modulated GaAs/GaAlAs Quantum Wells Grown on Vicinal Surfaces: Anisotropic Islands or Ordered Growth? J.J. Birch, U. Bockelmann, F. Laruette 9:20

MoA3 Preparation of 1D-2D Structures by Molecular Beam Epitaxy-growth on Patterned AlGaAs Buffer Layers K. Ebner, A. Kortenbach, P. Grambow, A. Lehmann, D. Helmreich, K. von Klitzing, M. Dillig, M. Hohenstein 9:40

MoA4 Fabrication of SiC/Si Quantum Wire Structures on a V-groove Patterned Si Substrate by Gas-source Si Molecular Beam Epitaxy N. Usami, T. Mine, S. Fukatsu, Y. Shiraki 10:00

Coffee break 10:20 - 10:30

MoB Transport Properties in Low-dimensional Systems 10:30 - 12:40

MoB1 Evidence of Directional Electron Heating in Doped GaAs B. Brill, M. Heiblum, H. Shtrikman (Invited) 10:50

MoB2 High-mobility Transport along Single Quasi 1-Dimensional Quantum Wires Formed by Cleaved Edge Overgrowth W. Wegscheider, W. Kang, L. N. Pfeiffer, K. W. West, H. L. Stormer, K. W. Baldwin 11:20

MoB3 Observation of Kondo and Gutzwiller Transport Regimes in a Two-dimensional Wire L.W. Molenkamp, M. J. M. de Jong 11:40

MoB4 Quantized Conductance and its Effects on Non-linear Drain Current Observed at 80 K in Mesa-etched InAs Quantum Wires with Split-Gate K. Yoh, A. Nishida, M. Imase 12:00

MoB5 Transport Properties of Lateral Superlattices Grown on Vicinal GaAs (100) Surfaces S. A. Lofke, P. M. Petroff 12:20

Lunch break 12:40 - 1:00

Poster Session:

MoP Growth, Characterisation, Transport 14:00 - 16:00

MoP1 MBE Fabrication of GaAs Quantum Wire Structures on Mesa Structures Along the [001] Direction M. Lopez, T. Ishikawa, I. Matsuyama, N. Tanaka, Y. Nomura 14:00

MoP2 Alternative Method to Produce Quantum Wires Using Dislocation Slipping C. Guisach, F. Volter, M. Cotran, J. P. Peyrard, E. Bedel, C. Fontaine, H. Atrami, A. Rocher 14:20

MoP3 Formation of N-AlGaAs/GaAs Edge Quantum Wire on (111)B Micro Facet by MBE and Magnetic Depopulation of Quasi-One-Dimensional Electron Gas Y. Nakamura, M. Tsuchiya, J. Motohisa, H. Noge, S. Koshida, H. Sakaki 14:40

MoP4 Lateral Potential Modulation in InAs/AlSb Quantum Wells by Wet Etching T. Uitzinger, K. Enslin, J. P. Kotthaus, C. Bologniet, C. Nguyen, H. Kroemer 15:00

MoP5 Optical Properties of GaAs Quantum Dots Fabricated by MOCVD Selective Growth Y. Nagamune, M. Nishioke, S. Tsukamoto, Y. Arakawa 15:20

MoP6 Fabrication of Nanometer-Scale Conducting Silicon Wires with a Scanning Tunneling Microscope P. M. Campbell, E. S. Snow, P. J. McMarr 15:40

MoP7 Selective Growth of SiGe Nanostructures by Low Pressure VPE G. Schmidt, W. Langheinrich, K. Helme 16:00

MoP8 Direct Epitaxial Growth of (AlGa)As/GaAs Quantum Wires by Orientation-Dependent Metal Organic Vapour Phase Epitaxy D. Bertram, B. Spill, W. Spolz, E. O. Gobel 16:20

AVAILABILITY	Notes
Small and/or	Special
<p>11</p>	

MoP9	GaAs/Al _{0.3} Ga _{0.7} As Quantum Wire Structures Fabricated by C ₆₀ -Induced Angle Molecular Beam Epitaxy on Reverse-Mo-Becked GaAs (100) Substrates S. Shinomura, K. Inoue, M. Tanaka, A. Adachi, M. Fujii, T. Yamamoto, T. Watanabe, N. Sano, K. Murase, S. Hayamizu	102
MoP10	Coverage Dependence of Migration Potential of Cation Adatoms on GaAs(001)-(2x4) Surface K. Shiraiishi, T. Ito, T. Ohno	104
MoP11	Raman Scattering Investigation on the Ordered Incorporation of Si Doped Atoms on (001) GaAs Vicinal Surfaces During MBE Growth M. Karstner, J. Wagner, G. Jung, D. Behr, L. Däweritz, R. Hey	110
MoP12	Disorder-Induced Raman Scattering of Folded Phonons in Quantum Wells and Superlattices T. Ruf, V. I. Belitsky, J. Spitzer, V. F. Sapryga, M. Cardona, K. Ploog	119
MoP13	FTIR Spectroscopy of Longitudinal Confined Phonons and Plasmon-Phonon Vibrational Modes in GaAs/AlAs _n m Superlattices Yu. Pusep, A. Mikhlin, A. Yonkov	123
MoP14	Raman Scattering Study of Longitudinal Acoustic and Optic Phonons in InSb/In _{0.5} Al _{0.5} Sb Strained-Layer Superlattices V. P. Gerasimov, D. J. Lockwood, J. B. Webb	124
MoP15	Optical Phonon Probes of Interface Roughness: A Theoretical Investigation S. de Gironcoli, E. Molinari	131
MoP16	Infrared Reflectivity of Strained GaSb/AlSb Superlattices C. Scarmiento, C. Galdete, A. Tagliente, L. Tapfer, K. Floeg, Y. Ohmori, H. Okamoto	139
MoP17	Quantitative Analysis of Strain Relaxation and Mosaicity in Short Period Si _{0.5} Ge _{0.5} Superlattices Using Reciprocal Space Mapping by X-ray Diffraction E. Koppert, P. Hambberger, G. Bauer, V. Hudy, H. Kibbel, H. Preising, E. Kasper	144
MoP18	Evidence of Non-commutativity of Band Discontinuities in InP-Al(In)As Ga(In)As Heterostructures E. Lugagne-Dupon, J. P. Andre, P. Vitiello	151
MoP19	Above Barrier Excitons Confined in InGaAs/GaAs Multiple Quantum Well Structures M. Capizzi, A. Frova, A. Pollini, F. Martelli, K. B. Ozanyan, T. Worren, M. R. Bruni, M. G. Simeone	157
MoP20	Spectroscopic Study of Photo-electric Field Effects in InGaAs/GaAs Multi-Quantum Wells Grown on (111)B Oriented GaAs Substrates T. A. Fisher, R. A. Hogg, A. R. K. Wilcox, D. M. Whitaker, M. S. Skolnick, D. J. Mowbray, J. P. R. David, A. S. Pabla, G. J. Rees, R. Grey, J. L. Sanchez-Rojas, J. Woodhead, G. Hill, M. A. Pate, P. N. Robson	163
MoP21	Optical Properties of AlP-GaP Short-period Superlattices A. Monti, T. Takano, J. Kitamura, K. Hara, H. Kulkarni, J. Yoshino, T. Yasuda	170
MoP22	InGaAs/InP Quantum Wells with Periodic Thickness Variation A. A. Bernus, M. J. S. P. Brasil, J. A. Brum, M. A. Cotta, R. A. Hamam, T. W. Suley, S. N. G. Chiu, L. R. Harriot, M. B. Panish, H. Temkin	173
MoP23	Determination of Built-in Electric Fields in Delta-doped GaAs Structures by Phase-sensitive Photoreflectance V. L. Alperovich, A. S. Jaroshevich, H. E. Scheibler, A. S. Terekhov	181
MoP24	Advantages of a Piezoelectric Field in a Quantum Well U. Ekenberg, D. Richards	182
MoP25	Determination of the Basic Parameters of Pseudomorphic GaAs Quantum Wells by means of Simultaneous Transport and Optical Investigations E. Litwin-Staszewska, F. Kobbi, D. Durr, C. Skierbiszewski, M. Kamal-Saadi, H. Sibari, K. Zekentes, V. Musser, A. Raymond, W. Knap, J. L. Robert	188
MoP26	The Conduction Band Spin Splitting in Type-I Strained and Unstrained (GaIn)As/InP Quantum Wells P. Onling, B. Kowalski, B. K. Meyer, D. M. Hofmann, C. Wetzel, V. Harle, F. Schulz	192
MoP27	Binding Energies of D ⁺ Ion in GaAs Quantum Well Y. H. Chang, J. J. Yeh, Y. M. Shiu, C. C. Wang, T. C. Chen, K. H. Chang, C. P. Lee	200

MoP28	Correlations of the Remote Impurity Charges - A Method of 2DEG Mobility Tuning in GaAs/AlGaAs Heterostructures T. Suski, P. Wierlewski, L. H. Dmowski, J. Gorszyc, J. Smoliner, E. Gornik, G. Böhm, C. Weimann	206
MoP29	Three-dimensional Boltzmann-Bloch Theory of Miniband Transport in Superlattices with Elastic Scattering R. R. Gerhardis	213
MoP30	Domain Formation in Modulation-doped GaAs/Al _x Ga _{1-x} As Heterostructures R. Düttling, E. Schöll	220
MoP31	Inside a 2D Electron System: Images of Potential and Dissipation R. Knott, U. Klass, W. Dietzche, K. von Klitzing, K. Eberl, K. Ploog	228
MoP32	DC Transport in Intense, In-Plane Terahertz Electric Fields in As ₂ Ga _{1-x} As Heterostructures at 300 K N. G. Asmar, A. G. Markelz, E. G. Gwinn, P. F. Hopkins, A. C. Gossard	234
MoP33	Microwave Miniband NDC in GaInAs/AlInAs Superlattices J. F. Palmier, J. C. Harmand, C. Minot, H. Le Person, E. Dutisseuil, H. Wang, C. Leroux	238
MoP34	Quasi-one-dimensional Ballistic Electron Transport in In-Plane-Gated Channels at Liquid Nitrogen Temperature D. K. de Vries, K. Ploog, A. D. Wieck	244
MoP35	The Dependence of Boundary Scattering in Split-gate Quantum Wires on the Transverse Mode Number M. Yamamoto, S. Nakata, K. Alhara, T. Mizutani	248
MoP36	Experimental Studies of Electronic Transport in Semiconductor Quantum Dot Structures J. P. Bird, K. Ishibashi, Y. Aoyagi, T. Sugano	252
MoP37	Photovoltaic Effect in Quasiballistic Electron Interferometer A. A. Bykov, Z. D. Kvon, L. V. Litvin, Ju. V. Nastaushev, V. G. Mensurov, V. P. Migal, S. P. Moschenko	261
MoP38	Dimensional Transition of Weak Localization Effects in Lateral Surface Superlattices P. E. Selbmann, M. Sührke	262
MoP39	Luminescence Studies of Resonant Tunneling in a Triple Barrier Structure with Strongly Coupled Quantum Wells T. S. Turner, P. M. Martin, L. Eaves, H. B. Evans, P. A. Harrison, M. Henini, O. H. Hughes, D. M. Whitaker, P. D. Buckle, T. A. Fisher, M. S. Stobnick, G. Hill	268
MoP40	Correlation Effects in Magnetoluminescence Spectra from Dense Quasi 2D Electron Gas in Selectively Doped InGaAs/GaAs Quantum Wells V. D. Kulakovskii, L. V. Butov, I. E. Itskovich, L. V. Kulik, T. G. Anderson, W. Shumin, A. Lomsadze	275
MoC	Growth, Characterization and Phonons (1610-1830)	
MoC1 1610	MBE Growth of GaAs Nanometer-scale Ridge Quantum Structures and their Structural and Optical Characterizations S. Koshiba, H. Noge, Y. Nakamura, H. Akiyama, T. Inoshita, T. Someya, K. Wada, A. Shimizu, H. Sakaki	281
MoC2 1630	Control of Interface Composition in InAs/GaSb Superlattices B. R. Bennett, B. V. Shanabrook, R. J. Wagner, J. L. Davis, J. R. Waterman, M. E. Twigg	290
MoC3 1650	Lateral Piezoelectric Fields - an Universal Feature of Strained III-V and II-VI Semiconductor Heterostructures M. Ilg, A. Heberle, K. H. Ploog	298
MoC4 1710	Band Discontinuity and Effects of Si-Insertion Layer at (311)A GaAs/AlAs Interface T. Saito, Y. Hashimoto, T. Ikoma	302
MoC5 1730	X-Ray Diffraction Analysis of GaAs/AlAs Multilayer Structures Grown by Molecular Beam Epitaxy on (311) and (210) GaAs Surfaces M. A. Tagliente, L. De Caro, L. Tapfer, R. Nötzel, A. Fischer, K. Ploog	307
MoC6 1750	Folded Acoustic Phonons in GaAs/AlAs Superlattices Grown on Non-(100)-Oriented Surfaces J. Spitzer, Z. V. Popovic, T. Ruf, M. Cardona, R. Nötzel, K. Ploog	314
MoC7 1810	Vibrational Properties of Si/Ce Superlattices: Theory and In-plane Raman Scattering Experiments R. Schorr, G. Abstreiter, S. de Gennaro, E. Molinari, H. Kibbel, E. Kasper	319

MoC3 18:30	Phonons and Electron-phonon Interaction in GaAs Quantum Wires F. Rossi, C. Bungaro, L. Rota, P. Lugli, E. Molinari	324
----- Tuesday, August 24, 1993 -----		
TuA	Quantum Wells - Electrical Properties (8:30 - 10:20)	
TuA1 8:30	Strained Si/SiGe Heterostructures for Device Applications F. Schaffler (Invited)	333
TuA2 9:00	Capture and Emission of Electrons in Quantum Wells under Applied Electric Field R. Vinter, F. Luc, P. Bois, L. Thibaudau, E. Rosencher	338
TuA3 9:20	Observation by Spin-Resolved Resonant Magnetotunneling of Oscillatory Landé Factor in Two-dimensional Electron Systems E. E. Mendez, J. Nocera, W. I. Wang	347
TuA4 9:40	Wire-like Incorporation of Degraded Alloys during MBE Growth on Vicinal GaAs(001) Surfaces L. Dieritz, C. Muggelberg, R. Hey, H. Kostial, M. Hörtel	354
TuA5 10:00	Slab Effects in the Transport Properties of Thin $\text{Si}_{1-x}\text{Ge}_x$ Epitaxial Layers Buried in GaAs R. Bogaerts, A. De Keyser, F. Herlach, F. M. Peeters, F. DeRosa, C. J. Palmstrom, D. Bruchman, S. J. Allen Jr.	369
Coffee break 10:20 - 10:50		
TuB	Vertical Transport - Resonant Tunneling (10:50 - 12:10)	
TuB1 10:50	Single-electron Tunneling and Coulomb Charging Effects in Double Barrier Resonant Tunneling Diodes M. Tewordt, V. J. Law, J. T. Nicholls, L. Martin-Moreno, D. A. Ritchie, M. J. Kelly, M. Pepper, J. E. F. Frost, R. Newbury, C. A. C. Jones (Invited)	368
TuB2 11:20	Hydrostatic Pressure Sensors Based on Solid State Tunneling Devices H. Brugger, U. Meiners, R. Ditz, T. Suttli, E. Gornik, A. Forster, H. Luth	377

VII

TuB3 11:40	Realization of a Novel Resonant-tunneling Hot-electron Transistor: Competition of Ultrasfast Resonant-tunneling and Energy Relaxation C.-H. Yang, R. A. Wilson	387
TuB4 12:00	F-X Electron Transfer in Type II Tunneling Bi-Quantum Wells A. Tackuchi, U. Strauß, W. W. Rohle, T. Inata, S. Muto	399
TuB5 12:30	Valley Mixing Effects on Electron Tunneling Transmission in GaAs/AlAs Heterostructures E. L. Ivchenko, A. A. Kiselev, Y. Fu, M. Willander	396
Lunch break 12:40 - 14:00		
TuC	Quantum Wells Superlattices - Optical Properties (14:00 - 16:10)	
TuC1 14:00	Luminescence Investigation on Strained $\text{Si}_{1-x}\text{Ge}_x/\text{Si}$ Coupled Quantum Wells S. Fukusaku (Invited)	403
TuC2 14:30	Fermi Sea Shake-up in Quantum Well Luminescence Spectra K. J. Nash, M. S. Sholevich, D. J. Mowbray, T. A. Fisher, D. W. Poggis, D. M. Whittaker, M. K. Saker, S. J. Bass, R. S. Smith	411
TuC3 14:50	Optical Investigation of Superlattice Orbital and Impurity States in $\text{InGaAs}/\text{GaAs}$ R. J. Warburton, J. G. Michels, P. Peyla, R. J. Nicholas, K. Woodbridge	416
TuC4 15:10	Metalband Formation in Graded-Gap Superlattices H. T. Grahn, F. Aguilin-Rueda, A. D'Intino, K. Schmidt, G. H. Dohler, K. Ploog	424
TuC5 15:30	Stark-Ladder Transitions in GaAs/AlGaAs Superlattices M. Yamaguchi, M. Morifuji, H. Kubo, K. Taniguchi, C. Hamaguchi, C. Gmühl, E. Gornik	431
TuC6 15:50	Modulated Blue Shift of the Quantum Well Electroluminescence in a GaAs/AlAs-Superlattice Resonant Tunneling Device O. Kuhn, D. K. Maude, J. C. Portal, M. Henini, L. Eaves, G. Hill, M. Pate	439

VIII

Poster Sessions:		
TuP	Transport, Optics (16:20-18:30)	
TuP1	A Metastable State in Self-Electric-Optic Effect Devices using Stark Ladder Transitions M. Hosoda, K. Kawashima, K. Tomimaga, K. Fujiwara	442
TuP2	"Spin"-Flip of Holes in Asymmetric Quantum Wells R. Ferreira, G. Bastard	446
TuP3	Interactions between Wannier-Stark States R. Ferreira, P. Vudlin, C. Bastard	454
TuP4	Resonant Coupling between Buried Single-Quantum-Well and Wannier-Stark Localization States in a GaAs/AlAs Superlattice I. Tanaka, M. Nakayama, H. Nishimura, K. Kawashima, S. Fujiwara	460
TuP5	Fermi Edge Singularities in Doped Quantum Wires and Quantum Wells F. J. Rodriguez, C. Tejedor	466
TuP6	Excitonic Enhancement of the Fermi Edge Singularity and Recombination Kinetics of Photo-generated Electrons in p-type δ -doped GaAs/Al _{0.2} Ga _{0.8} As Double-Heterostructures J. Wagner, D. Richards, H. Schneider, A. Fischer, K. Hoog	471
TuP7	Free to Bound Exciton Relaxation in {001} and {111} GaAs/GaAlAs Quantum Wells L. Mu, Y. L. Yin, N. Meures, W. J. Wang	479
TuP8	Resonant Quenching of Exciton Photoluminescence in Coupled GaAs/AlAs Quantum Wells: Effect of Exciton Binding Energy H. Schneider, J. Wagner, K. Ploog	485
TuP9	Pressure Dependence of Photoluminescence in In _{0.53} Ga _{0.47} As/Al _{0.2} Ga _{0.8} As Strained Quantum Wells with Different Widths Z.-X. Liu, G. H. Li, H.-X. Han, Z.-P. Wang	492
TuP10	Optical Transitions in GaAs/AlAs Superlattices with Different Miniband Widths K. Fujiwara, K. Kawashima, T. Yamamoto, K. Ploog	496
TuP11	Electromodulation Spectroscopy Study of a GaAs/GaAlAs Asymmetric Triangular Quantum Well Structure H. Qiang, F. H. Pollak, Y.-S. Huang, D. Mathine, G. N. Maracas	502
TuP12	Spectroscopic Studies of Ultra-thin Quantum-Wells of GaAs and GaInAs in InP grown by MOVPE D. Heszman, X. Liu, M. E. Pistol, L. Samuelson, W. Seifert	509
TuP13	Optical Properties of Symmetrically Strained (GaIn)As/Ga(PAs) Superlattices Grown by Metalorganic Vapor Phase Epitaxy (MOVPE) S. Luigen, T. F. Albrecht, T. Mentscher, W. Stolz, E. O. Göbel	515
TuP14	Impurity-Bound Excitons in Selectively Doped Strained-Layer Quantum Wells in High Magnetic Fields A. B. Dzyubenko, A. Yu. Suvchenko	522
TuP15	Optically Detected Magnetic Resonance Study of the Transition from Pseudodirect Type II to Type I GaAs/AlAs Superlattices N. G. Romanov, P. G. Baranov, I. V. Mashkov, P. Lavallard, R. Planel	525
TuP16	Valence-subband Level Crossing in GaAs/GaAsP Strained-barrier Quantum Well Structures Observed by Circularly Polarized Photoluminescence Excitation Spectroscopy H. Yaguchi, K. Ota, K. Onabe, Y. Shiraki, R. Ito	537
TuP17	Magneto-optics of Dense Electron Plasmas in Modulation-doped GaInAs/AlInAs Single Quantum Wells Y.-H. Zhang, J. L. Merz, M. Potemski, J. C. Maan, K. Ploog	533
TuP18	High Magnetic Field Effects on the Dynamics of Excitons in a GaAs Quantum Well S. Thacker, A. P. Heberle, M. Potemski, J. C. Maan, W. W. Rühle, G. Weimann	541
TuP19	Linear Optical Properties of Pseudomorphous Si/Ga Superlattices C. Tserbak, G. Theodorou	548
TuP20	Band-edge Photoluminescence of Si/Ga/Strained-Si/Si(Ge) Type-II Quantum Wells on Si(100) D. K. Nayak, N. Usami, H. Sunamura, S. Fukatsu, Y. Shiraki	553
TuP21	On the Two-dimensional Character of Absorption Spectra of Si/Ga Superlattices H. M. Polatoglu	559

TuP22	Systematic Study of the Infrared Absorption in Modulation Doped p-type Si/Si _{1-x} Ge _x Quantum Wells T. Fromherz, M. Helm, M. Seto, G. Bauer, J. F. Hölzel, C. Abstreiter	559
TuP23	Characterization of Valence Band Offset in p-Si/Si _{1-x} Ge _x /Si by Spin Charge Spectroscopy K. Schmalz, H. G. Grimmeis, B. Dietrich, H. Fraenkenfeld, J. Kim, G. Lippert, W. Meir, H. J. Oenan, P. Schley	565
TuP24	High Mobility 2D Hole Gases in Strained Ge Channels on Si Substrates Studied by Magnetotransport and Cyclotron Resonance C. M. Engelhardt, D. Többen, M. Aschauer, F. Schäffler, G. Abstreiter, E. Gornik	572
TuP25	Magnetotransport and Microwave Photoresistivity of Two-dimensional Hole Gases in Si/Si _{1-x} Ge _x Heterostructures Y. Guldner, J. M. Berroir, J. P. Vieren, M. Voon, I. Segnen, P. Warten, D. Dutartre	576
TuP26	Photoluminescence and Magnetotransport of 2D Hole Gases in Si/SiGe/Si Heterostructures R. Loo, R. Apetz, L. Vescan, U. Zastrow, A. Hartmann, A. Leuther, T. Schäpers, H. Lüth	581
TuP27	A New Technique for Directly Probing the Intrinsic Triability and its Temperature Dependence in a Resonant Tunneling Diode M. L. F. Lerch, A. D. Martin, P. E. Simmonds, L. Eaves, M. L. Leadbeater	585
TuP28	Mesoscopic Effects in Resonant Tunneling Diodes J. W. Sakai, N. La Scala, P. H. Beton, T. J. Foster, M. Henini, P. C. Main, L. Eaves, G. Hill	593
TuP29	Schottky Barrier Tunneling Spectroscopy of a 2D Electron System in Delta-doped Si(100) Layers J. Lindolf, B. Klehn, U. Kunze, W. Klunke, I. Eisele	600
TuP30	Photohole-induced Resonant Tunneling of Electrons in Selectively Etched Small Area GaAs/AlAs Double Barrier Diodes H. Buhmann, P. H. Beton, J. Wang, L. Eaves, M. Heath, M. Henini	605
TuP31	Interface Effects, Band Overlap and the Semimetal to Semiconductor Transition in InAs/GaSb Interband Resonant Tunneling Diodes U. M. Khan-Chemna, P. C. Klipstein, D. G. Austing, J. M. Smith, N. J. Mason, P. J. Walker, G. Hill	613
TuP32	InAs/Antimonide-Based Resonant Tunneling Structures with Ternary Alloy Layers J. N. Schulman, D. H. Chow, T. C. Hasenberg	617
TuP33	Thermally Deactivated Resonant Current in High Peak to Valley Current Ratio (6:1) GaAs/GaAlAs Resonant Tunneling Structures: A Spectroscopic View of the Emitter Density of State F. Laruelle, G. Falni	625
TuP34	Theoretical Analysis of Resonant Magnetotunneling Spectroscopy of Holes G. Guldioni, A. Fasolino	629
TuP35	Control of Electron Populations in the Quantum Well Levels of GaAs-AlGaAs Double Barrier Resonant Tunneling Structures P. D. Buckle, J. W. Cockburn, M. S. Skolnick, D. M. Whittaker, R. Gray, G. Hill, M. A. Pate, G. W. Smith	634
TuP36	Single-Electron Transistors Realized in In-Plane-Gate and Top-Gate Technology R. J. Haug, H. Pothier, J. Weis, K. von Klitzing, K. Ploog	635
TuP37	Quasi One-dimensional In-Plane-Gate Field-Effect Transistor U. Meiners, H. Brugger, B. E. Maile, C. Wolk, F. Koch	640
TuP38	Reflection of Ballistic Electrons by Diffusive 2D Contacts A. K. Geim, P. C. Main, R. Taborowski, H. Carmona, C. V. Brown, T. J. Foster, R. B. S. Oakeshot, E. Vele	645
TuP39	Giant Temperature Resonances of Noise in Submicron Quantum Well Structures S. T. Stoddart, A. K. Geim, S. J. Bending, J. J. Harris, A. J. Peck, K. Ploog	652
TuP40	Non-linear Transport Properties of Miniband Conduction in Presence of a Crossed Electric and Magnetic Fields: A Semi-classical Approach F. Arvinte, J. F. Palmier, A. Sibille, D. K. Maude, J. C. Portal, F. Molit	656

Wednesday, August 25, 1993

Thursday, August 26, 1993

W6A	Metal/Semiconductor and Type II Heterostructures (8:30 - 10:20)	
W6A1	Electronic Interactions at Semiconductor-semiconductor Interfaces H. Krömer, C. Nguyen, E. L. Hu (invited)	665
W6A2	Direct Observation of the Semimetal to Semiconductor Transition in Crossed Band Gap Superlattices at Magnetic Fields up to 150T D. J. Barnes, R. J. Nicholas, R. J. Warburton, N. J. Mason, P. J. Walker, N. Miura	675
W6A3	Magnetotransport Properties of MBE-Grown Magnetic Superlattices of Mn-Based Intermetallics on GaAs Heterostructures M. Tanaka, J. P. Harbison, T. Sands, J. DeBoeck, T. L. Cheeks, V. G. Keramidias	680
W6A4	Studies of GaSb capped InAs/AlSb Quantum Wells by Resonant Raman Scattering J. Wagner, J. Schmitz, M. Mäler, J. D. Ralston, P. Koidl	687
W6A5	Luminescence Up-conversion by Auger Process at InP-AlInAs Type II Interfaces A. Tilkov, W. Seidel, J. P. André, P. Volain, M. Voos	694
W6B	Atomic Scale Characterization (10:50 - 12:20)	
W6B1	High Resolution TEM of Heterostructures H. Cerva (invited)	700
W6B2	Cross Sectional STM on Heterostructures H. L. W. Salemink (invited)	712
W6B3	The Surface Evolution and Kinetic Roughening during Homoeptaxy of GaAs (001) B. G. Orr, J. Sudjono, M. D. Johnson, A. W. Hunt (invited)	714
	Excursion 13:00	
	Conference Dinner 19:00	

XIII

ThA	II-VI, IV-VI and Magnetic Structures (8:30 - 10:20)	
ThA1	Zeeman Tuning of II-VI-based Diluted Magnetic Semiconductor Superlattices J. K. Furdyna (invited)	729
ThA2	Novel Magnetic Phase Transition Behaviour in Short Period EuTe/PbTe Superlattices J. J. Chen, Z. H. Wang, M. S. Dresselhaus, G. Springholz, G. Bauer	738
ThA3	Band Offsets and Electronic Structures of (ZnCdHg)SSeTe Strained Superlattices T. Nakayama	742
ThA4	Light Induced Inversion of Magnetic Hysteresis in CdTe/(Cd,Mn)Te Superlattices V. P. Kocherzhevko, I. A. Merkulov, G. B. Pozina, I. N. Ural'sev, D. R. Yakovlev, W. Ossau, A. Wang, G. Landwehr	749
ThA5	Photomodulation Spectroscopy and Cyclotron Resonance of Cd _{1-x} Mn _x Te/CdTe Semimagnetic and Strained Multi-Quantum Well Structures S. C. Shen, L. J. Zhang, W. Lu, R. N. Bicknell	756
	Coffee break 10:20 - 10:50	
ThB	Dots and Wires - Optical Properties (10:50 - 12:40)	
ThB1	Optical Properties of Etched GaAs/GaAlAs Quantum Wires and Dots J. Y. Marzin, A. Izraël, L. Brocheau (invited)	763
ThB2	Radiative Recombination in Pseudomorphic InGaAs/GaAs Quantum Wires Grown on Nonplanar Substrates M. Grundmann, V. Tureck, J. Christen, E. Kapon, D. M. Hwang, C. Canau, R. Bhat, D. Bimberg	773
ThB3	Optical Characterisation of InGaAs/GaAs Quantum Dots Defined by Lateral Top Barrier Modulation A. Schmidt, A. Furtel, F. Faller, I. Iskevich, A. Vasiliev	777
ThB4	Electron-Phonon Scattering Rates in Quantum Wires P. A. Knipp, T. L. Reinecke	783
ThB5	Relaxation and Radiative Decay of Excitons in GaAs Quantum Dots U. Buckelmann, K. Brunner, G. Abt-Steiner	790

XIV

Lunch break 12:40 - 14:00

Poster Session:

Optical Magnetic Structures, Infrared Devices

- ThP1
(14:00 - 16:00)
Determination of Band Edge Offset by Weak Field Hall Measurement on MBE PbSe/PbSe Multi-Quantum Well Structures on KCL
Z. Shi, A. Lambrecht, M. Tacke
- ThP2
Static and Dynamical Properties of the Bound Magnetic Polaron in CdTe/Cd_{1-x}Mn_xTe Quantum Wells
P. Boudkhal, C. Barraud
- ThP3
Time-resolved Optical Study of Vertical Transport in Cd_{0.22}Mn_{0.18}Te/CdTe Superlattices
Ph. Roussignol, J. Martinez-Peñalor, A. Vinetier, C. Delalande, D. Lachet
- ThP4
Electron Subband Structure of HgCdTe Metal-Insulator-Semiconductor Heterostructure
J. Chu, R. Sizmann, K. Lili, I. Nachev, F. Koch
- ThP5
Zeraman Studies of CdTe-Cd_{1-x}Mn_xTe Multi-Quantum Wells
S. Jackson, S. R. Bardorf, T. Simer, W. E. Hagston, P. Harrison, J. E. Nicholls
- ThP6
Time-resolved Photoluminescence Studies of Stimulated Emission and Exciton Dynamics in ZnSe/ZnS_{0.15}Se_{0.85} Superlattices
C. J. Stevens, R. A. Taylor, J. F. Ryan, M. Dabbicco, M. Ferrara, R. Cingolani, Y. Kuroda, I. Sumeune
- ThP7
Strain, Confinement, Carrier Dynamics, and High Density Effects in ZnSe/ZnMnSe-Quantum Structures
F. Kreller, A. Schulzgen, J. Puls, F. Henneberger
- ThP8
PbSe MQW Lasers and the Effect of Quantum Well on Operation Temperature
A. Ishida, N. Sakurai, K. Aikawa, H. Fujiyazu
- ThP9
Electronic Structure of Thin Si Layers in CaF₂ Hybridization Versus Confinement
A. Fasolino, S. Ossicini, F. Bernardini
- ThP10
Coulomb Attraction in the Optical Spectra of Quantum Discs
B. Adolph, S. Glitsch, F. Bechtold

XV

- ThP11
Electronic Properties and Electron-Phonon Interaction in an Array of Anisotropic Parabolic Quantum Dots in the Presence of a Magnetic Field
R. Haupt, L. Wendler
- ThP12
Monte-Carlo Calculation of Few-Electron Systems in Quantum Dots
F. Bollen
- ThP13
Spectral Luminescence Enhancement in Three-dimensional Optical Microcavities Formed by GaAs Microcrystals
S. Juen, K. F. Lamprich, R. Rodriguez, R. A. Höpfel
- ThP14
Tailoring of the Carrier Capture Efficiency of a Quantum Well
J. M. Gerard, B. Deveaud
- ThP15
Stark-Wannier States in Nanostructures
E. A. M. Fagotto, P. A. Schultz, J. A. Brum
- ThP16
Multi-phonon Relaxation of Electrons in a Semiconductor Quantum Dot
T. Inoshita, H. Sakaki
- ThP17
Ground State Properties of Interacting Electrons in Semiconductor Quantum Dots: Exact and Unrestricted Hartree-Fock Results
L. Martin-Moreno, J. J. Palacios, C. Tejedor, G. Chiappe, E. Louis
- ThP18
Strong Lateral Quantization Effects in the Luminescence of InGaAs/InP Quantum Wires
P. Ili, M. Michel, A. Forchel, I. Gyuro, M. Klenk, E. Zielinski
- ThP19
GaAs/AlGaAs Quantum Well Infrared Photoresistors
T. Miyatake, S. Horikawa, T. Ezaki, H. Kubo, N. Mori, K. Taniguchi, C. Hamaguchi
- ThP20
New Type of Photoconductivity Induced by Continuum-Confinement States in Interband Transitions
C. Sicari, J. Fauré, F. Capasso, D. L. Sivco, A. Cho
- ThP21
Landau Levels of Bragg Confined Electrons and Holes
M. Zahler, E. Cohen, J. Salzman, E. Linder, L. N. Pfeiffer
- ThP22
Long Lived Photoexcited Electron-Hole Pairs in Modulation Doped GaAs/AlGaAs Quantum Wells Studied by Interband Spectroscopy
Y. Garini, E. Ehrenfreund, E. Cohen, A. Ron, K.-K. Law, J. L. Merz, A. C. Gossard

XVI

ThP23	Electron Transport in InAs-Ga _{1-x} In _x Sb Superlattices C. A. Hoffman, J. R. Meyer, E. R. Youngdale, F. J. Bartoli, R. H. Miles, L. R. Ram-Mohan	915	ThP33	Giant Third-order Nonlinear Susceptibilities for In-Plane Far- Infrared Excitation of Single InAs Quantum Wells A. G. Ariketz, E. G. Gvinn, M. S. Sherwin, C. Nguyen, H. Krcmar	970
ThP24	Comparison of Far-Infrared- and dc-Conductivity of Electron- Systems Laterally Patterned by Low-energy Ion Beam Exposure C. Lettau, M. Wendel, A. Schmeller, W. Hansen, J. P. Kuitthaas, G. Böhm, G. Weimann, M. Holland	916	ThP34	Enhancement of Free-to-bound Transitions due to Resonant Electron Capture in Be-doped AlGaAs/GaAs Quantum Wells K. Muraki, Y. Takahashi, A. Fujiwara, S. Fukatsu, Y. Shiraki	974
ThP25	Novel Tunable Far Infrared Detector Based on a Quantum Ballistic Channel L. E. Fedichkin, V. I. Ryzhii, V. V. Vyurkov	922	ThP35	Constructive Superposition of Field- and Carrier Induced Absorption Changes in Hetero-n-i-p-i Structures M. Kneisel, X. H. Guldem, P. Siesel, A. Luczak, S. Malzer, G. H. Döhler, X. Wu, J. S. Smith	978
ThP26	Cyclotron FIR Emission from Hot Electrons in GaAs-GaAlAs Heterostructures W. Zawadzki, C. Chaubet, D. Dur, W. Knap, A. Raymond	927	ThP36	Polarization of the Spontaneous Radiation of Stressed Laser Heterostructures A. A. Plashchenko, M. V. Deych, N. B. Mironchenko, F. A. Plashchenko	983
ThP27	Resonant Magneto-Polarons in Strongly-Coupled Superlattices F. M. Peeters, J. M. Shi, J. T. Devreese, J. P. Cheng, B. McCombe, W. Schaff	928	ThP37	Bi-Stability Effect in Laser-Transistor Resonant-Tunneling Structure V. Ryzhii, I. Khmyrova	992
ThP28	Far Infrared Response of Quantum Dots From Few Electron Excitations to Magneto-plasmons D. Pfannkuche, V. Gudmundsson, P. Hawrylak, R. R. Gerhardts	934	ThP38	Optoelectronic Properties of (001) and (111) Lattice-Matched and Strained Quantum Wire Lasers - Comparison with Quantum Well Lasers I. Vurgaliman, J. Singh	1000
ThP29	Cyclotron and Interband Resonance Studies in [100] and Pseudomorphic [111] InAs(Ga _{1-x} Jr _x)Sb Superlattices M. Lakrimi, T. A. Vaughan, J. J. Nicholas, D. M. Symons, N. J. Mason, P. J. Walker	943	ThP39	Photomodulation Spectroscopy of Narrow Minibands in the Continuum of Multi Quantum Wells J. Oikarinen-Schleier, E. Ehrenfreund, D. Gershoni, D. Ritter, R. A. Hamm, J. M. Vandenberg, S.-N. G. Chu	1009
ThP30	Magnetic Field Tuned Transition of Aharonov-Bohm Oscillations from h/e TO n/e Periodicity in the Array of AlGaAs/GaAs Rings G. M. Gusev, P. Basmajli, D. I. Lubyshchev, J. C. Portal, L. V. Litvin, Yu. V. Nasyushev, A. I. Toropov	949	ThC	Electronic Excitations - Superlattices (16.10-18.30)	
ThP31	Negative Conductance at THz Frequencies in Multi-well Structures W. S. Truscott	955	ThC1	Intersubband Lifetime in Quantum Wells with Transition Energies Above and Below the Optical Phonon Energy J. Faist, F. Capasso, C. Sirtori, D. L. Siven, A. Y. Cho, L. N. Pfeiffer, K. W. West	1015
ThP32	Perpendicular Transport Through Rough Interfaces in the Metallic Regime A. Brataas, G. E. W. Bauer	962	ThC2	Miniband Dispersion, Critical Points and Impurity Bands in Superlattices: an Infrared Absorption Study M. Helm, W. Hilber, T. Fromherz, F. M. Peeters, K. Alavi, R. N. Pathak	1016

ThC3 16:50	Inelastic Light Scattering by Electrons in GaAs Quantum Wires: Spin-Density, Charge-Density and Single-Particle Excitations A. Schmeidler, A. Pinczuk, J. S. Weiner, B. S. Dennis, J. M. Calleja, A. Gault, L. N. Pfeiffer, K. W. West	1022	FrA4 9:40	Strained InAs/Ga _{0.47} In _{0.53} As Quantum-well Heterostructures grown by Molecular-beam Epitaxy for Long-wavelength Laser Applications E. Tourmè, P. Grunberg, C. Fovillat, A. Baranov, A. Joullie, K. Ploog	1064
ThC4 17:10	Tunable Far Infrared Absorption in Logarithmically Graded Quantum Wells P. F. Hopkins, M. Sundaram, K. L. Campman, G. Bellomi, E. L. Yuh, S. J. Allen Jr., A. C. Gossard	1029	FrA5 10:00	Feasibility of Room Temperature Operation of Tunable Coupled-Quantum-Well Lasers M. Ogawa, E. E. Mendez	1068
ThC5 17:30	Widely Tunable Quantum Wire Arrays in MISFET-type Heterojunctions with a Stacked Gate C. Hertel, H. Drexler, W. Hansen, A. Schmeidler, J. P. Kotthaus, M. Holland, S. P. Beaumont	1033	FrB 10:50-12:40	Coffee break 10:20 - 10:50 <u>Ultrafast Processes - New Optical Phenomena</u> (10:50-12:40)	
ThC6 17:50	Infrared Spectroscopy of Lateral-Density Modulated 2DES in InAs/AlSb Quantum Wells M. Sundaram, S. J. Allen Jr., C. Nguyen, B. Brar, V. Jayaraman, H. Kroemer	1039	FrB1 10:50	Detection of Bloch Oscillations in a Semiconductor Superlattice by Time-Resolved Terahertz Spectroscopy and Degenerate Four-Wave Mixing C. Waschke, P. Leisching, P. H. Bulwar, R. Schwedler, F. Bruggemann, H. G. Roskos, K. Leo, H. Kurz, K. Köhler (invited)	1075
ThC7 18:10	Middle Infrared ($\lambda=2.55 \mu\text{m}$) High Quantum Efficiency Luminescence in GaSb/InAs II-type Multi-Quantum Well Structures S. V. Ivanov, B. K. Kurlakiev, N. N. Ledentsov, B. Ya. Meliser, A. A. Monakhov, A. A. Rogachev, S. V. Shapovalnikov, P. S. Kop'ev	1046	FrB2 11:20	Fermion-Cond Degenerate Four-wave Mixing on Unstrained (InGa)As/InP Multiple-Quantum Wells using an Optical Parametric Oscillator T. F. Albrecht, J. H. H. Sandmann, S. T. Cundiff, J. Feldmann, W. Stolz, E. O. Gobel	1081
FrA 8:30	Optical Properties - Lasers (8:30 - 10:20) Microdisk Lasers A. F. J. Levi (invited)	1049	FrB3 11:40	Time Resolved Spectroscopy of Electron Decay in Coupled Quantum Wells - Observation of Relaxation Induced Slow-Down I. Raz-Joseph, G. Cohen, B. Deveaud, P. Bergman, A. Regreny	1089
FrA2 9:00	GaAs-AlAs and Si-SiGe Quantum Well Structures for Applications in Nonlinear Optics M. J. Shaw, K. B. Wong, M. Jaros	1058	FrB4 12:00	Modulation of Wannier-Stark Transitions by Miniband Franz-Keldysh Oscillations in Strongly Coupled GaAs-AlAs Superlattices K. H. Schmidt, W. Geibelbrecht, N. Lindner, G. H. Döhler, H. T. Grahn, K. Ploog, H. Schneider	1094
FrA3 9:20	Charge Transfer and Electroabsorption in Zn Electric Field Tunable Double Quantum Well Structure K. Bernhard, A. Zrenner, G. Böhm, G. Trankle, G. Weimann	1059	FrB5 12:20	Photonic Bandgap of Two-dimensional Dielectric Crystals J. M. Gérard, A. Izrael, J. Y. Marzin, R. Pajon	1100

Conference Closing 12:40 - 13:00

Monday, August 23

- MoA** Growth of Wires and Dots
- MoB** Transport Properties in Low-dimensional Systems
- MoP** Growth, Characterisation, Transport
- MoC** Growth, Characterisation, Phonons

MoA1

Fabrication of Quantum Wires and Dots by MOCVD Selective Growth

Yasuhiko Arakawa

Institute of Industrial Science, University of Tokyo
7-22-1 Roppongi, Minato-ku, Tokyo 103, Japan

Abstract

We discuss fabrication of GaAs quantum wires and quantum dots using an *in-situ* MOCVD selective growth technique on SiO₂ patterned substrates, including the optical properties of those nano-structures. As for the GaAs quantum wires, triangular-shaped GaAs quantum wires with a lateral width less than 10 nm were obtained. The photoluminescence (PL) and magneto-PL measurements clearly demonstrate the existence of the quantum wire effect in the structures. In addition, InGaAs strained quantum wires were also fabricated. Using a similar but slightly different selective growth technique, GaAs dots with a dimension of 25nm x 25nm x 12nm surrounded by AlGaAs regions were prepared.

1. Introduction

A reduction of dimensionality of the electron motions in quantum nano-structures brings new phenomena in semiconductor physics. Moreover, it allows new device concepts to be considered and permits improvements in performance of the transistors and lasers. In 1980, the quantum wire was discussed for application to extremely high electron mobility channels [1]. In addition, in 1982, the quantum wire laser and the quantum dot laser were proposed, predicting significant improvement of lasing characteristics [2]. These proposals and discussions triggered the efforts toward semiconductor devices with lower-dimensional systems. Particularly, in the optical devices, the electronic states can be fully quantized. In contrast to the situation in transport devices, where the electrons need propagate along the channels.

Recently full confinement of photons (or optical waves) has been also discussed for the future super-threshold lasers in which the electron-hole pairs are coupled with only a single spontaneous emission mode. Consequently, as for the semiconductor lasers, the full-quantization of both electrons and photons is the ultimate direction forward [3]. The goal is, however, far away because the fabrication technology for such low-dimensional structures is still under development. In order to explore the frontier of the new physics experimentally and develop new optical and electronic devices, sufficiently small and uniform nano-structures need to be obtained so that all carriers are populated at the lowest subband for both the conduction band and the valence band. In addition, a three-dimensional optical cavity with extremely high reflectivity must be also prepared.

In this paper, after brief discussion of carrier relaxation phenomena in the quantum dot structures from the view point of laser applications, fabrication of the quantum wires using a developed *in-situ* MOCVD growth technique is investigated [4-6]. Using this technique, triangular-shaped GaAs quantum wires including photoluminescence (PL) and magneto-PL are studied in order to confirm the existence of the two-dimensional quantum confinement in the quantum wires. Strained quantum wires with a laser structure are also fabricated [7]. Using a similar but slightly different selective growth technique, GaAs quantum dot structures of 25nm x 25nm x 12nm are successfully prepared [8,9].

2. Bottleneck in Quantum Dots
Recently carrier relaxation phenomena from barrier region into the quantum dots have been discussed, predicting significant reduction of carrier relaxation rate due to the increasing energy separation between the barrier region and the quantized energy level of the quantum dot. In the full quantized system, the transitions of electrons to lower energy levels can occur only when the photon energy is resonant with the energy difference between the two energy levels. Weibach et al. [10] discussed this issue and exhibited the decreased PL intensity with the reduction of the lateral size of the quantum dots to this bottleneck. Moreover, they predicted that this bottleneck leads to drastic increase of the threshold current in the quantum dot lasers. Although the simple model shows us serious problems for the quantum dot lasers, the question whether this bottleneck problem really exists should be clarified by experiments. As discussed later, even from the quantum dots with the lateral size of 25nm, PL can be observed. Moreover, even if the bottleneck exists, there are several ways to avoid this bottleneck in the quantum dot lasers by designing carefully the quantum dot arrays, as discussed below.

Figure 1 illustrates one example of the structures where the bottleneck problem can be reduced. In Fig. 1 (a), the size of the quantum dot is determined so that the energy separation between the barrier region and the quantized energy level is two times larger than the longitudinal optical phonon energy (i.e., $\Delta E = 2\hbar\omega_{LO}$). In this case, the relaxation time is very fast because the energy difference is in resonance with the two LO phonon energy. Although some carriers are populated in the barrier region, the threshold current due to the population in the barrier region is improved by a factor of just two. By taking account of the fact that the threshold current can be improved by a factor of ten compared to that of the quantum wire lasers, the advantages of the use of the quantum dots definitely exist in the semiconductor lasers. The second example is shown in Fig. 2(b). In this structure, the resonant tunneling is utilized. It is, however, necessary that the quantum dot array is precisely fabricated so that the resonant condition is satisfied.

3. Fabrication of GaAs Quantum Wires (a.s)

In order to fabricate the quantum nano-structures, wet chemical etching, reactive ion etching [9], ion beam implantation and ion beam milling have been investigated. These methods, however, suffer from free surface effects, creation of a damage field during implantation, or a loss of interface control due to the random nature of the disordering mechanism. To avoid these problems, growth techniques on masked substrates and non-planar substrates [11-13] have been also investigated. Here, we discuss an *in-situ* fabrication technique for the quantum wires and quantum dots by utilizing MOCVD selective growth on a SiO₂ patterned substrate on which the V-groove structures are formed by the growth.

The MOCVD growth was performed in a low pressure, horizontal, rf-heated MOCVD reactor, using trimethylgallium (TMG), trimethylaluminum (TMA) and arsine (AsH₃) as group III and V sources, respectively. The ratio of group V to group III was 100. The growth temperature was 700 °C. Purified H₂ with a 6 liter/min flow rate was used as a carrier gas. The growth pressure was 100 torr.

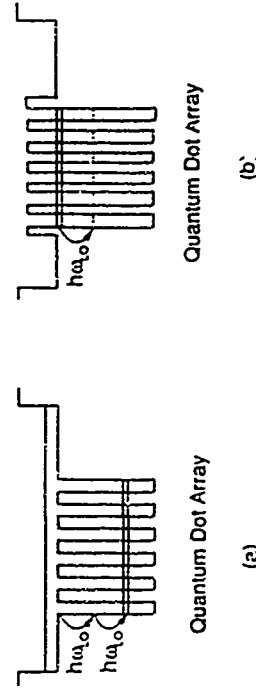


Fig. 1. Examples of the quantum dot laser structures where the bottleneck problem can be reduced.

Fabrication procedure for the quantum wires is as follows[4]. First, a SiO₂ layer with the thickness of 20nm is formed by plasma chemical vapor deposition on a semi-insulating (100) GaAs substrate. PMMA was then patterned on the SiO₂ layer by electron beam lithography technique, followed by a wet chemical etching to pattern the SiO₂. After this procedure, the triangular shaped GaAs with (111A) facet sidewalls were grown on the patterned substrate by MOCVD growth. The formation of the triangular structures is due to the large growth rate difference between (100) orientation and (111B) or (111A). Further continuation of the growth leads to the lateral growth above SiO₂ mask, making the gap between the triangular prisms small. The gap between the triangular prisms was then filled up with Al_{0.4}Ga_{0.6}As layer by twinning the growth layer from GaAs to Al_{0.4}Ga_{0.6}As. In contrast to GaAs, orientation dependence of the growth rate is weak in AlGaAs materials, although the dependence is strongly affected by temperature and Al content. As a result, a sharp corner at the bottom of the V-groove between the triangular prisms is formed by the growth of AlGaAs layer. At this point the growing layer is again switched to GaAs. Since at the V-groove corner there is a small point which has (100) orientation, triangular shaped quantum wires can be grown at the V-groove corner. This quantum wire is connected to thin quantum wells on (111A) sidewalls of large triangular GaAs prisms. Thus, GaAs quantum wires which are coupled with thin quantum wells are formed between the triangular prisms without being exposed to air. Figure 2 shows a high-resolution cross sectional



Fig. 2: A high-resolution scanning electron micrograph of GaAs triangular-etched quantum wire array structures with the lateral width of 10nm and its illustration.



Fig. 3: High-resolution scanning electron micrographs of the part of the quantum wires with lateral widths of -10, -15, -25, and -35 nm, respectively.

SEM image of the quantum wire array with 20nm period and its illustration. As shown in this photograph, even though there is ~20% lateral size fluctuation in SiO₂ mask, the quantum wires are uniformly formed, which is due to the relaxation of the size deviation by the lateral selective growth of the triangular prisms.

By changing the growth time of GaAs material for the quantum wires, we obtained the quantum wires with various lateral widths. Figure 3 shows high-resolution SEMs of the quantum wire region with lateral widths of ~10, ~15, ~25, ~35nm, respectively. Each quantum wire smoothly connects to quantum well layers with ~2, ~3, ~5, ~7nm thickness. As shown in this photograph, the quantum wire with L₂-10nm was obtained by systematic change of the growth time.

4. Photoluminescence and Magneto-Photoluminescence of Quantum Wires [9,10]

Photoluminescence (PL) spectra from the quantum wire structures are measured at 20K as a function of the lateral widths of 0, ~7, ~10, ~15, ~25, ~30, ~35nm as shown in Fig. 4(a). In this figure, the hatched PL peaks are corresponding to the quantum wires. Figure 4(b) shows the energy shift ΔE of the PL peak of the quantum wires versus the lateral width L₂. The ΔE is defined as the energy difference between the PL peaks of the GaAs bulk and the quantum wires. As shown in these figures, systematic blue shifts are observed with decreasing L₂, which is due to enhancement of the two-dimensional quantum confinement effect. The solid calculation curve in the figure is based on a simple one band model. These results indicate that a strong lateral confinement is achieved in the present structures.

PL measurements are a useful tool in order to confirm the quantum wire effects in the structures. However, it is necessary to obtain additional clear evidence. When the lateral potential exists in the quantum wires, the behavior of the Landau shift should depend on the direction of the applied magnetic fields. Therefore measurements of magneto-PL spectra were performed for the quantum wires with the lateral width of 20nm using pulsed magnetic fields at 4.2 K. The pulse duration of the magnetic field was 10 msec and the maximum field was about 40 T. PL spectra were detected with an optical multi-channel analyzer system installed at the exit of the monochromator through the optical fiber.

The PL peak position from the quantum wires and the bulk at the three configurations (i.e., B//x, B//y, B//z) are plotted as a function of applied magnetic fields in Fig. 5. As shown in this figure, the behavior of the PL peak shift ΔE is different between the bulk and the quantum wires. The bulk PL peak shifts at various magnetic fields are almost equally independent on the configurations throughout the magnetic field region. In contrast, PL peak shift of the quantum wires is clearly depending on the configuration. When the magnetic field is applied in parallel with the quantum wires (B//x), the energy shift with the increase of the magnetic field is the smallest. This can be explained by a classical picture in which the cyclotron motion on the plane perpendicular to the magnetic field is restricted by the two dimensional lateral potential of the quantum wires. On the other hand, there is also anisotropic effect when the magnetic field is applied in the two directions perpendicular to the quantum wires. The results indicate that the cross-sectional shape of the quantum wires are not isotropic.

In order to analyze these behaviors, we analyzed the experimental results assuming that the quantum wire potential is expressed by the following harmonic potential (x,y,z).

$$\psi(x,y,z) = \frac{1}{2} m^* \omega_x^2 x^2 + \frac{1}{2} m^* \omega_y^2 y^2 + \frac{1}{2} m^* \omega_z^2 z^2 \quad (1)$$

In this case, the energy shift ΔE due to the magnetic field applied perpendicularly to the quantum wires can be expressed as follows.

$$\Delta E = \frac{1}{2} \hbar \sqrt{\omega_x^2 + \omega_y^2} \quad : B//y \quad (2)$$

$$\Delta E = \frac{1}{2} \hbar \sqrt{\omega_x^2 + \omega_z^2} \quad : B//x \quad (3)$$

Where ω_c is equal to eB/m . By fitting the curve to the measured data using above relationship, the value of ω_x/ω_y are 2.9. It should be noted that the ω_x is approximately proportional to $1/L_2^2$ (1

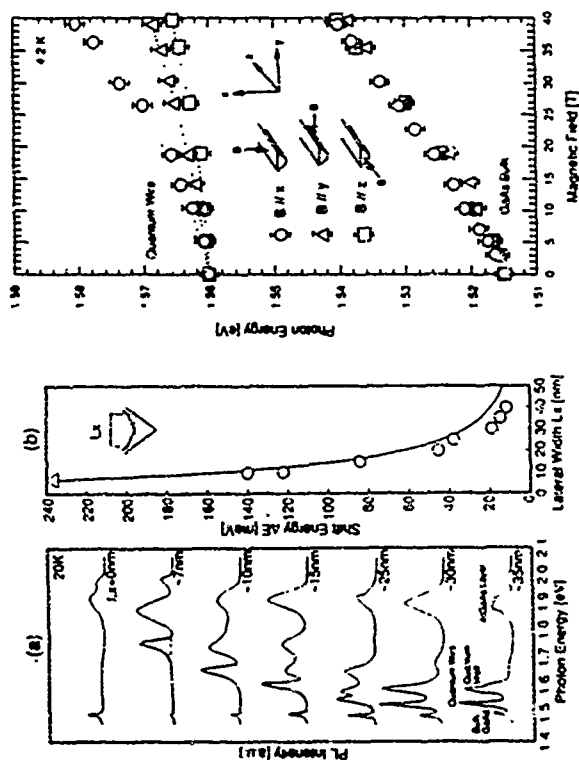


Fig. 4: (a) Photoluminescence (PL) spectra from the quantum wire structures measured as a function of the lateral width L_x at 20K. (b) The energy shift ΔE of the PL peak of the quantum wire versus the lateral width L_x .

Fig. 5: PL peak positions from the quantum wires and the bulk as a function of applied magnetic field for various configurations. Circles, triangles and squares represent the data for $B//z$, $B//y$, and $B//x$, respectively.

$= x$ or y), where L_x is the thickness of the quantum well. Since the SEM observation showed that L_x and L_y are about 12 nm and 20 nm, the value of $(L_x/L_y)^2$ is in good agreement with the value of $400/400$.

8. Fabrication of Strained InGaAs Quantum Wires and Laser Structures [7]

In the search for new materials useful in semiconductor lasers, strained systems have received great attention. In fact, low threshold current and high modulation frequency have been achieved in the semiconductor lasers with the strain effects. In addition, recent theoretical studies predicted that the strain effects lead to additional improvements of the laser characteristics in the quantum wire lasers [14]. Thus it is important to fabricate such strained quantum wire structures.

Here we fabricated InGaAs strained quantum wires using the same technique as that for the GaAs quantum wires because the growth behavior of InGaAs is quite similar to GaAs [15]. Figure 6 shows the PL spectra of the sample at 14 K for various In compositions. The sample was pumped by a CW Ar^+ laser. In this figure, the hashed spectral regions corresponds to PL from the quantum wires. As shown in this figure, the PL peak positions of the quantum wires are

systematically shifted toward to lower energy side with increasing In composition. Here, we assume that the composition of these quantum wire structures is the same as that of InGaAs bulk grown under the same conditions. The lateral width of the quantum wire is estimated to be in the range of 10 and 13 nm.

A laser structure was fabricated with these InGaAs strained quantum wires. Figure 7(a) shows a schematic illustration of the cross section of the structure. Before the deposition of SiO_2 , an $\text{Al}_0.4\text{Ga}_{0.6}\text{As}$ cladding layer was grown. After the InGaAs quantum wire structures were grown, the structures were embedded by GaAs in order to realize flat surfaces which can not be obtained with the AlGaAs layers because of differences of the growth behavior. Then finally an $\text{Al}_0.4\text{Ga}_{0.6}\text{As}$ cladding layer is formed again. The wires were cleaved into 800 nm-long cavity chip. The lasing property of this sample was measured at 10 K, using optical pumping method with a mode-locked Nd:YAG laser. Figure 7(b) shows output power of light from the sample plotted as a function of power of the pumping light.

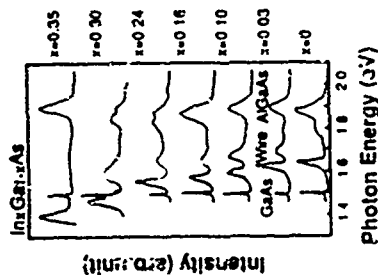


Fig. 6: PL spectra from the InGaAs strained quantum wires with various In contents.

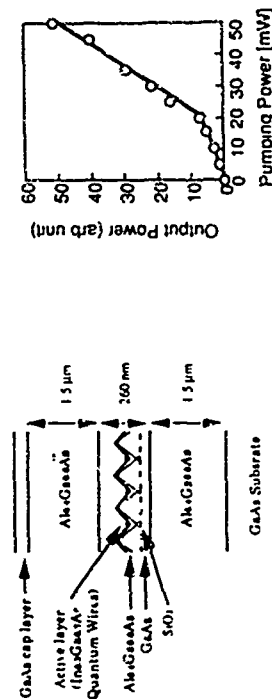


Fig. 7: (a) Illustration of a laser structure with the strained quantum wires (b) Light output characteristics of the laser structure pumped by Nd:YAG laser.

8. Fabrication of Quantum Dots (QDs)
 Fabrication trials of quantum dot structures using masked subwells have been intensively investigated by several groups. Here the GaAs quantum dots were fabricated by the MOCVD selective growth technique on SiO₂ patterned (100) GaAs substrates [8]. The masks are consisted of 100nm x 100nm and 2 windows with a period of 140nm. First, Al_{0.4}Ga_{0.6}As piliars are formed on the SiO₂ masks. Then, the GaAs is grown on the top of the Al_{0.4}Ga_{0.6}As piliars, followed by the growth of Al_{0.4}Ga_{0.6}As so that the GaAs quantum dots are embedded by Al_{0.4}Ga_{0.6}As.

Figure 8 is the cross sectional view of the GaAs surrounded by Al_{0.4}Ga_{0.6}As and its illustration. The photograph indicates that the lateral size of the quantum dots is 25nm x 25nm. We believe that this lateral size is the smallest so far as for the GaAs quantum dots embedded by Al_{0.4}Ga_{0.6}As materials.

Even from this small structure, PL can be observed. Figure 9 shows PL spectra of the quantum dot structures excited by an CW argon laser. In this case electron-hole pairs are excited in the barrier region and then relaxed into the quantum dot region. The energy shift of the PL peak from the quantum dot region is about 18meV. We believe that this energy shift is resulting from the lateral confinement of electrons. The full width of half maximum (FWHM) of the PL peak is

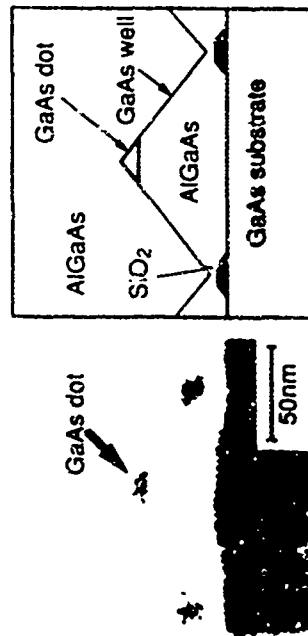


Fig. 8: The cross section of the GaAs quantum dot with a lateral width of 25nm as illustration.

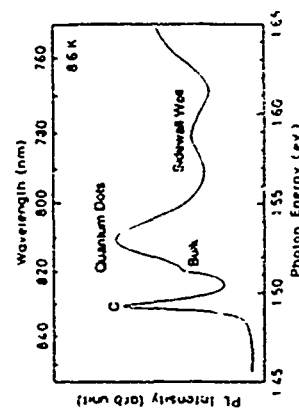


Fig. 9: Photoluminescence spectra of the GaAs quantum dot structures.

broad compared to those of the quantum wires. However, the tail of the luminescence at the low energy side disappears in the photo effect of the bulk GaAs. This indicates that the broadening is not due to strain and defect effects but due to size variation of the quantum dots. In the measurement, more than 100,000 quantum dots are simultaneously excited. Excitation of smaller number of quantum dots are discussed elsewhere.

7. Conclusion

We discussed fabrication of GaAs quantum dots and quantum wires using an in-situ MOCVD selective growth on SiO₂ patterned substrates. The optical properties of these nano-structures has been investigated. Triangular-shaped GaAs quantum wires with a lateral width less than 10 nm have been obtained. The PL and magnetop-PL measurements clearly demonstrate the existence of the quantum wire effects in these samples. In addition, the strained quantum wires with laser structures were also reported. Using a similar but slightly different selective growth technique, GaAs quantum dots with a lateral dimension of 25nm were successfully obtained.

The author expresses his thanks to Dr. Y. Nagamune for the fabrication of quantum dots and his excellent work on the electron beam lithography, to Dr. Tsukamoto for the fabrication of the GaAs quantum wires, to T. Arakawa for the fabrication of the Al_{0.4}Ga_{0.6}As piliars, and the laser structures, to Mr. M. Nishikawa for his excellent MOCVD growth work, respectively. He also expresses his thanks to Dr. Weisbuch of Thomson CSF for the discussion on the bottleneck problem and to Professor Y. Fujii, T. Ito, and H. Sakaki of University of Tokyo for their encouragement and support. We would also like to give our thanks for the support to the University-Industry Joint Project on Mesoscopic Electronics. This work is also supported in part by TEPCO Research Foundation.

References

- [1] H. Sakaki, *Jpn. J. of Appl. Phys.* **19**, L735 (1980)
- [2] Y. Arakawa and H. Sakaki, *Appl. Phys. Lett.*, **48**, 939 (1982).
- [3] For example, Y. Arakawa, Extended Abstracts of 1990 International Conference on Solid State Devices and Materials, Sendai, 745, Japan (1990)
- [4] S. Tsukamoto, Y. Nagamune, M. Nishikawa, and Y. Arakawa, *J. of Appl. Phys.* **71**, 533 (1992).
- [5] Y. Nagamune, Y. Arakawa, S. Tsukamoto, and M. Nishikawa, *Phys. Rev. Lett.*, **69**, 2963 (1992)
- [6] S. Tsukamoto, Y. Nagamune, M. Nishikawa, and Y. Arakawa, *Appl. Phys. Lett.*, **63**, 310 (1993)
- [7] T. Arakawa, Y. Nagamune, S. Tsukamoto, M. Nishikawa, Y. Arakawa, 1993 International Conference on Solid State Devices and Materials, Mahwah, submitted to *Jpn. J. of Appl. Phys.*
- [8] Y. Nagamune, S. Tsukamoto, M. Nishikawa, Y. Nagamune, *J. of Crystal Growth* **126**, 707 (1992)
- [9] Y. Nagamune, S. Tsukamoto, M. Nishikawa, Y. Arakawa, 1992 Gallium Arsenide and Related Compounds, Kanakawa, Int. Phys. Conf. Ser., **129**, 335 (1992)
- [10] H. Benisty, C.M. Soukoyev-Torres and C. Weisbuch, *Phys. Rev. B* **44**, 10945 (1991)
- [11] R. Blau, E. Kapon, D. M. Hwang, M. A. Koss, and C. P. Yu, *J. Cryst. Growth*, **93**, 850 (1988)
- [12] J. A. Leburu, C. S. Tsai, and K. J. Vahala, *Appl. Phys. Lett.*, **56**, 2643 (1990).
- [13] T. Fujii, S. Aono, and Y. K. Fukai, *Appl. Phys. Lett.*, **57**, 1209 (1990).
- [14] T. Yamauchi, T. Takahashi, J. Schulman and Y. Arakawa, *IEEE, J. of Quantum Electron.*, **QE-29**, June Issue (1993)
- [15] M. Nishikawa, S. Tsukamoto, Y. Nagamune, and Y. Arakawa, *J. of Cryst. Growth*, **124**, 502 (1992)

Polarization spectroscopy of modulated GaAs/GaAlAs quantum wells grown on vicinal surfaces : anisotropic islands or ordered growth ?

J. Bloch U. Buckelmann* and F. Laruelle*

Information des Microstructures et de Microdynamisme. CNRS. B.P. 107.

92223 Dugues Clou, France.

Walter Seifert, Technische Universität München, D-85748 Garching, Germany.

1987

We have investigated the adsorption of critical properties in quantum wells grown on vicinal surfaces and modulated by a fractional AlAs layer located in their middle. Photoluminescence (PL) excitation spectra have been measured as a function of the AlAs layer thickness. The PL excitation is systematically measured as a function of the AlAs layer thickness. The results indicate the influence of adatoms on critical properties.

1. Introduction

In the past decade, a growing interest has been devoted to quantum size effects due to the low dimensionality achievable in semi-conductor nanostructures, both from the viewpoint of fundamental solid state physics and of practical applications. In particular, the study of the electronic and optical properties of low-dimensional systems has attracted considerable attention, and has led to the development of a new branch of research on the atomic scale array of a crystal surface was prepared by Percot *et al.* [1]. During the last few years, numerous experiments have been carried out on the surface and incorporated in the bulk of semiconductors, allowing the study of quantum size effects. In particular, the study of the electronic and optical properties of the hetero-epitaxial growth of the layer-based optical devices, a classically well-known structure for its early experiments. Asymmetric optical properties of such structures, a characteristic feature of the quantum size effects, have been observed for the first time in the hetero-epitaxial growth of the layer-based optical devices [2]. The quantum size effects have been observed for the first time in the hetero-epitaxial growth of the layer-based optical devices [2]. The quantum size effects have been observed for the first time in the hetero-epitaxial growth of the layer-based optical devices [2].

2. Growth

Our samples are grown by Molecular Beam Epitaxy (MBE) simultaneously on three vicinal substrates to allow for a variable GaAs substrate GaAs substrates (GaAs) (111-A, Si-doped) (111-B) (111-C) (111-D) (111-E) (111-F) (111-G) (111-H) (111-I) (111-J) (111-K) (111-L) (111-M) (111-N) (111-O) (111-P) (111-Q) (111-R) (111-S) (111-T) (111-U) (111-V) (111-W) (111-X) (111-Y) (111-Z) (111-AA) (111-AB) (111-AC) (111-AD) (111-AE) (111-AF) (111-AG) (111-AH) (111-AI) (111-AJ) (111-AL) (111-AM) (111-AN) (111-AO) (111-AP) (111-AQ) (111-AR) (111-AS) (111-AT) (111-AU) (111-AV) (111-AW) (111-AX) (111-AY) (111-AZ) (111-BA) (111-BB) (111-BC) (111-BD) (111-BE) (111-BF) (111-BG) (111-BH) (111-BI) (111-BJ) (111-BL) (111-BM) (111-BN) (111-BO) (111-BP) (111-BQ) (111-BR) (111-BS) (111-BT) (111-BU) (111-BV) (111-BW) (111-BX) (111-BY) (111-BZ) (111-CA) (111-CB) (111-CC) (111-CD) (111-CE) (111-CF) (111-CG) (111-CH) (111-CI) (111-CJ) (111-CL) (111-CM) (111-CN) (111-CO) (111-CP) (111-CQ) (111-CR) (111-CS) (111-CT) (111-CU) (111-CV) (111-CW) (111-CX) (111-CY) (111-CZ) (111-DA) (111-DB) (111-DC) (111-DD) (111-DE) (111-DF) (111-DG) (111-DH) (111-DI) (111-DJ) (111-DL) (111-DM) (111-DN) (111-DO) (111-DP) (111-DQ) (111-DR) (111-DS) (111-DT) (111-DU) (111-DV) (111-DW) (111-DX) (111-DY) (111-DZ) (111-EA) (111-EB) (111-EC) (111-ED) (111-EE) (111-EF) (111-EG) (111-EH) (111-EI) (111-EJ) (111-EL) (111-EM) (111-EN) (111-EO) (111-EP) (111-EQ) (111-ER) (111-ES) (111-ET) (111-EU) (111-EV) (111-EW) (111-EX) (111-EY) (111-EZ) (111-FA) (111-FB) (111-FC) (111-FD) (111-FE) (111-FG) (111-FH) (111-FI) (111-FJ) (111-FL) (111-FM) (111-FN) (111-FO) (111-FP) (111-FQ) (111-FR) (111-FS) (111-FT) (111-FU) (111-FV) (111-FW) (111-FX) (111-FY) (111-FZ) (111-GA) (111-GB) (111-GC) (111-GD) (111-GE) (111-GF) (111-GG) (111-GH) (111-GI) (111-GJ) (111-GL) (111-GM) (111-GN) (111-GO) (111-GP) (111-GQ) (111-GR) (111-GS) (111-GT) (111-GU) (111-GV) (111-GW) (111-GX) (111-GY) (111-GZ) (111-HA) (111-HB) (111-HC) (111-HD) (111-HE) (111-HF) (111-HG) (111-HI) (111-HJ) (111-HL) (111-HM) (111-HN) (111-HO) (111-HP) (111-HQ) (111-HR) (111-HS) (111-HT) (111-HU) (111-HV) (111-HW) (111-HX) (111-HY) (111-HZ) (111-IA) (111-IB) (111-IC) (111-ID) (111-IE) (111-IF) (111-IG) (111-IH) (111-II) (111-IL) (111-IM) (111-IN) (111-IO) (111-IP) (111-IQ) (111-IR) (111-IS) (111-IT) (111-IU) (111-IV) (111-IW) (111-IX) (111-IY) (111-IZ) (111-JA) (111-JB) (111-JC) (111-JD) (111-JE) (111-JF) (111-JG) (111-JH) (111-JI) (111-JL) (111-JM) (111-JN) (111-JO) (111-JP) (111-JQ) (111-JR) (111-JS) (111-JT) (111-JU) (111-JV) (111-JW) (111-JX) (111-JY) (111-JZ) (111-KA) (111-KB) (111-KC) (111-KD) (111-KE) (111-KF) (111-KG) (111-KH) (111-KI) (111-KL) (111-KM) (111-KN) (111-KO) (111-KP) (111-KQ) (111-KR) (111-KS) (111-KT) (111-KU) (111-KV) (111-KW) (111-KX) (111-KY) (111-KZ) (111-LA) (111-LB) (111-LC) (111-LD) (111-LE) (111-LF) (111-LG) (111-LH) (111-LI) (111-LJ) (111-LK) (111-LM) (111-LN) (111-LO) (111-LP) (111-LQ) (111-LR) (111-LS) (111-LT) (111-LU) (111-LV) (111-LW) (111-LX) (111-LY) (111-LZ) (111-MA) (111-MB) (111-MC) (111-MD) (111-ME) (111-MF) (111-MG) (111-MH) (111-MI) (111-MJ) (111-MK) (111-ML) (111-MN) (111-MO) (111-MP) (111-MQ) (111-MR) (111-MS) (111-MT) (111-MU) (111-MV) (111-MW) (111-MX) (111-MY) (111-MZ) (111-NA) (111-NB) (111-NC) (111-ND) (111-NE) (111-NF) (111-NG) (111-NH) (111-NI) (111-NJ) (111-NK) (111-NL) (111-NM) (111-NO) (111-NP) (111-NQ) (111-NR) (111-NS) (111-NT) (111-NU) (111-NV) (111-NW) (111-NX) (111-NY) (111-NZ) (111-OA) (111-OB) (111-OC) (111-OD) (111-OE) (111-OF) (111-OG) (111-OH) (111-OI) (111-OJ) (111-OK) (111-OL) (111-OM) (111-ON) (111-OO) (111-OP) (111-OQ) (111-OR) (111-OS) (111-OT) (111-OU) (111-OV) (111-OW) (111-OX) (111-OY) (111-OZ) (111-PA) (111-PB) (111-PC) (111-PD) (111-PE) (111-PF) (111-PG) (111-PH) (111-PI) (111-PJ) (111-PK) (111-PL) (111-PM) (111-PN) (111-PO) (111-PP) (111-PQ) (111-PR) (111-PS) (111-PT) (111-PU) (111-PV) (111-PW) (111-PX) (111-PY) (111-PZ) (111-QA) (111-QB) (111-QC) (111-QD) (111-QE) (111-QF) (111-QG) (111-QH) (111-QI) (111-QJ) (111-QK) (111-QL) (111-QM) (111-QN) (111-QO) (111-QP) (111-QQ) (111-QR) (111-QS) (111-QT) (111-QU) (111-QV) (111-QW) (111-QX) (111-QY) (111-QZ) (111-RA) (111-RB) (111-RC) (111-RD) (111-RE) (111-RF) (111-RG) (111-RH) (111-RI) (111-RJ) (111-RK) (111-RL) (111-RM) (111-RN) (111-RO) (111-RP) (111-RQ) (111-RR) (111-RS) (111-RT) (111-RU) (111-RV) (111-RW) (111-RX) (111-RY) (111-RZ) (111-SA) (111-SB) (111-SC) (111-SD) (111-SE) (111-SF) (111-SG) (111-SH) (111-SI) (111-SJ) (111-SK) (111-SL) (111-SM) (111-SN) (111-SO) (111-SP) (111-SQ) (111-SR) (111-SS) (111-ST) (111-SU) (111-SV) (111-SW) (111-SX) (111-SY) (111-SZ) (111-TA) (111-TB) (111-TC) (111-TD) (111-TE) (111-TF) (111-TG) (111-TH) (111-TI) (111-TJ) (111-TK) (111-TL) (111-TM) (111-TN) (111-TO) (111-TP) (111-TQ) (111-TR) (111-TS) (111-TT) (111-TU) (111-TV) (111-TW) (111-TX) (111-TY) (111-TZ) (111-UA) (111-UB) (111-UC) (111-UD) (111-UE) (111-UF) (111-UG) (111-UH) (111-UI) (111-UJ) (111-UK) (111-UL) (111-UM) (111-UN) (111-UO) (111-UP) (111-UQ) (111-UR) (111-US) (111-UT) (111-UY) (111-UZ) (111-VA) (111-VB) (111-VC) (111-VD) (111-VE) (111-VF) (111-VG) (111-VH) (111-VI) (111-VJ) (111-VK) (111-VL) (111-VM) (111-VN) (111-VO) (111-VP) (111-VQ) (111-VR) (111-VS) (111-VT) (111-VU) (111-VV) (111-VW) (111-VX) (111-VY) (111-VZ) (111-WA) (111-WB) (111-WC) (111-WD) (111-WE) (111-WF) (111-WG) (111-WH) (111-WI) (111-W

1 Theory

In this section, we discuss what physical dependencies are expected for the theoretical case of a perfectly ordered layered structure. Ideally the half-momentary of ALi is interrupted in the QW should form a lateral superlattice with a period λ equal to the "strange length". We describe the resulting modulation of the QW energy levels by a periodic potential $U(x)$ of the form:

$$V(z) = V_1 + \sin \frac{2\pi z}{\lambda} \quad (1)$$

The amplitudes V_i are adjusted for the different 2D subbands and are of opposite signs for electrons and holes. In the present case, they are given by one half of the energy shift induced by one monolayer of AlGaIn on the surface of the GaAs substrate. The values of V_i are 1.0, 1.5, 1.6, 1.7, 1.8, 1.9, 2.0, 2.1, 2.2, 2.3, 2.4, 2.5, 2.6, 2.7, 2.8, 2.9, 3.0, 3.1, 3.2, 3.3, 3.4, 3.5, 3.6, 3.7, 3.8, 3.9, 4.0, 4.1, 4.2, 4.3, 4.4, 4.5, 4.6, 4.7, 4.8, 4.9, 5.0, 5.1, 5.2, 5.3, 5.4, 5.5, 5.6, 5.7, 5.8, 5.9, 6.0, 6.1, 6.2, 6.3, 6.4, 6.5, 6.6, 6.7, 6.8, 6.9, 7.0, 7.1, 7.2, 7.3, 7.4, 7.5, 7.6, 7.7, 7.8, 7.9, 8.0, 8.1, 8.2, 8.3, 8.4, 8.5, 8.6, 8.7, 8.8, 8.9, 9.0, 9.1, 9.2, 9.3, 9.4, 9.5, 9.6, 9.7, 9.8, 9.9, 10.0, 10.1, 10.2, 10.3, 10.4, 10.5, 10.6, 10.7, 10.8, 10.9, 11.0, 11.1, 11.2, 11.3, 11.4, 11.5, 11.6, 11.7, 11.8, 11.9, 12.0, 12.1, 12.2, 12.3, 12.4, 12.5, 12.6, 12.7, 12.8, 12.9, 13.0, 13.1, 13.2, 13.3, 13.4, 13.5, 13.6, 13.7, 13.8, 13.9, 14.0, 14.1, 14.2, 14.3, 14.4, 14.5, 14.6, 14.7, 14.8, 14.9, 15.0, 15.1, 15.2, 15.3, 15.4, 15.5, 15.6, 15.7, 15.8, 15.9, 16.0, 16.1, 16.2, 16.3, 16.4, 16.5, 16.6, 16.7, 16.8, 16.9, 17.0, 17.1, 17.2, 17.3, 17.4, 17.5, 17.6, 17.7, 17.8, 17.9, 18.0, 18.1, 18.2, 18.3, 18.4, 18.5, 18.6, 18.7, 18.8, 18.9, 19.0, 19.1, 19.2, 19.3, 19.4, 19.5, 19.6, 19.7, 19.8, 19.9, 20.0, 20.1, 20.2, 20.3, 20.4, 20.5, 20.6, 20.7, 20.8, 20.9, 21.0, 21.1, 21.2, 21.3, 21.4, 21.5, 21.6, 21.7, 21.8, 21.9, 22.0, 22.1, 22.2, 22.3, 22.4, 22.5, 22.6, 22.7, 22.8, 22.9, 23.0, 23.1, 23.2, 23.3, 23.4, 23.5, 23.6, 23.7, 23.8, 23.9, 24.0, 24.1, 24.2, 24.3, 24.4, 24.5, 24.6, 24.7, 24.8, 24.9, 25.0, 25.1, 25.2, 25.3, 25.4, 25.5, 25.6, 25.7, 25.8, 25.9, 26.0, 26.1, 26.2, 26.3, 26.4, 26.5, 26.6, 26.7, 26.8, 26.9, 27.0, 27.1, 27.2, 27.3, 27.4, 27.5, 27.6, 27.7, 27.8, 27.9, 28.0, 28.1, 28.2, 28.3, 28.4, 28.5, 28.6, 28.7, 28.8, 28.9, 29.0, 29.1, 29.2, 29.3, 29.4, 29.5, 29.6, 29.7, 29.8, 29.9, 30.0, 30.1, 30.2, 30.3, 30.4, 30.5, 30.6, 30.7, 30.8, 30.9, 31.0, 31.1, 31.2, 31.3, 31.4, 31.5, 31.6, 31.7, 31.8, 31.9, 32.0, 32.1, 32.2, 32.3, 32.4, 32.5, 32.6, 32.7, 32.8, 32.9, 33.0, 33.1, 33.2, 33.3, 33.4, 33.5, 33.6, 33.7, 33.8, 33.9, 34.0, 34.1, 34.2, 34.3, 34.4, 34.5, 34.6, 34.7, 34.8, 34.9, 35.0, 35.1, 35.2, 35.3, 35.4, 35.5, 35.6, 35.7, 35.8, 35.9, 36.0, 36.1, 36.2, 36.3, 36.4, 36.5, 36.6, 36.7, 36.8, 36.9, 37.0, 37.1, 37.2, 37.3, 37.4, 37.5, 37.6, 37.7, 37.8, 37.9, 38.0, 38.1, 38.2, 38.3, 38.4, 38.5, 38.6, 38.7, 38.8, 38.9, 39.0, 39.1, 39.2, 39.3, 39.4, 39.5, 39.6, 39.7, 39.8, 39.9, 40.0, 40.1, 40.2, 40.3, 40.4, 40.5, 40.6, 40.7, 40.8, 40.9, 41.0, 41.1, 41.2, 41.3, 41.4, 41.5, 41.6, 41.7, 41.8, 41.9, 42.0, 42.1, 42.2, 42.3, 42.4, 42.5, 42.6, 42.7, 42.8, 42.9, 43.0, 43.1, 43.2, 43.3, 43.4, 43.5, 43.6, 43.7, 43.8, 43.9, 44.0, 44.1, 44.2, 44.3, 44.4, 44.5, 44.6, 44.7, 44.8, 44.9, 45.0, 45.1, 45.2, 45.3, 45.4, 45.5, 45.6, 45.7, 45.8, 45.9, 46.0, 46.1, 46.2, 46.3, 46.4, 46.5, 46.6, 46.7, 46.8, 46.9, 47.0, 47.1, 47.2, 47.3, 47.4, 47.5, 47.6, 47.7, 47.8, 47.9, 48.0, 48.1, 48.2, 48.3, 48.4, 48.5, 48.6, 48.7, 48.8, 48.9, 49.0, 49.1, 49.2, 49.3, 49.4, 49.5, 49.6, 49.7, 49.8, 49.9, 50.0, 50.1, 50.2, 50.3, 50.4, 50.5, 50.6, 50.7, 50.8, 50.9, 51.0, 51.1, 51.2, 51.3, 51.4, 51.5, 51.6, 51.7, 51.8, 51.9, 52.0, 52.1, 52.2, 52.3, 52.4, 52.5, 52.6, 52.7, 52.8, 52.9, 53.0, 53.1, 53.2, 53.3, 53.4, 53.5, 53.6, 53.7, 53.8, 53.9, 54.0, 54.1, 54.2, 54.3, 54.4, 54.5, 54.6, 54.7, 54.8, 54.9, 55.0, 55.1, 55.2, 55.3, 55.4, 55.5, 55.6, 55.7, 55.8, 55.9, 56.0, 56.1, 56.2, 56.3, 56.4, 56.5, 56.6, 56.7, 56.8, 56.9, 57.0, 57.1, 57.2, 57.3, 57.4, 57.5, 57.6, 57.7, 57.8, 57.9, 58.0, 58.1, 58.2, 58.3, 58.4, 58.5, 58.6, 58.7, 58.8, 58.9, 59.0, 59.1, 59.2, 59.3, 59.4, 59.5, 59.6, 59.7, 59.8, 59.9, 60.0, 60.1, 60.2, 60.3, 60.4, 60.5, 60.6, 60.7, 60.8, 60.9, 61.0, 61.1, 61.2, 61.3, 61.4, 61.5, 61.6, 61.7, 61.8, 61.9, 62.0, 62.1, 62.2, 62.3, 62.4, 62.5, 62.6, 62.7, 62.8, 62.9, 63.0, 63.1, 63.2, 63.3, 63.4, 63.5, 63.6, 63.7, 63.8, 63.9, 64.0, 64.1, 64.2, 64.3, 64.4, 64.5, 64.6, 64.7, 64.8, 64.9, 65.0, 65.1, 65.2, 65.3, 65.4, 65.5, 65.6, 65.7, 65.8, 65.9, 66.0, 66.1, 66.2, 66.3, 66.4, 66.5, 66.6, 66.7, 66.8, 66.9, 67.0, 67.1, 67.2, 67.3, 67.4, 67.5, 67.6, 67.7, 67.8, 67.9, 68.0, 68.1, 68.2, 68.3, 68.4, 68.5, 68.6, 68.7, 68.8, 68.9, 69.0, 69.1, 69.2, 69.3, 69.4, 69.5, 69.6, 69.7,

of the lateral anisotropy is determined by the amount of N-ethyl milling. It is quite small in the present case because the conformational changes are induced by the shear stress caused by the lateral shearing.

Both energy and polarization of absorption peaks depend on the period Λ . The onset of the absorption shifts from 8 meV to higher energies with Λ decreasing from 22 nm to 8 nm. Parallel to that, the magnitude of P of the broad absorption peak decreases from 0.15 to 0.03 due to increasing scattering. The broad absorption peak is always polarized along the y-axis and the variation of the polarization effect over the energy range of the peak is very small.

4. Cyclical expertises

[illegible][illegible]

are present, polarized waves are placed between the laser (whose polarization is horizontal) and the sample. The PLE polarization spectra for the P2M4 is plotted in Figure 1. The PLE intensity $I(\lambda)$ corresponding to an absorbed light polarization parity (resp. perpendicular to the laser polarization) is denoted by I_{\parallel} (resp. I_{\perp}) and the depolarization ratio is defined by $D(\lambda) = I_{\perp}(\lambda)/I_{\parallel}(\lambda)$. The depolarization ratio $D(\lambda)$ is a function of the wavelength λ of the exciting light beam and not of the secondary-emitted optical axis.

$$P = \frac{1}{\left[\frac{1}{\left(\frac{1}{R_1} + \frac{1}{R_2} \right)} + \frac{1}{R_3} \right]} \quad (2)$$

The PSDM allows a typical accuracy of 0.50 in the polarization measurements with a 1 s counting time. It is limited by the signal to noise ratio. The PSDM increases PLR polarization accuracy without improving the exciting light beam as in the case when rotating CDH-thermo-polarizers. One also notices that the phase portion count moments are directly 1, and 4. The evaluation of P does not need any normalization procedure but requires fewer electronic than used by Waackner et al. [12].

Abstract

All samples with half an AlAs monolayer in the middle of the QW possess good optical properties at 2 K. PL intensity and Stokes-shift do not exceed 4 meV. The spectral position of the bi-excitonic transition corresponds in average to the 1.576 eV calculated gap (corrected by a 9 meV exciton binding energy) of a 36 ML GaAs QW with half a monolayer excess AlAs ML in the middle. This fractional layer introduces a 1% blue-shift of 27 meV relative to the bare QW.

To compare polarization anisotropy in P1 and in H1-L, we chose a temperature of 77 K so that excited QW levels are thermally populated. We have verified that polarized PL spectra weakly depend on temperature between 2X and 77 K. Figure 2 shows PL and corresponding polarization spectra of samples A, B and C. A narrow band of PL emission at 770 nm and a broad PL emission band at 780 nm are observed. Sample A and B exhibit similar polarization spectra; the low energy side of the fundamental transition is polarized along the σ_{wp} edges whereas the high energy side shows a pronounced polarization plane perpendicular to the σ_{wp} edges. The PL line transition is well resolved and is polarized parallel to the σ_{wp} edges. These results do not agree with theoretical calculations.

To determine the effect of the mixing between polarization selection layers, we have realized optical pumping experiments with the PEM and a quarter-wave plate. Circular polarization spectra are the same whether there is or there is not a quarter-wave plate in the middle of the PEM. As is well established [11], the $\lambda/4$ plate extinguishes linearly polarized light; it transmits unpolarized light. In our case, the linear polarization of the incident light is extinguished when the $\lambda/4$ transmission axis is perpendicular to the polarization PE. In our samples, the linear polarization direction does not allow the precise identification of heavy or light hole predominance in a given optical transition as vertical pumping does.

Sample C, grown at a lower temperature (520 °C) instead of 640 °C (NPTC), does not present any polarization anisotropy; rather, it shows isotropic behavior (shown in fig. 2). This demonstrates that the polarization anisotropy we observe in sample A is due to a thermally induced organization of the Al elements into anisotropic islands.

Preparation of low dimensional structures by molecular beam epitaxy-growth on patterned AlGaAs buffer layers

K. J. I. A. Kurbatov, D. Grashin, A. Leshman and A. Kluzing
Alfa-Patent-Institut für Polymerforschung, 70569 Stuttgart, Germany

13 | kelian

Illenbourg, (primary)

At Dlight and All Holdings

We studied the preparation of low-dimensional structures by molecular beam epitaxy (MBE) in overgrowth on patterned AlGaAs buffer layers. The detailed interface and surface structure was investigated by scanning electron microscopy and transmission electron microscopy. The active layers on the patterned Al_{0.35}Ga_{0.65}As buffer layer was passivated by a thin GaAs cap layer which is thermally desorbed in the MBE system prior to overgrowth. Small (110) and larger (111A) AlGaAs structures dominate the surface structure after MBE growth on the etched ridges along the (111) direction within the surface structure plane. Hall effect measurements demonstrate that an electron concentration of $1 \times 10^{11} \text{ cm}^{-2}$ is achieved in a 20 nm wide modulation doped quantum well with a 10 nm AlGaAs buffer layer thickness of only 0.5 nm. The free carriers are detected in the overgrown quantum well within the region where the etched Al_{0.35}Ga_{0.65}As surface was exposed to air.

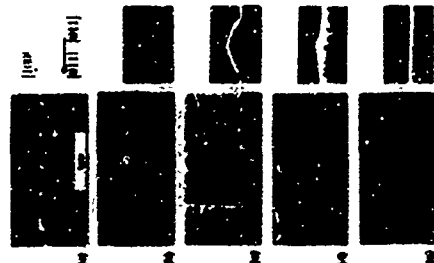
partial growth of GaAs/AlGaAs heterostructures on patterned GaAs substrates and AlGaAs buffer layers, the possibility to synthesize one and zero dimensional structures. Polar devices have been demonstrated and discussed in "growth after lithography and etching processes" [11-15]. It is known, that different facets evolve during the growth of GaAs on non planar substrates [3,6]. The detailed surface structure depends mainly on the orientation of the exposed surfaces and the growth parameters.

In this system we study the MBE growth on mesa etched lines in $[01\bar{1}]$ direction within the (110) surface on Al_{0.33}Ga_{0.67}As buffer layer and a GaAs cap layer. The Al_{0.33}Ga_{0.67}As buffer layer and a GaAs cap layer are deposited in a first MBE growth step. It is difficult to grow a step in AlGaAs which is a lattice mismatched material. The lattice mismatch between the GaAs cap layer and the AlGaAs buffer layer is about 1.5%. Because of the formation of very cubic semiconductor (the GaAs buffer layer) with this lattice strain, AlGaAs surface can be achieved by covering a MBE growth on the GaAs buffer layer with a thin GaAs capping layer. Growth can be directly observed by reflection high energy electron diffraction (RHEED) in the growth chamber. The AlGaAs growth on the GaAs cap layer has been reported in AlGaAs heterostructure [11].

[illegible]

Figure 1b shows a series of samples with increasing thicknesses of the overgrown layer acquired from 10 min to 220 min. The samples 1b and 1d are grown on substrately patterned a-C:Hs substrates. The growth was carried out in an furnace. GIN II system at a substrate temperature between 500°C to 580°C and with continuous water

Figure 1. AFM pictures. Patterned AKAAs buffer layer with (a) bridges along [011] on (100) GaAs substrate (a). After 120 min of etching (b). After 180 min of etching (c). After 240 min of etching (d). After 300 min of etching (e). The lateral period length of the patterning is 1.5 μm for all samples.

[illegible]

Al_{0.31}Ga_{0.69}As cap layer and Al_{0.31}Ga_{0.69}As/100nm GaAs cap layer on the interface between GaAs substrate and AlGaAs buffer layer on the bottom, and the profile of patterning is shown in Figure 1d. The growth rate on the ridge is dominated by the local Γ -valley observable in the TLM picture. The surface of the overgrown quantum on the ridge is dominated by the local Γ -valley observable in the TLM picture. The surface of the overgrown quantum well is marked in the area of the AlGaAs substrate, terminated (111A), and (111A) facets. The 100nm thick GaAs substrate well is marked in the area of the AlGaAs substrate, terminated (111A), and (111A) facets. The surface of the patterned Al_{0.31}Ga_{0.69}As buffer layer was patterned on the ridge, consequently we achieve perfect epitaxial regrowth in this region. It is however quite remarkable that there are also no extended defects observable in the TLM picture at the interface in the entire region where the Al_{0.31}Ga_{0.69}As was deposited to air.

The Al_{0.31}Ga_{0.69}As was deposited to air on the Al_{0.31}Ga_{0.69}As/100nm GaAs cap layer on the interface between GaAs substrate and AlGaAs buffer layer on the bottom, and the profile of patterning is shown in Figure 1d and e. The growth rate on the (100) surface is obviously much larger than on the (111A) and (111A) facets, so that the surface patterning is completely buried after 250nm thick overgrowth. Figure 1d is also shown in more detail in the TLM micrograph in Figure 3. In this sample we deposited a sequence of six times Al_{0.31}Ga_{0.69}As/100nm GaAs grown on a patterned GaAs substrate underneath Al_{0.31}Ga_{0.69}As/100nm GaAs grown on a patterned GaAs substrate. Before starting the regrowth the patterned wafer was heated to 620°C for 15 minutes to remove the oxide. The interface between the patterned GaAs substrate and the first overgrown 100nm thick AlGaAs layer is marked in the area of the AlGaAs substrate, terminated (111A), and (111A) facets. The surface of the patterned Al_{0.31}Ga_{0.69}As buffer layer was patterned on the ridge, consequently we achieve perfect epitaxial regrowth in this region. It is however quite remarkable that there are also no extended defects observable in the TLM picture at the interface in the entire region where the Al_{0.31}Ga_{0.69}As was deposited to air.

Figure 2
Cross-sectional TEM micrograph of the sample shown in Figure 1b. The sequence is: (1) 30nm GaAs marker layer / 40nm Al_{0.1}Ga_{0.9}As / 30nm Al_{0.1}Ga_{0.9}As cap layer. The structure was grown on a patterned 300nm thick Al_{0.1}Ga_{0.9}As buffer layer.





Figure 3: Cross-sectional TEM micrograph of the sample shown in Figure 1d. The overgrown layer sequence is 40 nm Al_{0.35}Ga_{0.65}As / 11 nm GaAs grown on a patterned GaAs substrate without AlGaAs buffer layer

the patterned Al_{0.35}Ga_{0.65}As buffer layer as one can clearly see in Figure 2, even though the Al_{0.35}Ga_{0.65}As samples have been annealed at 720°C for 10 minutes. The small (111)A facets on the patterned GaAs surface with lines along the [011] direction obviously evolve during the annealing process. Otherwise we did not observe significant differences in the regrowth behavior of AlGaAs/GaAs heterostructures for patterned Al_{0.35}Ga_{0.65}As buffer layers or GaAs substrates. Figure 3 demonstrates how the surface morphology develops on the thickness increases. The main aspects are:

- The deposition rate on the (111)A planes is significantly smaller than on (100). Therefore the (111)A facets become dominant on the ridges. After the etched grooves are filled up the (100) plane between the ridges start to overgrow the (111)A facets, and finally a smooth surface is regained (see also Figure 1c).
 - The (111) facets play a minor role as compared to regrowth on [011] oriented lines i.e. the patterned substrates (see for example Ref. [9]).
 - Co (111)A the AlGaAs layers are significantly thicker than the GaAs layers.
 - The GaAs layers are thicker than the AlGaAs layers on the small (100) flat in the middle of the ridges. Ga migrates on the (111) facets increase the growth rate on the (100) planes [6].
- These points in turn allow to prepare extremely narrow quantum wires on top of the ridges which are completely controlled as a fluently planarized structure. In the sample shown in Figure 1 the second GaAs quantum well forms a triangular coupled wire with a lateral width of about 10 nm.

For the characterization of the electronic properties of the MBE-regrown layers we performed Hall effect measurements. Both the active region on the ridge where the Al_{0.35}Ga_{0.65}As buffer was deposited and the area which was etched and exposed to air were investigated. Therefore we prepared a Van der Pauw geometry of a diamond in an unperforated area of the wafer and in a large 100 nm deep mesa etched section. The overgrown layer sequence was: 15 nm Al_{0.35}Ga_{0.65}As / 10 nm Al_{0.35}Ga_{0.65}As (Si doped) / 20 nm Al_{0.35}Ga_{0.65}As spacer / 20 nm GaAs quantum well / 10 nm Al_{0.35}Ga_{0.65}As spacer / 10 nm Al_{0.35}Ga_{0.65}As (N doped) / 10 nm GaAs cap layer. The structure was grown on a 100 nm Al_{0.35}Ga_{0.65}As buffer layer with a 10 nm GaAs cap layer which was deposited prior to regrowth. The curve (a) in Figure 4 shows the two dimensional (2D) electron density and the mobility for this sample. At room temperature we measure a density of $1.8 \times 10^{11} \text{ cm}^{-2}$ with a mobility of $3000 \text{ cm}^2/\text{Vs}$. The carrier density drops to less than 10^{10} cm^{-2} region at 77 K. In sample (b) we replace the first 15 nm Al_{0.35}Ga_{0.65}As layer by a superlattice with five periods of 10 nm AlAs / 2 nm GaAs. Thus, the total thickness of the regrown buffer below the 20 nm GaAs quantum well is again 40 nm. The curve (c) shows the data for a reference sample where the 100 nm thick Al_{0.35}Ga_{0.65}As buffer layer including the overgrown layer sequence like for sample (a) were deposited in one MBE process. The electron density at room temperature in this reference sample is $1.25 \times 10^{11} \text{ cm}^{-2}$ with a mobility of $800 \text{ cm}^2/\text{Vs}$. For the overgrown samples shown in Figure 4 (a) and (b) we did not detect free carrier within the etched region where the Al_{0.35}Ga_{0.65}As buffer layer was exposed to air.

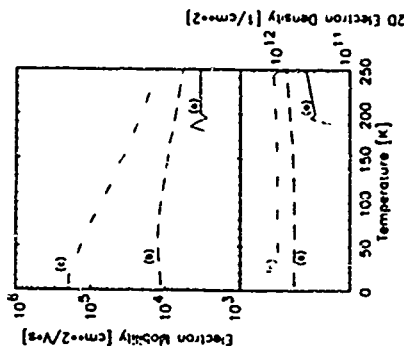


Figure 4: Hall effect measurement on modulation doped quantum well structures regrown in a 50 nm thick Al_{0.35}Ga_{0.65}As buffer layer. Overgrown layer sequence: 15 nm Al_{0.35}Ga_{0.65}As / 10 nm Al_{0.35}Ga_{0.65}As (Si doped) / 20 nm Al_{0.35}Ga_{0.65}As spacer / 20 nm GaAs quantum well / 10 nm Al_{0.35}Ga_{0.65}As spacer / 10 nm Al_{0.35}Ga_{0.65}As (N doped) / 10 nm GaAs cap layer. (a) 10 minutes thermal annealing at 720°C in As₂ atmosphere before regrowth. (b) like (a) however, periods of 20 nm GaAs / 10 nm AlAs instead of the 15 nm Al_{0.35}Ga_{0.65}As layer. (c) reference sample, 10 nm Al_{0.35}Ga_{0.65}As buffer layer and overgrown layer sequence are deposited in one MBE run without an intermediate patterning process.

Therefore, we can assume, that active quantum well structures with free electrons are formed in the ridges, which are electrically isolated by the inactive regions in the etched sections of the sample. (unintentional) spectroscopy on similar samples support this conclusion. The results have been presented in Ref. [11]. They strongly indicate that a quasi 1D electron gas is formed on top of the overgrown ridge.

In conclusion, we demonstrated that extremely narrow completely encapsulated modulation doped quantum wires can be prepared in a very controlled way by MBE-regrowth on [011] oriented mesa etched lines in AlGaAs buffer layers. This method allows to prepare low dimensional electronic device structures which are defined and separated by the etched areas which are electrically inactive.

We wish to thank M. Hauer, B. Schmitt, C. Lange, A. Goldhard and M. Riek for expert technical assistance.

References

- [1] W. Tsang and A. Y. Cho, Appl. Phys. Lett. 30, 293 (1977).
- [2] H. Tanaka and M. Nishigaki, J. Crystal Growth 111, 1043 (1991).
- [3] J. Kapteina, S. Simeonov, J.P. Harbeck, T.T. Thier, and P. Wierland, Appl. Phys. Lett. 54, 1825 (1990).
- [4] W.Q. Li, Y.J. Chan, P.K. Bhattacharya, J. Vac. Sci. Technol. B10, 1035 (1992).
- [5] J. S. Smith, P. L. Berry, S. Margalit, and A. Yarov, Appl. Phys. Lett. 47, 712 (1985).
- [6] H. P. May, J. Van Gasse, P. W. Ippert, C. Haider, W. Walter, M. Krah, and D. Bimberg, J. Crystal Growth 98, 66 (1990).
- [7] I. Bockschmidt and H. Doherty, J. of Crystal Growth 114, 619 (1991).
- [8] T. Takabe, M. Fujis, T. Yamamoto, K. Iijima, and K. Kuroyoshi, J. of Crystal Growth 127, 917 (1993).
- [9] Y. Nakamura, S. Koshihara, M. Tsukagawa, H. Kono, and H. Sakaki, Appl. Phys. Lett. 59, 703 (1991).
- [10] M. Wulfsberg, I. Rühr, G. Böhm, G. Traub, and G. Weimann, J. of Crystal Growth 127, 1045 (1993).
- [11] K. Thiel, V. Grubisov, A. Lehmann, A. Kurekshvili, K. Kilzring, D. Heun, M. Dolev, and M. Hohenstein, Appl. Phys. Lett. in press.

MoA4

Fabrication of SiGe/Si quantum wire structures on a V-groove patterned Si substrate by gas-source Si molecular beam epitaxy

N. Usami, T. Mine*, S. Fukatsu, and Y. Shiraki

Research Center for Advanced Science and Technology (RCAST)

The University of Tokyo

4-6-1 Komaba, Meguro-ku, Tokyo 153, Japan

Fabrication of SiGe/Si quantum wire (QWR) structures on a V-groove patterned Si substrate by gas source Si molecular beam epitaxy (GS-MBE) is reported. Cross sectional images of transmission electron microscopy (TEM) clarified a crescent shaped SiGe layer at the bottom of the V-groove. Evidence of the quantum state in QWR was estimated by photoluminescence (PL) spectra of the QWR grown by selective epitaxial growth (SEG) technique.

1. Introduction

Modulated semiconductor structures with reduced dimension have attracted considerable attention for the possibility of obtaining new and novel optical properties due to the quantum confinement effect. Among various techniques to fabricate quantum wire (QWR) structures, growth on non-planar substrates is promising since it is free from damage during processing. Recently, Kaplan *et al.* reported the successful growth of GaAs-AlGaAs QWR arrays on a V-groove patterned GaAs substrate by metal organic chemical vapor deposition (MOCVD) [1] and demonstrated room temperature operation of QWR laser [2]. Pan *et al.* fabricated GaAs (GaAs-P) QWR by also MOCVD and clearly showed the evidence of quantum state in QWR by cathodoluminescence (CL) [3]. These reports are actually some parts of great progress in the in situ fabrication of QWR in III-V material system [4]. However, SiGe/Si QWR has not been obtained yet in spite of recent rapid progress in research on QWR arrays on a V-groove patterned Si substrate using gas source Si molecular beam epitaxy (GS-MBE) [5]. A crescent-shaped SiGe layer was clearly seen in cross sectional image of transmission electron microscopy (TEM). Photoluminescence (PL) spectra of the QWR grown by selective epitaxial growth (SEG) technique showed photon resulted luminescence which might come from QWR region.

2. Experimental

Figure 1 shows the fabrication process of SiGe/Si QWR. At first, a 1.5 μm SiO_2 film was uniformly grown on a Si(100) substrate by thermal oxidation technique [6]. Subsequently, standard etching technique

* On leave from Hiroshi Central Research Laboratory,
1-280 Higashi-Tsugishiro, Akihabara-cho, Tokyo 135, Japan

lithography was carried out in order to generate line (1 μm) and space (0.3 μm) patterns along the (110) direction [6]. After removing resist completely by O_2 plasma irradiation, the substrate was dipped in N_2H_4 -based solution in order to create a V-groove pattern with Si(111) facets [6]. The SiO_2 layer acts as a mask for the chemical etching. QWR growth was performed in a GS-MBE (Dumbo House VCE S2020) system using disilane (Si_2H_6) and germane (GeH_4) as gaseous sources. The detail of the system reported elsewhere [6]. In some cases, the SiO_2 layer was removed with hydrofluoric acid (HF) before introduction into loading chamber. Prior to growth, the substrate temperature was raised up to 1050 $^\circ\text{C}$ and kept for 10 minutes so as to thermally desorb the contaminants and to obtain a clean surface. Then, the substrate temperature was lowered to 740 $^\circ\text{C}$ in order to obtain a high quality surface while maintaining geometry of the V-groove. The thickness of the Si buffer layer was reduced to less than 10 nm. It is noted that we should take three different regions into account when discussing the structure of the sample. One of them is a SiGe QWR layer formed at the bottom of the V-groove as shown in Fig. 1. The others are quantum well (QWL) structures on Si(100) flat region and Si(111) sidewall. In order to facilitate PL peak assignment, SEG was also performed. In this case, the Si(100) flat region between neighboring grooves was kept being covered with the SiO_2 layer. Under appropriate growth condition, no growth occurs on the Si(100) flat region. Hence, QWL on Si(100) flat region is not formed. PL spectra were measured in standard kx-kz configuration and detected by a liquid nitrogen-cooled Ge photo-detector (North Coast EO M7L). Excitation was provided by a defocused argon ion laser with an optical power density of 10^{-1} W/cm^2 .

3. Results and Discussion

Figure 2 (a) shows a typical cross sectional transmission electron microscopy (TEM) image of Si(100) Si QWR grown on a V-groove patterned Si substrate. Ge atomic composition was estimated by X-ray diffraction of QWL, which was grown on a Si(100) substrate using the same growth conditions. A very sharp V-groove is seen as a dark band which represents the interface between the substrate and the Si buffer layer. At the bottom of the groove, excellent crescent shape can be clearly seen in this micrograph. We believe that this is the first successful fabrication of QWR like SiGe layer. Any traces of multi-dilution were not found from a simple estimation by the nominal growth rate (4.4 $\text{\AA}/\text{sec}$) and the growth time (6 sec). The vertical wire width of this sample is expected as about 12 \AA . However, this micrograph shows that the vertical wire width is as thick as 100 \AA . On the other hand, well width of QWL fabricated on Si(111) facets is much smaller than the expected value. Hence, the unexpected large value of vertical wire width might be brought by the surface migration of adatoms on Si(111) to the bottom of the V-groove. Figure 2 (b) shows a typical cross sectional TEM image of a QWR fabricated by SEG technique. Epitaxial growth occurs only between the groove and no polysilicene Si layer can be found on the Si(100) layer. Figure 3 shows PL spectra of Si-SiGe/Si heterostructures grown on (a) on-axis Si(111) substrate, (b) a V-groove patterned Si substrate without SiO_2 layer, and (c) with SiO_2 layer. These three different samples were grown using exactly same growth conditions. The thickness of a Si buffer layer and the SiGe well width of this sample is nominally 40 \AA and 32 \AA for Si(111) flat region, respectively. In the spectra (a), no photon (NP) transition due to symmetry breaking allow

downward in the SiGe well layer and its transverse optical (TO) phonon replica can be clearly identified. The peaks labeled Si around 1197 meV come from the Si substrate with assistance of TO phonon. In the spectra (b), phonon replica spectra can be seen. The intense part is thought to come from the QWL formed on the Si (111) flat region between the gratings. Spectral blue shift can be seen compared to the spectral which comes from a reduced well width. This might be brought by a reduced effective wave vector due to a large surface area under the diffusion of adatoms in the grating. Since we can hardly identify the emission from the QWR at the bottom of the grating due to the intense luminescence from the QWL on Si (111), we carried out PL measurement of the QWR grown by SEG. The result is shown in Figure 3 (c). At the lower energy side of the emission from the Si substrate, we can observe a pair of two peaks. The energy separation (4meV) between the phonon replica of a quantized state. The QWL region on the (111) facet is a candidate which attributes to the emission. However, a QWL on Si (111) grown at the temperature selected here is known not to exhibit PL. [6] Moreover, the peak energy is much lower than the estimation by a numerical calculation using the well width in Si(111) obtained by TEM measurement. Hence, this quantized state can be attributed to the QWR layer fabricated at the bottom of the V-grating.

4. Conclusion

We succeeded in growing SiGe/Si QWR arrays on a V-grating patterned Si substrate by GS SIMBE. Excellent crescent shaped SiGe layer was confirmed by TEM cross sectional image. PL spectra of the QWR formed by selective epitaxial growth technique showed the existence of the quantized state in QWR.

Acknowledgement

We would like to acknowledge A. Nishida, I. Sakuma, and K. Suzuki for their expert technical support. H. Ota, T. Okada, and S. Okamura are gratefully acknowledged for developing the GS SIMBE system. We thank H. Sumitani and S. Ohkubo for their technical support. One of the authors (N.U.) was financially supported by Japan Science Promotion Society (JSPS) Fellowship for Japanese Junior Scientists.

References

1. E. Kapon, K. Kash, E. M. Chaves Jr., D. M. Huang, and E. C. G. Farias, Appl. Phys. Lett. 60, 477 (1992).
2. S. Yamahata, E. Kapon, E. C. G. Farias, D. M. Huang, N. G. Staudel, and P. Wisland, Appl. Phys. Lett. 59, 2225 (1991).
3. W. Pan, X. Ma, Z. Fu, H. Yaguchi, K. Okabe, Y. Shiraki, and R. Ito (unpublished).
4. S. Tsukamoto, Y. Nagamura, M. Nishikawa, and Y. Arakawa, Appl. Phys. Lett. 62, 49 (1993).
5. M. Wallner, E. Kapon, K. Kash, J. Chinn, D. M. Huang, and R. Bhui, Appl. Phys. Lett. 60, 421 (1992).
6. J. Chinn, M. Grundmann, E. Kapon, L. C. G. Farias, D. M. Huang, and D. Dimberg.

Appl. Phys. Lett. 61, 67 (1992).

7. Y. Nagamura, Y. Arakawa, S. Tsukamoto, M. Nishikawa, S. Sakai, and N. Miura, Phys. Rev. Lett. 69, 2963 (1992).
8. S. Fukatsu, H. Yoshida, N. Uemura, A. Fujimura, Y. Takahashi, Y. Shiraki, and R. Ito, Jpn. J. Appl. Phys. 31, L1110 (1992).
9. S. Fukatsu, Y. Kashi, N. Uemura, H. Sumitani, and Y. Shiraki (unpublished).

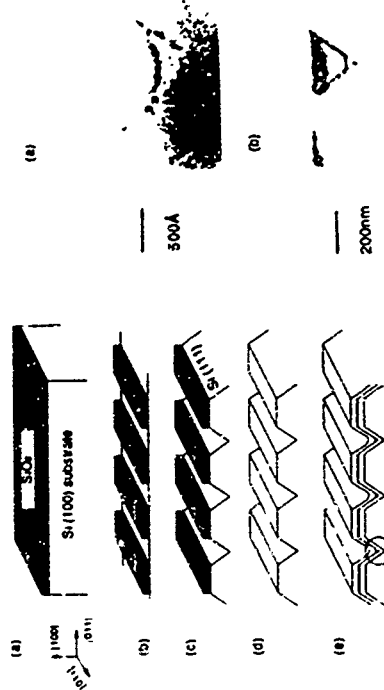


Fig. 2 Cross-sectional TEM image of SiGe/Si QWR. (unpublished) V-grating patterned Si(100) substrate.

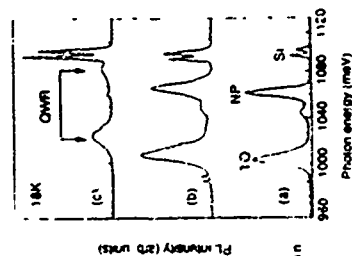


Fig. 3 Comparison of PL spectra of SiGe/Si grown on an unpatterned Si(111) (b) and a V-grating patterned Si substrate (c) by SEG.

MoB1

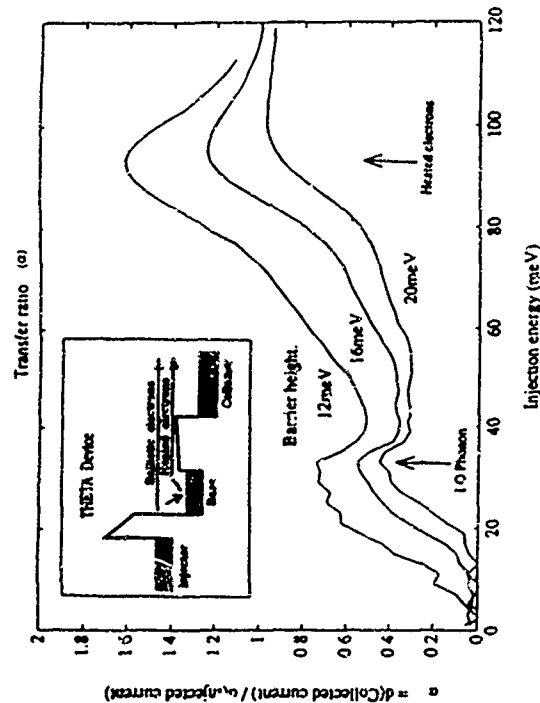
Evidence of Directional Electron Heating in Doped GaAs

B. B.-M., M. Heiblum, and H. Shtrikman
Braun Center for Submicron Research, Weizmann Institute of Science, Rehovot, Israel

As electrons gain energy or heat up their energy relaxation rate via phonon or electron scattering increases. This is mostly due to the available phase space that opens up for their final states after scattering. For very long samples, the electrons and the lattice reach thermal equilibrium with equal temperatures, however, when the transport region is very short, the electrons' and phonons' temperatures can be quite different. In extreme situations their distributions may be far from equilibrium and an electron temperature cannot be defined. Moreover, when the path length is on the order of the electron's wavelength, quantum size effects are expected to modify the cooling rate of the electrons.

We report of initial experimental results, via transport measurements, in narrow wells of doped GaAs, showing strong evidence of heated electron distribution with net momentum along the injected current direction. The measurements were done with a Hot Electron Device (THETA), having a 30 nm long transport region (base) doped to $(1.5 \cdot 2 \times 10^{18} \text{ cm}^{-3})$. Hot, non-equilibrium electrons were injected into the transport region utilizing a biased GaAs-AlGaAs-GaAs tunnel barrier and were collected above another barrier (collector barrier) that terminated the narrow base region. The collector barrier was designed to be only some 10-20 meV above the Fermi energy in the base, so that it prevented the collection of cold electrons while allowing forward moving hot electrons with normal energy higher than the collector barrier to be collected. In past works, when the collector barrier was higher, the differential transfer ratio, $\alpha = d(\text{collected current})/d(\text{injected current})$, approached unity, indicating the large fraction of ballistic electrons that had made it across the base. Measurements performed now, with the low-collector-barrier device, resulted, surprisingly, with α values peaking much above unity. Increasing the doping levels in the base or lowering the collector barrier height results with a higher α .

We suggest that directional electron heating takes place, namely, that the collected current has two contributions, resulting from the injected ballistic electrons and from electrons that were heated above the Fermi sea by the ballistic electrons. A simple model that assumes the heated electrons have a Fermi distribution with an electron temperature of some 20 K, while the lattice temperature is maintained at 4.2 K, can partially account for the experimental results. However, it is expected that the distribution may not be fully equilibrated and thus a more rigorous treatment is warranted. These results suggest a way to obtain three terminal devices with extremely high current gains (for $\alpha = 1$, $\beta = \alpha/(1-\alpha) \rightarrow \infty$)



Differential transfer ratio of the ballistic electrons through a $2 \times 10^{18} \text{ cm}^{-3}$ doped base as a function of the injection energy. At the collector barrier height decreases (from 20 to 12 meV), α increases with a distinct peak around 36 meV, where α exceeds unity. We attribute this peak to heated electrons with momentum along the direction of the injected ballistic electrons. The peak around 36 meV is due to the onset of LO phonon emission.

MOD2

High-mobility transport along single quasi one-dimensional quantum wires formed by cleaved edge overgrowth

W. Wegscheider, W. Kang, L. N. Pfeiffer, K. W. West, H. L. Stormer, and K. W. Baldwin
AT&T Bell Laboratories, Murray Hill, New Jersey 07974, USA

Abstract

We report on a novel contact scheme which for the first time makes possible magnetotransport measurements on individual quasi one-dimensional quantum wires prepared by cleaved edge overgrowth. Contacting is achieved via two isolated 2-dimensional electron systems that are connected to one another by the quantum wire under study. Two-terminal magnetoresistance measurements along our modulation-doped quantum wires exhibit electron mobilities in excess of 2×10^5 cm²/Vs and show pronounced Shubnikov-de Haas oscillations. Clear evidence for confinement of the electrons in two dimensions is deduced from the retarded depopulation of Landau levels at low magnetic fields. The results are in close agreement with a calculation of the magnetic field dependence of the number of occupied subbands in a narrow channel.

Introduction

Quantum sized semiconductor structures in which free carrier motion is restricted to one dimension, so-called quantum wires, are expected to show unique electrical transport properties such as extremely high electron mobilities [1], and quantized conductances that are independent of the wire length. These predictions have attracted considerable attention and motivation for the fabrication and the experimental investigation of these structures. While conductance quantization through narrow constrictions in a two-dimensional electron gas (2DEG) has been demonstrated [2,3], corresponding quantization in long one-dimensional (1D) wires has been elusive. This has been attributed to size fluctuations along the length of the quantum wires, and to the appearance of universal conductance fluctuations which wash out the effects associated with the reduced dimensionality. So far, the fabrication of quantum wire structures for transport measurements has mostly relied on lithographic techniques [4], which allow the fabrication of wires of widths well below 100 nm but are subject to considerable fluctuations of the wire width. Recently a molecular beam epitaxy (MBE) growth technique called cleaved edge overgrowth (CEO) has been developed, which involves regrowth on the sidewall of an *in situ* cleaved GaAs/AlGaAs heterostructure [5]. CEO is able to generate atomically precise quantum wires with minimum fluctuation of the wire width, however, the study of such highly uniform 1D wires via electronic transport has been hampered by inability to make reliable low-resistance electric contacts.

In this paper we introduce a new method to reliably contact CEO structures and in particular one-dimensional wires. Our technique makes use of the presence of two isolated 2DEGs defined by a shadow mask during the first CEO growth step. The transport properties of the quantum wires whose widths are defined on an atomic scale by the MBE growth process can be studied by

connecting current and voltage probes to the 2DEGs. Contacting can be achieved by conventional means, thereby avoiding complicated lithographic processing steps. Since the 2DEGs lie in a plane perpendicular to the (110) cleavage plane, magnetotransport characterizations of the quantum wires becomes independent of the contacting 2DEGs by proper orientation of the magnetic field.

Experimental procedures

Our technique is a variation of the CEO technique described in detail elsewhere [6]. First, a modulation-doped quantum well of thickness d embedded between $\text{Al}_{0.3}\text{Ga}_{0.7}\text{As}$ layers is grown on a $\text{GaAs}(001)$ substrate. The relevant layer thicknesses as well as the location of additional buffer and cap layers are indicated in Fig. 1. During deposition of the Si dopant ($n \approx 10^{12}$ cm⁻³) a shadow mask is positioned in close vicinity of the substrate surface. This mask blocks Si incorporation in the MBE film along stripes typically ≈ 40 - 100 μm wide, resulting in two spatially separated 2DEGs in the (001) plane. After the first MBE growth the substrate is removed from the machine, mechanically thinned from the backside and reinserted into the MBE growth chamber where an *in situ* cleave is performed. Within seconds after the cleave the second MBE overgrowth is started on the fresh (110) surface. The post-cleave sequence consists of a $\text{Al}_{0.3}\text{Ga}_{0.7}\text{As}$ spacer layer, a Si dopant spike ($n \approx 3 \times 10^{12}$ cm⁻³) and finally a $\text{Al}_{0.3}\text{Ga}_{0.7}\text{As}$ cap. As visualized in the perspective drawing of Fig. 1, this results in the formation of a quasi one-dimensional quantum wire connected over the corner to the two 2DEGs. While the width of the low-dimensional structure is given by the width of the quantum well d (70-1000 nm) of the first MBE growth, the wire length is defined by the width of the shadow mask which was in our case typically 40-100 μm .

For the shadow mask we use Ta wires etched in $\text{HNO}_3\text{:HF}$ (1:1) to the desired diameter. These are mounted on a Ta frame which, in turn, is attached to a hinge permanently connected to the sample holder block. Sample rotation by an angle of 180° in the vertical growth position moves the mask either in front of, or away from the sample surface aided by gravitation. Since the Si dopant cell is not a point source, a close proximity between the mask and the sample surface is required in order to guarantee complete shadowing. In addition, due to the sensitivity of the sample to contamination during MBE growth, extreme requirements are imposed on the mask as to the cleanliness so as to avoid outgassing as it is heated by the substrate during use. For that reason we prebake the chemically-cleaned empty substrate holder block and mask in a 10^{-11} Torr vacuum at a temperature of about 900°C before mounting the GaAs substrate and insertion into the growth chamber. This is followed by the usual outgassing procedure. As another precaution we terminate the $\text{Al}_{0.3}\text{Ga}_{0.7}\text{As}$ spacer layer by 3 monolayers of GaAs to protect the highly reactive $\text{Al}_{0.3}\text{Ga}_{0.7}\text{As}$ during mask manipulation.

Magnetotransport measurements were performed with standard lock-in techniques at a temperature of 300 mK. Four In-diffused contacts were made in each of the 2DEGs connected to the ends of the quantum wire. This allows us to perform two-probe magnetoresistance measurements along the quantum wire and after tilting the sample with respect to the magnetic field, to independently characterize each 2DEG region by four-probe Hall measurements.

Results and discussion

In order to verify the usefulness of the described contact scheme we characterized the properties

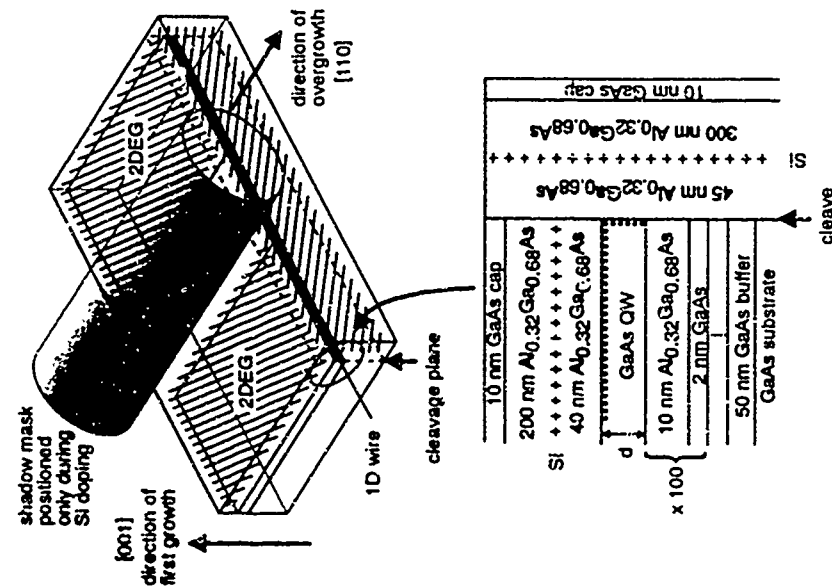


Figure 1: Schematic diagram of MBE overgrowth of a modulation-doped quantum wire structure on a cleaved interface (bottom) and perspective drawing of the quantum wire and the 2DEGs with respect to the shadow mask (top). Hatched areas indicate Si dopant layers; dots locate two and quasi one-dimensional electron gases.

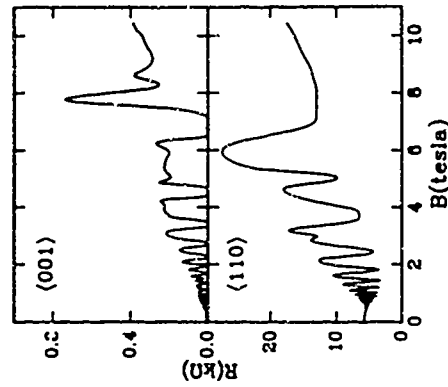


Figure 2: Four-probe magnetoresistance data in one 2DEG contact regions (top) and two-probe magnetoresistance across the $1 \mu\text{m}$ wide channel (bottom) of a CEO quantum wire sample.

of the resulting quantum well structure before the cleave and its overgrowth took place. Van der Pauw measurements of the modulation-doped quantum well regions reveal typical electron mobilities in the dark after exposure to light in the range of 1 to $3 \times 10^6 \text{ cm}^2/\text{Vs}$ at a carrier density of $3.6 \times 10^{11} \text{ cm}^{-2}$, comparable to our conventional quantum well samples. The resistance across the undoped quantum well stripe is found to be higher than $10 \text{ M}\Omega$ provided that a breakdown voltage of about 1 V is not exceeded.

Figure 2 shows the magnetoresistances of a fully processed CEO sample with a GaAs wire width of $d = 1 \mu\text{m}$. The (001) data in the upper panel are taken on one side of the contacting 2DEG with the magnetic field normal to the 2DEG plane. The high quality of the 2DEG in the (001) contact region is evident from the observation of the $\nu = 5/3$ fractional quantum Hall state at about 8.2 T in addition to the integral quantum Hall states. For the electron density and the mobility of these contacting 2DEGs in the (001) plane we obtain $3.2 \times 10^{11} \text{ cm}^{-2}$ and $2 \times 10^6 \text{ cm}^2/\text{Vs}$, respectively. The data in the bottom panel are taken on the $1 \mu\text{m}$ wide wire with the magnetic field normal to the "plane" of the wire [(110) plane] and parallel to the plane of the contacting 2DEGs [(001) plane]. The electric current proceeds from the first 2DEG through the wire into the second 2DEG and the voltage is measured at separate contacts between both 2DEGs. Although this constitutes a four-probe geometry it is not a truly four-probe electrical transport measurement, since the current and voltage probes are not truly independent. One current and one voltage contact is attached to each of the 2DEGs and each 2DEG in turn contacts the wire along a common edge. This

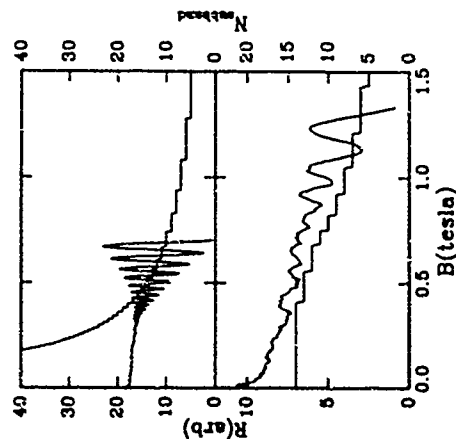


Figure 3: Comparison of low-field magnetoresistance across 1 μm (top) and 300 nm wide channels (bottom). The number of occupied subbands calculated after Eqs. (1) and (2) for both cases are also indicated.

unusual geometry leads to the mixing between magnetoresistance and Hall resistance observed in Fig. 2, reminiscent of two-probe measurements on 2DEGs. Such a mixing can be avoided by contacting four 2DEGs to the wire in future implementations. Under any circumstances the transport around the edge and into a true quantum wire opens interesting opportunities for future studies. Using an aspect ratio of 1:100 for the 100 μm long wire ($d \approx 1 \mu\text{m}$) we obtain a zero-field mobility of $2.8 \times 10^3 \text{ cm}^2/\text{Vs}$. This underestimates the true electron mobility in the wire since the resistances of the junctions from the 2DEGs to the wires have not been included. The deviations of the measured Hall plateaus from the quantized values at high magnetic fields indeed suggest a junction resistance of about 2–3 k Ω which is a considerable fraction of the total resistance of about 10 k Ω .

Low-field magnetoresistance data across 1 μm and 300 nm wide wires are shown in Fig. 3 together with the theoretically expected 1D subband population. The number of occupied subbands N at the Fermi energy E_F for a square well confining potential of width d is given approximately by [4(b)],

$$N \approx \text{Int} \left[\frac{2 E_F}{\pi \hbar v_c} \left(\arcsin \frac{d}{2l_c} + \frac{d}{2l_c} \left[1 - \left(\frac{d}{2l_c} \right)^2 \right]^{1/2} \right) \right], \quad \text{if } l_c > \frac{d}{2} \quad (1)$$

$$N \approx \text{Int} \left[\frac{1}{2} + \frac{E_F}{\hbar v_c} \right], \quad \text{if } l_c < \frac{d}{2}. \quad (2)$$

where $l_c = \hbar v_F / eB$ is the cyclotron radius at the Fermi energy and $\hbar v_c = \hbar e B / m$ is the Landau level separation. The onset of the SdH oscillations in the 1 μm wide wire is about 0.3 T, so that it is not possible to observe any one-dimensional behaviour which will appear only below the 1D to 2D crossover field of about 0.2 T. In the 300 nm wide wire, the crossover field is about 0.7 T and the quasi-one dimensional subbands can be resolved. Below 0.7 T we observe the retarded depopulation of Landau levels characteristic for lateral confinement of a 2DEG. The SdH oscillations are no longer periodic in $1/B$, confirming the presence of carrier confinement in two dimensions. At higher fields ($> 0.7 \text{ T}$) the $1/B$ periodicity is restored. Using the electron density n obtained from the high-field SdH data we achieve excellent agreement between the experimentally observed and the theoretically after Eqs. (1) and (2) calculated population of 14 electronic subbands. This close agreement confirms the implementation of a 300 nm wide quantum wire and the viability of our contacting scheme.

Conclusions

The contact scheme we reported here provides a simple and reliable way to probe individual quasi one-dimensional quantum wires fabricated by CEO. The high potential of this novel technique is demonstrated by the clear 1D subband population behaviour observed in 300 nm wide quantum wires with electron mobilities in excess of $2 \times 10^3 \text{ cm}^2/\text{Vs}$. However, in order to investigate narrower, ballistic channels whose length are comparable with the electron mean free path the dimensions of the shadow mask have to be further reduced. We expect that this can be achieved with lithographically prepared masks.

Acknowledgements

One of us (W.W.) gratefully acknowledges financial support from the Deutsche Forschungsgemeinschaft (DFG).

References

1. H. Sakaki, Jpn. J. Appl. Phys. 19, 94 (1980).
2. B. J. van Wees, H. van Houten, C. W. J. Beenakker, J. G. Williamson, L. P. Kouwenhoven, D. van der Marck, and C. T. Foxon, Phys. Rev. Lett. 60, 848 (1988).
3. D. A. Wharam, T. J. Thornton, R. Newbury, M. Pepper, H. Ahmed, J. E. F. Frost, D. G. Hasko, D. C. Peacock, D. A. Ritchie, and G. A. C. Jones, J. Phys. C 21, L209 (1988).
4. For reviews see, (a) *Nanotechnology Physics and Fabrication*, edited by M. A. Reed and W. P. Kirk (Academic, New York, 1989); (b) C. W. J. Beenakker and H. van Houten, in *Solid State Physics: Advances in Research and Applications*, edited by H. Ehrenreich and D. Turnbull (Academic, New York, 1991), Vol. 44, pp. 1–228.
5. L. N. Pfeiffer, K. W. West, H. L. Stormer, J. P. Eisenstein, K. W. Baldwin, D. Gershoni, and J. Spector, Appl. Phys. Lett. 56, 1897 (1990).
6. L. Pfeiffer, H. L. Stormer, K. W. Baldwin, K. W. West, A. R. Goni, A. Pinczuk, R. C. Ashoori, S. M. Dignam, and W. A. G. Schuler, J. Crystal Growth 127, 849 (1993).

MOB3

Observation of Knudsen and Gurzhi transport regimes in a two-dimensional wire

I. W. Moerkamp and M. J. M. de Jong*
Philips Research Laboratories, 5676 AZ Eindhoven, The Netherlands

Abstract

We have observed electronic Knudsen and Poisson flow in a current heat experiment on electrostatically defined wires in (AlGa)As heterostructures. (Current heating induces an increase in the number of electron-electron collisions in the wire, leading first to an increase (Knudsen regime) and subsequently to a decrease (Gurzhi effect) of the resistance of the wire as the Gurzhi effect of the resistance of the wire

In his famous 1909 paper on gas flow through a capillary, Knudsen [1] demonstrated that the pressure drop over the capillary first increases and then decreases with increasing density. The mechanism is that with increasing gas particle density, the number of interparticle collisions also increases. At low densities (what is now known as the Knudsen transport regime) this leads to increasing dissipation of forward molecular momentum at the capillary walls, while at higher densities (normal Poisson flow regime) it decreases the effective particle wall interaction.

Because of the analogy between classical diffusive transport of electrons and gas particles, one may anticipate that a similar transition from Knudsen to Poisson flow also occurs in electron transport, where normal electron-electron scattering events (NLEES) are the analogue of gas particle collisions. This issue has indeed been pursued since the early 1950's. However, it proved difficult to obtain reliable data [2], because the electron-phonon interaction is much more important than the electron-electron interaction.

So far, only preliminary indications of electronic Knudsen and Poisson transport effects have been found [3]. Most experiments were performed on potassium as an exemplary simple metal. However, the observed changes in the resistance as a function of lattice temperature were limited to about 0.01% of the total resistance, because on the limited impurity mean free path l_{imp} and the onset of electron-phonon scattering. Observations of a positive temperature derivative of the resistivity $d\rho/dT$ in potassium wires [4] could be assigned by Moshovitz and Wiser [5] as a Knudsen-like behaviour due to the combination of relatively infrequent normal electron-electron and electron-phonon collisions. However, until now there has been no observation of electronic Poisson flow

Electronic Poisson flow should lead to a negative $d\rho/dT$, a phenomenon predicted by Gurzhi in 1964 [6], and generally known as the Gurzhi effect.

Here we present a study of Knudsen and Gurzhi phenomena in two-dimensional wires, fabricated from high-mobility (AlGa)As heterostructures. Using this material to study NLEES effects offers several advantages, allowing a clear and unambiguous observation of the Knudsen and Poisson flow regimes. The resistance changes caused by NLEES processes can be larger than 10% of the total resistance. A full discussion of this work, as well as a detailed theoretical framework for calculations of NLEES effects on the resistance for arbitrary electron temperature will be given elsewhere [7].

The wires used for the experiments are defined electrostatically in the two-dimensional electron gas (2DEG) of (AlGa)As heterostructures. The layout of the 1.5 μm gates is given schematically in Fig. 1. We report here on two wires, both fabricated from an (AlGa)As wafer with electron density $n = 2.7 \times 10^{10} \text{ cm}^{-2}$ and $l_{imp} = 19.7 \mu\text{m}$. Both wires have a width $W = 1.0 \mu\text{m}$, but they differ a factor of two in length L : $L = 6.57 \mu\text{m}$ in one wire, and $L = 12.73 \mu\text{m}$ in the other. For transport measurements, the samples are kept in a crystal at 1.5 K, and at zero magnetic field. The differential resistance is measured with standard low-frequency lock-in techniques, using a 100 μV ac voltage.

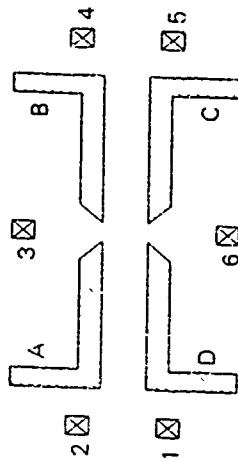


FIG. 1. Layout of the gates defining the wires used in the experiments. Current is passed between Ohmic contacts 2 and 1, and the voltage drop is measured between contacts 1 and 5. Ohmic contacts 3 and 6 can be used for measuring the thermovoltages across the point contacts in the wire boundaries. The wires studied here both have a width $W = 1 \mu\text{m}$, but differ in length ($L = 6.57$ and $12.73 \mu\text{m}$).

In order to be able to study the effects of NLEES separately from electron-phonon scattering effects, we utilize a peculiarity of (AlGa)As two-dimensional electron gases at low temperatures. In these materials, the coupling between lattice electrons and the lattice is orders of magnitude smaller than the coupling within the electron system. This allows one to achieve selective 'lattice heating' of the electron gas in the wires by passing a dc current I through the wire. This technique has proven to be very useful for the study of thermoelectric phenomena in nanostructures [8]. The wires studied here are equipped with opposing pairs of point contacts in their boundaries, allowing us to determine the electron temperature T as a function of I using the quantized thermopower of a point contact, as described in Ref. [9]. A typical example of such a measurement of T vs. I is shown in Fig. 2. We find that for $|I| \lesssim 20 \mu\text{A}$ and a lattice temperature $T_L \lesssim 2 \text{ K}$, the

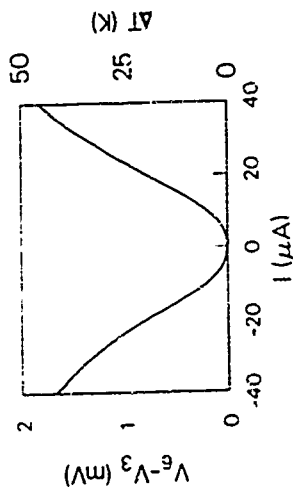


FIG. 2. Transverse voltage $V_6 - V_3$ as a function of heating current I . In this experiment, point contact AB is adjusted between the $V = 1$ and $V = 2$ for maximum quantized thermopower, and the thermopower of point contact CD can be neglected. The electron temperature in the channel can now be deduced from the size of the transverse voltage. See Refs. [8] and [9] for details.

electron temperature T in our wires is approximately given by

$$T = T_0 + (I/I_0)^2 \rho C, \quad (1)$$

where ρ is the resistivity of the channel. The constant C is of order $C \approx 0.05$ in $^2\text{K}/\text{W}$. In Fig. 1 we show our data (plotted lines) on the differential resistance (dI/dI) of both wires. The top trace was obtained from the longer, the bottom trace from the shorter wire. For both wires we observe first an increase, followed by a decrease of dI/dI with I . At low currents, where Eq. (1) applies, we observe a remarkable behavior of dI/dI an initial increase, followed by a decrease in dI/dI with increasing I [10].

To see whether NEES could in principle be responsible for this behavior, let us estimate the electron temperature in the wire at $I \approx 15 \mu\text{A}$ and $T_0 \approx 3.5 \text{ K}$. We have $L_{ee} \approx \tau_e v_F$, where v_F is the Fermi velocity, and τ_e the electron-electron scattering time, given by [11]

$$\frac{1}{\tau_e(T)} = \frac{E_F}{k} \left(\frac{k_B T}{E_F} \right)^2 \left[\ln \left(\frac{E_F}{k_B T} \right) + \ln \left(\frac{2I}{I_0} \right) + 1 \right] \quad (2)$$

Here q is the 2D Thomas-Fermi screening wave vector $q_F = m^2/2\pi^2 \hbar^2$. We find $L_{ee} \approx 0.8 \mu\text{m}$, which is much smaller than W . In this limit, the electrons undergo a random motion due to frequent NEES events, and we assume the decrease in dI/dI to the Gurzhi effect. For currents below $8 \mu\text{A}$, dI/dI is positive. As $L_{ee} \approx W$ for $I \approx 8 \mu\text{A}$ and $T_0 \approx 3.5 \text{ K}$, this additional feature occurs in the right current range for the electron Kohnen effect. Moreover, we see that the total increase in dI/dI in the long wire is twice the increase in the short wire. This proportionality to I rules out a contact resistance effect as an explanation for the anomalies.

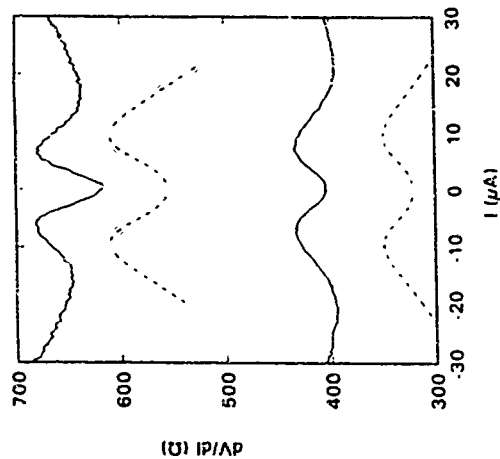


FIG. 3. Drawn curves: experimental dependence of dI/dI on heating current I for the $L = 127 \mu\text{m}$ (top curve) and $L = 63 \mu\text{m}$ (bottom curve) respectively. The dashed curves are the result of our calculations obtained using boundary scattering parameter α is 0.7, and width $W \approx L_{ee}/5.5$.

In order to substantiate our assignment of the anomalous behavior of dI/dI to hydrodynamic phenomena, we have performed model calculations of the effects of NEES on the differential resistance of a two-dimensional wire. We have included NEES events in an electron path tracing method originally due to Chambers [12], and obtained a solution for arbitrary L_{ee} , L_{ee} and W . In this method one follows the path of an electron until it relaxes at an impurity or the boundary of the system, and then determines a weighted average of the path lengths. The resulting effective mean free path L_{eff} is related to the resistivity ρ of the wire by

$$\rho^{-1} = \frac{m^2}{m\eta} L_{eff} \quad (3)$$

We assume that a fraction p of the incident electrons is reflected specularly at the bound-
ary, the remainder being scattered diffusely, and obtain for the effective mean free path
at position x along the width of the wire

$$L_M(x) = l - \frac{u}{\pi} \int_0^{\pi} d\alpha \sqrt{1 - u^2} \frac{1 - pu \cos \alpha}{1 - pu \sin \alpha} \\ + \frac{2}{\pi} \int_0^{\pi} d\alpha \frac{\sqrt{1 - u^2}}{u} \int_0^u dx' [L_M(x') + L_M(W - x')] \left[e^{-(x-x')/L_M} \theta(x - x') + \frac{p}{1 - pu \sin \alpha} \right]$$

where $l^{-1} \equiv l_{\text{imp}}^{-1} + l_{\text{sc}}^{-1}$, and $\theta(x)$ is the unit step function. The average effective mean
free path can now be obtained from $L_M = (1/W) \int_0^W dx L_M(x)$. Eq. (1) is solved self-
consistently using numerical methods.

For a comparison with the experiments, we relate L_M to L using Eqs. (1)–(4). The
resistance of the wire is obtained from $R \equiv V/I = h\pi/2e^2 L_M W + \rho L/W$, where the
first term is the two-dimensional Sharvin contact resistance [11]. Subsequently, dV/dI
is evaluated numerically. The dotted lines in Fig. 3 are the results of our calculation.
In both cases, the calculated dV/dI values are 60–80 Ω smaller than the experimental
values. This is due to the resistance of the wide 2DEG leading to the wires, which is
not included in the calculations. In addition, we did not include the lattice heating for
currents $|I| > 20 \mu\text{A}$ in our modelling. Apart from this the agreement between experiment
and theory is very good. Two remarks must be made regarding the parameters used in
our modelling. Firstly, one expects that due to depletion the electron width of the wires
is slightly smaller than the lithographic width; we have set $W = l_{\text{imp}}/3.5$ for both wires.
In addition, we noticed that using a constant value of p for all angles of incidence leads
either to a too large value for dV/dI at zero heating current or a too small Kondo effect.
It is well known from metal wires that in reality p depends on the angle of incidence θ ,
such that $p \rightarrow 1$ for grazing incidence ($\theta \rightarrow \pi/2$). According to Ref. [11],

$$p(\theta) = \exp[-(\alpha \cos \theta)^2] \quad (5)$$

Using this expression in Eq. (1) where $\alpha = \pi \cos \theta$ we obtain the numerical results of
Fig. 3. Good agreement with the experimental data is found with $\alpha \approx 0.7$, which implies
that some 80% of all boundary collisions are specular. A high specularity for boundary
scattering in split gate wires was previously found in magneto-resistance experiments [13].

In summary, we have found convincing evidence of the occurrence of electronic bound-
ary and Poisson-like transport regimes in the non-linear differential resistance of split gate
defined wires in a two-dimensional electron gas. Our results verify speculations on by-
drodynamic flow phenomena in solids that date back to the 1930's and 60's, which only
came within reach of the experimentalist after the development of methods of sufficiently
high mobility, and nano lithography techniques.

The heterostructures were grown by C. F. Loon at the Philips Research Laboratories
in Redhill (Surrey, UK). I. W. M. acknowledges the kind hospitality he enjoyed during
a visit to the Laboratory for Quantum Materials (RikSEN, Saitama, Japan, where this
research was initiated. M. I. M. de J. is supported by the Dutch Science Foundation
NWO/FOM.

REFERENCES

- [1] M. Keldos, *Ann. Phys.* **28**, 75 (1969).
- [2] I. M. Ziman, *Electrons and Phonons*, (Oxford Univ. Press, Oxford, England, 1960).
- [3] M. Kaveh and N. Wiser, *Adv. in Phys.* **33**, 237 (1981).
- [4] J. Zhao, W. P. Pratt, Jr., H. Sato, P. A. Schroeder, and J. Bass, *Phys. Rev. B* **37**, 5718 (1988).
- [5] D. Voskresenskiy and A. Wiser, *J. Phys.: Condens. Matter* **2**, 8053 (1990).
- [6] R. N. Gurzhi, *Zh. Eksp. ior Fiz.* **44**, 771 (1963) [*Sov. Phys. JETP* **17**, 521 (1963)].
- [7] J. Exp. Fiz. Nauk **94**, 650 (1968) [*Sov. Phys. Usp.* **11**, 275 (1968)].
- [8] L. W. Molenkamp and M. I. M. de Jong, submitted.
- [9] B. L. Galleher, I. Galloway, P. Beton, J. P. Oxley, S. P. Beaumont, S. Thomas, and C. D. W. Wilkinson, *Phys. Rev. Lett.* **64**, 2078 (1990); L. W. Molenkamp, H. van Houten, C. W. J. Beenakker, R. Eppenga, and C. T. Foxon, *Phys. Rev. Lett.* **65**, 1072 (1990).
- [10] L. W. Molenkamp, H. Gruber, H. van Houten, O. J. A. Bouck, M. A. A. Molewsone, and C. T. Foxon, *Phys. Rev. Lett.* **68**, 1765 (1992).
- [11] G. F. Giuliani and J. J. Quinn, *Phys. Rev. B* **26**, 4121 (1982).
- [12] R. G. Chambers, *Proc. R. Soc. London Ser. A* **202**, 378 (1950).
- [13] M. I. M. de Jong, submitted.
- [14] S. B. Soffer, *J. Appl. Phys.* **36**, 1710 (1967).
- [15] J. J. Thornton, M. L. Rother, A. Scherri, and B. P. Van der Gaag, *Phys. Rev. Lett.* **63**, 2128 (1989).

MoB4

Quantized Conductance and Its Effects on Non-linear Current-Voltage Characteristics at 80K in Mesa-Etched InAs/AlGaSb Quantum Wires with Split-Gate

Kazji Yoh, Akira Nishida and Masataka Inoue

Department of Electrical Engineering, Osaka Institute of Technology,
5-16-1 Omiya, Asahi-ku, Osaka 535

Abstract

We report electrical characteristics of InAs/AlGaSb quantum wire devices based on deep mesa-etched structures with split gate. Quantized current and conductance has been observed at around 80K for the first time. Current quantization analysis revealed that the quantized conductance showed constant value with the drain voltages up to ~ 100 mV suggesting that the Landauer's formula in one dimensional electron systems in finite voltages holds up to ~ 125 mV. The 3650\AA -wide, 3625\AA long InAs quantum wire showed non linear I-V characteristics with fixed gate voltage. The drain current dependence on matrix of gate and drain voltages revealed that the current increase at high drain voltages is caused by the so called drain-induced-barrier-lowering; sublevels at the point contact are actually lowered by the application of high drain voltage which has same effect as positive gate voltage application. Overall drain current saturation tendency is caused presumably by the saturation velocity effect in the high field region between the point contact and rest of the wire under high drain voltage.

Introduction

There have been extensive amount of work on the quantum wire transport mostly on (AlGa)InGaAs heterostructures [1-4] and on silicon based materials [5]. However, most of these phenomena were observed at 4.2K or much lower temperatures [6]. InAs quantum-effect devices [7] are potentially superior to the GaAs counterparts [8] in high temperature operation for their higher low-field mobility [9-11], higher conduction band discontinuity, and higher energy separation of sublevels. Because of this strong confinement nature and the low effective mass of electrons in the InAs well, quantum effects of the confined electron systems are expected to be observed at relatively high temperatures [7]. However, there have only been results measured at much lower temperatures than expected for several reasons [13-14]. One of the major reasons is that the lateral confinement is limited with the Schottky split-gate method. Reduction of the upper barrier is limited by the trade-off between confinement strength and tunneling currents. In this paper, we report the fabrication and characterization of deeply etched quantum wires on an (AlGa)Sb/InAs heterostructure with split-gate by utilizing electron beam lithography and wet-chemical etching. In order to avoid the inherent gate leakage current in heterostructures based on antimonides [11], deeply etched wire structures have been investigated.

Experimental

The heterostructures have been grown by molecular beam epitaxy using ANELVA MBE-620 system. The growth techniques of the InAs/AlGaSb are similar to what has been used to fabricate high performance heterojunction field-effect transistors [11,14].

The heterostructure of the device (#231) is shown in Fig.1, consisting of 2000Å of GaAs layer grown on unbuffered GaAs substrates, 1.0 μm AlSb buffer layer, 2000Å (Al_{0.5}Ga_{0.5})Sb buffer layer, 70Å of AlSb layer, 150Å of InAs, 150Å of (Al_{0.5}Ga_{0.5})Sb, and 100Å of GaSb cap layer. The inserted 70Å of AlSb was intended to prevent leakage currents through (AlGa)Sb buffer layer which becomes appreciable at high temperatures under high gate bias voltages. The carrier concentration and electron mobility of the present sample measured at 77K by Hall effect measurement were $1.07 \times 10^{12} \text{cm}^{-2}$ and $20,200 \text{cm}^2/\text{Vs}$, respectively.

Device fabrication has been performed by electron beam lithography and wet chemical etching with phosphoric-acid-based etchant and photoresist developer. Phosphoric-acid-based etchant was used to etch aramides and antimonides isotropically whereas photoresist developer was used as a selective etchant for antimonides [15]. Fabrication of deeply etched quantum wire structures using electron beam lithography and wet chemical etching is similar to what has been used to make ungated quantum wires [7,15]. Ti/Au was used as non-alloyed ohmic metal which is directly deposited on InAs layer after selective etching of antimonides. The nominal etch-depth were 1500Å. The JEOL multi-purpose Scanning Electron Microscope system, JSM840A, was used as the electron beam source. The width of the device was determined to be approximately 3650Å by measuring the SEM and AFM images.

The conductance of the devices have been measured using HP4145B semiconductor parameter analyzer. In order to collect as much data as possible in a wide range of drain and gate voltages a single shot of measurements, drain voltage step was taken to be 100mV. This relatively large drain voltage has extracting the conductance data has been justified by the current-voltage analysis which will be discussed in the results section. Voltage of only one of the split-gates, whichever has better Schottky quality than the other, was modulated and the other member of the split-gates is connected to the common ground and source terminal. This configuration was chosen to keep as much gate voltage range as possible by minimizing the total gate leakage current.

Results

Current-voltage characteristics of the split-gated quantum wire measured at 80K is shown in Figure 2. Clear current steps can be seen in the figure. Conductance dependence on gate voltage is shown in Figure 3 in various temperatures. A clear quantized conductance steps of three, four and five fold multiples of $(2e^2/h)$ were observed at temperatures between 55K and 80K. Beyond 104K, although clear conductance steps were observed up to 120K, conductance plateau did not agree with multiples of $(2e^2/h)$, suggesting the existence of a current leakage path other than the quantum point contact. This is probably due to parasitic MESFET effect which turns on very weakly at high temperatures.

Drain current increment at each current step in Figure 1 where wave mode number increases by unity. Thus, from this figure, one can extract the current increment data at each increment of the wave-mode by unity. The current increment dependence on drain voltage is plotted in Figure 4. The slope corresponds to device conductance increment at each wave-mode

length (3025 Å), extremely high field would possibly cause slight current saturation. Estimated saturation current agrees reasonably well with the experiment using the data from the separate velocity saturation experiments on the same heterostructure system [18]. This result supports the above model. The other possibility of non-parabolicity effects of InAs conduction band is eliminated by the separate experiment on the ballistic electrons in InAs which will be reported elsewhere.

Conclusion

We have reported electrical characteristics of InAs/AlGaSb quantum wire devices based on deep mesa-etched structures with split gate. Quantized current and quantized conductance have been clearly observed at around 80K for the first time. The non-linear drain current characteristics with fixed gate voltage were shown to be explained by the application of high drain lowering: sublevels at the point contact are actually lowered by the application of high drain voltage which has a same effect as positive gate voltage application. Overall drain current saturation tendency has been shown to have been caused by the saturation velocity effect in the high field region between the point contact and rest of the wire under high drain voltage.

Acknowledgements

The authors are grateful to H. Kawahara for the technical assistance in the device fabrication and measurements. This work was partially supported by Grant-in-Aid for Scientific Research on Priority Areas (Electron Wave Interference Effects in Mesoscopic Structures) from The Ministry of Education, Science and Culture. One of the authors, K.Y., also appreciates the partial support from The Murata Science Foundation.

References

- [1] K.-F. Berggren, T.J. Thornton, D.J. Newson and M. Pepper: *Phys. Rev. Lett.* 57 (1986) 1769.
- [2] M.L. Roukes, A. Scherer, S.J. Allen Jr., H.G. Craighead, R.M. Rulhien, E.D. Beebe and J. P. Harrison: *Phys. Rev. Lett.* 59 (1987) 3011.
- [3] K.-F. Berggren, G. Roos and H. van Houten: *Phys. Rev. B* 37 (1988) 10118.
- [4] C.C. Eugster and J.A. del Alamo: *Phys. Rev. Lett.* 67 (1991) 3586.
- [5] H. Matsukawa, T. Ichiguchi, T. Yoshimura and E. Takada: *IEEE Electron Device Lett.* EDL-13 (1992) 20.
- [6] There is a report on quantized conductance observed at 30K, but the quantized conductance can be just barely seen at 30K, showing how difficult it is to confine electrons by Schottky split-gate. G.L. Snider et al. *Appl. Phys. Lett.* 59 (1991) 2727.
- [7] K. Yoh, H. Taniguchi, K. Kiyomi, M. Inoue and R. Sakamoto: *IEEE IEDM Tech. Dig.* (IEEE, New York, 1991) p813.
- [8] B.J. van Wees, H. van Houten, C.W.J. Beenakker, J.G. Williamson, L.P. Kouwenhoven, D. van der Marel, and C.T. Foxen: *Phys. Rev. Lett.* 60, p 848, 1988.
- [9] G. Tuttle, H. Kroemer and J.H. English: *J. Appl. Phys.* 65 (1989) 5239.
- [10] G. Tuttle, H. Kroemer and J.H. English: *J. Appl. Phys.* 71 (1990) 3032.
- [11] K. Yoh, T. Moruchi, and M. Inoue: *IEEE Electron Device Lett.* 11 (1990) 526.
- [12] M. Inoue, K. Yoh, K. Kiyomi, A. Nishida, and T. Maemoto: *Extended Abstracts of Second International Symposium on New Phenomena in Mesoscopic Structures*, p.64, 1992.

increment point. It clearly shows that the conductance increment is equal to $(2e^2/h)$ with the drain voltages from 0V up to ~ 180 mV, suggesting that the Landauer's formula in one dimension in finite voltages [16] holds within this voltage range. This result gives foundation on the validity of our conductance measurements at finite drain voltage of 100mV. Beyond 180mV, quantized current seems to saturate with increasing the drain voltage suggesting the resistance increase at high field region of the quantum wire between the point contact (source edge where the sublevels have peaks) and the drain edge of the wire as shown in Figure 5. This topic will be elaborated in detail in the next section.

At much higher drain voltage conditions, the drain current increment starts to rise again. Drain current dependence on the matrix of gate voltage and drain voltage is shown in Figure 6. It clearly shows that the trace of the current increment (mode-change) point moves toward reduced gate voltages as the drain voltage is increased. The effect becomes most appreciable in the high end of the drain voltage axis where the drain voltage is 1.1V or higher. This effect is similar to what is observed in the short channel MOSFET: the drain-induced-barrier-lowering (DIBL) [17]. In short channel MOSFET, these effects cause high output conductance and it gradually becomes severer at higher drain voltages. In case of short channel "and" narrow wire as is the present case, DIBL occurs in such a way that it leaves a bundle of lower electron wave mode and switches to a higher mode bundle as shown in Figure 7. This is a quantum wire version of drain-induced barrier-lowering effect which must be overcome eventually if quantum wires are to be applied to high performance field-effect transistors.

Discussion

Current voltage characteristics of a different sample (#223) in a wider drain voltage region is shown in Figure 8. This sample has very low efficiency in modulating drain current by the split-gate voltage application indicating low efficiency in modulating sublevels at the point contact by the gate voltage presumably because of the imperfect Schottky contact of split-gates. However, we were able to measure current voltage characteristics in a wide range of drain voltage without suffering from severe gate leakage current by exactly the same reason. Sudden increase of the drain current is observed at drain voltages of approximately 1V and 2V as indicated in the arrows in the figure. The sudden gate leakage current at around 2V of drain voltage contribute only partially to the drain current increase. The ohmic contact can be shown to have no effect on non-linearities in a separate four terminal measurement on the present sample and other sample (#252). Drain current non-linearities can be divided into two parts: namely sudden current increase and gradual saturation tendency of the drain current as a function of drain voltage. The sudden increase of the drain current at high drain voltage bias points are presumably assigned to DIBL effect. No gate leakage effect nor ohmic contact resistance are responsible of the non-linearity. There remains a question of the physical origin of the current saturation tendency overlapped with the sudden increase caused by DIBL in the "quasi-ballistic point contact" structure. The schematic energy band diagram under high drain bias of Figure 5 well illustrates the situation. At low drain bias, the device is reasonably well described as a 1D quantum wire and drain voltage has small effect on pulling down the 1D sublevels. At high drain bias, the energy band is strongly pulled down by the drain voltage as shown in the figure and the device is pretty well described as a quantum point contact (QPC) connected in series with a quantum wire under high bias. The electrical properties of the 1D and 0D point contact are basically the same. But the series resistance of the rest of the wire region under high field comes in to alter the electrical properties of the device under high bias. Since present (#231) device is in quasi-ballistic regime with the mean free path of 3450 Å, which is comparable to the device

- [13] S.J. Kester, C.R. Bolognesi, M.J. Ronka, E.L. Hu, and H. Kroemer, Extended Abstracts of Second International Symposium on New Phenomena in Mesoscopic Structures, p.56, 1992
- [14] K. Yoh, K. Kiyomi, H. Taniguchi, and M. Inoue, Jpn.J. Appl. Phys. vol.30, No.12B(1991) 3833
- [15] K. Yoh, K. Kiyomi, A. Nisuda and M. Inoue, Jpn.J. Appl. Phys. vol.31, No.12B(1992) 4515
- [16] P.F. Bagwell and T.P. Orlando, Phys. Rev. B40 (1989) 1456
- [17] R.R. Troutman, IEEE Trans. Electron. Devices, ED-26, No.4 (1979) 461
- [18] K. Yoh, T. Monuchi and M. Inoue, Jpn.J. Appl. Phys. vol.29, No.12(1990) 12445

FIGURE CAPTIONS

Figure 1. Schematic diagrams of deep mesa-etched split-gated InAs quantum wire device of sample #231.

Figure 2. Current voltage characteristics of the split-gated InAs quantum wire device (#231). Gate voltage is taken from -5V to 3V and drain voltage is taken from 0V to 1.5V by 0.1V step.

Figure 3. Conductance dependence on split-gate voltage at various temperatures of sample #231.

Figure 4. Current increment dependence on drain voltage of sample #231 measured at 80K. The slope corresponds to the conductance increment when the electron wave mode increases by unity.

Figure 5. Schematic diagram of lowest sublevels of electrons confined in 2-D (source and drain) and 1-D (wire) freedom of motion. Quantized current flows through 1-D sublevels in the present system when each sublevel crosses Fermi level by drain-induced barrier-lowering (DIBL). (a) represent the energy band diagram under zero bias and (b) represent the situation with high drain bias voltage.

Figure 6. Drain current dependence on the matrix of gate voltage and drain voltage. The trace of the current increment (mode change) point moves toward reduced gate voltages as the drain voltage is increased.

Figure 7. Current voltage characteristics of the sample #231 measured at 80K. The gate voltage is taken from -5V to 3V by 0.5V step. Each curve can be seen to leave a bundle of lower electron wave mode and switches to a higher mode bundle as the drain voltage is increased. This is a quantum wire version of drain-induced barrier-lowering effect.

Figure 8. Current voltage characteristics of a different sample #223 in a wider drain voltage region. This sample had very low efficiency in modulating drain current by the split-gate voltage application indicating imperfect Schottky contact of split-gates. Current voltage characteristics in a wide drain-voltage range were measured without suffering from severe gate leakage current by the same reason. Sudden increase of the drain current is observed at drain voltages of approximately 1V and 2V as indicated in the arrows in the figure.

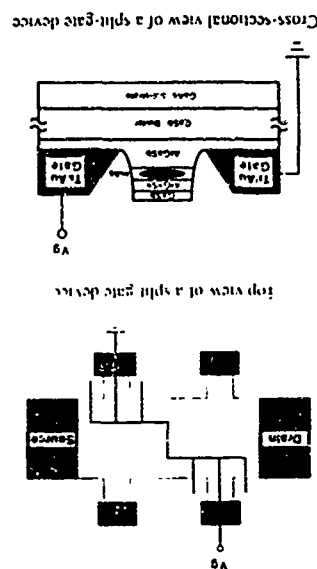


Figure 1

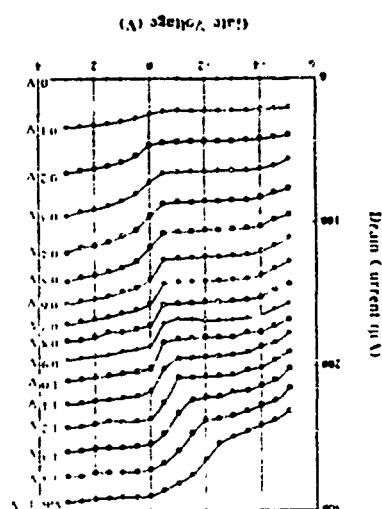


Figure 2

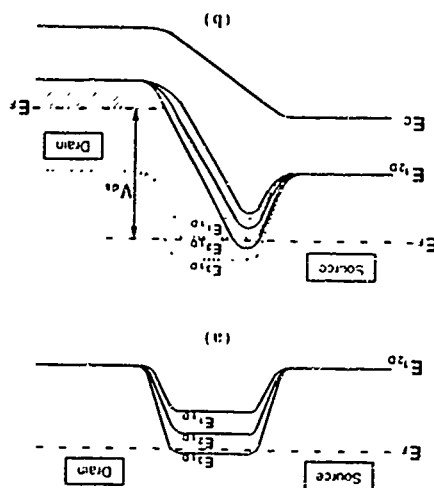


Figure 5

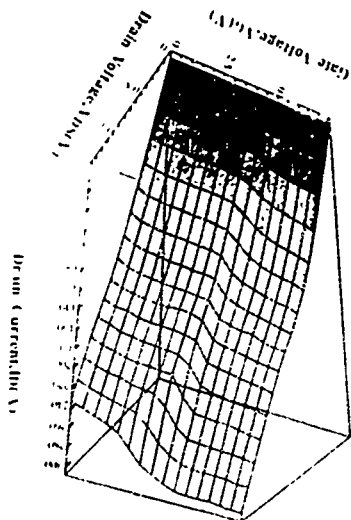


Figure 6

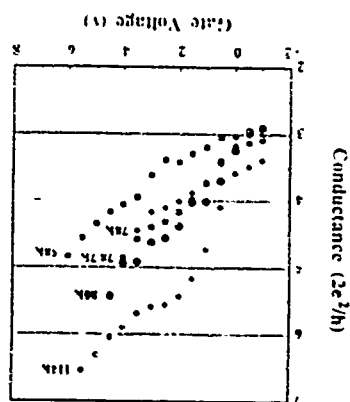


Figure 3

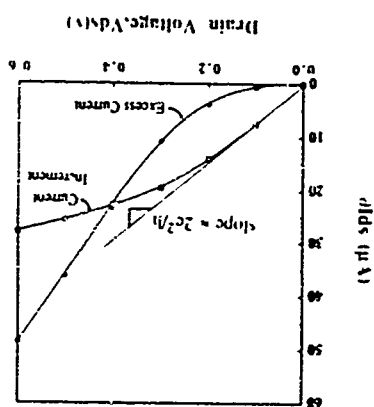


Figure 4

Transport Properties of Lateral Superlattices Grown on Vicinal GaAs (100) Surfaces

Axel Lorke and Pierre M. Petroff
Materials Department, University of California, Santa Barbara, CA 93106, USA

Abstract

We report on the growth and the transport characterization of sub-monolayer inserted quantum wells grown on vicinal GaAs (100) surfaces. The deposition conditions were carefully adjusted to ensure an ordered array of steps on the surface during growth. In magnetotransport measurements we observe that the Shubnikov-de Haas oscillations of the samples vanish at intermediate gate voltages. In the same regime, the resistance across the steps exhibits a pronounced plateau-like increase whereas the resistance along the steps remains essentially unchanged. Lateral miniband formation as well as the presence of a limited number of traps are discussed as possible explanations for the experimental findings.

Introduction

After the idea of vertical semiconductor superlattices was introduced in 1970 in the seminal paper by Esaki and Tsu [1], the concept soon was extended to lateral superlattices (LSL) [2]. In these systems, a two-dimensional electron gas (2DEG) is subjected to an in-plane (lateral) periodic potential with a period corresponding approximately to the Fermi wave length of the free carriers. Although the fabrication of LSL constitutes a great technological challenge, they are appealing under both technological and theoretical considerations. They provide for model systems in which basic solid state properties can be studied on a variable length scale. Furthermore, they allow one to apply electric and magnetic fields which can compete with the built-in potentials, a situation which is not, or only poorly, achievable in "real" solids.

First attempts to realize LSLs were undertaken by fabricating metal-oxide-semiconductor (MOS) field effect transistors on semiconductor substrates which were cut slightly off a major crystal axis ("vicinal substrates"). Many essential observations, establishing the existence of an artificial miniband structure, were made on these devices [3,6]. In MOS systems, however, the superlattice potential and the carrier density cannot be independently controlled. Furthermore, even for smooth or randomly corrugated oxide-semiconductor interfaces, intervalley scattering can lead to quasi-superlattice effects [4].

Epitaxially grown LSL on III-V semiconductors are expected to offer a number of advantages over MOS systems: (1) a considerably higher mobility, (2) a wide tunability of the lateral potential amplitude, largely independent of the carrier density, and (3) only small contributions to the miniband from the intervalley scattering [7]. A number of epitaxially grown LSL structures have been proposed and realized [7-11]. They are commonly fabricated by decorating (once or repeatedly) the regular step structure on a vicinal semiconductor substrate (e.g. GaAs) with a submonolayer of a different semiconductor (e.g. AlAs). Even though the preparation of a smooth and regularly stepped surface, as well as the submonolayer control of the growth, are of great difficulty, a number of novel physical properties have been reported on epitaxially grown LSL [8-11].

In the present work, we study the transport properties of submonolayer-inserted AlGaAs heterostructures at low temperatures with and without a magnetic field applied perpendicular to the plane of the LSL.

Design and Growth

The samples are grown by molecular beam epitaxy on GaAs (100) substrates, tilted towards the near (111)A plane by 0.5° . Such small tilt angles make the growth of a regularly stepped surface extremely difficult. The large terraces (average width $l \approx 320 \text{ \AA}$) require a large diffusion length of the impinging group III atoms to achieve "step-flow", necessary for step equalization. However, there are several advantages in choosing small angle vicinal substrates: Scanning tunneling microscopy shows that the raggedness of the step edges is given by the basic 2×4 reconstruction cell of length 16 \AA [12], which is already 20% of the terrace width l of a 2° vicinal substrate. Also, the randomness of the deposition process leads to a fluctuation of the terrace width $\Delta l/l \approx \sqrt{A/l}$ (with A

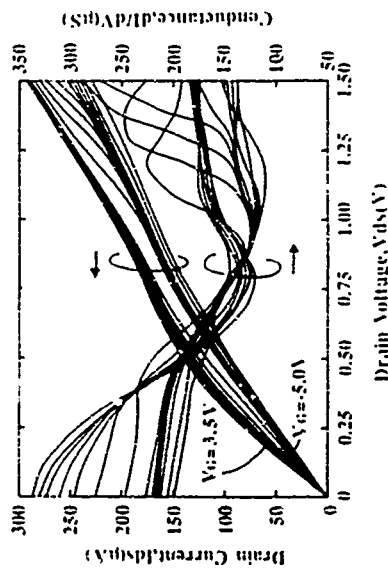


Figure 7

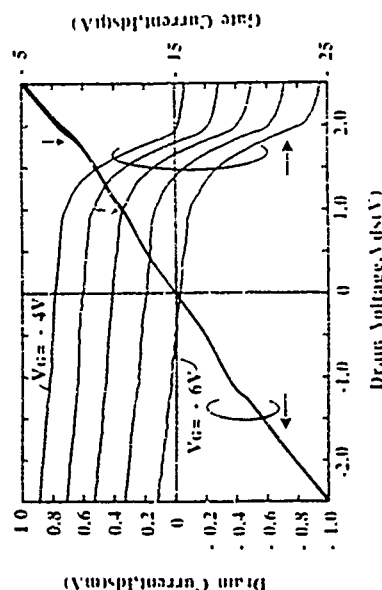


Figure 8

To assure step-flow mode, the samples are grown at a substrate temperature of $\approx 615^\circ\text{C}$ and at growth rates below $0.2\text{ }\mu\text{m/hr}$ for both GaAs and AlAs. The As flux is held at $3 \times 10^{-6}\text{ torr}$. The step-flow condition is verified by monitoring the absence of RHEED oscillations during growth. Shortly before depositing the AlAs submonolayer, a clear splitting of the 'specular' RHEED spot is observed, indicating a regularly striped surface. The complete growth sequence is then deposited: A smoothening superlattice of 20 periods (200 Å thick), a 200 Å thick GaAs buffer layer, 2500 Å short period superlattice consisting of 10 periods of 250 Å GaAs and 250 Å AlAs, a thick AlAs inserted quantum well (380 Å thick) and a 100 Å thick cap layer. The short period superlattice is grown through the interface. The growth of the quantum well is terminated by depositing a 100 Å thick AlAs submonolayer. AlAs are deposited to form a grading as determined by the temperature mobility of the samples as determined by Hall effect measurements.

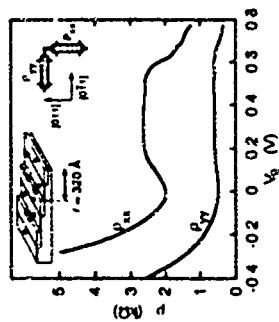


Fig. 1. Anisotropic resistivity of a LSL grown on (100) substrate tilted by 0.5° towards [111]A.

is as follows. On semi-insulating substrates are deposited 40 Å AlO_x, 40 Å AlAs, 7500 Å GaAs consisting of 50 Å Al_{0.98}Ga_{0.02}As + 50 Å GaAs; a thin layer of superlattices (40 Å AlAs + 40 Å GaAs); a Si-doped top layer (5 × 10¹² cm⁻², 230 Å). The well layer is schematically depicted in Fig. 1. The low temperature Hall measurements, two perpendicular Hall bars (*cfr.* inset in Fig. 1) are defined by standard lithography.

Experimental Results

All experiments are carried out at liquid He temperatures. Figure 1 shows the resistivity of a grating-inserted quantum well as a function of gate voltage, with the current (I) flowing across (p_{ax}) or along (p_{\parallel}) the steps. Close to the threshold voltage $V_g = -0.4$ V, in both directions the usual drop in resistance proportional to $1/(V_g - V_0)$ is observed. Between $V_g = 0$ V and $V_g = 0.5$ V, the resistance across the grating (p_{ax}) exhibits a pronounced increase of more than 30%. In the same regime, p_{\parallel} stays almost constant with only a small increase. At gate voltages above 0.6 V, both p_{ax} and p_{\parallel} decrease again with increasing gate voltage. Up to $V_g = 1.0$ V, only negligible gate leakage current $\leq 10^{-8}$ A is observed.

Figure 2 displays the magneto-transconductance of the same sample at different magnetic fields. Again, three distinct gate voltage regimes can be identified. Below $V_g = 0$ V (region I) the coexistent Shubnikov-de Haas oscillations are present. Their period is in agreement with the gate voltage - carrier density dependence derived

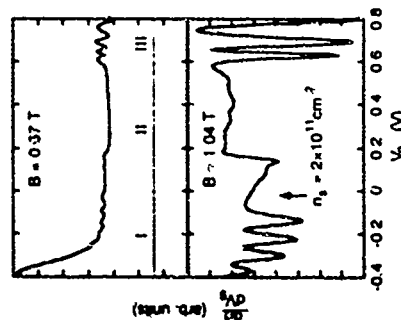


Fig. 2. Transconductance of a LSL at different magnetic fields. Between $V_g = 0$ V and $V_g = 0.6$ V, the SDH oscillation disappear

from the geometric capacitance of the sample. Between $V_g = 0$ V and $V_g = 0.6$ V (region II), the SDH oscillations completely vanish and a sharp, step-like structure at $V_g = 0.2$ V appears. For $V_g > 0.6$ V (region III), again SDH oscillations appear with a period which is almost identical with the one below. $V_g = 0$ V. In both regions I and III the period of the SDH oscillations shows the usual linear dependence on the magnetic field.

The (111) surface of GAs does not have a 4-fold symmetry, and even for just substrates of GaAs, the anisotropy of the surface is observed (for a systematic study of anisotropic island formation see, e.g. [13]). To investigate the possible influence of this inherent anisotropy on the observed transport features, we have grown a LSL on (100) substrate, tilted by 1° towards the [111] direction. The resistance of this sample as a function of gate voltage is shown in Fig. 3. It can be seen that the above sample and a planar-like increase in the gate voltage leads to a similar behaviour. We therefore conclude that the anisotropic transport along the [111] direction does not play a role in the observed transport. AJAs decorated steps along the [011] direction

It has been proposed [14] that the surface sinusoidal corrugations are oriented along the $[111]$ direction. However, apart from the difference in anisotropic magnetoelastic characteristics for both tilt orientations, the sinusoidal modulation in the sample tilted along the $[111]$ lateral direction is not observed.

Discussion

Many of the above experimental observations can be understood as resulting from an artificial mini-band structure caused by the periodic potential of the AlAs-decorated surface. Figure 4 schematically displays the Fermi surfaces expected for a 2DEG subjected to a one-dimensional periodic potential. For Fermi energies well below the gap (Fig. 4(b)), the Fermi surface is only little affected by the lateral modulation. In this regime, the LSL is expected to behave like an ordinary 2DEG. For $E_F = E_g$, the Fermi surface is strongly modified as shown in Fig. 4(c). Here, no closed orbits in k -space are possible, and hence no SDH oscillations are expected. In the gap, the states at the Fermi energy carry only little momentum along the z -direction, leading to an increase in μ_{eff} . For $E_F > E_g$, the second mini-band is occupied, closed orbits become possible again, and states with large k_z are available (Fig. 4(d)). Following this picture, the regions I, II, and III in Fig. 1 can directly be associated with the situations depicted in Fig. 4(b), (c), and (d), respectively. The increase in resistance and the vanishing of the SDH oscillations between $V_g = 0$ V and $V_g = 0.6$ V are then understood as a consequence of the Fermi energy being in the minigap of the LSL. Using the SDH oscillations in Fig. 2 as

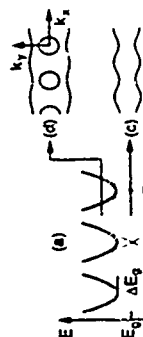


Fig. 4 Schematic representation of the dispersion (a) and different Fermi surfaces (b) - (d) of a lateral miniband

MBE Fabrication of GaAs Quantum Wire Structures on Mesa Stripes along the [001] Direction

M. Lopez, T. Ishikawa, T. Matsuyama, H. Tanaka, and Y. Nomura
Optoelectronics Technology Research Laboratory
5-5 Tokikodai, Tsukuba, Ibaraki 300-26, JAPAN

Abstract

We propose a novel mesa geometry for the fabrication of nanostructures by molecular beam epitaxy. We have found that (110) and (110) facets can be formed by GaAs growth on [001] oriented mesa structures. Smooth surface morphology and extremely low growth rate on the (110) facets are the advantages of using this mesa direction over the conventional [011] and [011]-cleaved directions. The width of the mesa top (100) plane, which is limited by the (110) facets, can be narrowed to the nanometer scale by GaAs growth. Quantum wire-like structures, as narrow as 30nm with a thickness of 30nm at its center, were successfully fabricated.

1 Introduction

Fabrication of quantum wire and quantum dot structures, in which charge carriers are confined in two and three dimensions, respectively, has attracted considerable attention recently. These low dimensional structures are expected to exhibit new physical properties which could be used for the development of new optical and electronic devices [1,2].

Crystal growth by metalorganic chemical vapor deposition on patterned or masked substrates has been used to fabricate the above structures [3,4,5]. Also, there have been several attempts for fabricating nanostructures by molecular beam epitaxy (MBE). For example, the MBE growth on (100) substrates patterned with mesa stripes along the [011] or [011] direction has been extensively investigated [6,7], however, the sidewalls formed during growth on these mesa stripes are often rough [8], thus complicating the fabrication of quantum wire structures.

In this work we have studied the growth mechanism of GaAs on [001] oriented mesa stripes. The growth of GaAs led to the formation of smooth

Even though many of the observed experimental features can well be understood within the framework of lateral miniband formation, a number of observations question this explanation. For example, the second miniband with its large curvature in k -space (cf. Fig. 4e) should exhibit more widely spaced subband oscillations than the lowest miniband [5, 6]. Clearly, this is not the case in Fig. 2. A possible explanation is that the presence of higher quantum well subbands influences the dispersion of the second miniband and lower its curvature [6]. Also, above $V_g = 0.6$ V, not the second miniband but the second subband might become occupied. Two-dimensional, self-consistent calculations of the band structure expected for our samples are presently under way to clarify these points.

A more important argument against the formation of a lateral miniband structure is the apparent insensitivity of the experimental observations on both the substrate vicinal angle and the vertical position of the AlAs submonolayer in the quantum well. Recently, a number of samples were grown with vicinal angles up to 4° . Even though for these structures the miniband gap is expected to lie well above Fermi energies that can be achieved in the (AlGa)As system, their transport properties closely resemble those of the 0.5° vicinal samples. At present, we do not have an explanation for this unusual behavior. On vicinal GaAs (110) surfaces, it has been observed that step bunching can lead to a local misorientation of 0.5° , independent of the microscopic miscut angle [17]. However, such a process is highly unlikely for the present structures, and no indication for step bunching has been observed in the RHEED pattern during growth.

As an alternate explanation for the transport anomalies, the presence of a limited number ($\sim 5 \times 10^{11} \text{ cm}^{-2}$) of traps in the samples might be considered, with the inserted AlAs submonolayer as a possible source. At intermediate gate voltages, these traps would become occupied, leading to a constant density of electrons in the 2DEG and hence to the absence of SDH oscillations. However, a number of experimental observations are incompatible with this explanation. (1) Illumination of the samples at low temperatures has only little effect on the transport properties of the samples. Both the increase in resistance and the vanishing of the SDH oscillations remain essentially unchanged. (2) A number of LSL samples were grown with differing doping schemes, growth temperatures, and growth interruptions before AlAs deposition. All these parameters have only little influence on the observed transport features. (3) Reference samples grown on just (100) substrates, with and without inserted AlAs, do not exhibit the above resistance anomalies. (4) In capacitance - gate voltage measurements, no indication for charge shifting within the samples could be observed.

Acknowledgments

We would like to thank A. Gossard, H. Sakaki, and K. Enslin for stimulating discussions. Financial support by AFOSR and the NSF Science and Technology Center for Quantized Electronic Structures (QUEST), grant #DMR 92-20007 is gratefully acknowledged.

References

1. L. Esaki and R. Tsu, *IBM J. Res. and Dev.* **14**, 61 (1970).
2. H. Sakaki, K. Waga, J. Hamada, and S. Saito, *Thin Solid Films* **36**, 497 (1976).
3. T. Cole, A. Lakham, and P. Sitic, *Phys. Rev. Lett.* **38**, 722 (1977).
4. L. J. Sham, S. J. Allen, Jr., A. Kamgar, and D. C. Tsui, *Phys. Rev. Lett.* **40**, 472 (1978).
5. T. G. Matheson, R. J. Higgins, *Phys. Rev. B* **25**, 2633 (1982).
6. T. Eitelbauer, A. Wixforth, and J. P. Kotthaus, *Z. Phys. B* **64**, 69 (1986).
7. L. J. Sham, *Appl. Phys. Lett.* **59**, 2010 (1991).
8. M. Tanaka and H. Sakaki, *Jpn. J. Appl. Phys.* **27**, L2025 (1988).
9. M. Tanaka and H. Sakaki, *Appl. Phys. Lett.* **54**, 1326 (1989).
10. J. Mauchisa, M. Tanaka, and H. Sakaki, *Appl. Phys. Lett.* **55**, 1214 (1989).
11. K. Tsutsumi, T. Honda, H. Saito, and T. Fukui, *Appl. Phys. Lett.* **58**, 376 (1991).
12. K. Pond *et al.*, *J. Vac. Sci. Technol. July/August 1993*, in press.
13. D. R. M. Williams and M. Krishnamurthy, *Appl. Phys. Lett.* **62**, 1350 (1993).
14. K. Yamaguchi and K. Okamoto, *Jap. J. of Appl. Phys.* **30**, L231 (1991); O. Brandt, L. Tapfer, and K. Ploog, *Surf. Sci.* **267**, 204 (1992).
15. T. Noda, J. Mauchisa, and H. Sakaki, *Surface Science* **267**, 187 (1992).
16. H. Sugawara, J. N. Schulman, and H. Sakaki, *J. Appl. Phys.* **69**, 2722 (1991).

(110) and (110) facets. It was found that the growth rate on these facets is extremely low. This is explained by the particular surface reconstruction of the (110) planes. Reducing the width of the (100) mesa top plane to the nanometer scale by GaAs growth, quantum wire like structures were fabricated.

2 Experimental

Mesa stripes aligned along the [001] direction were patterned on GaAs (100) substrates by conventional photolithography and wet chemical etching by $\text{NH}_4\text{OH}:\text{H}_2\text{O}:\text{H}_2\text{O}_2 = 1:1:20$. The pattern comprised mesas of different widths having a depth of $\sim 1\mu\text{m}$. The profile of the mesa stripe before growth is shown in the inset of Fig. 1. For a comparison, [011]- and [011]-patterned substrates with (111)A and (111)B exposed sidewalls, respectively, were also prepared and mounted side by side with the [001] patterned substrate on a molybdenum block. GaAs layers were grown under a variety of MBE growth conditions with a constant growth rate of $0.25\mu\text{m}$ and a substrate rotation of 10 rpm .

3 Results and Discussion

The growth of GaAs on [001] oriented mesa stripes led to the formation of (110) and (110) facets in all the growth conditions used in this work. The surface of these facets were very smooth as compared with the facets formed on the [011]- and [011]-mesa stripes[9].

Figure 1 shows (011) cross-section SEM photographs of 4000\AA -thick GaAs layers grown on [001] oriented mesa stripes under different growth conditions. 150\AA -thick AlAs layers were introduced as markers and are observed as dark lines in the photographs. The inset shows the shape of the mesa stripe before growth. GaAs growth led to the formation of (110) and (110) facets in all cases, however, (310) and (310) facets were also formed at low growth temperatures or high As pressures. These facets were formed in cases where bump like regions (indicated by arrows in Fig. 1) appeared on the (100) plane. The bump-like regions, formed by the diffusion of Ga atoms from the (110) facets, were not observed at high temperatures and/or low As pressures; growth conditions where the Ga migration length is expected to be large. Therefore, the development of the (310) facets seems to be associated to a reduction of the Ga migration length on the (100) plane at low growth temperatures and/or high As pressures.

Figure 2(a) shows the GaAs growth rate on the (110) facets relative to that on the (100) plane. The measurements were performed using $\sim 1\mu\text{m}$ wide (110) facets of $10\mu\text{m}$ wide mesa stripes in order to minimize the effects of a possible diffusion of Ga atoms from the (110) to the (110) facet, and vice versa. The GaAs growth rate on the (110) facets drastically decreased by decreasing the As pressure and/or increasing growth temperature. Figure 2(b) shows the width, $\%$, of the (110) facets after one hour of GaAs growth. The

(110) facets were wider when the growth was performed under low As pressures and/or high temperatures. In general, the formation of facets during growth is caused by the different growth rates on different crystallographic planes. Facets on which the GaAs growth rate is low are preferentially formed. Therefore, as observed in Figs. 2(a) and (b), the (110) facets were more easily formed when the growth rate on these planes was minimized. The (110) facets were narrow when the growth on these facets increased such that could become comparable to that of other shallow angle facets like the (310). As shown in Fig. 2(a), at 620°C under an As pressure of $0.9 \times 10^{-4}\text{ Torr}$, the growth rate on the (110) facets was two orders of magnitude lower than that on the (100) plane. The low growth rate on the (110) planes could be caused by the stable nature of the (110) surface.

Although the (110) plane is composed of an equal number of Ga and As atoms, the surface reconstructs in such a way that As atoms rotate 27° out of the surface and the Ga atoms inwards. Each As surface atom moves towards an s^2p^2 arrangement with three p electrons forming bonds with its three nearest neighbors and two s electrons forming filled s^2 orbitals. Each Ga atom moves toward an sp^3 configuration and uses all of its three electrons to bond with its nearest neighbors[10]. Since the s^2 orbitals of As surface atoms are satisfied, Ga atoms impinging on the (110) planes find few nucleation sites, and are expected to have a large migration length. On the other hand, the low chemical activity of the surface Ga atoms forming the sp^3 configuration yields to a low sticking coefficient of As on the (110) surface; thus a high As flux is therefore necessary in order to obtain significant growth on the (110) facets.

At high growth temperatures or low As pressures, the mobility of Ga atoms on the (110) facets is further increased and most of the Ga atoms impinging these facets can thus more easily diffuse to the adjacent (100) plane. As a result, the width of the mesa top (100) plane, which is limited by the (110) and (110) facets, can be reduced by the GaAs growth using such migration effects. Using an As pressure of $0.9 \times 10^{-4}\text{ Torr}$ and a growth temperature of 600°C , we fabricated quantum wire like structures. The width of the (100) facet was narrowed to about 50nm and then an AlAs/GaAs quantum well was grown. Figure 3 is a cross sectional STM photograph of the resulting wire structure formed on the top of the mesa stripe. The quantum wells on the (110) facets are very thin due to the low GaAs growth rate on these facets, while the AlAs barrier layers, with a considerable thickness, cover them due to shorter migration length of Al atoms. In this figure the wire structure is observed along the [011] cleaved direction, which is deviated by 45° from the [001] direction. The real size of this structure being as narrow as $\sim 30\text{nm}$ with a thickness of $\sim 30\text{nm}$ at its center.

4 Conclusions

The growth mechanism of GaAs by MBE on [001] mesa stripes was described.

We found that smooth (110) facets can be formed on this novel mesa geometry, and that the GaAs growth rate on these facets is extremely low using these unique characteristics. We fabricated quantum wire-like structures along the [001] direction

Acknowledgements

The authors would like to acknowledge stimulating discussions with Dr. Y. Katayama, Dr. M. Tamura, and Dr. H. Hayashi.

References

1. Y. Arakawa, K. Yabala, A. Yariv, Appl. Phys. Lett. 45, 950 (1984)
2. H. Sakaki, Jpn. J. Appl. Phys. 19, L735 (1980)
3. E. Kapon, K. Kash, E. M. Clausen Jr., D. M. Ilwang, and E. Colas, Appl. Phys. Lett. 60, 477 (1992)
4. T. Fukui, S. Ando, I. Honda, and T. Toriyama, Surf. Sci. 267, 233 (1992)
5. Y. Nagamune, S. Tsukamoto, M. Nishiohara, and Y. Arakawa, J. Cryst. Growth. 126, 707 (1993)
6. F. S. Turco, S. Simony, K. Kash, D. M. Ilwang, T. S. Ravi, E. Kapon, and M. C. Tamargo, J. Cryst. Growth. 104, 766 (1990)
7. Y. Makamura, S. Koshida, M. Sachiya, H. Kano, and H. Sakaki, Appl. Phys. Lett. 59, 700 (1991)
8. T. Takamori, K. Watanabe, and T. Kamiyoh, Electron. Lett. 28, 2708 (1992)
9. M. Lopez, T. Ishikawa, and Y. Nomura, submitted to Jpn. J. Appl. Phys.
10. S. Y. Tong and W. M. Mei, J. Vac. Sci. Technol. B2, 393 (1984)

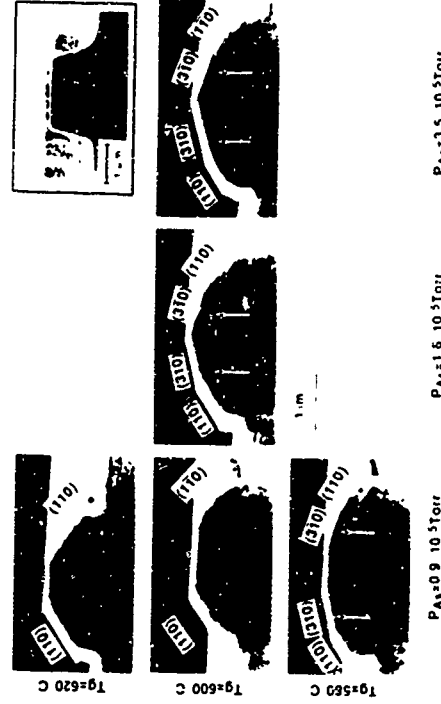


Fig. 1 Cross-sectional SEM photographs, taken along the [011] direction, of 150Å-thick AlAs layers grown under different conditions on [001]-oriented GaAs substrates. The AlAs layers were introduced as markers and observed as dark lines in the photographs. The arrows indicate the bump-like shaped regions which are formed by diffusion of Ga atoms from the (110) facets. The photograph in the inset shows the shape of the mesa stripe before growth.

MoP2

ALTERNATE METHOD TO PRODUCE QUANTUM WIRES USING DISLOCATION SLIPPING

C. GUASCH¹*, F. VOILLOT², M. GOIRAN³, J.P. PEYRADE⁴, E. BEDEL¹,
C. FONTAINE⁵, H. ATMANI⁶, A. ROCHER⁷

¹Laboratoire de Physique des Solides, LA074, 31077 TOULOUSE Cedex

²LAAS du CNRS, 7, av du Colonel Roche, 31077 TOULOUSE Cedex

³CNRS-LOF, BP 4347, 31055 TOULOUSE Cedex

ABSTRACT

We propose to generate quantum wires by a new method based on single crystal plasticity properties. In this method, the shift induced by the controlled dislocation slipping is used to cut a 2D structure in 1D structures. This method is not material specific and can be applied to any structure grown on crystalline substrates. We have used deformation by bending to control dislocation motion at high temperature on a 5 nm GaAs single quantum well MBE grown on a (100) GaAs substrate. Experimental observations show the efficiency of the method. PL spectra of the deformed structure exhibits a blue shift in regard to the single quantum well PL spectra, corresponding to an additional lateral confinement.

INTRODUCTION:

In many fields of physics the reduction of dimensions has become a challenge. This is particularly true for semiconductors where the nanometer scale is now considered since control of layer deposition by molecular beam epitaxy (MBE) is now nearly perfect. Although many techniques have been proposed either to pattern existing two dimensional (2D) structures or grow directly 1D or 0D structures, none has reached such a degree of perfection. We propose a new technique applicable to any crystalline system to obtain a sharp lateral confinement without loss of material. If used with appropriate conditions it leaves the active region free of damage and thus keeps the optical and transport properties of the system unaltered.

PRINCIPLE:

In principle the process is very simple: if we submit a single crystal to a stress higher than its elastic limit it will be plastically deformed. For adapted experimental conditions of temperature and strain rate it deforms by dislocation slipping. As observed by "in situ" transmission electron microscopy (TEM), randomly distributed dislocation

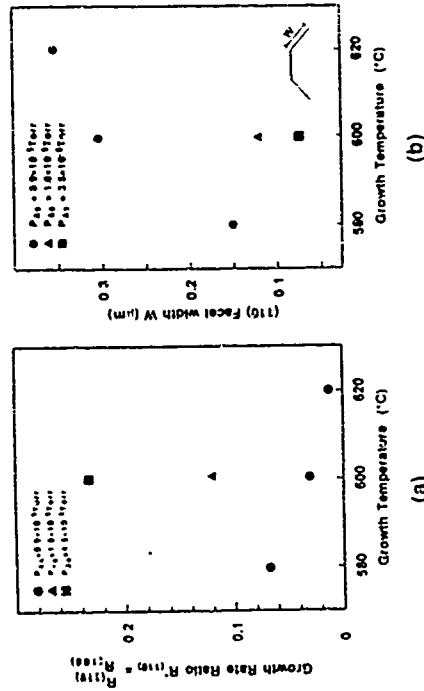


Fig2 Growth temperature and As pressure dependence of (a) GaAs growth rate on the (110) facet relative to that on the (100) facet, (b) width of the (110) facet after one hour of GaAs growth.

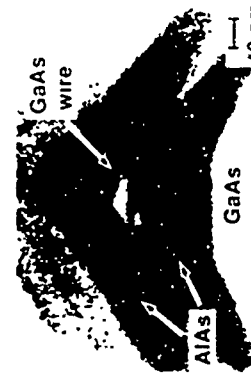


Fig.3 Cross-sectional SEM photograph, taken along the [011] direction, of a quantum wire-like structure.

sources in the volume or near the surface generate loops in the active slip planes [1]. The size of the loop increases in this slip plane until it reaches the surface where it creates a slip trace, i.e. a step, characterized by its Burgers vector b . During this process the crystal periodically is restored in the volume (Fig. 1). When a source has emitted n loops a slip trace having a height nb is created at the surface. If we consider an epilayer of thickness e in the crystal it will be cut in fact shifted by this process if $e \leq nb$ (where b is the component of b along the growth direction). So, if one can control the slip by choosing crystal orientation, stress conditions, temperature and source density (by artificial creation for example) one obtains the perfect tool to pattern a 2D structure in 1D or even 0D keeping all the active layer. We should mention here that these very straight and long slip traces at the surface can also be used as an alternative to patterned or misoriented substrates for direct growth techniques [2].

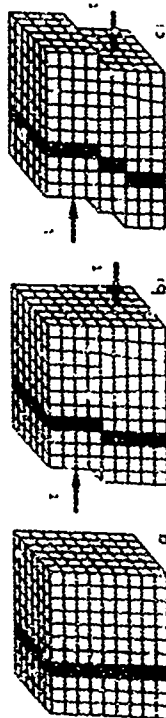


Fig. 1 Simple scheme for dislocation slipping: across a perfect cubic crystal a buried one monolayer of different composition is represented in dark (slipping structure a - one (b) and two (c) dislocation slippings). A wire is produced in figure 1c

DIFFERENT DEFORMATION CONDITIONS

The simplest configuration to realize this principle in spialent structure is the uniaxial compression

The edges of the parallelepipedic test-bar are cut along $\langle 111 \rangle$ and $\langle \bar{1}\bar{1}\bar{1} \rangle$ directions. A compressive stress is applied along the $[111]$ direction of the test-bar, in order to achieve a simple slip condition for deformation. In this configuration, the Schmidt factor of the 111 system is the highest, thus it will be the more efficient [2].

When the single crystal is stressed, dislocation sources emit loops formed by six dislocation segments (two screw dislocations, two $60^\circ \alpha$ and two $60^\circ \beta$). These loops increase with the stress and propagate through the crystal. When the dislocation loop reaches the edges of the sample, a $\langle 111 \rangle$ plane slips along the $[111]$ direction, leaving on the $\{111\}$ surfaces a step characterized by the Burgers vector of the dislocation. The direction of this step is $\langle 111 \rangle$.

So we have used n type GaAs single crystals elaborated by horizontal Bridgman in 10^{15} cm^{-3} . The mean residual dislocations density is 10^8 m^{-2} . The sample size is $12 \text{ mm} \times 2.7 \text{ mm} \times 3.5 \text{ mm}$. All faces are mechanically polished. In order to perform TEM on

surface replica, the $\{111\}$ face is mechanochemically polished. The chosen temperature is 673 K and the rate is $2 \cdot 10^{-7} \text{ s}^{-1}$.

Replica of such $\{111\}$ surface is observed by TEM. Fig. 2 shows a relatively homogeneous region over $20 \mu\text{m}^2$ area, in which the height value is 200 \AA and the step width 400 \AA . In some less homogeneous regions steps with height between 200 \AA and 400 \AA and width between 400 \AA and 600 \AA are observed.

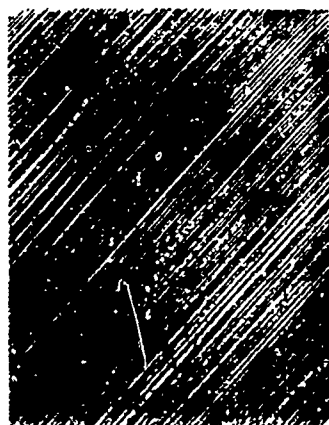


Fig. 2 TEM observation of the $\{111\}$ surface

Those results confirm that deformation of GaAs single crystal, in simple slip conditions, can generate step-like surfaces with geometrical characteristics compatible with quantum confinement. Step heights are about 10 times greater than the lattice width, so subsequent deposition by MBE on such surfaces would lead to the generation of quantum lines in an easy way.

The main problem in this deformation process is the heterogeneity of the steps size distribution on the surface on a large scale due to secondary slip, sources distribution and local hardening, so these structures will be useable only with local characterisation techniques.

This very simple situation can not be used since only MBE growth on $\{001\}$ substrates are available [3]. This case is more complicated but it is possible to choose two favourable stress orientations in which four slipping systems are activated which have in each case parallel traces on the $\{100\}$ surface: a stress applied along $[110]$ favours $(\bar{1}11)$, (111) , (111) , (011) and (111) slip systems, in the same way, a stress along $[110]$ will favour (111) , (111) , (111) , (011) and (111) slip systems.

We have used a pure bending tests which is a simple way to apply tensile stress in pure bending no cutting stress is involved, only a bending moment exists at the surface. In addition from the $\{100\}$ face to the $\{001\}$ one, the stress varies linearly from tension to compression. This situation will activate dislocation sources at the surface or close to the surface. Moreover the neutral plane at the center of the sample acts as a barrier for dislocation slipping which is a more favourable case to avoid inhomogeneities. The stress

orientation chosen is $[11\bar{2}]$ in order to favour the development of 100α dislocations sources from the surface on which the active layer is grown. The temperature is 673 K and the surface strain rate is about 10^{-5} s^{-1} in order to favour slipping deformation mechanisms [14]. We have tried both homogeneous four point bending and inhomogeneous three point bending.

SAMPLE CHARACTERIZATION

Single quantum wells (SQW) were grown by MBE on a $(100)\alpha$ GaAs semi-insulating substrate. They present a (0.15 ± 0.01) monolayer between two $\text{Ga}_{0.45}\text{Al}_{0.55}\text{As}$ barriers of thickness d and a cap layer of thickness e d varies from 30 nm to 100 nm and e is typically 20 nm.

RESULTS

Atomic Force Microscopy (AFM)

Fig. 1a displays a three dimensional image of a sample deformed by four point bending by an amount of 1.5%. The terraces created are defined by 125 parallel straight lines which continue throughout the sample as observed by optical microscopy. The average step height is 2.5 nm corresponding to 7 elementary slipping steps of the $\{111\}$ plane. Two different slipping planes from the $\{111\}$ family with parallel slip traces have been involved in this process. This explains why the surface does not present the aspect of a simple monotonic staircase.

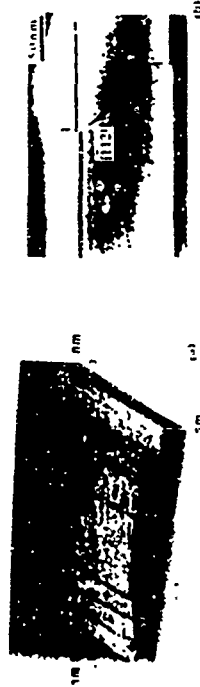


Fig. 1. (a) Indentationless AFM image of the $(001)\alpha$ GaAs surface after four point bending deformation (b) 2D AFM image of the same surface.

Transmission Electron Microscopy cross section (TEM)

Fig. 2b is an TEM micrograph of a deformed SQW. A sharp slip $\{111\}$ family is clearly revealed. A corresponding V-dot is observed at the barrier-buffer interface. The $\{111\}$ direction is $[11\bar{2}]$ which confirms that the slipping planes belong to the $\{111\}$ family. It should be mentioned that no dislocation is left inside the MBE 2D structure. Dislocations are only observed at about 1.5 μm from the surface.

Photoluminescence (PL) measurements

PL spectra were taken at 1.5 K on SQW before and after deformation with a 700 nm laser line excitation. After deformation the emission peak intensity is only slightly decreased. No blue shift is detected on samples with deformation smaller than 2%, which is expected due to the distance between two cuts inducing very large wires (150 nm) for larger deformations (in three points bending) we observed a blue shift which increases with the deformation according to calculations on the expected wire width for a given deformation. Typical spectra before and after deformation are presented on Fig. 4.

Preliminary XRD results allow us to evaluate the maximum tensile stress close to the surface at 10 MPa along the $[110]$ direction. The effort of uniaxial tensile stress is to reduce the active gap value E_g . Thus the measured PL spectra could be the result of two opposite contributions: a uniaxial tensile stress along $[110]$ and an additional lateral confinement with a 2.5 nm period along the same direction.

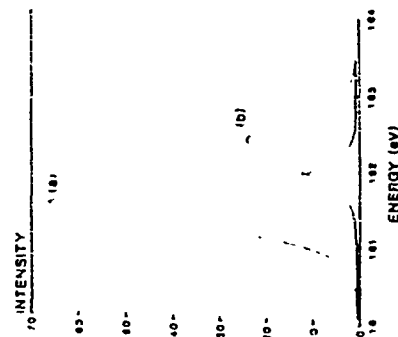


Fig. 4. PL spectra before (a) and after (b) a three point bending deformation.

ADVANTAGES OF THE METHOD

The different results exposed here confirm that quantum wires have been obtained by the proposed method and show that physics can be an alternate for quantum wires or quantum dots production. Our method has many advantages: 1) theoretically the critical toughness is no more than the atomic step; in principle there is no limitation in the size of the wire; neither in width nor in length; in simplicity and low cost; quantum wires are obtained by growing a 2D structure with an atomic scale tool (the dislocation) so there is absolutely no loss of active material; a very large field of application since only dislocation slipping is used; this method is basically applicable to any material or structure.

MoP3

Formation of N-AlGaAs/GaAs Edge Quantum Wire on (111)B Micro Facet by MBE and Magnetic Depopulation of Quasi-One-Dimensional Electron Gas

Y. Nakamura, M. Tsuchiya, J. Motohisa, H. Niige, S. Koshida, and H. Sakaki

Quantum Wave Project, JRPV, 4-3-24-302 Komaba, Meguro-ku, Tokyo 153, Japan, and Research Center for Advanced Science and Technology, University of Tokyo, 4-6-1 Komaba, Meguro-ku, Tokyo 153, Japan

Abstract

An edge quantum wire (EQWI) structure with a feature width of 120 nm was successfully prepared on (111)B micro facets; the structure was fabricated by an ensemble of several growth modes in molecular beam epitaxy (MBE) on a patterned (001) substrate without resorting to any advanced lithographic technique. A clear deviation from the linear relationship is observed in a Landau plot of magnetoresistance at low magnetic fields, providing the first evidence of magnetic depopulation of one-dimensional subbands in a facet EQWI. The sheet electron concentration measured is $5.4 \times 10^{11} \text{ cm}^{-2}$, which corresponds to the linear concentration of $4.8 \times 10^6 \text{ cm}^{-1}$, and mobility is $3 \times 10^4 \text{ cm}^2 \text{ V}^{-1} \text{ s}^{-1}$ or higher. These values indicate a high crystal quality of the facet EQWI thus prepared.

The edge quantum wire (EQWI) scheme provides a feasible way of forming very fine wire structures without requiring advanced fine lithographic technique [1]. The achievable lateral dimensions are expected to be far below 100 nm and will allow large separation of subband levels, leading to the various novel electronic properties predicted in the strongly confined quantum wire regime [1]. Fabrication of such EQWI requires two basic steps: the formation of edge surfaces in undoped quantum well (QW) layers [1], and the subsequent

long as we are dealing with a crystalline substrate, only its plastic properties have to be known and its plastic deformation has to occur at reasonable temperature. Nevertheless it has to be pointed out that plasticity studies are still strongly needed in order to control the homogeneity and the location of dislocations sources.

REFERENCES

- [1] Zaitsev M., Vaillet F., Pevrard J. P., Couret A. and Couquille R. Phil. Mag. A 65 (1) (1992) 195
- [2] Vaillet F., Guisan M., Gmouch C., Pevrard J. P., Dinh L., Rocher A., Bedel H. special issue of Journal de Physique III: Microelectronique et Optoelectronique III-V*, 1993 to be published
- [3] Karimouza M. Thesis University of Lille (France), 1984
- [4] Bouvier P. Thesis University of Poitiers (France) 1988
- [5] Poljak F. H. and Cardona M. Phys. Rev. B 22 (1968) 816

overgrowth of an electron supply layer onto the edge surface (2). Several methods have been proposed for those two processes.

The use of cleavage for the edge formation was first demonstrated by Pfeiffer et al. They fabricated a planar superlattice [2, 3] on a (011) surface using molecular beam epitaxial (MBE) overgrowth. Mochizuki and Sakai have formed an EQWI by this method and observed the magnetic depopulation (MD) of one-dimensional subbands [4], providing the first clear proof for quasi-one-dimensional electron gas (IDEG) formed in an EQWI. In this approach, however, the area of cleavage plane is extremely small, which makes the subsequent processing rather difficult, particularly for future device application.

As an alternative method, Fukui et al proposed the use of an epitaxially grown (001)-(111)B facet structure and demonstrated the formation of an EQWI by crystallographically anisotropic metalorganic chemical vapor deposition (MOCVD) [5]. Unlike the cleaved-edge-overgrowth (CEO) method this facet approach has advantages in that a large number of quantum wires can be prepared over the entire wafer by one consecutive run of epitaxial growth and the electrodes to the wires can be prepared much more easily by using standard lithography. In their sample, however, it was difficult to prevent the formation of a two-dimensional electron gas (2DEG) at (001) hetero-interface, and the parallel conduction of the 2DEG masked key features of IDEG on (111)B interfaces.

It was earlier suggested that a high surface selectivity of growth rates in MBE on a patterned substrate may be used to form a facet EQWI [6]. This MBE approach may have an advantage over the MOCVD method since, in addition to the crystallographic anisotropy, one can control the position and concentration of dopants by the oblique deposition technique and thereby prevent an undesirable parallel conduction outside an EQWI channel. In this paper, we report a successful fabrication of a EQWI by MBE and the first observation of MD in a facet EQWI. We describe a rather sophisticated ensemble of various MBE growth techniques employed to form the EQWI whose structure is schematically shown in Fig. 1 (a).

First, a line-and-space geometry of 2 μm depth was prepared on a SiO_2 -clad Cr-O doped semi-insulating (001) GaAs substrate by photolithography and SiCl_4 reactive ion etching [7]. The line width and spacing were both 5 μm . The stripes were set 2-3 degrees off from the (110) direction to provide eventually off-oriented (111)B facet surfaces where both morphology and Si donor activation are known to be better [8, 9]. After degreasing the

patterned substrate, the SiO_2 mask layer was removed to expose the mesa plateau. The substrate thus patterned was mounted on a Mo holder together with two flat (001) substrates. Those flat substrates were used to prepare the sample to monitor transport properties of electrons along the (001) interfaces.

Next, MBE growth of GaAs, AlAs, and AlGaAs layers was performed on the mesas in the following way to form the EQWI structure by paying attentions for crystallographic anisotropy and beam flux geometry (see Fig. 1 (a)). The growth rate of GaAs on flat (001) was set at 0.26 $\mu\text{m/h}$ by monitoring the oscillation of reflective high energy electron diffraction on unpatterned (001) substrates. The As/Ga flux ratio measured with a flux monitor was 26 on (001). Aluminum content x in $\text{Al}_x\text{Ga}_{1-x}\text{As}$ was 0.32 on (001) if grown with the Mo holder in rotation. The substrate was always rotated except in the last phase, where the oblique deposition was used to prepare GaAs QW and AlGaAs spacer, and to perform the δ -doping of Si. Substrate temperature (T_{sub}) was varied in the range of 580°C-665°C.

MBE was started with the deposition of undoped GaAs layer (260nm) at $T_{\text{sub}} = 580^\circ\text{C}$ to form a trapezoidal GaAs structure of Fig. 1 (a), which consists of (001) and two (111)B facets. This temperature is suitable to obtain a sharp facet corner at the boundary of (111)B and (001) planes. Then, a GaAs layer of 74nm was deposited, while T_{sub} was raised up to 665°C with the rate of 5°C/min to achieve good surface morphology. At 665°C, 50nm GaAs and 200nm AlGaAs were grown further. Although the growth at this temperature leads to somewhat rounded facet corners, it is effective to improve the quality of AlGaAs and also to reduce the outgassing from the substrate heater during the subsequent growth. Next, T_{sub} was gradually reduced to 580°C with the rate of 5°C/min, while 108nm AlGaAs was grown giving a rather sharp facet corner. Then to complete the bottom barrier, 100nm AlGaAs was grown. The (111)B surface was kept smooth in the growth of these AlGaAs layers. These AlGaAs layers are thick enough to prevent the accumulation of 2D electrons at the first AlGaAs/GaAs heterojunction.

Then the whole structure was covered with two-monolayer GaAs to prevent the oxidation of AlGaAs surface. Next, the substrate holder was adjusted so that the As beam was incident almost parallel ($\sim 0^\circ$) to the left facet plane of (111)B as shown in Fig. 1(a). After this adjustment 100nm GaAs layer was deposited to form a GaAs QW layer on the trapezoidal base as shown in Fig. 1 (a) and (b). Because of its low incident angle, the flux of As beam on the

(111)B surface was extremely low. Under this condition, the migration of Ga adatoms from the (111)B face to the adjacent (001) surface is very efficient, resulting in an extremely low growth rate ($\sim 9\text{nm/hr}$) on (111)B surface, which is 1/30 of that on the (001) surface [6]. As a result, the GaAs layer grown on the (111)B gets narrow ($\sim 3\text{nm}$) enough to prevent the accumulation of the 2D electrons. On this structure an undoped AlGaAs of 120nm was deposited as a thick spacer layer primarily on (001) plane, while the thickness of the AlGaAs spacer on the (111)B plane is about 20nm. Although the incident As flux and GaAs growth rates were both very low on the (111)B, it was found that the concentration of contaminating impurities at the (111)B surface was tolerably low and the crystal quality near the (111)B surface was rather high. This is possibly because the effective As/Ga flux ratio on the (111)B is almost equal to that on the (001) plane, as the effective population of Ga atoms is reduced by the inter-surface diffusion.

After the formation of the AlGaAs spacer two-monolayer GaAs was deposited to passivate the surface. Then δ -doping of Si donors was done with the oblique deposition technique, in which Si beam was adjusted to be incident almost normal ($70\sim 75$ degrees) to the left (111)B plane and almost parallel ($15\sim 20$ degrees) to the top (001) plane, as shown in Fig. 1 (a). In this geometry, the areal density of Si donors on the left (111)B facet is $\sim 2.5 \times 10^{12} \text{ cm}^{-2}$ and is about three times as high as that ($\sim 8 \times 10^{11} \text{ cm}^{-2}$) on the (001) plane. During the process of Si δ -doping, T_{sub} was raised up to 620°C to enhance the activation of Si donors on (111)B [9]. Because of the thick spacer layer and the low Si concentration on the top (001) plane, the formation of 2D electrons on (001) heterointerface was successfully prevented, while the supply of 1D electrons in the EQWI on (111)B plane was achieved. Finally, a 100nm undoped AlGaAs layer, a 4nm N-AlGaAs with Si dopants of $3 \times 10^{18} \text{ cm}^{-3}$, and an 30nm undoped GaAs cap layer were successively grown. This N-AlGaAs layer was inserted to prevent the surface depletion effect. During the growth of AlGaAs layer Al mole fraction x was maintained between 0.3-0.5 on both the left (111)B plane and the top (001) plane to avoid both parallel conduction of electrons and excessive oxidation in the air. For this purpose, the AlGaAs layers were grown at T_{sub} of 620°C where the inter-surface migration of Ga adatoms is relatively small. Figure 1 (c) shows a cross-sectional image taken by scanning electron microscope (SEM) for the edge-exposed QW structure thus prepared. The width W of the QW in (111)B is $\sim 120\text{nm}$. Its schematic structure is also shown in Fig. 1 (b).

To study the electron transport in this EQWI structure, we formed two AuGe ohmic electrodes using the lift-off technique by which fifty wires were connected in parallel. The electrode spacing L was $10\mu\text{m}$. The sample was conductive without light illumination, at 4.2K . The reference samples grown on (001) planes were almost insulating at 77K in dark, indicating the absence of 2D electrons in the (001) plane. We measured the transverse magnetoresistance of the EQWI sample by applying a field B from different angles with respect to the (111)B plane. A Clear Shubnikov de Haas (SdH) oscillation was observed for $B > 1.7\text{T}$ as shown in Fig. 2 (a). The oscillation is found to be determined almost by the magnetic field component B_{\perp} normal to the (111)B plane, indicating that the conductivity is due to the electrons accumulating at the (111)B heterojunction. The Landau plot for B normal to the (111)B is shown in Fig. 2 (b). A clear deviation from the linear relationship is seen for B less than 3T . This is due to the magnetic depopulation of 1D subbands and proves the quasi-one-dimensionality of electrons in our facet EQWI. The electron concentration N_{2D} derived from the Landau plot at high field was $5.4 \times 10^{11} \text{ cm}^{-2}$, which corresponds to the dashed line in Fig. 2 (b). Electron mobility μ estimated from the two-terminal resistance R (850Ω) was $3 \times 10^4 \text{ cm}^2 \text{ V}^{-1} \text{ s}^{-1}$ or higher. Note that R is $L/(en_{2D}\mu W_{\text{eff}})$, where n (~ 50) is the number of EQWIs and W_{eff} the effective wire width [10].

Finally, we analyze the Landau plot and estimate the effective width W_{eff} . If a parabolic potential is assumed along the lateral direction, the position of magnetoresistance maxima can be easily calculated [10]. The Landau plot of Fig. 2 (b) was best explained when we set the linear electron concentration N_{1D} to be $4.8 \times 10^6 \text{ cm}^{-1}$ and the quantized energy separation $\hbar\omega_c$ to be 3meV as shown by the cross marks in Fig. 2 (b). The effective width W_{eff} of the wire evaluated from N_{1D}/N_{2D} is 90nm , which is a little smaller than the width W ($\sim 120\text{nm}$) determined by SEM. The origin of this small discrepancy is not clear but may be related to the fact that our EQWI has a wedge-like structure of Fig. 1, where the effective confinement size may differ from the geometrical size. The calculation based on the square potential, which seems more suitable in our EQWI, has shown that non-linear features of the observed Landau plot are not significantly altered even when the square potential is used. This point will be clarified in the future work, in which Fermi level is varied systematically by the gate voltage.

In summary, a 120nm wide edge quantum wire has been successfully prepared by MBE

on a (111)B facet. The magnetic depopulation of one-dimensional subbands has been demonstrated in the facet EQWI for the first time.

Quantum wire samples were prepared at Process Center of RCAST, University of Tokyo. We thank Dr. S. Fukatsu, Mr. Y. Kadota, Dr. H. Kano, Prof. T. Ikoma, Dr. T. Saito, and Mr. H. Yano of Sumitomo Electric Industries for their cooperations. A part of this work is supported by Grant-in-Aid for Scientific Research from the Ministry of Education, Science and Culture.

References

- [1] H. Sakaki, *Jpn. J. Appl. Phys.* **19**, L735 (1980).
- [2] L. Pfeiffer, K. W. West, H. L. Stormer, J. P. Eisenstein, K. W. Baldwin, D. Gerahon and J. Spector, *Appl. Phys. Lett.* **56**, 1697 (1990).
- [3] H. L. Stormer, L. N. Pfeiffer, K. W. Baldwin, K. W. West and J. Spector, *Appl. Phys. Lett.* **58**, 726 (1991).
- [4] J. Motohisa and H. Sakaki, in *Proceedings of the 21st International Conference on the Physics of Semiconductors* (World Scientific, to be published).
- [5] T. Fukui and S. Ando, *Electron Lett.* **25**, 410 (1989).
- [6] Y. Nakamura, S. Koshiba, M. Tsuchiya, H. Kano and H. Sakaki, *Appl. Phys. Lett.* **59**, 700 (1991).
- [7] Y. Nakamura, M. Tsuchiya, S. Koshiba, H. Noge, H. Kano and H. Sakaki, *Jpn. J. Appl. Phys.* **32**, L383 (1993).
- [8] L. Vina and W. I. Wang, *Appl. Phys. Lett.* **48**, 36 (1986).
- [9] K. Tsuboi, H. Mizukami, O. Ishiyama, S. Nakamura and S. Furukawa, *Jpn. J. Appl. Phys.* **29**, 468 (1990).
- [10] K. F. Berggren, G. Roos and H. van Houten, *Phys. Rev. B* **37**, 10118 (1988).

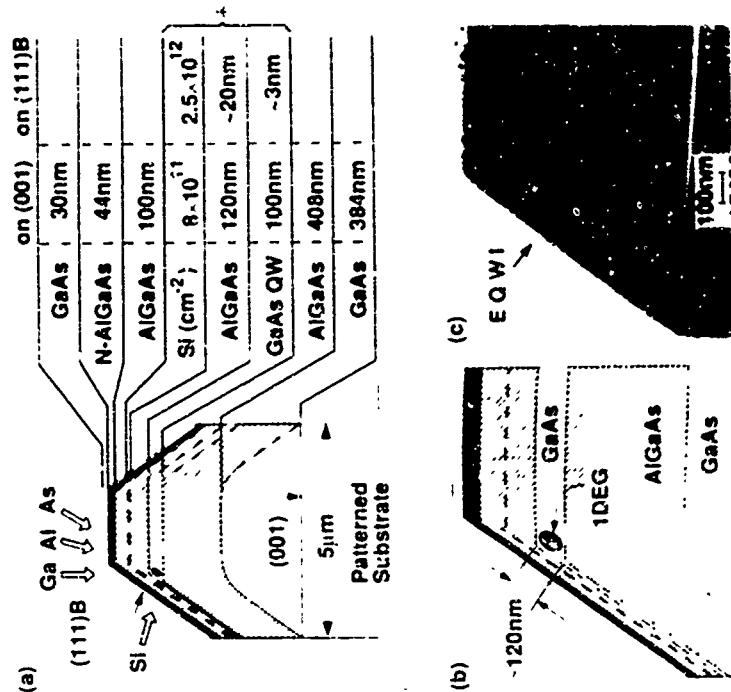


Fig. 1 Cross-sectional views of an edge quantum wire. In (a) the direction of each incident beam is shown by open arrows under the conditions for the oblique deposition modes. (a) In (b) magnified view of the facet EQWI is shown. The SEM photograph is shown in (c).

MoP4

Lateral Potential Modulation in InAs/AlSb Quantum Wells by Wet Etching

T. Urmeter, T. Schlöser, K. Ensslin, and J. P. Kotthaus
 Section Physik, LMU München, Geschw. Scholl Platz 1, D-80539 München, Germany

and

C. R. Bolognesi, C. Nguyen, and H. Kneer
 Materials Department, University of California, Santa Barbara, Ca 93106, USA

Lateral superlattices are fabricated on InAs/AlSb quantum wells using wet chemical etching. For magnetic fields where the cyclotron diameter matches an integer multiple of the superlattice period, commensurability oscillations in the magnetoresistance are observed. The spin-splitting of the Landau levels can be resolved for high magnetic fields. In this regime the height of the maxima in the magnetoresistance depends on the direction of current flow with respect to the superlattice orientation.

Introduction

High quality semiconductor heterostructures contain the free motion of carriers in the plane of the hetero-interface where a so-called two-dimensional electron gas (2DEG) is formed. A variety of technological methods has been applied to impose a lateral potential modulation onto the two-dimensional electron system [1]. In general, the fabrication of lateral superlattices on semiconductors starts from GaAs/AlGaAs heterostructures, a material system that offers large electron mobilities and well established technological procedures. Here we present experimental results obtained on InAs/AlSb quantum wells that provide a number of advantageous features [2, 3].

The huge conduction band offset of 1.35 eV between InAs and AlSb permits carrier densities of several 10^{12} cm^{-2} in the well. The small effective mass of $m^*/m_0 = 0.023$ at the conduction band edge favors large confinement energies in quantum structures for a given geometrical feature size. Without intentional doping in general the wells contain mobile electrons that dominantly originate from surface states [3, 4]. This fact lends itself to intentionally manipulate the surface and induce a lateral potential modulation. We show that wet etching being a straight forward technique can be used in combination with holographic lithography to impose a lateral potential modulation onto the 2DEG in InAs/AlSb quantum wells. The high quality of our samples as signified by the large electron mobilities $\mu > 1.500 \text{ (1000) cm}^2/\text{Vs}$ leads to a large mean free path λ_l of the carriers much longer than typical periods p of the lateral superlattice. The Fermi wavelength λ_F is more than an order of magnitude smaller than the lattice period. Electron transport in such systems can thus safely be regarded as operating in the classical ballistic regime.

We have realized lateral superlattices being periodic in one and two spatial directions with strong and weak potential modulation. Here we focus on the presentation of experimental results as obtained on one dimensionally weakly modulated potentials. Five current flow along the superlattice axis (i.e. perpendicular to the wells) maxima are observed in the magnetoresistance that are related to the commensurability of the lattice period and the classical cyclotron diameter at the Fermi energy [5, 6]. The magnitude of the potential modulation can be extracted from the positive magnetoresistance following the magnetic field regime of the commensurability oscillations and qualitative agreement with screening calculations is obtained. For high magnetic fields where the spin-splitting of the Landau levels can be resolved, a pronounced anisotropy in the magnetoresistance is observed depending on the direction of current flow with respect to the superlattice orientation. A tentative explanation is based on the modification of the edge states caused by the interplay of Zeeman splitting and the potential modulation.

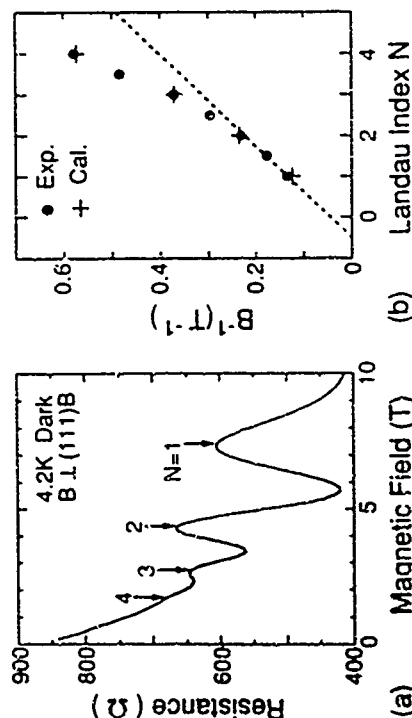


Fig. 2. Magnetoresistance of the (111)B facet at 4.2 K for the magnetic field B almost normal to the (111)B facet. (a) The Landau plot of the SdH oscillation (b), showing a clear deviation from the linear relationship for $B < 1 \text{ T}$. This is due to the magnetic depopulation of 1D subbands. Closed circles indicate observed peaks and valleys, whereas crosses show peaks calculated for $M_{1D} = 4.8 \times 10^6 \text{ cm}^{-1}$ and $M_{2D} = 5.4 \times 10^{11} \text{ cm}^{-2}$. M_{2D} was estimated to be $5.4 \times 10^{11} \text{ cm}^{-2}$.

Fabrication and Samples

The InAs-AISB quantum wells are grown by molecular-beam epitaxy on GaAs substrates. As a buffer a sequence of layers of AlSb, GaSb as well as superlattices of these two materials is grown to minimize the detrimental effects of the lattice mismatch with respect to GaAs. The InAs quantum well itself is imbedded between AlSb barriers and the capping material is GaSb or InAs. Two perpendicular Hall geometries are defined by wet etching onto the substrate. This enables us to measure simultaneously with current directions parallel and perpendicular to the wire-like superlattice. Ohmic contacts to the channel are made by zinc-doping In in reducing atmosphere. The low-frequency ($\nu = 30$ kHz) transport experiments are performed in a superconducting magnet (0-12 T) and the samples are cooled by He exchange gas at temperatures 0.5 K $< T < 4.2$ K. The magnetic field is oriented perpendicular to the plane of the electron gas.

One of the most spectacular features of InAs quantum wells imbedded between AlSb barriers is the high density of mobile carriers without intentional doping. It has been shown that the electrons originate from three different parts of the sample. Firstly from donors in the AlSb barriers, secondly from interface states at the InAs-AISB interface and thirdly and most importantly from surface states that lie about 0.85 eV below the AlSb conduction band edge. [3,4] The third mechanism can be used in two different ways.

One possibility is to change the surface material and therefore the Fermi level pinning at the surface. It has been shown by Nguyen et al. [7] that for a constant thickness of the cap layer the carrier density in the well depends on the material on the very top of the sample. In particular if the surface material is replaced from GaSb to InAs (a thin layer of InAs such that bound states are above the Fermi level) the carrier density is reduced by about a factor of two. The details of this approach are described in Ref. 17. Here we investigate a sample where the 2DEG is capped by a 30 nm AlGaSb layer and a 30 nm InAs layer. Using holographic lithography and suitable development conditions a one-dimensional periodic photorealist pattern is created on the sample surface as an etch mask. Using a selective etch the InAs is locally removed leaving stripes of InAs on the sample surface. [8] This is schematically depicted in Fig. 1 (a). The lateral potential modulation is expected to be such that the potential is lowered below the InAs stripes.

An alternative approach relies on the observation that for samples that have a uniform AlSbGaSb cap the carrier density significantly depends on the cap thickness. [9] Using a photorealist pattern fabricated in the same way as described before wet etching can be used to transfer the wire pattern onto the AlSbGaSb cap. The laterally varying cap thickness will then induce a lateral potential modulation as sketched in Fig. 1 (b). In the following we will present experimental data on two samples each fabricated by one of the two methods

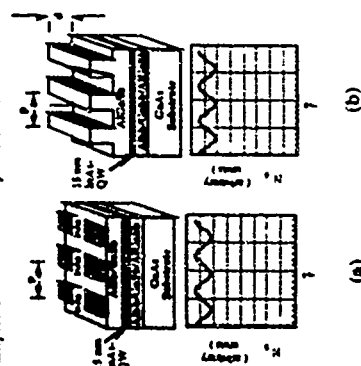
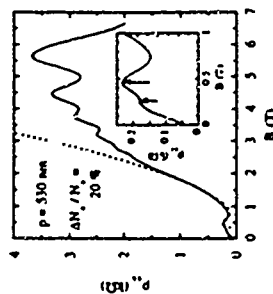


Fig. 1: Schematic for the two alternative procedures to fabricate lateral superlattices via wet chemical etching. On the left hand side (a) the thickness of the InAs cap layer is negligible. It is the lateral modulation of the Fermi level pinning caused by the lateral variation of the surface material that leads to a modulation of the carrier density. On the right hand side (b) the actual distance from quantum well to the surface laterally modulated. Thus the amount of mobile carriers that originate from surface states depends on the vertical dimension. The bottom parts of the figure indicate where the carrier density is expected to be raised and lowered

Experimental Results

We will first concentrate on a sample whose fabrication relies on the first method, namely the lateral variation of Fermi level pinning at the surface. In Fig. 2 the magnetoresistance ρ_{xx} for current flow across the wire-like barriers is presented for a sample with period $p = 530$ nm. The inset shows ρ_{xx} in an enlarged scale. Two maxima occur for low magnetic fields (as indicated by the arrows in the inset) that are related to the commensurability of the classical cyclotron diameter and the lattice period. This phenomenon has been studied in GaAs/AlGaAs heterostructures [5,6] and can be classically explained by the magnetic-field-induced modulation of the drift velocity [10] in a lateral superlattice. The fact that commensurability oscillations can be observed in our InAs-AISB quantum wells is another indication about the quality of the material as well as the fabrication procedure.

Fig. 2: Magnetoresistance for current flow across the wires of the lateral superlattice (full line) at $T = 4.2$ K. The dashed line marks the result of the fitting procedure to ρ_{xx} in the regime $0 < B < 2$ T as described in the text. The inset presents ρ_{xx} in an enlarged scale. The arrows mark the positions of the maxima that correspond to cyclotron orbits across one and two superlattice periods.



In order to estimate the effective potential modulation in the system the positive magnetoresistance following the regime of the commensurability oscillations is investigated. From the formulas as derived in the literature [6,10,11] for the magnetoresistance a parabolic increase is expected and was observed in the experiments [5,6,12]. We went one step beyond Ref. 12 and fitted the magnetoresistance in the regime $0 < B < 2$ T with the theoretical expression including the Bessel function that describes the low-field maxima. The dashed line in Fig. 2 depicts the results of this fitting procedure. The position and shape of the highest lying maximum that corresponds to an electron orbit of the size of the lattice period is nicely described by the theory. The lower lying maxima are less pronounced in the experiment probably because the scattering time in reality acquires a spatial dependence which is not taken into account in the theory. Nevertheless we can extract a value for the effective carrier density modulation from the behavior at higher magnetic fields $1 \text{ T} < B < 2 \text{ T}$ of $\Delta N_2 / N_2 = 20\%$.

Two homogeneous samples without lateral potential modulation where measured, one sample with the unstructured InAs cap layer and another sample with a completely removed InAs cap layer. We can thus estimate the bare potential modulation to be 50 %. The effective potential modulation is reduced with respect to the bare potential because of screening of the mobile electrons. Furthermore the closer the 2DEG to the surface of the sample the stronger the effective potential modulation in the electron channel will be. Both effects are taken into account according to Ref. 13 and a theoretical value of 28% for the carrier density modulation is found. The screening length [13] in InAs is 15 nm, much larger than in GaAs or Si. We conclude that the observed experimental features that occur at low magnetic fields and are related to the lateral superlattice are reasonably explained within the existing theoretical framework.

We also fabricated lateral superlattices by using the second fabrication method where the distance of the electron gas to the surface is periodically modulated. Again we clearly observe commensurability oscillations but now the oscillations are less pronounced and an overall negative magnetoresistance is observed that is not understood so far. The potential modulation that can be induced with this method is probably much smaller than in the experiment described before. Nevertheless an unexpected phenomenon is detected that we like to address in the following

The bare g -factor in InAs is very large $g \approx 15$ and spin splitting of the Landau levels can easily be resolved in a magnetotransport experiment. Figure 3 presents the components of the resistivity tensor for the current direction along the wires (ρ_{xx}) and across the wires (ρ_{yy}). The spectra are only shown in the magnetic field range $5T < B < 10T$ at low temperatures $T \approx 0.5$ K. The wide minima are related to the Landau splitting at even integer filling factors as indicated in the figure. The filling factor is defined as the number of occupied Landau levels below the Fermi energy. Every pair of maxima neighbors a minimum that is related to the spin splitting of a Landau level, i.e. an odd integer filling factor. The vertical arrows mark the magnetoresistance maximum on the low-field side of the spin-splitting. For current flow along the wires (a) the left maximum is always lower than the right maximum, for current flow across the wires (b) the situation is reversed. In the following we will refer to this effect by AMOF (anisotropy in the maxima neighboring an odd-integer filling factor).

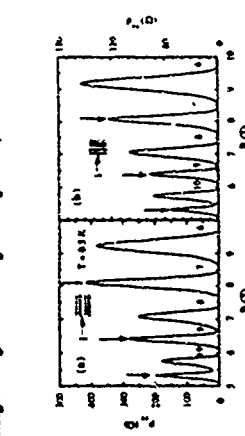


Fig. 3: Magnetoresistance along (ρ_{xx}) and across (ρ_{yy}) the wires in the magnetic field regime $5T < B < 10T$ at $T = 0.5$ K. The integer in the minima signify the number of occupied Landau levels. The vertical arrows mark maxima that lie on the low-field side of minima that reflect the position of the Fermi energy between two spin-split Landau levels (odd integers).

The AMOF was observed on more than ten samples with different superlattice periods fabricated by different fabrication technologies and never depended on cooling cycle or other external parameters of the experiment. On a homogeneous sample without a lateral superlattice the experiments revealed the same behavior for the magnetoresistance maxima as in the case of Fig. 1 (b) independent of the direction of current flow. We conclude that the AMOF is not related to possible anisotropies in the growth kinetics along the different crystal axis. In homogeneous samples it was observed that the height of a maximum in the magnetoresistance depended on the current level. [14,15] In our experiment the measurement current is changed over 4 orders of magnitude and the qualitative behavior of AMOF is not changed. The AMOF is identical under reversal of the magnetic field. As a function of decreasing temperature the minimum in the magnetoresistance related to the spin-splitting of Landau levels becomes more pronounced but the anisotropy of the neighboring maxima does not change qualitatively. The anisotropy is most pronounced for intermediate cases where the minimum related to an odd-integer filling factor is close to zero. For very low temperatures, high magnetic fields and high mobility samples where the Landau levels are well separated the AMOF becomes less pronounced. In the opposite limit where the spin-splitting of the Landau levels can barely be resolved the AMOF also becomes weaker. In general spin-splitting in GaAs-AlGaAs heterostructures is harder to resolve because of the smaller g -factor. However, after the observation of AMOF in InAs-AlSb quantum wells we were able to detect similar behavior in weakly modulated one-dimensional superlattices as well as in rectangular antidot lattices on GaAs.

For an explanation of AMOF it is important to remember that the height of the maxima neighboring a minimum in the magnetoresistance is modified with respect to a homogeneous sample in case the current flows parallel to the wires in the superlattice (Fig. 3 (a)). It is therefore this current direction that deviates from "usual" two-dimensional behavior. The fact that the magnetoresistance vanishes if the Fermi energy lies in between Landau levels can be understood in terms of absence of back-scattering in the quantum Hall regime. [16] The maxima in the magnetoresistance are supposed to arise from scattering from edge states into the bulk. If the current flows along the wires a Landau level will exhibit the minima and maxima of the potential modulation in the direction across the current direction. This situation is presented schematically

in Fig. 4. For two Landau levels that are energetically close to each other as in the case of spin-split Landau levels the Fermi energy may thus cross a Landau level several times. The scattering from an edge state into the bulk could therefore be greatly modified. This is completely different if the current flows across the wires in that case a Landau level will be flat across the direction of current flow and scattering from an edge state into the bulk should be the same as for an unmodulated sample. This simple model explains the direction dependence of the AMOF. It further suggests that the scattering rate from an edge state into the bulk could be modified if the current flows along the wire direction which would influence the shape of the respective maximum in the magnetoresistance. Nevertheless a more refined theoretical analysis is required to understand this phenomenon in more detail.

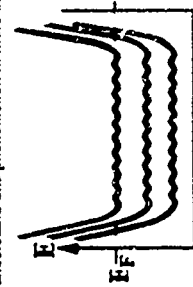


Fig. 4: Schematic of a series of spin-split Landau levels across the direction of the wires in the lateral superlattice. The dashed line marks the position of the Fermi energy. The wiggles of the Landau levels reflect the lateral potential modulation. The size of the cyclotron energy, Zeeman energy and potential modulation are not drawn to scale but to clarify the idea behind the explanation in the text.

We have presented two fabrication techniques that enable us to produce lateral superlattices on InAs-AlSb quantum wells. Commensurability oscillations occur in the low-field magnetoresistance which reflects the high quality of our samples. For high magnetic fields and low temperatures the spin-splitting of Landau levels can be detected in the magnetoresistance. The two spin-split Shubnikov-de Haas maxima reveal a pronounced anisotropy being related to the current direction with respect to the superlattice orientation. A simple model is presented that suggests a mechanism in terms of scattering from edge states into the bulk of the sample.

It is a pleasure to thank A. Wixforth for valuable discussion. Financial support from the Volkswagen-Stiftung is gratefully acknowledged.

References

- [1] for a review see: W. Hansen, U. Merkt, and J. P. Kotthaus, in Semiconductors and Semimetals, ed. R. K. Willardson, A. C. Beer, E. R. Weber, Vol. 35, ed. M. Reed, (Academic Press, San Diego 1992) p. 279.
- [2] G. Tuttle, H. Kroemer, and J. H. English, *J. Appl. Phys.* **65**, 5239 (1989)
- [3] C. Nguyen, B. Brar, H. Kroemer, and J. H. English, *Appl. Phys. Lett.* **60**, 1854 (1992)
- [4] C. Nguyen, B. Brar, H. Kroemer, and J. H. English, *J. Vac. Sci. Technol.* **B10**, 898 (1992)
- [5] D. Weiss, K. v. Klitzing, K. Ploog, and G. Weimann, in "High Magnetic Fields in Semiconductor Physics II", edited by G. Landwehr, Springer Series in Solid State Science **87**, 357 (1988)
- [6] R. W. Winkler, J. P. Kotthaus, and K. Ploog, *Phys. Rev. Lett.* **62**, 1177 (1989)
- [7] C. Nguyen, B. Brar, and H. Kroemer, to be published
- [8] C. Nguyen, B. Brar, V. Jayaraman, A. Lorke, and H. Kroemer, to be published
- [9] C. Nguyen, B. Brar, and H. Kroemer, to be published
- [10] C. W. J. Beenakker, *Phys. Rev. Lett.* **62**, 2020 (1989)
- [11] R. R. Gerhardts, D. Weiss, and K. v. Klitzing, *Phys. Rev. Lett.* **62**, 1173 (1989)
- [12] A. K. Geim, R. Taboryski, A. Krutsen, S. V. Dubonos, and P. E. Lindelof, *Phys. Rev. B* **46**, 4324 (1992)
- [13] J. P. Kotthaus and D. Heilmann, *Surf. Science* **113**, 481 (1982)
- [14] R. J. Haug, K. v. Klitzing, and K. Ploog, *Phys. Rev. B* **35**, 3933 (1987)
- [15] P. Svoboda, P. Streda, G. Nachev, A. Jaeger, M. Cukr, and M. Larnicki, *Phys. Rev. B* **45**, 8763 (1992)
- [16] M. Buttiker, *Phys. Rev. B* **38**, 9375 (1988)

MoP5

Optical Properties of GaAs Quantum Dots Fabricated by MOCVD Selective Growth

Y. Nagamune¹, M. Nishihata², S. Tsukamoto¹, and Y. Arakawa^{1,2}

¹Research Center for Advanced Science and Technology, University of Tokyo
4-6-1 Komaba, Meguro-ku, Tokyo 153, Japan

²Institute of Industrial Science, University of Tokyo
7-22-1 Koyohgi, Minato-ku, Tokyo 106, Japan

Abstract

In spite of a bottle-neck prediction, strong photoluminescence intensity was observed from nanometer-scale GaAs quantum dot structures *in situ* fabricated by selective growth technique using metal-organic chemical vapor deposition. The dot structures showed a large PL peak by excitation above AlGaAs barrier from 8 K to room temperature, while its intensity largely decreased by excitation below the barrier. This demonstrates that carrier diffusion smoothly occurs into the dots from the barrier region.

Introduction

Three-dimensional (3D) confinement of carriers in semiconductor quantum dots (QDs) has much attention for quantum device applications[1,2] as well as for fundamental study in quantum physics. Many workers have intensively investigated for fabricating structures inducing the predicted quantum effects[3-8], and estimated optical properties of the fabricated samples by spectrally resolved photoluminescence (PL) experiment, which directly depict radiative transition between density of states of the reduced dimensionality.

However, there have been facts that fabricated zero-dimensional (0D) or 1D nanostructures lead to almost diminished PL intensity[5,9]. This poor radiative efficiency in QDs was thought to be due to non-radiative recombination at surfaces or interfaces damaged by etching or other processings. But, recently it is pointed that the poor efficiency is intrinsic effect rather than the extrinsic effect caused by processing, so-called bottle-neck prediction[10], so that such the undesired effect is unescapable even in QDs fabricated by improved

techniques.

On the other hands, large efforts for making high quality nanostructures have been continuously made, in particular, to *in situ* fabrication techniques, which can largely reduce impurity and damages at hetero-interfaces. In *in situ* fabrication techniques, selective epitaxial growth on masked substrates by metal-organic chemical vapor deposition (MOCVD) is promising for fabrication of quantum wire (QWR) structures[7] or QDTs[8,11]. More recently large PL intensity was observed even from very narrow (7 nm) QWR structures[12]. Then, possibility for obtaining large PL intensity from QDTs is generated.

In this paper, we report PL spectra of nanometer-scale GaAs QDT structures fabricated by MOCVD selective growth. The QDT structures showed a clear blue-shifted PL peak with high quantum efficiency not only at low temperature but also at room temperature. In addition, we discuss carrier diffusion into the QDTs from the barrier region based on the result of PL excitation (PLE) spectra.

Fabrication Procedure

Samples were prepared by selective growth technique using MOCVD, which was carried out on (100) GaAs substrates with a low-pressure (100 torr) horizontal MOCVD reactor, where the substrates were masked by 20 nm thick SiO₂ films with square windows of about 700 x 700 nm² size made by plasma CVD, electron beam lithography and wet chemical etching. The sides of the windows were oriented in the direction of <011> and <011> of the substrates. The whole pattern was composed of 2000 x 2000 windows placed in the period of 1 μm and their sizes were 2 x 2 mm². Concerning the condition of MOCVD growth, partial pressure of arsine (AsH₃), trimethylgallium (TMG) and trimethylaluminum (TMA) were kept at 4 x 10⁻⁴, 4.4 x 10⁻⁶ and 1.5 x 10⁻⁶ atm, respectively. The group V/III ratio was 100 for GaAs growth, and the total gas flow rate including carrier gas H₂ was 6 liter/min. Before the MOCVD growth, at 700°C, thermal etching was performed at 800°C for 5 min in order to exclude an oxide film or a contaminated surface of the substrate.

Under this growth condition, GaAs or AlGaAs are selectively grown in the windows on the substrates, and a few hundred nanometer size GaAs QDT structures surrounded by Al_{0.4}Ga_{0.6}As can be made by switching the supplying material at the proper stage of the growth process. A scanning electron micrograph of the cross section of the fabricated GaAs

QDT structure for (011) are shown in Fig. 1(a), where dark parts are corresponding to GaAs and a little light ones to AlGaAs as shown in Fig. 1(b). The QDT structure have disk-shaped structure of which the dimension is $190 \times 160 \times 12$ nm, and are three-dimensionally surrounded by the AlGaAs barrier. This structure was made using the surface migration mechanism and difference of growth rate between (100) and other planes[6].

PL Spectra and Temperature Dependence

Figure 2 shows PL spectra of the sample including QDT structures at various temperatures between 8 and 300 K, where the PL spectra was obtained by use of Ar⁺ laser light with multi-lines, of which the energies are larger than the band gap of AlGaAs barrier. Here, laser beam diameter was about 0.2 mm and the power 10 mW. In Fig. 2, a PL peak at 805 nm of spectra measured at 8 K is corresponding to GaAs QDT structures while that at 817 nm is to GaAs bulk transition, probably (D₀X)[13,14], and that at 830 nm is to the transition at carbon impurities. A broad peak at 775 nm is considered to be corresponding to thin GaAs quantum wells with a thickness of about 5 nm grown on (311)A and mostly on (110) sidewalls of the AlGaAs epilayers shown in Fig. 1, and that at 730-610 nm in the inset is to AlGaAs with various compositions.

The energy shift of the PL peak position of the QDTs from that of the GaAs bulk is about 25 meV. This energy shift is considered to be induced almost by the longitudinal confinement of the disk-shaped dot-structures as is almost equal to that of a normal quantum well with the same thickness. However, the large intensity of the PL spectra in spite of small filling factor of the dots is expected to be caused by the zero-dimensional nature such as large interface-to-recombination volume rate, carrier diffusion from the outside.

As well as PL peaks of GaAs QDTs is larger than that of GaAs bulk and sidewall wells, the PL peak survive until higher temperatures. This is in contrast to the case that the PL peaks by the transition in GaAs bulk and that at carbon impurities disappear at comparatively lower temperatures. This weak temperature dependence of GaAs QDTs is considered to be caused also by the three-dimensional confined structures.

Excitation laser power dependence of PL spectra of GaAs QDTs at room temperature is shown in Fig. 3. A P¹ peak of the QDTs is clearly observed even at room temperature, and the peak intensity increases in proportion to the excitation power below about 50 mW.

showing linear response within this excitation power range.

Figure 4 shows PL spectra by excitation wavelength of 710 nm by a wavelength-tunable Ti:Sapphire laser, and PLE spectra detected at 805 nm by the tunable laser. In comparison with the case by the Ar⁺ laser light, PL intensity of the GaAs QDTs is much smaller and it is in a factor of 10^{-2} . This small intensity is according to its small spatial filling factor, while the large intensity by Ar⁺ laser light is mostly owing to carrier diffusion into the QDTs from the barrier region. This situation is also observed in PLE spectra. PLE intensity at PL peak position of the QDTs is almost zero, but it increases with increasing excitation energy. Therefore, it should be noted that PLE measurement is not equivalent to absorption measurement for GaAs QDTs, but that the PLE spectra include effect of carrier diffusion. It is considered that the PL intensity of the QDTs is caused by carrier diffusion from the sidewall well region, and that carrier diffusion from outside of the dots smoothly occurs.

Conclusion

In conclusion, we fabricated GaAs QDT structures three-dimensionally surrounded by Al_{0.4}Ga_{0.6}As by MOCVD selective growth, and observed a clear blue-shifted PL peak with high quantum efficiency not only at low temperature but also at high temperature. By PLE measurement smooth carrier diffusion into the dots from the barrier region was observed in spite of the bottle-neck prediction. These results demonstrate availability for the fabrication of QDTs by MOCVD selective growth technique and possibility of optical devices such as quantum dot laser using QDT structures.

Acknowledgement

We wish to thank Prof. T. Ikoma and H. Sakaki for their instructive discussion and encouragement. We would like to give our thank for supporting to the University-Industry Joint Project on Mesoscopic Electronics. This work was also supported in part by a Grant-in-Aid for Scientific Research on Priority Area, "Electron Wave Interference Effects in Mesoscopic Structures" from the Ministry of Education, Science and Culture, TEPCO Research Foundation, and Kanagawa Academy of Science and Technology Foundation.

References

- [1] Y. Arakawa, and H. Sakaki, Appl. Phys. Lett. 40, 939 (1982).
- [2] Y. Arakawa, Y. Vahala, and A. Yaniv, Appl. Phys. Lett. 45, 950 (1984).
- [3] H. Asai, S. Yamada, and T. Fukui, Appl. Phys. Lett. 51, 1518 (1987).
- [4] T. F. Kuech, M. A. Tischler, and R. Potemski, Appl. Phys. Lett. 54, 910 (1989).
- [5] J. A. Lobens, C. S. Tsai, and K. J. Vahala, Appl. Phys. Lett. 56, 2642 (1990).
- [6] T. Fukui, S. Ando, Y. Tokura, and T. Toriyama, Appl. Phys. Lett. 58, 2018 (1991).
- [7] S. Tritakomoto, Y. Nagamune, M. Nishioaka, and Y. Arakawa, J. Appl. Phys. 71, 533 (1992).
- [8] Y. Nagamune, S. Tsukamoto, M. Nishioaka, and Y. Arakawa, J. Crys. Growth. 126, 707 (1993).
- [9] H. Temkin, G. J. Dolan, M. B. Panish, and S. N. G. Chu, Appl. Phys. Lett. 50, 413 (1987).
- [10] H. Benisty, C. M. Sotomayor-Torres, and C. Weisbuch, Phys. Rev. B 44, 10945 (1991).
- [11] Y. D. Galeuchet, H. Rohlfsen, and P. Roenigen, Appl. Phys. Lett. 58, 2423 (1991).
- [12] S. Tsukamoto, Y. Nagamune, M. Nishioaka, and Y. Arakawa, to be published in Appl. Phys. Lett. (1993).
- [13] E. H. Bogardus and H. B. Bebb, Phys. Rev. 176, 993 (1968).
- [14] H. Kunzel and K. Ploog, Appl. Phys. Lett. 37, 416 (1980).

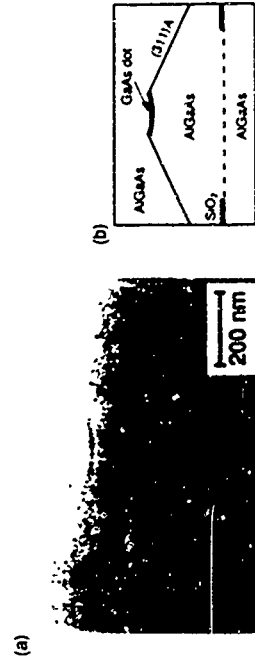


Fig 1 (a) A cross section for (011) of disk-shaped GaAs dot structures surrounded by AlGaAs, and (b) its schematic illustration.

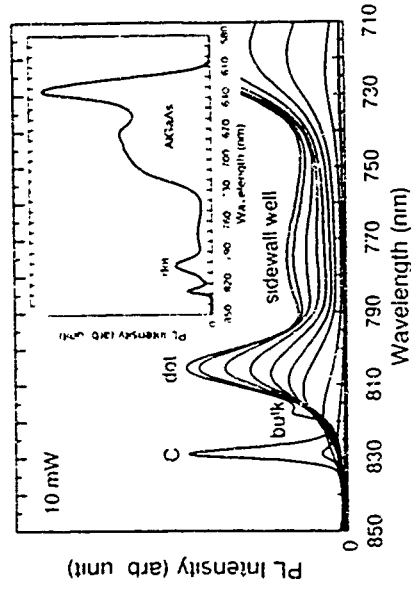


Fig 2 Photoluminescence spectra at various temperatures between 8 and 300 K of the sample shown in Fig. 1. Measurement temperatures of each of the spectra are 8, 20, 40, 60, 80, 100, 120, 160, 200, 250 and 300 K, respectively from the topmost of the spectra. The inset shows spectra of large wavelength scale at 8 K.

Fabrication of Nano Meter-Scale Conducting Silicon Wires with a Scanning Tunneling Microscope

P. M. Campbell, E. S. Snow, and P. J. McMarr*
Naval Research Laboratory
Washington, DC 20375-5000

ABSTRACT

We report the fabrication of nanometer-scale conducting silicon wires through the STM-induced modification of a passivated silicon $<100>$ surface followed by a selective liquid etch. The modified surface layer is a thin oxide a few monolayers thick which acts as a mask against subsequent liquid etching of the unexposed portions of the silicon. Silicon wires as narrow as 30 nanometers have been fabricated with this technique. More complicated patterns can be written selectively by pulsing the STM bias to a suitable writing voltage pixel-by-pixel during a low-bias (hence non-exposing) scan. The maximum pattern size is limited by the range of the piezoelectric transducer, which for our system is in excess of 100 micrometers. Conducting silicon wires between contact pads were fabricated on a silicon layer on top of a buried insulating layer of SiO_2 formed by oxygen implantation and subsequent anneal (SIMOX). Backgating of these structures permits the biasing of these wires into accumulation or inversion, thus allowing independent control of the conductivity of the wires. The techniques described here allow the simple, easy, and reliable fabrication of nanometer-scale device structures using relatively inexpensive and widely available equipment.

*Sachs-Freeman Associates

1 INTRODUCTION

The physics of nanometer-scale structures and their fabrication are topics of intense current interest. Various techniques have been employed to generate sufficiently small patterns and transfer them into the material of interest. The most widely used pattern-generation technique is electron-beam lithography of polymer resists, which is followed by pattern transfer techniques such as etching and metallization. While electron-beam lithography can generate patterns with features in the 10 nanometer range and below, the purchase and operation of a state-of-the-art electron-beam lithography system represents a large financial investment.

The scanning tunneling microscope (STM) has been proposed as a simpler and lower-cost alternative to electron-beam systems for the generation of nanometer-scale patterns. Originally developed as a means of surface characterization, the STM has been used to modify the properties of surface layers [1]. Recently, the STM was used to manipulate and position single atoms on a surface [2]. This potential for atomic-scale surface modification suggests that the STM may equal or surpass the electron-beam system size limit for pattern generation.

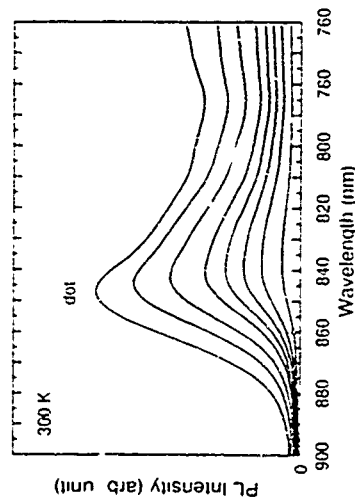


Fig. 3 Excitation power dependence of photoluminescence spectra of GaAs dot structures at 300 K. Powers corresponding to each spectrum are 10, 20, 30, 40, 50, 75, 100, and 150 mW, respectively from the lowest one.

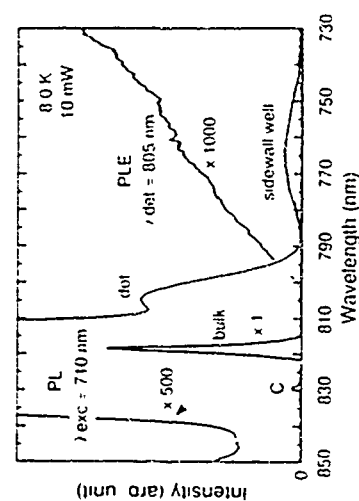


Fig. 4 Photoluminescence and photoluminescence excitation spectra of GaAs dot structures at 8 K, where excitation wavelength of the photoluminescence spectra is 710 nm and detection wavelength of the photoluminescence excitation spectra 805 nm.

One method of STM lithography uses the STM tunneling current to expose a layer of polymer resist, in a manner analogous to electron-beam lithography [3]. An alternate approach is to use the STM to modify the surface directly in such a way that the modified surface layer itself acts as a resist for pattern transfer. Dagata et al. demonstrated that the H-passivated Si <111> surface could be selectively oxidized by STM exposure [4]. This thin oxide layer was sufficiently robust to serve as a mask for the selective MBE growth of GaAs on the unexposed portion of the surface [5], but was only partially able to withstand a liquid etch of the unexposed surface [6].

We recently demonstrated that the H-passivated Si <100> surface can, in a manner similar to Dagata et al., be selectively oxidized by STM [7]. The etch rate of the Si <100> surface in conventional etches is much larger than that of the <111> surface [8]. The selectivity against degradation of the oxide mask during the liquid etch is consequently enhanced by a similar factor, which allows the controlled etching into silicon of useful nanometer-scale structures from patterns written directly on the silicon surface by the STM. The highly local nature of the STM tip-surface interaction, and the fact that the oxide mask is approximately 1 nanometer thick, suggest that this technique may ultimately approach near-atomic scale resolution.

In this paper we demonstrate that this technique of localized STM oxidation of a passivated <100> silicon surface, combined with the enhanced etch selectivity of this surface, can be used to fabricate nanometer-scale conducting silicon wires between metal contact pads. These wires, separated from the substrate by a buried insulating layer of SiO₂ formed by ion implantation, can by backgating be biased either into accumulation or into inversion. This allows independent control of the conductivity and carrier type of the wires. Such wires form the basic building blocks for more complex nanometer-scale silicon devices which are expected to play a central role in new generations of electronics technology.

2. STM PATTERNING AND ETCHING TECHNIQUES

The full details of the exposure and etching techniques have been treated in Reference 7 and will be summarized here. A <100> Si sample to be patterned is first passivated by a 60 second immersion in 10% HF and then blown dry. This process strips the native oxide from the silicon surface and replaces the oxide with a passivating dihydride layer [9]. Passivated samples were attached to a STM sample stage with a conducting mechanical clip. An etched tungsten STM tip operated in air was scanned over the passivated Si surface. Typical tunneling conditions to write patterns were tip bias of 3.5 to 4 V (tip negative relative to sample) and tunneling current maintained by feedback control at 0.2 nA. The tip was scanned across the surface at a speed of 1 to 10 micrometers/sec. Under these conditions, the regions exposed to the STM tip experienced modification of the surface. This was confirmed by subsequent atomic force microscopy (AFM) imaging of the scanned regions which showed that each line scan of the STM tip had generated a raised line on the order of 1 nanometer high. The width of these latent image lines can be as small as 15 nanometers, depending upon tunneling conditions and scan speed. We attribute this latent image to the growth of a local surface oxide formed when the STM tip interaction with the surface locally removes the H-passivation and the

exposed region oxidizes. Although we have no direct evidence to confirm this view, the properties of these films are consistent with those of a thin oxide [7]. Dagata et al. argued a similar oxidation mechanism on <111> Si [4].

There exist several liquid etches which etch silicon but do not etch silicon oxide (e.g., hydrazine [10]) or etch silicon oxide slowly (aqueous KOH solutions [11]). The STM-modified surface oxide layer should therefore act as a selective mask against etching. Figure 1 shows an AFM image of a .008 Ohm-cm n-type <100> Si sample onto which has been patterned a 50 nanometer period grating under the conditions described above and etched in an 11 molar KOH solution at a temperature of 60 C. The top half of the pattern was exposed at 3.5 V, while the bottom half was written at 4 V. The localized regions modified by the STM have withstood the etch, producing silicon wires approximately 30 nanometers wide at the top for the 3.5 V lines. The 4 V lines are slightly wider. The average etch depth is approximately 15 nanometers. Much deeper etches have shown that while the surface layer etch mask can be undercut by a long etch, it is not attacked by the hydrazine: the RMS roughness of the STM-modified region after a deep hydrazine etch is the same as before the etch. In contrast, a deep etch performed with a solution of KOH shows eventual degradation of the mask layer, which we attribute to the fact that KOH solutions etch silicon oxide, although at a rate several orders of magnitude slower than they etch silicon [11].

Another consideration for the formation of effective etch masks is dose. The slower the scan speed at a given bias, the larger the dose received by a given region. We find that an effective etch mask can be formed at virtually any tip-sample bias if a large enough dose is given. Conversely, a low bias at a high scan speed may not provide sufficient exposure to form an effective etch mask. This suggests that selective writing can be achieved by scanning a region at a sufficiently low bias and high speed in those areas where one does not wish to write, and pulsing the bias to a higher (exposing) value in those areas where one does wish to write. Performing this pixel-by-pixel in an area should allow the generation of arbitrarily complex patterns. We observe that it is quite easy to find conditions which will allow one to scan without writing a mask for KOH etches but somewhat more difficult for hydrazine. We attribute this to the fact that KOH will etch silicon oxide slowly but hydrazine will not. Therefore, a sufficiently low bias may generate a weak oxide layer on the surface which the KOH can dissolve but the hydrazine, owing to its extreme selectivity against silicon oxide, will not attack.

3. DEVICE FABRICATION AND RESULTS

While the etching of free-standing wires on the surface of bulk silicon constitutes a proof of principle of the technique, a more interesting structure would be a conducting wire connected at both ends to contact pads but electrically isolated from the substrate. Such a structure is one of the building blocks for more complicated dimensionally-confined devices. For this purpose we select as our starting material a piece of 1 Ohm-cm n-type <100> silicon which has been ion-implanted with a heavy dose of oxygen and annealed to form a buried layer of SiO₂ approximately 250 nm below the surface. This results in a thin layer of the host silicon being

electrically isolated by an insulating dielectric from the underlying substrate. This type of material, referred to as SIMOX, is used extensively in radiation-hardened electronics and is described elsewhere in more detail [12].

The sample was first coated with photoresist and patterned by standard photolithography to form open windows. This was followed by a deposition of 2 nanometers of Cr and 60 nanometers of Au which by lift-off formed metal contact pads separated by distances of 5 to 40 micrometers. The sample was then thoroughly cleaned to remove all residual photoresist. The sample was next passivated for 40 seconds in 10% HF. As described above, the STM was used to write (at 4 V, 0.2 nA) lines of oxide between pairs of contact pads. These were then etched in hydrazine at room temperature to remove all the unprotected silicon down to the buried SiO₂ layer formed by oxygen ion implantation, which acted as an etch stop for the hydrazine. As soon as the etch reached this layer, the sample was removed from the hydrazine to avoid undercutting of the wires masked by the thin surface oxide.

Figure 2 shows an AFM image of one end of a wire where it joins the contact pad. The wire is 250 nanometers high and 250 nanometers wide at the top. The flat plane at the base of the wire is the SIMOX oxide layer exposed by the etch. At the very top of the image one can see the metal contact pad. Extending out from the pad for a distance of approximately 300 nanometers is a region of unetched silicon. Rather than undercutting the metal contact pad (which is itself unaffected by the etch), the etch leaves a projection of silicon to which the silicon wire connects. The resistances of these contact pads, while greater than might have been obtained with a more complex contacting process, are still several orders of magnitude below the resistance of the fabricated wire devices and hence not a limiting factor in the electrical characteristics of the completed devices.

Several factors must be considered in the STM fabrication of conducting wires between contact pads, as well as more complex device structures derived from them. The first issue is surface cleanliness. Unlike the surfaces used to make free-standing wires in bulk silicon, which were relatively clean from contaminants, the process of writing lines between lithographically-defined metal pads implies that the surface has undergone considerable prior exposure to organic processing compounds, including photoresist, developer, resist remover, etc. Any remnant of these can interfere with the H-passivation of the surface and result in a poor pattern and hence an uneven etch. This is especially true if the etch used is hydrazine, which cannot cut through organic layers as easily as KOH does. The result in such cases is a rough etch with islands of unetched material, which would not occur with KOH. However, KOH is not appropriate for use with material which contains a SiO₂ insulating layer for electrical isolation because of the tendency for potassium to penetrate the oxide and compromise its dielectric properties [13]. Therefore, hydrazine is preferred over KOH for the fabrication of wires isolated by oxide, especially if backgating will be used to modulate the conductivity.

An additional factor to be considered is the joining of the wire to the metal contact. The wire pattern is usually written by starting the scan with the STM tip on one contact pad and scanning across to the other pad. When the tip leaves the edge

of the metal pad, the feedback control will lower the tip from the metal to the silicon surface. One must be certain that the tip is scanning slowly enough, or that the feedback loop time constant is fast enough, to lower the tip to the surface and expose it before the tip moves a distance greater than the exposure radius. If these conditions are not satisfied, the wire will not form a good connection to the metal contact pad. In practice, the unetched region surrounding the lateral contact pad shown in Figure 2 aids in establishing continuity between the wire and the contact.

The silicon wires fabricated as described above are more than simple wire resistors. Because they sit on a high-quality dielectric layer of SiO₂ which itself resists on an underlying silicon substrate, one can by application of an appropriate bias to the substrate use the field effect to drive the wire into accumulation or alternately into inversion [14]. Figure 3 shows the curve tracer characteristics of one such wire under both accumulation and inversion. This backgated FET action, although extremely weak from the standpoint of electronic gain, is useful because it affords independent control (over the conductivity (and even carrier type) of the wire.

The physical properties of semiconductor wires of this type are interesting from the standpoint of studying dimensionally-confined systems. In addition, such wires form the basic building blocks for fabricating more complex structures. The addition of a side gate to construct a narrow portion of the wire would constitute a narrow-gate field-effect transistor. In the appropriate size limit, such a structure could be operated as a ballistic point contact for the study of basic transport phenomena in dimensionally-confined semiconductors. The addition of several closely-spaced gated regions would allow the fabrication of lateral resonant tunneling structures and coupled quantum dots. The full realization of such structures will require the fabrication between conducting pads of wires much narrower than the 250 nanometer width shown in Figure 2. The limiting factor in the width of the wires described here is the thickness of the isolated top silicon surface of the SIMOX wafer. Because of undercutting, one cannot expect liquid etching to preserve features of width smaller than the depth to be etched. The wire shown in Figure 2 is at the limit of the one-to-one aspect ratio of width-to-depth. We have demonstrated that lines as narrow as 30 nanometers can be defined by STM and etched into silicon [7]. The fabrication of electrically isolated wires of this width on SIMOX will require material with an oxide buried 30 nanometers below the surface. This can be achieved by a shallower oxygen implant or by thinning the top layer of silicon to the desired value. We are currently pursuing work on thinner SIMOX material.

The ultimate limit on the size of structures achievable with this type of lithography will be determined by several factors. One factor is the thickness of the oxide mask (approximately 1 nanometer), since in general one cannot expect the lateral size of a feature to be much smaller than the thickness of the mask. Another consideration is the size of the smallest region of a silicon surface which can be selectively stripped of its passivating hydrogen layer by a STM tip. Recent work has shown that this can be as small as 10 atomic surface sites [15]. Therefore, the ultimate size limit of this technique may approach near-atomic scale pattern sizes. Because only the top few monolayers are modified, the bulk properties underneath should not be harmed. There are no proximity effects from backscattered beams; hence very

densely packed patterns can be fabricated. Finally, nanoscale fabrication becomes accessible through simple, easy, reliable techniques using relatively inexpensive equipment and widely available equipment.

REFERENCES

1. R. Wiesendanger, *Applied Surface Science* **53**, 271 (1992).
2. D. M. Eigler and E. K. Schweizer, *Nature* **344**, 524 (1990).
3. M. A. McCord and R. F. W. Pease, *J. Vac. Sci. Technol.* **B6**, 293 (1988).
4. J. A. Dagaia, J. Schneir, H. H. Harary, C. J. Evans, M. T. Postek, and J. Bennett, *Appl. Phys. Lett.* **56**, 2001 (1990).
5. J. A. Dagaia, W. Tseng, J. Bennett, C. J. Evans, J. Schneir, and H. H. Harary, *Appl. Phys. Lett.* **57**, 2437 (1990).
6. J. A. Dagaia, J. Schneir, H. H. Harary, J. Bennett, and W. Tseng, *J. Vac. Sci. Technol.* **B9**, 1384 (1991).
7. E. S. Snow, P. M. Campbell, and P. J. McMurtry, to be published in *Appl. Phys. Lett.*
8. E. D. Falk, V. M. Bermudez, and O. J. Glombicki, *J. Electrochem. Soc.* **132**, 871 (1991).
9. S. R. Kass, M. Licht, P. A. Thiry, H. Dellaportia, and M. Offenberg, *Appl. Phys. Lett.* **52**, 108 (1991).
10. R. M. Finne and D. L. Klein, *J. Electrochem. Soc.* **114**, 965 (1967).
11. E. D. Faulk, O. J. Glombicki, and R. E. Stahlbush, *J. Electrochem. Soc.* **135**, 3126 (1988).
12. P. J. McMurtry, D. J. Mroik, M. S. Barger, G. Bowden, and J. R. Blanco, *J. Appl. Phys.* **67**, 7211 (1990).
13. E. H. Nicollian and J. R. Breys, *MOS(Metal Oxide Semiconductor) Physics and Technology*, p. 759, Wiley Interscience, New York (1982).
14. Sorin Cristoloveanu and Stephen Williams, *IEEE Electron Device Lett.* **13**, 102 (1992).
15. R. S. Becker, G. S. Higashi, Y. J. Chahal, and A. J. Becker, *Phys. Rev. Lett.* **65**, 1917 (1990).

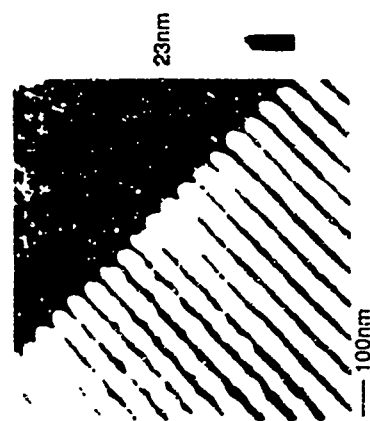


Figure 1. AFM image of 50 nanometer period grating written on $<100>$ Si with STM and etched in 11 M KOH. Etch depth is 15 nanometers.



Figure 2. AFM image of a Si wire (written with STM and etched in hydrazine) where it joins contact pad. Wire width and height are 250 nanometers. Wire sits on insulating SiO_2 layer formed by oxygen ion implantation.

MOP7

Selective growth of SiGe nanostructures by low pressure VPE.

C. Schmidt, W. Langheinrich and K. Heine
Institut für Halbleitertechnik, RWTH Aachen, Templergraben 55, D-52056 Aachen,
Germany

Tel : + +49/241/80 77 45 Fax : + +49/241/80 77 51

For the investigation of typical effects in low dimensional silicon germanium heterostructures it is necessary to transfer patterns into silicon germanium with a lateral scaling of less than 100nm. We use electron beam lithography and a special resist system to transfer the pattern into an SiO₂ mask. By selective low pressure vapour phase epitaxy small silicon germanium structures can then be grown. By this method surface damage resulting from subsequent etching can be avoided and an immediate coverage with silicon is possible. The process and first results are presented in this paper.

Introduction

In recent years Si/SiGe heterostructures have gained importance. In high speed electronics SiGe devices achieve a performance preserved up to now to III/V semiconductors [1]. Also SiGe heterostructures were expected to allow the application of silicon technology for optoelectronics especially high emitting devices [2,3].

Many experiments and theoretical computations have shown, that even by the use of superlattices light emission is restricted to very low efficiency [4]. A new approach to this subject is the investigation of 1D dimensional systems like quantum wires or even quantum dots. Since SiGe quantum wells show an increase of radiative recombination in photoluminescence [5], an additional spatial restriction should limit the movement of excitons and so exclude non radiative recombination paths.

As these effects are expected to appear in structures of a scale well below 100nm, lateral structuring in this range is required. Satisfactory tools to reach this aim are electron beam lithography and reactive ion etching. These methods have proved to be able to produce silicon structures down to some tens of nanometers [6,7].

As a great part of the volume of quantum dots has to be considered as surface, the processes in these structures are very sensitive to surface effects or defects induced by the structuring. So, proper patterning of semiconductors by dry etching diminishes any radiative quantum effects due to the radiation induced defects, as many experiments with III/V semiconductors have already shown [8]. For silicon germanium the effect should be even stronger because of the smaller dimensions required for quantum effects in this material.

We use an indirect way of patterning by selective growth of small SiGe structures. This way,

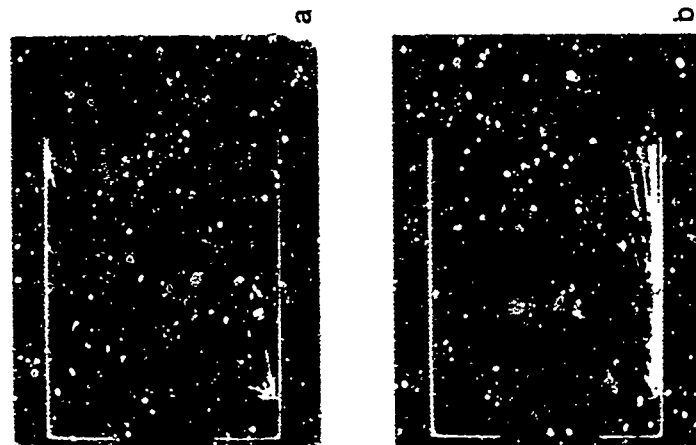


Figure 3. Curve tracer I-V characteristics of conducting Si wire, (as shown in Figure 2) backgated wires: a) accumulation and b) inversion. Wire length is 8 micrometers.

lateral dimensions in the range of 100nm and probably less can be achieved. In selective growth only the mask consisting of SiO_2 is affected during the patterning. Since the dots were grown only after patterning their surface is unaffected by the processing. An other point to be considered is the limited growth area. The very small lateral dimensions lead to higher critical layer thickness and allow much higher germanium concentrations than in large area growth without the formation of misfit dislocations [9]. Thus ideal conditions for optical effects should be given. In addition an in-situ coverage of the dots surface with pure silicon can be done. In this way any contact to air and any free lying SiGe surface can be avoided. This process will be described in this paper.

Resist system

The substrates we used were boron doped 100 oriented silicon substrates with a resistance of 10 Ω cm. After an RCA cleaning the substrates were thermally oxidized at a temperature of 1050°C for 15 minutes. This way a high quality SiO_2 layer of 170nm thickness was produced.

Since the desired lateral dimensions are ≤ 100 nm, a high aspect ratio has to be achieved. Hence an anisotropic RIE-process is required for patterning the SiO_2 layer. RIE of SiO_2 can be performed using fluorine-containing plasmas. A sufficiently high anisotropy and a high etch rate as well is achievable by using CHF_3 as an etch gas. However, this process is critical, especially if the resist covered area is large. In this case a shift of the chemical equilibrium of the RIE-process may occur and a passivation of the uncovered SiO_2 surface by carbonization is the consequence. Whether carbonization or etching dominates, mainly depends on the oxygen content within the plasma. A mixture of CHF_3 and O_2 for instance avoids carbonization but one has to take into account the enhanced etch rate of the resist (e.g. PMMA) in an oxygen containing plasma.

The main idea of the approach used in this work is the insertion of a thin titanium layer on top of the resist system. Although this titanium layer is etched by CHF_3 , the metal layer influences the etching in a way that carbonization is suppressed. One reason for this effect could be the presence of a thin TiO_2 layer on top of the Ti surface. This TiO_2 layer is believed to adjust the equilibrium during the initial stage of CHF_3 -RIE.

Figure 1. a describes the four level resist system. It consists of a double layered bottom polymer (50nm PMMA and 170nm polyimide), the titanium intermediate layer and finally on top the electron beam resist PMMA [10]. Electron beam lithography has been performed using a modified STEM with 100keV electron energy [11]. The critical exposure dose for squares larger than 100nm was 500 $\mu\text{C}/\text{cm}^2$ whereas the dose for a single dot was 12fC. After development in a mixture of 70% methanol and 30% ethylglycol (Figure 1. b) the titanium is etched using BCl_3 -RIE ($p=2.6\text{Pa}$, $P=0.28\text{W}/\text{cm}^2$) for 3 minutes (Figure 1. c). Subsequently, the double bottom polymer is patterned (Figure 1. d). Thereby the titanium acts as a mask, and as O_2 -RIE is used, a thin TiO_2 film is formed. The parameters for O_2 -RIE are $p=1.9\text{Pa}$, $P=0.32\text{W}/\text{cm}^2$ and etch time 2.3 minutes. Now the critical SiO_2 etch process follows (Figure 1. e). The parameters for this CHF_3 -RIE are $p=0.66\text{Pa}$, $P=0.16\text{W}/\text{cm}^2$ and etch time 8.5 minutes. The advantage of the double leveled bottom polymer is the easy removal of the complete resist system by lift off (Figure 1. f), since the lower PMMA layer is soluble in organic solvents like ethylglycol.

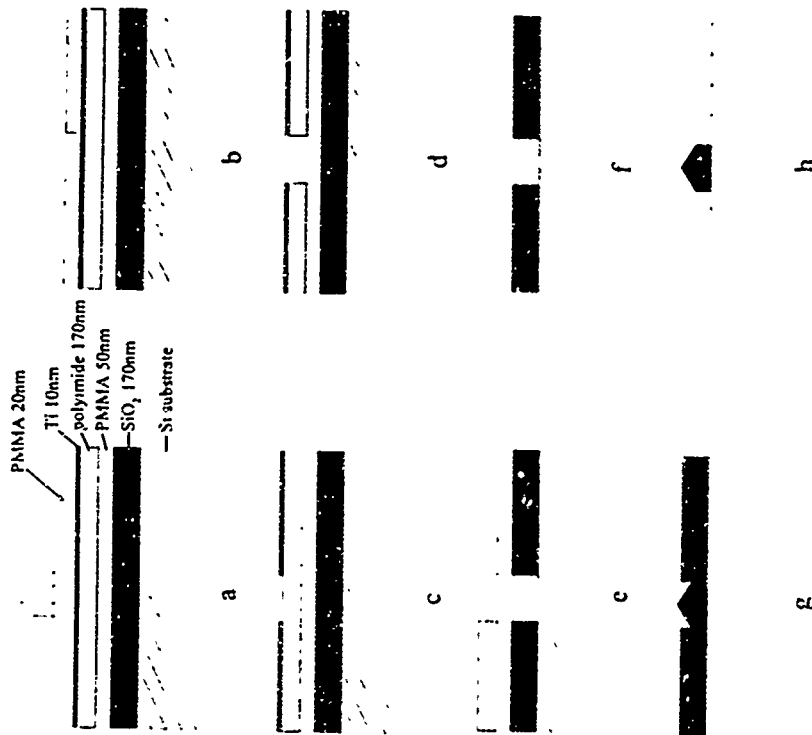


Figure 1: Process steps for fabrication of selectively grown SiGe nanometer structures. The SiO_2 layer is patterned using a multilayer resist system in order to avoid carbonization during RIE (See text)

Epitaxy

An established process for selective growth of silicon germanium layers is low pressure VPE [12]. The system we use consists of a horizontal reactor heated cold wall reactor with a graphite substrate holder. The tube can be evacuated to a pressure of 0.1 Pa. Further description was done elsewhere [13]. After the removal of the resist the samples were first cleaned in a mixture of H_2O , NH_4OH , and H_2O_2 . Next they were put for 15 minutes in H_2SO_4/H_2O_2 . Finally a short dip in HF/H_2O 1:100 was done. This dilution allows us to remove only some atomic layers of native oxide leaving the mask nearly unaffected. After a final rinse in deionized water the samples were introduced in the reactor.

At the beginning of the deposition process the reactor is heated up to a temperature of 900°C at a constant pressure of 14 hPa of pure hydrogen. The temperature is then lowered to 820°C and a buffer layer of pure silicon is grown to produce a perfect starting surface for the following SiGe deposition. The silicon germanium deposition (Figure 1 g) was performed at a temperature of 700°C or 650°C. The latter temperature is more suitable for device applications allowing sharp interfaces. The partial pressures during the deposition are as follows: Hydrogen 100 Pa, SiH_2Cl_2 6 Pa, GeH_4 0 to 0.3 Pa depending on the germanium content that shall be achieved. At a growth temperature of 650°C a small amount of HCl is added to the gas stream, to achieve perfect selectivity.

If needed a silicon layer may be grown on top to protect the surface of the structures. After growth the SiO_2 is removed by hydrofluoric acid (Figure 1 h) and an additional silicon layer can be grown to bury the dots, in order to keep surface depletion away from the Si/SiGe interface.

Results

Figure 2 shows an array of well defined dots with a diameter of 200 nm and 50 nm spacing. All sidewalls show facets with the (311)-plane. At the edge of a <110>-oriented structure no atoms can be added to the (100)-plane as the chemical bonds necessary for this reaction are not available. After growth of some (100)-monolayers near the SiO_2 sidewalls (311)-facets begin to form. Also dots grown in circular holes always show these facets. For edges along the <100>-orientation this problem is avoided and vertical sidewalls without facets can be produced.

The diameter of the smallest structures we have grown up to now is about 80 nm (Figure 3) with a height of 130 nm. In large area growth using the same process, layer thickness was 100 nm. In these small structures the facets mentioned before form at the beginning of the growth process. So the growth rate of the crystal plane, on which growth occurs, is reduced. Due to the aspect ratio of 1.7, these structures show vertical sidewalls, whereas the facets have formed on their top. The period of the array is 200 nm. The SiO_2 layer had a thickness of 170 nm.



Figure 2: Selectively grown SiGe structures. Diameter 200nm with 50nm spacing. All sidewalls show facets with (311)-planes.

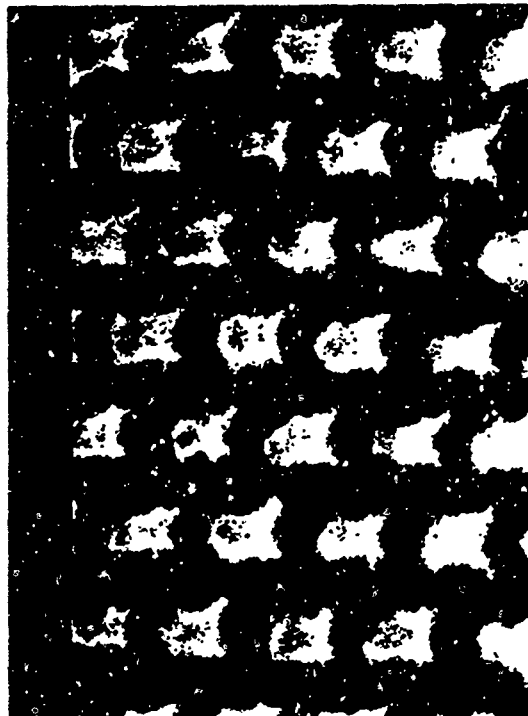


Figure 3: Array of selectively grown SiGe dots. 80nm diameter with a height of 130nm.

Conclusion

We have produced SiGe nanostructures by selective low pressure VPE. Using a special resist system and reactive ion etching very small patterns can be transferred into SiO₂. Up to now lateral dimensions go down to 80nm, a further diminution should be possible. Oxide layers of 50nm thickness or less will allow a higher precision in pattern transfer and thus lead to smaller structures. Also optimization of the aspect ratio would allow a decrease of the lateral dimensions. For photoluminescence studies large arrays of dots are necessary. Even with an array of thousands of dots only less than 1% of a laser beam with a diameter of 100µm would be used for excitation. In the case of high efficiency, this should be no problem, but for low luminescence intensities it will be necessary to work with arrays of about 100,000 to 1,000,000 dots. Using our electron beam lithography system 10,000 dots have been exposed in 10 minutes.

Acknowledgment

The authors wish to thank: B. Spangenberg for the RIE processing and H. P. Box from Forschungszentrum Jülich for the SEM photographs

1. A. Grubbe, H. Kibbel, U. Erben, E. Kasper, ELECTRONICS LETTERS 29 (4), 415 (1993)
2. G. Abstreiter, Thin Solid Films, 183, 1 (1989)
3. N. L. Rowell, J.-P. Noel, D. C. Houghton, M. Buchanan, Appl. Phys. Lett. 58 (9), 957 (1991)
4. U. Menzinger, G. Abstreiter, Physical Review B, 47 (7), 4099 (1993)
5. L. Vescan, A. Hartmann, K. Schmidt, C. Dieter, W. Jäger, H. Lüth, Appl. Phys. Lett. 60 (18), 2183, (1992)
6. P. B. Fischer, S. Y. Chow, Appl. Phys. Lett. 62 (12), 1414 (1993)
7. H. T. Liu, N. I. Maluf, R. F. W. Pease, D. K. Biegelsen, N. M. Johnson, F. A. Ponce, J. Vac. Sci. Technol. B 10 (6), 2846 (1992)
8. B. E. Maile, A. Forchel, R. Gernann, A. Mensching, H. P. Meier, D. Grützmacher, J. Vac. Sci. Technol. B 6 (6), 2108 (1988)
9. T. Stoica, L. Vescan, Journal of Crystal Growth, (to be published 1993)
10. W. Langheinrich, H. Beneck, Microelectron. Eng. 13, 225 (1991)
11. E. Kratschmer, D. Stehman, H. Beneck, Proc. of Microcircuit Engineering 81, 15 (1983)
12. Y. Zhong, M. C. Öztürk, D. T. Grider, J. J. Wortman, M. A. Littlejohn, Appl. Phys. Lett. 57 (20), 2092 (1990)
13. L. Vescan, H. Beneck, Journal of Crystal Growth, 76, 63 (1986)

Direct Epitaxial Growth of (AlGa)As/GaAs Quantum Wires by Orientation-Dependent Metal Organic Vapour Phase Epitaxy

D. Bertram*, B. Spill, W. Stolz, E.O. Göbel
Wiss. Zentrum für Materialwissenschaften (WZMW) und Fachbereich Physik,
Philipps-Universität, D-35032 Marburg, Germany

Abstract

The direct growth of (AlGa)As/GaAs quantum wire structures using metalorganic vapour phase epitaxy (MOVPE) is investigated. The present concept takes advantage of the different growth rates of GaAs and (AlGa)As on (100) and {111} planes to transfer a trapezoidal GaAs starting structure with dimensions in the µm-range into a quantum wire structure in the nm-range. For stripe dimensions below 500 nm significant changes in growth behaviour (enhanced growth rates and for special cases also the formation of other crystallographic facets) are observed by using scanning electron microscopy (SEM) studies. Based on these findings (AlGa)As/GaAs quantum wire structures are realized with lateral structure sizes of 30 nm as proved by SEM. The luminescence properties of these structures, which are determined by standard and polarization-dependent photoluminescence excitation spectroscopy, are presented and discussed in comparison to the properties of quantum well structures.

Introduction

Semiconductor heterostructures with carrier confinement in two and three dimensions (one-dimensional (1d-) and zero-dimensional (0d-) systems, respectively) have gained increasing interest in recent years due to their unique physical properties, e.g. the fundamental changes in the density of states distribution or in the Coulomb interaction of carriers in these systems [1-5]. Two principle approaches have been investigated in order to realize these modulated semiconductor structures. The first one is the lateral structuring of a 2D carrier system by using various submicrometer lithography techniques in combination with subsequent dry or wet chemical etching processes [6-15]. Because of defect formation problems of the dry etching techniques, direct epitaxial growth is becoming more and more interesting. Both molecular beam epitaxy (MBE) as well as metalorganic vapour phase epitaxy (MOVPE) have been used for growth studies to realize 1D- and 0D-systems by applying the fractional layer superlattice (FSL) process [16,17] as well as epitaxial growth on various kinds of prestructured substrate surfaces [18-27]. Recently, we have presented a new approach of direct epitaxial growth of quantum wire structures by MOVPE in the (AlGa)As/GaAs material system [27]. This approach takes advantage of the different growth rates on (100) and {111} planes as a function of substrate temperature [28,29], to transfer a trapezoidal GaAs stripe structure (stripe width in the µm-range), defined by simple photolithography and selective wet chemical etching, into an (AlGa)As/GaAs trapezoidal or triangular quantum wire structure in the nm-range. A growth rate enhancement on the top (100) stripe plane has been observed for a stripe width reduction below about 1 µm, presumably due to an increased diffusion of Ga-species from the {111} side planes to the (100) top plane. From this observation, which is of key importance for a precisely designed realization of quantum wire structures, it can be concluded that the epitaxial growth mechanism on narrow stripe structures is different from standard growth on planar (100) substrates. It is assumed that this change in growth behaviour takes place, if the geometrical extension of the growth planes becomes smaller as compared to typical surface diffusion lengths of ad-atom species on this plane. Therefore, after a brief description of our concept for realization of quantum wire structures, we concentrate in the present report on the investigation of the MOVPE growth on crystallographic planes with lateral dimensions in the nm-range. In the studied stripe structures, MOVPE growth proceeds on the (100) top stripe plane as well as on {111} or {111}Ga side planes, depending on whether the stripe is oriented in [011]- or in [011]-direction, respectively. The growth behaviour for both GaAs and (AlGa)As is investigated

as a function of substrate temperature by scanning electron microscopy (SEM) studies of cross-sectional cleavage planes of the deposited heterostructures. Finally, the optical properties of (AlGa)As/GaAs quantum wire structures, realized by the present approach, are briefly summarized.

Experimental

The MOVPE growth experiments have been performed in a commercial equipment (Aix 200, Aixtron Corp.) at a reactor pressure of 50 mbar. The substrate temperature has been varied in the range of 650°C to 750°C. In order to study the growth rate dependence of both GaAs and (AlGa)As on crystallographic planes in the nm-range, periodic (AlGa)As/GaAs multilayer structures have been deposited on prestructured GaAs trapezoidal stripe structures. Additional details of the MOVPE growth as well as the preparation of the trapezoidal GaAs starting structure using conventional contact photolithography and selective wet chemical etching ($\text{NH}_4\text{OH}:\text{H}_2\text{O}_2:\text{H}_2\text{O}$ etching solution) have already been published [27].

The structural investigations have been performed using SEM studies on cross-sectional (011)- and (011) cleavage planes of the deposited heterostructures. These cleavage planes have been selectively etched for contrast enhancement between the individual GaAs and (AlGa)As layers. A standard luminescence set-up has been used for the optical investigations. In the optical experiments only one quantum wire is excited, because of the chosen stripe separation of 80 to 125 μm . Thus, inhomogeneous broadening by interwire width fluctuations as well as grating effects in polarization dependent experiments are avoided.

Results and discussion

The principle of the present approach to realize quantum wire structures is schematically illustrated in Fig. 1. In a first MOVPE growth step an (AlGa)As/GaAs double layer is deposited. The (AlGa)As etch stop layer has a thickness of typically 0.5 μm , while the thickness of the GaAs layer is in the range of about 1 to 3 μm . This GaAs layer is structured by photolithography and the material as well as orientation selective $\text{NH}_4\text{OH}:\text{H}_2\text{O}_2:\text{H}_2\text{O}$ etching solution. In this etching process trapezoidal GaAs stripes are prepared with near (111)As side wall planes. The resulting stripe structure with stripe widths in the nm-range is schematically depicted in Fig. 1.a) for a stripe orientation along [011]-direction. This stripe width is reduced to values in the nm-range in the second MOVPE growth step (Fig. 1.b)), by taking advantage of the different growth rates of GaAs and/or (AlGa)As on the (100) top and (111) side planes. In a continuous process the quantum wire structure is then deposited on top of the stripe (Fig. 1.c)). For the other stripe orientation in [011]-direction, the shape of the GaAs starting trapezoid is reversed, with the narrower side formed at the GaAs/(AlGa)As interface [27]. For this stripe orientation growth proceeds on (100) top and (111)Ga side planes. The principle, however, is not changed.

In the following, the temperature dependence of the second MOVPE growth step is presented for structures with submicrometer stripe widths extending the growth experiments reported elsewhere [27]. The SEM micrographs of 10 period (AlGa)As/GaAs multilayer structures are summarized in Fig. 2, for the two stripe orientations ([011]-stripe orientation (left column) and [011]-stripe orientation (right column)) as a function of increasing growth temperature (from top to bottom of Fig. 2) in the range of 650°C and 750°C. Because of the selective etching of the GaAs layers in the respective cleavage planes, GaAs layers appear darker as compared to (AlGa)As layers. For the samples with [011]-stripe orientation the full trapezoidal GaAs starting structure is shown, while for the samples with [011]-stripe orientation only the top part of the trapezoid is displayed in the SEM micrographs.

First the MOVPE growth temperature dependence for the samples with [011]-stripe orientation (Fig. 2, left column) is considered. Here, we would like to concentrate on the growth behaviour on top of the GaAs starting trapezoid. As can be seen from the SEM micrographs, the principle concept, as illustrated in Fig. 1, can be applied for all growth

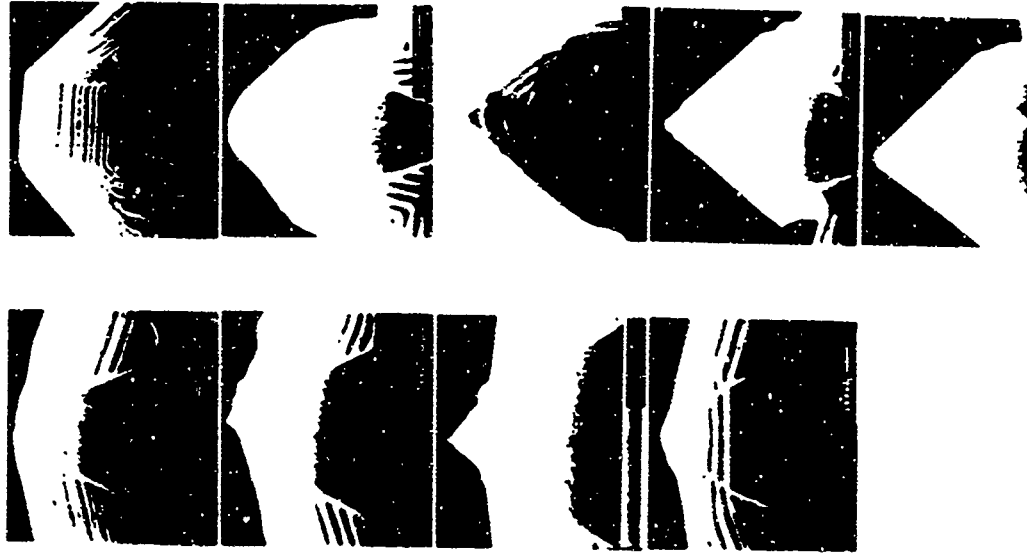


Fig. 1 Schematic sequence of realization of trapezoidal or triangular quantum wire structures. a) trapezoidal GaAs starting structure after photolithography and selective wet chemical etching. b) transfer of stripe widths in the nm-range to stripe widths in the nm-range by MOVPE growth of GaAs and (AlGa)As under appropriate growth conditions on (100) top and (111) side wall surfaces. c) growth of trapezoidal or triangular GaAs quantum wire structure.

temperatures using this stripe orientation. This is due to the almost negligible growth rate of GaAs and the small growth rate of (AlGa)As on the (111)As side wall planes. For growth temperatures above 700°C an increase in growth rate on the top (100) plane in the transition range to the (111)As side planes is observed. This is indicated by the small hump on the (100) plane at the left and right edge to the triangular side plane. The lateral extension of the humps on the (100) top plane are on the order of about 300 nm. It is assumed that this hump is caused by the additional diffusion of ad-atom species from the (111)As side planes onto the (100) top plane and/or an increase of the local gas phase concentration due to species desorbing from the (111)As side planes. Irrespective of the microscopic mechanism, this behaviour has to be taken into account in the design of the quantum wire structure. This becomes in particular true for (100) top stripe widths below about 500 nm, when the humps from the left and right corner of the trapezoid overlap, as can be seen in the top part of the triangle for the sample, grown at 700°C. So far, the formation of other crystallographic facets has not been observed for the [011]-stripe orientation and the corresponding (100) and (111)As growth planes.

For the other stripe orientation in [011]-direction the growth temperature dependence is shown in the right column of Fig. 2, in the range of 650°C to 750°C. In these structures, growth proceeds on the (100) top plane as well as (111)Ga side planes. Because of the temperature dependent growth rate on (111)Ga planes in contrast to the (111)As planes, the realization of the quantum wire structures is different as compared to the other stripe orientation. While for low substrate temperatures (650°C) the width of the stripe is becoming slightly larger, a narrowing of the stripe width with continuing growth is

Fig. 2 Scanning electron microscopy (SEM) micrographs of cleavage planes of (AlGa)As/GaAs multilayers deposited on stripe structures oriented in [011]-direction (left column) and in [011]-direction (right column) as a function of growth temperature in the range of 650°C to 750°C. For contrast enhancement the GaAs layers have been selectively etched, thus GaAs layers appear darker as compared to (AlGa)As layers.



observed for all the higher temperatures. This is caused by the reduction in growth rate on the $\{111\}$ planes with increasing growth temperature, as can be seen in the SEM micrographs. Also for this stripe orientation an increase in growth rate on the $\{100\}$ top plane near the transition to the $\{111\}$ side planes is observed. However, for this stripe orientation additional crystallographic planes develop for stripe widths below about 300 nm for growth temperatures of 700°C and above. This behaviour is identified most clearly for the sample grown at a temperature of 700°C. From the SEM micrograph one can deduce the occurrence of other crystallographic facets in the transition region of the $\{100\}$ top and $\{111\}$ side wall plane during the growth of GaAs (darker part in the SEM micrograph). The angle between this plane and the $\{100\}$ top surface of around 25° indicates that $\{311\}$ planes have been formed in this growth step for stripe widths below 500 nm. A similar facet formation has been observed recently also in overgrowth experiments using AlGaAs for the formation of arrow-head quantum wire structures on GaAs partially masked with SiO_2 stripes in the $[011]$ -direction [26].

The formation of $\{311\}$ facets, which seems to be characteristic for MOVPE growth on stripes oriented in $[011]$ -direction with dimensions below about 500 nm, can be seen in more detail in Fig. 3. In this figure, the SEM micrographs of a series of stripes with decreasing stripe widths (Fig. 3.a) through c)) are shown. These stripes have been overgrown first by a GaAs layer at a temperature of 700°C to realize stripe widths in the range of 600 nm to 400 nm. The humps in deposited material at the right and left edge of the $\{100\}$ top plane and the respective $\{111\}$ side planes is clearly seen in Fig. 3.a). For slightly narrower stripe widths these two humps overlap and the $\{311\}$ facets are formed together with a $\{100\}$ top surface (Fig. 3.b)). Finally, for even narrower stripe widths only the $\{311\}$ facets remain (Fig. 3.c)).

In order to establish whether or not the $\{311\}$ facets are stable also at lower growth temperature, once the facets have developed at high temperature, the substrate temperature has been reduced to 650°C after the deposition of the GaAs layer. Then, the stripe structure has been overgrown by an AlGaAs/GaAs multilayer structure at 650°C. As can be seen in Fig. 3.b) and c) the $\{311\}$ facets are not stable at this lower growth temperature. With continuing overgrowth the $\{100\}$ top and $\{111\}$ side wall plane are reestablished. Thus, it should be possible also for the $[011]$ -stripe orientation to realize trapezoidal or triangular as well as arrow-head quantum wire structures depending on the deposition temperature.

It is important to note, that the overgrowth in the top of the stripe depends very much on the actual geometrical stripe width. This is manifested by comparing the growth experiments for a growth temperature of 650°C as a function of the stripe width, i.e. the SEM micrographs in Fig. 2 (top, right column) and in Fig. 3 b) and c). For stripe widths



Fig. 3 Scanning electron microscopy (SEM) micrographs of cleavage planes of AlGaAs/GaAs multilayers deposited at 650°C on stripe structures oriented in $[011]$ -direction with decreasing wire width (a) through c)). The stripe structures have been realized by growing a GaAs layer at a temperature of 700°C. For contrast enhancement the GaAs layers have been selectively etched, thus GaAs layers appear darker as compared to AlGaAs layers

of about 500 nm (Fig. 2 (top, right column)) the stripe width is slightly increased during growth of the (AlGa)As/GaAs multilayer structure, while for a stripe width of about 600 nm (Fig. 3(b)) the width is slightly reduced during growth of the first three multilayer periods. For a slightly narrower stripe width of about 450 nm (Fig. 3(c)), however, a strong reduction in stripe width is observed, leading to a triangular quantum wire structure with a structure size of about 60 nm after deposition of three multilayer periods. These observations prove that the growth rate depends on the geometrical widths of the respective plane. It is assumed that this behaviour is directly correlated to the increased growth rate due to the diffusion of ad-atom species from the (111) side wall planes. The growth behaviour is changed significantly, if the geometrical widths of the crystallographic planes become smaller than typical surface diffusion lengths on these planes. Therefore, further growth experiments for structure sizes below 200 nm are necessary to understand the growth dependences on nanosized planes in detail.

For the optical experiments in the final part of this report we concentrate on quantum wire structures which are realized on [011] oriented stripe structures, because of the complication due to the formation of the crystallographic {111} facets for the other stripe orientation. The deposition of (AlGa)As at a growth temperature of 700°C has been used to realize the reduction in the top trapezoidal stripe widths to the nm-range. Trapezoidal or triangular GaAs quantum wire layers have been grown and covered directly by (AlGa)As layers. Series of samples with wire widths down to $L_1 = 30$ nm, as proved by SEM-microscopy [27] and presumably below. Additional high-resolution SEM- and TEM-investigations are underway to precisely determine the geometrical parameters of the realized quantum wire structures. The PL spectra of one of the realized quantum wire structures with $L_1 = 8$ nm (full line) together with the respective reference sample, grown simultaneously on a plan (100) substrate (dashed line) are shown in Fig. 4, on a logarithmic intensity scale. The marks on the scale indicate the orders of magnitude in PL intensity. The samples were excited using a photon energy of 2.41 eV (80 W/cm²) at a sample temperature of 5 K. For reference sample the luminescence recombinations lines of the (AlGa)As cladding layers are observed at wavelengths of 618.6 nm (line A, bound

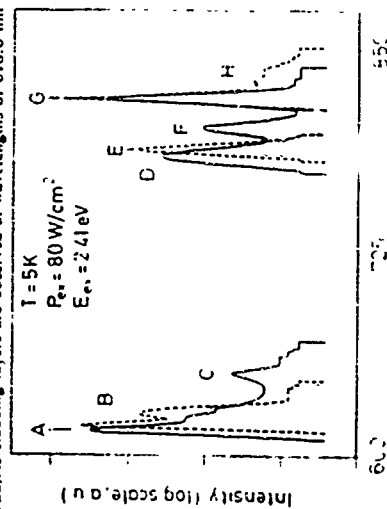


Fig. 4. Photoluminescence spectra of an (AlGa)As/GaAs quantum wire heterostructure (full line) and of a corresponding reference sample (dashed line) on a logarithmic intensity scale. For details see text.

exciton and/or (D^0, H^0) and 625.8 nm (line B, c.A.). These recombination processes of the GaAs buffer layer are detected at 819.0 nm (line G) and 830.1 nm (line H). The luminescence of the single quantum well structure with a well width of $L_2 = 8$ nm is observed at 788 nm (line E). For the quantum wire sample, realized on the structured surface, similar energetic positions of the luminescence of the (AlGa)As cladding layers, the GaAs buffer and the GaAs quantum well (line D) are observed as in the reference sample. In addition luminescence lines at 630.3 nm (line C) and 630.7 nm (line F) are detected. The luminescence line C is ascribed to the recombination in the GaAs (111) side wall quantum well, while line F is assigned to the recombination in the GaAs (111) side structure deposited in the top of the trapezoidal stripe structure. It is important to note that the quantum wire luminescence (line F) is red-shifted with respect to that of the quantum well layer deposited simultaneously in between the stripes. This red-shift is caused by the increased growth rate in z-direction on the narrow (100) top stripe plane, as described above. With a reduction in wire width a blue shift of line F is observed.

The assignment of the quantum wire luminescence line F is based on spatially-resolved PL as well as standard and polarization-dependent PLE investigations, which are presented in more detail elsewhere [27]. The PLE spectra of the quantum wire structures are always shifted in energy with respect to the corresponding spectra of the quantum well structures, proving the intrinsic character of luminescence line F. In addition, the wire luminescence intensity shows a distinct dependence on the orientation of the electric field vector of the linear-polarized light with respect to the quantum wire axis, while no such dependence is observed for the quantum well luminescence. As also reported in the literature [21], no evidence for an excitonic resonance or a peaked density of states is detected in the PLE spectra. Inhomogeneous broadening effects of the excitonic resonance due to wire width fluctuations along the wire axis and the reduced Sommerfeld-factor in 1D-systems [30] might cause the present experimental observations.

Summary

A new approach to realize trapezoidal or triangular (AlGa)As/GaAs quantum wire structures on (100) stripe facets by direct epitaxial growth using metalorganic vapour phase epitaxy (MOVPE) is presented. This concept takes advantage of the different growth rates on (100) and (111) planes as a function of substrate temperature to transfer a trapezoidal GaAs stripe structure (stripe width in the μ m-range), defined by simple photolithography and selective wet chemical etching, into an (AlGa)As/GaAs trapezoidal or triangular quantum wire structure in the nm-range. Growth investigations for GaAs and (AlGa)As in particular for facet dimensions in the submicrometer range as a function of growth temperature are presented using scanning electron microscopy (SEM) investigations. A growth rate enhancement on the (100) top stripe plane for submicrometer widths is observed for both GaAs as well as (AlGa)As, presumably due to the diffusion of ad-atom species from (111) side planes. Therefore, the growth rate strongly depends on the width of the growing plane, if the geometrical dimensions of the respective growth plane become smaller than typical diffusion lengths on planar surfaces. Further growth experiments on nm-scale crystallographic planes are necessary to clarify the respective growth mechanism in detail. The present approach can be applied for growth temperatures above about 675°C, thus, leaving a wide range of growth conditions for optimization of both the structural (geometrical width, fluctuations) as well as the optical properties (interface quality) of the respective quantum wire structure. Using high-resolution SEM investigations, the realization of (AlGa)As/GaAs quantum wire structures with lateral structure sizes of about 30 nm is proven. PL and PLE studies reveal the intrinsic character of the quantum wire luminescence. A distinct difference in the polarization dependence of this 1D-structures as compared to quantum well systems is found.

Acknowledgment

The authors are indebted to T. Och for expert technical support, to F. Scharner and H. U. Habermeyer (Max-Planck Institut für Festkörperforschung, Stuttgart) for preparation of the optical stripe masks. The expert support by A. Schaper during SEM investigations and by

MoP9

T.F. Albrecht during optical experiments is gratefully acknowledged. Part of this work has been sponsored by the Deutsche Forschungsgemeinschaft (DFG, Bonn).

* present address: Max-Planck-Institut für Festkörperforschung, D-70000 Stuttgart, Germany

References

- (1) Y. Arakawa and H. Sakaki, *Appl. Phys. Lett.* **40**, 939 (1982).
- (2) Y. Arakawa, K. Vahala and A. Yanv, *Appl. Phys. Lett.* **45**, 950 (1984).
- (3) I. Suemune and L.A. Coldren, *IEEE J. Quantum Electron.* **QE-24**, 1778 (1988).
- (4) A. Forchel, H. Leier, B.E. Maile and R. Gernann, in: "Advances in Solid State Physics" Vol. 28, p. 99, Ed. U. Rösler, Pergamon-Vieweg, Braunschweig (1988).
- (5) D. Heilmann, T. Demel, P. Grambow and K. Ploog, in: "Advances in Solid State Physics" Vol. 29, p. 285, Ed. U. Rösler, Pergamon-Vieweg, Braunschweig (1989).
- (6) Y. Hirayama, S. Tanaka, Y. Suzuki and H. Okamoto, *Phys. Rev. B* **37**, 2774 (1988).
- (7) J. Cibert, P.M. Petroff, G.J. Dolan, S.J. Pearson, A.C. Gossard and J.H. English, *Appl. Phys. Lett.* **49**, 1275 (1986).
- (8) K. Brunner, U. Bockelmann, G. Abstreiter, M. Wallner, G. Böhm, G. Tränkle and G. Weimann, *Phys. Rev. Lett.* **69**, 3216 (1992).
- (9) M. Kohl, D. Heilmann, P. Grambow and K. Ploog, *Phys. Rev. Lett.* **63**, 2124 (1989).
- (10) R. Gernann, A. Forchel, M. Briesch and H.P. Meier, *J. Vac. Sci. Technol.* **B7**, 1475 (1989).
- (11) H. Temkin, G.J. Dolan, M.B. Panitz and S.N.G. Chu, *Appl. Phys. Lett.* **50**, 413 (1987).
- (12) D. Gershoni, H. Temkin, G.J. Dolan, J. Dunsmuir, S.N.G. Chu and M.B. Panitz, *Appl. Phys. Lett.* **53**, 995 (1988).
- (13) K. Kash, J.M. Worlock, M.D. Sturge, P. Grabbe, J.P. Harbison and A. Scherer, *P.S.D. Lin. Appl. Phys. Lett.* **53**, 782 (1988).
- (14) K. Kash, J.M. Worlock, D.D. Maroney, A.S. Goetz, B.P. van der Gaag, J.P. Harbison, P.S.D. Lin and L.T. Florez, *Surf. Sci.* **229**, 245 (1990).
- (15) C. Grüt, A. Forchel, G. Mauckner, M. Emmertling, J. Straka and K. Pieger, *Surf. Sci.* **247**, 263 (1992).
- (16) J. M. Gaines, P.M. Petroff, H. Krömer, R.J. Simes, R.S. Geels and J.H. English, *J. Vac. Sci. Technol.* **B4**, 1378 (1988).
- (17) T. Fukui and H. Saito, *Jap. J. Appl. Phys.* **29**, L731 (1990) and references therein.
- (18) H.M. Cox, P.S. Lin, A. Yi-Yan, K. Kash, M. Seto and P. Bastos, *Appl. Phys. Lett.* **55**, 472 (1989).
- (19) E. Colas, E. Kapon, S. Simbony, H.M. Cox, R. Bhat, K. Kash and P.S. Lin, *Appl. Phys. Lett.* **55**, 867 (1989).
- (20) E. Kapon, S. Simbony, R. Bhat and D.M. Hwang, *Appl. Phys. Lett.* **55**, 2715 (1989).
- (21) M. Wallner, E. Kapon, D.M. Hwang, E. Colas and L. Nunes, *Phys. Rev. B* **45**, 6333 (1992).
- (22) S. Tsukamoto, Y. Nagamura, M. Nishioka and Y. Arakawa, *J. Appl. Phys.* **71**, 533 (1992).
- (23) K. Kojima, K. Mitsuoka and K. Kyima, *Appl. Phys. Lett.* **56**, 154 (1990).
- (24) R. Nözel, N.N. Ledentsov, L. Dawentz, K. Ploog and M. Hohenstein, *Phys. Rev. B* **46**, 3507 (1992).
- (25) F.E.G. Guimarães, B. Eisner, R. Westphalen, B. Spangenberg, H.J. Geelen, P. Balk and K. Heime, *J. Cryst. Growth* **124**, 199 (1992).
- (26) S. Tsukamoto, Y. Nagamura, M. Nishioka and Y. Arakawa, *Appl. Phys. Lett.* **62**, 49 (1993).
- (27) D. Bertram, W. Stolz, E.O. Göbel, J. Crystal Growth, to be published.
- (28) R.A. Lujan, F.K. Reinhart, *J. Appl. Phys.* **44**, 4172 (1973).
- (29) S.D. Hersee, E. Barbier, R. Blondeau, *J. Cryst. Growth* **77**, 310 (1986).
- (30) T. Ogawa and T. Tagahara, *Phys. Rev. B* **44**, 8138 (1991).

GaAs/Al_{0.3}Ga_{0.7}As Quantum Wire Structure Fabricated by Glancing Angle Molecular Beam Epitaxy on Reverse-Mesa-Etched GaAs (100) Substrates

S. Shimomura*, K. Inoue*, M. Tanaka*, A. Adachi*, M. Fujii*, T. Yamamoto*,

T. Watanabe*, N. Sano*, K. Murase*, and S. Hiyanishi*

- * Faculty of Engineering Science, Osaka University, Toyonaka, Osaka 560, Japan
- * Nissin Electric Co. Ltd., Umesu-Tabae-cho, Ukyo-ku, Kyoto 615, Japan
- * ATR Optical and Radio Comm. Res. Lab., Soraku-gun, Kyoto 619-02, Japan
- * Faculty of Science, Kansai Gakuin University, Nishinomiya, Hyogo 662, Japan
- * Faculty of Science, Osaka University, Toyonaka, Osaka 560, Japan
- * Research Center for Extreme Materials, Osaka University, Toyonaka Osaka 560, Japan

Selective growth of molecular beam epitaxy (MBE) on channelled substrates is one of the key technologies to fabricate laterally modulated structures with atomic-scale control. Glancing angle incident molecular beam enhances the growth rate dependence on different facets. In this paper, we report the fabrication of the quantum wire (QWR) structures by glancing angle MBE (GA-MBE) on reverse-mesa-etched GaAs (100) substrates (strips // [011]) and their characterization of optical properties by cathodoluminescence (CL).

10 periods of GaAs/AlAs (50 nm/50 nm) layers were grown by GA-MBE at 580°C under V/III = 26 (pressure ratio). Growth rates were 1 μm/h (GaAs) and 0.43 μm/h (AlAs). Substrates were not rotated during the growth. (111)B facets were preferentially grown for an epitaxial layer on the (100) top of the reverse-mesa structure in the [011] direction, when the incident molecular beam of the group III elements had a glancing angle of 42° from the (111)B facet surface. In this case, Ga and Al atoms do not impinge directly on the (111)B facet surfaces by the self-shadowing effect. After the growth of the GaAs/AlAs (50 nm/50 nm) multi-layers, an AlAs layer (200 nm) and GaAs cap layer (20 nm) were grown on both the (111)B facet and (100) face after rotating the substrate by 180°. Fig. 1 shows the cross sectional SEM photograph of the sample. The dark layers are AlAs and the bright are GaAs. The edge of each layer appears on the (111)B facet surface. Thus, this growth mode can be used for fabricating QWR structures. GaAs/Al_{0.3}Ga_{0.7}As T-shape QWRs were made using GA-MBE as shown in Fig. 2. The T-shape QWR consist of GaAs/Al_{0.3}Ga_{0.7}As (4.5 nm/20 nm) multi quantum wells (MQW) on the (100) plane and a 5-nm-thick GaAs layer covered by an Al_{0.3}Ga_{0.7}As barrier layer (30 nm). CL measurements at 78 K for the cleaved face of the sample showed spatially resolved two peaks at 771 nm and 784 nm. The higher energy CL peaks comes from MQW on the (100) plane and the lower energy peak comes from the T-shape QWRs. The intensity of the lower energy peak gradually increased with approaching the excited position by the electron beam to the T-shape QWR region. This shows that carriers excited by the electron beam in MQW region flow into the T-shape QWR region which have a lower energy state, indicating carriers were successfully confined within the very narrow T-shape QWR structures.

GaAs/Al_{0.3}Ga_{0.7}As Quantum Wire Structure Fabricated by Glancing Angle Molecular Beam Epitaxy on Reverse-Mesa-Etched GaAs (100) Substrates

S. Shimomura*, K. Ito*, M. Tanaka*, A. Adachi*, M. Fujii*, T. Yamamoto*,
T. Watanabe*, N. Sato*, K. Murase*, and S. Hiyamizu*



Fig. 1



Fig. 2

MoP10

Coverage Dependence of Migration Potential
of Cation Adatoms on GaAs(001)-(2x4) Surface
Kenji Shirasaka*, Tomonori Inoue*, and Takahisa Ohno*
*NII Basic Research Laboratories, Musashino-shi, Tokyo 180, Japan
*NTT LSI Laboratories, Atsugi-shi, Kanagawa 243-0292, Japan

We theoretically investigate the migration potential of cation adatoms on reconstructed As-rich GaAs(001)-(2x4) surface by *ab initio* calculation. By increasing the number of cation adatoms, we also study how migration potential depends on coverage. The calculated results for Ga adatoms suggest that the long bridge sites are energetically the most favorable at the initial stage of crystal growth. However, as the Ga coverage increases, the missing thimer row sites become the most favorable. Migration potentials strongly depend on the adatom coverage. Similar results were obtained for Al adatom migration. Furthermore, based on these migration potentials, we demonstrate the dynamical behaviors of cation adatoms on GaAs(001) surface including AlAs-GaAs binary systems by performing Monte Carlo simulations at finite temperatures.

1. Introduction

Adatom migration on solid surfaces is a fundamental problem in surface science. Also, adatom migration has been found to be a key mechanism in epitaxial growth. It is essential to increase adatom migration in order to obtain high quality samples when using epitaxial growth techniques. This is because adatoms migrate over a wide area, leading to a flat surface during the growth [1]. Consequently, the synthesized interfaces become sharp. Therefore, numerous experiments have been carried out to clarify the mechanism of adatom migration during epitaxial growth [2, 3]. However, the migration potentials obtained by these experiments are usually macroscopic, containing both intrinsic migration and extrinsic effects. It is not easy to obtain information on intrinsic adatom migration by experiment. Thus theoretical calculations are necessary in order to study the microscopic processes of adatom migration. Various theoretical works have been carried out: BCT theory [4], molecular dynamics (MD) [5], and Monte Carlo (MC) [6, 7] simulations are the most popular approaches, and have been widely studied. In these theoretical studies, the basic parameters are usually chosen to reproduce the experimental results. Therefore, the microscopic foundation of these parameters are not clear.

In order to study the microscopic parameters, we reported the *ab initio* calculation of the adatom migration potential of Ga adatoms on an As-terminated GaAs(001) surface [8]. However, the surface unit cells used in Ref. [8] were not large enough. Consequently, the results showed Ga migration at high Ga coverage. In this paper, we use a very large surface unit cell and study the migration potential for low Ga coverage. Furthermore, we investigate the dependence of the migration potential on adatom coverage by increasing the number of Ga adatoms. The migration potentials of Al adatoms are also investigated. In order to qualitatively investigate dynamical behavior of adatoms, we performed the Monte Carlo (MC) simulation of crystal growth including GaAs-AlAs binary systems based on these migration potentials.

2. Method

We use the *ab initio* pseudopotential method on the basis of local density functional formalism (LDF) [9]. We adopt Kleinman-Belinfante separable pseudopotentials and the kinetic energy cut-off value was set fully, chosen so as not to produce ghost bands [10]. The electron exchange correlation potential is approximated by Wu-Yang's improved form, formula. To simulate the GaAs(001) surface, the used repeated slab geometry is employed. The unit supercell consists of five atomic layers of GaAs, one atomic layer of intrinsic Al atoms, and a vacuum region equivalent to about five atomic layers in thickness. The validity of the thickness of this repeated slab model is carefully checked. Surface termination with the intrinsic Al atoms is a very powerful method for eliminating the interaction of the surface states of both sides of the slab, and this method is discussed in detail elsewhere [12].

To calculate the migration potential E_{mig} , we optimize the z coordinate of an adatom and the positions of substrate atoms. Inversely, the (x, y) coordinates of an adatom are fixed. The present

study uses a (111) surface unit cell of $\sqrt{3} \times \sqrt{3}$. This unit cell contains two (2x2) GaAs surface superstructures and is four times larger than that of our previous report [8]. In the present calculation, after one adatom is adsorbed on the surface unit cell, adatom coverage becomes 0.0625. Coverage dependence of the potential surface is investigated by increasing the number of adatoms in the surface unit cell. In this process, we fixed previously adsorbed adatoms to the most stable sites, and the migration potential of the adatom that arrives next is then calculated.

In this calculation, we used the nearest-neighbor model for the GaAs(001) surface, which consists of three surface sites: dimers and one missing dimer in a (2x2) unit cell. Talia *et al.* recently proposed additional models for the (2x2) GaAs surface, where two of the six surface As atoms are exchanged by two Ga atoms [11]. We calculated the relative stability of Talia's models compared with the usual missing dimer model. The results show that Talia's models are energetically unstable compared with the usual missing dimer model [11] over a wide range of As chemical potential [13]. Therefore, investigating migration potentials using the missing dimer model is realistic and reliable.

In the stochastic Monte Carlo (MC) simulation, kinetic rates are assumed to be of Arrhenius form

$$R = R_0 \exp(-\Delta E/k_B T) \quad (1)$$

where R_0 is the diffusion prefactor in hops per second, and ΔE is the activation energies which are determined from the obtained migration potential. Coverage dependence of the migration potential is also taken into account. In this study, the diffusion prefactor of Ga, $R_0(\text{Ga})$, is adjusted to the value used in ordinary MC simulation [14], i.e., the predominant migration path and the prefactor of Al is set to be $R_0(\text{Al}) = 1/67 R_0(\text{Ga})$ based on our *ab initio* molecular dynamics calculation [15]. MC formalism is described in detail below, where [17].

3. Calculated Results and Discussions

3.1 Migration Potentials

We first address the adsorption potential of Ga adatom migration on an As-stabilized GaAs(001) surface. In Fig. 1 (a), adsorption sites in the surface unit cell are indicated by the alphabet and Fig. 1 (b) (c) (d) and (e) show the migration potential surface of Ga adatoms at Ga coverage (0), 0.0625, 0.125, 0.1875, and 0.25, respectively. As seen in Fig. 1 (b), the most stable adsorption site at 0.0625 is a long bridge site (F site) where it is located between two As-dimer rows. Missing dimer region sites (A, B, C sites) are not stable in this figure. This shows that Ga adatoms tend to be adsorbed on F's dimer region at the initial stage of epitaxial growth. The favorable migration path is along the (110) direction on the dimer region.

After one As atom is adsorbed on the surface, migration potential changes. As seen in Fig. 1 (c), migration potential at 0.0625 shows that another long bridge site is the most stable as F's, 1 (b). The most noticeable change in this figure is that the missing dimer region becomes more stable after one long bridge site (F site) is occupied.

As the number of adsorbed Ga atoms increases (Ga coverage increases), this tendency becomes more clear. As seen in Fig. 1 (d), the Ga bridge site in the missing dimer region (B site) becomes the most favorable at 0.1875. The B site is energetically more stable than the second favorable site (EB site) by about 0.3 eV. From this figure, the most favorable migration path is along the missing dimer row. After the two long bridge sites (F sites) are occupied, Ga atoms tend to be adsorbed in the missing dimer rows and migrate through the missing dimer rows.

At the Ga coverage of 0.25, the missing dimer regions are much more stable than the dimer regions, and the migration path clearly lies in the missing dimer rows (E, G, I). Detailed structures of this migration potential at 0.25 are different from those in our previous report [8], which corresponds to 0.0625, however, the basic characteristics are very similar. A detailed comparison between these two migration potentials will be given below.

As explained above, migration potentials of Ga adatoms strongly depend on the Ga coverage, and the characteristics of Ga migration dramatically change as Ga coverage increases. Therefore, to study epitaxial growth by Monte Carlo simulations, it is essential to take into account the above coverage dependence of migration potentials.

We also calculated the migration potential of an Al adatom on the As-stabilized GaAs(001) surface. The calculated results show that the basic characteristics of Al migration potential are the same as those of Ga migration potential, but the absolute value of the activation barrier is about 1.1 times larger than that of Ga. Coverage dependence of Al migration potential is also similar to that of Ga migration potential.

3.2 Monte-Carlo Simulations

To investigate the dynamical behavior of adatoms qualitatively, we performed the MC simulations. Figures 2 (a) and (b) give the growth profiles at Ga coverage 0.061 and 0.25, where the MC simulation was carried out at 873 K with growth rate 3 ML/sec on an As-stabilized GaAs(001) (2x2) surface. As seen in Fig. 2 (a), randomly impinged Ga atoms predominantly occupy the lattice sites on the dimer region at 0.061.

As the coverage increases, the favorable lattice sites for Ga adatoms change from those on the dimer region to those along the missing dimer rows as seen in Fig. 2 (b). This reflects the migration potential where the energetically stable site is located at long bridge sites (F site) in the dimer region at 0.06125, while the Ga bridge site (B site) in the missing dimer region becomes favorable at 0.25.

In Figs. 3 (a) and (b), we show the growth profiles of GaAs-AlAs binary systems under the same conditions as the above pure GaAs systems. Figure 3 (a) and (b) correspond to the MC results of the cation coverage 0.061 and 0.25, respectively. The white circles, black circles, and shaded circles indicate the Ga adatoms, Al adatoms, and surface As atoms, respectively. The basic characteristics of the growth profile are very similar to those of pure GaAs systems. The noticeable fact is that movement of Al atoms with the increase of adatom coverage is much slower than that of Ga atoms. This reflects that migration barrier for Al atoms is larger than that for Ga atoms. In this calculation for the binary systems, the resultant growth profile shows that Ga and Al atoms are randomly distributed over the surface without any segregation observed in the experiment [17].

4. Conclusions

We investigated the migration potential of cation adatoms by the *ab initio* pseudopotential method, and based on the results, we performed a Monte Carlo (MC) simulation of epitaxial growth.

The following characteristics are obtained from the calculated migration potentials. The most stable sites of cation adatoms are located in the dimer region at the initial stage of epitaxial growth. However, stable sites change from the dimer region to the missing dimer region as the cation adatom coverage increases. Migration potentials of cation adatoms strongly depend on the cation coverage.

MC simulation reflects the coverage dependence of migration potential. At the cation coverage of 0.1, impinged cation atoms predominantly occupy the dimer region. However, the missing dimer region is occupied when the cation coverage is 0.25. This preliminary MC simulation for a GaAs-AlAs binary system does not reveal any experimentally observed segregation.

In the next step, we plan to investigate other processes such as the reactions at the step sites and elsewhere. When these processes are taken into account, our theoretical simulation will become more realistic and reliable.

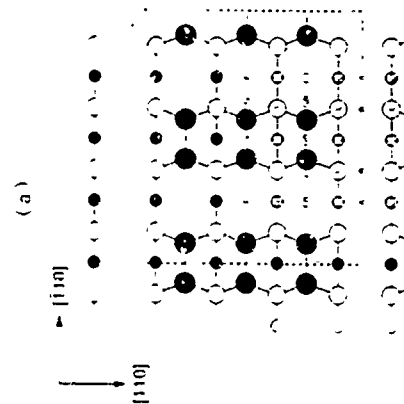
Acknowledgments

We would like to thank Dr. Yoshiji Horiuchi, Dr. Shintaro Miyazawa, and Kazuo Hayada for their fruitful comments and continuous encouragement throughout this work.

References

- [1] Y. Horiuchi, M. Kawashima, and H. Yano, *Int. Jpn. Appl. Phys.* **25**, L568 (1985); *Appl. Phys. Lett.* **50**, 1056 (1986).

Fig. 1



- [2] J. H. Neave *et al.* *Appl. Phys. Lett.* **47**, 100 (1985).
- [3] T. Nishimura and K. I. Cho, *Jpn. J. Appl. Phys.* **27**, L12 (1988).
- [4] A. K. Myers-Buchanan *et al.* *Phys. Rev. B* **42**, 5511 (1990).
- [5] D. K. Choi *et al.* *J. Cryst. Growth* **85**, 9 (1987).
- [6] S. Clark and D. D. Vvedensky, *J. Cryst. Growth* **95**, 28 (1989).
- [7] T. Ito, T. Ohno, and K. Shiraishi, *Proc. 21st Int. Conf. Phys. Semicond.* (Beijing, 1992) p. 550.
- [8] K. Shiraishi, *Appl. Phys. Lett.* **60**, 1163 (1992); *Appl. Surf. Sci.* **66/67**, 2105 (1992).
- [9] D. R. Hamann *et al.* *Phys. Rev. Lett.* **43**, 1191 (1979).
- [10] T. Ohno, *Phys. Rev. Lett.* **70**, 631 (1993).
- [11] J. F. Liu *et al.* *Phys. Rev. Lett.* **69**, 3968 (1992).
- [12] K. Shiraishi, *J. Phys. Soc. Jpn.* **59**, 3455 (1990).
- [13] K. Shiraishi and T. Ohno, unpublished.
- [14] S. V. Ghossein and A. Madhukar, *Phys. Rev. Lett.* **56**, 1066 (1986).
- [15] T. Ohno, K. Shiraishi, and T. Ito, submitted to 1993 Fall Meeting of the MRS.
- [16] K. Shiraishi, T. Ito, and T. Ohno, unpublished.
- [17] M. Tsuchiya *et al.* *Appl. Phys. Lett.* **54**, 1690 (1989).

Figure Captions

Fig. 1 Surface unit cell used in our calculation and the calculated migration potentials for Ga adatoms. (a) (1x1) surface unit cell. Adsorption sites are indicated by the alphabet. (b) migration potential at $\theta=0.025$, (c) $\theta=0.125$, (d) $\theta=0.157$, and (e) $\theta=0.25$.

Fig. 2 Calculated growth profiles for Ga adatoms at the coverage of (a) $\theta=0.10$ and (b) $\theta=0.25$. The profiles were obtained by MC simulation at a growth temperature of 373 K.

Fig. 3 Calculated growth profiles for GaAs MBE systems at the coverage of (a) $\theta=0.10$ and (b) $\theta=0.25$. The profiles were obtained by MC simulation at growth temperature of 373 K.

MoP11

Raman scattering investigation on the ordered incorporation of Si dopant atoms on (001) GaAs vicinal surfaces during MBE growth

M. Ramsteiner¹, J. Wagner², G. Jung¹, D. Behr², L. Dameritz¹, and R. Hey¹

¹ Paul-Drude-Institut für Festkörperelektronik, Hausvogteiplatz 5-7,

D-10117 Berlin, Germany

² Fraunhofer-Institut für Angewandte Festkörpertechnik Tullastraße 72,

D-79108 Freiburg, Germany

Abstract

Using Raman scattering by local vibrational modes (LVM) and collective electronic excitations we have investigated the ordered incorporation of Si dopant atoms on vicinal GaAs(001) surfaces. LVM spectra revealed for a sequence of δ -doped samples grown by molecular beam epitaxy (MBE) under specific conditions that the Si dopant atoms are predominantly incorporated on Ga-sites even at a doping concentration as high as $1.8 \times 10^{13} \text{ cm}^{-2}$. For a sample grown under conditions established by real-time high-energy electron diffraction (RHEED) to be favourable for the wire-like Si incorporation, a polarization asymmetry in the Raman scattering intensity of collective intersubband plasmon-phonon modes arising from the δ -doping layer has been found.

1. Introduction

A combination of lattice step growth with δ -doping on GaAs(001) vicinal surfaces has been shown to be a promising technique to prepare doping wires [1,2]. Thereby, under certain growth conditions, a preferential attachment of Si atoms at misorientation steps leads to an ordered array of dopant atom strings. A scheme of the growth mode¹ is shown in Fig. 1. So far, evidence for this self-organization during Si incorporation has been traced only from reflection high-energy electron diffraction (RHEED) measurements. Therefore, it is desirable to have other characterization methods at hand to confirm the above results. Raman spectroscopy is such a method. To investigate the lattice sites occupied by the Si dopant atoms in MBE layers Raman scattering by local vibrational modes (LVM) has been shown to very useful [3]. In addition, Raman scattering by plasmon excitations has been successfully used to characterize the two-dimensional electron gas in δ -doped GaAs [4] as well as the one-dimensional electron gas in quantum wire structures [5].

We have studied heavily Si doped samples grown by molecular beam epitaxy (MBE) on GaAs(001) substrates tilted towards the (111)Ga plane. The growth conditions to obtain the desired self-organization during Si incorporation have been established by in-situ RHEED measurements [2]. In order to proof the wire-like Si incorporation, Raman scattering by electronic excitations has been studied.

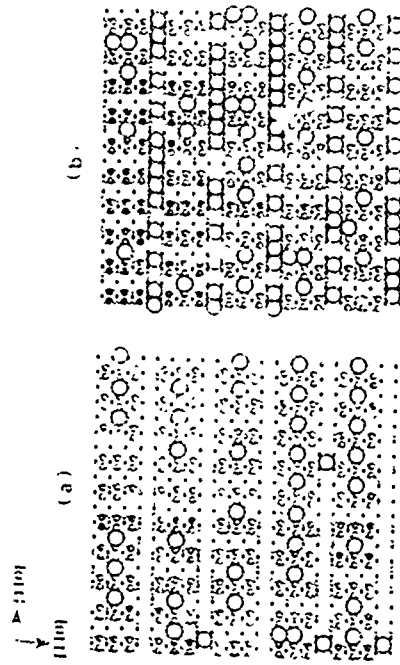


Fig. 2

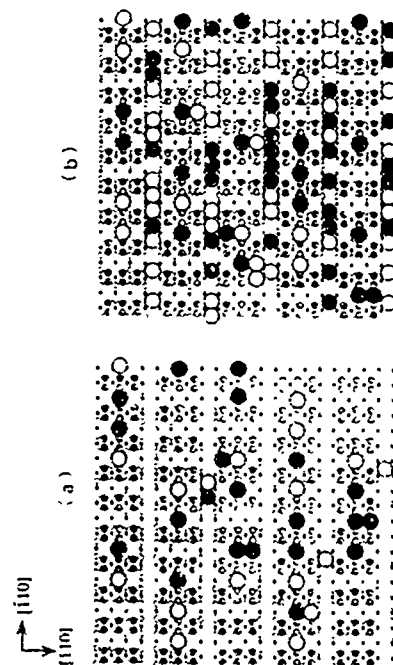


Fig. 3

2. Experimental

Raman scattering is in general sensitive to the inequivalence of the orthogonal crystallographic directions [110] and $\bar{1}\bar{1}0$ in polar semiconductors like GaAs [6,7]. Therefore, to study polarization asymmetries introduced by doping-wires aligned along the $\bar{1}\bar{1}0$ direction, a comparison with reference samples having a random arrangement of the dopant atoms is necessary. Therefore, three samples grown by solid-source MBE have been studied (see Tab. 1). For samples B and C we used GaAs(001) substrates misoriented 2° toward the $\bar{1}\bar{1}0$ plane, resulting in a misorientation step separation of 8 nm. Sample C has been grown using conditions favourable for a wire-like Si incorporation along the $\bar{1}\bar{1}0$ direction [2]. For sample B the substrate temperature during Si deposition was decreased, making the formation of doping wires less probable due to the smaller diffusion length of the Si atoms. Sample A was grown side by side with sample C on a perfectly oriented GaAs(001) substrate, where the absence of an ordered arrangement of misorientation steps prevents the formation of doping-wires. In all samples a single Si δ -doped layer with an intended dopant concentration of $1.8 \times 10^{13} \text{ cm}^{-2}$ was placed at a nominal depth of 10 nm below the surface. The growth details are described in Ref. 8.

	δ -doping with Si	misorientation steps	appropriate Si diffusion
sample A	x	—	—
sample B	x	x	—
sample C	x	x	x

Tab. 1. Growth characteristics of sample C and reference samples A and B. Favourable conditions for the wire-like Si incorporation along the $\bar{1}\bar{1}0$ direction have been used for sample C.

Raman measurements were carried out in backscattering from the epilayer surface with the sample cooled by He exchange gas in a continuous-flow variable-temperature He cryostat. Optical excitation was performed at 3.00 eV or 3.05 eV with a Kr ion laser in resonance with the GaAs Γ_1 band gap [3,4,9]. The optical probing depth $l(2\alpha)$ for these photon energies is about 10 nm, which is matched to the nominal depth of the δ -doping layers [3]. For Raman spectra of LVM a depolarized scattering configuration $\chi(y,z)\chi$ was used, where x , y and z denote $[001]$, $[010]$ and $[110]$ crystallographic directions. Polarized Raman spectra were recorded in the $\chi(z,z)\chi$ and the $\chi(y,y)\chi$ scattering configurations, where y and z denote $[110]$ and $\bar{1}\bar{1}0$ crystallographic directions.

3. Results and Discussion

Fig. 2 shows low-temperature (77 K) Raman spectra of sample A (Fig. 2(a)), B (Fig. 2(b)) and C (Fig. 2(c)) excited at 3.00 eV. All spectra show the LVM from Si on Ga site (Si_{Ga}) at the expected frequency of 384 cm^{-1} [10] superimposed on the second-order phonon spectrum of GaAs [9]. An additional contribution to the background arises from electronic excitations which are discussed below. LVM from the acceptors Si on As site (Si_{As}) at 399 cm^{-1} or the Si-X defect centre at 369 cm^{-1} [10] have not been resolved, which in-

icates a low electrical compensation of the Si donors (Si_{Ga}) in the present samples in spite of the high doping concentration in the δ -layer. This supports the RHEED results from which it has been concluded that most of the Si dopant atoms are incorporated on Ga site. In more recent RHEED studies it has been shown that the Si dopant atoms in sample C should be incorporated as Si_{Ga} - Si_{Ga} second-next neighbour pairs [8]. The present Raman data show the LVM of Si_{Ga} donors, however, it is not clear to what extent the formation of Si_{Ga} - Si_{Ga} second-next neighbour pairs should affect the LVM spectra.

For excitation at 3.05 eV scattering by collective intersubband plasmon-phonon modes (ω_A and ω_B) is observed in the polarized spectra besides scattering by one (Si_{Ga}) and two (Si_{As}) longitudinal optical phonons. This is shown in Fig. 3 for the scattering configuration $\chi(z,z)\chi$. As discussed for similar Si δ -doped GaAs layers, these collective modes are assigned to excitations involving various electron subbands [4,11]. The scattering by collective intersubband plasmon phonon modes was found to be strongly resonant with the Γ_1 band gap of GaAs [4]. The collective mode frequency ω_B increases from 980 cm^{-1} to 1110 cm^{-1} when going from sample B (Fig. 3(b)) to sample C (Fig. 3(c)). This effect can be discussed in terms of an additional lateral confinement and/or an locally increased carrier density because of the segregation of the dopant atoms at the misorientation steps. However, a quantitative analysis of the peak positions and widths for the collective mode spectra is complicated by the fact that several subbands are populated in the present structures, which leads to a coupling of the individual modes [11]. For sample C where wire-like Si incorporation is expected, self-consistent, two-dimensional, solutions of the Schrödinger and Poisson equations are required to calculate the spectra of collective intersubband excitations. For the present separation of the misorientation steps, and thus the Si doping wires, of 8 nm the individual wires are expected to be strongly electronically coupled [12] forming a lateral n - i - n superlattice. Nevertheless, the observation of the collective modes in the present sample structures indicates a high carrier density of $\geq 10^{13} \text{ cm}^{-2}$ [4]. Otherwise, at lower carrier densities, the δ -doped region placed only 10 nm underneath the sample surface would be almost entirely depleted with no individual intersubband excitations resolved [4]. This estimate of the carrier density is consistent with the low compensation ratio indicated by the above LVM data.

In order to investigate polarization asymmetries in the scattering intensities, polarized Raman spectra were recorded under the same conditions as described for Fig. 3 but with the scattering configuration $\chi(y,y)\chi$, i.e. with the sample rotated by 90° . As a measure for polarization asymmetries we computed the difference spectra $I(z,z) - I(y,y)$ between the spectra polarized along $z' = [110]$ and those polarized along $y' = [\bar{1}\bar{1}0]$. As can be seen in Fig. 4 the collective mode at the frequency ω_A shows an increasing polarization asymmetry when going from sample A (Fig. 4(a)) to sample B (Fig. 4(b)) and to sample C (Fig. 4(c)), i.e. in the direction of an increasing probability for the formation of doping wires. The asymmetries observed for samples A, B, are entirely due to the intrinsic inequivalence of the $[110]$ and $\bar{1}\bar{1}0$ crystallographic directions. The enhanced asymmetry observed for sample C can be explained by an ordered incorporation of the Si dopant atoms along misorientation steps, leading to a lateral modulation of the potential confining the

two-dimensional electron gas at the δ -doping layer. This supports the results obtained by RHEED measurements [2].

The origin for the polarization asymmetry induced by the wire-like incorporation of the dopant atoms is an additional polarization dependence in the efficiency of scattering by the collective mode at the frequency ω_L caused by a lateral modulation of the electron potential, which is attributed to a change of the lateral confinement potential in the conduction band. For the collective mode at the frequency ω_L such an increased polarization asymmetry in sample C was not found. This can be explained assuming a larger contribution of transitions involving higher lying subbands to this collective mode, which are less sensitive to the lateral potential modulation. Preliminary results obtained from Raman measurements using optical excitation in resonance with the $E_0 + \Delta_0$ band gap of GaAs confirm the above results.

4. Conclusions

We have used Raman scattering by local vibrational modes (LVM) and by collective intersubband plasmon-phonon modes to study Si δ -doped GaAs layers grown by MBE on GaAs(001) vicinal surfaces. LVM Raman spectra indicate a low compensation of the Si on Ga-site donor for the present δ -doped samples in spite of the high doping level of $1.8 \times 10^{13} \text{ cm}^{-2}$. For samples grown under certain conditions such as to promote the formation of Si doping wires, polarized Raman spectra of collective electronic excitations indicate a lateral electron potential modulation. This gives support to results obtained by real-time high-energy electron diffraction (RT-ED) measurements from which a wire-like incorporation of the Si dopant atoms has been inferred.

Acknowledgements

We would like to thank P. Koidl and H. S. Rupperecht as well as K. Ploog for continuous support of the work at the Fraunhofer-Institut für Angewandte Festkörperphysik and the Paul-Drude-Institut für Festkörperelektronik.

References

1. C.E.C. Wood, *J. Appl. Phys.* **71**, 1760 (1992).
2. L. Dierentz, K. Hagenstam and P. Schützengruber, *J. Cryst. Growth* **127**, 1051 (1993).
3. J. Wagner, *Mat. Science Forum* **65-66**, p. 1 (1990) and references therein.
4. J. Wagner, M. Ramsteiner, D. Richards, G. Fasol, and K. Ploog, *Appl. Phys. Lett.* **58**, 143 (1991).
5. T. Egeler, G. Abstreiter, G. Weinmann, J. Demet, D. Heunmann, P. Grambow, and W. Schlapp, *Phys. Rev. Lett.* **65**, 1804 (1990).
6. J. Méndez and M. Cardona, *Phys. Rev. Lett.* **51**, 1297 (1983).

7. J. Méndez and M. Cardona, *Phys. Rev. B* **31**, 3696 (1985).
8. L. Dierentz, C. Muggelberg, R. Hey, U. Kostal, and M. Hörner, this conference.
9. R. Trommer and M. Cardona, *Phys. Rev. B* **17**, 1865 (1978).
10. R. Newman, in *Proc. of the Int. Conf. on the Science and Technology of Defect Control in Semiconductors*, ed. by K. Sumino, p. 65 (North Holland, Amsterdam, 1990) and references therein.
11. D. Richards, J. Wagner, M. Ramsteiner, U. Flenberg, G. Fasol, and K. Ploog, *Surf. Sci.* **267**, 61 (1992).
12. G.L.W. Bauer and A.A. van Gorkum, in *Science and Engineering of One- and Zero-Dimensional Semiconductors*, ed. by S.F. Beaumont and C.M. Sotomayor Torres, p. 135 (Plenum, New York, 1990).

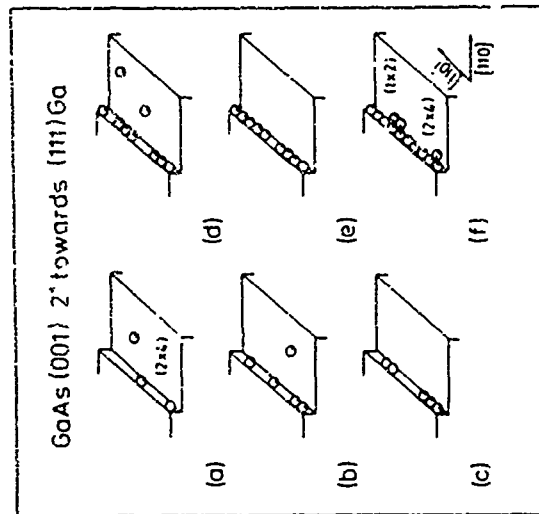


Fig. 1. Schematic model illustrating the ordered incorporation of Si dopant atoms at misorientation steps along the $[110]$ direction on a GaAs(001) vicinal surface $[21]$ with the Si coverage increasing from (a) to (f).

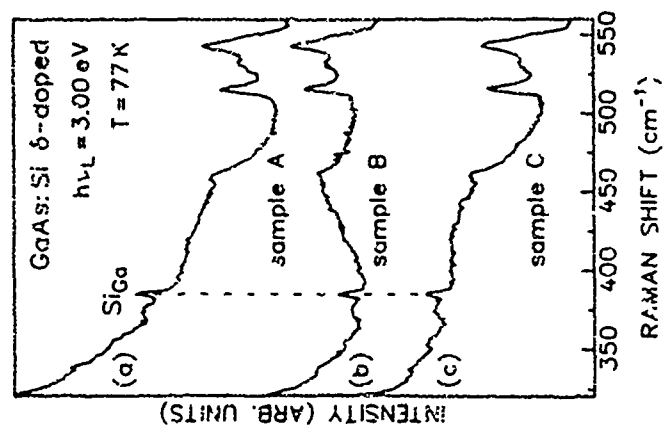


Fig. 2. Low-temperature (77 K) Raman spectra of Si δ -doped GaAs grown on perfectly oriented (a) and misoriented (b) and (c) GaAs(001) substrates. Optical excitation was at 3.00 eV close to resonance with the GaAs E_1 band gap.

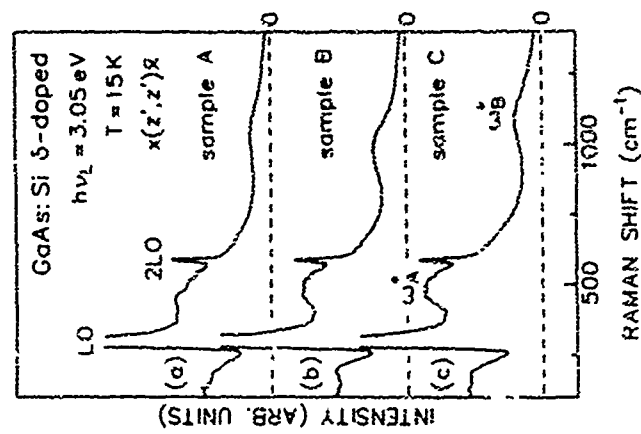


Fig. 3. Polarized low-temperature (15 K) Raman spectra of Si δ -doped GaAs grown on perfectly oriented (a) and misoriented (b) and (c) GaAs(001) substrates. Optical excitation was at 3.05 eV in resonance with the GaAs E_1 band gap.

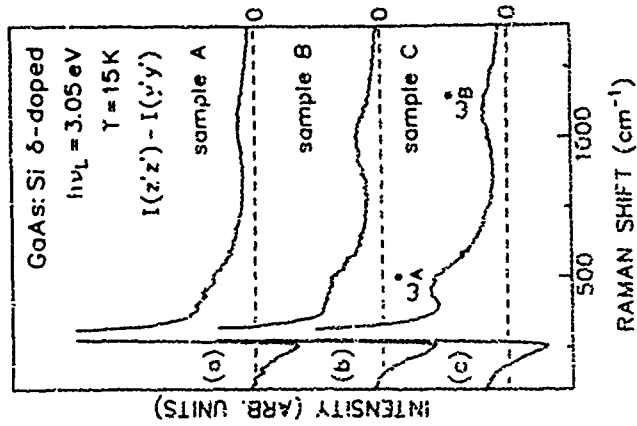


Fig. 4. Difference spectra $[I(z'z') - I(y'y')]$ between polarized low-temperature (15 K) Raman spectra recorded in the $x(z'z')x$ and the $x(y'y')x$ configurations, respectively, where y' and z' denote $[110]$ and $[110]$ crystallographic directions. Optical excitation was at 3.05 eV in resonance with the GaAs E_1 band gap.

Disorder-Induced Raman Scattering of Folded Phonons in Quantum Wells and Superlattices

T. Rüd, V. I. Belitsky, J. Springer, V. I. Spryda, N. I. Andronov and K. Ploog
Max-Planck-Institut für Festkörperforschung, Heisenbergstr. 1, D-7050 Stuttgart 80
Federal Republic of Germany

In addition to the well known folded modes, Raman spectra of GaAs-AlAs superlattices and multiple quantum wells show in the low energy regime a continuous acoustic phonon background related to scattering processes where crystal momentum q , along the growth direction is not conserved. Such a situation may occur when excitations become localized due to layer thickness fluctuations. This causes resonant Raman scattering from a random distribution of isolated wells. Superimposed on this background we find pronounced peaks and dips in the Raman intensity. These peculiarities occur at gaps of the folded longitudinal acoustic (LA) phonon dispersion and at energies where LA and transverse acoustic (TA) branches cross. The observations are explained by the dependence of the Raman efficiency on phase crystal momentum.

1. INTRODUCTION

In Raman experiments from semiconductor superlattices (SL) or multiple quantum wells (MQW) doublets of acoustic phonons are observed which reflect the "back folding" of bulk dispersions into a mini Brillouin zone [1,2]. The doublets arise from a coherent superposition of contributions to the scattering intensities from individual wells. This superposition is also the origin of crystal momentum conservation both along the growth direction (q_z) and perpendicularly (q_\perp) in the scattering process.

Recently additional features apart from the allowed folded phonon doublets, have been observed which can not be accounted for by standard selection rules. These structures consist of a continuous emission, background and pronounced intensity anisotropies (pr, as and dips). Due to its close vicinity to the exciting laser line the background has not attracted particular attention but was attributed to an incoherent scattering process. However, recent magneto-optical experiments, however, demonstrated that the continuous emission exhibits oscillatory intensity variations corresponding to interference between Landau levels [3,4]. It was noticed that the peaks and dips correlate with folded phonon gaps [1,3,6,4] but no explanation for their relation to the phonon dispersion and to mechanisms for Raman scattering has been given. The features were tentatively attributed to antiresonances associated with acoustic phonons at the reduced Brillouin zone edge [1] to doublets induced by q_z non-conserving scattering [5,7] or to local modes near the dispersion gaps [3].

In this report we present a model for Raman scattering by acoustic phonons from individual quantum wells due to interface roughness and layer thickness fluctuations. The dependence of the Raman intensity on phonon wave vector explains most of the observations. They are caused by a partial breakdown of crystal momentum conservation.

This case is illustrated in Figure 1. The solid line shows the Raman spectrum of a sequence of 11 GaAs quantum wells with $d = 100 \text{ \AA}$ embedded in AlAs layers with the same thickness. For simplicity the wave vector of incident and scattered light has been set to zero. Strong scattering only occurs at Raman shifts corresponding to zone center modes of the folded dispersion. The solid line was calculated with a constant detuning of $\Delta = 10 \text{ cm}^{-1}$ for all wells. Due to the finite size of the system the intensity between the zone center modes does not vary completely. Note the relative increase of the Raman signal due to outgoing resonance at a shift of 10 cm^{-1} . The dotted line in Fig. 1 was calculated under the assumption that the central one of the eleven layers has a larger confinement energy than the others by 10 cm^{-1} , e.g. due to a slightly smaller well width. In this case the exciting laser light is exactly in resonance with that one well whereas all other wells are slightly off resonance. The effect of such a perturbation is an increase of the Raman intensity near the laser line by almost two orders of magnitude.

The relative intensity of background and folded phonon doublet scattering is determined by the homogeneous width of the electronic structure and its inhomogeneous broadening due to layer thickness fluctuations and interface roughness. An interpretation of recent experiments along these lines has been given in Ref. [8].

While these considerations are valid for bulklike acoustic phonons, a treatment of superlattice effects has to take the influence of folded phonon dispersion gaps at the center and edge of the mini Brillouin zone into account. In a superlattice transmission and reflection at each interface cause the displacement field $u(q_z)$ of acoustic phonons along the growth direction to be a linear combination of two counterpropagating plane waves

$$u(q_z) = \frac{1}{2} [e^{iq_z z} + A e^{-iq_z z}] \quad (2)$$

The wave vectors k_z are given by the bulk dispersions of the constituent layers and the amplitude coefficients A_z are determined from periodicity and matching boundary conditions at the interfaces. We find that the Raman intensity for a mode $\omega(q_z)$ is proportional to the amplitude difference

$$A \approx |1/q_z| - A_z(q_z) \quad (3)$$

in the wells. Qualitatively this result can be easily understood for the special case of dispersion gaps. There the phonon displacement field is either symmetric or antisymmetric with respect to the center of the well i.e. the coefficients A_z are equal in magnitude but either equal or opposite in sign. The associated strain field which determines deformation potential electron-phonon interaction with acoustic phonons [3,10], is given by the first derivative of $u(q_z)$ with respect to the coordinate z and has therefore just the opposite symmetry. Thus the Raman intensity vanishes at one side of a dispersion gap whereas it has a non zero value at the other side. This

leads to characteristic peaks and dips in the spectrum far from the gaps intermediate situations occur. This behavior is clearly related to the oscillatory changes of dispersion gaps studied in Ref. [11].

At energies where LA and TA dispersions cross, interface gaps open for phonons with a non zero in-plane crystal momentum component q_\perp [12,13]. In backscattering Raman experiments q_\perp is conserved. A way to circumvent this selection rule is provided by impurity mediated second order Raman processes [14]. In quantum wells and superlattices interface roughness provides an elastic scattering mechanism in analogy to that of impurities. Therefore phonons $\omega(q_\perp, q_z)$ also contribute to the Raman intensity. From the width of interface gap structures and their strength compared to that of peak and dip associated with zone edge dispersion gaps information on length scales of interface roughness can be obtained.

III. EXPERIMENT

Figure 1c shows the Raman spectrum of a narrow GaAs-AlAs superlattice with a layer thickness of 10 monolayers. The resonant enhancement of the continuous emission intensity in a magnetic field was exploited to obtain these data (T=10 K, B=11 T, $\lambda_{\text{exc}} = 1.727 \text{ \mu m}$ excitation in resonance with the $n=2$ Landau level of the first subband transition) [3]. In Figure 2a the LA phonon dispersion for this structure is given vs. superlattice wave vector. Figure 2b displays the amplitude difference factor A superimposed on the continuous emission background. Fig. 2c shows a series of characteristic intensity anisotropies in comparison with Fig. 2a the coincidence of most of these features with phonon dispersion gaps becomes evident. The character of the intensity anisotropies is in complete agreement with the behavior of A on either side of the various gaps. The remaining features can be attributed to internal gaps. Most pronounced is the lowest LA-TA intersecting dip at 8 cm^{-1} . In a detailed analysis we find that in plane scattering from growth islands with a diameter of about 450 Å yields best agreement with the experiment.

The influence of roughness-mediated in plane scattering processes is further highlighted in Fig. 2b. The experimental spectrum from a symmetric GaAs-AlAs superlattice with layer thicknesses of 6.7 monolayers (top) is compared to the best theoretical description within our model (bottom). The spectrum was measured at a temperature of 77 K without magnetic field in resonance with the direct $1 \rightarrow 2$ transition of the superlattice. The folded phonon dispersion for all modes is shown in Fig. 2a at a non-vanishing value of crystal momentum $q_\perp = 0.1 \pi/d$ for propagation at arbitrary angles with respect to the (001) growth direction, the longitudinal branch intersects with one of the transverse branches. Depending on wave vector and energy, their character is only quasi-longitudinal (QL) or quasi-transverse (QT). The second

transverse branch remains unaffected (T). The dispersion in Fig. 2a was obtained by solving the Christoffel equation for the constituent materials [15] and matching of the appropriate boundary conditions for the phonon displacement and stress fields [12]. By comparison the QL-gap at about 25 cm^{-1} can be identified in the spectrum. The prominent feature at 20 cm^{-1} originates from the internal QL-QT gap. A link is observed at 15 cm^{-1} which can be attributed to the zone edge gap of the QT-phonon. Due to the vicinity of an internal gap, QT-phonons in this region still have enough longitudinal character to give a small contribution to the spectrum. To obtain best agreement with experiment the integration over q was performed up to $q_0 = 0.5\pi/d$. This corresponds to an uniaxial size of about 150 \AA , which is rather close to typical excitation radii in such systems [16]. Since excitons enter into Raman scattering as intermediate states, the value obtained for this sample might be limited by the sensitivity of the experimental method to length scales of this order. In the integration over q , a three-dimensional phonon density of states, modified by zone folding effects along the growth direction, is considered. This manifests itself in the vanishing of the Raman intensity for small shifts in agreement with experimental observations.

The behavior of the Raman intensity factor δ as a function of relative layer thicknesses $n = d(\text{AlAs})/d$ is shown in Fig. 4 for GaAs-AlAs superlattices with a total period of 3 nm . In analogy to the oscillatory behavior of the dispersion gaps [2] no changes are predicted for the lowest zone edge gap over the whole range of layer thicknesses. The second zone edge gap has two zones of n near 0.4 and 0.7. Consequently two changes of δ are expected for the zone center gaps, one and three zones are expected for the lowest ($n \approx 0.55$) and next higher gap ($n \approx 0.3, 0.8$), respectively. The intensity factor δ changes its character once and three times accordingly. The experimental verification of this behavior would provide a further test of the model presented.

IV. CONCLUSIONS

In Raman spectra of GaAs-AlAs multiple quantum wells and superlattices we have observed a characteristic emission background and pronounced intensity anomalies in the acoustic phonon regime. We find that the low scattering from isolated quantum wells due to interface roughness and layer thickness fluctuations provides a mechanism for a partial breakdown of crystal momentum conservation both parallel and perpendicular to the growth direction. This accounts for the observed features and provides a new way to obtain information on length scales of interface roughness.

V. ACKNOWLEDGMENTS

Two of us (V.B. and V.F.S.) acknowledge support from the Alfas Planck Gesellschaft. Thanks are due to V.P. Chumbarin for a critical reading of the manuscript. We would like to thank H. Hilt, M. Siemens and P. Wurster for expert technical assistance.

- * on leave from the A. F. Ioffe Physico-Technical Institute, Russian Academy of Sciences, 191021 St. Petersburg, Russia.
- [1] C. Colvard, T. A. Gant, M. V. Klein, R. N. Martin, R. H. Michel, H. Stork, and A. C. Gossard, *Phys. Rev. B* **31**, 2049 (1985).
 - [2] B. Jøssand, and M. Cardona, in *Light Scattering in Solids V*, Vol. 46 of *Papers in Applied Physics*, edited by M. Cardona and G. Gätkenroth, (Springer, Heidelberg, 1983), p. 41.
 - [3] V. F. Sushka, V. I. Belitsky, T. Ral, H. D. Joch, M. Cardona, and K. Floeg, *Phys. Rev. B* **40**, 6005 (1989).
 - [4] P. S. Koryun, D. H. Hill, V. F. Sushka, and A. A. Serebko, *Phys. Rev. B* **40**, 708 (1989).
 - [5] T. Ral, V. F. Sushka, J. Sutter, V. I. Belitsky, M. Cardona, and K. Floeg, in *Phonons in Semiconductor Nanostructures*, NATO-ASI Series edited by J. P. L. Loh, J. Sutter, J. Chaudhry, F. Alexander, and R. Atoulay, *Phys. Rev. B* **34**, 7119 (1986).
 - [6] A. B. Talochin, V. A. Stalov, I. G. Stetsko, O. P. Pribitshov, M. P. Stoyakov, and S. I. Stetsko, *Phys. Zh. Exp. Teor. Fiz.* **60**, 21 (1989), [*Sov. Phys. JETP Lett.* **50**, 24 (1989)].
 - [7] D. J. Nohbay private communication (1990).
 - [8] D. H. Hill, J. A. Morkel, V. I. Petri, I. I. Rekhina, and A. A. Serebko, *Solid State Commun.* **64**, 1051 (1992).
 - [9] A. Pierzak and E. Burstein, in *Light Scattering in Solids V*, Vol. 46 of *Papers in Applied Physics*, edited by M. Cardona, (Springer, Heidelberg, 1983), p. 21.
 - [10] P. V. Santos, L. Ley, J. Moberg, and O. Hübner, *Phys. Rev. B* **36**, 1858 (1987).
 - [11] S. Tamura and J. P. Wolfe, *Phys. Rev. B* **35**, 2528 (1987).
 - [12] E. Calle, M. Cardona, E. Richter, and D. Strauch, *Solid State Commun.* **72**, 1153 (1989).
 - [13] A. A. Gogolin and E. I. Rashba, *Solid State Commun.* **59**, 1177 (1986).
 - [14] B. A. Auld, in *Acoustic Fields and Waves in Solids*, Vol. 1 (Wiley, New York, 1973), p. 210.
 - [15] M. A. Hirman, D. Bimberg, and J. Chutista, *J. Appl. Phys.* **70**, R1 (1991).

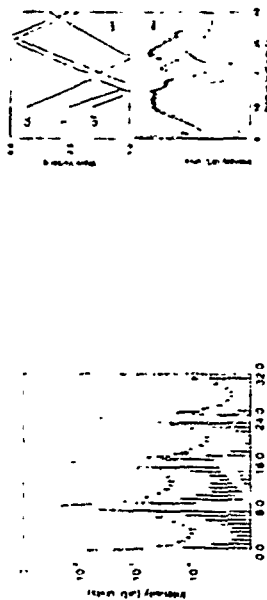


FIG. 1 Influence of disorder on the acoustic phonon Raman spectrum for a superlattice with 11 quantum wells. The excitation energy was chosen to be 10 cm^{-1} above an electronic resonance. The solid line was calculated assuming that all confinement energies are identical. The dashed line shows the enhancement obtained for the case when one of the wells has a confinement energy which is larger than that of the others by 10 cm^{-1} .

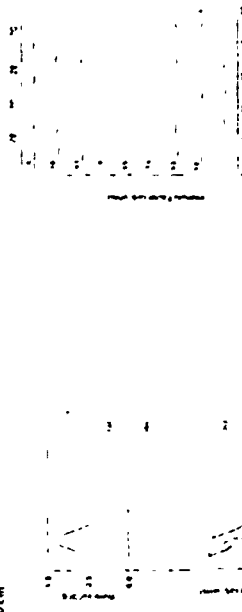


FIG. 2 (a) Folded LA phonon dispersion for a symmetric GaAs-AlAs superlattice with a total thickness of 16 monolayers. (b) Raman intensity factor δ showing the origin of anomalies near dispersion gaps in wave vector nonconserving scattering processes. (c) Experimental spectrum with bulk ground continuum and superimposed peaks and dips.

FIG. 3 (a) Folded phonon dispersion for a symmetric GaAs-AlAs superlattice with a period of 11 monolayers calculated for an in-plane wave vector of $q = 0.5\pi/d$. (b) Comparison of experimental Raman spectrum (top) with the best theoretical description (bottom) obtained by q integration.

FIG. 4 Dependence of the intensity factor δ on the layer thickness ratio n (given next to each curve) for GaAs-AlAs superlattices with a total period of 30 monolayers. Intensity anomalies show different oscillatory behavior for the various zone edge (2b) and zone center (2c) gaps.

FTIR SPECTROSCOPY OF LONGITUDINAL CONFINED PHONONS AND PLASMON-PHONON VIBRATIONAL MODES IN $\text{GaAs}_{1-x}\text{AlAs}_x$ SUPERLATTICES.

Yu. Pusep, A. Milekhin, A. Toropov
Institute of Semiconductor Physics, Siberian
Novosibirsk, Russia

The longitudinal optical (LO) and plasmon-phonon (L^+) vibrational modes have been investigated in $(\text{GaAs})_m/(\text{AlAs})_n$ superlattices (SL's) grown by MBE on (100) GaAs-Si substrates by Fourier-transform infrared (FTIR) spectroscopy. To measure the longitudinal modes of SL's the p-polarized reflection spectra with incidence angle $\approx 70^\circ$ were recorded in the spectral range of GaAs and AlAs optical phonons. In the short period SL's the modes originate from confined LO phonons have been observed (Fig. 1); the dispersion of LO phonons obtained by means of FTIR spectra is in good agreement with the Raman data.

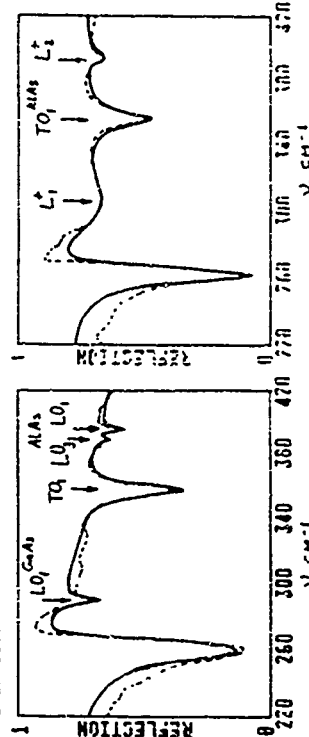


Fig. 1. p-polarized reflection spectra of the $(\text{GaAs})_{10}/(\text{AlAs})_3$ SL at $1.8 \times 10^{18} \text{ cm}^{-3}$. Broken line is the measured spectrum.

Fig. 2. p-polarized reflection spectra of the doped $(\text{GaAs})_{10}/(\text{AlAs})_3$ SL at $1.8 \times 10^{18} \text{ cm}^{-3}$. Broken line is the measured spectrum.

In order to study the plasmon-phonon vibrational modes the doped long period SL's with thin barriers were investigated. In this case at appropriate polarization of the light (p-polarization) the LO phonons are coupled with electrons moving in a half-filled miniband and thus the "vertical" transport of electrons can be studied. The fitting of calculated spectra to experimental ones allowed us to measure the "vertical" mobility of electrons that for the sample shown in Fig. 2, was $890 \text{ cm}^2/\text{V}\cdot\text{s}$.

Raman Scattering Study of Longitudinal Acoustic and Optic Phonons in $\text{InSb}/\text{In}_{1-x}\text{Al}_x\text{Sb}$ Strained-Layer Superlattices

V.P. Ginzburg, D.J. Lockwood, and J.B. Webb
Institute for Microstructural Sciences, National Research Council, Ottawa, Ontario K1A 0R6
Canada
Institute for Low Temperature Physics & Engineering, Ukrainian Academy of Sciences,
47 Lenin Avenue, 310164 Kharkov, Ukraine

Abstract

Detailed Raman scattering studies of $\text{InSb}/\text{In}_{1-x}\text{Al}_x\text{Sb}$ ($0.15 < x < 0.5$) strained-layer superlattices grown by magnetron sputter epitaxy on (001) InSb substrates are reported for the first time. A number of folded acoustic phonons appear in the Raman spectra and their frequencies are accurately predicted by Rylov's theory of acoustic vibrations in layered media. The longitudinal optic phonons in the $\text{In}_{1-x}\text{Al}_x\text{Sb}$ layers exhibit two-mode behavior and their shift due to the interlayer strain is discussed. Resonant Raman scattering was used to probe the electronic structure in the region of the E_1 and $E_1 + \Delta_1$ optical gaps. The two sets of peaks observed in the plots of the Raman cross section versus phonon energy are shown to originate from the independent electronic transitions in the alternating layers. Estimates of the strain and confinement effects were made and these agree with the observed differences from bulk material.

Introduction

Semiconductor superlattices (SLs) have now been of interest for nearly 20 years. Such interest has been stimulated by the thin film epitaxial growth techniques that show stable and reproducible behavior at the atomic level and through potential device application of new artificial materials. Raman spectroscopy has been one of the most widely employed experimental tools in the study of SLs and in the characterization of the materials used in devices [1]. The most extensively studied superlattices have been those composed of III-V compounds such as $\text{GaAs}/\text{Ga}_{1-x}\text{Al}_x\text{As}$. Recently, high-quality $\text{InSb}/\text{In}_{1-x}\text{Al}_x\text{Sb}$ strained-layer SLs have been grown by magnetron sputter epitaxy (MSE) [2]. This system is particularly interesting since information regarding InSb -based alloys is very limited and the high electron mobility and small effective mass associated with InSb would suggest superior performance of devices based on this system. The aim of this work was to perform a detailed study of $\text{InSb}/\text{In}_{1-x}\text{Al}_x\text{Sb}$ ($0.15 < x < 0.5$) strained-layer SLs using Raman scattering.

All 20 period SLs used in this study were grown by MSE on (001) InSb substrates and had different InSb and $\text{In}_{1-x}\text{Al}_x\text{Sb}$ layer thicknesses d_1 and d_2 , respectively. The top layer of the samples was InSb . The compositions of the ternary layers were determined from double-crystal x-ray diffractometer scans of single layer test structures and by fitting the x-ray diffractometer scans of the superlattices. The excellent crystalline quality of the epilayers was evaluated using x-ray diffraction and transmission electron microscopy. The individual layer thicknesses and ternary composition were chosen to ensure that the superlattices did not relax, as evidenced by x-ray line widths, transmission electron microscopy, and optical phase contrast microscopy.

The light scattering measurements were carried out using the quasi-backscattering geometry $z(y'y'z) \times y(z'z'z) \times y$, and z is perpendicular to the principal cubic axes, and z is perpendicular to the superlattice layers. The spectrum was excited with various lines of Ar^+ and Kr^+ lasers, and a

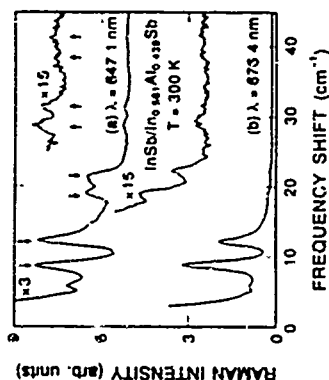


Figure 1. Room temperature Raman spectra of acoustic phonons in the $\text{InSb}(\text{In}_{1-x}\text{Al}_x)\text{Sb}$ ($x = 0-0.45$) superlattice excited with (a) 647.1 nm and (b) 676.4 nm laser light. The arrows indicate the folded acoustic modes. The experimental resolution is 0.8 cm^{-1} .

Acoustic Phonons

Low frequency Raman spectra obtained from an $\text{InSb}(\text{In}_{1-x}\text{Al}_x)_2$ superlattice is shown in Fig. 1. The spectra are typical of the other superlattices investigated in that all gave three or four well-resolved doublets, which are indicative of the high interface and surface quality of the MSE-grown samples. These sharp pairs of lines are attributed to the longitudinal acoustic (LA) phonons folded into the new Brillouin zone, which arises from the additional periodicity ($d = d_1 + d_2/2$) of the superlattice. According to the elastic continuum theory of Rytov [4] for layered media, the folded acoustic phonon dispersion well away from the zone center $q = 0$ and boundary $q = \pi/d$ is given by

$$\omega_{\text{cm}} = V_{\text{SL}} [(2\pi m/d \pm q)] \quad (1)$$

where

$$q = \{4\pi n_1(\lambda)\lambda\} / (1 + 4\pi n_1(\lambda)^2) \quad (2)$$

is the component of the light scattering wave vector perpendicular to the layers, $m = (1, 2, \dots)$, the zone folding index, λ , the incident laser light wavelength, n_{SL} , the refractive index of the superlattice at that wavelength, and V_{SL} the average superlattice sound velocity, which is a function of the component layer thicknesses, densities, and sound velocities. The predictions of the Rytov model are given by the arrows in Fig. 1 and are in excellent agreement with experiment. The layer thicknesses of $d_1 = 72.5$ Å and $d_2 = 41.0$ Å were obtained from the x-ray diffraction study; the following values for the sound velocity $V_{SL} = 3.581 \times 10^3$ cm/s and refractive index n_{SL} (647.1 nm) = 4.278 were used in the calculation.

The Raman intensity in the photoelastic coupling model for acoustic phonons is given by [5]

$$I \approx m^2 \sin^2 (m\alpha_1/d) \alpha_m (n_m + 1), \quad (3)$$

where η_{InSb} is the Bore factor. Equation (3) may be used to determine the InSb layer thickness d_1 . For example, the intensity of the $m = 1$ peak to that of $m = 2$ peak for the lower curve in Fig. 1 is 0.439. This gives the value of $d_1 = 66 \text{ \AA}$ for the superlattice with $x = 0.439$. This is in good agreement with the value of $d_1 = 72.5 \text{ \AA}$ obtained from the x -ray diffraction measurements. In order to obtain quantitative information about the layer thickness, it is necessary to use the experimental intensity data to obtain quantitative information about the layer thickness, it is necessary to note that under resonant conditions the intensity of the folded phonon scattering can be considerably reduced [5]. An example is the upper curve (a) in Fig. 1, which was measured with excitation close to resonance with a superlattice electronic transition.

Optic Phonons

The Raman spectrum of semiconductor superlattices at higher frequencies usually exhibits a number of first-order features characteristic of the two materials comprising the alternating layers. Figure 2 shows the high frequency region of the Raman spectrum of the $\text{InSb}(\text{In}_{1-x}\text{Al}_x\text{Sb})_x$ ($x = 0.364$) superlattice obtained using 530.9 nm Kr^+ laser exciting light. The peak labeled "A" corresponds to the longitudinal optic (LO) of the InSb layer, while the peaks labeled "B" and "C" correspond to the two LO phonons (InSb -like and AlSb -like, respectively) due to the two-mode behavior of optic phonons in $\text{In}_{1-x}\text{Al}_x\text{Sb}$ alloys. The frequency positions of the A, B, and C phonons in the Raman spectra for several SLs are summarized in Fig. 3, where the solid lines are the least-squares fit of a straight line to the frequency data. These fits yielded the concentration dependences

$$\omega_{\text{Nsb}} = 187.2 + 2.9x \text{ (cm}^{-1}\text{)} \quad (4)$$

for the IaSb line.

$$\omega_{\text{NSB}}/\text{Hz} = 186.8 \cdot 23.7\pi \text{ (cm}^{-1}\text{)} \quad (5)$$

for .he in Sb-like alloy line, and

$$\omega_{\text{AIBN}}(\text{Hz}) = 291.3 + 10.6x \quad (\text{cm}^{-1}) \quad (6)$$

For the AISB-1 file allow line.

The lattice mismatch in the superlattice composed of alternate layers of two materials with different lattice constants is classically accommodated, i.e., the materials inside the superlattice are elastically strained in order to match the substrate in-plane lattice parameter a . The lateral biaxial stress can be described as a biaxial stress. This is equivalent to a hydrostatic pressure and a uniaxial stress of opposite sign perpendicular to the interface. In the Raman scattering geometry, the stress causes a shift in the LO-phonon frequency ω by [6]

$$2((\epsilon_1 S + 1) S) b + \epsilon_1 S d \big|_{O_1^0} = m \varphi \quad (7)$$

where ω_0^{LO} is the phonon frequency of the unstrained cubic lattice, p and q are phenomenological parameters (known for AlSb [7] but not for InSb). S_{11} and S_{12} are the elastic compliances, and τ is the stress factor (positive for tensile and negative for compressive stress).

The higher frequency AIBS-like line lies well below the bulk AIBS LO-phonon frequency [8] of 340 cm^{-1} . Assuming a linear relationship between the two end points of 291.3 cm^{-1} (Eq. (6)) at $x = 0$ and 340 cm^{-1} , it is possible to predict the concentration dependence of the AIBS-like mode in bulk (relaxed) $\text{In}_{1-x}\text{Al}_x\text{Sb}$.

$$\omega_{\text{AICL}}^{\text{bulk}} = 2913 + 487x \text{ (cm}^{-1}\text{)} \quad (8)$$

Using the linear fits to $\omega_{\text{A1Sb-14e}}$ and $\omega_{\text{A1Sb-14e}}^{\text{bulk}}$ (Eqs. (6) and (8)) and a linear interpolation of

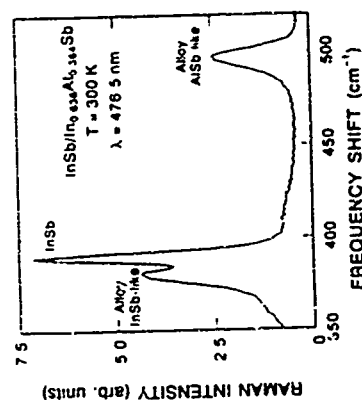


Figure 2 The room temperature Raman spectrum of optical phonons in the $\text{InSb/In}_{1-x}\text{Al}_x\text{Sb}$ ($x = 0.364$) superlattice excited with 476.5 nm laser light. The experimental resolution is 4.3 cm^{-1} .

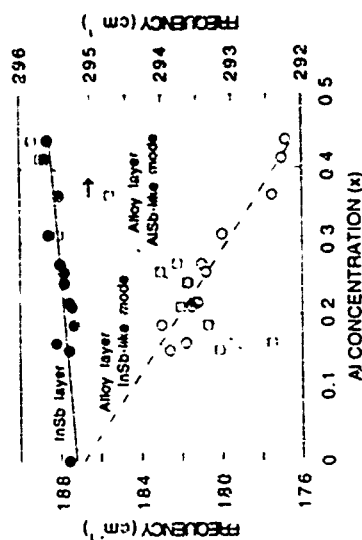


Figure 3 Concentration dependences of the peak frequencies of the InSb, AISb-like, and InSb-like lines in the Raman spectrum of $\text{InSb/In}_{1-x}\text{Al}_x\text{Sb}$ superlattices at room temperature. The compliances S_{11} and S_{12} [7,9] and lattice constants [9] of pure InSb and AISb, an estimate for the AISb-like mode stress factor for the $\text{In}_{1-x}\text{Al}_x\text{Sb}$ alloy may be obtained:

$$\gamma_{\text{AISb-like}} \approx 0.17x^2 - 3.8x + 11.3 \text{ (cm}^{-1}\text{/GPa)} \quad (9)$$

The stress X , in the alloy layers can be calculated from $\Delta\omega = \gamma X$ using Eqs. (6), (8), and (9) for AISb-like mode. At $x = 0.5$, $X = 2.0 \text{ GPa}$. As expected, the strain is mostly accommodated in the SL alloy layer, but the slight shift of the InSb line indicates that a small compensating strain

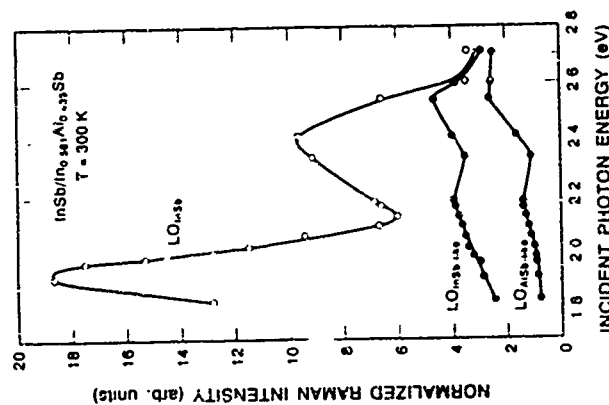


Figure 4. Resonant Raman profiles for the three main LO vibrations of the $\text{InSb/In}_{1-x}\text{Al}_x\text{Sb}$ ($x = 0.439$) superlattice. The lines are guides for the eye.

appears in the InSb layers. It is significant that the high strain in the alloy layers for larger x values results in a small compressive biaxial strain in the InSb layers, as this indicates a slight relaxation has occurred in the superlattices. The mechanism for this relaxation is not clear at present.

Resonant Raman

The significance of resonant Raman scattering as a spectroscopic tool for obtaining information on the electronic states of superlattices is now well known [1]. Although this method does not allow for exact determination of transition energies, it provides information on whether the electronic states under study are confined within the quantum wells or if they extend through the whole structure. This possibility is due to the exploitation of the modulation produced in the electronic states by the optical lattice vibrations that are characteristic of each type of layer and that are not significantly affected by the periodicity of the superlattices [10,11].

Most resonant Raman scattering work has been performed on direct band gap semiconductors in the vicinity of the Brillouin zone center and, although it is well recognized that Raman scattering investigations can provide a great deal of information about the E_1 and $E_1 + \Delta_1$ transitions in superlattices [1], only two reports are known in which Raman scattering has been used to study the

resonance at the E_1 gap in zinc-blende superlattices [12,13]. In these studies the resonant behavior of the longitudinal optical (LO) phonons of only one of the two alternating layers was analyzed.

Figure 4 shows the resonant Raman profiles for the LO phonons in the $\text{In}_{1-x}\text{Al}_x\text{Sb}$ ($x = 0.439$) superlattice. The shapes and interpretation of the resonances in bulk InSb are well understood [14]. As might be expected, the shapes and energy positions of both peaks in the resonant profile of the InSb phonon (see Fig. 4) are in good agreement with those found for bulk InSb [14]. The superlattice effect, which shifts the peak positions towards higher energies due to strain and confinement [1], is small. The strain dependent shift can be neglected for the InSb layers [1], while the possible shift for the confinement effect is expected to be less than 0.01 eV [8] and this is too small to resolve in a room temperature experiment. Contrary to the findings of Ref. [12], two weak but distinct resonant features are observed for the InSb -like mode. In addition, similar resonances are observed for the AlSb -like mode. The resonances at high energy are stronger than those at lower energy. It is also seen from Fig. 4 that the enhancements in the LO phonons originating in the alloy layers are smaller than those ones in the LO phonon originating in the pure InSb layers. Peak positions of the resonant profiles for InSb -like and AlSb -like phonon modes in Fig. 4 are shifted to higher energy relative to the positions of the corresponding peaks of InSb by values approximately equal to the differences in the E_1 and $E_1 + \Delta_1$ gaps of InSb and $\text{In}_{1-x}\text{Al}_x\text{Sb}$ [15]. The observation of the separate resonant enhancements in the InSb and $\text{In}_{1-x}\text{Al}_x\text{Sb}$ layers at energies close to the E_1 and $E_1 + \Delta_1$ gap energies in the respective bulk materials means that the electronic transitions that produce the resonances in the Raman scattering are independent, or nearly independent [1], for both materials in the superlattice.

Bulk material gaps have counterparts in superlattices and the energies of resonant peaks observed in both types of materials are related to each other by [12]

$$E_R(\epsilon, d) = E_R^{\text{bulk}} + \Delta_1(\epsilon) + \Delta_2(d), \quad (10)$$

where $\Delta_1(\epsilon)$ and $\Delta_2(d)$ are energy shifts produced by strain and confinement, respectively. The strain shift is calculated to be $\Delta_1(\epsilon) = 0.045$ eV using the dependence $\Delta_1(\epsilon) = 3.0(\epsilon/\Delta_2)$ in eV for InSb from Ref. [2] and strain ϵ evaluated from Ref. [6]. The confinement shift is found to be $\Delta_2(d) = 0.011$ eV from the experimental dependence [12] of the position of the resonant maximum (corrected for strain) versus d^{-2} for the $\text{InSb}/\text{In}_{1-x}\text{Al}_x\text{Sb}$ superlattice of well width d . Thus, the shift of 0.05 eV (see Fig. 4) between the position of the experimentally observed resonant peak near the E_1 gap energy in the superlattice and that deduced for the bulk alloy with the same Al content is very close to the calculated one of $\Delta_1(\epsilon) + \Delta_2(d) = 0.054$ eV.

Conclusion

In summary, strained layer superlattices of $\text{InSb}/\text{In}_{1-x}\text{Al}_x\text{Sb}$ have been prepared by magnetron sputter epitaxy. Superlattices with periods of less than 16 nm and alloy compositions $x < 0.5$ have been studied by Raman spectroscopy. The observed frequencies of the zone-folded longitudinal acoustic phonons are in good agreement with calculations based on Kytov's theory of acoustic vibrations in layered media. The higher frequency regions of the Raman spectra consist of the confined LO phonons in the InSb and $\text{In}_{1-x}\text{Al}_x\text{Sb}$ layers. The two-mode behavior of the $\text{In}_{1-x}\text{Al}_x\text{Sb}$ alloy layer phonons was clearly confirmed. A linear frequency-shift behavior was observed for all LO modes with increasing Al content. Resonant Raman experiments reveal the existence of two sets of interband transitions in the region of the E_1 and $E_1 + \Delta_1$ optical gaps of the InSb and $\text{In}_{1-x}\text{Al}_x\text{Sb}$ host materials. The existence of these two separate sets of resonances indicates that the electronic energy levels of the respective layers are essentially independent, i.e., the superlattice comprises a double set of multiple quantum wells for the E_1 and $E_1 + \Delta_1$ transitions. The resonance positions for the $\text{In}_{1-x}\text{Al}_x\text{Sb}$ layers show the effects of both strain and confinement.

Acknowledgment

We would like to thank H.J. Labbe for expert technical assistance.

References

1. B. Jusserand and M. Cardona, in *Light Scattering in Solids V*, edited by M. Cardona and G. Güntherodt, Topics in Appl. Phys., Vol. 66, p. 49, Springer-Verlag, Berlin (1989).
2. J.B. Webb, G.H. Yusefi, and R. Rousina, *Appl. Phys. Lett.* **60**, 998 (1992).
3. A. Compaan and H.J. Trodahl, *Phys. Rev. B* **29**, 793 (1984).
4. S.M. Rytov, *Akust. Zh.* **2**, 71 (1956) [*Sov. Phys. - Acoust.* **2**, 68 (1956)].
5. C. Colvard, T.A. Gani, M.V. Klein, R. Merfin, R. Fischer, H. Morkoç, and A.C. Gossard, *Phys. Rev. B* **31**, 2080 (1985).
6. G. Abstreiter, H. Brugger, T. Wolf, R. Zachai, and Ch. Zeller, in *Two-Dimensional Systems: Physics and New Devices*, edited by G. Bauer, F. Kuchar, and H. Heinrich, p. 130, Springer-Verlag, Berlin (1986).
7. E. Anastasiadis and M. Cardona, *Solid State Commun.* **63**, 893 (1987).
8. S. Ves, K. Strössner, and M. Cardona, *Solid State Commun.* **57**, 483 (1986).
9. *Landolt-Börnstein, Numerical Data and Functional Relationships in Science and Technology, New Series*, edited by O. Madelung, Group III, Vol. 22a, Springer-Verlag, Berlin (1987).
10. G. Abstreiter, E. Bauser, A. Fischer, and K. Ploog, *Appl. Phys.* **16**, 345 (1978).
11. J.E. Zucker, A. Pinczuk, D.S. Chemla, A. Gossard, and W. Wiegmann, *Phys. Rev. B* **29**, 7065 (1984).
12. F. Cordeira, A. Pinczuk, T.H. Chiu, and W.T. Tsang, *Phys. Rev. B* **32**, 1390 (1985).
13. C. Tejedor, J.M. Calleja, F. Meseguer, E.E. Mendez, C.A. Chang, and L. Esaki, *Phys. Rev. B* **32**, 5303 (1985).
14. M. Cardona, in *Light Scattering in Solids II*, edited by M. Cardona and G. Güntherodt, Topics in Appl. Phys., Vol. 50, p. 19, Springer-Verlag, Berlin (1982).
15. S. Isomura, F.G.D. Prat, and J.C. Woolley, *Phys. Stat. Sol.* **65**, 213 (1974).
16. V.P. Gnerzdlov, D.J. Lockwood, and J.B. Webb, to be published.

MoP15

Optical phonon probes of the lateral scale of interface roughness: a theoretical investigation

S. de Gironcoli

INFN - Institute of Condensed Matter Theory (FORUM),

Scuola Normale Superiore, Piazza dei Cavalieri 7, I 56100 Pisa, Italy

E. Molinari

Dipartimento di Fisica, Università di Modena, Via Campi 213/a, I 41100 Modena, Italy

Abstract

We study the effect of the different lateral scale of interface roughness on the optical phonon spectrum of thin Si/Ge (001) superlattices. We find that the first Si-like confined optical mode does localize either in the thinnest or in the thickest part of the Si well already for relatively small lateral sizes of the interface terraces, contrary to the corresponding behaviour in GaAs/AlAs structures. We show that this gives rise to distinct changes in the Raman lineshape, which should be useful to discriminate between short range intermixing and long range interface corrugation in Si/Ge superlattices. We finally discuss the optimal conditions to allow experimental observation of this effect.

Introduction

A number of important contributions have been recently devoted to the determination of the lateral scale of interface disorder in semiconductor superlattices (SL's), particularly GaAs/AlAs [1-3]. Early interpretations of optical experiments had led to the conclusion that structures with atomically sharp interfaces over very large regions ($\sim 1 \mu\text{m}$) had been achieved. The observed splittings of excitonic recombination lines were attributed to discrete (1 monolayer) variations in the well width and flat interface regions (terraces) much larger than the exciton diameter [1, 2]. However, a less optimistic view is now coming from experiments using different probes, including Raman spectra of optical modes [3-5], as well as more conventional structural characterization techniques (high resolution transmission electron microscopy (HRTEM) [6-8], x-ray diffraction and also scanning tunneling microscopy [9]). Moreover, the existence of systematic photoluminescence (PL) [1, 2, 10-11] and vibrational light scattering [1-3] studies on GaAs/AlAs samples grown in a wide range of conditions allows to conclude that the "optical growth parameters" (i.e. parameters yielding minimal disorder effects) depend strongly on the probe used to

characterize. On one hand, the observed excitonic transition lineshape splittings suggest that largest terraces are favoured by relatively high substrate temperatures T_s and growth interruption [10]. On the other hand, optical phonon features—which are expected to be especially sensitive to short scale roughness [12]—indicate that intermixing exists even in the best samples, and it decreases for low T_s growth while remaining quite insensitive to growth interruption [3, 4].

The most natural way to reconcile this set of results is the idea, independently supported by HRTEM data [6, 8], that interface disorder must occur over different lateral length scales, so that its spectrum in reciprocal space is at least bimodal [11], with different Fourier components depending differently upon the growth parameters and affecting the possible probes in different ways. A critical reexamination of PL spectra [11-13] has been crucial to reach this conclusion. The above interpretation is thus becoming increasingly accepted for GaAs/AlAs SL's.

A thorough work on similar issues has not been undertaken for Si/Ge structures so far, one of the reasons certainly being that a systematic photoluminescence lineshape study is impossible there. A probe which could be mostly sensitive to "long range" terraces seemed thus unavailable in this case.

In the present paper, we focus on the vibrational properties and show that in thin Si/Ge SL's optical phonons may be such a probe, i.e. phonon spectra should allow to discriminate between "large terrace" and "short scale intermixing" behaviors much more easily than in GaAs/AlAs [15]. In particular, we discuss the effect of disorder with different lateral length scales on the Si-like confined vibrations, and identify the sample geometry and the experimental conditions under which Raman spectroscopy may be most effective for this type of characterization.

Theoretical approach

As in previous studies of AlGaAs based heterostructures [14], we use accurate interatomic force constants which are calculated from first principles within density functional theory in the local density approximation by means of a linear response scheme. The ability of such force constants to reproduce the bulk vibrational properties of Si and Ge was demonstrated in [16]. In order to extend this approach to Si/Ge heterostructures, however, one has to face the additional difficulty of including strain effects in the *ab initio* force constant scheme. This has been recently achieved [17], by introducing higher order corrections, due to the different bond lengths, to the interatomic force constants.

To model SL's with disordered layers, an additional periodicity in the (xy) plane parallel to the interfaces has been assumed. In order to keep the size of the calculation tractable, we introduce an in-plane periodic corrugation only along the x direction, with alternating terraces and barriers p and q atomic layers wide. The lateral period is thus $(p+q)a/2$ and the three dimensional unit cell needed to treat a SL, with a period of $2n$ atomic layers contains $2n(p+q)$ atoms. For comparison, we have also simulated short range interface intermixing [18]. In that case Si and Ge atoms in the allowed planes are distributed at random in a 18 atom two dimensional unit cell according to the assumed concentration, and the calculated properties are averaged over ~ 10 different configurations.

Phonon spectra (frequencies and displacement profiles) are then obtained by direct diagonalization of the dynamical matrix, and the corresponding Raman strengths are estimated assuming the same bond polarizability in both materials [19].

Confined Si-like phonons the effect of short- and long-scale interface disorder

It is by now well known that in ideal Si/Ge SL's (i.e. SL's with perfectly abrupt interfaces) Si-like phonons are strongly confined in the Si region [20]. In particular for longitudinal (L) vibrations, which are allowed in the standard Raman backscattering configuration, it has been shown [21] that the confined mode frequencies ω_n are related to the bulk Si dispersion $\omega_{\text{bulk}}(q)$ by the condition $\omega_n \approx \omega_{\text{bulk}}(q_n)$ with

$$q_n = \frac{n\pi}{[n + 1]a/4} \quad (1)$$

n being the number of atomic planes in the Si layer and a the bulk lattice parameter. It has therefore become customary to plot the experimental SL phonon frequencies "unfolded" onto the bulk Brillouin Zone (BZ) according to (1), and to compare them with the appropriate bulk dispersion (in the same strain configuration [22]). Deviations between "unfolded" SL and bulk dispersions are thus attributed to disorder effects. We have recently been able to show [18, 23] that for high m confined modes (or large q_n unfolding) such deviations are accounted for by assuming a thin intermixed layer of Si_{1-x}Ge_x at the interfaces, which is also reasonable for the observed Si_{1-x}Ge_x like interface mode around 100 cm^{-1} [24].

In Fig. 1 we now show results for two different sets of $\text{Si}_{1-x}\text{Ge}_x/\text{Ge}_{1-x}\text{Si}_x$ (001) SL's grown on Si_{0.5}Ge_{0.5} alloy substrate with "nominal" thicknesses $n=4$ and $n=8$ respectively, and variable in-plane corrugation periodicity ($p+q \approx 12-21 \text{ Å}$ and $x \approx \pm p/(p+q)$). The symbols represent calculated SL Raman peaks of increasing intensity with increasing darkness in the grey scale while the solid line is the bulk L dispersion. Focusing on the first half of the bulk BZ it is apparent that some splitting of the first confined mode peak is always present for the thinnest ($n=4$) SL, even for the smallest terrace periodicity ($p+q \approx 12$, $x \approx 1/2$), although both split peaks have comparable intensity only to the largest $p+q$ values. This is not the case for the $n=8$ SL, where an in-plane periodicity $p+q \approx 12$ is clearly not sufficient to induce a splitting of the first confined Raman line. At larger values of $p+q$ some splitting $\Delta\omega$ does appear although still small in frequency ($\Delta\omega \lesssim 1-1.5 \text{ cm}^{-1}$).

To examine the origin of these splittings, in Figs. 2a and 2b we show the displacement amplitude corresponding to the individual frequencies for two particular SL's having $p+q \approx 12$ and $n=4$ and 8. The two split modes obtained for $n=4$ (Fig. 2b) clearly appear to derive from confined phonons which are localized either in the thickest or in the thinnest part of the Si layer. It is therefore not surprising that their frequencies turn out to be approximately consistent with confinement in a well of width 4 or 8 monolayers respectively. The displacement amplitude of Fig. 2a ($n=8$) is in fact quite delocalized over the Si layer, consistent with the amplitude lineshape of its corresponding peak (Fig. 2b). A similar analysis can be performed for all frequencies of Fig. 1 leading to the conclusion that the first Si-like confined

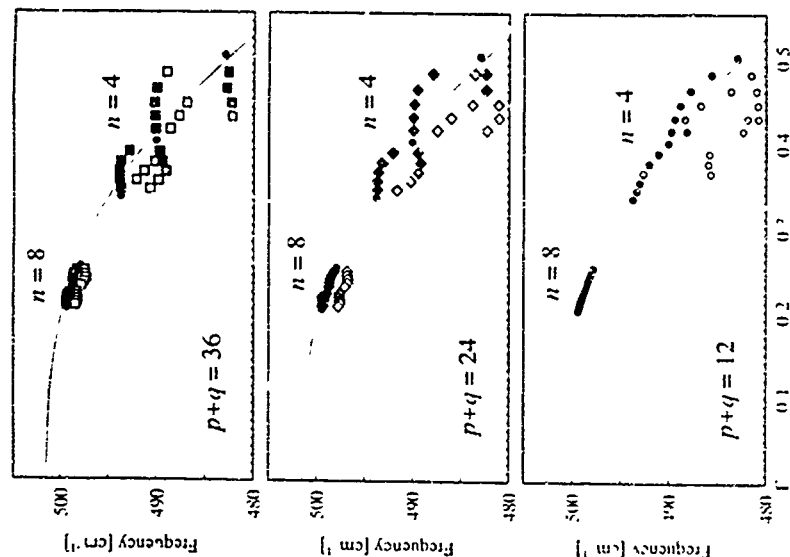


Fig. 1. Plot of in-plane corrugation periodicity versus calculated SL frequencies. Symbols first Si-like confined modes, unfolded onto the first half of the bulk BZ for strain-symmetrized $\text{Si}_{1-x}\text{Ge}_x/\text{Ge}_{1-x}\text{Si}_x$ with "nominal" thicknesses $n=4$ and $n=8$ respectively, and variable in-plane corrugation periodicity ($p+q \approx 12-21 \text{ Å}$ and $x \approx \pm p/(p+q)$). Increasing darkness of the symbols indicates increasing calculated intensity of the corresponding Raman peaks. Solid line: calculated dispersion for bulk Si in the same strain configuration as in the SL's.

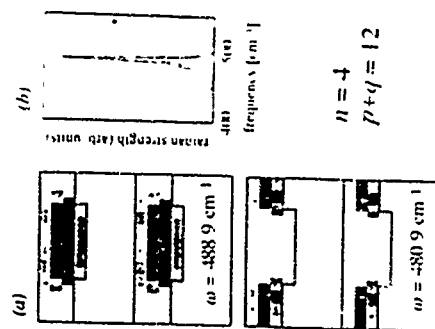


Fig. 2. (a) Spatial distribution in the (x, z) plane of the squared displacement amplitude corresponding to the two split frequencies of the first Si-like confined mode for $n=4$. (b) Calculated Raman strength in the Si-like frequency range of the same Si mode.

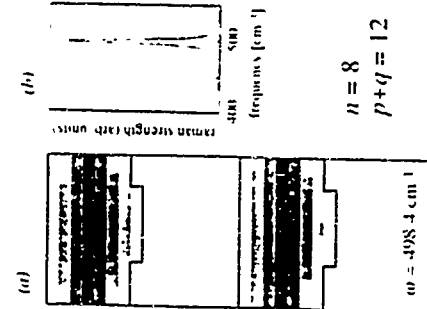


Fig. 3. (a) Spatial distribution in the (x, z) plane of the squared displacement amplitude of the first Si-like confined mode for $p+q=12$. (b) Calculated Raman strength in the Si-like frequency range of the same Si mode.

mode in Si/Ge-Si, may indeed give rise to monolayer splittings, similar to those by polarized for excitation lines [1].

It is thus meaningful to design a situation where this effect is expected to be most apparent in order to suggest an actual experimental application. By comparing a few sample geometries, we have found that Si's with $n=6$ should show at the same time relatively large splittings ($\Delta\omega \approx 1 \times 10^3 \text{ cm}^{-1}$ for $p+q$ in the range $23-36$) together with comparable intensities of the split lines, so that the spectrum corresponding to various Si's would differ significantly from that of broadened interfaces (Fig. 1). In particular, it appears that the broadening of the Si-like peak is only slightly affected by homogeneous broadening, which instead may induce significant frequency shifts (lowest curves in Fig. 1). On the contrary, an increasing splitting of the Raman lines (which might result in a broadened peak in the experimental spectra) originates from lateral corrugation with increasing period. This result suggests that a meaningful experiment would consist in monitoring the Si-like lines in nominal Si_{0.5}Ge_{0.5} grown under different substrate temperature and interruption conditions. Any splitting of

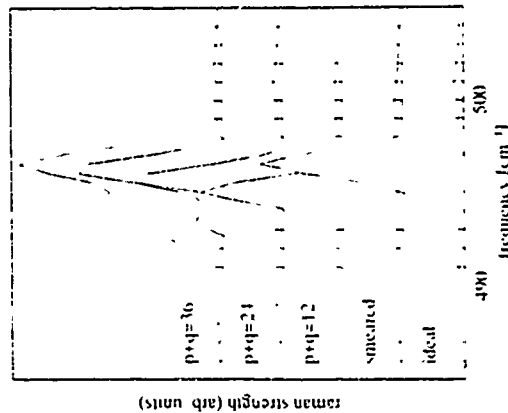


Fig. 4. Raman intensity profiles in the frequency range of the first Si-like L-confined mode for a nominal Si_{0.5}Ge_{0.5} with different interface profiles. The two lowest curves correspond to ideally abrupt interfaces and to interfaces with two interrupted layers of Si_{0.5}Ge_{0.5}. The three upper curves are for Si's with a "terraced" interface and variable in-plane corrugation periods ($p+q=12, 24, 36$).

marked broadening of the Raman lines would then indicate a transition from a regime dominated by homogeneous intermixing to a regime with more important terrace effects.

We finally come to the comparison with similar studies previously performed by B. Jassby and for GaAs/AlAs-Si [15]. In that case no splitting of the first confined mode frequency was found in the calculated spectra, even for the largest terraces and the thinnest wells that could be examined [25]. This was attributed [15] to the non-analytic properties of phonon dispersions close to BZ center arising from long-range Coulomb forces in polar materials. The very different behaviour of Si/Ge-Si's confirms this interpretation. Unlike in GaAs/AlAs, we indeed find that in Si/Ge the minimum terrace width λ needed to induce well defined phonon modes confined in the Si regions of different thickness is roughly consistent with the expression proposed for the same transition of confined electrons [26-17], namely

$$\lambda \approx d(d/2\Delta d)^{1/2} \quad (2)$$

d and Δd being the nominal thickness and its fluctuation (eq. (2) of Ref. [15] with the assumption of isotropic phonon dispersion).

INFRARED REFLECTIVITY OF STRAINED GaSb/AlSb SUPERLATTICES

G. Samundino C. Galdames

Departamento de Física, UNED, Universidad de Buenos Aires, Ciudad Universitaria, 1700BBA, Buenos Aires, Argentina

A. Tagliante L. Tapfer

F. V. M. Heringer, J. 2023, Brindley, Italy

K. Plohn

Physikalisches Institut für Festkörperelektronik, O. 1068 Berlin, Germany

Y. Ohmori

Electronics Engineering, Osaka University, 2-1 Yamadaoka, Suita, Osaka 565, Japan

H. Okamoto

Osaka University Faculty of Engineering, 2-1 Yamadaoka, Suita, Osaka 565, Japan

The optical properties of strained superlattices (SLs) have been studied by means of infrared reflectivity measurements. The optical properties of strained SLs are determined by the strain-induced band structure changes. The optical properties of strained SLs are determined by the strain-induced band structure changes. The optical properties of strained SLs are determined by the strain-induced band structure changes.

1. INTRODUCTION

Far infrared spectroscopy is well known to be a powerful tool for the investigation of structural properties of solids. Nevertheless, only recently its usefulness for the study of semiconductor superlattices (SLs) has been explored [1-4]. The ability of far infrared reflectivity (FIR) to probe confined phonons in SLs has been demonstrated very recently in the case of AlGaAs/AlGaAs SLs [5]. The influence of the strain on the optical properties of SLs is a function of the spatial configuration of the SL. The influence of the strain on the optical properties of SLs is a function of the spatial configuration of the SL. The influence of the strain on the optical properties of SLs is a function of the spatial configuration of the SL.

Particularly, the multilayered analysis of far and mid infrared reflectivity spectra, in the framework of the effective medium approximation, allows the determination of the structural parameters of the SLs with an accuracy comparable to that of double crystal x-ray diffraction [6]. To the best of our knowledge, an FIR investigation of strained SLs has been reported for the first time in this paper. The possible applications of strained SLs have attracted attention in the last few years [7]. Their structural properties are determined by the moderate (0.6%) lattice mismatch between the constituent materials. Strain and confinement effects have been previously investigated by means of ion channeling, x-ray diffraction [8] and Raman spectroscopy [9, 10]. Strain relaxation takes place for total AlSb thicknesses greater than the critical value $x_c \approx 1.5$ nm [9]. We report here far infrared reflectivity and x-ray diffraction of GaSb/AlSb superlattices. Our results show that a strain factor description of FIR spectra can be obtained provided that not only strain and phonon confinement but also strain relaxation processes are considered.

II. EXPERIMENTAL

GaSb/AlSb superlattices were grown by molecular beam epitaxy on GaAs or doped GaSb (001) oriented substrates. On doped GaSb, a 10 nm thick growth procedure reported in Ref. [11] was used. Structural data on the samples were obtained from x-ray diffraction. Diffraction patterns were recorded with a high resolution double crystal diffractometer using CuK α radiation close to the symmetric (400) and asymmetric (511) reflections in order to obtain the lattice mismatch and strain fields normal and parallel to the crystal surface. Structural parameters were obtained through comparison with the results of computer simulation based on the dynamical scattering theory [12]. The best fit values are listed in Table I.

IR measurements were performed under near normal incidence at 10 K by using a Fourier transform spectrophotometer operating under vacuum.

III. RESULTS AND DISCUSSION

Figure 1 shows the FIR reflectivity spectrum representative of the series grown on a doped GaSb substrate. The high reflectivity band extending in the low energy part of the spectrum up to about 200 cm^{-1} and the broad band around 400 cm^{-1} originate from plasma oscillations in the doped substrate. The intense structure extending in the range 200-400 cm^{-1} is due to the combined effect of "Reststrahlen" (RS) from GaSb and the SL. The edge at 225 cm^{-1} is attributed to the energy with the bulk GaSb TO and is ascribed to the

TABLE I. Structural parameters of GaSb/AlSb superlattices. Here N = number of periods of superlattice period, d_s = undoped layer thickness measured by x rays (samples 1-3) or FIR (samples 4-5), $(\frac{d_s}{d})_{\text{FIR}}$ = lattice mismatch parallel and normal to the (001) plane, respectively, values in <> brackets indicate mean values.

sample	substrate	N	d_s (nm)	layer	d_l (nm)	$(\frac{d_s}{d})_{\text{FIR}}$	$(\frac{d_s}{d})_{\text{FIR}}$
1	GaSb	50	18.04	GaSb	13.26	3.6×10^{-3}	$< 3.9 \times 10^{-3}$
				AlSb	2.89	1.1×10^{-3}	
2	GaSb	100	5.55	GaSb	3.55	$< 4.1 \times 10^{-3}$	
				AlSb	1.80		
3	GaSb	200	2.78	GaSb	1.74	0	0
				AlSb	1.04	1.29×10^{-3}	
4	GaAs	285	4.9	GaSb	3.1	$< 3.13 \times 10^{-3}$	$< 4.5 \times 10^{-3}$
				AlSb	1.6		
5	GaAs	148	5.6	GaSb	4.2	$< 6.14 \times 10^{-3}$	$< 6.68 \times 10^{-3}$
				AlSb	1.4		

substrate. The weak shoulder at 225 cm^{-1} appearing on the low energy side of the bulk GaSb RS band can be ascribed to GaSb-like TO phonons in the SL. The structure appearing in the range 300-330 cm^{-1} is due to RS from AlSb-like phonons in the SL. The RS bands around 230-320 cm^{-1} , respectively, are well separated from that of the substrate. A complete assignment of the spectral features of Figs. 1 and 2 shows the FIR spectrum of sample 5 which is grown on GaAs. Due to the different substrate, several changes can be observed with respect to the spectrum of sample 1. In particular, no plasmon-like reflectivity features are observed.

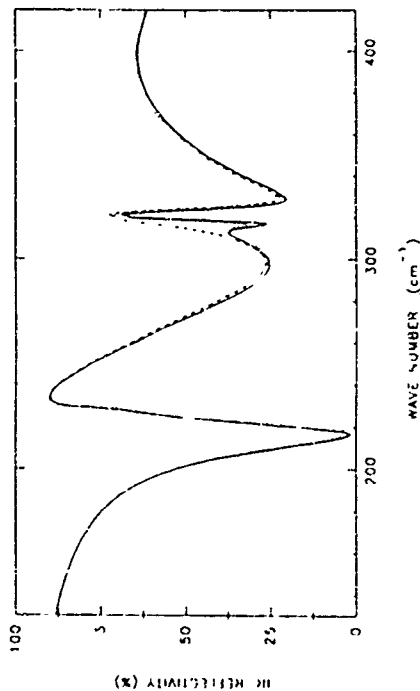


FIG. 1. FIR spectrum of GaSb/AlSb superlattice (sample 1) grown on a doped GaSb substrate. Continuous line: experimental data. Dashed line: spectrum calculated as explained in the text for abrupt interfaces. Dotted line: spectrum calculated considering 5% intermixing at the interfaces.

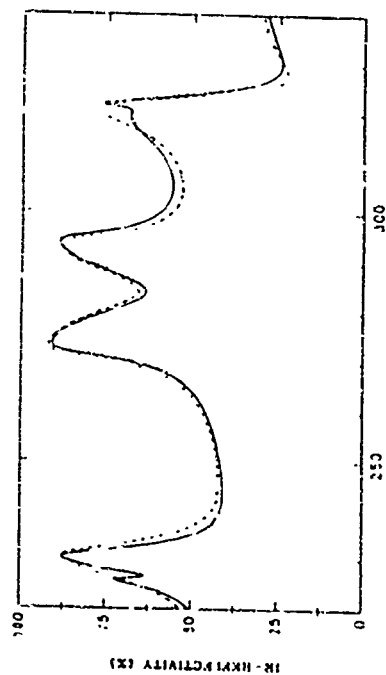


FIG. 2 FIR spectrum of $(\text{GaSb})_{1-x}(\text{AlSb})_x$ SL (sample 5) grown on GaAs substrate. Continuous line: experimental data. Dashed line: spectrum calculated for abrupt interfaces. Dotted line: spectrum calculated for a $\text{Al}_{0.1}\text{Ga}_{0.9}\text{Sb}_{0.1}\text{Al}_{0.1}\text{Ga}_{0.9}\text{Sb}_{0.1}$ SL as explained in the text.

The theory of ref. [14] gives a very satisfactory description of FIR for an "ideal" SL grown onto a semi-infinite substrate. The SL dielectric function is written in the effective medium approximation as the average of the dielectric function of the constituent layers weighted with the layer thicknesses [7]. For layers thinner than about 10 monolayers the confinement induced shift of phonon energies has to be considered [15]. In the case of strained layers the influence of lattice distortion on phonon energies needs to be evaluated, too.

The dashed line in Fig. 1 and 2 have been calculated according to the above model considering an ideal GaSb/AlSb SL with abrupt interfaces. For sample 1 the substrate doping has been properly considered by introducing a plasma oscillator in the substrate dielectric function. In the calculations we have taken the layer thicknesses of Table I. The following parameters have been adjusted for best reproduction of the experimental data: the plasmon frequency and damping γ , and ϵ_{∞} , the phonon frequency and damping in the Γ -th layer, ω_{TO} and Γ . Although a good overall agreement was obtained, several important structures cannot be reproduced at all. In particular, there is no way to reproduce the dip at 316.7 cm^{-1} in Fig. 1. The same is true for the structured GaSb -like and AlSb -like RS bands in Fig. 2. This discrepancy will be corrected by taking into account strain induced structural distortions, as explained in the following.

Strain relaxation: a superlattice structure manifests its

self by non-zero values of the in-plane lattice mismatch or by negative strain values in the GaSb layers. Values of Table I show a "natural" degree of relaxation near zero. $1-3$ grown on GaSb substrate, which increase at increasing the AlSb layer and the total superlattice thicknesses. This expected behaviour is related to the individual layer and total AlSb/AlSb thicknesses [9]. Lattice relaxation occurs through the formation of defects, i.e. dislocations and intermixed layers at the hetero-faces. This causes interface roughness and local fluctuations of strain fields in the layers. In fact, a satisfactory agreement between the calculated and experimental diffraction patterns of samples $1-3$ was obtained only if $0.1-0.2 \text{ nm}$ thickness fluctuations and $\sim 10^{-3}$ in fluctuations were considered. Hence, the simplistic assumption of homogeneous and abrupt interfaces has to be abandoned. Considering moderate thickness fluctuations in the model of FIR, does not give substantial improvement to the reproduction of the experimental features.

Fig. 1. On the other hand, the existence of an interface layer at the GaSb/AlSb interface can have a strong influence on the SL "Reststrahlen" profile mainly because the additional phonon resonances and the modification in the spatial configuration. Hence, we have included the model of FIR the presence of an $\text{Al}_{0.1}\text{Ga}_{0.9}\text{Sb}_{0.1}$ layer of thickness t at the interface. In this way we are considering one SL period as constituted by three layers: thickness d_1 (GaSb), d_2 (AlSb), and t ($\text{Al}_{0.1}\text{Ga}_{0.9}\text{Sb}_{0.1}$).

TABLE II Data on the intermixing in GaSb/AlSb SL samples deduced by the fitting of FIR spectra. Here t and x indicate the average thickness and Al mole fraction of the $\text{Al}_{0.1}\text{Ga}_{0.9}\text{Sb}_{0.1}$ layer at the interface. The percentage of intermixing is evaluated as $100 \cdot t/t_0$.

sample	t (nm)	x
1	0.27	0.18
2	0.40	0.40
3	0.10	0.22

The sum $(d_1 + d_2 + t)$ and the ratio $t/(d_1 + d_2)$ are fixed at the values of the period d and the ratio d_2/d_1 between the layer thicknesses, whereas t and the mole fraction x is left as fitting parameter. The layer parameter x also affects the phonon frequencies according to the known dependence from the chemical composition [16]. The dotted line in Fig. 1 was calculated considering a 0.87 nm thick $\text{Al}_{0.1}\text{Ga}_{0.9}\text{Sb}_{0.1}$ layer at each hetero-interface. All spectral values of Fig. 1 are now satisfactory. A unique representation is obtained also for samples 2 and 3. The best fit values of SL TO phonon frequencies are consistent with the moderate confinement and strain induced shifts calculated considering the measured structural parameters. Similar findings on the combined effects of

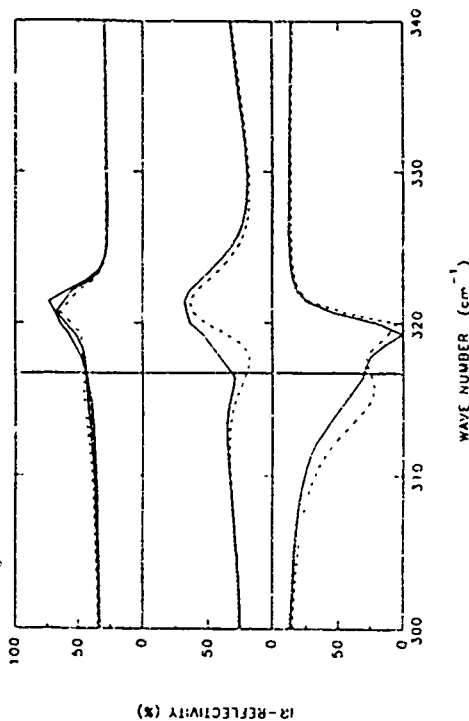


FIG. 3 AlSb -like "Reststrahlen" bands calculated for different values of plasmon frequencies: (a) $\omega_p = 0$, (b) $\omega_p = 1000 \text{ cm}^{-1}$, (c) $\omega_p = 1000 \text{ cm}^{-1}$. Continuous lines: abrupt interfaces. Dashed lines: 5% intermixing at the interfaces. Dotted lines: 10% intermixing at the interfaces. The vertical line marks the AlSb -like TO frequency of the alloy.

Quantitative Analysis of Strain Relaxation and Mortality in Short-Period SmGen Superlattices using Reciprocal Space Mapping by X-Ray Diffraction

E. Koppenscheimer¹, P. Hammerl¹, G. Bauer¹, V. Haly², H. Kibbel³, H. Presting³, E. Kasper³
¹ Institut für Halbleiterphysik, Johannes Kepler Universität, A-4040 Linz, Austria
² Department of Solid State Physics, Masaryk University, 61137 Brno, Czech Republic
³ Daimler Benz AG, Forschungszentrum, D-7900 Ulm, Germany

Abstract

Double crystal and triple axis x ray diffractionometry was used to characterize in detail the structural properties of several short period SiGe6 and SiGe6Ga superlattices grown by molecular beam epitaxy on thick step-graded SiGe alloy buffers resulting in reduced dislocation densities. Precise reciprocal lattice points were extracted from two-dimensional reciprocal space maps around (004) and (224) reciprocal lattice points. Due to the much higher instrumental resolution of triple axis diffractionometry, the triple axis diffractionometry Bragg reflection peaks from buffers and superlattices, which often overlap in such a manner, were clearly separated. The superlattices have been clearly separated experimentally, and minute changes in strain status and mean Ge content are determined. From the distribution of diffusely scattered intensity around reciprocal lattice points the correlation function of the deformation field is calculated. The deformation field is characterized by a model based on the kinematical theory of x-ray diffraction and on a formalism well known from statistical optics.

Introduction

The unique electronic properties [1-3] of ultrathin Si_mGe_n SLs depend strongly on their structural perfection and the strain adjustment of the SLs by a $\text{Si}_{1-x}\text{Ge}_x$ alloy buffer. A number of investigations was devoted to a study of the structural quality and stability of Si/Ge structures using mainly double crystal x-ray diffractometry (DCD) e.g. [4]. Recently, the use of triple axis diffractometry (TAD) has been introduced for the structural analysis of complex epitaxial multilayer structures, which allows the determination of the distribution of diffusely scattered x-ray intensity around reciprocal lattice points (RELSP) [5,6]. If graded buffers are used, a reduction of the number of threading dislocations by 3 to 4 orders of magnitude has been reported to occur [7,8] employing transmission electron microscopy (TEM). As a consequence in such samples the luminescence efficiency is higher [1-3].

It is the purpose of this paper to extend SLS's constraint on a 650 nm thick wet graded SiGe alloyed epilayer onto nominally SiGe_{0.8}Sb_{0.2} short period SLS's grown on a 650 nm thick wet graded SiGe alloyed epilayer followed by a buffer layer. We will compare the structural parameters in three nominally SiGe_{0.8}Sb_{0.2} samples with different compositions, namely 40%, 50% and 60% Sb content. We will also study the effect of the RLEP maxima above reflect the strain status and the Ge content in the corresponding layer, while the distribution of the intensity scattered diffusely around the RLEP maximum yields detailed information on structural imperfections like strain gradients,^{17,18} miscutty [110] and interface roughness.^{19,20}

roughness (142) has been developed for calculating the correlation function of the random displacement field of the deformation (fields due to structure) defects in two-dimensional layers and SLS's from measurements of the x-ray scattering (XSS) (111, 12). This method is applied to the DXS from SLS's by calculating the correlation function, and estimating the parameters of the defects. Calculated results are compared with experimental results. The size of regions which scatter coherently (143) and to estimates of the 'total dislocation densities (144). For the latter, the 'WIM' of x-ray diffractograms are used, whereas in the new approach the entire DXS distribution around the RELP maxima is compared to calculated data.

IV. CONCLUSION

Our results show that PIR is a powerful tool for the investigation of nitrated and nitroated propylene imine-based and nitroated polyimides. In addition to the nitro and nitrated polymers, the use of PIR in nitro and nitrated polymers allows to obtain important information on the structure of the polymers. Taking advantage from the easy measurement of weak ^{15}N resonances induced by the paramagnetic behavior of the doped substrate, the chemical composition and the average thickness of the ^{15}N layers formed at the surface are determined. X-ray diffraction is sensitive to thickness variations of the structure. It clearly merges the close complementary of the two techniques for the study of nitroated polymers.

- [illegible]

ALSB layers. For drawing more qualitative conclusions on this point the investigation of a larger number of samples is needed.

Our previous analysis shows that saturated layers do not serve as the transfer of nanosecond ultraviolet in the SL matrix reveal it remains as clearly detectable structure in the reflected spectra of Fig. 3. Indeed, the presence of a defect relative, whose reflectivity $\sim 40\%$ (near the value of a metal, strongly increases weak phonon absorption of the resonances. Figure 2abc show the AISB-485 spectra calculated for different values of the substrate plasma frequency ω_p and the $\text{AlGa}_{1-x}\text{As}$ layer thickness d . The remaining parameters in the calculation were the same used for the fitting of the spectrum of sample 1. In Figure 3a we see that only very weak difference exist among the spectra corresponding to $\omega_p = 0.3$ and 1.6 eV when ω_p and d are for an undoped substrate. In contrast, the "reflectable" and "leakage" changes dramatically in the $\text{AlGa}_{1-x}\text{As}$ metal behaviour is intertwined on by setting ω_p at 100 cm^{-1} , close to the actual value of ω_p in sample 1. A strong dip appears as the low energy side of the AISB-485 band close to the TO frequency of the alloy. By further increasing the doping level, i. setting ω_p at 300 cm^{-1} , causes a stronger modification of the whole spectrum which becomes absorptive (see Fig. 4). The spectrum closely resembles the reference of a thin detector film deposited onto a metallic substrate.²⁷

In the case of samples 4 and 5, by compensating the presence of a thin intermetallic layer at the interface three sequential improvement in the reproduction of spectral features is observed.

Concluding, we have shown that the presence of a thin intermetallic layer at the interface does not lead to significant false

The diffraction patterns of the superlattice deposited on GaAs substrates (samples 1 and 3) are characterized by a well-defined first-order Bragg peak, indicating a large amount of defect formation and, particularly, a strong interfacial interdiffusion. The structural determination in the superlattice samples is mainly caused by the large ($\sim 6^\circ$) lattice mismatch between GaAs and GaSb or AlSb layer. The above structural data indicated as to model the GaSb as a sequence of two alternating $\text{Al}_x\text{Ga}_{1-x}\text{Sb}$ and $\text{Al}_y\text{Ga}_{1-y}\text{Sb}$ layers, with the Al molar fractions x and y determined by the intensity ratio layer 0 and 1. The data of the θ vs. 2θ curve, as Fig. 2 was calculated with $x=0.1$ and $y=0.7$. Since the special quality of the π or diffraction patterns is not good enough to allow the determination of the individual layer thicknesses in this case, they were referred to the values of 2θ of 1 which give the best representation of 2θ of 1.20 units. In spite of the roughness of the superlattice model, a satisfactory reproduction of all the specified features is obtained. In particular, the dipole is at $2\theta = 42^\circ$ and at $2\theta = 31^\circ$ which are predicted by the GaSb-like and AlSb-like π "Kohnshub" bands, and the π dipole is at $2\theta = 35^\circ$ and $2\theta = 25^\circ$ respectively according to the theory

Strain analysis based on reciprocal space mapping

The principle of reciprocal space mapping as well as the procedure for a precise determination of the strain status of the buffer and SLS layers and of the thicknesses of the SLS constituting layers is described briefly, following Ref [6]. A reciprocal space map is performed by measuring a number of $\omega/2\theta$ scans (along the vector $q_{||}$) for a (hkl) reflection for different ω offsets (in the scan direction: new RELP perpendicular to $q_{||}$ in reciprocal space, where ω denotes the angle between sample surface and incident beam, and 2θ the angle between incident and diffracted beams). The center of the (hkl) oriented Si substrate reflector n is used as an internal standard, since the thick substrate is assumed to be unstrained and undistorted. If an SLS grows pseudomorphically on the substrate, in both symmetric (00l) and asymmetric (hkl) reflections the central SLS RELP SLO lies along the line $q_{||}(00l)$ through the substrate RELP maximum in reciprocal space. If the superlattice is completely free-standing from underlying layers (i.e., strain-symmetrized), theoretical critical SLS thickness is infinite, the relative position of the SLO RELP maximum lies along the direction $q_{||}(hkl)$ through the substrate RELP maximum for both symmetric and asymmetric reflections. Finally, if a SLS is partially relaxed, the position of the SLO RELP maximum lies in between the two extreme positions described above in reciprocal space, and from its angular deviations from the (known) position of the substrate RELP maximum in ω and $\omega/2\theta$ scan direction. Both the in-plane lattice constant $a_{||}$ and the ω -relaxed lattice constant a_{\perp} in growth direction are determined independently from each other and without any assumptions on elastic constants. In a SiGe SLS, where the individual layer thicknesses are below the critical layer thicknesses, the assumption $a_{||} = a_{\perp} = a_{\text{SiGe}}$ holds. Since the strain status of the individual layers in a SiGe superlattice is obtained as described, and the SLS period is determined from the angular deviation of higher order SLS peaks (denoted by SL-1, SL-2, etc.), the only free parameter in a simulation of a diffraction pattern from this structure is the relative thickness ratio of the Si and Ge layers in the SLS, which thus can be determined unambiguously.

The samples studied in this work are three nominally SiGe SLS's grown at $T_g = 500^\circ\text{C}$ (sample A), 470°C (sample B) and 450°C (sample C), and one nominally SiGe SLS (sample D, $T_g = 500^\circ\text{C}$), which are all grown on nominally the same buffers consisting of two parts. The first part is a graded SiGe alloy layer (graded buffer B1): Ge content increases by 3% each 50 nm up to 39%, 650 nm thick. T_g reduced continuously from 650 to 520°C, and the second part consists of a Si_{0.6}Ge_{0.4} alloy layer (buffer B2, 550 nm thick, $T_g = 500^\circ\text{C}$). In the case of almost free-standing superlattices grown on almost fully relaxed buffers B2 on top of fully relaxed graded buffers B1, as it is the case for samples A-D (see Table I), the SLO and B2 RELP's are lying very close together in reciprocal space. In order to separate these RELP's experimentally, which is essential for avoiding uncertainties in the strain analysis outlined above, it is necessary to use triple axis diffractometry which offers an about 15 times higher instrumental resolution as compared to DCD (see Figs. 1 and 2). The diffractometer (Philips MRD) uses CuK α radiation, a Bartels-type 4 crystal monochromator in the Ge(220) monochromator setting in the primary beam, and in the diffracted beam either a slit with a detector opening angle of $\lambda/20$ arcsec (DCD optics) or a two-reflection Ge(220) channel-cut analyser crystal (TAD optics, detector opening angle 1.2 arcsec).

Figure 1 clearly shows the peak separation between SLO (smaller peak) and buffer B2 Bragg reflections in $\omega/2\theta$ scans using TAD in comparison to DCD measurements of the three SiGe samples A-C. The reflections from the graded buffer part B1 are extended over the angular region between B2 and Si substrate. In the TAD reciprocal space maps shown in Fig. 2 the reflections from B1 are not visible because of their low intensity and the higher scan speed (0.5 seconds per 0.003 degree step) used for two-dimensional reciprocal space mapping compared to one-dimensional TAD measurements (2.4 s/step). In Fig. 2 symmetrical (00-4) (a) and asymmetrical (22-4) (b) reciprocal space maps are shown, in which the different distances of SLO and B2 from the Si RELP indicate slight changes both in strain status and mean Ge content in the three samples. Mere inspection of the relative positions of the Si, B2 and SLO RELP extrema in the (22-4) map indicates that not only the Ge content of the SLS in sample C is different from that of

the buffer B2. B2 is fully almost relaxed (see Tab I, $a_{||} = a_{\perp}$), however, since the center of SLO does not coincide with the line $q_{||}(224)$ through the Si RELP maximum, the whole SLS stack is under slight biaxial compression. The in-plane lattice constants of the SLS's are a useful measure for the degree of strain-symmetrization within the SLS's. The higher the values of $a_{||}$, the better the strain-distribution in these structures: a perfect strain-symmetrized SiGe as well as a perfect SiGe SLS would have a in-plane lattice constant of 3.514 Å (calculated from minimum of elastic energy stores, using values for elastic constants from Ref [15]), the measured in-plane lattice constants in the structures investigated are 5.509 Å (sample A), 5.502 Å (B), 5.503 Å (C), and 5.504 Å (D), respectively. Further structural parameters determined from (004) and (22-4) TAD reciprocal space maps are listed in Tab I.

Tab I: Structural parameters, layer strains and relative thicknesses in samples A to D.

sample	structure (°C)	layer	a (Å)	a _⊥ (SL) (Å)	a (Å)	a _⊥ (SL) (%)	a (Å)	a _⊥ (SL) (%)	meano- layers	(Si/Ge)	xGe	D _{SL} (Å)
A	500	Si	3.509	3.509	3.371	-1.11	5.526	9.18	1.58	0.386	22.02	
100x SiGe ₆	-	B2	5.509	5.509	5.526	-	-	-	-	0.386	5500	
B	470	Si	5.502	5.502	5.376	-1.01	5.528	9.40	1.63	0.380	23.57	
100x SiGe ₆	-	B2	5.502	5.502	5.519	-	5.70	-	-	0.377	5500	
C	450	Si	5.503	5.503	5.375	-1.03	5.531	9.15	1.56	0.385	23.96	
100x SiGe ₆	-	B2	5.503	5.503	5.518	-	5.85	-	-	0.370	5500	
D	500	Si	5.504	5.504	5.375	-1.03	5.520	7.5	1.74	0.364	15.87	
100x SiGe ₄	-	B2	5.504	5.504	5.519	-	4.3	-	-	0.364	5500	

Correlation function of the deformation field

Assuming the kinematical approximation and the two-wave case, the following equation for the diffusely scattered intensity I as a function of the coordinates q_x and q_z was derived [11] for a point in the plane of diffraction in reciprocal space:

$$I(q_x, q_z) = I_{\text{Dinc}} \pi K / \gamma_0^2 \int_{-\infty}^{\infty} d(x-x') \int_0^1 dz \int_0^1 d(x-x') \gamma_0(x-x') \times \exp[2\pi i q_x(x-x') + q_z(z-z')] \exp[-i(x-x')^2] \gamma_0(x-x') \quad (1)$$

The coordinate system chosen in real space (x, z, x_1, x_2) and in reciprocal space (q_x, q_z, q_1, q_2) is shown in Fig. 3, where 0 is the origin (000) of reciprocal space, H is a reciprocal lattice point with the Miller indices (hkl), k_0 and k_h are the wave vectors of the incident and the diffracted beams, and h is the diffraction vector. In Eq. 1 Dinc is the amplitude of the incident wave, K is the length of wave vector in vacuum ($1/\lambda$, λ = x-ray wavelength), $\gamma_0 = \cos(\phi_0)$ and $\gamma_h = \cos(\phi_h)$ are the direction cosines of the incident and the diffracted waves with respect to the internal surface normal n . x_1 and x_2 are the h -th and 0-th Fourier components of the polarization of the perfect crystal including the polarization factor, the asterisk denotes the complex conjugate. For an SLS, $\gamma_h(z)$ is a periodic function of z which can be expanded into a Fourier series [12]:

$$\gamma_h(z) = \sum_{H'} \chi_{hH'} \exp(2\pi i H' z) \quad (2)$$

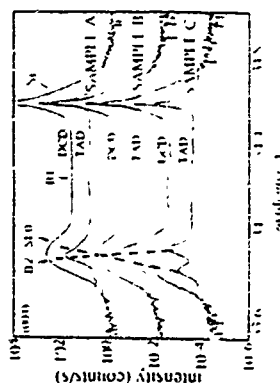


Fig 1 Double crystal (DCD) and triple axis (TAD) (004) and 2θ scans of samples A, B and C. For B and C, DCD and TAD measurements were shifted along the intensity axis by a factor of 100, respectively.

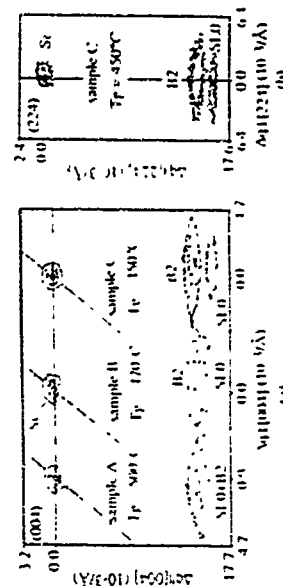


Fig 2 Triple axis reciprocal space maps in the vicinity of (004) (a) and (224) (b) substrate (Si), top buffer (constant Ge content, B2) and central superlattice (SLD) reciprocal lattice points of samples A to C as indicated. Two intensity contours are plotted at 1, 2, 5, 10, 20, 50, 100, and 1000 counts/s. The reflection from the graded buffer B1 is not visible because of the low intensity.

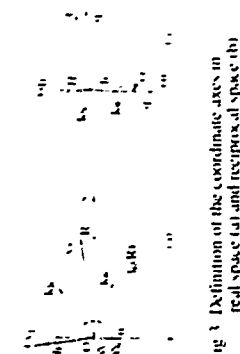


Fig 3 Definition of the coordinate axes in real space (a) and reciprocal space (b).

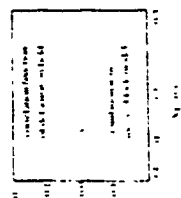


Fig 4 Calculated correlation function and simulation assuming a mosaic block model for central superlattice peak SLD in sample C.

where $H = m/D$, m is an integer (the diffraction satellite order) and D is the SLS period. The term which depends on the effective absorption coefficient $\mu = \pi K \text{Im}(S_{00})/(U_{00} - 1/\gamma_0)$ describes the influence of absorption. The first integral is performed for the distance in the x -coordinates X and X' of two observation points $R = (X, Y, 0)$ and $R' = (X', Y', 0)$ lying on the crystal surface along the lines $h_1(R)$ and $h_1(R')$ (Fig 3a). The latter are parallel to k_0 and connect $r = (x, y, z)$ and $r' = (x', y', z')$ within the layer (thickness l). r and r' mark the positions from which the two scattered beams originate. G denotes the correlation function of the random deformation field on the crystal surface [10]. Using this optical coherence approach, for volume defects like mosaic blocks we assume the random deformation field in the layer to be statistically homogeneous, and $G(r, r') = G(r - r')$ holds. Assuming a certain defect model, Eq. 1 is used to simulate the measured DXS intensity distribution in the vicinity of RELP's.

In the following we show that this correlation function of the atomic displacements u can be calculated directly from the measured DXS intensity. This procedure represents a significant simplification of the numerical analysis. Calculating the Fourier transformation $I(q_0, z_0)$ of $I(q_x, q_z)$ we obtain

$$I(q_0, z_0) = G(l, q_0, 0, z_0) R(z_0). \quad (3)$$

where $R(z_0)$ represents the Fourier transformation of the reflection curve of the perfect structure. Equation 3 means that the correlation function G of the random deformation field due to defects equals the Fourier transformation of the measured distribution of the diffusely scattered intensity near a RELP divided by the Fourier transformation of the reflection from the perfect structure. This approach is similar to the Patterson analysis well known from statistical optics, with the Fourier transformation of the DXS intensity treated as the Patterson function. In the case, where mosaic blocks are the main reason for the defect deformation field G , the DXS does not depend on the satellite order, and the ΔS intensity is centrosymmetric with respect to the RELP. We assume the coherence of crystallographic net planes to be completely destroyed, if two points r and r' are lying in two different blocks, and that the mosaic blocks are rotated with respect to each other. Then

$$G(r - r') = P(r - r') \exp[-2/\Delta (x_2 - x_2')^2], \quad (4)$$

where $P(r - r')$ is the probability of finding both points r and r' in the same block (which depends on the block size), Δ is the root mean square misorientation of the blocks. For the derivation of Eq. 4 we have assumed that the static IXBYE-Waller factor is much smaller than unity. In the case of blocks with diameter $2R$, both the contours of the DXS distribution as well as the contours of constant G are ellipses with the main axes q_1, x_1 and q_2, x_2 , respectively.

If the mosaic blocks are the dominant defects, then the block size $2R$ should not depend on the Bragg angle Θ of the particular RELP around which the DXS intensity has been measured. A random elastic deformation within different mosaic blocks (i.e. microstrain) would lead to smaller values for $2R$ for RELP's measured at larger Bragg angles Θ [11]. The true block diameter is then obtained by extrapolating to $\Theta = 0$. If random elastic deformation dominates in comparison to mosaic blocks, then in asymmetric Bragg reflections (i.e. for lattice planes tilted with respect to the sample surface) the main axes of the ellipses arising from DXS are no longer perpendicular and parallel to h , however, the DXS intensity is still centrosymmetric. We want to emphasize, that the DXS intensity around a central superlattice peak (SLD) is not sensitive to interface roughness.

Discussion

The whole analysis of the structural defects and the strain status described so far is based on the assumption that RELP contours or at least RELP maxima arising from different portions of the heterostructure are well separated experimentally in the plane of diffraction in reciprocal space.

The samples studied here consist of almost free-standing superlattices grown on almost fully relaxed buffers B2, the reflections of which are lying very close together in reciprocal space and are separated experimentally much better from each other in TAD than in DCD measurements.

The shape of iso-intensity contours around these RELP's is centrosymmetric if the RELP's do not overlap, e.g. in sample C), and therefore no strain gradient exists [9] in the top buffer part B2 and the SLS. The distribution of (diffusely scattered) intensity in the vicinity of the B2 and SLO RELP maxima is similar in all samples (as evident from the FWHM's, which are the same within the accuracy of ± 10 arcsec), indicating similar defect structures, but only in sample C the intensity distribution around both the (004) SLO and B2 RELP's measured by TAD has been used to calculate the correlation function of the deformation field (Fig. 4), which has been simulated on the basis of the mosaic block model explaining the shape of the contour maps. For the SLS and the buffer with constant Ge content B2, the mean block size turns out to be of the order of 310 and 390 nm in diameter, respectively, and the mean misorientation of the mosaic blocks with respect to growth direction is 370 and 360 arcsec, respectively. Using the measured FWHM's of 110 arcsec and 140 arcsec to estimate the size of coherently scattering regions using Scherrer's equation [13], values of 313 nm and 246 nm are obtained for B2 and SLS, which is in good agreement with the values found for 2R assuming the mosaic block model. The resulting dislocation density from the FWHM values would be $2.2 \cdot 10^7$ and $3.5 \cdot 10^7$ cm⁻² following the approximation in Ref. [14] and using a Burger's vector of 3.8 Å. This dislocation density is about one order of magnitude larger than that found by TEM [16].

Assuming the mosaic block model for a simulation of the correlation function G in these structures, it turns out that the average size of mosaic blocks would be larger than the thickness of the SLS, and that a wall between mosaic blocks (with a dislocation density of about 10^9 cm⁻², calculated from the mean Δ) would consist of only one dislocation over the SLS and only a few dislocations would pile up over the buffer B2 thickness. The pile-up of dislocations having the same Burger's vector (i.e., originating from the same dislocation source), which leads to a mosaic block-like structure, has been observed previously [5, 8]. We conclude therefore that the more pronounced mosaicity of the underlying graded buffer B1, which is evident from the about 50% larger values of the FWHM in the direction perpendicular to $q(1004)$ of the B1 RELP compared to that of the B2 [6], still influences the defect structure of the layers above. However, the mosaic block model is just one possible explanation for the shape of the DXS intensity. Another model is based on a random elastic deformation field, which may play a role in the buffer B2 in these samples. This is indicated by a slight deviation of the main axes of the elliptical contours of the DXS intensity around the asymmetrical (224) B2 RELP from being parallel and perpendicular to $q(12\bar{2}4)$ (Fig. 2b). Such an effect should not occur if the defect structure would be determined entirely by mosaicity. If this slight tilt is ignored and if the validity of the mosaic block model is assumed, the (224) Bragg reflection RELP data for buffer B2 were fitted. The values of $2R=350$ arcsec and $\Delta=360$ arcsec were obtained. The value for 2R increases slightly with decreasing Bragg

angle Θ which indicates a certain influence of random deformation on the results. Unfortunately the diffracted intensity from the (224) SLO RELP was too low for performing such an analysis. The TEM data of sample A show that in the SLS for distances which are one μ m apart from each other a few dislocations appear [16], which is not too different from the average values found here (for each 350 nm one dislocation) for sample C.

Conclusions

We show that triple axis diffractometry gives precise information on the strain status in complex multilayer structures, especially in the case of overlapping Bragg-diffraction peaks from NBE grown, strain-symmetrized SiGe₆ and SiGe₄ short period superlattices and from underlying buffers. In addition, reciprocal space maps yield the shape of iso-intensity contours of scattered radiation, from which - for the first time for Si/Ge structures - information on the correlation function of the deformation field due to structural defects is obtained. The latter can be expressed in terms of two statistical parameters assuming a defect model.

Acknowledgements: Work supported by ESPRIT Basic Research Action 7128, FWF Project No 9119PHY and Jubiläumsfonds der Österreichischen Nationalbank Project No 4542

References

1. For a recent review see e.g. W. Presting, A. Kibbel, M. Jaroš, R. M. Tunc, U. Menzinger, G. Absreiter, and H. G. Gmmeiss, *Semicond. Sci. Technol.* **7**, 1127 (1992)
2. J. Olajos, J. Engvall, H. G. Gmmeiss, U. Menzinger, G. Absreiter, H. Kibbel, E. Kasper, and H. Presting, *Phys. Rev. B* **46**, 12837 (1992).
3. J. Engvall, J. Olajos, H. G. Gmmeiss, H. Presting, H. Kibbel, E. Kasper, *Appl. Phys. Lett.* in print.
4. D. C. Houghon, D. D. Perovic, J. M. Barbeau, and G. Weatherly, *J. Appl. Phys.* **67**, 1850 (1990).
5. P. F. Frewster, *J. Appl. Cryst.* **22**, 64 (1989); **24**, 178 (1991)
6. E. Koppenscheiner, P. Hamberger, G. Bauer, A. Pesek, H. Kibbel, H. Presting, and E. Kasper, *Appl. Phys. Lett.* **62** (15) 1783 (1993).
7. E. A. Fitzgerald, Y.-H. Xie, M. L. Green, D. Brasen, A. R. Kortan, J. Mischel, Y.-J. Min, and B. E. Weir, *Appl. Phys. Lett.* **59**, 811 (1991).
8. W. Jäger, D. Sienkamp, P. Ehrhardt, K. Leifer, W. Sybertz, H. Kibbel, H. Presting, and E. Kasper, *Thin Solid Films*, **222** (1993) 221.
9. E. Koppenscheiner, G. Springholz, P. Hamberger, and G. Bauer, *J. Appl. Phys.*, submitted.
10. V. Holy, J. Kubena, E. Abramof, A. Tuck and E. Koppenscheiner, *J. Phys. D: Appl. Phys.* **26**, A146 (1993).
11. V. Holy, E. Koppenscheiner, K. Wolf, and M. Kasper, *J. Appl. Crystallography* submitted.
12. V. Holy, J. Kubena and K. Ploog, *Superlattices and Microstruct.* **12**, 25 (1992)
13. D. Scherrer, *Göttinger Nachrichten*, **3**, 98 (1918)
14. P. Gay, P. B. Hirsch, A. Kelly, *Acta Metall.* **1**, 315 (1953).
15. A. Segmüller and M. Murakami, "Treatise on Materials Science and Technology", eds K. N. Tu, R. Rosenberg, Academic Press, N.Y., 1988, Vol. 27, ppl 13
16. W. Jäger, E. Kasper, private communication

Abstract

In spite of the spatial separation of electrons and holes associated with its type II nature, the InP-Al(In)As system has excellent optical properties. In particular, it is possible to measure the photo-luminescence excitation and photo-current spectra in single hetero-junctions. In addition, the bandgap of a type II heterostructure varies linearly with the discontinuity of the conduction bands. This system thus offers a unique opportunity for a detailed experimental study of the band offsets. We find that offsets at InP-Al(In)As and Al(In)As-InP heterojunctions are quite reproducible, but differ by $(100 \pm 20 \text{ meV})$. It also appears that the average band offset is not transitive in the Ga(In)As-InP-Al(In)As family of heterostructures.

The basic problem of band discontinuities at a semiconductor-to-semiconductor contact has been a hotly contested topic [1-3] for the last twenty years. On one hand, there exists "global" approaches based on the assumption of a reference energy level, absolute like the vacuum level in the old electron affinity rule or the valence band extremum in Harrison's tight binding theory [4], or relative to the bulk material like the "charge neutrality level" introduced by Tejedor et al. [5] and by Tersoff [6]. Such approaches have built-in properties of commutativity and transitivity. More recently, super-computers have allowed a number of ab-initio calculation methods in which the redistribution of electronic charges at interface chemical bonds is evaluated for the actual atomic distribution [2,3,7]. In these approaches, band offset commutativity and transitivity are not imposed, but may actually appear as a de-facto result of numerical calculations. Also, it was proved already long ago that the deliberate (or non) introduction of a dipole layer, for instance by localized doping or addition of a chemical layer, will modify the measured band offset in a given system [8], which implies that in some circumstances, band offsets might not be an intrinsic property of an hetero-junction. Finally, evidences of band offset asymmetry were recently reported by Landesman et al. [9] for the InP-Ga_{0.47}In_{0.53}As interfaces from photo emission studies. However, there are considerable difficulties in characterizing properly the composition of ultra-thin semiconductor layers involved in such measurements, and more complete investigations are certainly necessary. In fact the experimental difficulty of measuring band offsets is such that until recently the commutativity of band offsets, ie the equivalence of the intrinsic A-B and B-A interfaces, has not been seriously questioned by the community of quantum well physicists who generally consider that semiconductor quantum wells are reasonably symmetric. The main reason why such a basic question remains open is that the majority of heterostructures which have been investigated in some details are of the type I, ie electron and holes are confined within the same layers. In this case, interband optical properties are rather insensitive to the value of the band offset ratio $\Delta E_c/\Delta E_v$, the consideration of uncertainties in the material or quantum well parameters and of the limited accuracy of theoretical models themselves explains surprising large fluctuations in the reported values. On the opposite, the band gap of a type II heterostructure (in which electrons and holes are confined in the adjacent layers) depends nearly linearly on the value of the conduction band offset,

and simple optical measurements should allow a direct and precise evaluation of the band offsets. Unfortunately, the type II systems investigated earlier in some details, the InAs-GaSb and Ge-CdSi systems and the GaAs-AlAs short period superlattices, have a number of intrinsic characteristics which make the analysis of a single hetero-junction rather difficult.

Recently, we realized that the almost unexplored InP-Al(In)As system [10-12], which presents a regular type II configuration with electrons confined in InP and holes in Al(In)As, has excellent optical properties which allow direct spectroscopic measurements on single interfaces [13], using various experimental methods like photoluminescence (PL), photoluminescence excitation (PLE) or photo-current (PC) spectroscopies. Here we report a set of observations on the "direct" InP-Al(In)As and "inverse" Al(In)As-InP hetero-junctions, as well as on multiquantum well structures. These results evidence that direct and inverse band offsets are quite reproducible, but differ by as much as 100 meV, which contradicts recently reported theoretical results [3,14,15]. We finally discuss the issue of band offset transitivity in the context of the Ga(In)As-InP, Ga(In)As-Al(In)As and InP-Al(In)As systems.

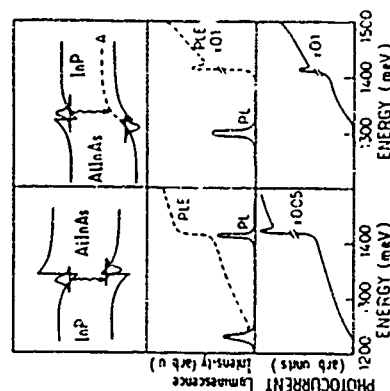


Fig. 1 (a) Low temperature PL, PLE and PC spectra for the "direct" InP-Al(In)As interface sketched in the insert, (b) same spectra for the "inverse" Al(In)As-InP interface.

All our samples were grown by atmospheric pressure metal-organic chemical vapor deposition (MOCVD) on n-doped InP substrates. They were characterized by X-ray double diffraction, which yields the precise value of $\text{Al}_{1-x}\text{In}_x\text{As}$ composition x , a crucial parameter for this study since the bandgap of this alloy varies quite rapidly: $E_g(\text{Al}_{1-x}\text{In}_x\text{As}) = 1520 + 27(x-x_0)$, where $x_0=0.48$ is the composition of the alloy lattice matched to InP. Electrical measurements on thick layers show that Al(In)As (InP) has a n-type residual doping in the 10^{16} cm^{-3} (10^{14} cm^{-3}) range. Figure 1a shows low temperature (2K) PL, PLE and PC spectra of a sample consisting in a single 1000Å thick $\text{Al}_{0.53}\text{In}_{0.47}\text{As}$ layer (4.8% Al-rich compared to the lattice-matched alloy) grown on undoped epitaxial InP. The luminescence consists in a single line, remarkably intense, ~30 meV broad and centered at 1.23 eV, well below both InP (1.42 eV) and Al(In)As (1.65 eV) bandgaps. This luminescence has a short decay time (a few ns) and gives rise to an absorption gap at nearly the same energy, as can be observed in both the PLE and PC [16] spectra. Absorption occurs between valence states localized in Al(In)As and conduction states localized in InP, as shown schematically in the insert. In fact, these states are confined close to the interface by the band bending resulting from the charge transfer of electrons from Al(In)As to InP, which probably helps the absorption. The smooth absorption profile is thought to result from the combination of 1) absence of parity selection rule for the absorption thence, many different

subbands can contribute to the absorption, ii) ~ 30 meV inhomogeneous broadening, mainly due to $\sim 1\%$ long range fluctuations of alloy composition, and iii) weakness of exciton binding energy due to electron hole spatial separation. It is noteworthy that our excitation source is an halogen lamp followed by a grating monochromator, with a maximum power of $50 \mu W$ only, and that estimates of the wavefunction overlap indicate an absorption of a few 10^{-4} . Observation of a PLE spectrum in these conditions witnesses the very high radiative efficiency of this type II system. The heterojunction bandgap is equal to the $Al_{0.47}In_{0.53}As$ bandgap E_g^{AlInAs} (1.65 eV, as observed directly in extended PLE and PC spectra) minus the conduction band offset ΔE_c plus the sum of electron and hole confinement energies E_1 and E_2 . Precise estimates of these confinement energies in the absence of complete electrical characterization are impossible, but 50 ± 20 meV should be a representative figure and a comfortable error bar for $H_1 \rightarrow E_1$ [17]. Hence, these data give a rather precise value of ΔE_c for this system, $\Delta E_c = 460 \pm 20$ meV.

Figure 1b shows the same PL, PLE and PC spectra observed on a different structure consisting of a 1000 Å thick $Al_{0.52}In_{0.48}As$ layer grown on a $GaInAs$ buffer (to avoid the presence of the direct interface), and topped with a thick InP layer. An intense luminescence line is also observed in this sample, but at a significantly larger energy, 1.3 eV, and with a completely different qualitative behavior: it has a very long decay time (non-exponential, with a characteristic time of 1 ns), and does not give rise to any absorption below InP bandgap. This luminescence is in fact most likely associated with the presence of a deep acceptor which emits a similar luminescence in InP grown by MOCVD on thick As-based alloys. We have observed a similar luminescence in InP grown on thick $GaInAs$ layers. Yet, the fact that no luminescence related to the interface can be observed is strange enough, and indicates that the interface transition is at a somewhat higher energy. Indeed, the PC spectrum shows a well defined absorption gap at 1.32 eV, with a line shape and an absolute value of the photo-current similar to those of Fig. 1a. This absorption gap, certainly associated with the interface transition, indicates that the offset at this interface is considerably larger than the one at the direct interface. Since the $Al_{0.52}In_{0.48}As$ composition is nearly the same for the two samples, and since band-bending effects cannot account for such a large difference, these data are a rather strong evidence that the direct offset (~ 460 meV) and the inverse offset (~ 360 meV) are intrinsically different. We would like to stress that these behaviors of direct and inverse interfaces, both qualitatively and quantitatively, are observed in all the samples (eight) that we have investigated so far.

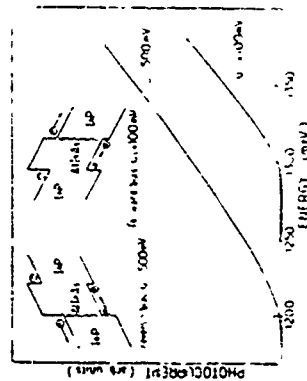


Fig. 2 Low temperature PC spectra for a $InP-Al(In)As-InP$ heterostructure. As illustrated in the insert, the direct interface is observed in reverse bias, and the inverse one in forward bias. In both cases, above a bias threshold of a few hundred mV, the PC spectrum becomes independent of the applied voltage.

An additional evidence is obtained from photocurrent spectra of a structure consisting in a 3000 Å thick $Al_{0.5}In_{0.5}As$ layer embedded between thick epitaxial InP layers, displayed in Fig. 2. As illustrated in the insert, in the forward bias the inverse interface contributes directly in the photocurrent, while the contribution of the direct interface is inhibited by the large potential barrier

that carriers have to overcome, and vice versa for the reverse bias, we thus expect, and do observe the direct interface in reverse bias and the inverse one in forward bias. Here, the $Al_{0.5}In_{0.5}As$ layer is the same, and electrical properties of the interfaces cannot differ significantly. From this, and from the general consistency of the whole set of data, we thus conclude that the 100 meV difference between the two interface transitions directly reflects a reproducible difference of the band offsets. Recently, the offset at the inverse interface has been measured by photo-emission spectroscopy [18], a method which has been rather successful in measuring band offsets in contested cases [19]. In these experiments, the ultra-thin InP layer was grown by MBE, and the reported offset is quite consistent with our result for the inverse interface. Conversely, our data for the direct interface and for multi quantum wells (see below) agree with the recently reported photo-luminescence data [11,12], which indicate an offset $\Delta E_c \sim 400$ meV.

The microscopic reason for this strong asymmetry is still unknown, and we can only add a few heuristic remarks. As discussed by several groups [3,15], the driving force for a strong intrinsic asymmetry is that chemical bonds at the two interfaces are completely different because the materials share no common atom. Ideally, the direct interface is predominantly built with $P-Al(In)$ bonds (shorter than the regular bonds), while the inverse one is primarily built with $As-In$ bonds (longer than the regular bonds). Therefore, strain and chemical-dipole contributions to the band offset may differ appreciably, and for instance Foulon and Prost (15) do predict an offset asymmetry of 50 meV for this system. However, it has been shown that exchange mechanisms [20] occur at the growing interface, and in particular that P atoms as soon as $AsIn_4$ is substituted to PH_4 in the reactor atmosphere [21]. If such a mechanism prevails, it should at first symmetrize the interfaces! On the other hand, if several monolayers are affected by these exchange mechanisms (as suggested by Brasel et al. [12]), this may result in non-symmetric interface non-stoichiometries. Conversely, it could be argued that the observed asymmetry is rather due to the reproducible presence of different defects at the interfaces. The observation of a specific deep acceptor level in InP grown on As-based layers indicates the possibility of such differences. However, since the long recombination time indicates a rather low density, it is unlikely that the dopant density may be large enough to affect the band offset. We rather expect that only a moderate increase of the band-bending effect would result from this possible p-type doping [22]. Another important issue is the interface sharpness. X-ray diffraction data for short period InP- $Al(In)As$ superlattices [13] indicate that the composition modulation is quite sharp, and the observation of quantitatively comparable PC signals from the two interfaces (see Fig. 2) proves that the electron-hole wavefunction overlaps are similar, which rules out a strong sharpness asymmetry.

The offset asymmetry has important consequences for the optical properties of InP- $Al(In)As$ superlattices, as illustrated in the insert of Fig. 3, to avoid the building-up of a macroscopic potential, the system has to create a built-in electric field by accumulating electric charges near the terminating planes, a classical mechanism which controls the quantum potential difference associated with the sum of band offset differences [23]. Calculations of the energy band structure and optical absorption for the structure depicted in the insert show that for reasonably narrow quantum wells, everything behaves nearly as if the offsets were symmetric, with the average value. We have examined the optical properties of a number of superlattices, grown in slightly different conditions and having slightly different alloy compositions. From the fit of their observed bandgaps we determine the variation of the average offset with $Al_xIn_{1-x}As$ composition, as shown in Fig. 3. With a remarkably small dispersion of the data points we get $\langle \Delta E_c \rangle$ (meV) =

$(410 \pm 20 + 1500 \delta x)$, where δx is the deviation from the lattice-matched composition $x_0 = 0.48$. These results thus give a precise value of $\langle \Delta E_c \rangle = 410 \pm 20$ meV for the lattice-matched system

There exists a general consensus for the offsets in the $GaInAs-InP$ ($\langle \Delta E_c \rangle = 260 \pm 10$ meV) and $GaInAs-AlInAs$ ($\langle \Delta E_c \rangle = 500 \pm 50$ meV) systems, which have been extensively studied because of their technological importance [24]. Both core level emission and electrical measurements on single heterojunctions, and optical properties of quantum well structures (which, as underlined above, are sensitive to the average band offset) seem to agree in these cases, although some recent measurements contradict this unanimity [9]. Our results indicate that band offsets are

Acknowledgements LPMC-ENS is Unité Associée à CNRS N° 1437 This work is supported by PIRNAT/DRET/DRED.

References

- 1 For a review, see "heterojunctions band discontinuities physics and applications", edited by F. Capasso and G. Magarinos, North-Holland, 1987
- 2 C. Priester, J. Phys. III, 1, 481 (1991), and references therein
- 3 R. G. Dandrea, C. B. Dote and A. Zunger, J. Vac. Sci. Technol. B 10, 1744 (1992), and references therein
- 4 W. A. Harrison, J. Vac. Sci. Technol. 14, 1016 (1977)
- 5 C. Tejedor, F. Flores and E. Louis, J. Phys. C 10, 2163 (1977)
- 6 J. Tersoff, Phys. Rev. Lett. 52, 463 (1984) and Phys. Rev. B 30, 4874 (1984)
- 7 M. Hybertsen, Phys. Rev. Lett. 64, 555 (1990) and references therein
- 8 G. Magarinos, J. Vac. Sci. Technol. 14, 430 (1986)
- 9 J. P. Landman, J. C. Garcia, J. Massies, P. Mauerl, G. Jazequel, J. P. Hirz and P. Ainhel, Appl. Phys. Lett. 60, 1241 (1992)
- 10 E. J. Cairne, H. Subbanna, H. Krimmer, J. L. Merz and A. Y. Cho, Appl. Phys. Lett. 45, 1123 (1984)
- 11 L. Aina, M. Mammi and L. Stetler, Appl. Phys. Lett. 53, 1620 (1988)
- 12 M. J. S. P. Brail, R. E. Nahory, W. E. Quinn, M. C. Tamargo and H. H. Farrell, Appl. Phys. Lett. 60, 1981 (1992)
- 13 E. Lugagne-Delpont, P. Vossin, J. P. Vernet, M. Voss, J. P. André and J. N. Pailion, Semicond. Sci. Technol. 7, 524 (1992); E. Lugagne-Delpont, J. P. André and P. Vossin, Solid State Comm. 86, 1 (1993)
- 14 M. Hybertsen, Appl. Phys. Lett. 58, 1759 (1991)
- 15 Y. Foulon and C. Priester, Phys. Rev. B 45, 6259 (1992); Y. Foulon et al., J. Vac. Sci. Technol. B 10, 1754 (1992)
- 16 Photocurrent spectra are obtained in the "vertical" geometry, with the electric field applied parallel to the growth axis
- 17 $E_{\text{H}} = 50$ meV and a sheet electron density of $2 \times 10^{11} \text{ cm}^{-2}$ are the figures coming out of the usual self-consistent calculation of the heterojunction (see ref. 1) for a n-type doping level of $2 \times 10^{16} \text{ cm}^{-3}$ in Al(In)As and a band offset of 450 meV. Increasing this doping level up to 10^{17} cm^{-3} doubles the electron density and yields $E_{\text{H}} = 71$ meV.
- 18 J. R. Waldrop, E. A. Kraut, C. W. Fairley and R. W. Grant, Appl. Phys. Lett. 69, 372 (1991)
- 19 R. W. Grant, E. A. Kraut, J. R. Waldrop and S. P. Kowalczyk, in ref. 1
- 20 J. M. Moisson, F. Houray, F. Barthe, J. M. Gérard, B. Jusserand, J. Massies and F. Turco-Sandroff, J. Crystal Growth 111, 141 (1991)
- 21 T. Y. Wang, E. H. Reihlen, H. R. Jen and G. B. Stringfellow, J. Appl. Phys. 66, 5376 (1989)
- 22 For a review of energy levels in heterostructures, see G. Bastard, "Wave mechanics applied to semiconductor heterostructures", les Editions de Physique (Les Ulis), 1988
- 23 This "macroscopic edge effect" screening a quantum (mesoscopic or microscopic) potential occurs in a variety of physical circumstances, like the "quantum photovoltaic effect" (Bum et al., Phys. Rev. B 33, 1063 (1986), or the built-in piezoelectric field in strained superlattices (Smith and Mailhot, Phys. Rev. Lett. 58, 1264 (1987)), or the simple fact that there is no permanent voltage across a polar semiconductor or a piezoelectric material.
- 24 M. Quilicet, SPIE vol. 1361, edited by M. Razzeghi (Bellingham, 1991), p. 34
- 25 W. Seidel, P. Vossin, M. Sacilotti, T. Benaitou and G. Guillot, unpublished

not transitive in this group of materials, since transitivity requires $\langle \Delta E_c \rangle \gg 240$ meV for the InP-AlInAs system

Finally, it should be noted that the average offset dependence observed in short period SLs does not perfectly fit the data in single heterojunctions, for which the average offset is somewhat smaller. We recently studied [25] a structure with 4% In-rich Al(In)As. This structure shows exactly the same qualitative behavior as the Al-rich sample of Figs. 1 and 2, and we find that the measured composition dependence of the average offset for single heterojunctions would be well fitted by the 15 meV/% law, but with $\langle \Delta E_c \rangle = 370 \pm 20$ meV for the lattice-matched system. This ≈ 40 meV difference with respect to superlattices remains within the error bars, but could also be significant and reflect a physical effect. Among possible causes for this observation, the role of plastic relaxation should be considered for the lattice mismatch and layer thicknesses involved in our Al-rich heterojunctions, the plastic relaxation of the layers is almost complete (as proved by the comparison of X-ray and optical data of the hosts), while for our short period superlattices, the small lattice mismatch is accommodated by elastic strain. For a given composition, the offsets might be slightly different for strained and relaxed layers.

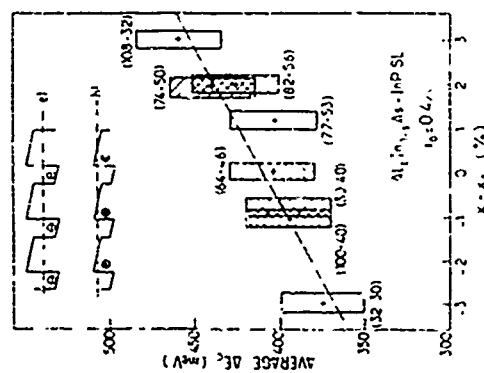


Fig. 3 Measured average offset for a series of short period Al(In)As-InP superlattices. Respective Al(In)As and InP layer thicknesses (as indicated for each sample) are in the 30-100 Å range, which ensures that band bending corrections are negligible. Calculations for the potential profile shown in the insert prove that optical properties are essentially sensitive to the average band offset.

In conclusion, from a number of highly consistent observations, we find that band offsets are simultaneously reproducible and non-commutative in the InP-Al(In)As heterojunctions, and non-transitive in the InP-Al(In)As, Ga(In)As-InP, and Ga(In)As-Al(In)As family of heterostructures. The microscopic origin of these effects is not fully established, and a more detailed knowledge of the chemical and structural properties of these interfaces is certainly needed to assert whether the leading term is the difference in strain and dipole contributions or the effect of non-stoichiometric interfaces. Yet, these properties are established with an unprecedented accuracy thanks to the type II nature of the InP-Al(In)As system, which allows, for the first time, direct spectroscopic investigations of single heterojunctions. This should stimulate a new interest in the comparison of theoretical and experimental results on heterojunction band discontinuities. The direct observation of single heterojunction optical properties also opens new areas of investigations like the dependence on the growth method or the effect of intermixing on the band offsets, for which there exists contradictory and unverified theoretical predictions.

Above Barrier Exciton Confinement in InGaAs/GaAs Multiple-Quantum-Well Structures

M. Cantini, A. Palmieri, and A. Proia

Dipartimento di Fisica, Università di Roma - La Sapienza, Piazzale A. Moro 2, I-00185 Roma, Italy

F. Martelli

Fondazione Ugo Bordoni, via B. Castiglione 59, I-00142 Roma, Italy

K. B. Oza and I. Wörren

Department of Physics, Norwegian Institute of Technology, N-7034 Trondheim, Norway

M. R. Bruni and M. G. Spascone

ICMAT CNR, Area della Ricerca di Roma, s.p. 10, I-00016 Montetomondo Stazzone, Italy

Abstract

Exciton confinement in the GaAs barriers of InGaAs/GaAs multiple quantum well structures is demonstrated by luminescence self-absorption and photoluminescence excitation spectroscopies. The confinement energy and absorption linewidth depend on the barrier width as predicted by a plain quantum mechanical model. For thin barriers, a splitting in the experimental lineshape is accounted for by including into the theoretical model the interaction among excitons confined in individual barriers. Evidence for a transition between a hole state in the well and an electron state confined in the barrier is also reported, which provides a direct way for estimating the band offsets.

The discovery of confined states in the energy continuum (i.e., above the top of the barrier potential) of modulated semiconductor structures has given new impulse to fundamental studies of these systems [1-5]. From a theoretical point of view, above-barrier carrier confinement (or resonances) can be easily modeled [6], its first discovery can be traced back to the independent reports by Ramsauer and Townshend, in the early twenties, that electrons scattering with noble-gas atoms have a minimum in the scattering cross section for very low kinetic energies, as described in most textbooks of quantum mechanics [7]. From an experimental point of view, an effective carrier localization has been achieved by means of electronic Bragg reflectors suitably designed superlattices [1,2]. In more simple structures, such as single- and multiple quantum wells (MQW), it has been shown, instead, that interference effects due to quantum reflection at the barrier/well interfaces give rise to a sizeable confinement of excitons in the quantum-barrier region [3-5]. In particular, electrons in the conduction band, and holes in the valence band, travelling in the GaAs barrier clad between two InGaAs wells, experience some reflection at the InGaAs/GaAs interfaces, thus undergoing partial confinement in the barrier region. Coulomb interaction between confined electrons and holes leads to the formation of excitons confined in the barrier, C-FE, with energy higher than that of the bulk free excitons, 3D-FE. This model has been verified by comparing the estimated values of the confinement energy with those obtained at 80 K by using a non-conventional, *ad hoc* designed, absolute absorption method, called "luminescence self-absorption" (LSA), as well as conventional photoluminescence (PL) [4,5].

In this work, LSA performed at 5 K, photoluminescence excitation spectroscopy (PLE) performed at 12 K, and PL performed in situ at 80 K, provide additional evidence of exciton confinement in the GaAs barriers of InGaAs/GaAs strained MQW structures. The increased resolution achieved at low temperature allows a better determination of the C-FE lineshape and linewidth. These have been successfully compared with the theoretical model, extended to include interactions among excitons confined in different barriers. Furthermore, earlier undetected absorption step-like structures have been observed in PLE spectra at energies below the GaAs 3D-FE. These structures have been interpreted in terms of a transition involving electrons confined in the quantum barriers and holes confined in adjacent quantum wells, thus allowing a direct way of estimating the band offsets.

The structures of all the samples studied in this work, InGaAs/GaAs MQW, grown by molecular beam epitaxy (MBE) on GaAs substrates, are reported in Table I. Buffer layers, quantum wells, and quantum barriers were all nominally undoped, the small linewidth of the QW ground-state PL at 5 K (about 1 meV) indicated a high quality material. All sample substrates are doped to $1-4 \times 10^{18} \text{ cm}^{-3}$, except those of samples 352-355, which are semi-insulating.

The luminescence self-absorption method is described in the following. Excitation by a Ti:Sapphire laser, at energy slightly above the GaAs band gap, creates electron-hole pairs in the whole multilayer structure, and in the substrate. At low temperatures, PL from epitaxial GaAs is virtually absent, compared to the broad band emitted from the degenerate substrate and centered around the band gap value of GaAs, which dominates the PL spectra. In the backscattering

geometry, used in conventional PL experiments, the substrate emission is detected after crossing the epitaxial layers: absorption in the buffer layer and in the quantum barriers shows up therefore as dips in the PL spectra (a more detailed discussion of this technique can be found elsewhere [4,5]). On the other hand, a sizeable PL signal from both buffer layer and quantum barriers can be obtained at all temperatures in the backscattering geometry by using an Ar⁺ laser to favor near-surface excitation. Conventional PLE is performed by monitoring the QW ground-state luminescence intensity.

Sample	N	L _b	L _q	L _h
S9J	4	30	5	5000
S102	6	35	5	80
S92	4	40	5	80
S99, S95, S96	4	40	5	5000
S103	4	40	5	80
S97, S98	2	40	2.5 × 25	5000
S111	4	60	5	80
S92	4	40	15	5000
S5J	4	20	15	5000
S58	4	10	15	5000
S55	4	5	15	5000

Table 1 Characteristics of the In_{0.95}Ga_{0.05}As/GaAs MQW structures used in this work. L_b, L_q and L_h indicate the thickness (in nm) of quantum barriers, quantum wells, and buffer layers, respectively. N gives the number of quantum wells and barriers. The sample parameters have been determined by means of RHE-FTD oscillations.

A series of absorption dips is observed in the LSA spectra of all samples described in Table 1, which have been grown on a degenerate GaAs substrate, at energies higher than that of 3D-FE (1.515 eV). This is illustrated in Fig. 1 for three samples: S111, S103, and S102, which normally differ only for the barrier thickness (40, 50 and 35 nm, respectively). These dips, with the only exception of the doublet structure observed for the first time at 5 K in sample S102, confirm the previous LSA measurements at 80 K, which have been interpreted in terms of transitions between states of excitons confined in the barrier region, C-1E [4,5]. The arrow in the figure points to the n = 2 state of C-1E in sample S111 [5].

As already discussed, in the perfectly abrupt heterostructure, particle confinement in the barriers can be obtained whenever the conduction band-edge conduction was dashed

$$L_b L_h \gg a^2 \quad (1)$$

where $L_b = (2m^* \Delta E / \hbar^2)^{1/2}$ is the particle wave vector in the barrier region, m^* is its effective mass, ΔE is the confinement energy defined as the difference between the confined and bulk particle energies, and n is an integer. The same result can be obtained by calculating the quantum-transmission coefficient for a particle incident onto a single quantum barrier [6,7], an approach formally equivalent to the determination of the optical transmission coefficient of a dielectric slab.

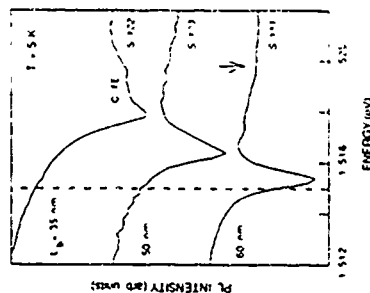


Fig. 1 LSA spectra at $T = 5$ K, for three In_{0.95}Ga_{0.05}As/GaAs multiple quantum-well structures, S111, S103 and S102. All samples have the same buffer thickness, 80 nm, and well width, 5 nm, but differ for barrier thickness L_b (40, 50 and 35 nm, respectively). The dashed line gives the position of the bulk-free exciton, 3D-FE, measured in samples with a thick buffer layer. The arrow indicates the position of the n = 2 state of the confined exciton, C-1E, in sample S111. The excitation wavelength is 801 nm.

In both cases, an inverse quadratic relationship between ΔE and L_b, where ΔE is the sum of confinement energies for an electron with mass m_e^* and a heavy hole with mass m_{hh}^* , can be derived,

$$\Delta E = \frac{\hbar^2 \pi^2}{2L_b^2} \left(\frac{1}{m_e^*} + \frac{1}{m_{hh}^*} \right) = \frac{\hbar^2 \pi^2}{2L_b^2} \frac{1}{m^*} \quad (2)$$

shown as a dashed line in Fig. 2, in excellent agreement with the experimental results. This is shown in the figure, where the values of the confinement energy, ΔE , as determined from the LSA, PL, and PLE spectra taken at different temperatures and averaged over several samples with the same quantum structure, have been reported. The theoretical line has been drawn considering a separate confinement of electrons and heavy holes in a GaAs barrier [8]. The good agreement between experiment and theory, as far as the slope is concerned, indicates that the confined exciton is formed by the Coulomb interaction among separately confined free carriers. Confinement of the exciton as a whole would imply the use of the exciton center-of-mass mass ($m_e^* + m_{hh}^*$) [9], thus resulting in much smaller confinement energies than those observed experimentally. On the other hand, the lack of agreement for what concerns the absolute values stresses the important role of deviations from ideality (real potential profiles, changes in the Coulomb interaction with barrier thickness, interaction between barriers, etc.)

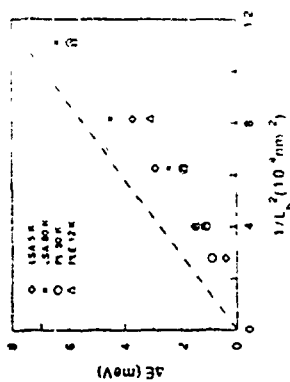


Fig. 2 Values of the experimental confinement energy ΔE , as determined at different temperatures by different photoluminescence techniques, together with the values evaluated from Eq. (2) (dashed line), vs the reciprocal L_b squared

In particular, the importance of the wavefunction overlap between electron states located at different barriers is shown in Fig. 3. In this figure, the PLE spectrum of sample S102 is compared with the absorption coefficient α of the GaAs buffer layer and barriers, extracted from the LSA spectrum in Fig. 1 for the same sample. In order to get the \hbar_0 baseline which appears in Lambert's law ($\alpha d = \ln(I_0/I)$), where d is the total GaAs epilayer thickness, we adopted an approach already successfully used in a previous case [10]: the PL level has been linearly extrapolated assuming $\alpha = 0$ at the energy of 1.513 eV, where the nominally undoped epilayers are virtually transparent, and assuming $\alpha = 1 \times 10^4 \text{ cm}^{-1}$ at the energy of 1.525 eV, i.e., above the excitation line, a value well established in the literature [11]. The close agreement between the lineshape obtained by the two different experimental techniques rules out the effect of artifacts

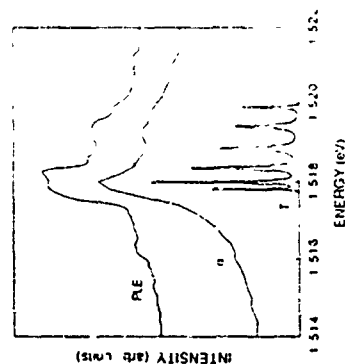


Fig. 3 Comparison of the PLE spectrum taken in sample S102 at 12 K with the absorption coefficient α estimated from the LSA spectrum of the same sample (see text). The theoretical estimate of the electron transmission coefficient in a similar six barrier structure is also shown

The experimental curves have been then convoluted with the transmission coefficient calculated for an electron in a structure like S102, where the termination at the surface has been simulated by a step 50 meV high and 5 nm wide. The theoretical curve, which has to be convoluted with the obtained for the heavy holes (confined a few tens of a meV), agrees almost perfectly with the experimental ones with respect to both its absolute energy and basic lineshape. It is worth noting that the doublet-like lineshape is dictated by the presence of a barrier at the surface (without it, all the individual split resonances would have a transmittance equal to one). Therefore, the above agreement has not to be overemphasized: the simulation of the surface being quite crude and needing further work. However, it already appears that the main features of the experimental lineshape can be successfully accounted for by the plain transmission model, despite the exclusion of hole contributions and Coulomb interaction [12]. In particular, the peculiar square-wave like lineshape with the abrupt rise in PL observed in the highly resolved PLE spectrum of sample S102 shown in Fig. 3, is characteristic of interacting resonance levels.

The above conclusions are further substantiated by the analysis of the experimental values of the full width at half maximum (FWHM) determined from the LSA spectra at 5 K (open circles) and reported as a function of barrier width on a log-log scale in Fig. 4. The experimental FWHM increases for decreasing barrier thickness L_b as the inverse cube. This behavior is quite well reproduced, with respect to its slope, by the electron transmission model (crosses in the figure)

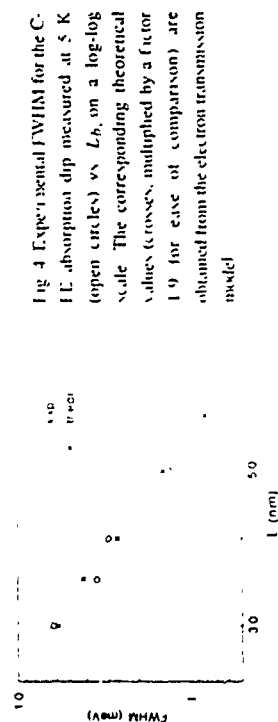


Fig. 4 Experimental FWHM for the CLE absorption dip measured at 5 K (open circles) vs L_b on a log-log scale. The corresponding theoretical values (crosses, multiplied by a factor 1.9 for ease of comparison) are obtained from the electron transmission model

The structure of the different samples has been taken explicitly into account while the surface has been simulated as done for the transmission spectrum shown in Fig. 3 (sample S102). For what concerns the absolute values, those extracted from the theoretical model have been multiplied by a factor 1.9, for ease of comparison (convolution with the hole band has not been considered, as well as other broadening factors).

Electrons confined in the quantum barriers also rise to transitions different from those responsible of the CLE line. In Fig. 5 we report the PLE spectra, below the GaAs gap, of

samples S52, S53, and S54. These samples have all the same well width (35 nm), but different barrier thickness, 40, 20, and 10 nm, respectively. In the spectrum of sample S52, a signal is observed with a threshold at 1.198 eV, shifted to higher energy in sample S53, and missing in sample S54. This feature is the only one in the below GaAs gap PLE spectra of samples S52 and S53, which shifts in the opposite direction as $1/\hbar\omega$ the transition from the $n=1$ electron state to the $n=1$ heavy hole state in the well. Moreover, it is not observed in samples with narrower barriers, such as S54 and S55 (the latter not shown in the figure).

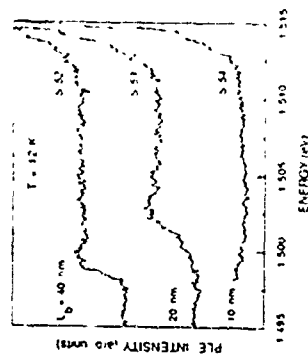


Fig. 5 Step-like features in the energy region below the GaAs gap of the 12-K-PLC spectra for samples S52, S53, and S54. All samples have the same well-width, 35 nm, but different barrier thickness, 40, 20, and 10 nm, respectively.

We believe that this transition involves an electron confined in the quantum barrier and a hole confined in the adjacent quantum well, i.e., the latter called (\bar{c}, h_h) . The step-like line shape of the PLE signal suggests that the two-dimensional continuum of the hole density of state is involved in the transition, most likely the heavy hole from a first qualitative analysis. In samples S54 and S55, this transition is not observed because it would take place at energies resonant with the buffer/barrier GaAs transition energies, and be too weak to be distinguished. The shift of the transition to higher energy, for a narrowing barrier width, can be interpreted in terms of an increased confinement energy for the electron, as outlined by comparison with the CLE shift corrected for the shift of the ground-state energy of the QW. For more quantitative results, one would need to know with adequate precision the In concentration, which is slightly different in the two samples and causes the above mentioned difference in the QW ground state emission. Therefore, the band offsets can be in principle derived from the comparison of (\bar{c}, h_h) with ground state transitions in samples grown with large In concentrations measurable by PL.

In conclusion, luminescence self-absorption, plan photoluminescence and photoluminescence excitation spectroscopies appear to be suitable techniques to study detailed aspects of excitation confinement in the GaAs barriers of InGaAs/GaAs multiple quantum well. A plain quantum

mechanical model, where the interaction between different barriers has been taken into account is able to predict the line shape of the experimental spectra as well as its dependence on barrier thickness. Finally, a transition between a hole state in the well and an electron state in the barrier has been observed, which can be used for estimating band offsets.

It is a pleasure to acknowledge useful and stimulating discussions with C. Presilla. This work has been partially supported by Ministero dell'Università e della Ricerca, and by Progetti Finalizzati "MADESS" and "Materie Speciali", both of CNR, and by the Norwegian Research Council. The work at Fondazione Igo Boncompagni has been carried out in the frame of the agreement between IUB and the Italian P.I. Administration.

- 1 M. Zoller, J. Breuer, G. Feen, J. Salzman, L. Cohen, and L. Pfeiffer, *Appl. Phys. Lett.* **61**, 949 (1992).
- 2 F. Capasso, C. Sirtori, J. East, D. T. Sivo, S. N. G. Chu, and A. Cho, *Nature* **358**, 565 (1992).
- 3 F. C. Zhang, N. Dai, H. Luo, N. Samarth, M. Dobrowolska, J. K. Furdyna, and L. R. Ram Mohan, *Phys. Rev. Lett.* **68**, 3220 (1992); H. Luo, N. Dai, F. C. Zhang, N. Samarth, M. Dobrowolska, J. K. Furdyna, C. Parks, and A. K. Ramdas, *ibid.* **70**, 1307 (1993).
- 4 F. Martelli, M. Capizzi, A. Trova, A. Polimeni, F. Sarto, M. R. Bruni, and M. G. Simeone, *Phys. Rev. B* **48**, 15 July (1993).
- 5 F. Martelli, M. Capizzi, A. Trova, A. Polimeni, F. Sarto, M. R. Bruni, and M. G. Simeone, *SPIE Proc.* **1985**, *Physical Concepts and Materials for Novel Optoelectronic Device Applications II - part II* in the press.
- 6 G. Bastard, *Wave Mechanics Applied to Semiconductor Heterostructures*, p. 8ff, Les Editions de Physique, Les Ulis (1988).
- 7 See, for example, D. Bohm, *Quantum Theory*, p. 568ff, Prentice Hall Inc., Englewood Cliffs, N.J. (1964).
- 8 The electron mass has been taken equal to $0.067 m_0$, the heavy hole mass to $0.62 m_0$ (S. Adachi, *J. Appl. Phys.* **53**, 8775 (1982)).
- 9 J. C. Kasano, Y. Segawa, M. Akita, Y. Aoyagi, and S. Namba, *Proc. of the 20th International Conference on the Physics of Semiconductors*, edited by I. M. Anastasakis and J. M. J. P. Jorj, World Scientific, Singapore, (1992), p. 1935.
- 10 F. Sarto, M. Capizzi, and A. Trova, *Semicond. Sci. Technol.* **8**, 1231 (1993).
- 11 J. M. Dell, M. J. Joyce, B. I. Usher, G. W. Yoffe, and P. C. Kenney, *Phys. Rev. B* **42**, 9496 (1990); D. D. Sell, *ibid.*, **B6**, 3750 (1972).
- 12 It may be worth noting that, for increasing temperature, the doublet line shape gradually evolves into the single broad dip observed in the ILS spectrum at 80 K (see Refs. 4 and 5), the narrower low energy component of the doublet weakening down to zero. No simple explanation of this behavior has been found.

MoP20

Structural and Optical Properties of $\text{In}_{0.5}\text{Ga}_{0.5}\text{As}/\text{GaAs}$ Multi-Quantum Wells Grown on Si(111)B Oriented GaAs Substrates

T. A. Fisher, R. A. Hogg, A. R. K. Vaidyan, D. M. Whitaker, M. S. Skolnick and D. J. Mowbray
Institute of Physics, University of Sheffield, Sheffield S10 7RH, UK
 J. P. R. Day, J. L. Sanchez-Romero, J. J. Woodhead, G. Hill, M. A. Fite and P. N. Robinson
Institute of Physics, University of Sheffield, Sheffield S10 7RH, UK

An optical study of a series of high quality $\text{In}_{0.5}\text{Ga}_{0.5}\text{As}/\text{GaAs}$ multi-quantum wells is reported. Well defined Δ_{AV} transitions (E1H12, E1H13 and E1H14) are observed with comparable strength to the Δ_{AV} transition, as a result of the asymmetric well profile induced by the piezo-electric field. In PLE the onset of the E1H11 continuum is clearly seen, allowing the detection of an exciton binding energy of 9 meV. Applying a bias to oppose the PZ field reduces the field in the well, which decreases the quantum confined Stark shift and weakens the Δ_{AV} transition. At high bias corresponding to flat band in the well, strong lifetime broadening is observed. Good agreement between theory and experiment is found with the use of a value for the PZ constant $\sim 70\%$ smaller than the commonly accepted value.

There has been considerable recent interest in the optical and electronic properties of strained layer quantum wells (QWs) structures grown in the (111) polar direction [1-7]. Due to the lack of inversion symmetry in the zinc-blende structure strain in the (111) direction produces a significant piezo-electric (PZ) field in the wells ($\sim 2 \times 10^6$ V/cm in $\text{In}_{0.5}\text{Ga}_{0.5}\text{As}/\text{GaAs}$ QWs) [1]. As a result, a strong quantum confined Stark effect (QCSE) is experienced in these structures without an external field [2]. This has been demonstrated both by the application of an opposing bias producing a large blue-shift of the transition energies [3-5], and by non-linear optical behaviour when photo-generated carriers screen the internal field [4,5].

In this paper we present an experimental and theoretical investigation of the optical properties of a series of high quality samples in which a number of $\text{PZ In}_{0.5}\text{Ga}_{0.5}\text{As}/\text{GaAs}$ multi-QWs (MQWs) are embedded in the intrinsic region of a p-n structure. Both photoluminescence excitation (PLE) and photoluminescence (PL) spectroscopies are used to measure the low temperature ($T < 4\text{K}$) absorption characteristics as a function of applied bias. Up to four prominent optical transitions are observed in the spectra, including Δ_{AV} lines [6] of comparable strength to the Δ_{AV} transition. In the highest quality PLE spectra of the series both the exciton transitions and the onset of the associated continuum transitions are observed allowing an exciton binding energy of 9.2 meV for E1H11 to be deduced. As the applied bias opposing the PZ field is increased, the QCSE is reduced, weakening the Δ_{AV} transition, until only E1H11 remains strong when the well profile is flat [2,7]. However, the field in the barriers is still large, leading to significant lifetime broadening of the exciton peak. Solutions to Schrödinger's equation support our interpretation of the results and show that the growth parameters are close to their nominal values. However, the fits suggest a value for the PZ constant ϵ_{12} (0.997 \pm 0.014 C/m²) considerably smaller than previously determined [8].

The samples were fabricated by molecular beam epitaxy and grown on (111)B semi-insulating GaAs substrates oriented 2 degrees towards (001). The layers in order of growth consist of 2.5 μm of GaAs (deposition), an intrinsic region in which the $\text{In}_{0.5}\text{Ga}_{0.5}\text{As}/\text{GaAs}$ MQWs of nominal width 100Å are incorporated centrally in GaAs, and 0.5 μm p⁺ GaAs (deposition). The number of QWs in a structure ranged from 1 to 25 [9-11]. In this paper we concentrate on two structures: sample M25 has 25 QWs (~ 0.13), with barrier widths of 150Å in an intrinsic region of width 610Å and sample M5 has 5 QWs (~ 0.13) with barrier widths of 900Å and an intrinsic region 620Å wide. Transmission electron microscopy (TEM) measurements indicate well widths close to 100Å with variations of $\pm 10\%$ for different structures in the series. The samples were processed into 400 μm diameter annular diodes with 200 μm optical access.

Fig. 1(a) shows PLE (filled) and PL (open) spectra obtained from the unprocessed sample M25. The samples are of high quality, comparable to the best (100) structures [11]. This is indicated by the narrow PL and lowest energy PLE linewidths of 3.5 and 3.0 meV respectively, and by the negligible Stokes shift between the PL and the lowest energy PLE peaks. The PLE spectra from the processed sample

M5 is shown in Fig. 2(a) at an applied bias of $V_{\text{A}} = -2\text{V}$. In general for the series, the PLE spectra show linewidths broader than in the PLE spectra (5 meV for lowest energy transition in PC of sample M5 in Fig. 2(a)). For example, in a 17 meV structure (~ 0.13) the lowest energy transition in PC of sample M5 is 6.5 meV in PC at low bias and 3 meV in PLE [9]. In PLE at the excitation energy is varied only one recombinational energy within the inhomogeneous linewidth is being detected. Therefore it is plausible that linewidth narrowing occurs in PLE due to the selective nature of the PL detection process. On the other hand, for PC the measured current is due to photo-generated carriers being swept out of the wells, so that the observed PC linewidth will generally be an average over all inter and intra-well fluctuations in width, and hence will have broader lines than for PLE. The series of samples all show PLE and PC spectra of similar quality to sample M25 and M5. These are discussed in more detail in Ref. [9] at low temperature and at room temperature in Ref. [10]. The measurements were taken using 100 mW/cm² of radiation, but varying the power from 10 mW/cm² to ~ 5 W/cm² does not affect the observed spectra, showing that photo-generated carrier screening effects are negligible.

Four prominent excitonic transitions are observed in the PLE of Fig. 1. The identifications are confirmed by the solutions of Schrödinger's equation (discussed in detail further on). The lowest energy transition (E1H11) involves absorption between the first heavy-hole state (HH1) and the first electron state (E1). The transitions to higher energy are E1H12, E1H13 and E1H14. A similar PC spectrum is observed for sample M5 at $V_{\text{A}} = -2\text{V}$ (Fig. 2(a)). The calculated transition energies (shown by arrows) are in good agreement with experiment for all of the series, the strain is expected to cause the light hole transitions to become Type II. Therefore they will be upshifted by ~ 20 meV and are expected to be weak [7,11] and as a result do not appear in the PLE of Fig. 1 or PC of Fig. 2(a). In Fig. 1(a) the Δ_{AV} transition (E1H12, E1H13 and E1H14) are of comparable strength to the allowed transition E1H11. This arises from the strong internal PZ field [1,2] which removes the usual selection rules in a flat well. The Δ_{AV} transitions are prominent in all of the processed structures measured near $V_{\text{A}} = 0\text{V}$ [9], as shown in the PC spectra of sample M5 at $V_{\text{A}} = -2\text{V}$ (Fig. 2(a)).

In addition to the prominent E1H11 and E1H12 excitonic transition observed in the PLE of Fig. 1(a) for sample M25 at $V_{\text{A}} = 0\text{V}$ and higher energy excitonic transitions broadened into the continuum edge. The absorption onset is composed of 25 and higher energy excitonic transitions broadened into the continuum edge. The E1H11 exciton energy is deduced to be 92.1 meV from Fig. 1 by taking the energy difference between the E1H11 exciton peak and the continuum onset marked by the downward pointing arrow. This value is very close to that found by Moore et al. [12] for a (100) $\text{In}_{0.5}\text{Ga}_{0.5}\text{As}/\text{GaAs}$ 40Å QW. This agreement is somewhat surprising considering the high electric field in the present structures and the narrower QW in the work of Moore et al. [12].

PC spectra as a function of applied bias V_{A} are shown in Fig. 2 for sample M25. A strong increase in the energy of the excitonic transitions of 16 meV is seen as the bias is increased from $V_{\text{A}} = -2\text{V}$ to $V_{\text{A}} = 0\text{V}$. This is also shown in the plot of the PC transition energies (filled circles) against bias in Fig. 3. As the field in the well is reduced the QCSE [15,16] is reduced causing the observed blue shift. The turning point in the graph corresponding to flat band in the well occurs at $V_{\text{A}} = -8\text{V}$. At low bias, $V_{\text{A}} = -2\text{V}$ (Fig. 2(a)) the Δ_{AV} transitions E1H12 and E1H13 are of similar strength to the Δ_{AV} transition E1H11 [6], increasing the reverse bias leads to a clearly observed reduction in the strength of Δ_{AV} transitions E1H12 and E1H13 as the field in the well is reduced. At $V_{\text{A}} = -8\text{V}$ E1H12 is not observed and E1H13 is very weak as expected for flat band in the well. A further trend observed with increasing bias above $V_{\text{A}} = -8\text{V}$ is for all excitonic transitions to undergo a strong broadening with only very broad features apparent at $V_{\text{A}} = 0\text{V}$ (Fig. 2(b)).

In order to interpret the experimental results in more detail the transition energies and oscillator strengths have been calculated as a function of V_{A} using numerical solutions to Schrödinger's equation. Since there is a significant probability of tunnelling out of the well especially at high reverse biases the rates are treated as resonances rather than true bound states. In the calculations standard interpolated values of the elastic parameters and deformation potentials [8] were used to calculate the effects of the strain on the band structure, and to calculate the PZ field [16]. The InGaAs electron mass was taken to be $0.07m_0$ [17] and the heavy hole mass along (111) to be $m_{\text{hh}} = 0.1m_0$, $m_{\text{lh}} = 0.7m_0$ [13]. This gives a good fit to the spectra of the observed heavy hole transitions.

Fig. 4 shows a typical potential profile for one of the wells in sample M5, calculated at $V_{\text{A}} = -2\text{V}$ along with carrier levels and associated wavefunctions of the first few states. At this bias the heavy hole states E1H12 and E1H13 are effectively under for HHs in the lower hole states. As a consequence at low bias the confinement potential is effectively under for HHs in the lower hole states. As a consequence at low bias

the energy separation of E11111 and E11112 is greater than that of E11112 and E11113, while at $V_g = -4$ V the spacing is reversed (Fig. 3).

Three fits to the experimental transition energies (circles) as a function of V_g for sample M5 are shown in Fig. 3, using various values of the PZ constant, ϵ_{12} , well width and indium concentration. The dashed line uses the standard value of $\epsilon_{12} = 0.143$ C/m² [14], linearly interpolated for the alloy, with nominal values of well width (100 Å) and indium concentration ($x = 0.15$), giving a piezoelectric field, $E_p = 2275$ V/cm [3]. The agreement with experiment is very poor. In order to improve the fit, ϵ_{12} and x were varied using this well width; reducing ϵ_{12} moves the curves towards zero bias, while reducing x shifts the transition energies upwards. The value of x is determined by fitting in the E11111 energy (1.410 eV) around $V_g = -4$ V, where the bottom of the well is flat and the transition energy is relatively insensitive to the other parameters [18]. An optimum fit, shown by the long dashes, is obtained for $\epsilon_{12} = 0.088$ C/m² and $x = 0.145$ ($E_p = 140$ kV/cm). Although this gives good agreement for E11111, the energies of the higher transitions are still well below the experimental values. The best fit (solid line), which agrees very well with experiment, was obtained by reducing the well width to 90 Å and using $\epsilon_{12} = 0.097$ C/m² with $x = 0.15$ ($E_p = 155$ kV/cm). The error in the ϵ_{12} determination is estimated to be $\pm 10\%$, most of the uncertainty arising from the precision with which the flat band voltage can be located in Fig. 3.

The values of ϵ_{12} used in the better fits are much smaller than the standard value of 0.143 C/m². The lower values of ϵ_{12} are necessary in order to make the bias which gives flat wells agree with the experimentally observed maximum in the transition energies. However, a similar result would be obtained if the intrinsic region were narrower than its nominal width of 6250 Å. Although capacitance-voltage measurements suggest that this is not the case, there is sufficient uncertainty to prevent the fits being a definitive determination of ϵ_{12} [19]. Very similar variations of transition energy against bias are observed for other samples in the series, except for a shift along the voltage axis. This shift can be well explained using the same values of ϵ_{12} as for the 5 well sample M5 and taking into account the larger number of wells [9, 10].

The calculated lifetime broadening only becomes significant in comparison with inhomogeneous broadening at biases beyond about $V_g = -6$ V where the barrier fields are high, but the well profile is close to flat band (see Fig. 3). At $V_g = -6$ V (Fig. 2(f)), where features can still be seen, the calculated broadening is 4.5 meV. The experimental linewidth changes from 6 meV at $V_g = -2$ V to 16 meV at $V_g = -6$ V, an increase of 10 meV. This is considered as good agreement, since the calculations are very sensitive to the input parameters. Increases in linewidth due to field variations in the structure at high V_g are not a likely explanation for the results of Fig. 2(f) since near $V_g = -8$ V the transition energy does not vary greatly with bias (Fig. 3). At $V_g = -8$ V, for sample M5, the calculations predict that, because the bottom of the well is flat, E11112 and E11113 are very weak and E11111 has only 3% of the strength of E11111, in agreement with the spectra of Fig. 2(c). As the reverse bias is reduced and the field in the well becomes larger, the zero transitions are predicted to become stronger, until at $V_g = -2$ V E11112 and E11113 are of comparable strength to E11111, again in good qualitative agreement with the spectra of Fig. 2(f).

In conclusion, the variation of transition energies and oscillator strengths with applied bias has been investigated in a series of high quality InGaAs/AlGaAs MQWs. Good agreement between theory and experiment is found, but only by using a value for the piezoelectric constant $\sim 10\%$ smaller than the commonly accepted value. Strong lifetime broadening is observed close to flat band conditions in the well. This result contrasts strongly with that in non-piezoelectric structures where the fields in the wells and barriers are equal, and lifetime broadening is observed at high fields in the wells. An excitation binding energy of 92 meV is deduced for E11111.

Acknowledgement - We would like to thank G. Duggan for helpful discussions. This work was supported by SERC (grant number GR0120425).

References

1. Permanent address: Departamento de Ingeniería Electrónica, Universidad Politécnica de Madrid, Madrid, Spain.
2. D. L. Smith, *Solid State Commun.* **57**, 919 (1986).
3. C. Mailhot and D. L. Smith, *J. Vac. Sci. & Technol.* **A7**, 609 (1989).
4. E. A. Caridi, T. Y. Chang, K. V. Goetsen and L. F. Esman, *Appl. Phys. Lett.* **56**, 659 (1990).
5. I. Sela, D. E. Watkins, B. K. Laurich, D. L. Smith, S. Subbana and H. Kriemer, *Appl. Phys. Lett.* **58**, 684 (1991).
6. K. Nishi and T. Anan, *J. Appl. Phys.* **70**, 4004 (1991).
7. G. Duggan, K. J. Moore, A. Raulkina, G. Th. Jazayria and K. Woodbridge, *Phys. Rev. B* **43**, 4604 (1991).
8. B. K. Laurich, K. Elovsky, C. G. Fonstad, J. B. Davis, C. Mailhot and D. L. Smith, *Phys. Rev. Lett.* **62**, 640 (1989).
9. R. A. Hegg, T. A. Fisher, A. R. K. Wilcox, D. M. Whitaker, M. S. Sholnick, D. J. Minnery, J. P. K. David, A. S. Palla, G. J. Rees, R. Gies, J. Woodhead, G. Hill, M. A. Pate and P. N. Robson, submitted to *Phys. Rev. (Rapid Commun.)*.
10. A. S. Palla, J. L. Sanchez-Rojas, J. Woodhead, R. Gies, J. P. R. David, G. J. Rees, G. Hill, M. A. Pate, P. N. Robson, R. A. Hegg, T. A. Fisher, A. R. K. Wilcox, D. M. Whitaker, M. S. Sholnick and D. J. Minnery, *Appl. Phys. Lett.* **1993**.
11. M. K. Saker, D. M. Whitaker, M. S. Sholnick, M. T. Emeny, C. R. Whitcombe, *Phys. Rev. B* **43**, 4045 (1991).
12. K. J. Moore, G. Duggan, K. Woodbridge, C. Roberts, *Phys. Rev. B* **41**, 1090 (1990).
13. L. W. Nohmi, R. Eppenga, G. W. H. Hoff, P. Dawson, C. T. Faxon and K. J. Moore, *Phys. Rev. B* **41**, 4314 (1990).
14. D. A. B. Miller, J. S. Weiner and D. S. Chikula, *IEEE J. Quantum Electron.* **QE-22**, 1816 (1986).
15. W. Chen and T. G. Andersson, *Semicond. Sci. Technol.* **7**, 878 (1992).
16. E. Anastasakis, *Phys. Rev. B* **46**, 4712 (1992).
17. R. Peyle and S. K. Spitz, *Phys. Rev. B* **41**, 3431 (1990).
18. For example a 10 Å change in well width, the maximum variation from the TEM measurement, would lead to a 5 meV shift in the transition energy, a 1% change in x changes the transition energy by 9 meV.
19. The relatively low value of $E_p = 155$ kV/cm corresponding to $\epsilon_{12} = 0.097$ C/m² could also arise if the strain in the structures were relaxed by 30% (the reduction of E_p from 227 kV/cm to 155 kV/cm). However, such large strain relaxation would lead to a 40 meV shift of the E11111 transition energy, to 26 meV, leading to predicted energies for $x = 0.15$ in strong disagreement with experiment.

Figure Captions

Fig. 1 (a) PL (dotted line) and PLT (full line) spectra from sample M25 at $T = 4$ K. The spectra show $\Delta n = 0$ transitions E11112, E11111 and E11113 of comparable strength to E11111. At -9 meV to higher energy the associated continuum onsets for the E11111 and E11112 overtone transitions are clearly observed.

Fig. 2 PL as a function of applied bias for sample M5. With increasing reverse bias the strength of the $\Delta n = 0$ transitions decreases, until at flat band in the well, $V_g = -8$ V (c) only E11111 is strongly observed.

Fig. 3 Experimental transition energies (circles) as a function of applied bias for sample M5. The lines are theoretical fits using various sets of parameters (see text for details). The inset shows the band profile at $V_g = -8$ V, where the well is flat.

Fig. 4 Potential profile for one of the wells in sample M5 calculated at $V_g = -2$ V, along with energy levels and associated wavefunctions of the first few states.

MoP21

Optical Properties of AlP-GaP Short-Period Superlattices

A. Morita, T. Takano, J. Kikunaga, K. Han, H. Kikunaga
Imaging Science and Engineering Laboratory, Tokyo Institute of Technology,
4259 Nagatsuta, Midori-ku, Yokohama 227, Japan

J. Yoshino

Department of Physics, Tokyo Institute of Technology,
2-12-1, O-okayama, Meguro-ku, Tokyo 152, Japan

and T. Yasuda

Photodynamic Research Center, The Institute of Physical and Chemical Research
Naga-machi, Aobe-ku, Sendai 982, Japan

Abstract

We present several optical properties of $(\text{AlP})_n(\text{GaP})_n$ short-period superlattices grown by metalorganic vapor phase epitaxy (MOVPE), which include the low temperature photoluminescence of samples with a shorter period, low temperature photoluminescence lifetime, and refractive indexes of the superlattices at room temperature. The photoluminescence characteristic of the superlattice with $n=3$ has been clearly observed. The radiative lifetime of the excited carriers in the superlattices is fairly long against expectation. It has been found that the refractive indexes of $(\text{AlP})_n(\text{GaP})_n$ superlattices are similar to that of AlGaP alloys.

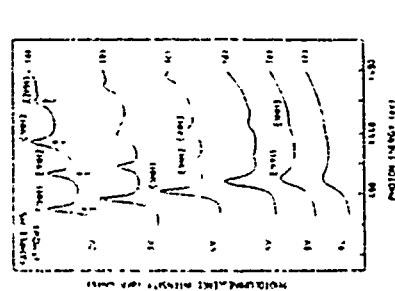


Fig. 1

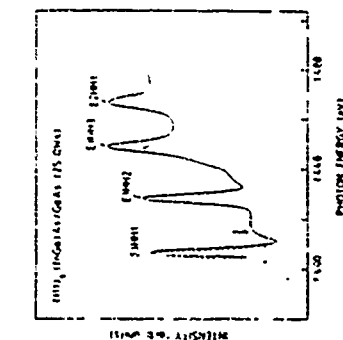


Fig. 2

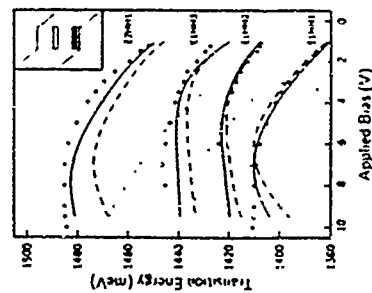


Fig. 3

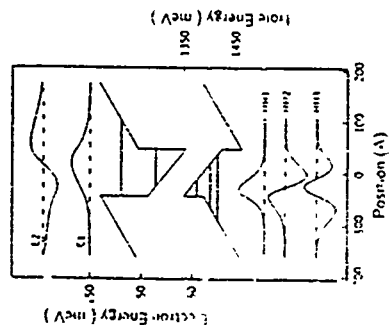


Fig. 4

Introduction

The AlP-GaP short-period superlattices composed of two indirect-gap semiconductors of AlP and GaP, with appropriate periods, are expected to have direct-gap due to the folding of the indirect conduction band minima at the X point to the center of the Brillouin zone (Γ), and the mixing of the electronic states of both materials [1]. We pay attention to this system for two reasons. One is that AlP and GaP can be nearly lattice-matched to each other with a small lattice mismatch of about 0.2%. The other is that the bandgap energy of the AlP-GaP superlattices corresponds with visible light in the red to green spectral region. Therefore, they are expected to offer potential for use in novel laser diodes operating in the yellow to green region.

The first optical study of $(\text{AlP})_n(\text{GaP})_n$ short-period superlattices has revealed blue shift and intensity enhancement of the characteristic photoluminescence with decreasing the number of sublayer, n [2]. More recent electrical and optical measurements have indicated that the band lineup of the AlP/GaP heterojunction is of the type II [3, 4], which is consistent with the photoluminescence peak shift, and that the observed photoluminescence is due to the electronic transition from the zone-folded conduction band at the Γ point to the valence band maximum [5, 6].

We have already observed the characteristic photoluminescence in the $(\text{AlP})_n(\text{GaP})_n$ superlattices with n ranging from 4 to 10, which were grown at 780 °C by metalorganic vapor phase epitaxy (MOVPE) [7]. One of our present concerns is with the characteristic photoluminescence to appear in the superlattices of much shorter periods. The other is with fundamental optical properties including radiative transition rate and refractive index, in conjunction with an application of this superlattice system for laser diodes.

In this paper we present the first observation of a dominant photoluminescence peak in a shorter-period superlattice of $(\text{AlP})_1(\text{GaP})_3$. Also, we show that the radiative lifetime of the excited carriers in this superlattice system is fairly long, against expectation, and that the

relative indexes of $(\text{AlP})_n(\text{GaP})_n$ superlattices with n ranging from 4 to 9 are similar to that of AlGaP alloys.

Photoluminescence of Shorter Period Superlattices

Growth of superlattice samples was carried out by MOVPE using the same growth system of the previous study [7]. The growth conditions were also the same as before except that the growth temperature was changed from the previous temperature of 780°C to 720°C. X-ray diffraction satellite lines were easily observed for the superlattices with $n=2, 3$ and 4 as shown in Fig. 1. It is noted that the satellite peak intensity for the sample of $n=3$ grown at 720°C was about 4 times higher than for the previous sample of the same n grown at a higher temperature of 780°C. Also noted is that the clear satellite diffraction was observable even for the sample of $n=2$, when the growth temperature was decreased to 720°C. These observations are similar to an improved abruptness at the AlP/GaP heterointerfaces of superlattices by reducing growth temperature, i. e., by suppressing a thermal interdiffusion of Al and Ga atoms within one or two monolayers adjacent to the AlP/GaP heterointerface during growth.

Low temperature photoluminescence spectra for three samples of different numbers of sublayer are shown in Fig. 2. Emission lines characteristic of the superlattices can be clearly seen for samples with $n=3$ and 4, in contrast with the previous case, where the spectrum for the sample with $n=3$ were similar to that for a typical AlGaP alloy sample [7]. This is also attributed to the improved abruptness at the AlP/GaP heterointerfaces of superlattices by reducing growth temperature.

The emission peak energy for the sample with $n=3$ is definitely determined from this spectrum, while one of the emission bands in the photoluminescence spectrum for a gas source molecular beam epitaxy grown sample was ascribed to the superlattice emission band by Azami *et al.* [5]. Our peak energy is different from theirs, and is located on the extrapolated line in the relation between photon energy and n .

Photoluminescence Lifetime

The samples used for the photoluminescence lifetime measurements were $(\text{AlP})_n(\text{GaP})_n$ superlattices ranging from 5 to 9 previously grown at 780°C, an $(\text{AlP})_3(\text{GaP})_3$ grown at 720°C, and a nitrogen-doped bulk GaP grown by liquid phase epitaxy. Samples were excited by 20-nsec pulses from a 318-nm KrF excimer laser at about 2 K. The time resolution of the measurement system was about 100 nsec for superlattice samples and about 10 nsec for a GaP-N sample. The luminescence decay for the superlattice samples with $n=3, 5, 6$ and 7 consisted of a single-exponential component, while that for $n=8$ and 9 double components. Figure 3 shows the decay time of photoluminescence peak intensity for different numbers of sublayer. The decay times ranging from 0.2 to 1.0 nsec are one or two orders of magnitude longer than that of GaP-N which is about 0.023 nsec at around 2.30 eV. These decay times for the superlattices are fairly long against expectation. Further studies are necessary for understanding the mechanism of luminescence decay and for fabricating superlattice samples of better quality in terms of periodicity and interface abruptness.

Refractive Index

The samples used for the refractive index measurements were those previously grown at 780°C. A 0.2- μm -thick GaP was grown on the n-type GaP nominally (100) oriented substrate, followed by an about 1.0- μm -thick $(\text{AlP})_4(\text{GaP})_4$ superlattice layer with $n=4$ to 9 or an about 1.5- μm -thick $\text{Al}_{0.5}\text{Ga}_{0.5}\text{P}$ alloy layer.

In the wavelength region where optical absorption in layers is negligibly small, a reflection oscillation appears in the spectrum due to the multiple internal-reflection interference effect. The conventional method of estimating the refractive index takes an advantage of this oscillation. That is, if layer thickness, d , is known from a separate experiment, the average refractive index, \bar{n} , is estimated from the wavelengths of two adjacent maxima or minima in the reflectance spectrum, λ and λ_2 ($\lambda_1 > \lambda_2$), by

$$2\bar{n}d = \left(\frac{1}{\lambda_1} - \frac{1}{\lambda_2} \right)^{-1} \quad (1)$$

Based on this method, Azami *et al.* estimated the refractive indexes of $(\text{AlP})_n(\text{GaP})_n$ superlattices ($n=2, 3, 4$), and concluded that the refractive index of superlattices is larger than that of alloys [6].

We have found that this method essentially involves a large error when applied to the layers which have refractive indexes with wavelength dispersion, as is the present case. We confirmed this by estimating the refractive index of an AlP layer on a GaP substrate. The refractive index evaluated from the oscillatory reflectance spectrum calculated using the reported wavelength-dependent refractive indexes of AlP and GaP [8], was about 20% larger than the refractive index of AlP which was initially used in the calculation of the reflectance spectrum. In the present study, therefore, we have used an alternative method reported by Heavens [9]. Suppose that a sample consists of a film with refractive index n_f and a substrate with refractive index n_s . On condition that either the reflection minima or maxima coincides with the reflectance of the substrate, the refractive index n_f is given by

$$n_f = \left(n_s \frac{1 + \sqrt{R}}{1 - \sqrt{R}} \right)^{1/2} \quad (2)$$

where R is reflectance maxima or minima of the reflectance spectrum depending on n_f is larger or smaller than n_s , respectively.

Figure 4 shows the reflectance spectrum of an $(\text{AlP})_3(\text{GaP})_3$ superlattice layer on the GaP substrate together with that of a GaP substrate itself. The reflectance of GaP substrate is accurate within 1% of the published value [8]. From the figure we find that the refractive index of the superlattice layer is smaller than that of GaP.

The refractive indexes of an $(\text{AlP})_3(\text{GaP})_3$ superlattice layer and an $\text{Al}_{0.5}\text{Ga}_{0.5}\text{P}$ alloy layer, obtained using eq. (2) and the reflectance minima, are shown in Fig. 5. Refractive indexes of superlattices did not depend on the superlattice period, locating between those of AlP and GaP, as is the case of AlGaP alloys. The results is surprising in view of the photoluminescence peak shift which depends largely on the superlattice period.

Summary

The low temperature photoluminescence characteristic of the superlattice with $n=3$ has been clearly observed by decreasing the growth temperature in MOVPE. It has been found that the radiative lifetime of the excited carriers in the superlattice is fairly long against expectation, and that the refractive indexes of $(\text{AlP})_n(\text{GaP})_n$ short period superlattices are similar to that of AlGaP alloys. These results should be taken into account for designing the laser diodes utilizing this superlattice system as an active layer.

One of authors (A. Murai) acknowledges support from the Japan Society for the Promotion of Science.

References

- [1] U. Grunzmann and K. Clausecker, *Appl. Phys.* 3, 9 (1974).
- [2] A. Morita, I. Ohno, A. Kanda, K. Arai, K. Tokudome, K. Hara, J. Yoshino and H. Kukimoto, *Japan. J. Appl. Phys.* 30, L1244 (1991).
- [3] A. Morita, H. Okagawa, K. Hara, J. Yoshino and H. Kukimoto, *Japan. J. Appl. Phys.* 31, L1161 (1992).
- [4] K. Adomi, N. Noto, A. Nakamura and T. Takenaka, *J. Crystal Growth* 124, 570 (1992).
- [5] K. Asami, H. Asahi, T. Watanabe, S. Gonda, H. Okumura and S. Yoshida, *Surf. Sci.* 267, 450 (1992).
- [6] K. Asami, H. Asahi, T. Watanabe, M. Enokida, S. Gonda and Sg. Fujita, *Appl. Phys. Lett.* 62, 81 (1993).
- [7] A. Morita, H. Okagawa, K. Hara, J. Yoshino and H. Kukimoto, *J. Crystal Growth* 124, 772 (1992).
- [8] T. Takagi, *Japan. J. Appl. Phys.* 21, L167 (1982).
- [9] O. S. Heavens, *Phys. Thin Films* 2, 193 (1964).

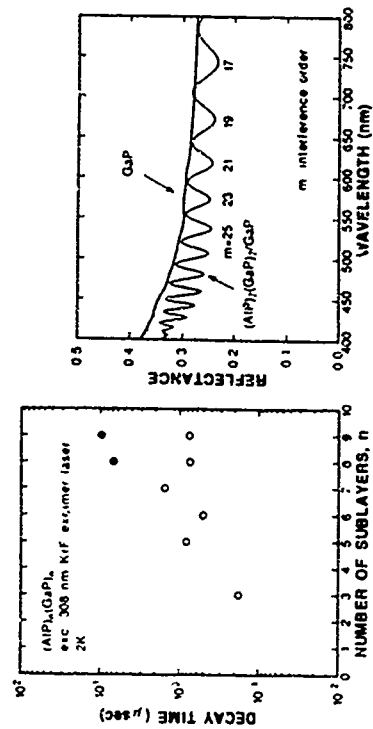


Fig. 3. Photoluminescence decay time at about 2 K for $(\text{AlP})_{1-x}(\text{GaP})_x$ superlattice samples.

Fig. 4. Reflectance spectra for an $(\text{AlP})_{1-x}(\text{GaP})_x$ superlattice sample and a GaP substrate at room temperature.

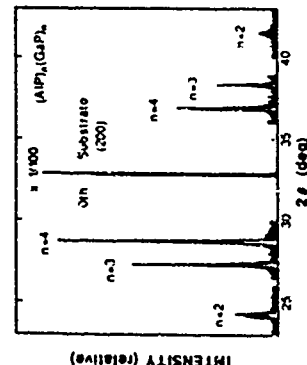


Fig. 1. X-ray diffraction satellite lines for $(\text{AlP})_{1-x}(\text{GaP})_x$ superlattice samples

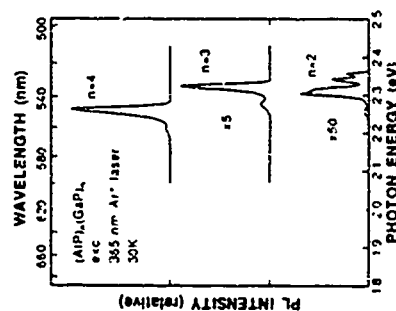


Fig. 2. Photoluminescence spectra at 30 K in $(\text{AlP})_{1-x}(\text{GaP})_x$ superlattice samples grown at 750°C. Excitation was made by an argon ion laser operating in the ultraviolet at about 350 nm.

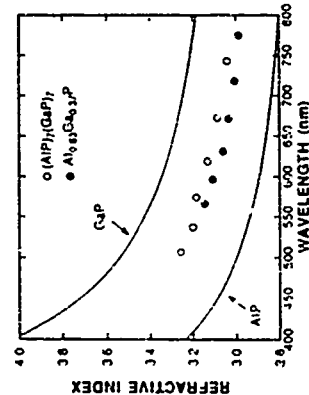


Fig. 5. Dispersion of the refractive indexes for an $(\text{AlP})_{1-x}(\text{GaP})_x$ superlattice sample and an $\text{Al}_{0.5}\text{Ga}_{0.5}\text{P}$ sample, which were estimated from the minima in reflectance spectra.

MOP22

InGaAs/InP quantum wells with periodic thickness variation

A.A. Demus¹, M.J.S.P. Brasil², J.A. Bium³, M.A. Colla⁴, R.A. Hamim⁵, I.W. Sialev⁶,
S.N.G. Chu⁷, L.R. Harriot⁸, M.D. Parash⁹, H. Temkin¹⁰

¹(Pq) - Telebras, Campinas, SP 13088-061, Brazil

²Instituto de Física, UNICAMP, Campinas, SP 13081-070, Brazil

³AT&T Bell Laboratories, Murray Hill, NJ 07971, USA

⁴Technical Engineering Dept., Colorado State University, Fort Collins, CO 80521, USA

We investigated the optical and structural properties of lattice-matched InGaAs/InP quantum wells grown by metalorganic molecular beam epitaxy. The growth conditions were chosen to provide a patterned InP buffer layer surface with elongated features aligned in the [011] direction. The morphology of the patterned surface was revealed by transmission electron and scanning force microscopy measurements. Low temperature photoluminescence results are correlated with the structural properties of the samples. The observation of multiple emission lines indicates the presence of elongated terraces with different thicknesses at the interface of the single quantum well. Information about the carrier dynamics between these elongated terraces is obtained from the photoluminescence temperature dependence.

3 - INTRODUCTION

The investigation of semiconductor heterostructure interfaces is of great interest because of its strong influence on the electro-optical properties of these systems. The understanding of the detailed characteristics of the interfaces is not only crucial for obtaining high quality semiconductor heterostructure devices, but it is the first step in use the interface control as a new tool to design special systems. In this work, we investigated a series of InGaAs quantum wells where the InP buffer layer was specially prepared to build-up periodic elongated features along the [011] direction [1]. This new growth technique may become a useful tool to obtain quantum wires eliminating intermediate ex-situ steps used in other methods [2, 3].

The observation of excitons confined in quantum wells is a powerful tool to investigate heterointerfaces and it can easily be performed by using photoluminescence spectroscopy [P1]. Since the effective probe of this technique is the excitation, which diameter is of the order of 100 Å, it gives information about features at the interface with sizes comparable to this value.

II - EXPERIMENT

The samples were grown by Metalorganic Molecular Beam Epitaxy. They consist of



Fig 1 - Transmission electron micrograph ([011] cross section) of InGaAs quantum well (dark) on top of InP film with elongated features along the [011] direction

Investigations on the InP growth [1] showed that the roughness increases and the surface evolves from a smooth two-dimensional growth to a pattern with features along the [011] direction. These structures can be observed on the Transmission Electron Microscopy picture presented in Fig. 1 for a single InGaAs/InP QW. This effect was attributed to an anisotropic diffusion of the In species along the crystallographic directions. For the present work, different morphologies of the InP surface were obtained varying the PII, flux and the thickness of the InP buffer layer, but maintaining both the temperature (510 °C) and the growth rate constants. The InGaAs layers were grown on top of these specially prepared surfaces and follow the InP profile. These parameters give some control on the basic characteristics of the InP surface, the height and period of the elongated terraces. Microroughnesses are also present on top of this anisotropic surface and they also depend on the growth parameters.

The PL measurements were performed using the 5145 Å line of an Ar⁺ laser as the excitation source and analyzed by a 0.5 m single spectrometer coupled to a nitrogen cooled Ge photodetector. The measurements were carried out at the temperature range of 2 to 300 K using a liquid helium Janis Supravillemp cryostat.

III. RESULTS AND DISCUSSION

To analyze the PL spectra, we have to compare its effective probe, the excitation, with the roughness scale. When the roughness scale is small compared to probe dimensions, the excitation experiences a fast varying thickness and a single PL broad emission is expected. When the roughness scale is relatively large excitons from different regions probe different thicknesses giving rise to multiple PL lines. A realistic interface is probably a combination of roughnesses with different frequencies.

Figure 2 shows the PL spectra at 2 K from four InGaAs/InP single QW samples

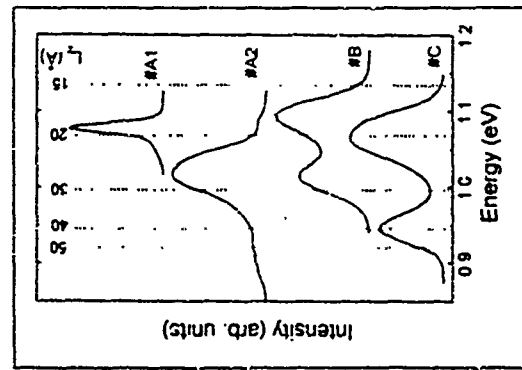


Fig 2 - 2K PL spectra from four InGaAs/InP single quantum well samples grown on InP surfaces with different morphologies

corresponding to different InP surface morphologies. Sample #A1 corresponds to a QW with a very smooth InP surface grown on (100) InP substrate at conditions in which the elongated terraces have not been developed yet. This result is in strong contrast with sample #A2 that was grown simultaneously with sample #A1 but with a slightly misoriented InP substrate. As it can be seen from this figure, the roughness development is very sensitive to the substrate orientation. Scanning Force Microscopy (SFM) measurements show that in the case of sample #A2 the terraces already started building up but they are still quite flat. These results also show that the microroughness for sample #A2 is enhanced as compared to sample #A1. This is in agreement with the PL data that show a single narrow (FWHM=16 meV) line for sample #A1 and broad emission bands for sample #A2 (FWHM=65 meV).

Samples #B and #C were grown on (100) InP substrates with slightly different parameters. SFM measurements confirm the presence of elongated terraces along the [011] direction for both samples. These measurements give an estimation of the height (11-10 Å), the length (4000-12000 Å) and the distance between adjacent terraces (0-20000 Å). The two PL peaks observed for these samples are attributed to fundamental excitonic transitions in the QW from two regions with different thicknesses. The origin of these regions is related to the growth on the patterned InP buffer layer.

Figure 2 also presents the results of a three band envelope function calculation for the energy transitions in InGaAs/InP QWs with different thicknesses using a conduction band offset value of 0.45 (Fig. 4, 5). The high energy peaks correspond to quantum well thicknesses of the order of 15-20 Å that is close to the nominal value. The low energy bands of the doublet correspond however to relatively thicker QWs, of the order of 25-40 Å. This thickness variation is expected because of the inhomogeneous growth rates on the anisotropic InP surface.

Figure 3 shows the temperature evolution of the PL spectra from samples #B and #C. As the temperature increases, the intensity of the higher energy band of the doublet like spectra decreases faster than the lower energy one. At room temperature the higher band is

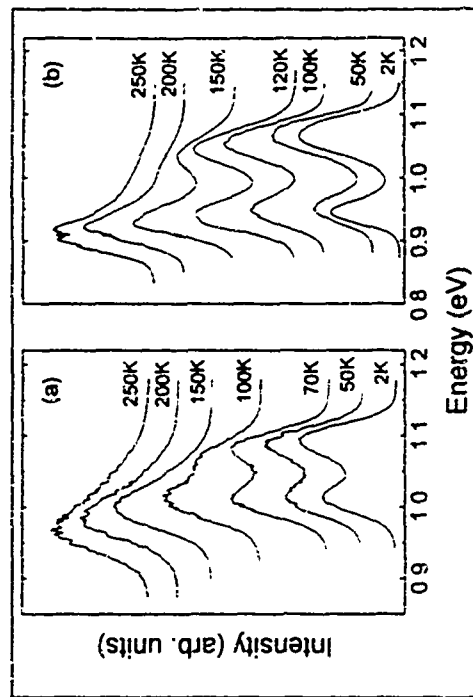


Fig 3 - PL spectra as a function of temperature from samples #B (part a) and #C (part b)

completely suppressed. The quenching of the high energy band occurs at different temperatures for these two samples. This is clearly observed at 100 K where the higher energy band from sample #B has almost disappeared, while the corresponding one for sample #C remains almost unchanged. Nevertheless the ratio intensity between the two bands at 2 K is very similar.

The total integrated PL emission intensity for samples #B and #C is almost constant up to 120 K and decreases exponentially for higher temperatures. This can be explained by the relative increase of competitive processes, mainly the thermal emission of the carriers out of the InGaAs well to the InP barriers followed by non-radiative recombination [6, 7].

As we discussed above, the PL band emissions, for samples #B and #C, originate from contiguous regions with different thicknesses and dimensions bigger than the excitation diameter. The PL intensity corresponding to each region should then reflect the relative area of each region and the carriers diffusion between these regions. The first parameter is a constant for each sample [8]. The second one is probably responsible for the variation of the intensity ratio between the PL bands as a function of the temperature. The exciton transfer from a region with a higher energy level to a lower one depends basically on the ratio between the excitonic diffusion constant and the dimensions of the regions, which is also a constant for each sample. The fact that the intensity ratio between the PL bands is constant for low temperatures and decreases exponentially above a given temperature suggests a

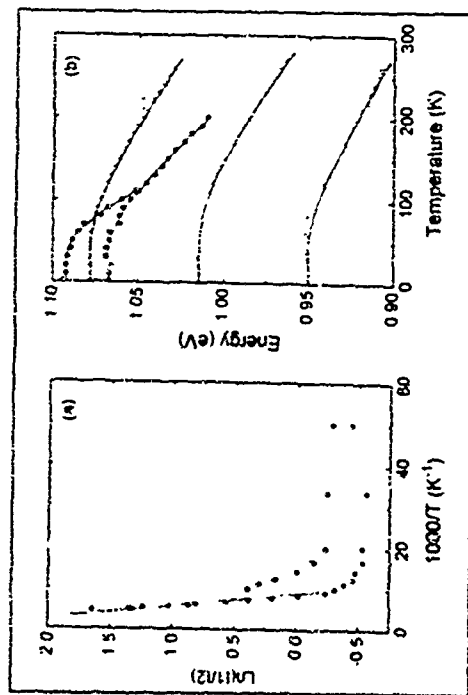


Fig. 4 - (a) Ratio between the intensity of the low over the high PL band for samples #B (●) and #C (○) versus the inverse of the temperature. (b) Peak energies for samples #A (▲), #B (●) and #C (○) and #C (■ and □) Open (full) symbols represent low (high) energy bands

mobility edge for the excitons. This edge has been observed by various authors and it was interpreted as a transition from localized to mobile excitons with relatively higher energy levels [9, 10]. This effect is attributed to microscopic statistical variations of the well width and the alloy composition that creates local fluctuations of the potential which localizes the exciton. However, it is difficult to quantitatively evaluate these effects. Experimentally, they result in an "effective activation energy" obtained from the dependence of the intensity ratio between the two PL bands for samples #B and #C as shown in Fig. 4(a). The energies obtained from linear square fittings on Fig. 4(a) are 3.5 meV for sample #C and 7 meV for sample #B. This "activation energy" should reflect the barrier height that the localized excitons have to overcome to become mobile excitons. We observe that this "activation energy" can assume relative high values and it is extremely sensitive to the sample parameters, making it difficult to correlate to the fundamental characteristics of the QW.

Finally, we present in Fig. 4(b) the variation of the PL peak energies as a function of the temperature for samples #A, #B and #C. Sample #A shows the behavior of a typical uniform QW, following the band gap energy of the well material. Similar energy dependence is presented by the low energy bands of samples #B and #C. In contrast, the high energy PL bands from these samples show a markedly different dependence with temperature. The

position of the high energy emission bands follows the band gap of InGaAs at low energies in the temperature range where the intensity ratio between the bands is almost constant. However, as the temperature is further increased, the peak of the high energy bands decrease in a much faster rate than the InGaAs band gap and become closer to the lower band. To understand this effect we have to take into account that the emission from each PL band does not originate from a single level, but from a set of levels due to the present roughness. The PL linewidth reflects an average occupation of these set of states. The "activation energy" for the transition localized-to-mobile experienced by the excitons should be relatively smaller for the higher energy levels. These excitons should then overcome the barrier to become mobile at relatively smaller temperatures, resulting in a PL peak shift to lower energies as the band intensity decreases.

IV - CONCLUSIONS

In conclusion, we have investigated InGaAs QWs grown by metalorganic molecular beam epitaxy on specially prepared InP surfaces with elongated terraces along the [011] direction. The build-up roughness results in periodic thicknesses of the InGaAs wells. The periodicity was observed by SFM measurements and reflects on doublets observed in the PL spectra at low temperatures. The PL experiments as a function of temperature give some insight on the dynamics of excitons in the regions created by long range roughness with a superimposed micro-roughness.

ACKNOWLEDGEMENTS: The authors gratefully acknowledge the financial assistance from CNPQ and FAPESP.

REFERENCES

1. M. A. Costa, R. A. Hamm, T. W. Siale, S. N. Chu, L. R. Harriot, M. B. Panish and H. Temkin, *Phys. Rev. Lett.*, in press.
2. K. Aoki, *J. Appl. Phys.*, 69, 69 (1990).
3. D. V. Lang, M. B. Panish, T. C. Capasso, J. Allian, R. A. Hamm, A. M. Sargent and W. F. Isang, *Appl. Phys. Lett.* 50, 736 (1987).
4. H. Kawanishi and H. Ikeda, *J. Appl. Phys.* 36, 27 (1991).
5. K. Fujiwara, K. Kanmori and N. Tsukada, *Phys. Rev. B* 40, 9698 (1989).
6. G. Bacher, J. Kovac, K. Streubel, H. Schweizer and F. Scholz, *Phys. Rev. B* 45, 1136 (1992).
7. X. Liu, S. Nilsson, I. Samuelson, W. Seifert and P. L. Souza, *Phys. Rev. B* 47, 2203 (1993).
8. J. Heyliger, L. Goldner and M. D. Sturge, *Phys. Rev. B* 30, 7146 (1984).
9. G. Delalande, C. Delalande, M. H. Meynadier, P. M. Fritink and M. Vroos, *Phys. Rev. B* 29, 7042 (1984).

V.L. Alferovich, A.S. Jaroshevich, H.E. Scheibler, and A.S. Terekhov
Institute of Semiconductor Physics, 630090 Novosibirsk, Russia

Photoreflectance (PR) technique, which in most cases is essentially a contactless form of electroreflectance, is based on the screening of built-in fields by photo-generated charged carriers created by the modulated illumination. One of the problems of the PR spectroscopy is that several regions of a sample may simultaneously contribute to PR, thus hindering the interpretation and quantitative analysis of the resulting spectra. In this paper we developed a technique for separation of contributions originating from different regions of a layered semiconductor structure. This technique explores differences in the temporal responses of the PR signal, which stem from differences in relaxation kinetics of screening of the built-in fields. As a result, the phase shifts of PR contributions with respect to the light pump are different. Therefore, proper selection of modulation frequency and of the phase angle of the synchronous detector allows us to suppress one of the contributions and to extract the other (or the superposition of the other contributions, if more than two interfaces contribute to a PR spectrum).

Using the proposed technique of phase suppression, the Fourier analysis of Franz-Keldysh oscillation, and the precise step-by-step etching of GaAs, we studied the built-in fields in the following MBE-grown structures: (1) GaAs with a single delta-doped layer, (111) delta-doped n-i-p-i superlattices with a "sawtooth" potential; (111) GaAs SIN-structure, which contained 100-nm undoped GaAs layer separated from the n⁺-substrate by a 1-μm n⁺-GaAs buffer layer. Along with the well-known above-bandgap Franz-Keldysh oscillations originating from the regions with homogeneous built-in field, we observed sharp near-bandgap features in the PR spectra of delta-doped structures. It was shown that these features stem from the built-in fields of buffer layers and are not associated with quantum-confined optical transitions. Built-in electric field at the interface of high-doped n⁺-GaAs buffer layer with n⁺-substrate was observed in a GaAs SIN-structure. The interface band diagram was determined, with the Fermi level being fixed within the range of 0.1 - 0.2 eV below the bottom of the conduction band. The observed Fermi level fixing is due to the interface defects, which arise at the initial stages of the molecular beam epitaxy. Thus, the development of photoreflectance spectroscopy performed in the present work enabled us to probe the built-in electric fields in layered semiconductor structures and, therefore, to evaluate the concentration of charged defects at surfaces and interfaces.

U. Ekenberg
Department of Theoretical Physics
Royal Institute of Technology, S-10044 Stockholm, Sweden

D. Richards
Cavendish Laboratory, Madingley Road, Cambridge CB3 0HE, UK

We have compared the properties of strained quantum wells grown along the (001) and (111) directions. In the latter case a piezoelectric field is created which we have found to have several advantages. We have analyzed in some detail quantum wells n-doped on one side by performing self-consistent subband structure calculations in the local density approximation and calculating scattering times due to remote ionized impurity scattering, which is an important limiting factor for the mobility. We find that the scattering times can be increased considerably by increasing the separation between the electrons and the ionized donors. We also predict electron densities in excess of $3 \cdot 10^{17} \text{ cm}^{-3}$, which should be useful for improving High Electron Mobility Transistors (HEMT's).

1. Introduction

So far layered semiconductor heterostructures have usually been grown along the (001) direction, but in the last few years other growth directions have also been used. This in particular applies to the (111) direction where the initial growth problems have been overcome to a large extent. Hayakawa et al. [1] showed that good crystal quality can be achieved by tilting the substrate. (111)-grown GaAs quantum well lasers were found to have lower threshold current densities compared to (001)-grown ones [2], which was explained by the lower parallel hole mass for (111) growth [2]. More recently, the critical layer thickness for strained layers was found to be larger [3] for (111) growth than for (001) growth. In GaAs/AlGaAs heterostructures grown along (311) the dopant Si turns out to be an acceptor, which has led to considerably enhanced hole mobilities [4].

It was pointed out by Smith [5] that a built-in longitudinal piezoelectric field (i.e. directed perpendicular to the layers) is created if a strained heterostructure is grown along anything but the (001) or (110) directions. For a given amount of strain this longitudinal piezoelectric field has its maximum for growth along the (111) direction. In this paper we will only consider (111)-grown samples and compare them with the corresponding (001)-grown samples. We will consider quantum wells n-doped on one side only in which the piezoelectric field concentrates the electrons to the interface region near the undoped barrier.

In a preliminary report [6] we examined the possibility of taking advantage of the piezoelectric field in such structures. Then, we only considered the often studied combination of InGaAs quantum wells and GaAs barriers and made some conclusions concerning sample design. With a well width of 200 Å one can have 1 % strain without forming dislocations [3, 7] and simultaneously the charge distribution can respond considerably to the piezoelectric field. We also compared different background doping in finite and semi-infinite buffer layers and found some advantage of having a wide n-type buffer layer as the undoped barrier. Hence, we only consider this case here. We take the background donor concentration to be 10^{16} cm^{-3} and the intentional donor concentration N_d to be $2 \cdot 10^{16} \text{ cm}^{-3}$. We have found that the results are remarkably insensitive to N_d . This can be explained by a simple argument. We consider two samples with intentional donor concentrations N_{d1} and N_{d2} , spacer layer widths d_1 and d_2 and depletion layer widths a_1 and a_2 . We further assume that the carrier concentration N_d is the same for the samples. This implies

$$N_{d1}n_1 = N_{d1}n_1 \quad (1)$$

The line up of the Fermi level in the electron gas and the doped barrier implies that the band bending in the barrier is the same for both the samples.

$$\frac{1}{2} N_{d1}e_1^2 + N_{d1}e_1d_1 = \frac{1}{2} N_{d2}e_2^2 + N_{d2}e_2d_2 \quad (2)$$

Together with eq (1) this gives

$$\frac{1}{2}e_1 + e_1 = \frac{1}{2}e_2 + d_2 \quad (3)$$

Thus the distance from the interface to the middle of the depleted layer and thereby the average electron-donor separation are the same in both the samples. We can then expect similar scattering times.

In this paper we have made a more systematic study and have considered several material pairs in which the compressive or tensile strain is 1%. $In_{0.15}Ga_{0.85}As$ quantum wells surrounded by $GaAs$ or $Al_{0.3}Ga_{0.7}As$ barriers and $In_{0.66}Ga_{0.34}As$ or $In_{0.39}Ga_{0.61}As$ quantum wells (under biaxial compression or tension, respectively) between InP or $Al_{0.48}In_{0.52}As$. Among the material pairs considered a good choice seems to be $In_{0.66}Ga_{0.34}As/Al_{0.48}In_{0.52}As$, partly due to the large conduction band offset. We have also calculated scattering times due to remote ionised impurity scattering which gives a measure of the potential improvements of the mobility.

2. Calculations

We have performed self-consistent subband structure calculations in the envelope function approximation. Using a modified variational approach we apply current-conserving boundary conditions [8] and the numerical work mainly consists of diagonalisation of 21×21 matrices. Exchange and correlation have been included in the local density approximation [9]. As a measure of the shift of the electron distribution we have determined the average position $\langle z \rangle$ numerically. The strength of the piezoelectric field is given by simple analytical expressions involving the lattice mismatch and experimentally determined material constants [5]. We have considered different values of the 2D electron density N_s and the spacer layer width d_p .

Using the results of these calculations as input we have also calculated scattering times for remote ionised impurity scattering. This we do within the Born approximation, determining the screened Coulomb interaction between an electron and the ionised donors within the random phase approximation [10]. The scattering time we consider is that for electrons at the Fermi wavevector, which is appropriate for low temperatures, as it is only electrons at the Fermi level which are then involved in transport. The mobility μ is related to the total scattering time τ by $\mu = e\tau/m^*$, where m^* is the electron mass. In this paper we only calculate the contribution from remote ionised impurity scattering to the total scattering time and only for cases with one occupied subband.

3. Results

a. Shift of electron distribution

For (001) growth, the electrons in a one-side doped quantum well are shifted towards the doped barrier because of the attraction to the ionised donors. This shift decreases the average electron-donor separation and increases the remote ionised impurity scattering. A typical example is given in fig. 1a. This effect can be opposed by a piezoelectric field, which causes the electrons to be strongly displaced towards the undoped barrier (fig. 1b)

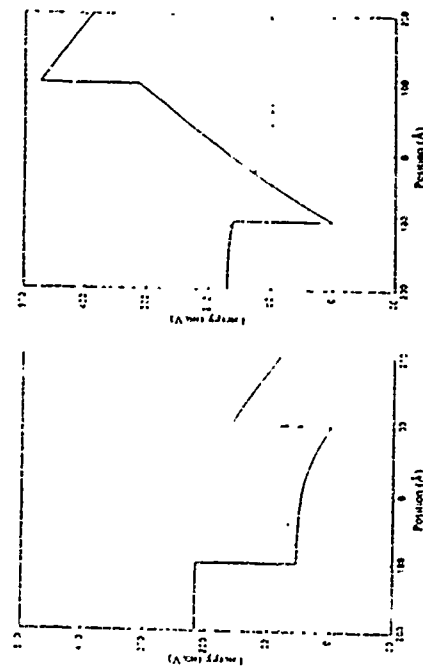


Fig. 1. Potential well (solid lines) and charge density (dashed lines) in a 200 Å $In_{0.15}Ga_{0.85}As$ growth, no piezoelectric field, $d = 92$ Å, and (b) (111) growth, piezoelectric field = $2.23 \cdot 10^{11}$ V/cm, $d = 391$ Å. In both cases the electron density is $6 \cdot 10^{11}$ cm $^{-2}$. Only the right barrier is intentionally doped.

The impurity scattering is decreased by this effect as well as by the effects described below. The appropriate sign of the piezoelectric field can be influenced by three factors: (i) the sample can be grown along the inequivalent directions called (111)A or (111)B, (ii) the quantum well can be under either compressive or tensile strain, and (iii) the doped barrier can be grown before or after the quantum well. We do not specify which case we have but only assume that the flexibility with these factors is used such that the piezoelectric field moves the electrons away from their parent donors.

It should be noted that the strong concentration of the electrons near the undoped barrier can lead to enhanced interface roughness scattering. This effect can be expected to vary from sample to sample and it is beyond the scope of the present article to evaluate it. Here we just try to minimise the effect of remote impurity scattering. But it should be noted that in designing the optimal structure a possible difference between (111) growth and (001) growth with respect to other scattering mechanisms should be taken into account.

b. Enhanced electron concentration

The piezoelectric field does not only influence the distribution of the electrons in the quantum well but also increases their number [6, 11, 12]. A similar idea was suggested by Snow et al. [13] who used a piezoelectric field in a barrier to produce a 2D electron gas without intentional doping in the barrier. We assume that the intentionally doped layer is thick enough that it is not completely depleted. Then the width of the depleted

layer is increased by the piezoelectric field and N_s , the number of electrons per unit area, increases. In the case of InGaAs/GaAs , N_s can be increased from $6.0 \cdot 10^{11} \text{ cm}^{-2}$ to $1.18 \cdot 10^{12} \text{ cm}^{-2}$ in a typical case [6]. If N_s is already rather large for the (001) grown samples, the relative increase due to the piezoelectric field is smaller. For example if we use $\text{Al}_0.3\text{Ga}_{0.7}\text{As}$ barriers but keep the spacer layer width fixed, the corresponding increase is from $1.5 \cdot 10^{11} \text{ cm}^{-2}$ to $1.84 \cdot 10^{11} \text{ cm}^{-2}$. The reason why this increase is smaller than for GaAs barriers, even on an absolute scale, is that here we have two filled subbands.

As discussed in c) below the maximal value of N_s is obtained if the spacer layer is zero. It is also found that a large conduction band offset leads to a high N_s , if the other factors are kept constant. In the optimal case with $\text{In}_{0.4}\text{Ga}_{0.6}\text{As}/\text{Al}_{0.4}\text{Ga}_{0.6}\text{As}$ we predict that an N_s value of $3.2 \cdot 10^{12} \text{ cm}^{-2}$ can be achieved provided that the conduction band offset, that we use as an input parameter, is correct. We have taken this to be 615 meV for this system. This is based on an interpolation between the calculated band offsets for lattice matched materials [14]. It is larger than what we would obtain from ref. [15] but smaller than the experimental value in ref. [16].

To our knowledge such high electron densities have not previously been achieved in standard modulation-doped structures. Above we have considered an Al content of 30% because then the AlGaAs still has a direct band gap. It is likely that higher Al contents will improve the results further, but it is dubious to use the one-valley envelope function approximation when one material has its conduction band minimum away from the Γ point. We have therefore refrained from such calculations.

c. Increased spacer layer widths

A thin ($\sim 100 \text{ \AA}$) undoped spacer layer of the barrier material is often grown between the doped layer and the quantum well. The purpose is to reduce the impurity scattering by increasing the electron-donor separation. However, a spacer layer also increases the band bending in the barrier and thereby decreases the carrier concentration N_s , which vanishes if d_p is too large. We saw above in b) that considerably higher electron concentrations can be obtained in (111)-grown samples than (001)-grown ones which are identical except for the growth direction. Thus, it is possible to increase d_p in the (111)-grown sample until N_s has been lowered to the same level as in the (001)-grown sample. In this way we can compare samples with the same electron densities N_s , but with different spacer layer widths d_p and electron distributions, as shown in fig. 1. Here we keep N_s at $6.0 \cdot 10^{11} \text{ cm}^{-2}$.

In table 1 we compare samples for both the growth directions and different material pairs. The results for different material pairs depend on the effective masses and dielectric constants as well as the piezoelectric field and the conduction band offset, but we have found that the latter two are the most important factors. For each case we include both the scattering time due to remote impurity scattering, τ , and the average electron donor separation given by

$$\langle L \rangle = \frac{L_s}{2} + d_p, \quad \tau = \frac{a}{2} - \langle z \rangle \quad (1)$$

Here L_s is the quantum well width, a is the depletion layer width and $\langle z \rangle$ is the average electron position relative to the middle of the quantum well. We note that both $\langle L \rangle$ and τ are increased considerably by the piezoelectric field. They are also larger for larger conduction band offsets. In general τ is increased more than $\langle L \rangle$ by these factors. If other scattering mechanisms could be ignored, the increase in scattering time, because of the piezoelectric field, from 55 to 2 ps for the case of $\text{In}_{0.15}\text{Ga}_{0.85}\text{As}/\text{GaAs}$ corresponds to an increase in the mobility from $2.6 \cdot 10^4 \text{ cm}^2/\text{Vs}$ to $1.0 \cdot 10^5 \text{ cm}^2/\text{Vs}$. Even if other scattering mechanisms are taken into account it is easy to verify that important improvements to the low-temperature electron mobilities are possible.

Table 1. Average electron donor separation ($\langle L \rangle$) in \AA and scattering time τ in ps due to remote ionised impurity scattering for different material pairs. The conduction band offset ΔE_c in meV and the piezoelectric field e_p in kV/cm (for (111) growth) are also given.

Quantum well	Barrier	ΔE_c	e_p	$\langle L \rangle$ (001)	$\langle L \rangle$ (111)	τ (001)	τ (111)
$\text{In}_{0.15}\text{Ga}_{0.85}\text{As}$	GaAs	161	223	92	391	0.055	2.21
$\text{In}_{0.15}\text{Ga}_{0.85}\text{As}$	$\text{Al}_{0.3}\text{Ga}_{0.7}\text{As}$	439	223	389	669	1.18	6.87
$\text{In}_{0.3}\text{Ga}_{0.7}\text{As}$	InP	158	171	81	288	0.045	1.04
$\text{In}_{0.3}\text{Ga}_{0.7}\text{As}$	$\text{Al}_{0.4}\text{Ga}_{0.6}\text{As}$	498	171	478	687	1.75	5.93
$\text{In}_{0.4}\text{Ga}_{0.6}\text{As}$	InP	275	115	202	322	0.233	0.941
$\text{In}_{0.4}\text{Ga}_{0.6}\text{As}$	$\text{Al}_{0.4}\text{Ga}_{0.6}\text{As}$	615	115	606	730	2.68	5.22

d. Higher N_s limit for filling of second subband

We have investigated how high carrier densities can be achieved for the different cases before the second subband starts to fill. For $\text{In}_{0.4}\text{Ga}_{0.6}\text{As}/\text{Al}_{0.4}\text{Ga}_{0.6}\text{As}$ we have found that this limiting N_s value is $8.25 \cdot 10^{11} \text{ cm}^{-2}$ in the (001) case and somewhat higher, $8.75 \cdot 10^{11} \text{ cm}^{-2}$, in the (111) case. The corresponding scattering times are 1.2 and 2.0 ps, respectively. If the main purpose is to achieve high mobilities one should probably try to stay slightly below this limiting N_s value, as for higher carrier concentrations in the subband scattering becomes important. This occurs in the case mentioned above with $N_s = 3.2 \cdot 10^{12} \text{ cm}^{-2}$. Calculations including this scattering mechanism will be presented elsewhere. In the present paper we have only calculated scattering times for samples with only one filled subband.

4. Discussion and conclusions

We have calculated subbands, electron distributions and remote ionised impurity scattering times for strained quantum wells doped on one side. We have compared (001)-grown samples with (111)-grown ones, where the main difference is the quite strong built-in piezoelectric field, which gives many advantages. The optimal design depends on what properties we want to improve. If we want to achieve high electron mobilities at low temperatures for studies of fundamental effects like the fractional quantum Hall effect, we should increase the electron donor separation, in order to reduce remote ionised impurity scattering in the quasi-2D electron gas. The piezoelectric field yields two effects contributing to this. The electron distribution is displaced towards the undoped barrier and one can increase the width of the undoped spacer layer by several hundred \AA .

For studies of the fractional quantum Hall effect, especially in the Wigner solid regime, it is often an advantage to have a low carrier density. In high electron mobility transistors (HEMT's), on the other hand, one often strives for very high carrier concentrations which, among other things, give rise to strong screening. For devices operating at room temperature, where phonon scattering is important, the saturation velocity can be more important than the impurity scattering limitation of the mobility at low temperatures and small current densities. In this respect we believe that the possibility of using the piezoelectric field to raise N_s above $3 \cdot 10^{12} \text{ cm}^{-2}$ can be very valuable.

In all the cases considered here the quantum well material is a ternary alloy and so the mobility is influenced by alloy scattering. In future work we plan to consider strained binary GaAs quantum wells between suitable barrier materials. Even if these structures are not optimal with respect to impurity scattering it is conceivable that the well developed GaAs technology and the absence of alloy scattering can make such structures promising for applications.

Determination of the band structure parameters of pseudomorphic GaInAs quantum wells by means of simultaneous transport and optical investigations

E. Litwin - Staszewska⁽¹⁾, F. Kobbi, M. Kamal-Saadi, D. Dur, C. Skierbiszewski⁽²⁾, H. Sibani, K. Zekentes³, V. Mosser⁴, A. Raymond, W. Knap, J. L. Robert

⁽¹⁾ Groupe d'Etude des Semiconducteurs Université Montpellier II
Place E. Bachelard, 34095 Montpellier Cedex 05, FRANCE
⁽²⁾ FORT III Institute of Electronic Structure and Laser, P. O. Box 1527,
Heraklion, 71110 Crete, Greece.
⁽³⁾ Schlumberger Montrouge Recherche
50, av. Jean Jaurès, BP 620-05, F-92342 Montrouge, France

Abstract

Combined studies of GaInAs/GaAs pseudomorphic structures have been performed by means of transport under hydrostatic pressure, luminescence and cyclotron resonance emission experiments. The structures investigated were 130 Å quantum wells. They were δ-doped outside the quantum well, with the spacer thickness ranging between 20 and 60 Å. These structures allowed us to study the influence of the carrier concentration on the mobility and on the position of the Fermi level above the first electrical sub-band. By using pressure and illumination, we changed the carrier concentration N_d from 0.5 to $1.8 \cdot 10^{12} \text{ cm}^{-2}$. In this range, only the first electrical sub-band is populated. A strong decrease of mobility at higher concentrations was shown and depicted essentially on correlation effects. High magnetic field transport measurements confirmed that only the lowest sub-band was populated. Moreover, cyclotron resonance emission gave the effective mass as a function of the carrier density in the well. On this basis, the importance of the non parabolicity effect was estimated. All these results were interpreted within the framework of the variational method leading to a determination of the most important physical parameters describing this system.

High quality pseudomorphic heterostructures can be grown epitaxially provided the thickness of the strained layer is small enough to avoid the generation of dislocations and defects. These structures, quantum wells and superlattices, have been studied intensively in the last years because of the wider range in the confinement related effects which they make possible. We focused our work on pseudomorphic GaInAs quantum wells which were δ-doped outside the well.

A combination of electrical transport and optical experiments have been performed to characterize these structures and to determine the parameters describing their electronic properties and their relation to the carrier concentration N_d .

The samples investigated were Si:δ doped $\text{Al}_x\text{Ga}_{1-x}\text{As}/\text{Ga}_{1-y}\text{In}_y\text{As}/\text{GaAs}$ structures grown by molecular beam epitaxy. The Al mole fraction, $x=0.32$, was checked by double X-ray diffraction as was the Indium content, $y=15\%$. The quantum well of thickness 130 Å was separated from the δ-doping plane by a spacer S_z ranging between 20 to 50 Å. The values of the effective doping density N_d amounted to $1.7 \cdot 10^{12} \text{ cm}^{-2}$ and $2.5 \cdot 10^{12} \text{ cm}^{-2}$. The samples were patterned in a Hall-bar geometry with six AuGeNi contacts.

Electrical characterizations

Hall measurements were performed between 4 and 400K using a helium continuous flow cryostat, reversing both the current and the magnetic field.
In order to study the behaviour of the structures as a function of the carrier concentration N_d , the metastable properties of the DX-Si centres present in the GaInAs were used. The combined effects of illumination [1] (by red LED), pressure (He-gas compressor system is used to change

Acknowledgements

U.E. is grateful to the Swedish Natural Science Research Council for economic support and D.R. wishes to thank St. John's College, Cambridge, UK, for support.

References

- [1] T. Hayakawa, M. Konno, T. Suyama, K. Takehashi, S. Yamamoto and T. Hiyakata, Jpn. J. Appl. Phys. **26**, L302 (1988)
- [2] W. Batty, U. Ekenberg, A. Glietti and E. P. O'Reilly, Semicond. Sci. Technol. **4**, 901 (1989)
- [3] T. Anan, K. Nishi and S. Sugaw, Appl. Phys. Lett. **60**, 3159 (1992)
- [4] J. J. Heremans, M. B. Santos and M. Shayegan, Appl. Phys. Lett. **61**, 1652 (1992)
- [5] D. L. Smith, Solid State Commun. **51**, 919 (1986)
- [6] U. Ekenberg and D. Richards, Surf. Sci. **263**, 580 (1992).
- [7] T. G. Anderson, Z. G. Chen, V. D. Kulakovskii, A. Uddin and J. T. Vallin, Appl. Phys. Lett. **51**, 752 (1987)
- [8] M. Altarelli, Phys. Rev. B **28**, 842 (1983)
- [9] T. Ando and S. Mori, J. Phys. Soc. Jpn. **48**, 1518 (1979)
- [10] T. Ando, A. B. Fowler and F. Stern, Rev. Mod. Phys. **54**, 437 (1982).
- [11] X. Li, K. F. Longenbach and W. I. Wang, Appl. Phys. Lett. **60**, 1513 (1992)
- [12] J. Sánchez-Dehesa, J. L. Sánchez-Rojas, C. Lopez and R. J. Nicholas, Appl. Phys. Lett. **61**, 1072 (1992)
- [13] E. S. Snow, B. V. Shanabrook and D. Gammon, Appl. Phys. Lett. **56**, 758 (1990)
- [14] M. S. Hylbertsen, Appl. Phys. Lett. **58**, 1759 (1991).
- [15] M. P. C. M. Krijn, Semicond. Sci. Technol. **6**, 27 (1991)
- [16] J.-H. Huang, T. Y. Chang and B. Lahrvic, Appl. Phys. Lett. **60**, 737 (1992)

the pressure even at low temperature) and temperature were used to produce different populations depending on the preparation cycles [2,3] (high pressure freeze out technique (HPFO) and persistent photoconductivity (PPC)). It should be noted that all the measurements were actually made at atmospheric pressure by means of this technique.

In figure 1-a, we show the Hall mobility μ_H measured at 4.2 K as a function of N_3 . As expected, the carrier concentration in the well was increasing with the δ doping density N_3 and was a decreasing function of the spacer thickness S_p . In figure 1-b the variation of μ_H at 77 K is presented for two samples having the same N_3 but different S_p . It should be noted that the mobility passes through a maximum in both cases. The increase of μ_H with N_3 has already been observed in heterojunctions and can be well explained taking into account the effect of screening by free carriers [4].

To explain the maximum and the decrease of the mobility [5] observed on our samples, we must consider the effect of spatial correlation of remote unpopulated charges in the Si δ -doped plane [6,7]. Indeed, other effects as the influence of the higher sub-band could not be involved since N_3 in the well was too small (see SdH experiments). The role of alloy scattering certainly could not explain the strong decrease of μ_H observed. The effect of correlation could be seen by measuring the mobility after different preparation cycles. In ref [8], it was demonstrated that depending on the way the remote impurity charges are distributed among the donor sites, different values of electron mobility were obtained for the same N_3 and in the same sample, which confirmed this hypothesis.

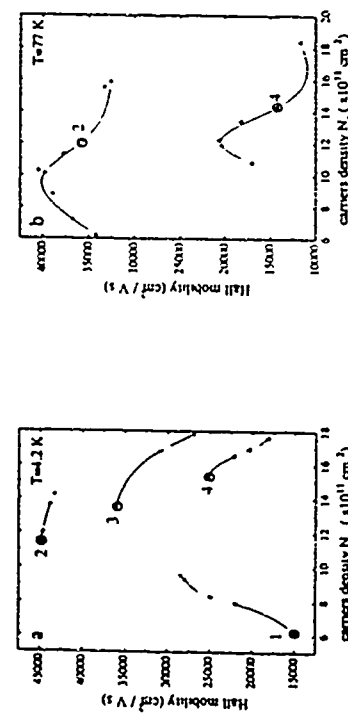


Fig. 1: Hall mobility μ_H versus carrier concentration N_3 for various samples. 1 ($N_3=1.7 \cdot 10^{12} \text{ cm}^{-2}$, $S_p=40 \text{ Å}$), 2, 3 and 4 ($N_3=1.7 \cdot 10^{12} \text{ cm}^{-2}$ and respectively $S_p=60, 40, 20 \text{ Å}$). The points inside the circles are obtained under equilibrium conditions.

Fig. 1-a) $T=4.2 \text{ K}$. \bullet , \circ , Δ , \times are obtained after illumination (PPC).

Fig. 1-b) $T=77 \text{ K}$. \bullet , \circ are obtained after different (HPFO) preparation cycles. Points for the highest concentrations are obtained after illumination (PPC).

Cyclotron resonance experiments

Cyclotron resonance emission was observed in the same samples. In these measurements, electrons heated by electric pulses to occupy higher Landau levels, relaxed by emitting photons of the cyclotron energy. The emitted radiation was detected by means of a selective GaAs detector operating at an energy of 4.43 meV. A detailed description of the experimental set up can be found in ref.[9]. An increase of the cyclotron mass with N_3 was observed as shown in figure 2.

The cyclotron resonance peak shifted towards higher magnetic fields with increasing N_3 in the quantum well. This effect was interpreted in terms of the variations of effective mass with energy in conduction band (non parabolicity effects) [10].

Shubnikov-de Haas experiments (SdH)

Carrier concentrations in the well were deduced from the period of ρ_{xx} magnetoresistance oscillations (SdH effects) [11]. The values deduced from these experiments were the same as those determined by Hall effect measurements. These results confirmed that in our samples only the lowest sub-band of the quantum well was populated (see electrical characterization). Thus it's possible, using the values of the effective masses deduced from cyclotron resonance experiments, to determine the position of the Fermi level above the conduction band minimum as a function of the carrier density. The results are shown in figure 3.

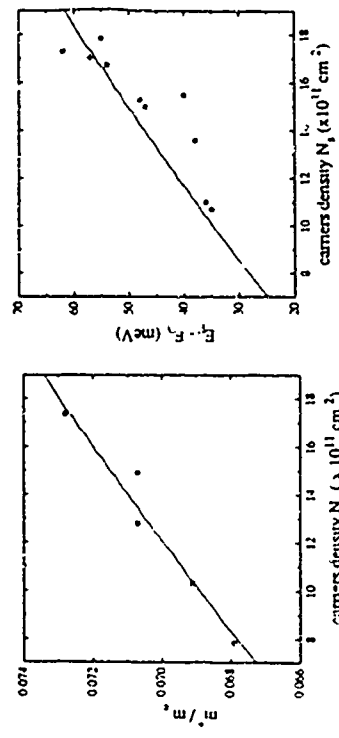


Fig. 2: Cyclotron resonance effective mass as a function of the carrier concentration N_3 . The solid line is the theoretical curve.

Fig. 3: The difference between Fermi energy E_F and the first electronic sub-band E_1 as a function of N_3 . \bullet are deduced from SdH experiments, \circ is obtained from photoluminescence spectra. The solid line represents theoretical results.

Luminescence experiments

Photoluminescence spectra [11, 12] were obtained at 12K using an He-Ne source operating at 632.8 μm with an intensity of 0.5 W/cm². The signal was detected using a Si photodetector. Under these experimental conditions, the concentration measured by the Hall effect was practically the same for each sample. The Fermi level position above the conduction band minimum was deduced from the Fermi edge singularity observed in the spectra. Its value is in good agreement with those deduced by SdH experiments (see figure 3).

MOP26

The conduction band spin splitting in type-I strained and unstrained (GaIn)As/InP quantum wells

P. Omling, B. Kowalski

Solid State Physics Department, University of Lund, Box 118, S-22100 Lund, Sweden

B.K. Meyer, D.M. Hofmann, C. Wetzel

Physik-Department, E 16, Technische Universität München, D-85747 Garching bei München, Germany

V. Härle, F. Scholz

Physikalisches Institut, Universität Stuttgart, Pfaffenwaldring 57, D-7000 Stuttgart, Germany

Abstract

We present the first successful optically detected magnetic resonance experiments (ODMR) on strained and unstrained $\text{Ga}_{1-x}\text{In}_x\text{As}/\text{InP}$ type I quantum wells. The resonances attributed to electrons are in general anisotropic and detailed results are given for the composition range $0.4 < x < 0.6$. Extrapolating to the binary end points i.e. InAs and GaAs close agreement with existing results is found. The anisotropy is explained within a simple model using subband calculations. It also explains why one sided p-type modulation doping reduces the electron-hole wavefunction overlap, increases the radiative life times and allows for optical detection of magnetic resonance. A detailed discussion why hole resonances can be ruled out is given.

Introduction

Optical detection of electron spin resonance (CESR, ODMR) is an ideal technique to determine the Landé factor g^* of conduction electrons [1]. The g -factor can be calculated by $\vec{k} \cdot \vec{p}$ theory and thus provides a test of band structure parameters and theoretical concepts. This is of special interest for the technologically important type-I quantum wells (QW) systems such as $\text{GaAs}/(\text{GaAl})\text{As}$ or $(\text{GaIn})\text{As}/\text{InP}$. However, the measurement of g -factors in these structures is not an easy task, since the radiative recombination times occur on a nanosecond time scale. A prerequisite to observe optically detected magnetic resonance (ODMR) is, however, to induce microwave transitions within the life-time of a decaying system. For the standard cw-ODMR technique life-times must be longer than $0.1 \mu\text{s}$. Therefore it is no wonder that the few experimental results on two dimensional structures using the ODMR technique were applied on type II quantum wells. Here the electrons and holes are separated in real space, e.g. with the electrons in the barrier material and the holes in the quantum well or vice versa. This separation leads to increased recombination times into the microsecond range. In type I quantum wells type-II behaviour, i.e. longer life-times can be achieved by the presence of an external electrical field applied perpendicular to the quantum well plane [2]. A built in electrical field as achieved by a one-sided modulation doping can play an equivalent role. We will demonstrate that one sided p-modulation doping allows for the first successful identification of electron g -values in strained and unstrained InGaAs/InP quantum wells.

Modeling

Using the variational method [13], we determined the Fermi level energy E_F and the first electrical sub-band E_0 as a function of N_s . By calculating the wave function of the electron at the Fermi level we determine its mean position z_0 in the well, and the corresponding energy $E(z_0)$ above the bottom of the conduction band. The Kane model was used to calculate the effective mass at the energy $E(z_0)$:

$$m^*(E(z_0)) = m_0^* (1 + 2 E(z_0)/E_g)$$

A good agreement with the experimental results (E_F and $m^*(E_F)$) was found by taking the following parameters $E_g = 1.355 \text{ eV}$, $m_0^* = 0.060 m_0$, and the trial functions given in ref.[13].

We wish to stress that good agreement between experimental and theory requires a full variational calculation and cannot be deduced from simple models of triangular or rectangular wells. This was due to the high values of N_s we have in our system and to the existence of the second barrier ($\text{InGaAs}/\text{GaAs}$).

Conclusion

Electrical and optical experiments performed on our $\text{AlGaAs}/\text{InGaAs}/\text{GaAs}$ structures have shown that only the first sub-band was populated up to $N_s = 1.8 \cdot 10^{12} \text{ cm}^{-2}$. Correlation effects must be invoked to explain the maxima and the decrease of the mobility when N_s was increasing. Cyclotron resonance experiments allowed us to establish the effect of non-parabolicity by measuring the electron effective mass as a function of N_s . PPC and HPPO techniques were used to change N_s in the well. Whatever the method used to change the carrier concentration N_s in the range of 0.5 to $1.8 \cdot 10^{12} \text{ cm}^{-2}$, accounts for the energy structure of the well. This also allows us to estimate the effect of non-parabolicity on the effective mass. This establishes the experimental method which we believe can be used to determine the properties of InGaAs quantum wells with different thicknesses and others growth parameters.

(x) Permanent address: UNIPRESS, Polish Academy of Sciences, 01-142 Warszawa, POLAND.

References:

- [1] M. Van der Burgt, A. Van Esch, F.M. Peeters, M. Van Hove, G. Borghs and F. Herlach, *Physica B* 184 p 211 (1993).
- [2] R. Piszarski, E. Litwin-Staszewska, T. Suki, L. Konecny and J.L. Robert, *Jpn. J. Appl. Phys.* Vol 32 (1993) suppl. 32: 1.
- [3] S. Konarska, L. Konecny, V. Mosser, J.L. Robert and K. Zakariasen, *Proc. 21 Int. Conf. of Physics Semicond. Beijing* (1992).
- [4] H. Okino, J.K. Luo, K. Masuoka and H. Iizawa, *Appl. Phys. Lett.* 54(1), p 36 (1989).
- [5] G.M. Yang, S.G. Park, K.S. Seo and B.D. Choi, *Appl. Phys. Lett.* 64(19), p 2340 (1992).
- [6] R. Piszarski, E. Litwin-Staszewska and J.L. Robert, *17 Int. Conf. of Defects in Semicond.*, Gmunden (1993).
- [7] T. Suki, P. Wawerowski, L.H. Duong, I. Guczyńska, J. Smolnicki, E. Gornik, G. Böhm and G. Weimann, *MSS 6 Conference*.
- [8] E. Litwin-Staszewska, T. Suki and J.L. Robert (to be published).
- [9] W. Knap, D. Dur, A. Raymond, C. Meny, J. Leclerc, S. Hénard and B. Eugene, *Rev. Sci. Instrum.* 63(6), p 3293 (1992).
- [10] W. Zawadzki, C. Chabert, D. Dur, W. Knap and A. Raymond, *MSS-6 Conference*.
- [11] H. Brägger, H. Mütting, C. Wölke, H. Kern and D. Hermonas, *Appl. Phys. Lett.* 59(21), p 2739 (1991).
- [12] J.M. Gilibert, J. Lascaris-Rojas, E. Munoz, E. Calleja, J.P.R. David, G. Hilland and J. Callegre, *Appl. Phys. Lett.* 61(10), p 1225 (1992).
- [13] G. Bastard, *Wave mechanics applied to semiconductor heterostructures*, Edition de Physique (1988).

Experimental

Our measurements were performed on $\text{Ga}_{0.4}\text{In}_{0.6}\text{As}$ single quantum well (SQW) and multiple single quantum wells (MQW). The structures were grown by metal organic vapour phase epitaxy (MOVPE) either lattice-matched ($x_{\text{Ga}} = 0.47$) to InP, having different well thicknesses or with varying composition ($0.4 < x_{\text{Ga}} < 0.6$) but fixed QW thickness ($d = 15 \text{ nm}$). The characteristic layer sequence was the same in all samples. The QW on top of several 100 nm of InP is followed by a single sided p-modulation doping, a 10 nm layer with an acceptor concentration of typically $2 \cdot 10^{18} \text{ cm}^{-3}$. It is separated from the QW by a 5 nm spacer. All structures were grown in a low pressure MOVPE system at 80 mbar and at a growth temperature of 620°C on semi insulating InP-Fe substrates. The quality of the samples was controlled by Hall effect, photoluminescence and magneto-luminescence. Hall effect measurements (77 K) showed mobilities around $100 \text{ cm}^2/\text{Vs}$ for the composition range studied ($0.6 < x < 0.4$).

For the ODMR experiments the sample was placed in an open TE₀₁₁ resonator itself located in the center of split-coil superconducting magnet (Magnex, $0-4 \text{ T}$) allowing for excitation with unpolarized light from the 514 nm line of an Ar^+ (typically 100 mW) laser. The luminescence emitted was focussed on the entrance slit of a $1/4$ 48 cm double monochromator (Spex) and detected by a LN_2 cooled Ge diode (North Coast). For the resonance experiments the circularly polarized components of the emission in Faraday configuration were analyzed by a combination of a linear polarizer and photo-elastic stress modulator (HINDS) working at 43 kHz . The spin resonance transitions were induced by applying microwaves at 21 or 36 GHz delivered from a Gunn diode or a klystron. The magnetic field was varied to tune to resonance.

Experimental Results

A typical photoluminescence spectrum from the $\text{Ga}_{0.4}\text{In}_{0.6}\text{As}/\text{InP}$ QW series is shown in the inset of fig. 1. A single line with a half width of 5 meV is observed, the peak maximum is at $E = 0.83 \text{ eV}$ ($x = 0.47$, $d = 15 \text{ nm}$). It is due to band to band recombination between the first electron and heavy hole subband (e_{1h_1}). The emission is circularly polarized (magnetic circular polarized emission, MCPE) with a degree depending on temperature and the applied magnetic field. This behaviour reflects an unequal spin-occupation in the Zeeman split states and is a necessary condition to perform magnetic resonance experiments. The difference in occupation, in our case not a Boltzmann equilibrium, can be changed by resonant microwaves and the magnetic resonance signal is observed as a decrease of the MCPE signal (see fig. 1). For the magnetic field parallel to QW plane (001) we obtain a g -value of $g_H = -3.27 \pm 0.04$, for clarity the field dependent background signal of the MCPE has been subtracted (the sign of the g -value has been checked independently [3]). The resonance signal has a Lorentzian line shape characteristic for homogeneous broadening. When rotating the sample from (001) towards the [011] direction the resonance position changes, the g -value decreases significantly. (see fig. 2). A complete 90° degrees rotation pattern could not be performed, since the MCPE signal on which we direct the ODMR decreased with increasing angle. The angular dependence was analyzed with the usual expression for the g -tensor in axial symmetry [4]

$$g(\theta) = (g_H^2 \cos^2 \theta + g_L^2 \sin^2 \theta)^{1/2} \quad (1)$$

where θ is the angle between the magnetic field and the quantum well plane, g_L is the only fitting parameter and the solid line in fig. 2 results from equ. 1 when using $g_H = -3.27 \pm 0.04$ and $g_L = -1.88 \pm 0.01$ (see also table 1).

As a function of composition the g -values decrease for higher Ga-content, also the g_L -components follow this trend (see fig. 3 and table 1). The anisotropy ratio g_H/g_L more or less remains the same for constant well width of $d = 15 \text{ nm}$ and varying composition. The data points lie on a straight line (see fig. 3), except for the values of the lattice-matched composition ($x_{\text{Ga}} = 0.47$). The reason is at present not understood, but this interesting observation deserves future investigations. The influence of size quantisation was studied in SQW's for $x_{\text{Ga}} = 0.47$. It was possible to observe resonances for a 100 nm (quasi-3-dimensional, 3D) QW down to thicknesses of 6 nm (see table 2). One notes that the anisotropy ratio decreases with increasing well width. For the quasi-3D QW no anisotropy is found, the g -value of -4.1 ± 0.01 is substantially smaller than reported by Johnson et al [5] of $g = 5.6 \pm 0.3$ (same composition and well width). Electrically detected spin resonance experiments gave values between 4 and 5, the authors [6] suggested that the bare or bulk spin splitting factor is $g = 4.1$, close to our experimental value.

Discussion and Interpretation

For an assignment of the resonances we first take a look on the band structure of the $(\text{GaIn})\text{As}/\text{InP}$ system. Strain and confinement considerably influence the ordering of the electron and hole levels in the QW's [7]. For $x_{\text{Ga}} < 0.17$, that means under compression of the layer, the radiative recombinations involve the conduction band and the $|J_z, I_z\rangle = |3/2, \pm 3/2\rangle$ heavy hole valence band states, under tension ($x_{\text{Ga}} > 0.47$) the light hole $|3/2, \pm 1/2\rangle$ has to be considered. Including the mass dependent confinement energy, the cross over point of the heavy and light hole energy as a function of Ga-content shifts. Calculations show that for x_{Ga} up to 0.5 the heavy hole is highest in energy for a QW width of 15 nm .

The large anisotropy of the g -tensor could on first sight suggest that the resonances could be due to holes. For the holes the Zeeman Hamiltonian in the Luttinger formalism can be written as [8]:

$$H_A = -\frac{1}{2}\mu_B \sum_i (\lambda A_i + g_i^h \mu_B) \quad i = x, y, z \quad (2)$$

with λ and g the Luttinger parameters and z parallel to [001]. In our samples the heavy hole band is separated from the light hole band by several 10 meV and it is highest in energy for $x_{\text{Ga}} < 0.5$. The heavy and light hole bands can thus be treated separately. Diagonalization of Eq. 2 gives the g -values for the heavy holes in the effective spin $J' = \frac{1}{2}$ formalism. $g_{A,H} = 6\kappa + 13.5g$, $g_{A,L} = 3g$ is usually very small (< 0.1), since it represents a correction due to 3rd order spin terms. Hence one expects a $g_H \cos \theta$ behavior for the heavy hole resonances, as found in the systems $\text{Sn}_{1-x}\text{Ge}_x/\text{Si}$ [9] and AlAs/GaAs (type II superlattices) [10]. In both cases $|g_L|$ is close to zero. Also the g_H -value should be less influenced when changing the composition, since on the In-rich side the Kohn-Luttinger parameters do not change considerably. Clearly, this is not in agreement with our experimental data, and therefore the assignment of the resonances to the spin splitting of the valence band is ruled out.

Furthermore all the spin split hole states near $\kappa = 0$ are occupied due to the two dimensional hole gas. Its Fermi energy E_F between 3 and 20 meV has to be compared with a

spin splitting of 0.1 meV. We conclude, that spin resonance is not possible at the valence band edge. This is supported by the fact, that we detect the spin resonance on the band-edge-PL ($k \approx 0$).

We attribute the resonances to electrons at the edge of the lowest conduction subband. Extrapolating the g -values to the binary end points (see fig.3), i.e. InAs/InP and GaAs/InP supports this interpretation. For GaAs we have values close to zero, the bulk g -value is $g^* = -0.44$ [10]. The extrapolated value on the InAs side is 7.2, for a 100 nm InAs/GaSb quantum well values between 7.8 and 8.7 were observed [11].

The spin splitting for the 100 nm lattice-matched QW (quasi 3D) is calculated using Roth three band formula [12]

$$g^* = \frac{2}{m^*} \frac{p^2}{3E_g(E_g + \Delta)} \quad (3)$$

where p is the interband matrix element, $p^2/2m$ is 25.5 eV, the bandgap energy E_g is 0.813 eV and the spin-orbit splitting energy Δ is 0.356 eV. With eq.3 we calculate $g^* = -4.34$ in reasonable agreement with the experimental value of 4.01.

For the 2D-system the band edge energy E_g and the lowest subband energies of the electrons E_{A1} , light E_{A1} , heavy E_{A1} and spin orbit split of holes E_{A1} are needed. g is given by

$$\frac{g_A}{g_0} = 1 - \frac{2}{3m^*} p^2 \left(\frac{3}{2(E_g + E_{A1} - E_{A1})} - \frac{1}{2(E_g + E_{A1} - E_{A1})} - \frac{1}{E_g + E_{A1} - E_{A1}} \right) \quad (4)$$

and g_0 by

$$\frac{g_A}{g_0} = 1 - \frac{2}{3m^*} p^2 \left(\frac{1}{E_g + E_{A1} - E_{A1}} - \frac{1}{E_g + E_{A1} - E_{A1}} \right) \quad (5)$$

From eq. 4 and 5 the composition dependence as well as the anisotropy ratio g_A/g_0 can be calculated, provided all parameters are known. In most cases the subband energies need to be calculated. Moreover, this calculations only hold for a flat bandprofile and the effects of the one side p-modulation doping on the bandstructure and subband energies are not considered. Preliminary selfconsistent calculations showed, that the energies of especially the hole states deviate considerably from the flat band case. The electron states in the conduction band seemed to be less affected.

Calculated g -values in the flat band assumption deviate from the experimental ones by 30%.

For the GaAs/(AlGa)As material system a theoretical model has been put forward by Ivchenko et al [13] which could explain the large anisotropy as well as the well width dependence. It has to be adopted to the GaInAs/InP system. Strain and the influence of the electrical field have to be included. These theoretical calculations are currently under way.

The recombination life-time in type I QW's is on the nanosecond scale, the observation of ODMR is an indication that the radiative life-time must be larger than 0.1 ns. The reason is, that the one-sided p-modulation doping changes the band structure. In fig.4 the calculated band edges are shown for a 15 nm QW with lattice matched composition. The subband edges of the first quantized states (e_1, h_1, h_2) are indicated. The holes from the asymmetric Zn-acceptor modulation doping on the left side are transferred into the deep quantum well in Ga_{0.47}In_{0.53}As: $\delta E_V = 353$ meV).

There is a strong electrical field between the dopant layer and the two-dimensional hole gas. It peaks at the interface between barrier and QW with $E \approx 1.7 \cdot 10^6$ V/cm. The field causes a spatial separation of hole states from electrons along the growth direction z . This is shown by the square of the wavefunctions χ_i for the electrons χ_i and heavy holes χ_{HH} . Due to the spatial separation of electrons and hole the overlap integral entering into Fermi's Golden Rule is reduced and hence the recombination life-time increases. For the order of magnitude of the electrical field a reduction of a factor 100 is calculated.

With increasing size quantization the separation is suppressed, the radiative life-times get shorter and shorter. This happens to be the case for $d < 6.0$ nm, resonance experiments so far failed for $d \approx 4$ nm. We currently set up time-resolved measurements to verify this estimate.

Conclusion

We have measured the conduction band spin splitting in type I (InGa)As/InP QW's with varying composition and well width. It was possible due to a built-in electrical field by a p-modulation doping enhancing recombination life-times. A influence of the confinement energies on the g values is described theoretically.

Acknowledgement

This work was supported by the Deutsche Forschungsgemeinschaft via SFB 348.

References

- [1] C Herman and C Weisbuch, Phys. Rev. B 15 (1977) 823
- [2] H.J. Pollard, L. Schulteis, J. Kuhl, E. Göbel and C. Tu, Phys. Rev. Lett. 55 (1985) 2610
- [3] B. Kowalski, Diploma Thesis, Munich 1993
- [4] C.P. Slichter, Principles of magnetic resonance, Harper and Row Publ. New York 1963
- [5] G.R. Johnson, A. Kana-ha, D.C. Cavenett and S.J. Bass, Semicond. Sci. Technol. 2 (1987) 182
- [6] M. Dobers, J.P. Vireen, Y. Guldner, P. Bove and M. Razhegi, Phys. Rev. B 40 (1989) 8075
- [7] D. Geraboni and H. Temkin, J. Lum. 44 (1989) 381
- [8] H.W. v. Kesteren, E.C. Cosman, W.A.J.A. VanderPool and C.T. Foxon, Phys. Rev. B 41 (1990) 5283
- [9] E.R. Glaser, J.M. Trombetta, T.A. Kennedy, S.M. Prokes, O.J. Glenboeck, K. Wang and C.H. Chern, Phys. Rev. Lett. 65 (1990) 1247
- [10] J.M. Trombetta, T.A. Kennedy, D. Gammann and S.M. Prokes, ed. by E.M. Anastassakis, J.M. Joannopoulos, 20 Int. Conf. of Semicond. Phys., World Scientific, Singapore, 1990 Vol. 2, p1361
- [11] Landolt Börnstein, Semiconductors, edited by O. Madelung, M. Schulz and H. Weiss, Vol. 17a, Springer, Berlin 1982
- [12] L.M. Roth, B. Lax and S. Zwerdling, Phys. Rev. 114 (1959) 90
- [13] E.L. Ivchenko, A.A. Kiselev, Sov. Phys. Semicond. 26 (1992) 827

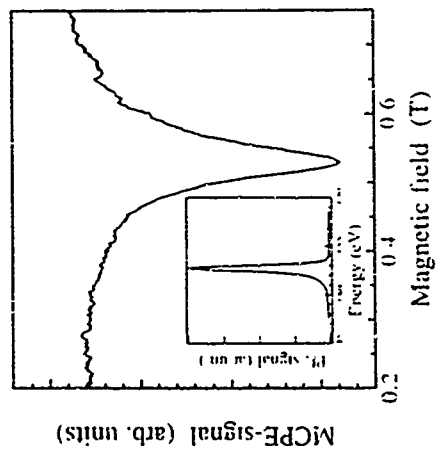


Fig. 1: Optically detected magnetic resonance spectrum of a 15 nm $\text{Ga}_{0.9}\text{In}_{0.1}\text{As}/\text{InP}$ single quantum well ($x = 0.17$) at $T = 1.6\text{ K}$, and a microwave frequency of 21 GHz. The inset shows the corresponding photoluminescence signal

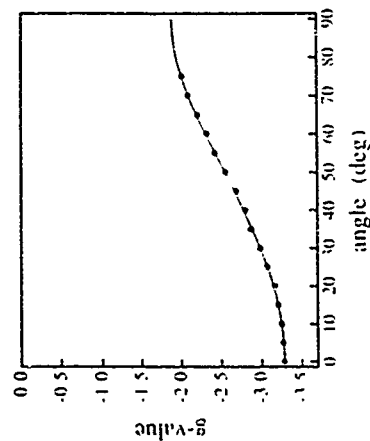


Fig. 2: The anisotropy of the g -factor for a rotation of the sample from the (001) plane towards the [110] direction with respect to the static magnetic field (solid circles: experimental points, the solid line is a fit to the experimental values with the help of eqn 1: parameters: $d = 15\text{ nm}$, $\alpha_{\text{Ga}} = 0.17$)

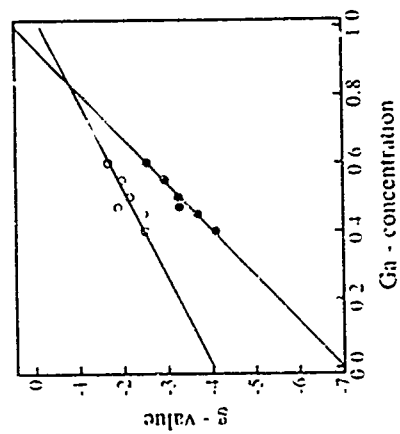


Fig. 3: The parallel (full circles) and perpendicular (open circles) components of the g -values for the different Ga compositions in $\text{Ga}_{0.9-x}\text{In}_{0.1+x}\text{As}/\text{InP}$ single quantum wells. The solid lines are linear fits to the data points

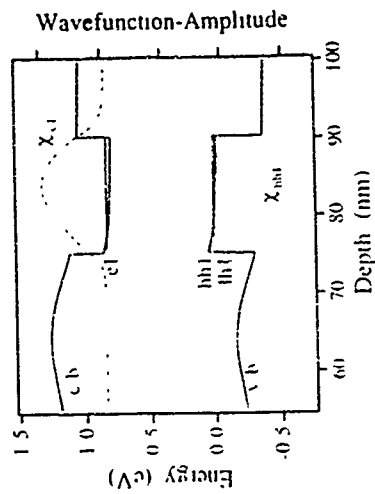


Fig. 4: Bandstructure and subband energies for a 15 nm single quantum well considering the influence of the one-sided p-modulation doping. The amplitudes of the electron (dashed curve) and hole (dotted curve) wavefunctions are indicated

Binding Energies of D Ion in GaAs Quantum Well

Y H Chang, J J Yeh*, Y M Shu, C C Wang, and T C Chen

Department of Physics, National Taiwan University, Taipei, Taiwan,
Republic of China

K H Chang, P Lee

Institute of Electronics, National Chiao-Tung University, Hsinchu, Taiwan,
Republic of China

x_{Ga}	g_1	g_2
0.40	-1.08 ± 0.01	-2.19 ± 0.06
0.15	-1.08 ± 0.01	-2.16 ± 0.06
0.17	-1.27 ± 0.01	-1.88 ± 0.01
0.50	-1.21 ± 0.01	-2.15 ± 0.01
0.55	-2.91 ± 0.02	-1.08 ± 0.05
0.60	-2.51 ± 0.02	-1.67 ± 0.01

Table 1 The g values for $Ga_{1-x}In_xAs/InP$ quantum wells with different Ga contents and a constant well width $d = 15nm$

$d(nm)$	g_1	g_2
100	-1.01 ± 0.01	-1.01 ± 0.05
15	-1.27 ± 0.01	-1.8 ± 0.01
10	-1.27 ± 0.01	-1.80 ± 0.01
8	-2.91 ± 0.01	-1.05 ± 0.04
6	-2.62 ± 0.02	-0.65 ± 0.05

Table 2 The g values for $Ga_{1-x}In_xAs/InP$ quantum wells with different thicknesses and a constant Ga composition $x_{Ga} = 0.15$

Abstract

Magnetic field dependent binding energies of D ion in the center of a 210 Å GaAs quantum well are determined from temperature dependent magneto-transport measurements. The binding energies increase from 2.1 meV at 2T to 4 meV at 8T, and are consistently higher than the transition energies obtained from magneto optics measurements performed with the same sample. We conclude from these data that in magneto-optics measurement the observed transitions are between ground and excited D states.

The properties of D ions in GaAs quantum wells have attracted much attention recently [1-9]. A D ion is a shallow impurity that binds two electrons with binding energy lower than neutral impurity (D⁰) because of Coulomb repulsion between electrons. This is a simple many electron system and is an analogue of the H ion in atomic physics. D ion can be created much easier in a quantum well system than in a three-dimensional system [10]. With shallow impurities placed both in GaAs quantum wells and in AlGaAs barriers the impurity atoms in the wells can capture an extra electron released from barrier

impurities to form a D ion. Because of the effect of quantum confinement, the binding energy of D ion in quantum well is enhanced over corresponding three dimensional D ion. For example, the binding energy of a D ion in bulk GaAs is 0.24 meV, while the binding energy of a D ion in the center of a 100 Å GaAs quantum is about 1.7 meV. In the presence of magnetic fields, the energy levels of D ion are strongly modified. From optical measurements, transitions between D ground state to other states can be observed. But there is still some controversy over whether the final states in the observed optical transitions are free electron Landau levels or excited states of D ion. In the former case, the binding energy of D ion can be easily determined from optical transition energies, while in the latter case, the binding energy of D ion can not be deduced from the transition energies directly. Here, we report our study on the activation energies of D ion in a 210 Å GaAs quantum well in the presence of magnetic field determined from transport measurements.

The sample used in this study is grown by molecular beam epitaxy with 20 layers of 210 Å quantum wells and 21 layers of 150 Å AlGaAs barriers. The center 70 Å of the wells are doped with n-type impurities of concentration $2 \times 10^{18} \text{ cm}^{-3}$ and the center 100 Å of the barriers are doped with n-type impurities of concentration $1 \times 10^{18} \text{ cm}^{-3}$. Hall pattern is defined by standard photo-lithography technique and contacts are made by alloying In dots into the sample. The sample, after being cooled down in the dark to 5K is illuminated with red LED for about one minute. The purpose of light illumination is to eject all the electrons trapped in AlGaAs into GaAs quantum well [11]. After the sample is illuminated with LED, there are $1.4 \times 10^{18} \text{ cm}^{-3}$ neutral impurity and $1.0 \times 10^{18} \text{ cm}^{-3}$ excess electrons in each quantum well if the sample is uncompensated. Because there are not enough excess electrons, not all the neutral impurities can capture an excess electron to form D ion. At low temperature, when thermal equilibrium is reached, there are $1.0 \times 10^{18} \text{ cm}^{-3}$ D ions and $0.4 \times 10^{18} \text{ cm}^{-3}$ D⁺ in each quantum wells. After LED is turned off, the sample resistance reaches a constant value in a couple of minutes. Data were then taken with constant current flowing through the sample in sweeping magnetic field and fixed

temperature. Far infrared photo-conductivity response of this sample has been published else where [6]. Both D⁺ and D related transitions can be clearly identified

Typical dependence of longitudinal and transverse resistivities, ρ_{xx} and ρ_{xy} , with magnetic field applied along crystal growth (z-) direction are depicted in Fig.1. Strong temperature dependence of ρ_{xx} and ρ_{xy} is a clear indication of activated transport. Since electron mobility in low magnetic field and low temperature is found to be around $2 \times 10^4 \text{ cm}^2/\text{V}\cdot\text{sec}$, the condition $\mu B > 1$ is satisfied and the free electron concentration (n) can be given approximately [12,13] by

$$n_s = \frac{1}{e} \frac{\rho_{xy}}{\rho_{xx}^2} B \quad (1)$$

But we also know that for thermally activated transport, n is given by $n = A \exp(-E_a/kT)$, here A is a constant, k is Boltzman constant and E_a is the activation energy. The free carrier concentration calculated according to equ. (1) for different temperature and magnetic fields, are plotted against inverse temperature in Fig.2. It is clear that n depends linearly on $1/T$ from 2 to 8T, and from the slopes of the curves magnetic field dependent activation energy can be determined. These activation energies are assigned as the magnetic field dependent binding energies of D ion in GaAs quantum wells. The justification of this assignment is that the binding energies of D ion is much lower than the binding energy of D⁺ impurity. Thus, in the temperature range studied, the conducting electrons mostly come from the process $D \rightarrow D^+ + e$. The number of free electrons released from the process $D^+ \rightarrow D^+ + e$ are too small and can be ignored. A detailed calculation taking into account the statistics of occupation of D⁺, D and free electron states is currently under study. Preliminary results indicate that the free electrons are indeed mostly come from electrons released from D ions.

The dependence of binding energies of a D ion in the center of a 210 Å GaAs quantum

well on magnetic fields are shown in Fig-3. Also shown in the figure are transition energies between D ground state ($|1S^2>$) and first excited state ($|1S^2P^1>$) obtained from magneto-photoconductivity measurements performed with sample cut from the same wafer. Here the notation of ref. 9 is used. As can be seen from Fig-3, the binding energy of D ion increases monotonically with magnetic fields and at low magnetic field region D binding energy increases faster than that in the high field region. These results are qualitatively consistent with theoretical calculation. For a quantitative comparison, we can only compare our results with available calculations for D ion in bulk GaAs and D ion in the center of a 100 Å GaAs quantum well. At $B = 6.7T$, the binding energies of D ion at the center of a 100 Å GaAs quantum well is $4.1[9] - 4.5[2]$ meV, and the binding energy of a D ion in bulk GaAs is 1.9 meV [2]. At same magnetic field, the binding energy obtained from our data is 3.8 meV which is close to the binding energy of D ion in the center of a 100 Å GaAs quantum well and is apparently quite reasonable.

From Fig-3 we can see quite clearly that the binding energies determined from transport measurements are different from the transition energies obtained from optical measurements. The optical transition energies are always higher than the transport binding energies. The differences are particularly evident in low magnetic fields. These results clearly indicate that in the optical measurements, the observed transitions are from ground to excited D states, i.e., $|1S^2>$ to $|1S^2P^1>$ transition, and not from ground D state to free electron Landau level. For if the latter is true, the binding energies obtained from optical and transport measurements will be the same. From these data, we can also conclude that the energy level of the first excited state of a D ion in a 210 Å quantum well is higher than the lowest free electron Landau level for magnetic field below 8T.

In conclusion, we have obtained the binding energies of a D ion in the center of a GaAs quantum well for magnetic field from 2 to 8T and the result is quite consistent with theoretical calculation. From comparing the transport and optical data, we conclude that the transitions observed in optical measurements are between D ground and excited states. We also show that for a D ion in a center of a 210 Å GaAs quantum well, the first excited

state of such an ion has an energy higher than the energy of ground state Landau level when the magnetic field is smaller than 8T.

This work is supported by National Science Council of the Republic of China under contract NSC-82-0208-M002-68

References

- * permanent address: AT&T Bell Lab, Murray Hill, NJ 07974, U.S.A.
- 1 S. Huang and S.P. Najda, Phys. Rev. Lett. **68**, 1486 (1990)
- 2. T. Pang and S.G. Louie, Phys. Rev. Lett. **65**, 1635 (1990).
- 3 D.M. Larsen and S.Y. McCann, Phys. Rev. B **45**, 3485 (1992).
- 4 E.R. Muller, D.M. Larsen, J. Waldman, and W.D. Goodhue, Phys. Rev. Lett. **68**, 204 (1992)
- 5. A.H. MacDonald, Solid State Commun. **84**, 109 (1992).
- 6 Y.H. Chang, T.C. Chen, C.J. Chen and Y.F. Chen, Phys. Rev. Lett. **69**, 2256 (1992)
- 7 S. Holmes, J.P. Cheng and B.D. McCombe, Phys. Rev. Lett. **69**, 2571 (1992).
- 8 A. Mandray, S. Huang, and B. Etienne, Europhys. Lett. **20**, 182 (1992).
- 9 X. Xia and J.J. Quinn, Phys. Rev. B **46**, 12530 (1992).
- 10 S.P. Najda, C.J. Armstead, C. Trager, and R.A. Stradling, Semicond. Sci. Technol. **4**, 439 (1989)
- 11 N.C. Jarosik, B.D. McCombe, B.V. Shanabrook, J. Comas, J. Ralston, and G. Wick, Phys. Rev. Lett. **54**, 1283 (1985)
- 12. R. Ransfield, J. Phys. C **4**, 2084 (1971)
- 13. J.L. Robert, A. Raymond, I. Konecny, C. Bousquet, Z. Zawadzki, F. Alexandre, I.M. Masson, J.P. Andre and P.M. Frijlink, Phys. Rev. B **33**, 5935 (1986).
- 14 to be published

Correlations of the Remote Impurity Charges -
a Method of 2DEG Mobility Tuning in GaAs/AlGaAs Heterostructures

T. Suaki, P. Winiwiaz, L.H. Dmowski, I. Gortczyca,
UNIPRESS, Polish Academy of Sciences, 01-142 Warszawa, POLAND
J. Smoliner, E. Goniak, G. Böhm, and G. Wernman,
Walter Schottky Institut, TUM, D-8046 Garching, GERMANY

Abstract

Low temperature 2DEG mobility and carrier concentration measurements made on two modulation doped GaAs/AlGaAs heterostructures are described. We demonstrate that, depending on the method which is used to populate the measurable donor states of Si-remote impurity, different values of electron mobility can be obtained for the same 2DEG density and in the same heterostructure. Concept of the correlation in the spatial distribution of the impurity charges (i.e. positively and negatively charged states of Si donor), caused by the Coulomb interactions is employed to explain our experimental finding. The invoked effect induces a strong reduction of the 2DEG scattering and can produce the mobility enhancement by as much as a factor of two over its value with a random distribution of impurity charges.

Introduction

Many attempts have been undertaken in order to improve a performance of electronic devices based on GaAs/AlGaAs heterostructures. High mobility of electrons and their high densities represent the major features important for applications. The first requirement has been achieved by means of modulation doped heterostructures (MDH) [1]. A spatial separation of donors located in AlGaAs barrier from the channel of two dimensional electron gas, 2DEG, situated in GaAs at the interface between two semiconductors, causes a substantial enhancement of electron mobility, μ . This originates in a strong reduction of efficiency of electron scattering by ionized impurities which constitutes the main mechanism limiting μ at low temperatures. With increasing a thickness of the undoped spacer, i.e. a AlGaAs layer incorporated between ionized remote donors and 2DEG, the impurity scattering is reduced (see e.g. [2]). There are two factors which determine the resulting effect: the falloff in Coulomb fields generated by individual impurities and drastic decrease of short-wavelength (large-wave-vector) potential fluctuations, which is the source of scattering by ionized impurities. However, at the same time the increase in the spacer thickness gives rise to a reduction in the concentration of 2DEG, n . The latter effect represents a drawback for many applications. Therefore, a particular design of high performance devices based on MDH, requires finding a compromise between the values of μ and n . The purpose of this paper is to point out an existence of a new mechanism which contributes significantly to the additional reduction in electron scattering by ionized impurities. It originates in a correlations in a remote-impurity-charges arrangement among the impurity sites in the doped region of AlGaAs barrier.

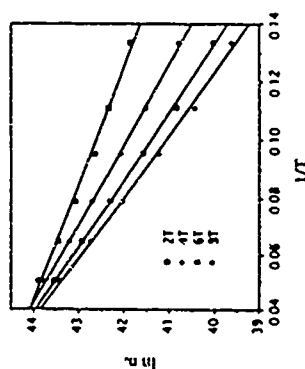


Figure 2 Temperature dependence of carrier concentration for different magnetic fields.

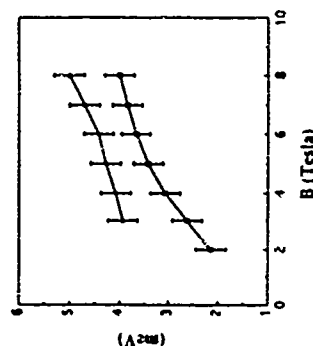


Figure 3 Binding energies obtained from transport measurements and transition energies obtained from optical measurements for a D ion at the center of a 210 Å GaAs quantum well.

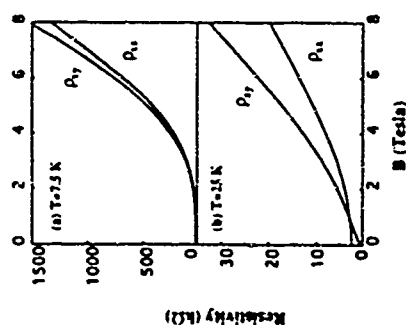


Figure 1 Magnetic field dependence of ρ_{xx} and ρ_{xy} at a) 7.5 K and b) 25 K.

It is well established now that donors in GaAs and AlGaAs form either positively charged substitutional d^+ centers or after trapping two electrons they transform to the interstitial DX^- states [3]. The latter states represent negatively charged centers. Both states of the donor take part in electron scattering by ionized impurities. Moreover, it has been demonstrated for uniformly doped bulk GaAs [4-7] and AlGaAs [8,9] crystals as well as for GaAs with δ doping [10] that the spatial arrangement of these two charge states of the donor in a dipole-like pairs of d^+ and DX^- causes a gain of crystal energy with respect to the uncorrelated arrangement of d^+ and DX^- centers. This energy gain results from minimization of Coulomb interactions between the two considered charge states of the donor. On the other hand creation of close dipoles d^+ - DX^- within the impurity region induces a strong reduction in the efficiency of electron scattering with respect to the situation when both charge states of the donor are distributed randomly.

It is natural to expect that the effect of spatial correlations in the system of remote impurity charges in GaAs/AlGaAs MDH's can cause also the effect of enhancement of μ [11]. Moreover, since an appearance of this phenomenon requires high density of impurities (empty donor centers d^+ and occupied DX^- ones should coexist in the system), a high concentration of 2DEG can be achieved in such MDH's. Concerning 2DEG mobility enhancement, it is suggestive to predict larger effect when more d^+ - DX^- dipoles appear in the doped region and smaller is a distance between d^+ and DX^- centers. We will show that this intuitive picture can be applied to the results of experiments performed on different MDH's. The decrease in efficiency of electron scattering caused by the correlations produces an increase of low temperature mobility of 2DEG as much as a factor of two or its value with a random distribution of charges.

Experiment

Experimental testing of the existence of the spatial correlation related contribution to the 2DEG transport, consists in examining of μ as a multivalued function of the 2DEG concentration, n . We will demonstrate that depending on the method of the "preparation" of the same heterostructure, various values of μ can be obtained for the same density of 2DEG. These preparation procedures utilize DX^- center metastable properties related to the existence of thermodynamic barriers for electron emission from and capture to the localized state of the donor. For Si-donor (the impurity used for doping of MDH's) the barriers block the electron transfer between two dimensional channel and DX^- states at temperatures below about 100K-160K [12]. Thus, below this temperature range the spatial arrangement of remote impurity charges, i.e. arrangement of d^+ and DX^- states, among the impurity sites freezes. Our experimental finding of different values of μ for the same n and for the same heterostructure, we interpret (by analogy with the situation for bulk GaAs and AlGaAs [7-9]) as originating from various distributions of charges among the donor sites within the AlGaAs barrier. In particular, we compare low temperature 2DEG mobilities measured for the maximum amount of spatial correlations with μ values corresponding to the situation with reduced correlations. This situation enables us to concentrate on the electron scattering by ionized impurities distributed differently in the region of the heterostructure barrier.

To alter 2DEG density (i.e., an amount of occupied DX^- centers) and μ we employed two procedures (the first one, Fig. 1, a-d, shows strong correlations, the second one, Fig. 1e and f, represents weak correlations):

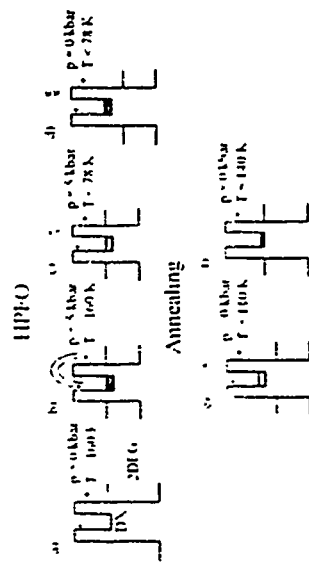


Figure 1 Schematic illustration of the procedure leading to changes in the spatial distribution of donor centers, d^+ and DX^- . (a) to (d) represent high pressure freeze-out of electrons onto DX^- states (HPFO) and (e) and (f) correspond to the annealing of heterostructures at different temperatures. Note the solid and dotted arrows which stand for free and hindered transfer of electrons between the conduction band and DX^- system due to barriers for electron emission and capture. The dashed arrows correspond to partially transparent barriers.

a) *high pressure freeze-out* (HPFO) [12,13] of electrons on the metastable DX^- states. This procedure consists in applying hydrostatic pressure at temperatures above 160K and releasing it at $T < 100K$. After applying hydrostatic pressure the donor levels corresponding to DX^- states penetrate deeper to the energy gap of AlGaAs which results in the enhanced transfer of electrons from the 2DEG to the donor states provided that the electron thermal energy exceeds the energy barrier (Fig. 1b). At temperatures below about 100K releasing the pressure does not change n because the trapped electrons cannot overpass the energy barrier between DX^- and the band states (Fig. 1c and 1d). Therefore in these pressure-induced processes of arrangement of impurity charges the minimization of their Coulomb interactions is achieved. The HPFO procedure allows to achieve the maximum value of μ for each value of n (determined by the magnitude of the freeze-out pressure). This effect was proved to reproduce μ_{max} versus n for bulk GaAs [7] and bulk AlGaAs [9].

b) *annealing*. Employing HPFO procedure makes it possible to form a reservoir of localized electrons which, at atmospheric pressure, are frozen in a metastable manner on DX^- states. Then a temperature increase in a controlled manner can modify n and the arrangement of donor charges. This consists of a subsequent annealing of the sample to temperatures above about 100K and then cooling down to 4 K or to 78K for performing measurements of n and μ . Each successive annealing step requires heating of the heterostructure to a higher temperature. Increasing temperature induces transfer of electrons from a metastable DX^- states to the two dimensional conducting channel (Fig. 1e). In the range of annealing temperatures between 110K and 140K, changes in the impurity-charges distribution are caused by the electron emission from randomly "chosen" DX^- centers. At this temperature range retrapping of electrons onto DX^- centers and thus rearrangement of their spatial positions minimizing Coulomb interactions is hindered by capture barrier. This results in a reduction in the amount of the correlations. A higher annealing temperatures causes ionization of a higher amount of DX^- states to d^+ states as

well as induction of correlations in spatial positions of impurity charges since a capture barrier becomes partially transparent (Fig. 1f). In other words, during the annealing processes both, the Fermi energy and electron kinetic energy increase leading to the decrease of the effective capture barrier. In addition, since the concentration of d^+ and 2D electrons raise significantly, the transfer of carriers from 2DEG to DX⁻ states is enhanced. One can see that the conduction band "mediates" the transfer of electrons between different DX⁻ centers leading to the appearance of the correlation effects. This situation requires that the both barriers become transparent (Fig. 1f). We have used two heterostructures with low and high value of μ (about 0.25 and $1.2 \cdot 10^6$ cm²/Vs at T=4.2K, respectively). Table 1 gives a description of the employed samples.

Table 1 Parameters of the Ga_{0.9}Al_{0.1}Ga_{1-x}As modulated heterostructures

Sample	n (T=4.2K) [10 ¹² cm ⁻²]	μ (T=4.2K) [10 ⁶ cm ² /Vs]	spacer [nm]	x [%]	doping layer thickness [nm]	density [10 ¹⁸ cm ⁻³]
H01	0.56	0.26	5	35	5	4
H70	0.365	1.16	24	29	36	2.8

Results

First, we will describe results of applying HPFO procedure to the H70 sample characterized by the higher value of μ . Open circles on Fig. 2 represent the obtained results. Increasing freeze-out pressure during subsequent sample cooling-down processes (highest pressure 5 kbar) results in the decrease of both n and μ measured at T=4.2K or at T=78K. An interplay between two effects determines the observed lowering of μ : a modification of the correlations and a decrease in efficiency of the scattering potential screening by 2DEG (lower concentration of carriers). Filled diamonds illustrate variation of μ with increasing n obtained after annealing of the sample. The first cycle of the annealing (T is raised up to about 110K) induces a decrease of μ . The origin of the μ reduction which accompanies the increase of n lies in a decrease in the amount of spatial correlations of d^+ and DX⁻ states. Thermal ionization of DX⁻ states occurs in a random manner. Consequently it leads to a more efficient 2DEG scattering due to remote impurities. The effect found here resembles behavior observed in bulk GaAs and AlGaAs [7-9]. Further annealing processes performed at higher temperatures cause a mobility increase although the "annealing branch" of the μ vs n dependence gives the mobility values lower than those obtained during HPFO. With increasing annealing temperature contributions from two additional factors influence μ value. i) increase in the 2DEG screening efficiency, ii) a process of equilibrium redistribution of electrons among the donor states. The second mechanism leads to a decrease of the crystal energy caused by inter-impurity Coulomb interactions and this results in a reestablishing of the correlations.

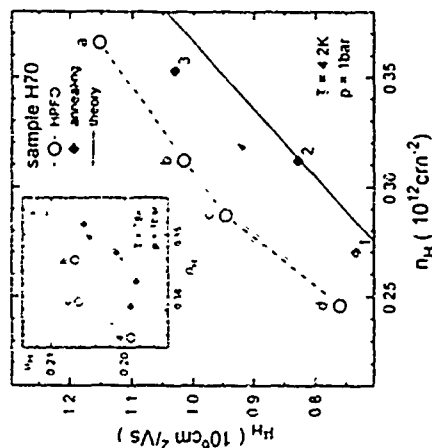


Figure 2 2DEG mobility variation with electron concentration measured at T=4.2K in the sample H70. The a, b, c branch of the plot represents a strong correlation path achieved by HPFO procedure performed at different freeze-out pressures, whereas filled diamonds correspond to a weak correlation path produced by the sample subsequent annealing. Solid lines represent results of theoretical calculations performed under the assumption of absence of the spatial correlations. The inset shows the corresponding dependence of μ versus n measured at T=78K.

Some information about the magnitude of the effect leading to mobility enhancement and originating in the spatial correlation of the donor charges can be deduced from a comparison of two μ values corresponding to the same 2DEG density. The maximum difference in the mobility values on the two branches of μ is about 30% which sets the lower limit of the examined effect. The solid line in Fig. 2 represents μ vs n for the examined heterostructure calculated under the assumption of absence of the spatial correlations [14].

To determine whether the correlation contribution to μ could be seen at higher temperatures we have repeated the same sequence of the sample preparation as described above but all measurements have been performed at 78K. The results obtained (insert in Fig. 2) clearly show that μ at 78K is approximately 6 times smaller than the value measured at T=4.2K. The gain in μ value corresponding to correlations of impurity charges at T=78K decreases in a similar manner as the absolute value of μ . This behavior results from the following effect. At higher temperatures electron scattering by phonons contributes more significantly to processes limiting 2DEG mobility. The latter effect raises the background scattering and therefore it masks changes of "unized" impurity scattering processes caused by the spatial correlation of impurity charges. At T=78K, one can expect much higher mobility gain due to this effect when MDH with a thinner spacer is employed.

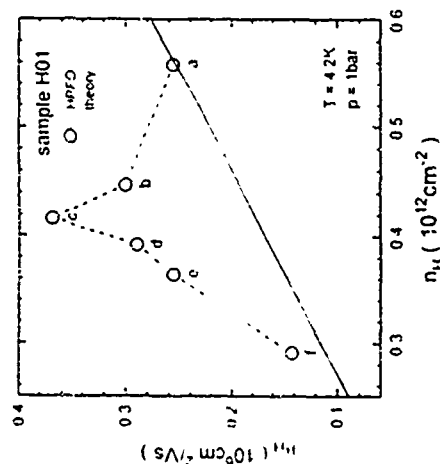


Figure 3. 2DEG mobility variation with electron concentration for the sample H01. The dashed line corresponds to the strong correlation path obtained by HPFO method. The solid line gives the results of calculations assuming that spatial correlations are absent.

The additional experimental test of correlation-related effects in GaAs/AlGaAs has been performed on the sample H01 which has the thin spacer and the low mobility value. Contrary to the usual behavior, a decrease in 2DEG concentration induced by the employed HPFO procedure causes an increase of μ in the initial stage, after which it decreases gradually (Fig. 3). The observed enhancement allows μ to reach value of $0.37 \cdot 10^6$ cm²/Vs compared with $0.26 \cdot 10^6$ cm²/Vs obtained after cooling of the sample to $T = 4.2$ K, at $p = 0$ kbar. Again we associate the origin of the μ enhancement with the spatial correlations of d^+ and DX^- states. We found a mobility increase of about 50% of its value detected after sample cooling at ambient pressure. At this early stage of HPFO the correlation related contribution to mobility increase overcompensates a decrease in the screening efficiency. The latter effect is due to the lowering of n and leads to the mobility decrease. This usual behavior of MDH is illustrated by the results of calculations neglecting correlations (see the solid line on Fig. 4). Comparison of experimentally determined μ value (maximum of correlations) with the calculated one (no correlations) gives the increase of μ by factor of two. Moreover, the result obtained for the sample H01 demonstrates that the spatial correlation induced enhancement of μ could reach its maximum value for the distribution of electrons between 2DEG and DX^- states different from that existing in the "as grown" heterostructure (i.e. during cooling at ambient pressure).

Conclusions

In conclusion, we examined variation of 2DEG mobility with carrier concentration in two different heterostructures of GaAs/AlGaAs. We have shown that depending on the way the

impurity charges are distributed among the donor sites in the AlGaAs barrier, different values of μ can be achieved for the same 2DEG density. This distribution depends in turn on a thermal treatment of the sample. The observed behavior of μ can be qualitatively attributed to changes in spatial correlation of the remote donor charges. This effect is responsible for very strong reduction of the 2DEG scattering by ionized remote impurities. The presented finding gives an important correction to understanding the electron transport in low dimensional structures [14-17]. It is very important to establish a theoretical description which gives the proper model of 2DEG scattering by ionized impurities. It would enable to incorporate the spatial correlation of impurity charges in processes of choosing parameters of the produced MDH (spacer thickness, doping density and doping profile). As it can be deduced from the results of papers by Sobkowicz et al. [10], better correlations can be achieved in a doping system of lower dimensionality. Accordingly, δ -like doping of the barrier would introduce larger reduction in a scattering efficiency due to ionized remote impurities.

Acknowledgements: We acknowledge valuable discussions with Drs. R. Potrzakowski, Z. Wilamowski and Prof. J. Kosut. This work was supported by the National Scientific Research Committee (Poland) under Project 20160 9101.

References

- [1] L. Störmer, R. Dingle, A.C. Gossard, and W. Wiegmann, *Inst. Conf. Ser. London*, **43**, 557 (1978).
- [2] G. Weinmann and W. Schlapp, *Appl. Phys. Lett.* **44**, 411 (1985).
- [3] D.J. Chadi and K.J. Chang, *Phys. Rev. Lett.* **61**, 873 (1988), *Phys. Rev. B* **39**, 10063 (1989).
- [4] E.P. O'Reilly, *Appl. Phys. Lett.* **55**, 1409 (1989).
- [5] T. Suski, P. Wiśniewski, E. Litwin-Staszewska, J. Kosut, Z. Wilamowski, T. Dietl, K. Świątek, K. Ploog, and J. Knecht, *Semicond. Sci. Technol.* **5**, 261 (1990).
- [6] J. Kosut, Z. Wilamowski, T. Dietl, and K. Świątek, *Proc. 20th Int. Conf. on the Physics of Semiconductors*, ed. E.M. Anastassakis and J.D. Joannopoulos (World Scientific, Singapore, 1990) p. 613.
- [7] D.K. Maude, L. Eaves, and J.C. Portal, *Appl. Phys. Lett.* **60**, 1993 (1992), L.H. Dmowski, B. Goulet, D.K. Maude, L. Eaves, J.C. Portal, and J.J. Harris, *Japan. J. Appl. Phys.* **32**, Suppl. 32-1, 221 (1993).
- [8] P.L. Coz, C. Ghez, and A. Pansini, *Semicond. Sci. Technol.* **8**, 13 (1993).
- [9] R. Potrzakowski, E. Litwin-Staszewska, and J.L. Robert, to be published.
- [10] P. Sobkowicz, Z. Wilamowski, and J. Kosut, *Semicond. Sci. Technol.* **7**, 1155 (1992) and *J. Phys.: Cond. Matter*, in press.
- [11] A.L. Efros, F.G. Pikus, and G.G. Samsonidze, *Phys. Rev. B* **41**, 8295 (1990).
- [12] T. Suski, E. Litwin-Staszewska, P. Wiśniewski, L.H. Dmowski, W.H. Zhuang, G.B. Liang, D.Z. Sun, and Y.P. Zou, *J. Appl. Phys.* **63**, 2307 (1988).
- [13] R. Potrzakowski, J.L. Robert, E. Litwin-Staszewska, J.P. Andre, *Phys. Rev. B* **37**, 1031 (1988).
- [14] G. Goryunov, C. Shierbisevsky, E. Litwin-Staszewska, T. Suski, J. Krupski, and K. Ploog, *Semicond. Sci. Technol.* **6**, 461 (1991).
- [15] T. Ando, *J. Phys. Soc. Japan* **51**, 3900 (1982).
- [16] F. Stern, *Appl. Phys. Lett.* **43**, 974 (1983).
- [17] W. Walukiewicz, H.E. Ruda, J. Lagowski, and H.C. Gatos, *Phys. Rev. B* **30**, 4571 (1984).

Three-Dimensional Boltzmann-Bloch Theory of Miniband Transport in Superlattices with Elastic Scattering

Rolf R. Gerhardt

Max-Planck-Institut für Festkörperforschung, Heisenbergstr. 1, D-70569 Stuttgart, Germany

Elastic scattering couples the quasi one-dimensional (1D) motion of electrons responding to an applied electric field in growth direction of a semiconductor superlattice effectively to the lateral degrees of freedom. We describe the superlattice by a simple miniband and elastic scattering explicitly by an appropriate collision term in Boltzmann's equation. As a function of the applied field, we calculate the heating of the electron system and its drift velocity, which shows pronounced negative differential conductance. Our results are qualitatively different from those of previous 1D theories, but compare favorably with results of recent experiments and balance-equation calculations.

72.20.Hi, 72.10.Fg, 73.20.Dx

Quasi-classical dynamics of Bloch electrons predicts fascinating phenomena such as Bloch oscillations and regimes with negative differential conductance (NDC), if the electrons can be forced by an applied electric field to follow the periodic band structure through a considerable region in k -space before being scattered. Whereas large Brillouin zones and wide energy bands prohibit these phenomena in natural bulk crystals, Esaki and Tsu [1] predicted a long time ago that they should become observable in semiconductor superlattices with artificial superlattices of sufficiently large lattice constants a . The prediction was that the drift velocity v_D of electrons responding to an electric field F applied in the growth (z) direction of the superlattice will decrease with increasing F , once F becomes larger than a critical value $F_{max} = \hbar v_F / ea$, at which the scattering rate ν equals the Bloch-oscillation frequency eaF/\hbar . Here $-e$ is the electron charge. A characteristic feature of this prediction is that the critical field F_{max} does not depend on the miniband width Δ . Previous generalizations of the Esaki-Tsu prediction to finite temperatures using the Boltzmann-Bloch equation in relaxation time approximation [2,3] confirmed this feature. Also Monte Carlo calculations of the drift velocity [4,5] produced no significant Δ -dependence of F_{max} and essentially confirmed the Esaki-Tsu prediction, long before it could be verified experimentally.

So far only two groups have claimed that their experiments reveal the Esaki-Tsu mechanism of miniband transport, and not hopping of electrons between localized states in adjacent wells of the superlattice. Sibille et al. [6] systematically studied stationary transport in several superlattices with different miniband widths and periods. They reported qualitative agreement with the Esaki-Tsu predictions, however, their F_{max} values seemed to decrease systematically with increasing Δ . The first direct observation of a v_D - F characteristic corresponding to NDC up to F -values far beyond the maximum, has been achieved in time-of-flight experiments by Grahm et al. [7]. They found a good agreement with the finite-temperature version of the Esaki-Tsu theory [2,3], at least for higher temperatures, $k_B T > \Delta$.

These experiments, especially the unexpected Δ -dependence of F_{max} , stimulated a renewed theoretical interest in the problem [8-10]. Lei et al. [8] applied a balance equation approach [11] to the superlattice model and reported an impressive agreement with the ex

perimental results of Ref. [6]. Similar to the Monte Carlo calculations [4,5], their calculation included explicitly the interaction of the electrons with acoustical and optical phonons as well as with randomly distributed impurities, and, in addition, the screening of these interactions. Although the ansatz of Ref. [8] is very general, it lacks transparency and does not clarify which particular interaction mechanism is responsible for the qualitative differences from the predictions of the Boltzmann-Bloch theories, notably for the Δ -dependence of F_{max} .

In order to clarify the situation and to gain a deeper physical understanding of the apparent insufficiencies of the previous Boltzmann-Bloch theories, we consider explicitly the role of elastic scattering. The basic idea is that elastic scattering by impurities or interface roughness will transfer energy, gained by the electron during its motion in the field direction, to the lateral degrees of freedom. Thus, elastic scattering will effectively render the problem a really three-dimensional one, and should be treated explicitly. In order to do this in the most simple and transparent way, we describe it by a simplified collision term in the Boltzmann-Bloch equation, in addition to the inelastic relaxation considered previously [2,3]. As in previous work [1-3,8-10], we take the tight-binding energy

$$E_z(k_z) = \frac{1}{2} \Delta (1 - \cos ak_z) \quad (1)$$

in z direction and free motion with effective mass m in the lateral directions,

$$E(k) = \frac{\hbar^2 k^2}{2m} + E_z(k_z), \quad (2)$$

with $k^2 = k_x^2 + k_y^2$.

The stationary Boltzmann-Bloch equation is written as

$$-\frac{eF}{\hbar} \frac{\partial}{\partial k_z} f(k) = -\nu_m [f(k) - f_0(E(k))] + C_d(f, k), \quad (3)$$

where the inelastic scattering rate ν_m describes relaxation towards the equilibrium distribution function f_0 . If elastic scattering is neglected, $C_d = 0$, and if non-degenerate statistics is assumed, one obtains the well known result for the drift velocity [2,3],

$$v_D = v_0 \frac{F/F_0}{1 + (F/F_0)^2} Q\left(\frac{k_B T}{\Delta}\right), \quad (4)$$

where $v_0 = -ea\Delta/2\hbar$, and $Q(t) = I_1(1/2t)/I_0(1/2t)$ with modified Bessel functions I_n . For $C_d = 0$, this theory is effectively one-dimensional, since the transverse motion (k_x) enters Eq. (3) only parametrically and drops out from Eq. (4). The maximum of v_D occurs at the electric field $F_0 = \hbar v_m / ea$, which is independent of Δ , whereas the amplitude factor Q is independent of F . The original Esaki-Tsu result follows in the limit $T \rightarrow 0$, with $Q(0) = 1$.

In order to simulate elastic scattering, we introduce in the Boltzmann equation (3) the collision term

$$C_d(f, k) = -\nu_d [f(k) - \phi_f(E(k))]. \quad (5)$$

Here

$$\Phi_j(E) = \alpha \int d^3k' \delta(E - E(k')) f(k') / D(E) \quad (6)$$

is the average of the distribution function taken over surfaces of constant energy, $E(k') = E$. $D(E)$ is the density of states, and $\alpha = 2/(2\pi)^3$. This ansatz describes forth and back scattering with equal weights between the state k and all states k' of the same energy. It effectively couples the motion in superlattice direction to the lateral degrees of freedom. Before proceeding, we stress that our 3D model is qualitatively different from the corresponding 1D model discussed by Ignatov et al. [9] (IDS). The IDS model couples the motion in z direction only to that in $-z$ direction, but not to the lateral degrees of freedom. As a consequence, the drift velocity can be calculated analytically. The result can be written in the form of Eq. (4), if one replaces v_0 with $v_0 \delta \nu = v_0 \delta \nu / \nu_{\text{tot}}$ and F_0 with $F_0 \delta \nu = \delta \nu / \nu_{\text{tot}} / \nu_{\text{tot}}$, where $\nu_{\text{tot}} = \nu_{\text{sc}} + \nu_{\text{el}}$ is the total scattering rate and $\delta \nu = \nu_{\text{sc}} / \nu_{\text{tot}}$. This model yields a suppression of the drift velocity below the value of Eq. (4). It can, however, not explain a Δ -dependence of F_{var} . Moreover, it predicts the same temperature dependence of the drift velocity as Eq. (1), namely a simple scaling factor which does not change the shape of the v_0 - F curve. For our 3D model, the drift velocity cannot be calculated analytically. With the dimensionless quantities $\epsilon = E/\Delta$ and $\xi = F/F_0$ where $F_0 = \hbar \nu_{\text{tot}} / e \Delta$, our Boltzmann equation subjected to the boundary condition $f(k_1, k_2 + 2\pi/a) = f(k_1, k_2)$ has the formal solution

$$f(k_1, k_2) = \frac{a}{\xi} e^{i k_1 x / a} \int_{-\infty}^{\infty} d\xi' e^{-i \xi' x / a} g_j(\xi(k_1, k_2')). \quad (7)$$

where

$$g_j(\xi) = (1 - r_s) f_0(\xi) + r_s \Phi_j(\xi \Delta) \quad (8)$$

and $r_s = \nu_{\text{el}} / \nu_{\text{tot}}$. Inserting (7) into the definition (6), we obtain an integral equation for g_j which can be written in the form

$$g_j(\xi) - (1 - r_s) f_0(\xi) = \frac{r_s}{\xi} \int_{-\infty}^{\infty} d\xi' \int_{-\infty}^{\infty} d\xi'' g_j(\xi - \sin^2 z + \sin^2(z + \xi u)) \quad (9)$$

Here, we have inserted the density of states, $D(E) = (2m/\pi^2 \hbar^3) z(E/\Delta)$, with $z(\epsilon) = \arcsin(\sqrt{\epsilon})$ if $0 < \epsilon \leq 1$, and $z(\epsilon) = \pi/2$ if $\epsilon \geq 1$. In view of the low electron densities in the experiments [6,7], we present numerical results only for non-degenerate statistics, $f_0(\xi) = \exp(-\xi/\theta)$, where $\theta = k_B T / \Delta$ is the reduced temperature. Figure 1 shows Φ_j for different situations. As compared with the equilibrium case ($\xi = 0$), in a stationary state with applied field ($\xi > 0$) electrons are redistributed from states with lower energy to states with higher energy. This 'heating' of the electron system is even increased, if part of the scattering is elastic. Apparently, this heating cannot be described by the equilibrium distribution at an elevated electron temperature $T_e > T$, since this would lead to a straight line in Fig. 1, because $\Phi_j = f$ if f depends on k only via the energy. The cusp behavior at $\epsilon = 1$ is, of course, closely related to the van Hove singularity of the density of states.

The drift velocity is defined by

$$v_D = \alpha \int d^3k v_z(k) f(k) / n_s, \quad (10)$$

with $v_z(k_s) = \hbar^{-1} dE_s/dk_s$. The normalization constant is the electron density,

$$n_s = \alpha \int d^3k f(k) = \int_0^\infty dE D(E) \Phi_j(E). \quad (11)$$

Since n_s in the stationary state has the same value as in the equilibrium state without applied electric field, we may replace in Eq. (11) Φ_j with f_0 . We used this sum rule for Φ_j to check our numerical results. With the formal solution (7) the integral in Eq. (10) can be evaluated to yield v_D again in the form of Eq. (4), but now with

$$Q(r_s, \xi, t) = \int_0^\infty d\xi g_j(\xi) \sqrt{\xi(1-\xi)} / \int_0^\infty d\xi z(\xi) f_0(\xi). \quad (12)$$

In the absence of elastic scattering, $r_s = 0$, one has $g_j = f_0$, and Q is independent of ξ . With $f_0(\xi) = \exp(-\xi/\theta)$ one exactly recovers Eq. (4). For degenerate statistics this factor $Q(t)$ is, of course, different. For $r_s > 0$, Q depends via ξ on the electric field. Then the shape of the v_D - F curves is different from the Esaki-Tsu result and changes with changing temperature. Two limits can easily be discussed analytically. The first is the linear response regime, $\xi \ll 1$. Here one obtains from Eq. (9) $g_j = f_0 + O(\xi^2)$. Thus, up to first order in ξ , the distribution function and the drift velocity depend only on the total scattering rate, and $Q(0, 0, t)$ is a sufficient approximation. A distinction between elastic and inelastic scattering is irrelevant in the linear response regime. The other trivial limit is that of extremely high temperatures, where $f_0(\xi)$ becomes a constant independent of ξ . In this limit the solution of Eq. (9) is the constant $g_j = f_0$, and again $Q(0, 0, t)$ is sufficient. Thus, our result should approach the 1D form (4) in the linear response regime and, for arbitrary values of ξ , in the limit of high temperatures, provided we define the scaling field as $F_0 = \hbar \nu_{\text{tot}} / e \Delta$.

In Fig. 2 we present typical results of our numerical calculations for three values of the temperature and for three values of the ratio $r_s = \nu_{\text{el}} / \nu_{\text{tot}}$, keeping ν_{tot} fixed. For $r_s = 0$ (dashed lines) we get the results of the 1D theories [1,9]: with increasing temperature the curves are reduced by an F -independent factor, but their shape does not change. For fixed reduced temperature and increasing r_s , the shape of the curves changes, the maxima are reduced and shifted to smaller values of F . This behavior is qualitatively similar to, but quantitatively different from the results of Ref. [9]. For fixed $r_s > 0$, the position of the maximum shifts with increasing temperature (or decreasing Δ) to larger values of F , so that the effect of elastic scattering is largest at low temperatures and becomes small at high temperatures. This result is qualitatively different from that of the 1D model of Ref. [9]. It is, however, in qualitative agreement with that of Ref. [8]. Systematic results for the dependence of the position F_{var} and the height $(v_D)_{\text{var}}$ of the maxima on the scattering-rate ratio r_s and the reduced band width $\Delta/k_B T$ are presented in Fig. 3. The results of the 1D model of Ref. [9] would appear in Fig. 3a as horizontal straight lines at $(F/F_0)_{\text{var}} = (1 - r_s)^{1/2}$ and in Fig. 3b as curves with the same shape as that for $r_s = 0$ (top curve), but rescaled by a constant factor $(1 - r_s)^{1/2}$.

In order to calculate the heating of the electron system, we consider the mean energy $\langle E \rangle_t$ in the stationary state, given by Eq. (10) with $v_z(k_s)$ replaced by $E(k_s)$. The result can be written as

$$\frac{\langle E \rangle_t}{\Delta} = \int_0^\infty d\xi g_j(\xi) z(\xi) / \int_0^\infty d\xi f_0(\xi) z(\xi) + \frac{1}{2} \frac{\xi^2}{1 + \xi^2} Q(r_s, \xi, t). \quad (13)$$

In thermal equilibrium, $\xi = 0$, only the first term on the r.h.s. survives, yielding $\langle E_0 \rangle = k_B T + (\Delta/2)[1 - Q(0, 0, t)]$. In the absence of elastic scattering, $r_e = 0$, only the second term contributes to the heating, since $g_j \approx f_0$. Then the increase of the internal energy density $n_s \langle E_j \rangle - \langle E_0 \rangle$ is just given by the Joule heating J^2/ρ_n , during the inelastic scattering time $1/\nu_{in}$, with $J = -en_s v_D$ the current density. It is interesting to note that this remains true if inelastic scattering is taken into account by the 1D model of Ref. [9]. For our 3D model the first term on the r.h.s. of Eq. (13) also contributes to the heating, and no analytic results are available. Numerical results are presented in Fig. 4. In all cases the heating saturates at high values of the applied field F . It is most effective for strong elastic scattering, $(1 - r_e) \ll 1$, and for low (lattice) temperature. We may define an electron temperature in the stationary state as the temperature of that equilibrium state with the same mean energy per electron.

In conclusion, we have emphasized the fact that elastic scattering makes the miniband transport through a 1D superlattice in a 3D semiconductor effectively to a 3D problem. Incorporating this into Boltzmann's equation in a simple relaxation time approximation, we obtain qualitative deviations from the results of the previously studied 1D theory. Our results are in good qualitative agreement with the very sophisticated calculation of Lei et al. [8]. Quantitative agreement cannot be expected, since our model does not contain any detailed information about scattering matrix elements or screening, and even assumes the scattering rates to be independent of energy. In principle such detailed informations could be incorporated into a Boltzmann-Bloch treatment. But this would be at the expense of transparency, and, perhaps more important, these details are not well known for semiconductors with superlattices. For a meaningful comparison with the experimental results of Shul'tet al. [6], we would have to assume that, at a given temperature, the scattering rates are the same for superlattices with different miniband widths Δ . Then we conclude from Fig. 3a that the electric field F_{max} at maximum drift velocity should decrease with increasing Δ . This is in agreement with the data of Ref. [6], but these data scatter by about 30 per cent, so that the assumption about the scattering rates becomes questionable. Therefore, we do not attempt a quantitative fit. From a rough estimate, we conclude that in their experiment the elastic scattering rate must be more than an order of magnitude larger than the inelastic one. This conclusion also applies to a very recent time-of-flight experiment by Minot et al. [12] with results which are in satisfactory agreement with our theory. Considering the experiments of Grahn et al. [7], it seems not surprising that at the relatively high temperature good agreement with the result of the 1D theory [3] is obtained, although this indicates that elastic scattering is not so predominant in this situation.

Stimulating discussions with Wolfgang Müller and Holger Grahn are gratefully acknowledged.

- [1] L. Esaki and R. Tsu, IBM J. Res. Dev. 14, 61 (1970).
- [2] F. G. Haas and E. A. Rubinshrein, Fiz. Tverd. Tela (Leningrad) 19, 1379 (1977) [Sov. Phys. Solid State 19, 800 (1977)].
- [3] R. A. Suris and S. S. Shchamkhalova, Fiz. Tekh. Poluprovodn. 18, 1178 (1984) [Sov. Phys. Semicond. 18, 738 (1984)].

- [4] D. L. Andersen and E. J. Asa, J. Appl. Phys. 44, 3721 (1973).
- [5] M. Artaki and K. Ilow, Superlattice Microsc., 1, 489 (1985).
- [6] A. Sibille, J. F. Palmier, H. Wang, and F. Mollet, Phys. Rev. Lett. 64, 52 (1990).
- [7] H. T. Grahn, K. von Klitzing, K. Ploog, and G. H. Döhler, Phys. Rev. B 43, 12094 (1991).
- [8] L. L. Lei, N. J. M. Horing, and H. L. Cui, Phys. Rev. Lett. 66, 3277 (1991).
- [9] A. A. Ignatov, E. P. Dodin, and V. I. Shakhin, Mod. Phys. Lett. B 5, 1087 (1991).
- [10] K. Huang and B. Zhu, Phys. Rev. B 48, 14404 (1992).
- [11] X. L. Lei and C. S. Ting, Phys. Rev. B 32, 1112 (1985).
- [12] C. Minot, H. Le Person, J. F. Palmier, and F. Mollet, Phys. Rev. B 47, 10024 (1993).

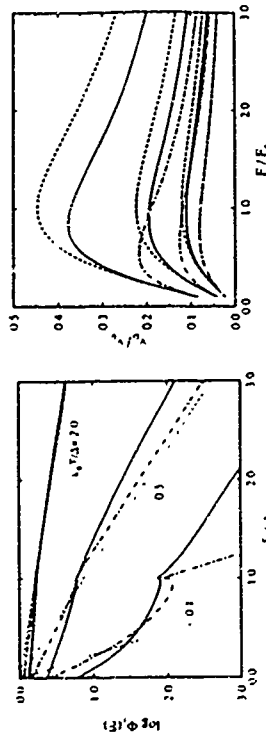


FIG. 1 Average of the distribution function over surfaces of constant energy, as defined in Eq. (6), versus energy for three values of the reduced temperature and, in each case, for thermal equilibrium $f_0(t) = \exp(-E/k_B T)$ ($F=0$, thin broken lines), for a stationary state with purely inelastic scattering ($F=F_0$, $r_e=0$, dash dotted lines), and for the stationary state with partly elastic scattering ($F=F_0$, $r_e=0.75$).

FIG. 2 Calculated drift velocity v_D versus electric field F for $r_e=0$ (dashed lines), 0.5 (solid lines), and 0.9 (dash dotted lines), and, in each case, for $k_B T/\Delta = 0.1, 0.5$, and 1.0 (from top to bottom). The units are $v_D = -n_s \Delta/2h$ and $F_0 = \hbar v_{in}/e a$, where v_{in} is fixed

Domain Formation in Modulation-doped $GaAs/Al_xGa_{1-x}As$ Heterostructures

R. Dittling and E. Schöll
Institut für Theoretische Physik
Technische Universität Berlin
Hardenbergstr. 36
D-10623 Berlin, Germany

Abstract

We develop a theory of self-organized domain formation arising in charge transport parallel to the layers of a modulation doped $GaAs/Al_xGa_{1-x}As$ heterostructure in the regime of real space transfer from the high-mobility undoped $GaAs$ layer into the low-mobility doped $Al_xGa_{1-x}As$ layer. We predict the existence of solitary travelling high-field domains associated with packets of real space transferred electrons propagating parallel to the layers with velocities of the order of $v = 2 \times 10^5$ m/s. This leads to transit time oscillations of $f = 2$ GHz for typical device dimensions of $l = 100 \mu m$ above fields of about $2 kV/cm$. Chaotic domain motion can occur under ac driving conditions.

Introduction

Negative differential conductivity (NDC) and electrical instabilities associated with parallel transport in modulation-doped semiconductor heterostructures have received much interest recently [1]-[13]. The occurrence of N-shaped current-voltage characteristics (NNDC) is due to real space transfer of hot electrons from undoped $GaAs$ to n-doped $Al_xGa_{1-x}As$ layers. At low bias U_0 applied parallel to the layers the electrons reside in the $GaAs$ channel, where they are separated from their parent donors. Therefore the mobility μ_1 of the electrons in the $GaAs$ channel will be high because of strongly reduced impurity scattering. A small electric field E_0 ($< 1 kV/cm$) will result in a current mainly due to the electrons in the $GaAs$ layer, because the carrier density and mobility in the $GaAs$ channel is much higher than in the $Al_xGa_{1-x}As$ layer. A high electric field ($\sim 2 kV/cm$) parallel to the layers induces carrier heating, and the electrons are thermionically emitted into the low-mobility (μ_2) n-doped $Al_xGa_{1-x}As$ layer, thus producing NNDC.

A physical mechanism for self-generated oscillatory instabilities under dc conditions in the real space transfer regime has been proposed in [9, 14]. The idea is based on the coupled nonlinear dynamics of real space electron transfer, the dielectric relaxation of the parallel electric field and of the space charge in the $Al_xGa_{1-x}As$ layer, which controls the interface potential barrier Φ_b [14, 15]. The spatially uniform system has been predicted to display hysteretic switching transitions between oscillatory and stationary states [16] and periodic or chaotic self-generated oscillations at frequencies of $20 - 100$ GHz [9, 14, 15]. The formation of travelling field domains has recently been predicted under current bias and an analytical description using methods of singular perturbation theory has been presented [17, 18]. In this paper we will theoretically develop the idea of domain formation due to real space transfer of hot electrons with a particular emphasis on the voltage controlled case, and present additional results on periodically driven heterostructures.

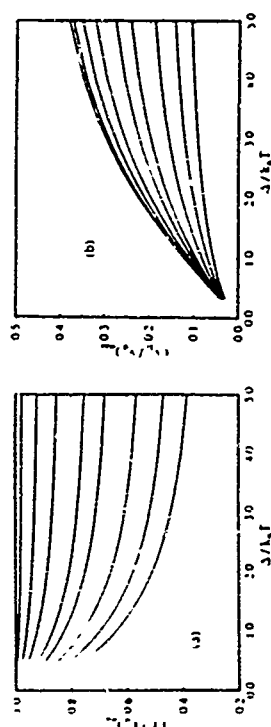


FIG. 3. Values of (a) the electric field and (b) the drift velocity at the maxima of curves as shown in Fig. 2 versus reduced miniband width for $r_s = 0.95, 0.9, 0.8, 0.7, 0.5, 0.3, 0.1$, and 0.0 (from bottom to top). For $r_s = 0$ the curve in (a) is $(F/E_0)_{max} \approx 1.0$. Symbols have the same meaning as in Fig. 2.

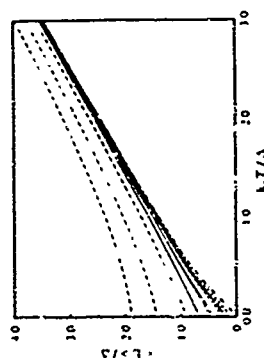


FIG. 4. Mean energy per electron vs. reduced temperature in stationary states with $r_s = 0$ (dashed line), 0.5 (solid line), and 0.95 (long dashed line), in each case for $E \approx F_0 a / h v_{th} = 0.5$, 1.0 , and 3.0 (from bottom to top), and in the thermodynamic equilibrium (dash-dotted line).

carrier concentration in transverse direction breaks down [19]. To simplify matters we have further assumed the mobility μ_i and the diffusion coefficient D_i in the GaAs to be constant, i.e. independent of the other variables. In (1)

$$j_{1 \rightarrow 2} = -en_1 \sqrt{\frac{k_B T_1}{2\pi m_1}} \exp\left(-\frac{\Delta E_c}{k_B T_1}\right) \quad (2)$$

$$j_{2 \rightarrow 1} = -en_2 \sqrt{\frac{k_B T_2}{2\pi m_2}} \exp\left(-\frac{\Phi_B}{k_B T_2}\right) \quad (3)$$

are the thermionic emission current densities (m_i^* are the electron effective masses) given by Behe's theory [19], ΔE_c is the conduction band discontinuity (Fig. 1b), and T_i ($i = 1, 2$) are the carrier temperatures. The thermionic emission theory corresponds to the following physical picture. Electrons in the GaAs with energy less than ΔE_c cannot penetrate into the adjacent $\text{Al}_i\text{Ga}_{1-i}\text{As}$ layer; all electrons with higher energy are emitted across the barrier without collisions. This assumption is correct only within a certain regime that is of the order of the mean free paths of electrons. If the GaAs/ $\text{Al}_i\text{Ga}_{1-i}\text{As}$ layers are wider, the thermionic emission current represents the current only close to the interface, and perpendicular diffusion (transverse dissipation of carriers in the $\text{Al}_i\text{Ga}_{1-i}\text{As}$ layer) will play a major role [2].

Intervalley transfer has been shown [20, 21] to be negligible compared to real space transfer at electric fields $\leq 4 \text{ kV/cm}$. This means that the transport processes are dominated by the Γ -valley in our case. At higher electric fields ($\sim 8 \text{ kV/cm}$) intervalley scattering will become more important.

Quantum effects like the quantum-transmission coefficient or tunneling through the barrier are also disregarded, of discussion in Ref. [20]. Size quantization effects, which arise if the layer widths are smaller than 100 \AA , are also neglected, since the current-voltage characteristic is not essentially affected by the quasi-two dimensional subbands below the barrier, except that the critical field for the onset of real space transfer is shifted to higher values [5].

As shown in Ref. [17] the dielectric relaxation of the parallel electric field is given by the balance of displacement current, total current, and conduction current:

$$\epsilon_0 \epsilon_s \frac{\partial E_{\parallel}}{\partial t} = j_{\parallel} - \frac{1}{L_1 + L_2} \left((m_1 \mu_1 L_1 + e n_1 \mu_1 L_1) E_{\parallel} + e D_1 L_1 \frac{\partial n_1}{\partial y} \right) \quad (4)$$

where ϵ_0 , ϵ_s are the absolute and relative permittivity, and the spatially averaged carrier concentration $n_i(y, t) = \int_{-L_i}^{L_i} n_i(x, y, t) dx / L_i$ in the $\text{Al}_i\text{Ga}_{1-i}\text{As}$ layer can be expressed by the averaged Poisson eq. $e n_i \epsilon_s \partial E_{\parallel} / \partial y = e (N_D - n_2) L_2 - n_1 L_1) / (L_1 + L_2)$ where N_D is the donor concentration in the $\text{Al}_i\text{Ga}_{1-i}\text{As}$. In (4) $j_{\parallel}(t) = \int_{-L_1}^{L_1} j_{\parallel}(x, t) dx / (L_1 + L_2)$ is a first integral equal to the current density flowing through the external circuit and is determined by the particular external circuit used in the experiment. For a resistive circuit as shown in Fig. 1a $j_{\parallel}(t)$ is determined by Kirchhoff's law such that the applied bias voltage $U_0 = \epsilon_0 \partial \phi / \partial t$ is a constant: $j_{\parallel}(t) = \sigma_1 (\epsilon_0 - \int_{-L_1}^{L_1} \epsilon_1(y, t) dy / l)$ where l is the sample length, $\sigma_1 = l / (A R_1)$ is connected to the load resistance R_1 , and A is the cross section of the current flow. Voltage bias means that $1/\sigma_1$ can be chosen arbitrarily small which reduces Kirchhoff's law to an

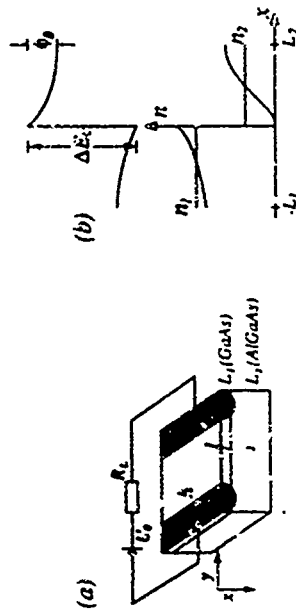


Figure 1: (a) Schematic sample and circuit configuration of a modulation doped GaAs/ $\text{Al}_i\text{Ga}_{1-i}\text{As}$ heterostructure with heterolayer widths L_1 and L_2 , respectively, and lateral dimensions h_1, l . (b) Energy-band diagram (top) and carrier density (bottom) versus the perpendicular coordinate x of the heterolayer (schematic).

Experimental evidence of spontaneous current oscillations of 1 GHz and static or slowly propagating high field domains in modulation-doped multilayer heterostructures has been reported recently under dc conditions [1].

Model

In our simple analytical model we describe the heterostructure by a set of local variables, whose time evolution is given by nonlinear transport equations coupled to Maxwell's equations. On a mesoscopic level we use a set of nonlinear partial differential equations for the carrier densities n_1, n_2 in the two layers of widths L_1, L_2 , for the dielectric relaxation of the applied lateral field E_{\parallel} and for the potential barrier Φ_B in the $\text{Al}_i\text{Ga}_{1-i}\text{As}$ layer as a function of the lateral coordinate x (the direction parallel to the layer interface) and the time t (see Fig. 1). The differential equations can be obtained by integrating the equation of continuity and the momentum and energy transport equations over the space coordinate x in transverse direction and neglecting spatial dependence in the z direction [17, 18]. The spatially averaged carrier density in the GaAs layer $n_i(y, t) = \int_{-L_i}^{L_i} n_i(x, y, t) dx / L_i$ as a function of t and y is then governed by the averaged continuity equation

$$\frac{\partial n_i}{\partial t} + \frac{1}{L_i} (j_{1 \rightarrow 2} - j_{2 \rightarrow 1}) + \mu_i \frac{\partial}{\partial y} (n_i E_{\parallel}) + D_i \frac{\partial^2 n_i}{\partial y^2} \quad (1)$$

where we have assumed that the carrier concentration and the parallel electric field are smoothly varying functions in the direction perpendicular to the layer interface. Eq. (1) is correct only within a finite distance from the heterojunction barrier which is comparable to the mean free distance of collisionless flight of the electrons. Far from the semiconductor barrier the average velocity of the carriers in the x direction is much smaller due to enhanced collisions with phonons, and the assumption of a nearly constant

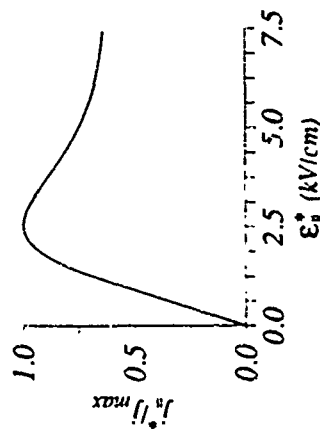


Figure 2: Static current density characteristic. The numerical parameters are listed in Table 1

Integral constraint for $\epsilon_1(y, t)$

$$U_0 = \int_0^l \epsilon_1(y, t) dy. \quad (5)$$

The dielectric relaxation of the interface potential barrier $\Phi(y, t) = -\int_0^y \epsilon_1(x, y, t) dx$ is governed by the space-charge dynamics in the $\text{Al}_x\text{Ga}_{1-x}\text{As}$ layer and the resulting internal electric field $\epsilon_1(x, y, t)$. As discussed in [17] the dynamic eq. for $\Phi(y, t)$ can be obtained by integrating the dielectric relaxation eq. for the perpendicular electric field ϵ_1 together with Poisson's eq. and the boundary conditions $\epsilon_1(-L_1, y, t) = \epsilon_1(L_2, y, t) = 0$:

$$\frac{\partial \Phi(y, t)}{\partial t} = -\frac{e n_0 N_D}{\epsilon_0 \epsilon_1} \Phi_1 + \frac{\partial^2}{\partial y^2} \left(\frac{\epsilon}{\epsilon_0 \epsilon_1} (N_D - n_1) L_2 - L_1 \frac{\partial \epsilon_1}{\partial y} \right) + \mu_0 \Phi_2 \frac{\partial \epsilon_1}{\partial y} \quad (6)$$

The steady uniform state (denoted by an asterisk) of (6) is given by $\Phi_0^* = e^2 L_1^2 n_1^2 / (2 \epsilon_0 \epsilon_1 N_D) = e^2 N_D L_1^2 / (2 \epsilon_0 \epsilon_1)$, which corresponds to the depletion approximation in the $\text{Al}_x\text{Ga}_{1-x}\text{As}$ layer within the effective depletion width $L_2 = n_1 L_1 / N_D$. The energy transfer between the heterolayers is described by the energy-balance equation containing Joule heating, convective, diffusive, and electron-pressure induced heat flow, and energy loss due to polar-optical-phonon scattering [9]. Adiabatic elimination of the mean energy and neglecting spatial derivatives yields in a first order approximation

$$T_1 = T_L + \frac{2}{3k_B} n_1 e \mu_0 \epsilon_1^2, \quad T_2 = T_L + \frac{2}{3k_B} n_2 e \mu_2 \epsilon_2^2 \quad (7)$$

with the lattice temperature T_L and the energy relaxation times τ_1 in the GaAs-channel and τ_2 in the $\text{Al}_x\text{Ga}_{1-x}\text{As}$ layer. The model equations (1), (4) and (6) represent a simplified description of the complex transport phenomena between the semiconductor layers at high electric fields. These

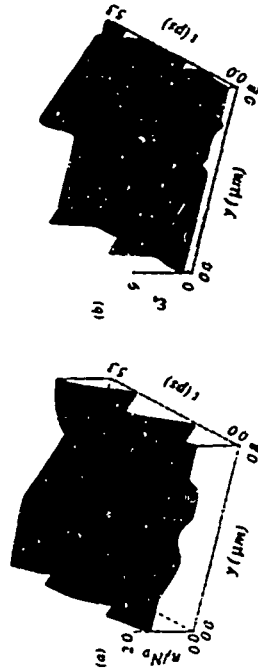


Figure 3: Travelling domain under voltage bias ($\epsilon_0 = 2.1 \text{ kV/cm}$, $R_L = 0$) and periodic boundary conditions (a) Carrier density distribution in the GaAs layer. (b) Corresponding high field domain of the parallel electric field. The lateral electric field is in units of kV/cm . (Calculated with the Parameters of Table 1).

equations have to be solved on a segment $0 < y < l$, with suitable boundary conditions that depend on the nature of the metal-semiconductor contact [22].

Travelling Domains

The homogeneous stationary states of the system are obtained by setting the spatial and temporal derivatives in (1), (4) and (6) equal to zero. The resulting static current-density-field characteristic is shown in Fig. 2. Real space transfer of hot electrons leads to a N-shaped characteristic with a regime of negative differential conductivity [17, 18]. The critical field for the onset of NDC is of the order of 2 kV/cm .

The uniform dynamical system which is obtained by neglecting the spatial derivatives in (1), (4) and (6) shows spontaneous current and voltage oscillations at frequencies of 100 GHz for a large enough load resistance R_L [17]. In the voltage controlled regime ($R_L \rightarrow 0$), however, no temporal instabilities occur.

The numerical solution of the full coupled partial differential equations (1), (4) and (6) with periodic boundary conditions under voltage controlled conditions exhibits spatio-temporal instabilities and is shown in Fig. 3. We have modelled the semiconductor by identical sections of length d joint by periodic boundary conditions neglecting the influence of the metal-semiconductor contacts at $y = 0$ and $y = l$. Nevertheless our solutions are expected to represent reasonable approximations of the full problem away from the contacts.

In Fig. 3a an initial small perturbation develops into a propagating depletion pulse of real space transferred electrons in the GaAs-channel. In the $\text{Al}_x\text{Ga}_{1-x}\text{As}$ the emitted carriers form an accumulation pulse moving with the same velocity as the depletion pulse in the GaAs. This can be explained by the following physical picture: A large enough local fluctuation of the electric field leads to real space transfer of hot electrons into the $\text{Al}_x\text{Ga}_{1-x}\text{As}$ layer. Because of the different mobilities in the semiconductor layers, the

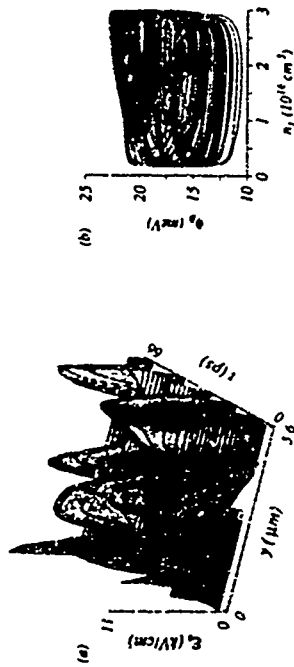


Figure 4: Chaotic domain for a driven system with $E_0 = 1.8 \text{ kV/cm}$, $E_s = 1.188 \text{ kV/cm}$ and $f_s = 75.41 \text{ GHz}$. (a) High field domain of the lateral electric field. (b) Phase plot of Φ_y vs n_1 at $y = d/2$. Parameters as in Table 1 except for $L_1 = 100 \text{ Å}$, $L_2 = 600 \text{ Å}$, $N_D = 10^{16} \text{ cm}^{-3}$, $\mu_1 = 10^4 \text{ cm}^2/\text{Vs}$, $\tau_1 = 2 \times 10^{-12} \text{ s}$ and $\tau_2 = 1 \times 10^{-12} \text{ s}$.

carrier fluctuation in the GaAs-channel moves fast with the electric field and is readily damped out due to lateral diffusion, while the emitted carrier fluctuation in the $\text{Al}_x\text{Ga}_{1-x}\text{As}$ layer remains almost unchanged. The local increase of the carrier density in the $\text{Al}_x\text{Ga}_{1-x}\text{As}$ diminishes the positive space charge controlling the band bending. The potential barrier Φ_s decreases therefore with some delay due to the finite dielectric relaxation time. This leads to an increased backward thermionic emission current, which decreases the carrier density and increases the space-charge and the potential barrier Φ_s in the $\text{Al}_x\text{Ga}_{1-x}\text{As}$. This local process of real space transfer of hot electrons in the $\text{Al}_x\text{Ga}_{1-x}\text{As}$ layer and backward emission into the GaAs channel can lead to a stable disturbance of carriers which cycle between the two semiconductor layers while the solitary pulse moves with constant velocity from the cathode to the anode.

In Fig. 3b the corresponding high field domain is shown under voltage bias for periodic boundary conditions. The velocity v of the propagating domain is of about $2 \times 10^8 \text{ m/s}$ and the pulse width is of the order of $0.2 \mu\text{m}$. For different parameters as in Table 1 we obtain similar results for the velocity of the travelling domains. These domains lead to transit time oscillations of $f = 2 \text{ GHz}$ for typical device dimensions of $l = 100 \mu\text{m}$ above fields of 2 kV/cm . As compared to the case of current bias [17, 18], the depletion pulse is less pronounced and narrower, but the domain propagation velocity is similar. More complex nonlinear phenomena occur when the semiconductor heterojunction is connected to a periodically driven voltage bias. In this case eq. (5) becomes

$$U_0 + U_A \sin(2\pi f_A t) = \int_0^l \epsilon_A(y) dy \quad (8)$$

where U_A is the amplitude and f_A is the frequency of the driving force. Depending on U_A and f_A we find quasiperiodic, frequency locked and chaotic states. Fig. 4 shows the spatio-temporal dynamics of a chaotic domain. The chaotic attractor has been generated

Table 1: The numerical parameters used in the simulation

N_D	10^{17} cm^{-3}
L_1	100 Å
L_2	200 Å
μ_1	$8000 \text{ cm}^2/\text{Vs}$
μ_2	$50 \text{ cm}^2/\text{Vs}$
T_L	300 K
ΔE_L	$250 \text{ meV} (\lambda = 0.3)$
m_1^*	$0.067 m_0$ (m_0 free electron mass)
m_2^*	$(0.067 + 0.083 \times x) m_0$
τ_1	$1.8 \times 10^{-12} \text{ s}$
τ_2	$6.4 \times 10^{-12} \text{ s}$
h	1 nm
ϵ_s	$12 \epsilon_0$

by an intermittency catastrophe of a torus. The topological property of this catastrophe is that the torus (which exists before the bifurcation event) lies inside the chaotic attractor (which exists after the bifurcation) [23].

Conclusion

The spatio-temporal self-organization due to real space transfer of hot electrons in modulation-doped heterostructures has been investigated theoretically on the basis of a system of nonlinear transport equations. Our model predicts stable solitary travelling domain solutions under voltage bias as well as under current bias. The high-field domains are connected with moving packets of real space transferred electrons, and propagate with velocities of about $2 \times 10^8 \text{ m/s}$ which typically correspond to oscillations in the GHz regime. These propagating domain solutions may serve as an explanation for the current oscillations observed at electric fields below the onset of intervalley transfer in semiconductor heterostructures [1, 2].

References

- [1] N. Balkan, B.K. Ridley and A. Vickers (eds.), Negative Differential Resistance and Instabilities in 2-D Semiconductors, Plenum, New York (1993).
- [2] B.K. Ridley, Rep. Progr. Phys. 54, 169 (1991).
- [3] Z.S. Gribnikov, Sov. Phys. Semicond. 6 1204 (1973).
- [4] F. Pacha, F. Paschke, Electron. Commun. 32, 215 (1978).
- [5] K. Hess, H. Morkoc, H. Shichijo, and B.G. Streetman, Appl. Phys. Lett. 35, 469 (1979).
- [6] H. Shichijo, K. Hess, and B.G. Streetman, Sol. State Electron. 23, 817 (1980).
- [7] P.D. Coleman, J. Freeman, H. Morkoc, K. Hess, B.G. Streetman, and M. Keever, Appl. Phys. Lett. 40, 493 (1982).
- [8] R. Sakamoto, K. Akai, and M. Inoue, IEEE Trans. Electron Devices 36, 2344 (1989).

MoP31

Inside a 2D Electron System: Images of Potential and Dissipation

R. Knott, W. Dietzsch, K. V. Klitsing, K. Eberl, K. Ploog,
MPI für Festkörperforschung, 70506 Stuttgart, FRG

ABSTRACT

Lateral potential distributions in two-dimensional electron systems are imaged under magnetotransport conditions with an electrooptic method. In low mobility δ -doped samples, the results agree with a classical picture in the ohmic regime. For high currents, a uniform breakdown is found. In high-mobility modulation-doped heterostructures, the change in the potential distribution at breakdown is strongly asymmetric upon current reversal.

INTRODUCTION

Two-dimensional electron systems (2DES) are established as the basis of various practical devices. In semiconductor heterostructures, remarkable microscopic qualities have been achieved. In addition, macroscopic homogeneity of the layers is also regarded essential for successful applications. Relative resistivity gradients around 0.005/nm have been reported on 3rd wafers [1].

In basic research, there has been much magnetotransport work on 2DES. Alloyed contacts are employed to feed the current and to sense the voltages. Global resistances can be extracted from these experiments, but their connection to the local resistivities has been unclear for some time [2]. Currently, there is a lot of discussion on the validity and usefulness of global and local descriptions of magnetotransport.

Alloyed contacts in the interior of a piece of 2DES have yielded some local information [3]. However, they are not flexible enough to yield a comprehensive picture of the potential distribution inside the 2DES. Furthermore, it is possible that these internal contacts will act as reservoirs or inject current. Clearly, a contactless spatially resolving method is desirable to investigate the previously marked degrees of freedom in the transport.

EXPERIMENTAL METHOD

Fortunately, optical measurements of electric potentials are possible by virtue of the linear electrooptic (Pockels) effect. In the present context, the electrooptic method has been introduced by Fontijn et al. [4].

The following optical setup (figure 1) is used. Subbandgap light from a collimated laser diode (850 nm, 2 mW) is circularly polarized by the calcite polarizer P and the appropriately set Soleil-Babinet compensator SBC. As it passes through the GaAs sample, it acquires some ellipticity [5]. We look at the light reflected from the gold coated rear side of the sample S, which also serves as a reference electrode. The front side electrode is provided by the structured and contacted 2DES itself. The

now at PDI für Festkörperelektronik, 10117 Berlin, FRG.

- [9] K. Aoki, K. Yamamoto, N. Mugibayashi, and E. Schöll, *Sol. State Electron* **32**, 1149 (1989).
- [10] A. Katsalisy, M. Milshstein, L.G. Shantharama, J. Harblson, and L. Florez, *Sol. State Electron* **32**, 1841 (1989).
- [11] A.J. Vickers, A. Straw, and J.S. Roberts, *Semicond. Sci. Technol.* **4**, 743 (1989).
- [12] P. Hendriks, E.A.E. Zwaal, J.G.A. Dubois, F.A.P. Blom, and J.H. Wolter, *J. Appl. Phys.* **69**, 362 (1991).
- [13] S. Luryi and M.R. Pinto, *Phys. Rev. Lett.* **67**, 2351 (1991).
- [14] E. Schöll and K. Aoki, *Appl. Phys. Lett.* **59**, 1277 (1991).
- [15] E. Schöll and K. Aoki, *Proc. 20th Int. Conf. Physics of Semiconductors*, ed. E.H. Anastassakis and J.D. Joannopoulos, p. 1125, World Scientific, Singapore (1990).
- [16] R. Dörling and E. Schöll, *Phys. Rev. B* **45**, 1935 (1992).
- [17] R. Dörling and E. Schöll, *Physica D* (1993) in press.
- [18] R. Dörling and E. Schöll, in: *Negative Differential Resistance and Instabilities in 2-D Semiconductors* eds N. Balkan, B.K. Ridley and A. Vickers, Plenum, New York (1993).
- [19] K. Hess, *Advanced Theory of Semiconductor Devices*, Prentice Hall, New Jersey (1989).
- [20] K.F. Brennan and D.H. Park, *J. Appl. Phys.* **65**, 1156 (1989).
- [21] T.H. Glisson, J.R. Hauser, M.A. Littlejohn, K. Hess, B.G. Streetman and H. Shichijo, *J. Appl. Phys.* **51**, 5445 (1980).
- [22] L.L. Bonilla and S.W. Telesworth, *Physica D* **50**, 545 (1991).
- [23] J.M.T. Thompson and H.B. Stewart, *Nonlinear Dynamics and Chaos*, J. Wiley, Chichester (1986).

reflected light is separated from the incident beam by the beam splitter BS and analyzed by the calcite analyzer A. A silicon photodiode PD serves as a detector. Its photocurrent is analyzed synchronously with the AC current through the sample (FETs). For a plane incident wave and a homogeneous electric field the AC photocurrent is then proportional to the electrostatic potential difference between the front and the rear side of the crystal.

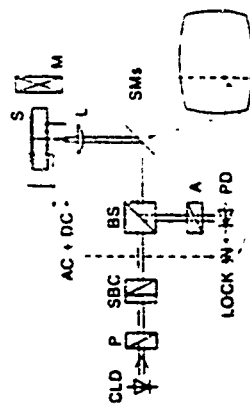


Figure 1. Schematic of the experimental setup. Symbols are mentioned in the text. The sample S and the lens L are immersed in superfluid helium in the bore of the superconducting magnet M.

To obtain spatial resolution, the laser beam is raster scanned across the sample surface by the galvanometer scanners XMs under computer control and focused onto the sample by the adjacent lens L. The AC photocurrent measured at each sample spot is displayed as the brightness a pixel on the computer screen.

In our setup, we deduce a spatial resolution of 20 μm . The potential resolution is around 3 mV/V_H, depending on the received optical power. These experimental values are sufficient for investigation of the Quantum Hall effect in the low current regime.

In practice, it is important to avoid any parallel channel bypassing the 2DES. Such a bypass would act as an undesired frontgate altering the electrostatic boundary conditions in the structure. Since electrooptics measures the potential difference between the front and back side of the sample, a parallel channel will mask the potential distribution in the 2DES.

LOW MOBILITY SAMPLES

Delta-doped layers [6] are an example of low mobility 2DES which intrinsically avoid parallel channels. We have prepared such layers by molecular beam epitaxy on [100] GaAs substrates. Upon a 500nm buffer layer a Si doping layer of $n = 7 \cdot 10^{16} \text{ cm}^{-3}$ was accumulated, which was in turn capped with 100nm GaAs. A Hall bar structure with dimensions $0.5 \times 1.5 \text{ mm}^2$ was defined using photolithographic techniques. Ohmic contacts were processed by alloying AuGe-Ni. On the polished rear side of the wafer, a

200nm Au layer was evaporated onto a 10nm Cr seed layer. When cooled in the dark to 1.5K, no conductivity was measurable. Upon illumination in the cold by a broadband visible source (intensity 10 mW/cm^2) however, a (quasi) 2DES was established with a density of $5.5 \cdot 10^{11} \text{ cm}^{-2}$ and a mobility of $2000 \text{ cm}^2/\text{Vs}$, as deduced from Hall measurements.

Such δ -doped layers are known to exhibit the Quantum Hall effect at low integer filling factors [7]. Experimentally, we find a broad plateau centered around $1/2$ in the magnetotransport trace, which is quantized to better than 1% at currents below 10nA. It is accompanied with a minimum in the longitudinal resistance of $\approx 500\Omega$. This rather large value clearly reflects the short elastic scattering times in the δ -layer.

A set of electrooptic images taken at $T = 1.5 \text{ K}$ is depicted as unprocessed data in figure 2. The current contacts are situated at the left and at the right hand side of the indicated 2DES area. Four additional voltage probe contacts are also discernible at the top and at the bottom side of the Hall bar. The measured potential difference between the front and rear side of the sample is brightness coded.

The upper picture was obtained without an applied magnetic field ($B = 0$). The AC current amplitude was 35nA. On the whole, a linear potential drop is recognized from the left to the right. This is just the result expected for a homogeneous conductor. A closer look at the image reveals, however, deviations from the ideal potential picture. They may be either due to uncorrected transmission inhomogeneities in the optical system or due to inhomogeneities in the conducting sheet. This point will be worked out further in connection with the measurements in a magnetic field.



Figure 2.

Electrooptic images of the potential distribution in a δ -doped layer. $I_{AC} = 35 \text{ nA}$, $T = 1.5 \text{ K}$.

B=0.

B=7T.

B=10.8T.

The central picture was taken in a magnetic field of 7T (filling factor 3.1) corresponding roughly to $\omega_c/\omega = 1$, where τ is the zero field scattering time. The current amplitude was 27 μ A. The potential distribution expected is reproduced quite nicely in the measurement: in the central part of the sample the equipotential lines intersect the sample boundaries with an angle of 45°. This is consistent with homogeneous current flow in this region and a Hall angle of 45°. Approaching the current contacts, the equipotentials tilt towards the injecting boundary to match the potential distribution in the contacts [8].

In the bottom picture of figure 2, the magnetic field was increased to 10.8T, which is the center value of the broad Hall plateau. From $\omega_c/\omega = 1$ a Hall angle of 56° is expected. Experimentally, however, an angle close to 90° is found in the central part of the sample assuming a homogeneous current flow in this area. This angle is in agreement with the minimum in the longitudinal resistance, which is typical for the QMx. Close to the current contacts the equipotentials converge towards a corner. Such a pattern is necessary to fit the potential distribution in the low resistivity contact.

The Hall potential drop, which is uniform and linear in the center of the sample, is confined to a narrow range close to the current contact. The whole current also has to transverse this narrow range. Therefore, the dissipating region is highly localized, as revealed by previous thermography experiments [9].

A closer look at the image reveals that the Hall bar cannot be perfectly homogeneous. Especially, the electric field vector between the voltage probes on the right side is not parallel to that in the center of the sample. This behaviour was even more pronounced in nonlinear transport experiments.

As an example, a bias current of 90 μ A was applied in figure 3 (B=10.8T). Transport measurements yield an increase of the longitudinal resistance from 5000 to 3k Ω . On the left of the image, the potential pattern is now very similar to that at B=7T. Obviously the conductivity is increased. On the right of the image the equipotential lines experience an odd distortion, which also depends on the bias polarity. Evidently, the current distribution in the sample is strongly inhomogeneous making the extraction of a Hall angle from the potential distribution alone impossible. We take this as an indication of a small density inhomogeneity in the sample.



Figure 3.

Potential distribution in the i-layer at large current.
B=10.8T, I_{DC} =90 μ A, T=1.6K.

HIGH MOBILITY SAMPLES

To compare the findings with experiments on high mobility 2DES, we have prepared samples of modulation-doped heterostructures by MBE. An undoped Al_{0.3}Ga_{0.7}As spacer upon the GaAs buffer separates the ionized Si donors from the 2D channel to achieve high mobility. All other sample processing steps were done as mentioned above for the δ -layers.

The sample for the electrooptic experiments was selected to show no conduction bypassing the 2DES under a variety of illumination conditions. When cooled in the dark, no conductivity was found in the heterostructure. Exposure to ambient light (intensity = 1mW cm⁻²) yielded a carrier density of $3.7 \cdot 10^{11}$ cm⁻² with a mobility of 50000 cm²/Vs. Magnetotransport traces show pronounced quantized Hall plateaus and accompanying zeros of the SdH voltage, as usual in samples of high quality. Critical current densities for breakdown of the QHE were around .5 A/m for filling factors 2 and 4 and for channel widths between 50 and 400 μ m.

In figure 4, electrooptic images are shown for filling factor 2 at T=1.6K. The boundaries of the 2DES (width 200 μ m) are indicated. Only a part of the structure is shown, with one current contact at the left of the images and a connection to a larger 2DES at the right. Current polarities refer to that contact. In figure 4a, there is a DC bias of 140 μ A with a square wave modulation amplitude of 30 μ A. In figure 4b, the bias polarity is reversed. The current values are switched between just below breakdown and far above it to enhance the contrast.

Contrary to the I-V characteristics, there is a large asymmetry in the potential distribution. With positive bias, the breakdown voltage drop occurs immediately after the current contact. The Hall potential drop then gradually moves from the upper to the lower side of the bar. On the right of the picture, the potential profile is homogeneous. With negative bias, the Hall potential drop always remains on the upper side of the sample, while the longitudinal drop occurs on the right of the strip. The overall behaviour of the potential distribution is obviously entirely different from the low mobility case discussed above. Its understanding will require a more elaborate picture than e.g. [9].

The dissipative current entry/exit point is always in the upper left corner of the sample. But since the potential landscape in its surroundings is different for both bias polarities, the asymmetry in the power dissipation reported in [9] is understandable.



Figure 4.

Potential distribution in a heterostructure sample.
Filling factor 2, T=1.6K.
(upper) I_{DC} =140 μ A,
(lower) I_{DC} =-140 μ A.
Polarity with respect to left current contact.

SUMMARY

The electrooptic technique has thus proven to be powerful in revealing the potential distributions in 2DES under magnetotransport conditions. In the low mobility 4-layers, the change in the potential landscape from zero to quantizing magnetic field has been analyzed and found to accord with conventional descriptions. Images of breakdown situations have revealed a reduction of the Hall angle back to 45° and a pronounced tendency towards density inhomogeneities. In high mobility heterostructures, potential distributions not envisaged previously have been encountered. They demonstrate the variability of the internal degree of freedom in two-dimensional magnetotransport.

REFERENCES

1. G. Böhm et al., J. Crystal Growth 127, 81 (1993).
2. J. Wakabayashi and S. Kawaji, J. Phys. Soc. Japan 44, 1839 (1979).
3. G. Ebert et al., J. Phys. C 18, L257 (1985).
4. P. Fontein et al., Phys. Rev. B 43, 12090 (1991).
5. A. Yariv and P. Yeh, Optical Waves in Crystals, Wiley, New York (1984).
6. K. Ploog, J. Crystal Growth 81, 304 (1987).
7. A. Zrenner et al., Semicond. Sci. Technol. 2, 1132, (1988).
8. B. Heudecker and K. Hoffmann, Solid State Comm. 62, 135 (1987).
9. U. Kläss et al., Z. Phys. B 82, 351 (1991).

DC Transport in Intense, in-Plane, Terahertz Electric Fields in AlGa_{1-x}As Heterostructures at 300 K

N. G. Amar, A. G. Markelz, and E. G. Gwinn
Center for Free-Electron Laser Studies and Department of Physics,
University of California, Santa Barbara California 93106

P. F. Hopkins and A. C. Gossard
Department of Electrical and Computer Engineering,
University of California, Santa Barbara California 93106

We report on K studies of the dependence of the in-plane, dc conductivity, $\sigma_{xx}(E_{\text{ap}})$, of a quasi 2D electron gas on the amplitude E_{ap} and frequency of intense far infrared fields ($\omega/2\pi = 0.24 - 3.5$ THz). We measure $\sigma_{xx}(E_{\text{ap}}, E_{\text{dc}})$ where E_{dc} is a small sensing field, and observe a monotonic decrease in σ_{xx} with increasing E_{ap} . Although a simple scaling analysis yields the measured $\sigma_{xx}(E_{\text{ap}})$ data into a single curve for frequencies from 0.25 to 4.5 THz (at low to moderate scaled fields), the decrease in conductivity is substantially more rapid than expected from comparison to similar data taken by Maslovskii et al [1] at 15 GHz. We tentatively attribute this difference to effects of a high frequency modulation in the electron temperature.

Development and application of high-speed devices made from modulation-doped semiconductor heterostructures require a better understanding of transport in large, rapidly varying electric fields. Electronic transport under intense high-field conditions in bulk GaAs has long been known to greatly differ from linear, low-field transport; for example, when an applied dc field is sufficiently large, GaAs exhibits Gunn oscillations due to negative differential mobility. Because high-speed devices are approaching the THz regime, it has become important to understand high-field transport in fields that vary periodically on the time scale of the fundamental energy and momentum relaxation processes. Currently, very little is known about electronic transport in this regime [2]. In order to probe high-field, high-frequency transport, we have studied the dependence of the dc conductivity of a quasi-two-dimensional electron gas (2DEG) in a modulation-doped heterojunction on the frequency and amplitude of applied, THz-frequency electric fields.

We have measured the 300 K, dc conductivity $\sigma_{xx}(E_{\text{ap}})$ of the 2DEG in far infrared (FIR) fields at frequencies from 0.25 to 3.5 THz. The FIR radiation is supplied by the UCSB Free Electron Laser (FEL), which provides intense, linearly polarized fields from 0.12 THz to 4.8 THz [3]. As shown in Fig. 1, the FIR radiation propagates in air and is directed onto the sample at normal incidence with a focusing mirror. A beam splitter couples a small fraction of the light to a fast pyroelectric reference detector. The attenuators used to vary the FIR intensity are mounted on the FEL beam port to avoid stray reflections. In the data shown here, the FIR radiation was polarized parallel to the small dc sensing field that biases the sample; an MBE-grown GaAs/Al_{0.3}Ga_{0.7}As heterojunction with an electron sheet density of $2.75 \times 10^{11} \text{ cm}^{-2}$ and a mobility of $8,500 \text{ cm}^2/\text{V}\cdot\text{sec}$ at 300K. This mobility yields a low-field momentum relaxation time, τ_m , of 0.32 ps, so that $\omega\tau_m$ varies from 0.45 at 0.24 THz to 6.5 at 3.6 THz.

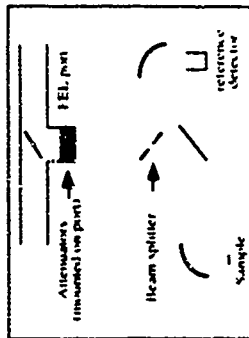


FIG. 1. Experimental setup. FIR propagates in air and is focused directly on the sample. Attenuators are used to vary its intensity, and a red prism induces its polarization. A small fraction of the light is focused into a reference detector.

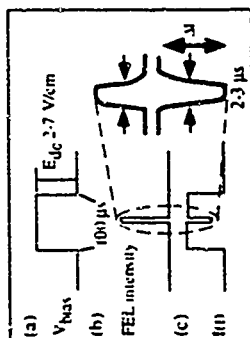


FIG. 2. Schematic diagram. (a) The sample is biased with a (100 ps, 2.7 V) pulse. (b) The sample is biased with a (100 ps, 2.7 V) pulse. (c) The sample is biased with a (100 ps, 2.7 V) pulse. (d) The sample is biased with a (100 ps, 2.7 V) pulse.

Figure 3 shows the dependence of $\sigma_{dc}(E_{\text{FIR}})$ on the terahertz field E_{FIR} . At representative frequencies from 0.25 to 1.5 THz, $\sigma_{dc}(E_{\text{FIR}})$ decreases less rapidly with increasing E_{FIR} . This dependence reflects the increasing phase shift between the high-frequency current and E_{FIR} , which decreases the power absorbed by the electron gas.

To analyze the frequency dependence of the data in Fig. 3, we make the ansatz that the d.c. conductivity is an (unspecified) function of P_{abs} , the power absorbed by the electron gas: $\sigma_{dc} = \sigma_{dc}(P_{\text{abs}})$. We further assume that the absorbed power has a Drude form, $P_{\text{abs}} = E_{\text{FIR}}^2/(1 + \omega^2 \tau_m^2)$, where τ_m is the low-field momentum relaxation time determined from the mobility. If these assumptions were valid, then plotting σ_{dc} versus the scaled field $E' = E_{\text{FIR}}/(1 + \omega^2 \tau_m^2)^{1/2}$ would collapse the data in Fig. 3 onto a single curve. Figure 4 shows that the data do indeed scale roughly with this ansatz over more than a decade in frequency, for

The sample is a micro-etched, 1 mm \times 0.5 mm bar with Ni-Au-Ge contacts. We voltage-bias the sample in series with a load resistor R_L , and measure the sample current from the voltage drop across R_L . The FIR electric field, which is polarized parallel to the direction of the d.c. sample current and in the plane of the electron gas, produces a decrease in the current through the load resistor due to an increase in the sample's resistance. As shown in Fig. 2, the 2.3 μsec FIR pulse arrives at the center of the small E_{FIR} (< 7 V/cm), 100 μsec d.c. voltage bias. We have varied the length of the FIR pulse to confirm that the observed increase in the sample resistance is not due to gross heating of the lattice.

We measure the total power incident on the sample with a photothermopile energy meter (Thomas Heating Ltd.) that is electrically calibrated. We measure the spot size using a micrometer-driven pyroelectric detector with a small aperture, and use a Gaussian fit to obtain the spot radius. The electric field E_{FIR} at the electron gas is different from the incident field due to interference between the parallel faces of the sample. We correct for this by using the measured FIR transmission of the sample to calculate the field inside. To determine the d.c. conductivity ratio, $\sigma_{dc}(E_{\text{FIR}})/\sigma_{dc}(0)$, from the sample resistance, we use the measured spot size and the spatial variation of the conductivity due to the nonuniform Gaussian sample illumination¹².

Figure 3 shows the dependence of $\sigma_{dc}(E_{\text{FIR}})$ on the terahertz field E_{FIR} at representative frequencies from 0.25 to 1.5 THz. At fixed ω , we observe a monotonic decrease in $\sigma_{dc}(E_{\text{FIR}})$ with increasing E_{FIR} . As ω increases, $\sigma_{dc}(E_{\text{FIR}})/\sigma_{dc}(0)$ decreases less rapidly with increasing E_{FIR} . This dependence reflects the increasing phase shift between the high-frequency current and E_{FIR} , which decreases the power absorbed by the electron gas.

To analyze the frequency dependence of the data in Fig. 3, we make the ansatz that the d.c. conductivity is an (unspecified) function of P_{abs} , the power absorbed by the electron gas: $\sigma_{dc} = \sigma_{dc}(P_{\text{abs}})$. We further assume that the absorbed power has a Drude form, $P_{\text{abs}} = E_{\text{FIR}}^2/(1 + \omega^2 \tau_m^2)$, where τ_m is the low-field momentum relaxation time determined from the mobility. If these assumptions were valid, then plotting σ_{dc} versus the scaled field $E' = E_{\text{FIR}}/(1 + \omega^2 \tau_m^2)^{1/2}$ would collapse the data in Fig. 3 onto a single curve. Figure 4 shows that the data do indeed scale roughly with this ansatz over more than a decade in frequency, for

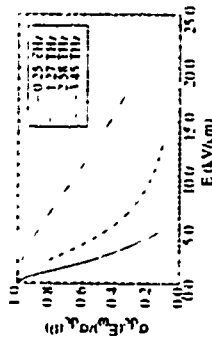


FIG. 1. d.c. conductivity ratio, $\sigma_{dc}(E_{\text{FIR}})/\sigma_{dc}(0)$, versus terahertz field, E_{FIR} . We observe a monotonic decrease in $\sigma_{dc}(E_{\text{FIR}})$ with increasing E_{FIR} . The decrease is more show at the higher frequencies.

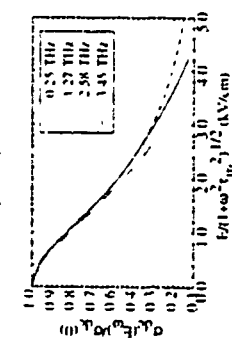


FIG. 2. d.c. conductivity ratio, $\sigma_{dc}(E_{\text{FIR}})/\sigma_{dc}(0)$, versus rescaled terahertz field, $E' = E_{\text{FIR}}/(1 + \omega^2 \tau_m^2)^{1/2}$, where τ_m is the low field momentum relaxation time. The data collapse onto a single curve, indicating that the decrease in σ_{dc} is due to the same mechanism at all frequencies.

the 2DEG. It also seems unlikely that the slightly higher mobility of our sample could be responsible for the difference between the microwave and terahertz-frequency data.

More interesting possibilities for the discrepancy between the 35 GHz data and our high frequency results for $\sigma_{dc}(E')$ are effects of modulation, at high frequencies, of the electron temperature, and of modification of the hot phonon population. In the 35 GHz data, $\omega \tau_m \ll 1$ and $\omega \tau_r \ll 1$, where τ_r is the low-field energy relaxation time, so that both the current and the electron temperature T_e of the gas follow E_{FIR} adiabatically. Furthermore, at 35 GHz the period of the microwave field is substantially longer than the lifetime of a non-equilibrium optical phonon, which ranges from ~ 0.5 psec to ~ 3.5 psec at 300 K in GaAs/AlGaAs quantum wells, depending on interface roughness¹⁵. In our data, $\omega \tau_r$ ranges from ~ 1.6 at 0.25 THz to ~ 22 at 3.45 THz, assuming $\tau_r \sim 1$ psec. Thus, the electron temperature T_e cannot follow the drive, and should oscillate about its time average value at frequency of 2ω , with an amplitude that decreases with increasing ω . This oscillation in T_e should lead to enhanced optical phonon emission twice per drive cycle. Because the optical phonon lifetime is comparable to or longer than the half period of the FIR drive for all of our

fields below ~ 2 kV/cm there τ_m has been adjusted slightly to obtain coincident curves at the lowest fields.

This good scaling over a wide frequency range leads one to expect the scaled data in Fig. 4 to agree with the $\sigma_{dc}(E_{\text{FIR}})$ curves measured in the presence of much lower frequency, microwave fields by Masselink and co-workers, who have studied bulk, n-GaAs and GaAs/AlGaAs 2DEG samples driven by a 35 GHz field¹¹. Thus, their bulk and 2DEG samples had mobilities of ~ 8000 cm²/V \cdot sec, comparable to that of the sample discussed here. At 35 GHz, $1 + \omega^2 \tau_m^2 \approx 1$, and $E' \approx E_{\text{FIR}}$. The 35 GHz data show that the 300 K $\sigma_{dc}(E')$ curves for both bulk and 2DEG samples are nearly identical for fields below ~ 2 kV/cm.

At 35 GHz, the decrease in $\sigma_{dc}(E')$ from $\sigma_{dc}(0)$ is $\sim 5\%$ at $E' = E_{\text{FIR}} = 1$ kV/cm, and $\sim 20\%$ at $E' = 2$ kV/cm¹¹. In contrast, in our scaled data in Fig. 4, $\sigma_{dc}(E')$ is reduced by $\sim 20\%$ from $\sigma_{dc}(0)$ at $E' = 1$ kV/cm, and by $\sim 50\%$ at $E' = 2$ kV/cm. The reason for this substantially more rapid fall-off in σ_{dc} with E' in our data is unclear. Although it is possible that this discrepancy between $\sigma_{dc}(E')$ at 0.25-3.45 THz and $\sigma_{dc}(E')$ at 35 GHz reflects a frequency-dependent error of a factor of 2 to 3 in our calibration of E_{FIR} , this exceeds any generous estimate of the random and systematic errors involved in finding the field at the plane responsible for the difference between the microwave and terahertz-frequency data.

More interesting possibilities for the discrepancy between the 35 GHz data and our high frequency results for $\sigma_{dc}(E')$ are effects of modulation, at high frequencies, of the electron temperature, and of modification of the hot phonon population. In the 35 GHz data, $\omega \tau_m \ll 1$ and $\omega \tau_r \ll 1$, where τ_r is the low-field energy relaxation time, so that both the current and the electron temperature T_e of the gas follow E_{FIR} adiabatically. Furthermore, at 35 GHz the period of the microwave field is substantially longer than the lifetime of a non-equilibrium optical phonon, which ranges from ~ 0.5 psec to ~ 3.5 psec at 300 K in GaAs/AlGaAs quantum wells, depending on interface roughness¹⁵. In our data, $\omega \tau_r$ ranges from ~ 1.6 at 0.25 THz to ~ 22 at 3.45 THz, assuming $\tau_r \sim 1$ psec. Thus, the electron temperature T_e cannot follow the drive, and should oscillate about its time average value at frequency of 2ω , with an amplitude that decreases with increasing ω . This oscillation in T_e should lead to enhanced optical phonon emission twice per drive cycle. Because the optical phonon lifetime is comparable to or longer than the half period of the FIR drive for all of our

MOP33

MICROWAVE MINIBAND NDC IN GaInAs/AlInAs SUPERLATTICES

J.F. Palmer, J.C. Hamand, C. Minot, H. Le Peron,
E. Dutivieux, H. Wang and G. Leroux
France Telecom, CNET/PAB 196 av. Bayard 92220 Bagneux (Fr)

Abstract

The negative differential conductance originating from electron Bragg scattering in miniband transport is demonstrated in a series of five GaInAs/AlInAs superlattices having miniband width from 18 to 81 meV. Sharp resonances or broad band amplification (0.55 GHz) are obtained according to the miniband width. The experimental values of the peak velocities deduced from the microwave resonances, and, to some extent, the DC values, are satisfactorily compared with semi-classical theory based upon the complete Boltzmann Transport Equation.

Introduction

Recent progress has been performed in the non-linear Esaki-Tsu [1] NDC in semiconductor superlattices [2-5]. This effect is different from the Wannier-Stark resonances, as the critical electric field does not depend at the first order upon the miniband width and, in principle, could be reduced in very low values. Most of these results have been obtained in the GaAs/AlAs system, and very few in other systems. Beltram *et al* have inserted a GaInAs/AlInAs superlattice in the collector of a pnp HBT and have concluded to the existence of the NDC [6] in terms of Wannier-Stark localization. In the present communication, we give another convincing evidence of the Esaki-Tsu NDC in a series of 5 GaInAs/AlInAs superlattices having different miniband widths from 18 to 81 meV. Our demonstration is based on two facts. The first one is the comparison of the static DC current-voltage characteristics with a semi-classical Boltzmann miniband transport numerical solution. The second one is based upon the microwave S-parameters measurements which is directly related to the carrier transmittance through the whole SL structure, and therefore to the drift velocity. In our first publication dealing with the miniband transport NDC in GaAs/AlAs superlattices, we were somewhat embarrassed by the proximity of X and L minibands from the first L one, and we argued that, even though a significant part of the electron distribution were "absorbed" in an inefficient X-miniband hopping transport, the observed effects were undoubtedly due to the L miniband. With GaInAs/AlInAs superlattices and for electric fields less than a few ten kV/cm, the contribution of X and L bands is negligible as their lowest extrema are almost resonant with the continuum above the InAlAs barriers. For that reason, and owing to the surprisingly good microwave performances of this first preliminary series of samples, GaInAs/AlInAs SLs may be of great interest in the development of further millimeter wave applications of SL devices.

Sample fabrication.

The epilayers have been grown by MBE on semi-insulating Fe-doped InP wafers. It consists of Si-doped ($N_A = 2 \cdot 10^{18} \text{ cm}^{-3}$) In, GaAs / Al_{0.3}In_{0.7}As SL layer of total thickness 1.1 μm sandwiched between two "n" layers and the active SL in order to provide a continuous variation of the lowest conducting state between the contact and the active layer. The five samples have been designed with a constant well thickness (45 Å) and different barrier thicknesses, as listed in table (1). Wide microwave bandwidth devices have been obtained by means of an SiO₂ insulated mesa technique, in a process very similar to the GaAs/AlAs recently published results [7]. The final step is particularly the same, consisting in a coplanar 50 Ω Ti-Au interconnection suitable to the 0.40 GHz Microtech Cascade probes used in S parameter measurements. In figure (1) the cross section of the sample and a schematic representation of the technology are drawn for indication. The mesa lateral dimensions are 14x12 μm .

data, an enhanced, non-drifting population of non-equilibrium phonons may occur at the high frequencies we have explored. This would tend to decrease the time-average conductivity $\sigma_{dc}(E)$ in terahertz-frequency fields relative to the d.c. conductivity at microwave frequencies. It is somewhat surprising that the very simple scaling ansatz above, which assumes a Drude form for the power absorption, works well to such high fields in Fig. 4. The deviation from this simple scaling with increasing E may reflect the frequency-dependent effects discussed above. It would be very interesting to extend the balance-equation calculations [2] of $\sigma_{dc}(E)$ that have been carried out for bulk n-GaAs at 35 GHz (which appear to agree fairly well with the 35 GHz data of Masselin *et al*) to the frequency regime explored here, to explore in detail the origins for the behavior shown in Fig. 4.

The authors acknowledge useful discussions with S. J. Allen Jr. and M. S. Sherrin, and the support of the staff at the Center for Free Electron Laser Studies. Work at the Center for Free Electron Laser Studies was supported by Office of Naval Research (N00014-92-1-1432). Clean room use was supported in part by the NSF Science and Technology Center for Quantum Electronic Structures, Grant No. DMR88-10410.

[1] W. T. Masselin, M. Braslau, D. LaTulipe, W. I. Wang, and S. L. Wright, *Solid State*

Electronics 31, 337 (1988).

[2] W. Cai and M. Lee, in *Physics of Hot Electron Transport in Semiconductors*, edited by C. S. Ting, World Scientific, London, (1992), and *Int. J. of Mod. Phys. B* 6, 1007 (1992).

[3] G. Raman, *Nuclear Instr. Meth. Phys. Res. A* 318, 225 (1992).

[4] N. G. Asmar *et al* to be published.

[5] J. R. Gupta, N. Balkan, and B. K. Ridley, *Phys. Rev. B* 46, 7745 (1992).

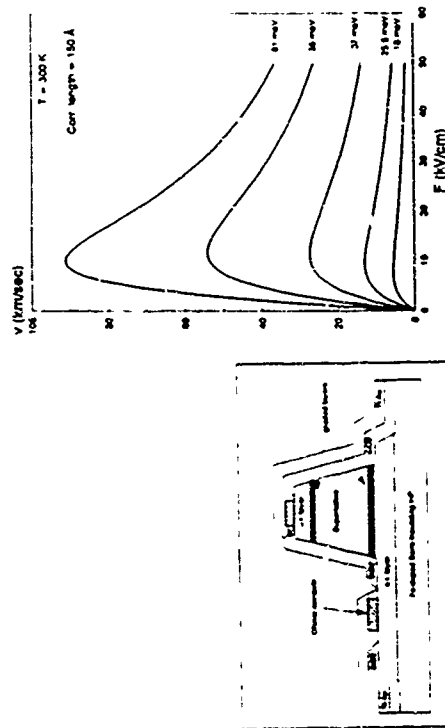


Figure 1 cross section of the SL device

Figure 2 Theoretical variations of the drift velocity versus F for the five minibands widths corresponding to the studied SLs

reter	a (Å)	b (Å)	a + b (Å)	period X rays	Δ meV	E_c meV
297W	45	40	85	84.8	17.7	140
304W	45	35	80	78.8	25.5	136
308W	45	30	75	72.4	37.1	131
313W	45	25	70	69.8	54.8	124
319W	45	20	65	64.7	80.6	114

Table 1 Superlattice geometrical and band parameters a and b are respectively the well and barrier width thickness. The period $a+b$ is compared to the measured one by X rays. As the lowest electron miniband width and E_c the position of the miniband origin from the Ga In As Γ band

Characterization

In table (1), the nominal periods are compared with the results as given by X-rays, one can note that the "error" is 0.5 Å in the worst case, resulting in a mean error less than 1% on the period. Up to four diffraction secondary peaks near (HKL) = (002) have been observed with about the same relative ratio to the main diffraction peak that provided by the diffraction model. We therefore consider that the crystallographic quality of the present SL series is sufficiently good

to assure the coherence of the Bloch wave function in the miniband. The miniband parameters Δ and E_c , also listed in table (1) are, respectively, the miniband width and the position of the miniband origin from the GaInAs Γ minimum. These parameters are obtained from a Kronig-Penney-Bartard derivation using 64% of the gap's difference for the band offset in the conduction band.

The static current voltage characteristics of all samples can be directly compared to the semi-classical drift-velocity versus electric field law $v(F)$, at least in the positive differential conductance range ($F < F_c$). The very coarse relations used in that direct comparison are $J = qN_d v$ and $V = FL$. This has been done in figures (2) and (3), respectively for the theory and the experiment taking N_d as the nominal doping value. One can remark from that coarse comparison that the experimental peak velocities are systematically higher than the theoretical ones. We advance the following explanation:

The actual N_d value is higher than wanted. The graded layers are doped $N_d = 2 \cdot 10^{18} \text{ cm}^{-3}$, and may electrically diffuse excess carriers in the active layer. One can remark an apparent shift of F_c for the widest minibands. This is due to a parabolic resistance caused by the n^+ buffer layer (see fig. 1). An estimated value of 12 Ω is in agreement with a separate TLM measurement of the buffer layer resistance per square and the observed shift of 0.5 volt for a current of the order of 50 mA.

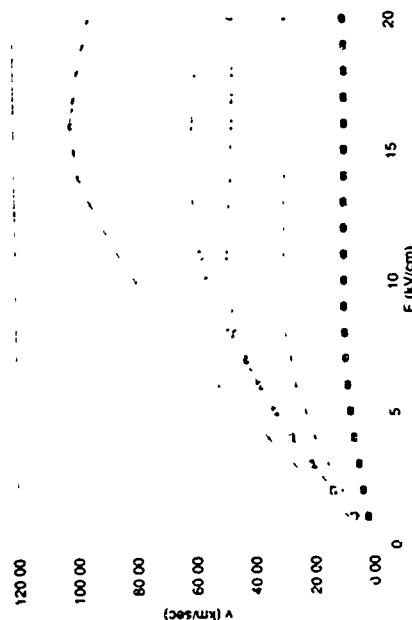


Figure 3 Experimental drift velocities v deduced from the $I(V)$ at 300 K

Anyway, in spite of a significant discrepancy for narrowest minibands, the agreement is quite good owing to the simplicity of the method. In the numerical simulation shown in fig (2) only one parameter has been used. The complete BTE has been numerically solved with only two dominant scattering mechanisms, $\Lambda = 300 \text{ Å}$, the electron-phonon scattering and the interface roughness scattering (II). The treatment of II scattering follows Diarra-Buicher's approach [8], numerous details are given in [9-10] for its application to the complete BTE numerical solution. The II scattering intensity is represented by only one parameter Λ which is the correlation length of the fluctuation on one monolayer at interfaces. Λ has been chosen equal to

150A for all samples in order to give the best fit of f_c for most samples. It is clear that the monolayer fluctuation for the present kind of SL could not be seriously maintained in a more conspicuous approach. On the other hand the agreement of the measured F_c with the semi-classical model of a rigid miniband discards the Wannier-Stark approach ($q\ell F_c = \Delta$) in favor to the Esaki-Tsu approach ($q\ell F_c = \hbar v$). The mean collision time is represented here by a more detailed BTE solution, but the mean collision time order of magnitude is also an interesting parameter, about 10^{-11} sec, in applying the simple formula. One of the major interest of AC measurements when NDC occurs is to provide a more complete analysis beyond the critical field than given by DC measurements.

Microwave measurements

Microwave measurements on these samples have been performed by a Wiltron 360 network analyzer in one port configuration in order to obtain the complex reflection coefficient S_{11} . In figure 4(a) and (b) are represented the variations of S_{11} , respectively for the narrowest miniband (7meV) and the largest one (81meV), at different applied voltages, in the frequency range 0-40 GHz. Intermediate cases are not represented to shorten the text. Let us first consider the narrowest miniband result (fig 4(a)).

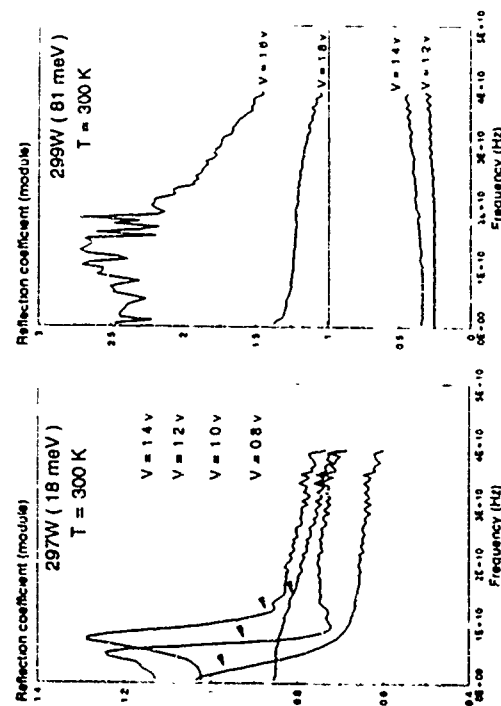


Figure 4a. Variations of the reflection coefficient module between 0.0 and 40 GHz for different applied voltages (sample 297W, miniband = 18 meV)

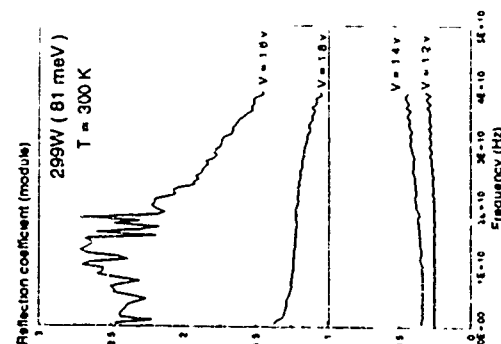


Figure 4b. Same than fig 4a but for the widest miniband (81 meV) sample 299W

At a voltage somewhat higher than the critical one ($V = 1$ volt) a sharp resonance occurs, with a significant central frequency at $f_c = 7$ GHz. The reflection gain is a direct consequence of the NDC, and similar to the Gunn amplifiers already described [11]. Another point is interesting to note: the cutoff point corresponding to $S_{11} = 1$, we note as f_c , rapidly drops when the voltage is increased for sample 297W and also for all the intermediate samples. We interpret this by a decrease of the mean drift velocity versus F_c , whereas the DC current varies little, due to a static division of the band diagram near the anode. In fig 4(b) the widest miniband results show much broader resonances, with f_c higher than 40 GHz. In table 2 we compare the results for all five samples through four velocity values: the theoretical peak velocity (fig 2), the DC peak velocity (fig 3), v_{me} and v_{me} for the applied voltage at which f_c is maximum. The f_c value is extrapolated when it is higher than 40 GHz. It is interesting to note that v_{me} and the theoretical peak velocities are very coherent for the three lowest miniband samples. This reinforces the interpretation in terms of a bulk NDC due to the miniband non-linear transferences in the frame of the Esaki-Tsu model. For samples 303W and 299W the microwave performances are not limited by the electron transport in the miniband, but merely by the sample capacitance on about 60 Ω (load plus access). The present series of SL samples have not been designed in order to obtain great microwave performances, but merely to extend earlier results to another class of materials. In spite of this significant microwave reflection gain values have been obtained, owing to the moderated value of N_d in the SL.

ref	λ	v_{me} km/sec	v_{me} km/sec	v_{me} km/sec	v_{me} km/sec
297W	18 meV	10	5.52	7	10
303W	25.5 meV	28	13	12	21
298W	17 meV	48	27.4	25	29
301W	55 meV	62	54.2	broad	38
299W	81 meV	100	92	broad	>40

Table 2. Comparison of different values of the drift velocity: v_{me} , the peak velocity from DC measurements, v_{me} , the peak velocity from BTE, and v_{me} and v_{me} from microwave data

Quasi-one-dimensional ballistic electron transport in In-Plane-Gated channels at liquid nitrogen temperature

D.K. de Vries, K. Ploog¹, and A.D. Wieck

Max Planck-Institut für Festkörperforschung, Heisenbergstraße 1, D 70569 Stuttgart
¹Paul Drude-Institut für Festkörperelektronik, Hausvogteiplatz 5-7, D 10117 Berlin

Abstract

In-Plane Gated quantum point contacts were fabricated in a pseudomorphic GaAs/InGaAs/AlGaAs heterostructure by focused ion beam implantation of 100 keV Ga³⁺ ions. We see an intrinsic conduction quantization structure at 4.2 K. As the temperature is increased, the quantization becomes less pronounced but clear remnants are observed even at liquid nitrogen temperature and above.

Introduction

After the discovery of quantized conductance in split gated point contacts in GaAs/GaAlAs heterostructures [1, 2], ballistic electron transport has been shown in devices of several kinds. Solid state devices modulate either the two-dimensional electron density by illumination or a (surface/back) gate or the "width" of the one dimensional channel by a split surface gate or in plane gate. Devices of both the electron density modulation type as well as the channel width tuning type can be made using focused ion beam (FIB) implantation to define the channel [3, 4]. A FIB fabricated device in which the channel width can be tuned is the In-Plane Gated field-effect transistor [4].

Most experiments on quantized conductance have been performed at temperatures below liquid helium temperature, 1.2 K. These temperatures are too low for most device applications. Considering the mean free path of electrons in high mobility heterostructures, it should be feasible to find remnants of quantization at higher temperatures. Such remnants were indeed found at up to 30 K in GaAs/AlGaAs [5] and InAs/GaSb [6] split gate devices. In these devices, the gates were brought close to the electron gas to increase the energy spacing of the one-dimensional bands.

In a GaAs/InGaAs/AlGaAs heterostructure where the electron gas is contained in a strained InGaAs layer, high transconductance in plane gated transistors have already been realized. [7] We consider GaAs/InGaAs/AlGaAs a promising structure for quantized conductance above 4.2 K because of its high electron density. Although the electron mobility is smaller than in GaAs/AlGaAs, the mean free path remains approximately 0.5 μm up to 100 K, above which the mobility is reduced by optical phonon scattering.

Experimental setup

A GaAs/InGaAs/AlGaAs modulation doped heterostructure was grown by molecular beam epitaxy on a semi-insulating GaAs (100) substrate. The two-dimensional electron gas is contained within the 12 nm thick strained In_{0.1}Ga_{0.9}As layer. The doped layer is a 40 nm thick Si doped Al_{0.31}Ga_{0.69}As layer (Si: $2 \times 10^{22} \text{ m}^{-3}$) separated from the 2DEG by a 3 nm thick undoped spacer layer. At room temperature, the electron sheet density is $1.3 \times 10^{16} \text{ m}^{-2}$, at a mobility of

Conclusions.

The present results constitute a clear experimental demonstration of miniband NDC in GaInAs/AlInAs superlattices giving more credit to the Esaki-Tsu semi-classical approach, already validated with GaAs/AlInAs SLs. We point out the remarkable agreement between the time of flight resonance occurring at v/L and the value predicted through BTE solution, whereas the DC values of the drift velocity obtained by a thumb rule do qualitatively follow the experimental ones within 50%. Such SLs have also interesting optical properties, in blocking contact structures and in the Wannier Stark localization conditions [12]. The broad band NDC amplifier demonstrated here, far from optimized, nevertheless opens a new class of millimeter wavelength active devices.

Acknowledgements.

The authors are indebted to J.C. Esnault, O. Dulac, and C. Benvenuti for their contribution to device fabrication, and J.P. Veldos for microwave measurements. Paul Vasin has impulsed the preliminary studies on GaInAs/AlInAs SLs from which the present series has been designed. The authors would like to thank M. Hadjari, A. Sibille, and G. Frennault for stimulating discussions.

References.

1. L. Esaki and R. Tsu, IBM J. Res. Dev., 14, 61 (1970)
2. A. Sibille, J.F. Palmer, H. Wang, and F. Mollot, Phys. Rev. Lett., 64, 52 (1990)
3. J. Feldmann et al., Phys. Rev. B, 46, 7252 (1992)
4. C. Waschke, H.G. Roskos, R. Schwedler, K. Leo, H. Kurz, and K. Kohler, Phys. Rev. Lett., 70, 3319 (1993)
5. A.A. Ignatov, K.F. Renk, and E.P. Dakhin, Phys. Rev. Lett., 70, 1996 (1993)
6. F. Beltram, F. Capasso, D.L. Saven, A.L. Hutchinson, S.G. Chu, and A.Y. Cho, Phys. Rev. Lett., 64, 3167 (1990)
7. M. Hadjari, J.F. Palmer, A. Sibille, H. Wang, E. Paris, and F. Mollot, Lett. 29, 648 (1991)
8. I. Dhuraut and P.N. Butcher, J. Phys. Condens. Matter, 2, 19 (1990)
9. J.F. Palmer, G. Frennault, A. Sibille, M. Hadjari, F. Mollot, and R. Planel, Surf. Science, 267, 574 (1992)
10. G. Frennault and J.J. Palmer, to appear in Solid State Comm.
11. B. Haka, J. Appl. Phys., 38, 806 (1967)
12. F. Bigan, M. Alloum, M. Carre, and P. Vasin, Appl. Phys. Lett., 57, 1271 (1990)

0.57 m²/Vs. At 77 K, electron mobility in the dark is 2.8 m²/Vs, hardly lower than the 1.2 h value of 3.0 m²/Vs. The sheet density at these temperatures is around $1.0 \times 10^{16} \text{ m}^{-2}$.

The samples were mesa etched to obtain electrically insulated areas with contact pads. By focused ion beam implantation of 100 keV Ga⁺ ions, nominally 100 nm wide insulating lines were directly written at normal incidence with a dose of $1 \times 10^{18} \text{ m}^{-2}$ to define in-plane gated channels. The in-set of Fig. 1 shows the geometry, for which only two FIB written lines are necessary. The channel between source (S) and drain (D) can be depleted or enhanced by applying a voltage to the in-plane gate (IPG) area. The channel width is zero gate voltage equals the geometrical width w_{geo} , minus the implanted line width of 100 nm, minus twice the width of the depletion zone between the implanted lines (p-type) and the conductive area (n-type). The geometrical widths were varied between 0.1 and 1.0 μm . After rapid thermal annealing at 700°C for 15 s, ohmic contacts were made with a AuGe/Ni alloy.

Transport measurements

Transport measurements were performed in the dark, with no magnetic field applied. With an HP 4142B parameter analyzer, current-voltage measurements were made at a finite drain source bias voltage in order to measure the conductance. The derivative of the conductance with respect to the gate voltage V_g was determined numerically. We also measured the AC voltage response to a 1 nA alternating current (81 Hz) through the channel by standard lock-in techniques, leading to ballistic structures at the same conductance values.

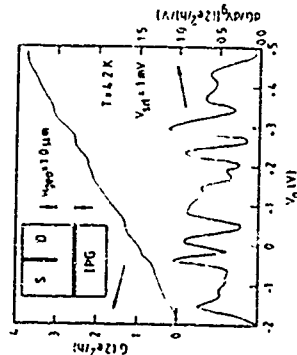


Fig. 1. Conductance G and dG/dV_g vs gate voltage at 4.2 K. The sample was cooled and measured in the dark. The inset shows the geometry of the channel directly by FIB implantation.

Figure 1 shows the conductance G of an in-plane gated channel at 4.2 K, at a source-drain voltage V_d of 1 mV, and its derivative with respect to the gate voltage. In calculating the conductance we neglected the series resistance. The gate leakage current is in the pA range. We observe a large number of plateaus in the conductance in the range of 0 to 4 times $2e^2/h$. The derivative shows corresponding minima, and some extra structure which is not quite apparent in the graph of the conductance. A similar complex structure has also been observed in strained

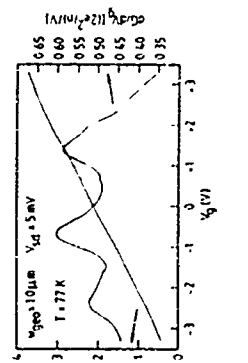


Fig. 2. G and dG/dV_g vs gate voltage at 77 K for the same channel as in Fig. 1

InGaAs channels below 1 K by Marc et al. [8].

The observed conductivity structure is independent of sweep direction. It is reproducible after thermal cycling, although the threshold voltage tends to drift. This drift has no structural effect on the measurement results.

On devices with smaller geometrical channel widths, we get qualitatively the same picture. This shows that an explanation of the complex structure in terms of states bound to a single impurity [9] does not apply here.

That the finite bias plateaus are relatively well-defined opens the way to measurements at higher temperatures. Figure 2 shows the conductivity of the same channel at liquid nitrogen temperature (77 K). The visible kinks in the conductance plot correspond to clear minima in the derivative dG/dV_g . In the case of ideal ballistic transport, we expect minima to occur at integer multiples of $2e^2/h$. The minima in Fig. 2 occur at somewhat higher values of G . Nevertheless they give direct evidence of quasi-ballistic transport at 77 K.

The peak to peak change in the derivative is well over 10 %, or $\sim \mu\text{S/V}$ on an average value of 40 $\mu\text{S/V}$. This change can be increased to 25 % in channels with smaller w_{geo} at the cost of tunability. Our narrower channels could not be enhanced to conductance values as high as the 1 μm channels.

To show that the peaks in dG/dV_g at 77 K are remnants of the 4.2 K peaks, we have measured the development of the conductance as a function of the temperature. We used a liquid helium flow cryostat in the temperature range 20 K to room temperature. In Fig. 3 we see how the intricate structure in the low temperature limit is averaged to less pronounced but still well defined structures at temperatures up to 100 K.

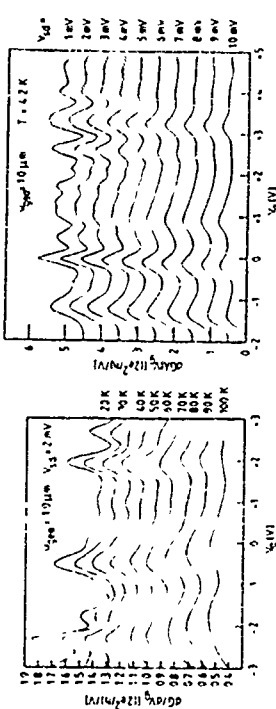


Fig. 3. dG/dV_g versus V_g as a function of temperature. For clarity, subsequent curves are offset 0.1 units with respect to the graph at 100 K.

For not too high temperatures, the averaging width of thermal smearing is $\sim k_B T$, centered around the Fermi energy E_F , which is the inverse slope of the Fermi-Dirac distribution function at E_F . A similar averaging, over a range of eV_d , is attained by measuring at a finite drain-source voltage. Figure 4 shows the effect of such different source-drain voltages. To compare curves from

Fig. 4. dG/dV_g versus V_g as a function of source-drain bias at 4.2 K. Subsequent curves are offset 0.5 units with respect to the 10 mV curve.

The Dependence of Boundary Scattering in Split-Gate Quantum Wires on the Transverse Mode Number

M. Yamamoto, S. Nakata, K. Aihara and T. Mizutani
NTT LSI Laboratories
3-1, Morinosato Wakamiya, Atsugi-shi 243-01, Japan

Abstract

Boundary scattering in quantum wires is investigated as a function of the transverse mode number, N , using a split-gate configuration. It is found that the specular factor, p , of boundary scattering increases toward 1 with decreasing N . Taking into consideration that the boundary roughness in the split-gate quantum wires, which is caused by the random positions of the ionized impurity ions in the doped layer, increases as the split-gate voltage decreases, then the increase in the specular factor indicates decreased intersubband scattering due to the reduction of the mode number.

1. INTRODUCTION

The quantum interference phenomena in microstructures offer the possibility of constructing viable three-terminal devices with a large on/off ratio and novel functional devices [1-5]. To realize quantum interference devices with a large coherence length and well-designed control characteristics, it is required to maintain the phase coherence length and the elastic scattering length much longer than the device length. In this sense, it is indispensable to suppress diffuse boundary scattering in quantum wires with which quantum interference devices are constructed. The purpose of the present study is to clarify the guidelines that ensure the suppression of diffuse boundary scattering. This study experimentally investigates boundary scattering in quantum wires as a function of the transverse mode number, N , using split-gate quantum wires. It was found that the specular factor of boundary scattering increased toward 1 with decreasing N . This result suggests that the diffuse boundary scattering is sufficiently suppressed by reducing the mode number.

2. EXPERIMENTAL METHOD

The samples investigated were split-gate quantum wires. The split-gate structures were made on high-mobility AlGaAs/GaAs heterostructures grown by molecular beam epitaxy (MBE). The carrier concentration and mobility of the two-dimensional electron gas (2DEG) were $4.2 \times 10^{11} \text{ cm}^{-2}$ and $2.1 \times 10^5 \text{ cm}^2/\text{Vs}$ at 4.2 K, respectively. The split gates were fabricated by electron beam lithography and a Ti/Au lift-off technique. The lithographic gap width between the split gates and device length were 0.5 μm and 2.0 μm , respectively. In this device, the two-dimensional electron gas beneath the split gate was depleted at the split-gate voltage $V_g = 0.26 \text{ V}$. By further decreasing V_g , the one-dimensional channel could be completely pinched off at $V_g = 0.6 \text{ V}$.

Magnetoresistance was measured using a low-frequency four-terminal ac technique with a lock-in amplifier at 4.2 K in a magnetic field up to 8 T.

3. EXPERIMENTAL RESULTS AND DISCUSSION

3.1 Magnetoresistance

Typical magnetoresistances, $R(B)$, are shown for various values of V_g in Fig. 1, in which a positive magnetoresistance peak at around 0.2 T and saturation of $R(B)$ at around $B \approx 1 \text{ T}$ were

Figs. 3 and 4, we note that at 4.2 K (Fig. 4) the channel could be tuned over a wider range than at higher temperatures. The peak at $V_g = -0.1 \text{ V}$ in Fig. 4 corresponds with the leftmost peak in Fig. 3. In comparing curves where $4k_B T \approx eV_d$ (10 K $\approx 3.4 \text{ meV}$), we observe that in the finite voltage curves, the structure of the peaks is less pronounced than in the curves at the corresponding temperatures.

Conclusions

The presence of ballistic properties in FET written in Plane-Gated transistors at liquid nitrogen temperature is a large step towards device application of one-dimensional transport phenomena. By making the channel width smaller, we expect that these phenomena will persist to even higher temperatures. The problem of decreasing tunability could be tackled by better control of the lateral doping profile, i.e. the ion beam focusing.

Acknowledgments

We thank Hans-Peter Schönherr for growing the InGaAs samples. This work was supported by the Bundesministerium für Forschung und Technologie of the Federal Republic of Germany.

References

- [1] B. J. van Wees, H. van Hest, C. W. J. Beenakker, J. G. Williamson, L. P. Kouwenhoven, D. van der Marel, and C. T. Foxon, *Phys. Rev. Lett.* **60**, 848 (1988).
- [2] D. A. Wharam, T. J. Thornton, R. Newbury, M. Pepper, H. Ahmed, J. E. F. Frost, D. G. Hasko, D. C. Preerck, D. A. Ritchie, and G. A. C. Jones, *J. Phys. C: Solid State Phys.* **21**, L209 (1988).
- [3] Y. Miyayama and T. Sakai, *Appl. Phys. Lett.* **54**, 2556 (1989).
- [4] A. D. Wieck and X. Ploog, *Appl. Phys. Lett.* **56**, 928 (1990).
- [5] G. L. Snider, M. S. Miller, M. J. Rooks, and E. L. Hu, *Appl. Phys. Lett.* **56**, 2727 (1991).
- [6] S. J. Koester, C. R. Eubank, M. J. Rooks, E. L. Hu, and H. Krenner, *Appl. Phys. Lett.* **62**, 1373 (1993).
- [7] A. D. Wieck and X. Ploog, *Appl. Phys. Lett.* **61**, 1048 (1992).
- [8] D. R. Mearns, M. P. Grimshaw, D. A. Ritchie, A. C. Churchill, M. Pepper, and G. A. C. Jones, *J. Crystal Growth* **127**, 601 (1993).
- [9] E. Tekmar and X. Ploog, *Phys. Rev. B* **43**, 7145 (1991).

observed. These structures in $R(B)$ are characteristic of diffuse boundary scattering [6, 8]. Furthermore, the magnetic field value corresponding to the positive $R(B)$ peak, B_p , was in good agreement with the theoretical value of $B_p(h) = 0.55 \phi_0 / 4\pi l_d$ for diffuse boundary scattering [6] where $\phi_0 = h/e$ is the flux quantum, W_{eff} is the effective channel width, and l_d is the Fermi wavelength.

The experiments revealed a characteristic feature: the resistance ratio $\Delta R/R_0 = (R(B) - R_0)/R_0$ decreased with decreasing V_g , as shown in Fig. 2. Here, R_0 represents the extrapolated value of $R(B)$ at $B = 0$ from the positive peak at $B = B_p$, as indicated in Fig. 1, which corresponds to approximately subtracting the contribution from the weak localization, and R_0 represents the resistance value at the plateau region around $B = 1T$, where diffuse boundary scattering is sufficiently suppressed.

Assuming Matthiessen's rule, that is, the bulk (impurity) and edge scattering (diffuse boundary scattering) rate are additive, the effective scattering time for $B = 0$, $\tau(B=0)$, is given using the probability of specular boundary scattering (specularity factor), p , as [6, 7],

$$\frac{1}{\tau(B=0)} = \frac{1}{\tau_0} + v_F \left(\frac{1-p}{W_{eff}} \right) \quad (1)$$

where v_F is the Fermi velocity and τ_0 is the bulk scattering time. Furthermore, the effective scattering time for $B = B_p$, where diffuse boundary scattering is sufficiently suppressed, $\tau(B=B_p)$, is simply given by τ_0 , that is,

$$\tau(B=B_p) = \tau_0 \quad (2)$$

For the present sample, it is shown below that $L_{eff} > L_d$, where L_{eff} is the effective wire length including the length of the depletion region along the wire direction, and $L_d = v_F \tau_0$ is the bulk mean free path. Therefore, the conductivity is represented by the Drude expression. Using the relationships of eqs. (1) and (2) for the Drude expression, the ratio, $\Delta R/R_0$ is given as

$$\frac{\Delta R}{R_0} = \left(\frac{1-p}{1-p_0} \right) \left(1 - \frac{L_d}{L_{eff}} \right) \quad (3)$$

To deduce the intrinsic parameter, p , from the experimental values of $\Delta R/R_0$ [9] as a function of the mode number, how W_{eff} , N and L_d vary with V_g were evaluated, as described in 3.2 and 3.3.

3.2. Evaluation of W_{eff} and N as a function of V_g

The values of W_{eff} and the mode separation energy, ΔE , were obtained from the analysis of a plot of the Landau index n versus $1/B$ for Shubnikov-de Haas (SdH) oscillations using a parabolic potential model [10]. The empirical dependences of W_{eff} and ΔE on V_g were expressed as follows,

$$W_{eff} (\mu m) = 0.275 + 0.255 V_g \cdot 0.115 V_g^2 \quad (4)$$

$$\Delta E (\text{meV}) = 0.975 + 0.664 V_g \quad (5)$$

The Fermi energy, E_F , was obtained from the slope of a linear region of a plot of n versus $1/B$ and was empirically expressed as

$$E_F (\text{meV}) = 15.17 + 15.0 V_g \cdot 12.8 V_g^2 \quad (6)$$

The transverse mode number, N , was estimated using the relation $N = E_F / \Delta E$ and varied from 21 to 3 corresponding to V_g values from 0.2 V to 0.5 V.

3.3. Evaluation of L_d

As shown below, the present sample was in the one-dimensional diffusive transport region in the sense that $L_d < L_{eff}$ and $W_{eff} \ll L_d$. Therefore, the resistance is expressed with the Drude rule and Ohm's law as

$$\sigma_1 = n_1 e \mu, \quad (7)$$

$$R = (L_{eff} / \sigma_1) L_{eff} \quad (8)$$

where σ_1 and n_1 are the one-dimensional conductivity and electron density, respectively, and μ is the mobility.

The experimental dependence of $L_d = v_F \tau_0$ was evaluated from the saturated resistance value, R_0 , at $B = B_p$. By using the approximation of $n_1 = n_2 W_{eff}$ in eq. (8) where n_2 is the two-dimensional electron density, R_0 is given as,

$$R_0 = \left(\frac{1-p}{n_1 e \mu} \right) L_{eff} = \left(\frac{1-p}{n_2 e \mu} \right) \left(\frac{L_{eff}}{W_{eff}} \right) \quad (9)$$

The obtained values of L_d as a function of V_g are shown in Fig. 3 in comparison to L_{eff} and W_{eff} . From these comparisons, the applicability of the one-dimensional Drude relation and Ohm's law was confirmed for the present sample, that is, $L_d < L_{eff}$ and $W_{eff} \ll L_d$.

3.4. Specularity, p , as a function of the mode number

It was found that the obtained values of p increased toward 1 with decreasing N , as shown in Fig. 4. The results of the quantum mechanical calculation of boundary roughness scattering in quantum wires, based on the model in which the boundary roughness is characterized by the root mean square deviation, Δ , and the correlation length, Λ , depend on the various parameters such as Δ/Λ , Λ/λ_F , the mode number, N , and the unperturbed potential model, that is, the hardwall or softwall potential [11]. Therefore, comparison of the present results, characterized by the single phenomenological parameter, p , with the theoretical results is not straightforward. Here, it should be noted that N varied substantially from 21 to 3 while λ_F varied only from 0.035 μm to 0.1069 μm in the experimental range of V_g . Furthermore, according to the calculated results [12], the boundary roughness of the quantum wires defined by a split gate, which is caused by the random positions of ionized impurity ions in the doped layer, becomes more pronounced with decreasing V_g . Thus, the observed increase in specularity with decreasing V_g ,

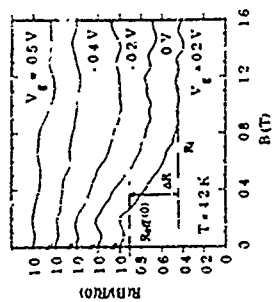


Fig. 1. Magnetoresistance for various V_g . $A(0) = 6.5, 3.8, 2.1, 1.5$ and $1.2 \text{ k}\Omega$ from top to bottom, respectively.

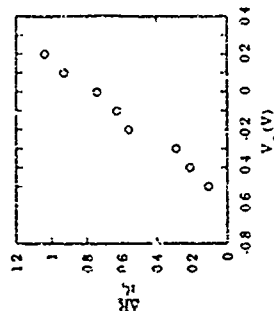


Fig. 2. $\Delta R/R_0$ as a function of V_g . ΔR and R_0 are indicated in Fig. 1.

Experimental Studies of Electronic Transport in Semiconductor Quantum Dot Structures

JP Birn, K. Ishiyoshi, Y. Aoyagi, and T. Sugano
Nanoelectronics Materials Laboratory, Frontier Research Program, RIKEN, 2-1 Hiwinawa,
Wako, Saitama 351-01, JAPAN.

Abstract

We have studied the low temperature electrical properties of semiconductor quantum dot structures at high magnetic fields. The devices consisted of lithographically defined aluminum gates deposited on the surface of a GaAs/AlGaAs heterojunction substrate and the dot structures were formed on the application of a suitable negative bias to the gates. At high magnetic fields electronic transport occurred via edge states and we were able to use the well known properties of these states to study transmission through the dot structures. In particular we observed large resistance resonances superimposed on the quantized magnetoresistance plateaus of the dot. These resonances were found to persist with reduced amplitude to above a degree Kelvin and showed a sensitive dependence on the applied gate voltage. We associate them with the increased edge state interaction introduced by the dot and discuss our results in terms of the various scattering mechanisms inherent in quantum dot structures.

The study of semiconductor quantum dot structures, in which electronic motion in all three dimensions is confined on the scale of the Fermi wavelength, is currently an area of strong theoretical and experimental interest [1]. Since the energy spectrum of such structures is quantized in a series of discrete levels, geometrical considerations are expected to exert a strong influence on the resulting device performance and several recent theoretical studies have predicted the existence of novel geometry dependent resonances in the corresponding electrical properties [2-4]. In this paper we demonstrate the presence of scattering resonances in quantum dots at high magnetic fields such that transport is in the edge state regime [4-6]. In particular we use the well known properties of these states to directly relate the measured electrical behavior to the transmission of electrons through quantum dots. The resonances were found to persist to temperatures above a degree Kelvin and also showed a sensitive dependence on the applied gate voltage. We associate them with the increased edge state interaction introduced by the dot and discuss our results in terms of the various scattering mechanisms inherent in quantum dot structures.

Probably the most versatile technique for the realization of quantum dot structures employs lithographically defined metal gates deposited on to the surface of a suitable semiconductor substrate; a negative bias applied to the gates then depletes electrons from underneath them leaving only a small conducting structure whose geometry is determined by both the lithographic design of the gates and the magnitude of the applied bias [6]. In this paper we discuss the results obtained in gated quantum dot structures geometrically defined using electron beam lithography and deposited on to the surface of a GaAs/AlGaAs heterojunction [7]. The aluminum gates were patterned into a stub structure which employed single quantum point contacts as the entrance and exit ports to a $4\mu\text{m}^2$ central dot (figure 1). The water was etched in to a standard Hall bar geometry and had a typical low temperature carrier density of $n \approx 3.5 \times 10^{14} \text{ cm}^{-2}$ and mobility of $\mu = 350,000 \text{ cm}^2/\text{Vs}$. After being mounted on a ceramic holder the sample was attached to the mixing chamber of a dilution refrigerator and audio frequency magnetotransport measurements were made at temperatures below 10 mK. Great care was taken to ensure good thermal contact to the sample and spurious heating effects were minimised by using a source in drain evaluation of under 1 nV. The measurements typically employed a geometry in which current was passed between probes 1 and 3 while the voltage drop across the dot was measured between probes 2 and 5. As has been described in the literature this corresponds to a two-terminal measurement in which all contact resistances are eliminated [1].

With the gates grounded at the drain potential the electron gas underneath them was undepleted and the device structure consisted of a two dimensional electron gas system. Spin resolved quantum Hall plateaus were clearly observed in the magnetoresistance and were quantified to better than 0.1%. The experimental accuracy of the measurement with a suitable negative bias applied to the gates the dot structure was formed and as can be seen in figure 1

in spite of the increased roughness, is probably attributed to the decrease of the intersubband scattering due to the reduction of the transverse mode number

4. CONCLUSION

In conclusion, it was experimentally shown that the specularly of boundary scattering in a quantum wire defined by a split gate increased toward 1 with a decreasing transverse mode number. The increase in the specularity was attributed to the decreased intersubband scattering due to the reduction of the mode number. The present results indicate that the diffuse boundary scattering in a quantum wire, which is a deteriorating factor for quantum wire-based devices such as quantum interference devices, is sufficiently suppressed by decreasing the mode number

REFERENCES

1. S. Datta, M. R. Melloch, S. Bandyopadhyay and M. S. Lundstrom, *Appl. Phys. Lett.* 48 (1986) 487, and S. Bandyopadhyay, M. R. Melloch, S. Datta, B. Das, J. A. Cooper Jr and M. S. Lundstrom, *IEDM* 86, 76
2. F. Solis, M. Macucci and K. Hess, *Appl. Phys. Lett.* 54, 350 (1989)
3. S. Datta, *Superlattices and Microstructures* 6, 43 (1989)
4. K. Akhara, M. Yamamoto and T. Mizutani, *Jpn. J. Appl. Phys.* 31, 1916 (1992)
5. K. Akhara, M. Yamamoto and T. Mizutani, *IEDM* 92, p. 491
6. T. J. Thornton, M. L. Rookes, A. Scherer and B. P. Van de Gaag, *Phys. Rev. Lett.* 63, 2128 (1989)
7. T. J. Thornton, M. L. Rookes, A. Scherer and B. P. Van de Gaag, *Granular Nanoelectronics* (Edited by D. K. Ferry, J. R. Barker and C. Jacoboni), p. 165 Plenum Press, New York (1990).
8. E. Ditlevsen and J. Lothe, *Philos. Mag.* 14, 759 (1966)
9. M. Yamada, K. Hirakawa, T. Odagiri, T. J. Thornton and T. Ikuma, *Superlattices and Microstructures*, 11, 261 (1992)
10. K. F. Berggren, G. Ross and H. van Houten, *Phys. Rev. B* 37, 10118 (1988).
11. H. Akita and T. Ando, *Phys. Rev. B* 43, 11676 (1991)
12. J. A. Nixon and J. H. Davies, *Phys. Rev. B* 41, 7929 (1990)

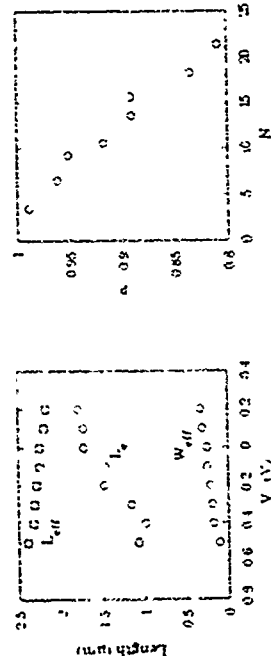


Fig. 3. L_{eff} and W_{eff} as a function of V_g

Fig. 4. Specularity vs transverse mode number

the resulting magnetoresistance showed very different behavior to the two dimensional system. In particular the plateau quantization was found to be significantly reduced and reproducible resonant like features were observed on the plateau (figure 1). As the negative bias applied to the gates was increased the plateau quantization was found to be further reduced while the resonant features became increasingly prominent (figure 2). An important feature of these resonances was that they occurred on plateau and not in the transition region between successive plateaux (although we point out that additional structure was also observed in the transition regions). Measurements at higher temperatures revealed the amplitude of the resonances to be temperature independent below approximately 400 mK and residual structure could still be resolved above a degree Kelvin (figure 3).

As it now well understood the observation of quantised plateaux in the magnetoresistance results from the perfect transmission of a finite number of edge states at high magnetic fields [1-5]. In the case of a simple two dimensional electron gas system there is a direct correspondence between the number of such edge states and the number of occupied Landau levels N . The resistance of the device can then be calculated by a Landauer-Büttiker approach and for the measurement geometry we employ [4]

$$R = (1/N) (h/e^2) \quad (1)$$

which is quantised and depends only on N . Equivalently the observation of quantised plateaux in the magnetoresistance of the dot also indicates perfect transmission of a finite number of edge states through the dot. In this case the situation is somewhat different from the bulk however since the point contacts of the dot are able to selectively transmit and reflect edge states [6]. The number of states fully transmitted through the dot is therefore no longer simply determined by N and under these conditions the magnetoresistance of the dot shows a different series of quantised resistance plateaux to that of the bulk (figures 2 and 3). Equation 1 must then be written as

$$R = (1/N_d) (h/e^2) \quad (2)$$

where N_d is the number of edge states perfectly transmitted through the dot and N_d is the number of completely reflected edge states ($N_d + N_r = N$). While the resistance in equation 2 is still clearly quantised, departures from quantisation will occur once one or more of the edge states become only partially transmitted through the dot. Associating a transmission probability t with the n th edge state ($t \leq 1$) we must then write

$$R = (1/T) (h/e^2) \quad (3)$$

where $T = \sum t_n$ is the overall edge state transmission probability and R is the overall edge state reflection probability ($T + R = 1$). Clearly this resistance is no longer necessarily quantised.

The important feature of the above equations is that they enable us to directly relate the measured magnetoresistance to the edge state transmission probability through the quantum dot. We have already shown that as the negative gate voltage was increased the plateau features of the dot shifted to resistance values larger than those predicted by equation 2 (figure 1 and 2). For the highest gate voltages this shift corresponded to a 20% increase above the expected quantised value and so indicates a corresponding reduction in the overall edge state transmission probability. This reduction presumably resulted from the increased interaction between oppositely propagating edge states as the width of the quantum point contacts was reduced and has previously been reported in smaller dot structures [9].

More interesting however are the large resistance resonances observed on plateau. These resonances correspond to an increase in the resistance above the quantised plateau and we associate them with a magnetic field induced increase in the edge state backscattering. As can be seen from figure 2 the magnetic field position and amplitude of the resonances was found to alter as the gate voltage was increased indicating a same dependence on the precise device geometry. The most likely origin of the resonances is that they arise from the interaction between localised and extended edge states within the dot. In particular under conditions such that $N_d \ll N$ edge states are perfectly transmitted through the dot. Additional edge states will also be localised within the dot. An electron in a transmitted edge state may then scatter into one of the localised states and finally backscatter out of the dot. Since this scattering involves a finite magnetic flux its associated phase change modulates the overall scattering probability and can be shown to give rise to a series of backscattering resonances as the magnetic field is varied [2]. In a similar fashion as the gate voltage is varied the associated

change in the edge state paths causes the resonances to occur at different magnetic field values.

The magnetic resonances described above were first observed in studies of small quantum dot structures in which the Hall resistance was found to dip unexpectedly to zero at certain magnetic field values [10]. In contrast we have demonstrated the presence of resonances which correspond to an increase in the magnetoresistance above the plateau value. While this feature may at first seem contradictory we point out that it is merely a consequence of the different measurement geometries employed in the experiments. In particular from equation 3 it can be seen that for the probe configuration described above an increase in the edge state backscattering probability will give an associated rise in the magnetoresistance. However we could equally measure the magnetoresistance using a geometry in which current is passed between probes 1 and 4 and in which the voltage drop across the dot is now measured across probes 3 and 4. Under these conditions equation 3 takes the form [4]

$$R = (1/N_r) (h/e^2) \quad (4)$$

and in this case an increase in the backscattering probability actually gives rise to a reduction in the measured resistance. In figure 4 we compare the results of measurements in the geometries of equations 3 and 4 and show the clear relationship between them. In the geometry of equation 4 the resonances now occur as a series of dips below the magnetoresistance plateau reminiscent of the Hall dips described above. Furthermore it can also be seen that in agreement with theory the resonances have the same amplitude in both geometries and are symmetric about the plateau value.

A surprising feature of the Hall resonances mentioned above was their persistence with almost unattenuated amplitude to temperatures in excess of a degree Kelvin [10]. This robustness to thermal averaging was actually predicted by theory and heuristically results from the fact that thermal smearing of the Fermi function is ineffective in averaging out the resonances which can only be upset by inelastic scattering [2]. We in fact observe a stronger dependence of the resonance amplitude on temperature in our experiment and we associate this with the increased diameter of the dot which we study [10]. As can be seen from figure 3 the amplitude of the resonances was temperature independent below 400 mK. Since the maximum path length around the circumference of the dot was 8 μm we suspect that at temperatures below 400 mK the inelastic scattering length of the electrons was comparable to or longer than this length. At higher temperatures however the reduced amplitude of the resonances suggests that the inelastic length became significantly shorter than 8 μm . In other words, even though electrons in high field edge states can propagate over hundreds of microns without equilibration [4-5] their phase is clearly only conserved over much shorter lengths. This is an important result and suggests that "quantum dot interferometers" may provide a useful system for the study of electron phase breaking at high magnetic fields [2].

We have already mentioned that the dot geometry studied here is significantly larger than that employed in previous experiments. This increased size is actually advantageous since the edge state population of a larger dot is expected to be well approximated by that of the bulk [11]. As a result we note that the resonances often occur at magnetic field values simultaneous with the depopulation of an edge state from the dot. For example consider the resonances at 4.1 Tesla in figure 1 and at 5.3 Tesla in figure 2, both of which appear to be enhanced by an associated edge state depopulation. However, since other resonances are also observed at magnetic fields not in any way correlated to a specific edge state depopulation it is difficult to make any quantitative conclusions with regards to this matter and here we merely note the coincidence for the sake of completeness.

While the edge state scattering mechanism described above is able to account for many of the features we observe experimentally, before concluding we make some comments on other possible origins of the resonances. In particular it is well known that aperiodic structure is often observed in the magnetoresistance in single point contacts [12]. However, in these experiments the structure is typically always observed in the transition between successive quantised plateaux and features have not yet been reported on plateau. In contrast, we have demonstrated the presence of striking, on plateau resonances and since we have observed the same generic features in measurements on three different devices we conclude that the resonances are indeed an intrinsic feature of quantum dots.

In conclusion we have studied the magnetoresistance of gated quantum dot structures in the edge state regime. Large resonant features were observed in the resistance plateau and

we evaluate these with an interference effect between localized and extended edge states within the dot. The resistance plateaus were also found to be shifted above their expected quantized values consistent with increased edge state interaction within the dot. Studies of the temperature dependence of the resonances indicate that the inelastic scattering length of electrons in high field edge states is very much smaller than their associated equilibration length. The observation of large resonant features on plateau and away from the transition region between successive plateau provides support that the features we observe are intrinsic to quantum dot structures.

The authors would like to acknowledge invaluable discussions with: C. Burnes, M. Suta, R. P. Taylor, Y. Ohtani, D. K. Ferry, and J. Speiser.

References

- [1] For a recent review of theoretical and experimental aspects of quantum dot structures see D.K. Ferry, *Prog. Quant. Electr.* **16** (1992), 251.
- [2] G. Kirczenow, *Phys. Rev. B* **42** (1990), 5357, and G. Kirczenow and E. Cantano, *Phys. Rev. B* **43** (1991), 7333.
- [3] H. Xu, Z. Ji, and K.F. Berggren, *Superlatt. Microstruct.* **12** (1992), 237; G.W. Bryant, *Phys. Rev. B* **44** (1991), 12837; Y. Takagaki and D.K. Ferry, *Phys. Rev. B* **43** (1991), 8399; P.F. Bagwell, *Phys. Rev. B* **41** (1990), 10354, and D.G. Ravenhall, H.W. Wyld, and R.L. Schult, *Phys. Rev. Lett.* **63** (1989), 1790.
- [4] H. van Houten, C.W.J. Beenakker, and B.J. van Wees, in *Semiconductors and Semimetals* **35** (Ed. M.A. Reed), Academic Press, 1992.
- [5] R.J. Haug, *Scand. J. Technol.* **8** (1993), 131.
- [6] C.G. Smith, M. Pepper, H. Ahmed, J.E.F. Frost, D.G. Hasko, D.C. Penceck, D.A. Ritchie, and G.A.C. Jones, *J. Phys. C* **21** (1988), L893.
- [7] K. Ishibashi, J.P. Bird, Y. Aoyagi, and T. Sugaw, to appear in *Jap. Journ. Appl. Phys.*
- [8] B.J. van Wees, L.P. Kouwenhoven, E.M.M. Willems, C.J.P.M. Hammans, J.E. Mooij, H. van Houten, C.W.J. Beenakker, J.G. Williamson, and C.T. Foxon, *Phys. Rev. B* **43** (1991), 12431.
- [9] R.P. Taylor, A.S. Sachrajda, J.A. Adams, P. Zawadzki, P.T. Coleridge, and M. Davies, *Surf. Sci.* **263** (1992), 247.
- [10] C.J.B. Ford, S. Washburn, R. Newbury, C.M. Kneadler, and J.M. Hong, *Phys. Rev. B* **43** (1991), 7339.
- [11] R.P. Taylor, A.S. Sachrajda, J.A. Adams, P.T. Coleridge, and P. Zawadzki, *Phys. Rev. B* **47** (1993), 4458.
- [12] B.J. van Wees, L.P. Kouwenhoven, C.J.P.M. Hammans, J.G. Williamson, C.T. Timmerling, M.E.J. Buckaert, C.T. Foxon, and G. Harris, *Phys. Rev. Lett.* **62** (1989), 2523.

Figure Captions

Figure 1: Magnetoresistance of the quantum dot structure measured both with the gates grounded and with an applied bias such that the dot was well defined. The inset shows a schematic of the gate geometry as well as the numbering scheme of the measurement probes. The central dot had a lithographic area of $4\mu\text{m}^2$ and the corresponding length and width of the point contacts was $0.1\mu\text{m}$ and $0.4\mu\text{m}$ respectively.

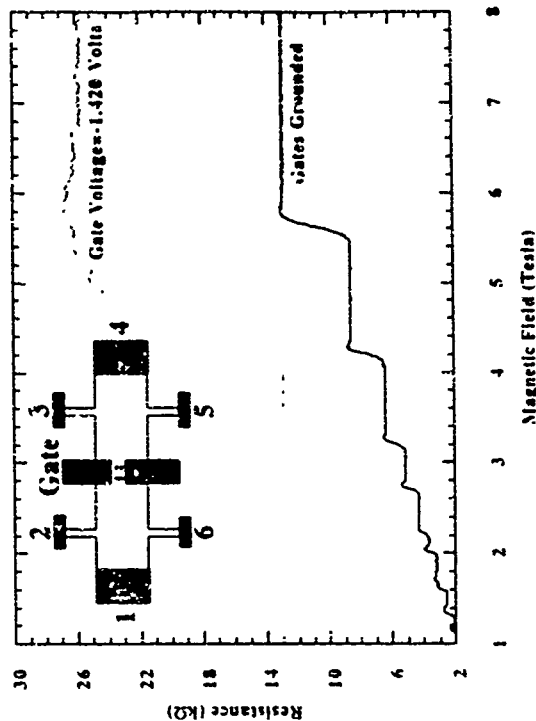
Figure 2: The evolution of the resonant structure for several well defined gate voltages. The corresponding magnetoresistance with the gates grounded is also shown for comparison.

Figure 3a: Temperature dependence of the resonance amplitude. For this gate voltage the dot was only just formed and over the magnetic field range shown two spin resolved edge states were occupied in both the bulk and the quantum dot. No resonant structure was observed in the corresponding bulk magnetoresistance trace however. For the sake of clarity, the curves at 105 mK , 400 mK , and 1200 mK have been offset by $+2k\Omega$, $+4k\Omega$, and $+6k\Omega$ respectively.

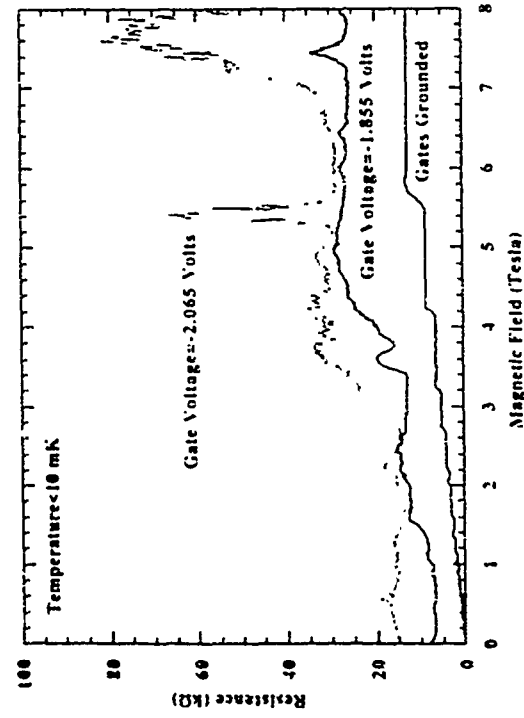
Figure 3b: Temperature dependence of two of the resonant features observed in figure 3a.

Figure 4: The dependence of the resonant structure on the measurement geometry. The probe combinations used in the two different measurements are shown as labels in the resulting magnetoresistance traces. In both measurements the resonances occur at the same magnetic field values, indicating their common origin.

JP Bird et al Fig 1

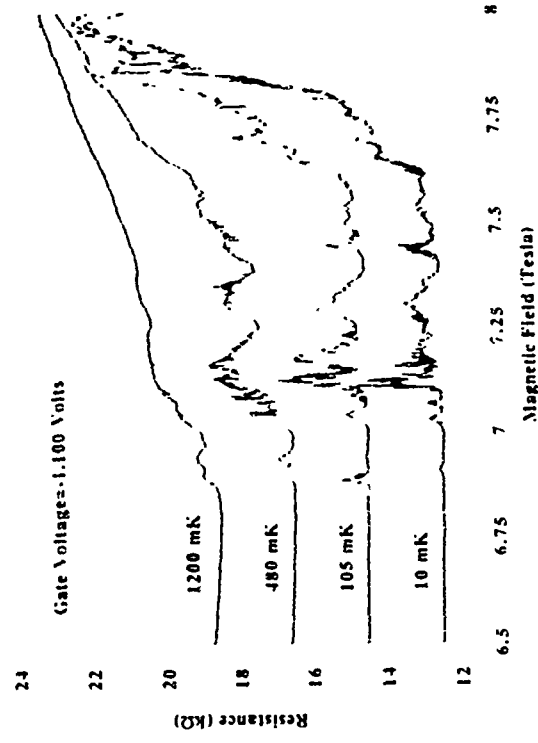


JP Bird et al Figure 2



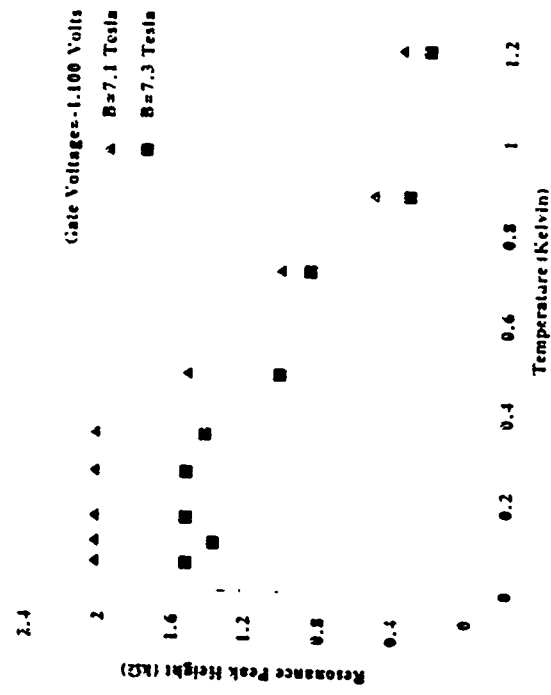
-257-

JP Bird et al Figure 3a

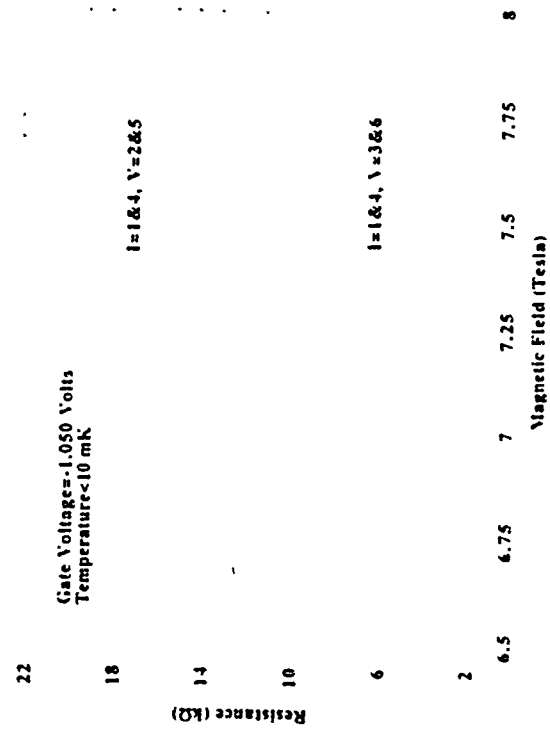


-258-

JP Bird et al Figure 3b



JP Bird et al Figure 4



Photovoltaic effect in quasiballistic electron interferometer

A.A. Bykov, D.D. Kvon, L.V. Litvin, Ju. V. Mastukov,
V.G. Vashurav, V.P. Mignat, S.P. Moschenko

Institute of Semiconductor Physics, Russian Academy of Sciences,
Siberian Branch, Novosibirsk 630090, Russia

It has been shown [1], that the lack of inversion symmetry in mesoscopic samples should give rise to a photovoltaic effect in the presence of microwave radiation. Later this effect has been observed and studied experimentally in various mesoscopic samples of single-connected geometry [2].

In this work we report the first observation of the photovoltaic effect in a quasiballistic electron interferometer exposed to microwave radiation with frequency lying in the range from 9 GHz to 140 GHz.

The experimental samples had a loop-shaped geometry and were fabricated by means of electron lithography with subsequent reactive ion etching. The 2D-electron gas parameters in the original AlGaAs/GaAs heterostructure at 4.2 K were as follows: $n_s = 2 \cdot 10^{11} \text{ cm}^{-2}$, $\mu_{300} = 10^5 \text{ cm}^2/\text{Vs}$. The effective ring diameter was about 0.5-0.7 μm .

At 75-82 K the application of microwave radiation to the interferometer results in appearance of a microwave emf oscillating with magnetic field. This emf has two constituents. The first one originates from the electron interference in π of the 1-cyclo channels and is analogous to those studied previously [3]. The second component of the microwave emf oscillates only with magnetic flux change Φ due through the area of the ring. As it is shown in [4] the magnetic field H is perpendicular to the plane of the ring. It is supposed that the component perpendicular with magnetic field is caused by the asymmetry of electron wave interference through the channels of the ring with respect to the ring center. At magnetic fields larger than ~ 1 Tesla the ring wave and ring wave interference disappear.

V.I. Pol'ko, D.E. Kuznetsov, D.V. Kuznetsov, D.E. Kuznetsov,
A.A. Bykov et al., in: Proceedings of the 1998 International
Conference on Physics of Semiconductors, 1998, p. 49.

Dimensional transition of weak localization effects in lateral surface superlattices

Peter E. Selmann^{a)} and Michael Suhrke^{b)}

^{a)} Max-Planck-Arbeitsgruppe Halbleitertechnik, O-1086 Berlin, Germany
^{b)} Institut für Theoretische Physik, Universität Regensburg, D-9300 Regensburg, Germany

Weak localization is investigated for a two-dimensional electron gas subject to a cosine-potential in one direction. With decreasing Fermi energy the system gradually develops into an array of almost isolated quantum wires of finite width. Interference effects are reduced in dimensionality if the coherent motion of the electrons between adjacent wires is suppressed. The weak-localization correction to the conductivity is remarkably enhanced then and changes its dependence on the phase coherence length from a logarithmic to a linear one. In the 1D limit the system shows a transition from weak to strong localization with increasing phase coherence length. The localization length changes from an exponential to a linear dependence on scattering length at the dimensional transition. Numerical results are presented for GaAs structures in dependence on Fermi energy.

1 Introduction. In addition to studies of two-dimensional systems weakly modulated by a periodic potential there exists a growing number of experimental investigations of carrier transport in strongly modulated structures which represent an array of quantum wires if the Fermi energy becomes smaller than the potential amplitude [1-3].

An interesting topic is the influence of interference effects such as weak localization in these systems. The 1D-2D transition of weak localization in a single quantum wire takes place if the phase coherence length becomes smaller than the wire width [6]. Subband effects and the transition to strong localization in a wire have been studied in Refs. [7, 8]. Weak localization in lateral surface superlattices has been investigated within a tight binding scheme [9]. In this calculation only one subband exists in each quantum wire which does not correspond to the experimental situation.

Our aim is to investigate the 2D-1D transition in weak localization in lateral surface superlattices with a more realistic model of the periodic potential. In semiconducting structures the total scattering length is usually much larger than the potential period of some hundred nanometers. The same applies to the phase coherence length which results in a transition from 2D to 1D behavior of weak localization if the Fermi energy becomes smaller than the potential amplitude. The mechanism of the transition has to be distinguished from that in a single wire due to the coupling of different wires via tunneling. It is expected to take place if coherent tunneling of the electrons from one wire to another is suppressed. In the limit of isolated wires a rapid transition to strong localization takes place with increasing phase coherence length. This will be taken into account approximately via a self-consistent treatment of the interference effects and will be used to estimate the localization length in dependence on Fermi energy. Details of the calculations will be published elsewhere [10].

2 Model of the system. We describe the uni-directional modulation of the 2DEG located in the x - y plane by a cosine-potential $V(y) = V_0 \cos(2\pi y/a)$. The solution of Schrödinger's equation yields a parabolic band in x -direction with the effective mass m^* and minibands in y -direction characterized by the band index n and the wave vector k_y which is restricted to the first Brillouin zone $(-\pi/a, \pi/a)$.

Investigating weak localization one has to consider elastic and inelastic scattering mechanisms, respectively. Elastic scattering is described within the model of Gaussian White Noise which corresponds to short-ranged scatterers in real space. Inelastic scattering limiting the phase coherence of electrons is assumed here for simplicity to be short-ranged, too. The total coupling constant $g = g^e + g^a$ is then the sum of the elastic and inelastic ones and given by the mobility μ_{2D} of the 2DEG. The inelastic coupling constant can be related to the phase coherence length L_ϕ via $\Delta_\phi \approx g^a/g \approx \ell/L_\phi$ [6]. ℓ is the total scattering length in x-direction.

For weak enough scattering ($E_F \gg \Gamma$) we can neglect interference effects in the equilibrium properties of the system and restrict ourselves to the self-consistent Born approximation [11]. The self-energy is averaged over the period a of the modulation potential which makes it independent of the quantum numbers n and k for short-range scattering. Numerical results for the density of states $g(E_F)$ which is related to the scattering rate via $\Gamma(E_F) = \pi g(E_F)$ are shown in Fig. 1 in dependence on Fermi energy for a modulation potential corresponding to usual experimental values [1-5]. Here and in the following figures the arrow indicates the position of the potential maximum.

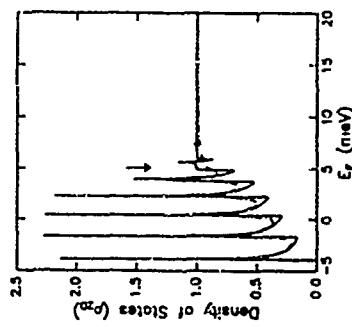


Fig. 1: Density of states in units of its value g_{2D} in a two-dimensional system in dependence on Fermi energy for a modulation potential of amplitude $V_0 = 5 \text{ meV}$ and period $a = 200 \text{ nm}$. The two different scattering strengths correspond to non-ohmicities of the 2D reference system $\mu_{2D} = 5 \times 10^4 \text{ cm}^2/\text{Vs}$ (solid line) and $\mu_{2D} = 5 \times 10^6 \text{ cm}^2/\text{Vs}$ (dashed-dotted line).

For energies well below the maximum at 5 meV , $g(E_F)$ behaves essentially as in one dimension. For stronger scattering the peaks are broadened by lifetime effects. Above the potential maximum the density of states approaches quickly its two-dimensional value which is energy independent. Close to the threshold the spectrum shows already dispersion in y-direction but the bands are still well separated by gaps. This leads to a step-like onset of the density of states at the lower band edge and a logarithmic divergence at the upper band edge for negligible scattering as usual for a band of finite width in two dimensions.

3 Conductivity. Regarding electron transport properties it is essential to include interference of electron waves leading to weak localization even if $E_F \gg \Gamma$ [11,12]. This means that in addition to diagrams with non-crossed interaction lines corresponding to the self-consistent Born approximation those with maximally crossed impurity lines have to be taken into account. We have done this by use of the non-equilibrium Green function technique [8,10]. First, we evaluate the conductivity of the system in self-consistent Born approximation. Without magnetic field and at zero temperature the diagonal tensor of band

conductivities is given by

$$\sigma_{ii}^0(E_F) = \frac{e^2}{h} \sum_{\mathbf{k}} v_i^2 A_{\mathbf{k}\mathbf{k}}^2(E_F), \quad v_i = \frac{\partial E_{\mathbf{k}}}{\partial k_i} \quad (1)$$

with the group velocity v_i and $i = x, y$. Here we have omitted the non-diagonal elements of the velocity matrix element in y-direction which correspond to scattering-induced interband transitions. The anisotropy of the system enters via the differing group velocities for both directions. Obviously, the group velocity in y-direction vanishes in the 1D limit since the spectrum shows no dispersion in this direction.

From the conductivity tensor one can obtain the tensor of diffusion coefficients with help of the Einstein relation $D_{ii}(E_F) = \sigma_{ii}^0(E_F)/e^2 g(E_F)$. The diffusion coefficients are related to the scattering lengths $l_i(E_F)$ by $l_i(E_F) = \hbar D_{ii}(E_F)/\Gamma(E_F)$. The latter are shown in Fig. 2 in dependence on Fermi energy.

The scattering length l_y along the equipotential lines is seen to be much larger than the potential period and subband effects are well resolved. This results in the pronounced oscillations of l_y in the one-dimensional region ($E_F < V_0$). Above the threshold it behaves as in two dimensions $l_y \sim \sqrt{E_F}$. The scattering length l_x in direction of the potential modulation is extremely small in the 1D region as expected. Contrary, for $E_F > V_0$ it shows a 2D energy dependence as l_x , but is smaller in amplitude due to the lower density of electrons which can move freely into this direction. At the threshold one recognizes the influence of the finite band width due to the enhanced tunneling between adjacent potential wells both on l_x and on l_y , which becomes finite there.

Within the non-equilibrium Green function technique [8,10] a self-consistent treatment of the Cooperon allows to investigate the transition from weak to strong localization and to estimate the localization length. For a modulated 2DEG the resulting conductivity is for zero temperature

$$\sigma_{xx}(E_F) = \frac{e^2}{h} \sum_{\mathbf{k}} \hbar^2 v_x^2 A_{\mathbf{k}\mathbf{k}}^2(E_F) (1 + F_{\text{AL}}(E_F))^{-1} \quad (2)$$

with

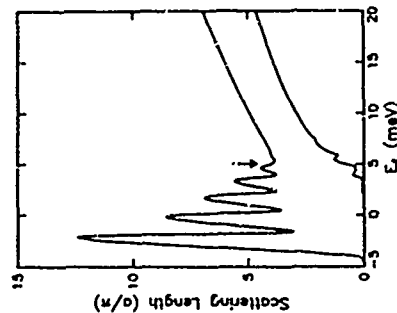


Fig. 2: Scattering lengths l_x (upper curve) and l_y (lower curve) in units of $a/2$ in dependence on Fermi energy for $\mu_{2D} = 5 \times 10^4 \text{ cm}^2/\text{Vs}$ and otherwise the same parameters as in Fig. 1.

$$F_{\Delta}(E_F) = g^2 C(E_F) A_{\Delta}(E_F) / \Gamma(E_F) \quad (3)$$

In Eq. (3) $C(E_F)$ represents the Cooperon averaged over the potential period as it has been done for the self-energy. Note that the Cooperon term appears in the denominator of the relation for the conductivity as a result of self-consistency. The solution for the Cooperon reduces to the expressions derived in Ref. [8] in the limit of an isolated quantum wire if the spectrum shows no dispersion in y -direction and to the usual expression* for a 2D system for vanishing modulation potential. For $L_y \gg a$, the result is

$$C(E_F) \approx \frac{1}{4\pi l_y l_z} \int_{-\infty}^{\infty} dt \exp\left[\frac{\pi l_y (t/r)^{1/2}}{a}\right] e^{-iEt/\hbar} \quad (4)$$

after an expansion for small q ($L_y \gg l_y$). Here, $\tau_0 = \hbar / V_{\Delta}$ is the phase coherence time, l_y and l_z are the scattering lengths defined above, and the total scattering time $\tau = \hbar / \Gamma$ has been used as the necessary short-time cutoff [12]. The limiting cases of Eq. (4) are $C(E_F) = L_y / 2l_y^2$ for $L_y \ll a$ and $C(E_F) = (1/2\pi l_y l_z) \ln(L_y/l_z)$ for $L_y \gg a$ where we have introduced the phase coherence length in y -direction $L_y = \sqrt{D_y \tau_0}$. The Cooperon acquires its one-dimensional form for $l_y \rightarrow 0$ and behaves as in two dimensions for $l_y \sim l_z \gg a$. This means that the 1D-2D transition in weak localization effects takes place in coupled wires when the electrons can tunnel between adjacent wires without losing phase coherence, i.e. if L_y becomes larger than the modulation period. This has to be distinguished from the usual 1D-2D transition in an isolated wire discussed e.g. in Ref. [6] which takes place if the phase coherence length becomes smaller than the wire width. For weak interference effects, i.e. not too large phase coherence length, one can expand the denominator in Eq. (2) which yields the usual perturbational relation $\sigma_{\Delta}(E_F) \approx \sigma_{\Delta}^0(E_F) - \Delta\sigma_{\Delta}(E_F)$ with the limits $\Delta\sigma_{\Delta}^0(E_F) = (3/2)(e^2/\pi\hbar)(L_y/a)$ and $\Delta\sigma_{\Delta}^0(E_F) = (3/2)(e^2/\pi\hbar) \ln(L_y/l_z)$. The small parameter for this expansion is $\delta = 4g^2 C(E_F) / \Gamma^2(E_F) \approx 4\Delta\sigma_{\Delta}(E_F) / 3\Delta\sigma_{\Delta}^0(E_F)$ [8]

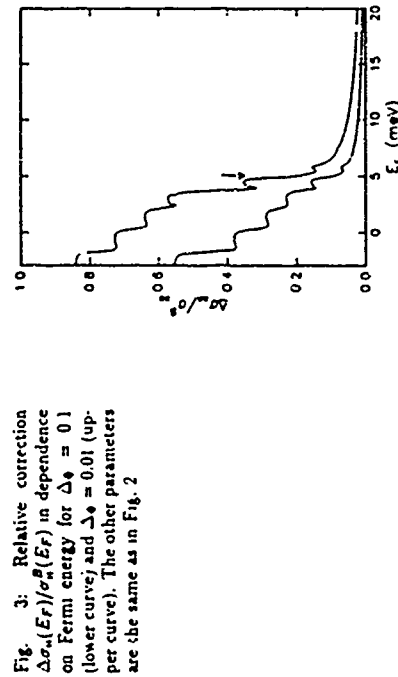


Fig. 3: Relative correction $\Delta\sigma_{\Delta}(E_F)/\sigma_{\Delta}^0(E_F)$ in dependence on Fermi energy for $\Delta\phi = 0.1$ (upper curve) and $\Delta\phi = 0.01$ (lower curve). The other parameters are the same as in Fig. 2

If δ becomes larger with increasing phase coherence length and for low electron densities the conductivity Eq. (2) approaches zero which describes the transition to strong localization. Now, the weak localization correction acts additive in the resistivity. The relative correction $\Delta\sigma_{\Delta}(E_F)/\sigma_{\Delta}^0(E_F)$ is shown in Fig. 3. The different ratios of elastic to inelastic scattering strengths, $\Delta\phi$, correspond to phase coherence lengths of about $1\mu\text{m}$ (lower curve) and $3\mu\text{m}$ (upper curve). The population of 1D subbands with increasing Fermi energy leads to a stepwise decrease of $\Delta\sigma_{\Delta}/\sigma_{\Delta}^0$. For low electron densities and weak inelastic scattering interference effects contribute considerably to the total conductivity and the usual perturbative result is not applicable. If the Fermi energy becomes larger than the potential amplitude the conductivity correction is much smaller and only weakly dependent on energy as expected for a 2DEG. The minima close to the threshold are due to the finite widths of the minibands leading to 2D behavior of weak localization. They become more pronounced for larger L_y when 1D behavior is preserved to larger Fermi energies.

The expansion parameter δ can be used to estimate the localization length l_{Δ} in our system from the assumption that the interference effects begin to dominate the conductivity if L_y becomes larger than l_{Δ} , $\delta(L_y = l_{\Delta}) = 1$.

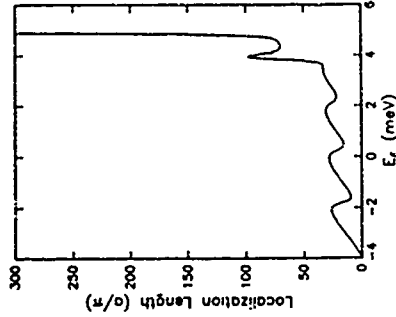


Fig. 4: Localization length l_{Δ} in units of a/x in dependence on Fermi energy for the parameters of Fig. 2

The localization length obtained from this assumption fulfills the correct limiting relations $l_{\Delta}^D = V l_z$ and $l_{\Delta}^D = l_z \exp(\pi k_F l_z / 4)$ where N is the number of occupied subbands in the 1D limit and k_F is the Fermi wave vector. It is shown in Fig. 4 its dependence on Fermi energy. Below 3 meV the localization length behaves essentially as in one dimension. Above the potential maximum l_{Δ} rises exponentially with Fermi energy as usual for a two-dimensional system. For $E_F \sim 4\text{ meV}$ the system undergoes a transition from being effectively one-dimensional to the 2D regime as the electrons become allowed to tunnel coherently between adjacent wires in the last subband below ϕ_0 .

4 Conclusions. A study of interference effects in a 2DEG subject to a uni-directional periodic modulation has been presented. With decreasing ratio of Fermi energy and potential amplitude the system turns from a weakly modulated 2DEG into an array of quantum wires which are coupled by tunneling. A transition from 2D to 1D behavior of the weak localization correction to conductivity is found if the coherent propagation of the electrons between adjacent wires is suppressed. This occurs when the period of the potential exceeds the transversal phase coherence length related to the diffusion coefficient in the direction perpendicular to the wires. We have presented numerical results for transport properties in dependence on Fermi energy, showing a smooth transition from the 2D to the 1D limit.

LIUMINESCENCE STUDIES OF RESONANT TUNNELING IN A TRIPLE
BARRIER STRUCTURE WITH STRONGLY COUPLED QUANTUM WELLS

T. S. Turner, P. M. Martin, I. Eaves, H. B. Evans, P. A. Harrison, M. Hemmi and
O. H. Hughes

Department of Physics, University of Nottingham, Nottingham NG7 3RD

D. M. Whitaker, P. D. Buckle, T. A. Fisher, M. S. Skolnick, and G. Hill*
Department of Physics, University of Sheffield, Sheffield S3 7RH

Abstract

The electrical and optical properties of an n-doped triple barrier resonant tunneling diode are investigated. A thin central AlAs barrier provides strong coupling between the two GaAs quantum wells which have equal widths. Photoluminescence (PL) arises from both spatially direct and spatially indirect transitions in the quantum wells. The intense spatially indirect transition shows a pronounced red shift with increasing bias. A strong intrinsic bistability effect is observed in one of the three resonant peaks in the current-voltage curve. This effect is also seen in the photon energy and intensity of the PL from the wells. Photoluminescence excitation spectroscopy is used to identify the optical transitions and the strength of the tunneling interaction.

The optical properties of coupled quantum wells separated by a thin tunnel barrier have been intensively investigated in recent years [1-3]. An interesting feature of these structures is that the thin central barrier leads to a strong quantum mechanical coupling between the two states in the quantum wells. In a device in which the two quantum wells have the same width, an applied electric field reduces this coupling and at sufficiently high electric fields the electron (and hole) wavefunctions become largely confined to one or other of the two quantum wells. A coupled quantum well structure comprising a thin central barrier and two wider outer barriers can be incorporated in the undoped, intrinsic (i) region of an n-i-n diode to form a modified version of the standard double barrier resonant tunneling device [4]. When a voltage is applied to this structure, resonant tunneling of electrons can occur from the doped contact regions into the quantum wells and peaks are observed in the current-voltage characteristics, $I(V)$.

Photoluminescence spectroscopy has proved to be a powerful tool for studying double barrier resonant tunneling devices [5-9] and provides detailed information about the charge buildup in the bound states of the quantum well [10-12] and of the energy relaxation and recombination processes. In this paper, we use photoluminescence (PL) and photoluminescence excitation (PLE) spectroscopy to investigate a triple barrier resonant tunneling structure with coupled quantum wells. Spectra were obtained over a wide range of bias and compared with the resonance effects observed in the current-voltage characteristics, $I(V)$. Electron hole recombination in the quantum wells gives rise to two intense PL lines. The line corresponding to spatially indirect recombination has the much higher intensity and its photon energy is tunable with applied bias. A very pronounced intrinsic bistability effect is observed in one of the resonances in the $I(V)$ characteristics due

respectively. Furthermore, we have estimated the localization length of the system which changes from an exponential to a linear dependence on scattering length.

M.S. acknowledges financial support by the DFG (Sonderforschungsbereich 348 - Teilprojekt YD). P.E.S. wishes to thank the GOS e.V., Berlin.

References

- [1] K. Imail, W. Chu, D. A. Antoniadis, and H. I. Smith, *Appl. Phys. Lett.* **52**, 1071 (1988).
- [2] J. Alneier, Ch. Sikorik, and U. Merkt, *Phys. Rev. B* **37**, 4314 (1988).
- [3] F. Brinkop, W. Hansen, J. P. Kotthaus, and K. Ploog, *Phys. Rev. B* **37**, 6547 (1988).
- [4] P. H. Beton, E. S. Alves, P. C. Main, L. Eaves, M. W. Dellow, M. Hemmi, O. H. Hughes, S. P. Beaumont, and C. D. W. Wilkinson, *Phys. Rev. B* **42**, 9729 (1990).
- [5] G. Berthold, J. Smolin, W. Demmerle, F. Hirler, E. Gornik, W. Etmüller, G. Böhm, and G. Weimann, *Semicond. Sci. Technol.* **6**, 709 (1991).
- [6] M. J. Kearney and P. N. Butcher, *J. Phys. C: Solid State Physics* **21**, 2539 (1988).
- [7] M. Suhrke, S. Wilke, and R. Keiper, *Solid State Commun.* **76**, 551 (1990).
- [8] M. Suhrke and S. Wilke, *Phys. Rev. B* **46**, 2400 (1992).
- [9] W. Szott, C. Jendrysek, and W. P. Kirk, *Superlattices and Microstructures* **11**, 199 (1992).
- [10] M. Suhrke and P. E. Selmann, submitted to *Phys. Rev. B*.
- [11] B. L. Altshuler, A. G. Aronov, D. E. Khmel'nitskiĭ, and A. I. Larkin, in *Quantum Theory of Solids*, edited by I. M. Lifshits (Mir Publishers, Moscow, 1982), p. 130.
- [12] G. Bergmann, *Phys. Rep.* **107**, 1 (1984).

to a space charge buildup process. This involves resonant electron tunneling into one of the wells, followed by a sequential tunneling process across the thin central barrier, accompanied by the emission of a longitudinal optic phonon.

Figure 1 shows a schematic band diagram of the device at a bias of around 0.6 V. The device consists of two GaAs quantum wells, each of width 6 nm, separated by a thin central barrier of AlAs, of nominal width 0.85 nm (3 monolayers). The two outer AlAs barriers are 5.1 nm wide. Two undoped GaAs spacer layers of width 7.6 nm separate the barriers and quantum wells from the Si-doped contact regions in which the doping is graded from $1 \times 10^{18} \text{ cm}^{-3}$ to $2 \times 10^{18} \text{ cm}^{-3}$. The top n^+ contact region incorporates an $\text{Al}_{0.15}\text{Ga}_{0.85}\text{As}$ window layer to transmit light to and from the region of the quantum wells. The devices are in the form of circular mesas of diameter 100 μm , with an annular Au/Ge top contact which provides optical access.

Figure 2(a) shows the $I(V)$ curve with the substrate biased negative. A similar curve is obtained in the opposite bias direction. Three resonant peaks are observed, corresponding to resonant tunneling into the three quasi-bound states of the conduction band quantum wells shown in Figure 1. Tunneling occurs from a two-dimensional electron gas in the accumulation layer adjacent to the left-hand barrier. The second peak (E2) exhibits a pronounced intrinsic bistability effect which, as discussed below, also appears in the PL emission spectra. Interestingly, this second peak has a higher maximum current in $I(V)$ than the third (E3), even though it occurs at about half of the applied voltage. Such behaviour is not observed in conventional double barrier resonant tunneling devices in which the current passed at successive resonances increases with increasing bias [see for example ref. 13].

Photoluminescence from the device was excited using a He-Ne laser ($\lambda = 633 \text{ nm}$). Photoexcited holes created in and around the electron depletion layer between the quantum wells and the positively biased contact layer are swept towards the tunnel barrier by the applied electric field (see Figure 1). They can then tunnel into the quantum well where they undergo recombination with electrically injected electrons, giving rise to PL. Figure 3 shows a series of spectra taken with an excitation power density of $\sim 0.5 \text{ W/cm}^2$, at a lattice temperature of 4 K. No change in the $I(V)$ curve is observed at these relatively low laser power densities. The PL spectra consist of three distinct features: the feature at around 1.5 eV corresponds to recombination of photoexcited holes in the n -type GaAs contact layers, and will not be discussed in detail in this paper, the two lines, QW1 and QW2, arise from electron-hole recombination in the quantum well region. Their intensities as a function of bias are shown in Figure 2(b) and reveal resonant features which can be related to those in $I(V)$. For most biases above about 0.1 V, the QW1 line has an intensity which is comparable to that of the near-band edge recombination (see Figure 3). It shows a pronounced peak in intensity at a bias corresponding to the peak of the E1 resonance in $I(V)$. A weak peak in the intensity of this line (peak H) is also observed at a lower bias (0.135 V) which we ascribe to resonant tunneling of the photoexcited holes into the quantum well regions. The intensity of the QW1 line is bistable in the region of the second (E2) resonance in $I(V)$. Interestingly, on the high current section of the bistable loop the intensity of QW1 is low, its intensity is about a factor of two higher on the low current section of the loop. An additional weak peak is observed in the intensity of QW1 at around 0.7 V. A corresponding broad feature is also observed in $I(V)$ and we ascribe both to electron tunneling into the E2 state of the quantum

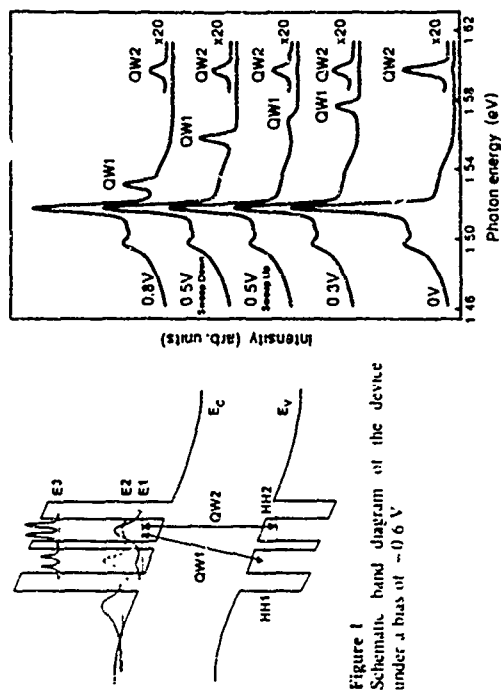


Figure 1 Schematic band diagram of the device under a bias of -0.6 V

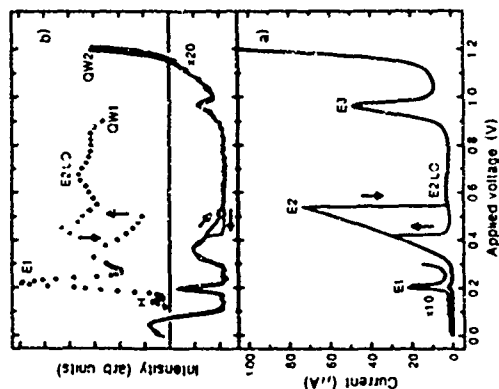


Figure 2 (a) The current-voltage characteristics, $I(V)$, taken at 4 K (b) The variation, as a function of bias, of the intensity of the two photoluminescence lines, QW2 and QW1

Figure 3 Photoluminescence spectra, taken at 4 K and various bias conditions. The spectra at $V = 0.5 \text{ V}$ were obtained in the high and low current sections of the bistable loop

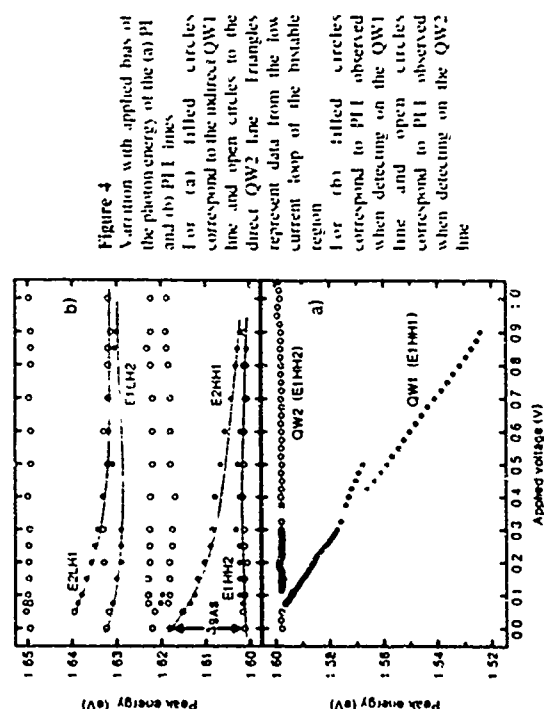


Figure 4
Variation with applied bias of the photon energy of the (a) PL line and (b) PLE lines. For (a) filled circles correspond to the indirect QW1 line and open circles to the direct QW2 line. Triangles represent data from the low current loop of the bistable region. For (b) filled circles correspond to PLE observed when detecting on the QW1 line and open circles correspond to PLE observed when detecting on the QW2 line.

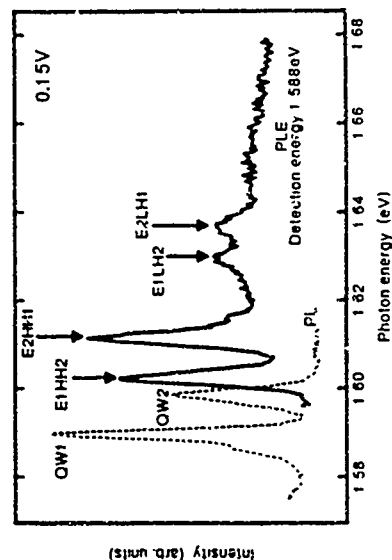


Figure 5
A typical PL spectrum and its associated QW PLE spectrum at 0.15 V.

well, accompanied by the emission of a longitudinal optic (LO) phonon. As shown in Figure 4(a) the QW1 line undergoes a significant red shift with increasing bias, shifting from 1.60 eV at 0.1 V to 1.525 eV at 0.9 V, where it merges with the band gap emission from the contact region. The weaker line, QW2, at 1.60 eV does not shift in energy with bias. Its intensity is typically ~ 20 times weaker than QW1. The variation of the intensity of the QW2 line with bias shows distinct peaks at the E1 and E2 resonances in LiV. There is also a peak at 0.325 V, at the onset region of the E2 resonance, a weak bistability is also observed at slightly higher voltages. At low bias between 0 and 0.1 V, the QW1 and QW2 lines merge and have a weak intensity relative to the PL from the GaAs contact regions.

We can understand the qualitative behaviour of the LiV characteristics and of the PL spectra by considering the effect of the applied voltage on the confined electron and hole states in the quantum wells. The thin central barrier couples the two quantum wells which in this device have the same thickness. At zero bias, the electron (and hole) wavefunction of the two lowest states E1 and E2 of the conduction (and valence) band quantum wells are of the familiar symmetric and antisymmetric type, extending over both wells. Increasing bias causes the electron wavefunctions to become increasingly localized in one or other of the two conduction band quantum wells as shown schematically in Figure 1. This effect is even more pronounced for holes because of their larger effective mass. The three peaks in LiV correspond to resonant tunnelling into states E1 and E2 and into the lower energy state E3 of the upper pair of coupled QW states, E3 and E4. No E4 resonance is observed, however.

We ascribe both PL lines to transitions involving electrons in the E1 state of the conduction band quantum wells. The QW2 line is due to a transition between E1 and HH2, the lowest hole state of the right hand well. The QW1 line arises due to a spatially indirect transition between E1 and HH1 (see Figure 2). The voltage-induced confinement effect leads to the pronounced red shift of transition QW1 with increasing bias. In contrast, the shift of QW2 is small as it effectively corresponds to a spatially direct transition. The relative weakness of the spatially direct QW1 line indicates that the hole population is much higher in the left hand quantum well.

This identification of the transitions corresponding to the QW1 and QW2 lines is confirmed by the PLE measurements which were obtained with a Ti-sapphire laser pumped by an Ar ion laser, detecting on either the QW1 or QW2 emission lines. A typical PLE spectrum at a bias of 0.15 V is shown in Figure 5 and reveals four clear QW transitions. The spectrum was obtained at a detection energy of 1.588 eV corresponding to the QW1 PL line. The QW PL spectrum at this bias is also shown in Figure 5. The variation of the principal PLE lines with bias is shown in Figure 4(b). These data give a value of the symmetric, antisymmetric splitting (electron + hole) of $\Delta = 17$ meV under flat band conditions at zero bias, in reasonable agreement with the value obtained from an effective mass model. The PLE measurements also confirm the identification of the QW1 and QW2 emission lines as E1 HH1 and E1 HH2 respectively, each of which involves the lowest heavy hole (HH) states of the respective quantum wells. Note that the E1 HH2 and E2 HH1 lines in PLE do not move symmetrically with increasing bias; the downward shift of E2 HH1 is considerably larger than the upward shift of E1 HH2. We attribute this to an excitonic effect in which the exciton binding energy decreases with increasing bias due to the increasing electron localization in the individual QWs.

References

- [1] A. Alexandrou, J. A. Kash, L. E. Mendez, M. Zechau, J. M. Hong, T. Fukuzawa and Y. Iase, *Phys. Rev. B* **142** (14), 9225 (1990)
- [2] T. Fukuzawa, P. E. Mender and J. M. Hong, *Phys. Rev. Lett.* **64** (25), 3066 (1990)
- [3] Y. J. Chen, L. S. Kotéles, R. S. Etkin and C. A. Armiento, *Phys. Rev. B* **36** (8), 4562 (1987)
- [4] L. I. Chang, L. Esaki and R. L. Tsu, *Appl. Phys. Lett.* **24** (1974)
- [5] J. F. Young, B. M. Wood, G. C. Aers, R. L. S. Devine, H. C. Liu, D. Landheer, M. Buchanan, A. J. Springthorpe and P. Mandelville, *Phys. Rev. Lett.* **60**, 2085 (1988)
- [6] N. Vojdani, D. Cote, D. Thomas, B. Sernage, P. Bois, E. Costard and J. Nagle, *Appl. Phys. Lett.* **56**, 33 (1990)
- [7] M. S. Skolnick, D. G. Hays, P. E. Simmonds, A. W. Higgs, G. W. Smith, H. J. Hutchinson, C. R. Whitehouse, L. Eaves, M. Henini, O. H. Hughes, M. L. Leadbeater and D. P. Halliday, *Phys. Rev. B* **41**, 10754 (1990)
- [8] C. R. H. White, M. S. Skolnick, L. Eaves, M. L. Leadbeater, M. Henini, O. H. Hughes, G. Hill and M. A. Pate, *Phys. Rev. B* **45**, 6721 (1992)
- [9] C. van Haest, J. Genoe, R. Mertens, G. Borghs and E. Goovaert, *Appl. Phys. Lett.* **60**, 77 (1992)
- [10] V. J. Goldman, D. C. Tsu and J. E. Cunningham, *Phys. Rev. Lett.* **58**, 1256 (1987)
- [11] L. S. Alves, L. Eaves, M. Henini, O. H. Hughes, M. L. Leadbeater, F. W. Sheard, G. A. Toombs, G. Hill and M. A. Pate, *Elect. Lett.* **24**, 1190 (1988)
- [12] M. L. Leadbeater, L. S. Alves, F. W. Sheard, L. Eaves, M. Henini, O. H. Hughes and G. A. Toombs, *J. Phys. Condens. Matter* **1**, 10605 (1989)
- [13] L. S. Alves, M. L. Leadbeater, L. Eaves, M. Henini and O. H. Hughes, *Solid State Electronics* **32**, 1627 (1989)
- [14] J. W. Cockburn, P. D. Buckle, M. S. Skolnick, D. M. Whittaker, W. I. E. Tagg, R. A. Hoeg, R. Grey, G. Hill and M. A. Pate, *Phys. Rev. B* **45**, 13757 (1992)

The observation of an intense QW1 line even when the device is biased on the E2 resonance implies that electrons which resonantly tunnel into E2 relax their energy and scatter into E1 prior to recombination. The energy separation of the E2 (HH1) PL line and the E1 (HH1) PL line indicate that the energy separation between the E2 and E1 levels exceeds the optical phonon energy in GaAs ($\hbar\omega_{ac} \approx 36$ meV) at bias voltages above about 0.38 V. Hence E1 phonon emission is energetically possible over most of the bias range of the E2 resonance. Further evidence for this relaxation process is provided by the strong peak in PLT due to the E2 (HH1) transition for detection on the QW1 (E1-HH1) transition.

Using magneto-tunneling measurements [12] we estimate that the electron sheet density in the right hand quantum well is $n_s \approx 1 \times 10^{11} \text{ cm}^{-2}$ on the peak of the E2 resonance at 0.525 V. The linewidth of the QW1 line also provides us with an estimate of the charge density in the E1 state. The linewidth varies with applied voltage, showing peaks at all three electron resonances in E1. From the linewidth at 0.525 V we obtain an estimate of $n_s \approx 1.3 \times 10^{11} \text{ cm}^{-2}$ (using the relation $J = n_s e / \tau_{\text{tunn}}$ and the measured value of the current density $J \approx 8.6 \text{ kA m}^{-2}$); we estimate the tunneling time to be 25 ns at this voltage. Both this time and the expected radiative recombination time of the spatially indirect QW1 transition $\tau_{\text{rad}} \approx 1$ ns are much longer than the E1 phonon emission time $\tau_{\text{E1}} \approx 0.3$ ps. Hence the absence of any observable PL from electrons in the E2 state is not surprising since the relative population of E1 to E2 is given by $\tau_{\text{E1}}(\tau_{\text{rad}}^{-1} + \tau_{\text{tunn}}^{-1}) \approx 10^3$ [14].

The red shift of the QW1 PL with increasing bias (see Figure 4(a)) shows an interesting dependence in the region of the E2 resonance. On the high current section of the bistability loop the rate of red shift of QW1 with increasing bias is smaller than on the low current section. A similar but less pronounced behaviour is also observed on the E1 resonance around 0.2 V and on the E1 phonon related peak at around 0.7 V. This effect is associated with the build up of space charge in the quantum well at resonance. When the device is biased on a resonance, the voltage drop across the emitter barrier remains constant and the additional voltage necessary to sweep through the resonance gives rise to charge buildup in the quantum well. This additional voltage is then dropped mainly across the collector barrier and depletion layer beyond. In this device the red shift of the QW1 line is effectively due to the increasing voltage drop across the two quantum wells with increasing bias. On the E2 resonance, the built up charge resides in the πs^* band quantum well and therefore the rate of red shift with increasing voltage is much smaller than it is for regions of bias voltage in which there is no resonant charge buildup.

In conclusion we have shown that photoluminescence and photoluminescence excitation experiments as a function of bias can provide detailed information about the energy levels and inter well transitions in a coupled well system under resonant tunneling conditions. The origin of the strong intrawell bistability observed in the E1 characteristics is explained in terms of a charge build up effect involving a sequential tunneling process, with E1 phonon emission across the central barrier.

This work is supported by the Science and Engineering Research Council and the European Community.

CORRELATION EFFECTS IN MAGNETOLUMINESCENCE SPECTRA FROM DEUTERON QUASI-2D ELECTRON GAS IN SELECTIVELY DOPED InGaAs/GaAs QUANTUM WELLS

V. J. Kulakovskii, V. V. Burkov, I. E. Itskovich, L. V. Kulik
Solid State Physics Inst. Russian Academy of Sciences, 142432, Chernogolovka, Russia

T. G. Andersson, W. Stuttmann
Department of Physics, Chalmers University of Technology, Gothenburg, Sweden

A. V. Lomsadze
High Pressure Physics Inst. Russian Academy of Sciences 142092, Troitsk, Russia

Abstract

Low temperature magnetoluminescence from a quasi-2D electron gas in $\text{n-AlGaAs/InGaAs/GaAs}$ quantum well with a partially filled $n=2$ subband has been investigated for $n=1$ electrons. The energy of interband Landau level transitions has been found to demonstrate an oscillating magnetic field dependence, and an additional structure in the emission lines has been revealed. The former is related with oscillations in the energy gap between the $n=1$ and $n=2$ subbands due to the redistribution of electrons between the subbands, while the latter indicates a strong enhancement of shake-up processes that allows different final states in the photoemission transition.

1. INTRODUCTION

High carrier density effects in quasi 2D (two dimensional) semiconductor quantum well (QW) heterostructures are of considerable interest from a fundamental point of view to test many-particles theories of structures with reduced dimensionality [1-4]. Most publications deal with the shrinkage of the fundamental energy gap, referred to as band gap renormalization which is due to exchange and correlation interaction.

In charged systems, the dynamic response of an electron Fermi sea to the optically generated holes is known to give rise to an enhanced interaction of correlated electron-hole pairs near the Fermi level. It results in an enhanced oscillator strength for optical transitions at the Fermi edge [5-8], referred to as Fermi-edge singularity. However, in the 2D magnetoplasma with the single occupied electron subband, the interband Landau level (LL) transition energies turn out to be almost linear in a magnetic field and separated by the electron cyclotron energy, $\hbar\omega_c$.

In the present paper we study peculiarities in the low temperature radiative recombination of the $n=1$ electrons in QWs with a partial filling of the next, $n=2$, subband in high magnetic fields under low excitation level. We have found that, first, the dependence of the LL transition energy on magnetic field becomes nonmonotonic and, second, an additional well resolved structure appears in the emission spectra. The latter cannot be described in a simple approximation that the $n=1$ electron-hole recombination leaves the free quasiparticle in the first conduction subband. With increasing temperature these effects become negligible at $T=10-12$ K. The oscillations of the transition energy with magnetic field are supposed to be related with variations in the energy gap between the first and second subbands. The latter is due to the redistribution of electrons between the subbands when their Landau levels cross each other [9,10]. The additional emission lines indicate a strong enhancement of the shake-up processes that give rise to different final states of the photoemission transition.

II. EXPERIMENTAL

Selectively doped single QW heterostructures were grown by MBE using solid source evaporation material. We used (001)-oriented substrates of semi-insulating GaAs . The layers were grown in the following succession - an 500 nm GaAs buffer layer, an undoped 25 nm thick $\text{In}_{0.18}\text{Ga}_{0.82}\text{As}$ QW, an undoped 5 nm $\text{Al}_{0.25}\text{Ga}_{0.75}\text{As}$ spacer, a δ -layer of Si ($N \sim 2.5 \cdot 10^{12} \text{ cm}^{-2}$), and a 50 nm $\text{Al}_{0.25}\text{Ga}_{0.75}\text{As}$ layer. The 2DEG concentration was $n_{2D} \sim 2.4 \cdot 10^{12} \text{ cm}^{-2}$.

Photoluminescence measurements were carried out with the use of a cw He-Ne laser with $\lambda=632.8$ nm. The sample was placed in a cryostat with a superconducting coil. It was immersed in liquid helium (4.2 K or 1.2 K) or located in helium vapor (4.2 K). To control the electron concentration in the QW we have used the quasi-hydrostatic pressure up to 3 GPa. In this case the sample was located in a low-temperature fixed pressure cell with diamond anvils, one of which was used as an optical window.

The plane of the QW was oriented normally to the magnetic field. A 0.6 mm quartz fiber was used to transmit both the excitation and luminescence light. The latter was dispersed by a grating monochromator and detected by a cooled photomultiplier.

III. EXPERIMENTAL RESULTS AND DISCUSSION

1. Emission spectra from 2DEG

To investigate the influence of the second subband filling on the emission spectra, we start from the case when it is empty. Figure 1 displays low excitation 2DEG emission spectra from a selectively doped $\text{n-AlGaAs/InGaAs/GaAs}$ 25 nm thick QW under 3 GPa for different magnetic fields at 1.8 K. Without external pressure a 2DEG density is $2.4 \cdot 10^{12} \text{ cm}^{-2}$, and $\hbar\omega_c$ corresponds to two subbands. The pressure of 3 GPa decreases n_{2D} down to $8 \cdot 10^{11} \text{ cm}^{-2}$ that results in depopulating of the second subband. The magnetoluminescence spectra consist of a few lines $J_e - O_h^1$ corresponding to the transitions between occupied LLs in the first (1) subbands of conduction (J_e) and valence (O_h) bands. In addition, there is a weak $J_e - O_h^1$ line that appears due to slow relaxation of photoexcited holes. The dipole-forbidden transitions $J_e - O_h^1$ with J_D appear mainly due to the defect induced carrier scattering. Both the small relative intensity of these transitions and the small halfwidth of the lines indicate the high quality of the QW investigated.

Figure 1 shows that the $J_e - O_h^1$ transition energies, $E_{J_e - O_h^1}$, are nearly linear in H . In the present paper only the recombination of holes from the $J_e - O_h^1$ LL is discussed, and we indicate only the numbers of the electron LL and subband. The energy gap between the near-by transitions, $\Delta E_{J_e - O_h^1} = E_{J_e - O_h^1} - E_{J_e - O_h^1}$, corresponds to a cyclotron energy of electrons with effective mass $m_0 = 0.084 m_0$, where m_0 is the free electron mass. This value is close to the calculated one (0.078 m_0) in the framework of Kane's model. These features are typical for the emission spectra from 2DEG with a single occupied subband.

Figure 2 shows an example of the magnetic field dependence of the emission spectra at higher 2DEG density, with the second subband partly filled. It displays the spectra from the same sample as Fig 1 but under pressure of 1.8 GPa, when n_{2D} increases to $\sim 1.3 \cdot 10^{12} \text{ cm}^{-2}$ that results in the population of the second subband. As a consequence, there appears a strong emission line $O_h^1 - O_h^1$ corresponding to the recombination of electrons from the O_h^1 LL. A high intensity of this line, I_0 , is due to the strong overlapping of the $n=1$ hole and $n=2$ electron wave functions resulting from the electric field normal to the QW plane because of selective doping.

Comparison of Figs. 1 and 2 shows that the 2DEG magnetoluminescence spectra from QWs with electrons in one and two subbands are markedly different. In the latter case the emission lines are significantly broader and reveal an additional structure. Magnetoluminescence studies of the sample under different pressure have shown that both the line width and additional structure are very sensitive to magnetic field and to filling of the second subband.

Comparison of the dependence of the $O^2-O^1_h$ energies on magnetic field for $p=1.5, 1.8$ and 3 GPa (10^{20} cm^{-3} , 1.5 and $1.5 \cdot 10^{20} \text{ cm}^{-3}$, respectively) is presented in Figs. 3 and 4. It shows that the filling of the second subband gives rise to the qualitative change in magnetic field dependence of $n_2=1$ transition energies. It becomes nonlinear and even nonmonotonic, whereas that for the $O^2-O^1_h$ transition demonstrates only very small deviations from linear. Dashed lines in Fig. 3 show the magnetic field dependence of the $n_2=1$ LL transition energies expected in the case of the empty second subband. To draw them, it is taken into account that at 1.8 GPa the second subband is depopulated at 14 T, and there were used the measured values of E_0 at 14 T and the slope of the E_1^1 (iii) dependences in QW with the empty second subband (at 3 GPa).

Figures 3 and 4 show that the filling of the O^2 LL results in the lowering of energy of the main emission line from the first subband. In some cases, the magnitude of this lowering exceeds a half of twice. Note, however, that there is a discrepancy between the position of extrema in the transition energies E_0^1 (ii) and in the $O^2-O^1_h$ line intensity. In particular, at 1.5 GPa the maximum of I_0^2 is at 11 T whereas the minimum of E_0^1 is at 12.2 T (Fig. 4).

Figure 2 shows that for 2DEG with two occupied subbands, the broad emission band $O^2-O^1_h$ consists of a few half-resolved lines. Their energetic position and intensity have quite different magnetic field dependences. The additional structure of the emission band is most pronounced at $8-14$ T, that is the range of crossing of the O^2 LL with the first and second LLs from the $n_2=1$ subband. At $11-16$ T, when the intensity of the $O^2-O^1_h$ line has a minimum, a line marked A' dominates in the emission spectra from the first subband. With increasing H till 10.4 T, the luminescence peak moves to lower energies, and simultaneously it broadens. This range of H corresponds to the high intensity of the $O^2-O^1_h$ line.

At $10.2-10.8$ T, a pronounced shoulder appears at the high energy side of the band A'. At higher H, when the intensity of the $O^2-O^1_h$ line strongly decreases, it transforms into the peak marked A. This peak becomes dominating at $11-12$ T, whereas the peak A' weakens and disappears. Fig. 2 shows also that at $11-10-12$ T there is another well pronounced shoulder at the high energy side of the peak A. At higher H it increases strongly and transforms into the line B which is relatively narrow when the O^2 LL becomes empty only that peak remains in the spectrum.

2. Discussion

When 2D-electrons transfer from the first to the second subband the lowering of the $O^2-O^1_h$ transition energy is due to the change of the electric field normal to the 2DEG plane. The latter is caused by the redistribution of electron density in this direction. In the frame of a simple approximation, this transition energy should lower with the filling of the second subband. However, the experiment shows that the largest lowering of the $O^2-O^1_h$ transition energy does not coincide with maxima in the

$O^2-O^1_h$ line intensity. The discrepancy might be related with incorrect determination of the transition energy as a spectral position of a maximum of the broad asymmetric $O^2-O^1_h$ emission line that reveals, in addition, the multicomponent structure.

The multicomponent structure of the emission band indicates that in the initial or final state of the photoemission transition there are a few different states. The excited initial states are to be excluded because of very low temperature of investigated 2DEG. The random potential fluctuations that are known to modify strongly the emission spectra of 2DEG in QW should mainly result in the line shift and broadening. They can be hardly responsible for majority of the observed peculiarities. Therefore we would like to discuss the contribution from the different final states in photoemission transition.

The radiative recombination of electron from a LL below Fermi level leaves the 2DEG in an excited state. Therefore one can write that the photon energy $\hbar\omega = E_0 - E_{exc}$ where E_0 is the energy of the transition to the 2DEG ground state, and E_{exc} is the energy of an additional excitation in the 2DEG if it arises with electron-hole recombination.

The excitation generated in the optical transition has a momentum $k=0$. For 2DEG with electrons in one subband, it can be described in terms of intrasubband magnetoexcitons or magnetoplasmons, with their energies coinciding at $k=0$. In 2DEG with $n_2=2$ electrons there is an additional possibility to leave the system with excitations belonging to intersubband magnetoplasmon branches. Two of them are expected to interact strongly at the resonance of their energies. These are the principal mode (corresponding to hole in the $n_2=1$ LL below the Fermi level) and the Bernstein one (corresponding to the excitation of electron from the $n_2=2$ LL to one of the $n_2=1$ LLs above the Fermi level) (iii). The generation of the Bernstein mode in the optical transition is related with shake-up processes. It can be hardly expected far from the resonance. However near the resonance the mixing of these modes should result in arising of an additional line. With increased H the emission intensity redistributes between two components, and the lower energy one becomes smaller and disappears, being transformed into the Bernstein mode. The arising high energy component transforms into the principal mode and becomes dominating. This is in qualitative agreement with observed behavior of the components in the emission spectra, i.e. the peaks A' and A near H and the peaks B and B' as well as the peaks C and D near 12 T.

Acknowledgements. We would like to thank A. V. Petinova and J.-M. Lefeuve for assistance in measurements. The Swedish National Board for Technical Development (STU) and the Fundamental Research Foundation of Russia are acknowledged for their financial support.

REFERENCES

- [1] S. Shmitt-Rink, C. Ell, and H. Haug, Phys. Rev. B 33, 1153 (1986).
- [2] G. Trankle, H. Leifer, A. Forchel, H. Haug, C. Ell, and G. Weimann, Phys. Rev. Lett., 58, 419 (1987).
- [3] Das Sarma, R. Jalabert, and S.-R. Eric Yang, Phys. Rev. B 41, 8288 (1990).
- [4] T. Ueno, Y. Nishida, and L. J. Sham, Phys. Rev. Lett., 65, 1048 (1990).
- [5] G. Mahan, Many Particle Physics, 2nd ed. (Plenum, N.Y., 1990).
- [6] A. F. Ruckenstein, S. Shmitt-Rink, and R. C. Miller, Phys. Rev. Lett., 56, 504 (1986).
- [7] W. Chen, M. Fritze, A. Nurmikko, C. Colvard, D. Ackley and H. Lee, Phys. Rev. Lett., 64, 2434 (1990).
- [8] P. Hawrylak, Phys. Rev. B 44, 11236 (1991), P. Hawrylak, H. Pulkard, K. Ploog, Phys. Rev. B 46, 15193 (1992).
- [9] P. E. Simmonds, M. S. Skolnick, L. L. Taylor, S. J. Bass, K. Nash, Solid State Commun., 67, 1151 (1988).
- [10] T. Richter, J. C. Maan, P. Wyder, F. Meseguer, K. Ploog, J. Phys. (Paris) 48, 389 (1987).
- [11] L. Wendler, R. Pechstedt, J. Phys. Condens. Matter 2, 8851 (1990).

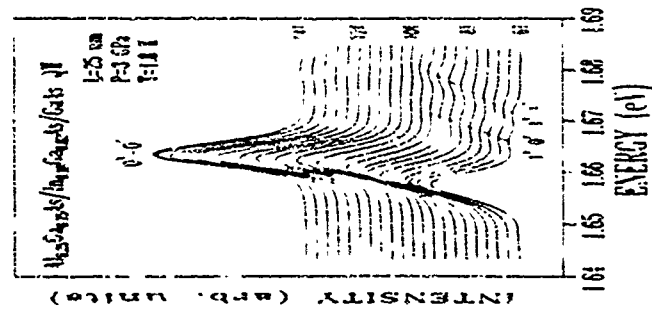


FIG 1 Emission spectra from n-AlGaAs/InGaAs/GaAs heterostructure at 3 CTs

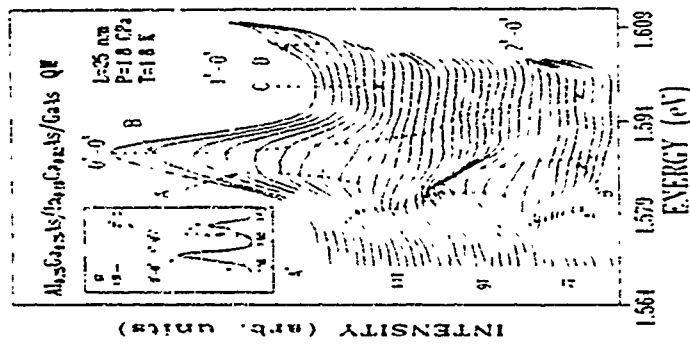


FIG 2 Emission spectra from n-AlGaAs/InGaAs/C heterostructure at 1.8 GPa corresponding to recombination of electrons from the first subband strong magnetic fields. Inset illustrates the full spectra recorded at 0 and 1.2

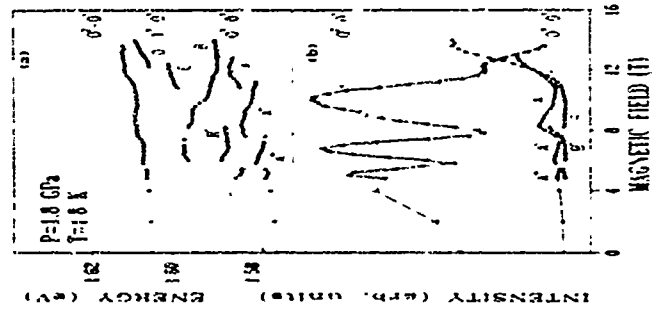


FIG 3 The energy (a) and the intensity (b) of transitions versus magnetic field at 1.8 GPa. Dashed lines show LL transitions energies expected in the case of the empty second subband

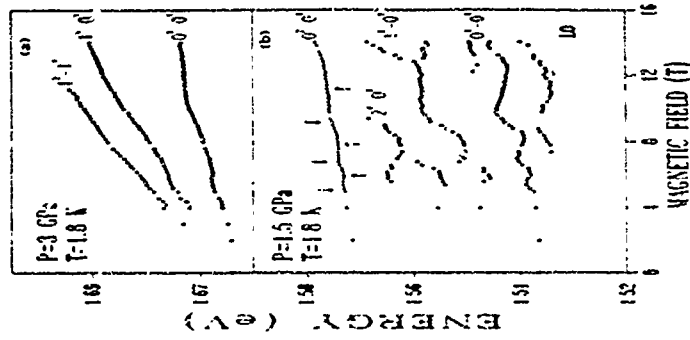


FIG 4 The transition energies versus magnetic field at 3 GPa (a) and 1.5 GPa (b). Arrows indicate the maxima and minima of the second subband line intensity

MoC1

MBE Growth of GaAs Nanometer-Scale Ridge Quantum Wire Structures and Their Structural and Optical Characterizations

S. Kouba, H. Naga, H. Kikuchi, H. Akiyama, Y. Nakamura, T. Inohara, K. Wada, A. Shimizu and H. Sakaki

* Quantum Wire Project, JNDC, 4-2-102 Komaba, Meguro-ku, Tokyo 153, Japan

** Research Center for Advanced Science and Technology, University of Tokyo,

4-6-1 Komaba, Meguro-ku, Tokyo 153, Japan

*** NTT LSI Laboratories, 3-1 Morinosato Wakamaya, Atsugi-shi, Kanagawa Pref. 243-02, Japan

**** University of Tokyo, 4-6-1 Hongo, Bunkyo-ku, Tokyo 113, Japan

Abstract A novel method for fabrication of the quantum wire structures has been investigated by which a quantum wire has been successfully fabricated on top of a (111)B facet structure with a very sharp ridge. Electron microscope study has shown that GaAs wires with the effective lateral width of 16-18 nm and with the thickness of 6-9 nm are formed at the ridge top. Photoluminescence and cathodoluminescence measurements indicate that one dimensional quantum confinement of electrons is realized at the ridge top and its blue shift agrees with the quantum confined energy calculated for the observed wire structure.

1. INTRODUCTION

Quantum wire (QW) structures with feature size comparable with de Broglie wavelength (~10 nm) of electrons are predicted to have unique electronic and photonic properties [1-3]. To realize them, various epitaxial methods have been tried such as selective growth on a vicinal surface [4-6], over growth on the cleaved edge surface of quantum wells (QWs) [7, 8], and selective epitaxy on patterned substrates. As a result, QWs are being formed at the bottom of V-grooves [9, 10], at the top of ridges [11-13], or on facet edges [14, 15]. In this work, we report molecular beam epitaxy (MBE) growth on a patterned substrate to form a novel QW structure on top of a GaAs ridge structure consisting of a very narrow (001) top surface and two (111)B side facets.

The advantages of facet growth used here are that the carrier confinement is achieved by smooth facet planes, and that the incorporation of damages and impurities can be minimized due to the continuous nature of facet growth. Selective epitaxy on patterned substrates to form such facet structure has been performed so far, mainly by means of organometallic vapor phase epitaxy, since the selectivity of its growth chemistry can be employed [9-12, 14]. In contrast, our method based on MBE utilizes the dependence of surface migration processes on crystalline orientation. Although

MBE has been considered less suited for facet growth because of inefficiency of desorption process, we have recently shown that well-defined facet structures consisting of (001)-(111)B planes can be grown by MBE on mesa structures [12].

In the MBE growth GaAs atom migration from the (111)B to the top (001) surface plays important role [16-19]. The width W of the top (001) surface or ridge region is narrowed as the growth of a (001)-(111)B facet progresses owing to the Ga migration. When the width W reaches some critical width, it can not decrease any further, because substantial portion of Ga atoms coming into the ridge region leave again by their frequent migration or desorption. To control the lateral width of the QW, we have investigated the factor which defines this critical width, and found that the ridge can be as narrow as 10 nm when formed at 580 °C. On the basis of these investigations, we have successfully fabricated GaAs QWs on top of the ridge structures. We have studied their structure by electron microscopy and also their electronic states by luminescence spectroscopy and compared them with theoretical calculation.

2. SAMPLE FABRICATION

In our experiment a (001) GaAs substrate with reverse mesa stripes was prepared by photolithography and reactive ion etching using SiCl_4 . Ti -mesa stripes running along the [110] direction were less than 2 μm in width, and about 2-3 μm in depth. On top of these mesas, a GaAs layer was grown by MBE at the substrate temperature T_s of 570 °C with the growth rate of 0.15 $\mu\text{m/h}$ and the flux ratio of $J_{\text{Ga}}/J_{\text{As}}$ of 3 if measured on a flat (001) substrate. During this growth, the substrate heater was rotated so that the As and Ga flux were uniformly supplied. As the growth progressed, the width of (001) top surface decreased, resulting in the facet structure consisting of a (001) top surface and two (111)B side surfaces, and eventually in a sharp ridge consisting of two (111)B faces. After the ridge is formed, a thin AlAs layer was grown as a lower barrier with the growth rate of 0.1 $\mu\text{m/h}$. Then a thin GaAs QW layer was deposited at $T_s = 550$ °C. Here two type of samples (A and B) with the different well thicknesses were prepared. Sample A has a 10 nm thick AlAs lower barrier layer, a 7 nm thick GaAs QW layer, a 150 nm thick $\text{Al}_0.3\text{Ga}_{0.7}\text{As}$ upper barrier layer, and a 30 nm thick GaAs cap layer. Sample B has a 5 nm thick AlAs lower barrier layer, a 5 nm thick GaAs QW layer, a 10 nm thick AlAs upper barrier layer and a 20 nm thick GaAs cap layer. All the layer thicknesses are defined as those measured when the layers are grown on a flat (001) surface.

3. EXPERIMENTAL RESULTS AND DISCUSSION

Figure 1(a) shows the cross sectional lattice image of the ridge region of sample A taken by transmission electron microscope (TEM), where a dark GaAs QW layer is seen on top of the bright AlAs layer. The thickness of this QW layer is position dependent and is largest (8-9 nm) at the top of the ridge because the incident flux of Ga atoms gets maximum at the top of the ridge and also the Ga migration from (111)B facet further enhances the growth on the ridge. On the other hand, the observed thickness of the side QW (S-QW) (≈ 4 nm) is about $1/\sqrt{3}$ ($\approx \cos 54.7^\circ$) of the

integrated flux ($\approx 7 \text{ nm}$) on the flat (001) surface. We expect that carriers in this ridge structure are confined two-dimensionally, since two side QWs are thinner and act as barriers for in-plane lateral diffusion. Note that the width W at the ridge is different for the three interfaces: W at the AlAs/GaAs interface formed at $T_1 = 570^\circ\text{C}$ is 20 nm, while W at the GaAs on AlAs interface formed at $T_2 = 570^\circ\text{C}$ is 16 nm. The width W on the GaAs QW surface formed at $T_3 = 550^\circ\text{C}$ is 15 nm. This indicates that the lateral width of the QW is dependent on growth conditions and compositions. The effective lateral width of the QW is estimated to be about $17 \sim 18 \text{ nm}$.

Figure 1(b) shows the cross-sectional TEM image of sample B. Thin bright layers are the AlAs barriers. The thickness of this QW structure is about 6 nm whereas the thickness of S-QW on the (111)B facet is found to be about $2 \sim 3 \text{ nm}$. The effective lateral width of the QW sandwiched by the AlAs barrier layers is about 16 nm.

Photoluminescence (PL) measurements were carried out on sample A at various temperatures by focusing 3 mW He-Ne laser light (632.8 nm) into $500 \mu\text{m}$ spot size. Measured PL spectra are shown in Fig. 2, where five peaks (a) - (e) and (QW1) are clearly seen. The origins of these PL peaks were identified by cathodoluminescence (CL) measurement at 15 K [22, 23]. The luminescence generated by $\approx 3 \sim 40 \text{ keV}$ electron beam with 1 nA current was collected by a mirror and its spectrum was analyzed as a function of position over the epitaxial layer. The magnetic field of 0.2 T was applied to suppress the carrier diffusion and improve spatial resolution [20]. A close examination of the CL data suggests that peak (QW1) comes from the top region of the ridge, peak (b) comes mainly from S-QW, and peak (a) originates mainly from the QW formed on the bottom of trench region between two mesas (B-QW).

Peak (QW1) has the full width at half maximum of 11 meV at 77 K, and keeps its shape up to 220 K which shows the stability of 1D excitons in the QW. It is also noteworthy that despite the small wire volume which occupies only the 1% of the patterned area, the intensity of peak (QW1) is as strong as other peaks. These facts near the good quality and uniformity of this QW structure and the efficient diffusion of electrons and holes from the AlGaAs barrier or S-QW into the QW. Time-resolved PL measurement for this sample revealed the smaller temperature dependence of radiative lifetime ($\tau \propto T^{-1/2}$) than that of a reference QW ($\tau \propto T$), which is attributed to the sharp density-of-state function of 1D excitons [24].

We have examined the shape of the ridge structure and the quantum levels in the respective QW1 and QW2. The detailed discussion is given in Ref. [23]. The conclusion is that the lowest state of QW1 is lower than that of S-QW because of the enhanced growth rate at the ridge region. The observed thickness of S-QW ($\approx 4 \text{ nm}$) is close to the value expected from PL energy. For the B-QW, incoming Ga flux to the bottom of the trench is partially interrupted by the adjacent mesas. Hence, the lowest energies B-QW is expected to be higher than that of S-QW.

For the quantitative discussion, we have calculated the energy levels of electrons and heavy holes for the QW structure formed on the ridge by using the finite element method. The structure was approximated as the region bounded by the two functions $F(x)$ and $G(x)$, where $F(x) = \sqrt{2b} \log_{10}(\cosh(x/b))$, $G(x) = F(x) + L$. The parameter b

defines the sharpness of the ridge and is assumed to be 8, 10, 12 nm. Figure 3 shows the calculated total quantization energies for the lowest states of QW1 (open circles), S-QW (solid line), and QW2 (dashed line) on a flat (001) plane as a function of the QW width L in the direction of (001). Here the excitonic effects are ignored. Note that the 1st quantized level of QW1 is lower than that of the S-QW and this supports reasonable lateral confinement in ridge QW1 structures. On the other hand, these levels are above those of the QW on flat (001) substrate which indicate that the quantized state by the narrow effective ridge width W . The shape of the ridge affects the level of QW1. The level of QW1 decreases with the increase of W , which is indirectly set by value of b and L , and gradually approaches the level of QW on flat (001). The calculated value of 63 meV was obtained for $L = 9 \text{ nm}$ and $b = 10 \text{ nm}$ ($W = 17 \text{ nm}$), and these sizes are estimated from the TEM (fig. 1(a)). This agrees well with the energy 64 meV of the peak (QW1) measured relative to the GaAs bulk. The detailed discussion will be found in Ref. [21].

For sample B, PL measurements were carried out at 77 K by focusing Ar⁺ laser light into $200 \mu\text{m}$ spot size. Measured PL spectrum is shown in Fig. 4(a), where the large peak at 1.62 eV and the small peak at 1.51 eV from GaAs bulk are clearly seen. As a reference, the PL spectrum from the QW grown simultaneously on a flat (001) substrate is shown by the dashed line with its peak located at 1.65 eV. The energy of the dominant peak is 30 meV lower than that of the reference QW. The origin of this PL peak has been also identified by CL measurement. Figure 4(b) shows the cross-sectional scanning electron microscope (SEM) image of sample B. Figure 4(c) shows the superimposed mapping of CL intensities on the SEM image of fig. 4(b), measured at the photon energy corresponding to the 1.62 eV PL peak. Figure 4(b) and (c) clearly indicate that the peak comes exactly from the top region of the ridge, where the QW1 is formed. The quantization energy of this QW1 is 110 meV, which is larger than that of sample A. In contrast to sample A, we observed no PL from S-QW nor B-QW. This is because the width of these QWs is so thin that the lowest states of the QWs exceed the X valley energy in the conduction band of AlAs (type II QW). In fact, the lowest state of the S-QW of $2 \sim 3 \text{ nm}$ thick is expected to be about 300 meV above the GaAs band edge which is higher than the X valley energy in AlAs [25, 26]. The lowest state of B-QW is expected to be higher than or at least equal to that of S-QW, because the width of the B-QW should be thinner than that of S-QW as in sample A. Furthermore, fast diffusion of electrons and holes from S-QWs to the adjacent QW1 may explain the absence of PL from S-QW [27]. The full width at half maximum of the peak from the R-QW of sample B is 21 meV at 77 K, and is larger than that of sample A. This is likely because the fluctuation of wire size affects the energy levels strongly in the narrower QW.

4. CONCLUSION

We have demonstrated that the MBE growth on a patterned substrate provides a very sharp ridge structure and results in a QW1 by which two-dimensional confinement of carriers is achieved.

We express our sincere thanks to Mr. H. Yano of Sumitomo Electric Industries and Mr. Y. Kadoya of Quantum Wave Project for their support in SiO₂ deposition, and Prof. M. Tsuchiya for stimulate discussions. We also thank to Professor Y. Shiraki and Dr. S. Fukasui for their collaboration at the Processing Center of RCAST. A part of the work is supported by Grant-in-Aid for Scientific Research from the Ministry of Education, Science, and Culture, Japan

References:

1. H. Sakaki, K. Waga, J. Hamaoka, and S. Saito, *Thin Solid Films* **3** 6, 497(1976)
2. H. Sakaki, *Jpn. J. Appl. Phys.* **19**, L235(1980)
3. H. Sakaki, *Surf. Sci.* **247**, 623(1992)
4. P. M. Petroff, A. C. Gozard, and W. Wegmann, *Appl. Phys. Lett.* **4** 5, 620(1984)
5. T. Fujii and H. Saito, *J. Vac. Sci. Technol.* **14**, 1373(1988)
6. M. Tanaka and H. Sakaki, *Jpn. J. Appl. Phys.* **27**, L2025(1988)
7. L. Pfeiffer, K. W. West, H. L. Stormer, J. P. Eisenstein, K. W. Balducci, D. Gerthsen, and J. Spector, *Appl. Phys. Lett.* **5** 6, 1697(1990)
8. J. Mochizuki and H. Sakaki, to be pub. in the Proc. of 21st Int. Conf. on Phys. of Semicond., Beijing, August, 1992 (World Scientific)
9. E. Kapon, D. M. Hwang, and R. Blot, *Phys. Rev. Lett.* **63**, 430(1989)
10. S. Takamori, Y. Nagamune, M. Nishiohara, and Y. Arakawa, *J. Appl. Phys.* **71**, 533(1992)
11. C. S. Tsai, J. A. Lert, C. C. Alm, A. Nohu, and K. J. Vahala, *Appl. Phys. Lett.* **6** 6, 210(1992)
12. S. Takamori, Y. Nagamune, M. Nishiohara, and Y. Arakawa, *Appl. Phys. Lett.* **6** 2, 49(1993)
13. K. Kiyama, K. Mitsuoka, and K. Kiyama, *Appl. Phys. Lett.* **5** 5, 882(1989)
14. T. Fukui and S. Ando, *Electron. Lett.* **25**, 410(1989)
15. Y. Nakamura, S. Koshida, M. Tsuchiya, H. Kano, and H. Sakaki, *Appl. Phys. Lett.* **5** 9, 700(1991)
16. S. Koshida, Y. Nakamura, M. Tsuchiya, and H. Sakaki, unpublished
17. X. Q. Shen, M. Tanaka, and T. Nishiohara, *Proc. Alloy Semiconductor Physics and Electronics Symposium, Japan (ASPEC)-II*, 333(1992)
18. M. Hara, T. Ito, A. Watanabe, and Y. Kasayama, *J. Vac. Sci. Technol.* **18**, 692(1990)
19. M. Kurekawa and Y. Horiuchi, *Jpn. J. Appl. Phys.* **27**, L483(1988)
20. K. Wada, A. Kurosawa, H. Fushimi, and M. Inoue, *Jpn. J. Appl. Phys.* **27**, L1952(1988)
21. T. Inoshita, S. Koshida, H. Akiyama, H. Naga, and H. Sakaki, unpublished
22. S. Koshida, H. Naga, H. Akiyama, Y. Nakamura, A. Shimizu, and H. Sakaki, *Int. Phys. Conf. Ser.* **125** (NIP Publishing, Bristol, 1993), p. 931
23. S. Koshida, H. Naga, H. Akiyama, T. Inoshita, Y. Nakamura, A. Shimizu, H. Sakaki, and K. Wada, unpublished (submitted to APL)
24. H. Akiyama, S. Koshida, T. Sumiya, K. Wada, H. Naga, Y. Nakamura, T. Inoshita, A. Shimizu, and H. Sakaki, unpublished (submitted to PRL)
25. S. H. Wei and A. Zunger, *J. Appl. Phys.* **63**, 5794(1988)
26. G. Ballard, J. A. Brum, and R. Ferreira, *Solid State Phys.* **44**, 229(1991)
27. M. Walther, E. Kapon, D. M. Hwang, E. Colas, and L. Nunes, *Phys. Rev. B* **45**, 6333(1992)

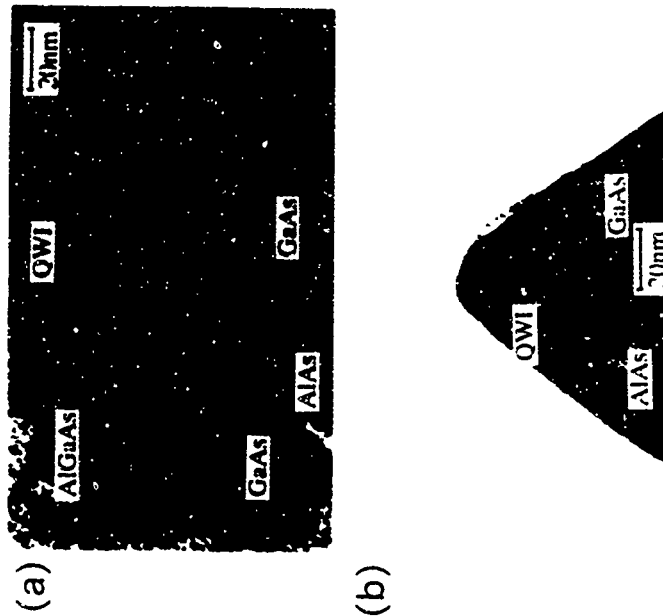


FIG. 1. Transmission electron micrographs of the cross-section of the ridge structures of sample A (a) and sample B (b). The dark line running obliquely in the upper right corner in fig. (b) is a dislocation.

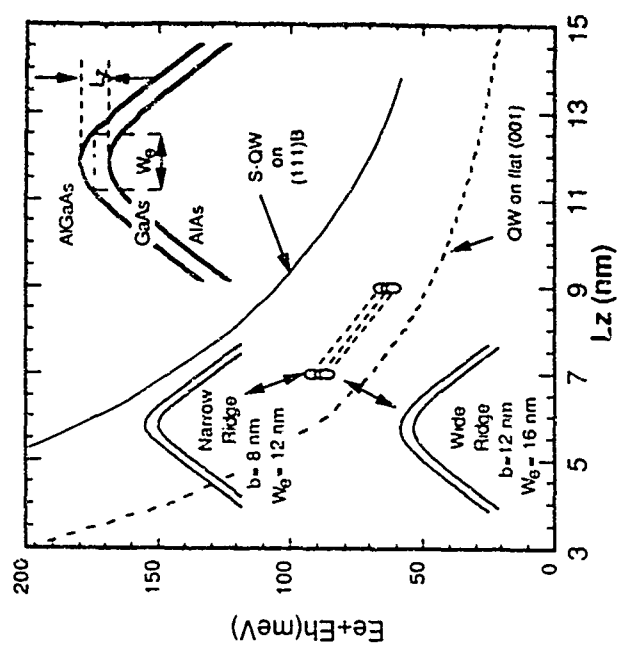


FIG. 3. The total quantization energies of electrons and heavy holes calculated for the lowest states in QW's are shown by open circles, those of S-QW by solid line, and those in reference QW by dashed line as a function of the QW thickness L_z and the width W_0 (in lateral direction).

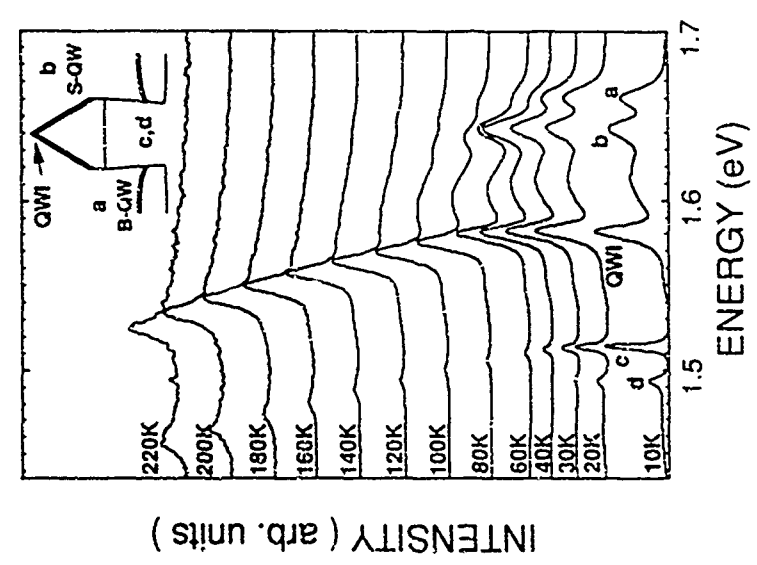


FIG. 2. Photoluminescence spectra measured at various temperatures excited by the π -factor for the QW's and QW's formed on ridge structure (sample A). The peaks are assigned as PL from subband quantum wells (QW's), bottom quantum well (B-QW) (a), side quantum well (S-QW) (b), and bulk GaAs (c,d).

Control of Interface Composition in InAs/GaSb Superlattices

B.R. Bennett, B.V. Shanbrook, R.J. Wagner,
J.L. Davis, J.R. Waterman, and M.E. Twigg
Naval Research Laboratory,
Washington, DC 20375-5347

ABSTRACT

The GaSb/InAs materials system, with two species of both cations and anions, permits the construction of heterostructures with either InSb or GaAs like interfaces. As a result, this system provides a unique opportunity to explore the limits of interfacial control that can be achieved by vapor phase growth techniques. We have characterized a series of superlattices (SL's) prepared with both types of interfaces by x-ray diffraction, Raman spectroscopy, transmission electron microscopy, and photoluminescence. The large differences in band lengths, electronic properties, and vibrational properties of InSb and GaAs interfaces allow these techniques to be sensitive probes of interfacial structure. By carefully measuring and minimizing the group V cross contamination in the SL layers, we are able to unambiguously demonstrate the growth of SL's with almost pure InSb like or GaAs like interfaces.

INTRODUCTION

Semiconductor heterostructures containing both As and Sb are of increasing interest for device applications. For example, the combination of a large conduction band offset for AlSb/InAs heterostructures and the high mobility of InAs has been exploited in the design of high speed transistors [1]. In addition, the staggered band line up and resulting small effective energy gap of InGaSb/InAs strained layer superlattices (SL's) may make this system suitable for use in infrared detectors [2, 3]. Very thin layers are often required to achieve the desired absorption characteristics in the SL's. Hence, interfaces will be a substantial fraction of the heterostructures and are expected to strongly affect optical and electrical properties.

In the case of heterostructures in which both the cation and anion change, the interfacial structure can be varied. For example, in an InAs/GaSb structure, interfaces with either InSb-like bonds or GaAs-like bonds (or a mixture) can be envisioned. Hence, these material systems are excellent candidates for basic studies of interfacial control in epitaxial growth. In this article, we report studies of InAs/GaSb superlattices grown by molecular beam epitaxy (MBE). By carefully measuring and minimizing the group V cross contamination in the SL layers, we are able to prepare SL's with almost pure InSb like or GaAs like interfaces. The differences in interfacial stoichiometry are shown to affect the structural, vibrational and electronic properties of the SL's.

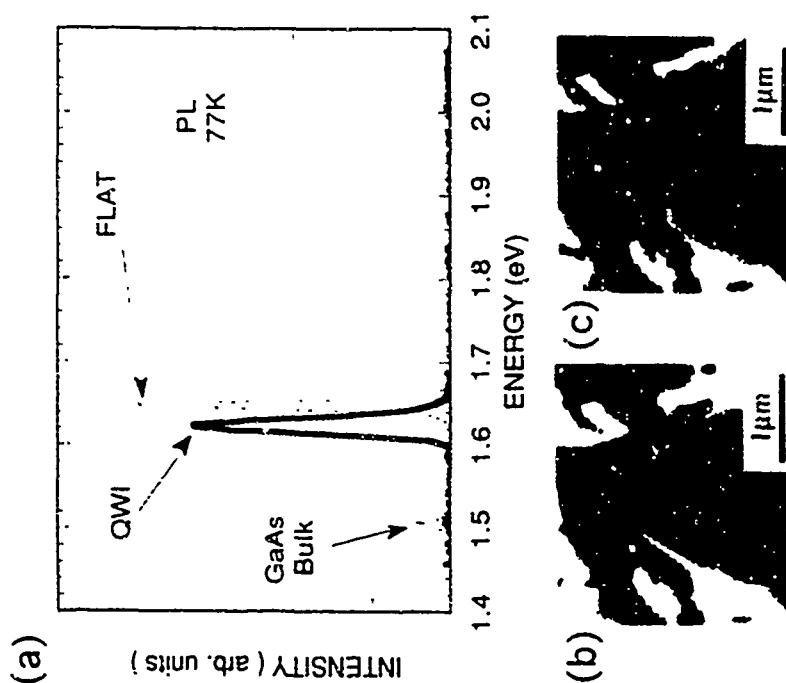


FIG. 4. (a) Photoluminescence spectrum of sample B measured at 77K. Shown by the dashed line is the spectrum of the reference QW grown on a flat (001) wafer. (b) Cross-sectional SEM image of the ridge structure of sample B. (c) Superimposed CL intensity mapping on the SEM image of fig. (b).

EXPERIMENTAL PROCEDURES

Epitaxial growth was carried out on a solid source MBE system equipped with a valved As cracker. The substrates were 50 mm, epitaxially semi-insulating, (001) GaAs wafers. After oxide desorption about 0.1 μm of GaAs was grown at 700°C using As₂. Next, the substrate temperature was lowered to 180°C and a 1.0 μm buffer layer of GaSb was grown with the temperature increasing to 700°C during growth [4]. Then, the substrate temperature was decreased to 180°C and the InAs/GaSb superlattice was grown using As₂ and Sb₂. Growth temperatures were determined by infrared transmission thermometry and are believed to be accurate to within 10°C [4]. Growth rates were calibrated by reflection high energy electron diffraction (RHEED) oscillations. As explained below, for most samples we chose growth rates of 0.15 monolayers (ml)/s for GaSb and 0.11 ml/s for InAs.

We grew 10 period superlattices with nominal structures of 8 ml InAs/12 ml GaSb, and 1 ml InSb on GaAs (designated as S121) as well as S1 and L2S1. The nominal interface type was varied by using the techniques of migration enhanced epitaxy [5, 6]. For example, to obtain a GaAs interface on GaSb, the Sb shutter is closed at the end of the GaSb layer. Next, the Ga shutter remains open for another 2.5 s to deposit an additional monolayer of Ga. Then, the Ga shutter is closed and the As shutter opened for a 1 s soak to saturate the Ga with As. Then, the In shutter is also opened and InAs is grown.

Structural properties of the SLs were measured by x-ray diffraction (XRD), using theta/two theta scans and Cu K α radiation. Raman spectroscopy (RS) was applied to evaluate the vibrational properties. RS measurements were taken at ~ 40 K in the Zn(N)/Z and Zn(N)/Z configurations where Z and Z are the directions of the incident and scattered light. ("Z" denote their polarizations and X, Y, and Z denote the [100], [010] and [001] crystallographic directions, respectively. Radiation from an Ar ion laser operating at 514.5 nm was employed in the measurements. Specimens were prepared for high resolution transmission electron microscopy (HRTEM) by mechanically thinning a cross sectional sample, which is then subjected to Ar⁺ beam milling on a stage cooled by liquid nitrogen. Both [100] and [110] oriented cross sections were imaged on a Hitachi H-9000S HR microscope operating at 300 kV.

RESULTS AND DISCUSSION

Due to transients, the flux of an element incident on a sample will not immediately drop to the background levels when its shutter is closed. Based upon ion gauge beam equivalent pressure (BEP) measurements, this problem is most severe for As. In the case of InSb like interfaces on InAs, there is a total of 12.7 s (7 s of In and 5 s of Sb) between the closing of the As shutter of InAs and the opening of the Ga shutter for GaSb. In the case of GaAs like interfaces, however, there is only a 2.5 s interval (deposition of 1 ml of Ga) between As and GaSb. To reduce GaSb contamination by As flux transients, we interrupted growth for 40 s after the As shutter was closed during each InAs to GaSb transition for sample A on S121 SL with GaAs like interfaces. Except for the growth interrupt, sample B was grown under identical conditions. The (001) diffraction peaks for the $n=1, 0$ and -1 SL satellites as well as the GaSb buffer layer are shown in fig. 1. The position of the $n=0$ peak is related to the average lattice constant of the SL via Bragg's law. The fact that sample A has a smaller Bragg angle than sample B means that its average lattice constant is larger. The average lattice constant of the SL is a function of the InAs and GaSb layer thicknesses.

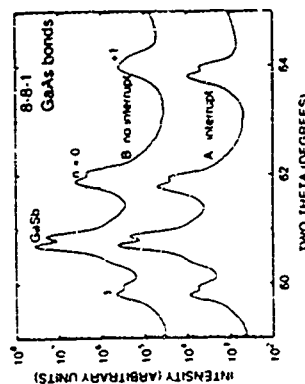


Figure 1. X-ray diffraction $\theta-2\theta$ scans for two 10 period superlattices. Each period consists of 8 ml InAs and 12 ml GaSb, along with two nominally GaAs like interfaces. Sample A was grown with a 40 s growth interrupt (see text). Sample B was grown without the interrupt. SL satellite peaks and the GaSb buffer peak are visible. The curves are offset for clarity.

The composition of the interfacial layers, and the actual composition of the nominally InAs and GaSb layers. It seems unlikely that the layer thicknesses or InAs composition would be a function of growth interrupts. The nominally GaSb layer, however, could contain As. If so, we could expect more As contamination in sample B (no interrupt). The lattice constant of GaAs is 3.5651 Å compared to 3.6051 Å for GaSb. Hence, As contamination in the GaSb will reduce the average SL lattice constant, as observed. Based upon these results, we used the 22: with interrupt on all subsequent GaAs bonded SLs.

Cross contamination can also result from the background pressure of the group V elements. The background pressure of an element is related to its cell temperature as well as the pumping efficiency of the MBE system. As a test, we grew two 8 x 1 SLs with nominally InSb like interfaces. Different autonomy cell temperatures were used, resulting in III P's of 7 and 11 $\times 10^{-7}$ for samples C and D, respectively. Sample D has an $n=0$ SL Bragg angle (not shown) which is 170 arc sec smaller than C's, translating to a lattice constant which is 0.024 Å larger. This can be explained by "InAs" layers in D with a composition of In_{0.999999}Sb_{0.000001}. The cross-contamination of As in GaSb layers was even more severe. To reduce it, we grew our SL structures at relatively slow growth rates and used the lowest As and Sb cell temperatures which provided atom rich surfaces. Based upon RHEED reconstruction patterns and uptake oscillations, we estimate our V III flux ratios to be between 1.0 and 1.5. Using XRD measurements of thick layers of InAs and GaSb grown under SL conditions, we estimate that the As contamination in GaSb is about 1% (e.g. GaSb_{0.9999}As_{0.0001}), and the Sb contamination in InAs is 0.1% (e.g. In_{0.9999}Sb_{0.0001}).

With group V cross contamination minimized, we are now in a position to quantify our ability to control interface type. In fig. 2 we show the XRD data for two superlattices with 10 periods of 8 ml InAs and 12 ml GaSb. Sample E was grown with nominally GaAs like interfaces and F was grown with InSb like interfaces. First, we note that both samples exhibit several SL satellite peaks, indicating reasonably good crystalline quality. Key key splitting is observed for some peaks. For simplicity, we reference the SL peak positions to

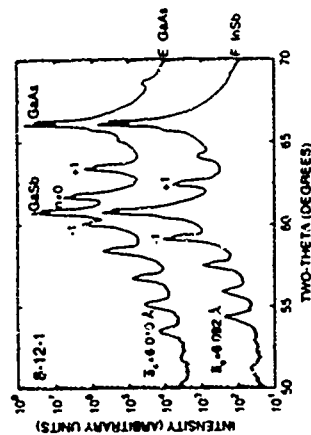


Figure 2. X-ray diffraction $\theta-2\theta$ scans for two 10-period superlattices. Each period consists of 8 ml InAs and 12 ml GaSb. Samples E and F were grown with nominally GaAs like and InSb-like interfacial bonds, respectively. SL satellite peaks, as well as the GaSb buffer and GaAs substrate peaks, are visible. The curves are offset for clarity.

the GaSb buffer peak. (Almost identical results are obtained if the GaAs substrate peak is used as the reference.) The $n=0$ SL peak for sample E is at a relative Bragg angle, $\Delta\theta$, of $+17.23$ arc sec, giving an average lattice constant of 6.018 \AA . For sample F, the $n=0$ peak is observed by the GaSb buffer peak. However, we can estimate its position from the $n=1$ and $n=2$ peaks. We obtain $\Delta\theta = +68$ arc sec, corresponding to 6.092 \AA . We can also determine the SL period from the separation between satellite peaks [8] for samples E and F. We obtain a period of 60.82 \AA and 62.40 \AA , respectively. These values are somewhat smaller than the theoretically predicted periods* 61.62 \AA (E) and 63.95 \AA (F). The discrepancies of $3-5\%$ may result from flux non-uniformities across the wafer.

We now compare our observed changes in lattice constant with interface type to theoretical predictions. In table 1, we list our measured $\Delta\theta$'s along with the theoretical values for all six structures studied. The $\Delta\theta$'s values are based upon the dynamical theory of X-ray diffraction [9], assuming the nominal thicknesses and interface types, no cross contamination, and no lattice relaxation in the SL with respect to the GaSb buffer. Our experimental values are always higher than the theory. These discrepancies can be reduced if we assume GaSb/InAs monolayers instead of pure GaSb. To estimate changes in interfacial composition we can look at the amount by which $\Delta\theta$ changes with bond type. In table 1, we show the differences in $\Delta\theta$ for the two types of interface bonds along with the percent change in bond type which we define as

$$\% \text{ change} = \frac{\Delta\theta_{\text{interfacial}} - \Delta\theta_{\text{GaAs}}}{\Delta\theta_{\text{GaAs}}} \times 100 \quad (1)$$

The measured SL period was always less than or equal to the predicted period, with differences as large as 1 \AA . By definition, each of the interfacial layers cannot be less than 0.5 monolayers. The InAs and GaSb layers, however, could be somewhat thinner than the nominal thickness. These predictions are based upon linear lattice theory assuming coherent layers with the in-plane spacing fixed by the relaxed GaSb buffer layer.

Table 1. Comparison of experimental and theoretical $n=0$ SL peak position in NRD of InAs/GaSb superlattices. $\Delta\theta$ values are in units of arc seconds.

Sample	Structure	$\Delta\theta_{\text{expt}}(^{\circ})$	% Change ^a	% Change ^b	% Change ^c
E	8-12-1 InSb	100 ± 68			
F	8-12-1 GaAs	1170 ± 172			
	Difference	1070	106	100	101 ± 6
G	8-8-1 InSb	110 ± 36			
A	8-8-1 GaAs	1820 ± 1926			
	Difference	1710	101	95	98 ± 6
B	12-8-1 InSb	1180 ± 238			
N	12-8-1 GaAs	1770 ± 1890			
	Difference	1590	101	99	101 ± 6

^a Assumes all monolayers are present (e.g., 8-8-1).

^b Assumes one monolayer is missing (e.g., 7-8-1 or 8-7-1).

^c Average value; error bar includes experimental errors in $\Delta\theta$.

values. If, for example, the InAs thickness in a nominal 8-8-1 structure is really only 7 ml, then the interfaces are a larger fraction of the SL, and the predicted change in $\Delta\theta$ will be larger. We assumed a missing ml (or 1 \AA) in determining $\Delta\theta$'s for the % Change^c column in table 1. The % Change^c column is an average of the other two values, with estimated errors in $\Delta\theta$'s included in the uncertainties. For all three structures (8-8-1, 8-12-1 and 12-8-1), we are able to change the interfacial bonding by about 100%.

Raman scattering spectra for five 8-8-1 SL's, taken in the Z(Y,X)Z configuration at $\sim 10 \text{ K}$, are shown in fig. 1. The large peaks at about 236 cm^{-1} result from the quasi confined longitudinal optic (LO) phonon modes of InAs and GaSb [10]. In sample A (nominal GaAs bonds), we observe a second peak at 253 cm^{-1} . We see no evidence of this peak in the SL with nominally InSb-like interfaces, sample K. The 253 cm^{-1} feature is also present in the 8-12-1 and 12-8-1 SL's with GaAs bonds, and absent in the 8-12-1 and 12-8-1 SL's with InSb bonds [7]. We attribute this peak to GaAs interfacial vibrational modes. We conclude that, to within the resolution of our Raman measurements, GaAs bonds are not present in the nominally InSb samples.

Although it is not obvious in fig. 1, we always observe a weak shoulder near 213 cm^{-1} when higher resolution Raman data is taken on our SL's. We associate this peak with the 1/4 As contamination in the GaSb layers. NRD data taken on sample J, grown under an excess As background, yields about 20% As in the GaSb. In fig. 3, we see that the contamination peak is the largest feature and has shifted to higher energies, as expected for the two mode behavior of GaAs-Sb [11].

Superlattice H was grown with no attempt to control the interface stoichiometry. The Ga and Sb shutters were closed at the same time the In and As shutters were opened and vice versa. The NRD data shows an $n=0$ SL peak between that of sample A (GaAs bonds) and sample K (InSb bonds), suggesting a mixture of interfacial bonds for sample H. This result is confirmed by the Raman measurement which reveals a GaAs interfacial mode which is shifted toward lower energies. A study of a series of samples with controlled but mixed interfaces revealed a clear contribution between the energy of the GaAs interfacial mode and

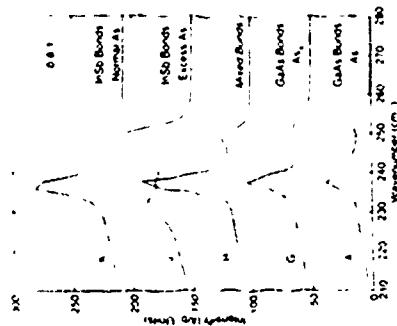


Figure 1 Raman scattering data at ~ 10 K with the $Z(N,X)Z$ geometry for five S.S.I superlattices. The curves are offset for clarity.

the interface composition [12].

Normally, we use a temperature of 875 °C for the As tracker zone, resulting in primarily As_2 . For sample G, however, the As zone was set at 100 °C, resulting in an As_4 beam on the sample. The nominal band type was GaAs. Several satellites are visible in the NRD data, demonstrating that a superlattice was achieved. The Raman scattering data are almost identical to those of sample A. We conclude that $InAs/GaSb$ S.S.I can be grown with uncracked As_4 , contrary to an earlier report [13].

Raman measurements taken in the $Z(N,X)Z$ configuration (not shown) reveal both LO phonons at higher energies (~ 100 , 100 , 100 cm^{-1}) and folded longitudinal acoustic phonons at lower energies (~ 100 cm^{-1}). These latter modes result from the additional periodicities imposed by the superlattice. SI periods calculated from their energies are in good agreement with the NRD results [6].

Using HRTEM, we observed apparent differences in the interfaces in sample N (12.8 \times GaAs bands) and sample O (12.8 \times InSb bands). To ensure that the differences were not an artifact of imaging conditions, we grew sample L, a 10 period S.S.I structure with InSb interfaces for the GaSb to InAs transition and GaAs interfaces for the InAs to GaSb transition. A [110] oriented cross-sectional image is shown in fig. 4. About three periods of the SI are visible. The GaAs interfaces are consistently brighter than the InSb interfaces. We also note that the GaAs interfaces appear to extend over about three monolayers. We speculate that this results from the fact that we are imaging through many atomic planes. Any roughness or steps in the structure would broaden the observed interfaces.

Interfacial band type has also been reported to influence electronic properties in the $InGaSb/InAs$ [14] and $AlSb/InAs$ [15] materials systems. We performed photoconductivity measurements at 77 K on seven $InAs/GaSb$ S.S.I. The effective band gaps were estimated from the photocurrent turn-on point. The results are shown in table 2. For each of the three

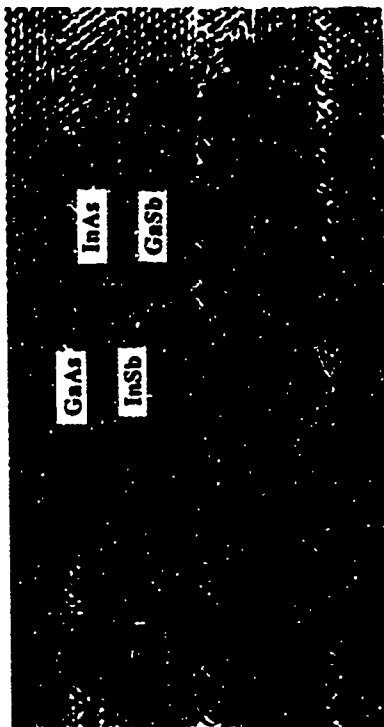


Figure 4 Cross-sectional [110] HRTEM image of sample L, with alternating interfacial bonds. The GaAs-like interfaces always appear brighter than the InSb-like interfaces.

structures, the InSb bonded SI, has a smaller band gap than the GaAs-banded sample, as expected. The differences range from 18.20 meV (8.12:1 and 12.8:1) to 10 meV (8.8:1).

CONCLUSIONS

Using migration enhanced epitaxial techniques, we varied the interface composition of $InAs/GaSb$ superlattices. After minimizing group V cross contamination, we demonstrated that structures with almost pure InSb-like and GaAs-like interfaces were achieved. The interface composition strongly affects the structural, optical, and electrical properties of these superlattices.

Table 2 Effective energy gaps for $InAs/GaSb$ superlattices measured by photoconductivity

Sample	Structure	Interface	77K Energy Gap (eV)
A	8:1	GaAs	0.253
L	8:1	InSb	0.236
M	8:1	InSb	0.209
N	12.8:1	GaAs	0.161
O	12.8:1	InSb	0.111
P	8.12:1	GaAs	0.254
P	8.8:1	InSb	0.206

MoC3

Lateral piezoelectric fields - a universal feature of strained III-V and II-VI semiconductor heterostructures

Mathias Bg and Albert Reiche
Max Planck Institut für Festkörperforschung D 70506 Stuttgart, Germany

Klaus H. Ploog
Paul Drude Institut für Festkörperforschung D 10117 Berlin, Germany

Strained II-VI and III-V semiconductor heterostructures in general are expected to have a piezoelectric polarization with a non zero component in the plane of the interfaces which generates lateral piezoelectric fields. We use InAs structures synthesized on virtual (110) GaAs surfaces as a model system to study such fields for the first time. These lateral fields manifest themselves in strong line shifts of the photoluminescence peaks and an energy dependence of the radiative lifetime. Our experiments unambiguously prove the existence of these electric fields and furthermore demonstrate their tremendous impact on the electronic and optical properties of our InAs/GaAs samples.

Strong piezoelectric fields have been shown to exist in strained III-V and II-VI semiconductor heterostructures with non (100) orientation [1, 2]. These fields are generated by interface charges due to an internal polarization \vec{P} which in general is expected to have a component P_x in the plane of the interface as well as a component P_z along the growth axis [3]. In an ideal quantum well structure only P_z prevails; the interfaces and creates piezoelectric fields whereas P_x remains without influence on the electronic properties of the well. A real heterostructure, however, always exhibits interface fluctuations and therefore a non zero P_x will also introduce charges and thus create piezoelectric fields. Figure 1 illustrates different scenarios for the special case of a (110) oriented heterostructure. These lateral fields are present with varying magnitude in heterostructures of any orientation with the sole exceptions of the (100) and (111) cases ($\vec{P} \approx 0$ and $\vec{P} \approx 0$ respectively) and therefore constitute a truly universal phenomenon. Their importance is two fold. First they significantly influence the electronic properties of the above mentioned heterostructures and second they provide a means to create large piezoelectric field effects via an appropriate lateral patterning of the interfaces. As a model system to study such effects we select the InAs/GaAs

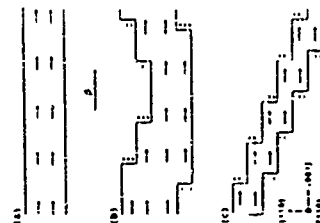
We use solid source molecular beam epitaxy (MBE) to synthesize our structures on (110) GaAs n^+ substrates with 1.2 micron period towards the [111] direction. Simultaneously grown on-axis (100) structures on semi insulating GaAs substrates serve as reference samples. The growth process is monitored *in situ* by reflection high energy electron diffraction (RHEED). Details about the growth procedure will be reported elsewhere.

acknowledgments. This work was done while B.R.B. held a National Research Council NRI Research Associateship. The work was supported in part by the Office of Naval Research. The authors thank M. Latum for the use of an X-ray diffractometer.

References

- [1] C. R. Bolognesi, J. D. Worke, I. J. Caine, H. Kroemer, and I. L. Ho, *IEEE Electron Dev Lett* **14**, 11 (1993).
- [2] D. L. Smith and C. Mailhot, *J Appl Phys* **62**, 2515 (1987).
- [3] D. H. Chow, R. H. Miles, J. N. Schulman, D. A. Collins, and I. C. MacGill, *Semicond Technol* **6**, C17 (1991).
- [4] B. A. Shanabrook, J. R. Waterman, J. L. Davis, and R. J. Wagner, *Appl Phys Lett* **61**, 2188 (1992).
- [5] D. H. Chow, R. H. Miles, and A. I. Hunter, *J Vac Sci Technol* **B10**, S88 (1992).
- [6] J. R. Waterman, B. V. Shanabrook, R. J. Wagner, M. I. Yang, J. L. Davis, and J. P. Omag, *Semicond Sci Technol* **8**, S106 (1993).
- [7] B. R. Bennett, B. V. Shanabrook, R. J. Wagner, J. L. Davis, and J. R. Waterman, *Appl Phys Lett* **63**, (16 Aug 1993).
- [8] V. Swaminathan and A. F. Macrauder, *Materials Aspects of GaAs and InP Based Structures*, p. 205, Prentice-Hall, Englewood Cliffs, NJ (1991).
- [9] Program RADs from Beale Scientific using the following values of lattice constant and Poisson's ratio: GaAs: 3.63125 Å, 0.311, InAs: 6.0581 Å, 0.352, GaSb: 6.0951 Å, 0.311, InSb: 6.4788 Å, 0.351.
- [10] C. López, R. J. Springer, R. J. Nicholas, P. J. Walker, N. J. Mason, and W. Hayes, *Surface Science* **267**, 176 (1992); I. Sola, I. A. Santos, C. R. Bolognesi, A. C. Gossard, and H. Kroemer, *Phys Rev B* **40**, 7290 (1992), and M. Imura, M. Yano, H. Furuse, N. Nasa, and Y. Iwata, *Semicond Sci Technol* **8**, S121 (1993).
- [11] D. W. Taylor in *Optical Properties of Mixed Crystals*, p. 15, Elsevier Science, The Netherlands (1988).
- [12] B. A. Shanabrook, B. R. Bennett, and R. J. Wagner, submitted for publication.
- [13] R. Lashe, I. I. Zhuravsky, I. D. Gubling, H. D. Shah, P. C. Chow, K. Matsushita, B. C. Coxington, A. Chu, J. Zhu, and H. F. Schaeke, *J Cryst Growth* **111**, 677 (1991).
- [14] G. Little, H. Kroemer, and I. L. English, *J Appl Phys* **67**, 4012 (1990).

the inset of Fig. 2 gives the sample structure. X-ray diffraction is performed with a double crystal x-ray diffractometer in Bragg geometry. The diffraction patterns are recorded in the vicinity of the symmetrical GaAs (220) and (004) reflections



For the PL experiments the samples are excited at 6K by the red line (637.6 nm) of a Kr⁺ laser. The emitted light is detected by a photomultiplier in the photon counting mode. Time-resolved PL experiments are carried out under pulsed excitation with an Ar⁺ laser pumped by a sapphire laser. The emission is dispersed by a 32 cm spectro meter followed by a Hamamatsu 2D streak camera with a time-resolution of 10 ps. We report on a set of three typical samples with different In contents. The parameters of the (110)- and the corresponding

(100) reference samples are given in table 1. First we direct our attention to the HRXRD spectra of the (110) samples together with reference sample #1(100) displayed in Fig. 2. For all samples we observe well defined *P*-*n*-*d* oscillation fringes indicative of high structural quality. The increase in In content from sample #1(110) to #3(110) results in expected in more pronounced and a larger number of observable fringes. Finally, we even observe a clearer and better defined pattern for sample #2(110) than for #1(100). Although a final assessment it has to wait for a theoretical simulation of the diffraction patterns this observation clearly underlines the structural excellence of our (110) samples.

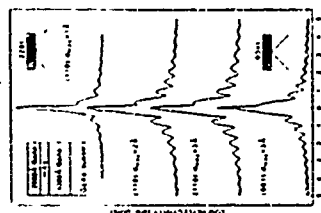


Figure 2. HRXRD patterns of all (110) and one (100) sample taken in the vicinity of the GaAs (220) and (004) reflections.

In order to find the first fingerprints of the expected strong internal electric fields we show in Fig. 3 the PL spectra of all investigated samples. The spectra of the (110) samples exhibit an extremely strong dependence on the excitation density whereas the (100) spectra remain virtually independent of this parameter. Therefore two spectra at different excitation densities are shown for the (110)- and only one spectrum for the (100) samples. Due to the low In content of samples #1(100) and #1(110) the respective spectra are dominated by the GaAs free excitation emission at 1.515 eV and a broad band originating in the n⁺-doped GaAs substrate respectively. In addition we observe in both cases carbon related features at about 1.19 eV for the samples with higher In

content the InAs related emission is the dominating feature. The energy and linewidth of all (100) reference samples agrees very well with studies carried out previously on such structures [2].

Second, again in strong contrast to the (100) case we observe a reduction of the PL linewidth with increasing excitation density. Since an increase of the PL linewidth with increasing electric field strength is a familiar feature of standard (100)-heterostructures under external electric fields [10] it is reasonable to assign the linewidth reduction observed here also to the screening of the internal piezoelectric fields by photogenerated carriers. With blueshift and linewidth reduction upon increase of the excitation density we thus observe two features which strongly imply the presence of internal electric fields in our (110) samples.

Because external fields are known to induce an enhancement of the radiative lifetime in (100)-heterostructures [10], it is an interesting test for our hypothesis of lateral piezoelectric fields to investigate the temporal emission characteristics of our (110) structures. Figure 1 displays the temporal evolution of the PL peak of sample #3(110) after pulsed excitation at 1.530 eV. We see a pronounced spectral diffusion of about 10 meV to the red. This finding is again in striking contrast to InAs/GaAs structures on vicinal (100) surfaces where under comparable conditions a spectral diffusion by about 2 meV to the blue was observed [6].

Figure 1. PL spectra for (110) and (100) samples taken at an excitation density of 5 mW/cm² and 30 W/cm². In which way do the internal fields manifest themselves in the PL spectra? For all (110) samples we see a clear blue-shift of the PL peak with increasing excitation density. This blue-shift ranges from a few meV in sample #1(110) where no definite value can be given due to partially superimposed carbon and InAs related peaks to striking 22 meV for sample #3(110). This observation contrasts with a shift of zero in the (100) reference samples and can be understood by the presence of strong internal electric fields in the (110)-samples which at larger excita-

tion contrast with a shift of zero in the (100) reference samples and can be understood by the presence of strong internal electric fields in the (110)-samples which at larger excita-

TABLE 1. Parameters of the investigated single quantum well (110) and (100) InAs/GaAs samples. High and low excitation densities are 30 W/cm² and 5 mW/cm² for samples #2 and #3 [5].

sample	$\Delta E_{\text{As}}/\text{Å}$	E_{PL}/eV	low I_{exc}	high I_{exc}	low I_{exc}	high I_{exc}
#1(110)	1	1.504	1.504	1.504	3.2	1.2
#2(100)	1	1.504	1.504	1.504	25	13.7
#2(110)	2	1.557	1.579	1.579	4.1	1.1
#3(100)	2	1.584	1.584	1.584	26.3	1.5
#3(110)	3	1.623	1.638	1.638	5	2

Band Discontinuity and Effects of Si-Insertion Layer at (311)A GaAs/AlAs Interface

T Saito, Y Hashimoto, and T. Ikoma
Institute of Industrial Science, University of Tokyo,
7-22-1 Roppongi, Minato-ku, Tokyo 105, Japan

Abstract - We present a theoretical analysis of the valence-band discontinuity ΔE_v at the (311)A GaAs/AlAs interface and a possibility of ΔE_v control by Si-intersection layers. The calculation is carried out by the self-consistent tight-binding method in a $(\text{GaAs})_n/(\text{AlAs})_m$ (311) superlattice. ΔE_v at the (311)A interface is calculated to be 0.50 eV, while it is 0.51 eV at the (100) and (110) interfaces. The orientation independence of the ΔE_v holds for the (311)A interface. The result is consistent with our experimental results. At the (311)A interface, inserted Si double-layers can have two possible layer spacings, one is $a\sqrt{4}/11$ on an As-terminated GaAs and the other $3a\sqrt{4}/11$ on a Ga-terminated GaAs, where a is the lattice constant. In the former case, ΔE_v is ~ 0.12 eV (reduced by 0.62 eV), while in the latter it is 1.67 eV (increased by 1.17 eV).

1. INTRODUCTION

A possibility to artificially control the band discontinuity at a hetero-interface by inserting group-IV element layers has been a hot issue from both scientific and application points of view [1-6]. Although the theoretical predictions [1,2] and the experiment [3] have shown that the band discontinuity is successfully controlled at the (100) GaAs/AlAs interface, Hashimoto *et al.* [4,5] have shown that the inserted Si atoms mainly act as donors and do not serve to control the band discontinuity because no interface dipole is formed. It is due to an experimental difficulty to control the occupation sites of Si atoms at the (100) interface, which is crucial in forming an interface dipole to control the band discontinuity [4,5].

On the other hand, it is known that on a (311A) GaAs substrate, Si can be both donor and acceptor depending on the growth condition [7,8] and therefore we have a higher possibility to successfully form an interface dipole and to control the band discontinuity. However, no theoretical calculation of the band discontinuity and on a possibility to control it is available on the (311A) GaAs/AlAs interface.

The purpose of this paper is to theoretically clarify, (1) how much the valence-band discontinuity (ΔE_v) is at the (111)-A GaAs/AlAs interface, and (2) how much ΔE_v can be controlled by insertion of Si-doped layers at the interface. The result of the former is compared with our experimental ΔE_v measured by the X-ray photoemission spectroscopy (XPS). This study is the extension of our previous calculations by the self-consistent tight-binding method [5,6].

2. METHOD OF CALCULATION

2. METHOD OF CALCULATION

The calculation is performed on the basis of the sp^3s^* semi-empirical tight-binding Hamiltonian [9]. The parameters are taken from the values of Vogl *et al.* [9]. Spin-orbit coupling is not included. The procedure for achieving an electrostatic self-consistency is essentially the same as that used by Muñoz *et al.* [10]. In this method, the atomic orbital energies are modified with the induced electro-

quantitative demonstration. By their very nature, lateral p-n junctions holds deeper strongly on the actual geometry of the quantum well structure and therefore a quantitative analysis, in contrast to the case of perpendicular fields, is extremely intricate.

In conclusion we have presented spectroscopic evidence for the existence of lateral piezoelectric fields in strained III-V heterostructures. Our results demonstrate the strong and dominating impact such fields can have on the electronic properties and the relaxation kinetics of a strained III-V heterostructure with arbitrary orientation. They further throw open as to the way to novel methods for optoelectronic devices based on piezoelectricity. In this regard, the introduction of a strained heterostructure with lateral patterning for carrier transport and lateral patterning for carrier recombination also hold for III-V heterostructures where even stronger effects are expected due to the much larger piezoelectric coefficients of the order of magnitude larger piezoelectricity in the zinc-blende materials.

We would like to acknowledge the expert help of A. Fischer with ABE growth. Part of this work was sponsored by the Bundesministerium für Forschung und Technologie of the Federal Republic of Germany.

- [1] J. M. Mailhot and D. E. Smith, *Phys. Rev. B* **35**, 1242 (1987).
- [2] J. F. Carole, Y. X. Chang, K. W. Evershed, and J. F. L. Thomas, *Appl. Phys. Lett.* **56**, 670 (1990).
- [3] P. M. Borsell, J. J. Nichols, J. J. Davies, B. Corcoran, and P. E. Wacht, *J. Appl. Phys.* **71**, 307 (1992).
- [4] D. E. Smith and J. M. Mailhot, *J. Appl. Phys.* **63**, 2717 (1988).
- [5] For samples $\#1$ we used $W/L=0$ and $\ln n/W/L=0$ to force the flow in front of the sample; we did not allow the contribution of a well defined $1D$ peak outside of this range.
- [6] O. Brandt, L. Unger, K. Ploog, H. Biersdorf, M. Hohenstein, A. Philipp, H. Luxe, and A. H. Heile, *Phys. Rev. B* **44**, 4011 (1991).
- [7] M. Heig, M. Voss, A. Lehmann, K. H. Ploog, and M. Hohenstein, unpublished results.
- [8] M. Heig, O. Brandt, and K. Ploog, *Appl. Phys. Lett.* **61**, 141 (1992).
- [9] M. Heig, O. Brandt, A. Ruz and K. Ploog, *Phys. Rev. B* **45**, 8825.
- [10] H. J. Pöhlard, L. Schulteis, J. Kuhl, E. O. Gdelt, and C. W. To, *Phys. Rev. Lett.* **55**, 240 (1985).

Two sources can contribute to this spectral red shift. The first influence certainly is the number of carriers which decreases in the course of time and leads to a less efficient screening of the internal fields. But the inset of fig. 1 demonstrates a strong dependence of the radiative lifetime on the PL energy which also contributes to the observed spectral diffusion. For the low energy part of the PL emission we observe a purely exponential decay, i.e. it is normally seen in GaAs/AlGaAs structures¹ with a decay time of 750 ps whereas for the high energy part a biexponential decay with an initially much shorter decay time of only 250 ps is observed. This difference in decay time can be understood the wavefunctions of the low energy states to be distorted by the internal electric fields. Therefore the electron hole overlap for low energy states is reduced compared to the high energy states so that the transition fields are screened only. A decrease of the field overlap however increases the radiative lifetime and results in the observed variation of the lifetime with energy.

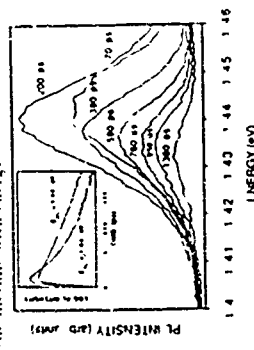


Figure 1. Transient photoluminescence spectra of the $\text{Al}_x\text{Ga}_{1-x}\text{As}$ (110) sample after pulsed excitation at 1.5 eV. The spectra are taken at different delay times after the excitation of the sample as shown in the figure. The first shows the time dependence of the emission spectra integrated over the low energy of $E_{\text{PL}} \leq 1.1\text{ eV}$, and the luminous part of the PL line at $E_{\text{PL}} > 1.1\text{ eV}$, in order to reveal the energy dependence of the relaxation time.

The time-resolved measurements thus strongly support our conclusions given above. The combination of the two spectroscopic methods therefore is a clear demonstration of the existence and importance of lateral piezoelectric fields. We point out, however, that at this stage we cannot give more than this

static potential at the interface [10]. In the present study, we apply this method to a GaAs/AlAs (311) superlattice and deduce ΔE_v . The similar studies on (100) and (110) superlattices were presented in our previous works [5,6].

We use a $(\text{GaAs})_2/(\text{AlAs})_2$ (311) superlattice. The period of this superlattice along the (311) direction is $a\sqrt{3}$, where a is the lattice constant of GaAs. Each GaAs well starts at a (311)B face and ends at a (311)A face. This means that both (311)A and (311)B GaAs/AlAs interfaces are included in the superlattice. Here A and B always refer to faces for As and Ga, not for AlAs. We focus mainly on the (311)A interface because it simulates the interface formed by AlAs growth on a (311)A GaAs substrate

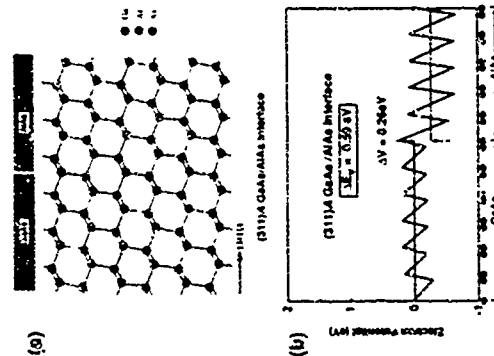


Fig.1. Atomic arrangement (a) and potential profile (b) at the (311)A GaAs/AlAs interface

Table 1. Valence-band discontinuities

Interface	Experiment	Theory
(100)	$0.44 \pm 0.05^{a,b}$	0.51
(110)	$0.44 \pm 0.05^{a,b}$	0.51
(311)A	0.42 ± 0.44^b	0.50
(311)B	0.45^a	0.52

^aGaAs on AlAs, ^bAlAs on GaAs)
^cRef. 11)

3. BAND DISCONTINUITY AT (311)A GaAs/AlAs INTERFACE

Figure 1 shows the atomic arrangement (a) and the potential profile (b) at the (311)A GaAs/AlAs interface. The potential sawtooth-like oscillates due to the negative and positive net charges at the anion and cation sites [10]. The dipole potential ΔV , which is defined as the difference between average potentials in AlAs and GaAs, is 0.26 eV. ΔV is modified by Si-insertion layers and consequently ΔE_v can be changed as shown in Section 4.

ΔE_v at the (311)A (and B) interface is calculated to be 0.50 eV (and 0.52 eV). At the (100) and (110) interfaces, it is 0.51 eV by our calculations [5, 6]. The result indicates that ΔE_v is almost constant for various interface orientations, even for high-index planes.

The apparent orientation independence of ΔE_v was experimentally shown by Hirakawa *et al.* [11] for major low-index planes: (100), (110), and (111)B. The measurement was done by XPS. In the present paper, we measured ΔE_v at the (311)A (and B) interface to confirm the theoretical result. The sample structures are: AlAs(30Å)/GaAs(1μm)/(311)A n⁺-GaAs(substrate) for the

(311)A interface, and GaAs(30Å)/AlAs(100Å)/GaAs(1μm)/(311)A n⁺-GaAs (substrate) for the (311)B interface. In the latter, the (311)B face of the top GaAs layer forms an interface with the underlying AlAs layer. The measurement technique is the same as reported in Ref.[11]. The values of ΔE_v measured in the present study and Ref.[11] are summarized in Table 1 together with our theoretical ΔE_v 's. In the experiment, ΔE_v is found to be independent of the interface orientation even in the (311)A (and B) interface, which confirms our calculation.

4. EFFECTS OF SI-INSERTION LAYER ON BAND DISCONTINUITY

Si double-layers inserted at the (311)A interface can have the two configurations as shown in Fig 2(a) and Fig 3(a); the former is formed on an As-terminated GaAs where the first Si layer occupies Ga sites and the second does As sites with the layer spacing of $a/4\sqrt{3}$. The latter is formed on a Ga-terminated GaAs, where the occupation sites are reversed and the layer spacing is $3a/4\sqrt{3}$. An extra interface-dipole [1] is expected to be formed by these Si double-layers. In the present calculation, a lattice distortion due to the Si-insertion layer is not included.

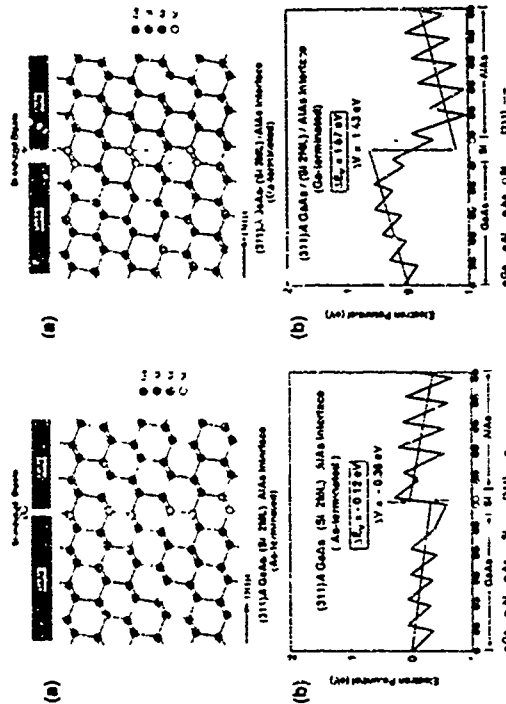


Fig.2. Atomic arrangement (a) and potential profile (b) at the (311)A GaAs/AlAs interface inserted with the Si double layers. GaAs is terminated at an As plane

Fig.3. Atomic arrangement (a) and potential profile (b) at the (311)A GaAs/AlAs interface inserted with the Si double layers. GaAs is terminated at a Ga plane

Figures 2(b) and 3(b) show the potential profiles at the (311)A GaAs/AlAs interface with the Si double-layers on an As-terminated and a Ga-terminated GaAs, respectively. ΔV is -0.36 eV in the former and 1.43 eV in the latter. The change of ΔV from the original value is -0.62 eV and +1.17 eV, respectively. Therefore, ΔE_v with the Si double-layers is reduced as: $\Delta E_v = -0.12$ eV on an As-terminated GaAs, and $\Delta E_v = 1.67$ eV on a Ga-terminated GaAs. The sign of ΔE_v change depends on the polarity of the terminated plane and the magnitude mainly on the layer spacing. The gradient of the average potentials in GaAs and AlAs in Figs. 2(b) and 3(b) is an artifact caused by the periodic boundary condition of the superlattice as shown in Ref. [1,6]. This does not influence ΔE_v .

In the previous work [5], we studied the effects of Si-insertion layers at the (100) and (110) interfaces. With Si-double layers, ΔE_v is calculated to be -1.36 eV and 2.1 eV at the As- and Ga-terminated (100) interfaces, respectively, and 0.35 eV at the (110) interface. It should be noted that an effect of Si-insertion layers on ΔE_v has a strong orientation dependence, although ΔE_v with no Si layers is almost independent of the interface orientation.

5. CONCLUSIONS

We analysed ΔE_v at the (311)A GaAs/AlAs interface and a possibility of ΔE_v control by insertion of the Si double-layers by using the self-consistent tight-binding method. The results are summarized as follows.

- (i) ΔE_v at the (311)A (and B) interface is 0.50 eV (and 0.52 eV), while it is 0.51 eV at the (100) and (110) interfaces. The orientation independence of ΔE_v holds for the (311)A (and B) interface, being consistent with our experimental observation by XPS.
- (ii) With insertion of Si double-layers, ΔE_v at the (311)A interface is calculated to be -0.12 eV (reduced by 0.62 eV) and 1.67 eV (increased by 1.17 eV) on an As-terminated and a Ga-terminated GaAs, respectively. The result predicts a possibility to control ΔE_v at the (311)A GaAs/AlAs interface, on which Si can be either an acceptor or donor depending on growth conditions.

Acknowledgements. We thank Dr. K. Hirakawa for valuable discussions. This work is partly supported by the Grant-in-Aid from the Ministry of Education, Science and Culture, Japan and also by the Industry-University Joint Research Program "Mesoscopic Electronics."

REFERENCES

1. A. Muñoz, N. Chetty, and R.M. Martin, *Phys. Rev. B* **41**, 2976 (1990).
2. M. Peressi, S. Baroni, W. Resta, and A. Baldereschi, *Phys. Rev. B* **43**, 7347 (1991).
3. I. Sorba, G. Bratina, G. Ceccone, A. Antonini, J.F. Walker, M. Micovic, and A. Franciosi, *Phys. Rev. B* **43**, 2450 (1991).
4. Y. Hashimoto, G. Tanaka, K. Hirakawa and T. Ikoma, in *Proc. of the 21st Int. Conf. on the Physics of Semiconductors*, p. 725 (Beijing, China, 1992).
5. Y. Hashimoto, T. Saito, K. Hirakawa, and T. Ikoma, in *Proc. of 19th Int. Symp. GaAs and Related Compounds*, Karuzawa, Japan, 1992, (Inst. Phys. Conf. Ser., No. 129, p. 259).

6. T. Saito and T. Ikoma, *Superlattices and Microstructures* **12**, 81 (1992).
7. W. Q. Li, P.K. Bhattacharya, S.H. Kwok, and R. Merlin, *J. Appl. Phys.* **72**, 3129 (1992).
8. K. Aizawa, Y. Hashimoto, T. Ikoma, T. Okumura, and S.-Q. Shao, submitted to *Proc. of 20th Int. Symp. GaAs and Related Compounds*, Freiburg, Germany, 1993.
9. P. Vogl, H.P. Hjalmarson, and J.D. Dow, *J. Phys. Chem. Solids* **44**, 365 (1983).
10. A. Muñoz, J. Sánchez-Dehesa and F. Flores, *Europhys. Lett.* **2**, 385 (1986), G. Platero, J. Sánchez-Dehesa, C. Tejedor and F. Flores, *Surface Science* **168**, 553 (1986).
11. K. Hirakawa, Y. Hashimoto, and T. Ikoma, *Appl. Phys. Lett.* **57**, 2555 (1990).

MoC5

X-Ray Diffraction Analysis of GaAs/AlAs Multilayer Structures grown by Molecular Beam Epitaxy on (111) and (110) GaAs surfaces

M. A. Tagliente^{a,1}, L. De Caro^a, I. Taylor^a, R. Maurer^b, A. Fischer^b, and K. Plagge^c

^a Centro Nazionale Ricerche Sviluppo dei Materiali
SS 7 per Macchine Km. 3,11-72022 Mesagne (Br), Italy

^b Max-Planck-Institut für Festkörperforschung
Heisenbergstrasse 1, D-7100 Stuttgart 80, Germany

^c present address: Paul-Drude Institut für Festkörperelektronik,
Hannoverstrasse 5-7 D 10117 Berlin, Germany

Abstract

In this work, we investigate the structural properties of single and multiple AlAs/GaAs heterostructures grown on (111) and (110) GaAs surfaces by molecular beam epitaxy. The strain state and lattice deformation of epitaxial layers grown on high index surfaces is determined. The components of the strain tensor are calculated by minimizing the strain-energy density and are implemented in the normalized strain function of the Takagi-Taupin equations of the dynamical x-ray diffraction theory for distorted crystals in order to simulate the experimental x-ray diffraction patterns. Experimental results on AlAs/GaAs single heterostructures and AlAs/GaAs multilayer structures reveal that the epitaxial layers are pseudomorphic and show a shear strain component different from zero in contrast to structures grown on (001) substrates. The measured data are in excellent agreement with the calculated strain fields.

1. Introduction

Semiconductor heterostructures grown on non-singular surfaces have recently attracted much attention for fundamental reasons as well as for their potential device applications. The growth of the epitaxial structure and the morphological properties of semiconductor multilayer structures grown on crystal substrates with high index crystallographic orientations have been studied extensively [1-8]. These studies show that the surface reconstruction during the growth, the surface morphology, the incorporation of impurity atoms (disorder), the band configuration and the sticking coefficient of atoms depend strongly on the surface orientation. However, few investigations were devoted to the analysis of the structural properties of heterostructures grown on low-symmetry surfaces [9,10].

The strain state of epitaxial layers grown on high index surfaces with less than two fold symmetry has been recently determined by minimizing the strain energy density of the epitaxial structure and using the appropriate boundary conditions at the film/substrate interface [11]. These expressions have revealed the presence of a non-tetragonal type lattice deformation in epitaxial layers with low-symmetry orientation. In fact the shear strain is found to be different from zero for all surface directions except for the high symmetry (111) and (110) surfaces. Furthermore, the shear displacement occurs normal to the direction of the highest symmetry of the interface plane. An exact knowledge of the lattice deformation is of high interest since strain fields govern electronic fields in the heterostructures and affect both microscopic properties, such as the band gap and the macroscopic properties of crystals, such as piezoelectric and photovoltaic effects [6].

In this work, we report on a structural and strain analysis of AlAs/GaAs heterostructures grown on (111) and (110)-oriented GaAs substrates by using high-resolution x-ray diffraction (HRXRD). The components of the strain tensor are included in the normalized strain function of the Takagi-Taupin equations of the dynamical x-ray diffraction theory for distorted crystals in order to simulate the experimental x-ray diffraction patterns. A comparison between experimental and simulated diffraction patterns permits us to determine the lattice deformation and strain fields in epitaxial films [12].

II. Experimental

The HRXRD study of epitaxial layers and superlattices was performed by means of a computer-controlled high resolution double crystal x-ray diffractometer [12]. A rotating anode was used as x-ray source ($\lambda = 1.54056$ nm) and an asymmetrically cut silicon (free germanium) crystal was used as monochromator and collimator of the incident beam. The angular divergence of the x-ray beam incident on the specimen crystal is about 11 mrad. Sample rotation is achieved by a stepping motor under a piezoelectric crystal (elementary step is variable between 7×10^{-6} and 1.5×10^{-5} rad). The intensity of the diffracted x-ray beam is measured with a "wide open" NaI scintillation counter.

The GaAs/AlAs quantum wells and superlattices studied were grown by MBE simultaneously on (111) and (110) or (110) and (110) surfaces of GaAs. The growth rate for both AlAs and GaAs layers, as well as the shutter operation, were calibrated by monitoring the intensity oscillations of the reflection high-energy electron diffraction (RHEED) pattern on the (110) growth face [9].

III. Lattice Deformation

Here, we consider a coherent heterointerface between an epitaxial layer and a substrate crystal both of them of cubic symmetry. If we assume that the film thickness is much smaller than the substrate crystal, then the whole strain will occur in the epitaxial layer and the elastic strain tensor is given by:

$$\epsilon_{ij}(x) = S_{ij} \cdot B_{ij} \quad (1)$$

where $i, j = (x, y, z)$, S_{ij} is the total strain tensor and B_{ij} is the misfit tensor of the lattice parameters of the two materials. For cubic materials, the misfit tensor B_{ij} is defined as follows:

$$B_{ij} = \delta_{ij} (d_L - d_S) / d_L = -\epsilon' \delta_{ij} \quad (2)$$

where d_L and d_S is the lattice constant of the layer (L) and substrate (S), respectively, δ_{ij} is the Kronecker delta tensor, and

$$\epsilon' = (d_S - d_L) / d_L \quad (3)$$

By minimizing the strain energy density starting from the commensurability constraint (or coherent interface hypothesis), the elastic strain tensor components, with reference to the coordinate system of the epitaxial film, can be obtained [11]:

$$\epsilon_{xx}(x) = \epsilon_{yy}(x) = 0 \quad (4)$$

$$\epsilon_{yz}(x) = \{ (C_{11} + 2C_{12}) \epsilon' (C_{44} R_{14} + C(R_{11} R_{14} - R_{13} R_{40})) / 2\Delta \}$$

$$\epsilon_{zx}(x) = \{ (C_{11} + 2C_{12}) \epsilon' (C_{44} R_{15} + C(R_{12} R_{15} - R_{14} R_{40})) / 2\Delta \}$$

$$\Delta = \epsilon' \epsilon_{zz}(x) = \{ (C_{11} + 2C_{12}) \epsilon' (C_{44}^2 + C C_{44} (1 - R_{11}) + 3C^2 (T_1 T_2 T_3)^2) \} / \Delta$$

where Δ is the tetragonal distortion, $\epsilon_{yz}(x)$ and $\epsilon_{zx}(x)$ are the shear strain elements, and Δ and C are given by:

$$\Delta = C_{11} (C_{44})^2 + (C C_{44} / 2) (C_{11} + C_{12} + 3C_{44}) + C^2 (C_{11} + 3C_{12} + C_{44}) (T_1 T_2 T_3)^2 \quad (5)$$

and

$$C = C_{11} - C_{12} - 2C_{44}$$

C_{11} , C_{12} , and C_{44} in eqs (4) and (5) are the elastic stiffness tensor elements for crystals with cubic symmetry in the crystallographic reference system. The stiffness tensor R_{ijk} describes the transformation of the stiffness tensor elements from the crystallographic reference system to the epitaxial layer reference system, and are given by

$$R_{ijk} = T_{11} T_{11} T_{11} + T_{12} T_{12} T_{12} + T_{13} T_{13} T_{13} + T_{21} T_{21} T_{21} + T_{22} T_{22} T_{22} + T_{23} T_{23} T_{23} + T_{31} T_{31} T_{31} + T_{32} T_{32} T_{32} + T_{33} T_{33} T_{33} \quad (6)$$

where T_{ik} is the matrix of the transformation. Here, α and $\beta = 1$, Δ indicate the symmetric pairs of the indices i and k are $\{1,2,3\}$, respectively.

According to these relations, the unit cell of a epitaxial layer grown on high-symmetry surfaces, i.e. (100), (110) and (111), is tetragonal, distorted. This means that the strain tensor ϵ_{ij} has only diagonal elements different from zero. On the other hand, if the film is grown on low-symmetry surfaces, the strain tensor has also shear strain components, which are different from zero. It should be noted that the axes x , y and z are always chosen in such a way that only one component of shear strain is different from zero (either x or y should coincide with a principal axis of the strain tensor). These findings are valid for all material systems with cubic symmetry and are independent of the magnitude of lattice mismatch between the epitaxial layer and the substrate crystal. In Table I are reported the elastic shear strain components ϵ_{ij} and the tetragonal distortion Δ for an epitaxial layer of AlAs grown on GaAs substrates for the crystallographic orientations under consideration. Here, the axes x and y of the epitaxial layer reference system are chosen to obtain only one of the shear strain components different from zero [11]. It should be noted that not only the tetragonal distortion but also the shear strain depends strongly on the lattice mismatch between epitaxial layer and substrate.

IV. X-Ray Diffraction Analysis

Double crystal x-ray Bragg diffraction experiments enable us to measure all the components of the strain tensor [12]. The position $\Delta\theta$ of the diffraction peak maximum of the film relative to the peak maximum of the substrate is given by

$$\Delta\theta \approx \frac{1}{2} \sin^2 \theta \frac{\Delta d}{d} = \frac{1}{2} \sin^2 \theta \frac{\Delta \epsilon_{11}}{\epsilon_{11}} \quad (7)$$

where the plus sign corresponds to the glancing incidence geometry and the minus sign to the grazing exit geometry. Here θ is the angle between the reflection planes and crystal surface, θ_B is the Bragg angle of the substrate crystal for the observed reflection and ϵ_{11} is the x component of the total distortion tensor, which contains also the rotations of the structure in the case of pseudomorphic growth. By substituting eqs (7) for the eq (4) we have

$$\Delta\theta \approx \frac{1}{2} \sin^2 \theta \frac{\Delta \epsilon_{11}}{\epsilon_{11}} = \frac{1}{2} \sin^2 \theta \frac{\Delta \epsilon_{11}}{\epsilon_{11}} \quad (8)$$

If we consider a symmetrical reflection in eq (8) is reduced to the following

$$\Delta\theta \approx \frac{1}{2} \sin^2 \theta \frac{\Delta \epsilon_{11}}{\epsilon_{11}} \quad (9)$$

Therefore, for a two-layer system film-substrate with a coherent interface we can determine both the normal strain ϵ_{11} and shear strain ϵ_{12} tensor components in the epitaxial layer by measuring the diffraction patterns in a symmetrical and asymmetrical reflection geometry (eqs (8) and (9)). By this method, we can determine all the components of the strain tensor, if the principal axes are known, while in the case of a superlattice, eqs (8) and (9) enable us to determine the average strain components of a superlattice period. Equation (7) is used for solving the Laue-Tauzin equation of the x-ray dynamical diffraction [14].

Furthermore, the angular distance $\Delta\theta$ between the satellite peaks gives the superlattice period length D as $\Delta\theta \approx \lambda / (2D \sin \theta_B)$

where λ is the x-ray wavelength and θ_B is the Bragg angle of the diffracted wave. The values of the strain components and thickness of the individual epitaxial layers, which constitute the SL period, can be obtained by

$$(10)$$

the simulation of the experimental diffraction curves. The position as well as the peak height of the satellites depends on the thickness and strain fields (strain modulation) of the individual layers. Since the strain in epitaxial structures is measured with respect to the substrate crystal, the calculated and measured strain components are related by the following expression:

$$\epsilon_{12}(\text{exp}) = -\epsilon_{12}(\text{calc}) \quad (11)$$

However, it should be noted that for AlAs/GaAs structures the factor $\epsilon_{12}(\text{exp}) = 1.0014$ can be neglected due to the small lattice mismatch between the two material systems.

V. Results and Discussion

Figure 1 shows the experimental (dashed lines) and calculated (solid lines) rocking curves recorded in the vicinity of the (111) and (400) GaAs Bragg reflection for an AlAs layer capped with GaAs, grown onto a (111) GaAs substrate. The dynamical theory in two recursive formalism has been used for the simulations. From the diffraction patterns we obtain by using eqs (8) and (9) the lattice strain along the growth direction $\epsilon_{11}(\text{exp}) = (2.49 \pm 0.07) \cdot 10^{-3}$ and the shear strain (invariant $\epsilon_{12}(\text{exp}) = (5.6 \pm 1.7) \cdot 10^{-4}$. The considered errors in the determination of strain components are due to an error of $3.5 \cdot 10^{-5}$ rad in the $\Delta\theta$ measurement. The comparison between the measured and calculated strain components values (see Tab. 2) shows an excellent agreement. According to this finding we may conclude that the growth of AlAs on (111) GaAs surfaces is pseudomorphic (coherent interface), i.e. there is no in-plane strain. The thickness of the AlAs epitaxial layer is found to be 313 nm and 7 nm, respectively, from the simulated patterns.

The lattice deformation in superlattices has been also investigated. In Fig. 2 is shown the experimental (a) and the calculated (b) rocking curves in the vicinity of the (400) reflection for an AlAs/GaAs superlattice consisting of 80 periods, grown on a (111)-oriented GaAs substrate. The SL period length determined by the angular distance between the satellite peaks is 11.6 nm. The best fit patterns have been obtained by considering an AlAs layer, 5.1 nm thick, in which the perpendicular strain $\epsilon_{12}(\text{exp}) = 2.5 \cdot 10^{-3}$, while the GaAs layer is 6.2 nm thick and strain free. The shear strain of the AlAs layer is $\epsilon_{12}(\text{exp}) = 4.1 \cdot 10^{-4}$ as determined from the (400) reflection measurement.

The maximum intensities of the first order satellite peaks $S_{1,1}$ and $S_{-1,1}$ (see Fig. 3) are smaller than the calculated values for a perfect superlattice with ideal interfaces. Moreover, the tails of the experimental satellite peaks are much more pronounced than the calculated ones. However, the full-width at half-maximum (FWHM) of the satellite peaks is not affected and no line broadening is observed experimentally. These findings may be explained by considering an ordered interface composition as observed by RHEED and TEM analyses. In fact, the presence of GaAs for AlAs wires, whose formation is due to the interface interdiffusion [6,9], gives rise to a diffuse x-ray scattering observed as an increase of the tail intensities of the satellite peaks.

Figure 4 shows the experimental (dashed lines) and calculated (solid lines) rocking curves for the asymmetric (400) reflection of a two-layer system composed of an AlAs layer and a GaAs cap layer grown onto a (110)-oriented GaAs substrate. The best fit reveals that the AlAs layer is 470 nm thick and the 20% mismatch along the growth axis is $\epsilon_{11}(\text{exp}) = (2.38 \pm 0.07) \cdot 10^{-3}$ and the shear strain is $\epsilon_{12}(\text{exp}) = (3.2 \pm 1.5) \cdot 10^{-4}$, while the GaAs cap layer is 10 nm thick and strain free. The difference between the theoretical $(2.48 \cdot 10^{-3})$ and the experimental $(2.38 \cdot 10^{-3})$ value of the normal strain ϵ_{11} can be explained by assuming a non perfect sample surface orientation, which leads to a small discrepancy for the $\Delta\theta$ value.

Figure 5 shows the (400) experimental (a) and calculated (b) diffraction patterns recorded in the grazing incidence geometry for a (110)-oriented GaAs/AlAs superlattice consisting of 100 periods. The angular separation between the satellite peaks gives the superlattice period length of 574 nm. The thickness of the individual GaAs and AlAs layers were determined from the simulation and are 2.62 nm and 1.12 nm, respectively. The strain values $\epsilon_{11}(\text{exp})$ and $\epsilon_{12}(\text{exp})$ of the AlAs layers of the superlattice are found to be $(2.48 \pm 0.07) \cdot 10^{-3}$ and $(4.12 \pm 0.10) \cdot 10^{-4}$, respectively. Comparing the experimental and calculated strain components (Tab. 1) we may conclude that the epitaxial growth of AlAs on GaAs is pseudomorphic also for the (110) surface orientation. The discrepancy between the experimentally measured satellite peak intensities and

A comparison between the data obtained from AlInGaSb heterostructures grown simultaneously on GaInAs and GaInP substrates is shown in Fig. 1. The AlInGaSb heterostructures grown simultaneously on GaInAs and GaInP substrates show a much more densely packed surface morphology than the AlInGaSb heterostructures grown on GaInP substrates alone. This is due to the fact that the (110) surface is much more densely packed than the (111) surface [6].

Abstract

- [11] S. Subhanwar, H. Krimmer, and J. L. Merz, *J Appl Phys* **59**, 488 (1986)
- [12] W. J. Wang, R. F. Tinkham, and L. Vase, *J Appl Phys* **59**, 937 (1986)
- [13] T. Fukunaga, T. Makimoto, and H. Nakashima, *J. of Crystal Growth* **81**, 85 (1987)
- [14] Z. Y. Pyun, M. Cuddebo, E. Rucker, D. Strach, L. Tapper, and K. Phlog, *Phys Rev B* **40**, 12107 (1989)
- [15] B. Gali, Y. El Khalil, H. Maubou, D. de Paulis, J. Masses, G. Neu, T. Fukunaga, and H. Nakashima, *Phys Rev B* **41**, 2885 (1990)
- [16] R. Nazari, L. Daweritz, and K. Phlog, *Phys Rev B* **46**, 4736 (1992)
- [17] T. F. Kuech, R. T. Collins, D. L. Smith, and C. Muthooz, *J Appl Phys* **67**, 2650
- [18] C. Muthooz and D. L. Smith, *Rev Mod Phys* **62**, 173 (1990)
- [19] R. Nazari, N. N. Lederman, J. Daweritz, K. Phlog, and M. Jochenstern, *Phys Rev B* **45**, 1907 (1992)
- [20] W. J. Beetz and W. Nippon, *J. Cryst Growth* **44**, 518 (1978)
- [21] L. D. Carroll and L. Tapper, *Phys Rev* **34** (1991), in press
- [22] Y. P. Khaykovich and F. N. Chakhrikov, *Sov Phys Crystallogr* **34**, 465 (1989)
- [23] L. Tapper and K. Phlog, *Phys Rev B* **40**, 9082 (1989)
- [24] W. J. Beetz, J. Huenenauer, and J. J. W. Luebke, *Acta Crystallogr A* **42**, 539 (1986)
- [25] R. Nazari, *Cryst. Phys., J. of Sci. and Technol.* **40**, 617 (1992)

Table 1. The calculated tetragonal distortion and elastic shear stress on GaAs for the $\{100\}$, $\{210\}$ and $\{111\}$ within the orientations

SUBSTRATE ORIENTATION	REFERENCE AXES			AlAs
	a	y	σ_{xx} (dy)	
[100]	[010]	[001]	$2.82 \cdot 10^{-5}$	0
[210]	[120]	[011]	$2.48 \cdot 10^{-5}$	$3.93 \cdot 10^{-5}$
[311]	[331]	[011]	$2.51 \cdot 10^{-5}$	$-4.11 \cdot 10^{-5}$

Figure Captions

Figure 1 Double crystal x-ray diffraction patterns recorded in the vicinity of the (311) and (600) GaAs reflections of an AlAs intercalated layer grown on (311)-oriented GaAs substrate

Figure 2 Experimental (a) and simulated (b) diffraction patterns of an AlAs/GaAs superlattice grown on GaAs (111)

Figure 1
crystalline (111) surface of the AlGaAs superlattice shown in Fig 2.

Figure 4
Experimental (dotted line) and simulated (solid line) double-crystal x-ray diffraction patterns
of the α -phase of an AlAs_{0.95}As_{0.05} grown on (210) GaAs.

Figure 5
Experimental (a) and simulated (b) diffraction patterns in the vicinity of the (400) reflection of an Al_{0.5}Ga_{0.5}As wire (diameter 1.0 μm) GaAs

Folded Acoustic Phonons in GaAs/AlAs Superlattices Grown on Non-(100)-Oriented Surfaces

J. Spitzer, Z.V. Popović, T. Ruf, M. Cardona, R. Nitsch, and K. Ploog
Max-Planck-Institut für Festkörperforschung, Heisenbergstraße 1,
Postfach 80 05 65, 70506 Stuttgart, Federal Republic of Germany

We present Raman spectra for folded acoustic phonons in GaAs/AlAs superlattices grown along the [111], [211], and [311] direction. The symmetry of these directions offers the possibility of observing transverse and longitudinal polarized folded acoustic phonons. The observed doublets of folded acoustic phonons are in accordance with the predicted selection rules, their frequencies and strengths are in agreement with calculations based on the continuum model. In the case of the [311]-oriented sample, folded-phonon to Brillouin ratios are calculated using elasto-optic constants of GaP in lieu of AlAs.

1 INTRODUCTION

Quantum wells and superlattices grown in directions other than [001] have generated increasing interest in the last few years [1-5]. It has been recently reported that high-quality superlattices can be grown by molecular-beam epitaxy (MBE) practically on any low-index crystallographic plane: (hkl), for $h, k, l = 0, 1, 2, 3$. The resulting GaAs/AlAs multilayer structures form asymmetric and symmetric quantum-dot structures on (111) and (211) GaAs, and quantum wire structures on (311) GaAs substrates [6,7]. The resulting lateral confinement of the carriers manifests itself in features such as increased exciton continuum energies or strong enhancement of the luminescence intensity compared to (100) reference superlattices [7]. Hence, this kind of structure is quite interesting for optical and electrical device applications. However, from the viewpoint of Raman spectroscopy high quality SL's grown in other directions than [001] are mainly interesting due to their symmetry properties. In contrast to superlattices grown along [001], in which only the longitudinal acoustic (LA) branch is Raman active in backscattering, samples grown along e.g. [111], [211] and [311] allow the observation of transverse and longitudinal acoustic modes.

In this paper we focus on the folded acoustic phonons of a series of GaAs/AlAs SL's grown along the directions mentioned above. The frequencies and intensities of the folded phonons are in good agreement with continuum model calculations. In the case of the [311] sample, folded phonon to Brillouin scattering ratios compare favorably with those predicted by using the elasto-optic constants of the electronically similar GaP, instead of those of AlAs which are not known.

2 EXPERIMENT

We studied GaAs/AlAs superlattices grown along the [111], [211], and [311] direction with a period between $d=39$ Å and $d=127$ Å. Details of the growth by MBE and the characterization with X-ray diffraction have been given earlier [6,7].

The Raman spectra were recorded in quasi-backscattering geometry, using a Spex Industries 1-m double-monochromator with 1500 grooves/mm holographic gratings and conventional photomultiplier tubes. For the [311] samples we used a SOPRA 2.12-m double-monochromator. The exciting laser was an Ar⁺ ion laser with an average power of 100 mW focused to a line were employed as excitation sources with the samples kept in vacuum at room temperature.

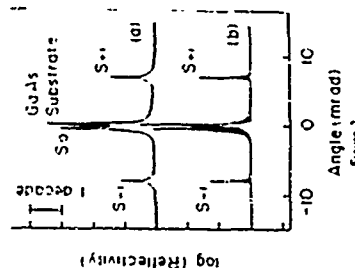


Figure 2
Experimental (a) and simulated (b) diffraction patterns of an AlAs/GaAs superlattice grown on GaAs (311)

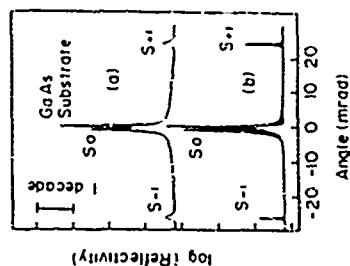


Figure 3
Experimental (a) and simulated (b) diffraction patterns of an AlAs/GaAs superlattice grown on GaAs (210)



Figure 4
Experimental (a) and simulated (b) diffraction patterns of an AlAs/GaAs superlattice grown on GaAs (111)

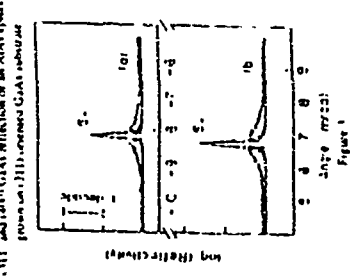


Figure 5
Experimental (a) and simulated (b) diffraction patterns of an AlAs/GaAs superlattice grown on GaAs (100)

Figure 6
Experimental (a) and simulated (b) diffraction patterns of an AlAs/GaAs superlattice grown on GaAs (111) (continued)

3 RESULTS AND DISCUSSION

The propagation properties of acoustic waves in a superlattice can be obtained from the propagation of acoustic waves in the parent material. [8]. For cubic solids (e.g. GaAs), there are three directions of propagation ((100), (110), and (111)) along which the long-wavelength acoustic waves are purely longitudinal and transverse in character (in the (110) case only for small q , i.e. within the elastic approximation). This results for the samples grown along [111] in a purely transverse and a purely longitudinal mode, whereas the [211] and [311] samples exhibit besides pure transverse polarized longitudinal modes, modes with mixed longitudinal and transverse character. The latter ones will be denoted as quasi-transverse (QT) and quasi-longitudinal (QL). The Raman selection rules for the folded acoustic phonons of superlattices in the elastic approximation can be extracted from the Brillouin tensors of the corresponding bulk crystals [8]. The details of this procedure have been described earlier [1-5], the selection rules for all growth directions considered in this work are compiled in Table I [5.9]. The linear combinations of elasto-optic constants which contribute to the scattering in the different polarization geometries of Table I are

$$\begin{aligned} a &= (p_{11} - p_{12} - p_{13} - 2p_{44})c_0^2/3\sqrt{2} \\ b &= (p_{11} + 2p_{12} - 2p_{44})c_0^2/3 \\ c &= (p_{11} - p_{12} - 2p_{44})c_0^2/3\sqrt{2} \\ d &= (p_{11} + 2p_{12} - 2p_{44})c_0^2/3\sqrt{2} \\ e &= (p_{11} + 2p_{12} - 2p_{44})2c_0^2/9 \\ f &= (2p_{11} - 2p_{12} - 4p_{44})c_0^2/11\sqrt{2} \\ g &= (p_{11} + 10p_{12} - 2p_{44})c_0^2/11 \\ h &= (p_{11} - p_{12} - 2p_{44})3c_0^2/11\sqrt{2} \\ i &= 5d p_{12}/11\sqrt{2} \\ j &= (27p_{11} + 94p_{12} - 54p_{44})c_0^2/121. \end{aligned} \quad (1)$$

Table I: The polarization selection rules in backscattering geometry for the folded acoustic phonons of GaAs/AlAs superlattices grown along the [111], [211] and [311] direction as carried over from those of the bulk crystal. a-j are elasto-optic tensor components as described in the text.

[hkl]	Configuration	Polarization			Scattering cross section		
		Incident	Scattering	TA _z	TA _y	TA _x	LA
[111]	$z(x'z')z$	[110]	[110]	0	a^2	0	0
	$x(x'y')z$	[110]	[112]	a^2	0	0	b^2
	$z(y'y')z$	[112]	[112]	0	0	a^2	b^2
[211]	$z(x'z')z$	[011]	[011]	0	c^2	0	d^2
	$x(x'y')z$	[011]	[111]	c^2	0	0	0
	$z(y'y')z$	[111]	[111]	0	0	0	e^2
[311]	$z(x'z')z$	[011]	[011]	0	f^2	0	0
	$x(x'y')z$	[011]	[233]	h^2	0	0	0
	$z(y'y')z$	[233]	[233]	0	0	i^2	j^2

Figure 1 shows the Raman spectra of a (111) oriented (17,30) Å sample for all three polarizations. In agreement with the selection rules of Table I one can observe both, doublets of transverse (TA_z) and longitudinal (LA) modes in parallel polarizations, whereas in crossed polarizations only the transverse (TA_z) doublet is allowed. Due to the symmetry of this growth direction the transverse modes are degenerate. The upper part of Fig. 1 shows good agreement between the measured frequencies and a continuum model calculation. Comparable agreement can be achieved for the samples grown along [211], as demonstrated for a (28, 26) Å sample in Fig. 2. In contrast to the [111] sample, here the degeneracy of the transverse modes is lifted and, in accordance with the selection rules of Table I, doublets from all three acoustic branches can be observed in the various polarizations.

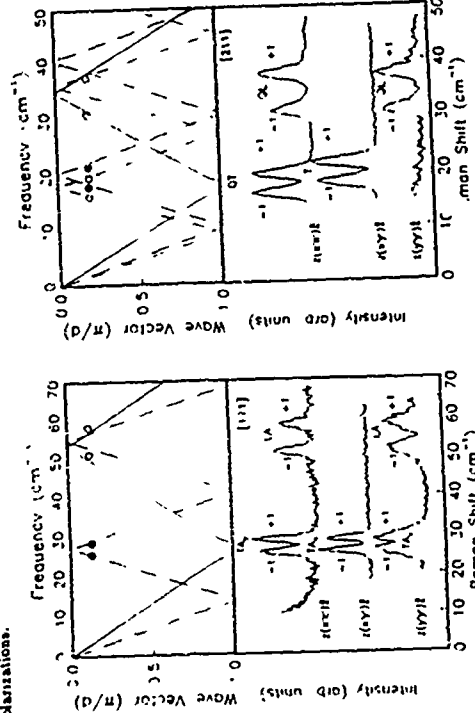


Fig. 1 Raman spectra of a (111)-oriented (17,30) Å superlattice, measured at $T=300$ K with an excitation wavelength of 4579 Å in three different polarizations. QL denotes the quasi-longitudinal, QL the quasi-longitudinal, and T the pure transverse mode. The upper part shows the comparison of measured phonon frequencies with the continuum model $z(x'z')z$, $x(x'y')z$, $z(y'y')z$.

We analyze next in some more detail the (311) oriented, (66,61) Å sample as typical example of the differently oriented samples we deal with in this work. Figure 3 shows the spectra of this superlattice, measured with a SOPRA 212 m monochromator to achieve better resolution and stronger suppression of elastically scattered light. Besides first order doublets, two weak features can be observed at 22.5 cm^{-1} and 25.6 cm^{-1} . We assign them to the third order QT doublet because of the agreement with the calculated frequencies (upper part of Fig. 3). In addition, also the QT-, QL- and T-Brillouin modes (labeled DQT, DQL, and DT) are observed. The relative intensities of the folded phonons with respect to the Brillouin mode can be used, in principle, to determine the ratio of the elasto-optic constants of GaAs and AlAs [10-13], using the expression

given in [10] or the more exact one in [11]. In our case, this yields the linear combinations of the elasto-optic constants contributing to the scattering intensities in the different polarization geometries, as given in Eqs (1). The accuracy obtained by applying this procedure is, however, very poor because of the small values of the elasto-optic constants of AlAs in our frequency range. While these constants (real and imaginary parts) have been measured recently [11] (frequencies for GaAs [11], those of AlAs are unknown. Therefore we calculated the relative intensities of the folded phonons with respect to the Brillouin modes using the elasto-optic constants of GaP [15,16] which should be very similar to those of AlAs in view of the fact that the band structures of both materials are nearly the same. The P_{ij} of GaAs and GaP for 1579 Å and 5145 Å are compiled in Table II. In Table III we give the experimental and calculated values for the relative intensities as the average of the $m=0$ and the $m=\pm 1$ modes. To account for the difference between GaP and AlAs we assume that their elasto-optic constants may differ by less than 10% (as corresponds to the differences in the relative direct gaps). This yields an error of $\approx 1\%$ for the calculated relative intensities. The measured and calculated values of all three intensity ratios agree then within the experimental uncertainty.

Table 2: Elasto-optic constants of GaAs [14] and GaP [15,16] defined as derivatives of the dielectric function (not its inverse) vs. strain.

Material	λ_L [Å]	Elasto-optic constants		
		P_{11}	P_{12}	P_{44}
GaAs	4379	115.7 ± 13.6	10.7 ± 1.99	199.7 ± 27.4
	5145	67.2 ± 128.7	11.7 ± 1.05	155.9 ± 110.7
GaP	4379	30.4	28.3	-5.8
	5145	13.9	19.9	-11.1

Table 3: Ratio of the intensities of the folded acoustic phonons to those of the corresponding Brillouin modes. The theoretical values were calculated using Eq (60) of Ref. [11] and the elasto-optic constants of GaAs [14] and GaP [15,16] (in lieu of AlAs). Both measured and calculated values represent the average of the $m=0$ and $m=\pm 1$ modes.

Acoustic mode	I_m/I_0	
	Experiment	Theory
Γ	0.375 ± 0.050	0.361 ± 0.001
QT	0.360 ± 0.051	0.311 ± 0.003
QL	0.360 ± 0.051	0.350 ± 0.001

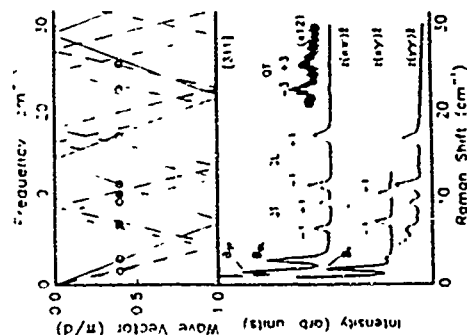


Fig. 3 Raman spectra of a (311) oriented GaP superlattice measured with a SOPRA 212 double-monochromator. In this case the Brillouin loss of all three branches by Rgr. Bgt. as well as QT doublets up to the third order can be observed.

This confirms that the elasto-optic constants of GaP can be used instead of those of AlAs in the region below the direct gap E_0 . The experimental values of Table III are taken from the spectra with $2\pi \times 10^3$ and $2\pi \times 10^4$ polarizations. In $2\pi \times 10^3$ polarizations Rayleigh scattering is stronger and the Brillouin mode could not be observed. This different behavior for both polarizations is presumably caused by the different orientation of the sample corrugation [6] with respect to the plane of incidence. However, this was the only hint of a possible influence of the corrugation on acoustic phonon spectra. A comparison of the linewidths of the folded acoustic phonons of this sample with a sample with the same thickness, but grown along [100] exhibited no differences. This is due to the fact that the acoustic waves are only sensitive to the average period of the superlattice.

4 CONCLUSIONS

We have measured folded acoustic phonons from GaAs/AlAs superlattices grown along [111], [211], and [311], respectively. In the case of the [111] samples, purely transverse and longitudinal acoustic phonon modes could be observed. The [211] and [311] samples exhibit transverse (T), quasi-transverse (QT) and quasi-longitudinal (QL) folded acoustic phonon modes. The measured frequencies of all modes compare well with calculations based on the elastic continuum model. In the [311] sample we have also measured the Brillouin modes of all three acoustic branches and have shown that the relative intensities of the folded phonons to the corresponding Brillouin modes can be described by the elasto-optic constants of GaAs and GaP.

References

- [1] Permanent address: Paul Drude Institut für Festkörperelektronik, Hansotterpl. 5-7, 10117 Berlin, Germany.
- [2] Z.V. Popovic, J. Trodhal, M. Cardona, F. Richter, D. Strauch, L. Tapfer and K. Ploog, Phys. Rev. B 40, 1202 (1989).
- [3] Z.V. Popovic, M. Cardona, E. Richter, D. Strauch, L. Tapfer and K. Ploog, Phys. Rev. B 40, 3040 (1990).
- [4] Z.V. Popovic, M. Cardona, E. Richter, D. Strauch, L. Tapfer and K. Ploog, Phys. Rev. B 41, 5904 (1990).
- [5] Z.V. Popovic, M. Cardona, E. Richter, D. Strauch, L. Tapfer and K. Ploog, Phys. Rev. B 43, 4925 (1991).
- [6] Z.V. Popovic, J. Spitzer, F. Ruf, M. Cardona, R. Naezel and K. Ploog, Phys. Rev. B 48, 15 July 1993.
- [7] R. Naezel, N.V. Le-Duc, L. Dawar, K. Ploog, and M. Hohenstein, Phys. Rev. B 45, 3507 (1992).
- [8] R. Naezel and K. Ploog, J. Vac. Sci. Technol. B 10, 2031 (1992).
- [9] B. Jusserand and M. Cardona in *Light Scattering in Solids V*, eds. G. Guntherodt and M. Cardona (Springer, Heidelberg 1989), p. 19.
- [10] Z.V. Popovic, Univ. Program Publ. Elektrotechn. Fak. Ser. Tek. fiz. 1-5 (1992).
- [11] C. Colvard, T. A. Gant, M. V. Kline, R. Merlin, R. Fisher, H. Morlock and A. C. Gossard, Phys. Rev. B 51, 2040 (1995).
- [12] J. He, B. Djafari-Rouhani and J. Szydlowski, Phys. Rev. B 37, 1006 (1988).
- [13] J. He, B. Djafari-Rouhani, R. Aoudia, and F. Melton, Phys. Rev. B 37, 1099 (1988).
- [14] P. Ertmer, J. Richter, M. Cardona, C. Green, and E. Boustarret, Phys. Rev. B 46, 15139 (1992).
- [15] F. C. and M. Grunwaldt and M. Cardona, Solid State Commun. 29, 523 (1979).
- [16] K. Srinivas, S. V. and M. Cardona, Phys. Rev. B 32, 6611 (1985).

MoC7

Vibrational Properties of SiGe Superlattices: Theory and In-plane Raman Scattering Experiments

R.Schorer¹, G.Abreiter¹, S.de Gironcoli², E.Molinari³, H.Kibbel⁴, and E.Kasper¹

¹Walter Schottky Institut, Techn. Universität München, D-8046 Garching, Germany
²INFN-Institute of Condensed Matter Theory (FORUM), Scuola Normale Superiore, Piazza dei Cavalieri 7, I-56100 Pisa, Italy
³Dipartimento di Fisica, Università di Modena, Via Campi 213/a, I-41100 Modena, Italy
⁴Daimler-Benz AG, Research Center Ulm, Wilhelm-Runge-Str.11, D-7800 Ulm, Germany

Abstract

Phonons in short-period (001)-Si_nGe_n superlattices (SL's) have been studied both theoretically, by a first-principles approach including strain and interface intermixing, and experimentally by micro-Raman spectroscopy where in-plane scattering geometries allow the observation of both longitudinal (L) and transverse (T) modes. Experimental data are found to deviate considerably from theoretical predictions for SL's with ideally sharp interfaces, both in frequency of higher-order confined SL-like modes and in the polarization dependence of the SiGe-like 'interface' peak (lineshape and L-T splitting). Supercell calculations representing interface intermixing within a simple model by 2-3 monolayers of SiGe alloy at the interfaces are found to reproduce these major experimental findings. Measurements of Raman resonance profiles of various SL phonon modes strongly confirm their calculated spatial localization.

The recent improvement of the growth technique of strained layers by introducing the graded buffer concept [1] has significantly raised the interest in short-period Si/Ge superlattices (SL's). Such structures now show a band gap related luminescence which is enhanced by two orders of magnitude as compared to the corresponding alloy [2]. However, for structures with single layer thicknesses only a few monolayers (ML) the interfaces play a crucial role, i.e. interface roughness due to Ge segregation and interdiffusion during growth has to be taken into account both for vibrational and electronic properties. Raman spectroscopy is a useful tool for characterizing short-period SL's, since their vibrational properties depend strongly on the microscopic structure.

The conventional backscattering geometry from the (001) growth surface is limited to the observation of longitudinal phonon modes. However, for establishing a full picture of the vibrational modes of SL's, their symmetry and their coupling to light, it is necessary to perform Raman scattering along each primitive axis of the SL crystal. These studies are enabled by a recently developed microprobe technique, where the probe laser is focused to a sub-μm spot by a microscope objective, thus allowing additional scattering geometries, such as from polished and cleaved sample edges [3-5]. According to the modified selection rules for SL's, polarization of the light parallel to the (001)-growth direction allows the observation of transverse phonon modes [5]. We studied (Si)_n/(Ge)_n SL's with $n = 4, 5, 6, 8, 12$ grown at 310°C on

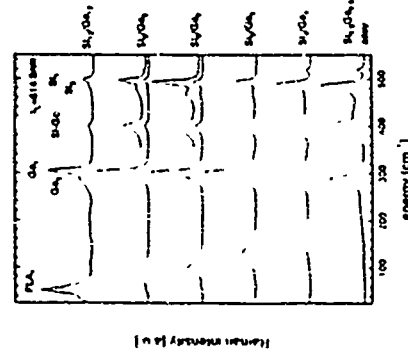


Fig.1 Raman spectra of various (Si)_n/(Ge)_n SL's and the corresponding alloy, normalized to the intensity of the Ge-like phonon mode.

strain-symmetrizing, partially relaxed Si_{1-x}Ge_x alloy buffers on Si (001) substrate [6,7]. The measurements were performed at room temperature.

Additionally a theoretical study on strain-symmetrized (Si)_n/(Ge)_n SL's was performed, taking into account both strain and interface intermixing. The calculations are based on interatomic force constants derived from first principles. Details on the method are given in Refs. 8,9. First we calculate the phonon frequencies for the SL's with ideally sharp interfaces (an example is given for the (Si)₄/(Ge)₄ SL in Fig. 2(c),(d)).

A first feature of the calculated spectra is the existence of optical modes well confined within the Si layers. Their frequencies can be described within a simple 'standing wave' model with an effective wave-vector of

$$q_{eff} = 2m\pi/\lambda_0(n+1/2) \quad (1)$$

where $m = 1, 2, \dots, n$ is the number of Si monolayers, λ_0 is the cubic lattice parameter and γ describes the extent to which the modes penetrate into adjacent layers [10]. The mode frequencies are almost perfectly mapped onto the calculated, strain-shifted bulk dispersion branch, if γ is chosen as follows: $\gamma=1$ for L polarization (n even or odd) and T1 polarization (n even), $\gamma=2$ for T1 and T2 (n odd) and $\gamma=3$ for T2 polarization (n even). The different values of γ are due to the dependence of the mode confinement on the mode symmetry. For L polarization the displacement pattern is similar for any choice of n , leading to $\gamma=1$. For T vibrations we have to consider that the interplanar forces connecting atomic planes are of two different types, one much stronger than the other. The two types are alternating along the growth direction, if n is even, for a given T polarization (T1), both interfaces are strongly coupled, while for T2 the interface bonds are light. Hence there are two interface modes for T1 and no interface modes for T2. Interface planes involved in interface modes do not participate in Si-like vibrations, since the modes must orthogonalize to each other. Thus we obtain $\gamma=1$ for T1 and $\gamma=3$ for T2, which is consistent with the displacement patterns. For n odd, one of the two interfaces in the SL unit cell has a strong bond, while the other one is weak, giving rise to one single interface mode. As a result, in this case $\gamma=2$. Thus for ideal structures, the frequencies of Si-like confined optical modes can be described by a simple unfolding rule. The description of the Ge-like modes in terms of confinement, however, is less accurate due to their coupling to the acoustic Si dispersion branch [10]. Therefore they are only 'quasi-confined'.

Fig.1 shows experimental Raman spectra of the L phonon modes, taken from the growth surface for all samples. The most pronounced feature of the SL spectra are the so-called folded-longitudinal acoustic modes (FLA) below 250 cm⁻¹, which gain in intensity and are shifting linearly to lower frequencies with increasing period. Their appearance is due to folding of the averaged longitudinal acoustic dispersion branch of the bulk materials into the reduced Brillouin zone of the SL. The mode frequencies are well described within an elastic continuum model [11], at least below 150 cm⁻¹, where the bulk dispersions are linear. For the quasi-confined Ge-like modes, the $m=3$ mode is resolved only for the (Si)₁₂/(Ge)₁₂ SL, whilst $m=3$ is

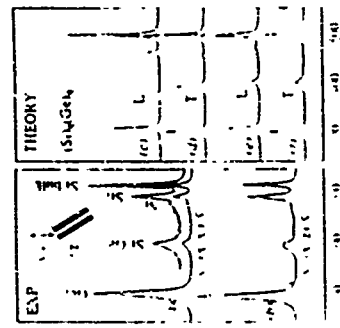


Fig.2 Experimental (a) and theoretical (b) results for L and T Raman spectra of (Si)_n/(Ge)_n SL's. (c) and (d) refer to ideal SL's (no interface intermixing), while (e) and (f) are for a SL with two intermixed Si_{0.5}Ge_{0.5} atomic layers at the interfaces. The vertical dotted lines are at the same frequencies in all panels

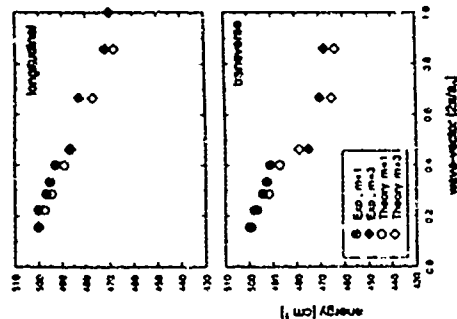


Fig. 3 Experimental (full symbols) and calculated (half symbols) frequencies of L and Si-like modes. (a) Longitudinal modes of strain-symmetrized $(\text{Si}_x\text{Ge}_{1-x})_n/\text{Ge}$ SL's, unfolded onto the corresponding bulk dispersion according to Eq.(1) with $\gamma = 1$. The calculations are for intermixed SL's with 3 monolayers $\text{Si}_x\text{Ge}_{1-x}$ with $x=0.25, 0.50, 0.75$ at the interfaces. Circles and diamonds correspond to $m=1$ and $m=2$ modes, respectively. Calculated γ values are an average over T1 and T2.

major experimental findings for the Si-Ge mode peak in the two polarization profiles. The basic features are independent of the exact interface composition profile. The broader and more symmetric line shape of the T mode is due to the less sharp localization compared to the L mode which can be seen from the calculated local density of states in Fig. 4. These effects are discussed in detail in Ref. 8. From the above discussion we conclude that interface roughness can not be neglected for our SL samples.

Now we come back to the confined Si-like modes. As could be expected, the experimental mode frequencies are found to deviate pronouncedly from the calculations for the ideal SL's both for L and T polarization, especially for modes associated with a large q_{\parallel} . In Fig. 3 we present the results of a calculation where the interfaces were represented by three homogeneous alloy monolayers with $x=0.25, 0.50$ and 0.75 . We note that, similar to the findings for the Si-Ge mode, the basic features are only weakly dependent on the exact profile. For simplicity, all values are plotted for $\gamma=1$, since we do not expect the unfolding rules derived for the ideal structures to be valid any longer for the intermixed SL's. Now the agreement between theoretical and experimental results both for L and T polarization is much closer, with the frequencies being considerably above the bulk dispersion for large q_{\parallel} . These results can be interpreted as follows. The modes whose frequency falls above the alloy bands of the interface alloy layers are confined to the pure Si layer.

resolved for the confined Si-like modes even for the $(\text{Si}_x\text{Ge}_{1-x})_n/\text{Ge}$ SL. Modes with even n are not observed, since they are Raman forbidden, to first order approximation. The appearance of a pronounced peak at 400cm^{-1} is contradictory to the calculation, where no interface mode is present for L polarization (see Fig. 2(c)). Therefore, in earlier work this was assigned to alloy-like vibrations of Si-Ge bonds due to the presence of alloy layers at the interfaces [12-14]. The T-spectra were experimentally obtained from measurements in backscattering geometry from a (110)-edge of the samples, which is shown as an example in Fig. 2(a,b) for the $(\text{Si}_x\text{Ge}_{1-x})_n/\text{Ge}$ SL. Also in the T-spectrum a Si-Ge-like peak is present, but the frequency is shifted downwards and the line shape is considerably changed. This gives clear evidence that the origin of this mode is different from that of the corresponding $\text{Si}_x\text{Ge}_{1-x}$ alloy, where no difference between L and T polarizations is observed. Fig. 2(c,d) presents calculated Raman spectra for a perfect $(\text{Si}_x\text{Ge}_{1-x})_n/\text{Ge}$ SL. No interface mode is present for L polarization, while in T polarization the well known "ideal" interface mode exists. However, its line shape is in sharp contrast with the experiment. Fig. 2(e,f) show the result of the calculation, when interface roughness is modelled by two homogeneous $\text{Si}_x\text{Ge}_{1-x}$ alloy monolayers at each interface. It is evident that even this simple intermixing model reproduces the major experimental findings for the Si-Ge mode peak in the two polarization profiles. The basic features are independent of the exact interface composition profile. The broader and more symmetric line shape of the T mode is due to the less sharp localization compared to the L mode which can be seen from the calculated local density of states in Fig. 4. These effects are discussed in detail in Ref. 8. From the above discussion we conclude that interface roughness can not be neglected for our SL samples.

Now we come back to the confined Si-like modes. As could be expected, the experimental mode frequencies are found to deviate pronouncedly from the calculations for the ideal SL's both for L and T polarization, especially for modes associated with a large q_{\parallel} . In Fig. 3 we present the results of a calculation where the interfaces were represented by three homogeneous alloy monolayers with $x=0.25, 0.50$ and 0.75 . We note that, similar to the findings for the Si-Ge mode, the basic features are only weakly dependent on the exact profile. For simplicity, all values are plotted for $\gamma=1$, since we do not expect the unfolding rules derived for the ideal structures to be valid any longer for the intermixed SL's. Now the agreement between theoretical and experimental results both for L and T polarization is much closer, with the frequencies being considerably above the bulk dispersion for large q_{\parallel} . These results can be interpreted as follows. The modes whose frequency falls above the alloy bands of the interface alloy layers are confined to the pure Si layer.

This is the case for modes with small q_{\parallel} which map close to the bulk dispersion for $\gamma=1$. For modes with large q_{\parallel} their frequency falls within the alloy bands. Thus they extend further into the alloy layers, which explains their deviation from the bulk dispersion. An effective confinement length n_{eff} can be extracted from the local density of states for a given intermixing configuration. This leads to $\gamma=0$ for LO modes, while for higher order modes $\gamma=2$ to 2.5 . Using this value, the SL mode frequencies are mapped closely onto the bulk dispersion. For T polarization, a splitting between T1 and T2 still remains for n even, although it is much smaller than for the ideal SL's. Thus n_{eff} still depends slightly on the SL symmetry. We believe the splitting is very difficult to be observed experimentally, since every monatomic step on the substrate would rotate the SL unit cell by 90° , thus disturbing the orthorhombic symmetry expected for n even. The scattering volume contains many defects of that kind so that the effective symmetry is always tetragonal. Therefore it is reasonable to average T1 and T2 before comparing with experiment.

Finally, we determined the Raman cross section of the observed SL phonon modes as a function of the excitation energy. This was done by normalizing the measured mode intensities to Si as a reference material for which the absolute Raman cross section is known. The Raman scattering cross section in a semiconductor material is enhanced, if the energy of the incoming or outgoing light equals a direct band-gap [15]. In a SL, the different phonon modes will thus display resonant behaviour at energies corresponding to electronic transitions which involve states extending to the same spatial region where they have their maximum vibrational amplitude. Resonance Raman experiments can thus be used to probe the actual localization of phonon modes, to be compared with the calculated local density of states.

We measured all samples in the visible range between 1.65 eV and 3.0 eV, thus covering the range of the E-like resonances of the bulk materials. These Raman resonance measurements will be discussed in detail elsewhere [16]. As an example, the result for the $(\text{Si}_x\text{Ge}_{1-x})_n/\text{Ge}$ SL for L polarized modes is shown in Fig. 4. The most pronounced feature is a strong resonance peak at 2.20 eV for the Ge mode, which may be attributed to transitions between electronic states localized in the Ge layers. For the Si mode no structure is observed below 2.5 eV. This complete decoupling from the Ge mode resonance is strong evidence for the almost perfect confinement of the Si mode to the Si layers. The latter is consistent with the theoretical predictions of Fig. 4, where the calculated vibrational density of states is shown for a $(\text{Si}_x\text{Ge}_{1-x})_n/\text{Ge}$ with two $\text{Si}_x\text{Ge}_{1-x}$ alloy layers at the interfaces. In contrast, for the Si mode a pronounced structure is observed close to the Ge resonance. From the local density of states it is obvious that the Si-like modes for $m>1$ have

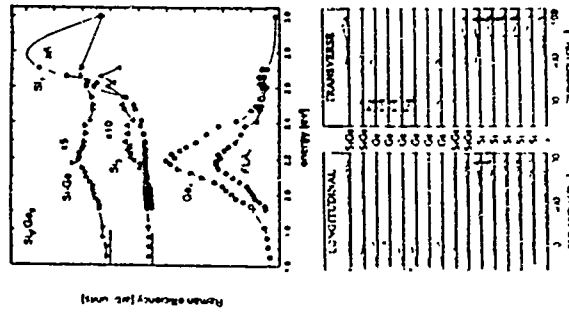


Fig. 4 (top) Measured Raman resonance curves for various phonon modes of a $(\text{Si}_x\text{Ge}_{1-x})_n/\text{Ge}$ SL. (bottom) Local density of states for L and T polarizations on the (001) atomic planes of a $(\text{Si}_x\text{Ge}_{1-x})_n/\text{Ge}$ SL with two intermixed $\text{Si}_x\text{Ge}_{1-x}$ atomic layers at the interfaces (the composition of each plane is indicated)

Phonons and electron-phonon interaction
in GaAs quantum wiresF. Rossi^{a,*}, C. Bucci^a, I. Rota^a, P. Lugli^b and E. Molinari^c

^a Dipartimento di Fisica, Università di Modena, Via Campi 213/a, I-41100 Modena, Italy
^b Fachbereich Physik und Zentrum für Materialwissenschaften, Philipps Universität Marburg, Renthof 5, D-3530 Marburg, Germany
^c International School of Advanced Studies (SISSA), Via Beirut 4, I-34100 Trieste, Italy
 Department of Physics, Clarendon Laboratory, Oxford University, Oxford OX1 3PI, England
 Dipartimento di Ingegneria Elettronica, II Università di Roma, Tor Vergata, Via della Ricerca Scientifica 1, I-00133 Roma, Italy

Abstract

Phonon dispersions and potential problems for thin rectangular GaAs wires embedded in AlAs are calculated by means of a microscopic approach based on an infinite micro-coupled force constants. Besides non-dispersive vibrations, well confined in GaAs, we find phonons with intrinsic character along one or both of the in-plane directions, the latter including modes with maxima at the edges of the wire. While confined phonon potentials are well described within the dielectric continuum (DC) model, interface mode profiles turn out to be more complex. Not only macroscopic models do not give analytic results in this case but also numerical implementations of the DC model reproduce only partially the microscopic results in the thin wire regime.

1 Introduction

Polar optical phonons in semiconductor nanostructures are receiving increasing interest in recent years due to their relevant coupling with carriers. In particular, they play an important role in determining the relaxation time of photoexcited carriers on the picosecond time scale as well as transport properties at high temperature. In order to reach a better understanding of the electron-phonon (e-ph) interaction, a detailed description of both phonon and electron properties in these low-dimensional systems is needed. The important quantity characterizing this interaction is the electrostatic potential associated with the polar optical phonons.

The dynamical properties of two-dimensional (2D) semiconductor systems have been widely studied both from the theoretical and from the experimental point of view. Accurate three-dimensional microscopic calculations have allowed a detailed understanding of the main features of the optical phonon modes involved in the scattering with confined electrons, and of the corresponding electrostatic potential [1].

considerable amplitudes at the border Si layers and even in the SiGe layers. This penetration enables a coupling to states confined to the Ge layers. The same holds for the Si-Ge mode which is mainly localized in the SiGe monolayers and the first Ge monolayer. Thus the coupling to Ge-like states is expected to be even stronger which is confirmed by the experimental resonance curve. The resonance behaviour of the FLA₁ mode is nearly identical to that of the Ge₁ mode, which is due to the completely propagating character of the acoustic modes. Around -65eV a common resonance for all modes is observed, which is likely to be related to alloy-like transitions in the intermixed interface region.

In summary, we have shown that a simple model of interface mixing accounts for the experimentally observed anomalous behaviour of the lineshape and the L-T splitting of the alloy-like interface modes as well as for the deviation between unfolded Si-like SL mode frequencies and the bulk dispersion. Resonant Raman scattering is a helpful tool for probing locally electronic states in SL's and enables, on the other hand, to verify the calculated spatial localization of SL phonon modes.

Acknowledgements

We are grateful to A. Fasolino for a helpful discussion. The calculations were supported in part by CNR under grant 92.01598.P569; the experiments were supported by ESPRIT Basic Research Project No 7128.

References

- [1] F.K. LeGoues, B.S. Meyerson, and F. J. Morar, *Phys. Rev. Lett.* **66**, 2903 (1991)
- [2] U. Menzinger, G. Abstreiter, J. Olajos, H. Gmünn, H. Kibbel, and H. Presting, *Phys. Rev. B* **47**, 4099 (1993)
- [3] R. Heßner, A. Huber, T. Egeler, M. Haines, G. Tränkle, G. Weimann, and G. Abstreiter, *Phys. Rev. B* **46**, 3071 (1992)
- [4] G. Scamarcio, M. Haines, G. Abstreiter, E. Molinari, S. Baron, A. Fischer, and K. Floeg, *Phys. Rev. B* **47**, 1483 (1993)
- [5] R. Schorer, W. Wegscheider, K. Eberl, E. Kasper, H. Kibbel, and G. Abstreiter, *Thin Solid Films* **222**, 269 (1992); R. Schorer, S. de Gironcoli, E. Molinari, H. Kibbel, E. Kasper, and G. Abstreiter, submitted to *Phys. Rev. B*
- [6] K. Eberl, E. Friess, W. Wegscheider, U. Menzinger, and G. Abstreiter, *Thin Solid Films* **183**, 95 (1989)
- [7] E. Kasper in *Physics and Application of Quantum Wells and Superlattices* ed. by E. Mendez and K. von Klitzing, NATO ASI Series B, Physics Vol. 170 (Plenum, New York, 1987), p. 10
- [8] S. de Gironcoli, E. Molinari, R. Schorer, and G. Abstreiter, accepted for publication in *Phys. Rev. B*
- [9] S. de Gironcoli, *Phys. Rev. B* **46**, 2412 (1992)
- [10] A. Fasolino, E. Molinari, and A. Qteish, in *Condensed Systems of Low Dimensionality* ed. by J.L. Breby et al. (Plenum, New York, 1991), p. 495
- [11] S. M. Rylov, *Sov. Phys. Acoust.* **2**, 68 (1956)
- [12] H. Brügger, E. Friess, G. Abstreiter, E. Kasper, and H. Kibbel, *Semicond. Sci. Technol.* **3**, 1166 (1988)
- [13] M.J. Alonso, F. Cerdeira, D. Nies, M. Cardona, E. Kasper, and H. Kibbel, *J. Appl. Phys.* **66**, 5645 (1989)
- [14] A. Fasolino and E. Molinari, *Journal de Physique C5*, 569 (1987); *Appl. Phys. Lett.* **54**, 1220 (1989)
- [15] M. Cardona, *Resonance phenomena in Light Scattering in Solids II*, ed. by M. Cardona and G. Güntherodt (Springer, Berlin, 1982)
- [16] R. Schorer et al., to be published

In particular the results of these microscopic studies also supported by experimental evidence,^{2,3} have clarified that a good approximation to the electrostatic phonon potentials in 2D structures can be obtained by one of the simplified macroscopic models previously proposed: the dielectric continuum model in its original [3] or improved Huang-Zhu [4] versions.

An increasing interest is currently devoted to one dimensional (1D) structures, a clear picture of the dynamical properties is therefore required also for these systems. The only available microscopic studies [5,6] focus on the frequency dispersions, and a systematic description of spatial mode profiles is still needed. Along the same line followed for 2D systems [1] we have performed a microscopic calculation based on ab initio interaction force constants of phonon dispersions and displacement patterns for thin rectangular GaAs wires embedded in AlAs. In this scheme the electrostatic potentials for the calculation of electron-phonon interaction are also obtained. In previous reports we have presented results for confined phonons, here we discuss in greater detail microscopic potentials for non confined modes, and compare them with phonon potentials derived by simplified macroscopic models which may be of practical use in simulations.

2. Microscopic analysis

Phonon frequencies and displacements are obtained by direct diagonalization of the dynamical matrix of the three dimensional crystal, which is in turn constructed from ab initio interaction force constants [9]. The electrostatic phonon potential associated to each optical mode at a given wave vector $q = (0, 0, q)$ is then calculated from the microscopic displacements [7]. The results presented in this paper are obtained for a quantum array of infinite (001) oriented GaAs quantum wires (QWR) of rectangular section embedded in AlAs. The dimensions of the GaAs QWR are 1 and 3 monolayers along x and y respectively ($\sim 5.5 \times 11 \text{ \AA}$) and the width of the AlAs barriers is of 11 monolayers in both directions. The dispersion of the topmost optical GaAs like modes for small wave vectors parallel to the wire direction is displayed in Fig. 1(a). Their angular dispersion at $q \rightarrow 0$ is displayed in Figs. 1(b) and 1(c). Here θ and α are the angles between the phonon wave vector and the x and y directions in the qz and xz planes respectively. As in 2D systems some of the modes have a non negligible angular dispersion, this is due to the long range Coulomb interaction which is anisotropic at

large angles with the 2D case one might expect that the angular dispersion of modes will be a fingerprint of their interface (IF) character, and that angle independent modes will be confined in the wire. The classification of the actual calculated modes is however more complex. We can distinguish (a) modes which are not dispersive with θ and α with α (a) modes which are dispersive either with θ or with α (a) modes which are dispersive both with θ and α .

As already shown in a partial account of the present calculations (cf. a good an detailed study of the non dispersive modes, class (a)), has been reached, they are usually well confined in the wire, and their potential profiles are several Å functions of x and y . For example the profile of Fig. 2(a) may be obtained as a product of two confined profiles along x and y both even with respect to the mirror planes through the center of the wire, the profile of Fig. 2(b) from two confined profiles of odd parity (cf.

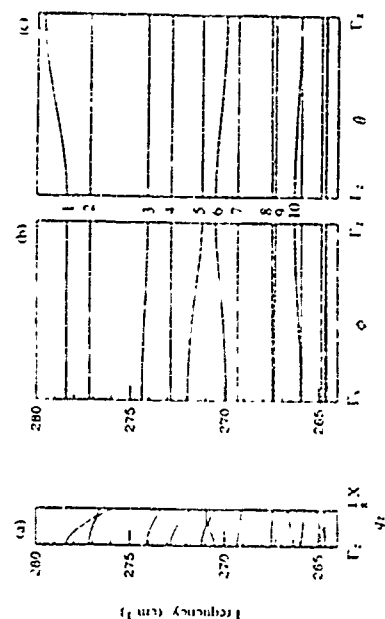


Fig. 1 Dispersion of the topmost GaAs like optical modes for the rectangular quantum wire array as obtained from the microscopic calculation. (a) Dispersion along the wire direction for $q = (0, 0, 125\pi/a)$. (b) and (c) Dispersion along the xz and yz center planes in the qz and xz planes respectively.

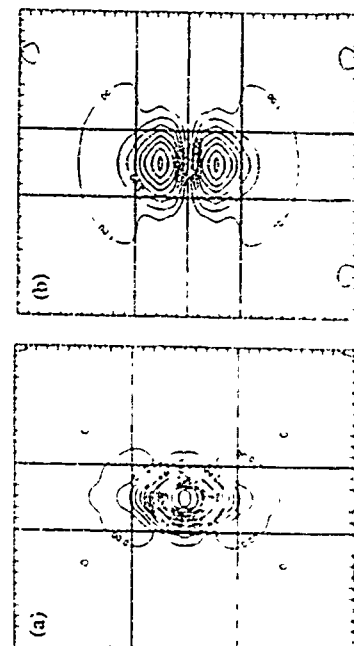


Fig. 2 Contour plot of the phonon potential (arbitrary units) in the xy plane for two non dispersive modes (modes 2 and 1 of Fig. 1) confined in the GaAs QWR. Here $q = (0, 0, 0.0125\pi/a)$. The straight lines indicate the interface planes.

The potentials of two modes belonging to class (a) are shown in Figs. 1(a) and 1(b). The ψ clearly have an H_z character along one of the in-plane directions and a confined shape in the other direction. Indeed, the potential in Fig. 1(a) is extended both in ψ and ψ directions, with a maximum on the interface perpendicular to this direction; along ψ the potential is instead confined in the ψ direction. Potentials of this type can still be written in separable form ($\psi = \psi(x)\psi(y)$).

Modes which are dispersive both with θ and ψ are not confined in both directions and have a well-defined interface character, which produces maxima at the edges of the wires (see for example Fig. 1). Contrary to the previous classes, clearly these mode profiles cannot be written as separable functions of x and y ($\psi = \psi(x)\psi(y)$).

The above classification describes the main features of the calculated spectra, but not all the modes can be associated with one of these classes. In particular, we have found some modes with very small or no angular dispersion (for example modes 1 and 5 of Fig. 1), whose potential is however extended both in ψ and ψ directions with some H_z character. We tentatively interpret this anomaly as due to coupling between states of different nature, although a more extensive study for different wire thicknesses would be needed for a conclusive assignment.

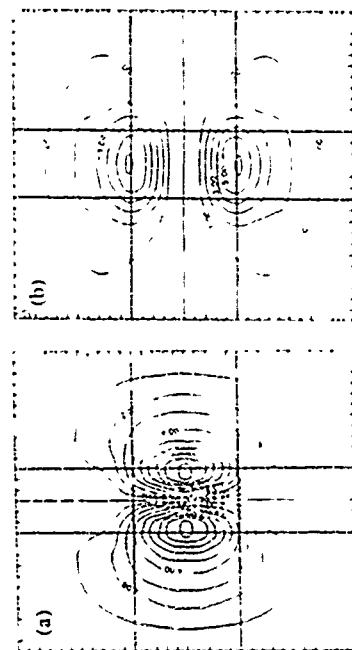


Fig. 3. Contour plot of the phonon potential (arbitrary units) in the xy plane for two QWR modes of class (a) (mode 1 and 5 of Fig. 1) whose angular dispersion is significant only vs. θ or ψ , respectively. Notations as in Fig. 2.

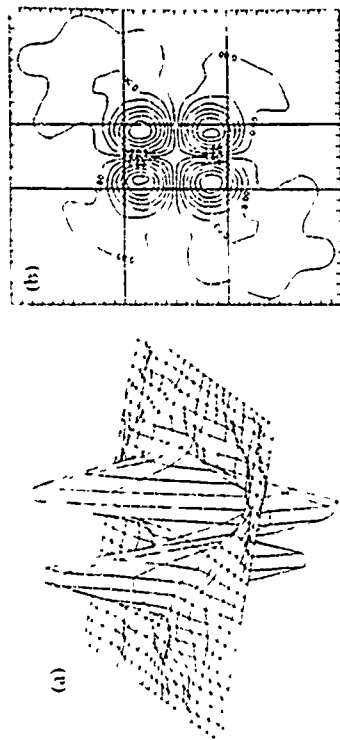


Fig. 4. (a) Three-dimensional and (b) two-dimensional contour plot of the phonon potential (arbitrary units) in the xy plane for a QWR mode of class (a) (mode 10 of Fig. 1) whose angular dispersion is significant both vs. θ and ψ . Notations as in Fig. 2.

3. Comparison with simplified macroscopic models

Macroscopic descriptions such as the one of the previous section are certainly rigorous but are not of very practical and flexible use. Given its successful description of the ψ interaction in 2D systems, it is therefore interesting to explore the possibility of extending the use of the macroscopic dielectric continuum model to the wire geometry.

In view of our microscopic results there are two major aspects of simplified macroscopic models to be discussed. The first is related to the fact that, within the DC model, interface and confined modes belong to two distinct sets of solutions of Laplace equations, i.e. a given mode can have either confined or non-confined character [7]. Therefore, modes belonging to class (a) of Sect. 2 seem to have no counterpart in the DC scheme. This intrinsic limitation of the DC model has never been discussed explicitly, although our calculated potentials show that the contribution of these modes to ψ rates should not be negligible unless for very large wires.

The second aspect concerns the accuracy of the separable approximation, which has been used extensively in conjunction with the DC model because of its simplicity [10]. There is no *a priori* justification for such approximation, except for very special wire geometries [11]. In wires of rectangular section, it turns out to be quite acceptable for confined modes [8], as apparent from the above discussion of modes of class (a). However, our results demonstrate that such assumption is not justified for modes of class (a). For phonons with purely interface character, Knapp and Remeke [12, 13] have shown that the problem can be overcome in wires of arbitrary geometries by means of a fully numerical treatment. From their calculated screening rates [8], it is

Tuesday, August 24

TuA	Quantum Wells - Electrical Properties
TuB	Vertical Transport - Resonant Tunneling
TuC	Quantum Wells, Superlattices - Optical Properties
TuP	Transport, Optics

Handwritten signature and date: 8/24/94

TIA1

STRAINED SI/SiGe HETEROSTRUCTURES FOR DEVICE APPLICATIONS

T. Schäffler

Daimler-Benz AG, Research Center Ulm, P. O. Box 2360, D-89013 Ulm, Germany

Abstract

A review is given of the most recent development in the field of modulation doped Si/SiGe heterostructures. Main topics are the successful implementation of high-quality, strain-relaxed SiGe buffers, the realization of n-type and p-type quantum well structures with unprecedentedly high electron mobilities, magnetotransport investigations of such structures, and their exploitation for devices with very high transconductance values.

Proper exploitation of the strain-dependent band alignment in the lattice mismatched Si/SiGe heterosystem allows the realization of enhanced electron and hole mobilities by means of modulation (or remote) doping of offset. Since a finite conduction band offset is only achieved, if the Si channel is put under a tensile in-plane strain^{1,2}, a partly or completely strain-relaxed SiGe buffer layer is required as a virtual substrate for n-type structures³. p-type quantum wells (QW), on the other hand, can be implemented using pseudomorphic SiGe channels, however, the low hole mobilities resulting from alloy scattering in such layers suggest the use of pure Ge QWs, which again require a relaxed SiGe buffer layer to maintain the mandatory compatibility with Si substrates.

Initially, Si_{1-x}Ge_x buffer layers with constant x were grown to a thickness somewhat above the critical thickness for strain relaxation by the formation of misfit dislocations. These were sufficient to demonstrate the strain-induced Type II band ordering and the electron-mobility enhancement by modulation doping in a subsequently deposited Si/SiGe heterostructure with a Si quantum well (QW).³ Also, the first n-type modulation-doped field effect transistors (MOSET) in this material system were

based on this buffer type.⁶ Despite gradual improvements⁷, however, the low temperature mobilities remained behind expectations. One of the main reasons was seen in the strain-adjusting SiGe buffer layers then used, which were known to contain a high density ($> 10^9$ cm⁻²) of unwanted threading dislocations that end at the surface, thus penetrating through the active layers. A major breakthrough with threading dislocation densities reduced by several orders of magnitude was achieved by introducing a linearly or step-wise increasing Ge content concomitant with relatively high growth

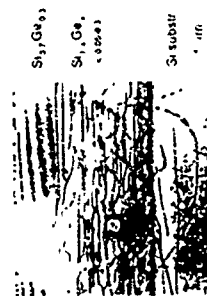


Figure 1: TEM cross sectional view of a Si_{1-x}Ge_x buffer layer with linear grading of the Ge content from 5% to 30%. Note the distribution of the misfit dislocation network over the thickness of the grading and the virtual dislocation free upper part of the buffer grown at a constant x.

temperatures.^{8,9,10} Because of the gradual increase of the lattice mismatch in such a buffer, the misfit dislocation network is distributed over the range of compositional grading rather than being concentrated at the interface to the Si substrate, which would be the case if a constant Ge content is used throughout (Fig. 1). The reduced interactions between intersecting misfit dislocations promotes, in connection with close-to-equilibrium growth temperatures, long misfit dislocation segments, and thus low threading dislocation densities.

The greatly improved buffer quality soon led to low-temperature electron-mobilities in excess of 100000 cm²/Vs¹¹, with the best value reported to date being 173000 cm²/Vs at 1.5 K (Fig. 2).¹⁰ This is the highest known mobility of a two dimensional electron gas (2DEG) in Si, which is almost a

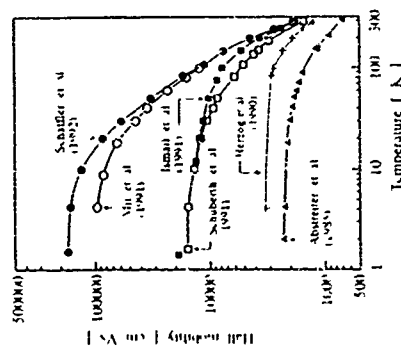


Figure 2: Development of the electron Hall mobility in modulation doped Si/SiGe heterostructures in recent years. The upper two curves were measured on samples with nearly graded SiGe buffer. Data from References 10, 13, 11, 7, 12, 3 (from top to bottom).

factor of five higher than the best values found in Si MOSFETs.¹⁴ Moreover, room temperature Hall-mobilities close to 2000 cm²/Vs were found in the MODFET samples, which not only exceeds the values of commercial MOSFETs by a factor of two, but also is higher than the bulk mobility in intrinsic Si. This is due to the fact that the strain dependent band-ordering in the (001)-oriented Si/SiGe heterosystems allows only a population of the two-fold degenerate electron valleys corresponding to the conduction band ellipsoids in the direction perpendicular to the (100) heterointerface. Thus 2D transport within the channel plane is associated with the transversal effective mass $m_t = 0.19m_0$, whereas the quantization (or subband) energies are determined by the much larger longitudinal effective mass parameter $m_l = 0.92m_0$. In terms of carrier mobility this is the optimum combination of mass parameters, which not only provides the lowest possible transport mass, but also the minimum penetration depth of the electron wavefunction into the heterointerface due to the large quantization mass. In contrast, the inferior mobility behavior of the MOSFET is mainly due to the inverse assignment of effective masses resulting from the fact that mainly the four-fold degenerate electron valleys are occupied at room temperature.

The success of n-MODQW structures grown on graded SiGe buffers with an effective composition of up to x=30% suggested an extension to higher Ge contents (up to 100%), to allow p-type QW structures with channels consisting of pure Ge. However, with increasing x_{eff} (and thus lattice mismatch), growth becomes more demanding. It requires a careful selection of growth parameters to maintain a low threading dislocation density without running into a three-dimensional growth mode which would spoil the surface morphology. A combination of Ge grading and down-ramping of the growth temperature at higher

Figure 3 Cyclotron resonance absorption of the sample in Figure 2 with the highest mobility. Note the sharpness of the absorption line corresponding to the high electron mobility.

Figure 5 Output characteristics of Ge channel (p type) MODFETs with and without gate recessing at room temperature and at 77K (from Ref 15)

The implementation of superior α - and p-MOFETs is a prerequisite for complementary transistors (CMOFETs) with

substrates were fabricated successfully. Although their performance has not entirely reached the level of their n type counterparts as yet, transconductances of 125 and 290 mS/mm at 300K and 77K, respectively, are very promising for future developments.

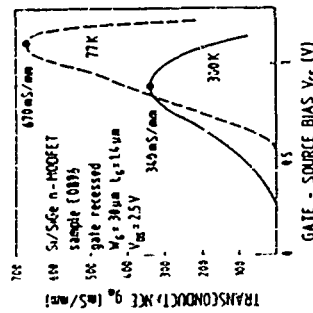


Figure 4 Output characteristics at room temperature and at 77K of a gate recessed n type (Si channel) MODFET device utilizing a high mobility Si/Si-Ge heterostructure grown on Si substrates (from Refs. 20)



Figure 6 First test vehicle of a CMOSFET with stacked p- and n-FETs. The common Drain metalization is on the left the separate Source contacts at the right. The common Y-shaped gate connects the p-FET in the 'foreground' with the stacked n-FET in the background

matched characteristics, which can not be realized in any of the established material systems because of the far inferior properties of the respective p-type devices. With almost identical mobilities of electrons in Si and holes in Ge, the Si/SiGe/Ge heterostructure could for the first time supply such matched transistor pairs, and moreover, remain widely compatible with Si very large scale integration (VLSI) technologies. Initial steps to implement such CMOSDETs are already under way. This is demonstrated in Fig. 6, which shows a simplified double-niassa CMOSDET with a layer sequence consisting of a n-MODEFET structure grown on top of a p-MODEFET without growth interruption. This development, which will certainly require more refined integration concepts and process steps, could once open the field of high-speed applications for the ubiquitous complementary logic, which is in its contemporary CMOSFET implementation the single-most important technology in microelectronics.

The contributions and helpful comments of D Többen, C M Engelhardt, M Sisson, G Absreiter, F Gornik, U König, H J Herron, and E Kasper are gratefully

CAPTURE AND EMISSION OF ELECTRONS IN QUANTUM WELLS UNDER APPLIED ELECTRIC FIELD

B. VINTER, F. LUC, P. BOIS, A. THIRAUDAU, and E. ROSENCHER
Laboratoire Central de Recherches
THOMSON - CSF
Domane de Corbeville
91404 - ORSAY (France)

Important characteristics of Quantum Well Infrared Photodetectors are determined almost entirely by the photoionization rate of electrons out of the Quantum Well (QW) and the recapture into the QWs. To elucidate these processes microscopically we have made structures in which the QWs are isolated from one contact by a completely blocking barrier, so that the steady state current vanishes. The transient current induced by photoionization out of the QWs gives a direct measurement of the photoionization cross section and the escape probability of a photoexcited electron. We have found that the variation of the latter with the electric field may be described by a simple barrier lowering model combined with statistical fluctuation of the QW width.

The capture process has been studied by impedance spectroscopy in samples containing only one well. The capture velocity thus measured is found to decrease with increasing applied electric field but within experimental uncertainties it does not depend on the width of the well for well widths between 3 nm and 7.5 nm. Theoretical results on optical phonon mediated transitions in the applied field from barrier to well states show a generally good agreement with experiment at low fields but less dependence on the field.

INTRODUCTION

The performances of Quantum Well Infrared Photodetectors (QWIPs) are determined by the rate at which electrons are ionized out of the Quantum Well (QW) either by photoionization or by thermal emission; and by the rate at which the excited electrons are recaptured into the QWs. The photoionization determines the response and background limited noise; the thermal emission determines the thermal or dark-current noise, and the capture probability determines the responsivity through the photoconductive gain [2,3]. In order to understand the microscopic physics of these mechanisms we have performed experiments on specially designed samples which give access to each mechanism in situations very close to that of the QWIP, i.e. unipolar conduction near a stationary state under an applied bias field.

PHOTOIONIZATION CROSS-SECTION

In order to measure the rate at which electrons will be ionized out of the QW without the complication due to photoconductive gain and dark current, we have made measurements of the transient photocurrent from a multi-quantum well structure in a Schottky diode. This technique is very similar to the Deep Level Optical Spectroscopy method developed to study the optical cross section of deep levels in semiconductors.

The sample (see Fig. 1), grown by molecular beam epitaxy, consists in ten periods of a 6 nm GaAs $5 \times 10^{11} \text{ cm}^{-2}$ δ -doped quantum well sandwiched between 35 nm Ga_{0.35}Al_{0.65}As barriers on the top of a 500 nm 10^{18} cm^{-3} Si-doped GaAs contact layer. The sample has been designed so that there are two bound levels in the well: E_1 and E_2 with $E_2 - E_1 = 138 \text{ meV}$ and that the second energy level E_2 is a few meV below the Ga_{0.35}Al_{0.65}As barrier E_B ($E_B - E_2 = 8 \text{ meV}$). The depth of the potential well as well as the barrier thickness have been chosen sufficiently high to suppress tunnel emission [4] as well as thermal emission for temperatures up to 60 K. Mesa structures $200 \mu\text{m} \times 100 \mu\text{m}$ were processed using standard lithography techniques. An evaporated AuGeNi layer provides an ohmic contact at the bottom of the structure while Cr was evaporated to provide a semi-transparent Schottky diode on the top. The Schottky diode ensures that

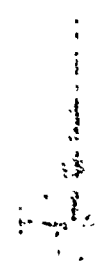
- 10 F. Schaffler, O. Tobben, K.-J. Herzog, G. Abstreiter, and B. H. Zander, *Semicond Sci Technol* 7, 260 (1992)
- 11 K. Ismail, B. S. Meyerson, and P. J. Wang, *Appl. Phys. Lett.* 58, 2117 (1991)
- 12 H.-J. Herzog, H. Jork, and F. Schaffler, *Thin Solid Films* 184, 237 (1990)
- 13 Y. J. Mi, Y. H. Xia, E. A. Fitzgerald, D. Monroe, F. A. Thal, B. E. Weir, and L. C. Feldman, *Appl. Phys. Lett.* 59, 1611 (1991)
- 14 I. V. Kukushkin and V. B. Timofeev, *Sov. Phys. JETP* 67, 594 (1991)
- 15 U. König and F. Schaffler, *IEEE Electron Device Lett.* 14, 205 (1993)
- 16 D. Monroe, Y.-H. Xia, E. A. Fitzgerald, P. J. Salverman, and G. Watson, *J. Vac. Sci. Technol.* (to be published 1993)
- 17 M. Basson, C. M. Engelhardt, F. Schaffler, and E. Gornik, to be published
- 18 see also the contribution of C. M. Engelhardt et al. at this conference
- 19 D. Tobben, F. Schaffler, A. Ziemer, and G. Abstreiter, *Phys. Rev. B* 45 (1992), to be published
- 20 U. König, A. J. Boers, F. Schaffler, and E. Kasper, *Electronic Lett.* 28, 160 (1992)
- 21 K. Ismail, B. S. Meyerson, S. Rahim, J. Chiu, S. Nelson, and J. Nocera, *IEEE Electron Device Lett.* 13, 229 (1992)
- 1 R. People, J. C. Bean, D. V. Lang, A. M. Sergent, H. L. Störmer, K. W. Wecht, R. T. Lynch, and K. Balmain, *Appl. Phys. Lett.* 45, 1231 (1984)
- 2 H. Jork and H.-J. Herzog, *J. Electrochem Soc.* 133, 998 (1986)
- 3 G. Abstreiter, H. Brugger, T. Wolf, H. Jork, and H.-J. Herzog, *Phys. Rev. Lett.* 64, 2441 (1985)
- 4 C. G. Van der Walle and R. M. Martin, *Phys. Rev. B* 34, 5671 (1986)
- 5 E. Kasper, *Surf. Sci.* 174, 630 (1986)
- 6 H. Dambkes, H.-J. Herzog, H. Jork, H. Kibbel, and E. Kasper, *IEDM Technical Digest*, IEEE New York 1985, p. 768
- 7 G. Schubert, F. Schaffler, M. Basson, G. Abstreiter, and E. Gornik, *Appl. Phys. Lett.* 59, 3318 (1991)
- 8 E. A. Fitzgerald, Y. H. Xia, M. L. Green, D. Braten, A. R. Kortan, J. Michel, Y. J. Mi, and B. E. Weir, *Appl. Phys. Lett.* 59, 811 (1991)
- 9 F. K. LeGoues, B. S. Meyerson, and J. F. Morar, *Phys. Rev. Lett.* 68, 2903 (1991)

acknowledged. This work was financially supported by the Bundesministerium für Forschung und Technologie (Bonn, Germany)

$$(i) \quad \frac{R}{N} \cdot \frac{1}{N} \cdot \frac{1}{N} \cdot \Phi(i) = \sigma_p(i)$$

$$(i) \quad \frac{R}{N} \cdot \frac{1}{N} \cdot \frac{1}{N} \cdot \Phi(i) = \sigma_p(i)$$
$$(i) \quad \frac{R}{N} \cdot \frac{1}{N} \cdot \frac{1}{N} \cdot \Phi(i) = \sigma_p(i)$$

$$R_{N_i} = \sigma_i \Phi(i, N_i, N_i) \quad (11)$$

$$(i) \quad \frac{R}{N} \cdot \frac{1}{N} \cdot \frac{1}{N} \cdot \Phi(i) = \sigma_p(i)$$
$$(i) \quad \frac{R}{N} \cdot \frac{1}{N} \cdot \frac{1}{N} \cdot \Phi(i) = \sigma_p(i)$$
$$(i) \quad \frac{R}{N} \cdot \frac{1}{N} \cdot \frac{1}{N} \cdot \Phi(i) = \sigma_p(i)$$
$$(i) \quad \frac{R}{N} \cdot \frac{1}{N} \cdot \frac{1}{N} \cdot \Phi(i) = \sigma_p(i)$$
$$(i) \quad \frac{R}{N} \cdot \frac{1}{N} \cdot \frac{1}{N} \cdot \Phi(i) = \sigma_p(i)$$


the experimental results. We therefore believe that the smooth variation of P_0 has a statistical origin i.e. the energy E_2 fluctuates in each QW with a Gaussian distribution, so that the P_0 vs E curve is the convolution of the Heaviside function with this Gaussian distribution. The best fit of the experimental result [1], taking into account this distribution, is obtained by a deviation of $\Delta E = 3.2$ meV around a mean value 4 meV below the barrier. The former value can be reasonably accounted for by a *one monolayer fluctuation* in the QWs on both sides.

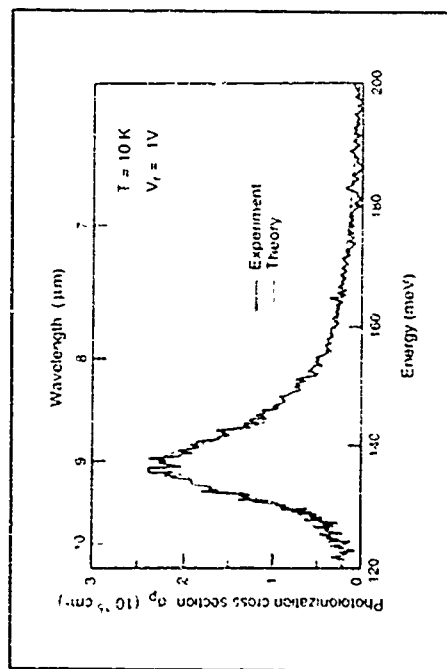


Fig. 2. Photoionization cross section σ_p of the QWs as a function of photon energy. The experimental curve (full line) is fitted by the simple quantum mechanical model for intersubband absorption with a linewidth of 5 meV (dotted line).

CAPTURE INTO A QUANTUM WELL

The second set of experiments determine the capture of electrons from the continuum in the barrier layers into a QW. The method used is that of impedance spectroscopy on a sample containing only one QW in a semiconductor-insulator-semiconductor structure.

The samples (see Fig. 3) consist of a sandwich of a 94 nm $\text{Al}_{0.4}\text{Ga}_{0.6}\text{As}$, 50 nm $\text{Al}_{0.2}\text{Ga}_{0.8}\text{As}$, a GaAs (undoped) QW of width L_w , 50 nm $\text{Al}_{0.2}\text{Ga}_{0.8}\text{As}$ structure. It is clad between two 500 nm 10^{18} cm^{-3} Si-doped GaAs contacts. The well parameters (length, barrier height) have been chosen so that for $L_w = 6$ nm the first energy level E_1 is bound (59 meV above the GaAs conduction band) and the second level E_2 is quasi resonant with the $\text{Al}_{0.2}\text{Ga}_{0.8}\text{As}$ conduction band ($E_2 - E_1 = 117$ meV). Moreover, on the one hand, the Al concentration of the $\text{Al}_{0.4}\text{Ga}_{0.6}\text{As}$ layer has been chosen sufficiently large so that this barrier is totally insulating at temperatures below 120 K, which has been experimentally verified. On the other hand, the Al concentration of the $\text{Al}_{0.2}\text{Ga}_{0.8}\text{As}$ intermediate barrier is low enough so that in the temperature range of our experiments (80 - 120 K), the QW is not far from the thermodynamical equilibrium with the electron reservoir of the lower contact. Consequently, the Fermi level in the well is set by the lower contact. This condition is the basis of the equivalent circuit analysis of interface traps in MOS structures so that we can extend this analysis to our SIS system [12]. Mesa structures

($265 \mu\text{m} \times 265 \mu\text{m}$) were fabricated using standard photolithography techniques and AuGeNi alloy contacts. The sample capacitance is independent of the applied bias in the ± 1 -V range at the temperature of 10 K and the value of 33 pF is in perfect agreement with the nominal total thickness of 200 nm. Admittance measurements are performed, using a lock-in technique, as a function of the frequency for different temperatures between 85 K and 115 K and for different applied biases.

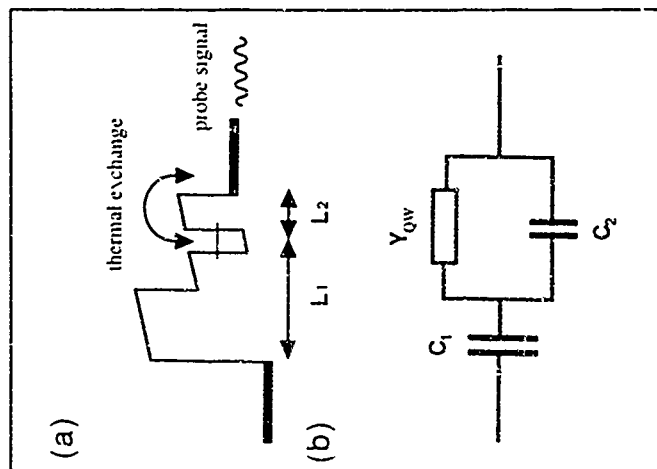


Fig. 3. (a) Schematic energy band diagram of the investigated samples for impedance spectroscopy and (b) equivalent electrical circuit.

From a *direct analogy* with MOS devices, the electrical equivalent circuit of the structure for a sinusoidal signal can be immediately deduced (see Fig. 4) by introducing the 'quantum well admittance' Y_{QW} [12]:

$$Y_{QW} = \frac{\partial I_{QW}}{\partial V} = G_{QW} + j\omega C_{QW} \quad (2)$$

where V_{QW} is the potential drop between the well and the lower contact, ω is the signal radial frequency and I_{QW} is the current flowing into the well $I_{QW} = -qA \partial N_{QW} / \partial t$, q is the elementary charge, N_{QW} is the electron density in the well and A is the sample area. The value of G_{QW} is deduced from the measured sample admittance and the known values of the geometrical capacitances C_1 and C_2 . In our case the values of C_1 and C_2 are respectively 44 pF and 132 pF. Considering the whole well as a single 2D trap, one can write the emission-recombination equation as:

$$A \frac{\partial N_{QW}}{\partial t} = c_n n \cdot e^{-AN_{QW}} \quad (3)$$

where n is the 3D distribution of carriers above the well c_n (s^{-1}) is the thermal emission rate from the QW while c_n (cm^3/s) is the classical capture coefficient in the QW. A classical treatment for small sinusoidal perturbations leads then to the expression of the equivalent impedance for such a mechanism [12]:

$$\frac{G_{QW}(\omega)}{\omega} = C_T \frac{\omega \tau}{1 + \omega^2 \tau^2} \quad (4)$$

with

$$C_T = \frac{q^2 A m^*}{\pi \hbar^2} \exp \left(\frac{E_f + q V_{QW} - E_1}{kT} \right) \quad (5)$$

where $\tau = AN_{QW}/c_n n_{eq}$, N_{eq} (resp. n_{eq}) is the 2D carrier density in the well (resp. 3D density above the well) in steady state. Since the well is undoped, N_{eq} is given by $N_{eq} = (m^*/\pi \hbar^2) kT \exp((E_f + qV_{QW} - E_1)/kT)$ where m^* is the effective mass of the electron in GaAs.

The experimental curves $G_{QW}(\omega)/\omega$ vs ω can be well fitted by one time-constant τ in Eq. (4). This is the signature of an emission-recombination process occurring between a single trap and the $Al_{0.22}Ga_{0.78}As$ conduction band. In our case of a 2D trap, the capture coefficient c_n is proportional to the sample area so that the significant capture parameter τ is the recombination velocity v_{QW} defined as $v_{QW} = c_n/A$ [14]. This quantum well recombination velocity is related to the time constant τ through the relation $v_{QW} = N_{eq}/\tau n_{eq}$. If we make the assumption that the 3D equilibrium density of states is not affected by the presence of the quantum well, so that n_{eq} is given by the classical expression [5] $n_{eq} = N_c(T) \exp((E_f + qV_{QW} - E_2)/kT)$ we find

$$\tau = \frac{1}{v_{QW}} \left[\frac{2\pi \hbar^2}{m^* kT} \right]^{1/2} \exp \left(\frac{E_2 - E_1}{kT} \right) \quad (6)$$

In Fig. 4a the corresponding Arrhenius plot is shown for a 1.6 nm wide quantum well. For the activation energy $E_2 - E_1$, a value of 113 meV is found independent of the field. This supports our assumption that the observed emission-recombination process occurs between the bound state of the well and the $Al_{0.22}Ga_{0.78}As$ conduction band. We also find $v_{QW} = 8 \times 10^4$ cm/s for an

electric field of 3 kV/cm. Moreover, in Fig. 4b we show that the experiments indicate a strong decrease of the recombination velocity for an increasing applied electric field. This can be seen to be the case for the samples of different well width, too. In contrast to what has been reported from time-dependent photoluminescence measurements [15], we find no clear dependence of the capture velocity on well width.

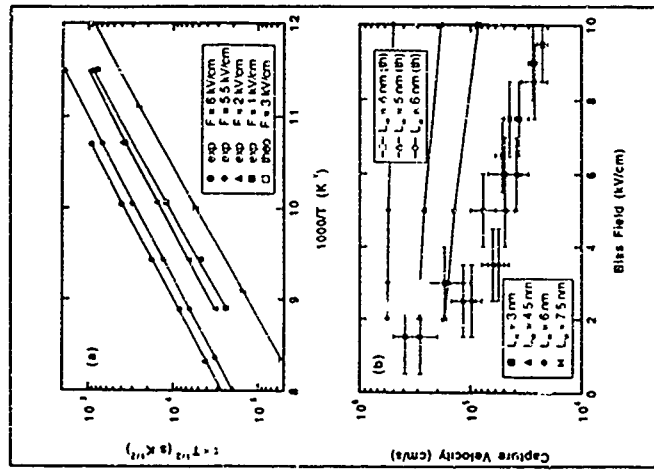


Fig. 3 (a) Arrhenius plot of $\ln(c_n/\tau)$ vs $(E_2 - E_1)/kT$ (it is the recombination time constant deduced from the frequency dependence of the admittance for a 6 nm QW). The corresponding theoretical results are also shown for one field. The intersection of the extrapolation lines with the abscissa yields the recombination velocity in the QW. This velocity is shown in (b) as a function of the applied electric field and for several different QWs. Low bias indicate the experimental uncertainties.

The capture coefficient may be connected to the capture probability p only if a velocity v is introduced, $\tau = 1/pv$. If we take a usual drift velocity of a QWIP $v = 1 - 5 \times 10^6$ cm/s [2] with a minimum value of $v_{QW} = 3 \times 10^4$ cm/s, we find a capture probability $p = v_{QW}/v = 0.03 - 0.006$. This is in good agreement with the values obtained by photoconductive gain in QW infrared detectors [10].

THEORY OF THE QW IMPEDANCE

We have performed calculations of the net capture rate into a QW in a constant electric bias field. The hypotheses of the calculation are that the polar optical phonon scattering processes from levels of the continuum to the fundamental bound state subband of the QW control the capture time, the continuum states are assumed to be in thermal equilibrium with the Fermi energy of the contact, and the electrons in the QW are in thermal equilibrium in the ground state QW subband. In the electric field the wavefunctions can be written as linear combinations of Airy functions in the barriers and in the QW. Using Fermi's golden rule to calculate the scattering rates $S(\epsilon_r, K \rightarrow \epsilon_0, K_0)$ between states of the continuum (denoted ϵ_r, K) and states in the QW (denoted ϵ_0, K_0) we have:

$$\frac{\partial N_{QW}}{\partial t} = \sum_{\epsilon_r, K} S_{em}(\epsilon_r, K \rightarrow \epsilon_0, K_0) f(\epsilon_r, K) (1 - f(\epsilon_0, K_0)) - \sum_{\epsilon_r, K} S_{abs}(\epsilon_0, K_0 \rightarrow \epsilon_r, K) f(\epsilon_0, K_0) (1 - f(\epsilon_r, K)) \quad (7)$$

which by using detailed balance between phonon emission processes in one direction and absorption processes in the opposite direction can be reduced to $\partial N_{QW} / \partial t = - (N_{QW} - N_{eq}) / \tau$, where N_{eq} is the number of electrons in the quantum well when no at voltage is applied, and

$$\frac{1}{\tau} = \frac{\pi \hbar^2}{m^* k T} \sum_{\epsilon_r, K} S_{em}(\epsilon_r, K \rightarrow \epsilon_0, K_0) \exp\left(\frac{\epsilon_0 - (\epsilon_r + \hbar^2 K^2 / 2 m^*)}{k T}\right) \quad (8)$$

Results of this calculation are also shown for a 6 nm wide QW in Fig. 4a. It can be seen that time constants in the 100 ps to 10 ns range are indeed reproduced by the theory and that the activation energy is the same as experimentally observed. However, the dependence on bias field is much smaller than observed. This can be seen in the theoretical recombination velocity (derived by making the same fitting procedure as for the experiment) which is also plotted in Fig. 4b for different QW widths. In addition, one can also see a stronger QW width dependence. It remains an interesting question which transport processes create competing time constants in the experiment in order to explain these less important discrepancies.

CONCLUSION

The picture of the QWIP which emerges from several independent experiments is very close to that of an extrinsic photoconductor in which the quantum wells simply act as point traps from which electrons are ionized and retrapped. We have measured the important parameters of these processes in specifically designed experiments and have found that they can be consistently explained by microscopic theory, and that they explain very satisfactorily the reproducibility and detection performance of QWIPs.

REFERENCES

1. For recent developments, see e.g. E. Rosencher, B. Vinter, and B. Levine, Eds., *Intersubband Transitions in Quantum Wells*, Plenum, New York (1992).
2. B. F. Levine, in *Intersubband Transitions in Quantum Wells*, E. Rosencher, B. Vinter, and B. Levine, Eds., p. 43, Plenum, New York (1992).
3. H. C. Liu, A. G. Szele, M. Buchanan, and Z. R. Wasilewski, in *Intersubband Transitions in Quantum Wells*, E. Rosencher, B. Vinter, and B. Levine, Eds., p. 57, Plenum, New York (1992).
4. E. Martinez, E. Rosencher, F. Chevoir, J. Nagle, and P. Bois, *Phys. Rev. B* **44**, 3157 (1991).
5. S. M. Sze, *Physics of Semiconductor Devices*, Wiley Interscience, New York (1981).
6. A. Chantre, G. Vincent, and D. Bois, *Phys. Rev. B* **23**, 5335 (1981).
7. B. F. Levine, A. Zussmann, S. D. Gunapala, M. T. Asom, J. M. Kuo, and W. S. Hobson, *J. Appl. Phys.* **72**, 4429 (1992).
8. E. Martinez, F. Luc, E. Rosencher, P. Bois, E. Costard, S. Delaune, and E. Bockelhoff, in *Intersubband Transitions in Quantum Wells*, E. Rosencher, B. Vinter, and B. Levine, Eds., p. 299, Plenum, New York (1992).
9. E. Rosencher, E. Martinez, F. Luc, P. Bois, and E. Bockelhoff, *Appl. Phys. Lett.* **59**, 3255 (1991).
10. H. C. Liu, *Appl. Phys. Lett.* **60**, 1507 (1992).
11. F. Luc, E. Rosencher, and P. Bois, *Appl. Phys. Lett.* **62**, 2542 (1993).
12. E. H. Nicollian and A. Goetzberger, *Bell Syst. Tech. J.* **46**, 1055 (1967).
13. F. Luc, E. Rosencher, and B. Vinter, *Appl. Phys. Lett.* **62**, 1143 (1993).
14. W. Shockley and W. T. Read, *Phys. Rev.* **87**, 835 (1952).
15. P. W. M. Blom, C. Smit, J. E. M. Haverkort, and J. H. Wollert, *Phys. Rev. B* **47**, 2072 (1993).

TuA3

Observation by Spin-Resolved Resonant Magnetotunneling of Oscillatory Landé Factor in Two-Dimensional Electron Systems

F. F. Mendley and I. Moxera
IBM Research Division, T. J. Watson Research Center
Yorktown Heights, N.Y. 10598, USA

and
W. I. Wang
Department of Electrical Engineering, Columbia University
New York, N.Y. 10027, USA

We have shown by magnetotunneling spectroscopy that at certain magnetic fields the Landé factor g of two-dimensional electrons is significantly enhanced relative to its three-dimensional value. The experiments were done using GaSb-AlSb InAs-AlSb GaSb heterostructures, in which a two-dimensional electron gas in the InAs layer is probed by holes from the GaSb electrodes tunneling in and out of it. The field dependence of the g factor is accounted for by the exchange interaction between electrons of the same spin.

When a strong magnetic field H is applied perpendicular to the plane of a two-dimensional (2D) gas, the density of states of the latter becomes discrete, with sharp peaks at energies corresponding to Landau levels E_n , defined by the well-known relation $E_n = \hbar\omega_c(N + 1/2)$, where ω_c is the cyclotron frequency ($\omega_c = e\hbar/m^*e$, and m^* is the effective mass). At very high fields each Landau level is split into its two spin components, the energy separation between which is the Zeeman energy $g\mu_B H$, where μ_B is the Bohr magneton and g is a proportionality constant called the Landé factor. If the exchange interaction between 2D electrons is taken into account, that simple expression for the Zeeman energy may no longer be valid since the magnetic energies are affected by exchange terms between electrons of the same spin. The energy difference depends on the relative population of the various spin states, as illustrated by Fig. 1. When the number of spin-up (up) and spin-down (down) electrons is equal, the exchange energy is the same for both types of magnetic states and their energy separation is not altered by the exchange correction. On the other hand, when the populations of the up and down states are not equal the different exchange terms result in an enhanced energy separation between those states. We can then define an effective g factor, g^* , which is larger than the single-particle Landé factor.

This many-body effect has explained the g -factor values measured in Si-SiO₂ devices [1,2] and it has been used in fitting magnetoresistance data of GaAs/GaAlAs heterostructures in the quantum Hall regime [3]. More recently, it has been manifested in angular-dependence measurements of Shubnikov-de Haas oscillations, which, with certain limitations, yielded enhanced g -factor values of 2D electrons in GaAs/GaAlAs structures [4].

Here we show that a tunneling current perpendicular to a 2D electron gas can provide a more direct way of determining the g factor, not only for states at the Fermi level but for any occupation number. This is demonstrated in GaSb-AlSb-InAs-AlSb-GaSb

heterostructures, whose unique properties make it possible the observation of features in the tunneling current-voltage (I - V) characteristics associated with magnetic states.



Fig. 1. Sketch of the density of states for Landau levels, at two magnetic fields. On the left, the field H_1 is such that two spin-resolved Landau levels ($N=0,1$) are fully occupied. The Zeeman energy is independent of whether the electron-electron exchange interaction is taken into account. On the center and right panels the field H_2 is higher, and the $N=0$ level is half occupied (11). The separation between the two spin states of the fully occupied $N=0$ state is larger when the e - e interaction is included.

The top of the valence band of GaSb lies above the bottom of the conduction band of InAs, so that in a heterostructure made out of GaSb-AlSb-InAs-AlSb-GaSb electrons flow from the GaSb thick regions to the InAs quantum well, leaving holes behind. The amount of charge transferred is controlled by the thicknesses of the InAs and AlSb layers, which for the structure discussed here are 150Å and 40Å, respectively. The 2D electron density in InAs is $1.2 \times 10^{11} \text{ cm}^{-2}$. (Although ideally the number of electrons balances the total number of holes accumulated on both GaSb interfaces, in real structures additional electrons from residual impurities or interface states brake that balance.) By applying hydrostatic pressure up to 1 kbar, that density was reduced to $5.2 \times 10^{10} \text{ cm}^{-2}$, as a result of the pressure-induced reduction of the overlap energy between the GaSb valence band and the InAs conduction band. When a voltage is applied via the two GaSb end layers acting as electrodes, current flows between them via resonant interband tunneling through the 2D quantum state, E_F , in the InAs well. (See

Fig. 2) The current is abruptly interrupted when the energy of the holes at the emitter is lower than E_1 , since then there are no states available for tunneling.

Because of the light effective mass of electrons in InAs, in the presence of a perpendicular magnetic field their cyclotron energy (≈ 5 meV), even at moderate fields, is much larger than the Fermi energy of the heavy holes in the GaSb emitter (≈ 4 meV). When, at a fixed field, an external voltage between the GaSb electrodes aligns the hole distribution with an electron Landau level, resonant tunneling occurs, and the current increases sharply. With a further increase of the voltage the holes are aligned with a gap between two Landau levels, tunneling is then inhibited and the current drops abruptly. The same process is repeated for subsequent Landau levels and, thus, the I-V characteristic shows a sawtooth behavior, with each current peak corresponding to a Landau level of InAs [5]. As the number of occupied levels decreases with increasing field so does the number of peaks; at a given field this number is determined by the electronic density under equilibrium conditions. At very high fields, even the Zeeman spin splitting becomes large compared to the hole Fermi energy (see Fig. 2) and it is possible to resolve in the I-V characteristics features associated with individual spin states [6].

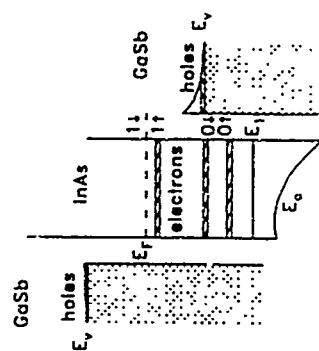


Fig. 2 - Energy band diagram of a GaSb/InAs/AlSb/GaSb heterostructure under a magnetic field perpendicular to the interfaces, when a bias is applied between the two GaSb electrodes. The field is large enough to resolve the spin splitting of the Landau levels of the electrons in the InAs quantum well. The small Landau level quantization of the heavy holes has been ignored.

The experimental I-V characteristics exhibit at low temperature ($T \sim 1$ K) the negative-differential-resistance and sawtooth behavior anticipated above, as illustrated in Fig. 3 for fields ranging from 0 up to 28 kT. At $H = 0$ the peak voltage (voltage for

maximum current) occurs when the quantum state E_1 is aligned in energy with the ground state of the accumulation layer of the GaSb emitter, and therefore that voltage is twice (assuming uniform distribution of the positive and negative states) the energy difference between electron and hole states. At moderate fields, e.g., several current peaks are observable, each corresponding to the alignment of an N -th Landau level with the GaSb heavy-hole state. With increasing field each peak moves to lower voltage, until it eventually disappears when it is above the quasi-Fermi level for electrons - in other words, when it becomes depopulated. The quantum limit (only $N=0$ occupied) is reached at ≈ 24 T, but, even before, the $N=0$ peak develops a shoulder (at $H \approx 15$ T) that gradually becomes a well-defined additional peak. A similar behavior is observed when the heterostructure is under hydrostatic pressure, the only difference being that the quantum limit is reached at lower fields, down to 11 T at the maximum pressure of 1 kbar, when the 2D density is $5.2 \times 10^{12} \text{ cm}^{-2}$.

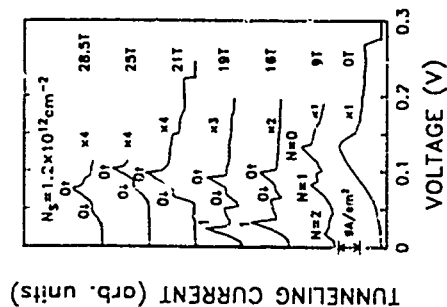


Fig. 3 - Low-temperature ($T \sim 1$ K) tunneling current-voltage characteristics of representative magnetic fields for a heterostructure like the one shown in Fig. 2. The thicknesses for the InAs and AlSb layers are 150 Å and 30 Å, respectively. The field was parallel to the current.

The Landau indices, as well as the 2D electron density, are readily deduced from a plot of the zero-bias tunneling conductance versus field, shown in Fig. 4 for both extreme pressures. The conductance exhibits Shubnikov-de Haas oscillations periodic with the inverse of the field, from which the 2D electron densities mentioned above are obtained. At high fields the deep minima approach zero, resembling the vanishing resistance of the quantum Hall effect of in-plane magnetotransport. This behavior is closely related to that well-known effect. At zero bias, the tunneling conductance vanishes while never the

Fermi level lies between two well-separated Landau levels and becomes maximum when it is in the center of a level. Then, the Landau-level indices can be derived from the relation between the 2D density, the magnetic field, and the spin-resolved filling factor ν . We explain the doublet observed in the I-V characteristics at high fields in terms of spin-polarized tunneling, based on the fact that in the $p \sim 1.3$ kbar case the low-voltage peak (01) passes through $\nu = 0$ precisely at the field (20 T) at which the conductance shows the minimum corresponding to the emptying of the 01 state ($\nu = 1$). Although at lower pressure the extreme quantum limit ($\nu = 1$) was not reached even at 40 T, based on a similar behavior with field, we ascribe the same origin to their respective $N = 0$ doublets.

After converting the voltage separation of the two $N = 0$ structures into energy, the g factor is derived simply by dividing that energy by the magnetic field and the Bohr magneton. The dependence of g with field for the configurations of extreme density is superimposed on Fig. 4. For the lowest density, g increases monotonically with field from a minimum value of 1 to a maximum of 9.

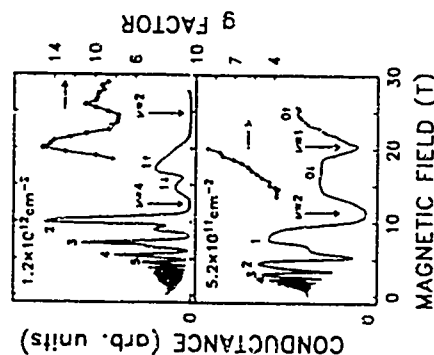


Fig. 4 Zero bias magnetoresistance (continuous curves, left hand scale) and Lande g factor (black dots connected by lines, right hand scale) for two different carrier densities. The values of the g factors are averages for both voltage pinbarriers in the I-V characteristics.

This enhancement of g with field can be understood from the nature of the exchange interaction, as explained in the introduction. At 11 T, the minimum in the zero-voltage conductance for the low-density case indicates that both the 01 and the 02 states are below the Fermi level ($\nu = 2$). As the field increases the 01 state becomes depopulated and the population difference between 01 and 02 increases, reaching a maximum at 20 T.

when 01 is very close to the Fermi level. The exchange-induced enhancement of the g factor follows precisely the increase in population difference.

These experimental g values, especially g_{max} , may at first sight seem too small for InAs. However, it is important to note that they correspond to measurements done under hydrostatic pressure, which increases the band gap of a semiconductor, thus increasing effective masses and decreasing g factors. In fact, a theoretical calculation of g that includes the effect of pressure on the relevant band parameters of bulk InAs yields for g_{max} a value of 4.5, which compares favorably with the experimental value of 4.

As for the enhancement of g from 4 to 9, it is qualitatively explained by a Hartree-Fock calculation, which predicts an enhancement more than three times larger. In that approximation, the maximum increase of the energy difference between the 01 and 02, when the $N = 0$ level is partially occupied, is

$$\Sigma_{01} - \Sigma_{02} = \frac{e^2}{f^2} \sqrt{\frac{\pi}{2}} N_{00} \quad (1)$$

where f is the dielectric constant of InAs, λ is the magnetic length ($\lambda^2 = \hbar/eB$), and $N_{00} = 1/7$.

At 20 T, this difference translates into a Δg of 18. This value, derived under the assumption of an ideal system with no impurities or defects, is larger than the experimental observation, which should not be too surprising, except maybe for the magnitude of the discrepancy.

For the highest density case, the splitting of $N = 0$ is observable even when $N = 1$ is partially occupied, as Fig. 3 illustrates. The g factor has a value of 8 at 18.5 T, a field at which, in equilibrium, 11 is still below the Fermi level. When the field increases, it does g , reaching a maximum value of 15 at 20 T. From then on, g decreases to 8 at 23 T and finally it recovers to values between 9 and 10 beyond 26 T. This oscillatory behavior is in qualitative agreement with the results obtained for the low-density configuration: g is minimum when the Fermi level is between two different Landau levels ($N = 1$ and $N = 0$) and is maximum when one of them is partially empty ($N = 1$).

A closer look, however, reveals a more complicated picture. The maximum g , g_{max} , should occur for a field at which the Fermi level is midway between two spin states within the same Landau level (or, equivalently, when the filling factor is odd), and g should be minimum when the Fermi level is between spin states of different Landau levels (that is, for even filling factors). Then, assuming that the plot of the conductance versus field reflects the 2D density of states, g_{max} should happen at 15 T, not at 20 T. Equally surprising is the observed enhancement of g at fields above 23 T, where the broad zero conductance region suggests a Fermi level between 1 and 0 levels.

Although we have no answer to this anomaly, the explanation may lie on the details of the density of states, especially in view of the presence of residual donor impurities in InAs that contribute to the imbalance between electrons and holes. It is known that impurities can lead to asymmetric density of states that shift the resistance minima of the QHE away from the expected magnetic fields [8]. For example, for a donor-induced attractive potential, an asymmetric density of states is predicted with an impurity band on the low energy side of the Landau levels. Such an asymmetry would be consistent with the observed shift of g_{max} to higher fields.

Calculations of the extreme g values agree well with the experiment. Thus, g_{max} is predicted to be 9, in comparison with an experimental $g_{\text{max}} = 8$. A Hartree-Fock expression for $\Sigma_{01} - \Sigma_{02}$, when the $N = 1$ Landau level is half-occupied reads the same as Eq. (1) re-

WIRE-LIKE INCORPORATION OF DOPANT ATOMS DURING MBE GROWTH ON VICINAL GaAs(001) SURFACES

L. DAWIDRZ, C. MUEGGER, R. HFX, B. KUSTAL and M. HORICKE
Paul Drude-Institut für Festkörperelektronik
Hausvogelplatz 5 - 7, D-10117 Berlin, Germany

ABSTRACT

The ordered incorporation of dopant atoms by combining lattice step growth on vicinal GaAs(001) surfaces and Si delta(d)-doping has been studied by real time reflection high-energy electron diffraction (RHEED) measurements. For Si deposition on 2° low and the (111)Ga plane misoriented surfaces and 0.4° toward the (111)As plane misoriented surfaces it is shown that the Si atoms arrange themselves preferentially along the step edges in a (3x2) structure consisting of an ordered array of Si dimers. For Si concentrations not exceeding substantially the amount expected to be attached at the step edges the GaAs growth can be continued at reduced substrate temperature without adverse effects on the growth front. By pulsed b-doping an unusual high concentration of Si atoms can be incorporated as donors on Ga sites.

1. INTRODUCTION

Delta-doping of GaAs with Si by molecular beam epitaxy (MBE) is now a well established method to incorporate an electrical active impurity in a sheet of a few atomic layers in thickness [1,2]. The usually applied procedure consisting of a suspension of GaAs growth, evaporation of dopant atoms on the non-growing surface while an arsenic flux is incident, and the growth of subsequent GaAs layers is assumed to result in a statistical in-plane distribution of the dopant atoms.

The introduction of an in-plane order of the dopant atoms would allow to study the intriguing electronic properties expected for such ordered structures. In particular it has been proposed to combine the lattice step growth on vicinal surfaces with planar doping to create a one-dimensional system of so-called doping quantum wires [3]. First studies on the deposition of Si atoms on vicinal GaAs(001) surfaces by reflection high-energy electron diffraction (RHEED) [4,5] suggest that a preferential attachment at the edges of misorientation steps occurs provided the vicinal surface is well ordered and the Si migration is strong enough. At present, however, neither the underlying surface processes nor the structure and ordering of the "wire-like" incorporated dopant atoms are well understood. In this work, we use real-time RHEED measurements for a systematic study of the incorporation of Si atoms on various vicinal GaAs(001) surfaces. Additional information on the site occupancy of the incorporated dopant atoms is derived from Hall effect measurements.

2. EXPERIMENTAL

The undoped semiinsulating GaAs(001) substrates misoriented 2° and 0.4° toward the (111)Ga or (111)As plane were prepared in the usual way: a buffer layer of 0.5 µm thickness was grown and annealed at 580 °C. The GaAs growth rate was 0.7 ML (monolayers) s⁻¹, and an As₂ + Ga beam equivalent pressure (BEP) ratio of 15 was used. At a substrate temperature ranging between 550 °C and 610 °C a clear (2x4) reconstruction was found. Before Si deposition, growth interruptions in the order of 1 h duration and the successive deposition of several monolayers GaAs with growth interruptions of 2 min were used to smooth the initial GaAs surface. Si was deposited with a continuous or interrupted flux of 1.08 x 10¹⁴ cm⁻² s⁻¹ (1.7 x 10¹⁴ ML s⁻¹). The subsequent GaAs layers on the Si modified surface were grown at a reduced substrate temperature of 540 °C. The Si flux was calibrated by capacitance-voltage (CV) depth profiling of a dopant staircase structure. To assess the site occupancy of the Si atoms at high concentrations, 300 K low field Hall effect measurements were performed by using chemical etching and a van der Pauw configuration.

For real-time RHEED measurements a 15 kV electron beam with an incidence angle close to

placing N_0 with $N_0 = 1/2$. At 2:1 this difference translates into $\Delta E = 9$, which is about twice the experimental enhancement. The fact that the difference is much smaller than in the case of low density may suggest that, in the latter, E_{ex} is not reached even at the highest fields at which the spin splitting is observable - a likely possibility especially when an asymmetric density of states is considered.

In summary, we have shown how magnetotunneling provides a good tool to obtain directly the Landé factor of two-dimensional systems. By probing the energy gaps in the density of states, the technique could in principle serve to detect anomalies in the density of states associated with fractional Landau level occupation responsible for the fractional quantum Hall effect. However, such an experiment would require a heavy-hole Fermi energy even smaller than that of the structure used in this work and possibly a 2D electron mobility superior to the one shown here. These are hard tasks - but hopefully not impossible.

The high-field measurements were done at the Francis Bitter National Magnet Laboratory, MIT, Cambridge, whose staff we thank for their help. This work has been sponsored in part by the Army Research Office (F. E. M.) and by the Office of Naval Research (W. I. W.).

References

1. F. E. M. and W. I. W., *Phys. Rev. Lett.* **43**, 823 (1969).
2. F. F. Fang and W. I. W., *Phys. Rev. Lett.* **43**, 823 (1969).
3. Th. Englert, D. C. Tsui, A. C. Gossard, and Ch. Uthlen, *Surf. Sci.* **113**, 295 (1982).
4. R. J. Nicholas, R. I. Haug, K. V. Klitzing, and G. Weimann, *Phys. Rev. B* **37**, 1294 (1988).
5. E. E. Mendez, H. Ohno, L. Esaki, and W. I. Wang, *Phys. Rev. B* **43**, 5196 (1991).
6. E. E. Mendez, J. Nueca, and W. I. Wang, *Phys. Rev. B* **47**, 13937 (1993).
7. A. H. MacDonald, H. C. Oji, and K. I. Lin, *Phys. Rev. B* **34**, 2681 (1986).
8. R. I. Haug, R. R. Gerhardt, K. V. Klitzing, and K. Ploog, *Phys. Rev. Lett.* **59**, 1349 (1987).

the first out-of-phase condition for the diffraction at the stepped surface was used. The specular beam intensity was recorded by using an arrangement consisting of a collimator, optical fibre and photomultiplier. The incident beam was parallel to the step edges. With this geometry the specular beam intensity is sensitive to changes in step edge roughness and strain induced effects, adatom density and nucleation processes on the terraces [6,7]. In this azimuth the terraces are not shadowed by the steps. Therefore, Si induced changes in surface reconstruction near the step edges on the lower terrace can be detected from the very beginning. To determine the full symmetry of the Si induced structures complementary measurements with the RHEED beam incident in the orthogonal (110) azimuths have been performed.

3. RESULTS AND DISCUSSION

3.1. Structure of the vicinal GaAs(001) surfaces

The first step in the synthesis of doping quantum wires is the preparation of a regularly stepped vicinal surface with smooth terraces. Using the transition from an oscillating to a constant RHEED intensity as a function of the GaAs growth temperature [8] the critical temperature T_{cr} for a change from two-dimensional nucleation and step propagation mechanism to the desired step flow mechanism has been estimated [5]. For the given growth parameters and the 2° and 0.4° misorientation toward the (111)Ga plane it amounts to about 560 °C and 640 °C, respectively. For the corresponding misorientations toward the (111)As plane these values are lower by about 20 degrees. This is consistent with a recent first-principle calculation on microscopic processes of Ga adatom diffusion on the (2x4) reconstructed surface according to that the Ga adatoms diffuse on the surface by passing through the missing dimer rows [9]. As can be seen in Figs. 1 and 2, this preferential diffusion path is normal to the As-terminated steps for the misorientation toward the (111)As plane but parallel to the Ga-terminated steps for the misorientation toward the (111)Ga plane. Figs. 1 and 2 show also schematically the different behaviour of the two different step types. From scanning tunneling microscopy (STM) studies it is known that Ga-terminated steps are relatively straight whereas As-terminated steps are very ragged [10]. As a consequence of the growth mechanism the terraces of the vicinal surfaces grown above T_{cr} are expected to be smooth, whereas on those grown below T_{cr} a certain concentration of holes and islands will exist even after annealing.

3.2. Si attachment

Fig. 3 shows the time evolution of the RHEED intensity during Si deposition on the 2° toward (111)Ga misoriented surface for different substrate temperatures that were kept constant during GaAs growth and Si deposition. The intensity change during the deposition of only 0.04 ML Si is in the same order as that during the deposition of 1 ML GaAs. The intensity behaviour observed for substrate temperatures below and above T_{cr} is quite different. In a first approximation, it can be understood by considering the two extreme cases, namely a random attachment of Si atoms on the terraces with statistically distributed defects and a preferential attachment of Si atoms at the edges of ordered steps. At 550 °C the intensity decreases linearly with the Si coverage. This suggests that the Si adatoms form a lattice gas of increasing density. The change of the slope of the intensity curve at a coverage of about 0.1 ML can be explained by the formation of islands with a (3x2) structure evidenced by the appearance of half-order spots in the [110] azimuth and of third-order spots in the [110] azimuth. At a coverage of about 0.24 ML asymmetric third-order spots are observed in the [110] azimuth due to the formation of a distorted (1x3) structure.

The intensity behaviour at 580 °C and 590 °C with a nonlinear intensity decrease, a minimum at a Si coverage of about 0.03 ML and the appearance of half-order spots at about the same coverage is considered to be typical for a wire-like attachment of the Si atoms at the step edges as will be discussed below in detail for the interrupted Si deposition. It should be noticed that compared to the case considered before the (3x2) structure develops at a lower coverage whereas the distorted (1x3) structure is formed at higher coverages.

Fig. 4a shows the RHEED intensity recorded during Si deposition on the 2° toward (111)Ga

misoriented surface in intervals of 90 s growth and 180 s growth interruption. The intensity decreases nonlinearly with the Si coverage and shows a slight recovery when the Si flux is interrupted. After reaching a coverage of 0.041 ML the intensity rises rapidly. At approximately the same coverage the (3x2) structure develops. These observations are consistent with the incorporation model schematically represented in Fig. 4b (cf. also Fig. 1). The nonlinear change in "kink" density and strain accompanying the attachment of migrating Si atoms as dimers at the step edges is reflected in a nonlinear intensity decrease. The recovery behaviour of the intensity suggests that this process including the ordering of the dimers can be completed by periodic interruptions of the Si flux. From symmetry and coverage arguments it is concluded that the Si dimers arrange themselves in units with two dimers and one missing dimer (model 1) or with one dimer and two missing dimers per unit mesh (model 2). The completion of (3x2) units along the step edge (to such extent that they can be detected by electron diffraction) and the attachment of a second row finally leads to the three-fold and two-fold periodicity in the [110] and [110] direction, respectively. The final intensity rise is attributed to changes in strain and reconstruction accompanying the Si attachment. For an ideal wire-like attachment of Si dimers the first strip of (3x2) units will be completed at a coverage of $4/3 \theta_{cr}$ (0.066 ML) and $2/3 \theta_{cr}$ (0.033 ML), respectively, for model 1 and model 2, respectively, where the critical coverage θ_{cr} is given by the number of Ga sites at the step edges. The value of 0.041 ML found in the experiment discussed lies in between. The data compiled in Table 1 for a series of experiments suggest, however, that the dimer arrangement according to model 1 dominates. The scatter in the data can be explained by taking into account that in the real experiment a second row of (3x2) units will start to grow before the first one is completed and that the step edges are kinked. The latter effect that would shift the critical coverage to higher values will be, however, not very important since Ga-terminated steps are relatively straight. The considered deviations from the idealized case can also explain why the half-order spots belonging to the (3x2) structure do not necessarily appear exactly at the coverage corresponding to the RHEED intensity minimum but often at slightly lower or higher coverages.

Similar as for the 2° misorientation toward (111)Ga also for the 0.4° misorientation toward (111)As a clear RHEED intensity minimum and at approximately the same coverage the development of a (3x2) structure was observed. A comparison with the Ga step-site density (cf. Table 1) reveals that the coverage of 0.021 ML Si corresponds nearly exactly to $2 \theta_{cr}$. The data reported by Wood [4] for a 0.2° misorientation toward (111)As satisfy the same relation. This is consistent with the model for the Si attachment presented in Fig. 2. The intensity rise and the appearance of the superstructure reflections coincide with the beginning of the formation of a second strip of (3x2) units with two filled and one missing dimer rows that are now parallel to the step edge. A slight shift of the intensity minimum from the expected coverage to higher values can be attributed to the pronounced meandering of As terminated steps.

The conclusions on a wire-like incorporation of dopant atoms drawn above from the intensity behaviour are supported by the quite different intensity versus Si coverage plots found for Si deposition on the 0.4° toward (111)Ga misoriented surface. As a consequence of the competition between step-edge incorporation of dopant atoms and their clustering on the larger terraces, the coverage given by the RHEED intensity minimum deviates now strongly from the value expected for a preferential attachment at step edges, even at a substrate temperature of 610 °C [5]. This is explained by the limited migration across the terraces due to the large activation energy for diffusion along the [110] direction [4].

3.3. GaAs overgrowth

To study the effect of a high local Si concentration at the step edges on the subsequent GaAs growth, for the 2° toward (111)Ga misoriented surface, RHEED intensity recordings for GaAs growth at 540 °C after Si deposition of 2×10^{13} atoms cm^{-2} and without the preceding Si deposition have been compared. The similar intensity behaviour shows that the Si modified surface can be overgrown by GaAs without adverse effects on the growth front morphology, although the reduced intensity indicates a reduced surface order.

To confirm the results of the RHEED measurements on the ordered Si incorporation Raman scattering by plasmon excitation was used. Difference spectra for light polarized parallel to the [110] and

[110] direction, respectively, showed a much stronger asymmetry for misoriented samples grown at conditions favorable for a wire-like Si incorporation than for reference samples grown on the perfectly oriented GaAs(001) substrate [11].

The well-ordered (3x2) structure observed during interrupted Si deposition on the appropriately misoriented GaAs(001) surface has been explained by the ordered incorporation of Si atoms on Ga sites. The Hall effect measurements of samples overgrown by GaAs confirmed that by pulsed δ doping Si can be incorporated in an unusual high concentration as donor. A sheet carrier concentration as high as $8 \times 10^{19} \text{ cm}^{-2}$ has been realized for the deposition of 0.61 ML Si on a 2° toward (111)Ga misoriented GaAs(001) surface at 590°C . Using these data it can be concluded that the distorted (1x3) structure observed at very high Si coverages is due to the incorporation of Si atoms in the As plane. For continuous δ doping this is observed at much lower Si coverages.

4. CONCLUSION

In conclusion we have shown that at appropriate conditions, in particular for interrupted deposition, Si atoms arrange themselves on vicinal GaAs(001) surfaces in a (3x2) structure along the step edges. This structure arises from an ordered array of filled and missing Si dimer rows parallel to the [110] direction. The critical terrace width for that a preferential attachment of the Si atoms at the step edges can be realized is much larger for a misorientation toward (111)As than for a misorientation toward (111)Ga. This shows that as for Ga adatoms also for Si adatoms the preferential diffusion path is along the [110] direction. From Hall effect measurements it is evident that nearly all Si atoms occupy their high local concentration at the step edges are incorporated as donors on Ga sites. This Si modified surface can be overgrown by GaAs without adverse effects on the growth or morphology.

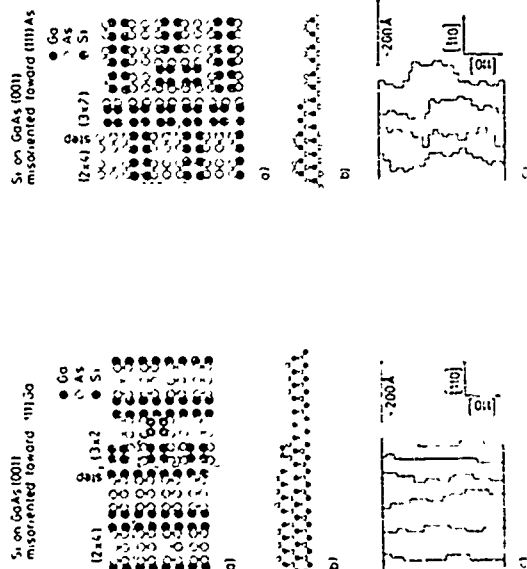


Fig. 1: Schematic models of the (3x2) reconstructed vicinal GaAs(001) surface misoriented toward (111)Ga and (111)As, respectively, with Si atoms attached in a (3x2) symmetry along the step edge in top (a) and side view (b). (c) is a schematic representation of the step edge roughness derived from STM studies [10].

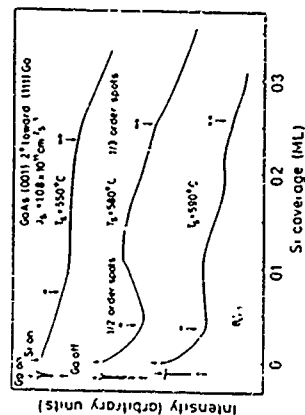


Fig. 3: RHEED intensity recorded in the [110] azimuth during continuous Si deposition at various substrate temperatures on GaAs(001) 2° misoriented toward (111)Ga. The crosses mark the appearance of half order and asymmetric taints under specular incidence. θ_{min} is equivalent to the density of Ga step-edge sites.

Table 1: Si coverages θ_{min} corresponding to the minimum in the RHEED intensity recording. Model 1 refers to a (3x2) unit mesh with two Si dimers, model 2 to a (3x2) unit mesh with one Si dimer. θ_{min} is equivalent to the density of Ga step edge sites.

misorientation	θ_{min} (ML)	θ_{min}	
		model 1	model 2
2° toward (111)Ga	0.049	$4/3 \theta_{\text{min}} = 0.066 \text{ ML}$	$2/3 \theta_{\text{min}} = 0.033 \text{ ML}$
0.4° toward (111)As	0.010	$2 \theta_{\text{min}} = 0.020 \text{ ML}$	$1 \theta_{\text{min}} = 0.010 \text{ ML}$
0.2° toward (111)As	0.005	$2 \theta_{\text{min}} = 0.010 \text{ ML}$	$1 \theta_{\text{min}} = 0.005 \text{ ML}$
			experiment
			(atoms cm^{-2})
			$(2.6 - 4.7) \times 10^{14}$
			1.3×10^{15}
			$(6.9) \times 10^{12}$
			ref. [4]

Size effects in the transport properties of thin $\text{Sc}_{1-x}\text{Er}_x\text{As}$ epitaxial layers buried in GaAs

R. Bogaerts*, A. De Keyser, F. Blitsch*, F. M. Poters*, J. Dellens*, C. J. Palmstroom*, D. Bredner*, and S. J. Allen, Jr.*

* Katholieke Universiteit Leuven, Department Natuurkunde, B-3001 Leuven
* Universitaire Instelling Antwerpen, Departement Natuurkunde, B-2610 Antwerpen
* Bellcore, Red Bank, NJ 07201-2000, USA
* University of California, Department of Physics, Santa Barbara, CA 93106

Size effects have been studied in the transport properties of $\text{Sc}_{1-x}\text{Er}_x\text{As}$ layers with the known thickness ranging from 20 nm to 0.5 nm. Shubnikov-de Haas (SdH) oscillations in tilted magnetic fields confirm the confinement of charge carriers in the $\text{Sc}_{1-x}\text{Er}_x\text{As}$ epitaxial layers. The layers with thickness less than 10 nm show magnetic oscillations in the longitudinal resistance. Different size mechanisms which may be responsible for the observed behaviour are discussed.

1. Introduction

The progress in epitaxial growth methods in particular Molecular Beam Epitaxy, has recently led to the fabrication of novel heterostructures consisting of semiconducting $\text{Sc}_{1-x}\text{Er}_x\text{As}$ layers buried in GaAs [1]. With a view to the potential technological applications of these high carrier density systems, it is important to achieve a thorough understanding of the mechanisms dominating their transport properties. In earlier publications [2-4] the Fermi surface of $\text{Sc}_{1-x}\text{Er}_x\text{As}$ layers with thicknesses of 71 monolayers (ML) (20 nm) and 20 ML (5.7 nm) was successfully described with a 3D model consisting of three electron ellipsoids at the vertices of the first Brillouin zone [2,4] and two hole spheres at the zone center [3,4]. SdH measurements in tilted magnetic fields on a 20 nm $\text{Sc}_{1-x}\text{Er}_x\text{As}$ sample however revealed that carrier quantization has to be taken into account. If SdH oscillations were observed below the classical Lifshitz transition [2], and if the SdH frequency attributed to one of the hole spheres deviated with the cosine of the angle θ between the surface normal and the magnetic field [1].

In this paper we study the angular dependence of the SdH oscillations at 1.2 K in strong parallel

magnetic fields for six samples with Er concentrations ranging from x=0.31 to x=1, and thicknesses ranging from 71 ML to 20 ML. A detailed analysis is made of the quantum size effect characteristics present in the frequency spectra of the oscillations. For $\text{Sc}_{1-x}\text{Er}_x\text{As}$ layers with thickness ≤ 10 ML, interface scattering is so strong that no quantum structure can be detected. Instead, a complex behaviour of the magnetoresistance is observed, with an increase of negative magnetoresistance for decreasing thickness. We discuss different mechanisms governing the magnetoresistance in this region of layer thicknesses: (i) indirect size effects due to the suppression of the antiferromagnetic order which is established below 5 K for bulk by order of the decrease of the spin disorder resistivity when the HFE spins are locked up in an increasing magnetic field, (ii) weak localization effects.

2. Quantum confinement

The samples were grown by MBE and consist of a 200 nm GaAs buffer layer on a semi-insulating substrate followed by a $\text{Sc}_{1-x}\text{Er}_x\text{As}$ layer and a 20 nm capping layer of insulating GaAs [1]. The mobility of the charge carriers in these structures is quite low ($\sim 1000 \text{ cm}^2/\text{Vs}$) and strong parallel

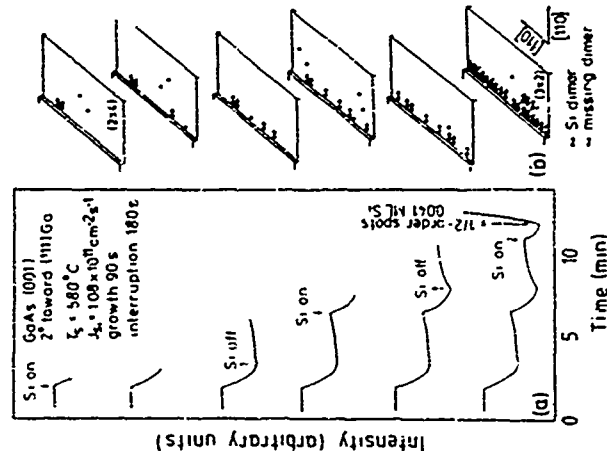


Fig. 4 RHEED intensity recorded in the [110] azimuth during interrupted Si deposition at 580 °C on a vicinal GaAs(001) surface. 2° misoriented toward (111)GaAs and the tilted incorporation model (b). The cross marks the appearance of half-order spots.

REFERENCES

- [1] K. Ploog, M. Hauser and A. Fischer, *Appl. Phys. A* **45**, 233 (1988).
- [2] E. F. Schubert, *J. Vac. Sci. Technol. A* **8**, 2980 (1990).
- [3] G. E. V. Baeij and A. A. van Gorkum, *Science and Engineering of One- and Zero-Dimensional Semiconductors*, (S. E. Baranovskii and C. M. Sponagor Torres, Eds.), p. 133, Plenum, New York (1990).
- [4] C. E. C. Wood, *J. Appl. Phys.* **71**, 1760 (1992).
- [5] L. Dierker, K. Hagenmüller and P. Schreder, *J. Crystal Growth* **127**, 1051 (1993).
- [6] M. G. Lagally, D. E. Savage and M. C. Tringola, *Reflection High Energy Electron Diffraction and Reflection Imaging of Surfaces* (P. K. I. Sen and P. J. Doherty, Eds.), p. 427, Plenum, New York (1990).
- [7] L. Dierker, *J. Crystal Growth* **127**, 949 (1993).
- [8] H. Neave, P. J. Doherty, D. A. Joyce and J. Zhang, *Appl. Phys. Letters* **67**, 100 (1995).
- [9] K. Sakai, *Appl. Phys. Letters* **64**, 1363 (1992).
- [10] M. C. Pashley, K. Hagenmüller and J. M. Gaillet, *Appl. Phys. Letters* **58**, 406 (1991).
- [11] M. Ramsteiner, J. Wagner, G. Jung, D. Behr, L. Dierker and R. Hey, *this conference*.

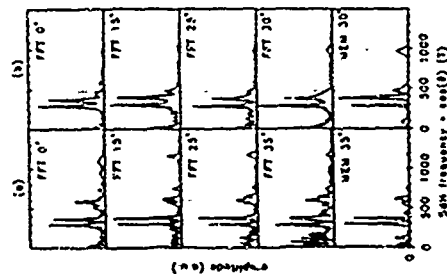


Fig. 1 Angular dependence of the SdH spectra for (a) 40 ML Se_{0.45}Te_{0.55} and (b) 20 ML Se_{0.45}Te_{0.55}. The frequency axis is recalculated with cos(θ). The dotted line indicates the hole frequency for θ = 25° in (a) and θ = 30° in (b). The FFT spectrum is compared to the MEX spectrum.

magnetic fields are required to observe the SdH oscillations generated by the hole spheres [1]. The experiments in tilted magnetic fields were performed at 4.2 K on Se_{0.45}Te_{0.55} samples of 21 ML with x = 0.33 and x = 0.68, a sample of 10 ML with x = 0.50, and samples of 20 ML with x = 0.34 and x = 0.70 and x = 1.

The frequency spectra of the oscillations were determined by Fast Fourier Transform (FFT) and the Maximum Entropy Method (MEM) [5]. The background in the MEM spectra is strongly reduced, and the peaks are more pronounced (Fig. 1). The latter method is thus well suited to identify the frequencies corresponding to different

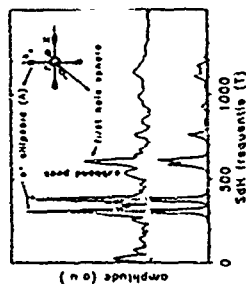


Fig. 2 Comparison between the experimental FFT spectrum for 40 ML Se_{0.45}Te_{0.55} (upper curve) and the spectrum calculated with the 3D Fermi surface model, which is shown in the inset. The peak labeled with 'subband peak' corresponds to the N = 1 subband of the holes in the first hole sphere.

carriers of the Fermi surface. Unfortunately, this method may generate spurious peaks, which can be eliminated by comparison with the FFT spectra.

The frequency axis of the spectra in Fig. 1, which are representative of the spectra of all investigated samples, are recalculated with cos(θ). In this way the angular dependence of the entire spectrum can easily be interpreted. For the frequencies generated by the hole spheres, the cos(θ) behavior strongly deviates from three-dimensional behavior and is indicative of magnetotransport in 2D subbands.

This observation leads us to assume that the dominant frequencies in our SdH spectra are generated by the N = 1 subbands, which are likely to have the highest mobilities. A further question is whether oscillations generated by the other subbands are experimentally observed. Reproducible peaks appear in the spectra of some of the samples on the left side of the frequencies associated with the N = 1 subbands in particular for the spectra of the hole-sphere with the lowest carrier concentration (the 'first hole-sphere' (1)st in model 2). In order to evaluate the possibility that

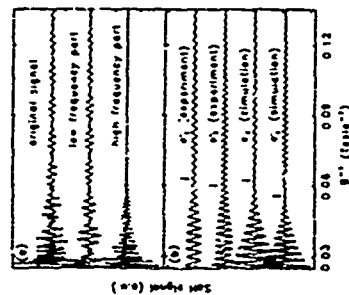


Fig. 3 (a) Decomposition of the SdH signal of 40 ML Se_{0.45}Te_{0.55} by means of inverse FFT. The low frequency part, which is dominated by the 'e' and 'e' frequencies attributed to electron ellipsoid (A) [5], contains all frequencies below the N = 1 subband frequency of the first hole sphere. The high frequency part is used to determine the effective mass of the holes.

(b) Further decomposition of the low frequency part. The two upper curves show the inverse FFT signals of the two dominant 'e' frequencies. The accompanying structure on the left side of the peaks is included for the inverse FFT. The lowest curves show a simulation of the 2D signal arising from the N = 1 and N = 2 subbands for 'e' and 'e'. The arrows indicate the nodes of the resulting beat pattern.

these peaks are generated by 2D subbands, the subband energies and thus the effective masses of the charge carriers must be determined.

For this purpose temperature dependent SdH measurements were performed on the 10 ML Se_{0.45}Te_{0.55} sample. The effective mass of the electron ellipsoids in the direction perpendicular to the long axis has already been obtained from SdH measurements in DC magnetic fields (m₀^{2D} = 0.17 m₀) [3]. Here we attempt to measure the effective mass of the holes. The SdH frequencies of

oscillations were decomposed into two parts by means of inverse FFT (Fig. 3a): one part containing the frequencies below the N = 1 subband frequency of the first hole sphere, and another part containing all higher frequencies. The low frequency part mainly consists of two dominant frequencies, corresponding to one of the electron Fermi surfaces (surface A) in Fig. 2, which is split due to the exchange interaction with the 4f Er spins [2]. The other part is dominated by the frequency of the first hole sphere, at least for magnetic fields up to 31 Tesla. An analysis of the temperature dependence of the SdH amplitude in this magnetic field region leads to an effective mass of m₀^{2D} = (0.52 ± 0.17) m₀ for the holes of the first hole sphere. The relatively large error is due to the small temperature region in which the experiments were carried out (1.4 K - 1.2 K). Also, we did not take into account the modulation of the amplitude by the exchange splitting of the hole Fermi energy, which is very small (ΔE_F/E_F ≈ 4.5%) though observable [4].

The 2D hole subband energies E_N = N²Δ²/2m₀^{2D} as well as the subband frequencies f_N = m₀^{2D}(E_N - E_F)/h have been determined using the value m₀^{2D} = 0.52 m₀. In these equations, f is the layer thickness and E_F is the Fermi energy calculated from the position of the hole peak in the FFT spectrum f_h = m₀^{2D}(E_F - E_h)/h = 0.13 Tesla. In this calculation, the exchange splitting of the bands is neglected. For the situation of Fig. 2, with t = 11.4 nm and E_F = 142 meV, we obtain E₂ - E₀ = 126 meV and E₂ - E₁ = 119 meV, which leads to a SdH frequency for the N = 2 subband of 535 Tesla. This is in good agreement with the observed additional peak at ≈ 538 Tesla in Fig. 1.

For the electron ellipsoid (A), m₀^{2D} is estimated using the expressions f_h = (f_h + f_h)/2 = Δ²/2h, m₀^{2D} = Δ²/2hf_h and f_h²/2m₀^{2D} = Δ²/2hf_h, and inserting the values m₀^{2D} = 0.17 m₀, f_h = 152 Tesla for the mean electron frequency, and m₀^{2D} = 3.1 · 10⁻⁴ cm⁻³ for the total electron concentration. The latter is obtained from an analysis of the SdH spectrum with the 3D Fermi surface model [3]. From the values of the electron effective masses, we obtain for the SdH frequencies of

spin-up and spin up electrons in silicon (A) and germanium (B). The values for the two lowest bands are 368, 378, 380, 390, 400, 410, 420, 430, 440, 450, 460, 470, 480, 490, 500, 510, 520, 530, 540, 550, 560, 570, 580, 590, 600, 610, 620, 630, 640, 650, 660, 670, 680, 690, 700, 710, 720, 730, 740, 750, 760, 770, 780, 790, 800, 810, 820, 830, 840, 850, 860, 870, 880, 890, 900, 910, 920, 930, 940, 950, 960, 970, 980, 990, 1000, 1010, 1020, 1030, 1040, 1050, 1060, 1070, 1080, 1090, 1100, 1110, 1120, 1130, 1140, 1150, 1160, 1170, 1180, 1190, 1200, 1210, 1220, 1230, 1240, 1250, 1260, 1270, 1280, 1290, 1300, 1310, 1320, 1330, 1340, 1350, 1360, 1370, 1380, 1390, 1400, 1410, 1420, 1430, 1440, 1450, 1460, 1470, 1480, 1490, 1500, 1510, 1520, 1530, 1540, 1550, 1560, 1570, 1580, 1590, 1600, 1610, 1620, 1630, 1640, 1650, 1660, 1670, 1680, 1690, 1700, 1710, 1720, 1730, 1740, 1750, 1760, 1770, 1780, 1790, 1800, 1810, 1820, 1830, 1840, 1850, 1860, 1870, 1880, 1890, 1900, 1910, 1920, 1930, 1940, 1950, 1960, 1970, 1980, 1990, 2000, 2010, 2020, 2030, 2040, 2050, 2060, 2070, 2080, 2090, 2100, 2110, 2120, 2130, 2140, 2150, 2160, 2170, 2180, 2190, 2200, 2210, 2220, 2230, 2240, 2250, 2260, 2270, 2280, 2290, 2300, 2310, 2320, 2330, 2340, 2350, 2360, 2370, 2380, 2390, 2400, 2410, 2420, 2430, 2440, 2450, 2460, 2470, 2480, 2490, 2500, 2510, 2520, 2530, 2540, 2550, 2560, 2570, 2580, 2590, 2600, 2610, 2620, 2630, 2640, 2650, 2660, 2670, 2680, 2690, 2700, 2710, 2720, 2730, 2740, 2750, 2760, 2770, 2780, 2790, 2800, 2810, 2820, 2830, 2840, 2850, 2860, 2870, 2880, 2890, 2900, 2910, 2920, 2930, 2940, 2950, 2960, 2970, 2980, 2990, 3000, 3010, 3020, 3030, 3040, 3050, 3060, 3070, 3080, 3090, 3100, 3110, 3120, 3130, 3140, 3150, 3160, 3170, 3180, 3190, 3200, 3210, 3220, 3230, 3240, 3250, 3260, 3270, 3280, 3290, 3300, 3310, 3320, 3330, 3340, 3350, 3360, 3370, 3380, 3390, 3400, 3410, 3420, 3430, 3440, 3450, 3460, 3470, 3480, 3490, 3500, 3510, 3520, 3530, 3540, 3550, 3560, 3570, 3580, 3590, 3600, 3610, 3620, 3630, 3640, 3650, 3660, 3670, 3680, 3690, 3700, 3710, 3720, 3730, 3740, 3750, 3760, 3770, 3780, 3790, 3800, 3810, 3820, 3830, 3840, 3850, 3860, 3870, 3880, 3890, 3900, 3910, 3920, 3930, 3940, 3950, 3960, 3970, 3980, 3990, 4000, 4010, 4020, 4030, 4040, 4050, 4060, 4070, 4080, 4090, 4100, 4110, 4120, 4130, 4140, 4150, 4160, 4170, 4180, 4190, 4200, 4210, 4220, 4230, 4240, 4250, 4260, 4270, 4280, 4290, 4300, 4310, 4320, 4330, 4340, 4350, 4360, 4370, 4380, 4390, 4400, 4410, 4420, 4430, 4440, 4450, 4460, 4470, 4480, 4490, 4500, 4510, 4520, 4530, 4540, 4550, 4560, 4570, 4580, 4590, 4600, 4610, 4620, 4630, 4640, 4650, 4660, 4670, 4680, 4690, 4700, 4710, 4720, 4730, 4740, 4750, 4760, 4770, 4780, 4790, 4800, 4810, 4820, 4830, 4840, 4850, 4860, 4870, 4880, 4890, 4900, 4910, 4920, 4930, 4940, 4950, 4960, 4970, 4980, 4990, 5000, 5010, 5020, 5030, 5040, 5050, 5060, 5070, 5080, 5090, 5100, 5110, 5120, 5130, 5140, 5150, 5160, 5170, 5180, 5190, 5200, 5210, 5220, 5230, 5240, 5250, 5260, 5270, 5280, 5290, 5300, 5310, 5320, 5330, 5340, 5350, 5360, 5370, 5380, 5390, 5400, 5410, 5420, 5430, 5440, 5450, 5460, 5470, 5480, 5490, 5500, 5510, 5520, 5530, 5540, 5550, 5560, 5570, 5580, 5590, 5600, 5610, 5620, 5630, 5640, 5650, 5660, 5670, 5680, 5690, 5700, 5710, 5720, 5730, 5740, 5750, 5760, 5770, 5780, 5790, 5800, 5810, 5820, 5830, 5840, 5850, 5860, 5870, 5880, 5890, 5900, 5910, 5920, 5930, 5940, 5950, 5960, 5970, 5980, 5990, 6000, 6010, 6020, 6030, 6040, 6050, 6060, 6070, 6080, 6090, 6100, 6110, 6120, 6130, 6140, 6150, 6160, 6170, 6180, 6190, 6200, 6210, 6220, 6230, 6240, 6250, 6260, 6270, 6280, 6290, 6300, 6310, 6320, 6330, 6340, 6350, 6360, 6370, 6380, 6390, 6400, 6410, 6420, 6430, 6440, 6450, 6460, 6470, 6480, 6490, 6500, 6510, 6520, 6530, 6540, 6550, 6560, 6570, 6580, 6590, 6600, 6610, 6620, 6630, 6640, 6650, 6660, 6670, 6680, 6690, 6700, 6710, 6720, 6730, 6740, 6750, 6760, 6770, 6780, 6790, 6800, 6810, 6820, 6830, 6840, 6850, 6860, 6870, 6880, 6890, 6900, 6910, 6920, 6930, 6940, 6950, 6960, 6970, 6980, 6990, 7000, 7010, 7020, 7030, 7040, 7050, 7060, 7070, 7080, 7090, 7100, 7110, 7120, 7130, 7140, 7150, 7160, 7170, 7180, 7190, 7200, 7210, 7220, 7230, 7240

3 Negative Transmembrane

res with thicknesses ≤ 10 ML, orientation anisotropy dominates the transport properties at low temperatures. The most in Fig. 1 shows the resistivity of a 20 ML and a 1 ML EXAF sample as a function of the temperature. The 20 ML sample shows the resistivity of the almost linear decrease with temperatures is followed by a leveling-off at lower temperatures, and a drop in the resistivity at about 5 K, which is due to antiferromagnetic ordering of the magnetic spins.³ For the 4 ML sample deviations from this behaviour are observed in the low temperature region: i) below 40 K the resistivity shows a logarithmic increase with decreasing temperature; ii) at the ordering temperature a rapid increase of the resistivity is observed. In Ref. [2], the latter is attributed to a suppression of the antiferromagnetic order in the thin layers, which leads to localisation of the charge carriers. The effect is most prominently present in the resistivity of the thinnest sample (4 ML). The logarithmic decrease which is clearly observed in the EXAF samples of 1 and 5 ML, extends over a larger temperature region for increasing sample thickness.

To gain insight into the mechanisms that cause the enhancement of the sensitivity at low temperatures we have carried out ^{13}C -cross-polarization and longitudinal magnetoresistance (LMR) measurements on ErAs samples of 3, 4, 5, and 6 μm at 4, 2, 1, 77, 4, and 150 K. We discuss here the results obtained for the thinnest samples at 4 K, which are shown in Fig. 4. The modulations of the charge car-

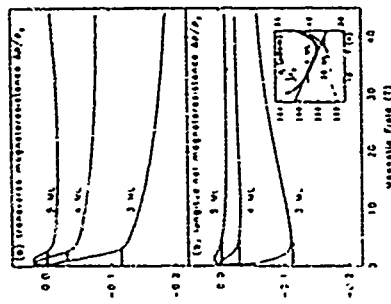


Fig. 6. (a) Transverse and (b) longitudinal NMR for the E₁A samples of 3 and 5 M. The inset shows the temperature dependence of the sensitivity for the 4 M sample and for a 36 M E₁A sample. The bottom curves are for ν_{H} and ν_{H} which differ only by a factor of 2 at ν_{H} and ν_{H} , corresponding to the negative NMR contrast for the high field NMR, respectively, due to the suppression of the antiferromagnetic order below 1 K, which is indicated in the inset.

exists in the layers are lower than the mobilities in the thicker $\text{Si}_{1-x}\text{Ge}_x$ layers. As a consequence, the quantum structure can be detected, and the transverse MR component for a classical orbital transverse MR component for a quantum structure with different types of carriers is strongly influenced both the transverse and the longitudinal measurements show an increase of negative MR with decreasing thickness.

At 1.2 K the behaviour of the MFR in magnetic fields below 3 Tesla is closely related to the antiferromagnetic-paramagnetic order transition. The initial increase of the resistance, which characterizes the transition in bulk-like layers [6], is followed by a decrease in the MFR, which can be attributed to the appearance of magnetic fields for the 4-MF, which

ed, and has disappeared for the 1 AU sample supporting the assumption of a true localisation due to suppression of the anti-magnetic order

The logarithm derived from the residuals above ± 1.5 K was extrapolated to ± 1.2 K as shown for the ± 1.5 K sample in the inset in Fig. 1. The difference between this extrapolated value and the measured value is attributed to the localisation effect and corresponds to a negative MH^* contribution and is used by measuring the localisation due to the alignment of the T spins in a magnetic field. A decrease in this negative contribution phenomenon will be due to an increase for the MH^* which are indicated in the curves in Fig. 1. It is probably a dominant negative high field component it is observed for the inverse MH^* and a dominant positive component for the longitudinal MH^* . Both contributions are proportional to the sample thickness increases. A negative contribution due to the decrease of the thermal quenching order so starting still has to be taken into account at ± 1.2 K; this is however a constant contribution over a large part of the magnetic field range, which does not change the general tendencies observed in the MH^* .

The log-odds ratio temperature dependence of the probability to be given a positive MRE (for the 100 samples) and χ^2 suggests the presence of a weak localization effect as an explanation for the observed MRE. Indeed, this mechanism can give rise to negative as well as positive MRE, depending on the latter behavior related to our sample. A careful analysis of the two mechanisms including a set of numerical simulations of the type of experiments for weak localization and spin disorder mixing will be carried out in future work.

Summary

Small amplitudes on S_1 and T_1 as samples with the losses ranging from 20 mm to 57 mm have been used as a criterion for 2D-simulation and spectra of the carrier frequency spectrum of the S_1 and T_1 states are shown with the same of the angle of the surface normal and the incident field on 2D-simulation frequencies are presented in the same of S_1 and T_1 to make technology the sub-

and frequencies theoretically we have extracted the value of the effective mass of one of the hole spinors from temperature dependent SdH oscillations.

For $\text{Sr}_{1-x}\text{Er}_x\text{As}_2$ samples with thicknesses ≤ 5 nm surface-related mechanisms, which are obviously present in the temperature dependence of the resistivity, lead to both negative and positive contributions to the magnetoresistance. A detailed quantitative analysis of the measurements is in progress in order to investigate the exact origin of these contributions.

Acknowledgements

HEW is a New York-based and FAF a Senior Research Associate of the Belgian National Fund for Scientific Research, which also provided funding for the experiments. We acknowledge helpful discussions with Fred G. Holtz who drew our attention to the MFM method.

References

- [illegible]

SINGLE-ELECTRON TUNNELING AND COULOMB CHARGING EFFECTS IN

ULTRASMAALL DOUBLE-BARRIER HETEROSTRUCTURES

M. Tervort, (a) V.J. Law, J.T. Nicholls, L. Martin-Moreno, (b) D.A. Ritchie, M.J. Kelly, (c)
M. Pepper, (d) J.E.F. Frost, R. Newbury, G.A.C. Jones

Cavendish Laboratory, University of Cambridge, Cambridge CB3 0HE, United Kingdom

An extensive study of charge transport through submicron-diameter double barrier heterostructure diodes is reported. The occupation of the quantum well with single electrons, starting from zero, is observed in the form of sharp steps in the tunneling current. The magnitudes of current steps can be controlled by changing the barrier thicknesses and thus their transparency for tunneling electrons. The plateau width of the current steps is related to the energies of the electron states in the quantum well which are affected by the combined vertical and lateral quantum confinement and by Coulomb charging effects. Diameter dependent studies of the tunneling current suggest that the lateral quantum confinement can result from the surface depletion potential, potential fluctuations, or single impurities. High magnetic field studies confirm this conclusion. The contribution of the Coulomb charging energy is investigated by using an asymmetric double barrier profile. It is shown that tunneling through submicron-diameter double barrier heterostructures provides valuable insight into the electronic properties of quantum boxes with very few electrons.

1. INTRODUCTION

Advanced technology now makes it possible to fabricate semiconductor nanostructures in which electrons are confined in small boxes with only a few hundred angstroms in size [1]. These tiny, artificially crafted electron systems are often referred to as "quantum dots" or "Coulomb islands". The interest in semiconductor quantum dots lies in their characteristic electronic properties. Firstly, when the size of the quantum dot is smaller than the Fermi wavelength and the electron mean free path, three-dimensional quantum confinement of the electronic states can be observed in vertical [2] and lateral [3] tunneling spectroscopy and in the optical spectra [4]. Secondly, the small size of the quantum dot implies that their electrostatic charging energy is quite significant. In analogy to the classical electrostatics of a capacitor C , the Coulomb charging energy of a quantum dot is $E_C(N) = N^2 e^2 / 2C$, where N is the number of electrons in the dot, and e is the electron charge.

Coulomb charging effects were first observed in small metal grains [5], but quantum confinement energies are much smaller and were never reported in these devices. However, in semiconductors, where both the electron effective mass and the Fermi energy are small, the confinement energies and the Coulomb charging energies [6] are comparable and can both be observed simultaneously [7]. This was first demonstrated in conductance studies of quantum dots formed in a high mobility two-dimensional electron gas (2DEG) [8].

A particularly interesting case occurs when the quantum dot is occupied by only a few electrons. This is difficult to achieve in microstructured 2DEG heterostructures, where Coulomb

islands with typically 100 electrons can be isolated. The lowest number of electrons ever reported in such structures is 7 [9]. Recently, several groups have successfully observed the hysteretic charging of a quantum dot with single electrons, starting from zero [2,10-16]. They studied transport through ultrasmall diameter resonant tunneling diodes (RTDs) in which the GaAs quantum dot is formed between the two AlGaAs barriers. If the vertical confinement is strong enough the lowest dot states lie above the Fermi energy in the emitter at zero bias, and no electron occupies the dot. At low temperatures, incremental charging of the dot can be observed in form of sharp current steps in the tunneling current. This experiment is very sensitive (low noise level) and it is easy to perform. However, the electrons are stored dynamically in the quantum dot, i.e. the system is not in equilibrium. In recent theoretical models for transport through sub-electron scale RTDs lateral quantum confinement [17], Coulomb charging effects [6], and both contributions at the same time [7, 18] were considered.

Asghori *et al.* [19] measured the capacitance signal of a quantum dot as it is charged up with single electrons, again starting from zero. In their device, no electrons tunnel through the dot, and therefore the discrete electron states can be probed under conditions closer to equilibrium.

In this paper, we present an extensive study of tunneling through nanometer scale AlGaAs-GaAs double-barrier quantum dots. The observation of single-electron charging is described under various experimental conditions that affect the electron transmission and the energetics of the quantum dot. Parameters studied include diameter, barrier thickness and asymmetry, magnetic field, and temperature. It will be shown that this system is a powerful experimental laboratory suited for the study of quantum dots in the limit of very few electrons.

2. SAMPLES AND EXPERIMENT

The diodes studied here were processed from 4 AlGaAs-GaAs double barrier heterostructures grown by molecular beam epitaxy on an n^+ -type (100) GaAs substrate. The undoped active layers of structure 1 comprise a GaAs quantum well (thickness $w=14\text{nm}$) sandwiched between two Al_{0.35}Ga_{0.65}As barriers (top barrier thickness $b_1=1\text{nm}$, substrate side barrier thickness $b_2=7\text{nm}$), and GaAs spacer layers ($b_3=7\text{nm}$). The top and bottom GaAs contacts, starting from the spacers, comprise a 350nm layer, Si-doped to $2 \times 10^{16}\text{cm}^{-3}$, a 25nm thick layer, with the doping graded from $2 \times 10^{16}\text{cm}^{-3}$ to $1.4 \times 10^{18}\text{cm}^{-3}$, and a 350nm thick layer, Si-doped to $1.4 \times 10^{18}\text{cm}^{-3}$. The other three heterostructures 2-4 are symmetric and have no graded doping profile in the contacts. The main design parameters of heterostructures 1-4 are summarized in table 1.

Free standing single RTDs with diameters between 0.1µm and 10µm were fabricated from the heterostructures by employing electron-beam lithography and Cl₄-H₂ metal-organic reactive ion etching [10].

All samples were measured at $T=4\text{K}$ or in a dilution refrigerator operation at base temperature of the mixing chamber ($T=20\text{mK}$). The diodes have to be measured under low temperatures, because the discrete electronic states can only be observed when the energy spacing

of the quantum dot states is smaller than the thermal broadening $k_B T$ of the Fermi energy in the contacts. This condition is typically fulfilled at temperatures around $T \approx 1\text{ K}$ (see section V).

Figure 1 shows the current-voltage ($I(V)$) characteristics of an asymmetric double barrier diode (structure 1) with large diameter $d \approx 10\text{ nm}$. Resonance peaks from tunneling through the first 2D subband are observed in both bias polarities. The asymmetry of the $I(V)$ results from considerable charging of the quantum well only in forward bias. In forward bias, the rate of tunneling into the well is higher than that of tunneling out, leading to much higher electron charging of the quantum well than in reverse bias [20]. Therefore, the current peak in forward bias is larger than in reverse bias. Charging also leads to more inefficient biasing of the quantum well, resulting in a higher peak voltage in forward bias as compared to reverse bias [20].

3. TUNNELING IN SMALL DIAMETER DIODES

The charging of the well increases with bias and it is proportional to the area of the diode. If the diode diameter is made very small, the incremental charging with single electrons can be resolved. Every electron that occupies the well contributes to the current by a discrete amount $\Delta I = e/\tau$, where e is the electron charge and τ is the transit time. The width of the resulting current plateaus in bias depends on the spacing in energy of the electronic states in the well. Main contributions to the spacing are the confinement energy and the electrostatic charging energy.

In Fig. 2 (a), a typical small diameter RTD is depicted schematically. Electrons tunnel from the contact regions through the AlGaAs barrier into the quantum well. The electron motion is laterally confined between the diode sidewalls in both contacts and in the quantum well. Thus, one-dimensional subbands are formed in the contacts and discrete zero-dimensional (0D) states are obtained in the well ("quantum dot"). The 0D states can be probed by measuring the tunnel current upon applying a bias between the contacts.

The discrete confinement energy in the well is $E_1 + E_{a,m}$, where E_2 is the energy from the vertical quantum confinement between the barriers. We naively assume that discrete states $E_{a,m}$ result from the lateral surface depletion potential. It is usually modeled using a two-dimensional, circular symmetric parabolic potential with quantum energies $E_{a,m} = (2m + \frac{1}{2})\hbar\omega_0$ with the radial $n = 0, 1, \dots$ and the azimuthal $m = 0, \pm 1, \pm 2, \dots$ quantum numbers. The lateral confinement energies can also be modeled using the hard-wall potential $E_{a,m} = (n^2 + m^2)\pi^2\hbar^2/2md^2$, where d is the well separation. The lateral confinement potential is not necessarily from the surface depletion potential. Particularly in systems with only very few electrons it can result from potential fluctuations [16] and from single impurities [13].

The Coulomb charging energy can be modeled using a single effective capacitance C . This is the usual approach in studies of resonant tunneling in quantum dots [6,7], although recently, it has been noted that electron-electron interactions within the dot can be important [23]. The resonant energies of the quantum dot states can be written as

$$E(n,m,N)_{\text{dot}} = (e^2/C)(N-1/2) + E_1 + E_{a,m} \quad (1)$$

The Coulomb charging energy of the quantum dot filled with N electrons gives the term $(e^2/C)(N-1/2)$ [7]. It can be estimated from the effective dot capacitance C by

$$C = (\epsilon_0 \epsilon_d \pi d^2/4) (b_1^{-1} + b_2^{-1}) \quad (2)$$

The tunnel current for a single electron through the quantum well is given by [10,12]

$$\Delta I = e(\Gamma_1 \Gamma_2 / (\Gamma_1 + \Gamma_2)) \quad (3)$$

where Γ_1, Γ_2 are the tunnel rates through the first and second barrier, respectively. Every time a discrete dot state falls below the Fermi energy in the emitter, a new current step ΔI will occur, leading to a current-voltage staircase. The tunnel rates Γ_1, Γ_2 depend exponentially on the barrier transparency and can be estimated in the WKB approximation by

$$\Gamma = (E_2/\hbar)T(E_2) = (E_2/\hbar) \exp(-(2b/\hbar)\sqrt{2m^*(V_0 - E_2)}) \quad (4)$$

where b is the barrier thickness, V_0 the barrier height, and E_2 the electron energy. Other models are more suitable when considering the influence of temperature and dimensionality of emitter contacts on the shape of the $I(V)$ steps [1, 6,7,8,10, 17]

Figure 2(b,c) shows a schematic band diagram to illustrate tunneling in a laterally confined asymmetric RTD from structure 1. Under reverse bias (Fig. 2(b)), there are 0D states in the accumulation layer at the interface of the thick barrier (box 1) and in the well (box 2). When in resonance, the energies of the 0D states in box 1 and box 2 line up and electrons can tunnel between the 0D states, leading to spikes in the $I-V$ characteristics [21,22]. The tunneling rate Γ_1 through the thick (emitter) barrier is much lower than the tunneling rate Γ_2 through the thin (collector) barrier (i.e., $\Gamma_1 \ll \Gamma_2$), and therefore, at low biases, there is at most one electron at a time in box 2. The spacing of adjacent single particle states $\Delta E_{a,m} = \hbar\omega_0$ is related to the measured spike spacing in bias ΔV_5 through the relation $\Delta V_5 = \hbar\omega_0 \Delta E_{a,m}/e$, where $\hbar\omega_0 = (\hbar^2/2m^*)(b_1^{-1} + b_2^{-1})$ is the fraction of the bias voltage dropped between the emitter and the well. Thus the resonance spacings in bias are related to the 0D single electron spectrum E_n in box 2.

The forward bias situation for tunneling is depicted in Fig. 2 (c). When the 0D states in the well fall below the electrochemical potential in the emitter contact, electrons can tunnel from the 1D subbands in the emitter through the thin barrier (with tunneling rate Γ_2), which is too transparent to form an accumulation layer. If a state below the Fermi energy is empty, an electron can tunnel from the emitter into the well after the time τ . Every electron that occupies the well will tunnel out

of it after a time t_e and thus contribute to the current with a current step ΔI given in eqn (3) ($I_{1,2} = I(t_{1,2})$). Increasing the bias will lead to incremental charging and thus to a current-voltage staircase. If the quantum dot contains N electrons, a current step will occur when an additional electron tunnels into the quantum dot, and the energy of the dot will increase by $\Delta E(N, N+1) = \Delta E_N + \Delta E_Q$. Thus, the plateau widths in bias, $\Delta V_P = \Delta E(N, N+1)/e$, may be larger than the spike spacing ΔV_S in reverse bias, where only the single electron spectrum E_N is probed.

4. RESULTS AND DISCUSSION

4.1. Fine structure at the current threshold

Figure 3(a) shows the $I(V)$ of a diode from heterostructure 1, with conducting diameter $d = 150\text{nm}$. The conducting diameter was estimated by extrapolating the 2D resonance peak current from a larger diameter diode. Since the asymmetry of the $I(V)$ curve is retained compared to Fig. 1, we can assume that the quantum well is charged considerably in forward bias. The interesting feature of this data is the appearance of fine structure at low biases.

In Fig. 3(b), the $I(V)$ curve of a diode from structure 1 with diameter $d = 300\text{nm}$ is shown at low biases. At $T = 4.2\text{K}$ (see inset), a smooth bump is observed at the current threshold in each current direction. At $T = 20\text{mK}$, fine structure in forward bias has developed into a sharp current-voltage staircase, whereas in reverse bias, a complicated sequence of current spikes has appeared. The steps in forward bias have a magnitude between 5pA and 14pA and the plateau widths range in bias between 1mV and 5mV . Spacings of the spikes in reverse bias are $\Delta V_S = 0.5\text{--}1\text{mV}$, i.e., they are an order of magnitude smaller than the plateau widths.

The current steps in forward bias are related to the incremental charging of the well with single electrons. The first current step corresponds to one electron tunneling through the well, the second to two electrons and so on. The magnitude of the current steps depends on t_1 and t_e , which can be calculated using the WKB approximation (see section 3).

The fine structure under low reverse bias seems to indicate that the well is not occupied with electrons between the spikes. The most reasonable explanation for this observation is that the first electron tunnels from discrete states in the accumulation layer at the emitter-barrier interface (box 1 in Fig. 2(b)). This is in accord with experimental data obtained from double quantum dot structures (21). The current step at -35mV may result from a second electron tunneling through box 2. It is not clear, however, why the magnitude of current spikes in reverse bias is larger than in forward bias, because the transit time should be smaller.

The smaller spacing of spikes as compared to the plateau widths is in qualitative agreement with the assumption that in reverse bias charging effects do not contribute, because only one electron occupies the well at a time. The fine structure in reverse bias contains information on the single-electron spectrum in box 2.

4.2. Diameter dependence

It was discussed in section 3 that both confinement energy and charging energy decrease with increasing quantum box size. We want to investigate if we can control this confinement by changing the diode diameter d . This control should be possible if the lateral confinement is dominated by the surface depletion potential of the diode sidewalls (2).

Figure 4 shows the $I(V)$ of four diodes from structure 1 with different conducting diameters 150nm , 300nm , and $10\mu\text{m}$ as a function of applied bias. In forward bias (Fig. 4(a)), the current displays sharp steps above the threshold voltage for all four diodes. Magnitudes of current steps are about 10pA for the 150nm and 300nm diameter diodes, and about 5pA for the $10\mu\text{m}$ device, i.e., there is only a very weak dependence on diode diameter. It is remarkable that nearly the same current steps are observed for diodes that differ in area by more than three orders of magnitude. This result shows that current steps are dependent on the heterostructure profile and clearly supports our model of single electron tunneling eqn (3) in which the magnitude of current steps is independent of the area of the diode. The value of the first current-step calculated using the WKB approximation (section 3) is $\Delta I = 15\text{pA}$. We have used eqn. (3), the values for b_1 , b_2 , w , b_0 (from Table 1 for structure 1), $V_0 = 250\text{meV}$ (for $x = 0.3$), and assumed linear voltage drop over the double-barrier profile. The calculation is in good agreement with the experimental current steps ΔI with $d = 10\mu\text{m}$. In the Coulomb blockade model a plateau width of a few mV (see Fig. 4(a)) implies a capacitance of the order 10^{-16}F and thus according to eqn (2) a diameter $d = 160\text{nm}$. Similar considerations hold when the plateau width is interpreted as related to lateral quantization. This result clearly favours an explanation in terms of localized states within the well (maybe due to potential fluctuations) and will have to be subject to further investigations. It can also be seen in Fig. 4 that the current threshold decreases with diode diameter, and at $d = 10\mu\text{m}$ it is just above zero bias. This latter observation will lead us below to argue in favour of a model of lateral confinement from potential fluctuations.

In reverse bias, the spike-like $I(V)$ fine structure is retained for all diode diameters. This observation supports our model, that electrons tunnel from fully quantized emitter-states into the well-quantum dot. The fine structure is difficult to quantify, but we cannot see any clear diameter dependence of the magnitude or spacing of spikes. Again we observe the decrease of the current threshold with increasing diode diameter.

4.3. Dependence on barrier thickness and symmetry

The tunnel current for a single electron through the quantum well is given by eqn (3). Therefore, we can use the experimental dependency of current step magnitudes on barrier thickness to test our model of single electron tunneling (eqn (3)) even further.

We have studied the dependence of current step magnitudes of four diodes with barrier thicknesses $b = 4\text{nm}$, 5nm , 7nm (nearly symmetric) and $b = 10\text{nm}$ (thicker barrier of the

asymmetric structure 1). All diodes have different diameters d , because the lateral confinement is difficult to control by processing. In Fig. 5, the first current step is plotted for four diodes with different barrier thicknesses b . The offset in bias has been changed for clarity. The temperature is $T=20\text{mK}$.

The magnitude of current steps decreases exponentially with barrier thickness. This is in agreement with eqn (3) for ΔL and eqn (4) for the tunnel rates. The experimental current steps are 5-10pA, 0.5nA, 12nA, and 50nA for barrier thicknesses 10nm, 7.1nm, 5nm, and 4.3nm, respectively (compare with table 1). The corresponding values calculated using the WKB approximation and parameters from table 1 are 15pA, 2nA, 18nA, and 50nA. While there is good agreement between experiment and theory, we can say that the dependency on barrier thickness supports the model of single-electron tunneling (eqn (3)). Other numerical calculations [9] show that in most cases, quantitative agreement is obtained between theory and model.

It is noteworthy that the structures 3 and 4 with thin barriers exhibit current steps in both bias polarities. This is to be expected, since barrier transparency is too high to allow an accumulation layer to be formed at the emitter-barrier interface.

4.4. Tunneling in high magnetic fields

The quantum dot resonance spectrum exhibits a very characteristic dispersion as a function of the magnetic field which is suited for modeling the energetics of the OD states. Alternatively, the OD states can be studied by tuning the lateral confinement using side gates, but this approach is much more problematic [13,14]. Finally, it is very difficult to process devices in which the electric field only squeezes the quantum dot and not the contact regions. Secondly, the complicated electrostatics makes a clean calibration between gate-voltage and confinement energy very difficult. All these problems can be circumvented by using magnetic fields to tune the OD states.

We have studied a large number of quantum dot diodes with various diameters, barrier and well thicknesses and doping profiles in high magnetic fields. The fine structure often exhibits different phenomena for each sample which are difficult to interpret. Here, we will discuss one interesting sample to describe typical problems we had to deal with during our investigations.

The data was obtained from an 83nm diameter R1-1 from structure 3 [16]. The current-voltage characteristics in a magnetic field parallel to the current direction are shown in Fig. 6 (a). Figure 6(b) shows resonance positions in forward bias as a function of magnetic field B applied parallel to the current direction. With increasing magnetic field, all steps shift to higher bias following a parabolic shape. This is in contrast to single electron theories for two-dimensionally and three-dimensionally confined, nearly cylindrical quantum boxes in magnetic fields [24] where some states increase in energy with B , while others decrease. In high magnetic field, the experimental traces run parallel to $V \propto (1/\eta)(\hbar\omega_c/2)$, with $(\hbar\omega_c/2)$ being the cyclotron frequency. The cross-over to the linear increase occurs at around $B=6\text{T}$. The lateral quantum confinement can thus be estimated to be in the order of the magnetic length $l_0 = \sqrt{\hbar/eB} = 10\text{nm}$. This strong

confinement implies quantum energies in the order of $\sim 20\text{meV}$, which is much greater than the energy $\Delta E = \eta \Delta V = e(0.3855\text{V} - 12\text{mV}) = 2.5\text{meV}$ obtained from the plateau widths. We therefore propose that electrons tunnel into laterally separated minima of a disorder potential in the quantum dot [16, 19].

In the circular symmetric, two-dimensional harmonic oscillator model, the eigenvalues are [21]

$$E(3)_{n,m} = (2n+4m+1)(\hbar\omega_c/2)^2 + (\hbar\omega_c/2)^2/2 + m(\hbar\omega_c/2) \quad (5)$$

We can fit the data in Fig. 6(b), using the formulas for the energy eqns (1), (2) and (5). Assuming that electrons occupy the lowest states with $n=m=0$ in the minima, we can fit several curves and obtain confinement energies between 9-35meV (for $\eta=0.3855-0.5$). The minima might arise from potential fluctuations in the central region which result from single impurities sitting in the well or from randomly distributed donors in the contacts (i.e., beyond the spacer layers, in a similar way as has been described for high mobility heterojunctions [25]). The parallel shift of the resonances with magnetic field suggests that the lateral extension of the wavefunctions of $d=10\text{nm}$ in all the states are about the same.

The model corroborates with the data obtained from the diameter dependence of the I(V) fine-structure in Fig. 4. With increased diode diameter, the probability for lower energy minima to occur in the disorder potential increases, resulting in lower bias current thresholds. For tunneling through such a low lying state the effective barrier height is increased and current steps are decreased according to eqn (3).

We note that in other data, many new and interesting phenomena can be observed which still have to be investigated in detail. It is therefore quite conceivable that a device can be processed that clearly exhibits all the electronic properties that are expected in a model of lateral confinement from surface depletion, as was observed in [2]. We can thus identify lateral quantum confinement from surface depletion, potential fluctuations from randomly distributed donors, and single impurities

4.5. Temperature Dependence

The temperature dependence of the shape of the fine-structure resonances is still controversial. In Fig. 7, a typical plot of the resonances arising in the low bias differential conductance-voltage (G(V)) characteristics is plotted for temperatures between $T=4.2\text{K}$ and $T=20\text{mK}$. The diode was processed from structure 3 and has a conducting diameter of 83nm. The two plots at $T=4.2\text{K}$ and $T=1.25\text{K}$ were taken in a conventional He^4 cryostat, whereas the other data was taken in a dilution refrigerator (T is the temperature of the mixing chamber).

The linewidth of the G(V) resonances is broadened as T increases. Raising the temperature causes a broadening of the Fermi energy in the emitter contact. Therefore, thermally excited electrons will contribute to the tunnel current and broaden the observed resonant structure. If the

thermal broadening $k_B T$ exceeds the spacing of the discrete electronic states in the quantum dot ΔE_{nm} and ΔE_C , resonance structures cannot be resolved anymore.

At $T=20\text{mK}$, the linewidth of the lower bias resonances is $\Delta V=3\text{mV}$. This corresponds to an energy broadening of $\approx 1.5\text{meV}$ which is more than one order of magnitude larger than the electron-state lifetime and the broadening of the Fermi energy in the contacts ($k_B T=0.086\text{meV}$ at 1K). The electron state lifetime of the 0D states of this diode are in the order of 0.1meV (which is consistent with the current step-height). It has been suggested by the authors that inelastic scattering may cause this broadening [9]. But it has not been possible to present a convincing model to explain the detailed broadening mechanism so far. Su *et al.* [12] suggested that the broadening may be due to electrical noise pick-up. However, it is difficult to understand how electrical noise pick-up leads to a linewidth broadening of 1.5meV ($k_B T=1.5\text{meV}$ corresponds to $T=17\text{K}$). The problem of the linewidth broadening will have to be addressed in future investigations.

5. CONCLUSIONS

A single electron that tunnels through a double-barrier potential has a well defined transit time τ and therefore it contributes to the tunneling current by a discrete amount $\Delta n=e/\tau$. We have observed the incremental charging of the double-barrier diode with single electrons by measuring the tunneling current increasing from zero in current steps with magnitude ΔI . Increasing the transmission by decreasing the barrier thickness leads to correspondingly smaller current steps. In good accord with simple model calculations. The step-like $I(V)$ is therefore a clear demonstration of single-electron tunneling.

Much more problematic is our understanding of the energetics involved. We have shown that the plateau-widths in bias of the current steps can explain the lateral confinement energies and electrostatic charging energies for submicron diameter quantum dot diodes. However, fine-structure was also observed in much larger diameter diodes. The plateau widths in that data was an order of magnitude too big to explain confinement or charging effects. High magnetic field data suggested that electrons in the lowest states are laterally confined to only $d=10\text{nm}$. From this, we have concluded that lateral confinement is due to a disorder potential. The drawback is that presently we cannot control this disorder potential. Therefore, our target is to find a way to control lateral confinement as well as we can control vertical confinement. Possible improvements could be obtained by decreasing the impurity concentration by growing smoother barrier interfaces, and by reducing the surface damage during reactive ion etch.

In conclusion, we have shown that submicron diameter RTDs are very promising devices to study the electronic properties of quantum boxes containing only very few electrons. However, we have to improve the experiment with respect to the purity of the heterostructures in order to eliminate potential fluctuations and impurities from the dot. This could be achieved by reducing the impurity concentration in the well, surface roughness and sidewall damage.

Tunneling in small RTDs allows us to study the energetics in the limit of very few electron systems [23]. They allow also the observation of excited states [8]. Furthermore, the coupling of two or more dots (molecules or 1D crystals) can be investigated. For all these interesting experiments, this system continues to be a very promising candidate.

This work has been supported by the Science & Engineering Research Council (SERC). M.T. acknowledges support from the Commission of the European Communities and a Charles and Katherine Darwin Fellowship of Darwin College, Cambridge. L.M.M. acknowledges the Spanish Ministerio de Educaci3n y Ciencia for support. J.T.N. is supported by the Leventhal Trust and the I. Newton Trust.

REFERENCES

- (a) Present address: Max-Planck-Institut für Festkörperforschung, Heisenbergstr. 1, W-7000 Stuttgart 80, Germany.
- (b) Present address: Instituto de Ciencias de Materiales, Consejo Superior de Investigaciones Científicas, Universidad Autónoma de Madrid, 28049 Madrid, Spain.
- (c) Present address: Department of Physics, University of Surrey, Guildford, Surrey GU2 5XH, England.
- (d) Also at the Toshiba Cambridge Research Centre, 260 Cambridge Science Park, Cambridge CB4 0NE, England.
- (1) Marc A. Kastner, *Physics Today*, Jan 1993, 25.
- (2) M.A. Reed *et al.*, *Phys Rev Lett* 60, 335 (1988); *Festkörperprobleme, Advances in Solid State Physics* 29, p. 267 (1989).
- (3) C.G. Smith *et al.*, *J Phys C: Solid State Phys* 21, L893 (1988).
- (4) Ch. Skierka and U. Merkt, *Phys Rev Lett* 62, 2164 (1989); T. Denzel *et al.*, *Phys Rev Lett* 64, 748 (1990); A. Lorke, J.P. Kotthaus, and K. Ploog, *Phys Rev Lett* 64, 2559 (1990).
- (5) T.A. Fulton and G.J. Dolan, *Phys Rev Lett* 59, 109 (1987); J.B. Barner and S.T. Ruggano, *Phys Rev Lett* 59, 807 (1987); I. Glaves and H.B. Zeller, *Phys Rev Lett* 28, 1504 (1983); J. Lenz and R.C. Jaklevic, *Phys Rev Lett* 23, 1371 (1969); reviewed by D.V. Averina and K.K. Lukharov, *Microscopic Phenomena in Solids*, edited by B. Altshuler, P.A. Lee, and R.B. Webb (Elsevier, Amsterdam, 1991), p. 169.
- (6) H. van Houten and C.W.J. Beenakker, *Phys Rev Lett* 63, 1993 (1989); L.J. Glasman and R.I. Shubner, *J. Phys Condens Matter* 1, S811 (1989).
- (7) Almasi Gruber, *Phys Rev* 42, 3895 (1990); C.W.J. Beenakker, *Phys Rev* 44, 1646 (1991).
- (8) P.L. McEuen *et al.*, *Phys Rev Lett* 64, 1926 (1991); A.T. Johnson *et al.*, *Phys Rev Lett* 68, 89 (1992); see also in this context U. Meirav, M. Kastner, and S.J. Wind, *Phys Rev Lett* 68, 771 (1990); L.P. Kouwenhoven *et al.*, *J. Phys B* 25, 507 (1991).
- (9) J. Weis, R.J. Haeg, K. von Klitzing, K. Ploog, *Phys Rev* 44, 12837 (1992).
- (10) M. Tewordt *et al.*, *J Phys Condens Matter* 2, 8969 (1990); *Appl Phys Lett* 59, 1966 (1991); *Phys Rev* 3 45, 14407 (1992).
- (11) S. Tanaka and Y. Huryama, *Phys Rev* 43, 9373 (1991).
- (12) B. Su, V.J. Goldman, M. Santos, N. Shayeghan, *Appl Phys Lett* 58, 747 (1991); B. Su, V.J. Goldman, J.E. Cunningham, *Science* 255, 313 (1992); *Phys Rev* 46, 7644 (1992).
- (13) M.W. Dellow *et al.*, *Phys Rev Lett* 68, 1754 (1992).
- (14) P. Guertel, N. Blane, R. Germain, H. Rohszen, *Phys Rev Lett* 68, 1896 (1992).
- (15) A. Rindani, G. Farn, and L. Lamm, *Phys Rev* 46, 3948 (1992).
- (16) M. Tewordt *et al.*, *Phys Rev* 46, 3948 (1992).
- (17) G. Garnett, W. Bryant, *Phys Rev* 39, 3145 (1989), 44, 12837 (1991).
- (18) D.V. Averina, A.N. Korolov, and K.K. Lukharov, *Phys Rev* 44, 6199 (1991).
- (19) R.C. Ashoon *et al.*, *Phys Rev Lett* 68, 3068 (1992); see also W. Hansen *et al.*, *Phys Rev Lett* 62, 2168 (1989); R.J. Silbey and R.C. Ashoon, *Phys Rev Lett* 64, 1591 (1990).
- (20) A. Zaitsev *et al.*, *Appl Phys Lett* 63, 1408 (1993).
- (21) M. Tewordt *et al.*, *Appl Phys Lett* 60, 595 (1992).
- (22) G. Garnett, W. Bryant, *Phys Rev* 44, 1064 (1991).
- (23) G. Garnett, W. Bryant, *Phys Rev Lett* 59, 1140 (1987); N.F. Johnson and M.C. Payne, *Phys Rev Lett* 67, 1157 (1991); U. Merkt, J. Hauer, and M. Wagner, *Phys Rev* 43, 7120 (1991).
- (24) C.G. Darwin, *Proceedings of the Cambridge Philosophical Society* 27, 86 (1930); V. Fock, *Z Phys* 47, 446 (1928).
- (25) J.A. Sison and J.H. Davies, *Phys Rev* 41, 7929 (1990).

Structure	Barrier width (nm)	Spacer (nm)	Layer (nm)	Layer (nm)
(1)	100	1.4	7	0.02
(2)	7.1(7.1)	5.5	3	-1.5
(3)	5.0(5.2)	5.5	3	-1.5
(4)	2.1(2.3)	6.1	3	-1.5

a Top (bottom) barrier.
b Doping of contacts close to the spacer layers.

TABLE 1. Summary of the double-barrier heterostructures.

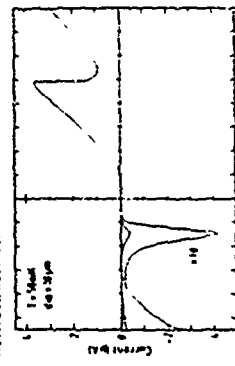


FIG. 1. (a) $I(V)$ characteristics of a large diameter asymmetric double-barrier diode from structure 1.

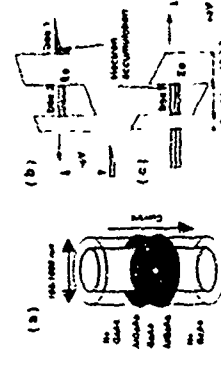


FIG. 2. (a) Schematic sketch of a submicron-diameter double-barrier diode. (b) Band diagram of structure 1 under reverse and (c) under forward bias.

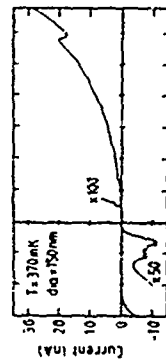


FIG. 3. (a) $I(V)$ characteristics of a 150nm diameter asymmetric RTD from structure 1 at $T=350\text{mK}$.

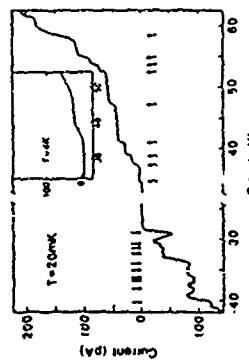


FIG. 3. (b) $I(V)$ at $T=20\text{mK}$ of a 300nm diameter RTD from structure 1 at low current levels, showing in forward bias the incremental charging of the quantum dot with single electrons, starting from zero. The inset shows that the steps are washed out at $T=4.2\text{K}$. In reverse bias, tunneling between two quantum dots in series is observed.

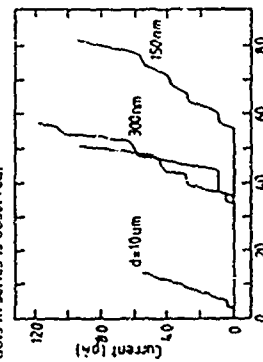


FIG. 4. (a) $I(V)$ of four diodes from structure 1 with conducting diameters 10nm, 300nm, 300nm, and 150nm, in forward bias.

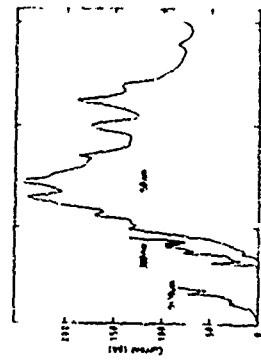


FIG. 4. (b) as (a), but in reverse bias.

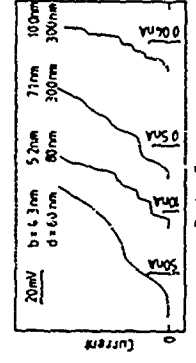


FIG. 5. $I(V)$ of four diodes structure 1-4 with increasing barrier thickness b and various electronic diameters d . The current steps decrease with increasing barrier thickness.

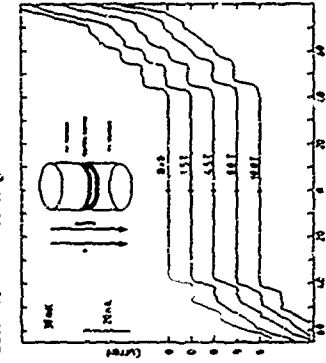


FIG. 6. (a) $I(V)$ characteristics of a symmetric RTD from structure 3 with a conducting diameter of 8nm, as a function of magnetic field applied parallel to the current direction.

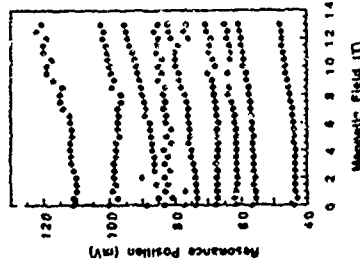


FIG. 6. (b) Positions of the resonance peaks in bias vs. magnetic field according to (a).

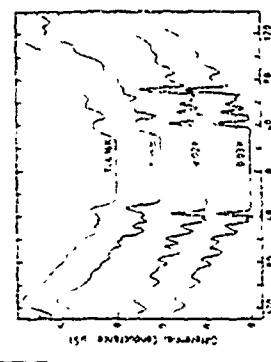


FIG. 7. Temperature dependence of the $dI(V)/dV$ characteristics of a symmetric RTD structure 3 with $d=8\text{nm}$.

TuB2

Hydrostatic Pressure Sensors Based on Solid State Tunneling Devices

H. Brugger and U. Meiners
Deutscher-Benz AG, Forschungszentrum Ulm, D-89081 Ulm, Germany
 R. Ditzel, T. Suter¹⁾, and E. Gornik
Walter-Schottky-Institut, TU München, D-85748 Garching, Germany
 A. Forster and H. Lüth
Institut für Schicht- und Ionentechnik, D 52425 Jülich, Germany

Abstract:

A new type of a hydrostatic pressure sensing device based on a thin AlAs/GaAs/AlAs double-barrier resonant tunneling (DBRT) structure is reported, which operates at room temperature. The current swing (ΔI) in the negative-differential resistance region depends linearly on the applied pressure (p). Diodes with an operating range of $\Delta p = 6000$ bar (12 000 bar) and a high sensitivity of $170 \times 10^{-3} \text{ kbar}^{-1}$ ($85 \times 10^{-3} \text{ kbar}^{-1}$) are realized with an AlAs barrier layer thickness of 2.3 nm (2.3 nm). Pressure sensing at 300 K is enabled by an elastic electronic tunneling process through the Γ -DBRT conduction band profile in combination with a sensitive pressure-dependent inelastic tunneling process through the transversal X-valleys in the AlAs barriers. The applied pressure decreases the GaAs/AlAs Γ -X discontinuity and yields to a significant enhancement of the valley current. The pressure coefficient ($\Delta I/\Delta p$) and operating range (Δp) can be adjusted by a variation of the AlAs barrier thickness.

1. Introduction

Double barrier resonant tunneling (DBRT) structures have been investigated intensively both for studying physical processes and for the development of novel device applications, mainly driven in direction of extremely high-speed electronic operations [1, 2, 3]. In the AlGaAs/GaAs material system the maximum achievable peak-to-valley current ratio (PVCr) values are limited by significant tunneling contributions through the indirect band-gap X-states in the AlGaAs barrier material ($\kappa > 0.4$) in addition to the resonant current, which is determined by the Γ -conduction band profile. Hydrostatic pressure [4, 5, 6] and uniaxial stress [7] experiments have been performed by different groups to study the influence of the tunneling conduction band minimum on the tunneling characteristics of AlAs/GaAs/AlAs DBRT structures at helium and liquid nitrogen temperatures.

In this paper a room temperature operating AlAs/GaAs/AlAs DBRT-diode pressure sensing device is reported which takes advantage of the two tunneling channels through AlAs barriers, elastic (through

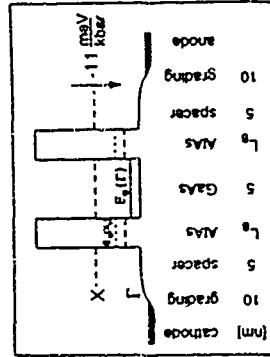


Figure 1. DBRT conduction band alignment for the direct Γ - (solid line) and indirect X- (broken line) valley minima. $E_g(\Gamma)$ and $E_g(X)$ are the first quasi-bound energy levels in the GaAs and AlAs QWs, respectively.

Γ - Γ band profile) and inelastic (through Γ -X band profile). DBRT structures with a GaAs quantum well (QW) of 5 nm thickness and with AlAs barriers of thickness (L_B) in the range between 6 monolayers (6 ML, 1.7 nm) and 10 ML (2.8 nm) are realized. There is strong evidence of a significant Γ -X tunneling contribution through the X-valley states in AlAs, which influences the IV characteristics. Applied hydrostatic pressure (p) yields to a decrease of the GaAs/AlAs Γ -X band offset and leaves the DBRT Γ - Γ profile almost unchanged. The dominant effect is an increase of the valley current density (j_v) and consequently a decrease of the PVCr. When the diodes are biased close to the negative-differential-resistance (NDR) region a linear behavior between the NDR current swing (ΔI) and the applied hydrostatic pressure (p) is observed. Spiking diodes with constant room temperature pressure sensitivities $S = \Delta I/\Delta p = 170 \times 10^{-3} \text{ kbar}^{-1}$ and $S = 85 \times 10^{-3} \text{ kbar}^{-1}$ over an operating range of $\Delta p = 6000$ bar and $\Delta p = 12000$ bar, respectively, are realized.

2. Layered Structure and Device Fabrication

The vertical layer sequence of the DBRT structure consists of two thin AlAs barriers with thickness L_B and a 3 nm thick GaAs quantum well (QW) grown by MBE in a VARIAN ModGen II system on (100) oriented n⁺-doped ($2 \times 10^{18} \text{ cm}^{-3}$) GaAs substrates. This is schematically shown in Figure 1 together with the conduction band profile. On both sides next to the DBRT structure 5 nm thick spacer layers and 10 nm thick dopant grading layers are used between the undoped DBRT layers and the 0.5 μm thick highly doped ($6 \times 10^{18} \text{ cm}^{-3}$) electrode regions.

The samples were grown at a fixed substrate temperature of $T_s = 600^\circ\text{C}$ (pyrometer measurement). The growth was interrupted at the normal interface (AlAs on GaAs) for 60 sec before the deposition of the AlAs layers in order to improve the morphological quality at the interfaces. From cross-sectional high-resolution TEM micrographs a roughness of only a one-monolayer fluctuation at these interfaces with large area terraces is observed. Highest PVCr values of 5 at 300 K are achieved on this type of samples with $L_B = 6 \text{ ML}$ [8]. Layer thicknesses were accurately established by measuring RHEED oscillations on reference samples prior to the DBRT growth.

Device structures were fabricated by a standard lift-off process. Top side (cathode) circular contacts with a diameter between 12 μm and 20 μm and a large area backside (anode) contact were fabricated by alloyed Ge/Au, followed by a Ti/Au initialization for the bonding pads. The diodes are isolated by wet chemical mesa etching. The wafers were mechanically thinned below 100 μm thickness and diced in small squares. The chips were mounted on a gold plated ceramic carrier by a highly conducting and ductile two-component silver filled epoxy resin. The diodes were bonded by 10 μm thick gold wires. Reliable ohmic contacts were realized and the diode chips are carefully fixed to avoid any stress in the semiconductor material for operating temperatures between 2 K and 400 K and for pressure values up to 13 000 bar.

Device performance was investigated at room temperature with the diodes inside a UNIPRESS pressure-cell. Hydrostatic pressures up to 13 kbar were applied with light-petroleum as a pressure-transmitting fluid. The pressure values were monitored by a calibrated highly Te-doped InSb sensor. The current/voltage (IV) behavior was measured in a pulsed mode to avoid thermal effects.

3. Experimental Results

In Figure 2 a series of room temperature IV-curves at different applied hydrostatic pressure values between $p = 0$ (atmospheric pressure) and $p = 7$ kbar is shown for a diode with an AlAs barrier thickness of $L_B = 10 \text{ ML}$. The electron flow direction was from the emitter top contact towards the collector substrate side. A monotonic enhancement of the peak current (j_p) and an exponential increase of the valley current is observed with increasing ambient pressure. This yields to a non-linear decrease of the PVCr which disappears completely for $p = 6$ kbar. The

¹⁾ on leave from UNIPRESS Warsaw (Poland)

The conduction band profile of the $\text{AlGa}_{0.5}\text{As}/\text{GaAs}$ DBRT structure is shown schematically in Figure 1. From a transfer matrix calculation the first electron subband in the GaAs QW is expected to be $E_{\text{g}}^{\text{GaAs}} = 103 \text{ meV}$ above the bottom of the conduction band. There is only a minor influence of the $E_{\text{g}}^{\text{GaAs}}$ on barrier thickness for E_{g} in the range between 6 and 10 meV. The AlAs Γ -band minimum and the X-valley minimum are assumed to be 1.05 eV and 160 meV above the GaAs Γ -conduction band, respectively, and the indirect X-band minimum in GaAs to be 450 meV above the Γ -conduction band. For the X-valley electrons the AlAs layers are a barrier. From a simple square-well box model calculation the first allowed subband of degenerate transversal valleys in the conduction band of the nonpolar GaAs layer is expected to be 10 meV above the conduction band minimum in GaAs. The interface is accepted to be perpendicular to the growth direction.

SECRET

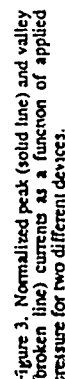


Figure 3. Normalized peak (solid line) and valley (broken line) currents as a function of applied gate voltage for two different devices.

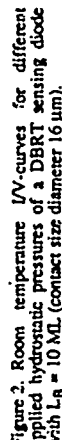


Figure 2. Room temperature I/V-curves for different applied hydrostatic pressures of a DBRT sensing diode with $L_A = 10 \text{ }\mu\text{m}$ (contact size diameter $16 \text{ }\mu\text{m}$).

The applied hydrostatic pressure leaves the DBRT Γ -profile almost unchanged but the Γ -X offset energy decreases linearly with p with a rate between -11 meV/kbar [9] and -12 meV/kbar [10, 11]. This enhances the non-resonant tunneling current through the A1As X-valleys which pushes mainly the valley current in the DBRT structures to higher values. Diniz et al. [12] have shown that tunneling through the four-fold X₁-valleys predominates at room temperature while at helium temperature tunneling through the two-fold X₁-valleys dominate the non-resonant current contribution.

Figure 3. Normalized peak (solid line) and valley (broken line) currents as a function of applied pressure for two different devices.

Figure 3. Normalized peak (solid line) and valley (broken line) currents as a function of applied gate voltage for two different devices.

L_B (ML)	j_p (kA/cm ²)	V_p (V)	PVCR	S (kbar ⁻¹)	Δp (kbar)
10	5	0.3	1.9	0.17	6
8	20	0.4	3.1	0.09	12
6	60	0.4	5.0	0.06*	>13*

c) pressure range limited by the experimental setup, non-linear $\Delta f(p)$ behavior for $p > 10$ kbar.

In Figure 3 the normalized room temperature current densities as a function of applied pressure are shown for two different sensor devices consisting of a DBRT diode with $L_B = 10$ nM (data from Figure 2) and $L_B = 8$ nM. For the thinner barrier device the current density with significantly lower rates as a function of p . This is attributed to the lower non-resonant X-tunneling contribution in thinner AIA's layers. This allows the $L_B = 8$ nM device to operate over a larger pressure range up to 12 kbar. In Tab. 1 the diode parameters of investigated samples are summarized. The highest operating pressure range of more than 13 kbar (limited by our experimental setup) was observed for a $L_B = 6$ nM (1.7 nm) diode. On this thin-barrier sample the influence of the X-tunneling contribution is rather small and the peak current already decreases slightly with applied pressure [12]. A decrease of the tunneling currents is expected from a pressure-induced increase of the tunneling electron mass. On the sample with $L_B = 8$ nM (see Figure 3) there was no resultant variation of $j_0(p)$ found. This is advantageous for device applications, because a change of j_0 can be used to monitor any additional extrinsic parameter, e.g. the ambient temperature.

The influence of electron-mass-induced and the Γ -X barrier-height-induced change of the current densities as a function of p was estimated quantitatively on the basis of a resonant tunneling model, neglecting any thermionic effects [12]:

$$\cdot v(p)/p, v(0) = \exp(-\alpha(0)) [m^*(0) \cdot \frac{1}{2} \frac{dm^*}{dp} + v(0) \cdot \frac{1}{2} \frac{dv}{dp} p] \quad (1)$$

with $j(0)$ as the zero pressure current density, $\alpha(0) = i_{\text{p}} \sqrt{8\pi^* m^* V(0)/h^2}$ as the transmission coefficient, $V(0)$ as the effective Γ -X barrier height at $p = 0$ bar, and $dV/dp = -1.1$ meV/bar. Equation (1) was obtained under the assumption that at resonant bias the emitter-barrier-side transmission coefficient (α_E) dominates the tunneling characteristics over the collector-barrier-side one ($\alpha_C \gg \alpha_E$).

The dominating effect in Equation (1) is the second term. For the $L_p = 10$ ML sample one obtains for the valley current component $j(v)/v(0) = \exp(\alpha n k \text{bar})$ with $\alpha = 0.15 \text{ kbar}^{-1}$ by using the transversal X-valley mass of $m^*(X_v) = 0.2 m_0$. This is in excellent agreement with a fit using the experimental data which yields $\alpha = 0.16 \text{ kbar}^{-1}$. For comparison, a significantly higher pressure sensitivity ($\alpha = 0.39 \text{ kbar}^{-1}$) would be expected from equation (eqn (1)) for the 10 ML sample tunneling through the longitudinal X-valley is considered ($m^*(X_l) = 1, 1 m_0$).

For thinner barrier samples $\alpha(V/V(0))$ is reduced and yields to a lower contribution of the elastic tunneling component in agreement with the observed behavior on samples with thinner interlayers and otherwise identical material properties. As a consequence, we conclude that the dominant pressure sensing mechanism at room temperature is the pressure-induced non-resonant tunneling through the low-mass transversal valleys (X_c) in the AlAs barriers.

References

1. F. Capasso, *Physics of Quantum Electron Devices*, Springer Series in Electronics and Photonics, vol. 28, Berlin (1990).
2. L.L. Chang, E.E. Mendez, and C. Tejedor, *Resonant Tunneling in Semiconductors: Physics and Applications*, Plenum, New York (1991).
3. E.R. Brown, *High Speed Resonant Tunneling Diodes*, in *Heterostructure and Quantum Devices*, ed. by N.G. Einspruch and W.R. Frenley, Series VLSI Electronics: Microstructure Science (1993), in press.
4. E.E. Mendez, E. Calleja, and W.J. Wang, *Appl. Phys. Lett.* 53, 977 (1988).
5. R. Pritchard, D.G. Austing, P.C. Klippenstein, J.S. Roberts, A.W. Higgs, and G.W. Smith, *J. Appl. Phys.* 68, 205 (1990).
6. Z. Obaman, A.J. Peck, S.J. Bending, G.A. Saunders, M. Rollman, K. Ploog, and S.S. Lu, *J. Appl. Phys.* 70, 1548 (1993).
7. H. Brugger, U. Meiners, C. Wolk, R. Deufel, J. Schroth, A. Forster, and H. Lüth, *Proc. 13th Int. IEEE/Cornell Conf. on Advanced Concepts in High Speed Semiconductor Devices and Circuits*, pp. 39-48 (1991).
8. S. Adachi, *J. Appl. Phys.* 38, R1 (1985).
9. A.R. Goni, K. Strömsner, K. Syassen, Y.C. Lu, and E. Bauer, *Phys. Rev. B* 44, 2985 (1991).
10. K. Reimann, M. Holtz, K. Syassen, Y.C. Lu, and E. Bauer, *Phys. Rev. B* 44, 2985 (1991).
11. R. Ditz, J. Smoliner, E. Gornik, U. Meiners, H. Brugger, P. Wisniewski, and T. Cusk, *Semiconductor Science and Technology* 8 (1993), in press.
12. H. Brugger, U. Meiners, A. Forster, and H. Lüth (to be published).
13. W.F. Sherman and A.A. Stadtmüller, *Experimental Techniques in High Pressure Research*, John Wiley, Chichester (1987).

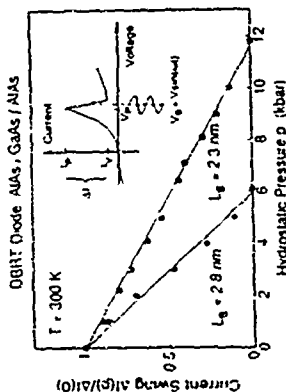


Figure 4. Hydrostatic pressure sensor characteristics for two different devices operating at room temperature.

The peak current is mainly dominated by resonant tunneling contributions. The role of X-tunneling is more complicated. The experimental results indicate an influence with applied pressure but with a less pronounced rate (see Figure 3). This suggests that both F-X and F-F related mechanism contribute to J_p . Continuously improved PVCR values were observed by reducing the barrier thickness up to maximum values of 5 (12) at 300K (77K) respectively for $L_g = 6$ nm. These are the highest observed values in standard $AlAs/GaAs/AlAs$ DBRT structures. However, for $L_g \leq 6$ nm the PVCR decreases again due to the broadening of the resonance level $E_0(F)$ inside the $GaAs$ QW [13].

Figure 4 shows the measured normalized current swing $\Delta I = J_p \cdot \Delta p / J_p(1 - 1/PVCR)$ as a function of applied pressure. A linear dependence of ΔI vs p is observed. A constant pressure sensitivity over the whole operating pressure range is useful for device applications. The sensor diode with a 10 ML thick barrier exhibits a maximum operating range of $\Delta p = 0$ kbar with a sensitivity of $S = 170 \cdot 10^{-3} \text{ kbar}^{-1}$. The 8 ML diode has a 12 kbar operating range with $S = 85 \cdot 10^{-3} \text{ kbar}^{-1}$. The inset shows schematically the I/V-curve of a DBRT sensing diode. The device is biased close to the NDR region. Oscillations are avoided by a stabilizing network. With an amplitude-modulated ac-signal a convenient and accurate measurement of the current swing ΔI is achieved. There is no need of an absolute current or voltage measurement.

4. Conclusion

The use of DBRT structures as hydrostatic pressure sensing elements operating at room temperature has been demonstrated. There is strong evidence for a non-resonant tunneling through the transversal X-valleys in thin-barrier $AlAs$ layers which enables pressure sensing. A constant pressure sensitivity is observed over a pressure range of more than 10 kbar. The NDR current swing shows a linear dependence on the applied pressure.

Presently used electrical high-pressure gauges are coils of fine cermet (a) and manganin (b) wires and InSb (c) manometer. The electrical resistance varies with applied pressure. Room temperature sensitivity values are in the range between $1.5 \cdot 10^{-3} \text{ kbar}^{-1}$ (a) and $34 \cdot 10^{-3} \text{ kbar}^{-1}$ (c) [14]. The DBRT diode achieves $S = 170 \cdot 10^{-3} \text{ kbar}^{-1}$ over a 6 kbar range. This is more than a factor of 5 more sensitive in comparison with commercially available electrical sensors.

Acknowledgement

The work was partially supported by the Bundesministerium für Forschung und Technologie (Bonn, Germany) under contract numbers NT 2754 2 and TK 03687. One of us (R.D.) thanks CNPq (Brazil).

TuB3

REALIZATION OF A NOVEL RESONANT TUNNELING HOT ELECTRON TRANSISTOR COMPLETION OF ULTRASONIC RESONANT TUNNELING AND ENERGY RELAXATION

C. H. Yang and R. A. Wilson

Department of Electrical Engineering, Joint program of advanced electronic materials, Laboratory for physical sciences, University of Maryland, College Park, MD 20742, U.S.A

ABSTRACT: We report a novel three-terminal hot electron transistor, where, at 77K, the transistor output characteristics can display novel features, including the negative differential resistance, extremely large peak-to-valley ratio, and a dc current gain. The operation of this novel transistor is based on quantum tunneling. The emitter injects hot electrons to the second lowest subband of a thin (100 Å) quantum well, and these non-thermalized hot electrons will then either resonantly tunnel to the collector or relax to the lowest subband and contribute to the base current. The resonant-tunneling probability of hot electrons between the emitter and the collector can be switched almost completely on and off, when either the base or the collector bias is swept. The new characteristics are shown to have application to dense logic circuits.

Hot electron transistors (HETs) are expected to have applications in ultrafast electronics [1], since the non-thermalized hot electrons can traverse at high speed in semiconductor for a relatively long distance. Because of the many advantages, recent experimental works [2-5] have been primarily focused on semiconductor heterostructures grown by MBE (molecular beam epitaxy). For enlarging the current gain, ideally, hot electrons injected by the emitter should ballistically travel through the base region without scattering, and they only relax their excess kinetic energy in the collector.

Thus far, the most difficult step in fabricating an HET is to electrically contact the "base". Typically, the mesa is etched down until the base layer is revealed. Subsequently, the base metal will be deposited. However, the Fermi level pinning [6] at the GaAs surface will deplete the exposed surface region by $\sim \sqrt{2N_A/q\epsilon_0\epsilon_{GaAs}}$ in thickness, where ϵ is the GaAs static dielectric constant, N_A ($\sim 10^{18}$ cm⁻³) is the surface Fermi level pinning voltage, and N_{area} is the doping level. For a doping level of 1×10^{18} cm⁻³, the depletion width is about 100 Å. So, the base could be no thinner than 100 Å for a GaAs base [7]. When InGaAs is used as the base material [2], the quantum well thickness has been reduced to 250 Å which still limited by the Fermi level pinning at the surface.

On the other hand, a base should be no thicker than about 1000 Å. The mean free path (MFP) of a ballistic non-thermalized hot electron can be estimated by taking a lifetime of 0.1 ps [8, 9], a velocity of 10^8 cm/sec, and MFP is found to be only 1000 Å. Therefore, the current gain (I_c/I_b) would diminish, if the base is much thicker than about 1000 Å.

In view of the difficulties, we have designed and fabricated an HET that is based on resonant tunneling (RT). The emitter injects hot electrons to the second lowest subband of a thin (100 Å) quantum well, and these non-thermalized hot electrons will then either resonantly tunnel to the collector (and form the collector current I_c) or relax to the lowest subband and contribute to the base current (I_b). The RT probability of hot electrons between the emitter and the collector can be switched almost completely on and off, when either the base or the collector bias is swept.

Figure 1(a) shows a schematic energy band diagram of the new HET, and the expected output characteristic. The hot electrons tunnel through the second lowest state in the quantum well, while the electrons at the lowest subband are used as a third terminal. A double barrier (DB) RT structure is used to inject hot-electrons with a narrow energy spread. The energy width of injected electrons can be experimentally obtained by using magnetotunneling spectroscopy. For example, 10 meV is measured for a DB diode with 30 Å barriers and a 100 Å quantum well. A narrow, peaked distribution can enhance the quantum selection rules. Given a full width of about 10 meV, when the energy of the second lowest quantum well state (E_2 in Fig. 1(a)) is shifted relative to the energy of injected hot-electrons (E_{hot}) by 10 meV, the RT current to the collector would be turned almost completely on and off. Fig. 1(b) illustrates such a three terminal transistor operation. Experimentally, this energy alignment (E_2 and E_{hot}) can be controlled by biasing the electrons in the QW base or by sweeping the collector voltage. Furthermore, when the E_2 and E_{hot} are off by an LO phonon energy, a phonon assisted RT process can also occur. The sufficient condition for observing the phonon-assisted RT tunneling is that the energy spread of non-thermalized hot-electrons at E_2 be less than both the LO phonon energy and $E_2 - E_1$.

Compared with conventional HETs, our HET has the following distinctive changes: (A) The base is now a quantum well, in which there are only a few quantum states. The hot electron transport perpendicular to the quantum well will therefore only involve a few states. (B) The hot electron energy spread is now reduced to be less than the GaAs LO phonon energy (36 meV). In conjunction with the fact that there are only a few quantum states involved in the tunneling process, the new HET will therefore be able to experimentally probe the energy distribution of injected hot-electrons with enough energy resolution to distinguish the true ballistic hot-electrons from those that have emitted one LO phonon. (C) The collector barrier can now be higher than the kinetic energy of injecting hot-electrons. The collector current therefore comes from a RT process.

A new tunneling and tunneling out approach is employed for contacting a thin quantum well. Standard fabrication processes are shown in Fig. 2. Starting from an as-grown wafer, the transistor mesa is first defined by wet-etching. The emitter and base contacts are then made by photolithography and metal evaporation. The region between the emitter and the base is etched, until there is barely any conduction between the emitter and the base at zero V_{bi} . Although the doped GaAs near the surface is not totally removed, the Fermi level pinning at GaAs surface can deplete the doped GaAs region at the surface, the DB RT structure and the doped QW. A schematic cross section of finished HET is shown in Fig. 3.

For an accurate structure design, numerical calculation for solving self-consistently the one-dimensional Poisson equation and Schrödinger equation is performed [10]. The positions of several important energy levels and their dependence on bias can be quantitatively predicted.

Grown on n⁺ (900) GaAs substrates by MBE, the model structure reported here consists of an n⁺ GaAs buffer layer as collector (Si doped, 10^{18} cm⁻³, 2000 Å) followed by an undoped $Al_{0.6}Ga_{0.4}As$ collector barrier (1000 Å) and an n⁺ GaAs QW (10^{18} cm⁻³, 100 Å), an undoped DB RT structure (DB $Al_{0.6}Ga_{0.4}As$ 100 Å GaAs / 10 Å $Al_{0.6}Ga_{0.4}As$) as an energy filter, an n⁺ GaAs cap layer (10^{18} cm⁻³, 2000 Å), and finally a 100 Å graded $In_{0.5}Ga_{0.5}As$ layer for non-aligning ohmic contacts.

Figure 1 shows the common emitter characteristics of an HET at 77K, where the collector current I_C is plotted against a sweeping V_{CE} at several different base currents I_B . No significant temperature dependence of the transistor characteristics was observed between 1.2K and approximately 77K. The double-peak feature as a result of the elastic and the phonon-assisted RF processes is clearly observed in I_C . When I_B is increased, the peaks in I_C shifts to higher V_{CE} owing to that the band bending will adjust itself self-consistently. The smooth rising background probably comes from a single-barrier tunneling current through the collector barrier, since there is no observable temperature dependence from 77K to 1.2K.

The observation of current gain of three (I_C/I_B) near resonance also verifies that at steady state 75% ($\approx I_C/(I_C + I_B)$) of the injected electrons can resonantly tunnel to the collector, while the rest 25% ($\approx I_B/(I_C + I_B)$) will relax to the lowest subband. This specific example demonstrates that the tunneling process can be faster than intersubband energy relaxation. In our particular case, the intersubband energy relaxation is known to be of the order of 0.1 ps, since the intersubband energy spacing is nearly 100 meV when the transistor is biased near resonance.

In summary, we have briefly reported our recent finding on a new HET, including the operating principles, the fabrication procedures, and the transistor output characteristics. The transistor has applications in dense static memory [14]. The lateral area of a static memory cell can be much reduced from current p-n junctions, because of the new output characteristics and that the electrical terminals can be stacked up. This new HET can also be applied in hot electron spectroscopy, and the resolution is improved to be able to distinguish a single LO phonon emission.

REFERENCES:

1. M. Heiblum, *Solid-State Elec.* **24**, 111 (1981), and references therein.
2. J.R. Hayes, A.F.J. Levi, and W. Wegmann, *Phys. Rev. Lett.* **54**, 1570 (1985).
3. N. Yokoyama, K. Inamura, I. Gamba, H. Noda, S. Muto, K. Kondo, and S. Hiyamizu, *International Electron Devices Meeting Technical Digest* (1984), p. 512.
4. M. Heiblum, M.J. Nathan, D.C. Thomas, and C. M. Kneedler, *Phys. Rev. Lett.* **55**, 2200 (1985).
5. K. H. Chou, P.G. Newman, and G. J. Lafferty, *Phys. Rev. B* **41**, 10270 (1990).
6. S.M. Sze, *Physics of Semiconductor Devices*, 2nd Edn, p. 77, eq. 15(a) Wiley New York, (1981).
7. K. Inamura, T. Adachi, S. Muto, and N. Yokoyama, *IEEE Trans. Electron Devices* **ED-39**, 179 (1992).
8. In three dimensions, see, e.g., E.M. Conwell, *High Field Transport in Solids*, 1st Ed. Furthall and H. Ehrenreich, *Solid State Physics* Suppl. **9**, Academic New York (1967).
9. In two dimensions, see, e.g., S. Das Sarma, F.K. Lam, and R. Jaldari, *Phys. Rev. B* **41**, 3561 (1990).

10. D.N. Mirlin, L.P. Nikitin, I.I. Reshina, and V.I. Sapozha, *ETP Lett.* **30**, 193 (1979).
11. D.N. Mirlin, I.Ya. Kochik, L.P. Nikitin, I.I. Reshina, and V.I. Sapozha, *ETP Lett.* **32**, 11 (1980), and D.N. Mirlin, I.Ya. Kochik, L.P. Nikitin, I.I. Reshina, and V.I. Sapozha, *Solid State Commun.* **37**, 777 (1980).
12. D.H. Auston, S. McAlver, C.A. Shank, E.P. Ippen, and O. Tesolke, *Solid State Lett.* **10**, 117 (1978).
13. M. Heiblum, D. Galai, and M. Winkler, *Phys. Rev. Lett.* **62**, 1057 (1989).
14. J. Chen, J.G. Chen, C.H. Yang, and R.A. Wilson, *J. Appl. Phys.* **70**, 1111 (1991).
15. For an example of using novel transistor characteristics in a memory cell, see J. Chen, C.H. Yang, and R.A. Wilson, *Appl. Phys. Lett.* **62**, 96 (1993).

FIGURE CAPTIONS:

1. (a) Schematic energy band diagram of the new HET, with the assumption that independent ohmic contacts can be made to the Emitter, the QW Base and the Collector (b). Expected output/input characteristic of the new HET, where the collector current would peak when E_2 and L_{DB} are brought to resonance.
2. The fabrication procedure of a THOHE. The transistor structure is not drawn to scale.
3. A schematic cross section of the new HET. The electrical components for characterization in the common-emitter configuration are also shown.
4. The common-emitter characteristics of an HET at 77K, where I_C is plotted against V_{CE} and I_B is stepped from $5 \mu A$ to $10 \mu A$.

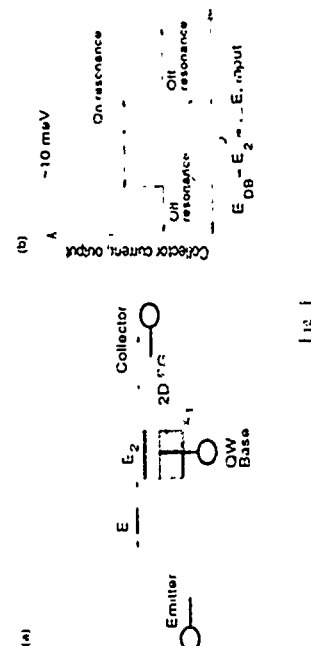


FIG. 1

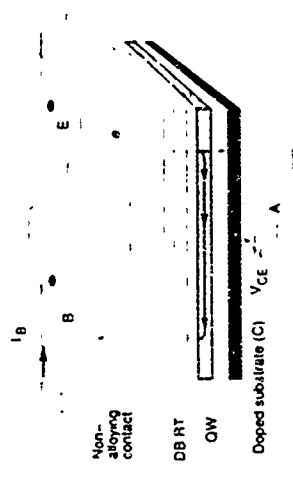


Fig 1

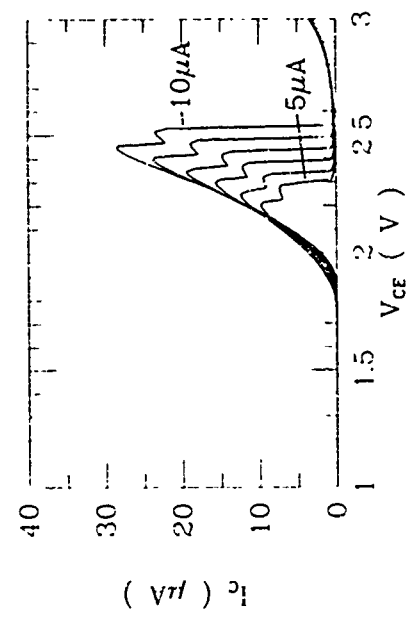


Fig 1

USE CROWN
TRANSISTOR
STRUCTURE

DEFINE
TRANSISTOR
MESA

InGaAs non-alloying
contact

n-doped GaAs

DB RT structure

QW

QW-Collector barrier

n-doped GaAs buffer

n-doped substrate

EMITTER
BASE AND
COLLECTOR
METAL
EVAPORATION &
LIFT-OFF

ISOLATION-ETCH
UNTIL THERE IS
NO CONDUCTION
BETWEEN THE
EMITTER AND THE
BASE WHEN
 $V_{CE} = 0$

Via Hole

Metal

CVD-Oxide

DB RT structure

QW

QW-Collector barrier

n-doped GaAs buffer

n-doped substrate

C

Fig 2

TuB4

Γ -X Electron Transfer in Type II Tunneling Bi-Quantum Wells

Atsushi Tackeuchi*, Uwe Strauß, and Wolfgang W. Rühle.

Max-Planck-Institut für Festkörperforschung, Heisenbergstr. 1, 70506 Stuttgart, Germany

Tsuguo Iwata and Shunichi Muto

Fujitsu Laboratories Ltd., 10-1 Morinosato-Wakamaya, Atsugi 243-01, Japan

*On leave from: Fujitsu Laboratories Ltd.

Abstract

We have studied the energy band structure and the Γ -X carrier transfer mechanism for type II tunneling bi-quantum wells consisting of GaAs wells, AlGaAs barriers of different thicknesses, and AlAs layers by cw and time-resolved photoluminescence measurements. The cw photoluminescence spectra of the indirect recombination of X electrons in the 7.1 nm thick AlAs layers with Γ holes in the 2.8 nm thick GaAs wells show weak zero-phonon lines indicating that the AlAs confined states at X_{xy} are lower than those at X_z . Time-resolved photoluminescence reveals that the carrier transfer time depends stronger on temperature for thicker AlGaAs barriers. Two scattering mechanisms, temperature-dependent phonon scattering and the temperature-independent interface scattering, are probably involved in the carrier transfer, the latter becoming smaller with increasing AlGaAs barrier thickness. Our results are compared with those obtained for similar type II GaAs/AlAs superlattices.

1. Introduction

Excitonic optical nonlinearity in quantum wells is useful for optical switching. Nonlinear absorption and refraction changes occur in MQWs with a time constant shorter than 1 ps due to photoexcitation of the exciton peak [1]. However, slow recovery of optical properties is often a severe restriction of these optical devices. The typical recovery time from excitonic absorption bleaching in a GaAs/AlGaAs MQW is 30 ns at 300 K [2]. Tackeuchi et al. [3] proposed the type II tunneling bi-quantum well (TBQ) structure to reduce and control the recovery time. The type II TBQ consists of a series of GaAs wells, AlGaAs barriers, and AlAs layers, as shown in Fig. 1. The structure uses optical nonlinearity at the exciton level in the GaAs well. The recovery time from excitonic absorption bleaching in the GaAs wells is governed by tunneling of electrons out of the well through an AlGaAs barrier into the X states in the AlAs layers. The recovery time can be made faster using thinner AlGaAs barriers without broadening the excitonic absorption peak of the GaAs wells. In type II TBQ, no significant optical absorption occurs in the AlAs layers during the excitation of Γ -hh1 excitons in the GaAs wells since the lowest direct transition energy in AlAs layers is larger than that of the GaAs wells. Therefore this structure can be used, in contrast to type I TBQ [4,5], also in

cavity devices. An all-optical gate operation of 17 ps has been already demonstrated with this structure in an etalon [6].

However energy band structure of this type II system and the carrier transfer mechanism are not clear, in contrast to the well-known type II superlattices (SLs) [7-10]. We investigate these features for different AlGaAs barrier thicknesses using cw and time-resolved photoluminescence measurements and compare our results with those which were obtained with similar type II SLs.

2. Energy band structure

The sample structures consist of 50 periods of 10 MLs (monolayers)-thick GaAs quantum wells, $\text{Al}_{0.51}\text{Ga}_{0.49}\text{As}$ barriers, and 25 MLs-thick AlAs wells. Four samples with different AlGaAs barrier thicknesses (from 4 MLs to 14 MLs) are studied. All structures were grown on a semi-insulating (100) GaAs substrate by molecular beam epitaxy.

Figure 2 shows the cw photoluminescence spectra at 4.2 K excited by a Kr^{+} ion laser at 530.9 nm. We observe the direct Γ -hh1 recombination in the GaAs wells at 704 to 711 nm. The Γ -hh1 peak shifts to higher energy with decreasing AlGaAs barrier thickness since quantization energy is enlarged if the high AlAs Γ potential is closer to the GaAs wells providing a stronger carrier confinement [3].

The indirect type II emission between the X state in AlAs and the lowest Γ heavy-hole level in the GaAs wells at wavelengths longer than 720 nm comprises mainly four peaks which are labeled a, b, c, and d starting at the high-energy side. Table 1 compiles the energy differences between the various peaks. The energy differences between a-c (28-31 meV), and a-d (47-48 meV) are close to the LA and LO phonon energies at the AlAs X point which are 28 and 50 meV, respectively [11]. These energy differences are also close to the data obtained for type II SLs by Dawson et al. [7], who identified these peaks as AlAs phonon replicas. However, we can not exclude the contribution of AlAs like phonons in the AlGaAs barriers since they have similar energies. In summary, the a, b, c, and d peaks correspond to the zero-phonon, AlAs-like TA, LA and LO phonon replicas, respectively. Recombination involving GaAs like phonons is obviously not important.

The energy differences between the direct Γ -hh1 recombination in the GaAs well and the zero-phonon lines of the indirect transition between the 10 MLs thick GaAs and the 25 MLs thick AlAs are only 42 meV, 25 meV, and 28 meV for 4 MLs, 8 MLs, and 12 MLs barriers, respectively. For comparison, in type II SLs with no AlGaAs barrier, this energy difference is 98 meV for a structure with 11 MLs thick GaAs and 24 MLs thick AlAs [9]. Obviously, energy crossover between X and Γ occurs at around 11 MLs thick GaAs wells in our type II TBQs, a value which is 1 to 2 MLs smaller than in type II SLs. This is a consequence of the reduced quantization energies due to the presence

of the AlGaAs intermediate layers in our TBQ structure.

One interesting feature of the present PL spectra is that the zero-phonon lines are relatively weak. In contrast, Dawson et al. [7] observed in type II SLs strong zero-phonon lines for 2.8 nm thick AlAs layers and weak zero-phonon lines for 6.8 nm thick and thicker AlAs layers. They interpret this phenomenon as the energy crossover between X_2 and X_{xy} states in the AlAs layers; PL shows the strong zero-phonon line due to band mixing between Γ and X_2 when the X_2 states are lower. This interpretation is supported by optically detected magnetic resonance experiments which show that X_{xy} is lower than X_2 when the AlAs layer is thicker than 5.5 nm in spite of the much larger effective mass of 1.1 m_0 at X_2 state (0.19 m_0 at X_{xy}) [12]. Since the AlAs layers have a finite lattice mismatch to the GaAs substrates, the layers are under biaxial compression, and the resulting uniaxial stress lowers the X_{xy} states with respect to the X_2 states. Therefore, the weak zero-phonon lines in our TBQ structures indicate that the X_{xy} states are lower than X_2 states for the type II TBQs with 7.1 nm thick AlAs layers.

3. Γ -X carrier transfer

Previously, the carrier transfer time from Γ states in the GaAs wells to X states in the AlAs layers were measured at room temperature using time-resolved absorption measurement [3], and carrier transfer time depended exponentially on barrier thickness demonstrating that the transfer is governed by tunneling. However, the scattering mechanism which is involved in the tunneling process has not been clarified. In type II SLs with GaAs wells thinner than 12 MLs, Feldman et al. showed that the Γ -X transfer is governed by interface scattering which does not depend on temperature [9].

We measure the time-resolved photoluminescence of ϵ_1 -hh1 emission of GaAs wells using a synchrotron streak camera system and a synchronously pumped Rhodamine 6G dye laser with 82 MHz repetition rate. The time resolution, the full width at half maximum of the laser pulse on the streak camera, is about 12 ps.

The time evolutions of ϵ_1 -hh1 photoluminescence peak at different temperatures are shown in Fig. 3 for the sample with 14 MLs AlGaAs barriers. The decay time becomes slower with lowering the temperature. This temperature dependence indicates that transfer in the type II TBQ does not exclusively occur via interface scattering. At high temperatures, a long-lived tail appears, its magnitude becoming larger with increasing temperature. A similar long-lived tail was observed previously at room temperature by time-resolved absorption measurements [3]. We believe the long-lived tail in luminescence and part of the long tail in absorption are due to thermally induced back-transfer of carriers.

Figure 4 shows the dependence of decay time on temperature: with increasing temperature, the decay times become close to the value measured at

room temperature by time-resolved absorption measurement. The increase of the decay time at low temperature (<150 K) for the 12 MLs and 14 MLs barriers is due to the increase of radiative recombination time with increasing temperature. Except for these samples in this temperature range, decay time is dominated by the tunneling transfer. In the latter regime, the decay times decrease with increasing temperature, and the change in the decay time is larger for thicker barriers. The ratio of the decay times between low and high temperatures are 2.2 and 3.0 for the structures with 4 MLs and 8 MLs barriers, respectively. This result differs from the data obtained by Feldman et al. [9] on type II SLs. They observed no temperature dependence for GaAs wells thinner than 12 MLs, whereas we observe the dependence of decay time on temperature for type II TBQ with even 10 MLs thin GaAs wells. They claim that interface scattering is the dominant temperature-independent scattering mechanism for thinner wells and that phonon scattering is the main scattering process for the thicker wells (>35 MLs).

This apparent contradiction is however well understood if we take into account that the AlGaAs barriers in our TBQ structures reduce the overlap of wavefunctions between Γ and X states at the interfaces. In type II SLs, the interface scattering due to the interface mixing potential and/or due to potential fluctuations caused by interface roughness at AlAs/GaAs interface are considered to be the dominant temperature-independent scattering mechanism [9]. In type II TBQs, AlAs/AlGaAs and/or GaAs/AlGaAs interface seems to mix similarly Γ and X states. We calculate the penetration probability of ϵ_1 electrons of the GaAs wells into the AlGaAs/AlAs interface (± 1 ML) using envelope function approximation. The penetration probability for the TBQ barriers as shown in Table 2. These values are clearly smaller than the penetration probability of 8.3 % for 10.3 MLs thick GaAs/17.1 MLs thick AlAs type II SLs which do not show any dependence of decay time on temperature. The values for the type II TBQs are close to the value of 0.45 % which is obtained for a 39.0 MLs thick Al_{0.36}Ga_{0.64}As/33.5 MLs thick AlAs type-II SL. Additionally, the ratios of the decay times at low and high temperatures, τ_{low}/τ_{high} , are also very similar for these three structures, namely 2.2 for 4 MLs thick barriers TBQ, 3.0 for 8 MLs thick barriers TBQ, and 2.3 for 39.0 MLs thick Al_{0.36}Ga_{0.64}As/33.5 MLs thick AlAs type II SLs. Obviously the penetration of electron wave functions at the AlAs/AlGaAs interface in our case are much more similar to those in type II 39.0 MLs thick AlGaAs/33.5 MLs thick AlAs SL, where phonon scattering is dominant, than to those in type II 10.3 MLs thick GaAs/17.1 MLs thick AlAs SL. Therefore we interpret the observed dependence of the decay times on temperature in our TBQ structures to be due to a combination of two scattering mechanisms: temperature-independent interface scattering and temperature-dependent scattering. The larger difference of decay times between low and high

temperatures with increasing AlGaAs barrier thickness is due to the decrease of interface scattering by less overlap of the wavefunctions at the interfaces which results in the relatively stronger contribution of temperature-dependent scattering. As for the temperature-dependent scattering, calculations show that phonon assisted scattering is the fastest scattering process [13,14]. Therefore phonon assisted tunneling seems to be the process which leads to the temperature dependence of the carrier transfer time in our TBQ structures.

4. Summary
We have studied the energy band structure and Γ -X carrier transfer of type II tunneling bi-quantum wells using cw and time-resolved photoluminescence measurements. Type II TBQ consists of GaAs wells, AlGaAs barriers, and AlAs layers. The cw photoluminescence spectra between X electrons in the 7.1 nm thick AlAs layers and Γ holes in the 2.8 nm GaAs wells exhibit weak zero-phonon lines indicating that the X-ray confined states are lower than the X_2 confined states. The time-resolved photoluminescence shows a stronger temperature dependence of the carrier transfer time for thicker AlGaAs barriers. This dependence on temperature and barrier thickness is explained by taking into account two scattering mechanisms: temperature-dependent phonon scattering and temperature-independent interface scattering, the latter becoming less efficient for thicker AlGaAs barriers.

Acknowledgments
We would like to thank K. Roiter and H. Klann for expert technical assistance. We also thank Professor H. J. Queisser for his hospitality during the course of this work. We acknowledge the work of Yoshiaki Nakata, Satoshi Nakamura, and Masao Yamaguchi with the sample growth.

References
[1] W. H. Knox, R. L. Fork, M. C. Downer, D. A. B. Miller, D. S. Chemla, C. V. Shank, A. C. Gossard and W. Wiegmann: *Phys. Rev. Lett.* **54**, 1306 (1985).
[2] D. S. Chemla, D. A. B. Miller, P. W. Smith, A. C. Gossard and W. Wiegmann, *IEEE J. Quantum Electron.* **QE-20**, 265 (1984).
[3] A. Tackeuchi, T. Inata, Y. Sugiyama, Y. Nakata, S. Nakamura and S. Muto, *Jap. J. Appl. Phys.* **31**, L667 (1992).
[4] A. Tackeuchi, S. Muto, T. Inata, and T. Fujii, *Jpn. J. Appl. Phys.* **28**, L1098 (1989).
[5] A. Tackeuchi, S. Muto, T. Inata, and T. Fujii, *Appl. Phys. Lett.* **58**, 1670 (1991).
[6] A. Tackeuchi, T. Inata, Y. Nakata, S. Nakamura, Y. Sugiyama, and S. Muto, *Appl. Phys. Lett.* **61**, 1892 (1992).

Table. 1 Energy differences between photoluminescence peaks.

	cl-hhl - a (meV)	a - b (meV)	a - c (meV)	a - d (meV)
L-B				
4 MLs	42	12	31	48
8 MLs	25	13	28	48
12 MLs	28	11	30	47

Table. 2 Penetration probabilities and the ratios of decay times between 5 K (10 K) and 300 K (295 K).

Type II TBQ	Penetration probability	τ_{low} / τ_{high}
GaAs/AlGaAs/AlAs		τ_{5K} / τ_{300K}
10 MLs / 4 MLs / 25 MLs	1.1 %	2.2
10 MLs / 8 MLs / 25 MLs	0.17 %	3.0
Type II SLs		τ_{10K} / τ_{295K} [9]
GaAs 10.3 MLs / AlAs 17.1 MLs	8.3 %	1.0
AlGaAs 39.0 MLs / AlAs 33.5 MLs	0.45 %	2.3

Table. 2 Penetration probabilities and the ratios of decay times between 5 K (10 K) and 300 K (295 K).

Valley mixing effects on electron tunneling transmission in GaAs/AlAs heterostructures

E. L. Ivchenko and A. A. Kiselev
A. F. Ioffe Physico-Technical Institute, Russian Academy of Sciences,
194021 St. Petersburg, Russia

Y. Fu and M. Willander
Department of Physics and Measurement Technology,
Linköping University, S-581 83 Linköping, Sweden

We propose a set of boundary conditions for electron envelope functions at GaAs/AlAs (001) heterointerfaces so as to take into account Γ -X mixing in the effective mass method. The proposed conditions enable one to obtain the dependence of the mixing effect upon the parity of monomolecular layer numbers in $(\text{GaAs})_M/\text{AlAs}$ superlattices. The electron transmission spectra of GaAs/AlAs M GaAs single barrier structures are calculated in the generalized effective-mass approximation. It is shown that the spectral fine structure depends essentially upon the parity of M . The low-temperature dc current-voltage characteristics of the single-barrier structure is derived taking into account the camel-back X-band structure in bulk AlAs and GaAs.

1. Introduction

Since mid 80s different pseudopotential and tight-binding models have been used for calculation of GaAs/AlAs (001) superlattice (SL) minibands and for the theoretical analysis of mixing between the Γ conduction band and (001) X valley (see the review [1]). The most striking common feature of the results is a qualitative sensitivity of the Γ -X mixing effects on the parity of monolayer numbers in AlAs and GaAs layers. Ando and Akera [2] (see also [3]) presented a formulation of the effective-mass method in which Γ -X mixing at interfaces is included by boundary conditions but in their formulation the parity of monolayer numbers has no influence on the miniband spectrum in contrast with the results of the empirical model calculations.

In the present paper it is shown that the boundary conditions of Ando and Akera are relevant to a single heteroboundary but they should be corrected in cases of double or multiple interface structures. If a dimensionless Γ -X mixing coefficient is supposed to change its sign from one monolayer to another then the effective-mass approximation leads as well to the dependence of Γ -X mixing in a $(\text{GaAs})_M/\text{AlAs}$ superlattice on the parity of M . We also present a theoretical study of resonant tunneling through a GaAs/AlAs M GaAs structure where the attention is focused on analytical properties of the transmission spectra and analytical description of the current vs. voltage dependence making allowance for a self-consistent electrostatic potential induced by the buildup X-electrons. It should be noted that there have been published numerous calculations of electron tunneling probabilities across a GaAs/AlAs single- or double-barrier heterostructures taking into account Γ -X mixing effects [2-9]. However only recently it has been realized [10, 11] that the transmission spectra depend on whether the AlAs layer contains an even or odd number of monomolecular layers.

2. Γ -X mixing in SLs in the effective mass approximation

Following Ando and Akera [2] we consider the three-band model taking into account mixing of Γ_1 states with those from two close-lying bands X_1 and X_3 . The electron wave function is written then as

$$\psi_e(r) = u(r)|\Gamma_1\rangle + v(r)|X_3\rangle + w(r)|X_1\rangle \quad (1)$$

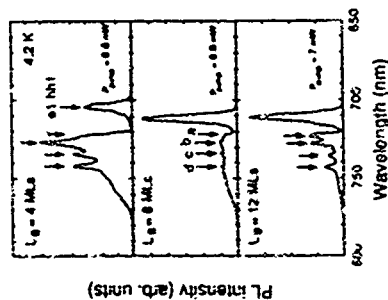


Fig. 2. CW photoluminescence spectra at 4.2 K.

Fig. 1. Schematic energy band diagram of a type-II TBQ structure.

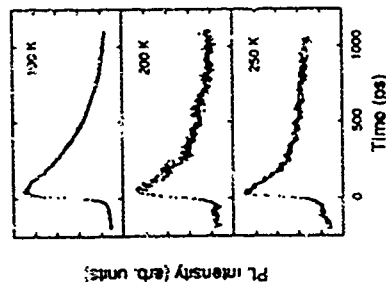
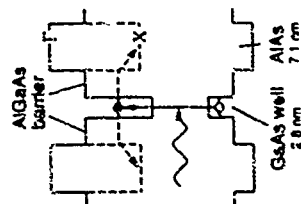


Fig. 3. Time resolved et-hhl photoluminescence for the TBQ structure with 14 MLs thick AlGaAs barriers at different lattice temperature

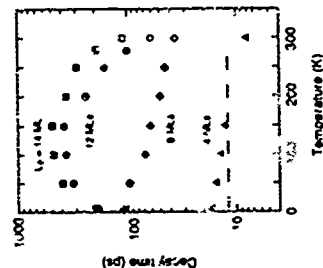


Fig. 4. Dependence of decay time on temperature. Also shown are the data (open symbols) obtained by time resolved absorption measurement at room temperature [3].

where $\Gamma_F > \Gamma_X$, Γ_X are the corresponding Bloch functions and w , v , u are envelopes in the effective mass method. We assume w , v , u and $\partial u/\partial z$ to be continuous at heterointerfaces and use the boundary conditions for derivatives $\partial w/\partial z$ and $\partial v/\partial z$ in the form [2, 12]

$$\nabla_F^A w_A = \nabla_F^B w_B + (z_F) u_B, \quad \nabla_X^A u_A = \nabla_X^B u_B + (z_F) w_B. \quad (2)$$

Here z_F is the heteroboundary coordinate.

$$\nabla_F^A = \frac{m_0}{a_0 m_1} \frac{\partial}{\partial z}, \quad \nabla_X^A = a_0 \frac{m_0}{m_X} \frac{\partial}{\partial z}.$$

a_0 is the lattice constant, m_0 is the free electron mass, m_1 is the Γ -electron effective mass in bulk GaAs (m_A) and AlAs (m_B), m_X is the effective mass describing parabolic term $A^2 k_z^2/2m_X$ in the two-band Hamiltonian of X -point electrons. The coefficient t was considered in [2, 3, 7] to be independent on the interface coordinate z_F . However, due to different translational properties of Γ - and X -point Bloch functions this coefficient changes its sign as a GaAs/AlAs interface is shifted by one monolayer along the principal axis z . Thus,

$$(z_F) = \Gamma_X \eta(z_F), \quad \eta(z_F) = \exp[iz_F/a_0], \quad (3)$$

where Γ_X is a real dimensionless constant. Note that for a single heteroboundary the phase of η can be chosen arbitrarily since the corresponding phase change can be introduced into the envelope w or into the envelopes v , u , but this choice unambiguously fixes the phase $\phi = 2\pi z_F/a_0$ at any other heteroboundary of the same structure.

In order to demonstrate the role of the phase factor $\eta(z_F)$ we consider the energy dispersion for the two lowest electron minibands in (GaAs) $_M$ (AlAs) $_M$ SLs near the transition from type I to type II. In this case one can first calculate the lowest minibands $e\Gamma_F$ and $e\Gamma_X$ for $\Gamma_X \neq 0$ and then include the Γ - X mixing between them. The details have been published elsewhere [10, 12] and here we present the final result for the electron dispersion curves obtained in the tight-binding approximation of the effective mass method

$$E_{\pm}(k) = \frac{1}{2} \left\{ E_F(k) + E_X(k) \pm \sqrt{[E_F(k) - E_X(k)]^2 + 16 V^2} \right\}. \quad (4)$$

Here k is the 3D electron wave vector in the SL, $E_F(k)$, $E_X(k)$ are the energies of the unmixed $e\Gamma_F$ and $e\Gamma_X$ states.

$$\tilde{V} = \frac{A^2 \Gamma_X}{2a_0 m_0} w e \Gamma_F(BA) v e \Gamma_X(BA), \quad \chi = \cos^2[k_z d + M\pi/2]. \quad (5)$$

$w e \Gamma_F(BA)$ is the electron envelope function in the state $e\Gamma_F$ in a GaAs single quantum well of the width $a = Na_0/2$, $v e \Gamma_X(BA)$ and $u e \Gamma_X(BA)$ are the envelopes in the $e\Gamma_X$ state in an AlAs single quantum well of the width $b = Ma_0/2$, $d = a + b$ is the SL period, the symbol BA means a coordinate of the heteroboundary AlAs/GaAs. The parity of AlAs monolayer number M is explicitly present in Eq (5) and, hence, in the dispersion (4). Note that the electron dispersion (4) is independent on the parity of N . The latter is due to a large value of the X -electron longitudinal effective mass which permits one to consider the GaAs/AlAs SL for X -electrons as a regular chain of isolated quantum wells and neglect the k_z -dependence of the curve $E_X(k)$.

3. Transmission through a GaAs(AlAs) $_M$ GaAs structure

Fig. 1 shows normal-incidence electron transmission coefficients for single-barrier heterostructures with the monolayer number M ranging from 8 to 12. Solid curves are calculated in the generalized effective mass approximation [10] for $\Gamma_X \neq 0$, dotted curves present the recent results of Ting and McGill [11] obtained by using an eight-band second-neighbor sp^3 tight-binding model. In Fig. 1 the incident electron energies lie below the conduction X -edge in GaAs and, therefore, the transmission probability is contributed by Γ - Γ , Γ - X , X - Γ but not by Γ - X , X - X processes. One can see a close agreement in the parity dependence of the fine structure in the spectra calculated by different methods [10] and [11]. The difference in the peak positions can be evidently removed by fitting band offsets and X -band parameters in the tunneling experiments [9, 13] the sharp structures are smeared out due to contributions to the current from electronic states with different energies. However the analysis of these structures can be used for making comparison between various computation methods.

In order to understand the fine structure of the spectra we apply here the perturbation theory to derive a formula for transmission coefficient for incident electron energies E close to the energy E_0 of a quibound X -state n in the AlAs layer.

It can be shown that the additional terms in the right-hand side of Eqs. (2) are equivalent to inclusion into the electron effective Hamiltonian of the operator

$$V_{\Gamma X} = \frac{A^2 \Gamma_X}{2a_0 m_0} \left\{ \delta(z - z_F) (-1)^M \delta(z - z_L) \right\}. \quad (6)$$

where z_F is the coordinate of the left- or right-hand interface and we set $\eta(z_F) = 1$ using Fermi's golden rule and the resonant scattering theory one can present the transmission probability in the form

$$T_A = \frac{1}{\hbar v_z} \int_{-\infty}^{\infty} dk' \delta(E_A - E_X) |V_{\Gamma X}|^2, \quad (7)$$

$$V_{\Gamma X} = V_F^* + \frac{V_{\Gamma X} V_{X\Gamma}}{E_X - E_0 + i0}. \quad (8)$$

Here k is the incident electron wave vector ($k \perp z$), $v_z = \hbar k/m_A$, Γ_0 is the escape rate from the E_0 level into the leads, V_F and $V_{X\Gamma}$ are the coupling constants connecting the bound state v to free G -states in the right and left leads, V_F^* is the coupling constant due to nonresonant tunneling via Γ -states of the AlAs layer.

Integrating Eq. (7) over k' and taking into account that $|V_{X\Gamma}| = |V_{\Gamma X}|$ and $\Gamma_0 =$

$$|V_{\alpha\beta}|^2/\hbar^2 u_2 \text{ we finally obtain}$$

$$T_k = \left| \frac{4J_{\alpha\beta}}{1+J_{\alpha\beta}} e^{-\kappa_{\alpha\beta} b} \pm \frac{\hbar \Gamma_{\alpha} (1-i)^M}{E_k \cdot E_{\alpha} + \hbar \Gamma_{\alpha}} \right|^2 \quad (9)$$

Here the sign \pm corresponds to even or odd envelope $v_j(z)$.

$$f_{\alpha} = \frac{m_{\alpha}}{m_B} \frac{\kappa_{\alpha}}{\kappa_{\beta}} \cdot k_{\alpha} = (2m_{\alpha} E_{\alpha} / \hbar^2)^{1/2} \cdot$$

$$\kappa_{\alpha} = (2m_{\alpha}^2 E_{\alpha} / \hbar^2) \cdot E_{\alpha} / \hbar^2)^{1/2} \cdot$$

E_j (AlAs) is the energy position of the Γ_j minimum in AlAs, $b = Ma_0/2$ is the AlAs layer thickness. Eq. (9) is valid provided the F - F tunneling probability is small, i.e. $\exp(-\kappa_{\alpha} b) \ll 1$. In this case the transmission peak position practically coincides with E_{α} . One can see that the parity dependence of the F - X mixing operator (6) is repeated in Eq. (9) because the product $V_{\alpha\beta} V_{\beta\alpha}$ is proportional to $(-1)^M v_{\alpha}(z) v_{\beta}(z)$. For the lowest state $\nu=1$ (e1X) the envelope $v_1(z)$ is even and $v_j(z)$ is odd and we should take the negative sign in Eq. (9). Thus, the energy position $E_j^{(d)}$ of the E_j -related dip is given by

$$E_j^{(d)} = E_j + (-1)^M \frac{1 + \int_0^b v_1^2}{4J_1} e^{-\kappa_1 b} \hbar \Gamma_1 \cdot (10)$$

the peak-dip distance being much larger than $\hbar \Gamma_1$. It follows then that for M odd the transmission zero is followed by the peak in agreement with the spectra in Fig. 1 for $M=9, 11$. On the other hand, if M is even the transmission zero occurs above the energy E_j (Fig. 1, $M=8$). For thick enough (AlAs) $_M$ layers, the resonant contributions to T_k due to the E_j and E_2 peaks exceed the nonresonant contribution in the whole region between E_j and E_2 and, for M even, the peak E_j is not followed by a zero (Fig. 1, $M=12$).

4. Resonant tunneling current in a single-barrier structure

The tunneling current density can be written as

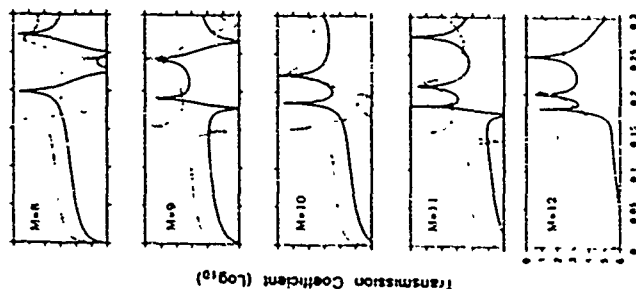


Fig. 1 Comparison between theoretical transmission spectra calculated for GaAs (AlAs) $_M$ GaAs structures with $M=8, 12$ by using the generalized effective mass approximation (10) (solid curves) and the eight-band second-neighbor sp^3 tight-binding model of Ting and McGill (from [11], dotted)

due to the E_j and E_2 peaks exceed the nonresonant contribution in the whole region between E_j and E_2 and, for M even, the peak E_j is not followed by a zero (Fig. 1, $M=12$).

$$J = \frac{1}{2\pi^2} \frac{em_A}{\hbar^3} \int dE_{11} dE_2 \pi(E_{11}, E_2) (F_1 - F_2) \quad (11)$$

where $E_{11} = \hbar^2 k_x^2 / 2m_A$, $E_2 = \hbar^2 k_y^2 / 2m_A$, $k_x^2 = k_x^2 + k_y^2$, $\pi(E_{11}, E_2)$ is the transmission probability under oblique incidence, $F_{1,2}$ are the electron distribution functions in the left and right leads described at low temperatures by the step functions $F_1 = \Theta(E_F - E)$, $F_2 = \Theta(E_F + eV - E)$, E_F being the Fermi energy and V being the bias between the leads. We take $V > 0$ so that the product eV is negative. We consider the region of electric fields where the level $E_{j,ex}$ is tuned to resonance with the left-lead states occupied by the degenerate electron gas and F_2 in Eq. (11) can be put to zero. The current is calculated self-consistently taking into account an electrostatic field induced by the electrons temporarily confined inside the AlAs layer. The whole electrostatic potential, $\phi(z)$, is determined from the Poisson equation

$$\frac{d^2 \phi}{dz^2} = - \frac{4\pi e N_j}{\epsilon} [u_j^2(z) + v_j^2(z)] \quad (12)$$

where N_j is the 2D density of the confined electrons. The structure is assumed to contain GaAs spacers of effective thicknesses L_1 and L_2 on both sides of the (AlAs) $_M$ layer. Neglecting the field-dependence of $L_{1,2}$ in the E_j -resonance region, we take for the potential the boundary conditions $\phi(-L_1 - b/2) = 0$, $\phi(L_2 + b/2) = V$, the origin $z=0$ being chosen at the center of the AlAs layer.

Note that in the narrow resonant regions, $|E - E_{j,ex}| < \hbar \Gamma_{j,ex}$, the nonresonant contribution in Eq. (9) is negligible while in off-resonant regions V_k can dominate if the AlAs layer is not very thick. Thus, the resonant and nonresonant contributions to the tunneling current can be calculated separately. In the following for simplicity we take into consideration only the resonant contribution to $\pi(E_{11}, E_2)$.

Neglecting the reflection of electron waves from spacer areas we can approximately present this coefficient in the form

$$\pi(E_{11}, E_2) = \frac{(\hbar \Gamma_j)^2}{[E_{11} + E_2(1 - m_A/m_X^*) - E_j - e\phi_0]^2 + (\hbar \Gamma_j)^2} \quad (13)$$

where

$$\phi_0 = \int dz \phi(z) [u_j^2(z) + v_j^2(z)]$$

m_X^* is the in-plane effective mass of an X electron. For normal incidence $\pi(E_{11}, 0)$ reduces to the resonant contribution to the transmission probability given by Eq. (9). Neglecting variation of $\Gamma_j(E_j)$ within the energy interval of the width E_F we can connect J and N_j by a simple relation

integer coefficients, g_j ($j=1,2,3$) being the basic translation vectors of the bulk lattice. These simple considerations can be modified to be valid for strained SLs.

References

1. J. Sham and Y.-T. Lu, *J. Lumin.*, **44**, 207 (1989).
2. T. Ando and H. Akera, *Phys. Rev. B*, **40**, 11619 (1989).
3. H. C. Liu, *Appl. Phys. Lett.*, **51**, 1019 (1987).
4. A. C. March, *Semicond. Sci. Technol.*, **1**, 320 (1986).
5. D. Y. K. Ko and J. C. Inkson, *Semicond. Sci. Technol.*, **3**, 791 (1988).
6. K. V. Rousseau, K. L. Wang and J. N. Schulman, *Appl. Phys. Lett.*, **54**, 1341 (1989).
7. J.-B. Xu, *Phys. Rev. B*, **41**, 3117 (1990).
8. T. B. Boykin and J. S. Harris, Jr., *J. Appl. Phys.*, **72**, 988 (1992).
9. Y. Carboneau, J. Beersens, L. A. Cury, H. C. Liu and M. Buchanan, *Appl. Phys. Lett.*, **62**, 1955 (1993).
10. Y. Fu, M. Willander, E. L. Ivchenko and A. A. Kiselev, *Phys. Rev. B*, **47**, 13498 (1993).
11. D. Z.-Y. Ting and T. C. McGill, *Phys. Rev. B*, **47**, 7381 (1993).
12. I. L. Aleiner and E. L. Ivchenko, *Fiz. Tikh. Poluprov.*, **27**, 594 (1993) (Sov. Phys. Semicond., **27**, (1993)).
13. E. E. Mendez, W. I. Wang, E. Calleja and C. E. T. Gonçalves da Silva, *Appl. Phys. Lett.*, **50**, 1263 (1987); R. Beresford, L. F. Luo, W. I. Wang and E. E. Mendez, *Appl. Phys. Lett.*, **55**, 1555 (1989).

$$J = \frac{1}{2} e N_f f_1 \quad (14)$$

Substituting Eq. (13) into Eq. (11), integrating Eq. (11) over E_1 and E_2 and taking into account Eq. (14) we obtain a final I - V characteristics

$$J(V) = J_0 \begin{cases} 0 & \text{if } V < V_{\min} \text{ either } V > V_{\max} \\ (V - V_{\min})/(V - V_{\max}) & \text{if } V_{\min} < V < V_{\max} \\ (V_{\max} - V)/(V_{\max} - V_{\min}) & \text{if } V < V_{\min} \text{ or } V > V_{\max} \end{cases} \quad (15)$$

Here

$$J_0 = \frac{1}{2\pi} \frac{em_A}{\hbar^2} f_1 E_F \cdot V_{\min} = \frac{E_1 \cdot E_F}{\hbar^2} \cdot V_{\max} = \frac{E_L}{\hbar^2} \cdot V_{\max} = \frac{E_L}{\hbar^2} \cdot \left(\frac{m_A}{m_N} \cdot \frac{c^2 m_A}{\pi^2} \left[\frac{2\pi^2}{\epsilon} (L_r - L_l) + \phi_0 \right] \right) \cdot \frac{L_l + b/2}{L_l + L_r + b} \quad \text{For } \epsilon \neq 1$$

convenience we introduced the function $\phi(z)$ so as $eN_f \phi(z)$ is an even solution of Eq. (12) with the boundary condition $\phi(-L_l) = b/2 = 0$.

$$\phi_0 = \int_{-L_l}^{L_r} dx \phi(x) [u_1(x) + u_2(x)]$$

It is clear that $\phi(z)$ is independent on the applied bias.

Fig. 2 shows a shape of the resonant $J(V)$ curve neglecting (dashed) and including the self-consistent potential influence (solid line). We use the notation

$$|e| \xi V_0 = E_1 - E_F (1 - m_A/m_N^*)$$

In general the parameters of a heterostructure can be such as V exceeds V_{\max} in which case the current-voltage dependence exhibits an intrinsic bistability.

5. Conclusion

The version of the effective mass approximation used in this work can be readily extended to treat valley-mixing in heterostructures grown along other crystallographic axes. Really, in general two Bloch states with the wave vectors K_1 and K_2 can be mixed by heteroboundary with the normal N if there exists a 3D reciprocal lattice vector B that satisfies the condition $(K_1 - K_2 - b)_\perp = 0$, where K_\perp means the in-plane component of the vector K . The envelope functions corresponding to the K_1 and K_2 valleys can be mixed by boundary conditions similar to those given by Eq. (2). It is evident that in such generalized boundary conditions the phases of K_1 - K_2 mixing coefficients should depend on the interface position as $\exp[i(K_1 - K_2 \cdot b)_\perp z]$, where the symbol z means the coordinate of a $3D$ vector parallel to the structure principal axis N and z_f is a linear combination of g_j with

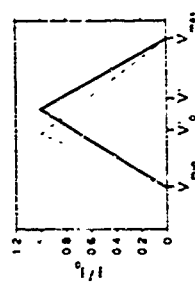


Fig. 9. Shape of the resonant current-voltage characteristics of GaAs/AlAs heterostructure (dashed curve) and including the self-consistent potential influence (solid line).

TuCl

Luminescence Investigation on Strained $\text{Si}_{1-x}\text{Ge}_x/\text{Si}$ Modulated Quantum Wells

S. Futatsuki
Research Center for Advanced Science and Technology (RCAST),
The University of Tokyo,
4-6-1 Komaba, Meguro-ku, Tokyo 153, Japan

Luminescence characterization is presented on potential-modulated strained $\text{Si}_{1-x}\text{Ge}_x/\text{Si}(100)$ quantum wells. Interval coupling was studied in a series of coupled quantum wells (CQW) with a heterostructure Si barrier for symmetric and asymmetric configurations. Symmetric red shift of photoluminescence peak energy was observed in symmetric CQWs with decreasing Si barrier width covered as CQW. Interval coupling was further evidenced in asymmetric CQWs luminescence as spectral densities which were broadened and shifted to the higher energy, reflecting the tunneling-controlled carrier transfer. Evolution of Kohn-Sham superlattice state was observed as consistent band-edge shift with change in the spectral parameters. Diffusion induced blue shift of luminescence peak amounting to 22meV was observed.

1. Introduction

Recent progress in epitaxial growth technology has enabled to control materials growth in atomic dimension, leading to discovery of novel quantum effects in a variety of doped structures. Potential profile modulation opens a way to a new research domain where interesting quantum physics is expected to manifest itself. Coupled quantum well (CQW) represents a new class of QW[1-4] with such a potential modulation that can be introduced by growth alone and has been a major focus of interest. Within these structures, interval coupling plays an essential role determining energy spectrum and resultant electronic as well as optical properties. Interval coupling also dictates the evolution of a superlattice state[4] which is a repeated extension of CQW. To date, luminescence investigation on the interval coupling in semiconducting materials has been limited to compound semiconductors whereas group-IV materials have been scarcely explored due primarily to the lack of emission efficiency. Owing to recent progress of vapor phase epitaxy technology, however, photon emissivity in strained $\text{Si}_{1-x}\text{Ge}_x/\text{Si}$ system has reached a point viable for realistic optical study using photoluminescence[5-18]. On the other hand, atomic diffusion at heterointerfaces is expected to induce a potential modulation in a different way due to profile extension driven by concentration gradient.

In this paper, we present a systematic photoluminescence (PL) study on strained $\text{Si}_{1-x}\text{Ge}_x/\text{Si}$ CQWs and interval coupling-driven potential profile modulation in QWs.

2. Construction of Potential Modulation

Potential modulation can be introduced either by growth, i.e., appropriate design of a heterostructure, or by post-growth manipulation. In this paper, CQW and diffusion induced modulation are demonstrated for the former and the latter, respectively. Shown in Fig.1 are schematic diagrams of potential-modulated strained $\text{Si}_{1-x}\text{Ge}_x/\text{Si}$ CQWs and the associated energy spectrum. In the remainder of the text, these specific structures are referred to as symmetric CQW(SCQW), a), asymmetric CQW (ACQW) (b), and superlattices (c). Fig.1(d) illustrates a diffusion-driven potential modulation as a consequence of Ge redistribution (solid line) deviating from its original rectangular profile (broken line).

In SCQW, ground states ($n=1$) both in the conduction and heavy hole (hh) bands split up into symmetric (S) and antisymmetric (A) states due to interval coupling. S state is lower in energy compared to $n=1$ state of SQW. This energy difference increases with decrease of Si barrier width due to increased overlap of wavefunctions. For a very thick Si barrier, the two wells are isolated, while SCQW system is reduced to a SQW of double width in the limit of vanishing Si barrier.

Superlattice can be regarded as a repeated sequence of SCQW[4] as shown in Fig.1(c) where interband formation is expected to occur according to Kohn-Pearcy calculation due to extension of carriers over the entire structure. Evolution of a superlattice state is observed as steady downward shift of luminescence peak energy with increasing number of wells coupled to each other.

On the other hand, in ACQW system, where two wells of different widths are separated by a Si thin tunnel barrier (Fig.1(b)), energy level splitting is not so pronounced as in SCQW. Nevertheless,

ACQW offers an interesting aspect of interval coupling in the form of tunnel transfer of carrier[2,3] through the Si barrier, from the narrower well (right well) to the wider (left well), as schematically shown in Fig.1(b). This can be visualized as relative intensity variations of PL with changing Si barrier width, and is interpreted in terms of tunneling time, or in the context of carrier flow kinetics controlled by tunneling rate and recombination lifetime.

Identification of heterointerface significantly modifies Ge profile, resulting in effective well width narrowing with concomitant uprise of confining potential inhomogeneity as indicated by the arrow. Resultant Ge profile is expressed as an error function provided that Ge concentration dependency can be neglected. Similar to the case of Ge surface segregation-induced potential modulation, which has already been addressed previously by the author[11] and Branner *et al.*[12], PL peak shift is likely to be brought in the same sense, viz. blue shift.

3. Experimental

All samples were grown in a purpose-built gas source Si MBE system (Daido Hoxan, VCE-S2020) with a base pressure of 4×10^{-10} Torr pumped by ultrahigh vacuum pumps. SiH_4 and GeH_4 were used as source gases. Further details of sample preparation are found elsewhere[19]. After standard degreasing, wafers were dipped for 1 min in 2.5 wt% diluted hydrofluoric acid to remove the surface oxide and to hydrogenate the surface. Following thermal clean at 800°C for 20 min in H_2 , $\text{Si}(100)$ uncoped QWs of Ge composition 0.177 and 0.15 were grown on off-axis P-type $\text{Si}(100)$ substrates at temperatures 620-740°C. Ge composition and layer thickness were controlled by a very precise and transmission electron microscope (TEM) for fully strained alloy layers and multiple QWs grown under the same conditions. Taking advantage of excellent controllability and reproducibility of gas source MBE, a series of single QWs (SQWs) and CQWs with a centered thin Si barrier were grown.

Steady state PL was collected in standard lock-in configuration using a defocused Ar^+ ion laser beam operating at an optical excitation power density of 0.1 mW/cm^2 over the sample surface. Luminescence was dispersed through a 1-m grating monochromator blazed at 1.5 μm , and detected using a liquid-nitrogen-cooled Ge detector (North Coast EO-817L). Time-resolved luminescence spectroscopy was performed using a synchronously pumped pyridine-2 dye laser operating at a wavelength of 673 nm being excited by a mode-locked Ar^+ ion laser. An ultra low dark-current S-1 type photomultiplier (Hamamatsu R3236) was operated in a photon counting mode with time resolution better than 1 ns[20]. Signal was processed through a time-to-amplitude converter and accumulated on a multichannel analyzer. Sample temperature was controlled by a closed-cycle refrigerator, a helium vapor stream vaporizer cryostat, or immersion in pumped liquid helium.

Post-growth annealing was performed in vacuum, $\sim 10^{-6}$ Torr, to prevent surface oxidation during annealing since a thermal oxide thicker than natural oxide was found to exert significant surface stress, leading to drastic band-gap shrinkage of QWs[21,22].

4. Results and discussion

4.1. PL spectra of SQWs and CQWs

19-K PL spectra of SQWs of $\text{Lz}=34\text{\AA}$ with Si barrier width (Lb) of 9.6, 19.2, 23.8, 38.4, 76.8, 94\AA are shown in Fig.2. PL spectra of single QWs of $\text{Lz}=34\text{\AA}$ and $\text{Lz}=68\text{\AA}$ are also shown for comparison. NP, TA, and TO refer to no-phonon and transverse-phonon-involving lines (A-acoustic, O-optical), respectively. Luminescence of Si substrate is seen on the higher energy side of QW luminescence around 1094-1097 meV.

PL peaks are seen to shift downward as Lb is decreased as shown in Fig.2, demonstrating the interval coupling between two symmetrically aligned wells due to wavefunction penetration across the Si barrier[1,4,23]. Accordingly, $n=1$ states in both the conduction and heavy hole (hh) bands split up into symmetric (S) and antisymmetric (A) states as shown in the inset. For $\text{Lz}=34\text{\AA}$, $n=1$ bound state is established in the valence band for all SQWs and CQWs, and $n=2$ bound state almost lines up with band-edge of the Si barrier. In contrast, $n=2$ state is not a real bound state in the conduction band. On the other hand, A-hh state is established only in the valence band and it is above the Si barrier band-edge in the conduction band. Thus the observed luminescence is plausibly attributed to the optical transition associated with the lower-lying S states of electron (e1) and heavy hole (hh1)[23]. Note here that the light hole (lh) state is expected to be split in a similar manner, but the S state is located well higher than symmetric hh1 state. Meanwhile, for a much thicker barrier, two wells are effectively isolated and NP peak is expected to exactly fall on the counterpart of a SQW with the same width, 1050 meV. This is what we observe in our samples for $\text{Lz}=80\text{\AA}$ where NP peak energy is centered at 1050 meV. For $\text{Lz}=0$, CQW system with $\text{Lz}=34\text{\AA}$ reduces to a SQW with a doubled width, $\text{Lz}=68\text{\AA}$.

NP peak energy, ENP, extrapolated to vanishing excitation is shown in Fig.3 as a function of Lb. Solid line represents the theoretical peak energy assuming a rectangular QW potential profile. Standard envelope function approach within the effective mass approximation was used in the calculation[19].

To check that the hole tunneling controls the PL profile variation with L_h , relative PL intensity of QW1 and QW2, I_{QW1}/I_{QW2} , as shown in Fig. 10 was compared with theoretical calculation. These points could not be obtained for $L_h = 70\text{\AA}$, since I_2 quickly rolled off due to faster tunneling. An assumption for particle transmission through a potential barrier and a kinetic equation of carrier recombination were combined to obtain the expression for the fitting curve of the form [27].

$$12\gamma_1 \frac{(1/\lambda^2)^2}{b} \frac{4EV \cdot D}{(1/\lambda^2)^2} \cdot (1) \quad (1)$$

[illegible]

The LB dependence estimated from Eq.(1) as tunneling rate gives by the rectangular bracket[27]. The tunneling time is then obtained as follows to be ~ 0.5 sec for $L=6-9\text{\AA}$. This value seems to be reasonably comparable with radiative decay time of the narrow well. This value shows that the intersubband tunneling time compares with the radiative decay times. Otherwise, carrier since the intersubband tunneling time compared on QW1 or tunnel escape to QW2 is dominant. These results indicate that the intersubband transition will be such that it is concentrated on QW1 as discussed in Sec. II. In addition, the intersubband transition will be observed in the photoluminescence spectra. However, the intersubband transition has been eventually observed for n-type GaAs and thinner Si barrier, respectively.

It is worth mentioning here that interval banding could be identified for rather wider Si band barrier compared to direct-gap materials systems like $\text{AlGaAs}/\text{GaAs}$ [17]. This seems to reflect an intrinsic aspect of SiGe luminescence, and is primarily because the cooling process, i.e., radiative inflection, is two to three orders of magnitude lower in SiGe than the typical radiative lifetimes of GaAs, $\sim 1\text{--}10\text{ns}$ [27]. Such a long-lived carrier in SiGe finds more chance of encountering the same barrier, leading to an apparent increase of classical period of motion [20] represented by the first parenthesis in the rectangular bracket, and thereby increasing the mean lifetime τ below which interval banding occurs happen.

Ge/Si interface diffusion

[illegible]

NP peak shift in Fig. 11 was found to be fitted with a single interdiffusivity of the form, $D = D_0 \exp(-E_a/RT)$, by software standard 1-D diffusion equation. D was assumed to be a function of T only. The activation energy E_a was determined to be 1.0 eV.

The effective masses of electrons (m_e) and heavy holes (m_{hh}) used were $m_e = 0.19m_0$ and $m_{hh} = 0.265m_0$, respectively, where m_0 is the free electron mass. m_{hh} was obtained by linearly extrapolating the values for Si and Ge. Excitonic NP peak energy was obtained by the relationship $E_{NP} = 115(\Delta E_c - \Delta E_v - \Delta E_{exc})$, where ΔE_c and ΔE_v represent the conduction and valence band edges, respectively. The exciton binding energy was assumed to be independent of the well width and fixed at 15 meV [16]. Recently, Gail et al. reported the well width dependence of exciton binding energy, showing that the binding energy varies ± 20 meV over $E_g = 1.1-3.0$ eV for $\text{GaAs}/\text{AlGaAs}$ heterostructures [17]. Therefore, the assumption of fixing the binding energy at 15 meV is expected to allow for an uncertainty of ± 20 meV in the present calculation. The ENP of a 1500-Å alloy was measured to be 990 meV at 10% where no quantum size effect manifested itself and therefore the sum of the band discontinuities should be 1500 meV. As ΔE_v is systematically increased, with a constraint that $\Delta E_c + \Delta E_v = 1500$ meV, the theoretical curve shifts toward higher energies. To an accuracy of ± 10 meV, the data fall on the curve with $\Delta E_c = 1450$ meV shown by the solid line. This value was then used to fit the experimental NP peak energy of SQWs as a function of x . An excellent match was obtained between the calculation and the data, consistent with the result reported previously by the authors that the conduction $\text{GaAs}/\text{AlGaAs}$ band discontinuity when a QW is present is 20 meV [18, 19].

It is interesting to check here the well-established formula, $\Delta E_F = 0.54(eV)$ ($0 < x \leq 1$) [25] obtained by Van de Walle and Martin for strained $\text{Si}_{1-x}\text{Ge}_x\text{S}/\text{Si}(100)$ on the basis of the deformation potential theory. Using this formula, we obtain $\Delta E_F = 14\text{meV}$ for $x = 0.177$, which is in close agreement with the experimental results. Hence one can say that the 0.54-eV holds as far as we are concerned with strained $\text{Si}_{1-x}\text{Ge}_x\text{S}/\text{Si}(100)$. With reference to this, the band alignment of strained $\text{Si}_{1-x}\text{Ge}_x\text{S}/\text{Si}(100)$ should be of type-I as shown in Fig. 4. This can be justified by the fact that no successful fit was obtained when the conduction band offset was neglected (broken line in Fig. 2) or a negative offset (dashed line) was assumed in the calculations. This seems to conflict with previous report [13,16] claiming the absence of conduction band discontinuity or type-II band (misnomer).

CONTEMPORARY CHINESE LITERATURE

Figure 5 illustrates the evolution of a population state with increasing number of coupled wells. The upper panel shows PL spectra and the lower panel shows EHP variation. EHP shifts to lower wavelengths with increasing number of coupled wells and the peak shift is in good agreement with a Kreeb-Priory type calculation.

[illegible]

CHILDREN'S SPEECH UNDERSTANDING: SPEECH RECOGNITION

19K PL spectra of ACQW's with two different wells, $L_1=40\text{\AA}$ (QW1) and $L_2=34\text{\AA}$ (QW2), are shown in Fig. 9 for $L_3=6, 8, 9, 11, 12\text{\AA}$. Note, QW2 was grown first and therefore is on the Si substrate side. In this arrangement, photo-carriers are created mostly in the Si substrate and diffuse into the QW2. Thus the apparent dominance of PL due to the narrower well (QW2) is observed for the first-grown QW [26]. The apparent dominance of PL due to the narrower well (QW2) for a decoupled case, say $L_3=100\text{\AA}$, is due to increased carrier flow into QW2. In contrast, spectral dominance is gradually switched to QW1 with decreasing L_3 . Although the second seramon seems to

Es. means to make smaller compared to what has been reported in a previous work reported by Van der Walle et al. [31]. Nevertheless, the action of Es was largest in recent x-ray characterization of metamorphic in situ melt layers by Enbass et al. [32] and Hollister et al. [33]. It is very difficult to explain the different results because they were allegedly grown by low temperature (1000°C) MBE growth. The reason for this is that the samples were grown by low temperature MBE growth [32,33] and strain enhancement of diffusivity would have brought a smaller Es, compared to unsaturated samples. Hence, we believe that the 'intermediate values' obtained here reflect improved stability in gas source grown samples which were grown in equilibrium conditions. It is worth noting that the stability of the solid source MBE grown samples exhibited a dramatic 10° peak within 10° to 15° to make gas source grown samples. This seems to be in agreement with a finding that solid source grown QW is not of a 'lath structure', stability compared to gas source grown QW [16,3].

In conclusion, we have demonstrated the luminescence investigation on the potential modulated quantum wells with different thicknesses. The results show that the PL intensity of SCQW, ACQW, and ICQW increases with increasing well width. In particular, the PL intensity of SCQW is lower than that of ACQW and ICQW. Interwell coupling was studied in the PL spectra of SCQW, ACQW, and ICQW. The calculated quantum energy variation was found in SCQW in close agreement with theoretical calculation. The interwell coupling effect was observed in the PL spectra of SCQW, ACQW, and ICQW. The modulation of the quantum energy variation was clearly observed in ACQW. Superlattice evolution was induced by changing structural parameters and the exciton localization was observed in superlattice-embedded single quantum wells. DMF-induced potential modulation was observed to bring large blue shift of luminescence peak energy.

- References
- 1 C. Delaunay, U.O. Zumballa, G. Bostard, M. Voon, A.C. Coatsworth, and W. Wegmann, *Sol. Sci.* **42**, 491 (1984).
- 2 R. Sauer, K. Thonke, and W.T. Tsang, *Phys. Rev. Lett.* **61**, 606 (1988).
- 3 R. Sauer, T.D. Harris, and W.T. Tsang, *Phys. Rev. B* **39**, 12929 (1989).
- 4 R. Dingle, A.C. Coatsworth, and W. Wegmann, *Phys. Rev. Lett.* **34**, 1322 (1975).
- 5 J. C. Sturm, H. Marchant, L. C. Lechinsky, M. L. Thewlis, N. L. Rowell, J.-P. Noél, and D. C. Hongton, *Phys. Rev. Lett.* **66**, 1363 (1991).
- 6 D. J. Robbins, P. Calvez, and W. Y. Leung, *Appl. Phys. Lett.* **59**, 1350 (1991).
- 7 D. Dworek, G. Brimble, A. Soufi, and T. Kizuyama, *Phys. Rev. B* **44**, 11152 (1991).
- 8 T.D. Sauer, R. Hengehoel, Y.K. Yen, D.J. Gebrey, E. Thompson, and G.S. Pomrenke, *J. Vac. Sci. Technol.* **B10**, 923 (1992); *J. Crystal Growth* **127**, 473 (1993).
- 9 J. Payer, K. Thonke, R. Sauer, H.K. Kibbel, H.-J. Herres, and E. Kasper, *Appl. Phys. Lett.* **66**, 1729 (1992).
- 10 L. Vasan, A. Harman, K. Smith, Ch. Dieler, and H. Lüth, *J. Appl. Phys.* **70**, 6218 (1992).
- 11 J. Payer, A. Harman, K. Smith, Ch. Dieler, E. Fries, and G. Abertner, *Thin Solid Films* **222/27** (1992); *Thin Solid Films* **124** (1993).
- 12 G. Abertner, *J. Vac. Sci. Technol.* **12**, 443 (1973).
- 13 G. Abertner, *J. Vac. Sci. Technol.* **10**, 1 (1972) (to be published).
- 14 J. Payer, H. Yoshida, N. Uemori, A. Fujiwara, Y. Takahashi, Y. Shiraki, and R. Ito, *Thin Solid Films* **232**, 1 (1993); *J. Crystal Growth* **127**, 489 (1992).
- 15 J. Payer, *Appl. Phys.* **31**, 1393 (1992); N. Uemori, S. Fukatsu, and Y. Shiraki, *Appl. Phys. Lett.* **61**, 706 (1992); S. Fukatsu, N. Uemori, Y. Shiraki, T. Chikari, A. Nishida, and K. Nakagawa, *Jpn. J. Appl. Phys.* **31**, L1015 (1992); S. Fukatsu, N. Uemori, and Y. Shiraki, *Jpn. J. Appl. Phys.* **31**, L1915 (1992); S. Fukatsu, N. Uemori, Y. Shiraki, A. Nishida, and K. Nakagawa, *J. Crystal Growth* **127**, 493 (1992).

FIG. 2 19 K PL spectra of strained Si0.83Ge0.17/Si SQWs with 1.2-14 Å with Si barriers of different thickness, 1b and SQWs with 1.2-14 Å and 1.2-18 Å.



FIG. 3 PL vs barrier width for strained $\text{Si}_{0.76}\text{Ge}_{0.24}/\text{Si}$ 177 Si superlattices. Solid line is the theoretical curve calculated by effective mass approximation. Broken line represents experimental data in the absence of conduction band offset. Inset shows the schematic of the coupled well with split energy levels.

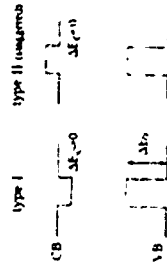


FIG. 4 Schematic potential line up for Type I and Type II configurations.

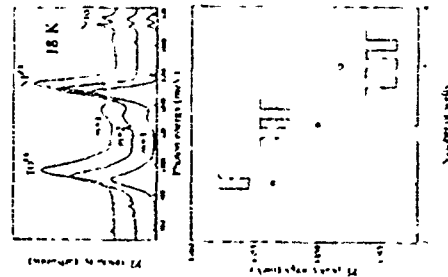
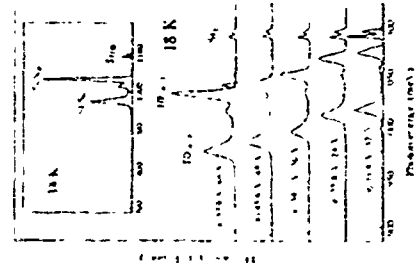


FIG. 5 Evolution of a Krong-Penny type superlattice. Upper and lower panels show PL spectra and PL peak energy with number of coupled wells. The schematic inset shows the associated energy spectrum.



M S Skolnick^a, K J Nash^a, D J Nowbady^a, M K Saker^a, T A Fisher^a, D M Whitaker^a, D W Pegg^a,
N Mura^b, S Sasaki^b, R S Smith^c, and S J Bass^d

^aDepartment of Physics, University of Sheffield, Sheffield S10 7RN, UK
^bDRA, St Andrew's Road, Marwell, Water, WRI4 3PS UK

^cInstitute for Solid State Physics, University of Tokyo, Roppongi, Minato-ku, Tokyo 106, Japan
^dGEC-Marconi Materials Technology Ltd, Caswell, Towcester, Northants NN23 9EQ, UK

Abstract

Evidence for many body shake-up in the magnetoluminescence spectra of quantum wells is presented. Results for bulk lattice matched InGaAs-InP and strained InGaAs-InGaAs GaAs structures, covering a wide range of carrier densities, are presented. In all the structures coupling between shake-up and LO phonon excitations is observed. Strong enhancement of the shake-up satellite of the N_0 ± 1 Landau level (LL) recombination due to resonant coupling with the $N_0 \pm 0$ LL is presented.

Fermi sea shake-up is a fundamental many body effect in which excitations of the Fermi sea arise during the recombination between a photoexcited hole and a high density electron system. It corresponds to the creation of an electron hole quasi particle pair on either side of the Fermi energy during recombination. The energy of the photon which is emitted in the presence of shake-up is lower than in its absence, the difference in the energies corresponds to the energy of the electron hole quasi particle pair created during shake-up. Such pair excitations across the Fermi level have a continuous range of energies, and thus give rise to a broad low energy tail to recombination spectra. For this reason, until very recently, the only evidence for shake-up processes in semiconductor spectra was obtained from line shape analysis of the observation of anomalously strong photoluminescence (PL) in the forbidden KLL geometry in GaAs-AlGaAs quantum well (QW) spectra [1]. However, we have shown within the last few months that definitive observations of 'shake-up' can be obtained from the study of the PL spectra of QWs in magnetic field [2]. In magnetic field the electron states are quantised into Landau levels, with the consequence that the only possible shake-up excitations are to unoccupied Landau levels (LLs) above the Fermi level. As a result the broad low energy tail in the PL spectra is transformed into a series of discrete shake-up satellites. Comparison of the zero and finite magnetic field spectra then shows that the $B = 0$ tail is also due to shake-up.

The work of ref 2 was carried out from 0 to 10T on a lattice matched InGaAs-InP QW containing $1.15 \times 10^{11} \text{ cm}^{-2}$ electrons. In the present paper these results are extended up to 20T. Interaction between the shake-up satellites and LO phonon lattice excitations is observed at very similar form to that reported recently for an AlGaAs-InGaAs-InP QW containing a relatively high density $n = 10^{11} \text{ cm}^{-2}$ of electrons [3]. New results for the strained InGaAs-InP QW up to higher fields are also reported. Strong evidence for the enhancement of the satellites due to resonant inter LL coupling will be presented. Finally, the satellite behaviour for the strained InGaAs-InP QW will be shown to be very similar to that observed in an InGaAs-InP QW also containing a high density of carriers ($1.9 \times 10^{11} \text{ cm}^{-2}$).

Details of the InGaAs-InP and AlGaAs-InGaAs QW samples are given in refs 2, 3 and 10. The PL experiments were carried out at 2 or 3K in either a 14T superconducting or 20T Bruker magnet. PL was excited with $\sim 25 \text{ mW/cm}^2$ of 633nm radiation from a He Ne laser dispersed by a grating spectrometer and detected using a cooled Ge photodiode.

The PL spectra for the lattice matched InGaAs-InP QW (1.15 $\times 10^{11} \text{ cm}^{-2}$) while QW $n_0 = 1.15 \times 10^{11} \text{ cm}^{-2}$ were presented in ref 2 and will not be repeated here. At $B = 0$, the spectrum consists of a zero phonon line (ZPL) at 347.4 meV and LO phonon satellite structure in the 800 to 820 meV region to lower energy. Above 820 meV the phonon satellites are resolved into contributions from the GaAs and InGaAs-like LO modes of the InGaAs QW material and from the InP modes of the barrier.

This behaviour is summarised in the fan diagram of transition energies against magnetic field shown in Fig 1. Splitting of the ZPL into $n = 0$ and $n = 1$ LLs is seen with the $n = 1$ LL depopulating at 2.7T at a filling factor $\nu = 2$, corresponding to $n_0 = 1.15 \times 10^{11} \text{ cm}^{-2}$. The ZPL variation with B is replicated at 2.7, 3.1 and 4.3 meV to lower energy by the 'InAs' GaAs and InP LO modes mentioned above. In addition, lower energy T_1 , T_2 and T_3 shake-up satellites are visible. The T_0 satellites correspond to inter Landau level Fermi sea excitations in which an additional electron is promoted from the $N_0 \pm 0$ state to $N_0 \pm 1$ or $N_0 \pm 2$ or higher LLs. The spacing of the T_0 satellites below the ZPL is close to integral multiples of $\hbar\omega_0$, the inter LL separation. Closer inspection of Fig 1 shows that the ZPL- T_1 separation is greater than the T_1 , T_2 , T_3 splittings, and that the

T_1 energy varies in a non linear fashion with B . The ZPL- T_1 spacing (ΔE) can be expressed in terms of an apparent effective mass m^* , using the expression $\Delta E = \hbar v_F / m^*$. The variation of m^* with B is shown in the inset to Fig 1. m^* varies from 0.037 m_0 at 2.3T to 0.047 m_0 at 9.6T, close to the QW band edge effective mass m_0 of 0.038 m_0 in these InGaAs-InP QWs. This behaviour was explained in ref 2 by noting that the shake-up excitations correspond to inter LL magnetoplasmon excitations of the Fermi sea. The energy of the magnetoplasmon excitations is only equal to $\hbar\omega_0$ for in-plane wave-vector $q = 0$ [1,3]. At $\nu = 1$, the departure from $\hbar\omega_0$ of the maximum in the magnetoplasmon density of states is given by $E_1 - 0.17\text{meV}/E_0$ where $E_0 = (\hbar v_F)^2$ is the magnetic length. The factor v_F in E_1 varies as $B^{1/2}$, and as a result the apparent effective mass m^* is expected to tend towards m_0 with increasing B as observed in the inset to Fig 1.

The T_1 satellite intensities decrease with increasing B in the low field range (0 to 10T). As shown in Fig 2, T_1 decreases in intensity by a factor of ~ 5 from 0.5 to 10T, where it is only barely visible with $\sim 0.01\%$ of the intensity of the ZPL. From 10.5 to 17.5T, T_1 is not observed, but it then reappears in the 18 to 19.5T range as shown in Fig 2c. For $B > 17.5$ T, T_1 is at lower energy than the LO phonon satellites (see Figs 1,2). Its re-appearance in the high field range arises from resonant mixing between T_1 and the much stronger LO phonon satellites of the ZPL. Very similar resonant interactions are discussed below for the high density AlGaAs-InGaAs QWs and InGaAs-InP QWs. In these cases the resonant interactions are observed at much lower field since higher LLs are populated to relatively higher fields. As a result the LO phonon satellites of $n \geq 1$ LLs interact with the T_0 satellites at lower magnetic field.

The $B = 0$ PL spectrum of the strained InGaAs-InP QW ($n_0 = 0.23 \times 10^{11} \text{ cm}^{-2}$) is shown in Fig 3a. It consists of a peak at 1.17 eV with QW $n_0 = 7.2 \times 10^{11} \text{ cm}^{-2}$ ($\nu = 2.4$ meV) is shown in Fig 3a. It consists of a peak at 1.17 eV with a shoulder to recombination at electrons at $q = 0$ at the bottom of the QW conduction band, together with a broad high energy tail extending to the electron Fermi energy at E_F . The $q = 0$ transitions up to the Fermi breaks up into LL transitions (N_0, N_1). At 10T ($\nu = 3$) only the $N_0 \pm 0$ and 1 LLs are populated. Recombination of $N_0 \pm 1$ electrons with holes in both the $N_0 \pm 0$ and 1 LLs is observed due to the nonthermal distribution of the photo-created holes. The intensity of the $N_0 \pm 1$ transitions decreases with increasing field from 10 to 14T (Figs 3b to 3c), as the $N_0 \pm 1$ LL depopulates towards $\nu = 2$ (14.9T). To lower energy below the 10T principal recombination line T_0 shake-up satellites and N_0 LO phonon satellites of the $N_0 \pm 1$ LL are observed. These results are summarised in the fan diagram of Fig 3. Spectra below 10T were presented in ref 2, together with a discussion of oscillations of intensity of the N_0 satellites with B which occur at crossing points with the T_0 satellites.

In the present paper we will concentrate on the new results above 10T in particular the resonant anti-crossing between T_1 and T_2 in the 14T region and the behaviour of the T_1 feature with B . As for the InGaAs-InP sample of Figs 1,2 the $(0,0) - T_1$ separation is greater than $\hbar\omega_0$. The dashed line representing the variation of the T_1 energy with B is drawn at an energy of 1.25 $\hbar\omega_0$ with the corresponding T_2 and T_3 energies at 2.25 $\hbar\omega_0$ and 3.25 $\hbar\omega_0$ below (0,0) as expected from the magneto-plasmon theory of Kallin and Halperin [1,3]. For this sample the variation of the T_1 energy with B is strongly perturbed by resonant anti-crossings with the N_0 satellites, thus precluding any determination of the variation of the departure of the T_1 energy from a linear variation with B equivalent to the variation of m^* with B in the inset to Fig 1.

The resonant interaction between T_1 and T_2 is clearly seen in the fan diagram of Fig 4, where anti-crossing is observed in the 9 to 14T region, away from resonance the T_1 satellite is dominant, as seen in the spectra of Figs 3b to 3c at 10 and 14T respectively. In the intermediate region T_1 gains intensity due to resonant mixing with T_2 with the two satellites having equal intensity at 11.5T. The variation of intensities between the two sides of the resonance is shown in the 11 and 12T spectra of Figs 5c, d respectively.

The variation of the intensity of T_1 the low energy shoulder ~ 5 meV below (0,0) at 10T is particularly interesting. In ref 3, this feature was tentatively ascribed to a shake-up satellite of (1,0) enhanced in intensity by resonant mixing with (0,0). This attribution is given strong support by the higher field data presented in the inset to Fig 4 where the intensity of T_1 relative to that of the (1,0) transition is presented. If T_1 is a satellite of (1,0) the ratio of the two intensities is expected to be a constant, independent of magnetic field. This is exactly the behaviour observed in the inset to Fig 4 where the intensity ratio of ~ 7.5 is seen to vary by less than 15%.

from 9 to 14 T is ~ 3 to 2. This observation provides strong support to the attribution of the T_1 feature to a shake-up satellite at (1,0). The shake-up excitation corresponds to the promotion of an additional electron from $N_0 = 0$ to $N_0 = 1$. T_1 occurs at 1.3 meV below (1,0), consistent with the separation observed between (0,0) and T_1 , as required since both T_1 and T_1' arise from $\Delta N_0 = 1$ inter-LL excitations.

The high intensity of T_1' relative to (1,0) is also noteworthy. (1,0) is relatively weak compared to (0,0), even when $N_0 = 1$ is filled at 7.4 T (~ 4), since (1,0) is a $\Delta N_0 = 1$ transition observed only due to the presence of weak disorder in the system.¹⁰ T_1' is ~ 7 times stronger than its parent line (1,0) since it is nearly degenerate with the dominant combination transition (0,0), and is strongly enhanced in intensity by resonant mixing with (0,0).

Finally we discuss the magneto PL results for an InGaAs-InP QW with high n_0 of 9×10^{11} cm⁻³, which shows very similar LO phonon and shake-up satellites to those described above for the AlGaAs-InGaAs-GaAs structure. This sample exhibits a strong Fermi energy edge singularity¹⁵ in its PL spectrum due to the strong localization of photo-generated holes in alloy fluctuations in the InGaAs QW. This contrasts with the behaviour for the more uniform AlGaAs-InGaAs QW of Figs. 3-4 where only a weak feature at T_1 is observed in Fig. 3a. In this paper we present only the variation of the transition energies against magnetic field, a discussion of the spin splitting in the satellite region being reserved for a separate publication. PL spectra for the principal LL transitions up to 10 T can be found in ref. 10.

The transition energies against magnetic field are shown in Fig. 5. An $n = 0$ LL transition ($N_0 = 0$) are observed for N_0 from 0 to 8. The straight lines through the experimental points correspond to $(N_0 + 1/2) \hbar\omega_c$ variables with $\hbar\omega_c = 0.05$ meV. Two points in particular should be noted concerning the ($N_0 = 0$) transition. Firstly the main transitions exhibit oscillations around the linear $(N_0 + 1/2) \hbar\omega_c$ variation as a function of filling factor. These oscillations have been attributed to oscillations of exchange and correlation energies or to variations in the self-consistent potential with filling factor.^{16,18} Secondly, the (1,0), (2,0) and (1,1) transition energies deviate to lower energy below the linear fit as soon as the respective LL begins to empty, with increasing B (i.e. (1,0) above $\nu = 4$ where $n_0 = 1$ begins to empty).¹⁹ This deviation probably arises due to the finite width of the distribution of LL energies. As the filling factor is reduced, recombination from the tail of the broadened distribution dominates the PL spectrum to a progressively greater extent, with the result that the observed LL transition energies deviate increasingly below $(N_0 + 1/2) \hbar\omega_c$.

To lower energy, N_0 LO phonon satellites and T_0 shake-up satellites are observed in a very similar manner to that reported in Figs. 3-4. The dominant LO phonon satellites T_1 , T_2 and T_3 arise from the 31 meV GaAs-like LO phonon modes of the InGaAs QW, as seen for the low density InGaAs-InP QW in Figs. 1-2. The satellite labelled T_4 arises 43 meV below the (1,0) transition and is due to emission of an InP barrier LO phonon (the InP LO phonon energy is 43 meV). The attribution of T_5 to an LO phonon satellite of (1,0) is supported by the very similar intensity variation of T_4 and (1,0) with field as $N_0 + 1$ depopulates towards $\nu = 2$.

The straight lines representing the T_1 and T_2 transitions which give the best fit to the experimental points are drawn at $\hbar\omega_c$ and $2\hbar\omega_c$ below the (0,0) energies. The difference between these splittings and the 1.25 meV $\hbar\omega_c$ 2.5 meV splittings of Fig. 4 may arise from the greater distribution of Landau level energies in this case as shown already by the departure below $(N_0 + 1/2) \hbar\omega_c$ of the ($N_0 = 0$) transitions for partially filled LLs. The results for the principal ($N_0 = 0$) transitions show that tail states dominate the recombination for small LL filling, such a distribution of LL energies may also perturb the observed shake-up energies and thus lead to the $\sim \hbar\omega_c$ and $\sim 2\hbar\omega_c$ energies observed. As discussed for the strained layer QW of Fig. 3, anti-crossing between the LO phonon and shake-up satellites is observed in Fig. 5 between the T_1 and T_2 satellites from 1.2 to 1.9 T. The splitting of the two energies at resonance is 10 meV, fairly close to that observed for the T_1 and T_2 anti-crossing of Figs. 3-4.

In conclusion, shake-up and LO phonon satellites in the magneto-PL spectra of lattice matched and strained QW structures covering a wide range of carrier density have been presented. Interaction between the Fermi sea and lattice excitations has been observed in all the samples investigated. Enhancement of the shake-up satellite 'intensity' by resonant coupling with the dominant $N_0 = 0$ LL recombination line has been demonstrated.

Acknowledgements: We thank J. C. Minn for collaboration at the Max Planck Institut, Grenoble where the experiments up to 20 T were performed.

1. See e.g.: G.D. Mahan, *Many Particle Physics* Plenum New York 1990) Chap. 3.
2. Y. A. Izrael and E. I. Raibin, *Zh. Eksp. Teor. Fiz.* 26, 757 (1989) (Sov. Phys. JETP 68, 430 (1989)).
3. T. Genoyama and L. J. Sham, *Phys. Rev. Lett.* 62, 1048 (1989).
4. K. J. Nash, M. S. Skolnick, M. K. Saker and S. J. Bass, *Phys. Rev. Lett.* 70, 3115 (1993).
5. See, for example, J. H. Cole, W. W. Rühle, M. Pugh, K. Leo and A. Million, *Phys. Rev. B* 40, 12296 (1989) and references therein.
6. R. Soodakumar, A. Pinzuk, A. C. Goswami, D. S. Chandra and L. J. Sham, *Phys. Rev. Lett.* 58, 1150 (1987).
7. G. D. Mahan and Y. C. Chang, *Phys. Rev. B* 32, 4521 (1985).
8. M. S. Skolnick, D. J. Nowozin, D. M. Whitaker and R. S. Smith, *Phys. Rev. B* 47, 6823 (1993).
9. Similar interaction phenomena between LO-phonon and shake-up satellites has also been reported by L. V. Butov, V. I. Grines, V. D. Kulakovskii and T. G. Andersson, *Phys. Rev. B* 46, 13627 (1992).
10. M. S. Skolnick, K. J. Nash, S. J. Bass, P. E. Simmonds and M. J. Kane, *Solid State Commun.* 62, 637 (1988).
11. C. Kallin and B. Halperin, *Phys. Rev. B* 31, 3635 (1985).
12. A. H. MacDonald, *J. Phys. C* 18, 1003 (1985).
13. A. Pinzuk, J. Valabrega, J. Helman, A. C. Goswami, J. H. English, C. W. Tu, L. Pfeiffer and K. West, *Phys. Rev. Lett.* 61, 2701 (1988).
14. At 10 T, the ratio of the (1,0) to (0,0) intensity is 20.
15. M. S. Skolnick, J. V. Ranson, K. J. Nash, D. J. Nowozin, P. R. Tapster, S. J. Bass and A. D. Phil, *Phys. Rev. Lett.* 58, 2130 (1987).
16. S. Katayama and T. Ando, *Solid State Commun.* 20, 97 (1989).
17. T. Genoyama and L. J. Sham, *Phys. Rev. B* 39, 11044 (1989).
18. R. Soodakumar, W. Koop, A. Rammo, G. Manner, T. Rogger, J. C. Minn and J. P. Andre in *High Magnetic Fields in Semiconductor Physics* edited by G. Landwehr (Springer-Verlag, Berlin), p. 62.
19. Similar but smaller deviations of the (1,0) and (2,0) transitions from linearity when the $N_0 = 1$ and 2 LLs are partially filled are visible in Fig. 3.

Figure Captions

1. Transition energies against magnetic field for InGaAs-InP quantum well of 150 Å width containing 1.5×10^{11} cm⁻³ electrons. Splitting of the zero phonon line (ZPL) into $n = 0, 1$ Landau levels is observed at low magnetic field. To lower energy LO phonon satellites and shake-up satellites (T_1, T_2, T_3) of the $n = 0$ LL recombination are observed. The inset shows the variation of mT with B, where mT is deduced from the $n = 0$ LL T_1 separation ΔE , where $\Delta E = \hbar\omega_c/mT$.
2. LO phonon and T_1 satellite spectra for InGaAs-InP sample at 8.5 T and 19 T. T_1 is observed at 19 T due to resonant interaction with the strong LO phonon satellites.
3. PL spectra at B = 0, 10, 11, 12 and 13 T in Figs. 3a-e for AlGaAs-InGaAs GaAs 150 Å wide, modulation doped strained layer quantum well. Landau level transitions (N_0, N_1) are observed in Figs. 3b-e with T_1 shake-up and T_2, T_3 LO phonon satellite lines to lower energy. The resonant exchange of intensities between T_1 and T_2 in the 11-12 T region is seen in Fig. 3c,d. Away from resonance the LO phonon T_1 line is the dominant satellite. The inset shows the variation of the intensity of T_1' the shake-up satellite ($n = 1$) relative to that of (1,0). The near constant intensity ratio of $T_1'/n(1,0)$ shows that T_1' is a satellite of (1,0), resonantly enhanced by interaction with (0,0).
4. Transition energies against magnetic field for AlGaAs-InGaAs GaAs quantum well. LL filling factors (ν) are indicated. The dashed lines to indicate the shake-up transitions (T_1, T_2, T_3) are drawn at energies 1.25 meV, 2.5 meV, 2.5 meV below (0,0). The fields indicated by the indices in the lower part of the figure correspond to the crossing points of T_1 with the N_0 satellites, at fields corresponding to the resonance condition $m = 1$ 2.5 meV, $\hbar\omega_c$ as discussed in ref. 7.
5. Transition energies against magnetic field for InGaAs-InP quantum well with $n_0 = 9.2 \times 10^{11}$ cm⁻³. $N_0 = 0$ LL transitions are observed, with $N_0 = 1$ to 3 GaAs-like and 1 A (InP) LO phonon satellites and T_1 and T_2 shake-up satellites are observed to lower energy, with clear resonant anti-crossing between T_1 and T_2 from 1.2 to 1.9 T. LL filling factors (ν) are indicated at the bottom of the figure.

Optical investigation of superlattice orbits and impurity states in InGaAs/GaAs

R. J. Warburton,¹ J. G. Michie,¹ P. Peyla,¹ R. J. Nicholas,¹
and K. Woodbridge²

¹Clarendon Laboratory, Parks Road, Oxford, OX1 3PU, U.K.

²University College London, Department of Electronic and Electrical Engineering,
Torrington Place, London, WC1E 7JE, U.K.

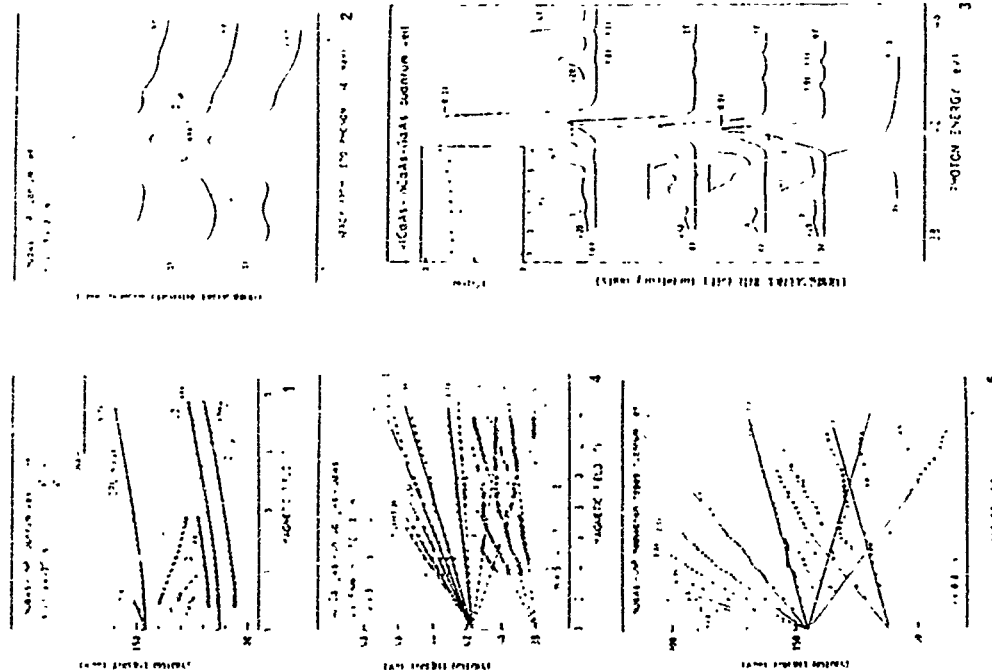
Abstract

We have measured optically-detected-cyclotron resonance on InGaAs/GaAs superlattices with large magnetic fields applied both parallel (Faraday) and perpendicular (Voigt) to the growth direction. Cyclotron resonance in the Voigt geometry reveals a band structure in the growth direction. A semi-classical quantization of the Kohn-Peierls dispersion gives good agreement with the data, providing that the cyclotron radius is larger than the superlattice period. We observe $1s - 2p_z$ transitions from residual impurities which lie predominantly in the barrier regions. The impurity transition has a remarkable behaviour in the Voigt geometry, moving from the bulk $1s - 2p_z$ field to close to the bulk free electron field as the barrier thickness increases, and is exactly mid-way between these two limits when the cyclotron radius equals the barrier thickness.

1 Introduction

A superlattice consists of quantum wells sufficiently close together such that inter-well coupling occurs. If a magnetic field is applied perpendicular to the growth direction, the electrons are forced to tunnel through the barriers. This can be pictured semi-classically because of the band dispersion in the growth direction. However, once the cyclotron diameter, $2r_c$ ($r_c = \sqrt{\hbar/efB}$), is smaller than, or comparable to, the superlattice period, L , then the effective mass picture breaks down. For a one-dimensional superlattice potential, the electron energy becomes dependent on the orbit centre [1], for a two-dimensional potential, a rich and fascinating energy level scheme emerges [2].

This transition when $2r_c \sim L$, from a semi-classical to a strongly quantum mechanical behaviour, has received only limited experimental coverage. Belle and co-workers [3] observed a weakening of PLF features when r_c^* and band level's energy exceeded the top of the miniband. Calculations showed that it is at this point that the electron energy becomes strongly dependent on the orbit centre. There is great advantage in probing the modes directly with far infrared (FIR) radiation, as has been reported by Duffield *et al* [4, 5] for GaAs/AlGaAs superlattices. These authors made cyclotron resonance experiments for $2r_c > L$, modelled successfully within



a semi-classical picture, but for $2\tau \sim l$ a new mode, corresponding to a state bound to the barriers, was observed.

The binding energy of impurities within a superlattice geometry is also of interest, as the impurity binding energy can depend strongly on the position of the impurity in the superlattice, which is in some ways analogous to the dependence of the Landau energy on orbit centre for $2\tau \leq l$. The impurity binding energy is a minimum when the impurity lies in the middle of the barrier, and a maximum when the impurity lies in the middle of the well [3]. If the impurities are spread evenly throughout the superlattice then there are two peaks in the density of states, leading to characteristic absorption edges [6]. Experimental work has in general concentrated on well bound impurities [7-9].

In this paper we present measurements on a series of $\text{In}_{0.5}\text{Ga}_{0.5}\text{As}/\text{GaAs}$ superlattices with the field B either $B \parallel z$ (Faraday) or $B \perp z$ (Voigt), where z lies along the growth direction. There are a number of differences to previous work. Most importantly, the electron band offset in $\text{In}_{0.5}\text{Ga}_{0.5}\text{As}/\text{GaAs}$ is only ~ 10 meV, giving sizeable miniband widths for relatively large barrier widths, l_b . This should be compared to the more familiar $\text{GaAs}/\text{AlGaAs}$ system in which superlattice behaviour is only apparent for very thin barrier widths, $l_b \leq 20$ Å. With $\text{In}_{0.5}\text{Ga}_{0.5}\text{As}/\text{GaAs}$ we are able to achieve not only $2\tau < l$, but also $2\tau < l_b$. Secondly, we have employed an optically detected technique in which the electrons are excited optically into the conduction band, allowing us to make cyclotron resonance experiments at low temperatures, without the constraints of impurity freeze out. Finally, we report measurements of barrier centred $1s - 2p_z$ impurity transitions, also in both field orientations.

2 Experiments

The samples were grown at Philips, Redhill, and consist of twenty periods of nominally undoped $\text{In}_{0.5}\text{Ga}_{0.5}\text{As}/\text{GaAs}$, with nominal well/barrier thicknesses (L_w/L_b) 50/50, 50/100, 50/150 and 50/200 Å. The actual sample dimensions, as measured by x-ray diffraction [10], differ slightly, although we refer throughout to the samples by their nominal thicknesses. Measurements on these samples, confirming their high quality, have already been published, notably a PL and PLE study [10] to determine the miniband widths and excitation binding energies.

The PL from each sample, excited with a 3 mW HeNe or solid state diode laser, consisted of a single line. Our optically detected cyclotron resonance (ODCR) technique involves monitoring the change in PL intensity induced by far infrared radiation. We found that the sign of the ODCR signal did not depend on the exact detection wavelength, and so the data were collected with poor resolution, to give as large a PL signal as possible. The sample was cooled to 2 K, and fields up to 15 T were applied. At resonance we could reduce the PL by up to 20% with our conventional optically pumped FIR gas laser. It should be borne in mind that the ODCR signal may not have a straightforward relation to the absorption of FIR.

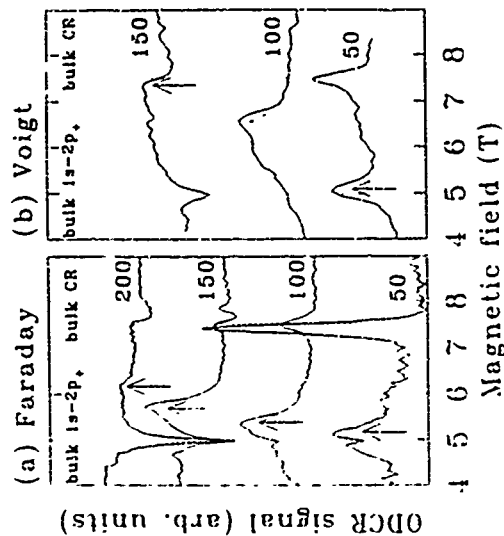


Figure 1. ODCR traces taken with the 96 μm FIR laser line for the four samples, labelled with the nominal barrier widths. The arrows mark the superlattice impurity transitions. The dashed lines show the fields of the bulk GaAs $1s - 2p_z$ and cyclotron resonance transitions.

3 Results

3.1 Faraday orientation

Typical ODCR traces, taken with the 96 μm FIR laser line, are shown in Fig. 1a. Each sample gives two main features, the one at lower field due to a $1s - 2p_z$ impurity resonance, and the one at higher field due to a cyclotron resonance. The impurity transitions are thought to be related to a low density of residual donors distributed throughout the superlattice. There are also particularly sharp features for the 50/150 and 50/200 samples, sharp features of opposite sign, related to values of these sharp features, and their independence from sample to sample, suggest that they arise from $1s - 2p_z$ and CR transitions in bulk GaAs , most probably from the GaAs capping layer, where any FIR absorption could affect the transfer of electrons into the superlattice, so contributing to an ODCR signal from the superlattice itself.

The CR field for the 50/50 sample occurs at a lower field than for bulk GaAs , but the field increases as the barrier width increases. This means that the cyclotron mass, $m^* = \hbar B/E$, increases for increasing l_b and this is a consequence of a reduction in inter well coupling. As the wells couple to form a superlattice, the confinement energy of the first electron level (E_1) decreases, so causing a reduction in the non-parabolicity enhancement to the band edge mass.

I_A	Δ	m^*/m_0	m^*/m_0	$1s-2p$	$1s-2s$	$r = I_A$
55.0	16.7	0.0665	0.0668	1.1	5.3	21.8
101.1	12.7	0.0671	0.0669	1.2	1.7	5.1
116.0	9.9	0.0677	0.0671	1.6	1.1	3.1
202.7	2.5	-	0.0675	1.0	3.5	1.6

Table 1 A summary of sample details and some results. I_A is the barrier width in \AA , Δ is the electron miniband width in meV, m^*/m_0 is the measured (calculated) effective mass at energy 10.13 meV in the Faraday orientation $1s-2p$ ($1s-2s$) or the $B=0$ impurity energy estimated experimentally (theoretically), and $r = I_A$ defines the magnetic field at which the cyclotron radius r is equal to the barrier thickness.

We have taken non-parabolics into account with an eight band k-p calculation [11]. The agreement with the data is good at cyclotron energies above ~ 8 meV (see Table 1) but at low energies the measured masses fall to anomalously low values. This behaviour is reminiscent of CR from conventional GaAs quantum wells where anomalously low effective masses have been observed at low field [12], attributed to shallow localizing potentials from well width fluctuations.

Fig. 1a shows two effects concerning the impurity transition with increasing barrier width: the field increases implying that the binding energy reduces, and the line shape becomes asymmetric with the signal falling rapidly on the high field side. Both imply that the impurities are predominantly in the barriers, although the broadness of the impurity resonance compared to the cyclotron resonance does mean that there is a distribution of impurities throughout the superlattice. The high field (low energy) absorption edge comes from the peak in the density of states from impurities in the middle of the barrier. As the barrier width increases, the superlattice potential draws the wave function further away from the impurity centre, so lowering the binding energy, as observed. Our calculations of the shallow donor $1s-2s$ energy reproduce this trend, and give reasonable agreement with the $B=0$ transition energy estimated experimentally (see Table 1).

3.2 Voigt orientation

ODCR traces in the Voigt geometry are plotted in Fig. 1b, again for the $96 \mu\text{m}$ FIR laser line. In this case, we have a clear CR only from the 50/100 sample, which occurs at higher field than in the Faraday geometry of Fig. 1a. We emphasize that the Voigt geometry enables us to sample the new band structure in the superlattice direction, and a semi-classical interpretation of cyclotron resonance consists of the electrons spiralling along the direction of the magnetic field, tunnelling through the barriers in the course of their cyclotron orbits. For the 50/100 sample, the cyclotron diameter is always larger than the superlattice period for the fields used here so we use a semi-classical quantization of the miniband dispersion to model the data. The superlattice dispersion $E(q)$, where q is the wave vector along the superlattice direction, implies a cyclotron mass according to

$$m^* = \frac{\hbar B}{v(q) \cdot \hbar} \quad q_0^2 = \frac{eB}{\hbar}, \quad q_1^2 = \frac{eB}{\hbar} \quad (1)$$

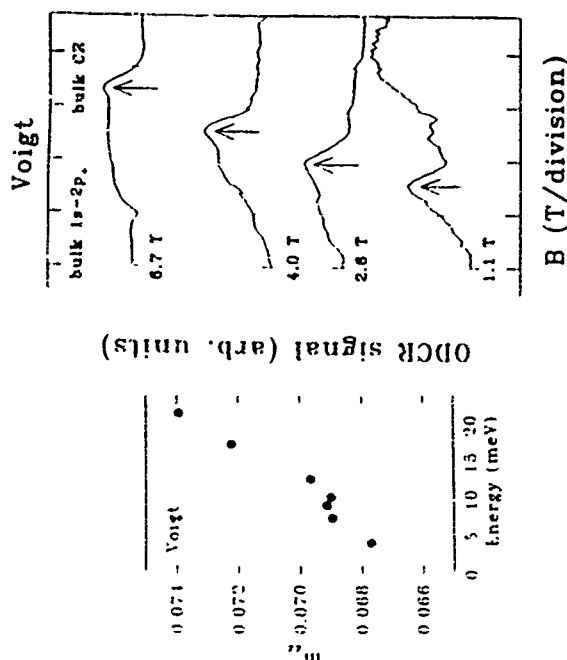


Figure 2 A comparison between the measured and calculated masses along the superlattice direction for the 50/100 sample. Figure 1 ODCR traces for the 50/100 sample, for four different laser wavelengths, 163, 118, 96 and 70 μm . The field has been offset such that the bulk $1s-2p$ fields (2.1, 3.6, 5.0 and 7.7 T respectively) are coincident. The arrows mark the superlattice impurity transitions.

We calculated $E(q)$ with the eight band program, although the result is not significantly different from the straightforward Kronig-Penney model. The measured mass m^* is actually a geometric average of m_{xx} and m_{yy} , where m_{xx} is the mass for in-plane motion. Fig. 2 is a plot of m^*/m_0 using the m_{xx} measured in the Faraday orientation for the same FIR energy, and shows how this semi-classical model gives good agreement with the data.

The semi-classical approach breaks down when q approaches π/L , the mini-zone edge in real space, this corresponds to $2\pi \sim L$ at 21.4 T for the 50/100 sample, but at 10.1 T for the 50/100. However we do not see any clear CR in the semi-classical regime for the 50/100 sample ($r \sim 1$) possibly because the field is too low. Furthermore, we do not see any of the new modes corresponding to well bound barrier bound or skipping orbits which might be expected for the 50/100, 50/150 and 50/200 samples once $2r < L$.

Instead Fig. 1b shows that the impurity resonance shifts remarkably with increasing barrier width, moving from close to the bulk GaAs $1s-2p$ field for $I_A \approx 50 \text{\AA}$ to close to the bulk GaAs

CR for $L_0 = 150 \text{ \AA}$. Fig. 1 contains data for the 50/100 sample for different FIR wavelengths illustrating how the impurity transition moves towards the bulk CR for increasing field. In fact we can collect the Voigt data for all samples and FIR wavelengths in the unified curve of Fig. 1, a plot of

$$100 \times \left(\frac{H(\lambda) - H_{1s-2p}(\lambda)}{H_{1s-2p}(\lambda) - H_{1s-2p}(\lambda)} \right) \text{ vs } \frac{L_0}{\lambda} \quad (2)$$

where $H(\lambda)$ is the measured field, and $H_{1s-2p}(\lambda)$, $H_{1s-2p}(\lambda)$ the fields for bulk $1s$ to $2p$ and free electron CR respectively, all for the same FIR wavelength λ . Fig. 1 shows how for $L_0/r \ll 1$ the resonance is close to the bulk $1s - 2p$ field, but for $L_0/r \gg 1$ the resonance moves to the free electron CR field, being exactly midway between the two when $L_0/r = 1$. We propose that the origin of this effect is a concentration of the wave function into the well close to the impurity as the field is increased.

We have calculated the L_0 and $1s$ energies in the Voigt geometry by adapting the exact calculation of Leavitt and Little [14], formally equivalent to a Born-Oppenheimer separation of the Schrödinger equation. The impurity is taken to lie in the middle of a barrier within the superlattice. The important effect of the magnetic field is to add a term

$$\frac{e^2 \hbar^2}{2m} (z - z_0)^2 \quad (1)$$

to the superlattice and impurity potentials in the effective Hamiltonian, where z_0 is the centre of the orbit. Fig. 3 shows the results for the 50/100 sample, with the orbit centre either at the middle of the well or at the middle of the barrier. It can be seen in Fig. 3a that for $H \ll 1$, the $1s$ well and barrier centred states are almost degenerate but the energies diverge at higher field. The divergence occurs at precisely the field when $r = L_0/6.1$ is the critical point observed experimentally in Fig. 1. An examination of the impurity wave function, Fig. 3b, reveals that there are appreciable nodes in at least four wells at low field, but at high field these nodes disappear and the wave function is Gaussian like, centred close to the middle of the well adjacent to the impurity.

The critical field, defined by $r_c = L_0$, can be understood semi classically as the coupling from one well to the next is much reduced once the cyclotron orbit centred on one well does not extend into the neighbouring well. This gives $r_c = L_0 + \frac{1}{2}L_0$, or, assuming that all the curvature of the orbit lies in the barrier, $r_c = L_0$. The important point is that the field concentrates the wave function into the well, not the barrier. In the latter case the critical field would be $r_c = L_0/2$ which is not observed experimentally.

Our model cannot easily include the $2p$ levels, and hence the exact transition energies are difficult to calculate. However, it appears likely that the divergence of the well and barrier centred $1s$ energies at $r_c = L_0$, and the associated concentration of the ground state wave function, is the cause of the experimental behaviour as it successfully reproduces the critical point at $r_c = L_0$. In fact the well centred $1s$ wave function is very similar to the first Landau eigenfunction (a Gaussian), suggesting that the transition energy for $r \ll L_0$ may well be that of a harmonic potential, i.e. the bulk cyclotron resonance energy.

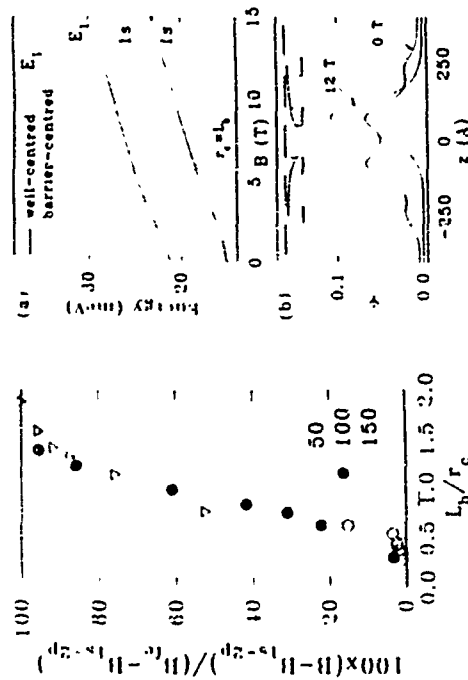


Figure 1. A summary plot of the experimental impurity resonances taken in the Voigt orientation. The dashed line is a guide to the eye (based on an error function). Figure 3: (a) The calculated $1s$ and $2s$ energies for the 50/100 superlattice, in the Voigt orientation. The orbit centre lies either at the centre of the well or at the centre of the barrier. (b) The calculated wave functions, at 0 and 12 T for the well centred $1s$ state. The impurity lies at $z = 0$, and the superlattice and impurity potentials are sketched.

4. Conclusions

We report a series of ODCR experiments on $\text{In}_{0.5}\text{Ga}_{0.5}\text{As}/\text{GaAs}$ superlattices, with magnetic fields applied both parallel and perpendicular to the growth direction. We prove that we have a well defined superlattice band structure by observing cyclotron resonance with the field perpendicular to the growth direction. The in plane mass is also found to be sensitive to inter well coupling. Mid barrier impurities are investigated and found to have a binding energy that reduces with increasing barrier width. In the perpendicular field case the transition energy of the mid barrier impurity decreases rapidly when the cyclotron radius equals the barrier width. This is explained as a concentration of the wave function into the quantum well adjacent to the impurity.

Miniband Formation in Graded-Gap Superlattices

H.T. Grahn¹, F. Agulló-Rueda², A. D'Amico³, K.H. Schmidt¹, G.H. Isbeler², and K. Ploog¹

¹Paul-Drude-Institut für Festkörperelektronik,
Hausvogelplatz 5-7, D-10117 Berlin, Germany

²Instituto de Ciencia de Materiales de Madrid (CSIC),
Universidad Autónoma, C.I.V. Cantoblanco, E-28049 Madrid, Spain.

³Institut für Technische Physik, Universität Erlangen Nürnberg,
Erwin-Rommel-Str. 1, D-91038 Erlangen, Germany.

ABSTRACT

A graded gap superlattice has been investigated to study the formation of miniband states at finite electric fields. In contrast to conventional superlattices only one type of states, either the conduction band or the valence band states, form a miniband. The transition from extended miniband states at finite electric fields back to localized states is clearly observed with increasing electric field. Calculations of the miniband structure using different methods support the formation of a miniband in the conduction band at finite electric fields.

1. INTRODUCTION

Artificial superlattices made from III-V semiconductors represent a model system for the investigation of quantum phenomena, e.g. resonant tunneling [1]. The study of semiconductor superlattices with strong coupling, i.e. wide minibands, has led to the observation of Wannier-Stark localization [2] and Franz-Keldysh oscillations from the lower and upper miniband edge [3]. Both effects have not been observed in bulk semiconductors. In conventional superlattices the conduction and valence minibands appear together at zero electric field. Due to the much heavier mass of the valence band ground state the conduction miniband is much wider than the lowest valence miniband. With increasing electric field the conduction and valence miniband states transform into Stark ladders. Eventually at large enough electric fields the system exhibits two-dimensional subbands as in a multi quantum well system. These effects have a promising potential for applications in electro-optic devices.

We have designed a novel compositionally graded superlattice which is quasiperiodic. The distance between wells, i.e. the spatial period, and the well width are constant but the composition is changed from well to well in order to monotonically increase the band gap keeping the same barrier height relative to the bottom of each well. A schematic diagram of the structure is shown in Fig. 1 for several applied electric fields. At zero electric field (cp. Fig. 1(a)) the superlattice is completely decoupled due to the graded gap. This system exhibits for a critical field different from zero a strong coupling between the conduction band levels leading to the formation of miniband states (cp. Fig. 1(b)). The valence band states are completely localized at this field strength.

Acknowledgements This work was funded by the S.E.R.C. of the U.K. R.J.W. would like to thank Christ Church, Oxford for the provision of a Junior Research Fellowship and P.P. would like to thank the Ministère Français des Affaires Françaises for financial support.

References

- [1] G. Belle, J. C. Maan, and G. Wernemann, *Solid State Commun.* **56**, 65 (1985).
- [2] D. R. Hofstadter, *Phys. Rev. B* **14**, 2249 (1976); F. H. Claun and G. H. Wanner, *Phys. Rev. B* **10**, 6068 (1974).
- [3] F. Duffield, R. Bhat, M. Koz, F. DeRosa, D. M. Hwang, P. Grahn, and S. J. Allen, Jr., *Phys. Rev. Lett.* **56**, 2721 (1986).
- [4] F. Duffield, R. Bhat, M. Koz, F. DeRosa, K. M. Ruch, and S. J. Allen, Jr., *Phys. Rev. Lett.* **59**, 2603 (1987).
- [5] P. Lane and R. I. Greene, *Phys. Rev. B* **33**, 5871 (1986).
- [6] F. Duffield, R. Bhat, M. Koz, M. C. Tamargo, J. P. Harbison, F. DeRosa, D. M. Hwang, P. Grahn, and S. J. Allen, Jr., *Solid State Commun.* **60**, 557 (1986).
- [7] N. C. Jarosik, B. D. McCombe, B. V. Shanabrook, J. Comas, J. Rakston, and G. Wicks, *Phys. Rev. Lett.* **54**, 1293 (1985).
- [8] G. Brozak, B. D. McCombe, and D. M. Laro, *Phys. Rev. B* **40**, 1265 (1989).
- [9] M. Helm, F. M. Peeters, F. DeRosa, E. Colao, J. P. Harbison, and L. F. Lorez, *Phys. Rev. B* **43**, 13983 (1991).
- [10] A. J. Moore, G. Duggan, A. Rankema, and K. Woodbridge, *Phys. Rev. B* **42**, 1326 (1990).
- [11] R. J. Warburton, R. J. Nicholas, L. H. Howard, and M. J. I. Mene, *Phys. Rev. B* **43**, 11121 (1991).
- [12] R. J. Warburton, J. G. Mitchell, R. J. Nicholas, J. J. Harris, and C. F. Loon, *Phys. Rev. B* **46**, 13391 (1992).
- [13] R. P. Frey and J. W. Little, *Phys. Rev. B* **42**, 11771 (1990).

II. EXPERIMENTAL

The superlattice consisted of 15 'periods' of 4 nm $\text{Al}_x\text{Ga}_{1-x}\text{As}$ alternating with 2 nm of $\text{Al}_y\text{Ga}_{1-y}\text{As}$ with a constant increase in the Al mole fraction from one period to the next. The nominal values of the Al mole fraction are $x = 0.03(n-1)$ and $y = x + 0.3$, where $n = 1, \dots, 15$ is the well number. The sample was grown by molecular beam epitaxy on a (100) n^+GaAs substrate. The growth was interrupted for 50 sec at each interface to adjust the fluxes and to reduce the interface roughness. Two Al effusion cells were used. One of them was open only during the barrier growth and its flux was kept constant to produce the constant barrier height. The other one together with the Ga cell was open during well and barrier growth and their fluxes were compensated to produce the desired composition profile. A 25 nm GaAs layer on the low concentration side and a 25 nm $\text{Al}_{0.3}\text{Ga}_{0.7}\text{As}$ layer on the high concentration side of the superlattice together with the superlattice itself were forming the intrinsic region of a $\text{p}^+\text{-i-n}^+$ diode. The n^+ -region consisted, in this order, of the substrate, a 100 nm GaAs buffer layer, and a 540 nm $\text{Al}_x\text{Ga}_{1-x}\text{As}$ window layer with $x = 0.6$ in the central 300 nm, all with a Si doping of $1 \times 10^{19} \text{ cm}^{-3}$. The p^+ -region contained a 370 nm $\text{Al}_x\text{Ga}_{1-x}\text{As}$ window layer with $x = 0.6$ in the last 300 nm and a 8.5 nm GaAs cap layer both with a C doping of $3 \times 10^{19} \text{ cm}^{-3}$. The high Al concentration side of the superlattice (well $n = 15$) was closer to the n^+ -region.

Individual devices were prepared by evaporating AuGe/Ni and Cr/Au contacts on the substrate and top side of the sample, respectively, and etching mesas of 120 μm in diameter down to the substrate. The mesa is bonded via a contact pad of 70 μm in diameter. We used photocurrent-voltage characteristics, photocurrent spectroscopy (PCS) and differential photocurrent spectroscopy (DPCS) illuminating through the p^+ -layer to investigate the field dependent optical properties of the superlattice. For the first two methods the white light from a Xe lamp was dispersed through a 0.6 m double monochromator with an excitation density smaller than $1 \mu\text{W cm}^{-2}$. The incident light intensity was modulated by a chopper and the photocurrent was recorded using a lock-in amplifier. The DPCS method, which is based on a wavelength modulation, was developed recently [4]. In DPCS only a small range of wavelengths of a halogen lamp passes through a monochromator and is guided with a mirror onto a slit. By moving the mirror different wavelengths of the transmitted spectrum pass through the slit. The periodic modulation of the wavelength results in a modulated photocurrent. Keeping the change in the wavelength small the modulated part of the photocurrent, which is detected with a lock-in amplifier, is proportional to the first derivative of the DC component of the photocurrent [4]. For a two-dimensional (2D) system the absorption spectra display step-like features when excitonic effects are neglected. The derivative of the absorption spectra of a 2D-system will therefore exhibit strong peaks. In PC spectroscopy the observed transitions always ride on a smoothly increasing background. Because DPCS is a first derivative technique this background will be strongly suppressed and a much better signal-to-noise ratio compared to the numerical derivative of the PC spectrum (cp. Ref. 5) can be achieved.

III. TRANSPORT PROPERTIES

Under a bias voltage V_{ap} , the electric field in the superlattice is homogeneously distributed and given by $F_{\text{ap}} = (V_{\text{ap}} - V_{\text{bi}})/W$, where $V_{\text{bi}} \approx 1.63 \text{ V}$ is the built-in voltage (determined as

the voltage for which the photocurrent (PC) crosses the zero value) and $W = 141 \text{ nm}$ is the intrinsic-region width. Due to the design of the sample an alignment of the conduction band levels of all quantum wells can only be achieved at a bias voltage $V_{\text{ap}} < V_{\text{bi}}$, i.e. at a finite electric field. Furthermore no carriers are injected from the contacts in this configuration. Fig. 1 shows schematically the potential profile (including the electrostatic contribution) of the conduction and the valence band in a graded-gap superlattice for three representative values of the applied electric field.

When the applied voltage is equal to the built-in voltage the effective electric field vanishes (Fig. 1(a)) and the conduction band states are decoupled. Note that the valence band states are always decoupled for a bias voltage $V_{\text{ap}} < V_{\text{bi}}$. The bandgap of the quantum wells increases between two adjacent wells by approximately 43 meV (cp. Ref. 5). The photocurrent spectrum should therefore consist of 15 transitions with an average separation of 43 meV starting at 1.66 eV ($n = 1$) and reaching 2.26 eV for the last we^+ ($n = 15$). No electron current is flowing at this field strength, since the photoexcited electrons cannot reach the n^+ -contact, which is located on the large Al mole fraction side of the superlattice. In Fig. 1(b) the electric field for the alignment of the conduction band levels is shown. The field strength for the coupling condition can be estimated from the spacing of the levels in the conduction band. For the nominal Al mole fraction this field strength is expected to be 46 kV cm^{-1} , which corresponds to an applied voltage of approximately 0.98 V. No photoexcited electrons can flow through the whole superlattice region and contribute to the current until the critical field strength is reached. In Fig. 1(c) the high field condition is shown, when all wells in the conduction band are decoupled again.

In Fig. 2 photocurrent-voltage traces for different excitation energies are shown. There is a clear onset behavior at 1.1 V for energies above 1.7 eV in reasonable agreement with the discussion of Fig. 1 above. This onset is caused by the blocking of electron transport at low fields, because the grading of the Al mole fraction forms a barrier for the electrons in this field range. When the applied field reaches the critical field strength all electrons excited in the superlattice region can reach the n^+ -contact. Below 1.7 eV only the first well close to the p^+ -contact is excited, while at 2.0 eV almost all wells are excited and therefore contribute to the current. This clearly demonstrates that the transport properties of this system are governed by the electrons. The system exhibits a strongly field dependent photocurrent edge, which is not an absorption edge, but originates from the graded gap in conjunction with the applied field [5].

In Fig. 3 photocurrent spectra are shown for several applied voltages. The wide spectrum displays a lot of fine structure which can be assigned to the transitions of the individual wells. The average spacing between two small peaks is about 34 meV, which is only 80% of the expected one. It can be explained by a reduced Al mole fraction in each well so that the average composition follows approximately $x = 0.025(n-1)$. This observation agrees with the fact that the threshold for transport through the superlattice occurs at 1.1 V. Due to the reduction in Al mole fraction the critical electric field should have a value of 37 kV cm^{-1} resulting in an applied voltage of 1.11 V. It is also consistent with a reduction of the spectral width of the graded-gap superlattice. All observed transitions correspond to the heavy-hole-to-electron intrawell transitions. The light-hole transitions have not been observed, their expected oscillator strength being a factor of three smaller.

It is apparent from Fig. 3 that it is impossible to observe the resonant coupling phenomenon, i.e. miniband formation at finite electric fields, discussed in Fig. 1 directly in the photocurrent spectra. We tried to take the numerical derivative of the PC spectra [5], but

the signal-to-noise ratio was not large enough. Only with the help of a modulation technique such as differential photocurrent or electroreflectance spectroscopy it becomes possible to observe the small modulation in the photocurrent spectra directly.

IV. MINIBAND FORMATION

Fig. 4 shows a series of differential photocurrent spectra of the graded-gap superlattice taken at 77 K for different bias voltages. Although complex in structure, they are very reproducible. Due to the first derivative of the photocurrent spectra the peak energies in the DPC spectra correspond directly to the transition energies. In contrast to standard superlattices where only one peak from all the wells is observed for each type of transition (e.g., heavy and light hole) each well of the graded-gap superlattice contributes a unique peak to the spectrum. It is therefore very difficult to observe the Wannier-Stark ladder transitions. Nevertheless, the formation and destruction of a miniband should be observable through a red-shift and blue-shift, respectively, of each quantum well transition (cp. Fig. 1), when the electric field is increased.

One can distinguish several regions of voltages in Fig. 4, which can be interpreted by the effect of the electric field on the conduction band. At higher voltages close to the built-in voltage the photo-generated electrons cannot surmount the increasing potential due to the increasing Al concentration (Fig. 1a), which separates them from the n^+ -contact (the substrate), and consequently they cannot be collected at the contact. Therefore, no photocurrent can be measured in this voltage range. For slightly smaller voltages the transport of electrons is still very slow and only the wells closer to the substrate contribute to the photocurrent. At 1.1 V the conduction band levels are approximately aligned (Fig. 1b) because this voltage corresponds to the critical field. Below 0.9 V all the wells contribute. Here we are mostly interested in the region between 1.2 V and 0.5 V where the change from coupled to uncoupled conduction band levels takes place.

The red-shift, which should occur at small electric fields when the miniband is formed, is difficult to detect with photocurrent spectroscopy, but we are currently investigating this regime with electroreflectance spectroscopy. The blue-shift at larger electric fields, when the transition from extended back to localized states occurs, can be clearly seen in Fig. 4 going from 0.9 to 0.6 V. It appears as a change in sign of the amplitude of the DPCS-signal, but it is actually a blue-shift. Between 0.9 and 0.6 V the DPCS spectra become very flat in the high energy transition region due to the Wannier-Stark localization. It is apparent from Fig. 4 that only wells 9 to 15 form a miniband in this field range. The blue-shift is about 15 meV, corresponding to a miniband width Δ of 30 meV. A simple Kronig-Penney model for a conventional 4 nm GaAs and 2 nm $\text{Al}_{0.2}\text{Ga}_{0.8}\text{As}$ superlattice leads to an upper bound for the actual miniband width of our system. Using the parameter cited in Ref. 5, we obtain 82 meV. However, due to the variation in the Al mole fraction only a subset of the wells is expected to couple simultaneously. Therefore, we have also solved the Schrödinger equation as a function of the applied electric field numerically for a portion of the graded-gap superlattice consisting of only wells 8 and 9, surrounded by outer barriers of 10 nm. The x values were taken equal to the nominal ones. The coupling between the two wells produces an anticrossing resonance with a minimum splitting of 25 meV. Consequently, the real miniband width of the graded gap SL should fall between 25 and 82 meV. This result is in good agreement with the observed blue-shift.

We have also estimated the Stark shift as described in Ref. 6 for a 4 nm GaAs well, resulting in a decrease of the heavy-hole-to-electron transition energy of less than 5 meV when increasing the electric field from 0 to 200 kV/cm (≈ -1.2 V). Consequently, the spectra do not show a significant red-shift between 0.5 and -0.2 V, which corresponds to the maximum displayed electric field.

One should note that similar effects should occur for the valence band states, but for opposite electric fields, i.e. for applied voltages above 1.63 V in this particular structure. Therefore, graded-gap superlattices offer the possibility of miniband formation at finite electric fields occurring separately for the conduction band and valence band. Due to the electrical injection of electrons and holes in the forward bias regime the measurement of PC and DPC spectroscopy is not suitable in this regime. To study the formation of a hole miniband the graded-gap superlattice should be grown in the reverse order, the low Al mole fraction wells near the n^+ -contact and the high Al mole fraction wells near the p^+ -contact.

V. SUMMARY

In summary, we have observed strong resonance effects between the conduction band states of a novel graded-gap superlattice leading to miniband formation at finite electric fields. The transition from miniband states to Wannier-Stark states is observed through a blue shift of the optical transitions from the individual wells. We are currently investigating the red-shift at low electric fields, which originates from the transition from localized to miniband states, with electroreflectance spectroscopy. Since the resonance in the conduction band can be achieved independently from that of the valence band, this kind of structure allows an independent control of the transport of electrons and holes.

VI. ACKNOWLEDGMENTS

We would like to thank A. Fischer for sample growth and U. Behn, K. von Klitzing and N. Linder for many fruitful discussions. One of us (F. A.-R.) thanks the Spanish CICYT for partial support under the project MAT91-0419. The work was supported in part by the Bundesminister für Forschung und Technologie.

VII. REFERENCES

- [1] See, e.g., H.T. Grahn, *Physica Scripta T48*, in press (1993) and references therein.
- [2] See, e.g., E.E. Mendez and F. Agulló-Rueda, *J. Lumin.* **44**, 223 (1989) and references therein.
- [3] K.H. Schmidt, N. Linder, G.H. Döhler, H.T. Grahn, K. Ploog, and H. Schneider, submitted to *Phys. Rev. Lett.* (1993).
- [4] K.H. Schmidt, A. D'Intino, N. Linder, M. Tuna, G.H. Döhler, H.T. Grahn, K. Kawashima, and K. Fujiwara, *Superlattices Microstruct.* **12**, 181 (1992).
- [5] F. Agulló-Rueda, H.T. Grahn, A. Fischer, and K. Ploog, *Phys. Rev. B* **45**, 8818 (1992).
- [6] G. Bastard, E.E. Mendez, L.I. Chang, and L. Esaki, *Phys. Rev. B* **28**, 3241 (1983).

VIII. FIGURES

Fig. 1: Schematic conduction band (Γ -edge) and valence band potential profiles in a compositionally graded superlattice like the one considered here for different values of the applied electric field: (a) flat band, (b) at the critical field, showing miniband formation in the conduction band, and (c) at high electric field. The z -axis corresponds to the superlattice direction with the substrate and the n^+ -contact on the right hand side, while the p^+ -contact is on the left hand side. A typical optical transition is marked by a vertical arrow

Fig. 2: Photocurrent (PC) vs. applied voltage for different photon energies at 6 K. The maximum value of the PC was of the order of 100 pA. The data have been corrected for the light source spectral dependence.

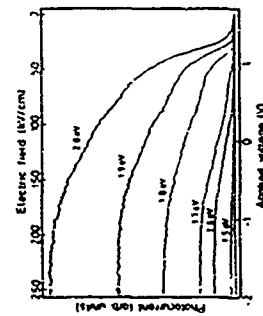
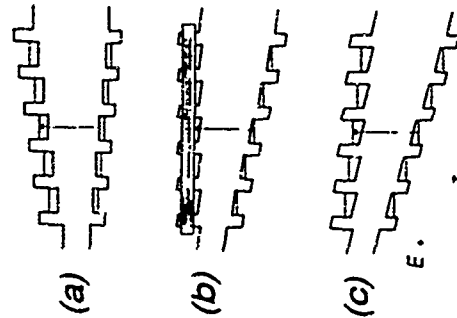
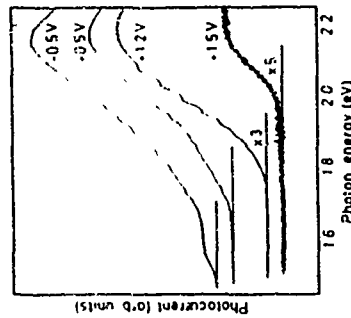
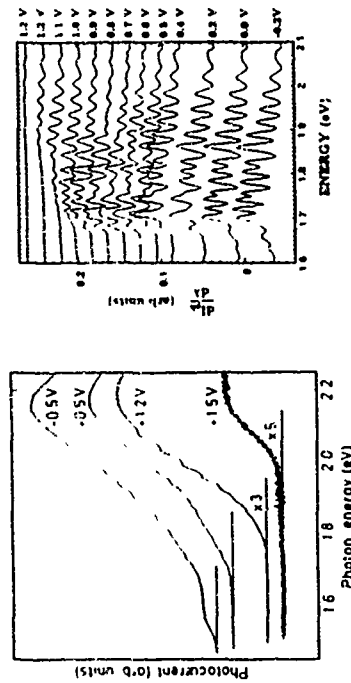


Fig. 3: Photocurrent (PC) spectra near the absorption edge at 6 K for different applied voltages. The electric field is given by $F_{\text{app}} [\text{kV cm}^{-1}] = 70.9 (V_{\text{app}} [\text{V}])$. The data have been corrected for the light source spectral dependence and shifted vertically for clarity. The maximum PC was of the order of 100 pA.

Fig. 4: Differential photocurrent spectra at 77 K for different values of the applied bias voltage. The spectra have been shifted vertically for clarity.



Stark-Ladder Transitions in GaAs/AlGaAs Superlattices

M. Yanaguchi, M. Morifuji, H. Kubota, K. Tanaka, H. and C. Hamaguchi
Department of Electronic Engineering, Faculty of Engineering,
Osaka University, Suita City, Osaka 565, Japan

F. Gornik
Walter Schottky Institut, Technische Universität München
Am Coulombwall, D-80335 Garching, Germany

F. Gornik
Institut für Festkörperelektronik, Technische Universität Wien
Gussbaumerstr. 25, D-1040 Wien, Austria

ABSTRACT

Electroreflectance measurements have been carried out in order to investigate Stark ladder transitions in a GaAs/AlGaAs (20Å) superlattice under various uniform electric fields, and compared with the transition energies calculated on the basis of a microscopic tight-binding description. The observed electroreflectance spectra in a wide range of energies (1.5 eV-2.2 eV) shift in proportion to an applied electric field. The signals in the higher photon energy region (1.5-2.2 eV) indicate an existence of the transition from the spin-split-off band in the valence band to the Wannier-Stark localization states in the conduction band. The assignment is supported by the tight-binding calculation. The resonant couplings of the localized states are also observed.

1. INTRODUCTION

Wannier-Stark (WS) localization in superlattices (SLs) has attracted a great interest recently [1-6]. In SLs consisting of a periodic repetition of quantum wells separated by narrow potential barriers, the discrete energy levels of the quantum well are localized to form a miniband. Under this condition the optical transition occurs from the miniband of the valence band states to the miniband of the conduction band states. When a uniform electric field is applied to the SL, the energy degeneracy between the wells is broken resulting in discrete levels. Therefore it is possible to observe new transitions which are called Stark ladder transitions.

This WS localization is studied experimentally by using electroreflectance (ER) and photoluminescence (PL) [2-3] and analyzed theoretically by the theories of effective mass approximation [5] and tight-binding (TB) approximation [6]. We have to note that many experiments and analyses are made in the low photon energy region related to the Stark ladder transitions from heavy-hole and light-hole states to the conduction band states. As far as we know, there has been no report in relation to the spin-split-off (SO) band in the valence band. In order to investigate the Stark ladder transition from the SO band, we study here the WS localization in a GaAs/AlGaAs SL under various uniform electric fields not only in lower photon energy region but also in higher photon energy region. We report the first observation of the Stark ladder transition associated with the SO band. The experimental results are compared with the transition energies calculated by the theory based on the microscopic TB description, where we take account of the applied electric field in the matrix.

2. EXPERIMENTS

We have carried out ER measurement for a GaAs/AlGaAs (20Å) SL. The uniform electric field is achieved by applying DC voltage to a *p-i-n* structure and the ER measurement is carried out by using modulation voltage of amplitude 100mV and frequency 1kHz. The sample of GaAs/AlGaAs (20Å) SL used in the present work was grown on an n⁺-GaAs (001) substrate by molecular beam epitaxy. The SL has 20 periods and is clad by undoped GaAs (001) and undoped AlGaAs (001) spacers. The *p-i-n* layers are sandwiched by 5.0 μ m thick 1×10^{18} cm⁻³ n-GaAs layer first grown on an n⁺-GaAs substrate and *p*-AlGaAs top layers (*p*- and *p*⁺-AlGaAs layers with 0.1μ m 5×10^{18} cm⁻³ and 0.2μ m 1.2×10^{19} cm⁻³ thickness, respectively) to form *p-i-n* structure.

Figure 1 shows the observed ER spectra of the GaAs/AlGaAs SL under various applied voltage (from 40kV to -10kV) at 77K. The ER signals in lower photon energy region shown in Fig. 1 exhibit peak shifts in proportion to the applied voltage toward both lower and higher energy sides. The shifts of transition energies indicate a progress of the WS localization. These peaks in the photon energy region 1.5-1.8 eV are assigned as the transitions with the Stark ladder index $\nu = 0, \pm 1$, and ± 2 , where the labels $H_{\nu, \nu \pm 1}$ ($L_{\nu, \nu \pm 1}$) indicate the transitions with the Stark ladder index ν between the most heavy-hole (light-hole) subband H_{ν} (L_{ν}) and ν th electron subband E_{ν} . The ER signals in the photon energy region 1.8-2.2 eV are also shown in Fig. 1, which will be discussed later. We find all the transition energies E_{ν} are well expressed by the following relation

$$E_{\nu} = E_0 + \nu eFd \quad (\nu = 0, \pm 1, \pm 2) \quad (1)$$

where E_0 is an interband transition energy, ν is a Stark-ladder index, F is the uniform electric field, e is the electronic charge, and d is the SL period.

3. ENERGY BAND CALCULATION

In order to analyze the ER experimental spectra, especially in higher photon energy region, we employ the output of TB theory for the energy band calculation [6]. We supply a real-space representation for the basis function along the direction of the electric field (z -direction) since the translational symmetry is lost in this direction. Thus the basis functions are specified in the atomic position l along the z -axis and a two-dimensional wave vector k_{\parallel}

$$\psi_{k_{\parallel}}(r) = \frac{1}{\sqrt{N}} \sum_l e^{ik_{\parallel}l} \psi_l(r) \quad (2)$$

where $\psi_l(r)$ is an atomic orbital located at the site of the crystal (l , j , b and μ denote the kind of atoms ($k \equiv x, y, z$ or μ), the type of atomic orbitals ($j \equiv x, y, z$ or μ), respectively). Considering Coulomb interaction that the optical properties are mainly governed by the band structure at the Γ point, we set $k_{\parallel} \approx 0$. We calculate energies and wave functions of WS localization states by solving the scalar equation

$$\det[H_{\nu\nu} - E] = 0 \quad (3)$$

where

$$H_{\nu\nu} = \langle \psi_{k_{\parallel}} | H | \psi_{k_{\parallel}} \rangle \quad (4)$$

The effect of the electric field is included in the diagonal elements of the Hamiltonian matrix, and the Hamiltonian contains the intra-atomic spin-orbit interaction. In order to solve the secular equation (3), we consider a finite domain in the z -direction because the number of the SL periods of a real system is finite and no translational symmetry exists along the z -direction. In the present study, we calculate the energy band structure for 10 periods of (GaAs)₁₀/AlGaAs. The valence band offset was set to be 0.11 eV.

4. DISCUSSION

From the TB calculation, we find that the heavy-hole states are well localized in each GaAs layer at 10kV/cm and that the conduction band states are not completely localized as the electric field reflects the higher effective mass. However, the TB calculation shows that the conduction band states are localized in a higher electric field.

Calculated charge densities of an SO state under several uniform electric fields are presented in Fig. 2, where the squared amplitudes of the eigenfunctions are plotted at each atomic site for several electric fields. The calculated results show that the SO states are gradually confined in a GaAs layer as the electric field increases. Thus an existence of the Stark ladder of the SO states are expected. In Fig. 2, the deformation of the charge density at $l = 10$ kV/cm is due to a mixing between a localized SO state and an extended state of miniband which was folded into the 1st Brillouin zone.

Figure 3 shows the calculated transition energy between the valence band states and the conduction band states as a function of the electric field, where the observed peaks of the ER spectra are also plotted as open circles. The electric field in the sample are estimated from the built-in voltage of 150V. The solid curves (a) in the lower energy region correspond to the transitions $H_{\nu, \nu \pm 1}$ ($L_{\nu, \nu \pm 1}$) and $H_{\nu, \nu \pm 2}$ ($L_{\nu, \nu \pm 2}$) while the solid curve (b) corresponds to $H_{\nu, \nu}$ ($L_{\nu, \nu}$) and the solid curves (c) in the higher energy region correspond to the transitions $H_{\nu, \nu \pm 1}$ ($L_{\nu, \nu \pm 1}$) and $H_{\nu, \nu \pm 2}$ ($L_{\nu, \nu \pm 2}$). The dashed curve (d) at 1.82 eV is the transition corresponding to the transitions $H_{\nu, \nu \pm 1}$ ($L_{\nu, \nu \pm 1}$) and $H_{\nu, \nu \pm 2}$ ($L_{\nu, \nu \pm 2}$). The dashed curve (d) at 1.82 eV is the transition corresponding to the

to $1,1,0$ and the dashed curve (d) extrapolated to 2.0 eV is $1,1,2-1$. In a good agreement between the observation and the calculation indicates that the Stark ladder is well described within the TB theory. In particular, the signals in the lower photon energy region ($1.5-1.8\text{ eV}$) are well explained as the Stark ladder transitions between the valence band states and the conduction band states. The calculated transition energy between localized SO states and the localized conduction band states are shown in this figure in dotted curves (a). Although there exists a slight deviation, the calculated curves fit to the observed LR signals in the photon energy region $1.9-2.2\text{ eV}$. This agreement indicates that the observed LR spectra in the higher photon energy region are attributed to the Stark-ladder transitions between the SO states and the conduction band states. We also found that calculated optical transition probabilities between SO states and conduction band states have a magnitude large enough to be observed.

Next we will discuss a resonant coupling of the Stark ladder states. Figure 4 gives a full detail of the LR spectra around the photon energy 1.64 eV at the applied voltages from -1.2 V to -1.07 V by a step 20 mV . This figure indicates that $1,1,1,0$ transition energy and $1,1,1,1-2$ transition energy do not cross each other indicating an apparent existence of a resonant coupling. A resonant coupling between neighboring localized states is expected to occur at a crossing point of their transition energies. In Fig. 4 we plotted the calculated transition energies by neglecting the splitting induced by the resonant coupling. However, the LR spectra in the lower photon energy region in Figs. 1 and 4 indicate an existence of the resonant coupling between neighboring localized states. As we can see in the figures, there exists a considerable change in the spectra near photon energy 1.64 eV when the applied bias is changed from -1.2 V to -1.0 V . This change is caused by the resonant coupling at the applied voltage around -1.1 V . Although the experimental results plotted in Fig. 4 show that the applied voltage -1.1 V (97 kV/cm) is the crossing point between $1,1,1,0$ and $1,1,1,1-1$ TB calculation indicates that the resonant coupling between $1,1,1,0$ and $1,1,1,1-1$ is very weak and that the crossing occurs at about 50 kV/cm . Therefore the distortion of the LR spectra near -1 V is not due to the resonant coupling between $1,1,1,0$ and $1,1,1,1-1$. TB calculation also indicates an existence of a resonant coupling between $1,1,1,0$ and $1,1,1,1-2$ at 70 kV/cm , and this resonant coupling is stronger. In addition to the resonant coupling at 97 kV/cm we find in Fig. 1 that distortion of the LR signal occurs at photon energy 1.64 eV at 120 kV/cm and 1.67 eV at 175 kV/cm which may be interpreted in terms of resonant couplings between $1,1,1,0$ and $1,1,1,1-2$, and between $1,1,1,0$ and $1,1,1,1-1$ respectively.

In conclusion we summarize the present results as follows. We carried out ER measurement at a $\text{GaAs}(100)/\text{AlGaAs}(200)\text{ SL}$. The observed peaks in the LR spectra shift with increasing the electric field along the growth axis of the SL, and they clearly indicate the existence of the Stark ladder states, field induced localization states. In addition, we also observed LR signals in the higher photon energy region which suggests the existence of Stark ladder of the SO states. In order to analyze the LR spectra we carried out an energy band calculation based on the TB theory including the intra-atomic spin-orbit interaction. By comparing the calculated results with the observed data, we found that the TB spectra in the lower photon energy region agree well with the calculated results and thus that the Stark ladder is well described by the TB theory. Furthermore, we found that the SO states are localized in an electric field as well as the states at the band edge. The calculated transition energies from the localized SO states to the localized conduction band states agree well with the LR spectra in the energy region $1.9-2.2\text{ eV}$. Thus these LR signals are attributed to the Stark ladder transitions from the SO states to the conduction band states. We also observed the three resonant couplings between $1,1,1,0$ and $1,1,1,1-2$, between $1,1,1,0$ and $1,1,1,1-1$ and between $1,1,1,0$ and $1,1,1,1-1$. The anti-crossing between $1,1,1,0$ transition and $1,1,1,1-2$ transition is clearly seen in ER measurement (Fig. 1), but the others are seen only as the distortion of the LR spectra.

5. REFERENCES

- [1] J. Bleuse, G. Bastard and P. Vashita, *Phys. Rev. Lett.* **60**, 220 (1988).
- [2] E. E. Mendez, F. Agullo-Rueda and J. M. Hong, *Phys. Rev. Lett.* **60**, 2126 (1988).
- [3] P. Vashita, J. Bleuse, C. Boulmer, S. Gaillard, C. Adami and A. Regreny, *Phys. Rev. Lett.* **61**, 1603 (1988).
- [4] K. Fujimura, *Jpn. J. Appl. Phys.* **28**, L1778 (1989).
- [5] M. Nakayama, J. Tanaka, H. Nakamura, K. Kawashima and K. Fujimura, *Phys. Rev. B* **44**, 1055 (1991).
- [6] M. Morifugu, Y. Nishikawa, C. Hamaguchi and I. Fujio, *Semicond. Sci. and Technol.* **7**, 1017 (1992).
- [7] D. J. Chadi, *Phys. Rev. B* **16**, 750 (1977).
- [8] P. Vogl and P. H. Plesch, and J. D. Dow, *J. Phys. Chem. Solids* **41**, 955 (1980).

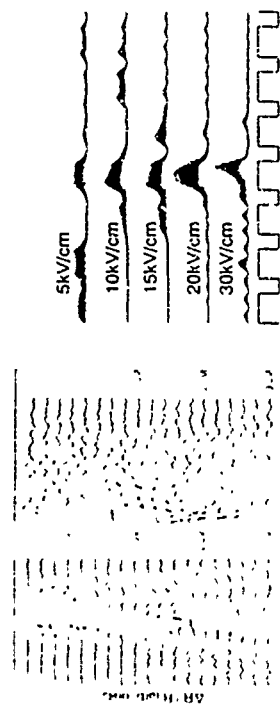


Fig. 1 Electron transition spectra for the superlattice at applied voltages from -1.2 V to -1.0 V by a step 20 mV . The voltage is indicated in the figure at 77 K .

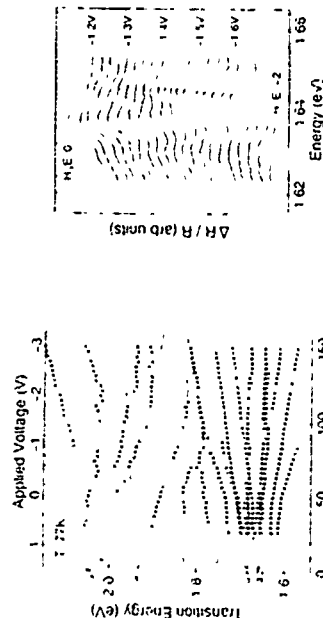


Fig. 2 Charge density distribution of the SO state calculated by the FB method.

Fig. 3 Electron transition spectra around the photon energy 1.64 eV for the superlattice at applied voltages from -1.2 V to -1.07 V by a step 20 mV . The voltage is indicated in the figure at 77 K .

Fig. 3 Electron transition spectra around the photon energy 1.64 eV for the superlattice at applied voltages from -1.2 V to -1.07 V by a step 20 mV . The voltage is indicated in the figure at 77 K . The solid curves (a) correspond to $1,1,1,0$ and $1,1,1,1-1$ and the dashed curves (b) to $1,1,1,0$ and $1,1,1,1-2$. The solid curve (c) extrapolated to 1.7 eV is $1,1,1,1-1$ and the dashed curve (d) is $1,1,1,1-2$. The dotted curves (e) show the transition energies from the localized SO states to the conduction band states. Observed peaks of LR spectra are shown by open circles.

TuC6

Modulated Blue Shift of the Quantum Well Electroluminescence in a GaAs/AlAs Superlattice Resonant Tunneling Device

O. Kuhn, D.K. Maude and J.C. Portal
CNRS-SNCl, B.P. 166 X, 38042 Grenoble CEDEX 9,
and CNRS-INSa, 31077 Toulouse, France

M. Henini and L. Eaves
Dept of Physics, University of Nottingham, NG7 2RD, U.K.

G. Hill and M. Pale
Dept. of Electronic and Electrical Engineering,
University of Sheffield, S1 4DU, U.K.

Abstract

Electrical transport and electroluminescence measurements have been performed on a p-i-n superlattice resonant tunneling device with a narrow 3.1 nm quantum well in the centre. The electroluminescence observed from the centre quantum well blue shifts with increasing electric field. The application of a magnetic field perpendicular to the layers modulates the blue shift of the quantum well recombination. Possible physical origins for the blue shift are discussed.

The behaviour of electrons and holes confined in GaAs/(AlGa)As heterostructures in the presence of external electrical and magnetic fields has been the subject of numerous optical experiments [1-4]. Recently double and triple barrier structures have been incorporated into p-i-n diode devices, and electroluminescence (EL) as well as magnetotransport studies have been performed [5-7]. In such a structure electrons and holes are electrically injected into the quantum well (QW) by resonant and nonresonant tunnelling processes. We have extended this work using a novel superlattice resonant tunnelling device (SLRTD) to study the simultaneous injection of electrons and holes into the centre QW and their subsequent radiative recombination.

In this paper, we report electrical transport and electroluminescence measurements on a p-i-n double barrier resonant tunnelling structure which incorporates superlattices in the emitter and collector region. The superlattices are designed to increase charge build-up in the QW and hence increase the electroluminescence efficiency. In contrast to previous work [1, 2, 5-7], for the extremely narrow (1.1 nm) QW in our structure, we observe a blue shift of the QW recombination with increasing applied voltage. The application of a magnetic field perpendicular

to the layers modulates the blue shift of the QW recombination. In order to explain the data, we propose a simple model in which the magnetic field modulates the electric field distribution across the device and thus modulates the blue shift of the QW recombination.

The structure used in the study was grown by Molecular Beam Epitaxy. It consists of an undoped region with a 3.1 nm GaAs-QW layer sandwiched between two 5 nm AlAs-barrier layers. Electrons and holes are injected into this centre QW via two superlattices. Each superlattice is formed by three coupled 6 nm wide GaAs-QWs, respectively n- and p-doped in the centre over a region of 2 nm with a nominal dopant concentration of $5 \times 10^{17} \text{ cm}^{-3}$. The AlAs-barrier layers in the superlattices have a thickness of 2 nm. As each superlattice only has three periods it would be technically more correct to speak of coupled quantum wells and hybridized quantum well states. However, for the sake of simplicity, in this paper we will refer to superlattices and minibands [8]. The active region is contacted with heavily doped ($2 \times 10^{18} \text{ cm}^{-3}$) n-type and p-type regions. A 25 nm thick $\text{Al}_{0.33}\text{Ga}_{0.67}\text{As}$ window layer is incorporated in the n+ contact to increase the efficiency of EL collection. Standard photolithographic and etching techniques were used to define mesas of between 2.5 and 800 μm . A transparent top contact was made by evaporating gold in the form of an annular ring. The device used for the measurements reported here was a circular mesa of 800 μm diameter.

The superlattices are intended to serve as energy filters. Each superlattice acts simultaneously as an emitter for majority carriers and as a collector for minority carriers which have tunneled through to the opposite contact. The superlattices enhance the charge build-up in the centre QW, since under an applied

bias carriers injected from the miniband in the emitter do not have a corresponding miniband in the collector to resonantly tunnel into. This situation is illustrated schematically in Figure 1 which shows the conduction and valence band of the device under an applied voltage of 1.8 V. Escape from the centre QW is thus limited to nonresonant tunnelling processes involving scattering or phonon emission. The structure is such that the electron (ET) and light hole (LH1) resonances occur at approximately the same bias, allowing the simultaneous resonant injection of electrons and holes into the QW. Therefore, in such a structure radiative recombination of electrons and holes should be greatly enhanced.

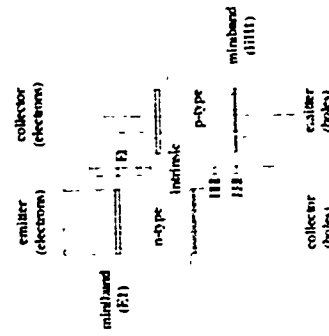


Figure 1: Schematic of the superlattice resonant tunneling device under an applied bias of about 1.8 V.

The experiments were performed using a superconducting magnet with the magnetic field parallel to the sample growth axis. The set-up allows for optical and transport measurements to be performed simultaneously in the temperature range 1.5 - 300 K. The EL from the sample was collected with an optical fibre, analysed with a single monochromator and detected using a standard multi-alkali photomultiplier tube and lock-in amplification.

Under forward bias, the device presents a diode-like current-voltage characteristic (Figure 2). Most of the turn on voltage of around 1.6 V is required to overcome the built-in voltage on the p-n diode structure. At least two resonances appear clearly in the current-voltage characteristic which are identified with the HH1 and the combined EL/LH1 resonances. These are seen more clearly in the d^2I/dV^2 plots also shown in Figure 2. At 77 K and under an applied bias of ≈ 2 V red light emission from the QW is clearly visible with the naked eye.

A typical EL-spectrum, taken with an applied bias of 2.0 V and at 4.2 K, is shown in Figure 3(a). EL is observed in three spectral regions of interest corresponding to recombination in the contacts, superlattice and centre QW. At low energies peaks originating from the GaAs-bulk contact regions are observed. The strongest at an energy of about 1.491 eV, 28 meV below the bandgap energy of undoped GaAs, is either the fundamental recombination from the band gap being renormalized due to the heavy doping or else corresponds to an electron-neutral acceptor transition. The two small peaks found at 1.525 eV and at 1.549 eV have yet to be identified. The energy of the lowest peak is close to the band to band recombination energy in bulk GaAs. The second spectral region is marked by the EL originating in the superlattices. The corresponding luminescence energy is 1.612 eV. The EL from the central 3.1 nm QW has an energy of 1.779 eV and shows a very narrow line width of less than 4 meV (FWHM) indicating the extremely high quality of the interfaces. The superlattice and QW recombinations are almost certainly excitonic in origin due to the increased overlap of the electron and hole wave functions caused by the confinement. It is interesting to note that no hot luminescence (EL-LH1) is observed even though at this bias voltage (2.0 V) there is significant hole injection into the LH1 state. This is because the relaxation time between the LH1 and HH1 states is much faster than the radiative recombination time which is of the order of nanoseconds.

The energy of the QW recombination blue-shifts slightly with increasing applied bias as shown in Figure 3(b). This is in contrast to the red shift reported for

wider QW's and triple barrier p-n's in which the major effect of the longitudinal electric field is to spatially separate the quantum confined electrons and holes lowering the ground state energy levels [1,5]. Since the electric field induced Stark shift varies as the fourth power of the well width [9], for the narrow (3.1 nm) QW in our structure the Stark shift is negligible. The blue shift may be due to an electric field induced decrease in the exciton binding energy [10,11]. Here it is important to note that our structure is close to the infinite well case, because of the large band offsets at the Γ -point of 1 eV and 0.55 eV in the conduction and valence band respectively. The penetration of the electron and hole wavefunctions into the AlAs-barriers is negligible and the excitons retain a highly two-dimensional nature. In the extreme two-dimensional limit, the exciton binding energy is four times the effective three-dimensional exciton Rydberg. In a deep and narrow QW, even though the electric field induced polarisation of the exciton is small, it reduces the two-dimensional nature of the exciton and thus lowers its binding energy. However, there is some doubt as to whether or not, in the extremely narrow QW of our device, the electric field induced decrease of the exciton binding energy is sufficient to account for the magnitude of the observed blue shift. It is also possible that the blue shift is associated with screening and many bodied effects [12].

The energies found for both the superlattice and QW recombination coincide within a few meV with those calculated within the effective mass envelope function approximation using a transfer matrix method which takes into account only the Γ -conduction band profile. For the 3.1 nm QW the calculated energy levels are $E_1 \approx 205$ meV and $HH1 \approx 58$ meV which, using a bandgap of 1.52 eV for GaAs at 4.2 K, gives a total energy of 1.783 eV. From this it is necessary to subtract the exciton binding energy in a 3.1 nm QW. From reference [13] we estimate the exciton binding energy to be ≈ 12 meV when no electric field is applied. This gives a calculated recombination energy of 1.771 eV under flat band conditions and is in good agreement with the value obtained by extrapolating the experimental data taken between 1.9 - 2.1 V (Figure 3(b)) down to flat band conditions at about 1.6 V. The good agreement between theory and experiment clearly demonstrates that the

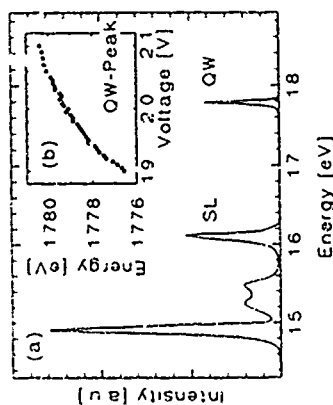


Figure 3: (a) Electroluminescence spectrum for an applied bias of $V = 2.0$ V measured at $B = 0$ T and $T = 4.2$ K. The peaks originating in the centre quantum well (QW) and in the superlattices (SL) are marked respectively. (b) Energy of the quantum well electroluminescence as function of applied bias.

The energies found for both the superlattice and QW recombination coincide within a few meV with those calculated within the effective mass envelope function approximation using a transfer matrix method which takes into account only the Γ -conduction band profile. For the 3.1 nm QW the calculated energy levels are $E_1 \approx 205$ meV and $HH1 \approx 58$ meV which, using a bandgap of 1.52 eV for GaAs at 4.2 K, gives a total energy of 1.783 eV. From this it is necessary to subtract the exciton binding energy in a 3.1 nm QW. From reference [13] we estimate the exciton binding energy to be ≈ 12 meV when no electric field is applied. This gives a calculated recombination energy of 1.771 eV under flat band conditions and is in good agreement with the value obtained by extrapolating the experimental data taken between 1.9 - 2.1 V (Figure 3(b)) down to flat band conditions at about 1.6 V. The good agreement between theory and experiment clearly demonstrates that the

The energies found for both the superlattice and QW recombination coincide within a few meV with those calculated within the effective mass envelope function approximation using a transfer matrix method which takes into account only the Γ -conduction band profile. For the 3.1 nm QW the calculated energy levels are $E_1 \approx 205$ meV and $HH1 \approx 58$ meV which, using a bandgap of 1.52 eV for GaAs at 4.2 K, gives a total energy of 1.783 eV. From this it is necessary to subtract the exciton binding energy in a 3.1 nm QW. From reference [13] we estimate the exciton binding energy to be ≈ 12 meV when no electric field is applied. This gives a calculated recombination energy of 1.771 eV under flat band conditions and is in good agreement with the value obtained by extrapolating the experimental data taken between 1.9 - 2.1 V (Figure 3(b)) down to flat band conditions at about 1.6 V. The good agreement between theory and experiment clearly demonstrates that the

X-minima in the indirect gap AlAs-barriers play no role in determining the energy of the bound states in the quantum well. This result is also in agreement with previous electrical transport measurements on GaAs/AlGaAs unipolar double barrier structures by Mendez and coworkers [14] and the calculation of Ko and Inkson [15].

For a bias voltage of 2.0 V, a magnetic field was applied perpendicular to the layers and EL spectra taken every 0.1 T up to 15 T. The energy of the QW recombination plotted in Figure 4 is an oscillatory function of the magnetic field and periodic in $1/B$. Similar oscillations, but in antiphase, also appear in the current versus magnetic field characteristic and also as an extremely weak variation in the intensity of the QW recombination. When the magnetic field is rotated, the fundamental period $\Delta(1/B)$ of the oscillations in the current follows a $\cos(\theta)$ law confirming the two dimensional origin of the oscillations. In addition to the oscillations, a small quadratic blue shift of the QW recombination energy with increasing magnetic field is seen as a background in Figure 4. It can be explained by a magnetic correction to the exciton binding energy [11,16].

Similar oscillations in the current versus magnetic field characteristic have been reported in unipolar double barrier resonant tunnelling devices [17]. The origin of the oscillations in such a case stems from the quantization into Landau levels of the two dimensional accumulation layer in the emitter which periodically modulates the density of states for tunnelling. A similar model, in which electron charge build-up occurs in the emitter superlattice QW directly adjacent to the double barrier can also explain the origin of the oscillations in our device. The magnetic field quantizes the electrons in the emitter into Landau levels. With increasing magnetic field the Landau level separation increases and to a first approximation $2eB/h$ electrons are ejected every time a Landau level passes through the Fermi energy. The modulation of the charge density in the emitter QW modulates the electric field across the double barrier and hence modulates the blue shift of the centre QW recombination. This current modulation also arises from the modulation of both the electric field across the double barrier and the charge in the emitter QW which changes the transmission coefficient of the barriers and the supply function for tunnelling respectively.

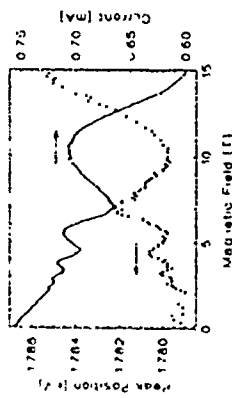


Figure 4: Oscillations in the current and in the peak electroluminescence energy of the centre quantum well as a function of magnetic field ($B \parallel J$) measured at $T = 4.2$ K and $V = 2.0$ V. The dashed line indicates the quadratic correction to the exciton binding energy in a magnetic field as given in reference [16].

From the period of the oscillations in $1/B$ space, $\Delta(1/B) = 11$ T at a voltage of 2.0 V, the change in the emitter QW is $5 \times 10^{11} \text{ cm}^{-2}$. Using Gauss's law it is possible to estimate the electric field variation across the emitter barrier and centre QW. We estimate that at 5.5 T, when the $n = 2$ Landau level passes through the Fermi energy, the electric field across the emitter barrier and centre QW is decreased by $4 \times 10^4 \text{ Vcm}^{-1}$. In reality this model is too simple and it is necessary to perform a self consistent calculation which takes into account the potential redistribution across the various regions of the device.

In conclusion, we have observed a blue shift with applied electric field of the exciton recombination in a narrow (3.1 nm) QW. This is in contrast to the red shift normally observed in wider QWs due to the quantum confined Stark effect which dominates over the electric field induced decrease in the exciton binding energy. For narrow QWs the Stark shift is negligible and screening and many bodied effects, together with the electric field dependence of the exciton binding energy may be important. Further theoretical work, including a detailed calculation of the electric field dependence of the exciton binding energy in narrow QWs is necessary to determine the origin of the blue shift.

Acknowledgements

O.K. and D.K.M. gratefully acknowledge the financial support of the EEC (ESPRIT). We acknowledge useful discussions with E.L. Ivchenko and A.A. Toropov. Part of this work was supported under ESPRIT project 7193.

References

1. E. E. Mendez, G. Bastard, L. L. Chang, L. Esaki, H. Marroc, R. Fischer; Phys. Rev. B 26, 7101 (1982). For a review see E. E. Mendez, F. Agullo-Rueda; Journal of Luminescence 44, 223 (1989).
2. D. A. B. Miller, D. S. Chemla, T. C. Damen, A. C. Gossard, W. Wiegmann, T. H. Wood, C. A. Burrus; Phys. Rev. Lett. 53, 2173 (1984).
3. D. C. Rogers, J. Singleton, R. J. Nicholas, C. T. Foxon, K. Woodbridge; Phys. Rev. B 34, 4002 (1986).
4. M. S. Skolnick, P. E. Simmonds, D. G. Hayes, C. R. H. White, L. Eaves, A. W. Higgs, M. Henini, O. H. Hughes, G. W. Smith, C. R. Whitehouse; Semicond. Sci. Technol. 7, B401 (1992).
5. C. R. H. White, H. B. Evans, L. Eaves, P. M. Martin, M. Henini, G. Hill, M. A. Pate; Phys. Rev. B 45, 9513 (1992). See also H. B. Evans, L. Eaves, C. R. H. White and M. Henini; NATO ARW on Frontiers of Optical Phenomena in Semiconductor Structures of Reduced Dimensions, Napa Valley, California, 1992 (to be published).
6. P. M. Martin, R. K. Hayden, C. R. H. White, M. Henini, L. Eaves, D. K. Maude, J. C. Portal, G. Hill, M. A. Pate, Semicond. Sci. Technol. 7, B456 (1992).
7. P. A. Harrison, H. B. Evans, P. M. Martin, T. S. Turner, L. Eaves, M. Henini and G. Hill; Proc. Int. Conf. on Electronic Properties of Two Dimensional Systems, Newport, Rhode Island, 1993; To be published in Surface Science.
8. R. A. Davies, M. J. Kelly and T. M. Kerr; Phys. Rev. Lett. 55, 1114 (1985).

TuP1

A metastable state in self-electro-optic effect devices using Stark ladder transitions

M. Hoshida, K. Kawashima*, and K. Tominaga
ATC Optical and Radio Communications Research Laboratories, Hikaridai, Seika-cho, Soraku-gun Kyoto, 619-02 JAPAN

K. Fujiwara
Department of Electrical Engineering, Kyoto Institute of Technology, Tobata-ku, Kitakyushu city, 804 JAPAN

Abstract: A self-electro-optic effect device (SEED) based on Wannier-Stark localization in GaAs/AlAs superlattices can show multiple negative differential resistance (NDR) regions in the photocurrent versus reverse bias voltage curve. This phenomenon is called Stark ladder transitions, which successively come into resonance with the optical energy of the SEED when the external electric field intensity is varied. Using these multiple NDR regions in a SEED configuration, we have found, for the first time, a metastable point isolated inside the bistable hysteresis curve of the optical switching characteristics. In the sense that it can be reached by conventional CW light without any optical pulse excitation, this metastable state has been observed in transmission by an optical pulse excitation method, and can be explained clearly with a novel global stability analysis of differential equations for photocurrents in the symmetric SEED system.

1 INTRODUCTION

Self-electro-optic effect devices (SEEDs) are potential elemental devices for signal switchers or optical interconnections or optical networks and logic gates and logical latches in optical digital signal processing systems, because of their low switching power, high sensitivity and integrability [1]-[3]. There are many reports on optical bistability in symmetric SEEDs (S-SEEDs) [4]. Achieving multistability in an optical processing element is a subject that has attracted a great deal of interest due to the potential applications to multivalued logic or threshold devices. To this purpose, S-SEEDs using the Wannier-Stark localization effect (WSL-S-SEEDs) have been able to easily demonstrate the multistability because their photocurrent versus reverse bias voltage characteristics (I-V curves) contain multiple peaks and multiple negative differential resistance (NDR) regions, resulting from the resonant peak shift of the Stark ladder transitions with an external electric field [5], [6]. This phenomenon comes from the multiple Stark ladder transitions which successively come into resonance with the optical input wavelength when the external electric field is varied [6], [7], [8].

By using these WSL-S-SEEDs, various types of stabilizers, for example multistability as

* Present Address: Semiconductor Research Center, SANYO Electric Co. Ltd. 1-18-13 Hashiridani, Hirakata City, Osaka 573 Japan

9. G. Bastard, E. E. Mendez, L. L. Chang, L. Esaki, Phys. Rev. B 28, 3241 (1983).
10. J. A. Brum, G. Bastard, Phys. Rev. B 31, 3893 (1985).
11. X.-L. Zheng, D. Heiman, J. Lu, F. A. Chambers, K. A. Saut, Appl. Phys. Lett. 52, 984 (1988).
12. H. Sakaki, H. Yoshimura and T. Matsusue, Japn. J. Appl. Phys. 25, L1 (1987).
13. R. L. Greene, K. K. Bajaj, D. E. Pielorz, Phys. Rev. B 29, 1807 (1984).
14. E. E. Mendez, E. Calleja, W. I. Wang, Phys. Rev. B 34, 6026 (1986).
15. David Yuk Kei Ku, J. C. Inkpen, Semicond. Sci. and Technol. 3, 791 (1988).
16. D. Heiman, Semiconductors and Semimetals 36, 1 (1992).
17. C. A. Payling, E. Alves, L. Eaves, T. J. Frater, M. Hennessy, O. H. Hughes, P. E. Simmonds, J. C. Portal, G. Hill, M. A. Pate, Proc. 3rd Int. Conf. on Modulated Semiconductor Structures, Montyvelier (1987).

well as bistability were obtained [8], [9], [10]. Recently, we have found a novel stable state, called a metastable state, isolated in the bistable hysteresis curve of a WSL-S-SEED system [11]. When an appropriate optical pulse excitation was used, this system showed an additional new stable point, metastable point. In this paper, we report this new type of stability of WSL-S-SEED systems with an analysis based on global stability analysis of differential equations for photocurrent balance in S-SEED circuit systems.

2 WSL-SEED having thin barriers

One class of SEEDs has been realized using the quantum confined Stark effect (QCSE) in multiple quantum wells [12]. The electroabsorption mechanism of the WSL effect is much different from that of the QCSE. When a strong resonant coupling between energy states in QW's form minibands of width ΔE_1 and ΔE_2 for conduction and valence band states, respectively. These eigenstates are distributed in the minibands and the electrons and holes do not localize in one well. When an electric field applied along the growth axis is greater than the miniband width, ΔE_1 or ΔE_2 , the eigenstates tend to localize over a few adjacent QW's due to the drastically reduced resonant coupling. This localization, called Wannier-Stark localization, raises up the band gap energy of the superlattice by $0.5(\Delta E_1 + \Delta E_2)$, which means a blue shift of the absorption band edge [13]. If the input wave

length is tuned to near this band edge region, these types of thin barrier superlattices can have an NDR region in their I-V curves. By using this NDR region, the WSL-SEED can be operated as a bistable optical switching device.

When the Wannier Stark localization occurs, a certain degree of the electronic wave function extends over a few periods of the superlattice due to the tunneling of the thin barrier. The overlap integrals of this "stretched" wave function of the electron from the adjacent wells, with that of the localized heavy hole in a well make possible spatially indirect transitions, called Stark ladder states, with evenly spaced energies, $E_g + n\hbar\omega$ ($n=1, 2, \dots$); where E_g is the band gap energy of an isolated QW [6], [13]. Because the Stark ladder transition energy of each index number " n " varies with the applied electric field F , if the input wavelength were properly tuned, the Stark ladder transitions can successively come into resonance with the optical input to the WSL-SEED by varying the applied voltage. The I-V curves of the WSL-SEED can have additional NDR regions.

Figure 1 shows these NDR regions resulting from the Stark ladder transitions. We used a sample which has a short period superlattice with very thin barriers. The superlattice p-i-n structured sample was grown on a (100)-oriented n-GaAs substrate by molecular beam epitaxy. The nominally undoped superlattice layer consisted of 100 periods of GaAs/AlAs, with GaAs QW widths of 31.3 Å and 3.7 Å, thick AlAs barriers. The sample was fabricated into p-i-n diode mesas of approximately 800 μm^2 with a 200 μm circular window, and about a 400 μm^2 area of the GaAs substrate underneath the optical window was etched off by selective wet chemical etching to fabricate a transmission device.

3 STABILITY ANALYSIS

These multiple NDR regions make it easy to realize multistability in SEED operations [10]. Usually, a load line graphical analysis has been used to find the stable point in the SEED operation, but this method becomes less convenient when the I-V curve becomes more complex. Moreover, with the load-line analysis, it is very difficult to trace the temporal track of voltage movement when the optical input temporally varies. For this reason, we propose a novel analytical method based on the global stability analysis of differential equations for photocurrent balance in SEED circuits. This method can

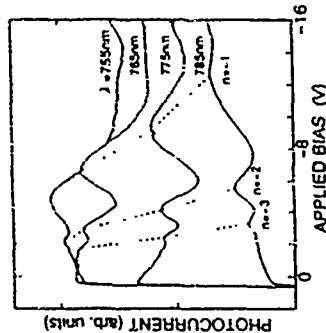


Fig. 1 Photocurrent versus applied reverse bias voltage curves for several illumination wavelengths. Each peak corresponds to the resonance of a Stark ladder state, so an incident optical wavelength

clearly describe the transitions between stable points, even when the system is in intermediate unstable state and even if the I-V curve is very complex.

Figure 2 shows a S-SEED circuit. The electrical current balance in the S-SEED system is denoted by

$$PcI(V_0 - V) - \frac{dQ_1}{dt} = PcI(V_0 - V) + \frac{dQ_2}{dt} \quad (1)$$

where PcI and $Pc2$ represent the photocurrent of SEED p-i-n diodes D1 and D2, respectively, and are functions of the applied voltage and the input optical intensity. Q_1 and Q_2 denote the charge in the device capacitance $C/2$ of each SEED diode. V_0 is the voltage of the constant voltage source, and V is the voltage between diodes D1 and D2 (Fig. 2). Suppose that both SEED diodes have the same capacitance, then the varying velocity of voltage V is derived from Eq. (1)

$$\frac{dV}{dt} = \frac{1}{C} [PcI(V_0 - V) - Pc2(V)] = \frac{1}{C} \Delta PcI(V) \quad (2)$$

In this analysis, for conciseness, the capacitance $C/2$ of each diode is assumed to be constant for all voltage changes. Assuming the existence of a potential-like function $U(V)$, the equation of motion for the voltage changes is described as

$$\frac{dV}{dt} = -\frac{\partial U}{\partial V} = -\frac{1}{C} [Pc2(V) - PcI(V_0 - V)] \quad (3)$$

This potential function represents the global stability of the differential equation (2) [14]. Explicitly, the potential function U is written as

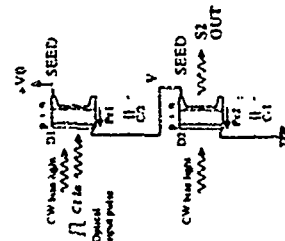


Fig. 2 Schematic diagram of a S-SEED circuit

$$U(V) = \frac{1}{C} \int [Pc2(V) - PcI(V_0 - V)] dV \quad (4)$$

Equation (4) can be numerically integrated explicitly because the functional form of the photocurrents, $PcI(V)$ and $Pc2(V)$, is already known as a numerical function of the data. This potential function specifies the stability points as well as the motion of the voltage. The local minima of the potential are stable points where the voltage V can no longer move. Using this potential function, the global stability analysis of the differential equations for the photocurrent and the analysis of temporal variations in voltage V are reduced to an analysis of the curve profile of the potential function $U(V)$. Compared to the ordinary method of load-line graphical analysis, the merit of this potential function method is that even far from the stable point, we can understand intuitively the dynamical behavior of the system, like the method of the potential function in classical mechanics.

4 METASTABLE STATE AND EXPERIMENT

Now, we introduce a metastable state. Figure 3 shows the I-V curves of the above sample at 770 nm wavelength. In this figure, the load lines of this WSL-SEED and their corresponding potential function curves for various intensities of optical input to diode 1 of the SEED are shown in addition to the dependence of the optical transmission rate of the SEED diode D2 on the applied reverse bias voltage. This S-SEED showed optical bistability clearly with CW (continuous wave) light irradiation

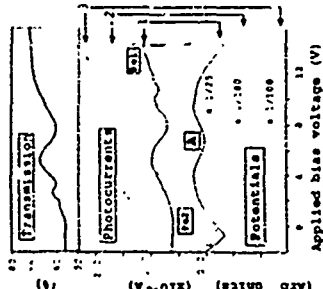


Fig. 3 Load-line graphs for a WSL-SEED with $V_0=13.5$ V at 770 nm illumination wavelength, and the corresponding potential curves. The index numbers 1 to 3 on the right hand side of the figure indicate the intensity of the optical incident intensities into SEED diode 1. These potential curves are scaled down vertically for view with the factors indicated in the figure. The top curve is the optical transmission rate versus voltage characteristics of SEED diode D2.

However, as shown in Fig. 3, the potential function, injected by number 1, has three local minima when both optical inputs to the SEEDs are nearly the same. Starting from the left most stable point, the potential function varies with increasing optical input power for diode 1 (as indicated by the numbers 1 to 3 in Fig. 3), and this unstabilized system falls to a new local minimum, i.e., the most right-hand stable point. Because the center stable point "A" also concurrently vanishes, the movement cannot stop at the center point and reaches the most right-hand end. Consequently, with an ordinary CW light input, this system shows optical bistability. This implies that the stable point "A" cannot be reached with a quasistatic process like DC incident light variation. So, we call it a *metastable point*.

However, because the transition requires a finite time, just after the voltage is passed near the point "A", the optical input intensities were reduced suddenly. It is possible to force the potential to return to the condition having three stable minima, i.e., an excitation with an optical pulse. This procedure makes it possible to reach the new metastable point hidden isolatedly inside the bistable hysteresis, and the voltage once settled in the point "A" can stay there until the potential shape changes. We may consider

"Spin"-Flip of holes in asymmetric quantum wells
R. Ferreira and G. Bastard
Laboratoire de Physique de la Matière Condensée de l'Ecole Normale Supérieure
24 rue Lhomond - 75005 - Paris

We consider theoretically "spin"-flip and "spin"-conserving processes for holes in single quantum wells. The presence of a spatial asymmetry in the hole envelope function has then a small linear-in-k perturbation lifts the parity degeneracy of the Luttinger dispersions of the symmetric quantum well. We show that in this case a D'yakonov and Perel' like mechanism holds for the relaxation of the holes "spin".

Semiconductor quantum wells (QW) present quasi-bidimensional confined states resulting from the quantum well like potential profile along the growth axis [1]. To each bound state are associated two (due to the spin) bidimensional dispersion branches associated with the free in-plane motion of the carriers. In general the free in-plane motion of an electron or of a hole depends upon its confinement along the growth axis, i.e., the quasi-bidimensional confinement in one direction affects the free motion in the layer plane. Let us consider initially (and briefly) the D'yakonov and Perel' spin-flip mechanism for conduction electrons

For structure based on wide gap III-V or II-VI materials we consider in a first approximation a parabolic (bulk-like) conduction dispersion. In that case the electron spin projection along the growth axis is a good quantum number and each state is doubly degenerate. Thus, any non magnetic scattering center in the QW region can induce only spin-conserving scatterings for conduction electrons. To study spin-flip processes for electrons in zincblende semiconductors we need to consider the small non-parabolic corrections to the hosts' conduction dispersions [2]. That non-parabolic correction mixes the two spin states and lifts the double degeneracy. Then spin-flip scatterings for electrons induced by a scalar potential become possible (Elliot-Yafet mechanism [3]). In addition, a weakening of the energy levels is present in real structures, due to the various possible scattering mechanisms. Let $k_z = (k_x, k_y)$ be the in-plane wavevector. Let the k_z dependent band-structure energy splitting $\hbar\omega_B$ be such that $\hbar\omega_B(k_z) \ll \epsilon_F(k_z)$ or $\hbar\omega_B \ll 1$, where $\epsilon_F = \hbar^2 k_F^2 / 2m^*$ for a given scattering mechanism and ϵ_F the spin-conserving scattering time for the parabolic states. Then, as shown by D'yakonov and Perel' for bulk semiconductors [2], the non-parabolic part of the conduction hamiltonian is responsible for spin-flip processes, but its effects are greatly reduced in the strong scattering limit (monotonic narrowing [4]). Their work has been extended to quantum wells by D'yakonov and Kachoravskii [5], who showed that the non-parabolic part of the conduction effective hamiltonian in a QW can be put in the form $(\hbar^2 \sigma_x^2 / 2m^*)$, where Ω_1 is a k dependent vector, with $\Omega_1^2 = \hbar^2 \sigma_x^2 / 2m^* = (\sigma_x^2 / 2m^*)$ and σ_x are the 2x2 Pauli matrices. This result means follows directly the "up" and "down" parabolic states are no more eigenstates of the full hamiltonian and so the electron spin should precess between these two pure states in presence of an in-plane effective magnetic field proportional to Ω_1 . Scattering events change the electron in-plane

5. SUMMARY

The operational mode of the WSL S-SEED using short optical pulses is some advantages. The switching properties, bistability or tri-stability, can be selected by adjusting the optical pulse width condition. Namely, a tri-state device can be obtained by using the same simple device configuration as that used for bistable devices, having considerable flexibility for designing functional photonic devices.

In summary, we have observed a metastable state in a WSL S-SEED system with optical pulse excitation. Through this metastable point, optical in-state switching is demonstrated. Our results show the great advantages of the S-SEED based on the Wannier Stark localization mechanism for applications in functional photonic devices.

References:

1. A.L. Lentine, H.S. Lim, D.A.B. Miller, J.H. Hunt, J.L. Cunningham and L.M.F. Chiriac, *JETP J. Quantum Electron.* (to be published).
2. A.L. Lentine, H.S. Lim, D.A.B. Miller, J.H. Hunt, J.L. Cunningham and L.M.F. Chiriac, *Appl. Phys. Lett.* 52, 1119 (1988).
3. D.A.B. Miller, *Optical Quantum Electronics* 22, 561 (1990).
4. D.A.B. Miller, D.S. Chemla, F.C. Danner, T.H. Wood, C.A. Burrus, A.C. Gossard and W. Wegmann, *IEEE J. Quantum Electron.* QP-21, 1462 (1985).
5. K. Kawabuchi, K. Fujiwara, T. Yamamoto, M. Sugita and S. Kishiyama, *Jpn. J. Appl. Phys.* 30, L293 (1991).
6. H. Strohriegl, K. Fujiwara, H.T. Grabo, K. V. Kluwe and K. Phang, *Appl. Phys. Lett.* 56, 1605 (1990).
7. E.E. Mendez, J. Aguillo-Rueda and J.M. Hong, *Phys. Rev. Lett.* 60, 2426 (1988).
8. K. Fujiwara, *Optical Quantum Electronics* 22, 590 (1990).
9. D.A.B. Miller, J.W. Gossard, J.M. Kuo, R. F. Kopf, D.A.B. Miller and J.S. Chisholm, *Appl. Phys. Lett.* 55, 100 (1989).
10. K. Kawabuchi, K. Fujiwara, T. Yamamoto, M. Sugita and S. Kishiyama, *Jpn. J. Appl. Phys.* 30, L1522 (1991).
11. K. Kawabuchi, M. Hoshida and K. Fujiwara, *Appl. Phys. Lett.* 62, L44 (1993).
12. D.A.B. Miller, D.S. Chemla, F.C. Danner, A.C. Gossard, W. Wegmann, T.H. Wood and C.A. Burrus, *Phys. Rev. B* 32, 1811 (1985).
13. J. Hefner, G. Bastard and P. Vashita, *Phys. Rev. Lett.* 60, 220 (1988).
14. H. Haken, *Synergetics*, 2nd ed. (Springer-Verlag, New York, 1978).

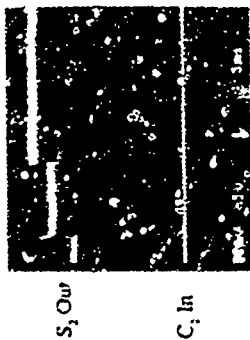


Fig. 4 Oscilloscope traces of a metastable transition. The upper trace shows the transition of optical input S2 shown in Fig. 2. The lower trace is optical excitation pulse C1. The double plateau of the upper trace returns to the metastable state.

has metastable point at a sort of temporally stable state because, when the slope of the potential function curve is changed with varying optical input intensity, it falls into the rightmost or leftmost bistable points.

Considering the above discussion, confirmation of the metastable state can be made by the following experimental setups. By irradiating both SEED diodes with equivalent CW bias lights, and making the potential function have three stable points as shown in Fig. 3, the observation of the metastable state can be made with an over-ridden optical pulse excitation. Figure 2 shows the optical input, and output signals for this experiment. A 770 nm CW light from a Ti:Sapphire tunable wave-length laser is divided to generate the CW bias lights in Fig. 2 and an optical excitation pulse C1 which passes through an acoustic optical modulator. The output light S2 from diode 2 is detected by a silicon avalanche photodiode and is displayed by an oscilloscope. Figure 4 shows experimental results of optical switching between the tri-stable states using approx. 200 psec optical pulses. Although this S-SEED shows only bistability in ordinary measurements with CW light excitation, this photograph shows the transition in the intermediate metastable state with an optical pulse input and the transition to the next final bistable point by an additional optical pulse. These three transmission states actually coincide with those expected from the transmission versus voltage curve in Fig. 1.

wavevector continuously and thus the precession axis. For decreasing $\omega_B \tau_c \ll 1$ the electron spin rapidly follows the rapid variation of Ω_L , and the spin relaxation becomes inhibited.

Contrarily in the conduction case the in-plane valence states of the QW are strongly non-parabolic [1,6]. The valence band hamiltonian in heterostructures is given by the 4x4 Luttinger matrix for the four uppermost host levels $J = 3/2, J_z = \pm 3/2, \pm 1/2, > 1/2$, where J is quantized along the growth axis (hereafter assumed to be the (001) direction). The diagonal part corresponds to a parabolic description of the hole states. The off-diagonal terms vanish at $k_x = 0$ and the eigenstates are decoupled into heavy ($J_z = \pm 3/2$) and light ($J_z = \pm 1/2$) hole states. At $k_x \neq 0$ the off-diagonal terms mix these $k_x = 0$ heavy and light hole states and give rise to the non-parabolic dispersions. In addition, for symmetric heterostructures each state is doubly degenerate for a given in-plane wavevector k_x (parity degeneracy), and the mean values of the projection of the total angular momentum along the growth axis for the two degenerate states have opposite sign: $\langle J_z \rangle(k_x) > 1$ at $k_x = 0 < J_z = \pm 3/2$ (heavy (light) states). Hence, it is convenient to label these two degenerate levels as two "spin" sublevels. Spin-orbit interactions are important for the valence states, and a non magnetic scattering center can induce hole scatterings where a change in the "spin" state is concomitant with the change in the "orbital" state ($\Delta k_x \neq 0$). Such "spin" flip processes are possible for holes in symmetric quantum wells in addition to the "spin" conserving scatterings [7,8]. Let τ_{sc} and τ_{sf} be respectively the k_x -dependent "spin" conserving and "spin" flip assisted elastic scattering times for holes in the Luttinger description. We have shown in ref [8] that for various scattering mechanisms of interest $1/\tau_{sf}$ in unbiased wells vanishes at $k_x = 0$ and rapidly increases with increasing k_x , whereas the "spin" conserving processes are much more probable at small wavevectors and present a very weak dependence upon k_x .

In this work we consider two different mechanisms leading to a breaking of the parity degeneracy and investigate its influence on the relaxation of the hole "spin".

The first one recalls D'yakov and Perel's model for electrons, i.e., it has also a band structure origin and is due to a small correction to the hole hamiltonian in a perfect heterostructure. In fact, the valence hamiltonian for bulk materials with zincblende-like structure displays small linear-in- k terms which account for the lack of centro-symmetry of the bulk unit cell [9]. They are generally neglected and vanish exactly for a diamond like structure. Let $\Psi_{k,1/2}$ and $\Psi_{k,3/2}$ be the k_x -dependent 4x1 wavevectors defined in ref [8] for the twofold degenerate ground valence dispersion of the symmetric QW. We diagonalize the linear hamiltonian $H_{lin}(k)$ within these two states. For the sake of generality we write the resulting eigenvalue hamiltonian as $H(k_x) =$

$$H(k_x) = \begin{pmatrix} H_{11} & H_{12} \\ H_{21} & H_{22} \end{pmatrix} = \begin{pmatrix} H_{11} + \epsilon & \epsilon \\ \epsilon & H_{22} + \epsilon \end{pmatrix} \quad (1)$$

where $\delta = \epsilon(k_x)$, $V(\theta) = \theta + \epsilon_2$ with ϵ_1, ϵ_2 real constants, $\epsilon_1(k_x) = \epsilon_1(k_x)$ are the twofold degenerate Luttinger dispersions of the symmetric QW given in ref [8], and ϵ' is the 2x2 unity matrix. For H_{lin} the pre-multiplicative term at small in-plane wavevectors reads $\delta = -\sqrt{3} C_k k_x/2$; $V(\theta) = -3\theta$ with C_k being the Kane constant in ref [9]. The linear hamiltonian lifts the "up"-down degeneracy (parity degeneracy) of the Luttinger dispersion and the energy splitting is given by $2\delta(k_x) = \sqrt{3} C_k k_x$.

The second mechanism we consider arises from an asymmetry in the total confining potential for the envelope function. We write for the total confining potential along the growth axis: $V(z) = V_S(z) + V_A(z)$ where $V_S(z) = \pm \epsilon_1 V_S(z)$, V_A defines the symmetric square well and V_A corresponds to a small asymmetry to be considered as a perturbation on the states generated by V_S . For instance, $V_A(z) = eFz$ by application of a weak external electric field F/z , or $V_A(z) = \Delta V$ if $z < L/2$ ($z > L/2$) when the two barriers have different energy heights (L is the well width and the z origin is taken at the center of the square well). For small wavevector and asymmetry we diagonalize $V_A(z)$ within $\Psi_{k,1/2}$ and $\Psi_{k,3/2}$. The resulting 2x2 hamiltonian is also given by eq (1) with $\delta = 2\eta_1 \sqrt{1 + \alpha^2 + \eta^2}$, $V(\theta) = \theta - \pi/2$, where α and η are normalization coefficients given in ref [8], $\eta = \sqrt{2} \int_0^L V_A(z) \Psi_{k,1/2}(z) dz$ with $\Psi_{k,1/2}(z)$ being the symmetric (χ_1) and antisymmetric (χ_2) quantum-well envelope functions for the two lowest bound heavy hole states at $k_x = 0$ (energies H_{11} and H_{22} respectively). The asymmetry term $V_A(z)$ lifts the parity degeneracy of the Luttinger dispersion [1,6], with an energy splitting given by $2\delta(k_x) \propto 1/k_x^3$ since $\alpha \propto 1/k_x^3$ and $\eta \propto k_x$ when $k_x \rightarrow 0$. Note that $2\delta(k_x)$ is proportional to the strength of V_A (i.e. to F or ΔV). This energy splitting is understood as follows. For a given $k_x \neq 0$ hole state only one component of the 4x1 spinor does not vanish, and it is either even or odd with respect to z (for instance for the ground $+3/2$ heavy hole state we have $\chi_1(3/2, z) = \chi_1(z)$ and $\chi_2(3/2, z) = 0$, where $\chi_1(z)$ are the four z -dependent components of the valence spinor). At $k_x \neq 0$ various components of the spinor do not vanish, but again each component is either an even or an odd function of z . Also, for a given spinor $\chi_1(3/2, z)$ (say the $J_z = +3/2$), the parities for the "up" and "down" energy degenerate states must be opposite to comply with the orthogonality condition. Thus, for each "spin" component the two degenerate states can in principle be coupled by an asymmetric external perturbation $V_A(z)$. (We can show also that for a given spinor the parities for the $+1/2$ and $-1/2$ components are opposite). The coupling interactions for all the "spin" components add. Finally, this dipole-like coupling can be viewed as an effective "spin"-orbit coupling (and vice-versa), which vanishes for vanishing in-plane wavevector. Note that $V_A(z)$ couples also the $k_x \neq 0$ hole states of different parities (and same heavy or light nature). V_A corresponds to an asymmetry induced dipole, which is responsible for a red shift of the ground QW state (quantum confined Stark shift for $V_A(z) = eFz$, also present for the conduction parabolic levels [11]). But this asymmetry induced shift of the $k_x \neq 0$ levels is neglected in this work, since (i) it is quadratic in V_A and (ii) we are

interested here mostly on the $k_z = 0$ states and suppose that $V_A(z)$ can be considered as a small perturbation.

Since $H_1 = H_1^+ + H_1^-$ and $H_1^+ = H_1^-$, we can rewrite H_1 in the more transparent form:

$$H_1 = H_1^+ + H_1^- = (b/2) \Omega_1 \sigma_1 \quad (2)$$

where $(b/2) \Omega_1 \sigma_1 = (b/2) (\Omega_1 \sigma_1) = [Re(H_1^+) - Im(H_1^+)] = \delta \cdot k_1 \cdot \theta$, where $k_1 = \cos V(\theta) \cdot \sin V(\theta) / \sin V(\theta)$ is an in-plane unit vector ($k_1 / k_1 = 1$ if $V(\theta) = \theta$). Thus, as expected, we recover a 2d pseudo spin 1/2 hamiltonian when folding the Luttinger matrix onto the "up" and "down" states of the degenerate ground heavy hole dispersion. If the off-diagonal term is sufficiently small ($\delta \ll b/2 \Omega_1$), we can follow the D'yakonov and Perel's treatment for electrons. We focus on the two HH_1 dispersions and write a general 2x2 density matrix $\rho = \langle \rho_{00} \rangle + \langle \rho_{01} \rangle \sigma_1 + \langle \rho_{10} \rangle \sigma_1 + \langle \rho_{11} \rangle \sigma_3$, where $\rho_{00} = \langle \rho_{11} \rangle = 1/2$, $\Delta \rho = \langle \rho_{11} \rangle - \langle \rho_{00} \rangle$ and we take $\langle \rho_{10} \rangle = \langle \rho_{01} \rangle$. According to ref [3] the D'yakonov and Perel contribution to the time evolution of the density matrix is given in our case (eqs (1-2) with $c_1 = 1$ or -1) by

$$\frac{\partial \langle \rho_{11} \rangle}{\partial t} = \langle \rho_{11} \rangle \Delta \rho / \tau_{sp} \quad (3)$$

where τ_{sp} is the (k_1) -dependent velocity relaxation time for the "spin"-conserving scatterings and $\Delta \rho$ means average over the in-plane direction of k_1 .

We obtain the "spin" relaxation rate $\langle 1/\tau_{sp} \rangle$ of a non-degenerate hole gas by averaging $1/\tau_{sp}(k_1)$ over a Boltzmann distribution. For the scattering mechanisms we consider in this work (see below) $\tau_{sp}(k_1)$ is practically (k_1) -independent for small wavevectors. Also, for $k_1 \rightarrow 0$ we have $\epsilon(k_1) = 1 - (b/2) \Omega_1 / \hbar^2 k_1^2 = 2/2(\mu_{HH_1})^*$, where $(\mu_{HH_1})^* = m_0 / (\mu_{HH_1})^*$. $1/\tau_{sp}^2 = \hbar^2 \lambda^2 / 2m_0^2 \cdot 1 / (HH_1 - LH_1)$, where $(\mu_{HH_1})^*$ is the parabolic in-plane heavy hole effective mass, m_0 the free electron mass, $\hbar^2 \lambda^2$ a non-symmetric Luttinger parameter and LH_1 the $k_z = 0$ ground light hole energy for the symmetric QW. On account of these approximations, we can show that for $\Omega_1(k_1)$ proportional to k_1^2 , we have

$$\langle 1/\tau_{sp} \rangle \approx n^2 \tau_{sp}^2 \Omega_1(k_1) / (1 + \lambda^2 (n+1)(n+2)) \quad (4)$$

where $\lambda = 3/2 \cdot (\mu_{HH_1})^* / m_0 \cdot \hbar^2 \lambda^2 / (HH_1 - LH_1)$ is the first order correction associated with the non-quadratic hole dispersion, $n = 1$ ($n = 3$) for the linear-in- (k) hamiltonian (for $V_A(z)$ contribution), and λ is defined by $\hbar^2 \lambda^2 / 2m_0^2 = N_B T$ (the thermal energy) $\lambda \ll 1$ at low temperature ($T < 20K$) and for thin wells ($L \leq 100 \text{ \AA}$). Then for the $V_A(z)$ asymmetry $\langle 1/\tau_{sp} \rangle \propto |A_2 T^3|$, whereas $\langle 1/\tau_{sp} \rangle \propto T$ for $HH_1(k)$. These trends are well reproduced in fig (1), where we show the calculated temperature dependence of the decimal logarithm of

$\langle 1/\tau_{sp} \rangle$ for a $L = 80 \text{ \AA}$ Ga_{0.47}In_{0.53}As-InP quantum well for three different cases: external electric field $F = 5kV/cm$; $\Delta V/N = 3\phi$, where $V_S = 365 \text{ meV}$ is the average hole barrier height, and linear-in- k hamiltonian with $C_1 = 7.5 \text{ meV \AA}$ (see [9] for an estimate). We consider in fig (1) "spin"-conserving scattering induced by alloy fluctuations in the ternary well region, which represents an important scattering mechanism in Ga_{0.47}In_{0.53}As based structures. For these delta-like scatterers ($\delta^2 \tau_{sc} = \tau_{sc}$), and we calculate $\tau_{sc}^2 = 1 \text{ ps}$ for $L = 80 \text{ \AA}$.

Acoustical phonons should dominate the "spin"-conserving scattering of low energy holes in very "clean" GaAs based quantum wells. However, in this case τ_{sc} depends upon the temperature: the acoustic phonon emission rate $1/\tau_{sc}(T)$ increases for increasing T , as shown in fig (2) for a 75 \AA GaAs-Ga_{0.47}In_{0.53}As QW. We evaluate $\langle 1/\tau_{sp} \rangle \approx 30 \text{ ps}^{-1}$ at $T = 17K$ and $\approx 12 \text{ ps}^{-1}$ at $T = 4K$, $10K$ and $20K$ respectively, with $C_1 = 3.4 \text{ meV \AA}$ [9]. We note that these values are close from Dutten et al's findings in a high quality GaAs-Ga_{0.47}In_{0.53}As QW [10].

We consider finally the "spin"-relaxation of minority (non-degenerate) holes in presence of an (eventually degenerate) electron gas (as for n-doped structures [11]). For scatterings by residual ionized impurities the screening by the electron gas of the scattering potential must be accounted for. In order to obtain a rough estimate of this effect the "spin"-conserving velocity relaxation time has been approximated by

$$1/\tau_{sp}(k_1, N_3, T) = \alpha_0 N_{imp} (k_1 \lambda_{De}^2 / \hbar^2) \int d\theta (1 - \cos \theta) |V(q_1, z_{imp})|^2 / (q_1^2 + q_2^2) \quad (5)$$

where $\alpha_0 = (2\pi/\hbar) (e^2/\kappa) \cdot \kappa$ is the relative dielectric constant, N_3 is the electron density (we consider only one electron level occupied), the ionized impurities (areal density N_{imp}) sit at the plane $z = z_{imp}$, $q_1 = 2k_1 \sin(\theta/2)$, $V(q_1, z_{imp}) = \sum_j \langle \xi_j \lambda_{De}^2 \rangle e^{i(q_1 z_{imp})} \langle \xi_j \lambda_{De}^2 \rangle$ is the impurity form factor, $q_2 = q_1 \cdot N_3 / T$ the RPA like screening of the electrons [11]. Finally, we neglect screening of the holes and direct hole-electron gas interactions. Note that eq (5) becomes exact for parabolic holes confined between hard walls. We present in fig (3) the temperature dependence of $\langle 1/\tau_{sp} \rangle$ for three electron densities (lower axis) and the N_3 dependence of $\langle 1/\tau_{sp} \rangle$ at $T = 4K$ (upper axis). The structure is the same as in fig (2). $H_{HH_1}(k)$, and for a degenerate electron gas. Decreasing N_3 weakens the static screening and rises the scattering rate and thus τ_{sp} increases with decreasing N_3 .

"Spin"-flip assisted scatterings between the "up" ($|N_{k, \uparrow} \rangle$) and "down" ($|N_{k, \downarrow} \rangle$) states add their contribution to $1/\tau_{sp}(k_1)$. The total "spin"-flip probability will be (for a given wavevector or for a thermal average) $1/\tau_{sf} = 1/\tau_{sf} + 1/\tau_{sp}$. We remark that at low enough temperature $\langle 1/\tau_{sp} \rangle$ is greater or much greater than $\langle 1/\tau_{sf} \rangle$, unless τ_{sc} is extremely short (i.e. "dirty" samples). Thus, the D'yakonov-Perel' mechanism for holes should be dominant in the generic case.

The D'yakonov and Perel' mechanism correlates the sample "quality" (via the velocity relaxation time) and the spin depolarization time. Holes in bulk materials lose their spin almost

instantaneously, and the D'yakonov and Perel' mechanism can be tested for electrons in p-doped samples by measuring the temperature dependence of both the electron mobility and the spin decay time [2,3]. In quantum wells both the electron and the hole spin relaxation times contribute to the measured c.w. polarisation or depolarisation time which correlate tightly the electron and hole motions complicate the interpretation of each species significantly. To circumvent these difficulties n-doped or p-doped wells are used: the sample polarisation is given by the minority photoexcited carriers which are in the presence of a sea of majority carriers of opposite charge which can reasonably (for weak laser intensities [10,11]) be taken as unpolarised. However, to our knowledge, no systematic study has been performed (in particular the temperature dependence of τ_{DP}) in test as in the bulk case the D'yakonov-Perel' mechanism.

Only a few c.w. and/or time-resolved spin-orientation experiments have been done on quantum wells [10-13]. Also, from work to work the sample "quality" is quite different. Generally speaking, real structures always present small asymmetries and deviations from the nominal square well shape, as (a) electrostatic fluctuations in the well region associated to a residual doping near a preferential interface or to different charge distributions in the two interfaces; (b) different doping contents in the two barriers, and (c) interface roughness. In addition, random fluctuations scatter elastically the carriers (e.g. alloy and roughness scatterings) and render the polarisation study in quantum wells strongly sample dependent. In fact, very different c.w. polarisation results and/or depolarisation times have been reported in the literature, even in the best known GaAs-GaAlAs QW systems. However, the observed inverse correlation between sample quality and the hole spin depolarization time [10-13] is what we believe a strong indication that a D'yakonov-Perel' mechanism holds for holes.

We would like to thank Drs. C. Delalande, G. Lampel, G. C. La Rocca, P. Rolland and Ph. Roussignol for very fruitful discussions. The LPMC is a "Unité de Recherche Associée au Centre National de la Recherche Scientifique (URA 1437)".

REFERENCES :

- [1] Bastard G., Wave Mechanics Applied to Semiconductor Heterostructures (Lex Editions de Physique, Les Ulis) 1988
- [2] D'yakonov M. I. and Perel' V. I., Sov. Phys. JETP 33 (1971) 1053; Sov. Phys. Solid State 13 (1972) 1023
- [3] Pikus G. E. and Titkov A. N., in Optical Orientation (ed. by F. Meier and B. P. Zakharchenya), North-Holland, Amsterdam (1984) p. 73 [Modern Problems in Condensed Matter Sciences, Vol. 87]
- [4] Shchier, C. P., Principles of Magnetic Resonance (Springer Series in Solid-State Sciences, Ed. P. Fulde, Springer-Verlag, 1978)
- [5] D'yakonov M. I., Kachorovskii V. Yu., Sov. Phys. Semicond. 20 (1) (1986) 110
- [6] See also Ekenberg U. and Altarelli M., Phys. Rev. B 30 (1984) 1560 for the hole levels

in asymmetrically p-doped structures and Ferreira R., Thesis (Paris 6 - 1992, unpublished) and Goldoni G. and Fasolino A., Phys. Rev. Lett. 69 (1992) 2567 for the hole states in asymmetric double quantum wells

- [7] Uenoyama T. and Sham L. J., Phys. Rev. B 42 (1990) 7114
- [8] Ferreira R. and Bastard G., Phys. Rev. B 43 (1991) 9687
- [9] Kane E. O., J. Phys. Chem. Solids 1 (1957) 249; also in "Handbook of Semiconductors", vol. 1, eds. T. S. Moss and W. Paul (North-Holland, 1982) pp. 193; see also Cardona M., Christensen N. E. and Fasol G., Phys. Rev. Lett. 56 (1986) 2831
- [10] Damen T. C., Viti L., Cunningham J. E., Shah J. and Sham L. J., Phys. Rev. Lett. 67 (1991) 3432
- [11] Roussignol Ph., Rolland P., Ferreira R., Delalande C., Bastard G., Vinatier A., Martinez-Pastor J., Carrazzi L., Colucci M., Palmier J.-F. and Etienne B., Phys. Rev. B 46 (1992) 7292
- [12] Bar-Ad S. and Bar Joseph I., Phys. Rev. Lett. 68 (1992) 349
- [13] Quivy da Silva E. C. F., Chitra V., Tuet D., Potemski M., Nuan J. C. and Phoo K., Semicond. Sci. Technol. 7 (1992) 1369

Interactions between Wannier - Stark states
R. Ferreira, P. Voisin and G. Bastard
Laboratoire de Physique de la Matière Condensée
Ecole Normale Supérieure, 24 rue Lhomond F75005 Paris (France)

We examine the interaction between the Wannier Stark ladders derived from two minibands in a semiconductor superlattice. We show that it leads to anticrossings whose magnitude and electric field position can be modelled in a simple way. The eigenenergies depart from a linear dependence upon the electric field. In the time domain, the wavepackets show spatial oscillations between the main locations of the particle in the two interacting states. The frequency of the absorbed and emitted photons between such unevenly spaced ladders become different. In contrast to the one band case, a net absorption or emission becomes possible, although not at the Bloch frequency ω_B .

The destruction of the quasi continuous electron spectrum of a crystalline material by a constant electric field and its replacement by ladders of evenly spaced levels, the Wannier - Stark ladders (energy separation: $\hbar\omega_B = eFd$, where d is the spatial period) has been predicted by Wannier in the late fifties [1] and since then considerably debated on the theoretical side [2,3]. The existence of such ladders has been established by steady state optical experiments performed on semiconductor superlattices [4,5]. These are high quality materials characterized by large periods along the growth axis ($\approx 60 \text{ \AA}$) and therefore small bandwidths ($\approx 60 \text{ meV}$) which become comparable to the electric field effects over a period ($eFd = 60 \text{ meV}$ if $F = 100 \text{ kV/cm}$ and $d = 60 \text{ \AA}$). Wannier's approach, a one band analysis, leads to discrete Wannier - Stark states and to a linear dependence of their energies upon F . The status of the interband couplings induced by the field, or equivalently the field induced couplings between the Wannier - Stark ladders belonging to different bands, is still a matter of debate [3], in particular because there is an infinite number of bands and hence an infinite number of field induced anticrossings between the ladders belonging to different bands in a finite energy range. This may transform the discrete levels of the one band approximation into resonant levels, eventually long lived. Early treatments of the interband couplings have relied on Kane's analysis [6] who first calculated the tunnel current associated with these interband transitions in a semi - classical approach. Formal treatments of Wannier - Stark ladders with two or a finite number of bands have been undertaken (see e.g. [7,8]) but no attention has been paid to the specific case of semiconductor superlattices, in particular to the fact that in these materials one may tailor situations in which one well defined discrete (or quasi discrete) Wannier - Stark level of one band is made to anticross another level belonging to another band, as demonstrated and analyzed by Schneider et al [9]. Recent time - resolved experiments on Wannier - Stark levels [10,11] have been analyzed in terms of an oscillatory motion of carriers at the Bloch frequency ω_B .

In this paper, we wish to address the questions of i) a simple, yet accurate enough, modelling of the anticrossings between two discrete Wannier - Stark levels belonging to two different bands and ii) the consequences that such anticrossings may have on the frequency of the motion of wavepackets of interacting Wannier - Stark levels as well as on the frequency of the absorbed or emitted light between the levels of such interfaced ladders.

In the envelope function approximation, the stationary conduction (Γ_6 related) eigenstates of a semiconductor superlattice in the presence of a longitudinal electric field are the solutions of

$$[T + V_{SL}(z) + eFz] \psi(z) = E \psi(z) \quad (1)$$

where $V_{SL}(z)$ is the piecewise constant superlattice potential with period d and T the longitudinal kinetic energy (equal to $\hbar^2 \partial^2 \psi / \partial z^2$). Without electric field the superlattice eigenstates are for a wide class of materials well described by nearest neighbour tight binding models as witnessed by the excellent fit of the exact dispersion relations to a single cosine law. We restrict our considerations to the two lower minibands. We call

Fig. (1) The calculated dermal logarithm of $\langle 2/T_{sp} \rangle$ is plotted versus temperature for a $L=80 \text{ \AA}$ $\text{Ga}_{0.47}\text{In}_{0.53}\text{P}$ quantum well. The scattering mechanism is the alloy scattering. Three inversion asymmetry terms are taken into account: (a) asymmetry barrier height $(\Delta V/V_{Sb} \approx 0.7)$, (b) a weak electric field (5 kV/cm) and (c) the linear-in-k hamiltonian ($C_4 = 0.75 \text{ meV \AA}$).

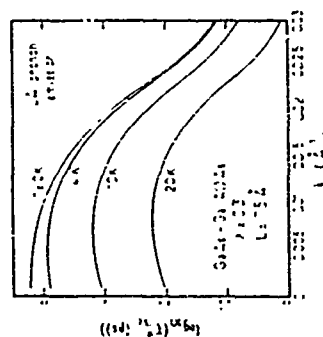
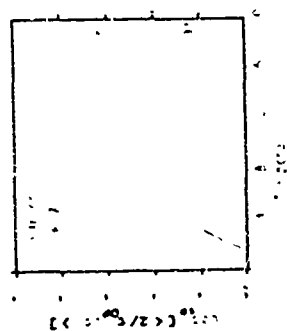


Fig. (2) Dependence with n of the spin conserving velocity relaxation time T_{vc} for a 75 \AA $\text{GaAs-Ga}_{0.47}\text{Al}_{0.53}\text{P}$ QW at various temperatures: $T=0\text{K}$, 4K , 1K and 20K . Emission of acoustic phonons deformation potential approximation.

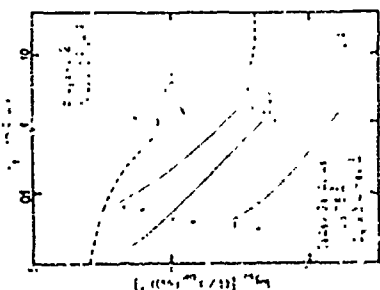


Fig. (3) Theoretical dependence of $\langle 1/T_{sp} \rangle$ with (1) the temperature for various electron densities (lower horizontal axis), (2) the electron density at $T=4\text{K}$ (upper horizontal axis) for a 75 \AA $\text{GaAs-Ga}_{0.47}\text{Al}_{0.53}\text{P}$ QW. Scattering by residual ionized impurities $n_{imp} \approx L^2$ and $N_{imp} \approx 10^{10} \text{ cm}^{-2}$.

(5)

confronted with the fact that the majority of the respondents have a low level of education and are in a position of economic dependence on their families.

$$s, w(z, \gamma) \geq w(z, \gamma') \Rightarrow Z_1 \delta_{\gamma, \gamma'} \cdot n' + Z_2 \delta_{n, n'} \cdot \pm 1 \quad (3)$$

works well for a variety of superlattices. Note that the Z_0 contribution is eventually an intra-well term; it represents for a single quantum well the polarization of the isolated wells with wavefunctions by the field (the one which gives rise to the Stark effect). We show in fig (1) the ϵ_{ij} dependence of the matrix element $\langle \phi_{n+1}^{(1)} | Z_0 | \phi_n^{(1)} \rangle$ where the $\phi_{n\pm 1}$'s are the isolated well eigenfunctions at zero field. This matrix element should provide a fair approximation of $\langle \psi_{n+1}^{(1)} | Z_0 | \psi_n^{(1)} \rangle$. Note that the values calculated for $n = 0, n < 80$ are not well represented by physical situations. The calculation at $\phi_0 = 0$ is meaningful: it is the intra-well contribution. As shown in fig (1), the intra-well ϵ_{ij} term ($\phi_0 = 0$) is the dominant one. For periods $d \approx 12$ nm, Z_0 is ~ 7 times smaller than Z_0 . It remains however important to keep it in the analysis in order to get an accurate description of the splitting at the n -th crossing for the following reason. Without interband coupling each miniband gives rise to an evenly spaced (to ϵ_0) ladder [1] with energies

$$E_{1,0} = \langle \varepsilon_1(q) \rangle + v_F p_d; \quad E_{2,0} = \langle \varepsilon_2(q) \rangle + v_F p_d \quad (4)$$

where u and v are relative integers and $\langle \epsilon_1(n) \rangle$ and $\langle \epsilon_2(n) \rangle$ are the average energies of E_1 and E_2 subband's respectively. $\langle \epsilon_1(n) \rangle$ and $\langle \epsilon_2(n) \rangle$ are close in energy from the isolated quantum bound states. The corresponding wavefunctions are

(5) $\rho = \frac{1}{m} \sum_{i=1}^m \rho_i$

$$\psi_{1N} = \sum_{\nu=0}^N J_{\nu, n} (\Delta \gamma / 2cFd) \psi_1(z - n\delta) \quad (6)$$

where J_{ll} is the Bessel function of integer order n . The uncoupled ladders intersect at fields $F_{\mu\nu} = \frac{1}{2} \mu \hbar \omega$. The inter-band couplings transform these crossings into anticrossings. The anticrossing between l, ν and $l+1, \mu = \nu - p$ gives rise to the energies $E_{\pm}(l, \nu, p)$. For $F = F_{\mu\nu}$, the $E_{\pm}(l, \nu, p)$ are the solutions of

$$\begin{pmatrix} E_{IV} - \underline{c}_V^-(v, p) & \delta_p \\ \delta_p & E_{2H} - \underline{c}_H^-(v, p) \end{pmatrix} \begin{pmatrix} c_1^+(p) \\ c_2^+(p) \end{pmatrix} = 0 \quad (7)$$

where we have only retained the two resonant contributions in the curly and

$$\delta\rho_p \approx \pi f |Z_0| J_{-p} \left[(\lambda_1 + \Delta_1/2\epsilon f d) + Z_1 \sum_{l=1}^{\infty} J_{-l} \left[(\lambda_1 + \Delta_1/2\epsilon f d) \right] \right] \quad (8)$$

Thus, the difference between Z_1 and Z_0 can be offset by the magnitude of the J_{-l} appearing in

$\delta\rho_p \in \mathbb{R}$ in strong fields when the arguments of the Bessel functions become small and if $p = 1$ the magnitude of $Z_1 J_0$ becomes comparable or even larger than that of $Z_0 J_{-1}$ and both terms have the same sign. At resonance the antiresonance gap is $2\delta\rho_1^2, \dots$.¹¹ Note also that

independent. This theorem states that the translation by d of the argument of one complex ψ with energy ϵ produces another eigenfunction of eq (1) with energy $\epsilon + eV$.

The non-resonant contributions can be inserted into eq (7) up to the second order. This amounts to taking diagonal contributions of the form $e^{-\beta_0} \sum_{j=1}^{\infty} |w_{2,j-1}|^2 |v_{1,j}|^2 e^{-(2-j)\beta_0}$. These terms are interchanged with 1 , v and w respectively. We have checked that the inclusion of those terms are not essential; they hardly affect the magnitude of the anticrossing gap, and merely amounts to shifting the $F_{\mu\nu}$'s towards higher fields. We summarize in fig (2) our modelling of the two band anticrossing for a 8 nm GaInAs superlattice. Since we do not know the w_1 and w_2 functions explicitly, we have replaced them by the ϕ_{kcc} 's defined previously in the evaluation of Z_0 and Z_1 . We note a fair description of the ϵ_{exci} - p versus F curves by eq (7), when compared with an "exact" i.e numerical calculation of the central eigenstates (to avoid edge effects) of a 15 period superlattice.

The oscillator strength of the optical transitions between the levels $1-v, p$ and $1-v', p'$ of a hybrid ladder is proportional to $(k-v, p) \pm (k-v', p')$ (see fig. (3)). The

energies of such transitions are $\epsilon_2(v', p) - \epsilon_1(v, p)$. Clearly, all the transitions $1 \rightarrow v, p \rightarrow 1 \rightarrow v', p$ occur at the energy $(v' - v)\epsilon_d, 1 \rightarrow v$; at the fundamental and harmonics of the Bloch energy. However, like in the one band case [14], the oscillator strengths of the absorption is exactly equal to that of the induced emission. Thus, there is no net absorption of the electromagnetic wave in an infinite superlattice due to $1 \rightarrow v, p \rightarrow 1 \rightarrow v', p$ transitions. Clearly, the same conclusion is reached if $1 \rightarrow v, p \rightarrow 1 \rightarrow v', p$ transitions are involved. In actual, i.e. finite materials, absorption or emission may take place due to edge effects [14]. Their signature would be their independence upon the superlattice thickness. Possible stimulated emission or absorption are associated with $1 \rightarrow v, p \rightarrow 1 \rightarrow v', p$ transitions. There is an absorption corresponding to $v = v'$ at the energy $\epsilon_2(v, p) - \epsilon_1(v, p)$, which is not compensated by an emission at the same energy, and with the same initial state. This solitary line is accompanied by an absorption sideband shifted in energy by ϵ_d and by an emission sideband at the energy $\epsilon_d - [\epsilon_2(v, p) - \epsilon_1(v, p)]$. Note that all these uncompensated (because the energies are different) absorption / emission processes are of the inter-subband type (like $E_1 \rightarrow E_2$ in a single quantum well) rather than of the Wannier - Stark type. They should produce net absorption or emission of an electromagnetic wave depending of the steady state (or transient) occupancy of the $v, p \rightarrow v', p$ hybrid levels.

Recent time-resolved optical experiments have been used to study the dynamical behaviour of electrons in superlattices under an electric field [10, 11, 12]. In particular, the time-varying polarization that accompanies the tunnelling back and forth of an electron between the wells of a double quantum well has been detected in the form of a 1.3 THz emission [11].

The time dependent counterpart of the anticrossings studied in eq (7) is a Rabi precession between the two interacting states if the system is prepared in an initial state which is not an eigenstate of eq (7). This is realized if a short light pulse (characteristic width $\delta t \ll \hbar/\omega$) is shined onto the crystal. Assume for simplicity that $\psi(t=0) = |1\rangle$. Then, the probability $P(t)$ to find the system in the state $|2\rangle$, $\mu = v \cdot p$ is equal to

$$P_{nm}(t) = \frac{1}{2} p \cdot m \cdot n \left[(\Delta_1^2 + \Delta_2^2 + 2\Delta_1\Delta_2 \cos(\omega_B t))^{1/2} / (2eF\hbar) \right] \quad (17)$$

$$\left\{ \sum_{\pm} c_1^{\pm} c_2^{\pm} + 2c_1^+ c_2^+ c_1^- c_2^- \cos[(\epsilon_+(v, p) - \epsilon_-(v, p))t/\hbar] \right\} \quad (17)$$

This probability depends, as expected, on two periodic functions of time. The first one corresponds to the intraband motions (period $2\pi/\omega_B$) in either bands while the second is related to the interband coupling as expressed by the energy difference $(\epsilon_+(v, p) - \epsilon_-(v, p))$. Note that P_{nm} is only a function of $n \cdot m$, a characteristic feature of perfect, infinite superlattices. In addition, we find that $P_{n \cdot m} \propto P_{m \cdot n}$, low energy transitions are favored, while, in a one band analysis the quantity equivalent to P_{nm} is an even function of $(n \cdot m)$. Eq. (17) is the discrete (in site and Wannier - Stark indices) version of the interband tunnelling probability. As pointed out by Kane [6], the latter is calculated in bulk materials under the assumption that the discrete Wannier - Stark levels in either bands are not resolved (because of the unfavorable $m\omega_B/\hbar$ broadening ratio). In semiconductor superlattices, where the Wannier - Stark levels are well resolved, we believe that the use of the bulk - like formula is unwarranted. The total interband probability $P = \sum_{n,m} P_{nm}$ is obtained from eq. (17) by summing over all the final sites m . This procedure erases the Bessel function in eq. (17), hence P becomes n independent. At the resonance fields $(F_{\pm})_{\pm}$, P is simply equal to $\sin^2[(\epsilon_+(v, p) - \epsilon_-(v, p))/2\hbar]$, irrespective of p . Therefore, the total interband probability can become equal to unity. It has however to be stressed that the narrowness of the anticrossings increases with p , which implies that unless one deals with low index resonances ($p \approx 1, 2$) the interband transition probability will for almost all field remain modest. Finally, it is worth pointing out that the existence of the other bands of the superlattice at zero field should modify the Rabi precession between the two well defined Wannier levels. The actual situation is that of two interacting levels which are each coupled to a quasi continuum, the one provided by all the Wannier - Stark levels belonging to the other bands of the superlattice and which are in the energy range of the anticrossing. These quasi - continuum will provide the source of an irreversible escape of the carrier while in the two levels model the carrier oscillates between the two eigenstates forever. Whether the escape time is shorter or longer than the Rabi frequency remains to be studied in actual superlattices. The fact that anticrossings have been optically detected is in favor of a negligible escape.

References
 [1] G. H. Wannier, "Elements of Solid State Theory", Cambridge Univ. Press, Cambridge, U.K., 1959.
 [2] J. Callaway, "Quantum Theory of the Solid State", Academic Press, Boston, U.S., 1991.
 [3] For a recent review see G. Nenciu, Rev. Mod. Phys. 63, 91 (1991) and references therein.
 [4] E. E. Mendez, F. Agullo-Rueda and J. M. Hong, Phys. Rev. Lett. 60, 2426 (1988).
 [5] P. Vashita, J. Bleuse, C. Bouche, S. Galliard, C. Allibert and A. Regreny, Phys. Rev. Lett. 61, 1639 (1988).
 [6] E. O. Kane, J. Phys. Chem. Solids, 12, 181 (1959).
 [7] J. E. Aron and J. Zak, J. Math. Phys. 18, 918 (1977).
 [8] X. G. Zhao, J. Phys. Condens. Matter, 4, L383 (1992).
 [9] H. Schneider, H. T. Grallin, K. von Klitzing and K. Ploog, Phys. Rev. Lett. 65, 2720 (1990).
 [10] K. Leo, P. H. Bolivar, F. Bruggemann and R. Schwetler, Solid State Commun. 84, 943 (1992).
 [11] H. G. Roskos, M. C. Nuss, J. Shah, K. Leo, D. A. B. Miller, A. M. Fox, S. Schmitt - Rink and K. Köhler, Phys. Rev. Lett. 68, 2316 (1992).
 [12] H. M. James, Phys. Rev. 76, 1611 (1949).
 [13] For a recent discussion of the Wannier functions for the Kronig - Penney model see F. B. Pedersen, G. T. Lenevill and P. C. Hemmer, Phys. Rev. B 44, 5470 (1991).
 [14] J. G. Bastard and R. Ferreira, C. R. Acad. Sci. Paris, 322, Série II, 971 (1991).
 [15] G. von Plessen and P. Thomas, Phys. Rev. B 45, 0185 (1992).

$$P(t) = |c_2|^2 \mu = v \cdot p \exp(-i t/\hbar) |1, v\rangle^2 \quad (9)$$

$$< z, v, p | z, \mu > = c_2^{\pm}(p) \delta_{v, v'} \quad (10)$$

$$< z, v, p | z, v > = c_1^{\pm}(p) \delta_{v, v'} \quad (11)$$

$$P(t) = |c_1^+ c_2^+|^2 + |c_1^- c_2^-|^2 +$$

$$2c_1^+ c_1^- c_2^+ c_2^- \cos[(\epsilon_+(v, p) - \epsilon_-(v, p))t/\hbar] \quad (12)$$

This Rabi precession is accompanied by an oscillatory displacement of the electron between the v th and the μ th period of the superlattice. We calculate the average position of the electron at time t ($\langle z(t) \rangle = \langle v | z | v(t) \rangle$) with the same assumptions as previously ($\langle v(t) \rangle = -i, v > 1$) and find

$$z(t) = (c_1^+)^2 < z, v, p | z | z, v, p > + (c_1^-)^2 < z, v, p | z | z, v, p > + 2c_1^+ c_1^- < z, v, p | z | z, v, p > \cos[(\epsilon_+(v, p) - \epsilon_-(v, p))t/\hbar] \quad (13)$$

$$< z, v, p | z | z, v, p > = (c_1^{\pm})^2 < 1, v | z | 1, v > +$$

$$(c_2^{\pm})^2 < z, \mu | z | z, \mu > + 2c_1^{\pm} c_2^{\pm} < 1, v | z | z, \mu >$$

$$= (c_1^{\pm})^2 \langle v | z | v \rangle + (c_2^{\pm})^2 \langle \mu | z | \mu \rangle + 2c_1^{\pm} c_2^{\pm} \delta_p / eF$$

$$< z, v, p | z | z, v, p > = c_1^+ c_1^- \langle v | z | v \rangle + c_2^+ c_2^- \langle v' | z | v' \rangle +$$

$$(c_1^+ c_2^- + c_1^- c_2^+) \delta_p / eF \quad (15)$$

We show in fig. (4) the calculated time dependence of $\langle z(t) \rangle$ for a $\Delta m / 4m$ GaAs/AlAs superlattice. The anticrossing between the $1, 0$ and $1, 2$ levels takes place at $F_1 = 96.8$ kV/cm. The different curves correspond to different field detuning $\Delta F = F - F_1$ from $\Delta F = -20$ kV/cm to $+20$ kV/cm from the resonance field. The (F dependent) time scale is the period of the Rabi precession, i.e. $\hbar / |\epsilon_+(v, p) - \epsilon_-(v, p)|$. It is only at exact resonance that the particle excursion extends over one period. Off resonance there is an increasing spatial localization with increasing detuning. There exists a slight asymmetry between the $-\Delta F$ and $+\Delta F$ curves. It is due to the fact that δ_p in eq. (7) is field dependent. Note that the $z(t)$ curves which correspond to the $1, 0$ and $1, 2$, $-p > p$ anticrossings would qualitatively be the same as those shown in fig. (3) with, however, much sharper resonance like profiles and, of course at the resonance field an excursion down to the $-p$ period. As has been shown by Schneider et al. [9] these resonant delocalizations of the eigenstates provide an efficient way for the vertical transport of the carrier.

Another kind of wavepacket can be studied. It corresponds to the creation of an electron around the v th site at $t = 0$ and to its detection at the μ th site at time t with a change in the "atomic" eigenstate. We model this situation by calculating

$$P_{nm}(t) = | < w_1(z - nd) | \exp(-i t/\hbar) | w_2(z - md) > |^2 \quad (16)$$

which is equal to

Resonant coupling between buried single-quantum-well and
Wannier-Stark-localization states in a GaAs/AlAs superlattice

I. Tanaka, M. Nakayama, and H. Nishimura
Department of Applied Physics, Faculty of Engineering, Osaka City University,
Sugimoto, Sumiyoshi-ku, Osaka 558, Japan

K. Kawashima
Optoelectronic Device Laboratory, Semiconductor Research Center,
Sumco Electric Corporation, Hoshizakura, Hirakata, Osaka 573, Japan

K. Fujiwara
Department of Electrical Engineering, Faculty of Engineering,
Kyushu Institute of Technology, Tokata-ku, Kitakyushu, Fukuoka 804, Japan

We have investigated the resonant coupling between the quantized state in a GaAs single quantum well (6.4 nm) buried in the center of a GaAs(3.2 nm)/AlAs(0.9 nm) superlattice and the Wannier-Stark-localization state in the superlattice by using photorefraction spectroscopy. It is found that the photorefraction-line shapes of the heavy-hole and light-hole exciton transitions associated with the first ($n=1$) subbands in the buried single quantum well drastically change under the resonant-coupling condition. The splitting feature of the line shapes due to the formation of the bonding and antibonding states and the intensity reduction due to the wave-function delocalization over the coupling space. We have detected the various resonant couplings of electrons and holes. The experimental results are discussed from a transfer-matrix analysis with Airy functions.

1. INTRODUCTION

Recently there has been a growing interest in electric-field effects on electronic and optical properties of semiconductor quantum wells (QWs) and superlattices (SLs) for various applications in optoelectronic devices. Much of interest has centered around the properties of Wannier-Stark (WS) localization corresponding to the wave-function localization induced by breakdown of the resonant condition of miniband states in a SL due to an applied electric field [1-15]. The WS localization leads to Stark-ladder transitions $F_n \pm (1/2) \hbar \omega_F$ ($n=0, 1, 2, \dots$), where F_n is an interband-transition energy in an isolated QW, ω_F is a SL period, and $\hbar \omega_F$ is a Stark-ladder index indicating an oblique transition in real space. Under the condition of $m\hbar\omega_F = \Delta E_n$ ($m=1, 2, 3, \dots$), where ΔE_n is the energy spacing between the $n=1$ and $n=2$ electron (hole) subbands, the WS-localization state of the $n=1$ subband in a QW resonantly couples with that of the $n=2$ subband in the m -nearest-neighbor QW on the lower (higher) electrostatic potential side [6, 7, 11, 14]. In our previous works [12, 14], we have indicated that the resonant coupling between the WS-localization states in a SL appears as the splitting feature of the photorefraction (PR) line shapes due to the formation of the bonding and antibonding states and the PR intensity reduction of the related Stark-ladder transitions due to the wave-function delocalization over the coupling space.

In the present work, we have investigated the resonant coupling between the quantized state in a GaAs single QW (SQW) with 6.4 nm buried in the center of a

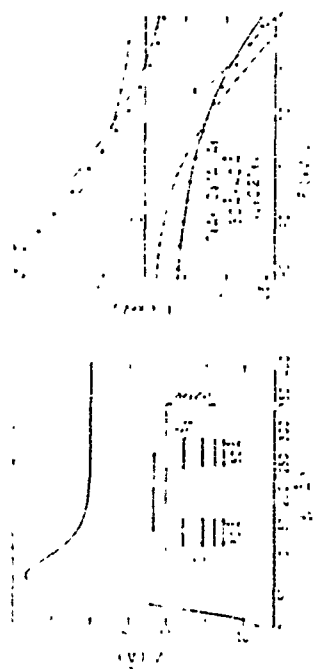


Fig. 1. $Z = \langle \phi_{n=1} | \mu | \phi_{n=2} \rangle / (2\hbar \omega_F)$ is plotted versus ϕ_F for a 80 Å - 40 Å GaAs/AlAs superlattice. The conduction band discontinuity is taken equal to 0.21 eV.

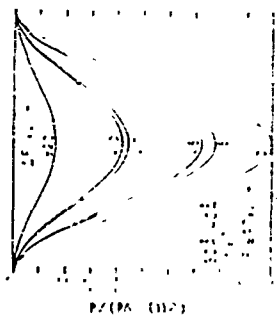


Fig. 2. Level scheme of a two-band Wannier-Stark ladder with positive optical transitions. The energy levels of the ground and first excited states of the superlattice are shown. The energy levels are separated by $\hbar \omega_F$. Here $F_F = 97$ kV/cm, ω_F corresponds to the energy of the unperturbed $v=0$ and $v=1$ subbands. Stark levels.

GaAs(1.2 nm)/AlAs(0.9 nm) SL and the WS-localization state in the SL by using IR spectroscopy. In the present case, the distance between the center of the buried SQW and that of the n-th-nearest-neighbor QW in the SL is given by $d_{WS} = 2 \cdot mD - d_{WS}/2$, where d_{WS} and d_{WS} are the layer thicknesses of the SQW and the QW in the SL, respectively. Therefore, the n-th-nearest-neighbor resonant coupling between the SQW state and the WS-localization state takes place under the condition of $ef(d_{WS} - 2 \cdot mD - d_{WS}/2) = \Delta E$, where ΔE is the energy spacing between the SQW state and the WS-localization state in the SL. Although Aguilu-Buella et al. [6] studied the similar resonant coupling by using photocurrent (PC) spectroscopy, they could not observe the resonant coupling between the hole states. From the IR profiles of the n=1 heavy-hole and light-hole exciton transitions [H1(SQW) and L1(SQW)] in the buried SQW as a function of electric field, we have detected the various resonant couplings of electrons and holes. We analyze the IR results of the resonant coupling by using a transfer-matrix (TM) method with any functions.

2. EXPERIMENTAL

The sample used in this work was grown on an n-type (Si-doped) (001)-GaAs substrate by multi-beam epitaxy. The GaAs SQW with 6.4-nm thickness is buried in the center of the GaAs(3.2 nm)/AlAs(0.9 nm) SL with 80 periods. The whole system is placed in the center of a p-i-n diode structure, where the n and p layers are Si-doped ($\sim 1 \times 10^{18} \text{ cm}^{-3}$) and Be-doped ($\sim 1 \times 10^{18} \text{ cm}^{-3}$) Al_{0.3}Ga_{0.7}As layers with $\sim 0.40 \text{ }\mu\text{m}$ and $\sim 0.18 \text{ }\mu\text{m}$, respectively. The method for making an ohmic contact is described in Ref. [5]. The IR measurements were performed at 77 K. The probe light was produced by combination of a halogen lamp (40 W) and a monochromator with 0.5-nm resolution. The reflected light was detected with a Si photodiode. The electric field was modulated with the amplitude of 50 mV and the frequency of the 210 Hz around a given dc bias. The IR signals were obtained by a conventional lock-in technique.

3. RESULTS AND DISCUSSION

We have calculated the electric-field dependence of the eigenenergies in the SL/SQW system by using the TM method proposed by Hutchings [16], which was already applied in our previous works [12-14]. Figures 1(a) and 1(b) show the calculated eigenenergies of the electron and light-hole states as a function of electric field respectively. In the TM calculations,

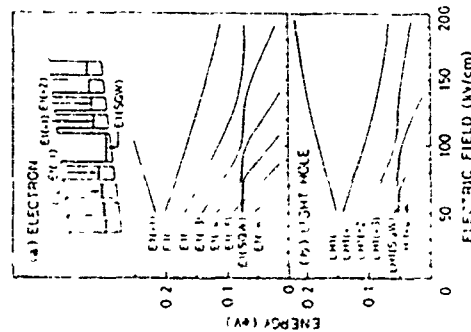


FIG. 1. Calculated eigenenergies of (a) the electron states and (b) the light-hole states in the SL/GaAs(6.4 nm)/SQW/SL system where the SL consists of six periods of 3.2-nm GaAs and 0.9-nm AlAs layers, the notations of L1(SQW), L1(-2), L1(SQW), and L1(-2) are explained in the text. The inset shows the potential profile of the SL/SQW/SL system.

GaAs(1.2 nm)/AlAs(0.9 nm) SL's on both sides of the central GaAs SQW are approximated by a system of six QWs, and the whole system is sandwiched by semi-infinite AlAs layers. In the present calculation, we used the following parameters: the conduction-band offset ratio is 0.66, and the effective masses of electrons, heavy holes, and light holes in units of m_0 are $m_e = 0.063$, $m_{hh} = 0.34$, and $m_{lh} = 0.15$, $m_{hh} = 0.4$, and $m_{lh} = 0.153$ for AlAs. All the values except for m_e for GaAs are the standard values taken from Ref. [17], and the value of m_e for GaAs is a little smaller than standard value of 0.0665 owing to fitting the calculated results to the experimental ones. Since the base line of the SL potential is proportional to the growth coordinate under the electric field, the energies are measured respect to the center of the SQW which corresponds to the center of the system. As shown in the inset of Fig. 1(a), the notation of L1(SQW) indicates the n=1 electron state in the central SQW, that of E1(-2 m) indicates the WS-localization state of the n=1 electron subband in the n-th-nearest-neighbor QW from the SQW, and the + (-) sign means the QW in the higher (lower) electron's potential side. It is the same with the light-hole states. In Figs. 1(a) and 1(b), we find various anticrossing behaviors due to the resonant couplings between the SQW and WS-localization states. We note that the SQW-electron state couples with the WS-localization state on the lower potential side, while the SQW-hole state couples with the WS-localization state on the higher potential side.

Noticing the electric-field range of 140-150 kV/cm in Fig. 1(a), we find the anticrossing of L1(SQW)-L1(-2), which originates from the resonant coupling between the SQW state and the WS-localization state of the n=1 electron subband in the second-nearest-neighbor QW. Figure 2 shows the IR spectra at 77 K in the energy range of the H1(SQW) and L1(SQW) transitions in the electric-field range of the E1(SQW)-L1(-2) resonant coupling. The value of the electric field is estimated from the built-in voltage of 1.77 V corresponding to the applied voltage at which the Stark-ladder transitions in the GaAs(3.2 nm)/AlAs(0.9 nm) SL converge. The IR spectra are not normalized by reflectance (R) because the surface ohmic electrode prevents us from obtaining the real R signal from the SL. Noticing the IR spectra at $F = 1.37 \text{ kV/cm}$ and 1.41 kV/cm , both the IR signal of the H1(SQW) transition and that of the L1(SQW) transition drastically change the shapes resulting from the formation of the bonding and antibonding states, which is due to the L1(SQW)-L1(-2) resonant coupling predicted by the TM analysis in Fig. 1(a). The anticrossing behavior will be shown together with other couplings in Fig. 4(c). In our previous works [12-14], we have

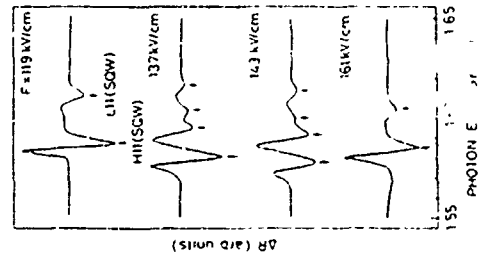


FIG. 2. IR spectra of the H1(SQW) and L1(SQW) transitions in the electric-field range of the L1(SQW)-L1(-2) resonant coupling.

demonstrated that IR spectroscopy is much more sensitive for detecting the resonant coupling than PR spectroscopy. In the present work, we could not obtain the clear information of the resonant coupling from the PR spectra.

Figure 1 shows the IR spectra at 77 K in the energy range of the $H1(SQW)$ and $L1(SQW)$ transitions in the electric-field range of the $E1(SQW)-F1(-3)$ and $E1(SQW)-F1(-4)$ resonant couplings, which correspond to ~ 100 kV/cm and ~ 75 kV/cm as shown in Fig. 4(c), respectively. Noticing the IR spectra at $F=75$, 77, 96, and 99 kV/cm, both the IR signal of the $H1(SQW)$ transition and that of the $L1(SQW)$ transition clearly exhibit splitting line shapes. Furthermore, the IR intensities under the resonant-coupling conditions are remarkably reduced, which is induced by the wave-function delocalization over the coupling space [12,14]. Focusing on the IR spectra, at $F \sim 100$ kV/cm, the split of the $L1(SQW)$ transition, ~ 13 meV, is larger than that of the $H1(SQW)$ transition, ~ 10 meV. The calculated results shown in Figs. 4(a) and 4(b) indicate that the $E1(SQW)-F1(-3)$ and $L1(SQW)-L1H(+2)$ resonant couplings simultaneously occur at $F \sim 100$ kV/cm, therefore, the large split of the $L1(SQW)$ transition is due to the overlap of the two resonant couplings.

Finally, we focus on the electric-field dependence of the IR intensities and energies of the $H1(SQW)$ and $L1(SQW)$ transitions. We assume that the transition intensity corresponds in the amplitude from the peak to the dip of the ER signals and that the transition energies correspond to the dip-position energies of the ER signals as indicated

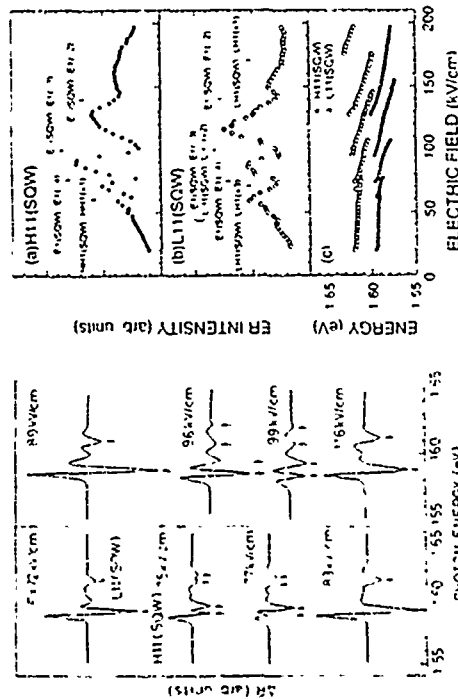


FIG. 3 IR spectra at 77 K in the energy range of the $H1(SQW)$ and $L1(SQW)$ transitions in the electric-field range of the $L1(SQW)-F1(-3)$ and $F1(SQW)-L1H(+2)$ resonant couplings.

by the arrows in Figs. 2 and 3. Figures 4(a) and 4(b) show the ER intensities of the (a) $H1(SQW)$ and (b) $L1(SQW)$ transitions as a function of electric field, respectively. The arrows in Figs. 4(a) and 4(b) indicate the calculated electric fields for the various resonant couplings by using the TM method. For the electron states, both the reduction of the ER intensity of the $H1(SQW)$ transition and that of the $L1(SQW)$ transition at $F=100$, 104, and 75 kV/cm result from the $L1(SQW)-F1(-2)$, $F1(SQW)-E1(-3)$, and $E1(SQW)-F1(-4)$ resonant couplings, respectively. The electric fields for the second-, third-, and fourth-nearest-neighbor resonant couplings between the SQW and WS-localization states should be in the ratio of $1.98:1.19:1.80 \approx 1.8:1.1$ because the resonant condition is proportional to the inverse of the distance between the center of the SQW and that of the nearest-neighbor QW in the SL: $cd(d_{sq}/2 + d_{ws}/2) \approx \Delta E$. The experimental ratio, $100:104:75 \approx 1.9:1.1:1.1$, is consistent with the expected one. In Fig. 4(a), only the ER intensity of the $L1(SQW)$ transition is reduced at $F=60$ kV/cm, resulting from the $H1(SQW)-L1H(+1)$ resonant coupling, which means the first-nearest-neighbor resonant coupling of the $n=1$ heavy-hole subbands. In Fig. 4(b), only the ER intensity of the $L1(SQW)$ transition is reduced around $F=170$ kV/cm owing to the $L1H(SQW)-L1H(+1)$ resonant coupling. The TM analysis predicts that the $L1H(SQW)-L1H(+2)$, $L1H(SQW)-L1H(+1)$ resonant couplings occur at $F \sim 100$ kV/cm and $F \sim 70$ kV/cm, respectively; however, the resonant conditions overlap with those of $E1(SQW)-F1(-3)$ and $E1(SQW)-F1(-4)$. Figure 4(c) shows the observed energies of the $H1(SQW)$ and $L1H(SQW)$ transitions indicated by the closed and open circles, respectively. We clearly find the anticrossing behaviors of the various resonant couplings. Thus, the above indicates that the quantized state in the SQW can be modulated by the resonant coupling between the SQW and WS-localization states.

4. SUMMARY

We have systematically measured the IR spectra of the GaAs SQW (6.4 nm) buried in the center of the $(\text{GaAs})_{1.2}$ nm $\text{AlAs}(0.9)$ nm SL at 77 K. It is found that the resonant coupling between the SQW state and the WS-localization state in the SL results in the change of the IR-line shapes of the $H1(SQW)$ and $L1(SQW)$ transitions, the splitting feature of the line shapes due to the banding and antibonding states, and the intensity reduction due to the wave-function delocalization over the coupling space. We have detected the various resonant couplings: the second-, third-, and fourth-nearest-neighbor resonant couplings of the $n=1$ electron subbands, the first-nearest-neighbor resonant coupling of the $n=1$ heavy-hole subbands, and the first-, second-, and third-nearest-neighbor resonant couplings of the $n=1$ light-hole subbands. The resonant coupling can be applied to modulate the buried SQW states.

ACKNOWLEDGMENT

This work was supported in part by Grant-in-Aid for Joint Research, No.05044109, from the Ministry of Education, Science, and Culture of Japan. One of the authors (T.T.) acknowledges the financial support of the Japan Society for the Promotion of Science for Japanese Junior Scientists.

Fermi Edge Singularities in doped quantum wires and quantum wells

F. J. Rodriguez and C. Tejedor
Departamento de Física de la Materia Condensada,
Universidad Autónoma de Madrid,
Cantoblanco 28019, Madrid Spain

Abstract

The optical properties of quantum wires and quantum wells are investigated. We are concerned with the effects produced by the localization of electrons and holes either in the same (direct transitions) or different $s_z = \pm 1/2$ regions (indirect transitions). The emission and absorption spectra are obtained by solving an effective Bethe-Salpeter equation including a static screened Coulomb interaction. First edge singularities (FES) are obtained and their dependence on temperature and density of carriers are analyzed. In order to obtain strong FES, it is necessary that two special points are fulfilled: (i) the hole mass goes to infinity and (ii) a spin-symmetry breaking of the system spatially indirect transitions. When the latter condition is satisfied, the bottom of the second conduction subband approaches the first one, a new channel of scattering is favored and the spectra show a large enhancement at the Fermi level. We compare our results with the experimental situations.

Available experiments [1] [2] [3] [4] [5] on the optical properties of modulation doped quantum wires (Q1D) and quantum wells (Q2D) show the possibility of observing many-body effects such as the Fermi edge singularities (FES). For Q1D systems, some optical absorption and emission measurements performed in the extreme quantum limit clearly show a strong peak at the Fermi energy. In contrast, some other experiments [4] [5] performed in quite similar conditions, in which electrons and holes are spatially separated, do not seem to detect such FES in the optical spectra. The theoretical models describing the optical properties of quantum wires [6] [7] [8] [9] [10] do not show a clear explanation for such apparent discrepancy. All of them always present a bottom singularity (typical of the one-dimensional density of states) accompanying the FES, which lacks in some experiments [2]. The aim of this paper is to consider a model of two conduction bands and a one hole band for spatially indirect quantum wires and consequently to allow the coupling between spatially extending and antisymmetric wavefunctions [10]. For the Q1D and the Q2D case we consider that both electrons and holes are completely confined in the xz plane. The electrons are free to move as a plane wave along the wire direction while they are confined by parabolic potentials in the transversal direction. In order to obtain a clear FES [2] [3] [4] extended holes with zero mobility due to random fluctuations of the potential are considered in the Q1D and Q2D cases.

The emission spectra are calculated using the relation between the linear optical susceptibility $\chi(\omega)$ and the interacting electron-hole Green function $G(\omega) = \sum_{\mathbf{k}, \mathbf{k}'} \chi(\mathbf{k}, \mathbf{k}') G(\omega)$,

$$\chi(\omega) = M^2 \sum_{\mathbf{k}, \mathbf{k}'} \frac{1}{\omega - \epsilon_{\mathbf{k}} - \epsilon_{\mathbf{k}'}} \quad (1)$$

where $\epsilon_{\mathbf{k}} = 0$ and $\epsilon_{\mathbf{k}'} = 0$ are valence and conduction states, respectively. \mathbf{k}, \mathbf{k}' are the hole and electron wavevectors and M^2 is the single particle dipole element which we take as a constant. As discussed in Ref. [10], $\chi(\omega)$ can be obtained from the noninteracting

REFERENCES

- 1 J. Bleuse, G. Bastard, and P. Vusim, *Phys. Rev. Lett.* **60**, 220 (1988)
- 2 I. L. Mendez, F. Agullo-Rueda, and J. M. Hong, *Phys. Rev. Lett.* **60**, 3426 (1988)
- 3 P. Vusim, J. Bleuse, C. Bouche, S. Guillard, C. Alibert, and A. Regreny, *Phys. Rev. Lett.* **61**, 1639 (1988)
- 4 F. Agullo-Rueda, E. E. Mendez, and J. M. Hong, *Phys. Rev. B* **40**, 1357 (1989)
- 5 K. Fujiwara, *Jpn. J. Appl. Phys.* **28**, L1718 (1989)
- 6 I. Agullo-Rueda, F. E. Mendez, H. Ohno, and J. M. Hong, *Phys. Rev. B* **42**, 1470 (1990)
- 7 H. Schneider, H. F. Gruber, K. V. Klitzing, and K. Ploog, *Phys. Rev. Lett.* **65**, 2720 (1990)
- 8 A. J. Shields, P. C. Klipstein, M. S. Skolnick, G. W. Smith, and C. R. Whitehouse, *Phys. Rev. B* **42**, 5879 (1990)
- 9 M. Nakayama, J. Tanaka, F. Doguchi, H. Nishimura, K. Kawachima, and K. Fujiwara, *Solid State Commun.* **77**, 303 (1991)
- 10 M. M. Digham and J. E. Sipe, *Phys. Rev. B* **43**, 4097 (1991)
- 11 Y. Tokuda, K. Kanamoto, Y. Abe, and N. Tokuda, *Phys. Rev. B* **43**, 7130 (1991)
- 12 M. Nakayama, J. Tanaka, H. Nishimura, K. Kawachima, and K. Fujiwara, *Phys. Rev. B* **44**, 5935 (1991)
- 13 A. M. Fox, D. A. B. Miller, G. Livescu, J. E. Cunningham, and W. Y. Jan, *Phys. Rev. B* **44**, 6231 (1991)
- 14 F. Tanaka, M. Nakayama, H. Nishimura, K. Kawachima, and K. Fujiwara, *Phys. Rev. B* **46**, 7656 (1992)
- 15 F. Tanaka, M. Nakayama, H. Nishimura, K. Kawachima, and K. Fujiwara, *Phys. Rev. B* **48** (1993) in press
- 16 D. C. Hutchings, *J. Appl. Phys. Lett.* **55**, 1082 (1989)
- 17 *Physics of Group Theory Elements and Applications*, edited by G. Madelung, M. Schultz, and H. Weiss, Landolt-Börnstein Numerical Data and Relationships, New Series, Group III, Vol. 17a (Springer, Berlin, 1982)

excitation hole Green's function $G_{\alpha\beta}^{(0)}(k, \omega) = G_{\alpha\beta}^{(0)}(k, \omega) + i\pi \delta(\omega - \epsilon_k) \delta_{\alpha\beta}$ and from the static electron-hole interaction potential $V_{\alpha\beta}(k) = V_{\alpha\beta}(k) + i\pi \delta(\omega - \epsilon_k) \delta_{\alpha\beta}$. Since α and β are described by a spectral function for the hole in order to give the adequate power law, the singularity $\delta(\omega - \epsilon_k)$ of the interacting electron-hole Green function is given by

$$G_{\alpha\beta}^{(0)}(k, \omega) = G_{\alpha\beta}^{(0)}(k, \omega) + i\pi \delta(\omega - \epsilon_k) \delta_{\alpha\beta} \quad (2)$$

From the wave functions of electrons and holes, it is straightforward to get the static Coulomb interaction between them as the necessary components of the interacting electron-hole interaction $V_{\alpha\beta}(k)$ we used are $V_{\alpha\beta}(k) = V_{\alpha\beta}(k) + i\pi \delta(\omega - \epsilon_k) \delta_{\alpha\beta}$. The screening of the Coulomb interaction $V_{\alpha\beta}(k)$ due to electrons, it is exactly the same than in direct wires where we used a RPA approximation [10]. The RPA polarizability for the two-dimensional case is taken from [11]. In contrast from the direct case, the coupling between electrons belonging to α and β and second subband $V_{\alpha\beta}(k)$ is different from zero allowing the coupling between α and β and even electronic bands which breaks the strong enhancement of the FES when the Fermi level lies just below the bottom of one of the bands as we will show below.

Experiments in which FES have been described [2] are performed with wires having a Fermi energy in the range 2.5 to 10 meV and an intersubband spacing Δ roughly 0.1 meV higher than F_1 . Therefore we work in the extreme quantum limit in which the Fermi level lies below the bottom of the second subband for Q_{2D} systems. We perform our calculations with $F_1 = 0.6 F_2$ and $\Delta = 0.7 F_2$ where F_0 is the band gap energy. Also to cover the experimental range, we take the temperature $0.6 k_B T / \hbar \omega \approx 1$ K, $F_1 \leq 0.1 F_2$ and $F_2 \leq 0.1 F_0$. The electron effective mass is that of GaAs while for the holes we take infinite mass in order to get a significant FES [10]. Experiment [2] with $a = 100$ nm show FES while others [2] with $a = 230$ nm do not. Therefore, we will cover the range $0.00 \leq a \leq 250$ nm.

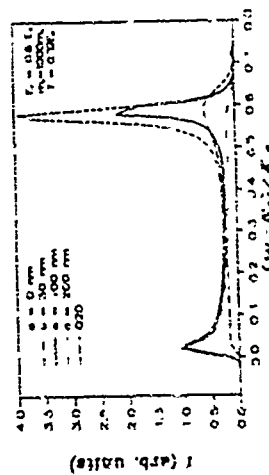


Figure 1: Emission spectra for direct Q2D system and indirect wires. All differences shown in here separation $a = F_1$ is the single particle band gap.

As we observe in a recent work [5], we obtain a very strong enhancement of the Fermi level when the difference between the Fermi level and the subband separation is of the order of $10 F_1$. If the difference is greater than this separation the FES becomes unappreciable.

Due to the asymmetry of the potential, $\epsilon_{\alpha\beta}$ couples $\epsilon_{\alpha\beta}$ with $\epsilon_{\beta\alpha}$. This gives a very strong contribution to the total emission. In a direct wire the off-diagonal term is zero and no strong singularity appears even when the intersubband separation is slightly larger than the Fermi energy [7,10].

Once the importance of the proximity of F_1 and Δ is established, let us analyze the importance of the electron-hole spatial separation as the key to understand differences between experiments. Figure 1 shows the emission spectra for several values of a . Both for small and large values of a the FES is rather weak. Only in the range between 50 and 100 nm, the singularity becomes strong. Our results show a maximum of $V_{\alpha\beta}(0)$ in these range while the two diagonal terms $V_{\alpha\alpha}$ and $V_{\beta\beta}$ decrease monotonously with increasing a . For $a = 0$ the symmetry tends to derouple the first and the second electron subbands and the singularity weakens. For very large a , the interaction between the spectrum and the hole is so small that the second term of equation (2) goes to zero and the Green's function tends to be $G_{\alpha\beta}$ which does not present singularity at all. Our results are in agreement both with experiment [2] which present FES in wires having $a \approx 100$ nm and with theory [10] which does not have singularity at $a \approx 250$ nm. Moreover, the FES is so strong that the bottom singularity becomes negligible in the whole emission spectrum as experimentally observed [2].

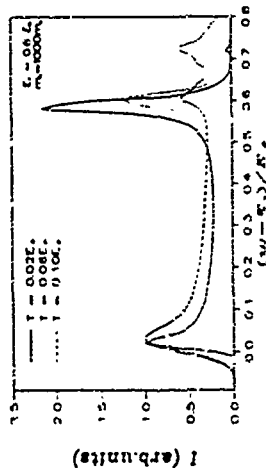


Figure 2: Emission spectrum of an indirect wire with electron-hole separation $a = 100$ nm, $\Delta = 0.7 F_1$, and $F_1 = 0.6 F_2$, for different temperatures. F_2 is the single particle band gap.

Another property comparable with the experiment is presented in figure 2. There the emission spectrum for a wire with $F_1 = 0$ and $\Delta = 0.7 F_1$ and $a = 100$ nm is given for several temperatures. For a temperature of 0.1 K, the FES has weakened so much that it is comparable to the bottom singularity of the first $\epsilon_{\alpha\beta}$ ($F_1 \approx 0$) and the second $\epsilon_{\beta\alpha}$ ($F_2 \approx 0.7 F_1$) subband is something appreciable in the experiment. This again agrees with the experimental temperature dependence.

Very important point must be stressed. The calculation has been performed in a single indirect wire while the experiments are done with multiple wires. In actual samples the hole does not move along the structure, most probably due to the limitations of the wire pattern. The position F_1 of such a $\epsilon_{\alpha\beta}$ subband is completely random for different wires. The FES of the array and the system is not comparable at all more.

In other words, the asymmetry is not restricted by the existence of a multiple array and all the results presented here for a single indirect wire are perfectly compatible with actual experiments.

TuP6

Excitonic enhancement of the Fermi edge singularity and recombination kinetics of photogenerated electrons in p-type δ -doped $\text{GaAs:Be/Al}_x\text{Ga}_{1-x}\text{As}$ double-heterostructures

J. Wagner^a, D. Richards^b, H. Schneider^c, A. Fischer^d, and K. Ploog^d
^a *Frankfurter Institut für Angewandte Festkörperphysik, Tullastrasse 72, D-70108 Freiburg, Federal Republic of Germany*
^b *Cambridge Laboratory, Madingley Road, Cambridge CB3 0HE, UK*
^c *Max-Planck-Institut für Festkörperforschung, Heisenbergstrasse 1, D-70506 Stuttgart, Federal Republic of Germany*
^d *Paul-Drude-Institut für Festkörperelektronik, Houvogelplatz 5-7, D-10117 Berlin, Federal Republic of Germany*

Abstract

We have studied the photoluminescence (PL) spectrum, and the strength of the Fermi edge singularity (FES) in the PL spectrum, of the two-dimensional hole gas (2DHG) formed in $\text{GaAs/Al}_x\text{Ga}_{1-x}\text{As}$ double-heterostructures as a function of the width of the GaAs layer, the centre of which is p-type δ -doped. A variation of the layer width allows us to tune, for a fixed doping concentration, the energetic spacings between the hole subbands. From these experiments, we conclude that the observation of a FES in the PL spectrum of a 2DHG is brought about by a resonant hybridization between occupied states close to the hole Fermi energy and exciton levels involving nearby lying unoccupied hole subbands. The recombination and spin-flip scattering times of the photogenerated electrons are found to decrease drastically with decreasing GaAs layer width which reflects the increase in the electron-hole wavefunction overlap.

1. Introduction

$\text{Al}_x\text{Ga}_{1-x}\text{As/GaAs/Al}_y\text{Ga}_{1-y}\text{As}$ double-heterostructures, p-type δ -doped in the centre of the GaAs layer, have proven to be very useful for the photoluminescence (PL) study of a two-dimensional hole gas (2DHG) [1-3]. The $\text{GaAs/Al}_x\text{Ga}_{1-x}\text{As}$ heterojunction barriers confine the photogenerated minority carriers (electrons), which are repelled by the space-charge induced potential well confining the holes, sufficiently close to the 2DHG to enhance the electron-hole wavefunction overlap for efficient radiative recombination [1,2]. A schematic energy-band diagram of such a double-heterostructure is shown in Fig. 1.

In the optical spectra of two-dimensional electron gases (2DEG) an enhancement of the emission intensity or the absorption strength at the Fermi edge has been observed [4,5]. This so-called Fermi edge singularity (FES) is a consequence of many-body interactions between the 2DEG and photogenerated holes [6,7]. To observe a Fermi edge enhancement in emitters, electrons with energies close to the Fermi energy E_F and consequently a wavevector close to the Fermi wavevector k_F , have to recombine

with photogenerated holes with a wavevector of essentially zero. If only momentum conserving transitions are allowed, this recombination would be forbidden and therefore, the FES would be strongly suppressed. Thus one possibility to observe a strong FES in emission is a localization, and thus a spread in k -space, of the holes [4]. Another possible mechanism for the observation of a FES in luminescence, suggested by Chen et al. [8,9], is the resonant hybridisation of occupied states at the Fermi edge with virtual excitons involving unoccupied electron subbands [10,11].

Recently, a FES has also been observed in the PL spectrum of a high-density 2DHG formed in a δ -doped $\text{Al}_x\text{Ga}_{1-x}\text{As/GaAs:Be/Al}_y\text{Ga}_{1-y}\text{As}$ double-heterostructure [1,2]. In this case, the photogenerated electrons are unlikely to be localized because of their much smaller mass. Instead, it has been suggested that the observation of a FES in the PL spectrum of a 2DHG is due to a resonant hybridisation between states at E_F and an unoccupied hole subband [2]. In the present paper we present experimental evidence in support of this suggestion. This evidence is based on the measured dependence of the 2DHG PL spectrum in $\text{Al}_x\text{Ga}_{1-x}\text{As/GaAs:Be/Al}_y\text{Ga}_{1-y}\text{As}$ double-heterostructures on the width of the GaAs layer, the centre of which is p-type δ -doped. Further, we report on the variation of the recombination and spin-flip scattering times with increasing electron-hole wavefunction overlap upon reduction of that layer width.

2. Results and Discussion

A. Fermi Edge Singularity

Fig. 2 shows a sequence of low-temperature (6 K) PL spectra of δ -doped $\text{GaAs:Be/Al}_x\text{Ga}_{1-x}\text{As}$ double-heterostructures where the width d of the GaAs layer was varied between 20 and 60 nm. The two-dimensional hole concentration was kept fixed at $4 \times 10^{12} \text{ cm}^{-2}$. For this doping concentration and a layer width of $d=60 \text{ nm}$ three or four hole subbands, namely the first (hh1) and the second heavy-hole (hh2) and the first (lh1) and possibly the second light-hole band (lh2), are expected to be occupied [2]. Thus the emission peak lowest in energy arises from recombination of holes in the first heavy-hole and light-hole subbands whereas emission at higher energies is due to transitions involving holes in the hh2 and possibly the lh2 subbands. The overall luminescence intensity is found to decrease by almost one order of magnitude with reduction of the GaAs layer width from $d=60$ to 20 nm. For the narrowest layer width of $d=20 \text{ nm}$ the whole luminescence spectrum is shifted to higher energies primarily due to the reduction in electron-hole separation. This reduction leads, for a constant electric field above and below the doping spike (see Fig. 1), to a blue-shift of the 2DHG emission.

For $d=60 \text{ nm}$ there is a well resolved Fermi edge enhancement at the high-energy side of the emission spectrum. When the GaAs layer width is decreased to $d=40 \text{ nm}$ the strength of the FES is considerably reduced and for $d=20 \text{ nm}$ there is no detectable enhancement left. Temperature-dependent PL spectra of the sample with the widest GaAs layer ($d=60 \text{ nm}$) are shown in Fig. 3. There is a monotonic

decrease in intensity of the Fermi edge enhancement with increasing temperature, which is a characteristic fingerprint of a FES [4,6]. For temperatures ≥ 40 K the intensity of the $\text{Mn}^{2+}/\text{Mn}^{3+}$ recombination band remains constant which indicates a complete disappearance of the FES due to the thermal spread of the holes. From the temperature dependence of the FES intensity the binding energy of the Mahan exciton can be determined to be about 1.5 meV. This value is about twice as large as the binding energy of 0.5 meV found for the FES in a 2DEG in a modulation-doped $\text{GaAs}/\text{In}_{0.7}\text{Ga}_{0.3}\text{As}/\text{Al}_{0.3}\text{As}$ quantum wells [12].

With increasing temperature an additional emission peak appears at the high energy side of the spectrum arising from recombination of holes which are thermally excited into the Mn^{2+} and/or Mn^{3+} hole subbands [2]. Thus the present temperature-dependent PL measurements allow us to determine the energetic spacing between E_F and the nearest hole subband not occupied at low temperature. In Fig. 4 PL spectra are plotted recorded at 6 and 50 K from the samples with GaAs layer widths of $d=60$ and 40 nm. The apparent energetic spacing, as determined from the half maximum points of the leading edges in the spectra, are 12 and 17 meV for $d=60$ and 40 nm, respectively. Taking into account the temperature shift of the GaAs band gap energy, the actual energetic spacings turn out to be ≈ 15 and ≈ 20 meV for the two different layer widths. For the sample with the narrowest GaAs layer of $d=20$ nm no emission from thermally populated hole subbands could be detected indicating an even larger energetic spacing between E_F and the nearest hole subband not occupied at low temperatures. This increase in subband spacing with decreasing GaAs layer width directly reflects the effect of the $\text{Al}_x\text{Ga}_{1-x}\text{As}$ barrier separation on the energy spectrum of higher lying hole subbands.

Combining the above results on the GaAs layer width dependence of the strength of the FES and of the hole subband spectrum, we can conclude that the FES decreases in strength with increasing energy separation between E_F and the nearest unoccupied hole subband. This finding gives full support to the view that the observation of a FES in the luminescence spectrum of a 2DHG is due to a resonant hybridisation between occupied states at the Fermi edge and excitation levels involving nearby unoccupied hole subbands [2]. For this hybridisation mechanism the strength of the Fermi edge enhancement is indeed expected to depend strongly on the energy separation [8-12]. It has been pointed out by Rodriguez and Tejedor [13] that a hybridisation between states from adjacent subbands is not possible for carriers confined in a symmetric potential. The present δ -doped $\text{GaAs}/\text{Be}/\text{Al}_x\text{Ga}_{1-x}\text{As}$ double-heterostructures are indeed symmetric by design. However, there are a number of possible reasons for the introduction of an asymmetry, such as the effect of the position of the Fermi level at the nearby surface on the electron-confining potential [2,14,15] and a segregation of the dopant atoms not detectable within the depth resolution of secondary ion mass spectroscopy [2].

Alternatively, one may think of an enhanced scattering of the photogenerated electrons by the ionized acceptor impurities upon reduction of the GaAs layer width

as a possible reason for the decrease in the strength of the FES. However, if this scattering had a strong effect on the FES intensity one would expect also a reduction in that intensity when, for a given GaAs layer width, the acceptor impurities are spread over a larger distance along the growth direction. An increase of the two-dimensional ($2D$) acceptor concentration results in a larger spread of the acceptors along the growth direction [4] because of diffusion and segregation of the dopant impurities. But in this case even an increase in the strength of the Fermi edge enhancement is observed with increasing $2D$ acceptor concentration, most likely because of a change in the hole subband structure [2]. For that reason we discard the idea of enhanced impurity scattering as a likely explanation for the observed decrease in FES strength with decreasing GaAs layer width, at least for widths $d \geq 40$ nm.

B. Recombination Kinetics

The recombination kinetics of photogenerated electrons are expected to depend strongly on the electron-hole wavefunction overlap and thus, for the present double-heterostructures, on the GaAs layer width. Therefore we have studied the recombination kinetics of the photogenerated electrons by time-resolved photoluminescence spectroscopy. The recombination time of 300 ps measured for the present hole concentration of $4 \times 10^{13} \text{ cm}^{-2}$ and $d=60$ nm is consistent with a recombination time of 400 ps reported previously for a hole concentration of $3 \times 10^{13} \text{ cm}^{-2}$ and the same GaAs layer width [2]. On the other hand, these time constants are much shorter than that of 2 ns reported for $d=60$ nm and a hole concentration of $8 \times 10^{12} \text{ cm}^{-2}$ [3]. Upon reduction of the GaAs layer width the recombination time is found to decrease, for a hole concentration of $4 \times 10^{13} \text{ cm}^{-2}$, to 130 and 35 ps for $d=40$ and 20 nm, respectively, as compared to 300 ps for $d=60$ nm. The above described dependence of the minority carrier recombination time on both the hole concentration and the GaAs layer width indicates a pronounced enhancement of the recombination rate with increasing electron-hole wavefunction overlap. As the decrease in recombination time with decreasing layer width goes along with a reduction of the cw luminescence intensity (see Fig. 2), we can conclude that with increasing wavefunction overlap the nonradiative recombination rate increases faster than the radiative one. As we deal with a highly p-type doped system Auger recombination is the most likely non-radiative process.

The short recombination time constants in the present samples prevented us from a direct measurement of the spin-flip scattering time of the photogenerated electrons as a function of the GaAs layer width [3]. However, using optical excitation with circularly polarised light and detecting the degree of circular polarisation of the emitted recombination radiation we could measure the average degree of circular polarisation P_{av} from cw PL measurements and the initial degree of polarisation P_0 was immediately after the exciting laser pulse in a time-resolved PL experiment. P_0 was found to be of the order of 20 % independent of the GaAs layer width whereas P_{av} decreased from ≈ 20 % for $d=60$ nm to ≈ 12 % for $d=40$ and 20 nm, respectively.

Using the relation $\tau_{sp} = \tau_{sp}^0 \{ \tau_{rec} / (\tau_{rec} + \tau_{sp}) \}$ [16], where τ_{rec} and τ_{sp} are the recombination and spin-flip scattering time constants, respectively, we can obtain a rough estimate for τ_{sp} from the measured values for P_{sp} , P_0 , and τ_{rec} . For $d=60$ nm τ_{sp} turns out to be much larger than the recombination time of 300 ps, whereas for $d=40$ and 20 nm spin-flip scattering times of ≈ 200 and ≈ 50 ps are obtained.

The above results clearly indicate a strong increase of the spin-flip scattering rate for electrons upon increasing electron-hole wavefunction overlap, as is expected from previous experiments on a less heavily p-type δ -doped GaAs:Be/AlGa_{0.5}As double-heterostructure with a GaAs layer width of 60 nm, for which a spin-flip scattering time of ≈ 20 ns has been reported [3]. The spin-flip scattering times of ≤ 200 ps observed for the two narrowest GaAs layers are comparable to those, which are of the order of 100 ps, reported for electrons in homogeneously p-type doped GaAs with decent concentrations in the mid 10^{19} cm⁻³ range [17].

3. Conclusions

We have analyzed the strength of the Fermi edge singularity in the emission spectrum, and the recombination kinetics, of photo-generated minority carriers in GaAs:Be/AlGa_{0.5}As double-heterostructures as a function of the width of the GaAs layer, the centre of which is p-type δ -doped. With decreasing layer width the energetic spacing between the Fermi edge and the nearest unoccupied hole subband increases and the strength of the FES is found to decrease. These findings lead us to the conclusion that the observation of a FES in the luminescence spectrum of a 2DHO is due to resonant hybridization between occupied states at the Fermi energy and exciton levels involving empty unoccupied hole subbands. The recombination and spin-flip scattering times of photo-generated electrons are found both to depend strongly on the GaAs layer width and to decrease with increasing electron-hole wavefunction overlap.

Acknowledgements

We would like to thank F. Koidl and H.S. Ruppert for stimulating discussions and for continuous support of the work at the Fraunhofer-Institut. Part of the work at the Max-Planck-Institut was sponsored by the Bundesministerium für Forschung und Technologie.

References

1. J. Wagner, A. Ruiz, and K. Ploog, Phys. Rev. B **43**, 12 154 (1991).
2. D. Richards, J. Wagner, H. Schneider, G. Hendorfer, M. Maier, A. Fischer, and K. Ploog, Phys. Rev. B **47**, 9639 (1993).
3. J. Wagner, H. Schneider, D. Richards, A. Fischer, and K. Ploog, Phys. Rev. B **47**, 4786 (1993).
4. M.S. Skolnick, J.N. Rorison, K.J. Nash, D.J. Mowbray, P.R. Tapster, S.J. Bass, and A.D. Pitt, Phys. Rev. Lett. **58**, 2130 (1987).
5. G. Livescu, D.A.B. Miller, D.S. Chemla, M. Ramaswamy, T.Y. Chang, N. Sauer, A.C. Gosard, and J.H. English, IEEE J. Quantum Electron. Q&E **24**, 1677 (1988).
6. S. Schmit-Rink, C. Ell, and H. Haug, Phys. Rev. B **33**, 1183 (1986).
7. A.E. Ruckenstein and S. Schmit-Rink, Phys. Rev. B **35**, 7551 (1987).
8. W. Chen, M. Fritze, A.V. Nurmikko, D. Ackley, C. Colvard, and H. Lee, Phys. Rev. Lett. **64**, 2434 (1990).
9. W. Chen, M. Fritze, A.V. Nurmikko, M. Hong, and L.L. Chang, Phys. Rev. B **43**, 14 738 (1991).
10. J.F. Mueller, Phys. Rev. B **42**, 11 189 (1990).
11. P. Hawrylak, Phys. Rev. B **44**, 6262 (1991).
12. W. Chen, M. Fritze, W. Walecki, A.V. Nurmikko, D. Ackley, J.M. Hong, and L.L. Chang, Phys. Rev. B **45**, 8664 (1992).
13. F.J. Rodriguez and C. Tejedor, Phys. Rev. B **47**, 13 015 (1993).
14. D. Richards, J. Wagner, K. Ploog, and A. Fischer, Mat. Res. Soc. Symp. Proc. Vol. **261**, 63 (1992).
15. D. Richards, J. Wagner, A. Fischer, and K. Ploog, Appl. Phys. Lett. **61**, 2683 (1992).
16. R.R. Parsons, Phys. Rev. Lett. **23**, 1152 (1969).
17. K. Zerruati, F. Fabre, G. Bacquet, J. Bandet, J. Frandon, G. Lampel, and D. Paget, Phys. Rev. B **37**, 1334 (1988).

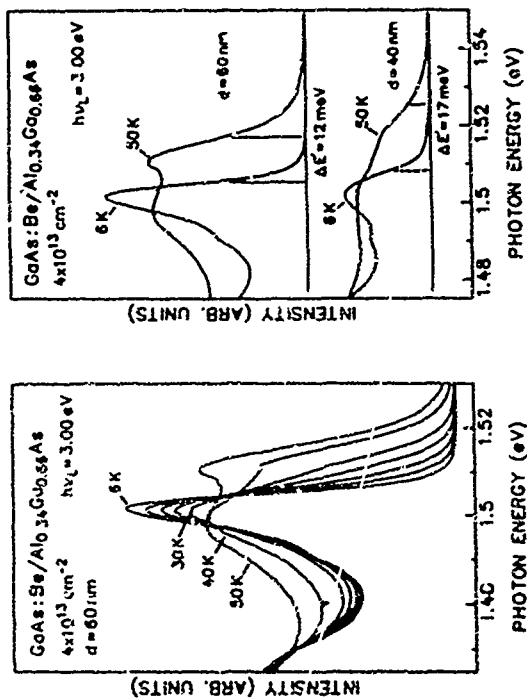


Fig. 3 (left) Temperature-dependent PL spectra showing the Fermi edge enhancement at the high-energy side of the emission spectrum of the sample with the widest GaAs layer width of $d=60$ nm. The temperature, at which each spectrum was taken, is given in the figure except for those spectra between 6 and 30 K which were recorded at 15, 20, and 25 K, respectively.

Fig. 4 (right) PL spectra recorded at 6 and 50 K for GaAs layer widths of $d=60$ and 40 nm, respectively. Apparent energy spacings $\Delta E'$ between the Fermi edge and the nearest hole subband unoccupied at low temperatures, determined from the half maximum points of the leading edge in the spectra, are marked in the figure.

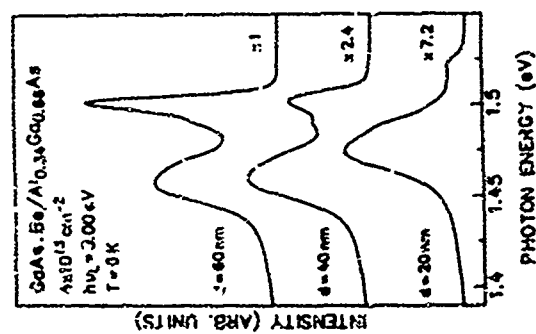


Fig. 4 (left) Schematic energy-band diagram of the Be δ -doped $\text{Al}_{0.34}\text{Ga}_{0.66}\text{As}$ /GaAs/ $\text{Al}_{0.34}\text{Ga}_{0.66}\text{As}$ double-heterostructures used in the present study.

Fig. 5 (right) Low-temperature PL spectrum of p-type δ -doped GaAs:Be/ $\text{Al}_{0.34}\text{Ga}_{0.66}\text{As}$ double heterostructures as a function of the width d of the GaAs layer in the center of which the doping spike is placed. The spectra were excited at 3.00 eV. Vertical lines mark the enhancement in photoluminescence intensity at the Fermi edge.

TuP7

Free to Bound Exciton Relaxation in [001] and [111] GaAs/GaAlAs Quantum Wells

L. Muñoz,^{1,2} L. Vila,^{1,2} N. Mesures¹ and W. I. Wang¹

¹Instituto de Ciencias de Materiales de Madrid, C.S.I.C., Cantoblanco, 28049 Madrid, Spain
²Departamento de Física de Materiales C.I.V., Universidad Autónoma, 28049 Madrid, Spain
³Elect. Eng. Department and Center for Telecomm. Research, Columbia University, New York, NY 10027, U.S.A.

Abstract

We have investigated the relaxation from free to bound excitons in [001] and [111] GaAs/Ga_{0.3}Al_{0.7}As quantum wells by analyzing the photoluminescence polarization in the presence of a magnetic field applied in the Faraday configuration. The Stokes shifts of our samples, which amount to ~ 3 meV, indicate that the photoluminescence is due to excitons bound to some kind of defects in the quantum wells. We have obtained a systematic decrease of the degree of polarization with increasing magnetic field for resonant excitation of heavy-hole excitons. We interpret this fact as a manifestation of the decrease of correlation between momenta and spins of the excitons as they decay from free to bound excitons. We obtain an effective out-scattering time due to the processes of energy relaxation from free to bound excitons of the order of 50 fs, which is independent of the crystallographic orientation.

1. Introduction

The optical properties of excitons in quantum wells (QW's) have been the subject of intense research in recent years for fundamental and applied reasons. A large body of experimental work deals with absorption, or pseudo-absorption, via photoluminescence excitation (PLE), and photoluminescence (PL) spectroscopy, in which excitons play a fundamental role. A usual finding is the shift of the peak of the PL below those of the absorption or PLE spectra. This is the so called "Stokes shift", which is widely used as a negative indicator of sample quality. Bassard et al. explained the Stokes shift in terms of exciton trapping at random interfaces defects of the order of 200 Å. In a more recent work, a linear relation between the line-width of the PLE excitonic peak and the Stokes shift has been found [2]. This behavior can be explained assuming the existence of randomly distributed interface defects and that the well width fluctuations extend over a length scale which is large compared with the size of the excitons [2].

Nowadays, it is generally accepted that good samples can exhibit Stokes shifts of a few meV, and that they are due to the difference in the binding energy between free and bound excitons. As the samples studied here present Stokes shifts of ~ 3 meV, we believe that their PL is due to bound excitons. In order to study the free to bound exciton relaxation we have used optical orientation methods.

Optical orientation, which allows the excitation of states with a preferential spin orientation, using selective optical excitation with circularly polarized light, is very powerful for investigating electronic properties of semiconductors [3]. The optical orientation manifests itself in a polarization of the PL, which is a consequence of the excitation of states with a preferential spin orientation, and it depends on the ratio between the lifetime and the spin relaxation time of excited states [4]. Usually, the polarization excited by circularly polarized light is quantified by means of the degree of circular polarization, \mathcal{P} . For one of the exciting helicities, \mathcal{P} is defined as the fractional difference of the PL intensities of two circular polarizations, σ^+ and σ^- , at a given energy, i.e. for σ^+ excitation $\mathcal{P} = (I^{\sigma^+} - I^{\sigma^-}) / (I^{\sigma^+} + I^{\sigma^-})$.

In this work, we investigate the relaxation between free and bound excitons by

studying the dependence of \mathcal{P} on magnetic field, under resonant excitation of the heavy-hole excitation and detection at the maximum of the Stokes-shifted PL.

2. Experimental details

The samples studied here were grown by MBE on [111]B semi-insulating GaAs substrates, with crystal orientation tilted 3° to improve their optical quality, and have been described previously [5]. Four different GaAs/Ga_{0.3}Al_{0.7}As samples with well thicknesses of 60, 75, 100, and 130 Å were investigated. We have also studied a [001]-oriented GaAs/Ga_{0.3}Al_{0.7}As QW of 100 Å for comparison purposes. PL and PLE spectra were obtained at 2 K, with magnetic fields applied in the Faraday configuration up to 13.5 T. The samples were excited with the light from a LD700 dye laser, a Rhodamine 6G dye laser or a Ti:Zr laser, pumped by ion lasers. The incident light was circularly polarized by means of an achromatic $\lambda/4$ plate. The emitted light was analyzed into its σ^+ and σ^- components, and it was detected with photon counting techniques.

3. Results and discussion

Figure 1 depicts PLE spectra of a 75-Å [111]-oriented QW at two different magnetic fields: the sample was excited with σ^+ light, and the emission, that was detected at the maximum of the PL, was analyzed into its σ^+ (solid PLE spectra) and σ^- (dashed PLE spectra) components. The upper traces of Fig. 1(a) and 1(b) correspond to the degree of polarization of the luminescence as a function of the exciting energy.

At zero magnetic field, Fig. 1(a), the pseudo-absorption spectra show two clear peaks, at 1.555 eV and 1.575 eV, which correspond to the ground state of the heavy-hole ($h_1(1s)$) and light-hole ($l_1(1s)$) excitons. The structure near 1.67 eV is due to the h_2 transition between the second confined electron and hole states. We have assigned the small peak at 1.562 eV in the σ^+ -PLE spectrum to a forbidden transition between the second heavy-hole and the first electron subband levels, h_1 . The degree of polarization as a function of the exciting energy, Fig. 1(a) upper trace, presents three clear structures: two peaks, corresponding to the $h_1(1s)$ and h_2 excitons, where \mathcal{P} exceeds 50%, and a deep at the $l_1(1s)$ excitation, where \mathcal{P} is slightly negative. These values of \mathcal{P} can be explained in terms of the spin of electrons and holes involved in the different excitonic transitions, considering that the spin-relaxation time of holes is much shorter than that of the electrons, and that the relaxation of holes occurs preferentially with conservation of hole parity [6]. In the case of the h_1 , the positive value of \mathcal{P} can be understood taking into account valence band-mixing effects.

Let us consider now the effects of a magnetic field. The PLE spectra recorded at our maximum field, Fig. 1(b), are much richer than those obtained at zero field. The new structures are due to excited states of excitons, whose observation is favored by the reduction of exciton radii and the increase in binding energies [7]. Conversely, the degree of polarization of the PL at 13.5 T (Fig. 1(b), upper trace) is almost zero for all the exciting energies. This result is in contrast with recent PLE experiments under high magnetic fields, which have shown that the relaxation time of the magnetic moment of electrons is much longer than the recombination time, and that the magnetic moment is conserved in the recombination as well as during the thermalization process from the excited states [8]. Moreover, calculations of the spin relaxation time of QW electrons in a magnetic field have obtained an enhancement of this time, in the $n=0$ Landau level, amounting to 1.6 when the field is increased from 6 to 15 T [9]. However, our results present a systematic decrease of the degree of polarization with increasing field for the different samples, as it is clearly seen in Fig. 1(b) for the 75 Å QW. Due to the fact that the decrease in \mathcal{P} is observed in the whole

spectral range, i.e. for the ground- and excited-excitonic states, we believe that it does not arise during the excited- to ground-state excitonic relaxation, but during the relaxation from free to bound excitons. In order to study this latter relaxation, we will concentrate in the case of resonant excitation of the $h_1(1s)$ exciton state.

Figure 2 shows the degree of polarization of the PL, exciting at the energies of the $h_1(1s)$ excitons observed in PLE, for the 60-Å (solid points) and the 100-Å (open points) [111]-oriented QW's as a function of the magnetic field. The exciting light was σ^+ polarized; the values of ρ were obtained at the maximum of the PL spectra. We also show in the inset of Fig. 2 the magnetic field dependence (up to 9 T) of ρ for the 100-Å [001]-oriented QW.

In some cases, it is possible to observe a Zeeman splitting between the σ^+ and σ^- components of the emission at high magnetic fields. For the [111]-oriented QW's, the Zeeman splitting of the PL is negligible, therefore, ρ was obtained with the spectrometer set at the same energy for both polarizations. However, in the case of the [001] QW, the presence of a Zeeman splitting for fields higher than 9 T originates a situation in which ρ depends markedly on the detection energy. Thus, we have limited our analysis for this sample up to 9 T, since for higher fields it is not possible to observe a clear trend in the behavior of ρ .

In the situation considered here of resonant creation of excitons, all the intermediate states during the absorption, energy and spin relaxation and emission processes are correlated electron-hole pairs [10]. However, one must consider that the initial and final states are not the same, since we are pumping free excitons, while the PL is due to excitons bound to some degree of defect in the QW. We have obtained that the zero-field degree of polarization, $\rho(0)$, is 43±10% for all the samples, including the [001]-oriented QW, while the drop between 0 and 13.5 T varies from 10% (130-Å QW) to 40% (75-Å QW). The $\rho(0)$ value indicates that the spin scattering time is not very short on the scale of the total excitonic lifetime, and the dependence of ρ on fields denotes that the spin-flip rate of the free exciton during its energy relaxation to bound exciton increases with magnetic field.

An analogous decrease of ρ has been reported for the hot luminescence of GaAs when the magnetic field, applied in the Faraday configuration, is increased [11]. This decrease is interpreted as a manifestation of the correlation between momenta and spins of the photoexcited carriers and it is found to follow the Lorentzian expression

$$\rho(H) = \frac{\rho(0)}{1 + (\omega_c^+)^2 \tau_1^2} \quad (1)$$

where ω_c^+ is the reduced cyclotron frequency and τ_1 represents an effective out-scattering time due to any processes of energy relaxation. For two-dimensional systems, Zakharenya et al. [12] have not observed any decrease of circular polarization up to 7 T and therefore they claim that the correlation between momenta and spins is absent in 2D systems. However, our results show a systematic decrease of the excitonic polarization for resonant excitation with increasing magnetic field, and we believe that this is due to the destroying of the aforementioned correlation during the free to bound excitonic relaxation. Assuming that Eq. (1) is valid to describe this process for excitons, with the knowledge of ω_c^+ ($\omega_c^+ = e\hbar/m^*$, where m^* is the in-plane reduced effective mass of the exciton) it is possible to obtain an indication of the relaxation time from free to bound excitons.

The cyclotron frequency can be easily obtained from an analysis of the magnetocircular data. Figure 3 shows the Far chart of the PLE peaks, exciting with σ^+ polarized light, for a [111]-oriented 100-Å QW. Two sets of transitions can be clearly distinguished: the ground

and excited states of the heavy-hole exciton, $h_1(n\uparrow)$, $n=1$ to 3 (solid circles), and the corresponding light-hole excitons, $l_1(n\uparrow)$ (open circles). Fitting the experimental results with a 2D hydrogenic-like excitonic model [13], it is possible to obtain the in-plane effective masses of the excitons. The result of fitting simultaneously the ground and excited states of the heavy- (light-) hole excitons are shown in Fig. 3 as solid (dashed) lines.

We have fitted ρ as a function of magnetic field with Eq. (1), using the values of m^* , which have been reported recently for the same samples [5]. The result of the fits, with $\rho(0)$ and τ_1 as adjustable parameters, are shown in Fig. 2 as solid lines for the 60-Å [111]-QW ($\tau_1 = 20 \pm 15$ fs) and for the 100-Å [001]-QW ($\tau_1 = 35 \pm 12$ fs), and as a dashed line for the 100-Å [111]-QW ($\tau_1 = 30 \pm 15$ fs). For the two other samples this effective scattering time is of the same order. The uncertainties in τ_1 are rather large since ω_c^+ is also obtained through a fitting procedure. The fact that the scattering times do not show any systematic dependence on QW width is not surprising since the defects to which the excitons bound may randomly fluctuate from sample to sample. Similarly, it seems that the process of relaxation from free to bound excitons does not depend strongly on crystallographic orientation.

Figure 4 depicts the spectral dependence of ρ for the 130-Å [111]-oriented QW exciting at $h_1(1s)$, for three different fields. The PL spectra, also shown in Fig. 4, were recorded exciting at 1.7 eV with σ^+ light. For this sample, the Stokes shift is negligible. We attribute the high- (low-) energy component of the PL spectra to free- (bound-) exciton recombination. It can be easily seen in Fig. 4 that the blue shift of the PL with increasing field is larger for the bound-exciton component of the PL than for the free-exciton one; in fact, at 13.5 T it is not possible to resolve both components. We believe that this is due to the different effective masses of the free and bound excitons.

The results shown in Fig. 4 yield further evidence of our claim that the decrease of ρ with magnetic field is related to the process of free to bound exciton relaxation. Although it is not possible to investigate ρ under resonant conditions at the free excitonic peak, we have indications that it does not decrease so markedly with increasing field as it does at the bound exciton emission. Actually, the stronger decrease of ρ with increasing field as the detection energy is scanned towards the low energy tail of the PL, where the bound exciton emission dominates the spectra, is apparent in Fig. 4. However, there are two peculiarities in this figure which indicate that further investigations are need in order to understand the relaxation of excitons in QW's: first, the higher polarization of the bound-exciton component of the PL as compared with that of free excitons at zero magnetic field, and, secondly, the negative degree of polarization in the low energy tail of the PL at high fields.

4. Summary.

We have investigated the relaxation from free to bound excitons using optical orientation methods in [111]- and [001]-oriented QW's. A systematic decrease of the degree of polarization of the photoluminescence has been found with increasing magnetic field, applied in the Faraday configuration. This behavior has been interpreted as a manifestation of the decrease of correlation between momenta and spins of the excitons as they decay from free to bound excitons. An analysis of the results have obtained an effective out-scattering time due to the processes of energy relaxation from free to bound excitons of the order of 50 fs independently of well width and crystal orientation.

Acknowledgments.

This work was sponsored by CIC-UT and PRJ-CAM Grants MAT-91-0201 and 170-92. The work at Columbia University was supported by the US Office of Naval Research.

- References
1. G. Bastard, C. Delalande, M.H. Meynaudier, P.M. Fijllink, and M. Voos, *Phys. Rev. B* **29**, 7042 (1984).
 2. F. Yang, M. Wilkinson, E.J. Austin, and K.P. O'Donnell, *Phys. Rev. Lett.* **70**, 323 (1993).
 3. See, for example, F. Meier and B.P. Zakharchenya, in *Optical Orientation*, M. Modern Problems in Condensed Matter Sciences, edited by V.N. Agronovich and A.A. Maradudin (North Holland, Amsterdam, 1984), Vol. 8, p. 1.
 4. L. Vība, J.C. Damen, J.E. Cunningham, J. Shah, and L.J. Sham, *Superl. and Microsc.* **12**, 377 (1992).
 5. L. Vība, L. Muñoz, F. Calle, N. Méndez, J.M. Calleja, and W. I. Wang, *Phys. Rev. B* **44**, 12234 (1992).
 6. T. Uemiyama and L.J. Sham, *Phys. Rev. B* **42**, 7114 (1990).
 7. G. Bauer and T. Ando, *Phys. Rev. B* **38**, 6415 (1988).
 8. M. Potemski, J.C. Maan, A. Fasolino, K. Ploog, and G. Weimann, *Phys. Rev. Lett.* **63**, 2409 (1989).
 9. G. Bastard, preprint.
 10. R. Planel and C. Benoit à la Guillaumie, *Ibid Ref.* **3**, p. 355.
 11. D.N. Mirlin, *Ibid Ref.* **3**, p. 133; I. Ya. Kadik, D.N. Mirlin, L.P. Nikitina, D.G. Polyakov, and V.F. Sapozhnikov, *IETP Lett.* **36**, 192 (1982).
 12. B.P. Zakharchenya, P.S. Kop'ev, D.N. Mirlin, D.G. Polyakov, I.I. Reshina, V.F. Sapozhnikov, and A.A. Sitenko, *Solid State Commun.* **69**, 203 (1989).
 13. A.H. MacDonald and D.E. Strick, *Phys. Rev. B* **33**, 8336 (1986); M. Potemski, L. Vība, G.E.W. Bauer, J.C. Maan, K. Ploog, and G. Weimann, *Phys. Rev. B* **43**, 14704 (1991).

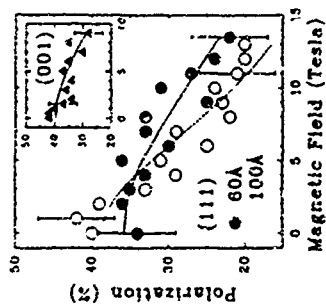


Fig. 2: Degree of polarization versus magnetic field for resonant excitation of the heavy-hole exciton in a 60-Å [111]-oriented QW (solid points) and in a 100-Å [111]-oriented QW (open points). The lines represent the best fit with Eq. 1. The inset shows the degree of polarization and the best fit for a 100-Å [101]-oriented QW

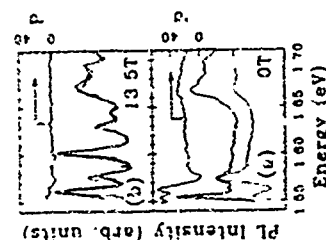


Fig. 3: Energy vs. magnetic field for σ^+ excitation of the ground and excited state heavy-hole (solid points) and light-hole (open points) excitons for a (a) 60-Å [111]-oriented QW and (b) 130-Å [111]-oriented QW. The triangles depict the forbidden h_v exciton. The full (dashed) lines show the result of the fit with a two-dimensional excitonic model for the heavy-hole (light-hole) excitons.

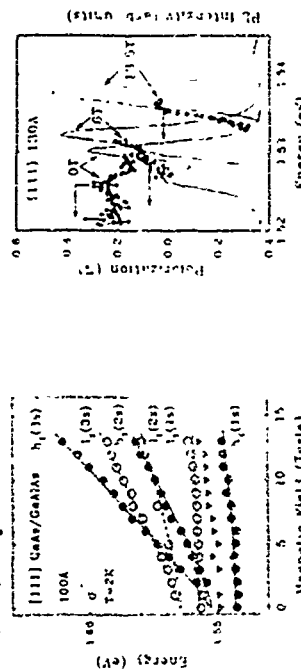


Fig. 4: Degree of polarization of the luminescence, as a function of the detection energy, for resonant excitation of the heavy-hole excitonic-ground state, $h_v(1s)$ (left axis), and photoluminescence spectra exciting at 1.7 eV (right axis) for three different magnetic fields. The sample was grown in the [111] direction with a QW width of 130 Å

Resonant Quenching of Exciton Photoluminescence in Coupled GaAs/AlAs Quantum Wells: Effect of Exciton Binding Energy

KARL SCHNIEDER,* JOACHIM WAGNER,† AND KLAUS FLOEGE[‡]
^{*} *Fraunhofer-Institut für Angewandte Festkörpertechnik, Tulln, Austria*
[†] *D-79108 Freiburg, Federal Republic of Germany*
[‡] *Paul-Drude-Institut für Festkörperelektronik, Hausvogteiplatz 5-7, D-10117 Berlin, Federal Republic of Germany*

Abstract

We have studied the electric field dependence of the photo-current and of the excitonic photoluminescence (PL) from the first and second conduction subband in weakly coupled GaAs/AlAs quantum wells. Resonant subband alignment between adjacent QW's results in a quenching of the PL intensity from the first subband, an enhancement of the PL from the second subband, and a maximum of the photo-current. These resonant extrema are observed at slightly different electric fields. We show that this behavior arises from the different binding energies of intra- and inter-well excitons.

Introduction

Sequential resonant tunneling processes between biased multiple quantum wells (MQW) have been studied by a variety of methods, including measurements of the steady-state photo-current [1-3], time-dependent photocurrent [4], steady-state photoluminescence (PL) [5,6], time-dependent PL [6], and by optical pump/probe experiments [7]. What one usually observes is a resonance induced decrease of the PL intensity and decay time and a corresponding resonant increase of the PL and of the transport rate. In addition, this transport effect induces a non-thermal carrier population of the final state, thus giving rise to additional PL emission lines involving higher subbands [8,9].

Relating these detection methods to each other, the conceptual question arises, which is the precise nature of resonant alignment that is probed using a specific detection method. Sequential resonant tunneling in a MQW of period d in an electric field F usually results from a resonant alignment of the subband energies E_1 and E_2 by $U_{12} = eFd$, giving rise to the resonance condition

$$eFd = E_2 - E_1 \quad (1)$$

However, if the transport behavior is probed by optical spectroscopy, the apparent resonance field may actually correspond to a different condition involving *exciton energies*. Two possible resonance configurations including exciton effects are indicated in Figs. 1(b) and 1(c).

Here E_{1e} , E_{1h} , E_{2e} , and E_{2h} are the banding energies of the spatially direct and spatially indirect e1-h1 and e2-h1 excitons, respectively. E_1 denotes the first heavy hole subband. As these banding energies are generally different, the resonance field for the situation of Fig. 1(b) is given by

$$eFd = E_{1e} - E_{1h} + E_{2e} - E_{2h} \quad (2)$$

whereas the resonance in Fig. 1(c) corresponds to

$$eFd = E_{1e} - E_{1h} + E_{2e} - E_{2h} \quad (3)$$

Since the binding energies E_{1e} and E_{2e} of the intra-well excitons are expected to be larger than those of the inter-well excitons E_{1h} and E_{2h} , the resonance in Fig. 1(b) occurs at a larger field than the resonance in Fig. 1(c), with the difference given by

$$\Delta F = \frac{1}{ed} (E_{1e} - E_{1h} + E_{2e} - E_{2h}) \quad (4)$$

We show in the following that each of the resonance conditions in Fig. 1 can be probed separately by appropriate detection methods, thus giving rise to different resonance fields.

Results and Discussion

For our experiments we use an undoped MQW structure with 50 periods of 12.3 nm GaAs wells and 2 nm AlAs barriers. The MQW forms the intrinsic region of a p-n diode structure. The sample is illuminated by 617.1 nm radiation from a cw Kr-ion laser with a spot size of about 100 μm on the sample. The PL is measured using a triple monochromator and an intensified linear Si diode array detector.

The electric field F is calculated from the applied voltage V by using the equation $F = (V - V_0)/L$, with the MQW thickness $L = 0.78 \mu\text{m}$ and the built-in voltage $V_0 = 1.55 \text{ V}$. The field screening parameter α was determined from the intensity dependence of the resonance fields. We obtained $\alpha = 0.95$ and 0.76 at excitation powers of 0.06 mW and 0.3 mW , respectively. These values also give satisfactory agreement between the field dependences of the e1-h1 PL wavelength at different excitation powers.

PL spectra at different electric fields in the spectral region of the e1-h1 and e2-h1 transitions are shown in Figs. 2(a) and 2(b), respectively. The e1-h1 transition is observed at 1.539 eV at low fields and is Stark-shifted with increasing field (1.308 eV at 116 kV/cm). We note that the thermally populated light hole exciton forms a PL line at about 11 meV above the e1-h1 exciton. The e2-h1 transition is observed at 1.617 eV (60 kV/cm). A strong reduction of the e1-h1 PL intensity and a pronounced enhancement of the e2-h1 emission is observed at around 60 kV/cm where the tunneling resonance is expected.

In Fig. 3, we have plotted the field dependence of the e1-h1 and e2-h1 PL intensities, as obtained from a numerical integration of a similar series of PL spectra as shown above, but for 0.06 mW excitation power. The resonance maximum of the e2-h1 luminescence is observed to occur at clearly smaller fields than the resonance minimum of the e1-h1 luminescence. As indicated by the dashed lines, the difference between these resonance fields in Fig. 3 is about 7.2 kV/cm . The data shown in Fig. 2 recorded with an higher optical power of 0.3 mW indicate a similar difference (5 kV/cm) in the e1-h1 and e2-h1 resonance fields.

The field dependence of the PC, measured under identical experimental conditions as those of Fig. 3, is shown in Fig. 1. Under steady-state conditions and at low intensity, the PC increases with increasing ratio between the transport and recombination rates. Therefore, the field value of 60 kV/cm, where the relevant maximum of the PC is observed, is associated with the tunneling resonance. This field value lies in between the resonance fields as obtained from the e1-h1 PL and from the e2-h1 PL, which are also indicated in Fig. 1. We note that the resonance maximum of the PC is less pronounced than the extrema of Figs. 2 and 3 since the PC saturates if the transit time becomes much smaller than the recombination time.

In Fig. 1, there are some additional structures which can also be observed in PL experiments [10]. The step like structure in Fig. 1 at 5 kV/cm is related to miniband conduction. The step at around 52 kV/cm corresponds to phonon assisted tunneling. The increase of the PC above 160 kV/cm is partly due to enhanced non resonant tunneling rates and to the e1-e3 resonance. It is not associated with avalanche multiplication processes which can only be observed above 220 kV/cm [3]. Previously, time-resolved measurements of the PC under pulsed optical excitation have been carried out [13] in order to determine directly the resonance field for photocarrier transport. Although essentially the same resonance fields have been obtained, the results are not directly transferable to the present situation since the precise influence of the space-charges in both experiments is probably not identical. Space-charge effects are also expected to play a somewhat different role [10] in previous higher subband luminescence studies [8] performed under pulsed excitation.

We now develop a physical picture to relate the different experimental approaches to the alignment conditions of Fig. 1. In a photoconduction experiment, the resonance condition corresponds to the alignment of the conduction subbands (Fig. 1(a) and Eq. 1). This is due to the fact that most of the drifting carriers are located in free carrier states and not in exciton states. In addition, only the free carriers induce a PC, whereas the electrically neutral excitons cannot contribute to the PC.

Conversely, as the PL is excitonic in nature, only the carriers located in the respective excitation states give rise to PL. Now, for the intra-well e1-h1 PL, the quenching is expected to be strongest when the respective exciton energy coincides with the energy of the spatially indirect e2-h1 exciton. Therefore we expect that the situation outlined in Fig. 1(b) and Eq. (2) is relevant for the resonance minimum of the e1-h1 PL intensity. Similarly, the minimum of the e2-h1 PL should occur if the energies of the intra-well e2-h1 exciton and of the inter-well e1-h1 excitons are in resonance, as shown in Fig. 1(c) (see also Eq. (3)). Indeed, the situation of Fig. 1(c) gives rise to an efficient population of the intra-well e2-h1 exciton states by carriers that have formed spatially indirect e1-h1 excitons. Carrier relaxation into inter-well e1-h1 exciton states is important because of the relatively strong Coulomb-interaction [11], in spite of the small oscillator strength of these excitons.

The binding energies of inter-well excitons have been calculated by Fox et al. [11] for similar sample parameters (9 nm GaAs wells, 1.5-5 nm Al_{0.3}Ga_{0.7}As barriers) with the result $E_{b1}^e \approx E_{b1}^h \approx 3.6$ meV and $E_{b2}^e \approx E_{b2}^h \approx 7.7$ meV. This gives rise to a difference in binding energies of $|E_{b1}^e - E_{b1}^h| \approx E_{b2}^e - E_{b2}^h \approx 1.25 \pm 0.25$ meV. Adopting

these values for the present situation, the theoretically expected field difference between the resonances shown in Figs. 1(c) and 1(b) (see Eq. (1)) is $\Delta F = 5.90 \pm 0.35$ kV/cm. This value is in quantitative agreement with the experimental value of 5.7 kV/cm.

In principle, resonant alignment between different subbands of adjacent wells induces a line splitting, which has been observed in MQW's with a stronger inter-well coupling [11-13] than in the present case. In those strongly coupled MQW structures, the resonance field where this line splitting is most pronounced, depends on the particular excitonic transition under study. The reason for this effect also arises from differences between the binding energies of the participating excitons [11,13]. Such a splitting cannot be observed in the present case since the spectral width of the transitions involved exceeds the expected line splitting. However, in these weakly coupled MQW's, the coupling between adjacent wells still has a strong influence on carrier transport. Therefore, the resonance splitting of the strongly coupled system translates into characteristic transport effects. Analogous signatures of different exciton binding energies, i.e. thus observed when the respective exciton states are probed in PL measurements.

Conclusion

We have presented a detailed study of the electric field dependence of the photocurrent of the e1-h1 PL, and of the e2-h1 PL, in a weakly coupled GaAs/AlAs MQW. Resonantly enhanced tunneling rates give rise to a maximum of the photocurrent, to a minimum of the e1-h1 PL intensity and to a maximum of the e2-h1 PL intensity. These resonance effects are observed at different fields. This difference in the resonance fields has been shown to be a consequence of the different binding energies of intra- and inter-well excitons. Consequently, the measured resonance field does not only depend on the subband spacing and on the MQW period, but also on the experimental detection method.

Acknowledgements

The authors are grateful to P. Koell (Fribourg) for the encouragement of this work. We also acknowledge partial support by the Bundesministerium für Forschung und Technologie.

References

- [1] F. Capasso, K. Mohammed, and A. V. Cho, *Appl. Phys. Lett.* **48**, 175 (1986).
- [2] S. Tarucha, K. Ploog, and K. v. Klitzing, *Phys. Rev. B* **36**, 1538 (1987).
- [3] S. Tarucha and K. Ploog, *Phys. Rev. B* **38**, 1498 (1988).
- [4] H. Schneider, K. v. Klitzing, and K. Ploog, *Superlatt. Microstruct.* **5**, 183 (1989).
- [5] H. Schneider, K. v. Klitzing, and K. Ploog, *Europhys. Lett.* **8**, 575 (1989).
- [6] H. Schneider, W. W. Rühle, K. v. Klitzing, and K. Ploog, *Appl. Phys. Lett.* **51**, 2676 (1989).
- [7] G. Laveson, A. M. Fox, D. A. B. Miller, T. Sizer, W. H. Knox, A. C. Gossard, and J. H. English, *Phys. Rev. Lett.* **63**, 118 (1989).
- [8] H. I. Grahn, H. Schneider, W. W. Rühle, K. v. Klitzing, and K. Ploog, *Phys. Rev. Lett.* **64**, 2126 (1990).
- [9] H. I. Grahn, W. W. Rühle, and K. Ploog, *SPIE, Vol. 1675 Quantum Well and Superlattice Physics IV*, edited by G. H. Döhler and E. S. Koteles, **16** (1992).
- [10] H. Schneider, J. Wagner, and K. Ploog, *Phys. Rev. B*, to appear.
- [11] A. M. Fox, D. A. B. Miller, G. Laveson, J. E. Cunningham, and W. Y. Fan, *Phys. Rev. B* **44**, 6231 (1991); A. M. Fox, D. A. B. Miller, J. E. Cunningham, W. Y. Fan, C. Y. P. Chao, and S. L. Chuang, *Phys. Rev. B* **46**, 15365 (1992).
- [12] H. Schneider, H. I. Grahn, K. v. Klitzing, and K. Ploog, *Phys. Rev. Lett.* **65**, 2720 (1990).
- [13] A. M. Fox, D. A. B. Miller, G. Laveson, J. E. Cunningham, J. E. Henry, and W. Y. Fan, *Phys. Rev. B* **42**, 1811 (1990).

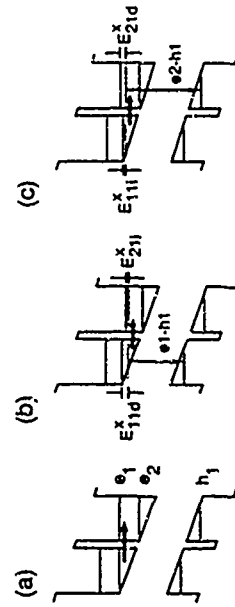


Figure 1: Schematics of resonant alignment of (a) the $e1$ and $e2$ subbands, (b) the intra-well $e2-h1$ and the inter-well $e2-h1$ excitons, and (c) the intra-well $e2-h1$ and the inter-well $e1-h1$ excitons in weakly coupled quantum wells. Dashed lines mark the energies of the excitons involving the $e1$ subband located in (b) the left quantum well and (c) the right quantum well, as counted from the respective valence subband energy E_{11d} , E_{21d} , E_{11u} , and E_{21u} . Vertical arrows indicate the spatially direct and spatially indirect $e1-h1$ and $e2-h1$ PL excitons, respectively (not to scale). Vertical arrows indicate the $e1-h1$ and $e2-h1$ PL.

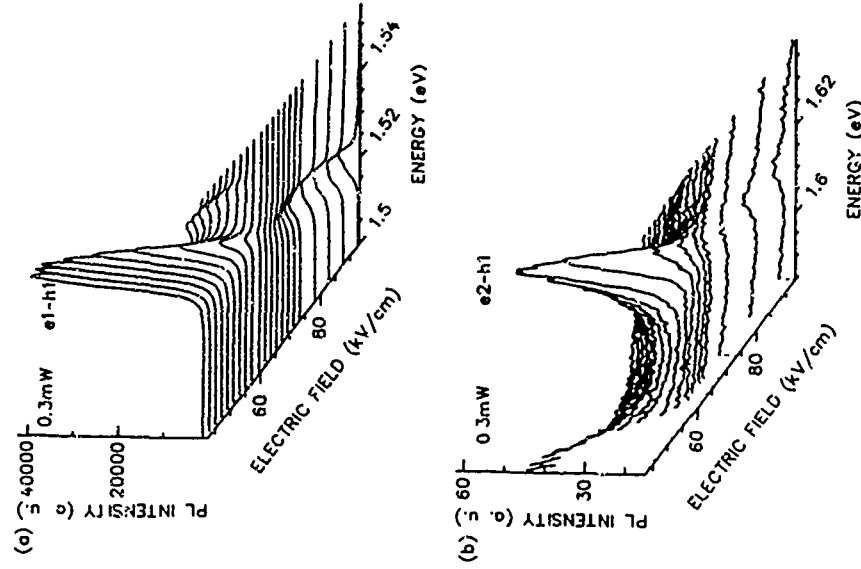


Figure 2: (a) 3D plot of PL spectra showing the spectral regions of the $e1-h1$ and $e2-h1$ transitions as a function of electric field at 77 K and an excitation power of 0.3 mW.

PRESSURE DEPENDENCE OF PHOTOLUMINESCENCE IN $\text{In}_{0.5}\text{Ga}_{0.5}\text{As}/\text{Al}_{0.5}\text{Ga}_{0.5}\text{As}$ STRAINED QUANTUM WELLS WITH DIFFERENT WIDTHS

Zhen-Xian Liu, Guo-Hua Li, He-Xiang Han and Zhao-Ping Wang

National Laboratory for Superlattices and Microstructures
Institute of Semiconductors, Chinese Academy of Sciences
P. O. Box 912, Beijing 100083, P. R. China

Abstract

A systematic investigation on the photoluminescence (PL) properties of $\text{In}_{0.5}\text{Ga}_{0.5}\text{As}/\text{Al}_{0.5}\text{Ga}_{0.5}\text{As}$ ($x=0.15$, $y=0$, 0.33) strained quantum wells (SQWs) with well widths from 1.7 to 11.0 nm has been performed at 77K under high pressure up to 40 kbar. The experimental results show that the pressure coefficients of the excitation peaks corresponding to transitions from the first conduction subband to the heavy-hole subband increase from 10.05 meV/kbar of 11.0 nm well to 10.62 meV/kbar of 1.8 nm well for $\text{In}_{0.5}\text{Ga}_{0.5}\text{As}/\text{GaAs}$ SQWs. However, the corresponding pressure coefficients slightly decrease from 9.93 meV/kbar of 9.0 nm well to 9.73 meV/kbar of 1.7 nm well for $\text{In}_{0.5}\text{Ga}_{0.5}\text{As}/\text{Al}_{0.5}\text{Ga}_{0.5}\text{As}$ SQWs. Calculations based on the Kronig-Penney model reveal that the increased or decreased barrier heights and the increased effective masses with pressure are the main reasons of the change in the pressure coefficients.

Introduction

There is currently much interest in strained quantum wells (SQWs) and superlattices, in which the lattice mismatch between layers is accommodated by the coherent elastic strain.^{1,2} This leads to a change in the band gap and a splitting of the valence band at the Γ point. Therefore the properties of SQWs are different from those of lattice-matched quantum wells, such as $\text{GaAs}/\text{AlGaAs}$ QWs. The study of PL under high pressure at 77K^{3,4} showed that the pressure coefficients of the excitation peaks corresponding to transitions from the first conduction subband to the heavy-hole subband for $\text{In}_{0.5}\text{Ga}_{0.5}\text{As}/\text{GaAs}$ SQWs decreased with increased well width, which is contrary to that of $\text{GaAs}/\text{AlGaAs}$ QWs.^{5,6} Therefore, it will be interesting that what is happened for $\text{In}_{0.5}\text{Ga}_{0.5}\text{As}/\text{AlGaAs}$ SQWs?

In this paper, we report systematic investigations of PL measurements on $\text{In}_{0.5}\text{Ga}_{0.5}\text{As}/\text{AlGaAs}$ SQWs with different well widths at 77K under high pressure up to 40 kbar. We found a slight increase in the pressure coefficient of the excitation peak with increased well width for $\text{In}_{0.5}\text{Ga}_{0.5}\text{As}/\text{AlGaAs}$ SQWs, which is in contrast to the case of $\text{In}_{0.5}\text{Ga}_{0.5}\text{As}/\text{GaAs}$ QWs. Calculations based on the Kronig-Penney model reveal that the increased or decreased barrier heights and the increased effective masses with pressure are the main reasons of the change in the pressure coefficients. The calculated results are in good agreement with the experimental data.

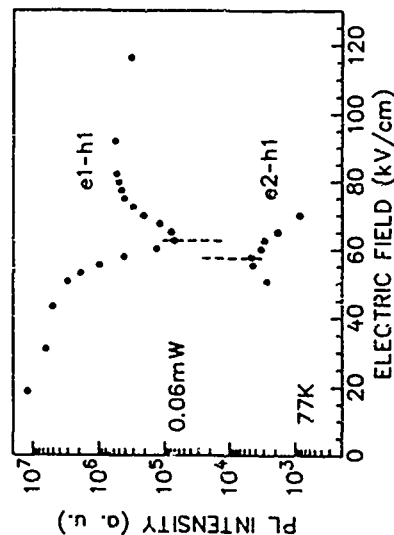


Figure 3: PL intensities of the e1-h1 and e2-h1 transitions at 0.06 mW excitation power versus electric field. The dashed lines indicate the resonance extrema.

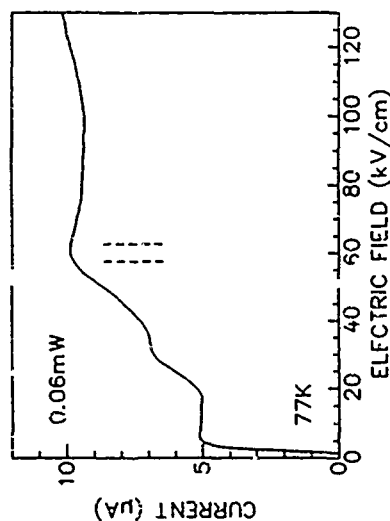


Figure 4: PC versus electric field at 0.06 mW excitation power. The dashed lines indicate the observed resonance extrema of the e2-h1 and e1-h1 PL intensities.

Experimental

The samples used in this study were prepared by molecular-beam-epitaxy (MBE). A 0.5- μm -thick buffer layer of GaAs was first grown on (001)-oriented GaAs substrate, then followed by five $\text{In}_{0.15}\text{Ga}_{0.85}\text{As}/\text{Al}_{0.1}\text{Ga}_{0.9}\text{As}$ SQWs with the well-width sequences of 11.0, 7.0, 4.6, 2.6, and 1.8 nm for $y=0$ and 9.0, 6.0, 4.0, 2.4, and 1.7 nm for $y=0.33$ along the growth direction, respectively, where the thicknesses of barrier layers are always 30 nm to prevent coupling between wells. Finally a 30-nm GaAs layer capped the structure.

The samples were mechanically thinned from the backside to approximately 20 μm and cleaved into $100 \times 100 \mu\text{m}^2$ square. The samples were loaded into a gasketed diamond-anvil cell, together with a piece of ruby to act as pressure gauge.¹¹ Pressure calibration was also done by the shift of the GaAs substrate band gap.¹⁶ This gives a high accuracy in the pressure determination and reliable coefficients can thus be obtained. Argon was used as a pressure medium in order to ensure hydrostatic conditions. The PL measurements were performed at 77K on a micro-optical system. PL was excited by the 488.0 nm line of an Ar⁺ laser, and dispersed by double monochromator, and detected by a photomultiplier and a photon counting system.

Results and Discussion

The PL spectra of $\text{In}_{0.15}\text{Ga}_{0.85}\text{As}/\text{GaAs}$ and $\text{In}_{0.15}\text{Ga}_{0.85}\text{As}/\text{Al}_{0.1}\text{Ga}_{0.9}\text{As}$ SQWs at 77K and different pressures are shown in Figures 1(a) and 1(b). The value of the pressure is indicated at the corresponding spectrum and the PL intensities are normalized according to the strongest peak. In the spectra, the transitions between the first conduction subband and heavy-hole subband are labelled with E_i ($i=1-5$) for five SQWs, respectively. The peak, E_1 , is attributed to emission from the GaAs substrate. With increasing pressure, the relative intensities of the peaks in Fig. 1(a) change dramatically but the absolute intensities of the narrow wells does not decrease obviously. On the other hand, the relative intensities of the

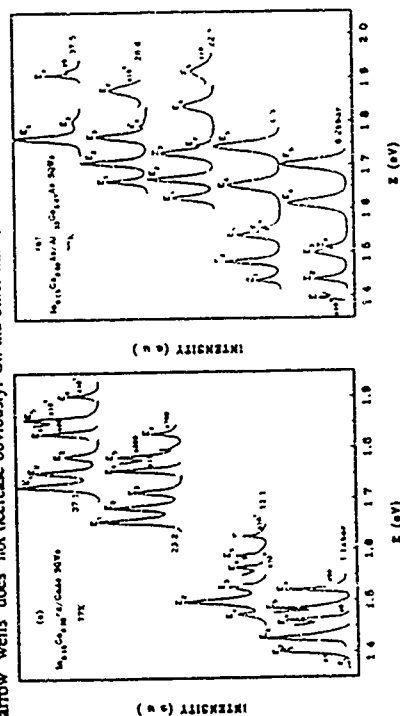


Fig. 1. 77K PL spectra for $\text{In}_{0.15}\text{Ga}_{0.85}\text{As}/\text{Al}_{0.1}\text{Ga}_{0.9}\text{As}$ SQWs at several pressures. (a) $\text{In}_{0.15}\text{Ga}_{0.85}\text{As}/\text{GaAs}$ (b) $\text{In}_{0.15}\text{Ga}_{0.85}\text{As}/\text{Al}_{0.1}\text{Ga}_{0.9}\text{As}$

peaks in Fig. 1(b) change drastically with increasing pressure and the intensities of the narrow wells become too weak to be observed under higher pressure. This rapid decrease attributes to the P-X subband crossover in the quantum-well structures.

Figures 2(a) and 2(b) show the dependence of the transition energy on pressure for each QW. For $\text{In}_{0.15}\text{Ga}_{0.85}\text{As}/\text{GaAs}$ and $\text{In}_{0.15}\text{Ga}_{0.85}\text{As}/\text{Al}_{0.1}\text{Ga}_{0.9}\text{As}$ SQWs, respectively. The solid lines are least-squares fits to the experimental data giving a linear function:

$$E_i(P) = E_i(0) + \alpha_i P, \quad (1)$$

where the energies are in eV and the pressure P is in kbar and the factor α_i is the linear pressure coefficient. Figure 3 shows the linear pressure coefficients (solid symbols) obtained from the SQWs data in Figs. 2(a) and 2(b) as a function of the well width. It can be seen that the well-width dependencies of these two kinds of SQWs have clearly different trends. For $\text{In}_{0.15}\text{Ga}_{0.85}\text{As}/\text{GaAs}$ SQWs the pressure coefficients decrease with increased well width, while those of $\text{In}_{0.15}\text{Ga}_{0.85}\text{As}/\text{Al}_{0.1}\text{Ga}_{0.9}\text{As}$ SQWs slightly increase. The transition energy of a SQW can be expressed as

$$E_{PL} = E_g + E_{1h} + E_{1e} - E_{ex}, \quad (2)$$

where E_g is the band gap of the well material, E_{1h} and E_{1e} are the confined energies of electrons and heavy holes, respectively, and E_{ex} is the exciton binding energy. Thus the pressure dependencies of these parameters determine to the change of the pressure coefficient with well width. We have used the Kronig-Penney model¹⁷ to calculate the well-width dependence of the pressure coefficients for the two studied samples, in which several main effects have to be considered. Firstly, the well width diminishes with the pressure and the pressure dependence of the well width L_z can be obtained from the elasticity theory:

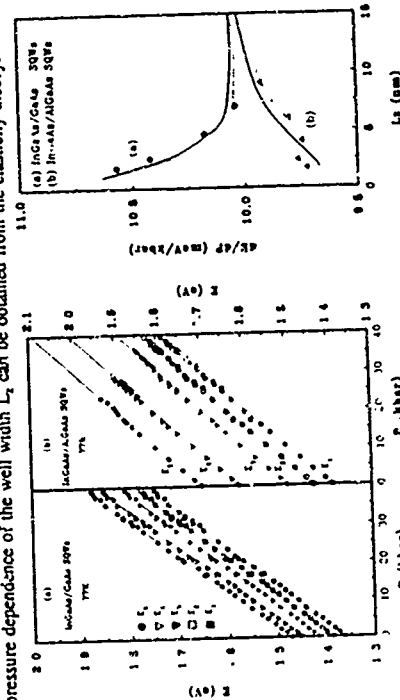


Fig. 2. Pressure dependence of the peak energies for $\text{In}_{0.15}\text{Ga}_{0.85}\text{As}/\text{Al}_{0.1}\text{Ga}_{0.9}\text{As}$ SQWs. (a) $\text{In}_{0.15}\text{Ga}_{0.85}\text{As}/\text{GaAs}$ SQWs (b) $\text{In}_{0.15}\text{Ga}_{0.85}\text{As}/\text{Al}_{0.1}\text{Ga}_{0.9}\text{As}$ SQWs

Fig. 3. The measured and calculated pressure coefficients in SQWs as a function of well width. The solid and dashed lines are the calculated results

TuP10

Optical Transitions in GaAs/AlAs Superlattices with Different Miniband Widths

A. Fujimura, K. Kawashima, T. Yamamoto* and Y. Ploog*
Kyushu Institute of Technology, Tobata, Kitakyushu 804, Japan
*ATR Optical and Radio Comm. Res. Lab., Soraky-gun, Kyoto 613-02
*Physikalische Institut für Festkörperelektronik, O-1000 Berlin

Abstract

Band edge optical transitions and their internal electric field effects are systematically studied in GaAs/AlAs superlattices with different miniband widths (Δ) by low temperature photoluminescence spectroscopy. Distinct H excitons related with saddle-type Δ_1 critical points at the miniband top are clearly observed both for heavy-hole and light-hole excitons. After the applied field strength F , discrete transitions due to band-edge localizations are observed and α is found their intensities of an order about ladder transitions with negative indices then $F^{-1/2}$ and Δ^{-1} dependences in agreement with the field blocking theory.

Introduction

Optical transitions involved with excitons in semiconductor superlattices (SL) and quantum wells (QW) have been attracted great attention [1]. One of the interesting properties of SL compared to QW is the tunability of miniband widths (Δ) by designing the layered structures and, as a result, controlling quantum mechanical tunneling. From the previous studies of optical absorption in GaAs/AlAs-x% SL, it is known that there are various types of fine structures originating from miniband dispersions [2-5], Stark ladder [5-9], and Franz-Keldysh oscillations [10]. However, attribution of such fine structures observed by one author is not always consistent with others' data, possibly because of non-uniform sample quality and different experimental conditions. Therefore, basic studies of optical transitions in SL and especially their relevance to miniband widths are important for understanding of the origins of the absorption spectral features. In this paper, optical absorption spectra are investigated in a series of GaAs/AlAs SL with different well and barrier parameters, thus varying the miniband width systematically, by means of low temperature photoluminescence (PL) spectroscopy. Direct spectroscopic evidences are provided for the miniband dispersion effects which show excitonic effects originating from the miniband bottom (Δ_1) and miniband top (Δ_2) critical points. We have also studied the external field effects as a function of both field strength F and miniband width Δ . It is shown that

$$L_1(P) = L_1(0) / (1 - S_{11} + 2S_{12}P) \quad (3)$$

where S_{11} and S_{12} are the elastic constants of the well material. Secondly, the well and barrier materials have different pressure coefficients. In the calculations, we take the pressure coefficients for GaAs and Al_{0.33}Ga_{0.67}As as 10.73 meV/kbar¹⁴ and 9.8 meV/kbar¹⁵ respectively. The experimental pressure coefficients for In_{0.15}Ga_{0.85}As have not been reported to date. Here we take the value as 10.1 meV/kbar. If we suppose the valence-band offset does not change with pressure, ϕ is the pressure-induced change of the barrier height can be expressed as

$$V(P) = V(0) + (\alpha_B - \alpha_W)P, \quad (4)$$

where α_B and α_W are the pressure coefficients of the barrier and well materials, respectively. In the case of In_{0.15}Ga_{0.85}As/GaAs SQWs, the barrier height will increase with pressure since $\alpha_B > \alpha_W$, while those of the In_{0.15}Ga_{0.85}Al_{0.33}Ga_{0.67}As SQWs will decrease with pressure. Finally, the size quantization and the change of the gap with pressure lead to an increase of the effective masses in the well and in the barriers. This change can be expressed by Kane's three bands model¹⁶

$$\frac{m(P)}{m(0)} = \frac{E_g + \alpha_B P}{E_g} + \frac{E_g + \alpha_W P}{E_g + \Delta} - \frac{2\Delta + 3E_g}{2\Delta + 3(E_g + \alpha_B P)} \quad (5)$$

where E_g is the band gap, Δ is the spin-orbit energy splitting, and α stands for B and W in barrier and well, respectively. As the pressure-induced change of E_g is very small, it can be neglected. After numerical calculation of the confined energy for electrons and heavy hole at $P = 41$ kbar ($t = 0.10$), we obtained the pressure coefficients of the PL-peaks energies according to the least-squares fits to the calculated data. The calculated coefficients for In_{0.15}Ga_{0.85}Al_{0.33}Ga_{0.67}As SQWs are also indicated in Fig. 4 by the solid curves. It can be seen that the results are in good agreement with the experimental data. The dashed lines in Fig. 4 represent the calculated results in which the compression of well width does not considered. These lines are very close to the corresponding solid lines, respectively. It implies that the influence of the well-width compression on the pressure coefficients can be neglected.

- [1] G. C. Osbourn, P. L. Gourley, I. J. Fritz, R. M. Biefeld, L. R. Dawson, and T. E. Zupparian, *Semicond. Semimet.* 24, 459(1987).
- [2] H. Q. Hou, L. J. Wang, R. M. Tang, and J. M. Zhou, *Phys. Rev. B* 42, 2926(1990).
- [3] G. H. Li, B. Z. Zheng, H. X. Han, Z. P. Wang, T. G. Andersson, and Z. G. Zhen, *Phys. Rev. B* 45, 3489(1992).
- [4] U. Venkateswarar, M. Chandrasekhar, and H. R. Chandrasekhar, *Phys. Rev. B* 33, 8416(1986).
- [5] H. K. Mao, J. Xu, and P. M. Bell, *J. Geophys. Res.* 91, 4673(1986).
- [6] D. J. Wolford and J. A. Bradley, *Solid State Commun.* 53, 1106(1985).
- [7] H. S. Cho and P. R. Prasad, *Phys. Rev. B* 36, 3237(1987).
- [8] E. O. Kane, *Semiconductors and Semimetals*, Academic, New York, Vol. 1, (1966).

The observed energies and oscillator strengths of the Stark ladder transitions are in good agreement with those predicted by the tight binding theory.

Experimental

High quality GaAs/AlAs SL samples were grown on n-type GaAs (100) substrates by molecular beam epitaxy (MBE) in a fully computer-controlled system. The nominally undoped SL layer is contained in the intrinsic layer of a p-n junction. Two series of seven SL samples are studied in this work. A first series consisted of AlAs barriers with a thickness of 5 Å and GaAs wells whose width was varied from $L_w = 6.6$ Å to 39 Å (29, 31, 33 Å). A second series consisted of AlAs barriers with a width of 5 Å and GaAs wells whose width was varied from $L_w = 7.4$ Å to 39 Å (29, 31, 33 Å). The sample 29 is common in the two series. The SL period was measured by small-angle X-ray diffraction experiments which were used to estimate nominal values of well and barrier parameters. The 100-period SL layers were confined between Al_{0.3}Ga_{0.7}As cladding layers in the heterostructure. PC experiments were performed around 4 K in the closed-loop helium cryostat using a combination of tunable-diode laser and monochromator for excitation and a standard electrometer for detection.

Results and discussion

Figure 1 shows PC spectra of the SL diode samples 29, 31, 33, 35, 37, and 39 for L_w variations. Solid curves correspond to the spectra measured

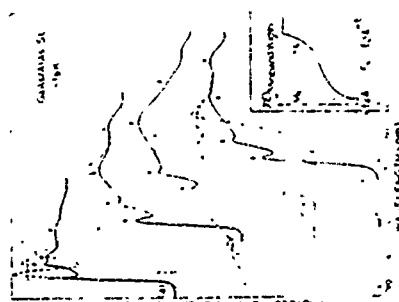


Fig. 1 Photocurrent spectra of GaAs/AlAs SL samples at 4 K. (a) (b) 29, 31, 33, 35, 37, and 39. Solid curves are corresponding to the spectra measured at 10 V reverse bias. The dashed curves correspond to the spectra measured at 1 V reverse bias. The solid curves are vertically shifted for clarity. Solid (dashed) horizontal bars are calculated (theoretical) ranges of valence-to-conduction subband transitions associated with heavy-hole (light-hole) excitations. An inset figure shows the calculated transition energies in the potential well of sample 29 (10 V, singularity at E_g).

at near the flat-band conditions (forward bias conditions), while dashed ones under a reverse bias voltage (VB) of 10 V. In the solid PC spectra sharp absorption thresholds are observed. The threshold wavelength (energy) decreases (increases) from the spectra (a) to (b) as the GaAs well width L_w decreases. At the absorption edge a sharp peak (indicated by left arrows) is observed in the spectra (a)-(d) indicating excitonic effects for the optical transitions. Beside the leading absorption peak, several peaks and/or shoulders are also seen in the solid spectra of Fig. 1. A relatively sharper peak (indicated by left downwards arrows) is observed next to the leading peak. Relatively broader peaks or shoulders (indicated by right arrows) are located at shorter wavelengths (higher energies) than the other hand, when the external electric field is applied along the growth z-axis, a number of new fine structures appear as shown in the dashed spectra. First we note that in the dashed curves a main steep edge appears at shorter wavelength sides of the threshold peak in the corresponding solid spectra and that the energy separation between them increases with decreasing L_w . Secondly, weaker edges are also seen in the dashed spectra of (b) to (d) at the longer wavelength. Their intensity increases with decreasing L_w .

The experimental results observed in Fig. 1 can rigorously be explained by the miniband dispersion effects as discussed below. In the SL structure, we have a slightly different energy scheme for the optical transitions from the bulk as schematically illustrated in the inset of Fig. 1. When the barrier thickness is thin enough so that the inter-QW layer coupling is enhanced, we have more three-dimensional characters for the miniband. That is, the miniband is formed along the growth direction whose bandwidth ΔE is basically determined by the SL structural parameters, L_z and L_w . In this case we have Van Hove singularities of N_D type at the miniband bottom and of N_V type at the upper edge. In order to more quantitatively show the effects of inter-well-coupling on the transition energies, the theoretical energies of the miniband transitions are calculated using the Kronig-Penney model within the effective mass approximation [5]. The calculated wavelength range for the transitions are indicated in Fig. 1 by horizontal solid (dashed) bars for the heavy-hole (light-hole) related transitions. Good relationship is observed between experimental and calculated values in spite of neglecting exciton effects. The sharper two leading peaks near the threshold in the solid spectra are therefore assigned to heavy-hole (HH) and light-hole (LH) excitations associated with the miniband bottoms. On the other hand, the high energy structures observed in the solid curves of Fig. 1 are attributed to the π excitations which are associated with the Van Hove singularity [3]. Peaked nature of the optical absorption indicates excitonic effects for their origins of the HH-related, as well as LH-related transitions. We would like to stress that

the peaks of high energy Π excitons and low energy Γ excitons, show excellent correlation with the calculated miniband width. At the best of our knowledge, the peaked structures in optical absorption spectra are the first observed for the saddle point Π exciton. Although not shown, we have also studied SL samples for L_0 variations. It is found that the transition energies and their barrier thickness dependence are in excellent agreement with those predicted by the simple theory for both Γ and Π excitons [11].

The external field effect on the PC spectra is reasonably explained by Wannier-Stark localization [12-14]. We have measured PC spectra as a function of F for each SL sample and evaluated the transition energies and their uncertainties in detail. The observed transition energies are found to coincide as $E_{\text{low}} = E_{\text{low}} + eFd$ as expected for the Stark ladder transitions. Here E_{low} is the eigenenergy of an isolated QW, d is a Stark ladder index ($n=0, 1, 2, \dots$), and D is L_0/L_1 . This confirms our attribution of the observed optical transitions under the applied field to Stark ladder transitions. In the dashed spectra of Fig. 1, the threshold peaks at lower wavelengths are attributed to the -1st and 0th order Stark ladder excitation transitions, as indicated by dashed vertical bars. From the energy difference between the localized QW ($n=0$) and the SL Π excitation transitions, we estimate half of the experimental miniband width, Δ_{exp} to be 15 (eV), 35 (eV), 61 (eV), and 73 (eV) meV, respectively, the difference of the excitation binding energy between the two cases (b). We note that this Δ_{exp} value gives a lower limit for Δ because of the smaller binding energy for the SL excitation.

In order to show field-induced variations of the oscillator strength of the Stark ladder transition, the relative intensity $I_{\text{rel}}(1/L_0)$ of the -1st order Stark ladder transition normalized by the 0th order transition is plotted in Fig. 2 for L_0 series of SL samples ($L_0 = 5, 7, 10, 15, 20, 30, 40, 50, 60, 70, 80, 90, 100, 120, 150, 200, 300, 400, 500, 600, 700, 800, 900, 1000, 1200, 1500, 2000, 3000, 4000, 5000, 6000, 7000, 8000, 9000, 10000, 12000, 15000, 20000, 30000, 40000, 50000, 60000, 70000, 80000, 90000, 100000, 120000, 150000, 200000, 300000, 400000, 500000, 600000, 700000, 800000, 900000, 1000000, 1200000, 1500000, 2000000, 3000000, 4000000, 5000000, 6000000, 7000000, 8000000, 9000000, 10000000, 12000000, 15000000, 20000000, 30000000, 40000000, 50000000, 60000000, 70000000, 80000000, 90000000, 100000000, 120000000, 150000000, 200000000, 300000000, 400000000, 500000000, 600000000, 700000000, 800000000, 900000000, 1000000000, 1200000000, 1500000000, 2000000000, 3000000000, 4000000000, 5000000000, 6000000000, 7000000000, 8000000000, 9000000000, 10000000000, 12000000000, 15000000000, 20000000000, 30000000000, 40000000000, 50000000000, 60000000000, 70000000000, 80000000000, 90000000000, 100000000000, 120000000000, 150000000000, 200000000000, 300000000000, 400000000000, 500000000000, 600000000000, 700000000000, 800000000000, 900000000000, 1000000000000, 1200000000000, 1500000000000, 2000000000000, 3000000000000, 4000000000000, 5000000000000, 6000000000000, 7000000000000, 8000000000000, 9000000000000, 10000000000000, 12000000000000, 15000000000000, 20000000000000, 30000000000000, 40000000000000, 50000000000000, 60000000000000, 70000000000000, 80000000000000, 90000000000000, 100000000000000, 120000000000000, 150000000000000, 200000000000000, 300000000000000, 400000000000000, 500000000000000, 600000000000000, 700000000000000, 800000000000000, 900000000000000, 1000000000000000, 1200000000000000, 1500000000000000, 2000000000000000, 3000000000000000, 4000000000000000, 5000000000000000, 6000000000000000, 7000000000000000, 8000000000000000, 9000000000000000, 10000000000000000, 12000000000000000, 15000000000000000, 20000000000000000, 30000000000000000, 40000000000000000, 50000000000000000, 60000000000000000, 70000000000000000, 80000000000000000, 90000000000000000, 100000000000000000, 120000000000000000, 150000000000000000, 200000000000000000, 300000000000000000, 400000000000000000, 500000000000000000, 600000000000000000, 700000000000000000, 800000000000000000, 900000000000000000, 1000000000000000000, 1200000000000000000, 1500000000000000000, 2000000000000000000, 3000000000000000000, 4000000000000000000, 5000000000000000000, 6000000000000000000, 7000000000000000000, 8000000000000000000, 9000000000000000000, 10000000000000000000, 12000000000000000000, 15000000000000000000, 20000000000000000000, 30000000000000000000, 40000000000000000000, 50000000000000000000, 60000000000000000000, 70000000000000000000, 80000000000000000000, 90000000000000000000, 100000000000000000000, 120000000000000000000, 150000000000000000000, 200000000000000000000, 300000000000000000000, 400000000000000000000, 500000000000000000000, 600000000000000000000, 700000000000000000000, 800000000000000000000, 900000000000000000000, 1000000000000000000000, 1200000000000000000000, 1500000000000000000000, 2000000000000000000000, 3000000000000000000000, 4000000000000000000000, 5000000000000000000000, 6000000000000000000000, 7000000000000000000000, 8000000000000000000000, 9000000000000000000000, 10000000000000000000000, 12000000000000000000000, 15000000000000000000000, 20000000000000000000000, 30000000000000000000000, 40000000000000000000000, 50000000000000000000000, 60000000000000000000000, 70000000000000000000000, 80000000000000000000000, 90000000000000000000000, 100000000000000000000000, 120000000000000000000000, 150000000000000000000000, 200000000000000000000000, 300000000000000000000000, 400000000000000000000000, 500000000000000000000000, 600000000000000000000000, 700000000000000000000000, 800000000000000000000000, 900000000000000000000000, 1000000000000000000000000, 1200000000000000000000000, 1500000000000000000000000, 2000000000000000000000000, 3000000000000000000000000, 4000000000000000000000000, 5000000000000000000000000, 6000000000000000000000000, 7000000000000000000000000, 8000000000000000000000000, 9000000000000000000000000, 10000000000000000000000000, 12000000000000000000000000, 15000000000000000000000000, 20000000000000000000000000, 30000000000000000000000000, 40000000000000000000000000, 50000000000000000000000000, 60000000000000000000000000, 70000000000000000000000000, 80000000000000000000000000, 90000000000000000000000000, 100000000000000000000000000, 120000000000000000000000000, 150000000000000000000000000, 200000000000000000000000000, 300000000000000000000000000, 400000000000000000000000000, 500000000000000000000000000, 600000000000000000000000000, 700000000000000000000000000, 800000000000000000000000000, 900000000000000000000000000, 1000000000000000000000000000, 1200000000000000000000000000, 1500000000000000000000000000, 2000000000000000000000000000, 3000000000000000000000000000, 4000000000000000000000000000, 5000000000000000000000000000, 6000000000000000000000000000, 7000000000000000000000000000, 8000000000000000000000000000, 9000000000000000000000000000, 10000000000000000000000000000, 12000000000000000000000000000, 15000000000000000000000000000, 20000000000000000000000000000, 30000000000000000000000000000, 40000000000000000000000000000, 50000000000000000000000000000, 60000000000000000000000000000, 70000000000000000000000000000, 80000000000000000000000000000, 90000000000000000000000000000, 100000000000000000000000000000, 120000000000000000000000000000, 150000000000000000000000000000, 200000000000000000000000000000, 300000000000000000000000000000, 400000000000000000000000000000, 500000000000000000000000000000, 600000000000000000000000000000, 700000000000000000000000000000, 800000000000000000000000000000, 900000000000000000000000000000, 1000000000000000000000000000000, 1200000000000000000000000000000, 1500000000000000000000000000000, 2000000000000000000000000000000, 3000000000000000000000000000000, 4000000000000000000000000000000, 5000000000000000000000000000000, 6000000000000000000000000000000, 7000000000000000000000000000000, 8000000000000000000000000000000, 9000000000000000000000000000000, 10000000000000000000000000000000, 12000000000000000000000000000000, 15000000000000000000000000000000, 20000000000000000000000000000000, 30000000000000000000000000000000, 40000000000000000000000000000000, 50000000000000000000000000000000, 60000000000000000000000000000000, 70000000000000000000000000000000, 80000000000000000000000000000000, 90000000000000000000000000000000, 100000000000000000000000000000000, 120000000000000000000000000000000, 150000000000000000000000000000000, 200000000000000000000000000000000, 300000000000000000000000000000000, 400000000000000000000000000000000, 500000000000000000000000000000000, 600000000000000000000000000000000, 700000000000000000000000000000000, 800000000000000000000000000000000, 900000000000000000000000000000000, 1000000000000000000000000000000000, 1200000000000000000000000000000000, 1500000000000000000000000000000000, 2000000000000000000000000000000000, 3000000000000000000000000000000000, 4000000000000000000000000000000000, 5000000000000000000000000000000000, 6000000000000000000000000000000000, 7000000000000000000000000000000000, 8000000000000000000000000000000000, 9000000000000000000000000000000000, 10000000000000000000000000000000000, 12000000000000000000000000000000000, 15000000000000000000000000000000000, 20000000000000000000000000000000000, 30000000000000000000000000000000000, 40000000000000000000000000000000000, 50000000000000000000000000000000000, 60000000000000000000000000000000000, 70000000000000000000000000000000000, 80000000000000000000000000000000000, 90000000000000000000000000000000000, 100000000000000000000000000000000000, 120000000000000000000000000000000000, 150000000000000000000000000000000000, 200000000000000000000000000000000000, 300000000000000000000000000000000000, 400000000000000000000000000000000000, 500000000000000000000000000000000000, 600000000000000000000000000000000000, 700000000000000000000000000000000000, 800000000000000000000000000000000000, 900000000000000000000000000000000000, 1000000000000000000000000000000000000, 1200000000000000000000000000000000000, 1500000000000000000000000000000000000, 2000000000000000000000000000000000000, 3000000000000000000000000000000000000, 4000000000000000000000000000000000000, 5000000000000000000000000000000000000, 6000000000000000000000000000000000000, 7000000000000000000000000000000000000, 8000000000000000000000000000000000000, 9000000000000000000000000000000000000, 10000000000000000000000000000000000000, 12000000000000000000000000000000000000, 15000000000000000000000000000000000000, 20000000000000000000000000000000000000, 30000000000000000000000000000000000000, 40000000000000000000000000000000000000, 50000000000000000000000000000000000000, 60000000000000000000000000000000000000, 70000000000000000000000000000000000000, 80000000000000000000000000000000000000, 90000000000000000000000000000000000000, 100000000000000000000000000000000000000, 120000000000000000000000000000000000000, 150000000000000000000000000000000000000, 200000000000000000000000000000000000000, 300000000000000000000000000000000000000, 400000000000000000000000000000000000000, 500000000000000000000000000000000000000, 600000000000000000000000000000000000000, 700000000000000000000000000000000000000, 800000000000000000000000000000000000000, 900000000000000000000000000000000000000, 1000000000000000000000000000000000000000, 1200000000000000000000000000000000000000, 1500000000000000000000000000000000000000, 2000000000000000000000000000000000000000, 3000000000000000000000000000000000000000, 4000000000000000000000000000000000000000, 5000000000000000000000000000000000000000, 6000000000000000000000000000000000000000, 7000000000000000000000000000000000000000, 8000000000000000000000000000000000000000, 9000000000000000000000000000000000000000, 100, 12000000000000000000000000000000000000000, 15000000000000000000000000000000000000000, 200, 300, 400, 500, 600, 700, 800, 900, 1000, 1200, 1500, 2000, 3000, 4000, 5000, 6000, 7000, 8000, 9000, 100, 12000, 15000, 200, 300, 400, 500, 600, 700, 800, 900, 1000, 1200, 1500, 2000, 3000, 4000, 5000, 6000, 7000000000$

Electromodulation Spectroscopy Study of a GaAs/GaAlAs Asymmetric Triangular Quantum Well Structure

Y.-S. Huang and W.-S. Chi
Department of Electronic Engineering, National Taiwan Institute of Technology
Taipei, Taiwan, Republic of China

H. Qiang[†] and Fred H. Pollak^{*}
Department of Physics, Brooklyn College of the City University of New York
Brooklyn, NY 11210, USA

D. L. Mathline and G. N. Maracas
Department of Electrical Engineering, Arizona State University
Tempe, AZ 85287, USA

ABSTRACT

Using the contactless electromodulation methods of photorefraction and contactless electroreflectance we have studied the interband transitions from a (001) GaAs/GaAlAs asymmetric, triangular quantum well (ATQW) structure at 300K and 80K. The sample was fabricated by molecular beam epitaxy using a digital alloy composition grading (DAC) method. Comparison of the observed interband resonances with a theoretical calculation (envelope function method) provided a self-consistent verification that the DAC method produced the intended result, i.e. an effective linearly graded profile, an external uniaxial stress (doping [100]) was used to confirm the heavy-or light-hole nature of some of the spectral features. Furthermore, the temperature dependence of both the energy and broadening parameter ($\Gamma(T)$) of the interband conduction to heavy-hole exciton feature were investigated in the wide temperature range 40K $< T < 450$ K. These observations, particularly the anomalous behaviour of $\Gamma(T)$, will be compared to the temperature dependence of the exciton wavevector of comparable dimensions.

NOBLE, JUDITH A.

1. INTRODUCTION

Graded bandgap materials are of great importance in band-gap engineering and are being widely used in photodetectors, lasers, heterojunction bipolar transistors, etc. For example, although rectangular quantum wells have been extensively employed as active regions of opto-electronic devices, they have certain limitations. These symmetrical rectangular quantum wells (SRQW) have an overlap integral between the fundamental conduction and heavy-hole wavefunctions that are very close to unity when no electric field is applied. However, in most opto-electronic devices the quantum well is subjected to internal and external fields from the device that increase this overlap because ΔE the separation of the conduction and valence bands is reduced. This reduction in the overlap integral creates a corresponding reduction in the emission or absorption process. In novel quantum well designs, such as those containing compositional gradients, there is a potential for increasing this overlap. Therefore, such novel quantum well structures should increase the absorption or emission process in opto-electronic devices. Recently, arbitrary shaped quantum wells have been implemented by molecular beam epitaxy (MBE) in such devices with an emphasis in asymmetric triangular quantum wells (ATQW) [1].

In this paper we report a study of the intersubband transitions from a (001) GaSb/Ga_{0.15}Al_{0.85}ATQW asymmetric triangular quantum wells (ATQW) structure at 300K and 80K using photoreflectance (PR)¹¹ and contactless electroreflectance (CER)¹². These modulation methods have proven to be extremely useful in the investigation and characterization of semiconductor microstructures. The sample was fabricated by molecular beam epitaxy (MBE) using a digital alloy composition grading (DACG) method. A number of *mnHIL* intersubband features were observed in the spectra, where *mnHIL* denotes a transition from the *m*th conduction to *n*th valence subband of heavy (vH) or light (l) hole character. The envelope function approximation¹³ was used to calculate the bound energy states using the DACG profile determined from the growth conditions. Comparison of the observed ATQW resonances with the theoretical calculation provided a self-consistent check of the ATQW composition profile. A comparison of the energy levels with the properties of a linearly graded

agreement with the obtained for the active Δ amplifier. If we use the exact dispersion relation for the slope indicated by a dashed curve, better agreement is obtained for the absolute values when the slope is evaluated at the experimental mean fields. The results given above show that the relative oscillator strength of the Stark ladder transitions basically depends on Δ , being consistent with the theory. Moreover, the F dependence of the relative transition intensity is valid over the wide range of the BL absorption wings studied.

In summary, miniband-edge optical transitions and their variations with the external field are investigated in photocurrent spectra of GaAs/AlAs 0.1- μ m diode structures with different miniband widths. Distinct spectroscopic features of the Π excitons due to the saddle-type Δ_1 singularity are directly observed in absorption spectra. Excellent correlation with the miniband width is obtained between the experimental and theoretical transition energies both for heavy-hole and light-hole excitations under the applied field. Stark ladder transitions are clearly observed over a wide range of well and barrier parameters, and $\tilde{\nu}^{-1}$ and Δ_1^+ dependences of their relative oscillation strengths are observed and explained with the tight-binding theory.

51025x921A05 215

ORDER TO SHOW CAUSE, FOR ANSWERING COMPLAINT FOR VIOLATION OF PROBATION, AND FOR REVOCATION OF PROBATION.

References

- [illegible]

well (LGVW) also will be presented. The heavy- or light-hole nature of various transitions was verified by a uniaxial stress ($\bar{\sigma}$) experiment for $\bar{\sigma} \parallel [100]$. Furthermore, the temperature dependence of both the energy position and broadening parameter (FWHM) of the 11H exciton feature were investigated in the wide temperature range 10K < T < 450K. These observations, particularly the anomalous behaviour of FWHM, will be compared to results for III-V and II-VI SQW's of comparable dimensions¹¹. We found no evidence for Franz-Keldysh oscillations due to the quasielastic field in the ATQW, as recently reported in DACO structures. Our spectra were due to intersubband transitions, similar to the electron beam electroreflectance experiment on a LGW.¹²

II. EXPERIMENTAL DETAILS

The ATQW used in this study was fabricated by the DACO method, which approximates the alloy composition profile by using alternating layers of Ga_{0.4}Al_{0.6}As and GaAs, where the ratio of layer thickness produces an average alloy composition. The average Al composition in an alloy cell (typically 25-30Å) is approximated by slanting the Al effusion cell such that the thickness of a layer of GaAlAs centered in the alloy cell provides enough Al to equal the required Al composition. The average Al composition in such a cell is given by

$$x_1 > x_2 = (d_1/d_2) \quad (1a)$$

where x_1 is the composition of the Al present in the GaAlAs layer and d_1 is the width of the Ga_{0.4}Al_{0.6}As layer centered in the i th cell of width i . The width of the GaAlAs layer is expressed as

$$d_i = i(1-0.5)/L_p \quad (1b)$$

where i ranges from unity to L_p/L_w and L_w is the width of the ATQW.

The ATQW was grown on a three inch semi-insulating (001) GaAs substrate using a solid source molecular beam epitaxy system. The resulting structure consisted of a 2000Å buffer layer of GaAs, followed by a 500Å cladding layer of GaAlAs. Next, a nominal 200Å ATQW was grown with the digital alloy approximation using a nominal 25Å alloy cell width. The structure was finished with a 500Å cladding layer of GaAlAs, followed by a 20Å cap layer.

The PR¹³ and CER¹⁴ methods have been reported in the literature. The pump beam of the PR experiment was the 6328Å line of a 3mW He-Ne laser at 200 Hz. The procedure for going to elevated temperatures is discussed in Ref. 14.

III. EXPERIMENTAL RESULTS AND ANALYSIS

A. Intersubband Transitions

Shown by the solid lines in Figs. 1 and 2 are the PR spectra of the sample at 300K and 80K, respectively. The CER data were quite similar. The first feature in the spectra corresponds to the direct band gap of GaAs, denoted E_g(GaAs), and originates in the GaAs buffer/substrate of the structure. The peaks at 1.753 eV (300K) and 1.842 eV (80K) are E_g(GaAlAs). The energy of this feature enables us to determine an Al composition of 23%.

The rich spectra between E_g(GaAs) and E_g(GaAlAs) are due to various mnl(L) quantum transitions of the ATQW. In order to accurately determine the energies of these resonances we have fit the experimental data with a first-derivative

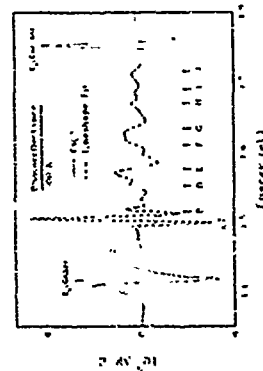


Fig. 1 Photoreflectance spectrum (solid line) at 300K from a GaAs/GaAlAs asymmetric quantum well. The dashed line is a least-squares fit to a FDGL function. The obtained energy values are denoted by arrows.

Gaussian lineshape (FDGL) function¹⁵, as shown by the dashed lines. The obtained energies of the features denoted A-J are indicated by arrows and are listed in Table I. The ATQW spectra in Figs. 1 and 2 are due to intersubband transitions, similar to Ref. 11, and are not Franz-Keldysh oscillations, as claimed in the PR study of Ref. 5.

In order to identify the nature of the large number of intersubband transitions observed from the ATQW we have performed a theoretical calculation based on the envelope function approximation¹⁶ using the measured DACO profile from the growth conditions. Non-parabolic effects were not included. The only adjustable parameter was L_p . We used a conduction band offset, $Q_c = 0.65^{17,18}$, and Ga_{0.4}Al_{0.6}As band masses for GaAs and Ga_{0.4}Al_{0.6}As listed in the literature and E_g(GaAs)/E_g(GaAlAs) taken from this experiment (see Figs. 1 and 2). Listed in Table I are the results of the calculation for 300K and 80K with 11L, B with 11L, C with 11L, etc. For the sake of comparison we also have performed a similar calculation for a LGW profile with the same L_p as displayed in the parentheses in Table I. There also is very good agreement between experiment and theory for this potential profile. This correspondence is verification that the DACO method has produced the desired result, i.e., an effective linearly graded potential profile.

B. Effects of $\bar{\sigma} \parallel [100]$

In order to verify the heavy- or light-hole nature of the observed mnl(L) transitions from the ATQW we have performed a PR experiment at 80K for $\bar{\sigma} \parallel [100]$ with the electric field vector \bar{E} of the incident light polarized parallel (\parallel) or perpendicular (\perp) to $\bar{\sigma}$. For such a stress it is well known that heavy/light-hole resonances have small/large stress-dependence because of the cancellation (addition) of the hydrostatic and shear components of the strain. Furthermore, when the stress-induced quantum confinement effects, mnl(L) features are allowed for both $\bar{E} \parallel \bar{\sigma}$ and $\bar{E} \perp \bar{\sigma}$, mnl(L) resonances are seen only for $\bar{E} \perp \bar{\sigma}$ and the intensity ratio $I_{\perp}/I_{\parallel} \approx 1/3$.

Displayed by the solid lines in Fig. 3 are the PR spectra at 80K for $\bar{\sigma} \parallel [100]$ and $\bar{E} \perp \bar{\sigma}$ in the region of the 11L-22H features for $\bar{\sigma} \parallel [100]$ and $\bar{E} \perp \bar{\sigma}$. The dashed lines are least-squares fits to a FDGL function.

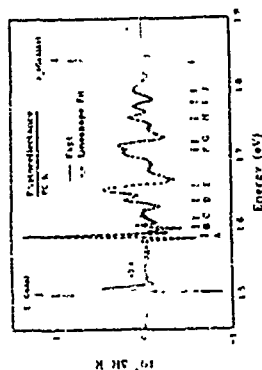


Fig. 2 Photoreflectance spectrum (solid line) at 80K from a GaAs/GaAlAs asymmetric quantum well. The dashed line is a least-squares fit to a FDGL function. The obtained energy values are denoted by arrows.

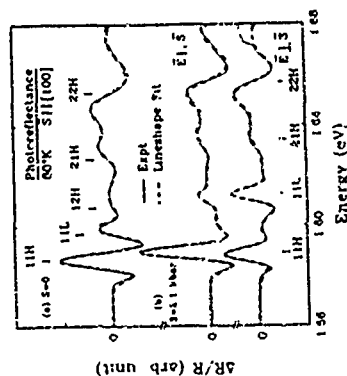


Fig. 3 Photoreflectance spectra (solid lines) at 80K for $\bar{\sigma} \parallel [100]$ and $\bar{E} \perp \bar{\sigma}$ in the region of the 11L-22H features for $\bar{\sigma} \parallel [100]$ and $\bar{E} \perp \bar{\sigma}$. The dashed lines are least-squares fits to a FDGL function.

element effects. Again the dashed lines are a FEXGL fit to the experimental data. The obtained energies are indicated by arrows. For the well resonances there is very little change in energy with the applied stress while for 11L there is a distinct blue shift. At $S \approx 2.1$ kbars the 11L peak becomes degenerate with the weak "symmetry-forbidden" 1211 feature and hence the latter is not resolved. Also, for the parallel configuration the intensity of 11L is weak while for the perpendicular case $I_{11L}^{\perp}/I_{11L}^{\parallel} = 1$. The ratio is not yet 1/3 since 2.1 kbars is not the high stress limit.

C. Temperature Dependence of E_{11L} and Γ_{11L}
We also have studied the temperature dependence of the energy and broadening parameter of the fundamental 1111 electronic transition in the temperature range 10K $< T < 450$ K using both PR and CER

relationships.²⁰ The temperature dependence of $E_{11L}(T)$ can be fit to either the Varshni semi-empirical relationship²¹

$$E_{11L}(T) = E_{11L}(0) - \alpha T^2 / (\beta + T) \quad (2a)$$

where $E_{11L}(0)$ is the energy at $T=0$ and α and β are the Varshni coefficients or a Bose-Einstein expression²²

$$E_{11L}(T) = E_{11L}(0) - 2\alpha_T \exp(E_g/kT) - 1 \quad (2b)$$

In Eq. (2b) α_T represents the strength of the electron-average phonon interaction and E_g corresponds to an average phonon energy.

Shown by the open circles in Fig. 4 are the experimental values of $E_{11L}(T)$ in the range 10K $< T < 450$ K obtained from PR/CER. The solid line is a least-squares fit to Eq. (2a). The obtained values of $E_{11L}(0)$, α and β are listed in Table II. We also have fit the experimental data to Eq. (2b) and have recomputed the obtained values of α_T and E_g in Table II. For comparison purposes corresponding numbers for the relevant parameters for bulk GaAs are also displayed.

The values for the parameters of the temperature dependence of E_{11L} are essentially the same as the consistent bulk material of the quantum wells. This can also be seen in Figs. 1 and 2 where the difference between E_{11L} and $E_d(\text{GaAs})$ is independent of temperature. This observation is consistent with studies of GaAs/GaAlAs²³ and InGaAs/GaAs²⁴ SRQW systems.

The variation of the linewidth with temperature also can be expressed by a Bose-Einstein type expression^{25,26}

$$\Gamma_{11L}(T) = \Gamma_{11L}(0) + \Gamma_p \exp(E_{11L}/kT) - 1 \quad (3)$$

The first term of Eq. (3) corresponds to broadening mechanisms due to both intrinsic lifetime, electron-electron interaction and extrinsic (well width fluctuations) effects. The parameter Γ_p is an electron-exciton-phonon coupling coefficient and E_{11L} is the zone center longitudinal optic (LO) phonon energy (36 meV for GaAs).

Displayed in Fig. 5 by the squares are the experimental PR/CER values of $\Gamma_{11L}(T)$. $\Gamma_{11L}(0)$ as a function of $\exp(E_{11L}/kT) - 1$ (with $E_{11L} = 36$ meV). The value of $\Gamma_{11L}(0) = 1.8$ meV. Clearly the data

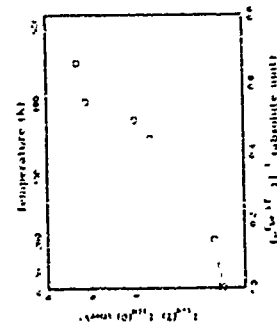


Fig. 5 Experimental values of $\Gamma_{11L}(T) - \Gamma_{11L}(0)$ vs $[\exp(E_{11L}/kT) - 1]$ with $E_{11L} = 36$ meV and $\Gamma_{11L}(0) = 1.8$ meV. The temperature scale is at the top of the figure.

do not lie on a straight line. This is in contrast to SRQW systems in which a linear relation is obeyed²¹, the slope yielding Γ_p . The exception is a recent work on a GaAs/GaAlAs SRQW in which a deviation from linearity was observed due to an internal electric field.²⁷ Our result could be due to the quasicrystalline field of the ATQW structure. Another possible reason for the anomalous behavior of our sample may be due to the contribution of interface modes.²⁸ Prior SRQW studies were performed on samples with well widths greater than 60Å. Our ATQW, although it has $L_w = 260$ Å, consists of many heterointerfaces spaced closer than 20Å apart and thus is in a regime where interface modes may become important. These points are under further investigation.

IV. SUMMARY

We have studied the intersubband transitions from a (001) GaAs/GaAlAs ATQW structure, grown by the DACG method, at 300K and 80K using PR and CER. Comparison of the observed ATQW resonances with a theoretical calculation, based on the DACG growth conditions, provided a self-consistent check of the ATQW composition profile in addition to the band offset parameter. There also is very good agreement between experiment and theory for a LGW potential profile. This correspondence is verification that the DACG method has produced the desired result, i.e., an effective linearly graded potential profile. The heavy- or light-hole nature of various transitions was verified by a uniaxial stress (S) experiment for $S \parallel [100]$. While the temperature dependence of $E_{11L}(T)$ was in agreement with results on SRQW microstructures an anomalous behavior for $\Gamma_{11L}(T)$ was observed. We found no evidence for Franz-Keldysh oscillations due to the quasicrystalline field in the ATQW.

V. ACKNOWLEDGEMENTS

The authors HQ and HJP acknowledge the support of US Army Research Office contract #DAAL03-92-G-0189 and the Olympus Corporation. The work of DLM and GNM was supported by US Air Force University Initiative contract AFOSR-90-0118.

REFERENCES

1. D. Hulin and H. Taylor, IEEE J. Quant. Electron. 25, 2164 (1989).
2. D. Gerber, R. Droopad, and G. N. Maracas, Appl. Phys. Lett. 62, 525 (1993).
3. T. Ishikawa and K. Tada, J. Appl. Phys. 78, L1982 (1995).
4. K.-K. Lau, P. H. Yan, A. C. Gossard, and J. L. Merz, J. Appl. Phys. 62, 6461 (1990).
5. H. Xu, X. Zhou, G. Xu, Q. Du, E. Wang, L. Zhang, and C. Chen, Appl. Phys. Lett. 61, 2193 (1992).
6. D. L. Mathine, G. N. Maracas, D. S. Gerber, R. Droopad, R. J. Graham and M. R. McCartney, submitted to J. Appl. Phys.
7. F. H. Pollak and O. J. Glembocki, Proc. Soc. Photo-Optical Instrum. Engineers (SPIE), Bellingham, 1988) 926-21988.
8. O. J. Glembocki and B. V. Shanabrook, Semiconductors and Semimetals, Vol. 67, ed. D. G. Semler and C. L. Lütler (Academic, New York, 1992) p. 222.
9. Y. Yu and E. H. Pollak, Appl. Phys. Lett. 59, 2305 (1991).
10. G. Bastard, Phys. Rev. B 24, 5693 (1981), also, Phys. Rev. B 25, 7584 (1982).
11. R. F. Kopf, M. H. Herman, N. L. S. Jones, A. P. Petley, G. Livescu and M. Ohring, J. Appl. Phys. 71, 5004 (1992).

12. H. Qiang, F.H. Pollak, C.M. Sotomayor Torres, W. Leitch, A.H. Kean, M.A. Stroscio, G.J. Iafrate and K.W. Kim, Appl. Phys. Lett. 61, 1411 (1992)
13. F.H. Pollak in *Photons in Semiconductor Nanostructures*, ed. J.-P. Leburton, J. Pasqual and C. Sotomayor Torres (Kluwer, Dordrecht, 1993) p. 341
14. Y.S. Huang, H. Qiang, F.H. Pollak, G.D. Pettit, P.D. Kirchner, J.M. Woodall, H. Stragier and L.B. Sorensen, J. Appl. Phys. 76, 7537 (1991)
15. F.H. Pollak in *Properties of Aluminum Gallium Arsenide*, ed. by S. Adachi (INSPEC, London, 1993) p. 53
16. M. Missous in *Properties of Aluminum Gallium Arsenide*, ed. S. Adachi (INSPEC, London, 1993) p. 73
17. S. Adachi in *Properties of Aluminum Gallium Arsenide*, ed. by S. Adachi (INSPEC, London, 1993) p. 58
18. S. Adachi in *Properties of Aluminum Gallium Arsenide*, ed. by S. Adachi (INSPEC, London, 1993) p. 66
19. F.H. Pollak, in *Semiconductors and Semimetals*, Vol. 32, ed. by T.P. Pearsall (Academic, New York, 1990) p. 17
20. F.H. Pollak, in *Properties of Aluminum Gallium Arsenide*, ed. by S. Adachi (INSPEC, London, 1993) p. 79
21. P. Launshlager, M. Garriga and M. Cardona, Phys. Rev. B 35, 9174 (1987), also, Phys. Rev. B 36, 4813 (1987)
22. A. Kargaliu, H. R. Chandrasekhar, Y. M. Kapoor, F. A. Chambers, B. A. Volak and J. M. Meese, Phys. Rev. B 37, 1035 (1988)
23. J. Filipowicz, C. Ghezzi and L. Tarricone, Solid State Comm. 74, 533 (1990)
24. M.A. Stroscio, G.J. Iafrate, K.W. Kim, M.A. Littlejohn, H. Goronkin and G.N. Narascan, Appl. Phys. Lett. 59, 1093 (1991).

TABLE I. Comparison of the experimental and theoretical (DAG) values for the mhl(L) transitions of the ATQW with $L_w = 20 \text{ nm}$. The numbers in parentheses are for a similar calculation for a LOW profile using the same L_w .

Spectral Feature	300K		80K		mhl(L)
	Expt (eV)	Theory (eV)	Expt (eV)	Theory (eV)	
A	1.503	1.5021 (505)	1.585	1.5871 (590)	11H
B	1.516	1.5151 (516)	1.598	1.6001 (601)	11L
C		1.5231 (527)	1.611	1.6081 (612)	12H
D	1.553	1.5581 (562)	1.636	1.6431 (647)	21H
E	1.577	1.5791 (584)	1.658	1.6641 (649)	22H
F	1.611	1.6231 (629)	1.709	1.7081 (714)	32H
G	1.635	1.6401 (648)	1.721	1.7251 (733)	33H
H	1.671	1.6711 (678)	1.754	1.7561 (763)	35H
I	1.691	1.6941 (702)	1.778	1.7791 (787)	44H
J	1.717	1.7101 (716)	1.794	1.7951 (801)	45H

TABLE II. Values of the parameters α , β , γ , and E_g which describe the temperature dependence of the energy of the 11H transition in the GaAs/GaAlAs ATQW

Material	α (10 ⁻⁴ eV/K)	β (K)	γ (meV)	E_g (meV)
ATQW	5.7 ± 0.3	228 ± 40	57 ± 3	21 ± 4
Bulk GaAs	5.31 (3) 5.115)	225 (74) 190 (82)	57 (29) 57 (29)	21 (10) 21 (10)

a. Ref. 20. The numbers in parentheses indicate error margins in units of the last significant digit.

TuP12

Spectroscopic studies of ultra-thin quantum-wells of GaAs and GaInAs in InP grown by MOVPE

D. Hasmann, X. Liu, M.E. Pistol, L. Samuelson and W. Skjott
Department of Solid State Physics, Lund University, Box 118, S-221 01 LUND, Sweden

Abstract

Quantum-well (QW) structures consisting of nominally 1, 2, and 3 monolayers of either GaAs or GaInAs, embedded in InP have been grown by low pressure metal organic vapour phase epitaxy (LP-MOVPE). Such QW structures are known to be strongly affected by interface layers due to As replacing P on the bottom interface and due to As carry-over from the QW into the top InP barrier. Theoretically one expects GaInAs/InP to form a type I QW while a "clean" GaAs layer embedded in InP is assumed to be of type II. However, the inclusion of the InAs-like interface layers has a strong effect on the type-I versus type-II conditions. Based on a systematic study of growth and interface interrupt conditions we have been able to find conditions which yield the best QW interfaces, as judged from photoluminescence (PL) combined with modeling of the electronic structure. PL peak half widths of 7-10 meV are obtained. First, conditions are described for the formation of such very thin, high quality QWs. We then report good qualitative agreement between the spectroscopic data and the results of the modeling of the QWs, which includes contributions from the growth-dependent interface layers.

1. Introduction

GaInAs/InP is a material system of great technological importance, offering a wide variability for fabrication of heterostructures for optical and high-speed applications. By varying the composition of the well material, this material system ranges from compressively strained InAs/InP, to lattice matched Ga_{0.47}In_{0.53}As/InP, and on to tensilely strained GaAs/InP. The band line-up of GaAs/InP is believed to be of type II [1, 2], meaning that the GaAs layer acts as a well for holes but a barrier for electrons, suggesting poor optical properties. For thin enough GaAs layers, however, the electron tunneling through the barrier is considerable, giving a non-negligible matrix element for electron-hole recombination. With the epitaxial techniques available today, quantum well (QW) structures can be grown with Ga_{0.47}In_{0.53}As thicknesses in the monolayer range. Clearly, for such thin QWs, the exact composition of the atomic layers close to the interfaces separating the well material from the barrier material becomes very important. An indication of the importance of these interfaces, is the spread in photoluminescence (PL) energies, measured for nominally 1 monolayer thick Ga_{0.47}In_{0.53}As/InP QWs, where values between 1.1 and 1.38 eV have been reported [3,4]. Theoretical calculations, neglecting interface contributions, predict values around 1.38 eV. The process responsible for these discrepancies is the unintended incorporation of As into the barrier material, at both the first and the second interface.

In this work, we have investigated the interface properties by measuring the PL of Ga_{0.47}In_{0.53}As and GaAs QWs, grown under different growth conditions. The PL peak energies are found to shift continuously with some conditions such as growth temperature, in contrast to the discrete set of PL peaks obtained when changing the growth time. This discreteness is understood as monolayer changes of the QW thickness, while the continuous shifting is an alloying effect at the interfaces. We also include the As incorporation at the interfaces in a theoretical calculation, giving qualitative agreement with the experimental results.

In section II, we describe the experimental conditions for the LP-MOVPE growth. In section III we give a brief theoretical background to the use of the effective mass theory on monolayer thin QWs, including a proposal of a simple method for defining the potential structure on the atomic scale. The experimental and theoretical results are presented in section IV, together with some discussion about the mechanisms of the As incorporation. The conclusions are given in section V.

II. Experimental

The samples used for this investigation were grown in a RF-heated LP-MOVPE apparatus (EPICUP RP-30) equipped with a vent/run switching and a pressure balance system. The total flow was 6.5 l/min H₂ and the total pressure was 50 mbar, 100 % PH₃ and AsH₃ and the metalorganics TMG (with a special dilution line) and TMI were used. Each switched component was compensated by a corresponding counterflow so that the pressure difference between vent- and run-lines during the switching process could be regulated to be ± 0.2 mbar. All samples consisted of an exactly oriented (100) InP substrate, a 500 nm InP buffer, a 500 Å GaInAs reference layer, and a stack of QWs. Two different types of QWs were grown: lattice matched Ga_{0.47}In_{0.53}As/InP and strained GaAs/InP. The QWs were grown using a 2s growth interruption when going from InP to the well material: 1 s after the TMG (and TMI) was switched on. The reverse procedure, 1 s of only AsH₃ flow followed by 1 s of only PH₃ flow, was used when going back to InP at the top interface. The QWs were grown under varying growth conditions, such as deposition temperature (typically 520-620°C) and molar fraction of AsH₃ (typically 0.5-2x10⁻³).

The samples were characterized by low-temperature (5 K) photoluminescence measurements. The excitation source was the 514 nm line of an Ar⁺-ion laser, giving an excitation power of about 10 W/cm². The emitted light was dispersed by a double monochromator and detected by a liquid nitrogen cooled Ge detector.

III. Theory

Since the mid-seventies, the effective-mass theory [5] (EMT) using an ideal square-well potential has been very successful in modeling the electronic energy levels of semiconductor quantum wells (QW). Despite its simplicity, this model gives good agreement with experiment also as the QWs become very thin, although some problems do arise. For example, the increased confinement energy, necessitates the inclusion of band non-parabolicity. This can be solved for instance by using an energy dependent effective mass or by generalizing the EMT to a multi band problem, allowing for explicit band mixing. Moreover, the uncertainty of parameters such as the band offset becomes more important as the confined states approach the top of the QW. The parameters of the barrier material also increase in importance, since the wave function of a carrier confined by a single monolayer will have a large penetration into the barrier material. Even including these refinements, it is still questionable that the EMT should be applicable to the ultra-thin QWs of this work, having thicknesses of only a few monolayers. The failure in modeling the experimental results on QWs intended to be one monolayer thick has previously been attributed to a possible break down of the EMT. However, as we report in this paper, additional interface layers, arising from different surface processes during growth, are incorporated in the structure. These interface layers have a large influence on the potential and on the resulting electronic states, and it is therefore crucial that they are included in the model. Two approximations in the (generalized) EMT that could be invalid in the case of monolayer sized QWs are the assumptions that (i) the potential is slowly varying compared to the atomic spacing and that (ii) the wave function of a confined state can be expanded in Bloch functions close to some critical point in the Brillouin zone. The first approximation can not be valid for the steps in the potential at the interfaces. However, this approximation would be fatal also in QWs with thicknesses of 10 monolayers or more, and is therefore not an issue specific for monolayer thin QWs. Why the EMT can be used in spite of the abrupt potential drop in a QW is a problem that still lacks a satisfactory explanation, though some progress has been made [6,7]. The second approximation is equivalent to a requirement that also the envelope function is slowly varying on the atomic scale. This is actually not a severe restriction, since the relatively small masses of electrons and holes in semiconductors cause the wave functions to penetrate far into the barrier material in ultra-thin QWs, with a corresponding localization in k-space.

Another problem that has to be addressed here is what potential structure to use. This is illustrated in figure 1a, which shows one monolayer of GaAs embedded in InP. Curve (i) shows the corresponding conduction band line-up, as usually used for thicker QWs. However, by pairing the atoms differently, this structure can equally well be described as one monolayer GaP and one monolayer InAs embedded in InP, as indicated by conduction band line-up (ii).

Comparing the two potentials, potential (i) might seem to be a more natural choice, however, at a closer look, it does not contain the symmetry of the atomic structure, as does potential (ii). In order to overcome this ambiguity, we propose a procedure that gives a unique potential for a specific atomic structure. In addition to that, the potential thus obtained will have the symmetry of the grown structure. The basic idea of this simple method, is to assign the band edge energy to the bonds connecting two planes of atoms. In this way we divide the structure into half-monolayer units, i. e. $\frac{1}{2}a$, where a is the length of the fcc unit cell. Using this concept, conduction band (iii) in figure 1a is obtained.

Figure 1a shows the atomic structure of a nominally one monolayer GaAs/InP QW. It is shown together with three different conduction band edge line-ups. Potential (i) is the one normally used. Potential (ii) is obtained by considering the Ga atom in being in a layer of GaP instead of GaAs as in case (i). Potential (iii) is constructed according to the model proposed in this work, which assigns the band edge energies to the bonds connecting the atoms. Note that only (i) and (ii) have the same symmetry as the atomic structure. In (b), the P atoms at the lower interface have been replaced by As atoms. The corresponding conduction and valence band structure is obtained using our model. With a partial P to As replacement the potential structure becomes that shown in figure 2b.

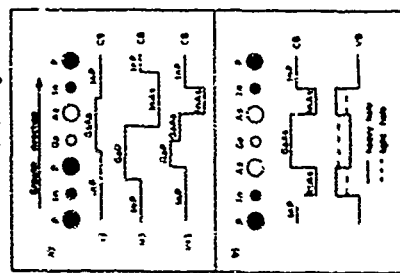


Figure 2. PL spectra of two QW samples, each of them containing three QWs with 1, 2, and 3 monolayer nominal thickness. a) Ga_{0.47}In_{0.53}As/InP and b) GaAs/InP. To the right are shown the corresponding potential structures for electrons, light holes and heavy holes, as used in the calculations. The only free parameter is the A_{SP}-ratio at the lower (left) interface.

If the grown structure is not perfect, e. g. if the composition of the atomic layers close to an interface differs from the intended one, the model potential has of course to be modified. As discussed in this paper, when starting to grow the GaAs layer the phosphorus atoms of the InP surface will almost instantaneously be replaced by As atoms. Assuming a complete P to As replacement, the atomic structure is that shown in figure 1b, where also the corresponding conduction and valence band line-up, obtained according to our proposal, is indicated. Note that both the atomic structure and the potential are symmetric with respect to the Ga atom, while the structure in figure 1a is not. With band line-up (i) in figure 1a, the pure GaAs/InP QW is of type II, with unbound electrons and bound holes. With band line-up (ii) however, the electrons become bound, though with a binding energy (≈ 1 meV) much smaller than a typical exciton binding energy, since this is an extremely thin well of only half a monolayer. Including the P/As replacement at the lower interface, a double-well structure is formed for the electrons, thereby slightly increasing their binding energy (< 5 meV), provided that the GaAs barrier is thin enough.

For all QWs in this study, the calculated PL recombination energies are for electron-heavy hole transitions, though for a thicker GaAs QW (> 1 monolayer), where the confinement energy is smaller, the electron-light hole transition has a lower energy. This is because the

tensile strain in the case of GaAs, lifts the light hole band above the heavy hole band, including strain to first order, the band edge energies of the conduction and valence bands are [1]

$$\begin{cases} V_{CB} = E_g + V_{\text{strain}} + a_1(\epsilon_{xx} + \epsilon_{yy} + \epsilon_{zz}) \\ V_{VB} = V_{\text{strain}} + b_1(\epsilon_{xx} - \frac{1}{2}(\epsilon_{yy} + \epsilon_{zz})) \end{cases} \quad (1)$$

where the $- (+)$ sign gives the heavy (light) hole valence band. E_g is the bandgap, V_{strain} the valence band offset relative to InP, a_1 is the hydrostatic deformation potential of the conduction band and b_1 is the shear deformation potential of the valence band (the hydrostatic deformation potential of the valence band is small and therefore taken to be zero). The strain tensor elements are $\epsilon_{xx} = \epsilon_{yy} = (a_{\text{GaAs}} - a_{\text{InP}})/a_{\text{InP}}$ and $\epsilon_{zz} = -(c_{\text{InP}}/c_{\text{GaAs}})\epsilon_{xx}$, where a_{GaAs} and a_{InP} are the lattice constants of InP and the unstrained material respectively and c_p are the components of the elastic moduli tensor. The parameters used in the calculations are taken from reference [1], where the parameters (apart from the bandgap) of ternary compounds are linearly interpolated from the parameters of the corresponding binary compounds.

Solving the Schrödinger equation for a piece-wise constant potential is just a question of fitting plane waves at each interface so that the envelope function, $F(z)$, fulfills

$$\begin{cases} F(d') = F(d'') \\ \frac{1}{m_1} F'(d') = \frac{1}{m_2} F'(d'') \end{cases} \quad (2)$$

where $d^{(1)}$ indicates interface approached from the left (right) side. With multiple interfaces, this may be extended using a transfer matrix technique [8].

The single band calculations described above have also been compared to the results of a more involved multi-band calculation, taking into account the electron, light hole and spin-orbit hole mixing due to strain and confinement. Both methods yield, however, approximately the same result for the electron heavy hole transitions. The multi-band model is based on the variational method of Ref. [6] with an eight-band $k \cdot p$ -Hamiltonian, including the strain [9].

When comparing the theoretical results with experiment, there are still many unknown parameters, e. g. the exact extent of the As incorporation into the lower and the upper barrier material. By varying the growth conditions, however, we have found conditions where such effects could be reduced. The agreement between the calculations and our experimental data, give no indication that the effective mass theory should be invalid for monolayer thick QWs.

IV. Results and discussion.

The highest quality Ga_{0.47}In_{0.53}As QWs, having the sharpest PL peaks, were grown at i) low growth rates (typically 0.5 ML/s for the QW and 0.25 ML/s for the barrier), ii) low hydride molar fractions (typically 1x10⁻³ for AsH₃ and 1x10⁻² for PH₃) and iii) deposition temperatures at about 380-400 °C. With these growth conditions, we obtain PL peak half-widths of 7-10 meV. Figure 2a shows a typical PL spectrum of a Ga_{0.47}In_{0.53}As sample. The different peaks correspond to Ga_{0.47}In_{0.53}As layers with nominal thicknesses of 0.5, 1.5, 2.5 and 5 monolayers. An increase of the growth time to yield nominal thicknesses of 1, 2 and 3 monolayers for the thinnest wells does not change the spectrum, indicating that, apart from any interface contributions, the QWs grow in monolayer steps. Changing the growth temperature or the AsH₃ pressure, however, shifts the PL peak position continuously. The reason for this continuous shift, which will be discussed in more detail later on, is mainly the incorporation of As at the second interface, i. e. at the interface between the Ga_{0.47}In_{0.53}As and the InP. There is, however, an important As incorporation also at the first (bottom) interface, a process which is much less sensitive to the growth conditions. Previous studies, under UHV conditions [11,12], have shown that, in the temperature interval used here, the surface P layer of InP is completely replaced by As atoms within less than a second, when exposed to AsH₃, while As replacement in deeper lying P layers is a considerably slower process [12]. This means that as soon as the PH₃ flow in the reactor has been changed into an AsH₃ flow, the P atoms sitting on the surface of the InP are expected to be replaced by As atoms and that almost no As gives into the depth of the InP during the short growth interruption.

If the growth temperature is decreased or if the AsH₃ partial pressure is increased, the PL peak position is shifted towards lower energy. Assuming, as discussed above, that the replacement of P atoms by As atoms at the first interface is instantaneous and, for the growth parameters used in this work, independent of growth conditions, this red shift of the PL must be indicating an increased As incorporation at the second interface. As we discuss below, the mechanism is that one or more layers of excess As are accumulated on the surface during the Ga_{0.47}In_{0.53}As growth, containing more As for lower temperatures and higher AsH₃ pressures. Most of this excess As will then remain on the surface, and as the TMI is switched on, the As is incorporated into the InP grows immediately after the upper interface, giving a graded InAs_{1-x}P_x interface layer.

The PL energies of Ga_{0.47}In_{0.53}As QWs grown at 640°C are plotted versus the AsH₃ molar fraction in figure 3. For low AsH₃ molar fraction, the PL energies seem to approach a constant value, suggesting that under these growth conditions, no excess As is incorporated at the second interface. Also included in the figure are the results of a calculation of the transition energies, assuming that no As is incorporated at the second interface but with different amounts of P replaced by As at the first interface. Including interface layers in the calculations, the experimental values are easily reproduced. Comparing experiment and calculation, the P layer does not appear in the gas switching, e.g. the delay before the AsH₃ pressure at the sample position reaches its maximum value, are possible explanations for the reduced P in As replacement compared to reference [11]. For the thicker QWs, the P to As replacement at the first interface appear to be enhanced. Most probably, however, this is a non-negligible As incorporation at the second interface, due to the increased As accumulation induced by the longer growth times. This explanation is supported by figure 3, where the thicker QWs clearly need lower AsH₃ pressures to reach a region of constant PL energy. i. e. the region of zero excess As at the second interface.

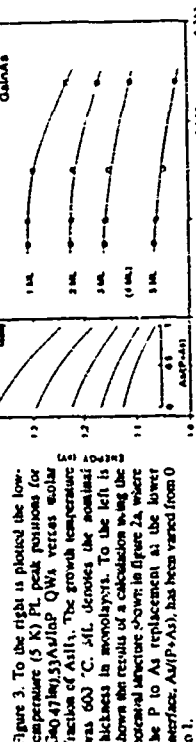


Figure 3. To the right is plotted the low-temperature (5 K) PL peak positions for Ga_{0.47}In_{0.53}As QWs versus molar fraction of AsH₃. The growth temperature was 640 °C. xPL denotes the nominal thickness in monolayers. To the left is shown the results of a calculation using the potential structure shown in figure 2a, where the P to As replacement at the bottom interface, AsH₃(P→As), has been varied from 0 to 1.

Figure 4. To the right is the low-temperature (5 K) PL peak positions for Ga_{0.47}In_{0.53}As QWs versus molar fraction of AsH₃. To the left is shown the calculated energies using the potential structure shown in figure 2a, where the P to As replacement at the bottom interface, AsH₃(P→As), has been varied from 0 to 1. The inset shows schematically a phase diagram of GaAs reconstructions versus AsH₃ pressure and inverse temperature. The growth parameters of this work are indicated by the shaded area.

V. Conclusions

We have optimized the growth of monolayer thick QWs of GaInAs and GaAs in InP, thus obtaining PL peak half-width of 7-10 meV. In addition to this, we have studied the As incorporation at the interfaces as a function of the growth conditions, using PL measurements as a probe. Theoretical calculations have been used as an important tool for understanding the spectroscopic results. The main conclusions are the following:

- When the InP at the bottom interface is exposed to AsH₃ as the growth of the well material is about to begin, a substantial fraction of the surface P atoms are replaced by As. This process is rapid and occurs, at all the studied temperatures and AsH₃ pressures, during a growth interruption of 1 s.
- During the growth of the well material, the growing surface is covered by one or more As layers. The amount of As is determined by the surface reconstruction, and is therefore strongly dependent on the growth conditions. With the growth conditions used in this work, a growing GaAs surface is always covered by more than one layer of As, as supported by studies of GaAs reconstructions under AsH₃ exposure. In the case of GaInAs, however, we have indications that we are able to decrease the amount of As to a single layer by choosing high temperature and low AsH₃ molar fraction. This suggests that the boundary between "2x4"-like and "4x4"-like reconstructions on GaInAs is moved towards higher AsH₃ pressures and lower temperatures compared to on GaAs.
- Terminating the growth of the well material, most of the excess As will remain on the surface. Then as the TMI is switched on to start growing the upper InP barrier, this As will be incorporated, giving a graded InAs_{1-x}P_x interface layer. The extent of this As carry-over effect is therefore mainly determined by the reconstruction of the growing Ga_{0.47}In_{0.53}As surface.
- Using the knowledge about the As incorporation at the two interfaces in the modelling, the spectroscopic data are reproduced by calculations using the effective mass theory. There are no indications of a break-down of the EMT. A consistent description on the atomic scale of the energy potential is obtained by assigning the band edge energy to the bonds connecting the atoms. In this way the symmetry of the atomic structure will also be maintained in the potential structure.

References

- D. Gerbasi and J. Temkin, *J. Luminance* 41, 481 (1989)
- M.-E. Hsu, M. Gerling, D. Hevman, and L. Samuelson, *Phys. Rev. B* 41, 1628 (1992) (1989)
- T. Y. Wang and G. B. Stringfellow, *J. Appl. Phys.* 67, 344 (1990)
- H. M. Cox, P. C. Moras, D. M. Hwang, P. Basile, T. J. Ganser, L. Nazar, J. M. Warkock, L. Yablonovitch, and S. G. Hermon, *Int. Phys. Conf. Ser.* No. 96, Int. Symp. GaAs and Related Compounds, Atlanta Georgia, 1988
- J. M. Luttinger and W. Kohn, *Phys. Rev.* 97, 869 (1955)
- G. A. Baraff and D. Gerbasi, *Phys. Rev. B* 41, 4011 (1990)
- M. G. Duff, *J. Phys. C* 4, 6631 (1992)
- E. Morbach, *Quantum Mechanics*, 2nd ed., p. 91, John Wiley and Sons, New York (1970)
- T. B. Bahder, *Phys. Rev. B* 41, 11992 (1990)
- W. Seifert, X. Lu, and L. Samuelson, *Appl. Phys. Lett.* 62, 949 (1993)
- N. Kobayashi and Y. Kobayashi, *J. Appl. Phys.* 30, 1199 (1991)
- A. Watanabe, T. Ito, M. Iida, and Y. Katsuya, *J. Crystal Growth* 115, 171 (1991)
- I. Kameyama, H. Tanaka, D. E. Aspes, L. T. Iwata, L. C. C. de, J. P. Harbison, and R. Blum, *Appl. Phys. Lett.* 60, 1238 (1992)

Optical Properties of Symmetrically Strained (GaIn)As/Ga(PAs) Superlattices Grown by Metalorganic Vapour Phase Epitaxy

S. Luigen, T.F. Albrecht, T. Marschner, W. Stolz, E.O. Göbel
Wiss. Zentrum für Materialwissenschaften (VZMW) und Fachbereich Physik,
Philipps-Universität, D-34032 Marburg, Germany

Abstract

Symmetrically strained (GaIn)As/Ga(PAs) superlattice structures (symm. SLS) have been realized by metalorganic vapour phase epitaxy (MOVPE). The high structural as well as optical quality of these symm. SLS has been established by detailed high-resolution X-ray diffraction (XRD) and in particular photoluminescence (PL) and excitation spectroscopy (PLE) investigations. The optical recombination at low temperatures is due to excitons localized in statistical potential fluctuations in the (GaIn)As well layer. The exciton binding energy is determined in these symm. SLS to (5.5 ± 1) meV according to a theoretical description of the PLE spectra using a two-dimensional (2D) absorption model. Therefore, the exciton binding energy is a significantly reduced as compared to unstrained GaAs quantum wells, caused by a considerably smaller in-plane hole mass for the top most valence subband. An estimate of this mass based on the determined exciton binding energy yields a value of about 0.05 m_0 .

Introduction

Strained III/V-semiconductor heterostructures are becoming increasingly important with respect to both fundamental physics [1] as well as applications in particular for optoelectronic devices [2]. This is due to the unique possibility of designing the effective band gap and the valence subband structure as a function of strain. For strained layer systems, however, two critical layer thicknesses with respect to strain relaxation by formation of misfit dislocations exist. These are the critical layer thickness of the individual strained layers and in case of SLS that of the total SLS structure. This leads to a severe restriction in the strain level and/or the number of SLS periods, which can be deposited before strain relaxation by misfit dislocation formation occurs. This becomes in particular true for one-side strained material systems like (GaIn)As/GaAs, which have been studied almost exclusively in the literature up to now. In order to overcome the limitations with respect to the critical layer thickness of the total SLS, the concept of symmetrically (symm.) or strain-balanced SLS, i.e. alternating layers with built-in compressive and tensile strain, has been introduced. Symm. SLS structures have been realized using gas source molecular beam epitaxy (GSMBE) [3,4] and metal organic vapour phase epitaxy (MOVPE) [5] in the (GaIn)As/Ga(PAs) material system on GaAs substrate as well as in the (GaIn)PAs on InP system [6,7].

In this work, we present a study of the optical properties of (GaIn)As/Ga(PAs) symm. SLS, which have improved structural properties as compared to those in the literature. The low-temperature photoluminescence (PL) and photoluminescence excitation spectroscopy (PLE) investigations reveal the achieved high-crystalline perfection of these structures. From the PLE studies the exciton binding energy in these symm. SLS is determined as a function of incorporated strain. These data are compared to the case of unstrained as well as one-side strained quantum well structures reported in the literature. From the exciton binding energy the in-plane hole mass is estimated in these symm. SLS as a function of strain, leading to values, which are comparable to the effective electron mass in these symm. SLS.

Experimental

The epitaxial growth of the (GaIn)As/Ga(PAs) symm. SLS has been performed by MOVPE in a commercial equipment (Aix 200, Aixtron Corp.) at a reactor pressure of 100 mbar and a substrate temperature of 650°C. The nominal layer sequence for the series of samples consists of 50 periods of a 9.5 nm (GaIn)As / 1.7 nm GaAs / 9.5 nm Ga(PAs) / 1.7 nm GaAs layer structure. Lattice mismatches of up to $\pm 2.4 \cdot 10^{-2}$ in the individual (GaIn)As

and Ga(PAs) layers have been realized ($x_{In} < 0.17$, $y_P < 0.35$). The thin GaAs intermediate layers in between the ternary (GaIn)As and Ga(PAs) layers have been deposited in order to avoid the possible formation of strained quaternary (GaIn)(PAs) interface layers. Details of the optimization of these symm. SLS structures have been published elsewhere [5].

The optical investigation have been performed in a standard luminescence set-up, using an Ar ion laser or a Ti:Sapphire laser as excitation source. The samples were mounted in a liquid He continuous flow cryostat. The luminescence signal was dispersed by a 1 m monochromator and detected by a GaAs photomultiplier using standard lock-in technique.

Results and Discussions

The structural properties of the symm. SLS have been evaluated by means of high-resolution X-ray diffraction (XRD) in combination with a theoretical description of the experimental XRD pattern using dynamical diffraction theory [3,8]. The average lattice mismatch in the samples in the present study is below $\pm 5 \cdot 10^{-4}$, proving the almost perfect strain balancing in these structures. The linewidth of the symm. SLS XRD satellite pattern is constant in the range of 20° to 30° (FWHM) irrespective of the value of the incorporated strain. These values of XRD linewidth are significantly narrower as compared to those reported so far for the (GaIn)As/Ga(PAs) material system [3,4], approaching the theoretical value of 18° (FWHM) for the above chosen layer structure. These results indicate the high structural perfection of the realized symm. SLS. The structural parameters (compositions, layer thicknesses and strain values) of the samples chosen for the present optical investigations are summarized in Table 1., as obtained from a detailed XRD study [8].

Table 1. Structural parameters of the (GaIn)As/Ga(PAs) symm. SLS as determined by X-ray diffraction analysis

#	x_{In}	$d_{(GaIn)As}$ (nm)	d_{GaAs} (nm)	y_P	$d_{Ga(PAs)}$ (nm)	ΔSLS (nm)
1	0.031	9.35	1.35	0.042	9.35	21.4
2	0.043	9.25	1.35	0.084	9.25	21.2
3	0.052	9.40	1.35	0.102	9.40	21.5
4	0.070	8.90	1.35	0.158	8.90	20.5
5	0.081	8.80	1.35	0.203	8.80	20.3
6	0.095	8.65	1.35	0.229	8.65	20.0
7	0.114	8.60	1.35	0.240	8.60	19.9
8	0.126	8.40	1.35	0.271	8.40	19.5
9	0.141	8.20	1.35	0.292	8.20	19.0
10	0.158	7.70	1.35	0.335	7.70	18.1
11	0.171	7.65	1.35	0.350	7.65	18.0

The low temperature (5 K) luminescence spectra of three samples out of this series, excited with a Ti:Sapphire laser, are shown in Fig. 1 for different In-concentrations x_{In} in the ternary (GaIn)As quantum well layer as indicated. With increasing x_{In} a red shift in energy is observed for both the PL spectra (dotted line) as well as the PLE spectra (full line), reaching a value of 165 meV with respect to the GaAs band gap for the PL line for $x_{In} = 0.171$ and a well width of 7.7 nm. Excitonic resonances also for higher subband transitions are observed in the PLE spectra of the different samples. A description of the subband structure of this novel symm. SLS material system is not attempted in the present study, because of the uncertainties in the values of the carrier effective masses, of the deformation potentials and in particular in the values of the band offsets (see for example the discussion in [9] and references therein for the (GaIn)As/GaAs strained material system).

For the lowest E_{th} transitions these excitonic resonances are resolved from the respective subband transitions, which allows to determine the exciton binding energy as described below. The luminescence spectra for the sample having an In-concentration $x_{In} = 0.114$ are shown in Fig. 2 in more detail around the lowest E_{th} subband transition. The luminescence line (dashed line), having a linewidth of 3.0 meV (FWHM), is "Stokes"-shifted by 2.0

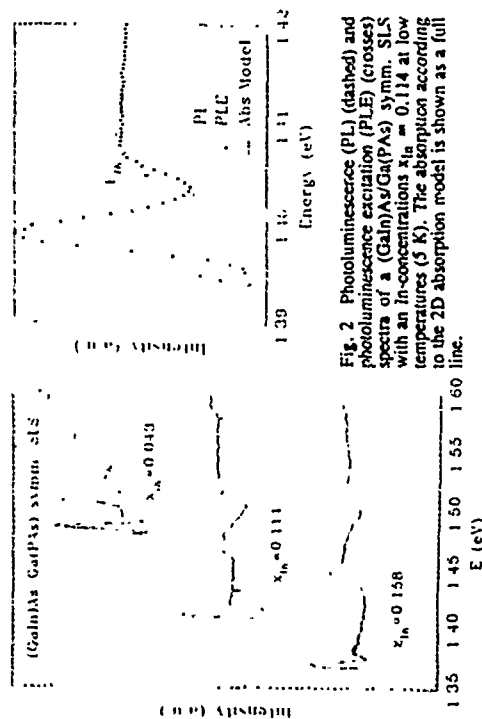


Fig. 1 Photoluminescence (PL) and photoluminescence excitation (PLE) spectra of (GaIn)As/Ga(PAs) symm. SLS samples with different In-concentrations x_{In} at low temperatures (5 K).

meV with respect to the excitonic resonance in the PLE spectrum (crosses). The resonance in the PLE spectrum has a linewidth of 4.3 meV (FWHM). It is characteristic for the symm. SLS in the present study that the PL linewidth is always narrower as compared to the excitonic resonance in the PLE spectra. For excitation densities in the range of 3 mW/cm² to 3 W/cm² using the Ar ion laser (2.41 eV) the energetic position and the linewidth of the luminescence line remain constant. For higher excitation densities (> 3 W/cm²) a broadening of the luminescence line to the high energy side is observed. These findings can be understood in the model of excitons relaxing energetically in a statistically fluctuating potential after resonant optical excitation. For the symm. SLS studied here, these potential fluctuations are caused by the intrinsic statistical alloy fluctuations of the ternary (GaIn)As well material and eventually by fluctuations in well width. For the absorption process the total bandwidth of the potential fluctuations contributes to the linewidth of the excitonic resonance. After excitation, the excitons relax to the local minima of the fluctuating potential before radiative recombination. This leads to a red shift as well as to a narrowing of the excitonic luminescence line with respect to the resonance in the absorption process. A quantitative theoretical description of this behaviour has been given recently using a topographical theory of exciton spectra in terms of statistical properties of a Gaussian random function [10]. According to this description a direct proportionality exists between the Stokes shift and the linewidth of the excitonic resonance in absorption. The coefficient of proportionality is found to be $\gamma \approx 0.553$ [9]. This correlation for the studied (GaIn)As/(GaPAs) symm. SLS is summarized in Fig. 3, where the Stokes-shift of the luminescence line is depicted as a function of the linewidth of the excitonic resonance in the PLE spectrum. A good agreement between the experimental values and the theoretical description, as given by the straight line in Fig. 3, is observed. This behaviour as well as the observation, that the excitonic luminescence line does not show a shift in energy with increased excitation density, prove that the observed

luminescence in these (GaIn)As/Ga(PAs) symm. SLS is due to the recombination of excitons, which are localized in statistical potential fluctuations. No additional localization processes due to extended interface defects and/or charged impurities are observed. This points to the high crystalline perfection, also with respect to the optical properties of the studied (GaIn)As/Ga(PAs) symm. SLS.

In the following, the exciton binding energy in these structures as a function of strain is determined and compared to unstrained quantum well structures. The exciton binding energy is evaluated from a theoretical description of the PLE spectra using the 2D absorption model [11]. This absorption model has been successfully applied to the determination of exciton binding energies for unstrained (AlGa)As/GaAs as well as (GaIn)As/(AlIn)As multiple quantum well heterostructures [12,13]. In the case of the (GaIn)As/Ga(PAs) symm. SLS the absorption model can be simplified as compared to the case of the unstrained quantum well systems. In the strained material system only one subband transition and the corresponding excitonic resonance has to be taken into account. This is due to the strain-induced energy splitting between heavy and light hole subbands, leading to a simpler structure of the two most valence subbands.

For all samples the PLE spectra have been described around the lowest subband transition by using this 2D absorption model, as already included in Fig. 2, with the E_{1h} subband transition energy as indicated by the arrow. A good agreement between the experimental PLE spectra and the 2D absorption model is found also for the other samples studied in this work. The exciton binding energy, as determined by the energy separation of the excitation resonance with respect to the E_{1h} subband transition, is shown in Fig. 4 as a function of the In-concentration in the (GaIn)As well material. An almost constant value for the exciton binding energy of the (GaIn)As/Ga(PAs) symm. SLS of (5.5 ± 1) meV is determined. These values are considerably smaller as compared to the case of unstrained (AlGa)As/GaAs quantum well structures having a similar well width of about 9 nm, where heavy hole exciton binding energies of (13 ± 1) meV were reported [12,14]. For small values of the In-concentration around $x_{In} < 0.07$, the (GaIn)As/Ga(PAs) symm. SLS form a shallow quantum well systems, because of the small band edge difference between (GaIn)As and Ga(PAs) for these concentrations. As we would like to point out, however,

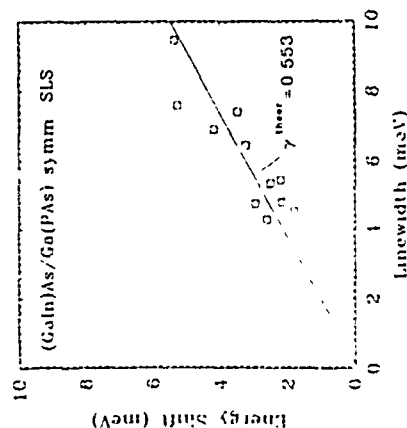


Fig. 3 "Stokes-shift" of the luminescence line of (GaIn)As/Ga(PAs) symm. SLS (squares) as a function of the linewidth (FWHM) of the exciton resonance in the PLE spectrum. The full line represents the theoretical values according to Ref. [9]

for In-concentrations above $x_{In} > 0.10$ the band edge differences in the (GaIn)As/Ga(PAs) material system are comparable or even larger than in the (AlGa)As/GaAs system for Al-concentrations of about $x_{Al} = 0.3$. Therefore, the quantum well depths are expected to be comparable for the two material systems. In this way, the change in exciton binding energy in the two material systems can be directly correlated to the amount of strain incorporated in the (GaIn)As/Ga(PAs) material system. The values reported here for the (GaIn)As/Ga(PAs) symm. SLS system with well widths of about 8 nm seem to be smaller than those in the one-side strained (GaIn)As/GaAs material system. In the latter material system exciton binding energies of 9 meV have been reported for quantum well structures with well widths in the range of 3 to 5 nm for In-concentrations $x_{In} = 0.15$ [15]. However, in the case of the (GaIn)As/GaAs material system, the E_{ex} subband transition is assumed at the top of the edge in the PLE spectrum [15], which does not agree with the theoretical 2D absorption model used in the present study. This difference in the determination of the subband transition energy might be the reason for the apparent discrepancy in exciton binding energies between the (GaIn)As/GaAs system [15] and the (GaIn)As/Ga(PAs) system, studied here.

The significant reduction in exciton binding energy in the strained (GaIn)As/Ga(PAs) material system as compared to the unstrained GaAs/(AlGa)As system leads to the conclusion, that the in-plane hole mass of the top most valence subband is reduced significantly for the strained material system as compared to the unstrained quantum well case. An estimate of the in-plane hole mass from the determined exciton binding energy can be obtained using the analytical description of excitons in a fractional dimension space [16,17]. Because the respective band offsets are unknown for the (GaIn)As/Ga(PAs) material system, we use the infinite well model for the description of the excitonic properties in our structures. This approximation would give a valid description of the experimental results for structures with In-concentrations $x_{In} > 0.10$, having deep enough quantum wells. All parameters entering the calculations (effective electron mass, Luttinger parameters) for the (GaIn)As well layer have been linearly interpolated between the values of the binary GaAs and InAs materials. The fractional dimension parameter σ is defined by

$$\sigma = 3 - \exp(-L_z/a_0^*) \quad (1)$$

where L_z is the well width and a_0^* the effective Bohr radius in three dimensions (3D). For these structures, this parameter is equal to $\sigma = 2.2$, justifying the application of the theoretical 2D absorption model for the description of the PLE spectra. According to this

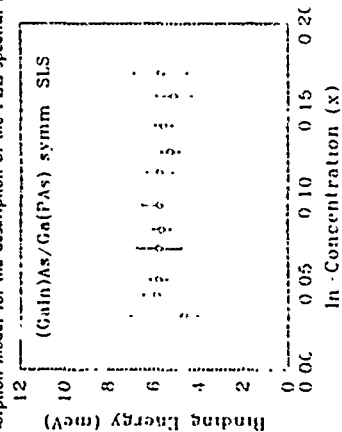


Fig. 4. Exciton binding energy of (GaIn)As/Ga(PAs) symm SLS as a function of In-concentration.

model the exciton binding energy in the quantum well E_b is given by the following expression [17]

$$E_b / E_0^* = (1 + (\sigma-3)/2)^{-2} \quad (2)$$

with E_0^* being the exciton binding energy in 3D. With the experimentally determined value of E_b and the parameter σ the value of E_0^* is obtained. From this value the reduced effective mass μ^* and, thus, the in-plane hole mass can be estimated using the known effective electron mass in the symm. SLS. Using this procedure for the (GaIn)As/Ga(PAs) symm SLS with In-concentrations $x_{In} > 0.10$, estimates for the in-plane hole mass of the top most valence subband of $m_{h,2D}^* = 0.05 m_0$ are obtained. These estimated values are a lower bound of the in-plane masses due to the used infinite potential well model. However, this estimate shows the possibility to design SLS with in-plane hole masses, which are comparable to the effective electron mass of $m_e^* = 0.06 m_0$ in these structures. This behaviour is of great importance in the design of optoelectronic device structures, in particular for semiconductor lasers with improved gain properties.

Summary
In conclusion, (GaIn)As/Ga(PAs) symm. SLS have been realized by MOVPE with lattice mismatches of up to $\pm 2.4 \cdot 10^{-2}$ in the individual constituent ternary layers. The high crystalline perfection is established by sharp XRD pattern with linewidths of 20-30° (FWHM) [5,8]. The almost perfect strain balancing in these structures with an average lattice mismatch of below $\pm 5 \cdot 10^{-4}$ for these symm. SLS results in a significant increase in the critical layer thickness of the total SLS in this highly strained system beyond values of 1 μm . With increasing In-concentration in the compressively-strained (GaIn)As well layer the luminescence peaks show a red shift of up to 165 meV ($\Delta E = 0.17$), $L_z = 7.7$ nm) with respect to the GaAs band gap. No shift of the PL line with increased excitation density in the low excitation density limit is found. Luminescence linewidths are about 3 meV (FWHM), while the Stokes-shift is about 2 meV with respect to the excitonic resonance in the PLE spectrum in optimized structures. The excitonic resonance is clearly resolved from the lowest E_{ex} subband transition with a linewidth typically of 5 meV (FWHM). These findings prove that the luminescence is caused by the recombination of excitons, which are localized in statistical potential fluctuations, caused by the ternary alloy disorder and eventually by well width fluctuations. No additional localization processes due to extended interface defects and/or charged impurities are observed, indicating the high crystalline perfection of these symm. SLS. The exciton binding energy is determined as a function of strain by use of a 2D absorption modelling of the PLE spectra. Values of the exciton binding energy of (5.5 \pm 1) meV are determined for these structures, which are considerably smaller as compared to unstrained (AlGa)As/GaAs quantum wells of similar well width, where excitons binding energies of (13 \pm 1) meV were reported in the literature. This considerable reduction in exciton binding energy indicates that the in-plane hole mass of the top most valence subband is significantly smaller in these symm. SLS. The in-plane hole mass has been estimated based on the analytical description of exciton properties in a fractional dimensional space in the infinite well approximation. This approximation has been applied due to the at present unknown values for the band offsets in the (GaIn)As/Ga(PAs) material system. This estimate leads to values of the in-plane hole mass, which are comparable to the effective electron mass of 0.06 m_0 in these symm. SLS.

Acknowledgments
The authors are indebted to T. Ochs for expert technical support. This work has been supported by the Deutsche Forschungsgemeinschaft (DFG, Bonn).

Impurity-Bound Excitons in Selectively Doped Strained-Layer Quantum Wells in High Magnetic Fields

A. B. Dravubenko^{a,†} and A. Y. Sivachenko^a

*General Physics Institute, R-45, Moscow 117912, Vavilov St.38, Russia
†Utrecht University of Technology, Dept. of Theoretical Physics,
Lorentzweg 1, 3528 CJ Delft, The Netherlands

We report on the theoretical study of quasi two-dimensional (Q2D) excitons bound to the ionized and neutral shallow donor, (D^+, V) and (D^0, V) , in high magnetic fields $B > 10^7$ in strained layer InGaAs/GaAs quantum wells (QWs) with simple valence band; our results are also semiquantitatively applicable to heavy-hole impurity bound excitons in GaAlAs/GaAs QWs. In a quantizing field B_z , due to the absence of kinetic energy (i) the effective mass ratio is not strongly coupled to the problem (so there always exist stable (D^+, V) states), and (ii) both interparticle interactions and that with the Coulomb impurity are strongly enhanced. We expand wavefunctions of an N -particle impurity bound complex with the total angular momentum projection M_z in terms of the non interacting wavefunctions from the constructed complete orthonormal set of Q2D s -states (e) and holes (h) in L_z , thus providing a systematic and convenient scheme for studying bound states [1].

We obtain the energies and wavefunctions of the (D^+, N) and (D^0, N) excitation complexes by diagonalizing the interaction Hamiltonian and derive the energies and oscillator strengths by direct diagonalization of the interaction Hamiltonian; we study their dependencies on the magnetic field strength of interband magneto optical transitions; we study their dependencies on the magnetic field strength H on a QW width, and on the position of the impurity in a QW.

Strictly, a Q2D consideration of the high magnetic field approximation the effect of unbinding B , on the position of the impurity in a QW, is not possible. However, we can consider the effect of the optically active impurity-bound excitons (P^+X^-) , (P^0X^-) and (P^-X^-) in our consideration. We examine (i) Q2D effects, taking into account, in particular, the difference in the wavefunctions of transverse motion of e and h $\psi_{0,1/2}^e \neq \psi_{0,1/2}^h$ and (ii) mixing between Landau wavefunctions of transverse motion of e and h $\psi_{0,1/2}^e \neq \psi_{0,1/2}^h$ in the in-plane wavefunctions of e and h when $\hbar\omega_0 \neq \hbar\omega_{\text{imp}}$ (which give rise to different corrections to the in-plane wavefunctions of e and h when $\hbar\omega_0 \neq \hbar\omega_{\text{imp}}$). We found, that the binding energies of the optically active excitons (in contrast to $\hbar\omega_0 \neq \hbar\omega_{\text{imp}}$) are weakly dependent on B , which is in a qualitative agreement with the experimental results [25]. The possibility to observe unbinding of optically active impurity bound excitons in available magnetic fields B in strained-layer Q2D QWs is discussed.

For contact address: Tel +31-15-781719 Fax +31-15 612156

1. A. B. Davudenko, *Soyuz Lett* 1173 (1993) 311
2. H. Ehrmann, R. Stepiński, G. Martinez and B. Luenne, *Helv. Phys. Acta* 65 (1992) 323

Tp15

OPTICALLY DETECTED MAGNETIC RESONANCE STUDY OF THE TRANSITION FROM PSEUDODIRECT TYPE II TO TYPE I GaAs/AlAs SUPERLATTICES

N.G. Romanov, P.G. Baranov, I.V. Mashkov,
A.S. Ioffe Physical-Technical Institute, Russian Academy of Sciences,
194021 St. Petersburg, Russia

P. Lavalard
Groupe de Physique des Solides - CNRS - Université Paris 6 et 7
Tour 23 - Place Jussieu - F75251 Paris Cedex 05, France

R. Planell
Laboratoire de Microstructures et Microélectronique - CNRS UP20
196, avenue Henri Rivera - F92220 Bagneux, France

Abstract

Optically detected magnetic resonance and level anticrossing spectroscopy have been applied for the first time for a study of GaAs/AlAs superlattices (SL) in the transition region type-II SL (Γ hole in the GaAs layer and X electron in the AlAs layer) - type I SL (Γ hole and X electron both in the GaAs layer). Three kinds of heavy-hole excitons which are typical for type-II SL, for the transition type-II/type-I and for type-I SL, with the lifetime down to 300 ps have been evidenced in the transition region and their g-factors and exchange splitting parameters have been measured.

Introduction

High sensitivity, spatial selectivity and very high resolution of optically detected magnetic resonance (ODMR) [1,2] and cyclotron resonance [3] make it possible to apply these powerful techniques for a study of excitons and unbound carriers in low-dimensional systems such as type-II GaAs/AlAs superlattices (SL) [4-7]. In these SL the lowest X-confined state of the conduction band in the AlAs barrier has a lower energy than the lower-Γ-conduction state in the GaAs well. The low-energy recombination occurs therefore between the electrons in the AlAs and the holes in GaAs layers. The excitons in type-II SL have rather long radiative lifetime (in the μs range) and small exchange energy splitting (in the meV range).

In [6,7] the exchange energy splitting parameters and g-factors of heavy-hole excitons in type-II GaAs/AlAs SLs have been studied by ODMR as a function of the SL composition and the emission wavelength. An importance of the measurements of level anticrossings (LAC) for the analysis of the exciton energy levels has been emphasized.

In this paper we report on the first study of GaAs/AlAs superlattices in the transition region between type-II SL (Γ hole in the GaAs layer and X electron in the AlAs layer) and type-I SL (Γ hole and X electron both in the GaAs layer) using ODMR and LAC spectroscopy.

Experimental results and discussion

The GaAs/AlAs SLs were grown by molecular-beam epitaxy. The sample B223 was a typical type-II SL. The GaAs/AlAs composition (in Å) was 17.4/28 and the emission decay time $\tau = 1$ ns, the sample E913 (18/12 Å, $\tau = 10$ ns) was a pseudodirect SL close to type-II/type-I transition. The sample E913 was grown with the spatial gradient of the GaAs/AlAs composition in the SL plane along the sample length: from 20.8/12.2 Å at $x=0$ to 22.8/11.2 Å at $x=23.4$ nm. A smooth transition from type-II SL ($x=0$) to type-I SL ($x=22$ nm) has been evidenced in this sample at $x = 13$ to 20 nm by the lifetime measurements [8]. Luminescence decay time decreases in this region down to 300 ps.

ODMR and LAC were recorded at 1.6 K by monitoring the circular polarization of photoluminescence or the intensity of one of its circularly polarized components. The excitation light of the argon-ion laser and the emission light were directed along the magnetic field while the sample could be rotated around an axis which was perpendicular to the field. The ODMR spectrometer is described in [2].

Fig. 1 shows LAC spectra in type-II SL B223 and E913 ($x=0$). Two broad resonance signals marked as AC1 and AC2 have different signs and belong to LAC of a non-radiative exciton level 1 with two radiative levels (2 and 3) as shown in the simplified energy level scheme (see Fig. 1a). The levels 1 to 4 correspond to the exciton spin states $|3/2, 1/2\rangle$, $|3/2, -1/2\rangle$, $|1/2, 1/2\rangle$, and $|1/2, -1/2\rangle$, respectively. LAC signals have also been detected as changes of the intensity of one of circularly polarized components of the emission and amounted up to 0.1 of this intensity. Depending on the excitation light intensity and the emission wavelength LAC signals change their value and shape. This seems to be due to a complicated interplay of the pumping, emission and relaxation rates and will be a subject of future studies.

New resonance signals corresponding to cross-relaxation (CR) between the exciton levels have been found in type-II SLs. These signals are more pronounced on the records made at higher intensity of the exciting light (lower curves in Fig. 1a and 1b). Since cross-relaxation implies an interaction between excitons it should be larger at higher light intensity. Some of GaAs/AlAs SLs: a) B223. Observation of LAC and cross-relaxation resonances in addition to ODMR in type-II SL allow to determine the complete set of the exciton exchange splitting parameters. Using the notations of Ref. 6 for the exchange interaction term of the spin-Hamiltonian $J \propto S$ we obtain for the sample B223 (composition 17.4/28 Å): $a_s = 1.486$, $a_n = 2.75$, $c_s = 4.97$ meV.

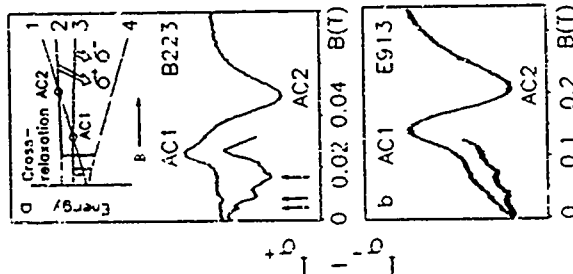


Fig. 1. Level anticrossing and cross-relaxation signals of excitons in type-II GaAs/AlAs SLs: a) B223. Observation of LAC and cross-relaxation resonances in addition to ODMR in type-II SL allow to determine the complete set of the exciton exchange splitting parameters. Using the notations of Ref. 6 for the exchange interaction term of the spin-Hamiltonian $J \propto S$ we obtain for the sample B223 (composition 17.4/28 Å): $a_s = 1.486$, $a_n = 2.75$, $c_s = 4.97$ meV.

$\epsilon_0 = 2.77$ uV, $\epsilon_0 = 0.85$ uV and for the sample E913 (type-II side, composition 20.8/22.4) $\epsilon_0 = 2.6$ uV, $\epsilon_0 = 2.6$ uV. It is to be noted that the exchange parameters vary by ca. 10 percent within the emission line. Variations of ODMR and LAC with the shift of the excitation spot from type-II side ($x=0$) to type-I side ($x=23.4$ mm) of the sample E913 are shown in Fig. 2. Although the emission decay time decreases from 300 ps we could detect ODMR. This implies the existence of excitons with a longer lifetime.

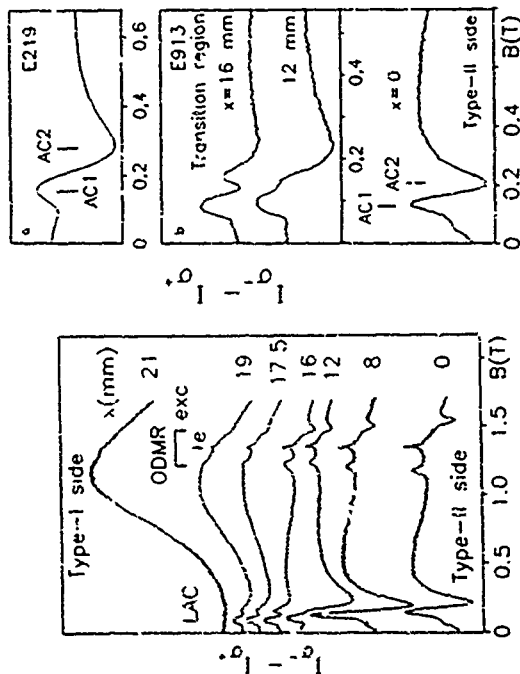


Fig. 2. Circular polarization of the emission under the action of 35 GHz microwaves in the sample E913 recorded with the shift of the excitation spot from type-I to type-II side. $B \parallel z$.

The splitting of the exciton ODMR lines which is proportional to ϵ_0 decreases showing a decrease of the isotropic splitting of the exciton levels. This should result in the shift of LAC signals to lower fields. Such LAC signals are really seen in the transition region but they are superimposed on another set of LAC signals corresponding to larger exchange. The LAC signals in type-II SL (E913, $x=0$) and in the transition region (E913, $x=12.16$ mm and E219) are plotted in Fig. 3 where the x-axis scale is normalized to ϵ_0 . With this scale additional LAC in E913 is similar to LAC in E219. The splitting between the radiative exciton levels has been measured in these samples with the quantum beats techniques [8] and was found to be 8.3 uV and 6.3 uV, respectively. The exciton radiative lifetime was about 20 ns what is too short for ODMR. The limitation arises from the condition $\gamma \ll \Gamma$.

where B_1 is the amplitude of the microwave field. Normally this prevents from the observation of ODMR for $\tau < 100$ ns. LAC effect is due to nonvanishing microscopic interaction (e.g. hyperfine interaction) coupling the approaching states. This interaction may be much stronger than the interaction with the microwave field and allow the observation of LAC for shortly lived states.

One can see in Fig. 2 that a very broad LAC-like signal appears in the sample E913 at the expense of the ODMR and low-field LACs with the shift of the excitation spot to type-I side. This signal is shown in Fig. 4. It seems to belong to excitons in type-I SL. We have observed similar signals in other type-I SL. No splitting between the exciton radiative levels is expected in type-I SL. The hole g-factor can be estimated from the general dependence on the GaAs width [7]. Thus, one can calculate the isotropic exchange splitting and electron g-factor. The positions and angular variations LAC in E913 (type-I side) can be in type-I SL explained with $g=2.6$, $g=0.9$ and $\epsilon_0=320$ uV.

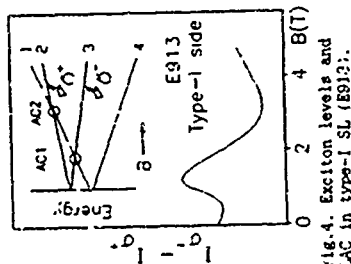


Fig. 4. Exciton levels and LAC in type-I SL (E913).

Conclusions

The measurements of ODMR, LAC and CR allowed us distinguish between three kinds of excitons in GaAs/AlGaSAs. Excitons 11^- with the lifetime ca. 1-10 ns are formed in type-II SLs by the electrons and the holes localized in different layers. They can be detected with both ODMR and LAC techniques. Excitons 11^- with shorter lifetime (down to 1 ns) and larger exchange energy appear in the transition region type-II/type-I where the energy difference between the X_a minima of the conduction band in AlGaS the F -minima in GaAs decreases and tunneling of the electrons between the layers is expected. In type-I SL in which both the electron and the hole are in the same GaAs layer we have detected LAC of excitons 11^- and estimated the exchange energy splitting and the electron g-factor. Since LAC can be detected even for very short exciton lifetimes the LAC spectroscopy seems to be very promising for a study of type-I SL and the transition type-II/type-I.

References

1. B. G. Cavenett, *Adv. Phys.* **30**, 475 (1991).
2. P. G. Baranov and N. G. Romanov, *Applied Magnetic Resonance* **2**, 381 (1992).
3. P. G. Baranov, Yu. P. Vashchunov, R. A. Zhitnikov, N. G. Romanov and Yu. G. Shreter, *JETP Lett.* **28**, 249 (1977).
4. H. M. van Kesteren, E. C. Coenen, W. A. J. A. van der Poel, and C. J. Foxon, *Phys. Rev. B* **41**, 5283 (1990).
5. J. H. Trombetta, T. A. Kennedy, D. Gammon, B. V. Shanabrook, and S. M. Prokes, *Material Science Forum* **83-87**, 1361 (1991).
6. P. G. Baranov, P. Lavallard, R. Planel and N. G. Romanov, *Superlattices and Microstructures* **12**, 327 (1992).
7. P. G. Baranov, I. V. Mashkov, N. G. Romanov, P. Lavallard, and R. Planel, *Solid State Commun.* (1993), in press.
8. C. Gourdon and P. Lavallard, *Phys. Rev. B* **46**, 4644 (1992).

Valence-Subband Level Crossing in GaAs/GaAsP Strained-Barrier Quantum Well Structures Observed by Circularly Polarized Photoluminescence Excitation Spectroscopy

Hironaka Yaguchi, Kazumasa Ota, Keitaro Onabe,
Yoshihiro Shiroki* and Ryoichi Ito

Department of Applied Physics, The University of Tokyo,
7-3-1 Hongo, Bunkyo-ku, Tokyo 113, Japan

*Research Center for Advanced Science and Technology (RCAST),
The University of Tokyo,
1-6-1 Komaba, Meguro-ku, Tokyo 153, Japan

Abstract

We have investigated the level configuration of the valence subbands in GaAs/GaAs_{1-x}P_x ($x = 0.23$) strained-barrier quantum well structures as a function of the well width. Circularly polarized photoluminescence excitation (CPLE) spectroscopy was used to identify the heavy- or light-hole character of the optical transitions. Distinct polarization properties were observed in the strain-split heavy- and light-hole bands in the GaAsP barriers, which indicates the photoexcited electrons in the barriers retain spin orientation well even after the capture into the $n = 1$ lowest energy level. Utilizing this polarization property of the transitions in the barriers, we could distinguish unambiguously the heavy- and light-hole character of the quantum well-related transitions. By varying the well width systematically, we observed the level crossing between $n = 1$ heavy- and light-hole transitions around the well width of 4 nm. This is in good agreement with the calculation based on the effective mass approximation.

1. Introduction

Recently, there has been considerable interest in strained-layer quantum wells and superlattices. Since the introduction of the strain modifies significantly the electronic and optical properties of semiconductor materials, it is expected to extend the possibility of the band gap engineering. In particular, strained-layer quantum wells are promising for the improvement of the semiconductor laser performances [1-4]. Among a number of strained-layer heterostructures, GaAs/GaAsP heterostructures have been widely studied [5-8].

When GaAs/GaAsP quantum well structures are grown on GaAs substrates, GaAsP barrier layers are strained to accommodate the lattice mismatch. In the GaAsP strained barrier layers, heavy- and light-hole bands, which are degenerate at the Γ point in the absence of strain, split into two bands owing to the tetragonal symmetry caused by the strain. Since the GaAsP barrier layers are under tensile strain, the heavy-hole band edge is located lower in energy than the light-hole one.

It is well known that the heavy and light holes in the quantum well are confined by the heavy- and light-hole barriers, respectively, ignoring the spin-orbit coupling effects. If

excited by a σ^+ polarized light made from the linearly polarized light of the Ti:sapphire laser such barrier height is the same, the $n = 1$ heavy-hole subband is located higher in energy than the $n = 1$ light-hole one because of the difference in the effective masses. In the GaAs/GaAsP strained-barrier quantum well structures, however, since the barrier height for heavy-hole is larger than for light-hole, the level crossing of the $n = 1$ heavy- and light-hole subbands should be observed by varying the well width.

In the present study, we report on the observation of the valence-subband level crossing in the GaAs/GaAsP strained-barrier quantum well structures using circularly polarized photoluminescence excitation (CPLE) spectroscopy [9]. For the excitation using the right circularly (σ^+) polarized light, the absorption by the transition associated with the heavy-hole $n = 1$ states, an electron with $m_j = -1/2$ and a heavy-hole with $m_j = -3/2$ according to the selection rule of the transition by circularly polarized light [9]. The circular polarization of photoluminescence is defined as $P = (I_+ - I_-)/(I_+ + I_-)$ depends on the character of the valence subband states related to the emission because the spin orientation of the photoexcited electrons is hardly changed in the relaxation process of energy and momentum while the hole spin is almost relaxed [10]. Here I_+ (or I_-) is the photoluminescence intensity with σ^+ (or σ^-) polarization.

In our CPLE measurements, the detection of the luminescence was fixed at the lowest-energy transition in the quantum well. If the lowest-energy transition is associated with the heavy-hole state, since a down-spin electron ($m_j = -1/2$) recombines a heavy-hole state with $m_j = -3/2$, σ^+ polarized luminescence should be observed. On the other hand, if the lowest-energy transition is associated with the light-hole, the luminescence with the σ^- polarization should be observed in the case of the recombination of a down-spin electron ($m_j = -1/2$) and a light-hole state with $m_j = 1/2$. Thus, we can extract the information about the valence band character from the polarization tendency. However, the CPLE measurement is valid only when there is a reference to judge the valence band character because the lowest-energy level in the CPLE always shows the σ^+ polarization. In our experiment, the reference is the electron-heavy-hole ($e-hh$) interband transition in the GaAsP strained barriers. We succeeded in clearly observing the polarization tendency associated with the heavy- and light-hole transitions in the barriers for the first time. From this polarization tendency of the $e-hh$ transition in GaAsP strained-barrier layers, we could unequivocally determine the character of the transitions and observe the valence-subband level crossing by varying the well width.

2. Experimental

GaAs/GaAsP strained-barrier quantum well structures were grown on GaAs (100) substrates by metalorganic vapor phase epitaxy (MOVPE). They consisted of an undoped GaAs/GaAs_{1-x}P_x ($x = 0.23$) single quantum well structure with the well width ranging from 21 to 174 Å. Strained-barrier layers were about 300 Å thick. The layer thickness and the phosphorus composition were determined by double-crystal x-ray diffraction [7]. Although the barrier layer thickness exceeds the critical thickness [11] the barrier layers were found to be almost fully strained from the asymmetric x-ray diffraction measurements.

CPLE spectra were obtained using a Ti:sapphire laser pumped by an Ar⁺ laser. The CPLE measurements were carried out at 7 K in a closed cycle cryostat. Samples were excited by a σ^+ polarized light made from the linearly polarized light of the Ti:sapphire laser by using a Balunet-Solel compensator. We fixed the detection wavelength at the lower energy side of the lowest-energy photoluminescence peak of the spectrum. The luminescence light containing both the σ^+ and σ^- polarized components was made into broadly polarized light by a V-plate. We could selectively detect the σ^+ or σ^- polarized luminescence light

by rotating the $\lambda/4$ -plate by 90° .

3. Results and Discussion

Figures 1 (a), (b) and (c) are the PLE and circular polarization spectra of GaAs/GaAsP quantum wells with the well width of 21, 82 and 39 Å, respectively. PLE spectra were obtained by the summation of the σ^+ and σ^- polarized luminescence. The label $m0H$ (or L) shown in these figures denotes the transition between the $m=0$ conduction subband and the $n=0$ valence subband of heavy-hole (or light-hole) character, which could be assigned as discussed later. As seen in these figures, the peaks associated with the intersubband transitions are distinctly observed as well as the transitions corresponding to the band gap of the strained GaAsP barrier layers.

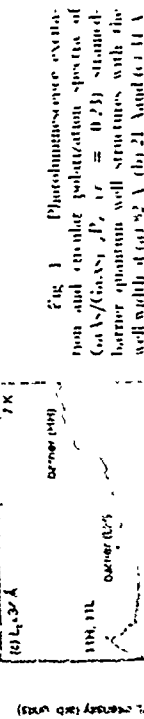
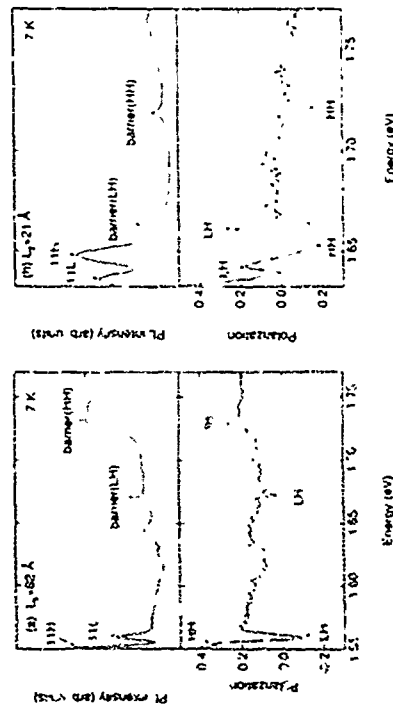


Fig. 1. Photoluminescence excitation and circular polarization spectra of GaAs/GaAsP $p_p \approx 0.25$ strained barrier quantum well structures with the well width of (a) 21 Å, (b) 21 Å and (c) 11 Å.

in Fig. 1(a), the polarization spectrum of the σ^+ (σ^-) transition in the barriers shows clearly the σ^+ (σ^-) polarization tendency. This indicates the photoexcited electrons in the barrier layers retain the spin orientation even after the capture into the well layer and the relaxation process. The lowest-energy transition has the same polarization tendency as the σ^+ (σ^-) transition in the barriers. Therefore, we can assign this transition as the $m0H$ transition. On the other hand, since the second lowest-energy transition has the opposite tendency, it is found to be due to the LH transition. On the contrary, in Fig. 1(b), the σ^+ (σ^-) transition in the barriers exhibits the σ^+ (σ^-) polarization. This indicates that the σ^+ (σ^-) transition in the barriers has the opposite tendency to the σ^+ (σ^-) transition in the well layers. The lowest-energy peak is associated with the LH transition and the second lowest-energy peak is associated with the $m0H$ transition. In Fig. 1(c), only one peak associated with the quantum well level could be observed since the difference between the LH and LH transition energies was very small compared with their linewidths. Moreover, distinct polarization tendency could not be observed all over the spectrum because both the LH and LH transitions were detected simultaneously in this PLE measurement.

It should be noted that the integrated intensity of the lowest-energy peak is larger than the second lowest-energy peak as shown in Fig. 1(a) and that vice versa in Fig. 1(b). This fact reflects that the oscillator strength of the σ^+ (σ^-) transition is larger than that of the σ^- (σ^+) transition. This is in good agreement with the theoretical calculation where the oscillator strength ratio of the σ^+ (σ^-) transition to the σ^- (σ^+) one is predicted to be 3 : 1.¹² Therefore, also from the difference in the integrated luminescence intensity, it is confirmed that the LH transition energy is lower than the LH in the wider well, as shown in Fig. 1(a). On the contrary, the integrated luminescence intensity shows that the LH transition energy is higher than the LH in the narrower well shown in Fig. 1(b). In this way, we can also distinguish the characters of the band on the basis of the luminescence intensity of the transitions.

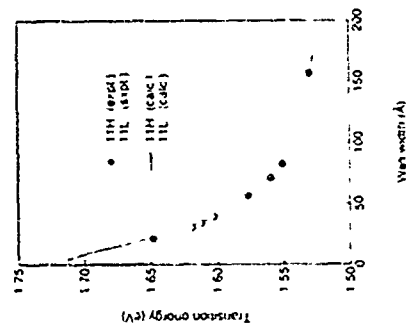


Fig. 2. Well-width dependence of transition energies in GaAs/GaAsP strained barrier quantum well structures. The solid and open circles represent LH and LH transitions obtained by the CPPL measurement, respectively. The solid and dashed lines show the LH and the LH transition energies, respectively, calculated by the effective mass approximation using the band offset ratio $Q = 0.57$.

In Fig. 2, the well-width dependence of the 11H and 11L transition energies is shown. The solid and open circles represent 11L and 11H transition energies obtained by the CPTLE measurement, respectively. The solid and dashed lines are the calculated 11H and 11L transition energies, respectively. The calculation was based on the effective mass approximation assuming the square well potential. The result of the calculation can explain well the experimental data. In this study, we could obtain directly the exact barrier height from the spectra. Thus, we do not have to use the literature values, e.g., the band gap energy of the barrier layer and deformation potentials, which may cause errors in the quantum well level calculation. In the calculation, we used band offset ratio $Q_c \approx 0.37$, where $Q_c = \Delta E_c / (\Delta E_c + \Delta E_v)$, for the GaAs/GaAsP heterojunction obtained from our previous study using photorefraction and photoluminescence measurements.[6, 7] This value is rather larger than that obtained by Van de Walle's model-solid theory ($Q_c \approx 0.39$).[13] The calculation using $Q_c \approx 0.39$ does not agree with the experiment. Therefore this CPTLE result supports our previous studies.

4. Conclusions

We have studied the valence-subband level crossing in the GaAs/GaAsP strained-barrier quantum well structures using CPTLE spectroscopy. Since we succeeded in directly observing the polarization tendency of the transitions in barriers, we could distinguish unambiguously the heavy- and light-hole related transitions in the quantum well. The valence-subband crossover behavior is observed in excellent agreement with the calculation based on the effective mass approximation using the band offset ratio $Q_c \approx 0.37$, which was obtained from our previous studies.

Acknowledgements

We would like to thank S. Miyoshi for his cooperation in the crystal growth and T. Machida for his assistance in measuring CPTLE spectra. We are very grateful to S. Ohtake for his technical assistance. We are also pleased to thank Dr. S. Fukatsu for his valuable suggestion and advice.

References

- [1] E. Yablonovitch and E. O. Kane, IEEE J. Lightwave Technol. LT-4, 304 (1986).
- [2] I. Suenium, L. A. Coldren, M. Yamamushi and Y. Kane, Appl. Phys. Lett. 53, 1378 (1988).
- [3] T. Ohtoshi and N. Chumeur, IEEE Photon. Technol. Lett. 1, 117 (1989).
- [4] L. F. Tien, P. J. A. Thijs, P. I. de Waard, L. J. Busscher and T. van Dongen, Appl. Phys. Lett. 58, 2738 (1991).
- [5] M. E. Picard and N. Lin, Phys. Rev. B 45, 1112 (1992).
- [6] X. Zhang, F. Onabe, Y. Nitta, B. Zhang, S. Fukatsu, Y. Shiraki and R. Ito, Jpn. J. Appl. Phys. 30, L1631 (1991).
- [7] H. Yaguchi, N. Zhang, K. Ota, M. Nagahara, F. Onabe, Y. Shiraki and R. Ito, Jpn. J. Appl. Phys. 32, 344 (1993).

- [8] X. Zhang, F. Onabe, H. Yaguchi, Y. Shiraki and R. Ito, Jpn. J. Appl. Phys. 32, L375 (1993).
- [9] R. C. Miller and D. A. Kleinman, J. Lumin. 30, 320 (1986).
- [10] T. Uemura and L. J. Sham, Phys. Rev. B 42, 7111 (1990).
- [11] J. W. Matthews and A. E. Blakeslee, J. Cryst. Growth 27, 118 (1971).
- [12] M. Yasutani and I. Suenium, Jpn. J. Appl. Phys. 23, L35 (1984).
- [13] C. G. Van de Walle, Phys. Rev. B 39, 1871 (1989).

Magneto-optics of dense electron plasmas in modulation-doped GaInAs/AlInAs single quantum wells

Yong-Hang Zhang¹, James L. Merz¹, M. Potemski², J. C. Maan², K. Ploog^{3,4}

¹QUEST, University of California, Santa Barbara, CA 93106, U. S. A.
²Max-Planck-Institut für Festkörperforschung, Hochfeldmagnetlabor, Grenoble, France
³Max-Planck-Institut für Festkörperforschung, Stuttgart, Germany

Abstract

Dense electron plasmas in modulation-doped GaInAs/AlInAs single quantum well structures have been studied with magnetoluminescence at 2 K. An electron-sheet-concentration (n_s)-dependent band-gap renormalization is measured in the magnetic field. The data agree well with that measured at zero magnetic field. This finding indicates that the inter- and intra-Landau-level many-body interactions are comparable at high filling factor for the electron plasma. A rigid effective-mass increase for electrons with different k -states in the conduction band is observed as n_s decreases, which is contrary to the results obtained for an electron-hole plasma in GaInAs/InP quantum well.

1. Introduction

Recently, the study of the two-dimensional dense electron-hole two-component plasma and electron one-component plasma in semiconductor quantum structures subjected to high magnetic fields has attracted considerable attention.[1-4] There are usually two ways to generate these plasmas, either by using intense photoexcitation or by modulation doping the barrier regions near the well. In the former case, the carriers usually have a much higher temperature than that of the host lattice. Both the photoluminescence and the magnetoluminescence spectra are consequently complicated due to at least two facts: i) the complicity of the valence band structure; and ii) the spatially inhomogeneous distribution of the photo-generated carriers due to lateral diffusion, lateral reabsorption of wave-guided light.[5] In high magnetic fields the density of states of these structures forms discrete Landau levels due to the quantization of carrier

⁴ Present Address: Paul-Drude-Institut für Festkörperelektronik, Hausvogtelplatz 5-7, Berlin, Germany.

movement. The energy splitting ($\hbar eB/\mu$) of the Landau-level peaks in magnetoluminescence is inversely proportional to the reduced mass ($1/\mu = 1/m_e^* + 1/m_h^*$). A recent magnetoluminescence study of the dense electron-hole plasma in GaAs/AlGaAs quantum wells has revealed a large reduction of the reduced mass for magnetoluminescence transitions with increase of the carrier concentration.[1] In addition, a gradient of this reduction of reduced mass as a function of Landau-level index has been observed for the dense electron-hole plasma in GaInAs/InP quantum well structures.[6] However, due to the involvement of the photo-generated holes in the valence band for the magnetoluminescence transitions, it is not possible to unambiguously separate the contributions from different types of carriers to the observed effect.

In the present paper, we report on a detailed magnetoluminescence study of dense electron plasmas in modulation-doped (MD) $\text{In}_{0.7}\text{Ga}_{0.3}\text{As}/\text{AlInAs}$ single-quantum-well (SQW) structures grown on InP substrates. The special design of these samples allows the observation of a collective recombination of the two-dimensional electron plasma with localized photo-generated holes. In this manner, we are able to study the density-dependent properties of the electron one-component plasma in a magnetic field without including the contribution of dense holes in the valence band. It is therefore possible to determine whether the origin of the reduction of the reduced mass results mainly from the conduction-band electron-electron interactions or from the complicity of the valence band. Furthermore, there are several additional advantages provided by this technique. First, since the experiments are performed under very low photoexcitation (0.7 W/cm^2 to 200 W/cm^2), the electron temperature in the samples investigated should be close to that of the lattice. Thermal effects are therefore avoided. Second, the lateral electron distribution is expected to be homogeneous because the light spot size is of the order of 200 microns, two orders of magnitude larger than the photo-generated carrier diffusion length.

II. Experiments

The samples used for the present study are n-type MD GaInAs/AlInAs SQW grown lattice-matched on InP substrates by solid-source molecular-beam epitaxy. The well widths are 90 Å and 110 Å for Sample 1 and 2, respectively. In the center of the GaInAs well a region of 63 Å is lightly doped with Be acceptors to $\sim 3 \times 10^{16} \text{ cm}^{-3}$. The unintentionally-doped AlInAs barrier layers (spacers) adjacent to the well region are 200 Å. Conventional low-temperature (4.2 K) Hall-effect measurements and

magnetoresistance measurements (2 K) are performed to determine the electron sheet concentration (n_s) in the well. A summary of the sample structural and electrical properties is given in Table 1.

The magnetoluminescence spectra are taken in a split-coil superconducting magnet with a Faraday configuration at 2 K. The excitation energy, 7800 Å from a dye laser pumped by a Kr^{+} laser, is slightly above the band-gap (1.5 eV) of the AlInAs barriers in order to minimize the heating of the electron gas in the well. The luminescence from the sample is dispersed with a double-grating monochromator and then detected with a cooled (77 K) Ge detector.

III. Results and Discussion

Fig 1 gives the magnetoluminescence spectra of Sample 1 in different magnetic fields. The photoexcitation density is about 1 W/cm^2 . At zero magnetic field, a rectangular spectrum is observed, which results from the collective recombination of electrons with different k -states and the photogenerated holes localized by the intentionally introduced acceptors. The step-like line shape of the spectrum at 0-field represents clearly the unique feature of the two-dimensional density of states. A detailed discussion of the optical properties of these samples at zero magnetic field can be found in Ref. 7. In high magnetic fields, the luminescence spectrum splits into distinct Landau levels due to the quantization of the electron movement. For instance, at 10 Tesla there are 6 Landau levels fully occupied. The degeneracy of each Landau level is $2eB/h = 4.83 \times 10^{10} \text{ B(T)} \text{ cm}^{-2}$. Therefore, the estimated electron sheet concentration is $2.9 \times 10^{12} \text{ cm}^{-2}$, which is in very good agreement with the value of $2.8 \times 10^{12} \text{ cm}^{-2}$ determined from the Shubnikov-de Haas oscillations of the magnetoresistance. This finding shows that under low photoexcitation the electron concentration *does not* change, providing a direct way to determine the electron concentration in the illuminated part of the sample. In the next section we use this result to obtain the electron sheet concentration under different excitations. This technique is essential to obtain the electron sheet concentration without fitting the experimental line shape. Since the Landau-level degeneracy is only a linear function of the strength of the magnetic field and is independent of the material parameters, we believe that this can more accurately determine the electron sheet concentration than line shape fitting, because the latter depends strongly on the theoretical model and the accuracy of used parameters used, which is not always guaranteed. For instance, due to many-body effects as well as the fact that the momentum (k) is not a good quantum

number in the crystal, the k -selection rule can be partially relaxed. If one uses a k -conserving model, the electron concentration may be overestimated. In addition, another uncertainty arises from the conduction-band electron effective mass, which is found strongly electron-sheet-concentration dependent in the present study, as well as by other authors [1.6]. Therefore, any line-shape-fitting model that does not take this effect into account introduces errors in the estimated electron concentration.

As having been discussed in Ref. 8, above a certain photoexcitation threshold the electron sheet concentration decreases with increase of the photoexcitation density due to a charge transfer effect. Since the photoexcitation energy used in these experiments is higher than the band-gap of the AlInAs barrier material, the electron-hole pairs are mainly generated in the barrier layer. The strong electric field in the barrier layer near the well then drives the photogenerated electrons away from the well into deeper barrier, while the holes are driven into the well. These holes then combine with the electrons in the well, causing the reduction of the electron sheet concentration in the well. Our previous study has shown that this effect can be used to simultaneously monitor the band-gap energy and the electron sheet concentration.[7] In the following we are going to discuss the evolution of the magnetoluminescence spectra as the photoexcitation density changes.

Fig. 2 shows the magnetoluminescence spectra of Sample 2 under different photoexcitation at 7 Tesla. Under low photoexcitation ($< 0.7 \text{ W/cm}^2$) there are 6 Landau levels fully occupied, giving an electron sheet concentration of $2.0 \times 10^{12} \text{ cm}^{-2}$, identical to the value determined by the Shubnikov-de Haas oscillations of the magnetoresistance. When the photoexcitation is increased to 20 W/cm^2 and 200 W/cm^2 , there are only 5 and 3 Landau levels fully occupied, respectively, corresponding to an $n_s = 1.67 \times 10^{12} \text{ cm}^{-2}$ and $1.0 \times 10^{12} \text{ cm}^{-2}$. The peak positions of different Landau levels are plotted in Fig. 3 as function of electron sheet concentration. Careful inspection of Fig. 3 reveals two major findings. First, the peak energies of the Landau levels move to higher energy monotonically as n_s decreases. The lowest Landau-level peak blue shifts about 11 meV to higher energy when the n_s reaches $1.0 \times 10^{12} \text{ cm}^{-2}$. Second, the energy splitting of the Landau levels also decreases monotonically as n_s decreases, from 15.2 meV to 12.5 meV within the n_s range mentioned above. In the next paragraph we address these two findings in more detail.

The lowest Landau level represents the band-gap. When the electron concentration decreases, the band-gap renormalization becomes smaller, which results mainly from the many-body interactions between electrons as well as between electrons and photogenerated holes in our case. This effect causes the blue shift of the lowest Landau level to higher energy. This 11 meV shift agrees well with the theoretical value (11 meV) drawn from the calculation by Jalabert et al. (Ref. 9) for an electron one-component plasma at zero magnetic field, which is confirmed by experimental results[8]. This excellent agreement implies that the density dependent band-gap renormalization is not perturbed by the magnetic field within the electron concentration range used for the present study. This behavior is actually understandable because our experiments satisfy the limit of large filling factor (the cyclotron energy, $\hbar\omega << \text{the Fermi energy, } E_F$). In that case the exchange interaction energy of the two-dimensional electron gas scales according to the total density of carriers, irrespective of their principle Landau level quantum number.[10] It is worth mentioning that the electron-hole two-component plasma generated by intense photoexcitation in some GaAs/AlGaAs QW samples has shown a saturation of the BGR under applied magnetic field,[11] while the photogenerated electron-hole plasma in GaInAs/GaAs as well as GaInAs/InP QWs does not show this saturation up to a very high carrier concentration ($5.0 \times 10^{12} \text{ cm}^{-2}$). [3] This discrepancy in experimental results is not well understood to date. Present data are consistent with those reported in Ref. 3.

The reduction of the Landau-level splitting with decrease of n_s results from the increase of the reduced mass. The splittings (2.5 meV and 15.2 meV) of the lowest Landau level at different electron sheet concentration give reduced m^* 's of 0.0652 and 0.0534, respectively. It is important to emphasize that in the samples investigated here the photogenerated holes are localized. It is thus reasonable to assume that the reduced mass is identical to the effective mass (m_e^*) of electrons. Our results then clearly reveal that the effective mass has a rigid 22% increase for all electrons in the conduction band, when n_s changes from $2.0 \times 10^{12} \text{ cm}^{-2}$ to $1.0 \times 10^{12} \text{ cm}^{-2}$. This tendency of the experimental data agrees qualitatively with the theoretical calculation.[11] The theory predicts a change of only about 2%, an order of magnitude smaller for the corresponding electron concentration range of interest. It is also worth noting that similar effects have been observed in other III/V QWs under intense photoexcitation.[1,6] In those cases the splitting of the Landau-level peaks decreases with increase of the Landau-level index. Since the contribution from the renormalization of the hole effective mass is included, in view of our new

data we believe that the gradient of the Landau-level splitting in those cases is probably due to the contribution of free holes.

IV. Conclusions:

In summary, the electron transfer effect induced by the photoexcitation of a MD SQW has been confirmed by the magnetoluminescence. An electron density-dependent band-gap renormalization for a cold electron plasma has been clearly observed in high magnetic fields. The measured value is very similar to that obtained at zero magnetic field, implying that for the electron system the inter- and intra-Landau-level many-body interactions are comparable at high filling factor. A large increase (22%) of the electron effective mass has been observed for electrons with different k -states.

References:

- 1) M. Potemski, J.C. Maan, K. Ploog, and G. Weimann, *Proceedings of the 19th Int. Conf. on Phys. of Semicond.*, p. 119, J.C. Maan, M. Potemski, K. Ploog, and G. Weimann: *Spectroscopy of Semiconductor Microstructures*, edited by G. Fasol, A. Fasolino, P. Lugli, p. 425, Plenum Press, 1989.
- 2) R. Cingolani, G. C. La Rocca, H. Kalt, K. Ploog, M. Potemski, and J.C. Maan, *Phys. Rev. B* **43**, 9662 (1991).
- 3) L.V. Butov, V.D. Egorov, V.D. Kulakovskii, and T. G. Andersson, *Phys. Rev. B* **46**, 15156 (1992).
- 4) M. Potemski, Y.H. Zhang, M. Hausenblas, J.C. Maan, G. Martinez, and K. Ploog, *Surface Science* **263**, 591 (1992).
- 5) H. Hillmer, S. Hansmann, and A. Forchel, *Phys. Rev. B* **45**, 8782 (1992) and the references therein.
- 6) L.V. Butov, V.D. Kulakovskii, A. Forchel, and D. Gritzmacher, *JETP Lett.* **52**, 121 (1990).
- 7) Y.H. Zhang and K. Ploog, *Phys. Rev. B* **45**, 14069 (1992).
- 8) Y.H. Zhang, R. Cingolani, and K. Ploog, *Phys. Rev. B* **44**, 5958 (1991).
- 9) R. Jalabert, S. Das Sarma and S.-K. Eric Yang, *Phys. Rev. B* **41**, 8288 (1990).
- 10) see the appendix of Ref. 2.
- 11) R. Jalabert and S. Das Sarma, *Phys. Rev. B* **40**, 9723 (1989).

Table 1: A list of the well widths, the electron sheet concentration determined by both conventional Hall-effect (n_{2D}) and the Shubnikov-de Haas (SdH) oscillations of the magnetoresistance (n_{SdH}), as well as the Hall mobilities (μ_H) for the studied samples.

Sample	Well width (\AA)	n_{SdH} (cm^{-2})	μ_H (cm^2/Vs)
1 (#51056)	90	3.8×10^{12}	36,000
2 (#51068)	110	2.2×10^{12}	54,000

Figure Captions:

Fig. 1 Low temperature magnetoluminescence spectra taken in different magnetic fields for Sample 1. The electron sheet concentration in the sample is $2.8 \times 10^{12} \text{ cm}^{-2}$, while the photoexcitation density is about 1 W/cm^2 .

Fig. 2 Low temperature magnetoluminescence spectra taken under different photoexcitation conditions in a magnetic field of 7 Tesla for Sample 2. The highest Landau level is depopulated as the photoexcitation increases. At a photoexcitation density of 200 W/cm^2 , there are only 3 Landau levels fully occupied, while there are 6 under low photoexcitations.

Fig. 3 Peak position of the optical transition for Sample 2. The peak position of the Landau levels as well as their splittings decreases with the decrease of electron concentration.

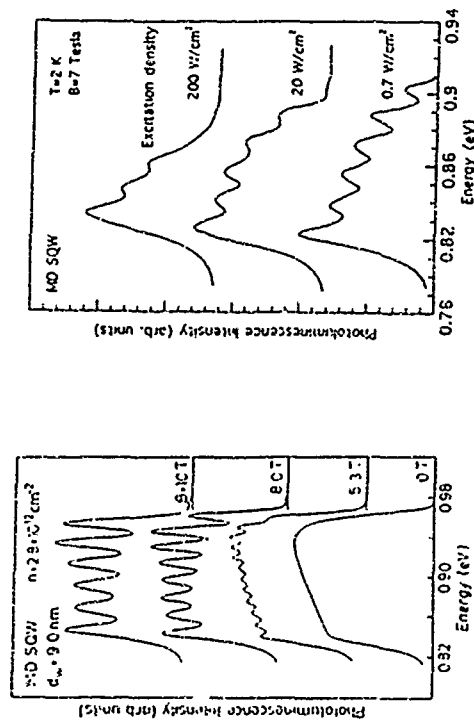


Fig 1

Fig 2

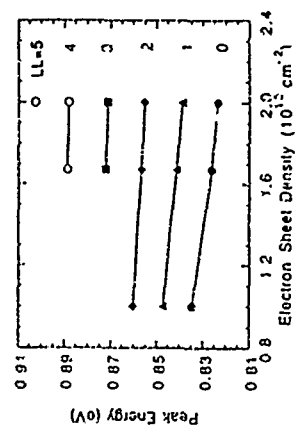


Fig 3

TuP18

High Magnetic Field Effects on the Dynamics of Excitons in a GaAs Quantum Well

S. Haackel¹, A.P. Heberle², M. Potemkin¹, J.C. Maan³, W.W. Rühle², and G. Weimann¹
¹Ordnelle High Magnetic Field Laboratory, JPL-FNRP/CHRS, L.P. 166, F-38012 Grenoble, France
²Max-Planck-Institut für Festkörperforschung, Heisenbergstr. 1, D-70706 Stuttgart, F.R.G.
³High Field Magnet Laboratory, University of Nijmegen, NL-6525 ED Nijmegen, Netherlands
⁴Walter-Schubert-Institut, Techn. Universität München, D-85713 Garching, F.R.G.

Abstract

The time-resolved photoluminescence of excitons in a 9 nm GaAs (Al,Ga)As quantum well structure under high magnetic fields (B_z 2 T) applied along the growth direction is reported. Magnetoexcitons related to the lowest light-hole subband with a well defined orientation of the magnetic moment are selectively excited. The thermalization between the two Zeeman split 1s heavy-hole exciton ground states is found to be accelerated by the magnetic field. Moreover, a decrease of the PL rise time is observed with respect to the zero field case where light-hole excitons and the electron heavy-hole continuum states are simultaneously excited.

Introduction

The energy diagram of quantum well (QW) excitons under high magnetic fields has been intensively studied in recent years by steady-state photoluminescence (PL) but far fewer experiments have focused on the dynamics of magnetoexcitons. Absorption spectra taken with the magnetic field parallel to the growth direction show discrete peaks associated with magnetoexcitons and a disappearance of any free-carrier continuum. Such a modified energy spectrum is thought to change the dynamics of magnetoexcitons when, for instance, thermalization processes are important. Moreover, magnetoexcitons are spin-split by the Zeeman effect according to their different orientation of magnetic moment ($M_S = \pm 1$). Steady-state PL experiments have suggested that the conservation of M_S during the relaxation from the excited states to the 1s ground state is favoured with increasing magnetic field and that the M_S -relaxation time between the two 1s heavy-hole magnetoexcitons with opposite M_S is comparable to the excitonic radiative lifetime [1].

At zero magnetic field the dynamics of QW excitons have attracted great interest [2][3], especially concerning the presumed enhanced radiative recombination due to the size confinement of excitons in QWs [4]. Magnetic moment relaxation times of 30-150 ps depending on the excitation density have recently been found for excitons at zero field [5]. High magnetic fields allow to excite excitonic states of a well-defined magnetic moment selectively by adjusting the laser energy and polarization to a given magneto-excitonic resonance, and to study the carrier dynamics in such a situation. Assuming a time-independent radiative lifetime at any moment, the photoluminescence (PL) intensity is proportional to the population of the magnetoexcitons. The aim of the present paper is to investigate the relaxation processes between the two lowest Zeeman-split heavy-hole magnetoexcitons implying a reversal of the magnetic moment by recording their PL decay. The PL rise gives information about the relaxation processes between the excited and the luminescent exciton state

Experimental Aspects

The sample investigated consists of three GaAs QWs of 90 Å thickness sandwiched between $Al_{0.2}Ga_{0.8}As$ barriers grown on an undoped (100) GaAs substrate. A large barrier thickness (1000 Å) allows us to consider the GaAs layers as decoupled single QWs.

The cw experiments have been carried out with a conventional PL set-up using a Ti:sapphire laser ($\lambda = 720-840$ nm) pumped by an Ar-ion laser. A spectral resolution of 1 Å (0.2 meV) is provided by a 1.5 m-monochromator.

For the time-resolved studies a Si:Ti:Al:8 dye laser ($\lambda = 720-820$ nm, autocorrelation pulse width 7-8 ps) synchronously pumped by a mode-locked Nd:YAG laser ($\nu = 76$ MHz) was used. A two-dimensional synchroscan streak camera in conjunction with a 0.32 m-monochromator was used in order to obtain a simultaneous recording of time- and energy-resolved PL spectra. The spectral and temporal resolutions are of 0.5 meV and 15-25 meV, respectively. Deviations of the electron beam in the streak camera by the stray magnetic field in the wavelength axis were corrected by recalibration for each magnetic field. The effect on the time-axis was negligible. The sample was placed in a He bath cryostat (1.5-2 K) mounted in the centre of a 21 T resistive magnet with the magnetic field and the exciting laser beam parallel to the QW growth direction (Faraday configuration). Achromatic $\lambda/4$ plates and polarizers were used to generate and to detect light of circular polarization.

Steady-state results

For zero magnetic field the luminescence spectra at $T = 2$ K show two transitions related to the 9 nm QWs at 1.550-1.555 eV separated by 1 meV and with a narrow line width of 1-1.5 meV (excitation density ≈ 50 W/cm², inset fig. 1a). The excitation spectra reveal a quite small Stokes shift of 1.3 meV with respect to the high energy PL peak. The dependence of the relative intensities of both transitions on the excitation density enables us to identify the high energy transition as the free ($e_1, h_{1/2}$)-exciton, the low energy transition being attributed to localized exciton states saturated by high excitation densities. For magnetic fields $B_{||} \geq 10$ T four transitions - two pairs of two transitions with opposite polarisation - can be resolved (fig. 1a). Both high energy transitions can be identified as the Zeeman split excitonic transitions (labelled excitons A and B) with opposite magnetic moment $M_S = \pm 1$ for the σ^+ and $M_S = \pm 1$ for the σ^- polarised transition following a diamagnetic shift with increasing $B_{||}$. The two localized transitions are labelled A' (σ^+) and B' (σ^-), respectively.

Excited magnetoexciton states have been probed by PL excitation (PLE) spectroscopy [1]. At 10 meV above the 1s state of the ($e_1, h_{1/2}$)-exciton one can distinguish the 1s state of the light-hole ($e_1, h_{1/2}$)-exciton showing a diamagnetic shift. For magnetic fields $B_{||} > 5$ T the excited states of the heavy-hole exciton (2s, 3s, ...) appear at higher energies than the 1s light-hole exciton with a more or less linear field dependence. It should be stressed that for $B_{||} > 12$ T and due to the narrow PLE linewidths (≈ 1 meV), magnetoexcitons of well defined magnetic moment can be selectively excited by tuning the laser energy resonant to the corresponding transition. As an example, fig. 1a displays the σ^+ and σ^- polarized PL spectra at $B = 14$ T for an excitation of the $M_S = \pm 1$ component of the 1s light-hole state (E_L in fig. 1b). The most striking feature of fig. 1a is the fact that the excitonic high energy peak B is roughly twice as big as peak A. With the reasonable assumption that A and B have the same probability for radiative recombination, it follows that A and B are not thermalized, i.e. their respective populations n_A, n_B do not follow a Boltzmann law $\frac{n_B}{n_A} \approx \exp(-\frac{\Delta E}{kT_L})$, with ΔE the energy separation (≈ 2 meV), and the lattice temperature T_L (2 K).

The preferential population of exciton B is due to the fact that it has the same electronic spin direction as the excited (e_1, h_1) exciton component. The observation of a non-thermal population of excitons A and B under cw excitation has indicated that the magnetic moment reversal time between the exciton B and A is of the same order of magnitude than the radiative lifetime [1]. In a similar way, exciton A can be made dominant with an excitation energy resonant to the M_2^- (-1.7) low energy component of the $1s(e_1, h_1)$ exciton (labelled E_1).

Increasing the magnetic field leads to an increase of the intensity ratio B/A (excitation of E_2). This intensity ratio will be followed in the time-resolved experiments as a function of the magnetic field.

Picosecond PL

Before we discuss the results of the time-resolved luminescence we will summarise the relaxation processes that govern the exciton dynamics (see fig 1b).

- 1 Relaxation from the excited light-hole state (either E_1 or E_2) down to the heavy-hole excitons A and B. Due to an energy difference of 10-11 meV, emission of acoustical phonons is expected to be the relevant relaxation process. When exciting in E_2 relaxation to A with the lifetime τ_{QA} requires reversal of the electron spin (see fig 1b). Relaxation down to B conserves the spin (lifetime τ_{QB}).
- 2 Relaxation from exciton B to A implying reversal of the spin of both electron and heavy-hole is characterized by a lifetime τ_2 . The energy separation between both excitons can amount to 2 meV at $B_{II} = 21$ T. The relaxation therefore requires emission of acoustical phonons.
- 3 Relaxation from the B or A exciton to the corresponding localized state B' and A' respectively with a lifetime τ_{therm} .

The PL decay rate of exciton B is a sum of $1/\tau_2 + 1/\tau_{therm} + 1/\tau_{rad}$ (τ_{rad} being the radiative exciton lifetime) whereas process 1 determines the PL rise-time.

A decay behaviour with two characteristic decay times is observed for the B exciton when the excitation energy coincides with the E_2 light-hole exciton state. In this excitation condition the B exciton is twice as intense as the A exciton in the cw spectra. The time-resolved data have been obtained under excitation conditions such that the time-integrated spectra are equivalent to the cw results. The mean exciton density is estimated to be 10^{10} cm^{-2} . The time evolution of the four PL transitions B, A, B' and A' at $B_{II} = 21$ T is displayed in fig 2a. Note the dominance (by a factor of 10) of the B exciton during the first 120 ps. After a rapid decay with a lifetime τ_1 , the B exciton shows the same decay than the A, A' and B' levels with a longer lifetime $\tau_2 = 180-200$ ps. The two slopes show a different dependence on the magnetic field. For $B_{II} \geq 12$ T a clear decrease of the τ_1 time can be observed. In fact, from the zero field value of $\tau_1(B=0) = 180 \pm 5$ ps the decay time decreases down to $\tau_1 = 44 \pm 2$ ps at $B_{II} = 21$ T. This two-component decay behaviour can be understood by looking at the other transitions represented in fig 2a. The localized states (A' and B') show a monoexponential decay with a slope τ of the same value as τ_2 . Apparently, for longer times ($t > 300$ ps) the exciton B and the localized states A' and B' are in thermal equilibrium, which means, for A' as an example, that the ratio of the populations ($n_{A'}/n_A$) is determined by a carrier temperature T_c following $\frac{n_{A'}}{n_A} = \exp(-\frac{\Delta E_{A,A'}}{kT_c})$. The shorter decay τ_1 can thus be interpreted as a relaxation time from the exciton B to all low-energy states, i.e. exciton A (with the lifetime τ_2) and the localized states A' and B' (lifetime τ_{therm}).

In the opposite excitation condition when the light-hole E_1 levels is excited selectively, the exciton A is preferentially populated and the high energy exciton B is roughly one order of magnitude smaller than the A luminescence. The temporal behaviour of the four PL lines is depicted in fig 2b for $B_{II} = 21$ T. The A exciton shows two decay times (τ_1, τ_2) much like the B exciton in the excitation condition discussed above. It is interesting to note that the τ_1 decay time of exciton A is the same (95 ps) here than under excitation of the E_2 level confirming the interpretation of this time as a thermalization time with the localized states.

In fig 3a the ratio B/A of the PL transients is depicted on a logarithmic scale for different magnetic field values. With the reasonable assumption that both excitons have the same combination probability, the intensity ratio is a direct measure of the ratio of exciton population $I(t) = \frac{n_B(t)}{n_A(t)}$.

Fig 3a shows a dominance of B excitons with respect to A by a factor $I_0 = 10-20$ immediately after the laser pulse ($t=0$) confirming the interpretation of the cw spectra that $\tau_{QB} < \tau_{QA}$ when the E_2 level is excited. The following thermalization process between the populations of B and A is characterized by an exponential decay with an inverse slope of $\tau = 52 \pm 3$ ps at $B_{II} = 21$ T. For $t \geq 250$ ps an equilibrium situation is reached with a temperature of $T_c = 18$ K. The dominance of the B exciton in the cw spectra can now be explained by the preferential population of B at short times. For lower values of the magnetic field the excess population ratio I_0 at $t=0$ decreases with respect to the equilibrium value I_c at long times (see fig 3b). That is the reason for the decrease of the B/A intensity ratio in the cw spectra with decreasing B_{II} . The dependence of τ on the magnetic field is displayed in fig 3b. A decrease of τ with increasing B_{II} is observed. It is not possible to conclusively identify the relaxation time τ with the M_2^- reversal time τ_2 for two reasons. It is not clear for the moment if the equilibrium between all radiative states is not rather determined by the low-energy localized states and it is also possible that the relaxation from B to A occurs through optically inactive intermediate states.

An effect of the magnetic field on the PL rise time can be found for low magnetic fields $B_{II} \leq 8$ T. In fig 4 the PL transients of exciton B under excitation of the light-hole level E_2 at $B_{II} = 0$ and 8 T demonstrate a displacement of t_0 , the time of maximum PL intensity, by roughly 100 ps towards shorter times. The same behaviour is observed for the A exciton under excitation of the light-hole level E_1 . Since the PL decay time is roughly the same for magnetic fields $B_{II} \leq 8$ T, the shift of t_0 must be the result of a shortening of the rise-time. On the other hand, for higher fields ($B_{II} = 12$ T) the displacement of t_0 (not shown here) is a consequence of the decrease of the decay time τ_1 .

Following Ref. 2 and 3 the slow rise-time at $B_{II} = 0$ T is always observed for laser excitation with excess energies of several meV above the heavy-hole exciton. The rise time reflects the slow exciton cooling through emission of acoustical phonons and it is decreased by reducing the excitation energy [3]. In our case, we kept the laser energy resonant with the light-hole exciton that is 11 meV above the heavy-hole exciton. The effect of the magnetic field is to shift the (e_1, h_1) continuum to higher energies than the $K=0$ states of the light-hole exciton for $B_{II} > 5$ T and at $B_{II} = 8$ T only $K=0$ light-hole excitons are excited. The faster PL rise time that we observe is consistent with rise-times found in Ref. 3 under similar excitation densities (10^{10} cm^{-2}) and for a larger QW sample where light-hole excitons could be excited selectively. In our case, the magnetic field allows to modify the energy spectrum and thus to shorten the PL rise time.

Summary, Conclusion

In summary, the time-resolved magneto-optical experiments show that relaxation between the light and heavy-hole magnetoexcitons occur preferentially with conservation of the electron spin

As a consequence, under excitation conditions which favour the higher Zeeman split component, a highly non-thermal population of the $1s$ heavy-hole excitons is created and can be observed during the first 100 ps after the excitation pulse. Increasing the magnetic field leads to a higher degree of spin conservation during the relaxation from the light to the heavy-hole excitons and also to a faster thermalization between the two Zeeman split components. The net result of these two effects explains the cw spectra and the first effect is in agreement with previous interpretations. The faster thermalization, hardly accessible with cw experiments, gives new insight into spin dynamics of magnetic excitons. Further experiments clarifying the role of the localized excitons are needed to identify the thermalization time within the $1s$ heavy-hole exciton components with the magnetic moment reversal time.

In addition, in the range of lower magnetic fields a field-induced decrease of the PL rise-time is observed which can be related to the selective excitation of light-hole excitons for $B_0 > 5$ T in our particular sample. In order to clarify such an effect of the density of states modified by the magnetic field, the low field region should be studied more carefully.

Acknowledgements. We would like to thank H. Kjaath for technical assistance. SH is grateful for a scholarship from the Deutscher Akademischer Austauschdienst (DAAD).

References:

- [1] M. Potemski, J. C. Naeff, A. Fasolino, K. Ploog, and G. Weinmann, Phys. Rev. Lett. 63, 2409 (1989).
- [2] T. C. Damen, J. Shah, D. Y. Oberli, D. S. Chemla, J. E. Cunningham, J. M. Kuo, Phys. Rev. B 42, 7434 (1990).
- [3] R. Eccleston, R. Strobel, W. W. Rohle, J. Kuhl, B. F. Feuerbacher, and K. Ploog, Phys. Rev. B 44, 1395 (1991).
- [4] B. Deveaud, F. Clerot, N. Roy, K. Satzke, B. Sermage, and D. S. Katzer, Phys. Rev. Lett. 67, 2355 (1991).
- [5] T. C. Damen, L. Vina, J. E. Cunningham, J. Shah, and L. J. Sham, Phys. Rev. Lett. 67, 3432 (1991).

Figures

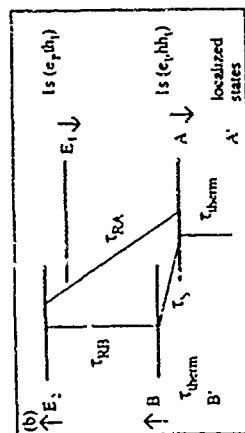
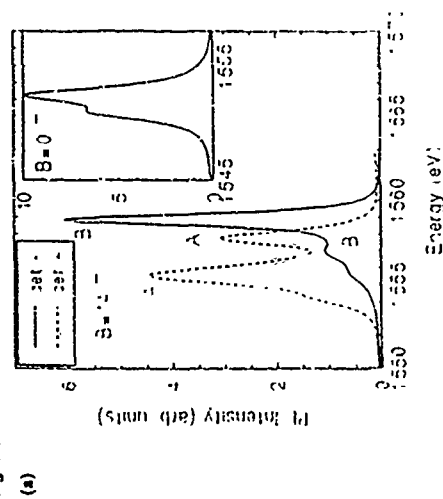
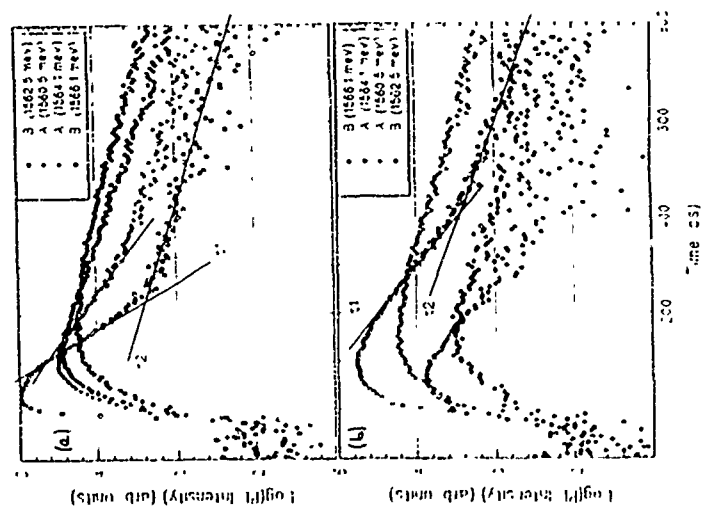


Figure 1. (a) Steady-state PL spectra at $B_0 = 1.4$ T under excitation of the light-hole level E_2 showing the four main transitions B, A, B', and A'. Inset: Steady-state PL spectrum at $B_0 = 0$ T. (b) Representation of the excited $1s$ light-hole levels E_1 and E_2 , the heavy-hole $1s$ ground states A and B and the respective localized states A' and B'. The different relaxation channels with the corresponding lifetimes are indicated (see text).



Optical Properties of Pseudomorphic $(\text{Si})_n/(\text{Ge})_{10-n}$ superlattices

C. Teerchak and G. Theodorou
Department of Physics
Aristotle University of Thessaloniki
54006 Thessaloniki, GREECE

Abstract

Calculations of linear optical properties of short-period pseudomorphic strain-symmetrized $(\text{Si})_n/(\text{Ge})_{10-n}$ superlattices, with $n = 1, 2, 7$, are presented. The calculations are based on an empirical tight-binding model in the three-center representation, which includes third-neighbor and spin-orbit interactions. These strain-layer superlattices (SLS) exhibit a direct gap and their band structure is calculated. Their dielectric function, ϵ_r , is also calculated and the behavior of ϵ_r and ϵ_i structures of ϵ_r is investigated. In addition the absorption coefficient, α , close to the band gap is evaluated, taking into account only direct transitions. It is found that for some cases α has a linear dependence on energy, while for others a more rapid increase. Finally their static dielectric constant is calculated.

Progress in the various methods of crystal growth and in particular the Molecular Beam Epitaxy has provided us with the capability of constructing pseudomorphic strained-layer superlattices (SLS)[1]. This can lead to a greater flexibility in the tailoring of electronic and optical properties in the field of semiconductor microstructures and in turn to the development of technologically advanced devices[2]. The possibility of creating a direct gap semiconductor, out of constituent materials that have indirect gaps, is what makes this class of SLS particularly interesting[3]. Among them the SLS Si/Ge is the most prominent one, because Si is a material with a highly advanced technology based on it, which can not be used directly in optical devices since it is an indirect gap semiconductor. Consequently the formation of a direct gap material based on Si will be of great technological importance.

Various studies have made the prediction that the $(\text{Si})_n/(\text{Ge})_{10-n}$ SLS with $n+m=10$ are the most promising candidates for the creation of direct gap materials, since the resulting folding brings the minimum of the Si conduction band along the growth axis at the center of the Superlattice Brillouin Zone (SBZ)[4-7]. In addition, a tensile lateral strain of the Si layers reduces the energy of the Si -like conduction band minima along the growth axis thus enhancing the possibility of obtaining direct gap materials. This tensile lateral strain can be accomplished by the growth of the SLS on a buffer alloy $\text{Si}_{1-x}\text{Ge}_x$ (001) rich in Ge .

Furthermore, experimental results support the prediction for the formation of (quasi) direct band gap materials. Zuchow et al [8] performed optical measurements on the strain-symmetrized $(\text{Si})_n/(\text{Ge})_{10-n}$ SLS. They found an intense photoluminescence peak close to 0.84 eV, attributing it to a fundamental quasi-direct band-gap transition with an enhanced dipole-allowed transition rate. Monerie et al [9] in photoluminescence measurements on the strain-symmetrized $(\text{Si})_n/(\text{Ge})_{10-n}$ SLS, reported a peak at 0.76 eV, also attributing it to a direct transition. Ojap et al [10] have performed detailed spectroscopic measurements on a series of strain-symmetrized $(\text{Si})_n/(\text{Ge})_{10-n}$ SLS ($n=1, 5, 6$). They have fitted the experimental results for the absorption coefficient close to the absorption edge by the expression $\alpha(\omega) = \chi^2 (\hbar\omega - E_g)^2$. Recently dielectric function spectra have also been reported for some Si/Ge SLS [11]. Many structures appear in these measured optical spectra, and therefore detailed theoretical calculations are needed in order to determine which of these structures are due to superlattice effects.

It is the purpose of this paper to study the optical properties of the strain-symmetrized $(\text{Si})_n/(\text{Ge})_{10-n}$ SLS with $n+m=10$. More specifically we will investigate the in

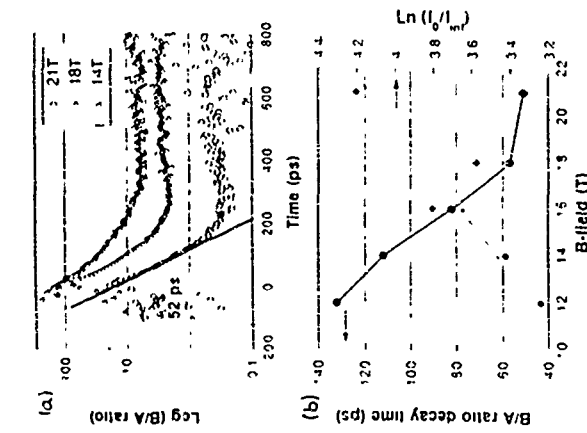


Figure 3. (a) Temporal behaviour of the intensity ratio P/A on a semi-log scale showing an exponential decay with a lifetime τ (≈ 52 ps at 21 T) for the relaxation of the excitation populations at different values of the magnetic field. Note the decrease of τ but the increase of the amplitude I_0 with increasing magnetic field. The curves for 14 and 18 T are vertically shifted for clarity. (b) Dependence of the thermalization time τ and of the excess population $I_0/(1-x)$ upon magnetic field. The dashed and solid lines are guides to the eye.

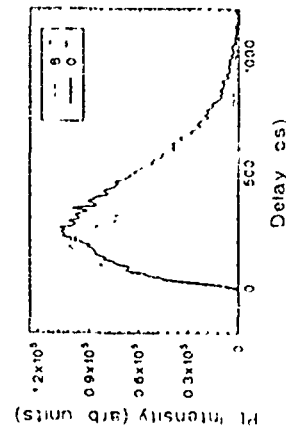


Figure 4. Normalized PL transients of exciton B under excitation of E_2 for 0 and 8 Tesla. The time of maximum PL intensity I_0 is displaced by 100 ps to shorter times at 8 T revealing a decrease of the PL rise-time.

fluence of the SLS composition, n/m , on the previously mentioned properties. The method used is the empirical tight-binding (ETB) in the three center representation with interactions up to third neighbor[7]. The spin-orbit interaction is also included in the calculations. The imaginary part ϵ_2 of the dielectric function was calculated in the range between 0 and 10 eV using the tetrahedral method[11,12] and a uniform mesh of k -points for the integration procedure. It should be noted that only direct transitions are taken into account while phonon-assisted transitions and excitonic effects are ignored. The real part of the dielectric function was obtained by the Kramers-Kronig relation, with the configuration from energies larger than 10 eV taken into account by the tail formula $\epsilon_2(\omega)/(\omega^2 + \gamma^2)$, where γ is taken equal to 4.5 eV and β is determined by the continuity condition[11].

Fig. 1 shows the band structure of the strain-symmetrized SLS $(\text{Si}_x\text{Ge}_{1-x})_n$ along some symmetry lines of the SBZ. Notice that this SLS has a direct gap, its value being $E_g^d = 0.73$ eV, while the indirect gap in the Δ direction parallel to the growth plane has the value $E_g^i(\Delta_1) = 0.94$ eV. The two lowest conduction bands parallel to the growth direction (PZ) exhibit small dispersion which indicates the confined character of these states. As far as

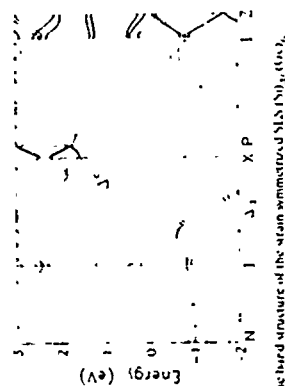


Figure 1 The band structure of the strain-symmetrized SLS $(\text{Si}_x\text{Ge}_{1-x})_n$. The energy dispersion of the rest of the SLS under consideration, strain-symmetrized $(\text{Si}_x\text{Ge}_{1-x})_n$, $(\text{Si}_x\text{Ge}_{1-x})_n$, $(\text{Si}_x\text{Ge}_{1-x})_n$ and $(\text{Si}_x\text{Ge}_{1-x})_n$, our calculations show that close to the fundamental gap the bands exhibit behavior similar to that of $(\text{Si}_x\text{Ge}_{1-x})_n$. This is justified by the same folding of the bands for these SLS.

Fig. 2 shows the dependence of the direct and indirect gaps E_g^d and $E_g^i(\Delta_1)$ respectively, on the composition. All these SLS exhibit a direct gap at Γ point strongly and

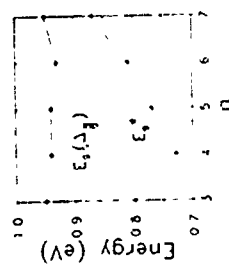


Figure 2 Direct (E_g^d) and indirect ($E_g^i(\Delta_1)$) gap values as a function of the strain-symmetrized $(\text{Si}_x\text{Ge}_{1-x})_n$ composition.

the composition and increases with the exception of $n=1$ with n . The indirect gap $E_g^i(\Delta_1)$ remains approximately constant, independent of the composition. For SLS $(\text{Si}_x\text{Ge}_{1-x})_n$, $(\text{Si}_x\text{Ge}_{1-x})_n$, $(\text{Si}_x\text{Ge}_{1-x})_n$, $(\text{Si}_x\text{Ge}_{1-x})_n$, the lowest transition V_1-C_1 is allowed, is polarized in the interface plane and has significant transition probability. In SLS $(\text{Si}_x\text{Ge}_{1-x})_n$, this transition is prohibited by symmetry. In last case, the lowest allowed transition is V_1-C_2 with energy 0.81 eV and relatively strong probability amplitude.

In order to investigate the optical behavior of the $\text{Si}_x\text{Ge}_{1-x}$ SLS we have calculated the imaginary part of the dielectric function $\epsilon_2(\omega)$. In fig. 3(a,b) we show the spectra of $\epsilon_2(\omega)$ for SLS $(\text{Si}_x\text{Ge}_{1-x})_n$ with $n=1, 3, 5$ and 7 , and for two polarizations ϵ_2^{\parallel} and ϵ_2^{\perp} denotes the average value $(\epsilon_2^{\parallel} + \epsilon_2^{\perp})/2$ parallel to the interface while $\epsilon_2^{\parallel} = \epsilon_2^{\perp}/2$ is the component along the growth direction. At this point we should mention that SLS $(\text{Si}_x\text{Ge}_{1-x})_n$ and $(\text{Si}_x\text{Ge}_{1-x})_n$ have orthorhombic symmetry and as a result they exhibit in addition an anisotropy in the interface plane. This anisotropy is relatively small. The anisotropy between the components ϵ_2^{\parallel} and ϵ_2^{\perp} has its larger value in the region 2-4 eV. For energies larger than 4 eV this anisotropy becomes smaller.

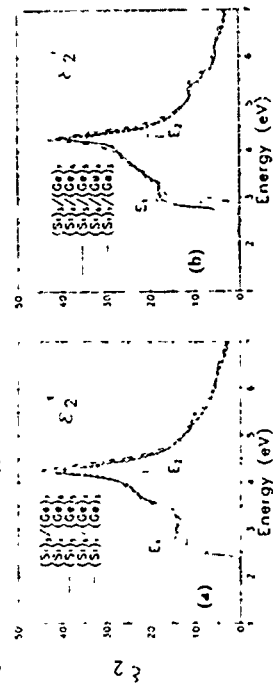


Figure 3 Imaginary part of the dielectric function $\epsilon_2(\omega)$ for the strain-symmetrized SLS $(\text{Si}_x\text{Ge}_{1-x})_n$ with $n=1, 3, 5$ and polarization (a) parallel and (b) perpendicular to the interface.

In the dielectric function spectra we observe mainly two structures. The first is in the region 2-3.5 eV, is relatively extended, and comes from the corresponding E_1 -structures of the constituent materials, Si and Ge. The E_1 -transitions of Si and Ge differ significantly (~ 1.2 eV). A consequence of this is the E_1 -type structure in the SLS spectrum to be relatively extended and significantly influenced by the composition of the SLS. As the number of Si layers increases the E_1 structure is shifted to greater energies and becomes more Si-like. The second and more intense structure around the 4 eV has its origin in the E_2 -structures of the constituent materials. The E_2 -structures of Si and Ge appear in similar energies and consequently the E_2 peak in the SLS will be sharp and its position will not be affected by the composition of the superlattice. The amplitude of the E_2 -peak increases and the one of E_1 decreases with an increase of the Si content of the SLS, resulting in a conservation of total strength. In the scale used in fig. 3, the behavior of ϵ_2 close to the absorption edge is not visible. The contribution to ϵ_2 in this region comes mainly from the quasi-direct transitions that are characterized by transition probabilities 2-3 orders of magnitude smaller than the corresponding ones of the average crystal.

The absorption coefficient of strain-symmetrized $(\text{Si}_x\text{Ge}_{1-x})_n$ SLS with $n=1, 3, 5, 7$, close to the absorption edge and for polarization parallel and perpendicular to the growth plane is shown in Fig. 4. For both polarizations the absorption coefficients for SLS $(\text{Si}_x\text{Ge}_{1-x})_n$ has stronger variation because of the larger values of the transition probabilities for SLS $(\text{Si}_x\text{Ge}_{1-x})_n$ and $(\text{Si}_x\text{Ge}_{1-x})_n$, and polarization along the $[100]$ direction.

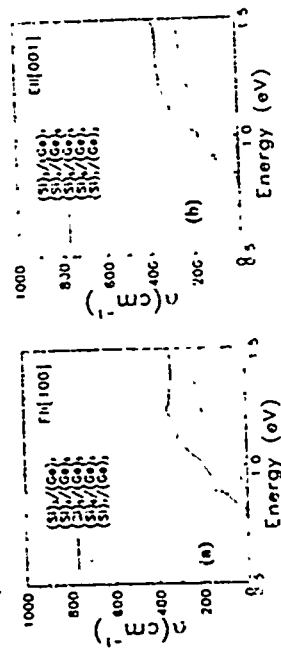


Figure 4. Change in coefficient for the strain uniaxialized $n_s(n_s)/(n_s)_{10,0}$ with $r = 1$. (a) parallel and (b) perpendicular to the interface.

the absorption coefficient close to the gap exhibits more or less a linear behavior with respect to the energy. For the rest of the SiS as well as for polarization along the [100] direction n exhibits a more rapid increase. Consequently, in a sample where the number of layers, as well as the polarization, are not sharply defined the absorption coefficient may exhibit behavior different than the linear one.

The real part of the dielectric function is obtained from ϵ_1 using the Kramers-Kronig relations. The static dielectric constant of the superlattice is then obtained. The results for strain-symmetrized $(SiS)/(Ge)_{10,0}$ and for polarization parallel ($\epsilon_{1||}$) and perpendicular ($\epsilon_{1\perp}$) to the growth plane are shown in table I. The value of ϵ_{10} decreases

Table I. Static dielectric constant for the strain uniaxialized $n_s(n_s)/(n_s)_{10,0}$ and $n = 1$, 7 and polarization parallel and perpendicular to the interface

	3	4	5	6	7
$\epsilon_{1 }$	12.3	12.0	11.6	11.4	11.1
$\epsilon_{1\perp}$	12.2	11.9	11.4	11.2	11.0

with the increase of n . This can be understood from the fact that the dielectric constant of bulk Si (equal to 11.7) is smaller than the corresponding one of Ge (equal to 15.8) [15].

ACKNOWLEDGMENTS. This work has been supported in part by the ESPRIT Basic Research Action N° 7128.

REFERENCES

1. E. Kasper, H. J. Hertzog, H. Dambkes, and G. Abstreiter in *Layered Structures and Epitaxial* edited by J. M. Gohman, G. C. Osbourn and R. M. Tromp. Materials Research Society Symposium Proceedings, vol. 56 (Materials Research Society, Pittsburgh, PA, 1986).
2. H. Presting, H. Kibbel, M. Jaros, R. M. Turton, U. Menzinger, G. Abstreiter, and H. O. Grimmelshaus, *Semicond. Sci. Technol.* 7, 1127 (1992).

3. U. Gnutzman and K. Clausenker, *Appl. Phys.* 3, 9 (1974).
4. S. Surpathy, R. M. Martin and C. G. Van de Walle, *Phys. Rev. B* 38, 13237 (1988).
5. R. J. Turton and M. Jaros, *Mater. Sci. Engineering B* 7, 17 (1991).
6. U. Schmidt, N. E. Christensen, M. Alouani and M. Cardona, *Phys. Rev. B* 43, 14397 (1991).
7. C. Tserbak, H. M. Polatoglu and G. Theodorou, *Phys. Rev. B* 47, 7114 (1993).
8. R. Zuchai, K. Ebert, G. Abstreiter, E. Kasper and H. Kibbel, *Phys. Rev. Lett.* 64, 1035 (1990).
9. U. Menzinger, J. Brunner, E. Fress, M. Gail, O. Abstreiter, H. Kibbel, H. Presting and E. Kasper, *Thin Solid Films* 222, 227 (1992).
10. J. Olajos, J. Engvall, H. O. Grimmelshaus, H. Kibbel, E. Kasper and H. Presting, *Thin Solid Films* 222, 243 (1992).
11. U. Schmidt, J. Humlicek, F. Lukes, M. Cardona, H. Presting, H. Kibbel, E. Kasper, K. Ebert, W. A. Schreier and G. Abstreiter, *Phys. Rev. B* 45, 6793 (1992).
12. O. Aivinen and O. K. Andersen, *Solid State Commun.* 9, 1763 (1971).
13. G. Lehmann and M. Tauc, *Physica Status Solidi* b54, 469 (1972).
14. Y. Petroff, M. Balkanski, J. P. Walter and M. L. Cohen, *Solid State Commun.* 7, 459 (1964).
15. C. Kittel, *Introduction to Solid State Physics* (John Wiley, New York 1970).

TuP20

Bang-edge Photoluminescence of SiGe/strained-Si/SiGe Type-II Quantum Wells on Si(100)

D. K. Nayak, N. Usami, H. Sunamura, S. Fukatsu, and Y. Shiraki
Research Center for Advanced Science and Technology (RCAST),
The University of Tokyo, 4-6-1 Komaba, Meguro-ku, Tokyo 153, Japan.

ABSTRACT

High-quality completely relaxed SiGe buffer layer is grown on Si(100) by gas source molecular beam epitaxy. Pseudomorphic Si layer is grown on this relaxed SiGe buffer to form SiGe/strained-Si/SiGe type-II (staggered) quantum wells. Intense bang-edge photoluminescence is observed from these quantum wells for the first time. Quantum confinement effect in SiGe/strained-Si/SiGe type-II quantum wells is demonstrated from the systematic shift of photoluminescence energy peaks with the width of the quantum well. Transitions from the strained-Si quantum well are identified as radiative recombination of excitons, which are confined into the quantum well.

Epitaxial Si_{1-x}Ge_x layers on Si are being studied extensively for potential use in Si-based optoelectronic device technology. In particular, strained-layer (Si)_{1-x}(Ge)_x superlattices (SLS) are important for possible efficient light emitting applications in the near-infrared region. (Si)_{1-x}(Ge)_x SLS show enhanced photoluminescence (PL) properties compared to indirect bandgap Ge and Si. Also, the possibility of artificially producing quasi-direct bandgap in SLS has generated much interest in (Si)_{1-x}(Ge)_x SLS [1-12]. In such SLS, Si layer must be under lateral tensile strain, which is produced by growing alternating layers of pure Si and pure Ge on a relaxed SiGe buffer layer. In this case, Si and Ge layers are strained, and radiative interband recombination occurs between minibands of conduction and valence bands.

Earlier report on the photoluminescence study of (Si)_{1-x}(Ge)_x SLS was controversial because of the poor quality of SiGe buffer [9,10]. With the recent development in SiGe buffer layer technology, however, enhanced luminescence from (Si)_{1-x}(Ge)_x SLS grown on graded SiGe buffer has been obtained [12]. The luminescence is described in terms of recombination of excitons localized at random potential fluctuations in SLS. However, no study on the properties of relaxed SiGe/strained-Si/relaxed-SiGe quantum well, which forms type-II (staggered) heterostructure and acts as the basic block for many optical devices, has been reported. In this letter, we report for the first time a systematic study of band edge photoluminescence characteristics of SiGe/strained-Si/SiGe quantum wells, which are grown on a thick relaxed Si_{1-x}Ge_x in buffer layer on Si(100). Quantum confinement effects and photoluminescence properties of excitons in this quantum well are presented.

Basic requirement for the growth of strained-Si layer is to obtain a good quality relaxed SiGe buffer layer on Si substrates. Recently, it has been shown that a high quality buffer layer can be grown by grading Ge concentration in the buffer layer [5]. In this study, we use step-graded buffer layer which is grown by gas source MBE (Daiko Sanzo VLE-S2020) at 800°C [16]. The starting material consists of 1-p-10% 5-10 Ω-cm, Si(100) wafer, 3000 Å Si buffer, 3.8 μm step graded Si_{1-x}Ge_x buffer (0 to 18% Ge in 9 steps), and 2.5 μm Si_{1-x}Ge_x in buffer cap layer. Five quantum wells with equal well width were grown on this buffer layer at 700°C. The barrier between adjacent wells was 350 Å Si_{1-x}Ge_x in, which eliminates any coupling between the quantum wells. All epilayers were undoped.

PL spectra were recorded using a standard lock-in technique. A multi-line argon laser was used for excitation. Signal was measured acoustically using a 1 m dispersive

monochromator, and was detected by a liquid-nitrogen cooled Ge photodetector. Temperature control was achieved by a closed-cycle refrigerator.

Figure 1(a) shows PL spectra from a thick (6.3 μm) step-graded relaxed Si_{1-x}Ge_x buffer layer at 4.2K. A peak at 1.093 eV, denoted as SUB10, is due to TO assisted excitonic recombination in Si substrate. A sharp peak at 1.072 eV corresponds to NP transition from the relaxed buffer layer. Transitions from buffer (barrier) layer are denoted by "B". Full-width at half-maximum of this peak is 4 meV at 4.2K, which shows that the top region of the buffer is of good quality. Phonon-assisted momentum-conserving transverse-acoustic (TA) and transverse-optical (TO) replicas are found at lower energies, TA at 16 meV, TO(Ge-Ge) at 36 meV, TO(Ge-Si) at 51 meV, and TO(Si-Si) at 38 meV. Locations of these energy peaks agree well with PL measurement results on SiGe buffer layers by others [17]. Complete relaxation of the buffer layer was confirmed by x-ray diffraction measurements. Broad peaks at 0.880, 0.906 and 0.923 eV are identified as dislocation- and point defect-related transitions D2, D3 and D4 [18,19]. Dislocation-related transition at 0.81 eV, D1, appears only for thin buffer layers, but it disappears as the buffer layer thickness exceeds 3 μm. These dislocation-related PL, D1-D4, have been also reported for fully relaxed SiGe buffer layers grown by solid source MBE [15,19].

Five quantum wells with equal well width were grown on the above buffer layer at a lower temperature (700°C) in order to avoid thermal relaxation of strain and Ge/Si interdiffusion in the quantum well. PL spectra from the multiple quantum wells are shown in Figure 1(b). All transitions from the strained-Si quantum well are denoted by "X". Well and barrier widths were 10 Å and 350 Å, respectively. Figure 1(b) looks identical to Figure 1(a) except that two new peaks (as a pair) appear at 0.983 and 1.043 eV in Figure 1(b). We assign the peak at 0.983 eV to be TO phonon-assisted band-edge transition of confined excitons in strained-Si quantum well. As shown in Figure 2, type-II band alignment results at the strained-Si/relaxed-SiGe-buffer heterointerface [20]. Therefore, TO-assisted excitonic transition occurs between the confined conduction band state (lowest lying in energy) of strained-Si quantum well and the top of valence band of SiGe buffer layer (Figure 2). The peak at 1.043 eV in Figure 1(b) can be assigned to NP transition from the quantum wells, and always appears as a pair with the TO-assisted transition. These two peaks were separated by 46 meV, which corresponds to TO phonon energy of Si-Si bond. In case of this narrow strained-Si quantum well, the excitonic wave function penetrates considerably into SiGe barriers, where NP transition is allowed due to the randomness of alloying, resulting in NP transition from the confined conduction band state of strained-Si layer (Figure 2).

In order to demonstrate quantum confinement effect in the SiGe/strained-Si/SiGe quantum well, samples with different quantum well width were prepared. In these samples, the buffer layer structure was kept exactly the same. Well width dependent PL peak energy shifts for excitonic phonon-assisted as well as NP transitions are shown in Figure 3. Figure 3(a) is PL spectrum from the buffer layer without any quantum well. As before, transitions from strained-Si quantum well are marked by "X". For a given well width, the high-energy peak ("X") is NP free excitonic transition from the quantum wells, whereas the low-energy peak is its TO replica. Both these peaks move to lower energy as the quantum well width is increased. Figures 3(a) and (b). As the well width is increased further, the relative intensity of NP peak becomes weaker with respect to its TO replica. Figures 3(c), (d) and (e). This is because the penetration of excitonic wave function into SiGe barriers diminishes with increasing well width, and therefore the NP transition probability becomes smaller. TO-assisted transition for the 10 Å well appears at 0.986 eV, and moves down to 0.947 eV for the 22 Å well. This shift of 19 meV can be used to estimate the conduction band discontinuity at the relaxed-Si_{1-x}Ge_x/strained-Si heterointerface. Using an envelope function calculation, this is found to be about 86 meV.

Temperature dependence of excitonic transitions from strained-Si quantum wells was found to be different from that of SiGe buffer (Figure 3). With increasing temperature, the NP transition intensity from the buffer layer, BVP, diminishes rapidly. At 25K, the NP peak almost disappears, while the transition from the quantum well, XTO, remains unchanged compared to its 16K value. XTO can be observed until 40K. This shows that the electrons are effectively confined into the quantum well and that strained-Si layer may provide a less nonradiative pathway for carrier recombination compared to its SiGe buffer counterpart.

In summary, intense band-edge photoluminescence for SiGe/strained-Si/SiGe type-II (staggered) quantum wells is reported for the first time. Quantum confinement effect in this quantum well is clearly demonstrated from the systematic shift of PL energy peaks with the width of the quantum well. Transitions from the strained-Si quantum well are identified as radiative recombination of excitons, which are confined in the quantum well.

Acknowledgement: We would like to thank H. Oki, Y. Ohnori, T. Ohnishi and K. Gushima of Daiichi-Kosha for their technical help in using gas source MBE. We also like to thank S. Ohtake of RCAI for technical assistance.

References

1. R. People and S. A. Jackson, *Phys. Rev. B* **36**, 1310 (1987).
2. M. S. Hybertsen and M. Schlüter, *Phys. Rev. B* **36**, 9983 (1987).
3. T. P. Pearsall, J. Beyk, L. C. Feldman, J. M. Bower, J. P. Manassens, and A. Chumazov, *Phys. Rev. Lett.* **68**, 729 (1987).
4. S. Froyen, D. M. Wood, and A. Zunger, *Phys. Rev. B* **37**, 6893 (1988).
5. S. Sathpathy, R. M. Martin, and C. G. Van de Walle, *Phys. Rev. B* **38**, 13237 (1988).
6. E. A. Moise, G. F. A. van de Walle, D. J. Graves, A. A. van Gorkum, and C. W. T. Bulle-Lieuwma, *Appl. Phys. Lett.* **56**, 340 (1990).
7. H. Okumura, K. Miki, S. Mizawa, K. Sakamoto, T. Sakamoto, and S. Yoshida, *Jpn. J. Appl. Phys.* **28**, 1189 (1989).
8. R. Zachai, K. Ebert, G. Abstreiter, E. Kasper, and H. Kibbel, *Phys. Rev. Lett.* **64**, 1033 (1990).
9. U. Schmid, N. E. Christensen, and M. Cardona, *Phys. Rev. Lett.* **68**, 2610 (1992).
10. R. Zachai, K. Ebert, G. Abstreiter, E. Kasper, and H. Kibbel, *Phys. Rev. Lett.* **68**, 2611 (1990).
11. J. Chojas, J. Engvall, H. G. Grimmeiss, U. Menzinger, G. Abstreiter, H. Kibbel, E. Kasper, and H. Preising, *Phys. Rev. B* **46**, 12835 (1992).
12. U. Menzinger, G. Abstreiter, J. Chojas, H. Grimmeiss, H. Kibbel, H. Preising, and E. Kasper, *Phys. Rev. B* **47**, 4099 (1993).
13. K. H. Jung, Y. M. Kim, and D. L. Kwong, *Appl. Phys. Lett.* **56**, 1775 (1990).
14. F. K. LeGoues, B. S. Meyerson, and J. F. Morar, *Phys. Rev. Lett.* **66**, 2903 (1991).
15. E. A. Fitzgerald, Y. H. Xie, M. L. Green, D. Brusen, A. R. Kortan, J. Michel, Y. J. Mi, and B. E. Weir, *Appl. Phys. Lett.* **59**, 811 (1991).
16. S. Fukatsu, H. Yoshida, A. Fujiwara, Y. Takahashi, Y. Shiraki, and R. Ito, *Appl. Phys. Lett.* **61**, 804 (1992).
17. J. Weber and M. L. Alonso, *Phys. Rev. B* **40**, 5683 (1989).
18. R. Sauer, J. Weber, J. Stolz, E. R. Weber, K. H. Kuster, and H. Alexander, *Appl. Phys. A* **36**, 1 (1985).
19. V. Higgs, E. C. Lightowler, E. A. Fitzgerald, Y. H. Xie, and P. J. Silverman, *J. Appl. Phys.* **73**, 1952 (1993).
20. R. People, *IEEE J. Quantum Electronics* **22**, 1696 (1986).

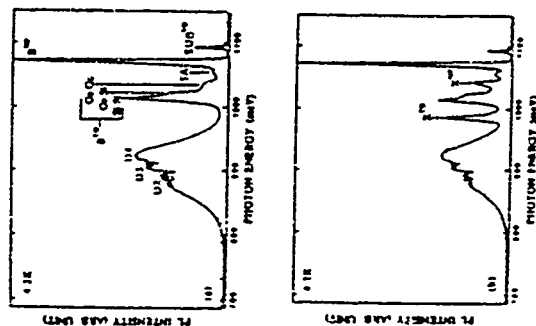


Figure 1. (a) PL spectra at 4.2K from a fully relaxed thick (6.3 μm) step-graded SiGe buffer layer. (b) PL spectra at 4.2K from 10Å strained-Si quantum wells grown on this buffer layer at 700°C.

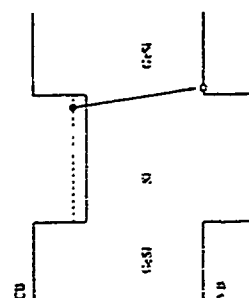


Figure 2. Schematic type-II band alignment at relaxed-SiGe/strained-Si heterointerface.

TuP21

On the two dimensional character of absorption spectra of Si/Ge superlattices

H.M. Polatoglu

Physics Department
Aristotle University of Thessaloniki Thessaloniki, GR-54006, GREECE

e-mail: caez@physics.upat.ac.il

fax: +30 (0) 51 206135

The optical properties of strained $(\text{Si})_n/(\text{Ge})_m$ superlattices grown on the [001] surface of $\text{Si}_{1-x}\text{Ge}_x$ have attracted recently great interest. Such modulated semiconductor structures are by now the main ingredients of many integrated optoelectronic devices developed on Si. Although much progress has been achieved in the past, it is the idea of strained-symmetrized superlattices which enabled absorption measurements on well that attracted much interest [1,2]. These absorption spectra indicate the existence of an absorption edge which can be related to the superlattice. The energy dependence of the absorption coefficient is found to be the one which for the case of the bulk semiconductor is connected to an indirect absorption edge. Theoretical work on the absorption spectra of these superlattices indicated that a large portion of the experimentally observed absorption spectral can be related to direct band-to-band transitions [3]. Converting the energy of the absorption edge a good agreement is found between theory and experiment. Theory predicts an almost linear energy dependence for the absorption coefficient, in this agreement with the experimental findings. However, as time, the energy dependence is not the one expected for such two-dimensional structures. The aim of the present work is to investigate the contribution of each direct transition to the absorption spectra and analyze their three- or two-dimensional character. To achieve these we decompose each contribution into the density of available superlattice states and the polarizability. It is found that polarizability is as important in determining the absorption spectra as the density of available states. Furthermore, the signature of direct transitions from the Z point of the superlattice Brillouin zone is predicted to be presented by a structure in the absorption spectra about 1 eV above the absorption onset. Therefore, if experimental results are available at the above energy range, there would be a good chance to observe direct superlattice transitions away from the Brillouin zone center.

[1] J. Olajos, J. Engvall, H.G. Grunmuss, J. Kibbel, E. Kasper, and H. Presting, International Conference on Electronic Materials, EMRS 1992 Spring meeting, Strasbourg, France (Thin Solid Films, in press).

[2] C. Menegat, J. Brunner, E. Kasper, M. Gail, G. Abstreiter, H. Kibbel, H. Presting, and E. Kasper, International Conference on Electronic Materials, EMRS 1992 Spring meeting, Strasbourg, France (Thin Solid Films, in press).

[3] H.M. Polatoglu, submitted.

The author has been partially supported by the EEC Esprit Basic Research Action program N° 7125

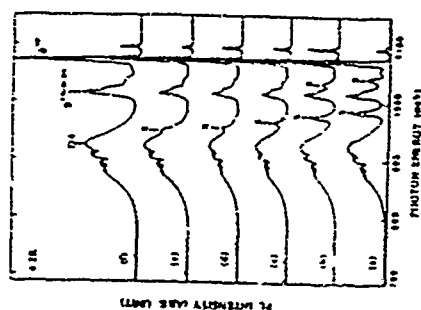


Figure 3: PL spectra at 4.2K from five quantum well structures, which were grown on the buffer layer described in Figure 1. (a) 10Å, (b) 15Å, (c) 20Å, (d) 25Å, (e) 30Å and (f) no quantum well.

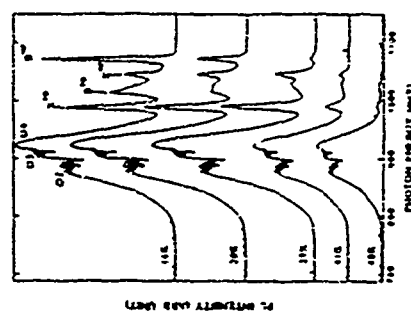


Figure 4: Temperature dependence of PL spectra at 10K, 20K, 30K, 40K, and 45K.

TuP22

SYSTEMATIC STUDY OF INTERSUBBAND ABSORPTION IN MODULATION-DOPED P-TYPE $\text{Si}_{1-x}\text{Ge}_x$ QUANTUM WELLS

T. Fromberts, E. Koppensheimer, M. Helm, G. Bauer
Institut für Halbleiterphysik, Universität Linz, A-4040 Linz, Austria
J. F. Nölzel, C. Abstreiter
Walter Schottky Institut, TU München, W-8046 Garching, Germany

ABSTRACT

A study of intersubband absorption in modulation-doped p-type Si/SiGe quantum wells is presented for a variety of SiGe well widths and Ge-contents. Narrow absorption lines (20 meV) between 470 cm^{-1} and 1035 cm^{-1} are observed. If the well width is 30 Å, the first excited heavy-hole subband is located close to the top of the quantum well, which results in a strong mixing between well- and barrier bound states. The latter arise from the hole transfer from the barrier into the well. A self-consistent calculation is used to fit the measured absorption spectra.

1. INTRODUCTION

The absorption of infrared radiation through intersubband transitions in quantum wells has been studied extensively in the past few years, because of its possible application for infrared detectors [1]. Besides the $\text{GaAs}/\text{AlGaAs}$ system, the Si/SiGe system has attracted a lot of attention recently. From the technological point of view, it is preferable to employ valence-band transitions in SiGe quantum wells, since the latter can be grown directly on a silicon substrate in a pseudomorphically strained fashion. Even though a number of results on this system have already been reported, [2,3] there is no detailed knowledge yet about the optimum sample parameters (e.g., layer thicknesses, Ge-content) for infrared detection. In this paper we present a study of the intersubband absorption in SiGe quantum wells for a variety of well thicknesses and depths, the latter being determined by the Ge-content of the alloy material.

2. EXPERIMENT

The samples investigated in this work were grown by molecular beam epitaxy on semi-insulating (100) Si wafers. The samples consist of 10 SiGe alloy quantum wells with a Ge-content of 20%-30%, separated by 180 Å Si barriers, the center 40 Å of which are known doped to a level of $2 \times 10^{18} \text{ cm}^{-3}$. Three groups of samples with different well widths (approximately 30 Å, 50 Å, 70 Å) were grown. During growth, the wafer was not rotated but rather kept fixed. This results in a controlled variation of the Ge-content and well- and barrier-width within one wafer. The exact structural parameters were determined by high-resolution triple axis x-ray diffraction and are listed in Tab. 1. The x-ray data show that the SiGe quantum wells are pseudomorphically strained with the in-plane lattice constant of the Si substrate. Infrared absorption measurements were performed in a Bruker IFS 113 Fourier transform spectrometer at a temperature of 5 K. The samples were prepared in multipass wavenumber geometry [4] as indicated in Fig. 1. The radiation is coupled into the sample at one facet which is wedged at an angle of 30°, and then undergoes approximately 4 reflections on the ratio of the thickness to the length of the sample) total internal reflections at a reflection angle of 50°. On top of the multiquantum well structure a layer of gold (300 nm) was deposited in order to enhance the electric field of the infrared radiation polarized parallel to the growth direction [5]. The transmission spectra were measured both in p-polarization (electric field parallel to the growth direction) and in s-polarization (electric field perpendicular to the growth direction). The ratio of the transmitted intensity of p- and s-polarized radiation was

normalized to the respective ratio measured at a reference Si substrate prepared in the same way as the multiquantum well samples.

3. RESULTS AND DISCUSSION

The solid lines in Fig. 1 show the absorption spectra of the 20 Å and 50 Å quantum wells, respectively. The broken lines in Fig. 1 are the result of a fit to a model describing the sample consisting of substrate, quantum wells and gold layer as a multilayer dielectric stack. The transmission through this dielectric stack was calculated using a standard matrix method [6]. According to the experimental geometry (Fig. 1), the sample transmission is determined by calculating the reflection coefficient R at the sample surface. Then, if n reflections occur, the transmission will be 10^{-R} . The optical properties of quantum wells (growth direction z) can be described by an anisotropic dielectric function given by [5]

$$\epsilon_{zz} = \epsilon_{\infty} - \frac{\epsilon_{\infty}(\omega_p^2)}{\omega^2 - \omega_{21}^2 + i0/\tau} \quad (1)$$

$$\epsilon_{xx} = \epsilon_{yy} = \epsilon_{\infty} - \frac{\epsilon_{\infty}\omega_p^2}{\omega^2 + i0/\tau} \quad (2)$$

Here ω_p is the plasma frequency defined by $\omega_p^2 = (n_0 e^2 / \epsilon_{\infty} m^* a) / 2$, where a is the well width, n_0 is the two-dimensional carrier density, ϵ_{∞} is the dielectric constant of the well, f is the intersubband transition oscillator strength, Γ is the intersubband linewidth and τ is the relaxation time for the in-plane transport. The frequency ω_{21} is defined by $\omega_{21} = E_2 / \hbar$, where E_2 is the transition energy between ground- and excited states of the quantum wells. As discussed in Ref. [7] for layers with thicknesses small compared to the wavelength of the incident radiation, the absorption for p-polarized light is determined only by ϵ_{zz} , which is a consequence of the gold overlayer. Therefore, the calculated transmission spectra shown in Fig. 1 do not depend on the value of ϵ_{xx} .

In the calculation, E_2 , Γ and f were treated as fitting parameters. The results for f range between 0.6 and 1 for both well widths and are in reasonable agreement with theory ($f=0.96$ for infinite quantum well). For E_2 we get the results listed in Tab. 1 and indicated in Fig. 1. As the calculations show, the maximum absorption does not occur at the transition energy E_{21} , but at energies shifted by approximately 40 cm^{-1} to higher values. This again is a consequence of the gold layer, which shifts the absorption peak from the maximum of $\text{Im}(\epsilon_{zz})$ to the maximum of $\text{Im}(\epsilon_{zz}) / (1 + \epsilon_{zz})$ [7]. For the intersubband linewidth Γ we get 150 cm^{-1} for both well widths. To our knowledge, this is the smallest linewidth so far observed in p-type $\text{Si}/\text{Si}_{1-x}\text{Ge}_x$ quantum wells and it is only twice as large as in comparable GaAs quantum wells.

In the lower part of Fig. 2 the absorption spectra of the 30 Å quantum wells are shown. Here, the absorption maxima shift from 725 cm^{-1} to 1035 cm^{-1} with increasing Ge-content (15% to 28%) and decreasing well width (36 Å to 26 Å). Furthermore the absorption linewidth is significantly larger than for the other samples. To understand the shape of the absorption lines, one has to calculate the energy levels of the multiquantum wells taking into account the electrostatic potential arising from the charge transfer from the doped region to the quantum wells. If we take the z -direction parallel to the growth direction and restrict ourselves to the case of zero in-plane wavevector, the heavy-hole band is decoupled from the light-hole and split-off band [8]. Therefore, the energy levels are the eigenvalues of the one-band Schrödinger equation of the form

$$\left[\frac{1}{2} \rho_2 \frac{1}{m_{||}(z)} \rho_2 + V_{||}(z) + e\Phi_{2,c}(z) \right] \chi(z) = E\chi(z) \quad (3)$$

and $\Phi_{2,c}$ is the solution of Poisson's equation

$$\Delta \Phi_{2,c} = -\frac{eN_A}{\epsilon_0} [\chi^+(z)\chi(z) - \theta(z)] \quad (4)$$

Here N_A is the sheet concentration of occupied acceptors per well, $\theta(z)$ is their normalized spatial distribution function, e is positive. The mass of the heavy holes along (100) direction in the SiGe is calculated from the well established values for Si ($m_H^* = 0.28 m_0$) and Ge ($m_H^* = 0.21 m_0$) [9] by linear interpolation. The band offset of the heavy-hole band in Si and SiGe was treated as a fitting parameter. For convenience, the energy of the hole states is counted positive in Eq. (3)

As an example, the results of the calculation for a quantum well with a germanium content of 24% and a well width of 30 Å are shown in Fig. 3. Due to band bending, bound states exist in the barrier. The transitions from the well bound ground state (labeled 1 in Fig. 3b) to these states (labeled 2, 3 in Fig. 3b) are indirect in real space and therefore have small oscillator strengths. The levels labeled 4 and 5 in Fig. 3b are mixtures between well- and barrier-bound states. The transitions from the ground state to these states have the highest oscillator strengths (see Fig. 3a) and therefore dominate the absorption spectra. The final states of these transitions are delocalized with a significant dispersion in k_x direction, which results in a rather broad absorption. The calculations show, but the transitions in the 30 Å quantum wells are most sensitive to the valence band offset, since the excited states with the highest oscillator strength have energies close to the top of the quantum well. Consequently, the absorption spectra of these samples were used to determine the valence band offset. Using a heavy-hole valence band offset of 740 meV between Si and pseudomorphically strained Ge (and linear interpolated values for the alloy) [10], the solution of Eq. (3,4) yields the transmission spectra plotted in the upper part of Fig. 2. The results of the calculation (not only reproduce the positions of the measured absorption maxima, but also the structures observed in the high energy shoulder of the absorption band (especially for the quantum well with 25% Ge content). We point out that it is crucial to take into account transitions to several excited states, which all contain considerable oscillator strength. Therefore, destructive simulation as above does not appear sensible due to the large number of fit parameters. For the 50 Å and 70 Å samples, however, the results of the calculation do not coincide well with the experimental results (see Tab.1). The reason for this discrepancy is not yet clear, but could be caused by intersubband transitions at finite in-plane wavevector values which are not taken into account in the present calculation.

To summarize, we have performed a systematic experimental study of the infrared absorption of modulation doped p-type Si/SiGe quantum wells with various Ge-content and well widths. As long as the wavefunctions of the excited states do not couple to continuum states, the linewidth of the absorption is only 20 meV, showing the high quality of the present samples. For the 30 Å samples, the results of a model calculation agree very well with the experimental results, if a band offset of 740 meV between Si and pseudomorphically strained Ge is assumed.

ACKNOWLEDGEMENTS

This work is supported in part by ESPRIT Basic Research Action 7125 by the FWF under Proj Nr 9119, and by the Jubiläumsfonds der Österreichischen Nationalbank.

REFERENCES

- [1] B. F. Levine, Semicond. Sci. Technol. **8**, S40 (1993).
- [2] R. P. G. Karunaratni, J. S. Park, Y. J. Mi, K. L. Wang, Appl. Phys. Lett. **52**, 2593 (1990), R. P. G. Karunaratni, J. S. Park, K. L. Wang, Appl. Phys. Lett. **52**, 2598 (1991).
- [3] B. Peuple, J. C. Bean, C. G. Bethea, S. K. Spitz, L. J. Pelletier, Appl. Phys. Lett. **61**, 1122 (1992).
- [4] H. Hertle, G. Schubert, E. Cornik, G. Abstreiter, F. Schaffner, Appl. Phys. Lett. **52**, 2997 (1991), H. Hertle, F. Schaffner, A. Zrenner, G. Abstreiter, E. Cornik, Thin Solid Films **222**, 20 (1992).
- [5] M. J. Kane, M. T. Emery, N. Apley, C. R. Whitehouse, D. Lee, Semicond. Sci. Technol. **3**, 222 (1988).
- [6] B. Harbeck, Appl. Phys. **132**, 165 (1986).
- [7] T. Frennherz, M. Helm, C. Bauer, H. Kibbel, E. Kasper, Thin Solid Films **222**, 251 (1992).
- [8] C. Barad, Wave Mechanics Applied to Semiconductive Heterostructures, Les Editions de Physique, 1984.
- [9] Landolt-Börnstein, New Series, III/17a, Springer Verlag Berlin, Heidelberg, New York, 1962.
- [10] L. Colombo, R. Kneis, S. Batten, Phys. Rev. B **44**, 5572 (1991).

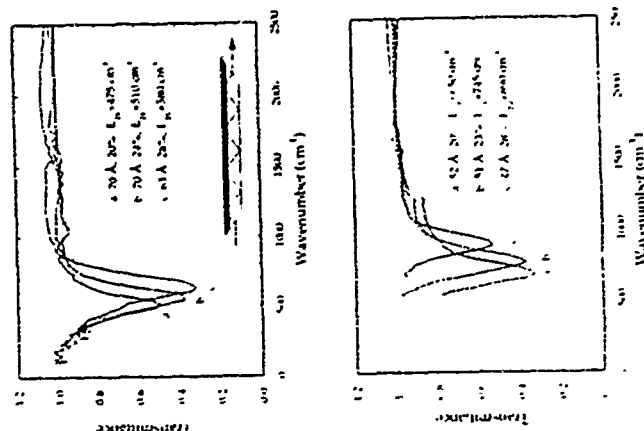


Figure 1: Transmission spectra of three modulation doped p-type Si/SiGe multi-quantum wells measured at 5 K (solid line). The respective Ge content and width of the quantum wells are indicated in the plot. The broken lines and the values of E₂₁ are the result of the fitting procedure described in the text. Note, that the peak absorbance occurs at energies greater than E₂₁.

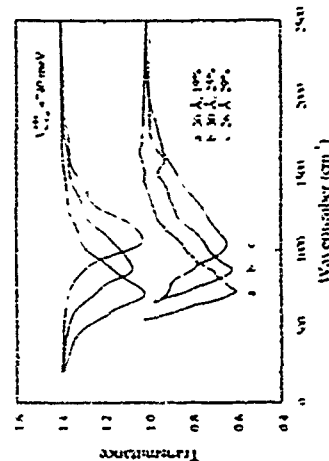


Figure 2: Calculated (upper curves) and at 5 K measured (lower curves) transmission spectra of 3 modulation-doped p-type Si/SiGe multiquantum wells. The well width and Ce content of the various quantum wells are indicated in the plot. For the calculation, a band offset of 760 meV between the heavy hole bands of Si and pseudomorphically strained Ge was assumed. For clarity, the calculated transmission spectra are shifted vertically by 0.4

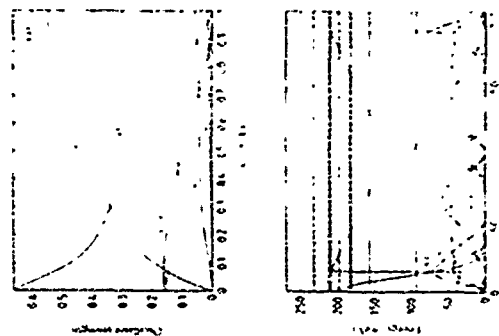


Figure 3: Results of the calculation described in the text for a modulation doped multiquantum system with 30 Å Si_{0.27}Ge_{0.73} quantum wells and 177 Å Si barriers. In (a) the oscillator strengths for transitions from the ground state to the first 6 excited states is plotted versus the reduced wavevector along the growth direction (L denotes the period in growth direction). The self-consistent potential and the energy bands are plotted in (b). For convenience, the energy of the holes is counted positive. Also shown in (b) are the wavefunctions of the miniband edge states. The first triplet of the labels of the wavefunctions indicates bandindex, the second the value of the reduced wave vector (in units of π/L).

Table 1: Sample parameters determined by high resolution triple axis x-ray diffraction and FIR transmission measurement. For the 30 Å quantum wells, the values marked with (*) represent the measured peak position, as for reasons explained in the text no dielectric simulation was performed for these samples. The values in the parentheses were used to obtain the best fit of the peak positions to the results of a self-consistently solved Schrödinger equation.

Ce content (%)	well width (Å)	barrier width (Å)	Transition energy (cm ⁻¹)	
			measured	calculated
20	70	193	475	350
24	70	178	510	390
28	63	160	580	400
20	52	193	680	520
23	51	176	745	610
28	47	162	860	750
19 (20)	36 (35)	180	725*	720
25 (24)	30 (30)	177	845*	860
29 (29)	26 (20)	160	1035*	1060

TuP23

Characterization of the valence band offset in p-Si/Si_{1-x}Ge_x/Si by space charge spectroscopy

K. Schmalz, H. Rucker, I. N. Yasyuevich*, H. G. Gmmeiss,
B. Dietrich, H. Frankenfeld, W. Mohr, H. J. Osten, P. Schley
Institute of Semiconductor Physics, Frankfurt (Oder), Germany
*Physico-Technical Institute, St. Petersburg, Russia

Abstract

Results are presented concerning direct comparison of admittance spectroscopy and DLTS in p-Si/Si_{1-x}Ge_x/Si quantum well (QW) structures with $x = 0.17$ using n⁺p mesa diodes with buried QW layer. The experimental results are analysed taking into account the external electric field as well as internal electric fields induced by holes confined in the QW. The temperature dependence of potential barriers at the QW and of the Fermi level determine the activation energy E_a of the conductance across the QW. From E_a a band offset of $\Delta E_v = 0.16$ eV was estimated. DLTS data suggest that hole emission from QW was observed with activation energy in correspondence with ΔE_v .

1. Introduction

The admittance spectroscopy [1] and the DLTS [1] can be considered as very similar diagnostic techniques for the investigation of carrier capture and emission in quantum wells (QW). The admittance spectroscopy measures the charge carrier transport over the QW, and by DLTS the carrier emission from the QW can be detected. In both cases there exists a thermally activated current limited by potential barriers closely related to the band offset ΔE . Although several DLTS-investigations [1-4] and admittance spectroscopy measurements [1, 5] were published for semiconductor heterostructures, there was not performed a direct comparison of these methods on the same device structure. This may be related to the fact that the specifications needed for the device structures are quite different. Recently, there is great technological interest in Si/Si_{1-x}Ge_x heterostructure layers due to possible applications in silicon based device technology. Admittance spectroscopy measurements of the valence band offset ΔE_v were performed on p-type Si/Si_{1-x}Ge_x/Si structures for Ge-concentrations up to 30 at.% [5]. The present work is focused on an experimental and theoretical study of carrier capture and emission processes in p-type Si/Si_{1-x}Ge_x/Si QW structures for conditions of admittance- and DLTS-investigations. For our investigations we have used specially designed n⁺p-diode structures allowing DLTS- and admittance spectroscopy on the same QW.

2. Theoretical study of carrier capture and emission processes

To obtain the valence band offset from experimental results of space charge spectroscopy measurements, it is necessary to examine carefully the capture and emission processes of holes in QWs for equilibrium and nonequilibrium conditions taking into account external electric fields as well as the local electric fields induced by confined carriers. The density of the emission current from a QW is given by $I_e = e \cdot n_{\text{eff}} \cdot v_{\text{eff}}$, where v_{eff} is the thermal emission rate and n_{eff} the hole surface concentration in the QW. In the framework of the thermionic theory, the capture flux density is given by $I_c = 2n_{\text{eff}} \cdot v_{\text{eff}}$, where n_{eff} is the free carrier concentration in the barrier layer and v_{eff} is the average thermal velocity of carriers. For the condition of thermal equilibrium $I_c = I_e$, one gets for the emission rate

$$v_{\text{eff}} = 2 \cdot \frac{e}{h} \cdot \frac{\lambda}{\pi} \cdot \frac{\exp(-\Delta E_v/kT)}{\exp(-E_F/kT)} \cdot \frac{1}{\Delta E_v} \quad (1)$$
 where $\lambda = (2 \cdot \pi \cdot \hbar^2 / m \cdot kT)^{1/2}$ is the thermal length of carriers with the mass m and E_F is the confinement energy of the first level in the well. For Boltzmann statistics the occupation factor g reduces in the limit of small wells ($E_1 \gg kT$) to $g = 1$ and in the opposite limit ($E_1 \approx kT$) we have $g = a/\lambda$, τ with a being the width of the well. The main peculiarities of a QW compared to a classical well consist in the existence of bound states in the QW and quasi-discrete levels in the continuous spectrum induced by reflection of carriers at the QW boundaries. The basic result is to replace the thermal average velocity $\langle v \rangle$ by the effective capture velocity v_{eff} , which accounts for optical phonon emission and is calculated in the framework of quantum theory [6]. In the nonpolar Si/Si_{1-x}Ge_x/Si QW structures, where the deformation potential controls the carrier-optical phonon interaction, the capture velocity v_{eff} for wells with $\Delta E_v = 140$ meV and widths a of about 30 nm oscillates between $0.5 \cdot 10^{10}$ cm/s (local minimum at $a = 29 \dots 30.5$ nm) and $4 \cdot 10^{10}$ cm/s (sharp maxima at 28.5 and 31 nm), and is practically temperature independent in the region from 100 K to 200 K [7]. For p-type Si/Si_{1-x}Ge_x/Si QW structures with large barrier layers which determine the position of Fermi level, the confined holes in the QW produce a depletion region in the vicinity of QW due to the charge neutrality condition. As a result the bottom of the energy levels in the QW and the potential barrier U_0 appears. For the calculation of the energy levels in the QW and the charge density, we have solved Schrödinger and Poisson equations self-consistently. The charge transfer between well and barriers aligns the barriers Fermi level close to the energy of the first heavy hole level in the well where the density of states is high. The calculated temperature dependence of the potential barrier eU_0 relative to the Fermi level E_F is given in Fig. 1 for different band offsets ΔE_v and acceptor concentrations N_A .

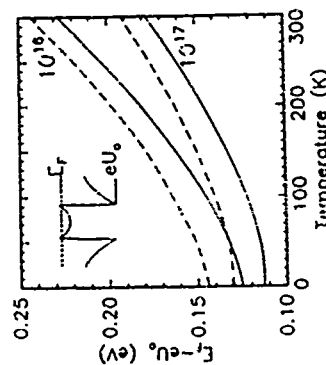


Fig. 1. Potential barrier eU_0 relative to E_F versus temperature for a 30 nm QW with valence band offsets $\Delta E_v = 0.14$ eV (solid lines) and $\Delta E_v = 0.16$ eV (dashed lines) for acceptor concentrations $N_A = 10^{16}$ cm⁻³ and $N_A = 10^{17}$ cm⁻³, respectively. The valence band edge in the vicinity of the QW is indicated in the inset

The potential barrier eU_0 induced by confined charge in the QW changes essentially the rates of carrier capture. For capture processes an effective velocity v_{eff} can be introduced by $I_c = 2 \cdot \frac{e}{h} \cdot \frac{\lambda}{\pi} \cdot \frac{\exp(-\Delta E_v/kT)}{\exp(-E_F/kT)} \cdot \frac{1}{\Delta E_v}$ with $v_{\text{eff}} = v_{\text{eff}} \cdot \exp(-U_0/kT)$, (2) where n_{eff} is the concentration in the neutral region of barrier layer. Now, we consider the time

dependence of the density of capture flux in the QW. The initial condition should correspond to the absence of carriers in the QW, i.e. $n_w = 0$. The change of the carrier concentration in the well is given by $dn_w/dt = (1/\tau_c) \cdot \frac{1}{2} \cdot \frac{1}{\tau_c} \cdot \frac{1}{\tau_c}$. For the capture flux density given by Eqs. (2, 3) U_0 should be replaced by $U_0 = U_0(0)$, the potential barrier induced by carriers captured in the time interval t_c . As a characteristic time for capture processes we obtain $\tau_c = (e \cdot E_0 \cdot N_A \cdot \Delta T / 2 \cdot e^2 \cdot n_0 \cdot \tau_c)^{1/2}$, where $e \cdot E_0$ is the electric constant. For times $t > \tau_c$ the population of the QW increases linearly with time. An estimation of τ_c for $N_A = 10^{17} \text{ cm}^{-3}$, $n_0 = N_A$ and $T = 100 \text{ K}$ gives $\tau_c \approx 10^{-12} \text{ s}$. In DLTS measurements the scale for pulses duration is usually $1 > 10^{-7} \text{ s}$. That means, that one can only observe an increase of the carrier concentration in QW in the vicinity of equilibrium concentration of the QW.

3. Experimental

In difference to the mesa-diode structures used in previous DLTS studies, a mesa diode geometry was developed for which the $\text{Si}_{1-x}\text{Ge}_x$ QW-layer exists as a buried layer. The three-chamber MBE equipment used in this work has been described elsewhere [8]. P-type Si (110)-substrates were prepared by an appropriate *ex situ* and *in situ* cleaning procedure, resulting in atomically clean and (2x1) reconstructed silicon surfaces as verified with RHEED. First, a Si buffer layer was deposited at a growth temperature of 600 °C with an e-beam evaporator. Elemental boron was evaporated from a high-temperature effusion cell with graphite crucible (EPF). Ge and Sb were evaporated from conventional water-cooled PBN Knudsen cells. The SiGe layers were grown at a substrate temperature of 500 °C. The following layer sequence was deposited: / 60 nm n^+ -Si cap layer, / 50 nm Si cap layer, undoped / 50 nm $\text{Si}_{1-x}\text{Ge}_x$ layer, undoped / 50 nm Si buffer layer, undoped / p -Si substrate, (110)-oriented. B doped with 10^{18} cm^{-3} . The undoped layers were of p -type due to the background boron contamination. The concentration at the interface buffer/substrate reaches up to few 10^{17} cm^{-3} . Employing mesa technology we have prepared n^+ -p-n diodes on the MBE samples. The depth of the mesa etching was 80 nm to realize buried $\text{Si}_{1-x}\text{Ge}_x$ layer. The area of the n^+ -contact was $A = 1.2 \cdot 10^{-5} \text{ cm}^2$. From the current voltage characteristics, an ideality factor of 1.4-2.0 was observed for the diodes. The reverse current I_R at $U_R = 2 \text{ V}$ was about 10^{-6} A . For the diodes the Ge-concentration of $\text{Si}_{1-x}\text{Ge}_x$ layer was controlled by means of Raman spectroscopy. The values obtained for the investigated diodes of samples DXT25 and DXT26 are $x = 0.17$ and 0.25 , respectively.

4. Admittance spectroscopy investigations

The temperature dependence of the sample capacitance $C = C(T)$ at $f = 1 \text{ MHz}$ for DXT25 and DXT26 shows a qualitatively different behaviour for $\text{Si}_{1-x}\text{Ge}_x$ -QW layers located in the neutral region or in the space charge region of the n^+ -p-diode. In the second case, realized for DXT25 at reverse bias $U_R = 4 \text{ V}$, the capacitance decreases only weakly with lower temperature (cf. Fig. 2). On the other hand, if the $\text{Si}_{1-x}\text{Ge}_x$ -layer is in the neutral region ($U_R = 0$), as checked by our CV measurements, the $C_p(T)$ -curve shows a characteristic decrease ΔC_p at lower temperatures. From the equivalent circuit for the space charge region of the n^+ -p-diode and the QW situated in the neutral region we get C_p and C_{p0} (C and G measured in parallel equivalent circuit) as a function of C_1 , C_2 , G and $\omega = 2\pi f$, where C_1 is the capacitance of the space charge region, C_2 the capacitance of QW and G the conductance across QW [5]. At higher temperatures leading to high conductivity, we get $C_p = C_1$ for low G. We have $C_p^{-1} = C_1^{-1} + (C_2^{-1} + G^2/\omega^2)^{-1}$. A maximum in $C_p(T)$ is achieved at $C_p = 2\pi f \tau_c (1 - C_1^{-1})$.

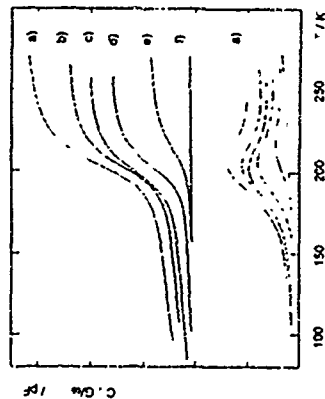


Fig. 2. Temperature dependence of capacitance C and normalized conductance G/ω for measurement frequency $f = 1 \text{ MHz}$ for different reverse bias U_R : (a) - $U_R = 0 \text{ V}$, (b) - 0.5 V , (c) - 1.0 V , (d) - 2.0 V , (e) - 4.0 V , (f) - 10 V .

From the experimental results presented in Fig. 2 we obtain the QW capacitance $C_2 = 80 \text{ pF}$ at about 100 K. The step ΔC_p decreases for larger reverse bias and diminishes for $U_R > U_R^*$. The value U_R^* corresponds to the U_R for which the QW becomes depleted from confined carriers, i.e. $C_2 = 0$. For the sample DXT25 we obtained $U_R^* = 4 \text{ V}$, and for DXT26 $U_R^* = 2 \text{ V}$. The width W of the depletion region for U_R^* which is obtained from our CV results, lies between the depth of the QW and the interface buffer/substrate, suggesting that the peak does not change with increasing reverse bias up to 2 V (cf. Fig. 2), suggesting that the QW is yet in the neutral region. For the step in $C_p(T)$ and the corresponding peak in $G_p(T)$ we have observed a shift to lower temperatures for lower measurement frequencies f . According to Eqs. (2, 3) the temperature dependence of conductance G of the QW is given by $G(T) = T^{1/2} \cdot e \cdot \mu \cdot (1 - U_0 - E_p) / kT$. The activation energy E_a was obtained from the resonance condition $G_p = 2\pi f (C_1 + C_2)$ drawing the Arrhenius plot $\ln(\alpha f / T^{1/2}) = -E_a / kT$ (α - constant), giving for the sample DXT25 $E_a = (0.14 \pm 0.01) \text{ eV}$. To obtain from E_a the band offset ΔE_v we have to compare E_a with $(eU_0 - E_p)$ averaged over the temperature range of measurement (100 - 200 K). The calculated temperature dependence of $(eU_0 - E_p)$ is given for $\Delta E_v = 0.14$ and 0.16 eV in Fig. 1. For $\Delta E_v = 0.16 \text{ eV}$ and $N_A = 10^{17} \text{ cm}^{-3}$ we get $(eU_0 - E_p) = 0.14 - 0.16 \text{ eV}$ in correspondence with $E_a = 0.14 \text{ eV}$. The calculated potential barrier $U_0 = 0.10 \text{ eV}$ at 100 K corresponds to an equilibrium hole concentration in the QW of $n_{h,eq} = 7 \cdot 10^{11} \text{ cm}^{-2}$. From the measured capacitance of the QW a depletion width $L_D = 80 \text{ nm}$ can be estimated. In order to obtain this L_D we have to assume an acceptor concentration of a few 10^{16} cm^{-3} in the vicinity of the QW in agreement with our CV measurements.

5. DLTS-investigations

The values U_R^* of reverse bias, for which the QW becomes depleted, determine the optimal U_R for DLTS investigations of carrier emission from the QW, because in this case the influence of the electric field on carrier emission is minimal. In the DLTS spectra measured for

U_R and U_R^2 we have detected peaks which could be attributed by DDLTS depth profiling to a region close to the depth of the $Si_{1-x}Ge_x$ layer. For the two levels observed for sample DDLTS (s. Fig. 3), the Arrhenius plot gives the activation energies $E_A = 0.17$ eV (A) and 0.42 eV (B) (s. Fig. 4).

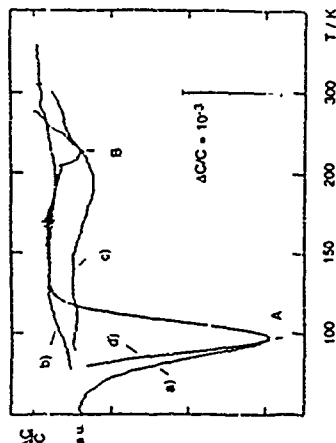


Fig. 3 DDLTS spectra measured for rate window $\tau_{sc} = 220$ s⁻¹, pulse duration $t_p = 50$ μs, reverse bias $U_R = 4$ V, and different pulse biases U_1 and U_2 : (a) $U_1 = 1.5$ V, $U_2 = 2$ V, (b) $U_1 = 0$ V, $U_2 = 0.5$ V, (c) $U_1 = 3.0$ V, $U_2 = 3.5$ V. Peak simulation for parameters from the Arrhenius plot: (d) - activation energy $E_A = 0.17$ eV, Gauss distribution of E_A is assumed with $\Delta E_A = 15$ meV

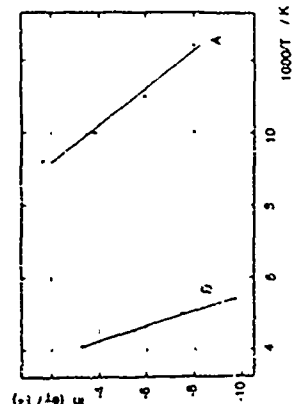


Fig. 4 - Arrhenius plot of the normalized emission rate e_1/T^2 versus $1/T$ for the DDLTS peaks A and B for measurements with reverse bias $U_R = 4$ V, pulse bias $U_1 = 0$ V, and pulse duration $t_p = 50$ μs

The concentration of the deep levels B was found to vary essentially for the different diodes of DDLTS and DDLTS. The relative concentration $\Delta C/C$ was for DDLTS and DDLTS in the

range $(0.5 - 4) \cdot 10^{-1}$ and $(0.5 - 3) \cdot 10^{-2}$, respectively, that means considerably larger for the higher Ge-concentration. It is important that peak A with $\Delta C/C$ up to 10^{-1} could be observed only, if the relative concentration of deep levels B was $\Delta C/C \leq 10^{-1}$. For diodes with higher $\Delta C/C$ of about 10^{-2} , a strong broadening of the peak shape was observed suggesting process-induced structural defects. The DDLTS spectra of DDLTS measured down to 50 K do not show any other peaks in the spectrum besides the peaks A and B, but a slowly increasing signal for temperatures below 100 K, which originates presumably from states at the interface buffer/substrate. The peak corresponding to $E_A = 0.17$ eV may be due to direct emission of holes from the QW, because the activation energy is nearly the same one as measured by admittance spectroscopy at the same diode. To get further evidence we have investigated the following points in more detail: (a) estimation of the pre-exponential factor of emission rate, (b) dependence of the emission rate on the electric field, and (c) capture of holes. For the conditions of DDLTS investigation of carrier emission, the emission rate e_1 is given by Eq. (1). The activation energy $E_A = \Delta E_V$ obtained from this Arrhenius plot is $E_A = (0.18 \pm 0.02)$ eV, and the pre-exponential factor is equal to $(2\pi k_B T)^{-1} = 5.9 \cdot 10^{11}$ s⁻¹. For the parameters of our QW we have calculated $g = 1$. Using the relation for λ_1 , we have estimated a capture velocity v_c of about $v_c = 6 \cdot 10^8$ cm/s close to the theoretical value of v_c . This supports the assumption that we have really observed hole emission from the QW. The shape of the DDLTS peak simulated with parameters taken from the Arrhenius plot is narrower than the peak shape measured. But, assuming Gauss distribution of the activation energy E_A with $\Delta E_A = 15$ meV, the peak shape can be fitted (s. Fig. 3). The broadening to lower temperatures should be related to the influence of states from the interface buffer/substrate. To obtain the valence band offset ΔE_V from the activation energy E_A , we have to consider the shift of the lowest confined level E_1 in dependence on the electric field F . The energy E_1 for the QW in the presence of external electric field can be calculated using the formula for energy levels in a triangular well, i.e. $E_1 = (\hbar^2/2m)^{1/3} (9\pi/8)^{2/3} [9] \cdot 91$. For $U_R = 4$ V, we have estimated from our CV data at 300 K that F is about $2 \cdot 10^4$ V/cm at the $Si_{1-x}Ge_x/Si$ interface of the QW, leading to $E_1 = 0.01$ eV. Therefore, we obtain for the valence band offset $\Delta E_V = E_A + E_1$ a value of $\Delta E_V = 0.19$ eV. In the case of DDLTS measurement with given rate window τ_{sc} (e.g. $\tau_{sc} = 22$ s⁻¹) for the emission rate e_1 , we have detected that the peak temperature T_p of the DDLTS peak decreases for larger reverse bias U_R . For $U_R = 6$ V, corresponding to F of about 10^5 V/cm at the $Si_{1-x}Ge_x/Si$ interface, we have found a decrease of the activation energy $\Delta E_A = 20$ meV compared to E_A at $U_R = 4$ V. The theoretical value $\Delta E_A = 40$ meV is somewhat larger. The hole surface concentration n_h captured in the QW can be obtained from the relation $\Delta C/C = n_h L / (2 N_A W^2)$, where L is the depth of QW layer, W the width of space charge region, and N_A the acceptor concentration. Taking $N_A = 1 \cdot 10^{17}$ cm⁻³, we get for $t_p = 50$ μs that $n_h = 2 \cdot 10^{10}$ cm⁻². The capture of holes into the QW was investigated by the dependence of the DDLTS peak $\Delta C/C$ on the filling pulse t_p . The relative signal $\Delta C/C$ of the DDLTS peak depends approximately logarithmically on t_p . The characteristic time t_0 obtained from the experimental dependence $\Delta C/C = \ln(t_p/t_0)$ by extrapolation to $\Delta C/C = 0$ is $t_0 = 10^{-6}$ s. This dependence of the hole concentration n_h in the QW on the pulse duration t_p cannot be described satisfactorily, because for $t_p > 10^{-6}$ s it is expected from the theoretical estimations for the capture process that n_h is nearly equal to the equilibrium concentration $n_h \approx 7 \cdot 10^{11}$ cm⁻². Maybe this discrepancy is due to donor-like defect states at the QW interfaces, which cause a lower effective capture velocity. Besides this, it can not be excluded that defect states at the interface buffer/substrate have also some influence due to the proximity to the QW

High mobility 2D hole gases in strained Ge channels on Si substrates studied by magnetotransport and cyclotron resonance

C. M. Engelhardt, D. Töben, M. Aichauer, F. Schäffler, G. Abstreiter, and E. Gornik
 Walter Schottky Institut, TU München, Am Coulombwall, D-85748 Garching, Germany, FAX: +49 89 320 66 20
 *Daimler-Benz AG, Research Center Ulm, Wilhelm-Runge-Str. 11, D-89081 Ulm-Erlangen, Germany
 *Institut für Festkörperelektronik, TU Wien, Gusshausstraße 25-27, A-1040 Wien, Austria

Abstract

High mobility two-dimensional hole gases have been achieved in p-type modulation doped Ge/Si heterostructures grown by MBE on a relaxed Ge/Si buffer. Hall mobilities of up to $15,000 \text{ cm}^2/\text{Vs}$ at carrier densities of $1.0 \times 10^{12} \text{ cm}^{-2}$ are observed at 0.4 K in magnetotransport. The cyclotron resonance (CR) shows a narrow (FWHM) 15 cm^{-1} and strong absorption up to 15 K . Quantum transitions are resolved splitting of the CR is observed, attributed to the lifting of the spin degeneracy of the $\pm 1/2$ states at $B = 0$ due to the asymmetric confinement potential. From CR masses of $0.14 m_0$ up to $0.20 m_0$ are found depending on well width and carrier density.

Introduction

Conventional Si-MOSFETs (metal-oxide-semiconductor field effect transistors) are intrinsically limited by the poor quality of the oxide-semiconductor interface [1]. The electron mobilities achieved in n-type modulation-doped Si-MOSFETs, however, have exceeded those of Si-MOSFETs both at low and at room temperatures within recent years [2-4]. This success is mainly due to the use of relaxed SiGe buffers with graded Ge contents which serve as a pseudosubstrate to even the required tensile stress on the Si layer containing the two-dimensional electron gas. Low-temperature mobilities of $170,000 \text{ cm}^2/\text{Vs}$ and above have been observed.

Two-dimensional hole gases (2DHGs) in the SiGe system have so far been realized either in pseudomorphic SiGe/Si quantum wells [5-7] or in Ge/SiGe structures grown on Ge wafers [8]. In the first case the 2DHGs are confined in the strained SiGe layers and their mobility is limited by alloy scattering. The second approach is not compatible with standard Si technology. Recently, however, high-mobility 2DHGs have been realized by depositing Ge channels on top of relaxed graded SiGe buffers grown by MBE on Si substrates [9-11]. These heterostructures displayed high hole mobilities and p-type MODFETs (modulation doped field effect transistors) were realized.

In this work we report on Shubnikov-de Haas (SdH) oscillations and cyclotron resonance (CR) investigations of such p-type modulation-doped Ge/SiGe heterostructures.

Sample structure and experimental technique

The samples investigated were grown at Daimler-Benz and have been described in detail in ref. [9]. The nominal parameters are listed in Table I. A rather thick relaxed SiGe buffer with linearly increasing Ge content was grown on an n-Si substrate. The active

structure consists of a Ge channel and a modulation-doped SiGe barrier. The Ge δ -doping layer has an integral concentration of $5 \times 10^{12} \text{ cm}^{-2}$. A thin Si cap layer was finally deposited to protect the structure against oxidation. TEM (transmission electron microscopy) micrographs of sample 1 have yielded an actual width of the Ge channel of 168 Å rather than the nominal 125 Å . Similar values are expected for samples 2 and 3. Because of the in-plane compressive strain the degeneracy of light-(lh) and heavy-hole (hh) bands at $k = 0$ is lifted. Therefore the hh-bands should be occupied and should exhibit a reduced effective mass.

For the CR measurements the sample substrates were wedged to avoid interferences. Ohmic contacts were allowed into the corners to determine the sheet density via two-point magnetoresistance measurements. The experiments were performed using a Fourier transform spectrometer at magnetic fields up to 17 T . Evaluation of the spectra is done by a Drude formalism to determine the resonance positions ω_c , from which the CR masses m_{CR} and m_{CR} can be deduced. The scattering rates $1/\tau$ and carrier densities n_s as described in ref. [12].

The samples used for the magnetotransport mea-

	sample 1	2	3
Si cap [Å]	30	30	20
spacer thickness [Å]	100	100	75
Ge content of barrier	0.6	0.6	0.5
channel width [Å]	125	125	75
final Ge content of buffer	0.7	0.7	0.7
graded buffer thickness [μm]	6	3	3

Table I Nominal sample parameters

6. Conclusions

For the investigation of capture and emission processes of holes in p-type $\text{Si}_{1-x}\text{Ge}_x/\text{Si}$ QW structures by means of admittance spectroscopy and DLTS we have used n/p meta diodes with a buried $\text{Si}_{1-x}\text{Ge}_x$ layer to prevent leakage current across the QW layer. To analyse the experimental results, it is essential to take into account the external electric field as well as the internal electric field induced by charge carriers confined in the QW. The potential barriers at the QW which are formed due to carrier confinement were calculated by solving self-consistently the Schrödinger and Poisson equations. The temperature dependence of these potential barriers and of the Fermi level determines the activation energy E_a of conductance across the QW. Therefore, the E_a depends sensitively on the acceptor concentration in the surrounding barrier layers. The DLTS data suggest that we have observed direct hole emission from the QW, but only for low defect concentration in the $\text{Si}_{1-x}\text{Ge}_x/\text{Si}$ structure. The $\Delta E_a = 0.19 \text{ eV}$ obtained by DLTS is in correspondence with the value $\Delta E_v = 0.16 \text{ eV}$ estimated from admittance spectroscopy. These values are somewhat larger than the calculated values $\sim 10 \text{ meV}$ and the photoluminescence measurements [11] of the band offset giving $\Delta E_v = 0.14 \text{ eV}$ for $x = 0.17$.

References

1. D. V. Lang, *Physics and Device Applications*, p.377.
2. Ed. by F. Capasso and G. Margalit, Elsevier Science Publisher, Amsterdam (1987).
3. N. Dohar, Dipankar Biswas, and Pallab Bhattacharya, *Phys. Rev. B* **40**, 1058 (1989).
4. X. Leang, D. Sleevan, and E. Barthier, *Appl. Phys. Lett.* **58**, 1047 (1991).
5. L. Vescan, R. Apetz, and H. Lüth, *J. Appl. Phys.* (1993), in press.
6. K. Nauka, T. J. Kamins, J. E. Turner, C. A. King, J. L. Hoyt, and J. F. Gibbons, *Appl. Phys. Lett.* **60** (2), 195 (1992).
7. I. N. Yassievich, K. Schmalz, and M. Beer, *Semicond. Sci. Technol.* (1993) to be published.
8. I. N. Yassievich, K. Schmalz, and M. Beer, *Proc. Internat. Conf. on the Formation of Semiconductor Interfaces*, June 1993, Jülich, in press.
9. et al. Ouen, G. Lippert, and J. Klatt, *J. Vac. Sci. Techn.* **B** **10**, 1153 (1992).
10. C. Weibuch and B. Vinter, *Quantum Semicond. Structures*, p.20, Academic Press, (1991).
11. W. X. Ni and G. V. Hansson, *Phys. Rev. B* **42**, 10301 (1990).

specimens had been processed into standard Hall bars by using optical lithography and wet chemical etching.

Magnetotransport

Fig. 1 displays Hall mobility and density of sample 1 as a function of temperature. A specimen in Hall geometry was used for the measurements up to about 60 K, while van-der-Pauw geometries were employed at higher temperatures. Good agreement is found in the data obtained from both geometries. The superior mobility of the Ge channel becomes obvious in the temperature range down to about 77 K. At this temperature 12 000 cm²/Vs are reached. However, the saturation behaviour at lower temperatures to a value of 15 500 cm²/Vs is indicative of a relatively high defect density or background doping concentration within the Ge channel. Further optimization of the growth x/d doping parameters is certainly required to match the high standards reached with n-type heterostructures on relaxed SiGe buffers [3]. Very recent reports claiming Hall mobilities as high as 55 000 cm²/Vs at very promising [11]. Nevertheless, the mobilities reached in these samples are high enough for a variety of magnetotransport and CR studies, which were formerly not possible.

The Sdfr and Hall traces of sample 1 at T = 370 mK are shown in Fig. 2. The Hall curve exhibits very precise quantum Hall plateaus accompanied by vanishing longitudinal resistance ρ_{xx} at higher magnetic fields. At a magnetic field of about 6 T the spin splitting begins to be resolved corresponding to a filling factor $\nu = 2$. The early onset of the oscillations, with respect to the mobility of 15 500 cm²/Vs, is a first evidence of a rather low transport mass. It is noteworthy that - contrary to magnetotransport work conducted on hole gases confined in strained SiGe layers - we observe Sdfr oscillations limited to even filling factors at small fields.

By evaluating the damping of the pure oscillatory part of ρ_{xx} as a function of the inverse magnetic field as described in ref [3] with an effective mass $m^* = 0.11 m_0$ obtained from the CR measurements (see

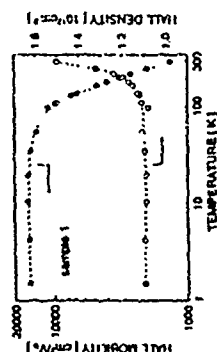


Fig. 1: Temperature-dependent Hall mobility and Hall density of sample 1

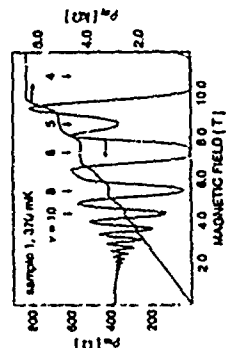


Fig. 2: Sdfr trace and Hall traces of sample 1 at 370 mK, measured in Hall geometry

below) one finds that the transport relaxation time τ is about 3.9 times larger than the single-particle relaxation time τ_s . The value of this ratio was found to lie in between 10 and 26 for high-mobility electron gases in Si/SiGe heterostructures [13]. We therefore conclude that the dominant scattering mechanism in the p-type structures investigated in this work is of long-range nature, but that there is still a significant short-range contribution as well. This would also account for the premature saturation of the mobility below T = 40 K described above.

Table 1 summarizes the low-temperature carrier densities of all three samples as determined by magnetotransport and CR, the Hall mobilities, and the CR masses in the low-magnetic field limit. Excellent agreement was found for the carrier densities obtained from the Hall, Sdfr, and CR data. The Sdfr experiments yielded the evidence of a bypass in sample 2. The hole mobility is therefore overestimated in this sample. At higher temperatures sample 2 always exhibits mobilities little below that of sample 1 [9].

Cyclotron resonance

Direct information on effective masses of holes is obtained from CR. In ref. [3] the CR of holes in a Si_{0.45}Ge_{0.55} channel on top of a Si substrate was reported. Due to the lower mobilities only a single broad

sample	1	2	3
magnetotransport, 0 K			
n_h [10^{16} cm ⁻³]	1.04	1.07	1.79
μ_{Hall} [cm ² /Vs]	15 500	21 700	9 800
cyclotron resonance / 3 K			
n_h [10^{16} cm ⁻³]	1.06	1.10	1.78
m_c [m_0]	0.112	0.131	0.200

Table 1: Low-temperature characteristics obtained by magnetotransport and cyclotron resonance in the low-magnetic field limit. n_h this mobility value appears to be distorted by a bypass

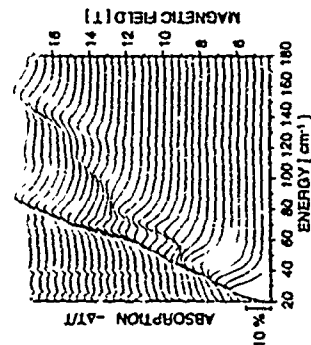


Fig. 3: Sample 1 at 1.5 K. Series of cyclotron resonance spectra for magnetic fields of 2.2 T up to 17 T. The CR absorption $\sim 3T - T_0 - T_{D0}$ is plotted in the vertical scale, the spectra for different magnetic fields are shifted vertically for convenience

and shallow resonance was observed, allowing the determination of an effective mass. In contrast the CR of the Ge p-doped layers investigated in this work reveals a rich structure due to the much higher mobility.

A series of CR spectra of sample 1 for magnetic fields from 2.2 T up to 17 T measured at 1.5 K is displayed in Fig. 3. At low magnetic fields the resonance exhibits up to 15% absorption and a FWHM of 15 cm⁻¹.

Fig. 3 gives the evaluation of the spectra in Fig. 3 for sample 1. At low fields a CR mass of 0.112 m_0 is determined by fitting the resonance with a single line. The sharp resonances and the rather low CR masses allow quantum transitions to be resolved at higher magnetic fields in all samples. At fields above B = 6 T

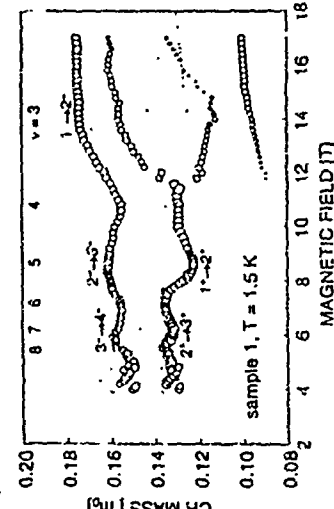
two resonances are clearly resolved. Below 6.7 T the fit with two lines is stable and independent of starting values. Therefore also in this regime two CR masses are plotted. Typical scattering rates are 1.0×10^{11} s⁻¹ for samples 1 and 2, and about 1.5×10^{11} s⁻¹ for sample 3.

In Table II the carrier densities and CR masses of the three samples are given as determined by fitting the resonances with a single line at low magnetic fields. The absolute values confirm the expectation that the in-plane mass is light. For the most CR masses a strong variation is found for the three samples. Since all three Ge channels are subjected to the same amount of strain, variations in CR mass are attributed to the different well widths and carrier densities. The increased subband energy and higher carrier density in sample 3 leads to a higher Fermi energy. The increased CR mass reflects the strong anisotropy of the valence band.

In all three samples two different CR masses are found at low fields. Note that due to the strain only sub-bands with axial quantum number $\pm 3/2$ are occupied. The splitting is found to be 13-18% of the total CR energy. It is attributed to the lifting of the spin degeneracy of the $\pm 3/2$ and $\pm 1/2$ bands at B = 0 and $k = 0$ by the asymmetric confinement potential [15]. Such a splitting has been observed in GaAs p-type heterostructures [16]. This effect was often confused with the Kramers degeneracy in the literature. The inconsistency has recently been clarified [17].

The two CR masses oscillate with the magnetic field. The lower trace splits at about 12 T. The branch with the higher CR mass is observed as an asymmetry in the high energy tail of the lowest energy resonance. Also, at 12 T a high energy resonance appears, corresponding to the lowest CR masses in Fig. 4. It gains intensity just as much as the resonance at lower energy loses it. The periodicity of the mass oscillations

Fig. 4: Combined plot of CR masses and carrier densities (size of the circles) for sample 1 at 1.5 K as evaluated from the spectra shown in Fig. 3. The filling factors $\nu = n h e B$ corresponding to a carrier density of $n_h = 1.06 \times 10^{16}$ cm⁻³ are given by the dotted lines. Also shown by the dashed lines is the result of a model calculation giving the expected CR masses for the different possible transitions at a given filling factor which may serve as a guide to the eye



Magnetotransport and microwave photoresistivity of two-dimensional hole gases in Si-Si_{1-x}Ge_x heterostructures.

Y. Guldner, J.M. Berroir, J.P. Vieren, M. Voos
Laboratoire de Physique de la Matière Condensée, Ecole Normale Supérieure, 24 rue
Lhomond, 75005 Paris, France

I. Sagnes, P.A. Badoz, P. Warren and D. Duzanne
France Télécom-CNET, BP 98, 38243 Meylan, France

Abstract

Shubnikov-de Haas and quantum Hall effect measurements in p-type modulation doped Si-SiGe double heterostructures with both symmetric and asymmetric doping grown by rapid thermal chemical vapor deposition, show that the two interfaces are highly equivalent and that the charge (hole) transfer can be quantitatively explained by a simple model. The two-dimensional hole gas effective mass parallel to the interfaces is determined by microwave photoresistivity experiments. Furthermore, the limitation of the hole mobility is discussed in terms of alloy scattering.

Introduction

In recent years, two-dimensional (2D) hole gases in Si-Si_{1-x}Ge_x heterostructures have received a great deal of attention, which is due, in particular, to their potential interest in microelectronics, and it is clearly important to investigate and understand in detail the transport properties of this quantum well system. Transport experiments have been performed on high-quality p-type modulation-doped Si-SiGe heterostructures [1, 7] fabricated by different growth techniques. We describe here transport, magnetotransport, and microwave photoresistivity experiments on such structures grown by rapid thermal chemical vapor deposition (RTCVD) with a single or a symmetric double hole gas. Shubnikov-de Haas oscillations and integral quantum Hall plateaus were observed at 1.6 K and the 2D hole mass parallel to the interfaces is obtained from microwave photoresistivity data. Our results show unambiguously that these structures present equivalent Si-SiGe and SiGe-Si interfaces and that the charge transfer is governed by the undoped spacer layer thickness. We discuss also the hole mobility limitation in these heterostructures.

Experimental Results and Discussion

Our samples are listed in table 1 and are constituted by a Si-Si_{0.8}Ge_{0.2} double heterostructure deposited on a (100) Si substrate using the RTCVD technique. The 40 nm thick SiGe layer is unintentionally doped. For the symmetrically doped samples (S1-S8), the two Si barriers contain a 16 nm *in-situ* doped region with an acceptor density $\approx 2 \times 10^{18} \text{ cm}^{-3}$. In the single-side doped samples, only the last (S4) or the first (S5) grown barrier contains a similar doped region. Undoped Si spacer layers of thickness *d* are inserted between the doped regions and the SiGe layer. A cap layer (undoped 40 nm Si layer followed by a p-type 20 nm Si layer) was grown on top of all samples.

The valence band diagram is determined (figure 1) by requiring that the Fermi level *E_F* remains constant throughout the structure. The heavy-hole valence band discontinuity is $\Delta E_{\text{hh}} \approx 160 \text{ meV}$ for *x* = 0.2 [2]. The ground hole subband HH₁ is in the cusp of the self-consistent potential and, as a result, two parallel hole gases occur in the symmetric samples. Due to the large 2D hole density of states, the separation *E_F* - HH₁ is a few meV for hole densities $\leq 10^{12} \text{ cm}^{-2}$ and

References

- [1] T. Ando, A. B. Fowler, F. Stern, *Rev. Mod. Phys.* **54**, 437 (1982).
- [2] F. Schaffler, D. Többen, H.-J. Herzog, G. Abstreiter, B. Hötter, *Semicond. Sci. Technol.* **7**, 260 (1992).
- [3] E. A. Fitzgerald, Y.-H. Xie, D. Monro, P. J. Silverman, J. M. Kuo, A. R. Kortan, F. A. Thiel, B. E. Weir, *J. Vac. Sci. Technol. B* **10**, 1207 (1992).
- [4] S. F. Nelson, K. Inanai, J. J. Nozema, F. F. Fang, E. E. Mendez, J. O. Choi, B. S. Meyerson, *Appl. Phys. Lett.* **61**, 64 (1992).
- [5] R. People, J. C. Brann, D. V. Lang, A. M. Sergent, H. L. Stormer, K. W. Weick, R. T. Lynch, K. Baldwin, *Appl. Phys. Lett.* **45**, 1231 (1984).
- [6] J. F. Nötz, F. Meier, E. Fritsch, G. Abstreiter, *Thin Solid Films* **222**, 150 (1992).
- [7] L. Vescia, R. Leo, A. Hartmann, U. Zaurow, A. Leuther, T. Schapers, T. Stolz, H. Lüth, to be published in *Proc. of ICPSI-4* (1993).
- [8] M. Nivao, E. Nura, H. Etoh, K. Nakagawa, A. Nishida, *J. Cryst. Growth* **111**, 912 (1991).
- [9] U. Köhler, F. Schaffler, *IEEE Electron. Dev. Lett.* **14**, 205 (1993).
- [10] Don Monroe, Y.-H. Xie, E. A. Fitzgerald, P. J. Silverman, G. Watson, to be published in *Proc. of ICPSI-4*, *Vac. Sci. Technol.* (1993).
- [11] Don Monroe, Y.-H. Xie, E. A. Fitzgerald, P. J. Silverman, G. Watson, to be published in *Proc. of EPDS-10*, *Surf. Sci.* (1993).
- [12] C. M. Engelhardt, E. Cornik, M. Besson, G. Böhm, G. Wernmann, to be published in *Proc. of EPDS-10*, *Surf. Sci.* (1993).
- [13] D. Többen, F. Schaffler, A. Zrenner, G. Abstreiter, *Phys. Rev. B* **46**, 1314 (1992).
- [14] J.-P. Cheng, V. P. Keld, D. A. Gruzman, T. O. Sedgwick, *J. Appl. Phys. Lett.* **62**, 1322 (1993).
- [15] T. Ando, *J. Phys. Soc. Jpn.* **54**, 1528 (1985).
- [16] H. L. Stormer, Z. Schirmer, A. Chong, D. C. Tsu, A. C. Gossard, W. Wegmann, *Phys. Rev. Lett.* **51**, 125 (1983).
- [17] G. Goldoni, A. Fasolino, *Phys. Rev. Lett.* **69**, 3507 (1992); G. Goldoni, A. Fasolino, *Phys. Rev. Lett.* **70**, 2031 (1993).
- [18] K. Suzuki, J. C. Hensel, *Phys. Rev. B* **9**, 4118 (1974); J. C. Hensel, K. Suzuki, *ibid.* **p. 4219** (1974); W. Erhardt, W. Stachulski, P. Byers, M. von Ortenberg, G. Landwehr, G. Weimann, L. van Bockstaele, P. Jansen, F. Herlach, *J. Vac. Sci. Technol.* **17**, 181 (1984).
- [19] Y. Iwasa, N. Mura, S. Tanaka, H. Okamoto, T. Ando, *Surf. Sci.* **170**, 357 (1986).

appears to be linked to the filling factor which is calculated from the carrier density determined at low magnetic fields.

In the following we shall use the notation introduced in ref. 18, which is the basic work on the CR of holes in strained bulk Ge. The dashed lines in Fig. 4 represent a calculation of the CR masses for the different possible transitions according to the filling factor of the system. The model assumes different energy-dependent densities of states for the $\pm 1/2$ bands. It has been fitted to the data in the range between 5 T and 9 T. In this model the transitions are identified as labeled in Fig. 4. The decrease of the CR masses with magnetic field occurs because the splitting between $n-1 \rightarrow n$ and $n \rightarrow n+1$ transitions is not resolved when the n -th Landau level passes the Fermi energy. This interpretation is supported by the observation of increased scattering rates, i.e. linewidths of the resonances in this region.

However, this model fails to describe the high field data. Above 12 T additional transitions are resolved. With respect to the filling factor of the system the highest energy resonance has to be attributed to an excitation from the lowest Landau level. The apparent splitting within the $1^- \rightarrow 2^-$ transition above 12 T comes as a surprise. The observation of more than three transitions implies either a crossing of two levels at the Fermi energy or the observation of previously forbidden transitions. The latter has been suspected in the case of GaAs 2DHG [19, 20]. Furthermore, in this high field region the evaluated total carrier density appears to increase with magnetic field. Understanding of the CR in the limit of low filled Landau levels therefore has to await detailed bandstructure calculations including z -quantization, strain and magnetic field.

Conclusion

High mobility Ge p-channels have been achieved on Si substrates using the graded buffer technique. The good quality of the samples has been demonstrated by magnetotransport and CR. A dominance of remote ionized impurity scattering over short range scattering is found. The determined CR masses confirm the expectations that the hh-bands have a light in-plane effective mass when the hh-degeneracy is lifted by strain. The lifting of the spin degeneracy at $B = n$ in the asymmetric confinement potential provides a qualitative understanding of the low field CR. Further theoretical work is required for a more quantitative understanding.

Acknowledgements

The authors would like to thank U. Köhler and J. F. Nützel for valuable discussions and V. Rookhof for experimental help.

only H_{H1} is populated at low temperature. Carrier densities obtained at 1.6 K from quantum Hall (ρ_{QH}) and Shubnikov-de Haas effects (ρ_{SH}) are given in table 1. In the symmetric situation (S1, S3), $\rho_{SH} \sim 0.5 \rho_{QH}$. This has been observed previously by other groups [4,7] and suggests that the two interfaces are equivalent and that the wavefunctions of the two 2D hole gases are nearly independent. For example in sample S1, a wavefunction extension of ~ 3 nm is calculated from a simple triangular potential model, yielding a 34 nm distance between the two symmetric hole gases. Due to the SiGe band bending a potential barrier of a few tens of meV separates the two gases, so that tunneling between the two channels is negligible and no splitting of the H_{H1} ground subband is evidenced. For S4 and S5, similar ρ_{SH} values are obtained, which shows that the charge transfer is equivalent at Si-Ge and Si-Ge-Si interfaces. Sample S4 corresponds to a "normal" modulation-doped Si-SiGe heterojunction, and $\rho_{SH} = \rho_{QH}$ as expected if there is no parallel conduction. Sample S5 corresponds to an "inverted" modulation-doped SiGe-Si heterojunction, and there is a difference of $\sim 1.4 \times 10^{11} \text{ cm}^{-2}$ between ρ_{SH} and ρ_{QH} which can be explained by an additional charge transfer from the boron doped cap layer to the SiGe layer, leading to another 2D hole gas with a lower density at the upper Si-SiGe interface.

The analysis of the charge transfer can be achieved from a simple electrostatic calculation. The Fermi level E_F is constant throughout the structure and the following expression is obtained at low temperature:

$$\Delta E_v = H_{H1} + \pi^2 (0.65 \text{ eV/nm}^2) + e^2 \rho_{SH} / 2\epsilon N_A$$

Here $m/\mu = 0.4 m_0$ is the 2D hole mass parallel to the interfaces, and $\epsilon = 12\epsilon_0$ is the SiGe dielectric constant. Using a triangular potential approximation to calculate H_{H1} and the data shown in table 1, one obtains $\Delta E_v = 165 \pm 10 \text{ meV}$ for all samples (S1 - S5). This result, which is consistent with previous determinations of ΔE_v [2], shows that the charge transfer is essentially governed by the thickness d of the undoped spacer layer and is not too dependent on the nature of the interfaces.

The Hall resistance as a function of the magnetic field B at 1.6 K is given in figure 2 for samples S1 and S2, and it has been pointed out that these curves depend on the angle θ between B and the surface normal as $(\cos \theta)^2$. Quantized plateaus of resistance h/e^2 with filling factor i up to $i = 32$ can be seen (cf. $B \geq 1.5 \text{ T}$ (fig. 2b)), which evidences the high quality of the 2D hole gases. For $B < 4 \text{ T}$, the Landau level spin splitting is not detected due to level broadening, and plateaus are observed only for $i = 4n$, where n is an integer ($i = 12, 16, 20, 24, 28, 32$ in sample S1 and $i = 8, 12, 16, 20$ in sample S2). However, plateaus at $i = 2n$ are observed in the asymmetric samples: the inset in figure 2b presents the Hall resistance at low B in sample S4 where plateaus occur at $i = 8, 10, 12, \dots, 18$, and similar plateaus at $i = 2n$ are also observed in sample S5. These results demonstrate that two parallel highly equivalent channels contribute to the Hall effect in the symmetrically-doped structures. Indeed, between two successive plateaus, four Landau levels are crossing the Fermi level instead of two in a single 2D hole gas. Similarly, for higher B where the spin splitting is resolved, plateaus are observed only for even filling factors in samples S1 to S3, while plateaus at both odd and even i can be seen in the asymmetric samples. As previously reported [6], the plateaus and magneto-resistance minima at odd filling factors in the single-side doped samples are likely to be due to the large spin splitting of the Landau levels which can be comparable or larger than the cyclotron energy in the studied 2D hole gases.

Hall measurements in S1, S2 and S3 show that the 2D hole mobility μ is enhanced when the temperature T is decreased as a result of the spatial separation between the ionized impurities and the holes. One obtains $\mu = 4000 \text{ cm}^2/\text{Vs}$ at low T for $d = 10 - 20 \text{ nm}$. As can be seen in figure 2 and in figure 3 which will be described later, the onset of oscillations or Hall plateaus occurs at $B \sim 1.5 \text{ T}$, which corresponds to $\mu = 6000 \text{ cm}^2/\text{Vs}$. An important mobility limitation could result from alloy scattering since the 2D hole gas is essentially confined in the SiGe alloy. If one uses a simple model (one-band approximation, Fang and Howard wavefunction for the 2D hole ground state [8], short range scattering, same spatial average of the fluctuating alloy potential as in III-V ternary compounds [9]), one can obtain the alloy-limited mobility, namely $\mu_{al} = 5000 \text{ cm}^2/\text{Vs}$. This is in good agreement with our values and those of other groups [3,4,7]. As a result, alloy scattering is likely to be a limiting factor for the mobility.

at low temperature, even if other factors should also be considered like the background impurity concentration in the SiGe layer or the interface quality.

We have also measured the 2D hole mass parallel to the interfaces m_{\parallel} from photoresistivity measurements under microwave illumination which is a more accurate method than direct transmission measurements to obtain the cyclotron mass. With a DC bias current $I = 1 \mu\text{A}$, changes $\Delta\rho$ in the magneto resistivity ρ due to the chopped microwave radiation were detected using a lock-in amplifier. Figure 3 gives typical data obtained for ρ and $\Delta\rho$ in S4 at 1.6 K. Magneto-oscillations in $\Delta\rho$ correspond to the Shubnikov-de Haas effect and arise from 2D carrier heating. An important enhancement can be seen around $B_0 = 4 \text{ T}$ at 270 GHz and 4.5 T at 333 GHz, which corresponds to the 2D hole cyclotron resonance (CR) when the hole absorption of the microwave radiation is maximum. The CR absorption correlates with the envelope of $\Delta\rho$ as shown in figure 3 by the dashed line. The half width at half amplitude ($\Delta B = 2T$) at 333 GHz yields $\mu = 3000 \text{ cm}^2/\text{Vs}$ at low T in a classical ϵ - m model, and $\mu = 4700 \text{ cm}^2/\text{Vs}$ from $\Delta B = 0.65 B_0/\mu_{\parallel}^{1/2}$ which has been used in the case of 2D electron gases [10,11]. These values are in agreement with those obtained from transport experiments and the onset of the Shubnikov-de Haas oscillations in S4. The maximum of the dashed line gives $m_{\parallel} = (0.42 \pm 0.02)m_0$ in S4, and similar experiments in S1 and S2 yield $m_{\parallel} = (0.45 \pm 0.02)m_0$ and $m_{\parallel} = (0.42 \pm 0.02)m_0$, respectively. These values are comparable or larger than results obtained previously from Shubnikov-de Haas measurements in analogous structures [1,4], but we think that the microwave photoresistivity method is actually more reliable.

Conclusion

The electronic properties of 2D hole gases have been investigated in p-type modulation-doped Si-SiGe heterostructures fabricated by RTCV. We have evidenced that the charge transfer is equivalent at each interface and depends only on the undoped spacer thickness. The hole mass in the plane of the layers has been determined, showing that it does not vary appreciably with the hole concentration. We have finally shown that alloy scattering is certainly an important limiting mechanism at low T for the carrier mobility.

Acknowledgments

This work has been partly supported by the Direction des Recherches, Etudes et Techniques (DRET), The Laboratoire de Physique de la Matière Condensée de l'ENS is associated to CNRS and to University Paris VI.

References

1. R. People, J.C. Dean and D.V. Lang, *J. Vac. Sci. Technol.*, **A3**, 846 (1985).
2. R. People, IEEE J. Quantum Electron. **QE22**, 1696 (1986).
3. T. Mishima, C.W. Fredrickson, G.F.A. van der Wal, D.J. Graveston, R.A. van den Heuvel and A.A. van Gorkum, *Appl. Phys. Lett.*, **57**, 2567 (1990).
4. P.J. Wang, F.F. Fang, B.S. Meyerson, J. Nocera and B. Parker, *Appl. Phys. Lett.*, **54**, 2333 (1989).
5. P.J. Wang, B.S. Meyerson, F.F. Fang, J. Nocera and B. Parker, *Appl. Phys. Lett.*, **55**, 2701 (1989).
6. F.F. Fang, P.J. Wang, B.S. Meyerson, J. Nocera and K.E. Ismail, *Surface Science*, **263**, 175 (1992).
7. V. Venkataraman, P.V. Schwartz and J.C. Sturm, *Appl. Phys. Lett.*, **59**, 2877 (1991).
8. F.F. Fang and W.E. Howard, *Phys. Rev. Lett.*, **16**, 797 (1966).
9. G. Bastard, *Wave mechanics applied to semiconductor heterostructures*, Les Editions de Physique, Paris, p. 219 (1985).
10. C. Absurener, J.P. Kothaus, J.F. Koch and G. Dorda, *Phys. Rev. B*, **34**, 2480 (1976).
11. P. Minih, Y. Guldner, J.P. Verrier, M. Voos, P. Deloche and N.T. Linh, *Appl. Phys. Lett.*, **52**, 982 (1988).

Sample	Spacer d(nm)	P_{SiH} (10^{11} cm^{-2})	P_{QHE} (10^{11} cm^{-2})
Symmetrically doped structures			
S1	10	6.2	12.4
S2	20	4.0	7.8
S3	40	2.25	4.3
Single side doped structures			
S4	10	6.8	6.8
S5	10	6.7	8.1

Table 1 Parameters of the symmetrically and asymmetrically doped Si-Ge structures used here

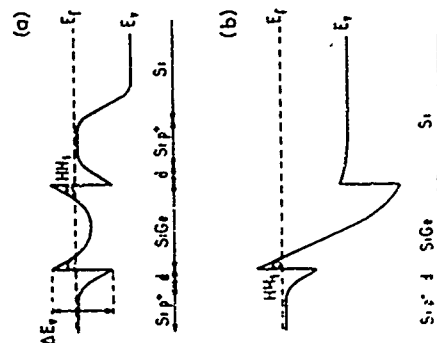


Figure 1 Valence band diagram for (a) a symmetrically doped structure and (b) a single side doped structure as S4. The cap layer is not shown

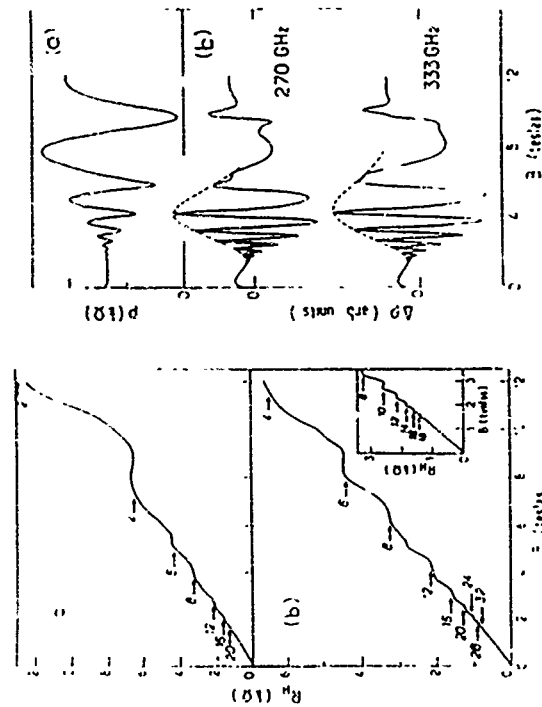


Figure 2 : Hall resistance versus B at $T=1.6K$ for (a) S2 and (b) S1. The arrows give the position of the quantized plateaus with the corresponding filling factors. The inset represents the Hall resistance at low B in S4.

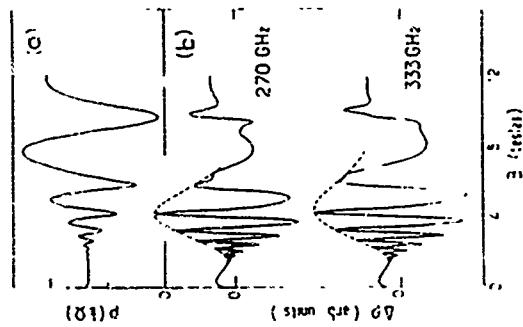


Figure 3 : (a) p and (b) Δp versus B at $1.6K$ in S4

TuP26

Photoluminescence and magnetotransport of 2D hole gases in Si/SiGe/Si heterostructures

R. Leo, R. Apeiz, L. Vescan, A. Hartmann, U. Zastrow, A. Leuther, T. Schäfers and W. Lüth

Institut für Schicht- und Ionentechnik (ISI), Forschungszentrum Jülich GmbH, D-52425 Jülich, Germany

Abstract

p-type modulation-doped Si/Si_{0.8}Ge_{0.2}/Si strained layer double heterostructures with $x \sim 0.2$ have been epitaxially grown on (100) Si substrates using low pressure chemical vapor deposition (LPCVD). The modulation doping effect has been obtained by two remote boron-doped Si layers ~ 10 nm thick. Hole mobilities as high as $3900 \text{ cm}^2/\text{Vs}$ have been obtained at 4.2 K comparable to the best reported values, so far. The temperature dependence of the 2D hole concentration and mobility shows characteristic remote ion-dominated scattering. Clear quantum Hall plateaus and Shubnikov-de Haas oscillations were observed. The photoluminescence (PL) from the SiGe quantum well (QW) shows excitonic behaviour in its variation with excitation power. A general trend of increasing PL intensity with the mobility of the 2D hole gas was observed. The high hole mobility and strong PL reflect the good interfacial quality of the LPCVD Si/SiGe/Si heterointerfaces.

1 Introduction

In recent years the Si/SiGe system has attracted much interest because of its potential applications in silicon-based circuits. In particular, 2D hole gases play the key role in the p channel modulation doped field effect transistor (MODFET). There is also some hope that Si/SiGe structures could be used for optoelectronic devices like detectors as well as light emitting diodes. In this paper, we present optical and electrical investigations of modulation doped Si/SiGe/Si QW structures grown by LPCVD. It results that LPCVD is a suitable method for the fabrication of structures containing 2D hole gases with mobilities comparable to the best published values. We report the observation of strong PL from modulation doped Si/SiGe/Si structures and explain the origin of the different peaks, first presented by us in

[1]. A very interesting property is a considerable enhancement of the PL intensity from the modulation doped SiGe QW relative to undoped QW structures.

2 Experiment

The Si/SiGe/Si heterostructures were epitaxially grown by LPCVD on n-type Si (100) 1000 Ωcm . The samples consist mainly of an undoped Si_{0.8}Ge_{0.2} layer (~ 15 nm) between two remote p⁺Si layers (~ 10 nm, doped $\sim 3 \times 10^{18} \text{ cm}^{-3}$) separated by undoped Si spacers (10-40 nm). The self-consistent calculation of the band edges of this samples is shown in Fig. 1. The Hall effect was measured on samples patterned with van der Pauw geometry, while for Shubnikov-de Haas measurements the Hall bar geometry was used. Ohmic con-

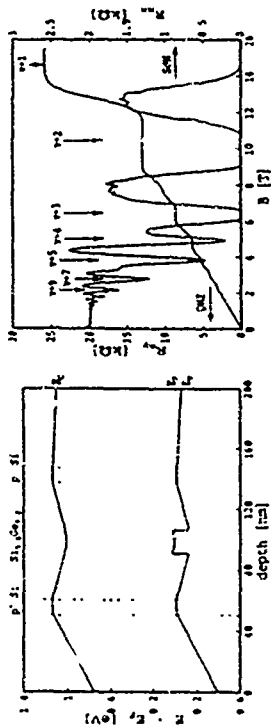


Fig. 1. Self-consistent calculated band edges of a modulation doped Si/Si_{0.8}Ge_{0.2}/Si structure at 20 K without illumination. The hole density in the QW was computed to $5.3 \times 10^{11} \text{ cm}^{-2}$.

tacts were Al/Ti/Au/Cr alloyed at 380°C for 2 min. Photoluminescence was carried out with a Fourier transform spectrometer equipped with a cooled Ge-detector. The samples were mounted in a continuous flow He-cryostat and excited by an Ar ion laser (488 nm).

3 Magnetotransport

In low field Hall effect measurements we observed a weak temperature dependence of hole mobility and concentration below 30 K and a clear dependence on space thickness in our samples. This demonstrates clearly the presence of a 2D hole gas where remote ion scattering is dominating. Fig. 2 shows well defined Shubnikov-de Haas (SdH) oscillations and carrier quantum Hall (QHE) plateaus of the sample with the largest Hall mobility, exhibiting $\mu = 3900 \text{ cm}^2/\text{Vs}$ at 4.2 K and $\mu = 870 \text{ cm}^2/\text{Vs}$ at 50 mK. These values are comparable with the best published results so far [3, 4]. The onset of SdH oscillations is already observable at fields as low as $B = 0.5 \text{ T}$. Apart from filling factor $\nu = 2$ a d 4 only odd filling factors were observed.

4 Photoluminescence

PL spectra of a modulation doped sample containing a 15 nm SiGe layer are presented in Fig. 3. They show no-phonon transitions and their TO-phonon replicas arising from

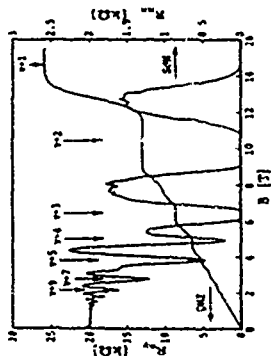


Fig. 2. QHE and SdH measurements at 50 mK of the modulation doped sample with the highest mobility.

This is possibly due to the overlap of Landau levels due to spin splitting at lower fields [3, 4]. The low field Hall effect hole density was $p_H = 4.5 \times 10^{11} \text{ cm}^{-2}$ while the density determined from SdH was $p_{SdH} = 4.8 \times 10^{11} \text{ cm}^{-2}$. This indicates that only one 2D conducting channel is present in the SiGe layer in agreement with self-consistent calculations (Fig. 1). From the calculations we obtained the value $p_{SdH} = 5.3 \times 10^{11} \text{ cm}^{-2}$ using the characterisation data for doping and layer sequence and effective masses obtained by solving the 6x6 Luttinger-Kohn Hamiltonian. There are no harmonic components in the SdH oscillations showing that only one sub-band is occupied which is also in agreement with the calculations. Furthermore, there are no parallel conducting channels in the sample at low temperatures demonstrated by the vanishing longitudinal magnetoresistance R_{xx} at the QHE plateaus.

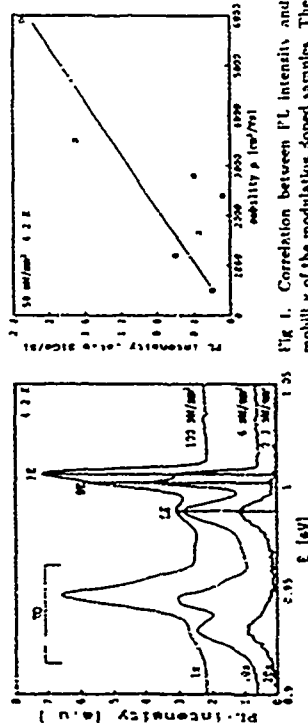


Fig. 3. PL spectra of a modulation doped sample at different excitation power densities at 4.2 K.

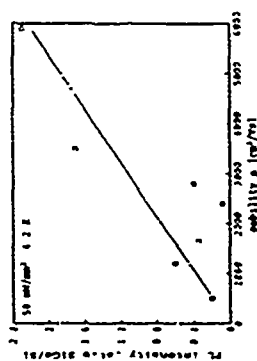


Fig. 1. Correlation between PL intensity and mobility of the modulation doped samples. The PL intensity ratio is given by the ratio of the PL peak height of SiGe and Si at 4.2 K.

the SiGe quantum well similar to that observed by many other authors in undoped structures [5, 6]. By temperature and excitation power density dependent measurements the different no-phonon peaks were assigned to localized excitons (LE), bound excitons (BE), and free excitons (FE). In Fig. 3 spectra with three different excitation power densities P are shown. The intensity $I \sim P^n$ of the FE peak exhibits linear to superlinear behavior with $n=1-1.3$ while the BE peak varies sublinearly with $n=0.79-0.94$. The LE peak shows saturation behavior typical for localized excitons [6]. The FE and BE peaks are very sharp with half widths of 4.6 meV. With increasing temperature only the FE peak remains. The energy difference between the FE and the BE peak (~ 3 meV) is the typical binding energy for excitons at shallow impurities, very probably residual boron ($\sim 1 \times 10^{16} \text{ cm}^{-3}$) in our samples. The energy shift with excitation power density of the FE peak is small being of the order of 2 meV. So there is no marked difference in undoped samples except that the PL intensity is enhanced more than one order of magnitude. This is in contrast to measurements we compare samples where different param-

eters (spacer thickness, doping concentration etc.) are changed. Furthermore, some kinds of impurities not easily controllable in the epitaxy process may have a much greater influence on PL than on mobility. Possibly they determine in some samples the PL efficiency.

5 Conclusions

In conclusion, we observed high mobility and strong PL of L-PCVD grown modulation doped Si/SiGe/Si structures. This demonstrates the high quality of the Si/SiGe heterointerfaces and the low concentration of impurities and defects. It was shown that p-type modulation doping leads to a strong enhancement of luminescence compared to undoped samples. This was explained by the additional confinement of the photoexcited electrons by an attractive potential caused by the modulation doping.

6 Acknowledgments

The authors are grateful to G. Abstreiter for interesting discussions. The authors also wish to thank P. Gartner for the effective mass calculations, T. Stoica for the Hall bar samples and K. Wambach for technical assistance.

References

- [1] L. Vescan, R. Loo, A. Hartmann, U. Zastrow, A. Leuther, T. Schäfers, T. Stoica and H. Lüth, to be published in *Proc. Int. Conf. on the Formation of Semiconductor Interfaces 4*, Jülich, Germany, eds. H. Lüth, W. Mönch, J. Follmann, World Scientific (1993).
- [2] L. Vescan, K. Schmidt, C. Dieker, H. P. Lang, F. Vescan and H. Lüth, *Thin Solid Films* 222, 3 (1992).

- [3] F.F. Fang, P.J. Wang, B.S. Meyerson, J.J. Nozera and K.E. Ismail, *Surface Science* 236, 173 (1992).
- [4] J.F. Nitzel, F. Meier, E. Fress and G. Abstreiter, *Thin Solid Films* 222, 150 (1992).
- [5] J.C. Sturm, H. Manoharan, L.C. Lenchysyn, M.L.W. Thewalt, N.L. Rowell, J.-P. Noël and D.C. Houghton, *Phys. Rev. Lett.* 66, 1562 (1991).
- [6] L.C. Lenchysyn, M.L.W. Thewalt, J.C. Sturm, P.V. Schwartz, E.J. Prinz, N.L. Rowell, J.-P. Noël and D.C. Houghton, *Appl. Phys. Lett.* 60, 3174 (1992).
- [7] M.S. Skolnick, J.M. Rorison, K.J. Nash, D.J. Mowbray, P.R. Tapster, S.J. Bass and A.D. Pitt, *Phys. Rev. Lett.* 58, 2130 (1987).

Tup27

A NEW TECHNIQUE FOR DIRECTLY PROBING THE INTRINSIC TRISTABILITY AND ITS TEMPERATURE DEPENDENCE IN A RESONANT TUNNELING DIODE

M. L. F. Lerch, A. D. Martin and P. E. Simmonds
Department of Physics, University of Wollongong, Wollongong, NSW 2522, Australia.

L. Eaves and M. L. Leadbeater
Department of Physics, University of Nottingham, Nottingham NG7 2RD, England.

ABSTRACT

A new measurement technique employing a positively sloping load line has been used to probe the region of apparent bistability near a tunneling resonance in the electrical characteristics of a resonant tunneling diode. This technique is equivalent to using a voltage source and negative series resistance. The appearance of bistability is an artifact of the conventional measuring technique which uses a load line with negative slope. The complete characteristic is found to be a continuous Z-shaped curve between 20 K and 150 K, corresponding to tristability and in accordance with theoretical models based on the effects of charge accumulation in the central quantum well of the diode. The width of the tristable region passes through a maximum at 40 K and, at 150 K, disappears as the resonance broadens. Above this temperature the resonance develops a region of negative differential resistance (NDR). As the device is cooled below 20 K additional structure develops in the central arm of the Z, with some portions of the characteristic exhibiting five stable current states at temperatures below 15 K. At 1.2 K, the effect of an in-plane magnetic field mimics that of increasing temperature.

INTRODUCTION

The occurrence of intrinsic bistability in the electrical characteristics (I-V curves) of semiconductor double-barrier structures (DBSs) has attracted considerable recent attention, both experimentally and theoretically. When a DBS device is biased, electron tunneling through the barriers and enclosed quantum well can show large resonances which occur when incoming electron coincide in energy and transverse momentum with quantum states quasi-localized in the well. The characteristic in the vicinity of these resonances have regions of either negative differential resistance (NDR) [1] or apparent bistability [2-5] and devices which display both types of curve have been subject to detailed experimental study. In the bistable case there has been some initial debate as to the cause, since circuit oscillations in a region of NDR, or NDR together with a series resistance, can simulate this effect [6-8]. It is now clear that bistability which is intrinsic to the device has been realized experimentally in appropriately designed structures [3-5] and is caused by electrostatic feedback due to charge buildup in the well [2,5,9-11]. This effect is particularly pronounced in devices with asymmetric barriers. The asymmetry facilitates the accumulation of free charge in the well when the device is biased so that the probability of tunneling into unoccupied well states through the emitter barrier greatly exceeds that of tunneling out through the thicker collector barrier [3-5]. The conventional technique for measuring the device characteristic uses a voltage source in series with the device together with some positive resistance. Although the resistance can be made arbitrarily small, the interior of the bistability remains inaccessible to this technique. The appearance of bistability may therefore be an artifact of the conventional measuring technique and could conceal an important portion of the static characteristic which would indicate charge accumulation in the well [9,11], predict a characteristic models, which include effects of charge accumulation in the well [9,11], predict a characteristic in the form of a continuous Z-shaped curve provided that the tunneling resonance is sufficiently sharp. Such a characteristic should more correctly be called tristable [10]. The form of the

characteristic in this region could yield useful information on the details of the tunneling process, particularly where there is substantial charge density in the well. In this paper we show that the interior of the bistability in one such device is indeed accessible to a measurement technique which employs a load line with positive slope, corresponding to a voltage source and a negative series resistance. The characteristic near the first tunneling resonance of the device under study is a continuous Z-shaped curve between 150 K and 20 K and develops additional structure as the device is cooled further. At 4.2 K, the effect of a small in-plane magnetic field ($B < 1$ T) mimics that of increasing temperature.

DEVICE STRUCTURE AND CHARACTERISTICS

The active region of the asymmetric device studied consists of a 5.8 nm GaAs quantum well, sandwiched between Al_{0.3}Ga_{0.7}As barriers of different widths, 8.3 nm and 11.1 nm. Lightly doped GaAs spacer layers separate this region from the heavily doped n⁺ contact regions. An applied bias voltage causes an accumulation layer and associated two-dimensional electron gas (2DEG) to form adjacent to the emitter barrier. Resonant tunneling occurs when this voltage brings one of the two quasi-bound states in the well into energy coincidence with the quasi-bound state in the emitter. Full details of the layer structure are given in Refs. 4 and 5 and a schematic diagram of the conduction band edge under forward bias is shown in the inset to Fig. 1(a). The electrical characteristics have already been reported in detail and show two resonances in each bias direction [5]. Under reverse bias (electrons tunneling into the well through the thicker barrier) the resonances are sharp and exhibit NDR. Under forward bias the respective peak resonant currents are more than an order of magnitude larger, much broader and show apparent bistability. The characteristic due to the first resonance measured conventionally at 2 K is shown in Fig. 1(a). The region of apparent bistability near a bias of 0.7 V is studied in the present work. The charge buildup in the well which causes the extended voltage range of the first forward bias resonance (0.3 V to 0.7 V) has been confirmed by detailed magneto-capacitance and luminescence studies [5,14]. The fact that the device exhibits NDR under reverse bias (where no charge build up is detected) is in itself strong evidence in support of the intrinsic nature of this bistability.

MEASUREMENT TECHNIQUE AND CIRCUIT STABILITY

The measurements reported here (Fig's 3 and 4) were taken using a voltage supply designed to have a negative output resistance (NOR), corresponding to a load line with positive slope. This enables the portion of the characteristic inside the region of apparent bistability to be probed (see Fig. 2(a)). An active circuit designed to meet the NOR requirement is shown in Fig. 2(b). Additional details of this circuit will be reported elsewhere. Provided that the device characteristic is continuous, the load line can be made to intersect any part of it inside the bistability at a point Q if $|R_L| > R_d$. Here R_d is the dynamic resistance dV/dI of the device at Q and $-1/R_L$ is the slope of the load line. Under these conditions the total circuit resistance $R_L + R_d < 0$ and circuit oscillations can occur due to the exponential growth of any initial perturbation. Circuit analysis based on dynamic circuit models of the NOR measuring circuit [15] and device [5,12,13], predicts a narrow range of values of R_L and C_L for which stability should occur. (C_L is a capacitance which appears in parallel with R_L in the NOR equivalent circuit. Both parameters are adjustable). These values form an "island of stability" in R_L - C_L space. Stable measurements, for which no oscillations up to 400 MHz were observed, could be made with values of R_L and C_L close to those predicted, giving some confidence in the circuit models used. Varying R_L or C_L outside this range caused large amplitude oscillations at frequencies up to a few hundred kHz.

MEASUREMENTS USING THE NOISE CURVE AND DISCUSSION

Measurements made with the NCR circuit on the device characteristic outside the bistable region gave the same results as those obtained using conventional techniques and, for measurements obtained at 4.2 K, correspond closely to published data for an essentially identical device [4]. Adjusting the position of the load line by varying V_{in} and R_L (see Fig. 2(b)) gave a smooth, continuous and reversible transition into the interior of the bistability. The results of these measurements are shown in Fig. 3, where the complete characteristics of the device near the peak of the first tunneling resonance close to a bias of 0.7 V are plotted for a number of temperatures between 160 K and 4.2 K. For temperatures between about 150 K and 20 K these results clearly demonstrate the continuous and unstable nature of the intrinsic device characteristic inside the region of apparent bistability as measured conventionally. The re-entrant form of the (IV) curve (resonance overhang) predicted in Ref. 10 (3DEG in the emitter) and Ref. 11 (2DEG in the emitter) corresponding to the present device is reproduced qualitatively in the experimental data. As the temperature is reduced below 20 K the overhang region of the characteristic develops more complex behaviour. Between 20 K and 4.2 K the resonance exhibits marked narrowing close to the current peak and an additional broader shoulder develops between the peak and foot. This coincides with a decrease both in the overall voltage width ΔV of the overhang and in the peak current. Very similar behaviour is observed for three different devices on two separate chips and is insensitive to (in fact usually) small variations in the slope of the load line.

Plots of the voltage width ΔV , together with bias at the current peak V_p , against T are shown in the inset to Fig. 3. As expected, very similar data are obtained from conventional bistability width measurements [12] although switching between high and low current states in conventionally measured data occurs at bias voltages near the peak and foot of the resonance overhang. As this temperature is increased above 4.2 K, both ΔV and V_p initially increase, with ΔV reaching its maximum value near 40 K. At still higher temperatures, broadening of the resonance causes a decrease in ΔV and the bistability vanishes near 150 K. Above this temperature the resonance exhibits NDR, an observation consistent with previous measurements [12].

The detailed origin of the low temperature structure in the overhang region is unclear. The sharp corresponding reverse bias resonance displays no such satellite structure and quite separate LO phonon satellites lie at higher biases. The broad shoulder is possibly caused by an inelastic process due to some form of electron-electron interaction, for example electron shake-up or emission of a plasmon at a near k_F in the emitter 2DEG. Either of these processes would be expected to give satellite structures separated by a few mV from the main emitter to well resonance voltage. Further experiments on different device structures would be required to establish that the complex characteristic observed here is an intrinsic feature of the tunneling process in devices displaying bistability. In the present asymmetric structure which exhibits strong charge build-up in the well at the first resonance, the peak-to-valley current ratio is significantly degraded relative to the sharp reverse bias resonance, and weak off-resonance and satellite tunnelling processes appear relatively enhanced. This is because the peak forward bias current is limited by the maximum carrier density, $n_{w,max}$, which can accumulate in the well at resonance ($E_F = E_1$) together with the low transmission probability of the wide collector barrier. This value of $n_{w,max}$ ($2.2 \times 10^{11} \text{ cm}^{-2}$) occurs when the Fermi energies of the 2D emitter and the well (and hence the sheet densities n_e , $n_{w,max}$ respectively) are approximately equal, as has been confirmed experimentally [4,5].

Another feature of interest in Fig. 3 is the initial increase in ΔV and V_p with temperature despite the obvious broadening of the re-entrant resonance curve (made evident by the new technique which exposes the full lineshape). This observation suggests that $n_{w,max}$ can be enhanced by thermal effects beyond its 'resonance' value so that $n_{w,max} > n_e$. It has been previously demonstrated that strong enhancement in the value of $n_{w,max}$ at resonance can be achieved by application of a quantising magnetic field (BQU) with consequent large increase in peak current and ΔV [14]. Alternatively, a smaller increase in $n_{w,max}$ and ΔV is obtainable by

application of a small in-plane field ($B \parallel J$). Results taken at $B \parallel J = 0.5$ and 1 T , at 4.2 K are shown in Fig. 4. The effect of the field is strikingly similar to that caused by an increase in temperature. This observation suggests a possible explanation for the temperature induced increase in V_p and overhang ΔV shown plotted in the inset to Fig. 3. The in-plane B field generally causes spreading and a shift in the resonance cut off to slightly higher emitter to well voltage [16]. At the new resonance cut off the levels $E_1(well)$ and $E_1(emitter)$ are misaligned with E_1 lying at energy δE below E_1 . This allows the stored charge density for $B > 0$ to exceed its maximum zero field value (i.e. $n_{w,max} > n_e$) since as mentioned above, $n_{w,max}$ corresponds to alignment of emitter and well Fermi levels. Field induced enhancement of the resonance overhang and increased V_p and peak current are expected, and observed (see Fig. 4), since all three depend on $n_{w,max}$ (peak current is approximately $\propto n_{w,max}$). From the discussion in Ref. 16 we estimate a B field induced spreading $\delta E = \hbar^2 k_F \Delta k / m$ where $\Delta k = eBL_{em}/\hbar$, k_F is the emitter Fermi wavevector and $L_{em} = 18 \text{ nm}$, the effective emitter to well separation [4]. For $B = 1 \text{ T}$, this yields $\delta E \sim 1 \text{ meV}$ corresponding to $\sim 15\%$ increase in $n_{w,max}$, from which an increase in ΔV of $\sim 65 \text{ meV}$ is estimated, in good agreement with $\sim 70 \text{ mV}$ obtained experimentally. Since elevated temperature and applied magnetic field have similar effects on the characteristic there may be an underlying common mechanism in which thermal broadening of the resonance plays a role analogous to the field induced spreading.

ACKNOWLEDGEMENTS

The expert technical assistance of Dale Hughes is gratefully acknowledged. This work was partially supported by the Australian Research Council and the U.K. Science and Engineering Research Council.

REFERENCES

- 1 See, e.g. E. E. Mendez, 'Physics of resonant tunneling in semiconductors', in *Physics and Applications of Quantum Wells and Superlattices*, edited by E. E. Mendez and K. von Klitzing, NATO ASI Series B Physics, Vol 170, p. 159 (Plenum, New York, 1988).
- 2 Y. J. Goldman, D. C. Tsui and J. E. Cunningham, *Phys. Rev. Lett.*, **58**, 1256 (1987).
- 3 A. Zaslavsky, V. J. Goldman, D. C. Tsui and J. E. Cunningham, *Appl. Phys. Lett.*, **53**, 1408 (1988).
- 4 M. L. Leadbeater, E. S. Alves, L. Eaves, M. Henini, O. H. Hughes, C. A. Payling, F. W. Sheard and G. A. Toombs, *Semicond. Sci. Technol.*, **3**, 1060 (1988).
- 5 M. L. Leadbeater, E. S. Alves, F. W. Sheard, L. Eaves, M. Henini, O. H. Hughes and G. A. Toombs, *J. Phys.: Condens. Matter*, **1**, 10605 (1989).
- 6 T. C. L. G. Sollner, *Phys. Rev. Lett.*, **59**, 1622 (1987).
- 7 V. J. Goldman, *Phys. Rev. Lett.*, **59**, 1623 (1987).
- 8 W. D. Goodhue, T. C. L. G. Sollner, H. Q. Le, E. R. Brown and B. A. Vojac, *Appl. Phys. Lett.*, **49**, 1086 (1986).
- 9 M. Tsuchiya and H. Sakaki, *Appl. Phys. Lett.*, **49**, 88 (1986).
- 10 F. W. Sheard and G. A. Toombs, *Appl. Phys. Lett.*, **52**, 1228 (1988).
- 11 D. D. Coon, K. M. S. V. Bandara and H. Zhao, *Appl. Phys. Lett.*, **54**, 2115 (1989).
- 12 F. W. Sheard and G. A. Toombs, *Semicond. Sci. Technol.*, **7**, B460 (1992).
- 13 M. L. Leadbeater, Ph.D. Thesis, University of Nottingham (1990).
- 14 F. W. Sheard and G. A. Toombs, *Solid State Electron.*, **32**, 1443 (1989).
- 15 L. Eaves, M. L. Leadbeater, D. G. Hayes, E. S. Alves, F. W. Sheard, G. A. Toombs, P. E. Simmonds, M. S. Stollnick, M. Henini and O. H. Hughes, *Solid State Electron.*, **32**, 1101 (1989).
- 16 A. D. Martin, M. L. F. Lerch, P. E. Simmonds, L. Eaves and M. L. Leadbeater, *Elgth International Conference on Hot Carriers in Semiconductors* (Oxford, U.K. 1993).
- 17 M. L. Leadbeater, L. Eaves, P. E. Simmonds, G. A. Toombs, F. W. Sheard, P. A. Clifton, G. Hill and M. A. Pate, *Solid State Electron.*, **31**, 707 (1988).

FIGURE CAPTIONS

Figure 1 (a) (b) characteristics at 2K of the asymmetric double barrier structure, measured using a conventional (near vertical) load line. Only the first resonance is shown in each bias direction. In forward bias the current switching directions observed using this measurement technique are indicated by arrows and delineate the region of apparent bistability. The broad peak near 0.9 V is associated with LO phonon assisted tunneling. Inset: Schematic conduction band energy diagram for the device under forward bias.

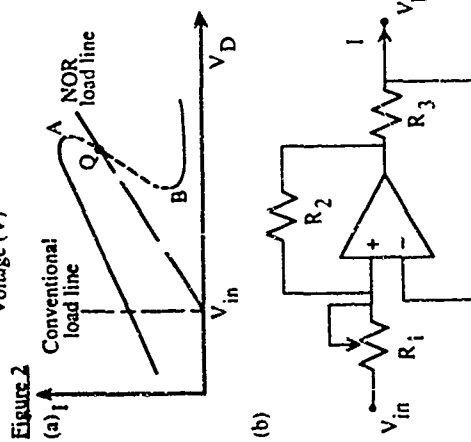
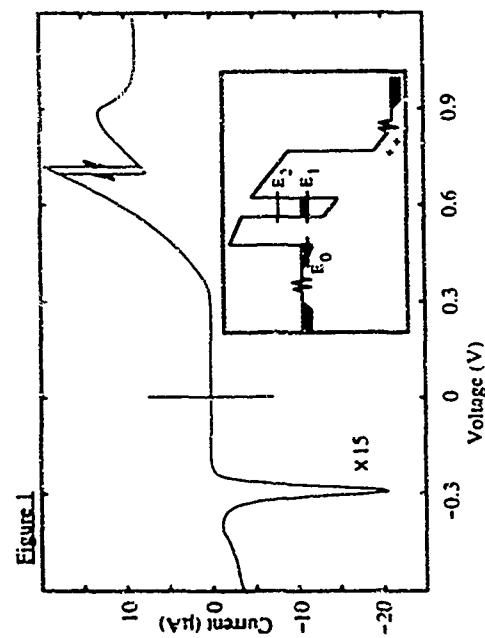
Figure 2 (a) Schematic region of apparent bistability shown on an expanded voltage scale. The conventional load line corresponds to a voltage source V_{in} and a (small) positive series resistance R_L . The gradient of the load line is $-1/R_L$. Switching occurs at A and B as the load line is swept through the device characteristic by varying V_{in} and any part of the characteristic between A and B is inaccessible for any positive value of R_L . The load line for a voltage source and a negative series resistance (an NOR supply) has a positive slope and can be used to probe the region between A and B provided the slope of the load line is less than the slope of the device characteristic at Q (1/R_Q). This is equivalent to the requirement that $R_L + R_Q < 0$.

(b) Circuit diagram for a NOR voltage supply. The output voltage is given by $V_D = V_{in} + (R_L R_3 / R_2) I$ (i.e. V_D increases as more current I is drawn from the supply). This is the equation of the NOR load line shown in Fig. 2(a). The circuit is equivalent to a voltage source V_{in} in series with a negative resistance $R_L = -R_1 R_3 / R_2$.

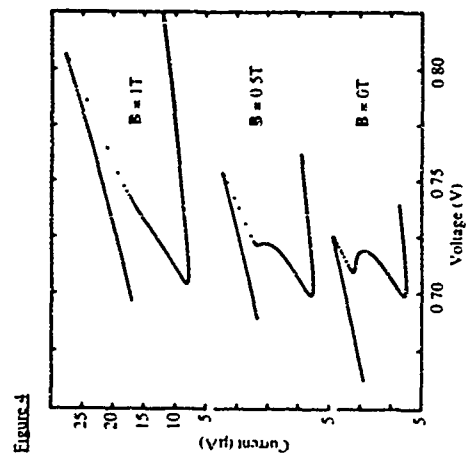
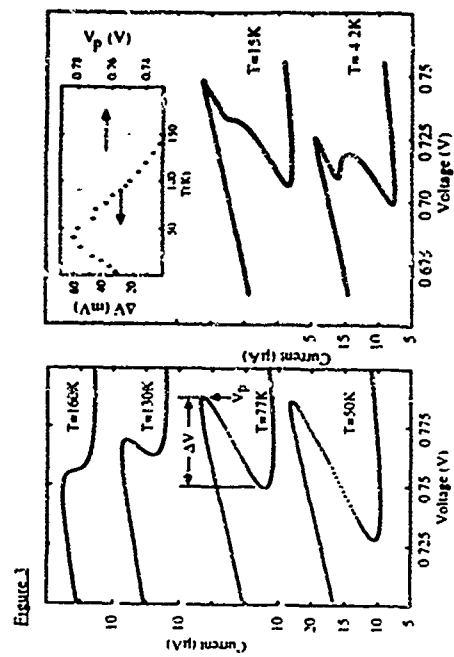
Figure 3 Temperature dependence of the device characteristics measured near the peak of the resonance using the NOR supply. The onset of instability and the development of more complex structure is shown as the temperature is lowered. Inset: Variation with temperature of the width, ΔV , of the voltage overhang and V_p , the voltage at the resonance peak.

Figure 4

Effect of an in plane (B 1 J) magnetic field on the device characteristic at 4.2K. The field extends the range of the voltage overhang and has a similar effect to that caused by increasing the temperature between 4.2 K and 50 K, as shown in Fig. 3.



-591-



-592-

Mesoscopic Effects in Resonant Tunneling Diodes

J W Sakai^a, N La Scala Jr^a, P C Main^a, P H Beton^a, T J Foster^a, A K Geim^a,
L Eaves^a, M Henini^a, G Hill^b and M A Paic^b

^a Department of Physics, University of Nottingham, Nottingham, NG7 2RD, UK.
^b Department of Electrical Engineering, University of Sheffield, Sheffield, UK.

Abstract

We have investigated resonant tunnelling in GaAs/AlGaAs heterostructures which have been fabricated into mesas of cross section 0.6 $\mu\text{m} \times 0.6 \mu\text{m}$. A δ -layer of donors ($n = 2 \times 10^{24} \text{ m}^{-3}$) has been incorporated at the centre of the quantum well which is 9 nm wide. The $I(V)$ characteristics show a feature at $\sim 70 \text{ mV}$, which is below the threshold for the main resonance and is due to resonant tunnelling through single donor states in the well. This feature is also present in large area mesas. At lower biases and at low temperatures we see a pair of resonances which, although they occur in all small area mesas, differ in detail between devices with regard to their strength and bias position. The form of the low-bias structure is strongly dependent on temperature. Below 4 K where several very sharp steps appear, becoming sharper as T is decreased. We have also investigated the dependence of the new structure on magnetic field, B , parallel to the current direction. The features become sharper with increasing B in forward bias while, in reverse bias, the structure breaks up into a set of smaller peaks and we are able to see spin-splitting effects. We attribute the new features to tunnelling through potential fluctuations on the mesoscopic scale due to donor clustering. Although our devices are not small enough to observe OD quantization or size-related Coulomb blockade, the effects we observe are qualitatively and quantitatively similar to those seen in sub-micron mesas by other authors and attributed to these effects.

There has been a great deal of recent interest in the electronic transport properties of systems in which there is confinement of the electrons in all three dimensions. One method of attempting to achieve this confinement is to fabricate a resonant tunnelling diode (RTD) with lateral dimensions less than $1 \mu\text{m}$ [1-6]. An RTD involves electron tunnelling through levels in the quantum well formed between two barriers and for wells a few nm wide, quantum effects can be observed even at room temperature. However, the quantum effects due to the lateral confinement have proved more elusive to identify unambiguously. Although a number of extra features in the current-voltage characteristics, $I(V)$, have been observed in small area diodes at low temperatures, they have been variously attributed to quantum confinement [1,2,4], single electron charging effects [2,4,6] and impurities [3]. In earlier work [3] we have demonstrated that, whatever other effects may be important in a given device, it is vital to consider impurities which may segregate or diffuse into the quantum well.

In this paper, we investigate the effects of impurities by studying devices in which we have incorporated a δ -layer of impurities into the quantum well. Furthermore, the devices are intermediate in lateral dimension ($\sim 0.6 \mu\text{m}$) between the sub-micron and the large area ($\sim 100 \mu\text{m}$) diodes. These devices are not small enough to show lateral quantum effects but are *mesoscopic* in the sense that they show sample-specific features, qualitatively similar over a range of different devices but differing in quantitative detail.

0.6 μm	GaAs	$n = 2 \times 10^{24} \text{ m}^{-3}$
80.6 nm	GaAs	$n = 2 \times 10^{23} \text{ m}^{-3}$
50.9 nm	GaAs	$n = 2 \times 10^{22} \text{ m}^{-3}$
10.2 nm	GaAs	undoped spacer
5.7 nm	$\text{Al}_{0.4}\text{Ga}_{0.6}\text{As}$	barrier
4 nm	GaAs	undoped 1/2 well
1 nm	GaAs	$n = 2 \times 10^{22} \text{ m}^{-3}$
4 nm	GaAs	undoped 1/2 well
5.7 nm	$\text{Al}_{0.4}\text{Ga}_{0.6}\text{As}$	barrier
10.2 nm	GaAs	undoped spacer
50.9 nm	GaAs	$n = 2 \times 10^{22} \text{ m}^{-3}$
80.6 nm	GaAs	$n = 2 \times 10^{23} \text{ m}^{-3}$
2 μm	GaAs	$n = 2 \times 10^{24} \text{ m}^{-3}$
	GaAs	n^+ substrate.

Table 1

segregation of dopants during growth. Mesas $\sim 6 \mu\text{m}$ square were fabricated using photolithography and dry etching. Electrical measurements were made using standard dc techniques at temperatures down to 280 mK.

In Figure 1 we show $I(V)$ at $T = 4.2 \text{ K}$ in both forward and reverse bias for a $6 \mu\text{m}$ square mesa incorporating a δ -layer of impurities and grown with a substrate temperature of 630°C . We define forward bias as the top contact positive so that the electrons are travelling up from the substrate. The curve is essentially identical to that of a large area mesa, suitably scaled. There is a small shoulder at $\sim 70 \text{ mV}$, visible in the $\times 50$ expanded curve, which we have shown previously is due to tunnelling via states bound to single donors in the quantum well [7]. Devices which are grown at 550°C , where there is far less segregation of dopants, show this feature far more clearly. When the scale is expanded $\times 25000$ some additional structure with $I < 100 \text{ pA}$ appears at low bias ($|V| < 50 \text{ mV}$). Unlike the principal resonant peak at approximately $\pm 150 \text{ mV}$ this structure is strongly asymmetric between forward and reverse bias. In addition, although we see similar features in all devices incorporating donors in the well, the detailed peaks are different, characteristic of a mesoscopic system. Generally, for higher concentration of impurities or higher substrate temperature during growth, the structure occurs at biases closer to zero. For consistency, all curves shown in this paper will be for the same device but we shall emphasize which features of the data are universal and which are device specific. In the control samples, where we have taken considerable trouble to reduce the number of stray donors by incorporating larger spacer layers and growth at low temperatures, there is still some additional structure but it occurs very close to the threshold for the main resonance. In one or two control devices we have observed single, isolated peaks at $V \sim 60 \text{ mV}$.

The sub-threshold structure in the doped devices is strongly temperature-dependent below $T = 4.2 \text{ K}$. This is illustrated in Figure 2 where we plot $\ln(I)$ versus V to emphasize the low bias structure. Curves for the five temperatures are offset for clarity and the current scale refers to the lowest curve. The dotted lines represent our noise threshold. The curve at $T = 4.2 \text{ K}$ is the

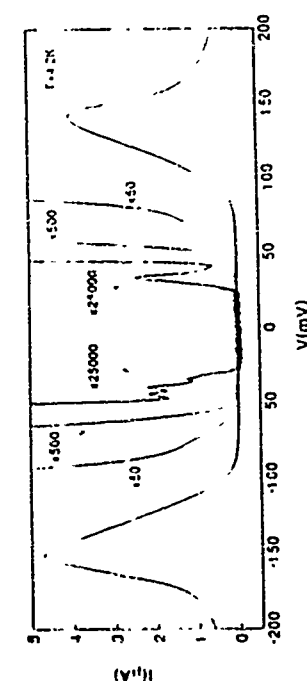


Figure 1.
I(V) characteristics at 4.2 K of a device of lateral dimension $b = 6 \mu\text{m}$ in forward and reverse bias.

same as is shown in Figure 1. As temperature is decreased, although the curve at high bias is unchanged, two notable features emerge. First, the structure becomes more pronounced at low temperatures although it is more or less unchanged below 1 K. Secondly, the onset of the structure, defined as the point at which the current is measurable above the noise, becomes very sharp indeed and at slightly higher bias there is a series of further sharp steps in both forward and in reverse bias. The sharpness of these curves is illustrated by the fact that the slopes of the onset and the next step (at -48 mV and $+45 \text{ mV}$) in both bias directions are limited only by the bath temperature. This is shown in Figure 3 where we plot the slope of the onsets of the structure of Figure 2 versus temperature. The solid line represents the equation

$$I = I_0 \exp \left\{ -\alpha e \Delta V / k_B T \right\} ; I_0 = 50 \pm 10 \text{ pA and } \alpha = 0.32$$

where ΔV is the measured voltage relative to the onset at $T = 0$. The constant α represents the relationship between energy difference and applied voltage near the onset of the structure. Equation 1 implies that the sharpness of the current onset is limited only by the thermal activation of electrons from the emitter chemical potential, implying that the emitter electrons are in thermal equilibrium with the main heat bath. Despite the peak structure being quantitatively different in different devices the sharpness of the onset appears to be universal, appearing in all devices studied, including the controls. This activated behaviour is discussed in more detail below but we note the similarity between our data and that seen elsewhere in smaller, sub-micron, devices and attributed to quantisation effects and Coulomb blockade [2].

Figure 4 illustrates the pronounced effect of a magnetic field on the sub-threshold features in I(V). The graph plots $\ln I$ versus V at $T = 1.24 \text{ K}$ for magnetic fields, B , of 0 to 16 T applied parallel to the current direction. Successive curves are offset for clarity and the current scale refers to the $B = 0$ curve. The dotted lines represent the noise level. Below about 4 T, the magnetic field has very little effect in both forward and reverse bias. At higher fields in forward bias, there is a general sharpening of the features and a shift of the onset to lower voltage will

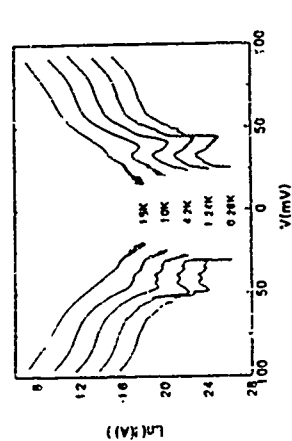


Figure 2.
In (1) versus V near the current threshold for 5 temperatures. The dotted lines represent the noise level. Curves are offset for clarity and the current axis refers to the lowest curve.

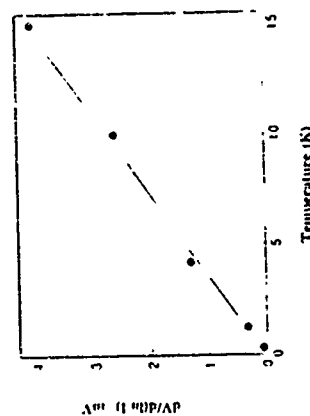


Figure 3.
 $\ln(I)$ versus T near the current threshold plotted against temperature. The straight line is the best fit.

structure is always sharper in reverse bias than in forward bias, (b) peaks develop and become sharper as B increases but eventually disappear for sufficiently large B , (c) the structure moves to lower bias, ie closer to zero and (d) spin splittings occur.

All the results displayed refer to a device $\sim 6 \mu\text{m}$ square. On this length scale there is no possibility of lateral quantum confinement causing the structure. Equally, the Coulomb charging energy for a single electron, $e^2/2C$, where C is the capacitance of a $6 \mu\text{m}$ planar diode, is ~ 100

increasing B . The features decrease in amplitude at the highest fields and there is also some evidence for additional structure appearing at intermediate values of B . The effect of the field is much more pronounced in reverse bias. The same general observations apply in forward bias but, in addition, for $7 \text{ T} < B < 11 \text{ T}$ we see the emergence of a set of sharp peaks, more or less evenly spaced in V . Furthermore, although the structure beyond onset at $B = 0$ is independent of temperature below 2 K (see Fig. 2), the features around $B = 10 \text{ T}$ become sharper as T is reduced below 1 K. This is shown in detail in Figure 5 in which we plot actual $I(V)$ in reverse bias at $T = 280 \text{ mK}$ for $7 \text{ T} < B < 13 \text{ T}$. Successive curves are offset by 100 pA. At $B = 10 \text{ T}$ the sharp, T-limited onset to the structure remains but there are now also six well-defined and evenly spaced peaks, four of which are split. We believe that this splitting, which has not previously been observed in sub-micron RTD's, is due to spin (see below). The spin-split peaks have a linewidth which is limited by temperature, even at 280 mK.

The presence of the six well-defined peaks at $B = 10 \text{ T}$ is not a universal property of the devices. However, it is quite generally the case that, with increasing B , (a) the structure is always sharper in reverse bias than in forward bias, (b) peaks develop and become sharper as B increases but eventually disappear for sufficiently large B , (c) the structure moves to lower bias, ie closer to zero and (d) spin splittings occur.

neV, which is far too small to explain the observed effects. Considering the thermally activated onset of the structure, equation 1 implies that, in the vicinity of the onset, we can relate applied voltage, V , to an energy scale, E , by $E = 0.32V$ eV. An energy of 100 neV is entirely negligible compared with the ~ 10 meV (ie $V \sim 30$ mV) which is required for onset of the structure. Nevertheless, our observations are very similar both qualitatively and quantitatively to those reported by other authors in sub-micron diodes which have been ascribed to Coulomb blockade.

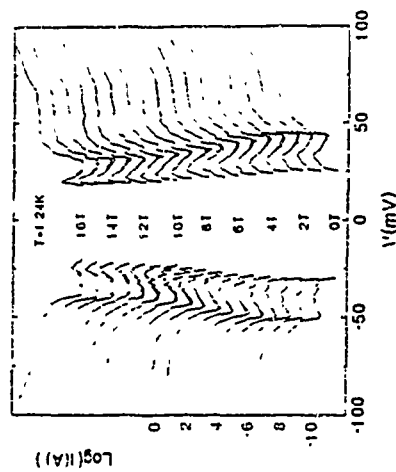


Figure 4. In (I) versus V at 1.24 K for various magnetic fields. The dotted lines are the noise level and curves are offset for clarity with the current axis referring to the lowest curve.

On the principal resonance of a RTD of this type, in which a spacer layer separates the barriers from the electrical contacts, it is well established that tunnelling takes place from a two-dimensional electron gas (2DEG) in an accumulation layer next to the emitter barrier into two-dimensional bound states in the well [8]. Our observed structure occurs at voltages well below the threshold for this process and lower even than that for tunnelling into shallow states in the well which are bound to single donor atoms [7]. Therefore, we are led to the conclusion that the structure must be due to tunnelling into deep localised states, possibly associated with clusters of donors in the well. Deeper energy levels allow tunnelling at biases closer to zero as seen in the experiment. We estimate that there are ~ 700 donors in the quantum well which, if we assume a random distribution, implies that there is a very high probability ($\sim 95\%$) of two donors lying within an effective Bohr radius of each other and a reasonable probability of three ($\sim 25\%$). The localised nature of the states has been confirmed by measurements made with B perpendicular to the current direction which will be reported elsewhere [9]. However, at such low biases in a disordered material we consider it unlikely that there is a uniform and continuous 2DEG from which to tunnel. Rather, it is likely that the electrons accumulate next to the emitter barrier as localised puddles in regions of low potential. At the relevant biases the mean sheet density is a few times 10^{14} m^{-2} . Some of these puddles may be associated with the same clusters of donors which give rise to the localised states in the well. Our model is that the structure at $B = 0$ at least, is due to tunnelling between an emitter state, possibly only containing a few electrons, and a more strongly localised state in the well. The shift of the onset of the structure to lower biases with increasing B is also consistent with the emitter state being more weakly confined. The sharpness of the onset is limited by thermal activation from the quasi-Fermi level in the emitter accumulation layer into the localised state if

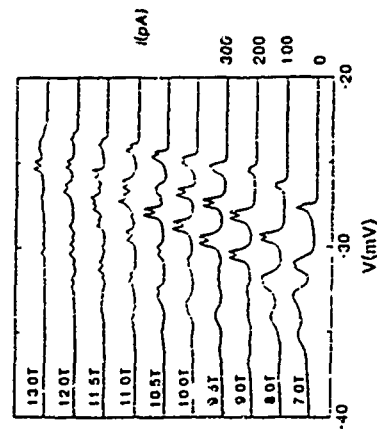


Figure 5. I(V) on a linear scale at $T = 280$ mK and various magnetic fields. Successive curves are offset by 100 pA.

the well, which is consistent with the observed experimental results. The natural linewidth of the state in the well may be very small if it is limited by the dwell time in the well, which we estimate to be about 3 ns. The sharp onset indicates that the electrons in the emitter are in thermal equilibrium with the main thermal reservoir even though we are in the regime where $eV \gg k_B T$. Note that there is no need to invoke Coulomb blockade as the origin of the step-like structure although it is likely that electron charging energies may be important in the localised states. Steps in I(V) which occur at higher values of bias may then be due to a succession of localised states in the well.

An important feature of our data is that the structure appears in I(V) and not in the differential conductance. In an RTD, the current is essentially a measure of the charge in the well. The initial current step, therefore, is probably a signature of a single electron in the well. The current of 50 pA would correspond to a lifetime ~ 3 ns for the state in the well, consistent with the barrier height and thickness. The structure we observe at higher magnetic field, as shown in Figure 5, is different in that it comprises a set of well defined peaks whose width is limited only by temperature. This is very important because it means that in between the peaks there is no charge state to another. There are however two important points to be made with regard to the peaks. First, at 10 T for example, the voltage spacing of the peaks is only ~ 2 mV. Even if we associate this directly with an energy difference, it is much smaller than the Landau level spacing at 10 T (~ 17 meV) which should represent the minimum energy separation of single particle states. Secondly, assuming that spin is conserved in the tunnelling process, the observation of peaks split by the magnetic field indicates that there must be a different spin splitting for the two states. Furthermore, the splitting itself is voltage dependent at a given magnetic field although at a given bias the splitting is reasonably linear in B. At 10 T it varies from $\sim 280 \mu\text{V}$ at $V = -26$ mV to $\sim 420 \mu\text{V}$ at $V = -28$ mV indicating a strong dependence on energy. These splittings can be related to a difference in the effective Landé g -factor, g_B^* , between the two states using $\Delta E = \Delta g^* \mu_B B$ where ΔE is the splitting in energy, μ_B is the Bohr magneton and $m^* = 1/2$. Assuming the energy is related to voltage by $E = eV$ with $\alpha = 0.32$, this gives values of $\Delta g^* = 0.3 \pm 0.5$ to be compared with the value $g^* = -0.44$ for electrons in bulk GaAs.

The above observations are consistent with the model of tunnelling from a weakly localised state near the emitter barrier into a more strongly localised state in the well. The different values of

SCHOTTKY-BARRIER TUNNELING SPECTROSCOPY OF A 2D ELECTRON SYSTEM IN DELTA-DOPED Si(100) LAYERS

J LINDNER, B KLEIN, and U KUNZE,
Institut für Technische Physik, Universität Erlangen-Nürnberg, D-91051 Erlangen, Germany
and

W KILINKI and I EISELE,
Fakultät für Elektrotechnik, Universität der Bundeswehr München, D-85577 Neubiberg, Germany

Abstract—Schottky-barrier tunneling junctions have been prepared on Si(100) layers with the sequence p-type buffer, Sb δ -doping layer, and an intrinsic layer ranging from zero to 10 nm thickness. The tunneling characteristics show structures arising from subband edges, from the bulk conduction band edge, and from the tunneling of holes into the metal. Exact layer thickness and doping parameters are gained from a self-consistent calculation of the subband structure.

In a number of experiments quantized two-dimensional (2D) electron systems have been investigated by electron tunneling spectroscopy, where the bias position of subband-edge-induced features in the second derivative d^2I/dV^2 of the current(I)-voltage(V) characteristic directly reflects the subband energies. The electron layer has been induced by native interface donor states in InAs [1], by the work-function difference of the electrodes in PbTe [2], Si [3], and InGaAs [4] metal-oxide-semiconductor (MOS) structures, by barrier doping in GaAs-AlGaAs heterostructures [5], and by planar-delta(δ)-doping layers in GaAs [6,7] and Si [8-10]. In particular for the tunneling experiments on Si the Schottky barrier junctions on δ -doped layers [8-10] showed considerably poorer quality than MOS-junctions with electron inversion layers [3]. In the latter samples subband levels could be detected up to energies of more than 500 meV above the Fermi level, subbands of the lower (unprimed) and higher (primed) series could be clearly distinguished, and the occurrence of large and reproducible subband-edge-induced structures in d^2I/dV^2 prevented one from misidentifying additional structures that arise from impurity-assisted tunneling. In the present work we demonstrate a substantial progress in fabricating Schottky-barrier tunneling junctions on Si(100) resulting in a new insight into the tunneling mechanisms in these quantum layer devices.

The preparation started from high-resistive Si(100) wafers. A several μ m thick p-type layer was diffused from a spin-on boron dopant source. Then the δ -doping layer was grown by molecular beam epitaxy (MBE). The layer growth started with a 100 nm (wafer A) or 300 nm (wafer B) undoped buffer. Annealing for 15 min at 1000 °C flooded the buffer layer with boron, resulting in a surface concentration of about 10^{18} cm $^{-2}$. Subsequently an Sb δ -doping layer of about $2 \cdot 10^{11}$ cm $^{-2}$ covered with 2-3 nm Si was grown by solid-phase epitaxy followed by about 10 nm normally undoped Si grown at 700 °C [8]. From these wafers samples with different intrinsic layer thicknesses were prepared by anodic oxidation and subsequent etching with hydrofluoric acid. Details of this controlled removal of Si up to 30 nm with an accuracy of better than 1 nm will be described elsewhere. Finally, 25 nm Ti and 200 nm Au were evaporated and 35,

g^* are consistent with the difference in localisation [10]. However, the presence of peaks with equal spacing in energy much less than the Landau level spacing indicates that the structure is probably due to the addition of electrons to the electron puddle localised near the emitter barrier. The observed spacing of ~ 1 meV is reminiscent of the charging energies observed by Ashoori et al [11] but in a device more than an order of magnitude smaller in lateral dimension than our mesas.

In summary, we have observed strong sub-threshold structure in the $I(V)$ characteristics of RTD with lateral dimensions $\sim 0.5 \mu$ m. At all magnetic fields there is a very sharp onset to the structure which is limited by temperature even at $T = 280$ mK. For $D > 7$ T a series of peaks appears in $I(V)$ whose width is also limited by $k_B T$ and which show spin splitting at the lowest temperatures. We interpret these results tentatively in terms of tunnelling between two localised states, one which is considerably more localised than the other. Further, we are able to see structure which we can only attribute to Coulombic effects. There are two important features to emerge from our work. First, it is possible to observe quantum box effects in devices which themselves are far too large to cause the quantisation directly. This means that the interpretations of results in all devices must be carried out very carefully to distinguish between effects due to impurities and effects due to confinement provided either by the device geometry or by a gate potential. Secondly, we have been able to observe spin-splitting effects which are due to a different value of g^* in the two localised states. We find that Δg^* is dependent on bias, and hence energy, and this may prove to be a new technique for studying the variation of g^* with increasing localisation.

Acknowledgements

This work is supported by the SERC (UK). JWS and NLS wish to thank CNPq (Brazil) and PHB the Royal Society (UK) for financial support.

References

- [1] M A Reed, J N Randall, R J Aggarwal, R J Marti, T M Moore and A E Wetsel, Phys. Rev. Lett. **60**, 535 (1988)
- [2] B Su, V J Goldman and J E Cunningham, Science **258** 313 (1992).
- [3] M W Dellow, P H Beton, C J G M Langerak, T J Fuster, P C Main, L Eaves, M Henini, S P Beaumont and C D W Wilkinson, Phys. Rev. Lett. **68**, 1754 (1992).
- [4] M Tenaud, L Martin-Moreno, J T Nicholls, M Pepper, M J Kelly, V J Law, D A Ritchie, J E F Frost and G A C Jones, Phys. Rev. B **45**, 14407 (1992).
- [5] S Goutet, N Blanc, R Germann and H Rühlken, Phys. Rev. Lett. **68**, 1986 (1992).
- [6] S Tarucha, T Honda, T Saku and Y Tokura to be published in Surf. Sci. (Proceedings of EP2DS10, Newport, USA, 1993).
- [7] J W Saker, T M Fromhold, P H Beton, M Henini, L Eaves, P C Main, F W Sheard and G Hill, Physica B **184** 241 (1993).
- [8] M L Leadbeater, E S Alves, F W Sheard, L Eaves, M Henini, O H Hughes and G A Tumbrs, J. Phys. Condens. Matter **1** 10605 (1989).
- [9] For an explanation of the technique see J W Saker, T M Fromhold, P H Beton, L Eaves, M Henini, P C Main, F W Sheard and G Hill, to be published in Phys. Rev. (1993).
- [10] M J Stedling, G P Flinn, A S Plaut, R T Hatley, A C Tropper, R Eccleston and C C Phillips, Phys. Rev. B **44** 11345 (1991).
- [11] R C Ashoori, H L Stormer, J S Weiner, L N Pfeiffer, S J Pearton, K W Baldwin and K W West, Phys. Rev. Lett. **68** 3088 (1992) and to be published in Surf. Sci. (Proceedings of EP2DS10 Newport, USA, 1993).

50, and 70 μm square contacts lithographically defined. The counterelectrode was formed by another Schottky contact of several nm^2 separated from the tunneling contact by a 5 μm gap.

Figure 1 illustrates the band structure of the Schottky-barrier tunneling junction as calculated self-consistently for an intrinsic layer (thickness $d_i = 5 \text{ nm}$), a δ -doping density $n_D = 1.8 \times 10^{13} \text{ cm}^{-2}$ with a uniform distribution of width $d_D = 1 \text{ nm}$, a bulk doping level $N_A = 1.8 \times 10^{18} \text{ cm}^{-3}$ and a Ti Schottky barrier height of $\phi_s = 0.5 \text{ eV}$. The parameters d_i , n_D , d_D , and N_A have been gained from a fit to the experimental data as described below.

The sheet electron density n_s in the δ -layer is given by

$$n_s = n_D - n_{\text{in}} - n_{\text{dep}} \quad (1)$$

Here the surface charge density at the metal electrode n_m corresponds to an electric field in the intrinsic layer $F_s = e n_m / \epsilon_0 \epsilon_s$. For a δ -layer with populated electron subband the surface potential drops across the intrinsic layer, which results in $F_s = (\phi_s - eV) / e d_i$. The depletion charge density in the p-type buffer is given by $e n_{\text{dep}} = (2 \epsilon_0 \epsilon_s N_A / F_s)^{1/2}$, where we assume that the acceptor concentration is uniform and the bulk Fermi level coincides with the valence band edge. It is obvious from eqn (1) that at low d_i and high reverse bias V , n_m increases and the electron layer becomes depopulated. In the limiting case of $n_s = 0$ the surface potential drops across the total depletion layer, consisting of d_i and the bulk depletion zone $d_{\text{dep}} = n_D / n_{\text{dep}}$. This leads to a weaker increase of F_s as bias is increased than for the case of populated electron layer.

The measurements were performed at a sample temperature of 80 and 4 K taking the I - V , dI/dV and d^2I/dV^2 characteristics. Figure 2 shows a typical set of characteristics taken at 7–4 K from a junction on wafer B with 2 nm removed layer. Distinct kinks in I - V corresponding to maxima in the conductance and to oscillations in d^2I/dV^2 arise from the subband levels of the quantized 2D electron layer. Maxima in the tunneling conductance close to the subband edges rather than a step-like increase as in MOS tunneling [4] probably result from the crystalline barrier, which leads to a wave-vector dependent tunneling probability [11]. The stretching of the oscillation period at reverse biases in excess of 500 mV cannot be explained by an increase of the subband separation in the triangular potential well as F_s increases with bias. The origin is the gradual depletion of the electron layer, which leads to the distribution of the voltage drop across the total depletion zone. As a result, the potential well is raised in energy as illustrated in Fig. 3. Some additional bias shift may arise from the series resistance of the electron layer, in particular at biases $V < 500 \text{ mV}$, where the current increases. Around zero bias tunneling into subband states is effectively suppressed due to the energy-dependent thickness of the triangular barrier. The large dip structure at $V = -1.15 \pm 0.01 \text{ V}$ reflects the onset of tunneling into the extended conduction band states of the bulk. As can be seen from Fig. 3, its bias position is independent of the population of the potential well.

The structures mentioned above are reproducible from different junctions, in contrast to the series of narrow peaked structures at forward and large reverse biases. However, this random pattern is not due to noise but is reproducible from consecutive bias runs. We attribute these structures to tunneling via localized impurity levels in the barrier.

At elevated temperatures the impurity-induced fine structure is not resolved. If now the intrinsic layer is sufficiently thin tunneling spectroscopy of the very weak subband-induced structures around zero bias becomes possible. Figure 4 shows an example of a junction prepared on wafer A with 6 nm removed layer. At 180 K the enlarged recording reveals small dips at low

forward and reverse bias that arise from the lowest three subbands E_{D1} , E_{D2} , and E_{D3} . Another three large dip structures occur at about the same bias position as in the 7–4 K characteristic. According to the result of the self-consistent calculation indicated in Fig. 4 we assume that these structures reflect the primed subbands as in MOS tunneling junctions [4] due to their larger density of states and lower effective mass in the tunneling direction.

The junction modelling, details of which are discussed below, indicates a beginning of the electron layer depopulation at $V = -460 \text{ mV}$, which is close to the value $V = -470 \text{ mV}$ obtained from eqn (1). These results are confirmed in Fig. 4 by the fading of the oscillatory component at larger negative bias. When the electron layer becomes depopulated the Fermi level in the potential well is no longer pinned by the high density of states in the subband and large potential fluctuations lead to an averaging of the subband-edge induced structures. It should be noted that the large structure at $V = -1.15 \text{ V}$ arising from the conduction band edge is still present at 7–80 K. At reverse bias $V < -1.3 \text{ V}$ a strong current rise leads to the steep slope in d^2I/dV^2 which probably reflects the onset of hole tunneling. As indicated in Fig. 3 a substantial lowering of the hole barrier occurs at small d_i and at high reverse bias where the electron layer is depopulated, which facilitates tunneling of holes. At forward bias $V = 250 \text{ mV}$ the bell-shaped maximum indicates the transition from the exponential Schottky diode I - V characteristic to the saturation of the conductance dI/dV due to the series resistance.

Figure 5 summarizes the results from samples on wafer B with the removed layer thickness as parameter. It is obvious that the subband structure is extremely sensitive to the intrinsic layer thickness. At 6 nm removed Si the electron layer is nearly depleted, at 9 nm the only current component is hole tunneling. A removal of more than 9 nm Si will not lead to further changes in the tunneling characteristics. A numerical calculation shows that at $d_i < 1 \text{ nm}$ the δ -doping layer has only a weak influence on the hole barrier height. Therefore we estimate the initial thickness of the undoped layer at $10 \pm 1 \text{ nm}$.

We have used the estimate of the remaining intrinsic layer thickness d_i as a parameter for the model calculation, where in the fit to the experimentally determined subband energies under bias the variation of d_i is limited to the uncertainty of 2 nm. Further fit parameters are the δ -doping density n_D , the δ -doping spread d_D , and the buffer doping concentration N_A . For the Ti Schottky barrier height a value $\phi_s = 0.5 \text{ eV}$ has been assumed. In spite of the large number of four different fit parameters the determination of a conclusive set of d_i , n_D , d_D , and N_A is feasible because each of the parameters efficiently influences only some part of the subband spectrum. The δ -doping n_D strongly influences the energy position of the lowest subbands E_{D1} , E_{D2} , E_{D3} , and E_{D4} relative to the Fermi level, whereas the spread d_D determines their separation. Higher subband energies mainly depend on d_i and N_A . Reducing both d_i and N_A while keeping a given E_{D4} constant leads to a stronger decrease of the subband separation with increasing energy. A critical test of the parameters is possible because the changes of the subband structure due to the Si removal has to be modeled only by the known variation of d_i .

The resulting parameters of wafer A are an initial $d_i = 11 \text{ nm}$, $n_D = 1.8 \times 10^{13} \text{ cm}^{-2}$, $d_D = 1 \text{ nm}$, and $N_A = 1.8 \times 10^{18} \text{ cm}^{-3}$ and of wafer B $d_i = 9.5 \text{ nm}$, $n_D = 1.6 \times 10^{13} \text{ cm}^{-2}$, $d_D = 1 \text{ nm}$, and $N_A = 2.2 \times 10^{18} \text{ cm}^{-3}$, where the average deviation from the experimental $E_{D4} - E_{D1}$ is about 5%. It should be noted that the calculation is based on an idealized model, e is the true donor distribution, image-force corrections, and the imaginary k dispersion in the band gap have been

neglected. The systematic deviation of the calculated E_F level towards lower energies is probably the result of neglecting the O -population due to band tailing. However, also the experimentally determined subband energies are inaccurate because of the voltage drop across the series resistance.

In conclusion, we have observed three different tunneling channels in Schottky-barrier contacts in i - $8n$ - p structures on Si(100) with intrinsic layer thickness u_i 510 nm. Around zero bias and at reverse biases up to several 100 mV the d^2I/dV^2 curves exhibit subband edge induced dips and at a fixed bias $V = 1.5$ V a large structure arising from the bulk conduction band edge. The onset of hole tunneling from the bulk valence band edge to the metal is observed at high reverse bias and small thickness u_i , where the potential well is depopulated. The results of a model calculation agree reasonably with the experimentally determined bias and thickness u_i dependent subband structure.

Acknowledgement—This work was supported by the Deutsche Forschungsgemeinschaft.

REFERENCES

- 1 D C Tsui, *Phys. Rev. B* 4, 4438 (1971)
- 2 D C Tsui, G Kaminski, and P H Schmidt, *Phys. Rev. B* 9, 3524 (1974)
- 3 P-F Lu, D C Tsui, and H M Cox, *Appl. Phys. Lett.* 45, 772 (1984)
- 4 U Kunze, *J. Phys. C* 17, 5677 (1984)
- 5 J Smoller, M Hauser, and E Gornik, *Appl. Phys. Lett.* 52, 33 (1988)
- 6 M Zachau, F Koch, K Ploog, P Roening, and H Beneking, *Solid State Commun.* 59, 561 (1986)
- 7 F Batmaji, A C Notari, B Schrappe, M H Degani, L Ioraiti, and O Hipolito, *Surf. Sci.* 263, 231 (1992)
- 8 H P Zeindl, T Wegehaupl, I Eisele, H Oppolzer, H Reisinger, G Tempel, and F Koch, *Appl. Phys. Lett.* 59, 1164 (1991)
- 9 I Eisele, *Superlatt. Microstruct.* 6, 123 (1989)
- 10 H-M Lin, K-F Berggren, W-X Ni, B E Sernelius, M Willander, and G V Hansson, *J. Appl. Phys.* 67, 1062 (1990)
- 11 C B Duke, *Tunneling in Solids*, Academic, New York 1969

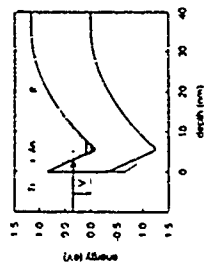


Fig. 1 Calculated band diagram of a tunneling junction with 5 nm intrinsic layer under reverse bias $V = -0.14$ V. Solid and dashed horizontal lines represent the energies of the lowest subbands F_n and F_{n+1} respectively. The arrow indicates the tunneling channel that detects the E_F subband level. Thin lines represent the band diagram at zero bias.

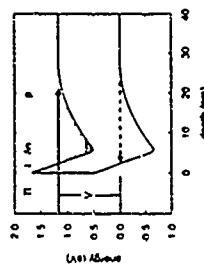


Fig. 2 d^2I/dV^2 and d^3I/dV^3 tunneling characteristics of a junction on wafer B with 2 nm removed layer. The alignment of dip structures with calculated subband levels and the conduction band edge (CB) is indicated.

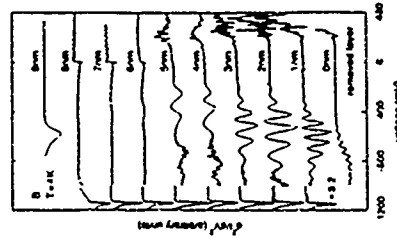


Fig. 3 d^2I/dV^2 characteristics of samples on wafer B with different removed layer thickness as given.

Fig. 3 As Fig. 1, with electron layer depopulated by the large reverse bias $V = -16$ V. Tunneling into the conduction band states of the p -type layer and hole tunneling from the valence band into the metal is indicated by arrows.

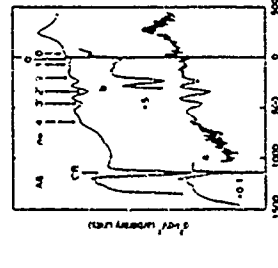


Fig. 4 Tunneling characteristics of a junction on wafer A with 6 nm removed layer measured at (a) 7-4 K and (b) 7-40 K. Calculated subband levels are indicated.

PHOTOHOLE-INDUCED RESONANT TUNNELING OF ELECTRONS IN SELECTIVELY ETCHED SMALL AREA GaAs/AlAs DOUBLE BARRIER DIODES

H. Buhmann, J. Wang, L. Mansouri, P.H. Beton, L. Eaves, M. Heath
and M. Henini

Department of Physics, University of Nottingham, Nottingham, NG7 2RD, U.K.

Abstract

The influence of light of wavelength 670 nm on the low temperature ($I(V)$) characteristics of selectively etched small area resonant tunneling diodes (RTD) has been investigated. These diodes have with physical dimensions down to 0.5 μm and their design allows easy optical access. Under illumination new sub-threshold peaks appear in $I(V)$. The sub-threshold peaks are also observed in large area diodes, and are found to be strongly influenced by the presence of a magnetic field applied either parallel or perpendicular to the plane of the barriers. We show that our results cannot be explained in terms of resonant tunneling of photo-excited holes and propose an explanation based on the Coulomb electron-hole interaction.

Resonant tunneling diodes (RTDs) are an attractive system for the study of quantum transport since the strong non-linearities observed in their current voltage characteristics, $I(V)$, are a direct consequence of the quantum confinement of carriers within a quantum well [1]. The incorporation of donors within the quantum well of an RTD leads to the formation of laterally bound hydrogenic-like states which are localized within the plane of the quantum well. These bound states are lower in energy than the quantum well continuum and provide an additional channel for resonant tunneling, which in turn leads to additional non-linearities in $I(V)$ [2, 3]. Resonant tunneling therefore provides a means of detecting the presence of any low energy states which are formed within the quantum well.

In this paper we describe a series of experiments in which we investigate the possibility of using RTDs to probe the presence of holes in the quantum well. The holes are introduced by means of photo-excitation and they give rise to sub-threshold peaks in $I(V)$. We argue that these peaks are a close analogue of the peaks generated by the presence of donors.

Our experiments are conducted on both large (100 - 100 μm square) mesas (which are suitable for optical access) and also a range of small area diodes with dimensions down to 0.5 μm . An important element of our work is the development of a fabrication process for a sub-micron RTD which is suitable for optical access. This process, based on optical lithography and wet etching and as described below, does not require the use of either wet-etching (a possible source of damage) or dielectric layers (which might impair the optical access of the devices) for isolation of bonding pads and metallic tracks.

The devices were fabricated from a GaAs/AlAs double-barrier heterostructure grown on a semi-insulating (100) GaAs substrate, using molecular beam epitaxy (MBE). The

layer composition of the heterostructure is given in Table 1.

100.0 nm	GaAs	$n = 2 \times 10^{18}$	top contact
80.6 nm	GaAs	$n = 2 \times 10^{17}$	
50.9 nm	GaAs	$n = 2 \times 10^{18}$	
20.1 nm	GaAs		spacer
5.9 nm	AlAs		barrier
9.1 nm	GaAs		well
5.9 nm	AlAs		barrier
20.3 nm	GaAs		spacer
50.9 nm	GaAs	$n = 2 \times 10^{18}$	
80.6 nm	GaAs	$n = 2 \times 10^{17}$	bottom contact
200.0 nm	GaAs	$n = 2 \times 10^{18}$	
7.6 nm	AlAs		etch stop
1000.0 nm	GaAs		semi-insulating Substrate

Table 1: Sample structure. Growth direction from bottom to top. The donor is Si and the MBE growth temperature was 550°C.

To fabricate the small area diodes the GaAs (top contact) layer is selectively etched using $\text{NH}_4\text{OH}/\text{H}_2\text{O}_2$ (5:95), to form a narrow lines with a width in the range of 0.5 to 3 μm . The lines are formed between large ohmic contacts ($\sim 100 \mu\text{m} \times \sim 100 \mu\text{m}$). Note that optical lithography is used for pattern definition, so that significant undercut etching is required to achieve sub-micron dimensions. A second (non selective) etch was used to penetrate the AlAs barriers and reveal the lower GaAs doped (bottom contact) layer. Finally, this buried n type GaAs layer was also selectively etched to form a freestanding GaAs bridge in the emitter layer. Au/Ge/Ni ohmic contacts were then deposited on the top and bottom contact doped layers. A schematic representation of the final device is shown in Figure 1. Note that the metallised region on the top contact is connected to the active region of the device by the freestanding GaAs bridge. This serves to isolate the bottom contact from the doped region beneath the top contact eliminating any possible parallel conduction path. This novel fabrication route produces small area diodes with low contact resistance which can be easily illuminated. The dimensions of the small area devices discussed below are: I $\sim 0.5 \mu\text{m} \times 60 \mu\text{m}$, II $\sim 1.0 \mu\text{m} \times 60 \mu\text{m}$ and III $\sim 3.0 \mu\text{m} \times 60 \mu\text{m}$. We have also investigated large area control devices with metal contacts which are sufficiently small for light to penetrate the device.

The low temperature current-voltage characteristics ($T = 4.2 \text{ K}$), $I(V)$, for device I, II and III are shown in Figure 2 a). For all measurements the convention of positive bias implies a positive potential applied to the top contact. Comparing the $I(V)$ of the small area and large area devices (inset Fig. 2a), no significant difference is observed, except for the smallest device (I). The main electron peak positions remain approximately the same, and a small asymmetry in the bias region beyond the main resonance is common to all devices.

The $I(V)$ for the smallest diode, device I, shows a broadening of the main electron resonance together with a shift to higher voltage in forward bias, while in negative bias it

exhibits no obvious changes. A similar asymmetry has been observed in gated resonant tunneling devices [4], when the active tunnel area is progressively decreased with increased gate voltage. This has been explained in terms of the shape of the equipotential close to the tunnel barriers.

We may estimate the side wall depletion, d_s , in the small area diodes from the value of the peak current, I_{peak} , of the main resonance from the relation: $I_{\text{peak}} = J_{\text{peak}}(l_1 - d_s)l_2$, where J_{peak} is the peak current density and l_1 and l_2 are defined in Figure 1. From the values of I_{peak} for devices I, II and III we find $J_{\text{peak}} = 0.17 \text{ nA } \mu\text{m}^{-2}$ and $d_s = 0.4 \text{ } \mu\text{m}$. Note that this means the conducting width for device I is $0.1 \text{ } \mu\text{m}$. Our experimental value for J_{peak} is in good agreement with the peak current density measured for the corresponding large area devices, $J_{\text{peak,large}} = 0.18 \text{ nA } \mu\text{m}^{-2}$.

The devices were illuminated in a flow cryostat via an optical fibre. Under constant illumination ($P_L \leq 100 \text{ } \mu\text{W cm}^{-2}$) with 670 nm wavelength laser light, changes in $I(V)$ are observed. In Figure 2(b) $I(V)$ for device II is plotted for various levels of illumination. The features which are observed for device II are typical of all devices. The main electron resonance peak position and threshold voltage shift to lower voltage and new resonances occur in the sub-threshold region just below the threshold voltage for the main resonance. The new features are indicated by arrows in Fig. 2(b). The strength of these additional resonances increases with excitation power. In addition to the appearance of these features we also observe an increase in the peak and valley currents of the main resonance with increased illumination. The valley current is greatly enhanced in forward bias.

To understand the effects of illumination we refer to the band profiles of the device shown in Figure 3. The incident light creates electron-hole pairs in the depletion region beyond the collector barrier. The photo-created electrons (majority carriers) drift up into the deposed collector region, but the photo-created holes (minority carriers) drift towards the collector barrier where they form an accumulation layer. This process has been discussed previously in the context of photoluminescence experiments on resonant tunneling devices [5, 6, 7]. The presence of the photo-created holes close to the collector barrier facilitates the band bending in the device and accounts for the shift of the threshold and peak of the main resonance to lower voltage.

Similar effects have previously been observed in the $I(V)$ of large area resonant tunneling diodes under illumination [6, 7] which were attributed to resonant tunneling of photo-created holes in the depletion region. This data indicates that the dependence of the photo-induced peaks on magnetic field. This data indicates that the additional peaks we observe cannot be described solely in terms of the conventional model involving independent resonant tunneling of photo-created holes. Instead we suggest that they may arise from resonant tunneling of electrons through excitonic bound states formed due to the presence of photo-created holes in the quantum well of the device. Note that this quantum-bound state model is analogous to the tunneling of electrons via donor states in the quantum well as discussed in Refs. 1 and 2.

One dimension of the magnetic field dependence refers to $I(V)$ for large area diodes, since for these devices we have a more complete set of data, and can make a direct comparison with previous work [6, 7]. Figure 1(a) shows $I(V)$ up to the threshold voltage for the main resonance for a $160 \text{ } \mu\text{m}$ square device illuminated with an excitation power $P_L \leq 10 \text{ mW cm}^{-2}$ in the presence of a magnetic field B between 0 mT and 10 T oriented

perpendicular to the plane of the barriers. For $B = 0$ (lowest curve) we observe a sub-threshold resonance in each bias direction at $V \sim -110 \text{ mV}$ and $V \sim 120 \text{ mV}$ (peaks marked D in Fig. 4 a). For $B < 4 \text{ T}$ this peak remains unaffected by magnetic field, however as B is progressively increased it shifts to larger voltage and its amplitude is reduced. For $B > 3 \text{ T}$ several more peaks appear which occur at even lower voltage. These are labelled A, B and C on Fig. 4 a). The peaks show a fair degree of symmetry between bias directions, although their amplitude is higher in forward bias (because of an effective difference in the light intensity incident on the depletion region in forward and reverse due to absorption effects). The voltage positions of peaks A, B and C are only weakly dependent on magnetic field, however their amplitude is a strong function of field. At the highest magnetic fields peaks A and B split into two peaks. This can be seen more clearly for peak B, for which the split peak is stronger. The separation of the split peaks in voltage is $\sim 5 \text{ mV}$.

$I(V)$ for the same diode under illumination in the presence of a magnetic field oriented parallel to the barrier is shown in Figure 4 b). Note that for our experimental arrangement illumination of a sample oriented parallel to the field is more difficult. The maximum level of illumination is lower than for the perpendicular case and the corresponding photo-induced peaks have smaller amplitude than the data in Fig. 4 a). For $B = 0 \text{ T}$ we observe two sub-threshold peaks as in Fig. 4 a) (peaks marked D), however as B is increased beyond 3 T another more peak appears (peak B). As the magnetic field is increased peak D moves to higher voltage, and a weak splitting is observed.

The behaviour of the peak in $I(V)$ corresponding to the main resonance displays quite different behaviour for parallel and perpendicular oriented fields. For a perpendicular field its voltage position and amplitude are only weakly dependent on field, however for a parallel field the threshold moves to higher voltage. Note that peak D in the parallel field moves to a higher voltage at a similar rate to the threshold for the main electron resonance.

Thus our data shows a series of photo-induced peaks whose amplitude and voltage position are extremely sensitive to magnetic field. We first consider whether the dependence of their amplitude and voltage position on magnetic field is consistent with conventional resonant tunneling of photo-created holes. We focus on peak D since this peak is observed even for $B = 0 \text{ T}$. Previous work on p-p resonant tunneling diodes [8] shows that the voltage position of the lowest two hole resonances referred to as hh1 and hh2 (corresponding to resonant tunneling via the lowest heavy and light hole subbands respectively) is almost independent of magnetic field for $B < 11 \text{ T}$, the range shown in Fig. 4 b). Clearly peak D cannot be due to hole resonant tunneling via the hh1 or hh2 subbands since its voltage position is shifted by a parallel field. Hayden et al. found that the lowest hole subband resonance which has a strong parallel field dependence of its voltage position is hh2, the first excited state heavy hole state. However, firm identification of peak D as the hh2 resonance is not possible, since in that case we would expect to observe a peak in $I(V)$ of comparable amplitude at lower voltage corresponding to the hh1 resonance as observed by Hayden et al. In addition we have calculated the expected peak positions for electron and hole resonances using a simple model for the band bending of the device which uses the 1D flow and wavefunction to model the state in the electron accumulation layer and treat the state in the hole accumulation layer as an Airy function. This model predicts

that the $h\nu/2$ resonance should occur at a higher voltage than the electron resonance. We also note that in similar $p-i-n$ resonant tunneling diodes the $h\nu/2$ peak always occurs at higher voltage than the lowest electron resonance [9].

Another result established in the study of $p-i-p$ resonant tunneling diodes is that the amplitude and voltage position of the peaks in $I(V)$ due to hole resonances are insensitive to the presence of perpendicular magnetic fields for $B < 10$ T. Certainly nothing comparable with the dramatic magnetic field enhancement of peaks A, B and C in Fig. 4 has been observed for $p-i-p$ devices. We are thus unable to account either qualitatively or quantitatively for our data in terms of conventional resonant tunneling of photo-excited holes.

We have also investigated these effects in several other wafers which differ from the heterostructure shown in Table 1 only in the thickness of the AlAs tunnel barriers. For barrier widths of 4.5 and 3.0 nm we do not observe such clear additional peaks under illumination, but see a step like behaviour at lower voltage which is highly reminiscent of the data shown in Ref. [7]. For barrier widths 5.9 and 7.5 nm we observe structure similar to that in Fig. 4. Note that the peak current density for our devices, J_{peak} , is two orders of magnitude smaller than that for the material used by Vooljdian et al. [7]. This dependence of the peaks on barrier width clearly complicates the comparison of our data with that previously reported.

We have stressed above that our data cannot be explained solely in terms of resonant tunneling of photo-excited holes. Our alternative explanation is that the presence of a hole in the quantum well gives rise to an alternative resonant conduction path which is lower in energy than the quantum well continuum due to the Coulomb interaction of the electron and hole, i.e. tunneling of electrons via an excitonic state. Similar peaks have been observed in $I(V)$ for devices in which ionized donors are introduced into the quantum well. The threshold for peak D is approximately 30mV below that of the main resonance. According to our band bending calculations this corresponds to an energy below the continuum of ~ 5.5 meV. This should be compared with the binding energy of ~ 7 meV for a light hole exciton and ~ 9 meV for a heavy hole exciton. Although these numbers are not in exact agreement they are close, however we are not able to determine the type of exciton from our present data set. Note, however, that associating peak D with an excitonic transition is at least consistent with its shift to higher voltage in parallel field. However our model is so far unable to explain the appearance of the lower voltage peaks A, B and C with increasing magnetic field.

In conclusion we have observed a series of peaks which appear when a resonant tunneling diode is illuminated. The dependence of these peaks on magnetic field is no consistent with resonant tunneling of holes. We have proposed an alternative explanation based on resonant tunneling via hole-induced excitonic states in the well. Further work, in particular photoluminescence studies, are required to clarify the detailed origin of these peaks.

References

- [1] L.L. Chang, L. Esaki and R. Tsun, Appl. Phys. Lett. 24, 591 (1974)

- [2] M.W. Dellow, P.H. Beton, C.J.G.M. Langrak, T.J. Foster, P.C. Main, L. Eaves, M. Henini, S.P. Beaumont and C.D. Wilkinson, Phys. Rev. Lett. 64, 1734 (1992).
- [3] J.W. Sakai, T.M. Fronthold, P.H. Beton, M. Henini, L. Eaves, P.C. Main, F.W. Sheard and G. Hill, to be published in Phys. Rev. B.
- [4] P.H. Beton, M.W. Dellow, P.C. Main, T.J. Foster, L. Eaves, A.F. Jezierski and M. Henini, Appl. Phys. Lett. 60, 2508 (1992).
- [5] J.F. Young, B.M. Wood, G.C. Aern, R.L.S. Devine, H.C. Liu, D. Landheer, M. Buchanan, A.J. SpringThorpe and P. Haudeville, Phys. Rev. Lett. 60, 2085 (1988).
- [6] C.R.H. White, M.S. Stohnick, L. Eaves, M.L. Leadbeater, M. Henini, O.H. Hughes, G. Hill and M.A. Pate, Phys. Rev. B 45, 6721 (1992).
- [7] N. Vooljdian, D. Cote, D. Thomas, B. Serenge, P. Dosi, E. Costard and J. Nagle, Appl. Phys. Lett. 56 (1), 23 (1989).
- [8] R.K. Haydon, D.K. Maude, L. Eaves, E.C. Valadares, M. Henini, F.W. Sheard, O.H. Hughes, J.C. Portal and L. Cury, Phys. Rev. Lett. 66, 1749 (1991).
- [9] R.K. Haydon, Thesis, University of Nottingham, 1992.
- [10] P.M. Martin, R.K. Haydon, C.R.H. White, M. Henini, L. Eaves, D.K. Maude, J.C. Portal, G. Hill and M.A. Pate, Semicond. Sci. Technol. 7, 436 (1992).

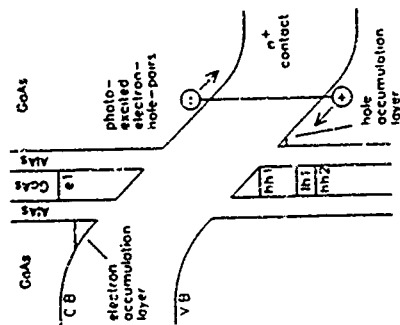


Figure 3. Schematic band profile of the device.

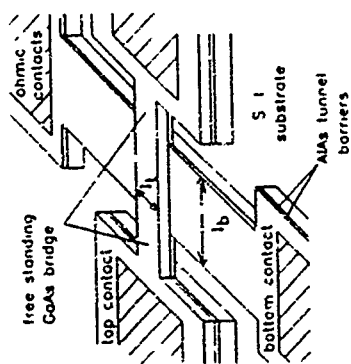


Figure 1. Schematic picture of the small area device

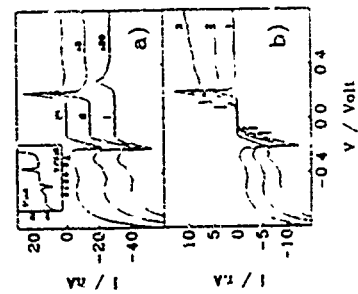


Figure 2: a) $I(V)$ characteristics of device I II and III in darkness. Inset $I(V)$ of a large area device $100 \mu m \times 100 \mu m$ b) $I(V)$ characteristics of device II under illumination $10 \mu W/cm^2$, $\pm 1 \mu W/cm^2$ and $3 \mu W/cm^2$

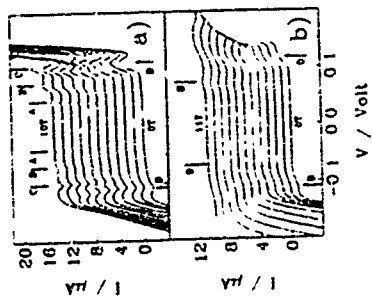


Figure 1. $I(V)$ characteristics for a $100 \mu m$ square mesa in a) perpendicular and b) in parallel magnetic field configuration

TuP31

INTERFACE EFFECTS, BAND OVERLAP AND THE SEMIMETAL TO SEMICONDUCTOR TRANSITION IN InAs/GaSb INTERBAND RESONANT TUNNELING DIODES

U. M. Khar-Chernov*, P. C. Klipstein*, D. G. Aueling*, J. M. Smith*, N. J. Maue*, P. J. Walker* and G. Hill*
 * Department of Physics, Clarendon Laboratory, University of Oxford, Parks Road, Oxford, OX1 3PU, U.K.
 * Department of Electrical and Electronic Engineering, The University, Marple Street, Sheffield, S1 3JD, U.K.
 * Present Address: NTT Research Laboratories, 3-9-11 Midori-cho, Musashino-shi, Tokyo 180, Japan

We report some of the high- γ 77K peak in valley ratios (PVRs) for single heterojunction InAs/InSb resonant tunneling diodes. The devices were grown with low background doping ($n \approx 10^{16} \text{ cm}^{-3}$) on (100) oriented substrates by atmospheric pressure MOVPE, and were prepared by etching the precursor in a predetermined order, to leave "InSb" or "GaAs" like interfaces. We observe a stronger resonance with a weaker temperature dependence when the interface is "InSb" like. In all samples, the voltage of the resonance and the peak current both decrease with hydrostatic pressure, due to the pressure induced decrease of band overlap. Our results are consistent with a shift of $\sim 10 \text{ meV/Å}$ and overlap of $120 \pm 20 \text{ meV}$ and $250 \pm 50 \text{ meV}$ respectively for "InSb" like and "GaAs" like interfaces, and are in agreement with high pressure parallel transport results in superlattices with "InSb" like interfaces.

InAs/GaSb structures, particularly when combined with AlSb , offer the possibility of interband tunneling devices exhibiting Negative Differential Resistance (NDR), with a very high Peak to Valley Ratio (PVR), and a large peak current density, two qualities which are desirable for high frequency applications [1-3]. The GaSb/InAs material system is distinguished from the more conventional GaAs/AlAs by a novel band alignment where the InAs conduction band edge lies approximately 145 meV below the GaSb valence band edge [1], and by the existence of two types of interface, with either "GaAs" or "InSb" character [4]. In this paper we examine the role of the interface on interband tunneling in single heterojunction structures.

Five structures were grown by atmospheric pressure Metal Organic Vapour Phase Epitaxy (MOVPE), and each comprised a $\text{GaSb } p^+$ substrate, $0.3 \mu\text{m u-GaSb}$, 100 Å InAs , and $0.5 \mu\text{m n-InAs}$ ($n \approx 4 \times 10^{16} \text{ cm}^{-3}$). For both materials, the background carrier concentration at room temperature was $1.2 \times 10^{16} \text{ cm}^{-3}$. For samples A, B and C the interface was biased to "InSb" by switching the flow of precursors in the following order: Ga off, In on, Sb off, As on with a 1s pause between each event. Sample D was biased to "GaAs" (Sb off, As on, Ga off, In on), while sample E was unbiased (all four switching events occurring simultaneously). The structures were processed into $16 \mu\text{m}$ diameter mesa structures prior to contacting.

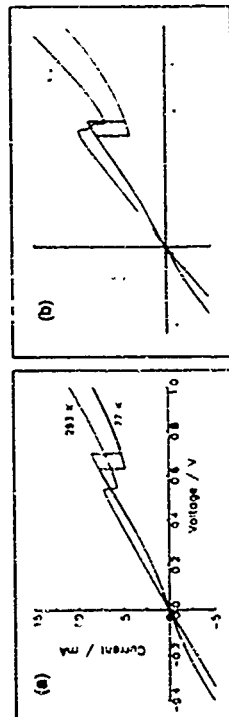


Figure 1 I-V characteristics for (a) sample B2 and (b) sample D2 at 293 and 77K.

In figure 1, the forward bias characteristics (InAs negative with respect to GaSb) are shown for (a) an "InSb" interface and (b) a "GaAs" interface. In this bias direction a resonance is observed, in which the peak occurs when the bottom of the subband from the first confined electron state in the approximately triangular potential well of the conduction band aligns close to the top of the first light hole subband in the equivalent valence band potential well [5]. For different n and p in the same wafer, the voltage of the peak can be variable (typically lying between 0.2 and 0.6 V in all cases) due to a significant contact resistance, but the peak and valley current densities are generally more reproducible, showing a scatter within about $\pm 5\%$ (which we attribute to a parasitic parallel conductance, perhaps due to the state of the etched surface of the mesa). It is apparent from figure 1 that with increasing temperature the resonance shifts down in bias, consistent with previous reports [6], although the PVR shows a larger decrease, particularly for the InSb interface. This downshift can be explained by the shift of the Fermi level at zero bias towards midgap in both materials (a simple calculation gives a shift of 0.19V), which may be offset slightly by an increase in the band overlap due to thermal expansion (equivalent to a negative pressure of a few kbar). The stronger resonance and weaker suppression with temperature in the "GaAs" case is indicative of a larger band offset compared to the "InSb" case, which would tend to suppress the thermionic emission of both electrons and holes at high temperatures. Further evidence that this is the case is obtained by considering the effect of high pressure.

In figure 2, the forward bias characteristics of sample C are plotted at different pressures. For the mesa shown, the resonance occurs at a very low bias suggesting that for this mesa contact resistance effects are negligible. It is apparent from figure 2 that the resonance is almost totally suppressed by 11.6 kbar. The suppression is explained by a reduction of the band overlap with increasing pressure. Results for all the samples are summarised in figures 3(a) and (b) respectively, where the PVR and the resonance voltage, normalised to its 1 bar value, are plotted as a function of pressure.

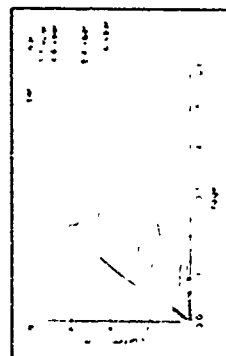


Figure 2 Forward bias characteristics for sample C at 77K for different pressures

With the exception of the "unbiased" interface, a clear pattern seems to emerge, where the "GaAs" interface exhibits a higher PVR at 1 bar and is not suppressed by pressure as quickly as the "InSb" interface. Unfortunately, it is not so straightforward to estimate from the data the exact pressure, P_c , at which the band overlap goes to zero. One might expect that because the alignment of confined electron and hole subbands is no longer possible above P_c , resonant behaviour should clearly vanish at this pressure. However, although the confinement energies go to zero at this pressure, so do the electron and hole concentrations in the subbands, so the strength of the resonance will also go to zero at P_c , making it hard to observe. Furthermore, above P_c the device may start to exhibit tunnel diode behaviour at low bias, when electrons near the bulk conduction band edge of InAs tunnel into hole states near the bulk valence band edge of GaSb . Since the concentration of both types of carrier is quite small, any resonance of this type should be fairly weak. Nevertheless, a weak resonance may persist beyond P_c , making a clear identification of P_c difficult. Such an effect may explain why the resonance voltages for the "InSb" samples in figures 2 and 3(b), do not appear to go to zero at high pressure, but instead saturate at about 10% of the initial 1 bar values. Therefore, in figure 3(b), it is probably more reliable to extrapolate data taken below about 8 kbar to the point at

which it intercepts the x-axis, to obtain an estimate for P_c . This is the procedure which we follow below. Even though the contact resistances (assumed pressure independent) influence the resonance voltages in figure 3(b), as discussed above, it is clear from figure 2 that the intrinsic

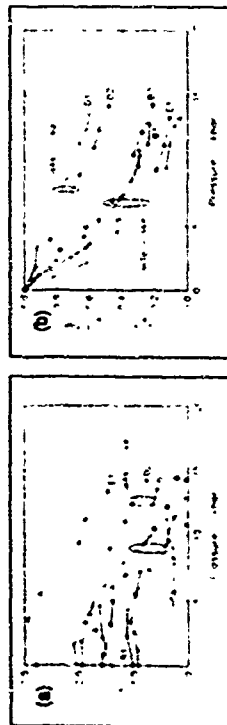


Figure 3. Sample PVRs and (b) their corresponding normalized resonance voltages vs. pressure at 77K.

device resistance is not a strong function of pressure, increasing by no more than a factor of 2 in about 10 kbar. Therefore even if in some cases the contact resistance at 1 bar is comparable to the intrinsic device resistance, the normalized bias voltage as plotted in figure 3(b) will still be within about 70% of the true intrinsic value at 10 kbar. Thus, contact effects may account for the small variation between different samples or measurements of the same interface type in figure 3(b), but they cannot account for the larger variation between samples with "InSb" or "GaAs" interfaces, which is therefore taken to be a genuine effect.

Extrapolation of the data in figure 3(b) as discussed above suggests that for the "GaAs" samples $P_c \approx 25 \pm 5$ kbar, while for the "InSb" samples, $P_c \approx 12 \pm 2$ kbar. A slightly lower value, but within the stated error limits, is predicted from figure 3(a) for the "GaAs" samples. Notwithstanding the difficulties in obtaining a precise value for P_c , it is clear that its value for "GaAs" is approximately 13 kbar larger than for "InSb". Symons et al. [7] have performed Quantum Hall measurements on superlattice samples from the same MOVPE reactor as the present samples, where "InSb" interfaces were used to achieve the high carrier mobilities necessary for the measurements. They derived values for the band overlap and pressure shift of 145 ± 5 meV and -9 ± 1 meV/kbar. These values are in good agreement with our value of P_c for the "InSb" samples. Assuming that the pressure shift, which is close in magnitude to the pressure shift of the bandgaps of InAs and GaSb (~ 10 and 14 meV/kbar respectively [8]), is not strongly dependent on the interface type, our results predict an increase in band overlap of about 130 ± 70 meV on going from an "InSb" interface to a "GaAs" one. This increase has been predicted in recent calculations by Feulon and Priester [9], and by Hemstreet et al. [10], who report values of 31 and about 50 meV respectively. Our result is therefore not surprising, although the value of about 130 ± 70 meV for the increase in the overlap is somewhat larger than expected.

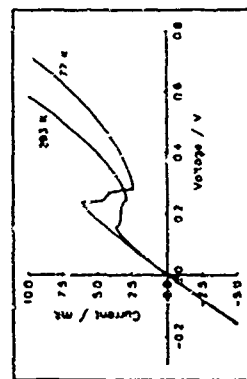


Figure 4. I-V characteristics for an "unbiased" interface (sample E2) at 295 and 77K.

Finally, we note that the sample with

the "unbiased" interface gave a PVR at 77K and 1 bar of 2.6, which to our knowledge is the largest PVR reported for a single heterojunction device of this type. The large PVR is due to a particularly low valley current compared to other samples. This may reflect the fact that the interface was grown without pauses. To decide the nature of the interface is a little problematic, since the data in figure 3(a) appears to extrapolate to an intercept on the x-axis close to that for the "GaAs" samples, whereas in figure 3(b) the behaviour is clearly "InSb" like. The low valley current may simply reveal a tunnel diode resonance once the resonance due to band overlap at the interface has been suppressed, so the PVR data in figure 3(a) may be misleading, whereas the bias data in figure 3(b) is more directly related to the offset. Therefore, we suspect that the "unbiased" interface has essentially "InSb" character. This attribution is confirmed by the strong temperature dependence of the NDR in the "unbiased" sample, plotted in figure 4, which is clearly characteristic of an "InSb" interface as discussed above.

In conclusion, we have presented electrical data on a number of similar single heterojunction InAs/GaSb interband tunneling devices, in which the only difference has been to vary the character of the interface between "InSb" or "GaAs". The "GaAs" interface appears to give a stronger resonance, with a weaker temperature dependence, than the "InSb" interface. The resonance is suppressed by pressure in all cases, with a threshold, P_c , which is approximately 13 kbar higher on going from an "InSb" to a "GaAs" interface. Our results are consistent with overlaps of 120 ± 20 and 250 ± 50 meV respectively for the two interfaces. Further measurements are in progress, looking at more "GaAs" interface samples up to higher pressures, which should yield a more precise value for the difference in band overlap for the two interface types. Finally, measurements on an "unbiased" interface indicate that the interface may have adopted an "InSb"-like character.

References

1. D. H. Chow, J. R. Soderstrom, D. A. Collins, D. Y. Tang, E. T. Yu and T. C. McGill, *SPIE Quantum Well and Superlattice Physics III*, 1283, 2 (1990).
2. J. R. Soderstrom, D. H. Chow and T. C. McGill, *IEEE Electron Device Lett.* 11, 27 (1990).
3. K. F. Logothetis, L. F. Luo and W. L. Wang, *Appl. Phys. Lett.* 57, 1554 (1990).
4. C. Lopez, R. J. Sprengel, R. J. Nicholas, P. J. Walker, N. J. Mason and W. Hayes, *Sref. Sci.* 267, 176 (1992).
5. D. H. Collins, E. T. Yu, Y. Kajikumarasake, J. R. Soderstrom, D. Y. Tang, D. H. Chow and T. C. McGill, *Appl. Phys. Lett.* 57, 683 (1990).
6. F. E. Mendez, *Surf. Sci.* 267, 170 (1992).
7. D. M. Symons, M. Lakshmi, R. J. Warburton, R. J. Nicholas, N. J. Mason, P. J. Walker and M. J. Lemaire, to be published (1993).
8. Landolt-Börnstein, New Data Series, vol. 17a, *Physics of Group II elements and III-V compounds*, ed. C. Moll, Springer, Berlin (1982).
9. Y. Feulon and C. Priester, *Phys. Rev. B* 45, 6259 (1992).
10. J. A. Hemstreet, C. Y. Fung and J. S. Nelson, *Bull. Am. Phys. Soc.* 38, 183 (1993).

* Oxford sample numbers: A 92R B 1189 C 1192 D 1191 E 1190

TuP32

InAs/AlInMnOxide-Based Resonant Tunneling Structures with Ternary Alloy Layers

J. N. Schulman, D.H. Chow, and T.C. Hasenbergl
Hughes Research Laboratories
3011 Malibu Canyon Road
Malibu, California 90263 USA

Abstract

We have studied two modifications of mixed arsenide/antimonide resonant tunneling structures, in which one of the binary components is replaced by a ternary alloy. The first structure is based on an InAs/AlInSb/GaSb resonant interband tunneling structure with the GaSb quantum well layer replaced by a GaAs_{1-x}Sb_x alloy layer. The added As decreases the lattice constant in the well, and the resulting strain can shift the heavy hole subbands below the incoming electron energy. We find that the negative resistance effect can be enhanced by properly adjusting the splitting via the As concentration. A maximum enhancement in the peak-to-valley ratio was obtained with a 10% As concentration in the doped well.

The second structure is a modification of a conventional InAs/AlInSb double barrier structure, in which the AlInSb barriers are replaced by Al_xGa_{1-x}Sb with $x \approx 0.5$. In these structures, the pronounced type-II band alignment results in an entirely new type of current versus voltage characteristic exhibiting intrinsic current bistability (double-valued currents for a given voltage) instead of the conventional voltage bistability. Peak-to-valley voltage ratios as high as 1.5 have been observed with current densities in the 10^5 A/cm² range.

Introduction

Resonant tunneling structures based on the InAs/AlInSb/GaSb material system have produced diodes with unique characteristics and enhanced performance. Two systems have been studied in detail in recent years. First is the interband tunneling structure, which utilizes the broken-gap band line-up of InAs and GaSb, usually in combination with AlInSb barrier layers [1-3]. In these structures band gap blocking for bias voltages above the tunneling resonance results in extremely high peak-to-valley current ratios. The second structure of current interest is the relatively conventional InAs/AlInSb double barrier structure. This structure has demonstrated the highest oscillation (700 GHz) and switching speeds (1.7 ps) to date for resonant tunneling devices [4,5]. The individual layers in both of these devices are usually made from binary compounds, i.e., InAs, GaSb, and AlInSb. Here we investigate the effects of replacing one or more of these layers with ternary alloys, GaAs_{1-x}Sb_x for GaSb in the case of interband structures, and Al_xGa_{1-x}Sb for AlInSb in the case of conventional double barrier structures. We demonstrate dramatic variations in both cases, including an improved peak-to-valley ratio in the first case, and a novel bistable current feature in the second.

InAs/AlInSb/GaAs_{1-x}Sb_x Interband Tunneling Structure

Figure 1(a) is a band edge diagram of a typical InAs/AlInSb/GaSb structure. In these devices, electrons are emitted from the InAs conduction band, tunnel through the AlInSb barrier into the GaSb valence band resonances, and then out the other side. Other variations which have been studied include reversing the roles of the InAs and GaSb as the cladding and well layers, and making various asymmetric structures [6-8].

Here we are only concerned with cases in which the quantum well portion is in the valence band, as in Fig. 1(a). Shown schematically is the band edge diagram of the structure and two of the valence band resonances, the first heavy hole (HH1) and first light hole (LH1) levels. The HH1 level lies above the LH1 level, as is always the case for unstrained materials. The close proximity of HH1 above LH1 produces a degradation in the negative differential resistance effect, however, which can be understood as follows. The LH1 state is the dominant channel for tunneling due to the large coupling between the InAs conduction states and the GaSb light hole state [9]. The coupling in the heavy hole state is small due to the differing orbital composition of

the heavy hole states near the Brillouin zone center. As bias is applied to the diode, the incoming electrons will encounter the HH1 resonance at higher biases than the LH1 resonance. Thus, depending on the precise widths of the layers and other structural parameters, tunneling through the HH1 level contributes to the valley current and tends to degrade the peak-to-valley current ratio of the device. In addition, if the well layer is thick enough, there may be one or two additional heavy hole levels above the LH1 level contributing to the valley current.

The valley current can be divided into two contributions, that due to scattered and due to unscattered electrons. Theoretical calculations usually include only the unscattered portion [9,10]. This calculated heavy hole current contribution to the valley current is small and is probably undetectable, especially at higher temperatures. The main contribution, however, is probably the more difficult to account for contribution due to scattering. This is certainly the case for conventional structures such as n-type GaAs/GaAlAs double barrier diodes. In this case, experimental values for the valley currents are usually much larger than the theoretical predictions. The major missing theoretical ingredient is generally agreed to be the scattering through the indirect conduction band valleys, via phonons, impurities, defects, or other mechanisms. It would be reasonable to expect that similar mechanisms involving scattering through the heavy hole band are significant in the InAs/AlInSb/GaSb system.

We have attempted to eliminate the heavy hole channel by adding As to the central GaSb well layers. Since GaAs has a smaller lattice constant than GaSb, the introduced As creates a lattice mismatch which splits the heavy hole band to lower energy than the light hole band. Figure 1(b) shows a schematic diagram of such a structure. If the mismatch is sufficient, this splitting can dominate over the quantum confinement induced splitting and actually push the heavy hole band below both the light hole level and the InAs conduction band minimum energy. It is then entirely inaccessible for tunneling at any applied bias.

We have grown by MBE and fabricated InAs/AlInSb/GaAs_{1-x}Sb_x structures with As concentrations of 0, 10, 15, and 30%. The arsenic concentration in the GaAs_{1-x}Sb_x layer was controlled by utilizing a valved arsenic cracking effusion cell. The well and barrier thicknesses were 51 Å and 12 Å, respectively, with the InAs electrodes doped to 2×10^{18} cm⁻³, separated from the AlInSb barriers on either side by lightly doped AlInAs spacer layers. Figure 2 shows the room temperature current-voltage curve for one such device, with $x=0.1$ in the GaAs_{1-x}Sb_x layer.

Table 1 summarizes the average peak-to-valley ratios and the peak currents in the four structures. Due to variations in device area produced by the processing procedure, the differences among the values of the peak currents for the 0%, 10%, and 15% As samples are not large enough to be significant, and should be considered as roughly similar. The peak-to-valley ratios do not depend on area, and it can be seen that the 10% As sample has the maximum peak-to-valley ratio among the set. We believe that this enhanced peak-to-valley ratio is due to the lowering of the heavy hole resonance energy below the light hole resonance energy for this alloy concentration.

Calculations of the energy levels in these structures were of no using a twenty-band tight-binding model, to include the heavy hole-light hole coupling [10]. The standard offset of 150 meV was used for the offset between the InAs conduction band and the GaSb valence band. A valence band discontinuity of 41% of the band gap difference was used between AlInSb and GaSb to set the AlInSb band edges [3]. These values are relatively well determined in the literature. A much more uncertain parameter is the dependence of the band offsets on the As concentration in the GaAs_{1-x}Sb_x layers. In lieu of any better technique to determine this value, a constant 43% discontinuity rule for the unstrained GaAs_{1-x}Sb_x band offset was used. This is somewhat arbitrary, since the accuracy of this procedure is unknown, and therefore the theoretical results should be taken as qualitative only.

The calculation for the 0% As case gives a HH1 energy about 60 meV above the LH1 energy. Adding 10% As brings the LH1 energy to within 15 meV of HH1, but still above it. An additional 10% As, to 20% total, shifts HH1 to 35 meV below LH1, which is about 10 meV above the InAs conduction band edge. The experimental result of an enhanced peak-to-valley ratio for 10% As implies that band edge. The experimental result of an enhanced peak-to-valley ratio for 10% As implies that the HH1 energy should have already passed to below the LH1 level for this concentration, but given the aforementioned uncertainties, this level of agreement is all that can be expected. We believe that the abrupt decrease in the measured peak-to-valley ratio for 15% and 30% As is due to the compensation induced shift of the light hole resonance itself towards the InAs conduction band edge. As LH1 decreases in energy, the overlap of its density of states with the

increasing InAs density of states eventually decreases, resulting in smaller currents and degraded peak-to-valley ratios. Thus, we have shown that adding As in the central GaSb layers has a significant effect on the current-voltage characteristics. Similar effects should be found in related structures, e.g., InAs/AlSbGaSb/AlSbGaSb and other structures.

InAs/Al_{0.5}Ga_{0.5}Sb Current Controlled Negative Differential Resistance Structure

The starting point for the second system to be discussed, InAs/AlSb double barrier heterostructures, utilize relatively conventional conduction band resonant tunneling. Their main advantages arise from the use of high excitability InAs in the cladding layers, which provides low contact resistance. The AlSb barriers have large conduction band offsets with InAs and are nearly lattice matched. These structures have been used to make oscillators with frequencies up to 712 GHz [4] and switches with 10%-90% rise times as short as 1.7 ps [5].

As in the previously described InAs/AlSbGaSb structures, the devices reported here are also based on a type II resonant tunneling structure. However, in this case the staggered lineup involves the barrier layers, instead of the wells. The operating principle of the device is that, under certain conditions, two different steady state charge distributions are obtainable for a single bias voltage. These conditions arise due to the presence of hole states in the quantum barrier layers, providing regions for positive charge to be trapped. As device current is strongly affected (via band bending) by changes in the steady state charge distribution, a pronounced bistability in device current is observed.

In all of the structures studied here, the active device region consists of an InAs(n)/Al_{0.5}Ga_{0.5}Sb/Al_{0.5}Ga_{0.5}Sb/Al_{0.5}Ga_{0.5}Sb/Al_{0.5}Ga_{0.5}Sb stack in which the middle three layers form a double barrier structure for electrons tunneling from one InAs(n) electrode to the other. Figure 3(a) shows a schematic band edge diagram of this structure at zero bias. The cladding layers consist of $\sim 1 \mu\text{m}$ n⁺ InAs, lightly doped (500 A/cm²) and undoped (10¹⁷ cm⁻³) Al_{0.5}Ga_{0.5}Sb spacer layers are used to bracket the active double barrier region. The InAs quantum well layer is 75 Å thick in all samples, while barrier layer compositions and thicknesses are intentionally varied from sample to sample. Each structure is completed by a 200 Å InAs(n⁺) cap layer.

The I-V curves are taken on an HP4145A Semiconductor Parameter Analyzer configured either to input a current sweep while measuring voltage, or to input a voltage sweep while measuring current. Due to the nominally symmetric layer sequence used for the structures investigated here, we observe nearly symmetric I-V curves in all of the devices studied.

Figure 4(a) is an I-V curve displayed by a structure with symmetric, 18 Å thick (AlSb)(ML/GaSb)(ML) ordered alloy barriers, taken by sweeping the voltage from 0 mV up to 750 mV and then back down to 0 mV, while measuring the current through the device. A pronounced hysteresis is displayed in the figure, with the lower current line corresponding to the sweep from low to high bias. The observation of hysteresis in the DC I-V curve is indicative of a bistability in device current for a given applied bias. In contrast, no hysteresis is observed in the I-V curve obtained from a structure with symmetric, 18 Å thick AlSb barriers (a "conventional" InAs/AlSb resonant tunneling diode), taken using the same measurement configuration.

Figure 4(b) is the current-voltage curve obtained from the device used for Fig. 4(a) taken by sweeping the current while the voltage is measured. The curve displays a current-controlled ("S"-shaped) negative differential resistance region, in contrast to the voltage-controlled ("N"-shaped) curves displayed by conventional resonant tunneling diodes. We note that in this measurement configuration there is no voltage bistability (the voltage as a function of current is a single valued function), and that conventional resonant tunneling diodes will normally display hysteresis when tested under this measurement configuration. We have also observed the I-V behavior displayed in Figs. 4(a) and (b) in samples with symmetric: (i) 21 Å thick Al_{0.4}Ga_{0.6}Sb barriers, (ii) 15 Å thick Al_{0.6}Ga_{0.4}Sb barriers, and (iii) 18 Å thick Al_{0.5}Ga_{0.5}Sb barriers.

At 400 mV applied bias, the current ratio between the high and low states of the I-V curve displayed in Fig. 4 is greater than 2. This figure of merit might be expected to have implications for static operation in digital circuit applications. A potentially more significant figure of merit is the current density obtained from the device, which is greater than $2 \times 10^5 \text{ A/cm}^2$ in the current-controlled negative differential resistance region of the curve. Large current densities in these

devices generally indicate potential for high speed operation due to short RC time constants [11]. The current densities observed here are only a factor of 1.5 smaller than the peak current density of an InAs/AlSb resonant tunneling diode that was demonstrated 1.7 ns switching times [5]. Therefore, we anticipate that the class of devices reported here will be suitable for future high speed circuits.

The special characteristics of this double barrier structure that produce the unique double-valued current behavior can be understood by considering the band edge diagrams shown in Figure 3. Figure 3(a) shows the bands with no applied bias. The conduction band edges are similar to those of a conventional double barrier structure. However, the Al_{0.5}Ga_{0.5}Sb layers are barriers for electrons only; they form wells for the holes, with the InAs layers acting as barriers. These hole wells can trap positive charge, depending on the applied bias and the Fermi level in the positively biased side, and significantly alter the potential distribution in the structure.

For small bias the current can still be described by conventional conduction band double barrier resonant tunneling. A key point here is that the voltage drop in the space charge region adjacent to the barriers on the positively biased side can be substantial, depending on the doping concentration, and is a large contribution to the total measured voltage. For sufficiently large applied bias the Fermi level on the right approaches the allowed hole energy levels in the right Al_{0.5}Ga_{0.5}Sb well. At some point, depending on bias and tunneling rates, the hole population in the Al_{0.5}Ga_{0.5}Sb layers will increase to the extent that the holes substantially screen out the electric field in the space charge region. This occurs near 0.6 volts in Fig. 4. The potential drop will then become greater across the double barriers themselves and smaller in the space charge region. Since the tunneling current follows the voltage across the barriers, this causes the sudden jump in current at that voltage. Figure 3(b) and (c) show band diagrams for the two possible potential distributions for a given total bias. The current is relatively small in (b) due to the smaller voltage drop across the double barriers, while the current is larger in (c) due to the larger voltage drop there. Measurements at low temperature reveal that the conventional negative differential resistance effect due to tunneling through the conduction band resonance also occurs, but at higher bias.

In summary, we have designed and demonstrated a novel resonant tunneling device based on type-II, InAs/Al_{0.5}Ga_{0.5}Sb heterostructures. Due to hole accumulation in the active device layers, these structures are capable of possessing multi-state charge distributions at a given applied bias, resulting in bistable device currents. The demonstrated devices display hysteretic I-V behavior under voltage-controlled measurement conditions, and "S"-shaped negative differential resistance under current-controlled conditions. Device operating currents are in excess of $1.5 \times 10^5 \text{ A/cm}^2$, suggesting the potential for good high speed performance due to low RC time constants.

The authors wish to acknowledge helpful technical discussions with A.T. Hunter, E.T. Crooke, and R.H. Miles and the technical assistance of L.D. Warren.

References

1. M. Sweeney and J. Xu, Appl. Phys. Lett. 54, 546 (1989).
2. J.R. Soderstrom, D.H. Chow, and T.C. McGill, Appl. Phys. Lett. 55, 1194 (1989).
3. L.F. Luo, R. Brestford, and W.I. Wang, Appl. Phys. Lett. 55, 2123 (1989).
4. E.R. Brown, J.R. Soderstrom, C.D. Parker, L.J. Makiney, K.M. Mulvar, and T.C. McGill, Appl. Phys. Lett. 58, 2291 (1991).
5. E. Özyay, D.M. Bloom, D.H. Chow, and J.N. Schulman, to appear in Elsev. Dev. Lett.
6. R. Brestford, L.F. Luo, K.F. Longenecker, and W.I. Wang, Appl. Phys. Lett. 56, 952 (1990).
7. D.Z.-Y. Ting, D.A. Collins, E.T. Yu, D.H. Chow, and T.C. McGill, Appl. Phys. Lett. 57, 1257 (1990).
8. M.P. Houng, Y.H. Wang, C.L. Shen, J.F. Chen, and A.Y. Cho, Appl. Phys. Lett. 60, 713 (1992).
9. D.Z.-Y. Ting, E.T. Yu, and T.C. McGill, J. Vac. Sci. Technol. B9, 2405 (1991).
10. M.S. Kikodjian, J.N. Schulman, K.L. Wang, and K.V. Rousseau, Phys. Rev. B46, 16012 (1992).
11. S.K. Diamond, E. Özyay, M.J.W. Rudwell, D.M. Bloom, Y.C. Pao, and J.S. Harris, Appl. Phys. Lett. 54, 153 (1989).

Table 1. Room temperature peak-to-valley ratios (P/V) and approximate current densities for InAs/AlSb/GaSb double barrier structures with 0, 10, 15, and 30% As concentrations.

x	P/V	Peak Current Density (A/cm^2)
0	8	2.5×10^4
0.1	11	1.5×10^4
0.15	3	1.3×10^4
0.30	3	0.5×10^4

Figures

Figure 1. Band edge diagram of (a) InAs/AlSb/GaSb and (b) InAs/AlSb/GaSb double barrier resonant tunneling structures.

Figure 2. Room temperature current versus voltage curve for InAs/AlSb/GaSb double barrier structure with 10% As in the GaSb.

Figure 3. Schematic band edge diagram of the InAs/AlSb/GaSb structure with three potential distributions. (a) has no applied bias, and (b) and (c) have the same applied bias. Holes may accumulate in the AlSb barriers for sufficient bias.

Figure 4. (a) I-V curve, taken by sweeping the voltage in both directions while measuring current, for an InAs/AlSb/GaSb double barrier structure with 18% thick barrier layers. (b) I-V curve taken by sweeping the current in both directions while measuring voltage. Room temperature

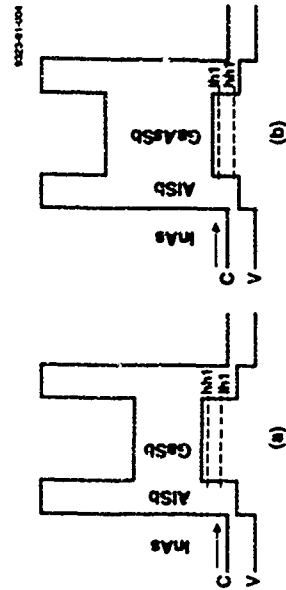


Figure 1

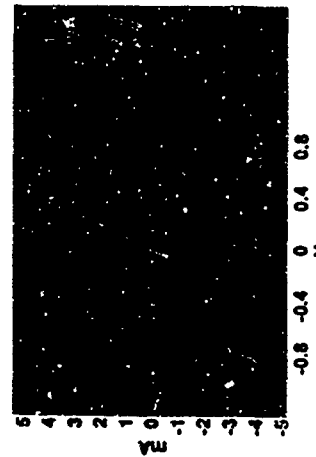


Figure 2

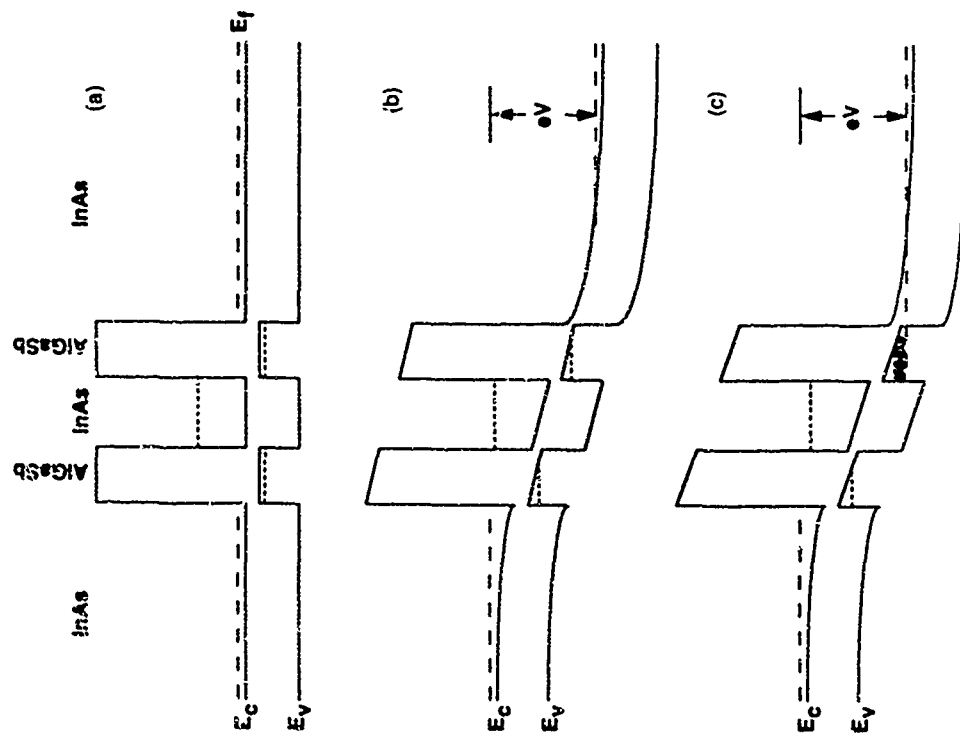


Figure 3

-623-

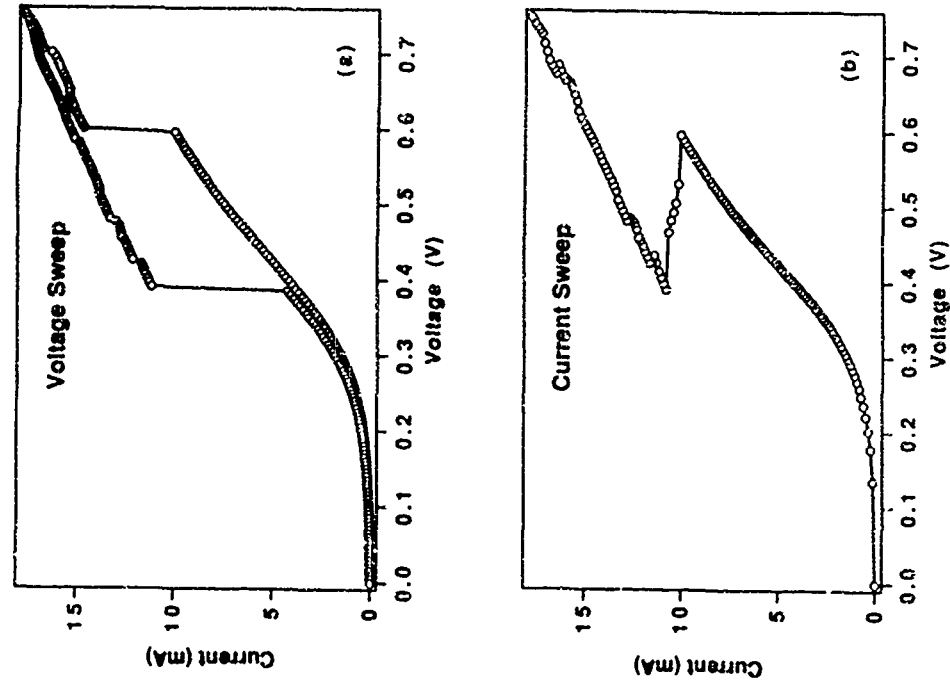


Figure 4

-624-

TuP33

Thermally desactivated resonant current in high peak to valley current ratio (69:1) GaAs/GaAlAs resonant tunneling structures : a spectroscopic view of the emitter density of state.

F. Lanielle and G. Faini

Laboratoire de Microstructures et de Microélectronique, C.N.R.S.
B.P. 107, 92225 Bagneux Cedex, France

Abstract

We describe the realization of very high peak to valley current ratio double barrier resonant tunneling structures by molecular beam epitaxy. We find that the resonant current through the ground state resonances decreases as the temperature is raised. This unique behavior is explained within the Esaki-Tsu formalism and originates in the Fermi-Darwin statistics.

1- Introduction

Since the first observation of resonant tunneling by Chang, Esaki and Tsu [1] the peak to valley current ratio (PVR), known as the figure of merit of double barrier resonant tunneling structures (DBRTS), keeps increasing with time due to technological efforts. However the best PVR's are well below values predicted by resonant tunneling theories that ignore relevant scattering mechanisms in these systems [2-3]. As first shown by Minot et al. [4], undoped spacer layers, inserted between heavily doped electrodes and tunneling barriers, prevent the incorporation of segregated impurities into the active part of the structure during epitaxial growth. It is now well established that localized impurities are very efficient scatterers in these systems which strongly degrade the PVR [5]. It has been recently suggested that, provided impurity segregation is minimized, extremely high PVR can be obtained [6]. We will confirm this idea and further show that these high quality structures help to gain insights into the thermal and bias dependence of resonant tunneling.

2- Experiments

The DBRTS has been grown by molecular beam epitaxy (MBE). The sample is grown on a n⁺ type, Si doped substrate and consists of : 5000 Å GaAs, Si 1x10¹⁸ cm⁻³, 5000 Å GaAs, Si 2x10¹⁷ cm⁻³, 3000 Å GaAs, undoped, 170 Å Ga_{0.9}Al_{0.1}As, 90 Å of GaAs, 170 Å Ga_{0.9}Al_{0.1}As, 120 Å GaAs, undoped, 5000 Å GaAs, Si 2x10¹⁷ cm⁻³, 5000 Å GaAs, Si 1x10¹⁸ cm⁻³. Growth rates are precisely measured in situ with the help of reflection high energy electron diffraction : 2.09 Å s⁻¹ for Ga and 0.545 Å s⁻¹ for Al. The growth temperature is 640 °C and the Al_x flux is monitored to ensure the As rich growth front in the 3x3 surface reconstruction. 100x100 µm square mesas are defined by photolithography with SiO₂ reactive ion etching. Ohmic contacts are made of alloyed AuGeNi multilayers. The back contact is made on the backside of the n⁺ wafer. J-V curves are measured in a variable temperature cryostat from T= 1.8 K up to 150 K. Forward bias refers to electrons propagating from the substrate toward the surface : the large spacer layer lies then on the emitter side of the DBRTS. The current density is simply obtained by dividing the measured current by the DBRTS nominal rectified area, measured during scanning electron microscope inspection.

3- Results and discussion

We will first concentrate on the low temperature J-V characteristics. As can be seen in figure 1, the first resonance under forward bias consists of a very narrow peak at 78 mV followed first by a pronounced valley at 130 mV and then by a shoulder at 175 mV. To convert external voltages into energies relative to the emitter Fermi energy, we solve Poisson's equation in the Thomas-Fermi approximation. We use nominal thicknesses and alloy composition. Doping densities are extracted from the best fit with the experimental J-V curve : they are found slightly lower than what was expected from doping calculations. The multiplicity coefficient to get energy from voltage is 0.315 for forward bias and 0.063 for reverse bias. It is worth pointing out that these coefficients are smaller (down to 20%) than if we assume a constant electric field across the DBRTS. This potential profile is then used to solve Schrödinger's equation in the effective mass approximation to get the energy dependent transmission coefficient T(E,V) for each external voltage. We determine the threshold voltage and the total width of the resonance by extrapolating the linear part of the peaks on both sides. We find 69 mV and 32 mV respectively. The width of the resonance is related in the Fermi energy of the emitter i.e. 10.1 meV which corresponds to a three dimensional Fermi sea of 7.8x10¹⁶ cm⁻³, a value close to the density of the doping level in the contact layer. The threshold voltage is related to the energy difference between the emitter Fermi level and the quantum well (QW) ground state : 18.9 meV. This gives a ground state energy of 29.0 meV in good agreement with envelope function calculation done with the nominal thicknesses and Al composition : 11.8 meV. The peak current is measured for a voltage of 78 mV and the peak current density is 4.50 µA cm⁻². The peak current arises when the QW

ground state lies 4.4 meV above the bottom of the emitter conduction band. The valley current density around 116 mV is only 6.5 µA cm⁻², setting the PVR to 69.1 which is a typical value measured for several double barrier structures. The shoulder around 175 mV is offset by 115 mV or 36.3 meV with respect to the first resonance threshold. We attribute it to a first resonance replica with emission of a GaAs LO phonon. The valley current is dominated by the emergence of acoustic optical phonon scattering : it is of intrinsic origin.

The reverse bias J-V curve looks very similar except that the bias scale is cut about roughly 3 times since the thick undoped spacer layer lies now on the collector side. We find a Fermi energy of 13.7 meV (Fermi sea density of 1.2x10¹⁷ cm⁻³) and a ground state energy of 33.8 meV in agreement with the forward bias determination. We notice that the PVR is much smaller (26:1) compared to the other polarity whereas the peak current density is quite similar (600 µA cm⁻²). We find that the shoulder after the valley current appears at 807 mV and is offset only by 30.7 meV. This is smaller than the GaAs LO phonon energy. This suggests that for the reverse polarity, the valley current is not dominated by phonon diffusion. The phonon contribution (36.3 meV) can be easily seen around -500 mV (note that the slope of the J-V curve is changing at this value).

In another DBRTS, identical to this one except a thinner QW (70 Å instead of 90 Å), we measure a current density of 10 nA cm⁻² and a PVR of 61:1 under forward bias at T= 1.8 K, showing that this structure is well suited for high PVR structures provided the required current density is not too large.

Cundeghe et al. reported similar measurements on DBRTS grown by gas source MBE and claim higher PVR's up to 130:1 at 1 K [6]. However there are some discrepancies with our results : for positive bias their resonance appears at 400 mV with a current density around 350 µA cm⁻². We use the same polarity convention as Cundeghe et al. [7]. With such peak voltage and current density, we are tempted to say that the polarity is not correct. Otherwise, they observe the second resonance that we also observe at 400 mV for positive bias, with a current density of 150 nA cm⁻² in our sample. In that case, their current density is much too low. The resonance in ref. [6] exhibits a hysteresis loop that we do not observe around our first resonance which has a very unichain shape. Other electrical data obtained on comparable structures published by the same group [7] with resonance line shape similar to ours reveal a PVR of 54:1 for forward bias with current densities around 1 A cm⁻² : the PVR in such samples is also limited by polar optical phonon scattering. Figure 2 shows the J-V characteristics for several temperatures up to 100 K. The thermal activation of the valley current is well known. The first resonance disappears above 150 K : it is entirely dominated by the current flowing through the second resonance. We also note the thermal activation of the current on the low voltage side of the first resonance due to the electronic state population above the Fermi level. More surprising is the pronounced drop of both peak current and peak voltage which is present for both polarities although this effect is stronger for direct bias.

To elucidate the origin of this phenomenon, we have calculated the J-V characteristics using the Tho-Esaki formula [8] :

$$J(V) = \frac{em^*kT}{2\pi\hbar^2} \int_{T(E,V)}^{\infty} \ln \left(\frac{1 + \exp\left(\frac{E - E_F}{kT}\right)}{1 + \exp\left(\frac{E - E_F}{kT}\right)} \right) dE \quad (1)$$

where T(E,V) is the transmission probability coefficient for an incident electron of energy E upon the double barrier biased with potential V. Equation (1) can be simplified since T(E,V) is sharply peaked around E_g with a maximum value T_{max} and a width γ, these three values depending on V implicitly :

$$J(V) = \frac{em^*kT}{2\pi\hbar^2} \ln \left(\frac{1 + \exp\left(\frac{E_g - E_F}{kT}\right)}{1 + \exp\left(\frac{E_g - E_F}{kT}\right)} \right) T_{max} \gamma \quad (2)$$

In our calculation, the Fermi energy (and the related doping level) is determined as the best parameter to fit the J-V curve at low temperature following the above described procedure to measure the width of the resonance.

From equation (2) we deduce that all J/T curves cross for the polarization such that E_g equals E_g provided that eV is large compared to kT and that E_g does not depend on temperature. In principle this allows to determine with a good precision the threshold voltage for which the Fermi level is in resonance with the QW ground state. Inspection of figure 3 on which J/T curves are displayed shows that this is not the case neither for reverse nor for direct bias. Comparing equation (2) with a constant Fermi energy leads to an increasing current density with temperature : the hypothesis that the Fermi energy does not depend on temperature implies that the emitter electron density increases with temperature because the three dimensional density of states is a growing function of energy. To compare equation (2) correctly, we have to calculate the Fermi energy for each temperature in order to keep the electron density constant. We then get a good agreement with our experimental results. The Fermi energy variations are very large in our experiments : the inset of figure 4 shows the calculated relative Fermi energy variation between 0 K and 100 K for two electronic densities : 8x10¹⁶ and 1x10¹⁷ cm⁻³. It is clear that, when the Fermi energy gets larger and larger, the 3D density of states varies more and more slowly.

To understand the decrease of both peak current and peak voltage we have to keep in mind the consequences of the elastic tunneling selection rules, namely electron energy and in-plane momentum (x,y components) conservation. For each bias, tunneling electrons are located on a disk, intersecting the emitter Fermi sphere at energy E_g [9]. The emitter electron

density participating to the elastic tunneling current resonance is given by:

$$n(E) = \int \frac{1}{1 + \exp\left(\frac{E - E_F}{k_B T}\right)} dE. \quad (3)$$

From equation (3) it is clear that smaller E_F implies, larger $n(E)$, whereas decreasing E_F has the opposite consequence. For higher voltages, there are more tunneling electrons (the disk area is larger) but each state carries less current: the momentum component along the z direction gets smaller and smaller. In other words: as voltage increases, tunneling electrons have a larger and larger incident angle respectively to the plane of the barrier. When the temperature is raised, the Fermi energy decreases. If the resonant level lies well below (above) the Fermi energy, the current decreases (increases). This implies that (i) the peak voltage shifts toward lower bias and (ii) the peak current drops.

Figure 4 presents calculated J-V curves for different temperatures. They reproduce qualitatively the thermal behavior of the measured DBRTS. It is not clear why the measured current variation with temperature is larger than the calculated one. One possibility is the build-up of a two-dimensional accumulation layer which would change the density of state used in the calculation. The larger emitter Fermi energy for reverse bias explains the smaller temperature sensitivity for this relation. Another striking difference is the pronounced current rise at high temperature and low bias in the theoretical calculation. This discrepancy with experimental results is puzzling. We finally note that the onset of the J-V curve gets sharper and sharper when the temperature is lowered in contrast with the experimental behavior where the onset sharpness saturates at 15 K. Spectroscopy around this onset should allow to determine the width of the resonance which is probably inhomogeneously broadened by interface roughness scattering.

Chen et al. report a similar temperature study concerning the second resonance of a similar DBRTS and find the same overall behavior [10]. They attribute temperature changes to the modification of the accumulation layer electron density in the emitter rather than to a statistical effect. If the accumulation layer is strongly affected by the temperature, this can be checked easily with magneto-tunneling experiments [11].

IV - Summary

In conclusion we have demonstrated that in high quality DBRTS the PVR is dominated by optical phonon scattering at low temperature and can reach 69%. The J-V characteristics dependence on temperature is simply explained by first considering the electron statistics with a constant electron density and a variable Fermi energy and then by taking into account elastic tunneling selection rules. The resonance occurs from a simple compromise: as bias increases, the tunneling electron density increases but each state brings a smaller contribution to the total current. We evidence that the resonance occurs when the QW ground state lies several meV above the bottom of the emitter conduction band, in contrast with the usual idea that the current drops sharply when the ground state lies below the emitter conduction band edge. When the resonant level is aligned with the emitter conduction band edge, electrons are allowed to tunnel only parallel to the plane of the DBRTS and no current is flowing from one side of the DBRTS to another.

Acknowledgements

We wish to thank V. Thierry-Mieg for providing help during the growth of the samples, F. R. Ladan and C. Mayeux for their valuable support during the process in the DBRTS. We gratefully acknowledge fruitful discussions with D. Filenue, A. Stahli, and J. F. Palmier.

References

1. L.L. Chang, L. Esaki, and R. Tso Appl Phys Lett, 24, 393 (1974)
2. F. Chevalier, and B. Vinter, Phys Rev B, 47, 7260 (1993)
3. P. Roblin, and W.R. Louis, Phys Rev B, 47, 2146 (1993)
4. S. Mino, T. Inasa, H. Okushi, N. Yokoyama, and S. Iiyamazu Jpn J Appl Phys, 25, 577 (1986)
5. F. Lantelle, A. Rancoule, and G. Faint, Surf Sci, 267, 396 (1992)
6. J.E. Cunningham, V.J. Goldman, B. Su, and W.Y. Jan, J Cryst Growth, 127, 695, (1993)
7. V.J. Goldman, B. Su, and J.E. Cunningham, Phys Rev B, 46, 7644 (1993)
8. R. Tso, and L. Esaki, Appl Phys Lett, 22, 562, (1973)
9. S. Luryi, Appl Phys Lett, 45, 490 (1985)
10. J. Chen, J.G. Chen, C.H. Yang, and R.A. Wilson, J Appl Phys, 70, 3131 (1991)
11. Y. Galvao Goharo, F. Chevalier, J.M. Demer, P. Bink, Y. Guldner, J. Nagle, J.P. Vieren, and B. Vinter, Phys Rev B, 43, 4843 (1991).

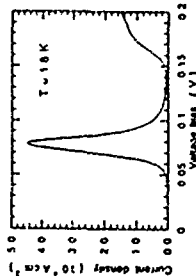
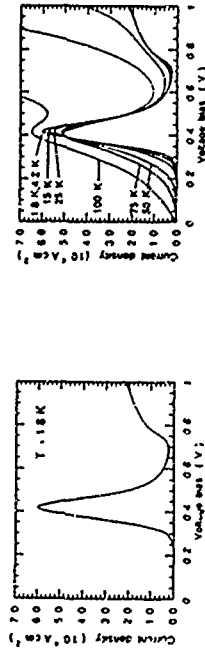


Figure 1: Low temperature J-V characteristics of DBRTS at $T = 1.8$ K. Bottom: forward bias; top: reverse bias. The plot is made with absolute values.

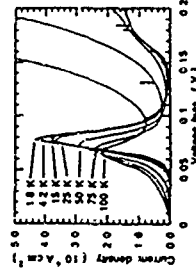
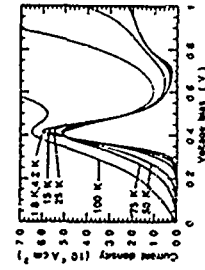


Figure 2: J-V curves of the same device as in Fig. 1 for different temperatures. Bottom: forward bias; top: reverse bias. The plot is made with absolute values.

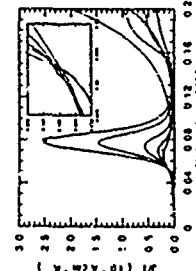
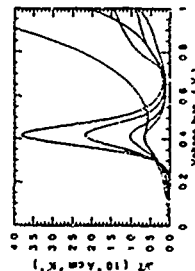


Figure 3: J-V characteristics of the same device as in Fig. 2 but with forward bias. Bottom: forward bias; top: reverse bias. The plot is made with absolute values. The inset shows the calculated relative Fermi energy E_F versus temperature T for the device. The curves are for E_F at 1.8 K, 2.5 K, 5 K, 10 K, 20 K, 50 K, 75 K, 100 K, 150 K, 200 K, 250 K, 300 K, 350 K, 400 K, 450 K, 500 K, 550 K, 600 K, 650 K, 700 K, 750 K, 800 K, 850 K, 900 K, 950 K, 1000 K.

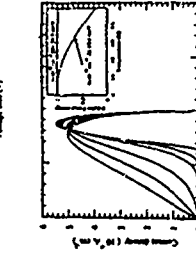
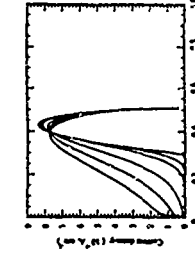


Figure 4: Theoretical J-V curves for the DBRTS described in the text. Bottom: forward bias; top: reverse bias. The plot is made with absolute values. The inset shows the calculated relative Fermi energy E_F versus temperature T for the device. The curves are for E_F at 1.8 K, 2.5 K, 5 K, 10 K, 20 K, 50 K, 75 K, 100 K, 150 K, 200 K, 250 K, 300 K, 350 K, 400 K, 450 K, 500 K, 550 K, 600 K, 650 K, 700 K, 750 K, 800 K, 850 K, 900 K, 950 K, 1000 K.

Theoretical Analysis of Resonant Magnetotunneling Spectroscopy of Holes

¹ C. Galdoni and A. Fasolino,
Scuola Internazionale Superiore di Studi Avanzati, in *Brescia* 2:2, 1912; Trieste, Italy.
² Istituto degli Studi di Matematica, Dipartimento di Fisica,
in *Campi* 2:1 A, 2:1109; Modena, Italy.

We calculate the hole energy band structure in Ga_{1-x}Al_x Quantum Wells (QW) with high in-plane magnetic fields and simulate Resonant Magnetic Tunneling (RMT) experiments. RMTs experiments, recently proposed as a probe of the hole energy dispersion. We find that the high magnetic fields used in RMTs result in small modifications of the QW hole subbands in turn QW. However for wide QW's or very large magnetic fields, the first strongly affected is the hole dispersion by changing the heavy hole light hole mixing. We give a simple expression to evaluate to such extent the mixing is modified as a function of the QW width and field strength.

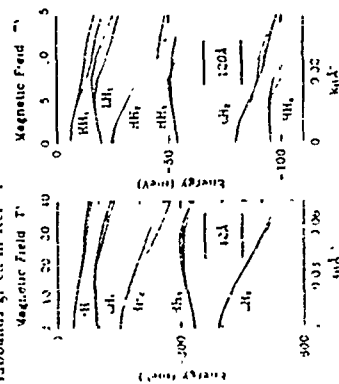
Resonant Magnetotunneling Spectroscopy (kMBS) of p-doped GaAs-AlAs double barrier structures has recently been proposed as a probe of the complicated hole subband distribution in quantum wells (QWs).² kMBS has also been realized in bulk GaAs.³ In kMBS holes are injected from an accumulation layer into an adjacent QW through a barrier. The quantized levels of the QW are brought in resonance with the emitter Fermi level by an electric field perpendicular to the interfaces. The carriers which tunnel into the QW moving in the plane of the interfaces acquire an in-plane wave vector k_{\parallel} . The acquired k_{\parallel} has to match that of the quasi-bound QW hole levels for resonant tunneling to take place. Therefore the magnetic field is in one-to-one correspondence with

8. In GaAs-AlAs double barrier structures the shifts of the resonance peaks with magnetic field maps very well onto the theoretical QW hole dispersion ω_k calculated at zero field (Fig. 1.4). The agreement is rather surprising in view of the high in-plane magnetic fields (several T) in the experiments, since high fields are expected to shift the energy through the heavy-hole-light-hole mixing and field spin splitting of the hole bands.

[illegible]

where Δ is the average distance carried by ions in going from one station level to another. We must also include mixing by the + & - lattices' admittance with the substitution $k \rightarrow k - A$. The admittance can be calculated as follows: since

energy dispersion vs k in ^{11}B . The magnetic field removes the degeneracy between the two lowest energy solutions that would apply to symmetric QW's at zero field.

[illegible]

ination R is with hole energies calculated at $\omega = 0$ by Eq. (4) as a function ω of the magnetic field H and $\omega = 4.2 \times 10^{12}$ rad/sec. Solid lines marked with dots are calculated for $\omega = 0$ and dashed lines marked with dots are calculated for an applied bias in the growth direction $\omega = 0.1$ rad/sec. The full and LH nomenclature is used for the magnetic field H and the lower and higher Landau levels, respectively. The LH and LL nomenclature is used for the lower and higher Landau levels, respectively. The LL and LH nomenclature is used for the lower and higher Landau levels, respectively.

[illegible]

terms introduced in the Hamiltonian by the field depend mainly on the field strength, the larger the ω , the more effective is the field in modifying the HH-LH mixing.

Magnetic field at $k_z = 0$

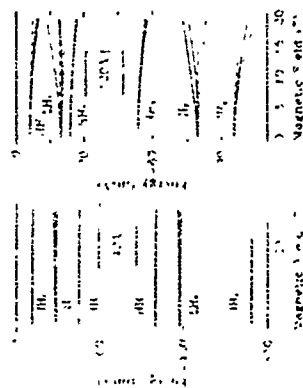


Fig. 2. Energy bands as a function of the magnetic field. Solid lines, hole magnetic energy at $k_z = 0$; dashed lines, electron magnetic energy at $k_z = 0$. The HH and LH abbreviations refer to the hole character at $B = 0$.

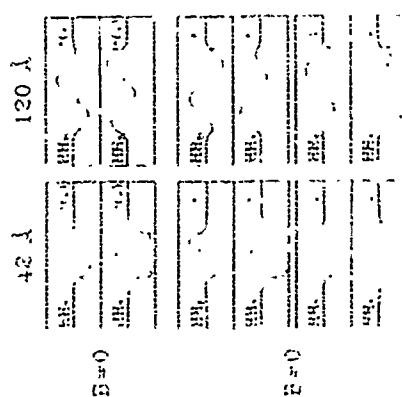


Fig. 3. Energy bands for HH and LH bands at $k_z = 0$. Solid lines, hole magnetic energy at $k_z = 0$; dashed lines, electron magnetic energy at $k_z = 0$. The HH and LH abbreviations refer to the hole character at $B = 0$.

As it can be seen, by comparing the simulated RMS spectra for the two QW's, in fact, while the spin splitting is of the same order of magnitude for the two QW's (note the different energy scales), in the latter QW the HH-LH mixing is strongly modified with respect to the zero-field subbands. This is evident by comparing antissymmetries between different subbands: HH-LH, HH-LH, LH-LH, etc. Note in particular how the LH-LH, antissymmetric, is strongly affected by the field. Note also that antissymmetries shift differently both in k_y and in energy for the two spin-split subbands.

For carriers with parabolic energy dispersion, as in a conduction band electron, the in-plane magnetic field forms a parabolic effective potential in the growth direction, with curvature determined by the effective mass. This effective potential rigidly shifts upwards the subbands as soon as the magnetic length becomes comparable to the QW width. The situation for holes is far more complicated since holes have a mixed HH-LH character. The field moreover modifies the HH-LH coupling. In Fig. 2 we plot the shift of the subband edges ϵ_k of holes as a function of the magnetic field for the 12 Å and the 120 Å QW's and see. The dashed lines represent the magnetic shift that would be expected for pure HH and LH (a Zeeman splitting has been added in this case for LH's subbands). At $B = 0$ HH's and LH's are exactly decoupled in the Luttinger Hamiltonian so that solid and dashed lines coincide. In the 12 Å QW, the HH's and LH's remain nearly decoupled up to high fields. For the 120 Å QW, however, the shift of the subband edges deviates from the Zeeman shift. The hole subband mixes LH's with HH's even at $k_z = 0$, the assumed heavy moment induces a positive magnetic shift of LH's. The opposite is true for HH's, since that positive magnetic shift appears when HH and LH edges with same parity happen to be near in energy: since the hole relation terms at $k_z = 0$ can be shown to mix HH's and LH's with same parity, HH's and LH's edges, instead, shift according to the decoupled case.

The magnetic field can also affect the HH-LH mixing at finite in-plane wavevector $k_z \neq 0$ (Fig. 3). As for the $k_z = 0$ case, the antissymmetries of the subbands labeled HH and LH in Fig. 3 are compared to the wavefunctions at $B = 0$ and $B \neq 0$. It is evident from the figure that in the 12 Å QW the wavefunctions are only slightly modified by the field so that, apart from spin splitting, small deviations of the RMS spectra are expected with respect to the unperturbed subbands. For the 120 Å QW, however, the $k_z \neq 0$ wavefunctions are significantly different from the $B = 0$ ones.

To identify the important couplings introduced by the field, we use a simple representation of the Luttinger Hamiltonian in the truncated basis formed by the intralayer states at $k_z = 0$. HH, LH and HH' the relevant wavefunctions are taken to be those of the infinite well $W = 1$ (it is clear that the largest off-diagonal term couples the LH and HH' edges

$$\langle \text{HH} | H | \text{HH}' \rangle = \frac{1}{2} \left(\frac{1}{m} + \frac{1}{m'} \right) \frac{\hbar^2}{2m} \frac{1}{L} \frac{1}{L}$$

with the unperturbed constants $\chi = 1/L^2$ and $\chi' = 1/L'^2$ and be zero until in the two spin cases. The second term in H is absent present at $B = 0$ and is responsible in our simple representation of the system for the mixing of the HH and LH subbands. The first term instead is responsible for the spin splitting, since it mixes the HH-LH coupling. By comparing the energy of the unperturbed states, we can estimate a value of the field effects the coupling χ and χ' in terms of the unperturbed energy. For the 12 Å QW, we have $\chi = 1/L^2 = 1/12^2 = 0.0069$ and $\chi' = 1/L'^2 = 1/120^2 = 0.000069$, so that the spin splitting amounts to 0.0069 of the zero-field coupling.

TuP35

Control of Electron Populations in the Quantum Well Levels of GaAs-AlGaAs Double Barrier Resonant Tunneling Structures.

P D Buckle, J W Cockburn, M S Skolnick and D M Whitaker
Department of Physics, University of Sheffield, Sheffield S1 3JD, United Kingdom

R Grey, G Hill, and M A Pate

Science and Engineering Research Council Central Facility for III-V Materials, Department of Electronic and Electrical Engineering, University of Sheffield, Sheffield S1 3JD, United Kingdom

G W Smith

Defence Research Agency, St Andrews Road, Malvern, Worcestershire WR14 3PS, United Kingdom

In double barrier resonant tunnelling structures (DBRTS), the potential exists to control independently the populations of individual quantum well (QW) confined levels. For example, when biased on the second electron tunnelling resonance the ratio of the electron populations of the ground (E1) and first excited (E2) state of the QW (n_2/n_1) within the DBRTS is controlled by the ratio of the inter-sub-band scattering time (τ_1) to the ground state tunnelling out time (τ_1).¹ In this work both electroluminescence (EL) and photoluminescence (PL) techniques are employed to provide spectroscopic information on the level populations as a function of bias. From these results we demonstrate the control of the population ratio n_2/n_1 by independent variation of both τ_1 and τ_1 in different structures.

The tunnelling-out time (τ_1) from the E1 level is expected to be a very sensitive function of collector barrier width. We demonstrate a 40 times enhancement of n_2/n_1 by reducing the collector barrier width from 80Å to 50Å in a structure with 80Å QW, in good agreement with the decrease in τ_1 predicted from a tunnelling resonance calculation. Furthermore, by application of a magnetic field perpendicular to the plane of the QW, a strong oscillatory variation of the EL intensity from E2 electrons, periodic in $1/B$, is observed. These oscillations in EL intensity, proportional to the changes in E2 population, are shown to arise from modulation of the inter-sub-band scattering time (τ_1) as Landau levels from the E1 sub-band are swept through the E2 level. As a result, the control of the n_2/n_1 ratio by variation of the inter-sub-band scattering time (τ_1) is demonstrated in a very clear manner.

inally, the observation of a population inversion between highly excited states of a wide well (200Å) DBRTS is reported. In this case the population ratios are shown to be controlled by the differences in longitudinal optic phonon inter-sub-band scattering times between the highly excited states of the QW. The experimentally determined values of the inverted population ratios are found to be in good agreement with a rate analysis.

J W Cockburn, P D Buckle, M S Skolnick, D M Whitaker, W F F Yare, R A Haver

-634-

In conclusion, we have calculated the hole magnetic levels in a QW with strong in-plane magnetic field and we simulated RAS spectra for two different regimes of the QW width. For a 12 Å QW our calculations give support to the interpretation of RAS in p-doped QW as a probe of the hole dispersion for a 120 Å QW. Instead, our calculations show that the III-V mixing and the subband dispersion are significant in the field, in particular, the position of the anti-crossing between the zero field subbands shifts in a different fashion for the two spin split partners as a function of the field.

This work has been partially carried out within the European Program Human Capital Mobility project MAGNET in ERB4050P(L2)1451.

- 1 R K Hadden, P K Maude, L Eaves, L Eaves, M Henni, J W Sheard, H Hughes, J P Portalano, J Jor, Phys Rev Lett 66, 1719 (1991)
- 2 M Vassallo, J Ekembere and A Fasolino, Phys Rev B 52, 3173 (1995)
- 3 J Jor, J P Portalano, J Ekembere, L Eaves, L Eaves, M Henni, J W Sheard, H Hughes, Phys Rev Lett 67, 2922 (1991)
- 4 R K Hadden, J Takamasa, P K Maude, L Eaves, L Eaves, M Henni, J W Sheard, H Hughes, Phys Rev Lett 67, 2922 (1991)
- 5 J Jor, J P Portalano, J Ekembere, L Eaves, L Eaves, M Henni, J W Sheard, H Hughes, Phys Rev Lett 67, 2922 (1991)
- 6 J Jor, J P Portalano, J Ekembere, L Eaves, L Eaves, M Henni, J W Sheard, H Hughes, Phys Rev Lett 67, 2922 (1991)
- 7 J Jor, J P Portalano, J Ekembere, L Eaves, L Eaves, M Henni, J W Sheard, H Hughes, Phys Rev Lett 67, 2922 (1991)
- 8 J Jor, J P Portalano, J Ekembere, L Eaves, L Eaves, M Henni, J W Sheard, H Hughes, Phys Rev Lett 67, 2922 (1991)
- 9 J Jor, J P Portalano, J Ekembere, L Eaves, L Eaves, M Henni, J W Sheard, H Hughes, Phys Rev Lett 67, 2922 (1991)
- 10 J Jor, J P Portalano, J Ekembere, L Eaves, L Eaves, M Henni, J W Sheard, H Hughes, Phys Rev Lett 67, 2922 (1991)

-633-

Part of the work has been supported by the Bundesministerium für Forschung und Technologie (BfF) into account in all devices using in-plant-rate technology (transistors etc.)

A Conclusions

Part of the work has been supported by the Bundesministerium für Forschung und Technologie (BfF) into account in all devices using in-plant-rate technology (transistors etc.)

* present address: Paul-Ude-Institut für Festkörperelektronik, O-026 Berlin, Germany

[1] e.g. *Semiconductor Technology and Materials*, edited by H. Krost and H. Löhmann, Springer Series in Electronics and Photonics, Vol. 31 (Springer, Berlin, 1982).

[2] e.g. *Tungsten Carbide*, edited by S. Gruber and M. H. Dornost (Plenum, New York, 1982).

[3] e.g. *Single Crystals*, V.J. Lee, J.T. Nicholas, L. Martin-Moreno, D.A. Ritchie, M. Kelly, M. Poppert, I.E.F. Frost, R. Newbury, G.A.C. Jones, *Solid State Electron.* (this volume) and references therein.

[4] A.D. Welch and K. Phang, *Appl. Phys. Lett.* **56**, 728 (1990).

[5] A.D. Welch and K. Phang, *J. Appl. Phys.* **68**, 228 (1990).

[6] A.D. Welch and K. Phang, *Phys. Rev. B* **42**, 1040 (1990).

[7] K.J. Haug, A.D. Welch, K. Phang, and K. Phang, *Physics B* **164**, 197 (1993).

[8] J. Nieder, A.D. Welch, P. Giamboni, H. Lager, D. Heilmann, K. v. Klitzing, and K. Phang, *Appl. Phys. Lett.* **61**, 2785 (1992).

[9] Y. Fein, T. Thornton, J.J. Harris, and D. Williams, *Appl. Phys. Lett.* **60**, 94 (1992).

[10] K. Nakamura, C.J. Thornton, J. White, and H. Ahmed, *Appl. Phys. Lett.* **61**, 2165 (1992).

[11] B. Pöschel, Z. Wen, R.J. Haug, K. v. Klitzing, and Phong, *Appl. Phys. Lett.* **62**, 3176 (1993).

[12] U. Meier, M.A. Kastner, and S.J. Wind, *Phys. Rev. Lett.* **68**, 771 (1990).

[13] P. McEuen, E.B. Fomina, U. Meier, M.A. Kastner, Y. Meir, N.S. Wingars, and S.J. Wind, *Phys. Rev. Lett.* **66**, 1926 (1991).

[14] L.P. Kouwenhoven, N.C. van der Vaart, A.T. Johnson, K. Woon, C.P.J. Harman, J.G. Williamson, and A.M.M. Staring, *Z. Phys. B* **88**, 347 (1991).

[15] R.J. Haug, J.M. Hag, and E.Y. Lee, *Surf. Sci.* **263**, 415 (1992).

[16] A.M. Staring, B.W. Albrecht, H. van Hoofte, L.W. Molenkamp, H.A.A. Mabeene, and O.J.A. Bay, *Phys. Rev. B* **46**, 7238 (1992).

[17] R.N. Taylor, A.S. Sachdev, P. Zawadzki, R.T. Colbridge, and T.A. Adams, *Phys. Rev. Lett.* **69**, 1849 (1992).

[18] J. Wen, R.J. Haug, K. v. Klitzing, and K. Phang, *Phys. Rev. B* **46**, 12317 (1992).

[19] C. Panquier, U. Meier, F.B. Williams, D.G. Glath, Y. Jin, and B. Elman, *Phys. Rev. Lett.* **70**, 69 (1993).

[20] R.J. Haug, K.V. Lee, and J.M. Haug in Ref [1], J. Woon, R.J. Haug, K. v. Klitzing, and K. Phang, *Physics B* (to appear).

[21] J. Wen, R. Haug, K. v. Klitzing, and K. Phang, Proceedings of EPDS-10, to be published in Surf. Sci.

[22] A.T. Johnson, L.P. Kouwenhoven, W. de Jong, N.C. van der Vaart, C.J.P.M. Harman, and C.T. Fouts, *Phys. Rev. Lett.* **69**, 1592 (1992).

[23] E.B. Fomina, P.L. McEuen, U. Meier, N.S. Wingars, Y. Meir, P.A. Bell, N.R. Bell, M.A. Kastner, and S.J. Wind, *Phys. Rev. B* **47**, 10070 (1993).

[24] J. Wen, R.J. Haug, K. v. Klitzing, and K. Phang, (to be published).

[25] W. Pöschel, D. Weismann, U. Meier, N.S. Wingars, B. Pöschel, B. Kastner, and U. Wenz (preprint).

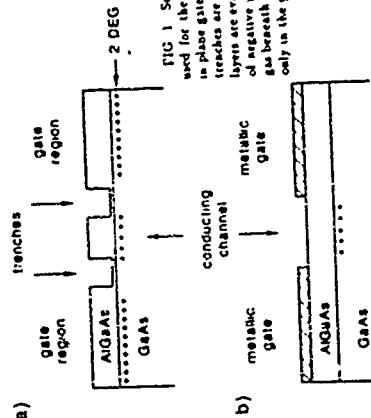


FIG. 1 Schematic pictures of the different approaches used for the reductions of single-electron transistors (a) in planar gate technology, (b) for the top-gate technology, where gate electrodes are etched, (c) for the top-gate technology, where layers are evaporated onto the sample surface, by application of negative gate voltages relative to the IDEG the electrons gain in the gap region

TuP37

Quasi One-Dimensional In-Plane-Gate Field-Effect-Transistor

U. Meiners, H. Brugger, B. E. Mail, and C. Wolk
Daimler-Benz AG, Forschungszentrum Ulm, D-89081 Ulm, Germany
F. Koch
Physik-Department, TU München, D-85748 Garching, Germany

Abstract:

A new type of a quasi one-dimensional planar field-effect-transistor (FET) with two lateral and symmetric in-plane-gate electrodes (IPG) is realized. The vertical layer sequence consists of a GaAs/AlGaAs heterostructure and a δ -doped pseudomorphic InGaAs quantum well with a high-density two-dimensional electron gas. The device configuration results in a strong lateral concentration of the confining electric field in the 2DEG plane. The fabricated devices operate excellently at room temperature with maximum currents (I_{DS}) above 0.3 mA and transconductance (g_m) values of 0.2 mS. Perfect pinch-off is achieved by a negative gate-voltage. Devices with planar arrays of quasi one-dimensional channels exhibit $I_{DS} > 6$ mA and $g_m = 5$ mS. A PMMA electron beam lithography process followed by a selective isolation implantation is used for the fabrication of IPG-FET devices.

1. Introduction

Low dimensional transport properties are intensively investigated for future electronic and optoelectronic device applications. In a one-dimensional electron-gas (1DEG) system a drastic suppression of the scattering rate was predicted theoretically by H. Sakaki [1]. The expected mobilities should be well beyond the values of a corresponding two-dimensional electron-gas (2DEG) system. One of the many novel device structures being investigated today is a quasi-1DEG field-effect-transistor (FET) with a lateral in-plane-gate (IPG) electrode configuration which was first proposed and demonstrated by A. T. Weick and K. Ploog [2]. The expected reduced scattering rate in one-dimensional channels and the inherent low gate-channel-capacitance of the IPG structure makes this type of device very promising for high speed operation. The fully planar device configuration, and the simple fabrication process offers the possibility of in-situ epitaxial regrowth for multi-functional, three-dimensional integration. IPG-FETs have already been realized by trench etching [3] and resistive p-type barrier isolation by focused-ion-beam (FIB) implantation of Ga ions [4, 5, 6].

In this paper we report about a novel IPG-FET and a selective isolation implantation technique for fabricating planar device structures. Starting from MBE-grown AlGaAs/GaAs heterostructure with a pseudomorphic InGaAs

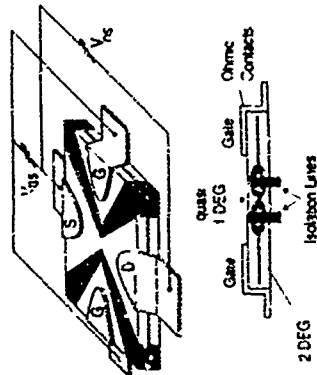


Figure 1. Schematic of the IPG-FET device. The quasi one-dimensional channel conductance is controlled by a lateral electric field via two symmetric gate electrodes.

-640-

FIG 2. Schematic picture of a single-electron transistor. The geometry was used for the realization of the in-plane gate single-electron transistor. The different gates are numbered, whereas source and drain of the conducting channel are characterised by S and D. The shaded areas show the etched regions.

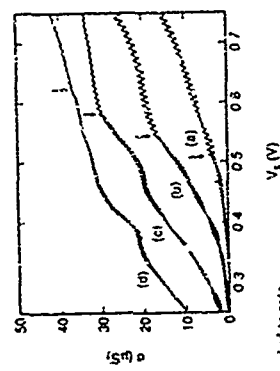
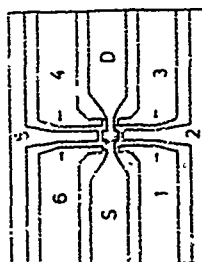


FIG 3. Conductance versus gate voltage V_g applied to gate 5 of the in-plane gate geometry as shown in Fig. 2. While for the different curves the voltage $V_D = -0.5V$, $V_S = -0.0V$ and $V_6 = 0$ are kept constant, the gate voltages $V_1 = V_2$ are varied: (a) $-40mV$, (b) $0mV$, (c) $40mV$, (d) $80mV$. The arrows indicate the position of the abrupt changes in the periodicity of the conductance oscillations.

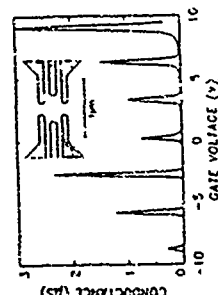


FIG 4. Conductance versus back gate voltage measured for a quantum dot defined by the top-gate geometry as shown schematically in the inset. The voltages applied to the top gate had been kept constant at values of about 0.7V.

-639-

2DEG-layer quasi-1DEG channels are formed by two closely spaced isolation barriers. The fabricated devices operate excellently at room temperature. Current levels of more than 0.3 mA and transconductance values of 0.2 mS are realized on single-channel devices. These are to our knowledge the highest ever reported values on one-dimensional FETs. Perfect pinch-off is achieved at a gate voltage of $V_{GS} = -2$ V. On IPG-FETs with multiple quasi 1-DEG channels device source-drain currents above 6 mA and maximum transconductance values of 5 mS are realized. The electrical isolation of the gate-electrodes from the channel region is realized by a selective dual energy implantation with single charged boron ions. The achieved resistance of $> 10^9 \Omega/\square$ is higher than the corresponding value of the used seminsulating substrate and yields to a very low gate leakage current density and to a high break-down voltage.

2. Layered Structure and Device Fabrication

A schematic illustration of the device layout is shown in Figure 1 together with a cross-sectional view of the intrinsic part of the device. The vertical layer sequence consists of an MBE-grown pseudomorphic GaAs/InGaAs/AlGaAs heterostructure with a high-density 2DEG. Details about the epitaxial layers are summarized in Table 1.

Table 1. MBE layer sequence used for the fabrication of IPG-FET devices. The substrate temperature was 620 °C up to the growth of the buffer layer and was reduced to a value of 530 °C for the growth of the final heterostructure layers.

layer	material	thickness	Si-doping
cap	GaAs	10 nm	$5 \times 10^{18} \text{ cm}^{-3}$
barrier	$\text{Al}_{0.25}\text{Ga}_{0.75}\text{As}$	10 nm	$5 \times 10^{17} \text{ cm}^{-3}$
quantum well	$\text{In}_{0.2}\text{Ga}_{0.8}\text{As}$	12 nm	$2 \times 10^{12} \text{ cm}^{-2}$
buffer	GaAs	750 nm	undoped
superlattice	AlAs/GaAs	2 nm / 2 nm	undoped

To improve carrier confinement and to enhance the 2DEG electron density in the quantum well (QW) a pseudomorphic InGaAs layer was used as a channel material. The InGaAs QW is doped with a nominal Si concentration of $2 \times 10^{12} \text{ cm}^{-2}$. A thin top-side and moderately doped AlGaAs barrier region is incorporated for a strong 2DEG confinement. A final, thin and highly doped GaAs cap-layer is used for the fabrication of low-resistance ohmic contacts. In order to avoid any parallel conductance through the cap layers the doping concentrations and layer thicknesses of the AlGaAs/GaAs heterostructure layers are completely surface-depleted. The 2DEG carrier density (n_s) and mobility (μ_{H}) were measured by Hall. Typical values are $n_s = 1.7 \times 10^{12} \text{ cm}^{-2}$ and $\mu_{\text{H}} = 2060 \text{ cm}^2/\text{Vs}$ at 300 K.

As shown in Figure 1 the IPG-FET devices are defined by wet chemically etched mesa squares ($12 \mu\text{m} \times 12 \mu\text{m}$) which contain source (S), drain (D) and two symmetric gate (G) electrodes. The ohmic contacts are fabricated by photolithography and standard alloyed NiGeAu metallization. The quasi one-dimensional current channel is realized in the center of the mesa by a small spacing between two thin V-shaped isolation lines along the mesa diagonal. The isolation regions are fabricated in the following way: The wafers are covered with a 0.6 μm thick polymethyl methacrylate (PMMA) resist layer. E-beam lithography is used for patterning the PMMA layer without a spatial dose variation to correct proximity effects. The resist pattern acts as a mask for the following implantation process. A dual implantation by boron ions is used with two different energies of 25 keV and 80 keV and dose values of $5 \times 10^{11} \text{ cm}^{-2}$ and $5 \times 10^{14} \text{ cm}^{-2}$, respectively, for the isolation. A high resistance behaviour is achieved by damage-induced carrier trapping in the implanted regions. The measured sheet resistance on test structures is beyond $10^9 \Omega/\square$, which is higher than the corresponding resistance of the used

semi-insulating GaAs-substrate. The ion energies and dose values are optimized with the help of a Monte-Carlo simulation [7] to achieve extremely high resistances.

Realized isolation line widths (w_i) are in the range between 100 nm and 1.1 μm . The quasi one-dimensional channel width (w_{ch}) is varied between 200 nm and 2.0 μm . Outside the channel region wider isolation lines are used to minimize the capacitance and to reduce the leakage current as can be seen in Figure 1. The effective isolation line width is expected to be larger than the geometrical width w_i due to lateral straggling effects during the implantation and due to lateral depletion zones between the implanted regions and the channel. The 0.6 μm thick PMMA resist absorbs completely the high energy boron ions and protects the underlying semiconductor material to be damaged. For the fabrication of multi-channel devices a series of single-channels are connected in parallel by use of an airbridge technology. Details about the process technology are published elsewhere [8].

3. Experimental Results

A typical transistor room temperature current/voltage (I/V) curve is shown in Figure 2. The IPG FET device consists of only one single IPG-FET with a nominal width of $w_{\text{ch}} = 2.0 \mu\text{m}$ and an isolation line width of $w_i = 0.4 \mu\text{m}$. The channel is totally pinched-off by a gate voltage of $V_{GS} = -2$ V. A very low gate leakage current of less than 70 nA is measured even for $V_{DS} = 6$ V and $V_{GS} = -2.5$ V. This is attributed to the excellent resistivity of the gate isolation region. The DC I/V performance was measured by a HP 4145B parameter analyzer with the device in the dark. The IPG-FET exhibits a maximum measured source-drain current (I_{SD}) of above 0.3 mA in the saturation range and a maximum transconductance (g_m) of 200 μS at a gate voltage of $V_{GS} = 0$ V. These are to our knowledge the highest ever reported values for an IPG-FET device.

The devices realized by the reported selective isolation implantation technique operate in a depletion mode. The transistor can be slightly enhanced by a positive gate voltage. The excellent controllability of the channel conductance is attributed to the QW-shaped 2DEG structure. By applying a negative gate voltage the electric field is directed in the plane of the 2DEG outside the quasi one-dimensional channel as can be seen schematically in the lower part of Figure 1. In the proposed surface-depleted vertical layer sequence there exist no free charges in the AlGaAs and GaAs layers and therefore the conductance is strictly limited to the thin 2DEG QW layer. This yields to a nearly perfect lateral field-effect.

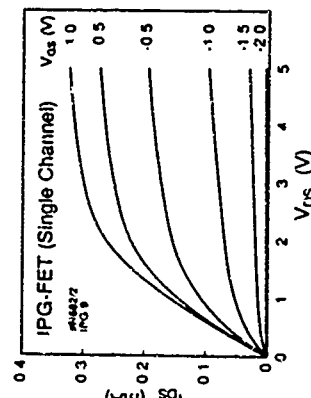


Figure 2. Room temperature I/V characteristics of a single channel IPG-FET in the dark

Experiments on conventional modulation-doped 2DEG samples have shown significantly lower transconductance values and reduced maximum current levels of the IPG-FET device. Only for $w_{\text{ch}} \leq 1 \mu\text{m}$ a complete depletion is achieved by a negative gate voltage. For $w_{\text{ch}} > 1 \mu\text{m}$ a gate/drain breakdown occurs before pinch-off. Therefore a more effective lateral field-effect is expected in QW-shaped structures in comparison with modulation-doped heterostructures.

The maximum channel current and the device transconductance are directly influenced by the spacing of the isolating barriers which determines the width of the channel

region. In Figure 3 the dependence of I_{DS} on V_{GS} ($V_{DS} = 4$ V, $V_{GS} = 0$ V) and I_{DS} on the channel width (w_{ch}) is shown. The curves are obtained from devices with a constant isolation of $w_i = 0.4$ μ m and the measurement performed in the dark. With increasing number of carriers in the channel also the transconductance increases steadily with w_{ch} . At a channel width of $w_{ch} = 350$ nm the channel is completely depleted even for $V_{GS} = 0$ V. Therefore the effective electrical width of the channel is expected to be 350 nm smaller than the nominal one. This is attributed to the lateral straggling of the boron ions during the implantation process and due to lateral depletion zones between the isolated regions and the conductive channel. Additional experiments on the dependence of I_{DS} and g_m on the isolation width have shown that w_i has only a minor influence on the device performance. An IPG-FET device with $w_{ch} = 0.6$ μ m and $w_i = 0.6$ μ m exhibits an enhancement of g_m by about 20 % if the isolation width is reduced to $w_i = 100$ nm.

In the saturation range of the operating transistor the observed linear dependence of I_{DS} on w_{ch} can simply be described by the following formula:

$$I_{DS} = e \cdot n_s \cdot w_{ch} \cdot v_{sat} \quad (1)$$

with the electronic charge e , the 2DEG carrier density n_s , $w_{ch} = (w_{ch} - 350 \text{ nm})$ as the effective electronic channel width and the saturation velocity v_{sat} . From the experimental data in Figure 3 and the measured two-dimensional carrier density $n_s = 1.7 \times 10^{12} \text{ cm}^{-2}$ a saturation velocity of $v_{sat} = 0.9 \times 10^7 \text{ cm/s}$ is obtained from equation (1). This value is close to the expected saturation velocity in GaAs material at high electric fields ($\approx 10^7 \text{ cm/s}$).

In Figure 4 the I/V performance of a multi-channel device with 48 single channels in parallel is demonstrated. Maximum current levels above 6 mA are observed. The electrical connection of individual quasi one-dimensional "neck" is realized by micro-bridges in a capillar design. The maximum observed transconductance is 5 mS. Perfect pinch-off is achieved for gate voltages $V_{GS} = -2.5$ V. The individual channels are fabricated with $w_{ch} = 0.8$ μ m and $w_i = 0.6$ μ m. The current level and the transconductance value of the multi-channel device directly scales with the number of the quasi-1DEG channels connected in parallel. This demonstrates the high performance of the used technology in fabricating this new type of FET device. Also the gate leakage current of the multi-channel device is less than 1 μ A at an applied gate voltage of $V_{GS} = -2$ V and $V_{DS} = 5$ V. A maximum source-drain voltage of $V_{DS} = 9$ V at $V_{GS} = -3$ V can be applied before gate-drain break-through occurs. Due to the intrinsic current limitations of 1DEG FETs a parallel conducting matrix-array arrangement is necessary to push the current level in the mA-range for real device applications.

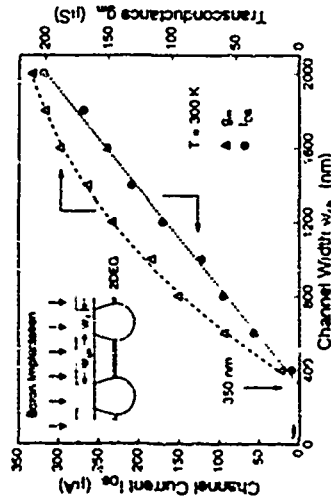


Figure 3. Measured source-drain currents at $V_{DS} = 4$ V and $V_{GS} = 0$ V and maximum transconductance values of single-channel IPG-FETs as a function of the channel width in the dark. The isolation barriers are $w_i = 0.4$ μ m.

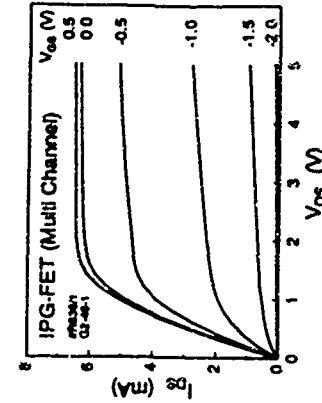


Figure 4. Room temperature I/V characteristics of a multi-channel IPG-FET (planar array of 48 channels).

The maximum available speed of the IPG-FET device is expected to be limited by extrinsic parasitic capacitances and internal capacitances (C_{GD}). Therefore the overall dimensions of IPG-FET devices (esp. the multi-channel configuration) should be kept as small as possible and a low loss connecting transmission line network is necessary to minimize extrinsic capacitances and resistances. Otherwise the inherent advantage of this novel quasi-1DEG FET (a very small gate capacitance) is dominated and limited by extrinsic effects. A detailed analysis on speed limiting effects in IPG-FET devices is performed by high frequency characterization experiments and will be published elsewhere.

4. Conclusion

A selective isolation implantation technique is used for a successful fabrication of a fully planar quasi one-dimensional field-effect-transistor with in-plane gates. A strong lateral electric field concentration is achieved by a QW-shaped 2DEG layer sequence. Highest room temperature transconductance values of 0.2 mS and maximum channel currents of more than 0.3 mA are realized on single-channel devices. The high performance of the used technology is demonstrated on devices with a planar array of parallel conducting channels yielding $I_{DS} > 6$ mA and $g_m = 5$ mS.

Acknowledgement

The work was partially supported by the Bundesministerium für Forschung und Technologie (Bonn, Germany) under contract number III BM 123/7.

References

- [1] H. Sakaki, *Jap. J. Appl. Phys.* 19, L735 (1980)
- [2] A. D. Wieck and K. Plagw. *Appl. Phys. Lett.* 56, 928 (1990)
- [3] J. Nieder, A. D. Wieck, P. Grambow, H. Lage, D. Heilmann, K. v. Klitzing, and K. Plagw. *Appl. Phys. Lett.* 57, 2695 (1990)
- [4] A. D. Wieck and K. Plagw. *Appl. Phys. Lett.* 61, 1048 (1992)
- [5] Y. Hirayama, *Appl. Phys. Lett.* 61, 1667 (1992)
- [6] J. A. Adams, L. M. Templeton, E. V. Kometov, and S. P. McAlister, *Proc. of the Int. Semiconductor Device Research Symposium*, Charlottesville (U. S. A.), Dec. 4-6 (1991)
- [7] J. Ziegler, J. Biersack, and V. Litmark, *Doping and Range of Solids*, Pergamon Press, New York (1985)
- [8] U. Meiner, B. E. Maile, and H. Brugger (to be published)

TuP38

Reflection of Ballistic Electrons by Diffusive 2D Contacts

A. K. Geim, P. C. Mahai, R. Taboryski*, H. Carmona, C. V. Brown, T. J. Foster, P. B. S. Oakeshott*, and E. Vojte*

*Department of Physics, University of Nottingham NG7 2RD, England

*Niels Bohr Institute, The Oersted Laboratory, DK-2100 Copenhagen, Denmark

*Department of Physics, Imperial College, Prince Consort Road, London SW7 2JZ

We report quenching of high-magnetic-field Shubnikov-de Haas oscillations and shrinking of the Hall plateaux with decreasing temperature in a quantum Hall effect conductor with low-mobility contact leads. Selective He-ion bombardment has been employed to reduce the mobility of a two-dimensional electron gas (2DEG) in the contacts. We explain the results in terms of the Milne reflection of electrons from these disordered regions. At sufficiently low temperatures, inelastic scattering is suppressed and electrons are scattered back by elastic collisions before thermalisation can occur.

The Landauer-Büttiker formalism provides a method of characterising conduction processes in a quantum conductor. Usually, the conductor is conceptually divided between regions of non-dissipative transport in the bulk of the conductor and contact regions ("thermal reservoirs") where electrons are completely thermalised [1]. The boundary between these two regions is not clearly defined in real experiments and may depend on external parameters such as temperature and magnetic field. In quantum Hall effect (QHE) experiments, low-mobility alloyed AuGe contacts are usually considered as "ideal" contacts which totally absorb and thermalise incident electrons. This simplistic model that AuGe contacts act as ideal thermal reservoirs has appeared to explain experimental results well [2]. This is a surprising fact since it is known from astrophysics and neutron physics that ballistic particles penetrating into a strongly scattering medium are mainly reflected back if the inelastic scattering length l_i is much longer than the elastic length l_e (the Milne problem [3]). The condition, $l_i \gg l_e$, is always valid for alloyed metal contacts at helium temperatures. It is probably the mismatch in electron concentration and dimensionality at the metal-2DEG interface which is responsible for the suppression of the expected backscattering from alloyed contacts in the range of temperatures usually employed [4].

To investigate the role of the Milne reflection and contact dissipation in quantum resistance measurements we have fabricated 2DEG devices with long and narrow diffusive leads where the mobility was reduced with respect to the rest of the conductor by He-ion bombardment. Unlike conventional QHE devices, our samples have no distinct boundary between the quantum conductor and the contact regions since electrons thermalise in mobility contact leads. Changes in the inelastic scattering rate with temperature cause in the effective position of the contacts relative to the quantum conductor which dramatically influences resistance measurements. The devices with disordered 2D leads exhibit a rapid quenching of the high field Shubnikov-de Haas (SdH) oscillations and a significant decrease of the width of the quantum Hall plateaux as the temperature decreases, in contrast to the behaviour of unimplanted devices and larger conventional QHE devices.

We explain the observed behaviour by considering the thermalisation of electrons in the disordered regions. At high temperatures, electrons entering the disordered region from the edge states in the high-mobility region are able to thermalise rapidly and the implanted areas act as conventional contacts. At low temperatures the electrons are backscattered by elastic collisions in the disordered regions before thermalisation can occur. We present a model which shows that the longitudinal resistance goes to zero and the quantum Hall plateaux shrink as the inelastic scattering rate decreases with decreasing temperature. The model assumes that the innermost edge state is mostly influenced by the disorder and elastically scattered back when $l_i \gg l_e$ (the analogy of the Milne problem for the edge state regime).

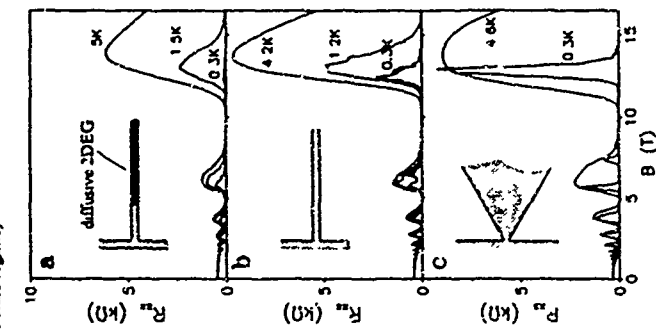


Figure 1 Longitudinal magnetoresistance at different temperatures in QHE devices with various configurations of the contact leads shown in the insets

Three types of devices have been used in our experiment. Hall bar structures with several voltage probes were fabricated using electron beam- and photo-lithography from a modulation-doped GaAlAs heterostructure with 2D electron concentration $\approx 4 \times 10^{10} \text{ m}^{-2}$ and mobility $\mu_{2D} \approx 200 \text{ m}^2/\text{Vs}$. The devices differ in their configurations of the contact leads as shown schematically in the insets to Figure 1. The first two types of Hall bar (Fig 1a,b) have a conducting width $w \approx 1 \mu\text{m}$ of all 2DEG sections and a distance between adjacent voltage probes Δ between 10 and 20 μm . The measurement leads have a relatively long length of $\approx 50 \mu\text{m}$ terminated by conventional AuGe contact pads. Type-A devices (see Fig 1a) were exposed to bombardment by 50keV alpha-particles of a total dose $3 \times 10^{10} \text{ m}^{-2}$ with the central part of the device, including $5 \mu\text{m}$ sections of the contact leads, protected by a thick metal mask. The bombardment dramatically reduced the mobility of the exposed 2DEG (the measured 2DEG mobility of an unmasked device is $\mu_{2D} \approx 200 \text{ m}^2/\text{Vs}$) while the mobility in the central part is found to be unchanged. Details of the He-ion implantation procedure and characteristics of implanted 2DEGs can be found elsewhere [5]. We refer to unimplanted Hall bars of the same geometry as type-B devices. For completeness, we have also fabricated control samples (type C) from the same heterostructure with the contact lead geometry as shown in Fig 1c. The width of the leads rapidly increases from $\approx 1 \mu\text{m}$ to $10 \mu\text{m}$ where they are terminated by the alloyed contact pads (see Fig 1c).

A central qualitative result is presented in Figure 1a where the longitudinal magnetoresistance R_{xx} of a type-A device is shown for three different temperatures. It is clearly seen that, as temperature decreases from 5K down to 0.3K, the amplitude of SdH oscillations above 3T decreases considerably and the last peak in R_{xx} at about 14T ($\nu=1.5$) virtually disappears. A detailed temperature dependence in the range 0.3-5K for this peak is shown in Figure 2. Note the strong resistance fluctuations at low temperatures in Fig. 2 which have been attributed to resonant tunnelling between opposite edge states in these mesoscopic devices [6]. The quenching of R_{xx} at low temperatures is in stark contrast to the usual behaviour of QHE devices [7] and in theory (see e.g. [8]) which both give nearly constant amplitude of Shubnikov-de Haas peaks as temperature decreases. Figure 1c shows the behaviour of R_{xx} in the control device. The high-field SdH peaks become narrower at low temperatures but their amplitudes remain nearly constant as temperature decreases. Type-B devices exhibit an intermediate behaviour as shown in Fig. 1b and the peak at $\nu=1.5$ decreases by a factor of 4 with decreasing temperature from 4.2K to 0.3K. The amplitude of this peak is found to saturate below 0.6K. Note that two other peaks at about 3T and 7T in the samples A and B (Figs 1a,b) are also suppressed as temperature decreases although the effect is not as pronounced as for the peak at 14T. In addition, different degrees of spin-splitting of the peak at about 7T (see Fig. 1) make it rather difficult to compare the temperature dependences of R_{xx} for this magnetic field.

Figure 3 shows the Hall resistance R_H in a

type-A device at different temperatures. The width of the quantum Hall plateau at $\nu=2$ decreases at both high and low temperatures and the plateau is widest at about 5K. The lower plateau at $\nu=4$ also has some tendency to shrink at low temperatures (not visible in the figure). This behaviour is in contrast to the behaviour of conventional QHE devices [7,8] and our control samples where the plateau are always wider at lower temperatures. Note that there is an interval of magnetic fields, for example from 10 to 11T, where the longitudinal resistance goes to zero as temperature decreases while the Hall resistance goes up and away from its quantised value (compare Fig. 2 and 3). We conclude that zeros of the longitudinal resistance in type-A devices do not necessarily imply quantised values of the Hall resistance as is normally the case in QHE devices.

Considering the qualitative behaviour of R_{xx} with temperature we first address the temperature dependence in magnetic fields far away from the field of magnetoresistance maxima. The changes in this regime are exponential and can be described for all the devices by the functional form $R_{xx} \propto \exp(-\alpha/T)$ [7,9] where α is a field dependent constant. We find $\beta \approx 0.5$ for both B and C devices and on both sides of the high-field magnetoresistance peak. Examples of this behaviour are shown in Fig. 4a where R_{xx} is plotted versus $T^{-1/2}$ for a type-B device at 13.5 and 15T. The solid lines in Fig. 4 show the case of $\beta=1/2$. The same temperature dependence can also describe $R_{xx}(T)$ in type-A devices far away from the resistance maximum

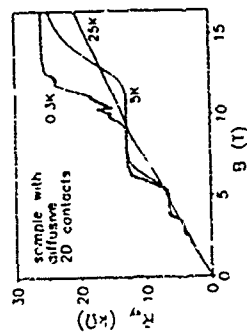


Figure 3 The Hall resistance in a type-A device (see Fig. 1a) for three different temperatures

(see Fig. 4b, the filled circles are for $B=15T$). However, due to the strong microscopic fluctuations at low temperatures the accuracy of the measurements of β is much lower and only implies $\beta \approx 0.7 \pm 0.4$ for this device. The observed exponential dependence with $\beta=1/2$ is in agreement with theory, which attributes this behaviour to a variable-range-hopping conduction modified by the Coulomb gap in the density of states [9] (see also [7]). The temperature dependences in the immediate vicinity of the SdH maximum are different and vary between the different devices. For C devices the magnetoresistance changes are weak, corresponding to a nearly constant height of the R_{xx} peak. In contrast, for type-A devices the changes at the maximum near 13T are exponential and are described by a stronger function of temperature than in the case well away from the maximum. Fig. 4b shows the temperature dependence for the magnetic fields of 13T and 15T in a type-A sample (open symbols). The best fit to the experimental dependence over the whole temperature interval in Fig. 4b yields $R_{xx} \propto \exp(-\alpha/T)$ as shown by the dashed line

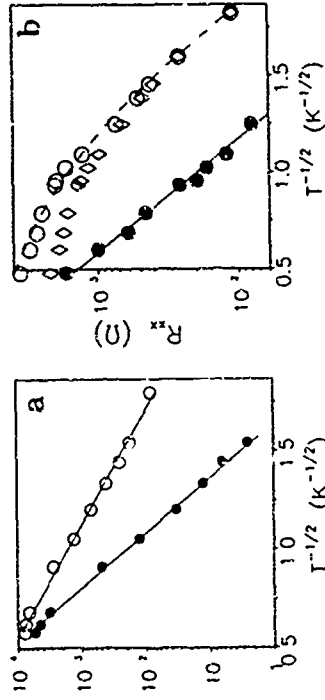


Figure 4 Changes of the longitudinal magnetoresistance with temperature for different magnetic field (a) - type-B sample at $B=13.5T$ (open circles) and $15T$ (closed circles) (b) - type-A device at $B=13.5T$ (open circles) and $15T$ (diamonds). The latter two values are at the position of the peak maximum. The solid line shows the best fit to the dependence $R_{xx} \propto \exp(-\alpha/T)$. The dashed line corresponds to $R_{xx} \propto \exp(-\alpha/T^{1/2})$.

To explain the results we assume that it is the innermost occupied edge state which is mostly influenced by the disorder [1] and strongly scattered back by the low-mobility contact leads. An electron entering the diffusive region can be either scattered back elastically or thermalised in the lead which then is effectively a contact. As the temperature decreases, the inelastic scattering rate also decreases so that the electrons can spend more time in the lead before undergoing an inelastic event. This increases the probability of back-scattering by involving a longer section of the lead in the process and effectively moving the position of the boundary between the quantum conductor and the contact further inside the contact leads. For an infinitely long lead and no inelastic scattering there would be 100% probability of back-scattering. We expect that this result, obtained for zero magnetic field [3,4], is also valid for the case of the edge-state transport.

For a quantitative analysis we consider a model of the type-A device shown schematically in Fig 5 [10]. Only 10 occupied Landau levels are taken into account, corresponding to the experimental situation for the high-field peak at 1.3T. Note that the edge states of the central part of the device remain well defined in the disordered 2DEG regions where $\mu_{im}B \gg 1$ at these magnetic fields. The backscattering in the central part is neglected since $\mu \gg \mu_{im}$ and this section is relatively short. We model the back-scattering in the implanted leads assuming that there is some characteristic length of the edge state thermalisation $L_k(T)$. Referring to the qualitative considerations of the previous paragraph and to avoid an involved analysis for the distributed QHE networks [11], we assume that the thermalisation of the edge states occurs at a distance of L_k inside the disordered regions. Following ref [12], we express the transmission probability T of the inner edge state into the thermal reservoir placed at the distance L_{th} as

$$T = \frac{1}{1 + \alpha_{xx} L_k (L_k^2 / L_{th} w)} \quad (1)$$

where $\alpha_{xx} L_k$ is a parameter which can be interpreted as the electron conductivity of the uppermost Landau level [12]. The temperature dependence of $\alpha_{xx} L_k$ is metallic near half-integer filling factors when the electron states are extended [8]. For other magnetic fields, it is expected that $\alpha_{xx} L_k \propto \exp(-\alpha T^{-1/2})$ due to variable-range hopping [9].

In Fig 5 the transmission probabilities T and through the current and voltage leads, respectively, are chosen to be different. This corresponds to our experimental geometry but also reflects the fact that the voltage probes are noninvasive, whereas passing a current could influence the properties of the current leads in the real experiment. Following the standard procedure for QHE networks [1,12], we obtain for the geometry in Fig 5

$$R_{xx} = \frac{h}{e^2} \frac{L/L_k - D}{2(1+T)(1+T)} \quad (2)$$

$$R_{yy} = \frac{h}{e^2} (1 - \frac{T}{2(1+T)}) \quad (3)$$

A similar analysis for the Hall geometry gives

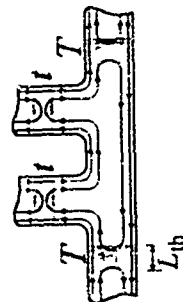


Figure 5 Model of the edge state reflection from the disordered regions in type-A devices

If T or L goes to either zero or unity, R_{xx} varies. When either T or L equals unity, R_{yy} corresponds to its normal quantised value $h/2e^2$ and if $T=0$, $R_{yy}=h/e^2$.

To explain the observed behaviour of R_{xx} and R_{yy} in type-A devices, we consider the magnetic field interval 10-11T where the anomalies are most pronounced. In this regime we have observed near-zero values of R_{xx} while R_{yy} goes away from $h/2e^2$ up to near h/e^2 . Referring to Equations 2 and 3, this behaviour unambiguously implies a rapid decrease of both T and L toward zero as the temperature decreases.

The temperature dependence of the transmission coefficients is determined by both $\alpha_{xx} L_k$ and L_{th} (see Eq 1) which have opposite temperature dependences, i.e. L_{th} increases with decreasing temperature while $\alpha_{xx} L_k$ decreases or remains constant. Near the R_{xx} maxima, the changes in the conductivity $\alpha_{xx} L_k$ are slow and $L_{th}(T)$ dominates in the temperature dependence of T and L . From the observed exponential decay of R_{xx} near $\nu=1/2$ in Fig 4b, we infer that the thermalisation length can be described by an activated behaviour, i.e. $L_{th} \propto \exp(C/T)$. This dependence is in agreement with experiment, where the inter-edge scattering rate has been found to depend exponentially on temperature, [13] and also with theory which predicts exponential dependences for both inter- and intra-edge scattering [13-15]. Far away from the resistance maxima, the temperature dependence of R_{xx} is determined by the competition between $\alpha_{xx} L_k$ and $L_{th}(T)$. This competition can explain other features in the behaviour of type-A samples and, in particular, the shift in the position of the maximum seen in Fig 2.

Finally, we discuss the observed difference in the behaviour of R_{xx} and R_{yy} for the different devices. The reason is presumably due to the different relationship between L_{th} and the length of the 2DEG contact leads for the different devices. When the contact leads are shorter than L_{th} , their length should be substituted into Eq (1) instead of L_{th} since the edge state electrons are rapidly thermalised in the alloyed contacts [4]. This situation is expected to be valid for type-C devices at helium temperatures. In the type-B sample, the increase of L_{th} can describe the initial decay of the SdH peak with decreasing temperature while at 0.6K L_{th} probably becomes comparable with the length of the leads and the amplitude of the peak saturates at lower temperatures. In type-A devices, the thermalisation length in the leads is suppressed with respect to the B-devices by the He-ion bombardment [13,14] and we can expect that it is always shorter than the length of the leads for the employed temperature interval.

In conclusion, we have studied reflection of edge state electrons at the boundary between high and low mobility 2DEGs. The quenching of the longitudinal resistance and the narrowing of the Hall plateau with decreasing temperature are explained in terms of the temperature dependent position of the Landauer thermal reservoirs. The experiment emphasises the important role of dissipation in quantum resistance measurements. We note that the proposed model of the effect can also explain nonlocal magnetoresistance oscillations which have been observed at elevated temperatures in n-GaAs quantum wires [16].

This work was supported by SERC. We want to thank Y B L'vovskii and L Eaves for helpful discussions.

Giant Temperature Resonances of Noise in Submicron Quantum Well Structures

A.K Geim¹, S.T. Stoddart, S.J. Bending,
School of Physics, University of Bath, Claverton Down, Bath BA2 7AT, UK

J.J. Harris
Interdisciplinary Research Centre, Imperial College, Prince Consort Road, London SW7 2BT
A.J. Peck

Max-Planck-Institute fuer Festkörperforschung, Heisenbergstr. 1, D-70569 Stuttgart, Germany
K. Ploog

Paul-Drude-Institute fuer Festkörperelektronik, Hausvogelplatz 5-7, O-1086 Berlin, Germany

We show that excess noise in micron-sized samples fabricated from Si-doped GaAs/GaAlAs quantum wells and heterostructures is a strong non-monotonic function of temperature with several sharp peaks below room temperature. The noise power at the peaks exceeds the background noise by several orders of magnitude. The observed behaviour represents a classical noise source where only a single type of switching defect with a well-defined activation energy is present. We attribute the resonances to deep metastable donors and provisionally identify one of the donors as the known DX-center in GaAs and GaAlAs.

Low-frequency noise in solids has received considerable attention in recent years. It has been shown that almost any resistor demonstrates excess noise with an approximately 1/f-shaped power spectrum and it is well established that this noise can be described as arising from the thermally activated switching of defect states [1,2]. Each defect gives rise to a Lorentzian power spectrum whose superposition leads to 1/f-noise if the distribution of relaxation rates is fairly flat. Recently, using sufficiently small-length-scale devices random telegraph noise due to single defect switchings has been observed [3-5]. If the sample size is increased, the number of the elementary noise sources increases and it is possible to follow the transformation of this telegraph noise into 1/f-noise [2-4]. New noise sources can also be activated by raising the temperature which changes the spectrum into 1/f-form and leads to a monotonic increase of the noise power.

In this paper we report noise with a resonant-like temperature dependence. Sharp peaks in the noise have been seen against a negligibly small background in micron and submicron devices fabricated from δ -doped GaAs quantum wells and GaAlAs/GaAs heterostructures containing a high-mobility two-dimensional electron gas (2DEG). The temperature resonances in the noise are in striking contrast with one's common experience that noise is a monotonic or, at least, smooth function of temperature (see reviews [1],[2]). Despite the fact that this type of noise behaviour has never been observed before, we show that it corresponds to the simplest model of random telegraph noise [1,2,6]. The observed noise arises when the switching defects are exactly the same and differences in their thermally activated relaxation times τ are minimal. This condition appears to be fulfilled in Si-doped GaAs and GaAlAs where the dominant defect (Si) becomes metastable at high concentrations [7]. A Si atom can only occupy a few strictly determined sites in the crystal lattice of GaAs and its energy is not affected by lattice imperfections as in the case of polycrystalline and amorphous materials which have previously been studied. We show that the dominant contribution to the observed noise arises from the thermally activated switching of DX-like centres [7]. The noise can be persistently quenched by

References

1. For a review, see H van Houten and C W J Beenakker, in *Solid State Physics*, edited by H Ehrenreich and D Turnbull (Academic, New York, 1991), vol 44.
2. Note that in several papers the non-ideal behaviour of the alloyed contacts has been reported [S Komiyama, H Hirai, S Sasa, and T Fujii, *Solid State Commun* 73, 91 (1990); H van Houten, C W J Beenakker, and B J van Wees, in *Semiconductors and Semimetals*, edited by M A Reed (Academic, New York, 1991)].
3. P M Morse and H Feibach, *Methods of Theoretical Physics*, McGraw-Hill, 1953.
4. Y B Levinson, in *Proceedings of EPJDS-10*, Newport 1993 (to appear in *Sur Sci*).
5. R. Taboryski and P E Lindelof, *Semicond Sci Technol* 5, 933 (1990).
6. A K Geim, P C Main, C V Brown, R Taboryski, H Carmona, T Foster, P E Lindelof, and L Eaves, in *Proceedings of EPJDS-10*, Newport 1993 (to appear in *Sur Sci*).
7. H P Wei, D C Tsui, M A Paalenen, and A M M Putsken, *Phys Rev Lett* 61, 1294 (1988).
8. S Koch, R J Haug, K v Klitzing and K Ploog, *Phys Rev B* 43, 6828 (1991). Note that QHE devices (e.g. H P Wei, S Y Lin, D C Tsui, and A M M Putsken, *Phys Rev B* 45, 3926 (1992)) can also exhibit a decreasing amplitude of SDHO with decreasing temperature somewhat similar to the behaviour found in our type-B devices. This behaviour has not been explained but can be understood in terms of the present paper.
9. J Kucera and P Sireda, *J Phys C* 21, 4357 (1988).
10. D G Polyakov and B I Shklovskii, *Phys Rev Lett* 70, 3796 (1993) and references therein.
11. To avoid confusion we note that the ion bombardment also slightly decreases the electron concentration in the contact leads [5]. We have measured change of $\approx 10\%$ in an unmasked device after bombardment. The different electron concentration in the contact leads makes type-A devices somewhat similar to QHE devices with gated contacts [1]. We have proved directly that this difference does not influence the observed temperature effects. In our experiment, we have illuminated type-A devices and discretely increased the electron concentration in the leads leaving the concentration in the masked central part unchanged. For all illumination doses we observe the quenching of SDH oscillations and the shrinking of the Hall plateaus. There is no concentration difference in type-B devices.
12. P L McEuen, A Szafer, C A Richter, B W Alphenaar, J K Jain, A D Stone, R G Wheeler and R N Sacks, *Phys Rev Lett* 64, 2062 (1990).
13. S Komiyama, H Hirai, M Ohuwa, Y Matsuda, S Sasa, and T Fujii, *Phys Rev B* 45, 11085 (1992) and references therein.
14. D L Maslov, Y B Levinson, and S M Badalzin, *Phys Rev B* 46, 7002 (1992).
15. Note that impurity scattering is mainly responsible for the inter-edge scattering [13,14]. However, this is not sufficient to reach the true equilibrium and some inelastic process has to be involved in the thermalisation. On the other hand, the elastic process may be the one which determines the observed temperature dependences as in the case of impurity scattering in normal metals.
16. A K Geim, P C Main, P H Beton, P Sireda, L Eaves, C D W Wilkinson, and S P Beaumont, *Phys Rev Lett* 67, 3014 (1991).

infra-red illumination which also leads to persistent photoconductivity (PPC) in our structures. The switching defects influence the electrical conduction due to the sensitivity of the resistance of a small sample to the state of every single impurity within it.

Two types of structures have been investigated in our experiment. The δ -doped GaAs quantum wells were grown by molecular-beam epitaxy on semi-insulating GaAs substrates and consisted of 20nm of undoped $\text{Ga}_{0.9}\text{Al}_{0.1}\text{As}$ followed by a GaAs quantum well of the width in the range 10-20nm and terminated with 250nm of undoped $\text{Ga}_{0.9}\text{Al}_{0.1}\text{As}$ and 20nm GaAs capping layer. A Si δ -doped plane of nominal concentration in the range $(2.5-3) \times 10^{16} \text{cm}^{-2}$ was placed in the centre of the quantum well. The quantum confinement of the Si doping layer increases the separation between the two-dimensional (2D) electron subbands and allows one to work in the simplest situation when only one 2D subband is occupied. Further information about the structures and their characterisation can be found elsewhere [8]. The second type of structure we have studied is the standard modulation-doped GaAlAs heterostructure with 2D electron concentration $\approx 2.7 \times 10^{16} \text{cm}^{-2}$ and mobility $\approx 750000 \text{cm}^2/\text{Vs}$ at 4.2K.

Hall bar structures with several voltage probes were fabricated using photolithography and wet chemical etching. Samples with different conducting widths b between 0.5 and 8 μm have been investigated and the separation between the centres of adjacent voltage probes is twice the characteristic sample width. DC currents between 1 and 100 $\mu\text{A}/\mu\text{m}$ are passed through the sample and signal fluctuations at the voltage probes ($\sqrt{\langle \Delta I^2 \rangle}$) are measured using the noise option of a EG&G 5210 Lock-in amplifier at a chosen frequency f in the range 1-10kHz. Bandwidths Δf in the range 0.1-11Hz around the centre frequency were selected. Figure 1 shows typical examples of the temperature dependence of the noise at $f=10\text{Hz}$ for both types of structure studied. Three peaks near 50, 80 and 170K are clearly seen for the case of the 10nm wide δ -doped quantum well ($n_s \approx 5 \times 10^{16} \text{cm}^{-2}$) and only one peak near 180K has been observed for the modulation-doped sample.

We find that the noise signal changes linearly with the current ($\sqrt{\langle \Delta I^2 \rangle} \propto I$) indicating that these are fluctuations in the resistance R . Consequently, experimental data are presented using the normalized noise power $S(f) = \omega \langle \Delta I^2 \rangle / I^2 = \langle \Delta R^2 \rangle / R^2$. The power S is found to be inversely proportional to the distance between voltage probes and the sample width b (i.e. $S \propto 1/b$ where b is the sample area). In the plots, S is multiplied accordingly by the active area ($S_s = S \times A$) and is given in units m^2/Hz .

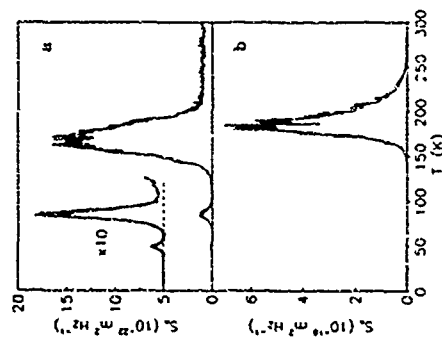


Figure 1 (a) Noise power as a function of temperature in a 2 μm wide sample fabricated from a 10nm wide δ -doped GaAs quantum well and (b) in a 0.5 μm modulation-doped heterostructure sample. The low temperature section of Fig 1a is magnified by a factor of 10 and shifted for clarity.

The positions and the amplitudes of the noise peaks as a function of temperature depend on the measurement frequency f . Figure 2 shows an example of this dependence for the top trace in Fig 1. In Fig 3a,b the positions, T_m , and heights, S_m , of two of the noise maxima observed in the quantum well are plotted as a function of frequency. We note that S_m decreases with frequency as $1/f$ and $1/T_m$ decreases as $\ln(f)$. At a fixed temperature, $S(f)$ has exactly the Lorentzian form $S(f) = [1 + (2\pi f \tau)^2]^{-1}$ as also shown in Fig 3a for the peak near 170K.

All our results follow directly from the standard theory of excess noise [1,2]. A switching defect can be characterised by its relaxation time τ and the magnitude ΔR of changes in the sample resistance $\Delta R(t) \equiv \Delta R \exp(-t/\tau)$. The noise power spectrum due to N identical but uncorrelated defects is given then by

$$S(f) = N(\Delta R)^2 \tau^2 / (1 + (2\pi f \tau)^2) \quad (1)$$

At moderate temperatures the switches are usually thermally activated and can generally be described by $\tau = \tau_0 \exp(-E_a/kT)$. If there are many defects present with a wide spread in their activation energies E_a , the integration of Eq (1) leads to a $1/f$ dependence and the noise is a smooth function of temperature [1,2].

However, in the case where E_a and τ_0 have well-defined values, a noise peak will occur. A characteristic frequency of the random resistance switches ($1/\tau$) changes exponentially rapidly with temperature, resulting in a resonance when ν matches the measurement frequency. Due to this exponential behaviour the resonance can survive over a very wide frequency band.

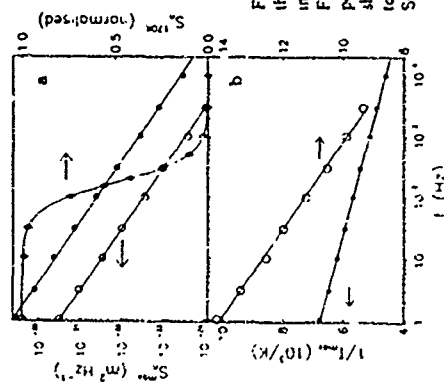


Figure 3 (a),(b) Frequency dependence of the magnitude and position of noise maxima in the δ -doped quantum well structure of Fig 1. Open and closed circles are for the peaks near 80K and 170K respectively. Also shown is the noise power spectrum for a fixed temperature of 170K (rhombic symbols). Solid lines are the best fits to Eq (1).

Figure 2. Noise peaks in the δ -doped GaAs quantum well of Fig 1 at two different measurement frequencies.

and for the maximum bandwidth $\Delta f \approx 10^4$ Hz available in our experimental set-up (the integral noise power in the range $f \approx 1-10^4$ Hz) the peak widths in Fig 1 would only increase by a factor of three. We note that more detailed models of two-state random telegraph noise [9,10] which take into account the balance between generation and recombination processes can not explain resonances in the noise. The appearance of peaks requires that the recombination process is a background process and its relaxation rate not be coupled to the generation frequency via a balance equation

Equation (1) implies that $S_{\omega} \propto 1/\omega$ and $E_a/T_m = -\ln(2\pi/\tau_1)$. Solid lines in Fig 3 show the best fits to the experimental dependencies for the quantum well structure. We obtain $E_a \approx 0.1$ eV, $E_a' \approx 0.145$ eV, $E_a'' \approx 0.37$ eV, where the upper index denotes different switching defects in the order of appearance with increasing temperature, and τ_1 is found to lie in the range $10^{-11}-10^{-10}$ sec. When the values of E_a and τ_1 are known, Eq (1) allows us to compare directly the experimental temperature dependencies of S_{ω} with theory without using any fitting parameters. An example of such a comparison is shown in Fig 4 where the theoretical curve follows the observed temperature dependence perfectly. The agreement is excellent for peaks 1 and 2 although peak 3 is 30% wider than expected from Eq (1) probably indicating that there is some small spread in the value of the activation energy for this type of defect. The same analysis for GaAlAs/GaAs heterostructure samples gives $E_a = 0.42(\pm 0.02)$ eV and $\tau_1 \approx 10^{-11}$ sec.

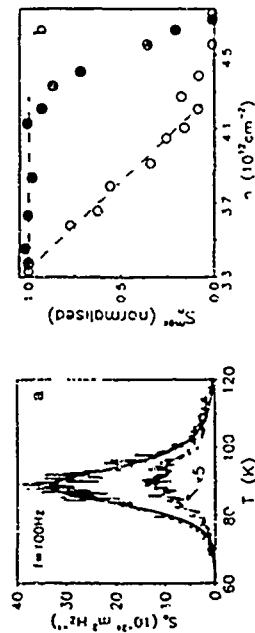


Figure 4. Persistent suppression of the noise peak by infra-red illumination in the δ -doped quantum well structure of Fig 1. (a) Noise in the dark (upper curve, $n = 3.3 \times 10^{17} \text{ cm}^{-3}$) and after partial illumination (lower curve, $n = 3.8 \times 10^{17} \text{ cm}^{-3}$). Solid line in Fig 4a shows temperature dependence of noise calculated directly from Eq (1). (b) Variation of the height of the noise peaks with total electron concentration.

Both studied types of structure demonstrate strong low temperature persistent photoconductivity (PPC) indicating that deep metastable donors are present in a concentration comparable with the Si doping level. Figure 4 shows a direct connection between the noise and PPC in the quantum well structure. As the electron concentration increases upon infra-red illumination the noise decreases rapidly indicating that deep donors (probably DX-like centres whose concentration decreases under illumination) are responsible for the observed noise. All the peaks are significantly suppressed by illumination. Note that neither the position nor the shape of

the peaks alters while the Fermi energy of the 2DEG increases substantially. This implies that conduction electrons at the Fermi level do not directly participate in the noise and we observe switches between the deep-donor state and some intermediate state rather than the shallow-donor state. It is very probable that the dominant peaks near 170K in the noise spectra of both our structures are due to the known DX-center. The activation energy for this peak in the GaAlAs/GaAs heterostructure is in good agreement with the known value of 0.43 eV for the DX-center in GaAlAs [7]. However, the dominant peak in the quantum well has $E_a' \approx 0.37$ eV which is only in fair agreement with ≈ 0.33 eV measured by DLTS for the DX-center in δ -GaAs [7]. This is probably due to considerable changes in the band structure arising from δ -doping in a quantum well [8]. Another deep donor in the quantum well device with an activation energy of 0.145 eV can possibly be attributed to a donor which was found in $\text{Al}_{0.5}\text{Ga}_{0.5}\text{As}$ for $x \approx 0.15$ and has a thermal emission energy in the range 0.13-0.16 eV [10]. The donor responsible for the small peak near 50K remains unidentified.

Note that different types of donor are present in the δ -doped GaAs quantum well rather than a single donor with different energy levels. This is evident from Fig 4b which shows the dependencies of S_{ω} on electron concentration after illumination for the two major peaks in the quantum well sample. The very different behaviour of the peaks under illumination implies that different defects are responsible for these resonances. It is clear from Fig 4b that illumination removes the captured electrons much easier from defects of type 2 and only then starts to depopulate type-3 deep donors. This difference in sensitivity to illumination for the two states has been directly confirmed by measuring the time variation of the total concentration under continuous illumination which shows two distinct levels of saturation, one with a short and another with a long time constant.

Finally, we discuss the scaling of the noise and its absolute magnitude. A switching DX-like center changes the scattering cross-section for conduction electrons (a) by a value $\delta\sigma$. First order corrections to the Boltzmann equation due to the switching of a single impurity lead to resistance changes $\delta R/R = (1/N)\delta\sigma/a$ where N is the total number of impurities in a sample which differs from the number of switching defects N [11]. The noise power in the peak (see Eq 1) is given $N(\delta R/R)^2 \propto N/N^2 \propto 1/N$ as observed in the experiment. Assuming that the impurity concentration N/A is equal to the doping level, data in Figures 3a and 4b can be used to show that $\delta\sigma/a \approx 0.1$ and 0.3 for peaks 2 and 3 in the quantum well structure, respectively. The fact that the inferred values of $\delta\sigma/a$ are of the order of unity confirms that coupling between the switching defects and the conductance occurs via a change in the scattering cross-section of the DX-like centres. This simple consideration is not directly applicable to the modulation-doped heterostructure since donors are remote from the carriers, phonon scattering is dominant for the 2DEG at these temperatures and a parallel conductance in the Si-doped GaAlAs layer is probably present.

In conclusion, micron-sized samples of δ -doped GaAs quantum wells and modulation-doped heterostructures show giant peaks in the temperature dependence of the excess noise power. This noise is caused by the temperature-activated switching of many Si donors with a single well-defined relaxation rate. The defect leading to the strongest resonance near 170K is tentatively identified as the known DX-center. Noise measurements of the type described here represent a powerful tool for the identification and characterisation of deep metastable defects and have clear implications for practical limits on the operation of submicron quantum well devices.

This work was supported by SERC grant No GR/H23573

NON-LINEAR TRANSPORT PROPERTIES OF MINIBAND CONDUCTION IN THE PRESENCE OF CROSSED ELECTRIC AND MAGNETIC FIELDS: A SEMI-CLASSICAL APPROACH

F. Aristone^{1,2}, J.F. Palmier³, A. Sibille², D.K. Maude¹, J.C. Portal² and F. Mollot⁴
¹ CNRS-SNCL B.P. 160-X, 38042 Grenoble Cedex - France
² CNRS-LPS-NSA, Complexe Scientifique de Rangueil, 31077 Toulouse Cedex - France
³ CNET, 195 Av. Henri Ravera, 92220 Bagneux Cedex - France
⁴ ENSTA - Dept. d'Electronique, 32 Boulevard Victor, 75015 - Paris - France
⁵ IEMN - DHS / UNIR - USTL, 59655 - Villeneuve d'Ascq - France

ABSTRACT In this paper we compare a series of perpendicular transport measurements for short period GaAs-AlAs superlattices in presence of a magnetic field applied parallel to the layers with the semi-classical calculations of the miniband conduction properties. The theoretical approach takes into account the local solution of the Boltzmann equation in the presence of scattering mechanisms such as phonons and interface fluctuations. The Poisson and drift-diffusion equations have been self-consistently solved to obtain the current density versus the applied electrical field characteristics which is directly compared with the experimental measurements. A good agreement is found at 300K for all values of the electric and magnetic fields. At low temperatures a pronounced disagreement is observed when the electric field E is greater than the critical value E_c that determines the negative differential resistance regime in the current-voltage characteristics. We discuss the physical origin of this difference.

in the presence of a sufficiently large applied electrical field. The NDV regime is a direct consequence of the negative effective mass experienced by the carriers.

This new type of material with a miniband width controllable only by external (growth) parameters has attracted much interest due to the potential applications for the elaboration of devices such as ultra-high frequency (≥ 100 GHz) oscillators. Very recently Hadjazi et al [2] have obtained a 60GHz oscillator with a GaAs-AlAs SL structure. SL's have been studied either by electrical transport measurements, such as thermal-saturation of miniband transport [3], tunneling between weakly-coupled SL's [4], under hydrostatic pressure [5] and also using optical techniques such as photoluminescence [6] and electro-reflection [7].

The existence of the NDV regime in SL's as a bulk material effect has been demonstrated by Sibille et al [8] in undoped samples. Studying n-type doped samples they also demonstrated the existence of the negative differential resistance (NDR) in

The concept of superlattices (SL's) was introduced some years ago by L. Esaki and R. Tsu [1] as a new class of semiconductor material. SL's are formed by the alternate growth of electronically different materials (typically two) along one direction, with individual widths small enough to give significant quantum effects, i.e., of the order of 100Å. This new one-dimensional man-made crystal presents a Brillouin zone smaller than that of the bulk materials due to the larger period of the artificial lattice. The energy spectrum along the growth direction is composed of minibands and minigaps. The first miniband width for conduction electrons is typically of the order of a few meV up to 200meV in comparison to the usual 4eV for the conduction band in pure materials. These minibands occur because of the non-zero tunneling probability between two consecutive wells. The energy-momentum dispersion of these minibands should allow the observation of the negative differential velocity (NDV) regime for electrons moving

LIST OF REFERENCES

1. P. Dutta and P. M. Hoon, *Rev Mod Phys* **53**, 497 (1981)
2. M. B. Weissman, *Rev Mod Phys* **60**, 537 (1988)
3. K. S. Ralls, W. J. Sloop, L. D. Jackel, R. E. Howard, L. A. Fetter, R. W. Epworth, D. M. Tennent, *Phys Rev Lett* **52**, 228 (1984)
4. C. T. Rogers and R. A. Buhrman, *Phys Rev Lett* **55**, 859 (1985)
5. C. T. Rogers, L. N. Smith, *Appl Phys Lett* **49**, 1107 (1986)
6. C. E. Parmian, N. E. Israeloff, K. Kakalios, *Phys Rev B* **44**, 8389 (1991) and *Phys Rev Lett* **69**, 1097 (1992)
7. A. L. McWhorter, in *Semiconductor Surface Physics* edited by R. H. Kingston (University of Pennsylvania, Philadelphia, 1957)
8. P. M. Mooney, *J Appl Phys* **67**, R1 (1990)
9. J. J. Harris, R. Murray and C. T. Foxon, *Semicond Sci Technol* (to appear)
10. S. M. Schlup, *J Appl Phys* **25**, 341 (1954)
11. J. R. Kirtley, T. N. Theis, P. M. Mooney, S. L. Wright, *J Appl Phys* **63**, 1541 (1988)
12. R. S. Sorbello, G. S. Chu, *IDM J Res Develop* **32**, 58 (1988)

Present address: Physics Department, University of Nottingham, Nottingham NG7 2RD, England

short period SL's [4]. Palmer and co-workers [10] have calculated in detail the effects of a crossed electric and magnetic fields in the velocity versus the electrical field relation $V(F)$, by solving the Boltzmann transport equation in the presence of a limited number of scattering mechanisms.

As a starting point we take the local $V(F)$ relation and calculate the current density as a function of the applied bias voltage solving a self-consistent system of the Poisson and drift-diffusion equations taking into account the conservation of the carriers. These results are directly compared to the experimental curves, obtained for different values of the applied magnetic field and over a range of temperature.

The samples studied consist of a series of periodic SL's of GaAs-AlAs hetero-layers grown by molecular-beam-epitaxy. They are highly Si-doped (i.e. $n \approx 2 \times 10^{18} \text{ cm}^{-3}$) and were grown on a highly doped substrate ($n \approx 2 \times 10^{18} \text{ cm}^{-3}$).

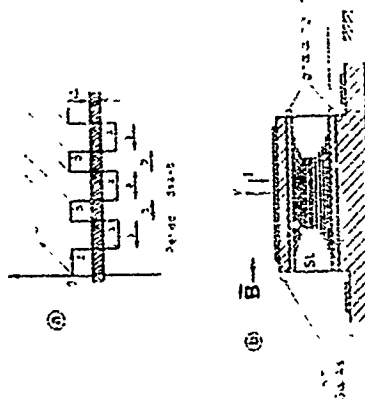


Figure 1. Schematic SL device and the experimental set-up. (a) Potential profile for a periodic SL of materials A and B. Δ is the miniband width of accessible energy for electrons. (b) SL device in presence of the applied electric and magnetic fields.

The doping concentration was graded on either side of the active region to avoid abrupt hetero-junctions between the SL and the contacts. Standard contact techniques with typical mesa's areas of $200 \mu\text{m}^2$ were used.

In this work we present results obtained for 3 samples of miniband widths equal to 4, 9 and 16 meV. These samples are nonvalley of 2/2, 1/1 and 2/2 monolayers of GaAs/AlAs respectively. The active region is about $1 \mu\text{m}$, which means typically a total of 1.5 periods in each sample. The miniband widths have been calculated using a K-P model, taking into account a constant averaged mass of GaAs and AlAs. Identical results have also been obtained using a transfer matrix approach.

In Fig. 1 a schematic representation of the sample structure is shown. The miniband width, the applied electric field and the orientation of the magnetic field are represented. Only the Γ conduction band for the GaAs and for the AlAs is shown.

Transport properties of electrons moving along the growth direction of a SL were first investigated by Shkly [11]. He also considered the presence of a magnetic field applied perpendicular to current. However, in his approach only low values of B for which the energy quantization by the magnetic field was negligible have been taken into account. Recently Palmer et al [10] have presented a detailed numerical solution of the Boltzmann equation under the same conditions and they obtained the local $V(F)$ -velocity versus the applied electrical field characteristics for different values of the magnetic field intensity. In their work the temperature T and the interface fluctuation Δ that describes the interface roughness, are additional parameters in the formulation of the problem.

We have considered the solution of the Boltzmann equation in presence of polar optical and transversal phonons together with the interface roughness scattering mechanisms, as described in ref [10]. To calculate the $V(F)$ -current density versus the applied bias voltage curve in order to compare it with

experimental results we have used the Poisson equation

$$\frac{\partial E}{\partial z} = -q(n - N_d) \quad (1)$$

and the drift-diffusion equation

$$J_n = q(n \mu_n E + D_n \frac{\partial n}{\partial z}) \quad (2)$$

where n is the density of negative carriers, N_d is the doping concentration of donors, μ_n is the static dielectric constant and D_n is the diffusion constant. The carriers conservation equation in the absence of any generation and recombination mechanism (dark conditions of measurements) and in steady-state condition is given by

$$\frac{1}{q} \frac{\partial J_n}{\partial z} = 0 \quad (3)$$

In order to apply suitable boundary conditions we simply write Eq (1) in terms of the electrostatic potential ϕ , given by

$$F = -\frac{\partial \phi}{\partial z}, \text{ and from Eqs (2) and (3) we obtain}$$

$$\frac{\partial}{\partial z} \left(q \mu_n \nabla_n(F) + q D_n(F) \frac{\partial n}{\partial z} \right) = 0 \quad (4)$$

Assuming a starting known expression for the $n(z)$ distribution and the $F(z)$ in Eqs (1) and (4) re-achieved is routine (1) and (4) in terms of differential equations using the finite-element method (P1) [12]. The non-linear decoupled system is solved by the Newton-Raphson algorithm. The iterative procedure is repeated until a stable and convergent solution for $n(z)$ and $F(z)$ is

simultaneously obtained. We note that the present model may not be applied when $\frac{\partial V_n}{\partial F} \approx 0$ nor when N_d exceeds a certain critical value [13], where L is the length of the active SL region. This procedure has been validated for pure GaAs samples, whose $V_n(F)$ law is well known.

In our experiments we have measured the current-voltage characteristics for a series of samples in presence of a magnetic field applied parallel to the SL's interfaces, i.e. perpendicular to the current direction. In Table I we present the most important parameters of our samples.

Typical $I(V)$ characteristics for each sample are shown in Fig. 2 for different temperatures. The current increases with applied bias for applied electric fields less than the critical value F_c . At room temperature we observe that the current intensity does not really decrease but remains almost constant when the applied electric field is higher than F_c .

When the temperature decreases the current intensity decreases abruptly for electric fields such that $F > F_c$, i.e. the NDI is more pronounced and the peak in the $I(V)$ curves is clear. The increase of the current when the temperature decreases is essentially due to the decrease of the scattering relaxation time τ , which occurs because phonons scattering is less important at lower temperatures. At very low temperatures ($T \approx 50\text{K}$) the current decreases with the decreasing temperature. A more detailed discussion of these effects will be included in a future publication.

Sample	Δ (meV)	widths (Å)	# of periods
S1	4	62/72	118
S2	9	53/70	135
S3	16	62/74	131

Table I. Main parameters of the 3 samples studied in this paper. The miniband widths have been calculated with a Kronig-Penney model using a constant averaged mass and also using the transfer matrix technique. The period of these SL's have been obtained from X-ray diffraction. The electrical contacts were formed using standard lithographic techniques and had an area of $200 \mu\text{m}^2$. The active region of the samples were doped at $n \approx 10^{18} \text{ cm}^{-3}$.

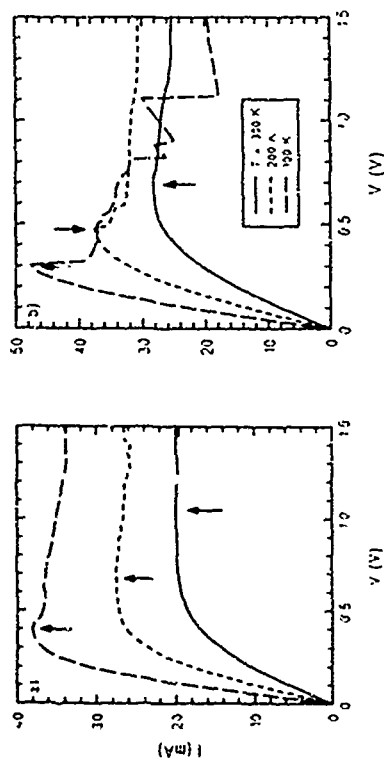


Figure 2 Experimental $I(V)$ characteristics for samples S2 (a) and S3 (b) - see Table 1 - for $H=0$ T. The variation of temperature is shown in the insert. The critical electric field F_c is indicated by the arrows and shifts to high values when the temperature increases. We note that the NDR is more pronounced for low temperatures.

for all temperatures and miniband widths we have observed that with increasing magnetic field F_c shifts to higher values. This effect occurs mainly because of the distortion of the electronic orbits... presence of the magnetic field, which tends to localize the electronic movement. A small effect due to the nature of scattering mechanism is present, although it is only a second order correction.

In Fig (3) we have plotted both experimental and calculated $I(V)$ curves. In spite of the fact that our model can not be applied for electric fields higher than F_c we do not observe a strong disagreement between theory and experiment at high temperature for electric fields in the NDR region. However, in the low temperatures regime the experimental results in the NDR region diverge from the calculated values. A satisfactory agreement is achieved in the

non-linear but positive domain of the differential resistance. We do not obtain from our analysis a decrease in the current density, i.e., the NDR, because the assumptions on which our model is based are no longer valid in this region. The shift of the critical field F_c to higher values due to the presence of the applied magnetic field is understood in terms of a competition between electric localisation, i.e., the Dragg reflection at the Brillouin zone and the magnetic localisation.

From our analysis we have observed that a relatively simple classical description of the transport properties in a SE, lead to a satisfactory agreement in all of the positive domain of the differential resistance. However, a better quantitative agreement between the theoretical and experimental results of the NDR region remains to be obtained.

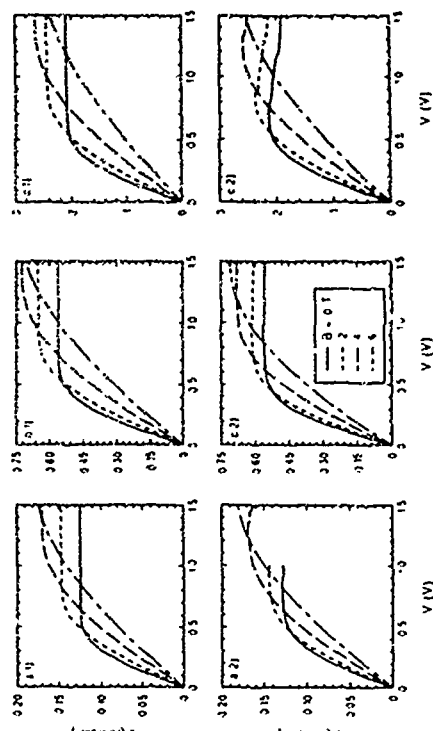


Figure 3 Direct comparison between experimental results (a, b, c) and calculated curves (a, b, c) for samples S1 (a), S2 (b) and S3 (c) - see Table 1 - for $T=300$ K. Very good agreement is obtained for all curves below the critical electric field F_c . Fairly good agreement is obtained in the NDR region. We note that the disagreement in the NDR region increases with decreasing temperature.

ACKNOWLEDGEMENTS

We thank S Vuze and J C Esnault for sample mounting and M Rabary for technical support. F A is grateful to CAPES-Brazil for a grant. We acknowledge CNCT, EEC and Conseil Regional des Midi-Pyrenees for financial support.

REFERENCES

- [1] L. Esaki and R. Tsu, *IBM J. Res. Develop.* 14 (1970) 61.
- [2] M. Hadjazi, J. F. Palmier, A. Sibille, H. Wang, E. Jans and F. Mollet, *Electr. Lett.*, 29 (1993) 648.
- [3] G. Brozak, M. Helm, F. de Rosa, C. H. Perry, M. Kozza, R. Bhat and S. J. Allen Jr., *Phys. Rev. Lett.* 64 (1990) 3163.
- [4] R. A. Davies, M. J. Kelly and T. M. Kerr, *Phys. Rev. Lett.* 55 (1985) 1111.
- [5] J. F. Anstome, A. Sibille, J. F. Palmier, B. Gouyons, J. C. Portal and F. Mollet, *Jpn. J. Appl. Phys.* 32 (1993) 144.
- [6] J. Skromme, R. Bhat, M. A. Kozza, S. A. Scharz, T. S. Ravi and D. M. Huang, *Phys. Rev. Lett.* 65 (1990) 2050.
- [7] P. Voinin, J. Blaise, C. Bouche, S. Gallard, C. Albert and A. Legreny, *Phys. Rev. Lett.* 61 (1988) 1639.
- [8] A. Sibille, J. F. Palmier, H. Wang and F. Mollet, *Phys. Rev. Lett.* 64 (1990) 52.
- [9] A. Sibille, J. F. Palmier, H. Wang, J. C. Esnault and F. Mollet, *Appl. Phys. Lett.* 53 (1993) 256.
- [10] J. F. Palmier, G. Etenshah, A. Sibille, M. Hadjazi, F. Mollet and R. Planel, *Surface Science* 267 (1992) 574.
- [11] A. Y. Shuk, *Soviet Phys. Semicond.* 7 (1973) 187.
- [12] J. F. Palmier, *Resonant Tunneling in Semiconductors*, Edited by L. L. Chang et al., Plenum Press, New York, 1991, p. 161.
- [13] H. Aki, B. W. J. Appl. Phys. 38 (1967) 808.

Wednesday, August 25

WeA Metal/Semiconductor and Type II Interfaces

WeB Atomic Scale Characterization

WeA1

Electronic Interactions at Superconductor-Semiconductor Interfaces

Herbert Kroemer, Chanh Nguyen, and Evelyn L. Hu
Department of Electrical and Computer Engineering
University of California, Santa Barbara, CA 93106

Abstract

Two current flow mechanisms across a superconductor-semiconductor-superconductor double heterostructure are discussed: The conventional proximity effect, and Andreev reflections. The emphasis is on Nb-InAs-Nb structures, with the InAs being in the form of a quantum well with AlSb barriers, for which current flow by multiple Andreev reflections can lead to an enhancement of the zero bias conductance by a large factor. For sufficiently short inter-electrode spacings, the multiple Andreev reflections can lead to a true supercurrent flow.

Introduction

When a superconductor and a semiconductor are brought together into atomically intimate contact, with an interface that is free from intervening oxides and/or contaminants, and which does not form an electron-blocking Schottky barrier, the electrons in the two materials can interact with each other in ways that can drastically alter the current flow through what may be called "super-semi-super double heterostructures." An example of a particularly suitable structure for the observation of such interaction effects is shown in Fig. 1 [1-3]. It consists of a thin layer of InAs, in which the electrons are confined at top and bottom by AlSb barriers, forming a 2D electron gas. This gas is then contacted by superconducting Nb electrodes

One of the reasons for the use of InAs is that the Fermi level at Metal-InAs contacts tends to be pinned inside the InAs conduction band, thus leading to an absence of Schottky barriers impeding the flow of electrons. As a result, such structures behave like pure resistors above the critical temperature of the Nb electrodes (9.2 K), and any new effects due to super-semi interactions are especially pronounced, unencumbered by non-superconducting complications. The reason for singling out a quantum well over a bulk structure is to achieve high electron concentrations by modulation doping while retaining high mobilities [4], and to suppress mobility reductions due to surface scattering, a problem especially severe with InAs, because of the absence of surface band bending. Typical sample parameters are: Well width of 15 nm, a

channel length ranging from sub- μm dimensions to several μm , and an electron sheet concentration of several-times 10^{12}cm^{-2} .

The super-semi interaction effects in such structures are pronounced. Fig. 2 shows the 4.2 K differential conductance of a structure as in Fig. 1, as a function of bias voltage [3]. The device shows a very narrow conductance spike around zero bias, inside which the conductance is enhanced by a factor 7 relative to the conductance just above the critical temperature of Nb (9.2 K). With increasing bias the conductance decreases, but shows a rich structure up to bias voltages equivalent to the superconducting gap of Nb ($\sim 3.2\text{ mV}$). These phenomena disappear when the Nb electrodes "go normal."

The structure and the behavior shown are by no means the only manifestation of super-semi interactions, nor are advanced quantum well structures necessary for all such observations. A variety of interaction phenomena have been observed in a variety of structures, employing a variety of semiconductors, including GaAs [3], (Ga,In)As [6], and Si [7]. Complete references can be found in the papers cited.

Proximity Effect, Weak Links and Josephson FETs

There are two distinct basic forms of super-semi interactions: The well-known *Proximity Effect*, and the less-well-known, but perhaps more important *Andreev Reflections*.

In the conventional proximity effect, the Cooper pairs that are the carriers of supercurrent inside the superconductor, can tunnel into the a normal conductor, causing induced superconductivity there, falling off exponentially with distance, with a characteristic length called the *coherence length*. If the separation between the superconducting electrodes is sufficiently small — typically of sub- μm dimensions — this can lead to what is called a *weak link*, a structure capable of carrying a true resistance-less supercurrent through the semiconductor.

In 1980, Clark et al. [8] drew attention to the promise of semiconductors rather than conventional metals as the non-superconductor in proximity effect studies. They proposed a Hybrid Josephson FET (= JOFET), basically a weak link the critical current of which can be modulated, leading to a current-voltage characteristic resembling that of a field effect transistor, except for a very different voltage scale, in the low-millivolt range, and of course a very different physics. The central idea was that the critical current that can be passed through a weak link employing the proximity effect depends strongly on the superconductive coherence length inside the semiconductor, which in turn depends on the electron

concentration in the semiconductor, which can be modulated with a gate electrode. The overall result would be a current-voltage characteristic as shown schematically in Fig. 3.

What distinguishes JOFETs from conventional FETs are not only the much lower voltage (and current) scales, but the existence of a true zero-resistance on-state. This makes a JOFET a device of potential interest as a current routing switch in superconducting networks. There is some doubt as to whether such JOFETs would ultimately be useful as amplifiers or logic gates. The gate voltage at $\sim 10^5$ V required for current modulation tend to be larger than the drain voltage swings obtainable from the constant modulation.

Clark et al. pointed out that InAs appeared to be the ideal semiconductor for such studies, not only because of the absence of Schottky barriers at metal-to-InAs interfaces, but also because of its unusually high electron mobilities, which in turn reflect the low effective mass of electrons in InAs. Because of this low effective mass, heavily n-type doped InAs has a Fermi velocity approaching that of many trap metals, and as a result, InAs in contact with a superconductor behaves more like a high-mobility metal than like a semiconductor. In particular, larger coherence lengths should be achievable.

Weak links and JOFETs employing a Nb-InAs-Nb structure were subsequently demonstrated, by Takayanagi et al. [2, 10], followed by others. However, the current-voltage characteristics of these early structures were relatively poor, and JOFETs with much better characteristics were obtained in GaAs and even Si [7], despite the theoretical superiority of InAs. Perhaps the most interesting of these early JOFET structures was that of Ivanov et al. [5], which appears to have been the first to employ a quantum well channel [GaAs-(Al,Ga)As] in a weak link or JOFET, demonstrating the superiority of such a design.

Following the development of a technology for high-quality InAs-AlSb quantum wells during the '80s, we ourselves turned to the problem of InAs weak links, and the balance of this paper deals with that work. In 1990 we were able to demonstrate weak links showing unprecedentedly high critical current densities above 2×10^5 A/cm² for a remarkable large 11×1 electrode spacings of 0.6 μ m [1]. We were naturally interpreting these results as caused by the conventional proximity effect. More recent observations challenge this interpretation, and suggest a different superconductivity mechanism in terms of multiple Andreev Reflections, our next topic.

Andreev Reflections

Consider a semi-super interface between a degenerately doped semiconductor and a superconductor, with a band diagram as shown in Fig. 4. On the semiconductor side, a superconducting energy gap has opened up. If now a small bias voltage V is applied, as shown, the existence of the gap then prevents a single electron at the Fermi level of the semiconductor from entering the superconductor. This argument suggests that, in the absence of the proximity effect, the onset of superconductivity in the metal thus actually increases the electrical resistance to current flow across the interface, due to this gap formation. However, even a single electron may pair up with a second electron at the bias energy qV below the Fermi level, forming a Cooper pair, which can enter the superconductor, causing a doubling of the current compared to that in the absence of superconductivity, rather than the reduction that would occur in the absence of this pair formation. As the electron below the Fermi level is removed from the semiconductor, it leaves behind a hole below the surface of the Fermi sea. The generally accepted jargon associated with this phenomenon is to say that the incident electron is *reflected as a hole*, a kind of reflection process called an *Andreev reflection*, honoring the originator of the concept [11]. The *Andreev hole* left behind, being a "bubble" under the surface of the Fermi sea in the conduction band, must not be confused with a valence band hole.

In a semiconductor with a large mean free path for the electrons ($\sim 3 \mu$ m in our structure), the Andreev hole left behind at the interface has a large mean free path itself, roughly equal to that of the electrons, and theory shows that the hole travels back into the semiconductor along a trajectory that is essentially the time reversal of the trajectory of the original incident electron. If its mean free path is sufficiently large, the hole will eventually reach the negative superconducting electrode. If the bias across the structure is sufficiently small, the energy of the hole is still within the superconducting gap on that side. Such a hole cannot enter the superconductor, but it can be annihilated by breaking up a Cooper pair inside the adjacent superconductor. One of the electrons of the pair annihilates the hole, the other electron takes up the annihilation energy, and is injected into the semiconductor as a ballistic electron above the Fermi level, at an energy above that of the initial electron. This process, illustrated in Fig. 5, can evidently be repeated, until either an electron or a hole has been "pumped up" to an energy outside the superconducting gap, on one of the two sides of the structure. If all the reflections of electrons and holes were Andreev reflections rather than "ordinary" reflections, the result would be an enhancement of the conductivity by a factor equal to the number of ballistic round trips before escape or before collision events randomize either the electron or the hole flow in this chain reaction. As a rule, the conductance enhancement in past structures has been much smaller, presumably due to a low AR probability, itself caused by strong normal reflections due to residual potential barriers at the interfaces.

One of the "fingerprints" of multiple ARs is a rich "sub-harmonic gap structure" in the conductance-vs.-voltage characteristic, with steps occurring at voltages equal to the integer fractions of the superconducting gap voltage [12-14]. A discussion of this structure lies outside the scope of the present paper, but the occurrence of such a structure is evident in the characteristics of Fig. 2, thus clearly indicating the multiple-AR origin of the conductance peak. What is new compared to earlier data reported in the literature is the huge enhancement in the differential conductance, by a factor of seven in the example of Fig. 2. The behavior appears superficially as if the proximity effect were present. However, we will show below that contact resistance measurements rule out such an explanation.

Andreev-Reflection-Induced Superconductivity?

The large conductance enhancement suggests that it might be instructive to carry the above multiple-AR argument to its extreme limit, the case of zero applied bias, and assuming that all reflection events at the Sp-Sm interfaces are AR events, and that no scattering of any kind inside the semiconductor randomizes the electron and hole velocities. In this case, a given AR "chain" would go on forever. During each electron-hole round trip, one Cooper pair is annihilated at one of the electrodes, and re-constituted at the other electrode on the opposite side, leading to the net transfer of one Cooper pair per round trip. Given an initial net current, this current would persist, just as in the proximity effect, but by an altogether different mechanism.

These are extreme assumptions, especially the assumption of a 100% AR probability, yet the final conclusion appears to be correct. The quantum mechanics of this hypothetical multiple-AR mechanism has recently been analyzed in detail by Schluster and Kummel (SK) [15], using a model assuming the existence of a *definite fixed phase difference* between the pair potentials in the two superconducting electrodes, and neglecting scattering in the semiconductor channel, but not assuming a 100% AR probability. The authors showed that under their conditions the multiple Andreev Reflections of phase-conjugate ballistic quasiparticles (i. e., electrons and Andreev holes) form indeed a very effective mechanism for Cooper pair transfer between the electrodes, capable of carrying a much higher zero-resistance current densities than the conventional proximity effect.

We believe that the narrow central conductance spike shown in Fig. 2, with the up-to-seventyfold enhancement of the differential conductance, is a *precursor* of the true Andreev-caused supercurrent postulated above, and analyzed by SK. We have to call it a precursor, because our data indicate a still-finite conductance, occurring over a narrow but nonzero voltage range ($\sim 5k_B T$). Presumably, the finite height and width of the central conductance

spike is the result of residual scattering events present in the relatively long (1 μm) InAs-AlSb QW channel, eventually randomizing the quasiparticle velocities. Furthermore, we believe that the true superconducting limit can indeed be achieved in Nb-InAs-Nb quantum well structures with a shorter inter-electrode spacing.

In their work, SK assume that there is a fixed phase relation between the pair wave functions in the two superconducting electrodes, and analyze the consequences. They do not address the question of how such a phase relation, and with it any supercurrent, might be maintained in the presence of scattering in the semiconductor channel. In the absence of such scattering, the assumption of a fixed phase relation between the pair wave functions in the two superconducting electrodes is entirely self-consistent. On the other hand, in the presence of sufficiently strong scattering, as in the case of a sufficiently wide inter-electrode spacing, any current not driven by an external voltage must eventually decay. This raises the question as to the nature of the transition to the SK superconducting limit, as the scattering in the semiconductor channel is reduced, by reducing the temperature and/or the inter-electrode spacing: Will the zero-bias resistance of the overall structure drop towards zero continuously without ever reaching the true superconducting limit? Or will collective effects cause a "condensation" of the Andreev pairs into a new correlated many-body state, in which the dephasing effects of scattering are quenched, similar to the way the BCS transition quenches the ordinary resistivity in a BCS superconductor?

We believe that the latter is indeed the case, and that our earlier observation of very large weak link current densities in structures with 0.6 μm electrode spacing was indeed an manifestation of such a mechanism. To pursue this idea further, we have utilized laser holography to prepare what is essentially a grating of ~ 300 parallel Nb lines making periodic contact to an InAs quantum well with AlSb barriers, with a 1 μm period and a $\sim 0.4 \mu\text{m}$ spacing between the Nb lines. The rest of the technology was basically the same as in the structure whose data were shown in Fig. 2. In "the direction perpendicular to the grating lines, the structure acts basically as a series-connection of 300 diodes of the type shown in Fig. 1. At 4.2K, this structure showed a characteristic qualitatively similar to that of Fig. 2, with the "Andreev fingerprint" of sub-gap harmonics, but with a ~ 300 -fold enhanced voltage scale. More importantly, the conductance enhancement was by a factor 75, presumably as a result of the shorter inter-electrode spacing. With decreasing temperature, the zero-bias resistance dropped further, reaching an immeasurably low value between 3.9 and 3.8K.

This grating structure was still being evaluated at the time of the deadline for this manuscript; up-to-date results will be presented at the conference.

The Contact Resistance Problem

Our interpretation of the conductance enhancement in terms of multiple ARs rather than as a precursor of the ordinary proximity effect is supported by measurements of the specific contact resistance at the Nb-InAs interface, using the conventional *transmission line method* widely used in semiconductor technology [16]. The latter consists of measuring the set of voltage drops across a monolithic array of metal contacts to a thin semiconductor layer, with various lithographic inter-contact spacings L , and fitting the measured voltages and their current derivatives to an expression of the form

$$\frac{dV}{dI} = 2 \frac{dV_c}{dI} + \rho_s \cdot \frac{L}{w} \quad (1)$$

Here I is the current through the array, w is the width of the array, and ρ_s is the ordinary sheet resistance of the semiconductor layer in the limit that L and w are large compared to the electron mean free path. In (1), the length-proportional term represents the "ordinary" path resistance of a semiconductor path of length L , and $2dV_c/dI$ represents the effects of whatever additional voltage drops are present at or near the two contacts. The latter include the true contact resistances at the two interfaces, plus any deviations from *bulk* behavior inside the semiconductor near the electrodes, for example due to any proximity effect. If the latter is present, a DC current across the SpSm interface would be carried entirely by Cooper pairs. We would then expect the true contact resistance associated with the Nb-InAs interface to be zero, and the resistive portion of the semiconductor path to be shortened below the lithographic length, leading to a *negative* value of the intercept voltage $2V_c$, and to a negative *apparent* contact resistance, represented by the leading term in (1). Our measurements, shown in Fig. 6, indicate that the apparent contact resistance remains positive, thus ruling out the proximity effect as an explanation of the zero-bias conductance spike.

Acknowledgments

This work was supported in part by the Office of Naval Research and in part by the National Science Foundation, the latter through the NSF Science and Technology Center for Quantized Electronic Structures, Grant #DMR 91-20007, as well as through the NSF Materials Research Laboratory Program, Award #DMR 912-3048. One of us (C.N.) wishes to acknowledge the financial support from the UCSB Vice Chancellor's Fellowship for Advanced Research on Quantized Structures

References

- [1] C. Nguyen, J. Working, H. Kneimer, and E. L. Hu, Appl. Phys. Lett. 57, 87 (1990).
- [2] C. Nguyen, H. Kneimer, and E. L. Hu, Phys. Rev. Lett. 69, 2847 (1992).
- [3] C. Nguyen, H. Kneimer, and E. L. Hu, to be published (1993).
- [4] C. Nguyen, B. Brar, C. B. Bolognesi, J. J. Pekarik, H. Kneimer, and J. H. English, J. Electron. Mater. 22, 255 (1993).
- [5] Z. Iqbal, T. Claeson, and T. Anderson, Jpn. J. Appl. Phys. 26 Supplement 3, DF31 (1987) (Proc. 18th Internat. Conf. on Low Temperature Physics, Kyoto, 1987).
- [6] A. Kasulsky, A. W. Kleinsasser, L. H. Greene, R. Bhat, F. P. Milliken, and J. P. Harbison, Phys. Rev. Lett. 67, 1326 (1991).
- [7] T. Nishino, M. Hatano, H. Hasegawa, F. Murai, T. Kuro, A. Hiraiwa, K. Yagi, and K. Kawabe, IEEE Elect. Dev. Lett. 10, 61 (1989).
- [8] T. D. Clark, R. J. Prance, and A. D. C. Grassie, J. Appl. Phys. 51, 2736 (1980).
- [9] H. Takayanagi and T. Kawakami, Phys. Rev. Lett. 54, 2449 (1985).
- [10] H. Takayanagi and T. Kawakami, Proc. of Internat. Electron Devices Meeting, 1985, p. 98.
- [11] A. F. Andreev, Sov. Phys. JETP 19, 1228 (1964).
- [12] T. M. Klapwijk, G. E. Blonder, and M. Tinkham, Physica B+C 109&110, 1657 (1982).
- [13] M. Octavio, M. Tinkham, G. E. Blonder, and T. M. Klapwijk, Phys. Rev. B 27, 6739 (1983).
- [14] K. Flensberg, J. B. Hansen, and M. Octavio, Phys. Rev. B 38, 8707 (1988).
- [15] U. Schuster and R. Kummel, Phys. Rev. B 47, 2754 (1993).
- [16] R. E. Williams, Gallium Arsenide Processing Techniques (Artech House, Inc., 1984).

Figure Captions

Fig. 1. Schematic InAs-AISb quantum well structure with superconducting Nb electrodes, for the investigation of electron-electron interaction effects across a super-semi interface

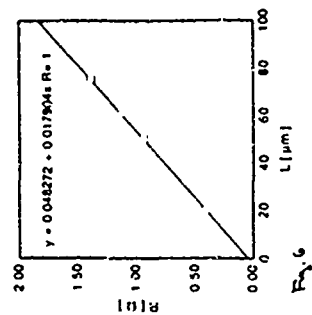
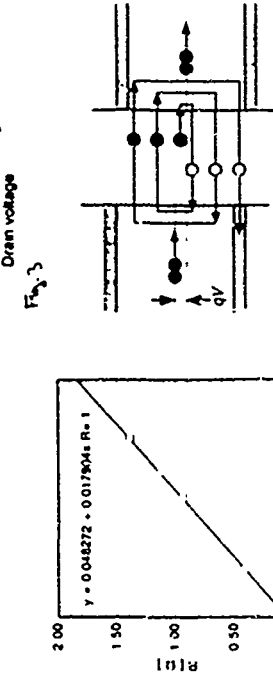
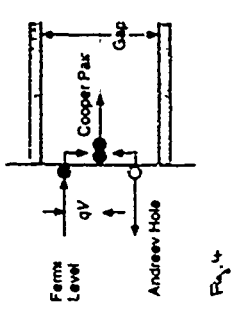
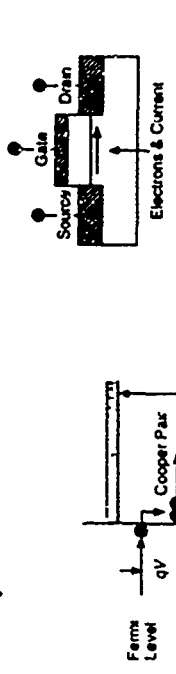
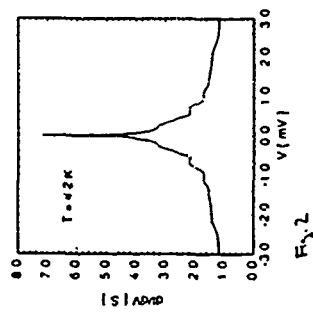
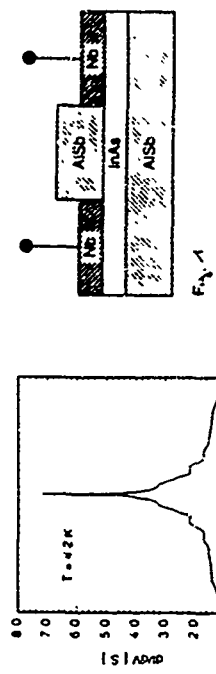
Fig. 2. Very strong enhancement at zero bias of the differential conductance of a recent InAs-AISb quantum well structure with Nb electrodes [3], of the type shown in Fig. 1, with $\approx 1\mu\text{m}$ electrode separation. The rich structure shown on the flanks of the central identifies the conductance peak as due to multiple Andreev reflections (see text)

Fig. 3. Schematic JOFET structure and its $I-V$ characteristics.

Fig. 4. Andreev reflection (AR) of an electron at a biased super-semi interface.

Fig. 5. Multiple Andreev reflections (AR) alternating between the super-semi interfaces at opposite ends of the semiconductor region

Fig. 6. Zero-bias differential resistance $R = dI/dV$ at 4.2K of a set of Nb-InAs(QW)-Nb structures with different inter-electrode spacings, plotted as function of spacing. The straight line is a linear fit through the data, including a point at $L = 200\mu\text{m}$, not shown on the plot. The intercept value, representing twice the line contact resistance, is positive.



Direct Observation of the Semimetal to Semiconductor Transition in Crossed Band Gap Superlattices at Magnetic Fields of up to 150T

D.J. Barnes^{a,*}, R.J. Nicholas^{a,b}, R.J. Warburton^b, N.J. Mason^b, P.J. Walker^b and N. Miura^a^a ISSP, Tokyo University, Roppongi 7-22-1, Tokyo 106, Japan
^b Physics Dept., Clarendon Lab., Parks Rd., Oxford OX1 3PU, U.K.

Abstract

Ultra-high magnetic field (>150T) cyclotron resonance has been performed on type II InAs/Ga(In)Sb superlattices. The electron density data reveals a dramatic depopulation at a critical magnetic field corresponding to the uncrossing of the lowest electron and hole Landau levels. The magnitude of this critical field decreases with decreasing superlattice period.

The type II heterostructure InAs/GaSb has an extreme band gap line-up such that the valence band of the GaSb lies at a higher energy than the conduction band of the InAs, resulting in charge transfer across the interface until the band bending equalises the Fermi energy across the two materials. Thus, electron and hole gases are intrinsically generated on either side of the interface [1]. When a superlattice is constructed from these materials the subband confinement energy can strongly modify this behaviour. The relatively light mass of the electron in the quantum wells of InAs ($m^* \sim 0.023$) makes the subband energy extremely sensitive to the well width and so the electron energy can be pushed up through the valence band energy within a feasible layer thickness of order 85 Å InAs [2]. Once this has been achieved, the band lineup is essentially semiconductor-like and the structure shows a rapid depopulation of the carriers.

The semimetal to semiconductor transition can also be generated magnetically [3], in a completely reversible manner for a single structure. As the hole Landau levels fan downwards in energy with increasing magnetic field and the electron levels upwards, at a sufficiently high magnetic field the lowest hole and electron Landau levels uncross, leading once again to depopulation. The threshold magnetic field depends on the magnitude of the original band gap overlap, determined by the period. For a typical superlattice with a band gap overlap of 70 meV, the uncrossing has been calculated to occur in the region of 40T [4] and for long period structures with overlaps of order 100 meV or more, the transition is expected to occur at still higher fields up to the megagauss region.

There have been many transport and FIR studies performed on both semimetallic and semiconducting InAs/GaSb superlattices. Simple Hall measurements [5] and later two-carrier fits to Hall measurements [6,7] have demonstrated the semimetal to semiconductor transition due to subband confinement, while cyclotron resonance (CR) data has exploited the strong non-parabolicity of InAs to confirm the presence of well developed superlattice subbands which raise the electron mass well above the band edge mass value [8]. Moreover, low magnetic field CR studies have observed complex data in multiply populated subbands, which have been interpreted as due to both interband (ie electron to hole) resonances as well as the expected intralevel electron cyclotron resonances [9-11].

We present a comprehensive study of the magnetically induced semimetal to semiconductor transition examined as a function of superlattice period over the range 30 to 150T. We have studied the superlattices using electron CR which allows simultaneous access to the effective mass and carrier density through the resonance position and the integrated absorption of the resonance. (The heavy mass of the hole, around 0.1 m_0 , puts the resonance field well beyond the maximum magnetic field accessible.) The experiments were performed at the Institute of Solid State Physics, Tokyo University where up to 150T for 5µsec can be generated by the fast discharge of a 1000J, 40kV capacitor bank across a copper, single turn coil. The IR wavelengths used were provided by CO₂ and CO lasers and the transmitted radiation measured by a fast action, N₂ cooled HgCdTe detector. The samples, unwedged, were held in place by a phenol cryostat and cooled to about 30K by the continuous flow of liquid Helium. Embedded in the

cryostat was a pickup coil able to measure the magnetic field to better than 2%. Further details of the technique of CR at 150T are available in refs 12 and 13.

A series of InAs/GaSb and InAs/Ga_{1-x}In_xSb superlattices have been grown by MOVPE at Oxford University. The superlattices were grown onto semi-insulating GaAs substrates with a 2µm thick buffer layer of GaSb to accommodate the strain from the first substrate GaSb interface. During the growth, the gas switching at the interface between the InAs and GaSb layers is timed to favour the formation of an InSb monolayer interface [14], whose presence has been detected by Raman scattering [15], in order to reduce the presence of interface defects [16]. Thus, these superlattices possess a much higher intrinsic carrier density than their MBE grown predecessors which were only in the order of 25% intrinsic. The high quality of these superlattices and the high density of the hole gas has been proven recently by the measurement of hole CR [17]. As short period superlattices are known to have low carrier concentrations, a larger number of layers were grown to enhance the absorption.

The superlattices were grown simultaneously onto two substrate orientations (001) and (111)A. As the (111)A direction is piezoelectrically active, the small strain inherent in InAs/GaSb, 0.6%, induces a strong electric field which acts to further increase the band overlap, and thus also increase the carrier concentration in long period structures [18]. More significantly, Symons *et al* [19] have shown that the band structure is strongly orientation dependent due to the presence of an interface dipole, which leads to an additional overlap of order 65 meV for (111)A samples. The InAs/GaSb superlattices were grown with a thickness ratio 5:3 and the InAs/GaSb superlattices with the ratio 5:1. The addition of 10% In into the GaSb layer has the effect of shifting the valence band and thus increasing the band gap overlap by ~30 meV [20]. The addition of In also affects the lattice mismatch causing the strain to increase to, of order, 1%, which is expected to be significant for the (111)A superlattices.

Cyclotron resonance was performed for a wide range of InAs/GaSb superlattices with periods in the range 60 Å to 600 Å at wavelengths of 10.6µm and 9.2µm. In contrast with the complex CR structure seen in low field measurements, the striking aspect of all the data is its simplicity: all the superlattices produced single resonances corresponding to electron CR. The long period superlattices exhibit narrow and strong resonances which become weaker and broader and move up in magnetic field as the periodicity decreases, until at very short periods the resonances disappear almost entirely. Due to the presence of a small proportion of extrinsic carriers the depopulation is not total, and the remaining CR allows the extrinsic carrier density to be measured and the effective mass to be determined even beyond the depopulation point. The decreased mobility associated with short periods is attributed to the increased importance of scattering at the interfaces, which are thought to be significant sources of charged defect states, and the increasing influence of layer width fluctuation which are found by TEM in the smaller structures. Three of the best superlattices - 1249, 1252 and 1253 - were then chosen as representative of semimetallic, zero band gap and semiconducting superlattices and studied further at 5.7µm and 5.3µm in order to gauge the magnetic field dependence of the depopulation effects.

To illustrate these trends, a set of CR data is shown for InAs/GaSb superlattice 1252(001) (InAs layer thickness 106 Å). At low magnetic fields, around 40T, the resonance is strong corresponding to a high carrier density. By 50T, as the transition field is approached for this superlattice and the carrier density reduced, the resonance is considerably weaker, and by 110T, the hole and electron Landau levels have completely uncrossed and the sample depopulated.

As the integrated absorption area of a resonance is directly related to the total carrier concentration, the collapse of the cyclotron resonance due to the semimetal to semiconductor transition can be quantified. The electron density deduced from the CR for a selection of superlattices has been used in Fig. 2 to show the general trends in behaviour. This figure clearly demonstrates the link between a high, low field carrier concentration and depopulation occurring at high magnetic fields. In long period superlattices the large band gap overlap generates high density 2D electron gases essentially isolated by the resultant strong band bending. The large band overlaps of these superlattices are only overcome, and the sample depopulated, with the large Landau level energy caused by large magnetic fields. As the superlattice period is decreased

and the confinement energies increased however, the effective band gap is reduced, thus lowering the carrier concentration and reducing the magnetic field required to depopulate the superlattice.

The structures grown on the (111)A substrate show essentially the same behaviour as their (001) counterparts (Fig. 1), except that their carrier densities are significantly higher (typically doubled) and that the transition magnetic field moves to an appreciably higher value (Fig. 2). This is attributed to the effects of the piezoelectric field and the larger band gap as reported recently by Symons *et al* [19].

The InAs/GaSb superlattices were studied at 10.6 μm , 9.2 μm and 5.5 μm and showed similar behaviour to the InAs/GaSb superlattices [24] (Fig. 2), though the resonances show less distortion. The higher carrier densities are due to the larger band gap caused by the wider InAs layer and due to the shift of the GaSb valence band [20]. A comparison of the CR before and after depopulation shows that about 95% of the carriers are intrinsic, which agrees with low field Hall data that the ratio of electrons to holes in these superlattices is close to 1:1.

The dependence of the effective mass on both energy and superlattice period has been examined. Even at such high energies, both the InAs/GaSb and InAs/GaInSb superlattices on both (001) and (111)A substrate directions, can be described by the simple linear dependence, $m^* = m_0^* (1 + 2.6\omega_c/E_g)$ which is the functional form expected for a simple two band non-parabolic approximation for the effective mass, using the InAs band gap and an increased value of the energy prefactor. As an example, the (001) and (111)A data for InAs/GaSb and InAs/GaInSb superlattices are shown in Fig. 3. Also plotted is the effective mass taken from the magnetic field dependence of the lowest two Landau levels which was calculated using a full eight band $k \cdot p$ perturbation theory for both a net band gap of 0 meV and -70 meV. The effective mass from the calculation fits the data and the observed linear dependence well. The effective mass values for the InAs/GaSb superlattices are slightly lower than the InAs/GaInSb superlattices due to the larger InAs thicknesses which lead to lower confinement energies and so, by non-parabolicity, to a lower mass. In contrast, the (111)A structures have a slightly higher mass due to the larger confinement energies which result from the stronger self-consistent confinement potential caused by the higher carrier densities which result from the increased band overlap for this orientation.

The effective mass has also been studied as a function of InAs layer thickness for a fixed laser wavelengths of 10.6 μm and 9.2 μm for both (001) and (111)A InAs/GaSb superlattices in Fig. 4. The InAs thickness is more significant than the superlattice period as the electron resonance is dominated by the contribution from the InAs conduction band. A systematic increase in mass can be seen as the thickness is decreased due to the corresponding increase in the quantum well confinement energy increasing the mass through the non-parabolicity. This effect can be modelled with the expression:

$$m^* = m^*_{\text{InAs}} (1 + 2.6\omega_c/E_g) + (E_g + 2.6\omega_c/E_g) / (E_g + 2.6\omega_c/E_g) \quad [\text{Eq. 1}]$$

where m^*_{InAs} and E_g are the band edge InAs mass and band gap, and E_c the confinement energy, again calculated by $k \cdot p$ theory. The first term accounts for the InAs non-parabolicity at the cyclotron frequency, as discussed above for the energy dependence, and the second term is the non-parabolicity from the superlattice confinement. There is a smooth change in effective mass across the semimetal to semiconductor transition (which occurs, e.g., for (001) superlattices at 10.6 μm at about 100Å), which implies relatively little mixing between the lowest conduction and valence bands due to the large difference in quantum number for these two states.

In conclusion, we can state that we have shown clear evidence for the existence of a magnetic field induced semimetal to semiconductor transition in a wide range of structures, which is particularly dramatic due to their low extrinsic doping levels.

1. L.L. Chang, *J. Phys. Soc. Jpn* 49 997 Supp A (1990);
2. L. Esaki and L.L. Chang, *J. Magn. Mater* 11 208 (1979);
3. L.L. Chang and L. Esaki, *Surf. Sci.* 96 70 (1980);
4. N.J. Kawai, L.L. Chang, G.A. Sai-Halasz, C. A. Chang and L. Esaki, *Appl. Phys. Lett.* 36 369 (1992);
5. D.J. Barnes, R.J. Nicholas, N.J. Mason, P.J. Walker, R.J. Warburton and N. Miura

6. L.L. Chang, N. Kawai, G.A. Sai-Halasz, R. Ludeke and L. Esaki, *Appl. Phys. Lett.* 33 939 (1979);
7. E.E. Mendez, L. Esaki and L.L. Chang, *Phys. Rev. Lett.* 55 2216 (1985);
8. H. Munekata, E.E. Mendez, Y. Iye and L. Esaki, *Surf. Sci.* 174 449 (1986);
9. H. Bluyssen, J.C. Maan, P. Wyder, L.L. Chang and L. Esaki, *Solid State Comm.* 31 35 (1979);
10. Y. Guldner, J.P. Vieren, P. Voisin, M. Voos, L.L. Chang and L. Esaki, *Phys. Rev. Lett.* 45 1719 (1980);
11. J.C. Maan, Y. Guldner, J.P. Vieren, P. Voisin, M. Voos, L.L. Chang and L. Esaki, *Solid State Comm.* 39 683 (1981);
12. J.C. Maan, Ch. Uihlen, L.L. Chang and L. Esaki, *Solid State Comm.* 41 755 (1982);
13. K. Nakai, E. Herlach, T. Goto, S. Takeyama, T. Sakakibara and N. Miura, *J. Phys. F: Met. Phys.* 13 1018 (1983);
14. S.P. Najda, S. Takeyama, N. Miura, P. Pfeiffer and W. Zawadzki, *Phys. Rev. B* 40 6189 (1989);
15. M. Lakrimi, R.W. Martin, N.J. Mason, R.J. Nicholas and P.J. Walker, *J. Cryst. Growth* 110 677 (1991);
16. C. Lopez, R.J. Springett, R.J. Nicholas, P.J. Walker, N.J. Mason and W. Hayes, *Surf. Sci.* 267 176 (1992);
17. J. Luo, H. Munekata, F.F. Fang and P.J. Stiles, *Phys. Rev. B* 38 10142 (1988);
18. G.M. Sundaram, R.J. Warburton, R.J. Nicholas, G.M. Sundaram, N.J. Mason and P.J. Walker, *Semi. Sci. Technol.* 7 985 (1992);
19. M. Lakrimi, C. Lopez, R.W. Martin, G.M. Sundaram, G.M. Sundaram, K.S.H. Dalon, N.J. Mason, R.J. Nicholas and P.J. Walker, *Surf. Sci.* 263 575 (1992);
20. D.M. Symons, N. Lakrimi, R.J. Warburton, R.J. Nicholas, N.J. Mason, P.J. Walker and M.J. Eremets, *To be published (1993)*;
21. S.K. Haywood, E.T.R. Chidley, R.E. Mallard, N.J. Mason, R.J. Nicholas, P.J. Walker and R.J. Warburton, *Appl. Phys. Lett.* 54 922 (1989);
22. D.J. Barnes, R.J. Nicholas, N.J. Mason, P.J. Walker, R.J. Warburton and N. Miura, to be published.
23. D.J. Barnes now at: Sektion Physik, Universität München, Geschwister-Scholl-Platz 1, 8-500 München 22, Germany

	Number of Periods	InAs (Å)	GaSb (Å)	GaInSb (Å)
1:65(100)	20	500	-	100 *
1:65(111A)	20	500	51	100 *
1:52(100)	100	106	77	-
1:52(111A)	100	155	32	-
1:53(100)	100	64	33	-
1:53(111A)	100	66	112	-
1:49(100)	20	223	100	-
1:49(111A)	20	202	-	-

Table 1: Superlattice details. Thickness measured by TEM except * calculated by time of growth.

Magnetotransport Properties of MBE-Grown Magnetic Superlattices of Mn-Based Intermetallics on GaAs Heterostructures

M Tanaka*, J.P. Harrison, T. Sandz, J. DeBoeck**, T.L. Cheeks and V.G. Kermidas
 Bellcore, 335 Newnan Springs Road, Red Bank, NJ 07701-7040, U.S.A.
 *On leave from Dept. of Electrical Engineering, The University of Tokyo, Japan.
 **Present Address: Interuniversity Microelectronics Center (IMEC), Belgium.

We have studied magnetic and magnetotransport properties of two kinds of new epitaxial magnetic superlattices, MnGa/NiGa and MnAl/NiAl, consisting of ferromagnetic tetragonal NiGa (MnAl) and nonmagnetic C3Cl-type NiGa (NiAl), grown by molecular beam epitaxy (MBE) on (001) GaAs substrates. Strong perpendicular magnetization is evidenced in both types of superlattices, with the values of remanent magnetization higher than those of MBE-grown MnGa and MnAl thin films reported previously. At room temperature, the hysteresis loops in the extraordinary Hall effect (EHE) measurements on the MnGa/NiGa superlattices exhibit evenly-spaced multiple steps, while the MnAl/NiAl superlattices show rectangular single-stepped EHE hysteresis loops with nearly perfect squareness. The capability of growing these kinds of new epitaxial magnetic superlattices gives a new degree of materials design of the magnetic thin films on GaAs substrates, offering the possibility of integrating magnetic devices with III-V semiconductor electronics and photonics.

Introduction

The progress in heteroepitaxial growth techniques such as molecular beam epitaxy (MBE) has made it possible to prepare a variety of heterostructures consisting of materials that are dissimilar in terms of crystal structure, chemical bonding, electronic and magnetic properties [1]. One of the most unique and attractive future directions, both for materials science and device applications, is the integration of magnetic materials and compound semiconductors [2]. Epitaxial ferromagnetic films grown directly on III-V semiconductors offer a wide range of possibilities for the fabrication of new devices including non-volatile memory coupled with underlying high speed optical/electronic III-V circuitry.

We have recently demonstrated successful MBE growth of metastable ferromagnetic MnAl thin films [3][4], and thermodynamically stable ferromagnetic 8MnGa [5] thin films on GaAs substrates. In both these MnAl and MnGa thin films, we have used MBE heteroepitaxy to align the c-axis of the tetragonal unit cell of the MnAl and MnGa, which is the easy magnetization axis, perpendicular to the substrate. This perpendicular magnetization is desired for many applications of magnetic thin films, since it allows high storage density in nonvolatile magnetic memory applications, and allows the use of the extraordinary Hall effect (EHE) and the magnetooptic Kerr effect (MOKE). Furthermore, we have also explored MBE growth of (MnNi)Al [6] and (MnNi)Ga [7] alloy thin films with perpendicular magnetization, and have found that the structural and magnetic properties can be controllably changed by Ni additions.

In order to derive more functionality and to increase the freedom in materials design by utilizing the atomic-scale controllability of the film thickness in MBE, we have created two kinds of new ultrathin epitaxial magnetic superlattice (SL) structures of metallic compounds, MnGa/NiGa superlattices and MnAl/NiAl superlattices, on (001) GaAs substrates. These superlattices consist of ferromagnetic tetragonal NiGa (MnAl) and nonmagnetic cubic C3Cl-type NiGa (NiAl). In this report, we present the magnetic and magnetotransport properties of both the MnGa/NiGa and MnAl/NiAl SLs, with emphasis on their extraordinary Hall effect (EHE) characteristics.

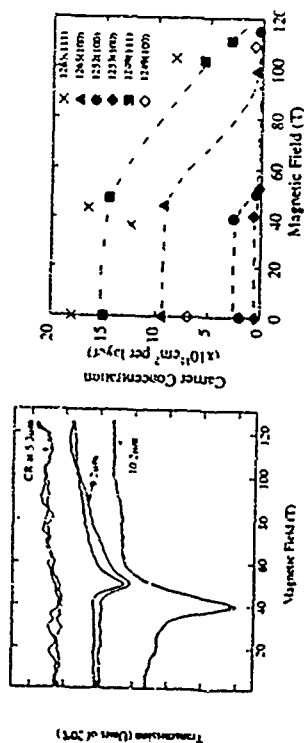


Figure 1: Cyclotron resonance data for InAs/GaSb superlattice 125/5(001)

Figure 2: The electron concentration per layer of InAs/GaSb and InAs/GaInSb (1265) superlattices deduced from cyclotron resonance measurements. The dotted lines are guides for the eye only.

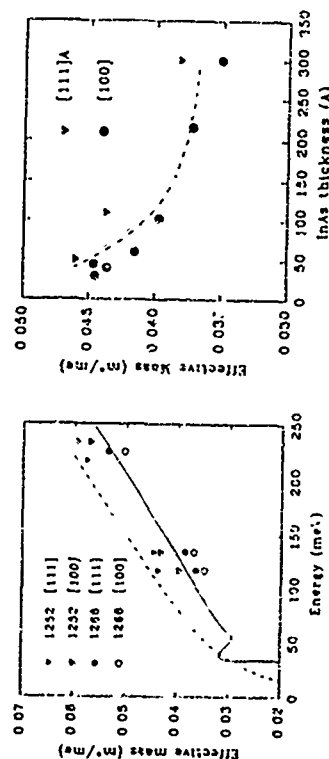


Figure 3: Effective mass (m^*) deduced from CR measurements as a function of energy for InAs/GaSb superlattices 125/5 and InAs/GaInSb superlattice 1265, both on the (100) and (111)A substrate directions. The m^* extracted from 8 band $k \cdot p$ theory calculations are shown for 10meV (solid line) and 10meV (dotted line) band gaps.

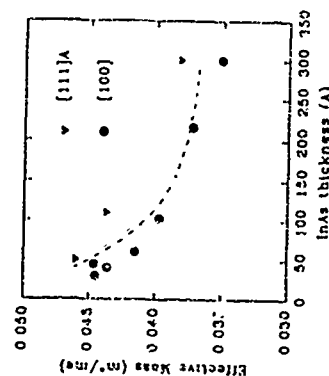


Figure 4: Effective mass of InAs/GaSb superlattices deduced from CR measurements as a function of InAs layer thickness for both (001) and (111)A substrate directions at 100 meV. The fit to the data is from conduction band $k \cdot p$ theory and the conduction energy E_c calculated from 8 band $k \cdot p$ theory.

magnetization axis is the c-axis in both materials. The lattice constants a_0 in the basal plane of the tetragonal unit cell of the MnGa and MnAl are 0.272 nm and 0.277 nm, respectively, and c_0 along the c-axis are 0.369 nm and 0.354 nm, respectively. On the other hand, both NiGa and NiAl with stoichiometric composition are nonmagnetic intermetallics, with cubic CsCl-type crystal structures having the lattice constant a_0 of 0.289 nm. Since the a_0 values of these transition metal (TM) - group III intermetallics are close to half (0.283 nm) the lattice constant of GaAs, one can expect that both MnGa/NiGa and MnAl/NiAl heterostructures should be compatible in heteroepitaxy with GaAs and related III-V semiconductors, with the desired "cube-on-cube" crystal orientations of $[110(001)]$ TM-III // $[110(001)]$ GaAs.

The growth of MnGa/NiGa and MnAl/NiAl SLs on GaAs (001) substrates was performed with a conventional III-V MBE machine (Riber-2300) equipped with Mn and Ni effusion cells. Schematic sample structures are shown in Fig. 1. Since the details of the MBE growth and characterizations are described in recent publications [8][9], we briefly summarize the growth procedure here. After growing a 100 nm-thick undoped GaAs buffer layer at 580°C on the semi-insulating GaAs substrate, the substrate temperature T_s was cooled to 200°C - 220°C while completely eliminating the As flux in the growth chamber. The Ni shutter was opened to deposit one monolayer (ML) of Ni on $c(4 \times 4)$ GaAs surface, and then Ni and Ga were codeposited to grow n MLs of NiGa, followed by the codeposition of Mn and Ga to grow m MLs of MnGa. The Ni/Ga and Mn/Ga ratio were set to 50/50 and 60/40, respectively. After growing the MnGa/NiGa SLs with p periods at 200 - 220°C, a postgrowth annealing was done at 300°C for 1 - 2 minutes to improve the structural and magnetic properties of the MnGa/NiGa SLs [8]. The sample structure and the growth process of the MnAl/NiAl SLs are similar to that of the MnGa/NiGa, but the metallic layers of aluminides were grown on a 5 nm-thick AlAs layer and the growth temperature and postgrowth annealing temperature were higher, 250°C and 350°C, respectively [9]. Throughout the growth, the reflection high energy electron diffraction (RHEED) patterns were very streaky and sharp, indicating that epitaxial monocrystalline metallic layers with good quality are successfully grown. Figures 1 (a) and (b) also show cross sectional transmission electron microscopy (TEM) images of the MnGa/NiGa SL with $m=n=6$ and $p=5$ and the MnAl/NiAl SL with $m=n=3$ and $p=10$, respectively, giving the direct evidence of the successful formation of the compositional SLs with atomically abrupt and smooth interfaces. We have confirmed the "cube on cube" epitaxial relationship as expected, where the c-axis of the tetragonal MnGa and MnAl is aligned perpendicular to the film plane, by these RHEED and TEM analyses. From the TEM diffractions, both the MnGa and the MnAl in the SLs are found to have reduced tetragonality, with the c_0 of 0.35 nm (MnGa) and 0.33-0.34 nm (MnAl), the values smaller than those of bulk. This reduced tetragonality influences on the magnetic properties, particularly on the coercive field of the ferromagnetic films.

MnGa/NiGa Superlattices on GaAs: Magnetic and Magnetotransport Properties

To investigate the magnetic properties, we have performed magnetization measurements at room temperature by using vibrating sample magnetometry (VSM). The M-H curves of the MnGa/NiGa SLs measured by VSM show square-like hysteresis loops for the magnetic field applied perpendicular to the film plane.

indicating the perpendicular magnetization of the SL samples. This perpendicular magnetization is desired for many interesting device applications, including high density non-volatile memory coupled with underlying high speed III-V electronics and photonics. Table I shows the magnetic properties of the $(\text{MnGa})_m/(\text{NiGa})_n$ SLs with p periods, in comparison with those of a single 100-nm-thick $\text{Mn}_{0.5}\text{Ga}_{0.5}$ film [6] and a single 100-nm-thick $\text{Mn}_{0.5}\text{Ni}_{0.5}\text{Ga}_{0.5}$ alloy film [7], grown on

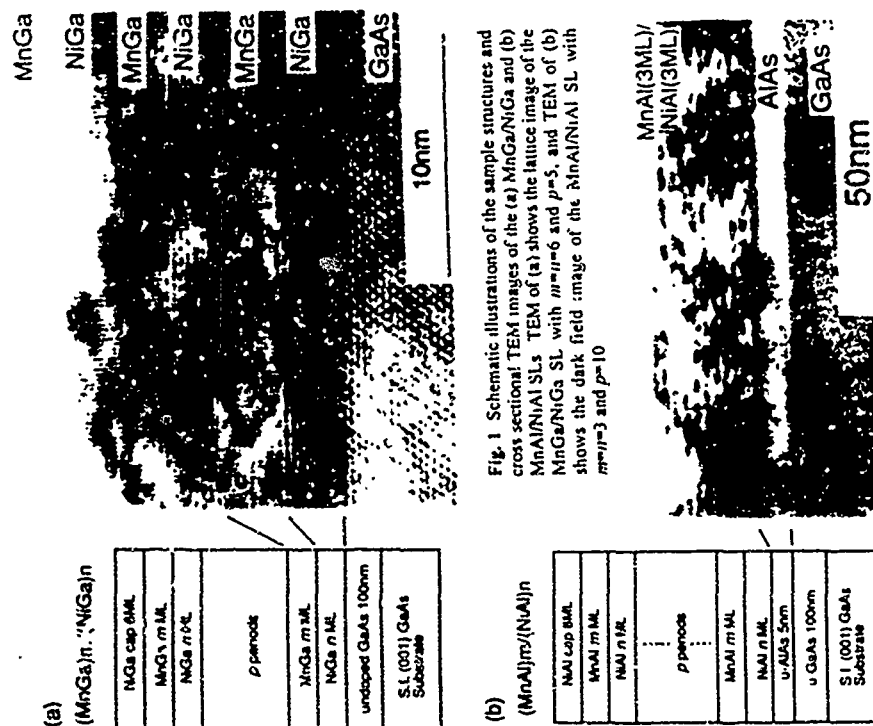


Fig. 1 Schematic illustrations of the sample structures and cross sectional TEM images of the (a) MnGa/NiGa and (b) MnAl/NiAl SLs. TEM of (a) shows the lattice image of the MnGa/NiGa SL with $m=n=6$ and $p=5$, and TEM of (b) shows the dark field image of the MnAl/NiAl SL with $m=n=3$ and $p=10$.

Formation of $\text{Mn}_x\text{Ga}_{1-x}$ and MnAl/NiAl Magnetic Superlattices on GaAs

In the bulk, both $\text{Mn}_x\text{Ga}_{1-x}$ and $\text{Mn}_x\text{Al}_{1-x}$ with the Mn content x around 0.6 have ferromagnetic phase with tetragonal crystal structure. The tetragonal MnGa is a thermodynamically stable phase, while the tetragonal MnAl is a metastable phase. The easy

m (MLs)	10	6	6	6	6	Mn _{0.1} Ni _{0.9} Ga _{0.1}
n (MLs)	10	6	1	10nm	10nm	
p	3	5	5			
M_r (emu/cm ³)	267	302	286	113 - 225	1.4	
H_c (kOe)	2.60	2.29	5.35	1.30 - 3.15	1.27	

Table 1. Magnetic properties of the (MnGa)₁₀(NiGa)₁₀ SLs with p periods, in comparison with those of a single 10nm-thick MnGa film and a single 10nm-thick Mn_{0.1}Ni_{0.9}Ga_{0.1} alloy film, grown on (001) GaAs by MBE. The values of remanent magnetization M_r and coercive field H_c measured at room temperature are shown.

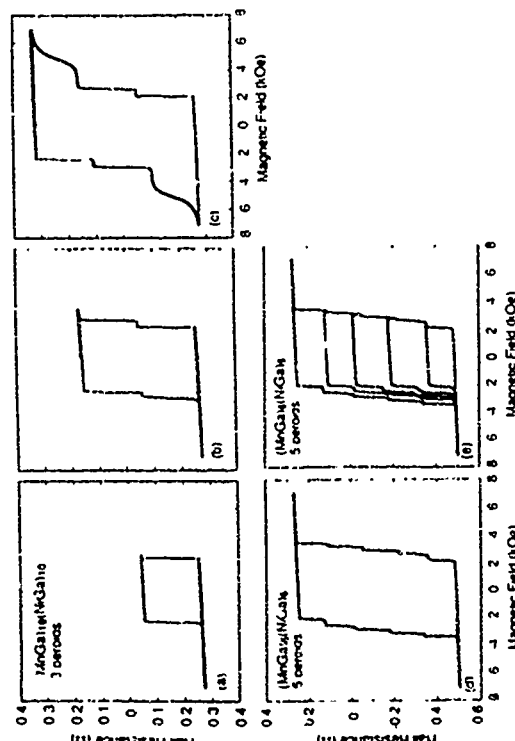


Fig. 2. EHE hysteresis loops of the MnGa/NiGa SLs with (a)-(c) $m=10$ and $p=3$ and with (d)-(e) $m=10$ and $p=5$, measured at room temperature with differing the maximum values H_{max} of the applied magnetic field perpendicular to the substrate plane. The H_{max} value was set to (a) 2.7 kOe, (b) 4.0 kOe and (c) 7.0 kOe for the (MnGa)₁₀(NiGa)₁₀ SL with 3 periods, and (d) 7.0 kOe and (e) 2.6 - 7.0 kOe for the (MnGa)₁₀(NiGa)₁₀ SL with 5 periods.

(001) GaAs by MBE. All these SLs and thin films showed square-like M-H curves with perpendicular magnetization. The values of remanent magnetization M_r of the present MnGa/NiGa SLs are 267 - 302 emu/cm³, when normalized by the total volume of the ferromagnetic MnGa layers, the values which are higher than those of the MBE-grown 10nm-

thick MnGa thin film and 10nm-thick MnNiGa alloy thin film. This is probably because the crystal quality of the epitaxial layers of the SLs is better than that of the MnGa and MnNiGa films, as indicated by the RHEED studies [6][8].

It is known that the Hall effect measured in a ferromagnetic film has an "extraordinary" component resulting from the asymmetric s-d scattering of carriers with magnetic atoms. This extraordinary Hall effect (EHE) is a very powerful probe to characterize the properties of perpendicularly magnetized thin films, because the Hall resistivity measured in a patterned Hall bar is proportional to the magnetic moment perpendicular to the film plane [10]. We have found that EHE is more sensitive, and therefore, more suitable than VSM for clearly detecting the detailed magnetic structures in such SLs with periods of only several monolayers.

Figures 2 show the EHE hysteresis loops of the MnGa/NiGa SLs with (a)-(c) $m=10$ and $p=3$, and with (d)-(e) $m=10$ and $p=5$, measured at room temperature with differing the maximum values H_{max} of the applied magnetic field perpendicular to the substrate plane. The H_{max} value was set to (a) 2.7 kOe, (b) 4.0 kOe and (c) 7.0 kOe for the (MnGa)₁₀(NiGa)₁₀ SL with 3 periods, and (d) 7.0 kOe and (e) 2.6 - 7.0 kOe for the (MnGa)₁₀(NiGa)₁₀ SL with 5 periods. When the applied field is as high as 7.0 kOe, the entire magnetic structure is saturated for both SLs. Note that the EHE hysteresis loops have evenly-spaced multiple steps when H_{max} is 7.0 kOe, as shown in Fig. 2 (c) and (d), where three steps and five steps are clearly seen in the EHE loops of MnGa/NiGa SLs with 3 periods and 5 periods, respectively. Since the number of steps in the loops are the same as the number of ferromagnetic MnGa layers, each step is formed by the reversal of magnetization in one of the MnGa layers. This is because the MnGa layers have different coercive forces H_c from one to another. In principle, these phenomena can be applied to multi-level signal recording, which can lead to much higher storage density. The capability of reading and writing multi-level signals is demonstrated for the MnGa/NiGa SL with 3 periods in Fig. 2 (a) - (c), where four different static values of Hall resistance are realized with varying the value of H_{max} . Likewise, in Fig. 2 (e), six different values of Hall resistance are shown for the MnGa/NiGa SL with 5 periods.

The possible origin of the different H_c values in the MnGa layers of the SLs is the difference in lattice strain. Since the bulk a values of tetragonal MnGa and CsCl-type NiGa have the lattice mismatch of -3.8% and -2.1%, respectively, the c/a ratio in the lattice of the epitaxial MnGa layers of the SLs can be slightly different due to the difference in strain, leading to the difference in H_c . Another possible reason for the different H_c may be the difference in the interface roughness or defect density. The full understanding of the mechanisms and the artificial "design" of the EHE hysteresis will be interesting future issues.

MnAl/NiAl Superlattices on AlAs/GaAs: Magnetic and Magnetotransport Properties

To investigate the magnetic properties of another type of magnetic superlattices, MnAl/NiAl SLs, we have performed ⁵⁷Fe measurements at room temperature. Table II shows the values of remanent magnetization M_r and coercive field H_c for various (MnAl)₁₀(NiAl)₁₀ SLs with p periods, in comparison with those of a single 10nm-thick Mn_{0.1}Ni_{0.9}Al_{0.1} film and a single 10nm-thick Mn_{0.1}Ni_{0.9}Al_{0.1} alloy film, grown on AlAs/GaAs by MBE. For the magnetic field applied perpendicular to the substrate, all these SLs and thin films showed M-H curves with almost perfect squareness, indicating strong perpendicular magnetization. The M_r values of the present MnAl/NiAl SLs, when normalized by the total thickness of the MnAl, are higher than those of the MnAl and the MnAl thin films, and even higher than those of MnGa/NiGa SLs (see table I and II). On the other hand, the H_c values of the MnAl/NiAl SLs are relatively low. The lower coercivity of the SLs is due to the reduced tetragonality, as evidenced by the TEM analysis, of the MnAl layers in the SLs, which is caused by the strain.

Table II Magnetic properties of the $(\text{MnAl})_{1-x}(\text{NiAl})_x$ SLs with p periods in comparison with those of a single 10nm-thick MnAl film and a single 10nm-thick $\text{Mn}_{0.5}\text{Ni}_{0.5}\text{Al}$ alloy film, grown on AlAs/GaAs by MBE. The values of remanent magnetization M_r and coercive field H_c measured at room temperature are shown

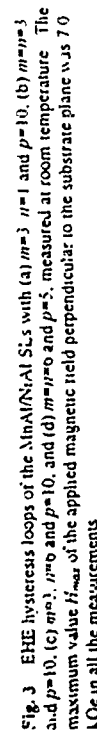


Fig. 5 shows EHE hysteresis loops of the MnAl/NiAl SLs with (c) $m=3$, $n=1$ and $p=10$, (b) $m=1$, $n=3$ and $p=10$, (c) $m=3$, $n=6$ and $p=10$, and (d) $m=10$ and $p=n$, measured at room temperature. Here the maximum value H_{max} of the applied magnetic field perpendicular to the substrate plane was 70 Oe in all the measure, as EHE loops of the MnAl/NiAl SLs have a non-rectangular EHE characteristics of the MnGa/NiAl SLs.

This set of magnetic properties of the present SLs, strong perpendicular anisotropy, perfect generated fields in combination with high current pulses

We have studied room-temperature magnetic properties and EHE characteristics of two kinds of MBE-grown magnetic SLs of metallic compounds, MnGa/NiGa and NiAl/NiAl . Strong perpendicular magnetization have been revealed for both types of SLs, with M_r higher than those of MBE-grown NiGa , NiAl and related alloy thin films. The EHE hysteresis loops of the MnGa/NiGa SLs are found to have multiple steps. These new epitaxial magnetic SLs show rectangular EHE hysteresis loops with perfect squareness. These new epitaxial magnetic SLs, having appealing magnetic properties as well as good compatibility with existing III-V semiconductor technology, offer a wide range of possibilities for device applications such as non-volatile memory coupled with III-V electronics/circuitronics.

Acknowledgments
The authors wish to thank B. Philips, D.M. Hwang, and L.T. Florez for their valuable cooperations. One of the authors (M.T.) acknowledges financial support by the Japan Society for the Promotion of Science (JSPS).

References
(1) For example, Materials Research Society Symp Proc Vol 221 "Heteroepitaxy of Dissimilar Materials" edited by R. Farrow, J. Hathison, P. Peercy and A. Zangwill.

- 989-

Studies of GaSb-capped InAs/AlSb quantum wells by resonant Raman scattering

J. Wagner, J. Schmitz, M. Mauer, J.D. Rolsion, and P. Koidl
 Fraunhofer-Institut für Angewandte Festkörperphysik,
 Tullastraße 72, D-79105 Freiburg, Federal Republic of Germany

Abstract

We have used resonant Raman scattering to study GaSb-capped AlSb/InAs/AlSb quantum wells grown by molecular-beam epitaxy. The shutter sequence for the growth of the InAs/AlSb heterointerfaces was such as to promote the formation of an InSb-like interface. Scattering by an InSb-like mode at $\approx 190 \text{ cm}^{-1}$ is found to resonate at approximately the InAs $E_1/E_1 + \Delta_1$ gap energy, supporting its assignment to an interface mode. Resonance effects in scattering by longitudinal optical (LO) phonons enabled us also to distinguish between scattering by the almost degenerate LO phonon modes in the InAs quantum well and in the GaSb cap layer. The GaSb and the AlSb one-LO phonon spectra indicate the unintentional incorporation of As at concentrations up to 18-19 % in the GaSb and AlSb layers for As background pressures in the growth chamber exceeding 10^{-9} Torr. The incorporation of As was confirmed independently by secondary ion mass spectroscopy.

1. Introduction

Nearly lattice matched InAs/AlSb quantum wells are interesting semiconductor heterostructures for the study of two-dimensional electron systems because of the large conduction band offset of 1.35 eV and the small electron effective mass in the InAs well [1]. Potential applications for such heterostructures include high-speed field-effect transistors [2]. Across the InAs/AlSb heterointerface there is no common anion or cation, resulting in two different types of interfaces, either InSb- or AlAs-like. It has been shown that the in-plane transport properties of the two-dimensional electron gas (2DEG) formed in the InAs quantum well depend critically on the type of heterointerface [3].

Raman spectroscopy has proven to be a valuable experimental technique for the analysis of the InAs/AlSb heterointerface via inelastic light scattering by interface modes [4-6]. However, all these studies published so far are based on Raman spectra recorded with optical excitation at a fixed photon energy. On the other hand, it is known from numerous studies on GaAs/Al_xGa_{1-x}As quantum wells that, when the optical excitation is tuned into resonance with an electronic interband transition, resonance effects in the Raman scattering cross-section can enhance the Raman signal considerably, and thus facilitate a more detailed study of vibrational modes in such heterostructures [7].

In the present study we have used resonant Raman scattering by longitudinal optical (LO) phonons and by interface modes to analyse GaSb-capped InAs/AlSb quantum wells grown by molecular-beam epitaxy (MBE). We show that tuning the incident

photon energy into resonance with an appropriate band-gap energy of one of the constituents allows the vibrational properties of that particular layer to be probed with a high degree of selectivity. Exploiting such resonance effects, a splitting of the GaSb LO phonon mode and a high-frequency shift of the AlSb LO phonon is resolved for As background pressures in the growth chamber exceeding 10^{-9} Torr, indicating the unintentional incorporation of As at concentrations up to 18-19 % in the AlSb and GaSb layers.

2. Results and Discussion

Sample growth was performed by solid-source MBE on (100) GaAs substrates. InAs/AlSb single quantum wells with a width of 15 nm were grown on a buffer layer consisting of 1 μm of AlSb and a 10-period 2.5nm GaSb/2.5nm AlSb superlattice. The InAs quantum well was sandwiched between a 40 nm wide AlSb barrier on the substrate side and a 10 nm wide AlSb barrier on the surface side. The top barrier was capped with 10 nm of GaSb to prevent the oxidation of the underlying AlSb. The shutter sequence for the growth of the InAs/AlSb heterointerfaces was chosen such as to promote the formation of InSb-like interfaces [3]. Growth of the quantum well structure was performed at a substrate temperature of 300 °C. Three different samples were investigated, differing only in the As background pressure during the deposition of the AlSb and GaSb layers. Sample A was grown using a conventional As effusion cell producing an As₄ molecular beam and an As background pressure of 2×10^{-8} Torr with the shutter closed. For the growth of sample B and C a valved cracker cell was used as the source of an As₂ molecular beam. Sample B was grown with the valve open resulting in an As background pressure of 4×10^{-9} Torr. During the deposition of the AlSb and GaSb layers of sample C both the shutter and the valve were closed, leading to an As background pressure of 5×10^{-10} Torr.

In Fig. 1, low-temperature (77 K) Raman spectra of sample A are plotted. The spectra were excited at 2.71 eV, close to the E_1 band-gap resonance of InAs [8], and recorded in backscattering from the (100) growth surface. Spectra were recorded with the polarizations of the incident and scattered light selected to be either parallel to the same (100) crystallographic direction [$x(z,z)\bar{x}$] or perpendicular to each other [$x(y,z)\bar{x}$]. In polarized spectra [$x(z,z)\bar{x}$], intrinsic two-LO phonon scattering is allowed, whereas one-LO phonon scattering by the deformation potential mechanism is symmetry-forbidden. For resonant excitation, however, intrinsic one-LO phonon scattering via the Fröhlich mechanism, as well as defect-induced one-LO phonon scattering, contribute to the Raman spectrum [9]. The present spectra show one-LO phonon scattering by the InAs quantum well and by the AlSb barriers, as well as two-LO phonon scattering from InAs. The presence of an InAs two-LO phonon signal, and the observation that InAs one-LO phonon scattering is stronger for parallel than for crossed polarizations, show clearly the resonant enhancement of LO phonon scattering from the InAs quantum well [8]. The non-resonantly excited AlSb one-LO phonon signal, in contrast, is, as expected [9], most intense for crossed polarizations. For this scattering configuration [$x(y,z)\bar{x}$], the spectrum shows also a

peak at 190 cm^{-1} which is assigned to scattering by a longitudinal InSb interface mode [IF(InSb)] [4,5].

The phonon energy dependence of scattering by the InSb-like interface mode is shown in Fig. 2, which presents three room-temperature Raman spectra excited at photon energies varying from 2.41 to 2.71 eV. The InSb-like interface mode is strongest in intensity for excitation at 2.71 eV, matching the $\text{InAs } E_1/E_1 + \Delta_1$ band gap resonance, and is only weakly resolved for 2.41 eV excitation. This resonance behaviour is consistent with the assignment to an interface mode, since scattering by such modes is expected to be strongest for excitation in resonance with interband transitions of the quantum well [7]. From studies on ultrathin Ge layers embedded in crystalline Si it is known that for layer thicknesses exceeding three to four monolayers, Raman scattering from the embedded layer shows a resonance behaviour similar to that of the corresponding bulk material [10]. For the present case of InSb a bulk-like resonance behaviour would lead to an enhancement of the InSb-like mode for excitation in resonance with the $E_1 + \Delta_1$ band gap at $\approx 2.4 \text{ eV}$ [11], contrary to the experimental observations. Thus, the measured resonance behaviour of the InSb-like interface mode places an upper limit of three to four monolayers on the thickness of the interfacial layer producing this mode.

Fig. 3 shows a series of depolarized Raman spectra $(\chi_{yy} z \chi_z)$ recorded from samples A, B, and C for excitation in resonance with the $\text{GaSb } E_1 + \Delta_1$ band gap [11]. There are pronounced resonance effects in the Raman spectra of sample A as seen from the comparison of the spectrum recorded for excitation at 2.41 eV (Fig. 3 a), which is well below the InAs E_1 gap resonance, and that recorded with 2.71 eV excitation (Fig. 1, lower curve) in resonance with that band gap [8]. For 2.41 eV excitation the relative strength of the InAs one-LO phonon line is drastically reduced, as compared to excitation at 2.71 eV, and two peaks appear above and below the InAs one-LO phonon line. These new peaks arise from one-LO phonon scattering in the GaSb cap layer. In the spectrum excited at 2.71 eV these two GaSb-related phonon peaks are only just resolved as weak shoulders on either side of the InAs one-LO phonon peak. Two GaSb one-LO phonon modes, namely a GaSb-like ("GaSb") and a GaAs-like ("GaAs") mode [12], are observed because of the formation of $\text{GaSb}_{1-x}\text{As}_x$ rather than binary GaSb. The formation of a pseudo-ternary alloy is due to the unintentional incorporation of As caused by the relatively high As background pressure. The InSb one-LO phonon line shows no splitting but is shifted to higher frequencies, as compared to binary InSb, indicating the formation of $\text{InSb}_{1-x}\text{As}_x$ [13]. The difference in mode behaviour is consistent with the reported single-mode behaviour for $\text{InSb}_{1-x}\text{As}_x$ [13], which is in contrast to the partial two-mode behaviour found in $\text{GaSb}_{1-x}\text{As}_x$ [12].

Upon reduction of the As background pressure (sample B), the splitting of the two $\text{GaSb}_{1-x}\text{As}_x$ LO phonon modes is reduced (Fig. 3 b), and for the structure grown at the lowest background pressure (sample C) just one GaSb one-LO phonon line is resolved (Fig. 3 c). From the splitting between the GaSb-like and the GaAs-like

phonon modes As concentrations of 19 and 7 % are deduced for samples A and B, respectively [12]. The InSb one-LO phonon line shifts to lower frequencies with decreasing As background pressure. From the measured shift of the InSb one-LO phonon line (Fig. 3), As concentrations of 18 and 8 % are inferred for samples A and B, respectively, in good agreement with the values extracted above from the $\text{GaSb}_{1-x}\text{As}_x$ mode splitting. The InSb LO phonon frequency observed in sample C, in contrast, is that of binary InSb [13].

For an independent confirmation of the above findings, secondary ion mass spectroscopy (SIMS) has been used for a semi-quantitative analysis of the As incorporation in the InSb layers of the present samples. The measurements were carried out using a Cs^+ primary ion beam at an energy of 3 keV impinging on the sample surface at an angle of 45 degrees. CsX^+ molecular ions were detected since for these ions the SIMS matrix effect is small. Fig. 4 shows SIMS depth profiles of CsAs^+ and, for reference purposes, of CsAl^+ . For all three samples, there is a maximum in the CsAs^+ signal at the expected depth of the InAs quantum well, accompanied by a minimum in the CsAl^+ signal intensity. However, the CsAs^+ signal observed in the regions above and below the InAs layer, which consist of nominally binary InSb, increases strongly with increasing As background pressure. There is a difference of almost three orders of magnitude in the As background concentration between the structure grown at the highest As background pressure (sample A) to that grown at the lowest pressure (sample C). In the latter case the As signal drops below the detection limit of the SIMS apparatus. The CsAs^+ signal intensity for sample B is only about one third of that measured for sample A (Fig. 4 a and b), which compares favourably with As concentrations of 8 and 18 %, respectively, measured by Raman spectroscopy.

The present finding of a significant As incorporation in the GaSb or InSb layers of MBE grown InAs/InSb or InAs/GaSb heterostructures, for As background pressures in the growth chamber exceeding 10^{-9} Torr, is consistent with recent Raman spectroscopic [6] and SIMS data [14] reported by other groups. On the other hand, the present results clearly demonstrate that, using a valved cracker As effusion cell, the As background pressure can be reduced significantly, facilitating the growth of truly binary/binary InAs/InSb and InAs/GaSb heterostructures.

3. Conclusions

We have shown how resonant Raman scattering by LO phonons at the interface modes can be used to analyse GaSb-capped InAs/InSb quantum well structures. Tuning the incident photon energy into resonance with an appropriate band-gap energy of one of the constituents allows the vibrational properties of that particular layer to be probed with a high degree of selectivity. The LO phonon spectra of GaSb and InSb are found to depend critically on the As background pressure during layer growth, which indicates the unintentional incorporation of As at concentrations up to 18-19 % for background pressures exceeding 10^{-9} Torr.

Acknowledgements

We would like to thank G. Bihlmann for valuable technical assistance in the MBE growth, F. Pohl for expert technical support of the Raman measurements, and F. Fuchs for helpful discussions and comments.

References

1. See, e.g., A. Nakagawa, H. Kroemer, and J.H. English, *Appl. Phys. Lett.*, **54**, 1803 (1989); S. Ideshita, A. Furukawa, Y. Mochizuki, and M. Mizuta, *Appl. Phys. Lett.*, **60**, 2549 (1992); Ch. Gauer, J. Senba, A. Wixforth, J.P. Kotthaus, C. Nguyen, G. Tuttle, J.H. English, and H. Kroemer, *Semicond. Sci. Technol.*, **8**, S137 (1993); M.J. Yang, P.J. Lin-Chung, R.J. Wagner, J.R. Waterman, W.J. Moore, and B.V. Shanabrook, *Semicond. Sci. Technol.*, **8**, S129 (1993).
2. G. Tuttle and H. Kroemer, *IEEE Trans. Electron Devices* **ED-34**, 2358 (1987); J.D. Werking, C.R. Bolognesi, L.D. Chang, C. Nguyen, E.L. Hu, and H. Kroemer, *IEEE Electron. Device Lett.*, **13**, 164 (1992).
3. G. Tuttle, H. Kroemer, and J.H. English, *J. Appl. Phys.*, **67**, 3032 (1990).
4. I. Sela, C.R. Bolognesi, L.A. Samoyla, and H. Kroemer, *Appl. Phys. Lett.*, **60**, 3283 (1992).
5. M. Inoue, M. Yano, H. Furuse, N. Nasu, and Y. Iwai, *Semicond. Sci. Technol.*, **8**, S121 (1993).
6. J. Spitzer, H.D. Furtis, P. Fichtegoin, M. Cardona, B. Altar, and H. Kroemer, *Appl. Phys. Lett.*, **62**, 2274 (1993).
7. See, e.g., B. Jusserand and M. Cardona, in *Light Scattering in Solids V*, eds. M. Cardona and G. Güntherodt (Springer, Berlin, 1989), p. 49.
8. R. Carlos, N. Saint-Cricq, J.B. Renucci, A. Zwick, and M.A. Renucci, *Phys. Rev. B*, **22**, 6129 (1980).
9. See, e.g., M. Cardona in *Light Scattering in Solids II*, eds. M. Cardona and G. Güntherodt (Springer, Berlin, 1982), p. 19.
10. J.C. Tsang, S.S. Iyer, J.A. Calise, and B.A. Ek, *Phys. Rev. B*, **40**, 5886 (1989).
11. See, e.g., W. Richter in *Springer Tracts in Modern Physics*, Vol. 78, ed G. Höhler (Springer, Heidelberg, 1976), p. 121.
12. T.C. McGlimm, T.N. Krabach, M.V. Klein, G. Bajor, J.E. Greene, B. Kramer, S.A. Barnett, A. Lasras, and S. Gorbalkin, *Phys. Rev. B*, **33**, 8396 (1986).
13. I. Sela, C.R. Bolognesi, and H. Kroemer, *Phys. Rev. B*, **46**, 16 142 (1992).
14. J.T. Zborowski, W.C. Fan, T.D. Golding, A. Vigilante, P.C. Chow, H.D. Shih, and J.M. Anthony, *J. Appl. Phys.*, **71**, 5908 (1992).

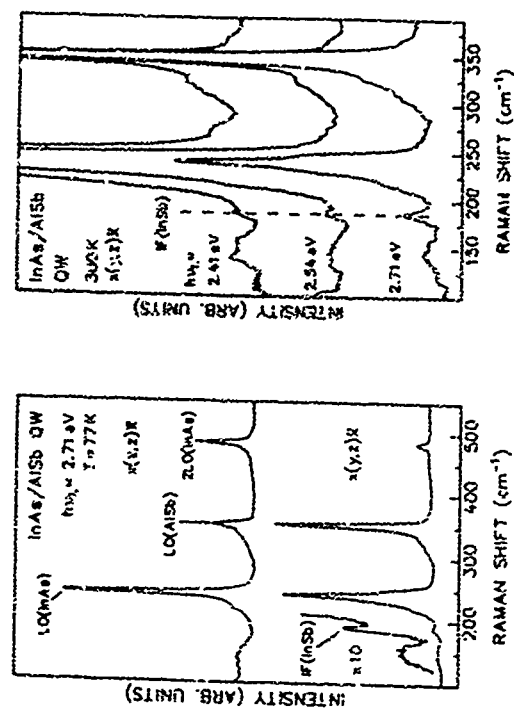


Fig. 1 (left) Low-temperature (77 K) Raman spectra of an InAs/AlSb single quantum well (sample A). The spectra, excited in resonance with the InAs E_1 band gap, were recorded with the polarization of the scattered light either parallel $[x(z, z)]$ or perpendicular to that of the incident light $[x(y, z)]$ (bottom). Here x , y , and z denote (100) crystallographic directions.

Fig. 2 (right) Room-temperature Raman spectra of an InAs/AlSb single quantum well (sample A) recorded for different incident photon energies $h\nu_i$ indicated in the figure. The spectra were recorded with the polarization of the scattered light perpendicular to that of the incident light $[x(y, z)]$.

WeAs

Luminescence up-conversion by Auger process at InP-AlInAs type II interfaces

A. Tikhov*, W. Sordel*, J.P. Andre**, P. Vuisin* and M. Voss*

*Laboratoire de Physique de la Matière Condensée de l'Ecole Normale Supérieure
24 rue Lhomond, F75005 Paris, France

**Laboratoire d'Electronique Philips
22 av. Descartes, F94453 Limeil-Brevannes, France

Abstract

Luminescence of bulk InP at 1.42 eV is observed when exciting a type II InP-AlInAs single heterojunction above the heterojunction bandgap at 1.23 eV. We show that this energy up-conversion results from Auger process producing high energy holes which redistribute over the heterostructure and recombine with native electrons in the InP layer.

Auger processes in semiconductors have both a fundamental interest as three-particle recombination mechanisms and a practical importance as the main limitation to radiative efficiency under high injection. For instance in semiconductor light-emitting devices [1], Auger constants are usually determined somewhat indirectly from the saturation of photo-luminescence intensity when increasing the pump intensity [2-4]. The nature of the main process (one electron-two holes, two electrons-one hole...) can also be determined by comparing the situation of p-type and n-type materials. Calculations [5] of Auger recombination rates are uneasy because they involve high-energy states in the conduction or valence band, which cannot be described by simplified k.p models. Auger effects in bulk materials like GaAs [2,3], GaSb [2,4] and InGaAs [6] have been carefully studied, but the case of semiconductor heterostructures, in spite of the technological importance of heterostructure lasers, is not completely clarified. It seems, however, that in the case of InGaAs-based quantum wells, Auger coefficients are close to the bulk value [6]. Type II heterostructures offer a completely new situation with respect to radiative as well as Auger recombination processes, since electrons and holes are spatially separated and recombination is allowed only by the weak overlap of the wavefunction tails outside the wells where they are localized. Recently, we observed low threshold laser emission in InP-AlInAs superlattices [7], which are certainly the most "regular" type II systems, with F-electrons (holes) localized in InP (AlInAs) [8]. This intriguing observation, which seems to contradict the standard expectation as well as a theoretical prediction of enhanced Auger rates [9], due to the increased accessible phase-space, is a strong motivation to study Auger effects in these materials. In addition, we anticipated that the type II configuration offers a unique opportunity to detect directly Auger hot carriers through a luminescence up-conversion effect: hot carriers produced by Auger events can indeed recombine over the heterostructure and recombine with the other particles, which are confined in the "barrier". Hence, Auger carriers will induce barrier luminescence, possibly at a higher energy than the pump itself. Here, we report first results of the investigation of the "Auger fountain" effect in a InP-AlInAs single type II heterojunction.

Our sample was grown by MOCVD, using a schematic in Fig. 1a, simply consists of a 100 Å thick InP buffer layer undoped, with a n-type residual doping in the 10¹⁴ cm⁻³ range, deposited on a p⁺ InP substrate, and followed by a 1000 Å AlInAs layer, non-intentionally doped in n-type residual doping in the 10¹⁶ cm⁻³ range. The free surface is protected by a 50 Å InGaAs cap. Calculations [10] of the charge transfer at the heterojunction for a conduction band offset ΔE_c = 470 meV [8] and a doping level N_D = 2 · 10¹⁶ cm⁻³ in the AlInAs layer yields a two-dimensional electron gas with an

-694-

Fig. 3 (left) Depolarized (x(y,z)) low-temperature (77 K) Raman spectra of an InAs/AlSb single quantum well excited at 2.41 eV. The spectra were recorded (a) from sample A, (b) from sample B, and (c) from sample C with the As background pressure in the growth chamber decreasing from sample A to C.

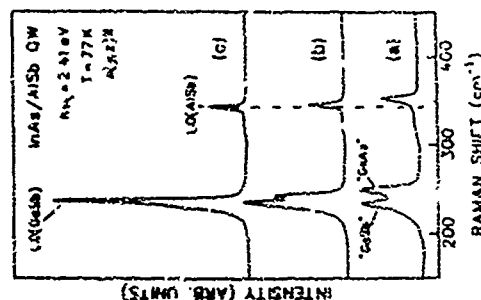
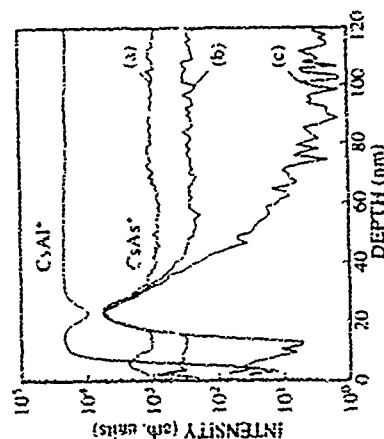


Fig. 3 (right) SIMS depth profiles of Al (CsAl⁺) and of As (CsAs⁺) for (a) sample A, (b) sample B, and (c) for sample C. The As background pressure in the growth chamber decreases from sample A to C.



-693-

areal density $n_s = 3 \times 10^{11} \text{ cm}^{-2}$, and corresponding to an electron Fermi level of 10 meV. The electric field at the interface is 30 kV/cm. Electron and heavy hole confinement energies in their respective quasi-mangular quantum wells are 30 meV and 20 meV respectively.

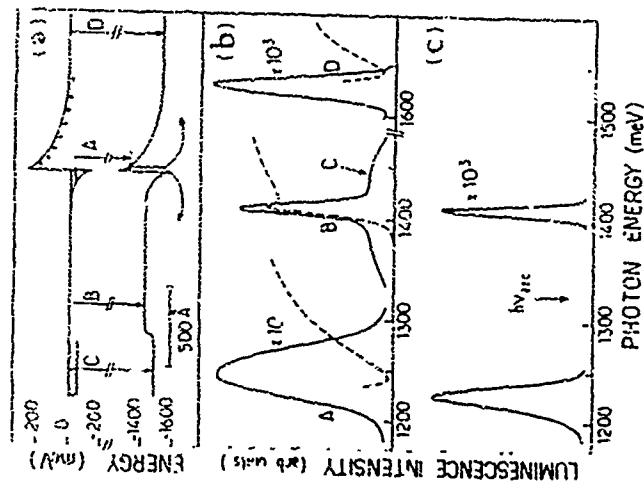


Fig. 1: (a) Sketch of the band structure of the InP-AlInAs heterojunction. (b) Luminescence spectrum (solid line) under low power excitation with an He-Ne laser, and excitation spectra (dashed lines) of the various lines (B, C, D). (c) Luminescence spectrum with a 20 mW excitation power at $h\nu_2 = 1.325 \text{ eV}$, showing the up-converted InP luminescence.

The low temperature (2K) luminescence spectrum under low power excitation by a He-Ne laser is shown in Fig. 1b. A strong line "A", corresponding to recombination through the type II interface, is observed at 1.23 eV. The luminescence from the InP buffer layer is seen as a sharp peak "B" at 1.41 eV, emerging from a broad background "C" due to the substrate luminescence. In addition, a weak luminescence line "D" from the Al_{0.33}In_{0.67}As layer (which is 5% Al-rich with respect to the lattice matched composition $x=0.48$) is observed at 1.63 eV. Excitation spectra [11] of these different lines (dashed lines in Fig. 1b) exhibit the absorption gaps associated with the InP and AlInAs layers. More surprisingly, the gap associated with the interface can also be measured directly from the excitation spectrum of the 1.23 eV luminescence line, in spite of the very small absorption coefficient associated with the type II single heterojunction. From the calculation of the ground-state wavefunction overlap, the threshold absorption should indeed be as small as 3×10^{-5} , to be compared with $\sim 10^{-2}$ in the case of a type I quantum well.

In the following, we discuss results obtained using a Ti:Sapphire tunable laser with a power of a few tens of mW and tightly focused on the sample using a long focal (0.8 m) lens. The diameter of the exciting spot, determined as the product of the normal divergence of the laser beam ($1.2 \times 10^{-4} \text{ rad}$) by the focal length, is 1 mm. For an excitation energy above the InP bandgap ($h\nu_1 = 1.51 \text{ eV}$), the luminescence spectrum shows very little dependence on the excitation power. In particular, as shown in Fig. 2a, the integrated intensities of the InP ("B") and interface ("A") lines vary linearly with the pump power over several decades. This proves that the radiative efficiency is nearly constant. It is also noteworthy that the lineshapes do not change in this range of excitation powers. However, when the sample is excited at $h\nu_2 = 1.32 \text{ eV}$ (ie between the InP and the interface bandgaps), a very unusual feature can be observed: as shown in Fig. 1c, the luminescence from the InP buffer layer can still be observed, although much weaker than before. We now observe a quadratic dependence of the "B" line on the laser intensity while the dominating interface line "A" still shows the linear dependence (Fig. 2b). As great care has been taken to ensure perfect spectral filtering of the laser beam, this InP luminescence clearly corresponds to an up-conversion of the exciting photon energy, and the laser intensity dependence proves that this is due to a non-linear effect. Various mechanisms can be envisaged, like two-photon absorption, intra-band absorption by photo-carriers, or, more likely, Auger processes.

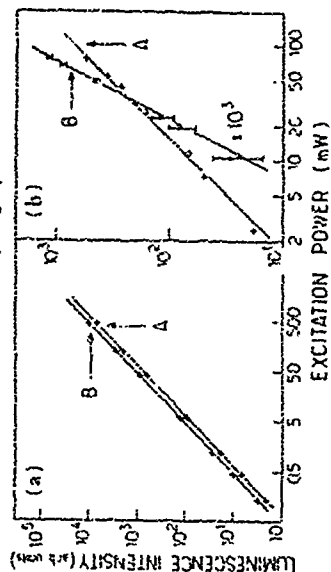


Fig. 2: Integrated intensities of the interface "A" and InP "B" luminescence lines versus the pump intensity (a) for an excitation energy $h\nu_1 = 1.51 \text{ eV}$ and (b) for an excitation at $h\nu_2 = 1.325 \text{ eV}$

To discriminate between these possible explanations, we have examined the excitation wavelength dependence of the InP luminescence, at a fixed pump intensity. We find that the signal varies like the square of the interface absorption coefficient α_A , deduced from the PLE spectrum of Fig. 1b. Considering that in the range of excitation power density used in our experiment ($< 1 \text{ W/cm}^2$), the areal density of photo-carriers is by far lower than the density of native electrons in the two-dimensional electron gas, this result proves that the up-converted luminescence signal is directly proportional to the square of the photo-hole density p , which rules out intra-band absorption (which would depend linearly on p , hence on α_A) and two-photon absorption, which would not depend on p or α_A . Clearly, the only mechanism which explains the I_{ex}^2 and α_A^2 dependences is a one electron-two hole Auger recombination process. The way we interpret the up-conversion is illustrated in Fig. 1a: Auger recombination processes involving a native electron and two photo-holes provide high energy holes which, during thermalization, are redistributed in the heterostructure. Those falling into the InP side are finally pushed away from the interface by the

electric field, and they thermalize at the top of the InP valence band and recombine there with native electrons (or, possibly, with excess electrons provided by an other Auger process): this is the "Auger fountain" effect.

In order to discuss these results more quantitatively, we use simplified rate equations governing the ratio of the luminescence signals. Under cw excitation, a luminescence signal L can always be written as:

$$L = g \eta G \quad (1)$$

where g is an external coupling constant (which is the same for the A and B luminescence lines), η the radiative efficiency and G the carrier generation rate. For photo-carriers, G is given by:

$$G = \alpha I (1-R) / h\nu \quad (2)$$

where σ is the absorption, $R = 0.3$ the sample reflectivity, I the pump power and $h\nu$ the energy of the exciting photons. For Auger holes, we assume that the generation rate can be written, in formal analogy with the bulk situation, as:

$$G = 0.5 S C_p \eta p^2 \quad (3)$$

where S is the surface of the excited region. As already mentioned, η is essentially constant and equal to the area density of native electrons in the two-dimensional electron gas. The 0.5 factor accounts for the fact that a maximum of only one half of the Auger holes will be fed to the InP buffer layer.

η is clearly different for the interface and the InP luminescences, since the huge difference in absorptions ($\sim 10^{-4}$ and ~ 0.1 , respectively) results in nearly equal integrated intensities. With the superscripts A, B referring to the interface and InP luminescence lines and the subscripts 1, 2 referring to the excitation energies 1.51 eV and 1.32 eV respectively, we thus write four equations:

$$L^A B_{1,2} = g \eta A, B G^A B_{1,2} \quad (4)$$

where $G^A B_{1,2}$ and $G^B B_{1,2}$ are given by Eq. 2 and $G^B B_{1,2}$ by Eq. 3. Finally, we assume that the interface recombination follows an exponential law with a time constant τ^A . Hence, the steady state density of photo-holes is simply:

$$p_{1,2} = G^A B_{1,2} \tau^A / S \quad (5)$$

This system of equations immediately gives the Auger coefficient as:

$$C_p = 2 \frac{L^B_2 L^A_1 \alpha^B_1 \alpha^A_1}{L^A_2 L^B_1 \alpha^A_1 (\tau^A)^2} \frac{1}{\alpha^A_2} \frac{1}{(1-R) I_2} \frac{1}{n} \quad (6)$$

From the interface PLE spectrum, we know that $\alpha^A_1 / \alpha^A_2 = 3$. Besides, the absorption coefficient of bulk InP at 1.51 eV is 10^4 cm^{-1} , hence the absorption by the 1000 Å thick layer is $\alpha^B_1 \approx 0.1$. Equation 6 unfortunately still contains two unknown quantities, α^A_2 and τ^A . In order to determine τ^A we have measured the time decay of the interface luminescence.

using a cavity-dumped Ar⁺ laser delivering ~ 15 ns pulses. The decay curves of the InP (which essentially reflects the exciting pulse) and the interface luminescences are shown in Fig. 3. Although a deconvolution of the two responses is needed for better accuracy, it is clear that the interface luminescence involves a characteristic time constant of ~ 15 ns, which is indeed significantly longer than the decay times usually observed at low temperature in type I heterostructures of bulk materials (< 1 ns).

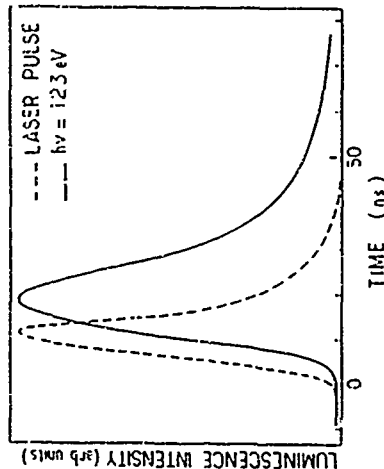


Fig. 3: Time decay of the interface (solid line) and InP luminescences (dashed line). The dashed line essentially represents the shape of the exciting pulse of the cavity dumped Ar⁺ laser, convoluted with the response of our detection. The broadening of the interface response indicates a lifetime $\tau^A \sim 15$ ns.

Unfortunately, the absolute value of the absorption by the interface cannot be measured directly, and our evaluation of C_p has to rely on the theoretical estimate of α^A_2 . As already mentioned, the numerical calculation of the overlap of the ground-state wavefunctions indicates a threshold absorption equal to $3 \cdot 10^{-5}$. The absorption at $h\nu_2 = 1.325$ eV, about 75 meV above the interface bandgap, may be significantly larger because other two-dimensional subbands can contribute to the absorption, which, incidentally, do not obey any parity selection rule. The number of hole subbands is probably restricted because the corresponding quantum well is rather deep (see Fig. 1a), but the situation of electron subbands is more difficult to handle because we deal with an accumulation rather than with an inversion situation. However, from the smooth lineshape of the PLE spectrum, and its comparison with various numerical simulations, we believe that $\alpha^A_2 = 10^{-4}$ is a representative figure, and should not be wrong by more than a factor of 2. Using this value, and the experimental data $L^B_2 / L^A_2 = 10^{-3}$ for a pump intensity $I_2 = 20 \text{ mW}$ at 1.325 eV, focused on a 0.8 mm^2 spot, we get $p = 10^7 \text{ cm}^{-2}$ (hence $p \ll n$) and:

$$C_p = 1.2 \cdot 10^{11} \text{ cm}^3 \text{ s}^{-1} \quad (7)$$

The main uncertainties in this determination certainly lies in the evaluation of the interface absorption α^A_2 , and, as usual with investigations of Auger effects, in the estimation of the size of the excited region. All together, we estimate that these uncertainties should not exceed a factor of 10. More questionable might be the assumption, implicit up to now, that all the Auger holes falling into the InP layer actually thermalize and recombine in InP instead of tunneling back to the AlInAs side of the interface. This assumption is in fact supported by the examination of the extended interface PLE spectrum [8,10]: the absorption by InP manifests itself by a moderate raise (merely a factor of two) in the interface luminescence, which proves that only a very small fraction

High-Resolution Transmission Electron Microscopy of Heterostructures

H. Cerva
Siemens AG, Research Laboratories (Otto Hahn Ring 6,
D-81730 München, Germany

Abstract

Chemical information on a near-atomic scale may be obtained from high-resolution transmission electron microscope (HREM) images. This requires first a distinct contrast difference in the adjacent semiconductor materials in a particular projection direction for a wide range of objective lens defoci and specimen thicknesses for the given microscope parameters (acceleration voltage, spherical aberration constant). Second this contrast difference must behave almost linear with layer composition. The contrast formation in the systems AlGaAs and SiGe, where such conditions may be found and which are representatives for amplitude and phase contrast respectively, is discussed. The method of chemical lattice imaging is applied to AlGaAs structures and reveals differences in the abruptness of GaAs on AlGaAs and AlGaAs on GaAs interfaces. Selected area diffraction is shown to yield the period length of short period superlattices in unstrained AlGaAs and strained SiGe systems with high accuracy.

Introduction

Semiconductor heterostructure layer systems with their geometric structures and compositional variations in near-atomic dimensions are suitably characterized by transmission electron microscopy (TEM) because of its high spatial resolution. Dark-field imaging with the (200) reflection and bright-field imaging of conventionally ion-beam-milled thin cross sections or cleaved 90° wedge-shaped specimens are nowadays routinely used to characterize layer growth and processing [1]. High-resolution electron microscopy (HREM) provides not only structural but also quantitative chemical information of interfaces at atomic or near-atomic scale. This requires to relate the image intensities observed with appropriate imaging conditions in the specifically different HREM contrast patterns at the interface and on both sides of the interface to the chemical variation across the interface, and develop an algorithm to extract the chemical signal quantitatively [2]. Over the last years this algorithm [2,3], applied to images projected in <110>, has been extensively used for various systems such as AlGaAs and HgCdTe to study structural and chemical interface properties and point defects [4,5,6]. A theoretical treatment of the image contrast in <110> projection based on the non-linear imaging theory was described for the AlGaAs and SiGe system [7,8] and was experimentally demonstrated for the AlGaAs system by using a different algorithm for quantitative analysis [7,9]. This algorithm was used to verify the different abruptness of the AlGaAs and the GaAs/AlAs interfaces [10]. Successful quantitative analysis of strained SiGe superlattices in <110> and <110> projection has been reported recently by using a similar approach as in [7,8,9] but by taking also into account in the

of the holes photo-created in InP actually tunnel and feed the interface luminescence. Finally, it is certainly desirable to attempt a comparison between our new two-dimensional Auger recombination process and the situation of bulk materials (InP, GaAs) where Auger coefficients are in the range:

$$C_p^{3D} \approx 10^{-28} \cdot 10^{-30} \text{ cm}^6 \text{ s}^{-1} \quad (8)$$

It is not clear whether this procedure is fully justified, but, in analogy with what was done in the case of type I quantum wells [6], a simple way to derive an "equivalent 3-dimensional Auger coefficient" consists in writing:

$$\approx C_p^{3D} = C_p^{2D} L_p^{-2} / (L_c + L_p) \quad (9)$$

where $L_{c,p}$ are characteristic lengths for the electron and hole wavefunctions along the z-direction taking the extension of the classical motions. $L_c \approx 100 \text{ Å}$ and $L_p \approx 70 \text{ Å}$, we get:

$$\approx C_p^{3D} \approx 3 \cdot 10^{-24} \text{ cm}^6 \text{ s}^{-1} \quad (10)$$

This value is several orders of magnitude larger than the reported values for bulk materials with small spin-orbit splitting, like GaAs or InP. This result supports the idea that phase-space and matrix-elements considerations make Auger processes more "efficient" in type II interfaces [9]. This conclusion seems at odds with the observation of laser emission in InP-AlInAs superlattices [7]. The solution of this apparent paradox is probably the fact that our investigations also indicate that the type II interface has a much better radiative efficiency than the bulk material ($\eta_A \approx 30 \text{ nJ}$), which favors lasing at low carrier density.

In conclusion, we have evidenced a novel energy up-conversion mechanism, the Auger hot-carrier fountain effect in type II InP-AlInAs heterojunctions. This effect, which may become quite efficient, at unusually low pump power, might have potential applications. On a more fundamental ground, it allows a new experimental approach to Auger recombination in semiconductor heterostructures. Extension of this first study to the case of InP-AlInAs superlattices will help the elucidation of the apparent contradiction between high Auger recombination rate and fair laser effect in these materials.

Acknowledgements: we thank T. Leblhen and C. Delalande for their help and the use of their Ti:Sapphire laser, and P. Roussignol for fruitful discussions. LPMC-ENS is Unité Associée N° 1437 at CNRS

References:

1. H.C. Casey and M.B. Panish, *Heterostructure Lasers*, Academic Press, New York (1978)
2. G. Benz and R. Conradt, *Phys. Rev. B* 16, 843 (1977)
3. U. Staus, W. W. Rühle and K. Köhler, *Appl. Phys. Lett.* 62, 55 (1993)
4. A.N. Titkov, G. N. Ilundze, I.F. Nironov and V.A. Cheban, *Sov. Phys. Semicond.* 20, 14 (1986)
5. A. Haug, *J. Phys. C* 16, 4159 (1983)
6. B. Semprage, D.S. Chemla, D. Sivco and A.Y. Cho, *IEEE J. Quantum Electronics*, QE-22, 714 (1986) and references therein.
7. E. Lugagne-Delpont, P. Voisin, M. Voos and J.P. André, *Appl. Phys. Lett.* 60, 3087 (1992)
8. E. Lugagne-Delpont, J.P. André and P. Voisin, this conference, and *Solid State Comm.* 86, 1 (1993)
9. The Unknown Russian Theoretician, private communication
10. E. Lugagne-Delpont, Doctoral Thesis, Université Paris VI (1993) (unpublished)
11. These excitation spectra are obtained using an extremely low-power excitation set-up using an halogen lamp followed by a monochromator as the excitation source

algorithm the lattice distortions at the interface [1,12]. First, the important issues of the imaging process as well as the algorithm for extracting the quantitative information will be discussed and reviewed. Then, the applications to an AlGaAs resonant tunneling structure and a short period superlattice (SPS) are presented. Finally, it is shown that selected area electron diffraction (SAD) yields additional information of strained and unstrained SPS structures.

Quantitative Chemical HREM Analysis

(a) General unit AlGaAs <100> Images

The main task is to find the appropriate imaging conditions (ranges of defocus Δf , and specimen thickness t) for a given TEM to distinguish between two adjacent materials with identical lattice but different elemental constituents by their HREM contrast which should be quantifiable. The HREM image in fig. 1 shows a cleaved 90° wedge-shaped specimen of an AlGaAs system. At the defocus $\Delta f = 25 \text{ nm}$ and for the thickness range $7 < t < 13 \text{ nm}$, the AlGaAs layer is characterized by a strong (200)-pattern contrast with the white dots corresponding to Al-atom columns and black dots to As-atom columns, whereas in GaAs a (220)-pattern contrast prevails where white dots represent positions of Ga- or Al-atom columns and black dots are tunnels in the structure. When crossing the interface these contrast change gradually. At the given imaging conditions this change in contrast going along with a change of the Al-content can be described by those Fourier components of the image intensity which contain the linear beam interactions between the transmitted and the (200) beams as well as the non-linear interactions between (200) and (220) beams [7,9]. This behaviour stems from the fact that in the <100> projection the amplitudes of the (200) beams in AlGaAs increase with the Al-content x whereas those of the (220) beams remain almost constant for the chosen imaging conditions.

In the contrast patterns the smallest unit cell is chosen which contains all the chemical information for the quantification procedure. In the case of AlGaAs in <100> projection this is a 0.28 nm^2 square shaped cell [2,3]. This is due to the fact that the (200) beams with their 0.28 nm spacing contain the chemical information. The reference cells for AlAs and GaAs are shown by the white small frames in fig. 1. The resolution of this method, however, is not only determined by the size of the unit cell. Assuming perfect coherent illumination, the imaging conditions are periodic with defocus. Then, however, the Fourier-transformed contrast transfer function, which is a function of the TEM parameters, is broadened at higher defocus. At larger defocus this results in larger deviations in the quantitatively determined compositions of individual columns from the actual values because of the influence from neighbouring columns with different compositions [9]. In the AlGaAs system quantifiable images may be obtained with a few JEMEX microscope at $\Delta f = 20$ and 70 nm [9,13] but spreading starts at 1.2 nm [9]. In material systems where a much smaller unit cell can be chosen because of the smaller spacings of the reflections which contain the chemical information, a TEM with improved resolution would have to be used.

There exist various pattern-recognition approaches to extract the compositional information from the intensity distribution [2,3,9,14]. In our approach only those Fourier components are derived from the intensity distribution which contain the chemically sensitive linear and non-linear contributions of the (200) beams [9]. The sum of these chemically sensitive Fourier components yield a chemical signal which is normalized with help of the reference cells in the, e.g., AlAs and GaAs layers and is almost linear with the Al-content. This chemical signal

becomes 0 for GaAs and 1 for AlAs. Testing this algorithm on simulated images of sharp and graded interfaces at the optimum imaging conditions showed that the composition profiles across the interfaces deviate from the given profiles by only $\Delta x \approx 0.03$ for each unit cell [9]. In comparison to the cross-correlation method of Oumazal et al. [2,3] which is a real-space method including all Fourier components almost exactly, the same results for AlGaAs interfaces were obtained [9]. Since in HREM imaging we are dealing with projected images the accuracy of about $\Delta x \approx 0.03$ within each unit cell allows to detect a vacancy of one Al-atom (or a replacement by one Ga-atom) in a column of a 1 nm thick specimen [3,9]. Experimentally beam and crystal tilt can be controlled to be ≤ 1.4 and 2.8 mrad by checking fine contrast details in the image at other defoci, and the systematic error becomes $\Delta x \approx 0.05$ [9].

Electron irradiation at 400 kV leads to knock on damage in AlAs and GaAs but does not affect the contrast as long as images are taken within 15 minutes irradiating the same area [3,9]. In order to reduce the random error caused by quantum noise (amplified by the photographic process) and surface roughness of the specimen, the chemical signal for the reference unit cells is obtained by averaging over several cells in the reference layers. This reduces the noise for a best signal to noise ratio reported to be $SN \approx 20$ [3] whereas it is about 10 for cleaved wedge specimens [9] and 5 for ion-beam thinned samples [3,9]. The accuracy is then given by the sum of the systematic and random error and in the best case is $\Delta x \approx 0.1$. The accuracy of compositional profiles may, however, be improved by averaging over several cells along the interface. Cleaved 90° wedge-shaped specimens of AlGaAs structures have the advantage that they are quickly prepared and that the specimen thickness is easily controlled (fig. 1). Moreover, from the change of the contrast with thickness, the width of an interfacial transition layer may qualitatively be estimated [9,10].

(b) SiGe images

In the case of Si or Ge there exist no so called chemically sensitive reflections, such as the (200) beams in the compound semiconductors, owing to their diamond structure. Taking the <100> projection as example mainly the transmitted and the four (220) beams contribute to the HREM image. In contrast to the AlGaAs case where the difference in the amplitudes of the (200) beams yields information on the Al-content, the amplitudes of the (220) reflections do not differ significantly in Si and Ge for thicknesses $< 18 \text{ nm}$. However, there is a distinct difference in the phases of the (220) beams in Si and Ge. Considering the linear beam interaction between transmitted and (220) beams, an image contrast difference between Si and Ge will be obtained at imaging conditions where the generalized transfer functions (GTF) $\cos(\theta_{220} - \theta_{000} + \chi_{220})$ for Si and Ge are different (θ - phase shift due to scattering, χ - phase shift by objective lens). Defocus and thickness may be chosen such that the difference is $\pi/2$ or π . In the first case one layer shows a strong (220)-pattern contrast ($|GTF| = 1$) while in the other layer "half-spacing" contrast dominates (440)-pattern). GTF=0 which originates from non-linear beam interactions between the various (220) beams [8]. In the second case the GTF is +1 for the layer where the atom columns appear as white dots and the tunnels as black dots, while the GTF is -1 for the layer with reversed contrast. This situation is shown for 400 kV in the simulated images of a SiGe superlattice (fig. 2). Si-atom columns are dark, Ge-atom columns are bright. The sharp interfaces chosen in the model are marked by the arrows and lie between the pair of bright dots which are 0.14 nm apart. In the upper left corner of fig. 2 the Fourier component (220) of the image intensity is plotted for Ge and Si as a function of t at $\Delta f = 55 \text{ nm}$. From this plot it can be

seen that a phase difference of π is obtained in the thickness range 135-180 nm. The image simulation reveals that this contrast is stable for δ values 5-9 nm [8]. The same results were reported by Sienkamp and Jager [11,12]. Moreover, they showed that the contrast becomes linearly quantifiable for Si, Ge, (05551). In the $\langle 110 \rangle$ projection it is the phase of the (111) beams which has to be considered similarly to the (220) beams in the $\langle 100 \rangle$ case. Experimental $\langle 110 \rangle$ HREM images of Si, Ge, SPS have been successfully quantified by applying a similar Fourier approach as described in [9] but implementing a new method taking into account the tetragonal lattice distortions [12]. They also report that the cross-correlation method fails in this case because it is not selective in those Fourier components which are chemically sensitive for the chosen imaging conditions but also includes Fourier components which behave non-linearly.

(c) $\text{AlGaAs} \langle 110 \rangle$ images

When $\langle 100 \rangle$ and $\langle 110 \rangle$ HREM images recorded at 400 kV of the same MOCVD (metal organic chemical vapour deposition) grown AlGaAs superlattice were compared by visual inspection, different interface abruptnesses were observed (fig. 3a and fig. 4b) [1]. The interface was analyzed quantitatively from the $\langle 100 \rangle$ image in fig. 3a which was taken at optimum imaging conditions. The Al-concentration profile is shown in fig. 3b and reveals an interfacial transition zone being five cation layers broad. By averaging over 64 cells along the interface the statistical error for the Al-content x in the cation layers of the transition region was reduced to about 0.04. The error bar $\Delta x = \pm 0.01$ drawn in fig. 3b gives an upper limit of the uncertainty for the composition determination resulting from both statistical and systematic errors.

Judging visually the $\langle 110 \rangle$ image of the same superlattice, the interface zone may be estimated to be only one to two cation layers broad. $\langle 110 \rangle$ HREM images of AlGaAs layer-structures are often imaged under conditions where one layer shows up with a strong (111)-pattern while in the other layer "half-spacing" contrast dominates (fig. 4b) [15]. In such $\langle 110 \rangle$ images the (111)-pattern contrast comes mainly from the linear contributions of the (111) beams whereas the half-spacing contrast stems from non-linear contributions of the (111), (200), and (220) beams [16]. In contrast to the $\langle 100 \rangle$ projection this specific contrast difference comes only from a difference in the phase [16]. Half-spacing contrast and (111)-pattern contrast occur in one or the other layer for numerous imaging conditions. For e.g., the imaging conditions $\Delta f = -35$ nm, and $t = 20$ nm the (111)-pattern dominates in the GaAs whereas a half-spacing contrast appears in the AlAs layer (fig. 4b). Figure 4a shows the corresponding chemical signal as a function of Al-content x . Only for a narrow composition range 0.65-0.9 a linear relationship exists. For lower x values the function is ambiguous. Hence, the interface appears to be much sharper in the $\langle 110 \rangle$ image. Such imaging conditions are not suitable for quantification and also a qualitative visual evaluation of the interface is unreliable or even erroneous. Moreover, the ranges of Δf and t for imaging the layers with these contrasts are not very broad and alternate rapidly with thickness [16].

Applications

(i) $\text{AlGaAs} \langle 110 \rangle$ double barrier quantum wells

The interface quality of double barrier quantum wells (DBQW) used in resonant tunneling structures determines their electrical properties and, therefore, the interface quality is of decisive importance. Figure 5a shows a $\langle 100 \rangle$ HREM image of a conventional thin cross section from a

$\text{Al}_{0.5}\text{Ga}_{0.5}\text{As}/\text{GaAs}$ DBQW structure grown by molecular beam epitaxy (MBE) [10]. Specimen thickness and defocus are within optimum range. There is a clear difference in interface abruptness between normal $\text{Al}_{0.5}\text{Ga}_{0.5}\text{As}$ on GaAs and inverted interfaces (GaAs on $\text{Al}_{0.5}\text{Ga}_{0.5}\text{As}$). The normal interfaces appear abrupt and the inverted ones diffuse. To quantify this impression the Al-concentration profiles across the interfaces were determined using the algorithm described above (fig. 3b). By averaging over 64 cells along the individual interfaces the statistical error for the Al-content x in the cation layers of the transition region was reduced to ± 0.04 . The normal interface exhibits a transition region extending over one cation layer whereas the diffuse inverted interface extends over three cation layers. This difference between normal and inverted interface is also observed in AlGaAs DBQWs and can be explained by the higher surface mobility of Ga atoms on the GaAs surface compared to that of the Al atoms on the AlGaAs surface during MBE growth. These results are in perfect agreement with asymmetries in electrical transport measurements [10].

(b) Short period superlattices

Short-period superlattices (SPS) of compound and elemental semiconductors deposited by MBE reveal interesting physical properties. Multiquantum well structures using GaAs/AlAs , SPS instead of AlGaAs alloy layers as barriers reveal better optical properties. Strained-layer Si_3Ge_4 SPS have a modified electronic bandstructure compared to Si and Ge. Besides, new electronic devices which become possible, they offer to realize a quasi-direct band gap semiconductor made from the indirect host materials. Characterization of period length, thickness and composition of individual layers, and layer thickness fluctuations is important to optimize growth conditions.

Superlattices of the type GaAs/AlAs , grown on $\langle 100 \rangle$ substrates have an artificial tetragonal structure with reduced point group symmetry compared to the host materials. The spacegroup of the superlattice depends on whether the total number of monolayers in the unit cell is even or odd [17]. Each layer of GaAs or AlAs is a double-layer (DL) consisting of a cation layer and an arsenic layer with the DL thickness being that of the (200) lattice spacing d_{200} . Thus, for a given SPS the number $(m+n)$ of DLs corresponds to the period $d_{\text{DL}} = (m+n) d_{200}$ of the SPS in $\langle 100 \rangle$ direction. The artificial superlattice structure causes superlattice spots (SLS) in the diffraction pattern lying on rows between the reflections of the bulk material having reciprocal lattice vectors $h100$ perpendicular to the $\langle 100 \rangle$ surface. The SLSs have a spacing of $1/d_{\text{DL}} = 1/(d_{200}(m+n))$ [18,19]. Only for $(m+n)$ being an integer the $k_{\text{min}} = \pi/m$ SLSs coincide with a reflection of the bulk material. Due to double diffraction in thick TEM specimen areas (typically 20-50 nm thickness) the rows of SLSs appear centered on each bulk reflection. Hence, for non-integer periods $(m+n)$ a SLS "splitting" occurs as the SLSs do not coincide [20,21]. Figure 6 shows a section of the $\langle 100 \rangle$ SAD pattern of a nominally GaAs/AlAs , SPS, 1 μm thick, obtained from a cleaved 90° wedge-shaped specimen. The aperture diameter used for SAD which defines the area where the diffraction information comes from was typically 0.3 to 0.5 μm . The arrows in fig. 6 indicate the SLSs which are centered on the (200) and (000) spots. The fact that these rows of spots do not coincide reveals that the periodicity is incommensurate. The reciprocal spacing of the spots is in both cases $d_{\text{DL}} = 10.76$ DLs. If the diameter of the SAD aperture is smaller than the total thickness of the SPS structure, then several SAD patterns may be recorded as a function of growth direction. This allows to search for growth irregularities such as areas with different superlattice periodicities. The individual layer thicknesses are difficult to measure in conventional bright- or dark-field images of conventional cross sections or cleaved specimens when the thickness approaches or is below 1 μm [1]. Then HREM imaging

in $\langle 100 \rangle$ projection is useful to determine interface abruptness and average individual layer thickness. Both SAD and HREM imaging may rather quickly be carried out on cleaved 90° wedge-shaped specimens. Figure 7a shows the $\langle 100 \rangle$ lattice image recorded at optimum imaging conditions for 400kV together with the optical diffraction pattern (ODP) obtained from the negative with a small aperture corresponding in the image to a circular area with a diameter of about 25 nm. The ODP reveals also SLSs yielding a periodicity of 10.77 DLs. The Al-concentration profile was calculated $n \cdot$ about 2.5 periods of the SPS by averaging over 12 cells parallel to the interface. The total error in determination of the Al-content is ± 0.1 . When averaging the Al-content x of all cation layers this SPS corresponds to an alloy with $x = 0.25$ which is in good agreement with the results obtained from photoluminescence measurements. The profile in fig. 7b also shows that the period is not strictly 10 DLs but varies between 10 and 11 DLs. Both interfaces are not abrupt which for AlAs on GaAs is in contrast to the finding of the DBQW structure (see above). Both structures were grown with similar growth parameters, but probably because of the thinner GaAs layers in the SPS structure the GaAs surfaces do not become flat. The individual layers consist of: 7-8 GaAs layers (4-5 cation layers with $x=0.01$) and 1-2 cation layers with $x=0.25 \pm 0.1$ and 1-4 AlAs layers (1-2 cation layers with $x=1.0$) and 1-2 cation layers with $x=0.7 \pm 0.1$.

Another situation exists for SPSs of the type $\text{Si}_{1-x}\text{Ge}_x$ because they are strained due to the 4.2% lattice mismatch of the host materials, and in contrast to the compound semiconductors on (100) surfaces the thinnest individual layer that may be grown is either a monolayer (ML) of Si or Ge with the thickness d_{ML} . This leads to various possible spacegroups for various combinations of m/n whether m and/or n are even or odd [17]. For the case (m,n) even the number $(m+n)$ of MLs corresponds to the period $d_{\text{SPS}} = d_{\text{ML}} \cdot (m+n) \cdot d_{\text{SL}}$ of the SPS in $\langle 100 \rangle$ direction, whereas for (m,n) odd twice the number $(m+n)$ of MLs corresponds to the period $d_{\text{SPS}} = 2(m+n) \cdot d_{\text{ML}}$. This causes an interesting effect in the SAD patterns of $\langle 110 \rangle$ zone axes recorded parallel to the interfaces: for (m,n) odd there is a "doubling" of SLSs between (200) and (000). Thus, a SPS $\text{Si}_{1-x}\text{Ge}_x$ with (m,n) odd shows the same number of spots as a SPS $\text{Si}_{1-x}\text{Ge}_x$ [22]. This effect is due to Umweganregung of the kinematically forbidden (200) reflection via the (111) reflections. Figure 8 shows sections of $\langle 110 \rangle$ SAD patterns between two fundamental spots for a series of $\text{Si}_{1-x}\text{Ge}_x$ SPSs. From the left to the right in fig. 8 the measured period $(m+n)$ decreases from 8.4 to 6.6. Arrows which are linked indicate positions of related SLSs emanating from the same fundamental spot. Comparing fig. 8b and 8d the number of SLS positions has doubled for the SPS with the odd period length. The SLSs emanating from one fundamental spot lie exactly in between those SLSs coming from the other fundamental spot. This causes a virtual doubling of the period length [23]. Experimentally this effect is only observed for very short SPSs when the rows of SLSs overlap [22]. Since the SPSs are strained the total thickness is small (typically 20-200 nm) to avoid plastic relaxation. The selected area aperture (diameter typically 0.3-0.5 μm), therefore, contains mainly diffraction information from the substrate. Hence, the superlattice spots are much weaker than in the case of the thick $(\text{GaAs})_n/(\text{AlAs})_m$ SPS in fig. 6. Besides, the intensity of the SLSs is a criterion for the perfection of the layers and interfaces [24].

In $(\text{GaAs})_n/(\text{AlAs})_m$ SPSs the effect of SLS doubling does not occur for odd $(m+n)$ because the smallest individual layer possible is two MLs thick. However, due to the Umweganregung in $\langle 110 \rangle$ orientation a doubling of the number of SLSs may occur for half-integer periods. The doubling of the number of SLSs may also happen in $\langle 100 \rangle$ projection of SiGe SPSs if the period length is half-integer $(2(m+n)+1/2)$. Then, the number of SLSs between (000) and (400) spots is theoretically the same as for a SiGe SPS with the period $2(m+n)+1$.

As noted before the $\text{Si}_{1-x}\text{Ge}_x$ SPSs are strained and, therefore, (100) spots with $1/2a_0$ of the Si or Ge substrate do not coincide with SLSs. The separation may be well observed in the SAD pattern at the positions of higher orders of (000). Assuming a totally elastically strained SPS the lateral lattice constant of the SPS corresponds to that of the substrate. Then, the average perpendicular lattice constant of the SPS may be determined from the SLSs period d_{SL} while the substrate spots are used for calibration. Moreover, this allows to calculate the composition of the SPS with an accuracy of about 5% [23]. If it is assumed that the lattice parameter within the layer of that $\text{Si}_{1-x}\text{Ge}_x$ constituent is not changed which is identical with the substrate material, the perpendicular lattice parameter in the layers of the other constituent may be calculated: $d_{\text{L}}^{\text{other}} = d_{\text{SL}} - d_{\text{L}}^{\text{SiGe}}$ and $d_{\text{L}}^{\text{other}} = d_{\text{L}}^{\text{SiGe}} \cdot \frac{a_{\text{other}}}{a_{\text{SiGe}}}$ [25]. If the SPS is plastically relaxed then the lateral lattice parameters of SPS and substrate are different and this may be observed in a "splitting" of the diffraction spots of the lateral planes [26].

Conclusion

Chemical information may be obtained from high-resolution lattice images with near-atomic resolution. For every material combination the electron beam specimen interaction has to be studied in order to find imaging conditions where the contrast depends almost linearly on the layer composition. The imaging conditions (defocus and thickness) have to be stable in a wide range for a given projection direction and a given TEM with its specific electron optical parameters and acceleration voltage. Contrast differences may either arise due to a monotonic behaviour of the amplitude of a specific - so called chemically sensitive - reflection with layer composition (this case applies to the AlGaAs system) or is due to a phase difference for a particular reflection (this case applies to the SiGe system). The resolution for the quantification procedure depends on the lattice plane spacing of the reflection which shows the amplitude or phase variations, the size of the unit cell used in the quantification algorithm, and the electron microscope parameters. An accuracy of $\Delta x \approx 0.1$ can be achieved. Various applications, either in this paper or in the literature, have demonstrated the usefulness of this method. Selected area diffraction has been shown to be an important additional method available in the TEM to characterize the period lengths of short-period superlattices. Cleaved 90° wedge-shaped specimens of compound semiconductors were shown to allow rapid investigation by HREM imaging and electron diffraction.

Acknowledgements: The author thanks Drs. H. Riechert and L. Korte for supplying the AlGaAs samples and for discussions.

References

- [1] e.g. H. Cerva, H. Oppolzer, Prog. Crystal Growth and Character. 20, 231 (1990), H. Cerva, Appl. Surf. Sci. 50, 19 (1991).
- [2] A. Ourmazd, D.W. Taylor, J. Cunningham, C.W. Tu, Phys. Rev. Lett. 62, 933 (1989).
- [3] A. Ourmazd, F.H. Baumann, M. Bode, Y. Kim, Ultramicroscopy 34, 237 (1990).
- [4] M.H. Bode, A. Ourmazd, J. Vac. Sci. Technol. B10, 1787 (1992).
- [5] Y. Kim, A. Ourmazd, R.D. Feldman, J. Vac. Sci. Technol. B8, 1116 (1990).

- [6] A. Omri, M. Scheffler, M. Henkemann, J.-L. Rouvier, *MRS Bulletin* 12, 24 (1992)
- [7] S. Thoma, H. Cerva, *Ultramicroscopy* 35, 77 (1991)
- [8] S. Thoma, PhD Thesis, Technical University München, Germany (1992).
- [9] S. Thoma, H. Cerva, *Ultramicroscopy* 38, 265 (1991).
- [10] S. Thoma, H. Riechert, A. Miulajsky, H. Oppolzer, *J. Cryst. Growth* 123, 287 (1992).
- [11] D. Stenkamp, W. Jäger, *Proc. EUREM'92* 1, 545 (1992).
- [12] D. Stenkamp, W. Jäger, *Inst. Phys. Conf. Ser.* (1993) to be published
- [13] F.H. Braumann, M. Bode, Y. Kim, A. Ourmad, *Ultramicroscopy* 47, 167 (1992)
- [14] A.F. De Jong, D. Van Dyck, *Ultramicroscopy* 33, 269 (1990)
- [15] A. Poudoulec, B. Guenais, C. D'Anterries, A. Regreny, *J. Cryst. Growth* 100, 529 (1990).
- [16] S. Thoma, H. Cerva, submitted for publication
- [17] M.J. Alonso, M. Cardona, G. Kanellis, *Solid State Communications* 69, 479 (1989), *Corrigendum* 70, 1 (1989)
- [18] P.M. Petroff, A.C. Gossard, W. Wiegmann, A. Savage, *J. Cryst. Growth* 44, 5 (1978).
- [19] P.M. Petroff, *Inst. Phys. Conf. Ser.* 74, 259 (1984)
- [20] K. Kifune, S. Kajii, Y. Komura, N. Sano, H. Terauchi, *Proc. 11th Int. Cong. on Electron Microscopy, Kyoto, (1986)*, p.475
- [21] B. Guenais, A. Poudoulec, P. Auvray, M. Baudet, A. Regreny, B. Lambert, *J. Cryst. Growth* 88, 125 (1988).
- [22] K. Eberl, W. Wegscheider, G. Abstreiter, H. Cerva, H. Oppolzer, *Superlattices and Microstructures* 9, 31 (1991)
- [23] G. Lütjering, Diploma Thesis, Technical University München, Germany (1992)
- [24] T.S. Kuan, W.I. Wang, E.L. Wilkie, *European Cong. on Electron Microscopy, Budapest, (1984)*, Vol. 1, p. 535
- [25] W. Wegscheider, K. Eberl, G. Abstreiter, H. Cerva, H. Oppolzer, *Appl. Phys. Lett.* 55, 448 (1989)
- [26] W. Wegscheider, PhD Thesis, Technical University München, Germany (1991)

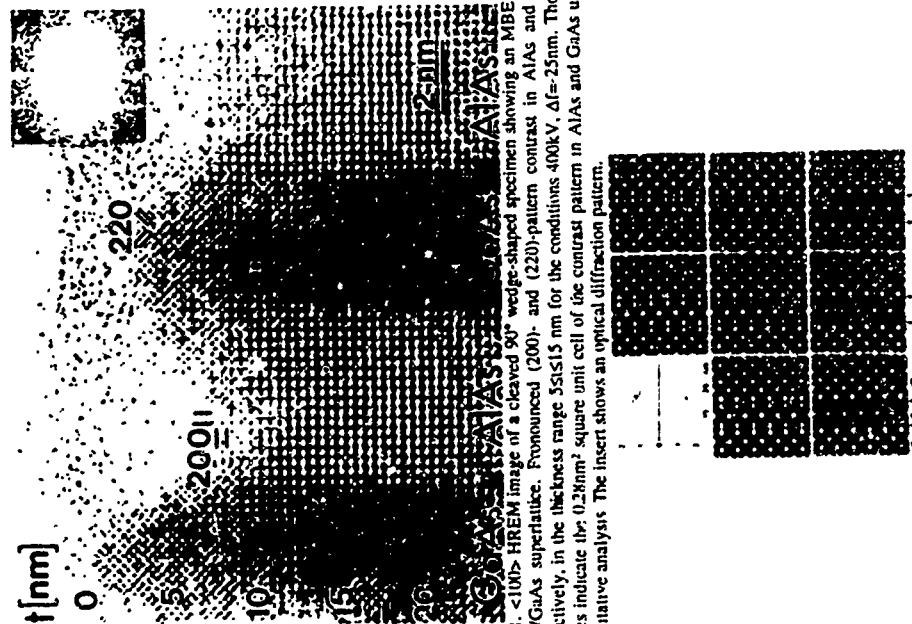


Fig. 1. <100> HREM image of a cleaved 90° wedge-shaped specimen showing an MBE grown AlGaAs superlattice. Pronounced (200)- and (220)-pattern contrast in AlAs and GaAs, respectively, in the thickness range 35±15 nm for the conditions 400kV, Δf=25nm. The white frames indicate the 0.2nm² square unit cell of the contrast pattern in AlAs and GaAs used for quantitative analysis. The insert shows an optical diffraction pattern.

Fig. 2. Simulated <100> HREM images of a SiGe short period superlattice with abrupt interfaces (arrows indicate position of the interfaces). All simulated images show white spots at the positions of the Ge-atom columns and black spots at the positions of Si-atom columns for the thickness and defocus ranges given in the images (in nm). (480kV, defocus spread 9nm, beam semi-convergence angle 0.7 mrad). The insert shows plots of the Fourier component I(220) of the image intensity for Si and Ge as a function of thickness

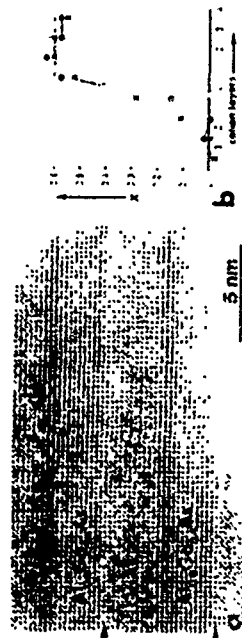
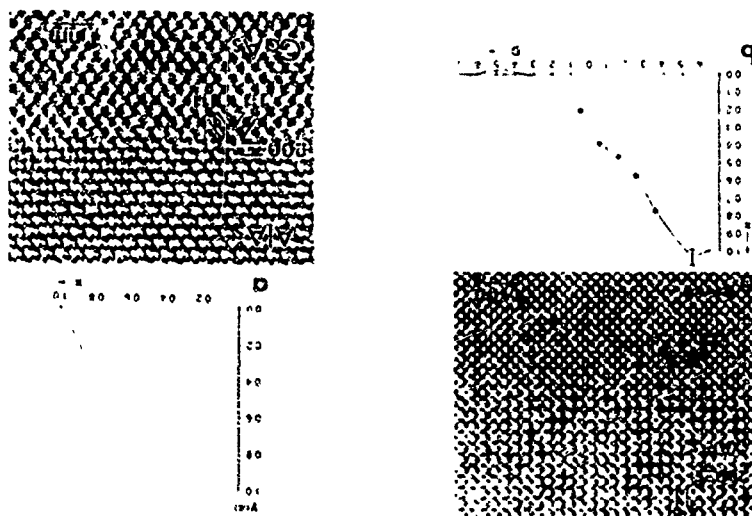
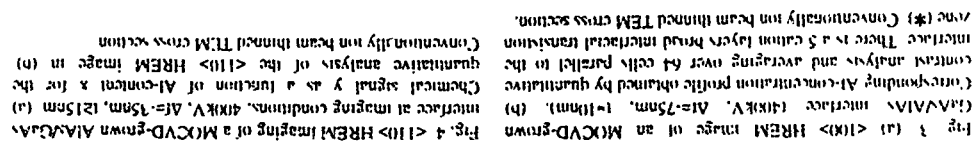


Fig. 5 (a) Experimental $<100>$ HREM image of a cross-sectional specimen containing an MBE-grown $\text{GaAs}/\text{Al}_{0.4}\text{Ga}_{0.6}\text{As}$ double-barrier quantum well structure recorded with $\Delta f = 20$ nm. $\text{Al}_{0.4}\text{Ga}_{0.6}\text{As}$ on GaAs interfaces are marked by arrows. (b) Al-concentration profiles determined for the $\text{Al}_{0.4}\text{Ga}_{0.6}\text{As}$ on GaAs interface (—) and the reverse interface (--- in a). The profile of a perfectly abrupt interface is also plotted (---)



Fig. 6. Section of a $\langle 100 \rangle$ electron diffraction pattern of a nominally $(\text{GaAs})_x(\text{AlAs})_{1-x}$ short period superlattice showing superlattice spots between (200) and (000) spots. Measured period length is 10.76 (200) spacings.



Cross-Sectional STM on Superlattices and the Effect of Doping

H.W.M. Salemink, M.B. Johnson, O. Albreksten* and P. Koetzrad#
IBM Research Division, Zurich Research Laboratory, CH-8803 Rüschlikon,
Switzerland
*Telecommunications Research Laboratory, DK-2970 Hørsholm, Denmark
#Physics Dept., Eindhoven University of Technology, NL-5600 MB Eindhoven,
The Netherlands

Extended Abstract

The analysis of semiconductor multilayer structures by cross-sectional STM is discussed. The majority of the work reported is concerned with observations on the UHV cleaved (110) plane of epitaxially grown III-V compounds [1]. The group-III (empty state) or the group-V (filled state) sublattices are selectively imaged by tunneling into the conduction states or out of the valence states, respectively [2]. The heterostructure interfaces are quantified on both the group-III (Al-Ga) and group-V (As) sublattices with atomic resolution in direct space [3]. In particular we demonstrate the definition of the AlGaAs-GaAs interfaces at the atomic scale. Sublattice ordering is observed in domains with a dimension of a few nanometers, and we discuss the consequences of this "clustering" for the homogeneity of ultrathin ternary layers [4].

Fig. 7 (a) $\langle 110 \rangle$ HREM image of an (GaAs)₁₀(AlAs)₂ short period superlattice (cleaved 90° wedge-shaped specimen, 400kV, $\Delta f = 20$ nm). The optical diffraction pattern reveals additional superlattice spots. (b) Al-concentration profile obtained from 2.5 periods of the superlattice. Averaged over 12 cells parallel to the interface.

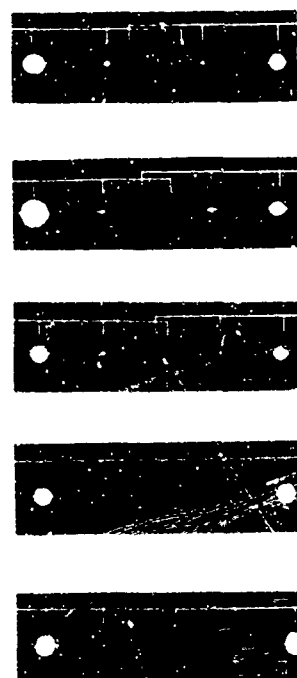


Fig. 8. Sections of electron diffraction patterns of the $\langle 110 \rangle$ zone axis of $\text{Si}_{1-x}\text{Ge}_x$ short period superlattices. The (200) reflection and the superlattice spots emanating from it are excited because of Umweganregung via the (111) reflections. Nominal m/n value: (a) 2/6, (b) 3/5, (c) 2.5/5, (d) 2/5, (e) 2/5. Measured periods ($m+n$) are given in the images.

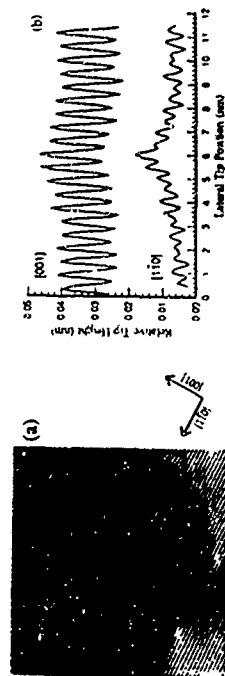


Fig. 1. (a) Filled-state image of GaAs (110) buffer layer, Be doping level $1 \times 10^{19} \text{ cm}^{-3}$. Sample voltage is -2.1 V , dimensions are $31 \times 29 \text{ nm}$. The individual As sites are visible. The hillocks are attributed to the signature of individual doping sites in the topmost layer(s). (b) Charge density corrugation traces across an assigned Be doping site in $[001]$ and $[1-1]$.

The effect of the doping concentration is visible in two ways. First, we observe the electronic signature of the individual active dopant sites in the top several layers (Fig. 1). Such measurements have been made across modulation-doped GaAs multilayers, and the observed doping site density compares well with SIMS data (Be

dopant density is $10^{18}\text{-}10^{19}\text{ cm}^{-3}$ [5]. In addition, clear indications are found for the incorporated delta layer.

The second effect of the doping density is observed via the band-bending inside the semiconductor surface, caused by the electric field strength of the tunneling potential (Fig. 2). The tunneling current (out of the valence band in Fig. 2) traverses two consecutive barriers, the subsurface band-bending zone, which is doping dependent, and the usual vacuum tunnel barrier. Using a numerical model for this tunneling process, we expect an attenuation of the valence band current (Fig. 3) when the doping density is lowered, in agreement with our experimental results. The important role of the doping concentration has been used to analyze the spectroscopic data across heterojunctions [5].

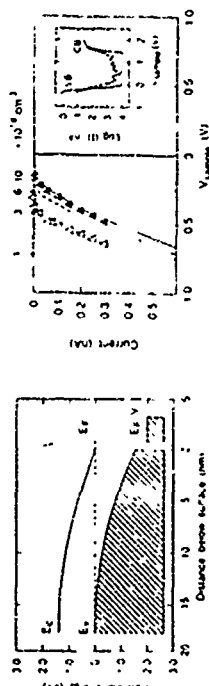


Fig. 2. Energy diagram for tunneling out of valence states; note subsurface band-bending.

Fig. 3. Calculated valence band current for various dopant densities of Be in GaAs. The symbols are experimental data from current voltage spectroscopy for concentrations of nominally 5 (Δ) and $10 \times 10^{18}\text{ cm}^{-3}$ (▲).

[1] H.W.M. Salemink and O. Albrektson, *J. Vac. Sci. Technol. B* 10, 1799 (1992).
 [2] R. Feenstra et al., *Phys. Rev. Lett.* 58, 1192 (1987); O. Albrektson et al., *Appl. Phys. Lett.* 57, 31 (1990).
 [3] H.W.M. Salemink et al., *Phys. Rev. B* 47, 16044 (1993).
 [4] M.B. Johnson et al., *Appl. Phys. Lett.* 62, (1993) in press.
 [5] M.B. Johnson et al., submitted to *Appl. Phys. Lett.*
 [6] H.W.M. Salemink et al., *Phys. Rev. B* 45, 6946 (1992).

The Surface Evolution and Kinetic Roughening during Homoepitaxy of GaAs (001)

B.G. Orr, J. Sudijono, M.D. Johnson, and A.W. Hunt
 The Harrison M. Randall Laboratory
 University of Michigan
 Ann Arbor, MI 48109-1120

Scanning tunneling microscopy studies have been performed on GaAs homoepitaxial films grown by molecular-beam epitaxy. Images show that in the earliest stages of deposition the morphology oscillates between one with two-dimensional islands and flat terraces. After the initial transient regime, the system evolves to a dynamical steady state. This state is characterized by a constant step density and as such the growth mode can be termed step flow. Comparison with RHEED shows that there is a direct correspondence between the surface step density and the RHEED specular intensity. Thin films (up to 1450 monolayers) display a slowly-increasing surface roughness. Analysis of the scaling properties and comparison with theories of film growth will be made.

Thin film deposition has become a critical technology for the advancement of modern electronics. A large number of artificial heterostructures have been produced by using various growth techniques. Molecular Beam Epitaxy (MBE) is particularly important because it affords monatomic layer thickness control over films growing from the vapor phase at relatively low temperatures under supersaturation conditions [1]. This means that thermodynamically unstable structures can be made by tuning the growth rate and temperature. In fact, with careful choice of the growth parameters to control the surface kinetics, one can create different multi-layered structures in which individual layers maintain their chemical integrity and form compositionally abrupt interfaces with one another.

To understand the growth kinetics, one needs to focus on the growth process at the atomic level. The importance is clear. Semiconductor heterostructures and superlattices possess novel electrical and optical properties. For optimum performance of devices based on these artificial materials, the morphological sharpness of the interfaces is required. Roughness leads to increased carrier scattering in active regions, lowering the carrier mobility. A detailed microscopic examination of the surface kinetic processes will therefore enhance our ability to produce higher quality device structures. In this paper we concentrate on three major processes during MBE growth of GaAs on GaAs (001), i.e. nucleation, growth, and coarsening. Nucleation occurs when adsorbed adatoms make a random walk on the surface until they meet another adatom and form islands. Growth follows when islands larger than a critical nucleus extend with further attachment of adatoms. Coarsening is considered as the transition stage when growth approaches steady-state. This occurs when the step density becomes so high that the growth mode evolves to step flow.

For many years Reflection high-energy electron-diffraction (RHEED) has been the standard *in situ* characterization tool for thin film MBE [2]. In addition to providing information on the evolution of surface structures, RHEED specular intensity oscillations are widely used to monitor growth from the transient (2D nucleation) regime to steady-state (Step-flow) mode. However, being a macroscopic averaging diffraction technique, RHEED fails to give local topographic information. Efforts aimed at modeling nonequilibrium film growth phenomena are thus hindered due to the lack of a real space picture of the growth front as it evolves. This provides motivation for using scanning tunneling microscope (STM) to obtain real space pictures of the surface evolution during growth.

The first part of these experimental studies is to examine the relationship between the RHEED oscillations and the surface evolution of GaAs during deposition. The second part has to do with the investigation of surface roughening during the steady-state growth, i.e. regime where RHEED specular beam no longer oscillates. The experiment consists of initiating growth from a recovered surface and then terminating deposition at a specific point during the growth process. This procedure is then repeated for various termination points. Because the samples are removed from the

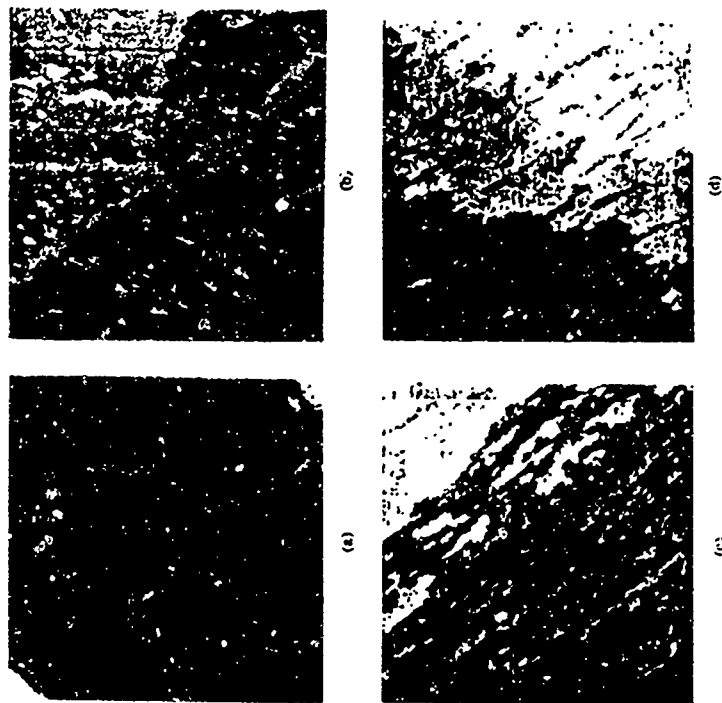


FIG. 1 (a) STM image of a GaAs(001) buffer layer. The scan range is 200nm x 200nm. The tunneling voltage (V) was +2.0V, applied to the sample, and the tunneling current (I) was 80pA. (b) STM image of GaAs(001) surface after deposition of 0.25 monolayer of GaAs. (c) and (d) STM image of GaAs(001) surface after termination of growth at the fourth RHEED minimum and maximum. Notice the change in the local direction of the vicinality in the figures.

STM for regrowth, so direct comparison can be made between any specific feature in the progression of the images. We have imaged large areas at multiple sites on multiple samples. The images shown are thus representative of the surface.

Deposition was performed in a standard ultra-high vacuum system, base pressure 7×10^{-11} Torr. Effusion cells were used to produce both the Ga and As₂ fluxes. Commercial GaAs(100) substrates were first chemically cleaned then loaded in the vacuum system where the oxide was removed at 580°C under an As₂ flux. Prior to the experiment a 300 nm thick buffer layer was grown. The substrate temperature during deposition was 555°C. The As to Ga pressure ratio was 15 and the deposition rate was 0.18 micron/hr. The sample miscut as determined by STM was approximately 0.15 degree. The direction and magnitude of the local vicinality was found to vary appreciably. The incident angle of the RHEED beam was approximately 0.9° and corresponded closely to the "in-phase" Bragg condition. The diffraction condition was chosen to yield a reduction in specularly scattered electron intensity as growth commences.

Rheed oscillation data

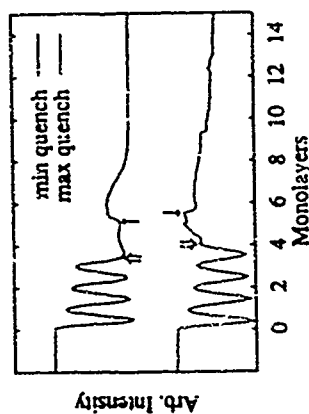


FIG 2 RHEED specular intensity oscillations for GaAs on GaAs(100). The incident angle was 0.9° and the azimuth was along [110]. The 4 labels the point at which growth was terminated for each sample and the 1 indicates an experimental artifact due to the quenching procedure. STM data presented in figures 2c and 2d were acquired from these samples.

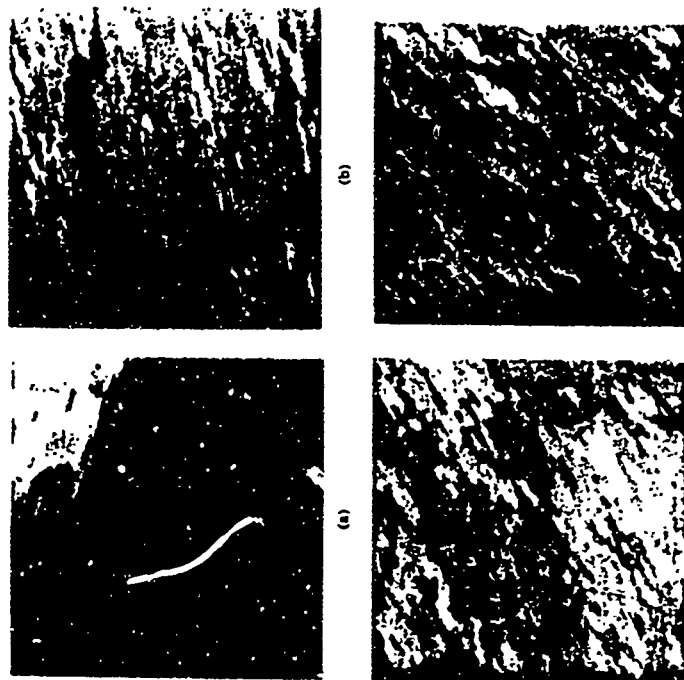


FIG 3 (a) STM image of GaAs(100) after termination of growth of 60 monolayers (VLs) (b), (c), and (d) are STM images of GaAs(100) after deposition of 120 VLs, 540 VLs, 1150 VL, respectively. The size of all images is 200nm x 200nm

The key feature of the experiment was the ability to quench the surface morphology as it appeared during growth. To accomplish this a resistively heated low thermal mass sample was used. The sample temperature could be reduced from that during growth (535°C) to below 450°C in 1.5 sec. A Li_2 cooled baffle with a cooled shutter shields the sample [3]. The quench procedure has been described previously [4]. Upon the completion of quench, the sample was transferred *in situ* to the analysis chamber equipped with an STM. The RHEED intensity was recorded up to the time of the transfer. We found that the RHEED intensity is quite steady during this period indicating that no significant surface evolution has occurred.

Figure 1a shows an STM image of a recovered surface. The terrace size is large and the step edges are smooth. This is the GaAs surface as it appears before growth. Figure 1b shows the surface after deposition of 0.25 monolayer of GaAs. The typical size of islands and the average separation between islands are 80 and 300 Å respectively. The coverage seems to be less than 25 percent because growth may have occurred at some preexisting step-edges. Figures 1c and 1d are respectively images of the surface as it appeared at the fourth RHEED intensity minimum, and the fourth maximum during the oscillatory regime. The quenched RHEED curves are reproduced in Fig. 2 for completeness.

There is clearly a morphological change in the sample surface profile as it evolves from a RHEED maximum to a RHEED minimum. The surface quenched at an intensity maximum shows few islands on terraces and an approximately equal number of monolayer deep holes. In contrast, the surface quenched at a RHEED minimum shows many two-dimensional islands on the terraces. There is a much lower density of monolayer deep holes. The terrace edges for both samples are relatively smooth.

To understand the observed morphological evolution in the context of temporal variation of the RHEED specular intensity, we briefly review various models on the interpretation of the diffraction process. Our simple approach uses a kinematic approximation to determine the interference of the scattered electrons with the surface. In this picture the measured intensity is due to the interference of the electrons scattered from different terraces on the surface. At the correct incident angle (off-Bragg condition) this leads to an oscillation of the specularly reflected intensity due to a changing terrace occupation during deposition. As each growing layer proceeds from zero coverage through half filling and finally to a complete layer the specular intensity cycles through one period. A second, largely phenomenological model which attempts to incorporate diffuse scattering has been proposed to explain RHEED oscillations. In this model the relevant quantity is not the terrace occupation but the step edge length per unit area, termed step density [6]. Steps provide a mechanism for diffuse scattering of the electron beam. With an increase in step density the specularly reflected intensity decreases. As in the previous model, if the surface morphology cycles from islanded to flat then the RHEED intensity would vary accordingly. Monte-Carlo growth simulations [7] have shown an excellent correspondence between the step density and experimental RHEED data taken on vicinal surfaces. [5] There has been criticism

of these models due to the incomplete treatment of multiple scattering (MS). While it has been experimentally demonstrated that the behavior of the scattered electrons is a complicated function of both azimuthal and polar angles [8] results from the dynamical approach [9] remain impractical due to step-surface structure idealization. However, much progress has been made in understanding RHEED through the MS approach. Mitura and Nakayama [10] have recently used MS to successfully study the RHEED Azimuthal Plots, i.e. the specular beam intensity under rotation about the perpendicular axis of the surface. Furthermore, it has been shown that for the out-of-phase diffraction condition, the MS results for specular intensity behavior agree with that of the kinematical approach [11].

Our STM data can be interpreted within the context of the step density model [12]. The diffraction conditions correspond to the "in phase" Bragg condition where electrons reflected from adjacent terraces constructively interfere. The specular intensity varies not because of interference but, because of diffuse scattering from step edges. There is a correspondence between films with higher step density and lower RHEED specular intensity. On closer inspection, we find that, within a modified Born approximation, the Bragg scattering from holes less than 5 nm in diameter contribute much less to the diffuse scattering than do islands and terrace edges. As a first approximation, if the step density contribution from small holes is subtracted from the total then the agreement between this modified step density and RHEED intensity is quite strong, see Figure 4.

To further investigate the growth process, we have also examined the sample surface after the decay of RHEED oscillations. Figure 3a shows the surface after 60 monolayers have been deposited and the RHEED oscillation amplitude has decayed to less than 5% of its original value. The sample is quenched in the same manner as before. The typical feature size has increased and in contrast to the earlier data the two-dimensional islands and terrace edges are now quite ramified. Figure 3b displays the surface after deposition of 120 monolayers. The surface in figure 3a has coarsened so much that it starts to roughen and nucleate 2D islands on top of the terraces. This may explain the increase in step density between 60-monolayer deposited surface and that of 120 monolayers. Nevertheless, the overall morphology remains flat, with about four layers present. Surprisingly, further growth does not seem to increase the surface roughness, as evidenced by figure 3c and 3d. These STM images obtained after depositing 540 and 1450 monolayers (figs. 3c, 3d respectively) show essentially identical topography to that of the 120 monolayer film. The rms roughness of these surfaces is ~ 2.5 Å. This points to a central feature of the data, that is the decay of the oscillation amplitude has occurred without an increase in the interface roughness. As shown in Figure 4a, the interface width of the grown surface increases extremely slowly. Furthermore, the surface has achieved a steady state configuration, through a balance of island nucleation and step-edge attachment, which evolves with a constant step density. In short, the surface has reached the step flow growth mode.

During deposition an adatom can either diffuse to an existing upward step or kink

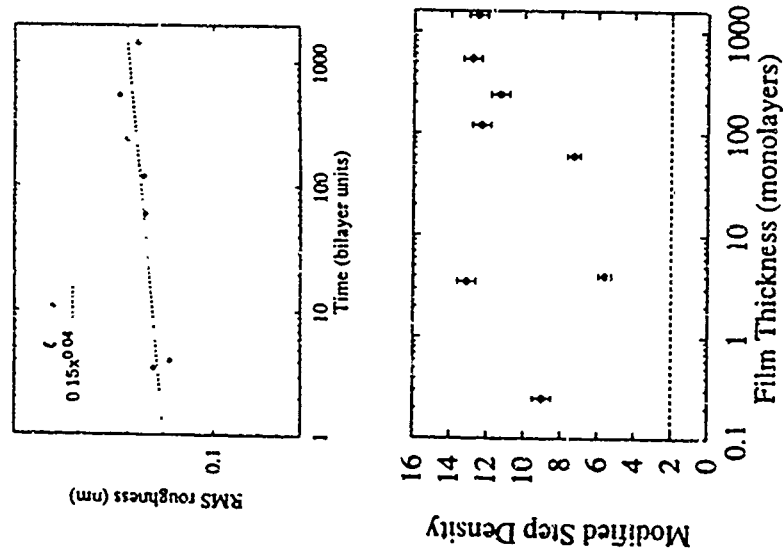


FIG. 1 (a) RMS roughness (in nm) of the surfaces as a function of deposition time (bilayer units). The rms roughness is defined as $\sqrt{\frac{1}{A} \sum (h_i - \bar{h})^2}$ where h_i is the height and the area is over a $200 \text{ nm} \times 200 \text{ nm}$ area. (b) Plot of the surface step density (in units of 10^{-4} nm^{-2}) as a function of thickness (in monolayers). The modified step density is explained in the text. The dashed line represents the starting growth rate.

on a terrace edge and be incorporated, diffuse to an existing downward step and be incorporated in the lower terrace, or collide with another adatom and form a new stable island. If the formation of new stable 2D nuclei is dominant then the growth is called layer-by-layer[13]; however, if diffusion to an existing step dominates then the growth is termed step flow. The relative probability of an adatom to follow one of these trajectories is a complicated function of the substrate temperature, growth rate, and surface morphology. The experimental results indicate that evolution of growth of GaAs can be characterized by a change in the relative probability to nucleate a new island versus attaching to an existing step edge. This evolution may be thought of as a dynamical transition to step flow growth. What is remarkable is that even though the substrate temperature and growth rate are constant, the surface morphology has been transformed to allow a new growth mode. This type of growth is not what is conventionally called step flow, i.e. a uniform progression of the steps across the surface. The classic step flow occurs when the substrate has a sufficient density of steps and very mobile adatoms. The new feature presented here is that deposition has dynamically generated a sufficient step density to allow for the change from layer-by-layer growth to step flow growth mode.

With this picture in mind, we will now perform the scaling analysis on the steady-state surface, i.e. during step-flow growth. Many theoretical models have been recently proposed to study kinetic roughening of surfaces grown with Molecular Beam Epitaxy (MBE) [14-22]. The interest stems from the success at understanding such diverse growth phenomena as directed polymers in random media, evolution of bacterial colonies, UV Chemical Vapor Deposition (UVCVD), and sedimentation in lake beds. These systems, it turns out, share common universality classes and display interesting non-trivial scaling behavior in the dynamics of their interfaces. However, there has not been agreement in how to apply these models to the case of MBE or in fact which universality class MBE growth falls under. This controversy is due in part to the lack of experimental evidence to decide which model and universality class is appropriate to describe MBE growth.

Despite the large amount of literature describing MBE growth, the only measurements of dynamic scaling in MBE growth roughening we know of are on films which were grown with low substrate temperatures and thus rough by MBE standards[23-25]. The diffusion length of an adatom on a terrace in these systems is relatively short and it is possible that these systems are governed by a different dynamics than that of typical MBE growth with rapid surface diffusion.

Dynamic renormalization group implies that in order to determine the asymptotic time evolution of a growing surface $h(x,t)$ one need only consider the contributions from long wavelength modes. The higher order terms are irrelevant and will not affect the long-time behavior. A universality class can be characterized by a simple equation for the growing interface involving only the relevant operators and from which the scaling properties can be determined. The primary quantities used to describe kinetic roughening are the asymptotic growth exponents α and β which are

expected to satisfy: $\xi^2 \propto L^{2\alpha} f(t)/L^{2\alpha\beta}$ [26] where ξ is the rms roughness, L is the size of the system, and $f(x) = x^\beta$ for short times eventually saturating to a constant at $x \sim O(1)$

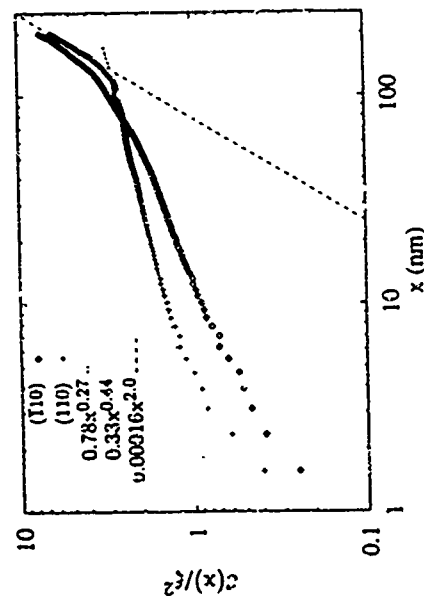


FIG 3 A Logarithmic plot, for two perpendicular crystallographic directions, of the normalized height correlation function, $C(x) = 1/2 \langle (h(r) - h(r+x))^2 \rangle$, where ξ is rms roughness. The plots were calculated by averaging the height-height correlation function of 10 independent 200nm x 200nm images which were phase subtracted so that terraces had no slope. The steep region of the function indicates the runoff of scaling due to vicinality.

Although MBE growth appears to be conceptually quite simple, i.e. no reevaporation of deposited particles and no formation of voids [27] an analytic description has not yet been determined to describe the scaling behavior. On the other hand, many numerical simulations of various growth models have been performed to determine the growth exponents α and β . In order for universality to be meaningful the details of the rules used in the simulations should not effect the asymptotic behavior of the interface. However, this does not appear to be the case for the numerical simulations. Despite various models, a conclusive statement has yet to be made regarding the MBE growth [11-20].

Nevertheless, our experimental measurement of $\beta=0.01$ (see Fig. 4a) appears to agree with the prediction of the Edwards-Wilkinson (EW) model, i.e. $\beta=0^+$ [11]. We should mention at this point a need for caution when interpreting the experimental results in terms of theoretical models. To determine the growth exponent $\beta < 0.1$ one needs to measure the roughness over a length scale L for which the interface width has not yet saturated. The time to saturation goes as L^4 , where $z = c/\beta$. For a real system this crossover time is very large, however we cannot be sure that for our measurement of β we are not still in an initial transient regime before scaling has set in. In order to be completely confident one would need to grow long enough to see the interface width saturate. Since this would involve growing to many more than 10^4 monolayers, this time will never be reached for typical device quality growth. While it is possible to grow with lower substrate temperatures to reduce the time to saturation, most experimenters and device growers are trying to produce as smooth a surface as possible and may never reach long term growth.

In an attempt to further study the surface characteristics of these films we have examined the height-height correlation function defined as $C(x) = \langle (h(r) - h(r+x))^2 \rangle$. Figure 5 shows $C(x)$ for a surface after deposition of 1450 monolayers. The correlation function is predicted to scale as $C(x) \sim x^{2\alpha}$ [28]. In fig. 5 one can observe two distinct regimes in the correlation function. The small distance dependence indicates a maximum value for the growth exponent $\alpha \leq 0.2$. The extent over which this behavior is exhibited is approximately one decade in distance. For larger distances the behavior is dominated by the vicinality of the sample. For a miscut substrate (all physically realizable samples are miscut) asymptotically $C(x)$ approaches x^2 . Our data shows this crossover at approximately $x = 100$ nm. For our experiment the sample miscut was relatively small, $\sim 0.1^\circ$, producing a typical terrace width of 100 nm. The STM images show quite clearly that during growth, there is the dynamic generation of steps and roughness with length smaller than the terrace spacing. However, as shown in the dependence of the height-height correlation function $C(x)$ the longest wavelength behavior is dominated by the terrace width for deposition thicknesses up to 1450 layers. The discrepancy between the measured $\alpha=0.2$ and the EW values ($\alpha=0^+$, $\beta=0^+$) is larger than that for measured $\beta=0.01$. This is most probably due to a greater effect which the vicinality has on surface correlations than on surface roughness.

In conclusion, we have studied the evolution of the GaAs surface during MBE growth. Starting from a recovered substrate, upon the initiation of growth the surface progresses through a transient regime, where cyclic changes in the step density are found, to a steady state. Using in-phase diffraction conditions, we have shown a clear connection between the surface morphology in terms of step density and RHEED intensity oscillations. A striking result is that the decay of the RHEED oscillations is not due to an increase in surface width, but the dynamical evolution of the surface to step flow growth, defined as a steady state with a constant step density. The measured surface roughness is consistent with the EW universality class.

The authors would like to thank Dr. D. Kessler and Professor L. Sander and Professor A. Zangwill for stimulating discussions. We also thank M. B. Elowitz and R. Sears for assistance with data analysis. This work has been supported by Grants No. N00011-89 J-1319 and No. NSF/DMR 8857828.

REFERENCES

- [1] B.A. Joyce, *Contemporary Physics*, **32**, 21 (1991) and references therein.
- [2] *Reflection High Energy Electron Diffraction and Reflection Electron Imaging of surfaces* NATO ASI series B vol. 128 edited by P.K. Larsen and P.J. Dobson (Plenum, New York, 1988).
- [3] B.G. Orr, C.W. Snyder, and M.D. Johnson, *Rev. Sci. Instrum.*, **6**, 1400 (1991).
- [4] J. Sudjono, M.D. Johnson, C.W. Snyder, M.B. Elowitz, and B.G. Orr, *Phys. Rev. Lett.*, **69**, 2811 (1992).
- [5] P.R. Fukute, C.S. Lent, and P.J. Cohen, *Surf. Sci.*, **161**, 39 (1985).
- [6] S. Clarke and D.D. Vvedensky, *Phys. Rev. Lett.*, **58**, 2235 (1987).
- [7] T. Shitara, D.D. Vvedensky, M.R. Wilby, J. Zhang, J.H. Neave, and B.A. Joyce, *Appl. Phys. Lett.*, **60** (12), 1504 (1992).
- [8] P.J. Dobson, B.A. Joyce, J.H. Neave, and J. Zhang, *J. Crystal Growth*, **81**, 1 (1987).
- [9] T. Kawamura and P.A. Maksym, *Surf. Sci.*, **161**, 12 (1983).
- [10] Z. Mitura and P.A. Maksym, *Phys. Rev. Lett.*, **70**, 2904 (1993).
- [11] M.G. Knibbs, preprint.
- [12] Our STM data are not meant to rule out other models. The experimentally chosen diffraction condition provides little information on the models.
- [13] J.H. Neave, B.A. Joyce, P.J. Dobson, and N. Norton, *Appl. Phys. A*, **31**, 1 (1983).
- [14] S.F. Edwards, and D.R. Wilkinson, *Proc. R. Soc. Lond. A*, **381**, 17 (1982).
- [15] M. Kardar, G. Parisi, and Y.C. Zhang, *Phys. Rev. Lett.*, **56**, S89 (1986).
- [16] D.E. Wolf and J. Villain, *Europhys. Lett.*, **13**, 389 (1990).
- [17] Z.W. Lai and S. Das Sarma, *Phys. Rev. Lett.*, **66**, 2348 (1991).
- [18] S. Das Sarma and P. Tamborenea, *Phys. Rev. Lett.*, **66**, 325 (1991).
- [19] D.A. Kessler, H. Levine and L.M. Sander, *Phys. Rev. Lett.*, **69**, 100 (1992).
- [20] J. Villain, *J. Phys.*, **1**, 19 (1991).
- [21] H. Yang, *Phys. Rev. Lett.*, **68**, 3018 (1992).
- [22] M. Siegt and M. Plachke, *Phys. Rev. Lett.*, **68**, 2035 (1992).
- [23] J. Chevier, V. Le Thanh, R. Boys, and J. Derrien, *Europhys. Lett.*, **10**, 737 (1991).
- [24] Y.L. He, H.N. Yang, T.M. Lu, and G.C. Wang, *Phys. Rev. Lett.*, **69**, 3770 (1992).
- [25] R. Chazotte, V. Panella, J. Krim and C. Thompson, *Phys. Rev. Lett.*, **67**, 3108 (1991).
- [26] F. Family, *J. Phys. A Math. Gen.*, **19**, L441 (1986).
- [27] The conservative nature of MBE growth, i.e. no voids, leads us to eliminate theories which do not conserve surface currents.
- [28] B.B. Mandelbrot, *The Fractal Geometry of Nature* (Freeman, New York, 1982).

-728-

-727-

Thursday, August 26

- | | |
|-----|--|
| ThA | II-VI, IV-VI and Magnetic Structures |
| ThB | Dots and Wires - Optical Properties |
| ThP | Optics, Magnetic Structures, Infrared, Devices |
| ThC | Electronic Excitations - Superlattices |

ZEEMAN TUNING OF II-VI-BASED DILUTED MAGNETIC SEMICONDUCTOR SUPERLATTICES

J. K. Furdyna
Department of Physics, University of Notre Dame, Notre Dame, IN 46556 U.S.A.

ABSTRACT

Electronic levels in II-VI-based diluted magnetic semiconductors (DMSs), e.g., $\text{Zn}_{1-x}\text{Mn}_x\text{Te}$, experience extremely large Zeeman shifts when a magnetic field is applied, reaching values of the order of 100 meV at low temperatures. Zeeman shifts of the conduction and the valence band can then have profound consequences on the properties of DMS/non-DMS superlattices, since they provide the opportunity of tuning the band alignments in such structures simply by varying the applied field. We discuss the consequences of such Zeeman-tuning, with emphasis on the creation of spatial spin modulation and on mapping of wave function distribution in superlattices.

1. INTRODUCTION

Semiconductor superlattices owe most of their spectacular properties to our ability of depositing a sequence of alternating layers of different materials, so as to form one monolithic structure. The resulting energy gap discontinuities at the interfaces of the constituent layers then define the new band structure of the system, and thus its electronic and optical properties. Investigation of the effect of band alignment in such multilayer structures is clearly of fundamental importance to the understanding of those systems. To do so, however, in most cases (e.g., in the well-known GaAs/AlAs system) requires the preparation of a series of samples, each with a different alloy composition. It would of course be much more desirable to have the means of tuning the band alignment continuously in a single sample during the experiment. Here II-VI-based diluted magnetic semiconductors offer a number of attractive possibilities, as discussed below.

Diluted magnetic semiconductors (DMSs) are semiconducting ternary or quaternary alloys whose lattice is made up in part of substitutional magnetic ions [1,2]. $\text{Zn}_{1-x}\text{Mn}_x\text{Se}$, $\text{Cd}_{1-x}\text{Mn}_x\text{Te}$, or $\text{Pb}_{1-x}\text{Mn}_x\text{Te}$ are examples of such systems. One of the most interesting and important properties of DMSs is the spin-spin exchange interaction between the band electrons and the magnetic ions localized in the lattice. This interaction -- often referred to as the sp-d interaction -- leads to an enormous amplification of Zeeman splittings of conduction and valence band edges, which at low temperatures can reach values of the order of 100 meV in moderate magnetic field (e.g., 5 Tesla). This in turn has exciting implications for quantum wells and superlattices consisting of combinations of non-magnetic and DMS layers, since it provides a handle for "tuning" the band alignment at the interfaces of constituent layers over a significant range (typically over several tens of meV) simply by varying an applied magnetic field.

2. SPIN-SPIN (sp-d) EXCHANGE INTERACTION

Before proceeding with specific structures, we first briefly describe the sp-d exchange interaction itself, since this mechanism is responsible for all effects presented in this paper. Let us, for specificity, consider $\text{Zn}_{1-x}\text{Mn}_x\text{Se}$, which will appear in several superlattices to be discussed below. In order to account for the effect of exchange interaction between the band electrons and the localized Mn spins in $\text{Zn}_{1-x}\text{Mn}_x\text{Se}$, one must include a new term into the band-structure Hamiltonian, as follows:

$$H_{\text{ex}} = \sum_i \kappa_{\text{eff}} \mathbf{S}_i \cdot \mathbf{S}_i^{\text{eff}} \quad (1)$$

where κ_{eff} is the effective Mn concentration, \mathbf{S}_i is the exchange integral appropriate either for the conduction or for the valence band, $\mathbf{S}_i^{\text{eff}}$ is the electron spin, and $\langle S_z \rangle$ is the thermally averaged Mn spin, given by

$$\langle S_z \rangle = -\frac{1}{2} B_{5/2}(\beta \mu_B B / k_B T + T_0) \quad (2)$$

Here $B_{5/2}$ is the Brillouin function of the

argument in square brackets, μ_B is the Bohr magneton, B is the applied magnetic field, k_B is the Boltzmann constant, T is the temperature, and T_0 is a parameter representing antiferromagnetic interactions between the Mn ions [3]. The consequences of Eq. (1) have been extensively discussed in the literature [2]. The resulting Zeeman splitting of the conduction and valence band edges is schematically depicted in Fig. 1. Spin-up and spin-down states are symbolized by arrows in the figure, and the light-hole band splitting is shown by horizontal dashed lines. Allowed interband transitions are shown by vertical lines, with corresponding circular polarizations indicated by σ_+ and σ_- .

As seen in the figure, the splitting of the heavy-hole band is considerably larger than for the conduction band, and is opposite in sign (i.e., the energy for spin-up electrons increases, and for spin-up heavy holes it decreases, when a magnetic field is applied). The behavior of light holes, on the other hand, is nearly identical to that of electrons, in sign and in magnitude. In the present paper we shall be interested in the dominant features observed in optical properties of DMS-based superlattices, which are determined by the spin-conserving transitions indicated by arrows in Fig. 1. Since transitions involving light holes (broken lines in the figure) are generally much weaker than those associated with heavy holes, in this brief presentation we will restrict ourselves to effects associated only with the heavy holes.

The Zeeman splittings in Fig. 1 can be conveniently represented by an effective g-factor in the form

$$\Delta E = g_{\text{eff}}^{\text{hh}} \mu_B B \quad (3)$$

where the subscript h refers to the conduction or the heavy-hole band, and $g_{\text{eff}}^{\text{hh}}$ is given by

$$g_{\text{eff}}^{\text{hh}} = g_s^{\text{hh}} - N_0 \kappa_{\text{eff}} \langle S_z \rangle / \mu_B B \quad (4)$$

$$g_s^{\text{hh}} = g_{\text{hh}}^{\text{hh}} - N_0 \kappa_{\text{eff}} \langle S_z \rangle / \mu_B B \quad (5)$$

Here g_s^{hh} is the g-factor obtained from the band structure without the exchange contribution (typically of the order of unity), and N_0 and $N_0 \beta$ are the traditional designations for the s-like conduction electron and p-like heavy hole exchange integrals [1]. The terms containing α and β are strongly temperature dependent because of the presence of $\langle S_z \rangle$ (see Eq. (2)), and can be as large as 100 or more at low temperatures.

As already pointed out, the sp-d exchange interaction has particularly important implications for DMS/non-DMS superlattices, since it can be used to vary the superlattice potential profile in a single sample. Below we will focus on two striking examples of such "Zeeman tuning" in DMS-based superlattices: spin segregation, and "mapping" of the spatial wave function distribution.

3. SPIN-SEPARATING STRUCTURES

A. Spin Superlattices

A "spin superlattice" (SSL) is a superlattice in which carriers with opposite spin states are confined in different layers. In order to achieve such spin-modulation, we look for a structure in which the energy gaps of the constituent layers are initially (i.e., in the absence of magnetic field) equal, and the band offsets at the interfaces are initially zero, as shown at the top of Fig. 2 (where DMS regions are designated by shading). When a magnetic field is applied, the large Zeeman splitting of the band edges in the DMS layers results in induced band offsets and, consequently, in a spatial separation of the spin-up and spin-down states, as shown in Fig. 2

(bottom). The SSL phenomenon has already been observed experimentally in several DMS/non-DMS multi-quantum well systems [4,5].

One particularly attractive DMS system for achieving the structure described above is the $\text{ZnSe}/\text{Zn}_{1-x}\text{Mn}_x\text{Se}$ superlattice. The energy gap of $\text{Zn}_{1-x}\text{Mn}_x\text{Se}$ exhibits a rather striking bowing with Mn concentration x at low temperatures, first decreasing with x , and then rapidly increasing [6]. It is thus possible to find a value of x at which $\text{Zn}_{1-x}\text{Mn}_x\text{Se}$ has the same energy gap as ZnSe (this occurs for $x = 0.04$ at 1.5 K). Furthermore, since the valence band offsets at $\text{ZnSe}/\text{Zn}_{1-x}\text{Mn}_x\text{Se}$ interfaces are close to zero by the common anion rule (which works reasonably well in wide gap II-VIs), the value of x which gives equal energy gaps in ZnSe and $\text{Zn}_{1-x}\text{Mn}_x\text{Se}$ automatically leads to zero (or, in practice, to very small) band offsets in the conduction and the valence bands, thus satisfying the properties stipulated in the preceding paragraph.

Examining Fig. 1 we note that, when the magnetic field is applied, the band edge of $\text{Zn}_{1-x}\text{Mn}_x\text{Se}$ for spin-down electrons will move down, and it will move up in energy for spin-up holes. The $\text{Zn}_{1-x}\text{Mn}_x\text{Se}$ layers thus become wells for both carriers of the spin-down orientation. Similarly, for spin-up states the conduction band moves up in energy, and the heavy-hole band moves down, so that for this spin orientation the ZnSe layers become wells. This magnetic field-induced band offset has therefore the consequence of spatially separating electron and hole states of different spin orientation. It is particularly convenient to observe the formation of such spin separation in magnetoabsorption experiments with the magnetic field applied perpendicular to the SSL layers (the Faraday geometry), in which only spin-conserving transitions are allowed ($\Delta S = 0$). Using left- and right-handed circular polarizations (from here on designated by σ_L and σ_R), one can then observe separately transitions between spin-up valence and conduction band states (corresponding to σ_R), and those between spin-down states (σ_L).

Fig. 3

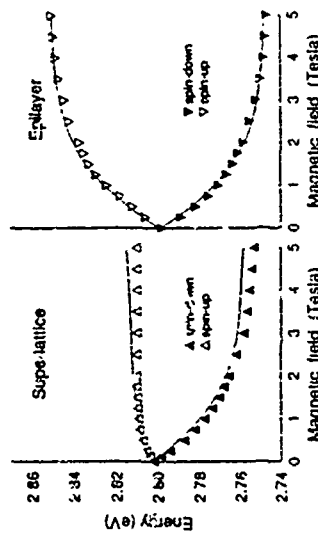


Figure 3 (left) shows the magnetic field dependence of excitonic transitions observed with the σ_L and σ_R polarizations in a $\text{ZnSe}/\text{Zn}_{0.96}\text{Mn}_{0.04}\text{Se}$ SSL, with DMS and non-DMS layers 112 Å wide. The figure illustrates very nicely the spatial separation of spins occurring in the SSL. Considering first the spin-down (σ_L) transition, we see the rapid red shift of the σ_L absorption line, since the initial and final states of the transition are both in the DMS layers as finite magnetic field, and follow the field dependence of the valence and conduction band edges of the DMS material (see Fig. 1). In contrast, the spin-up transitions take place between states localized in the ZnSe layers, which become wells for this spin orientation when the field is applied. This is responsible for the flatness of the transition energy at higher fields — in the effect becomes well defined. The small initial rise in energy seen in Fig. 3 at low fields is due to the fact that the static well pinning to form) arises from the fact that in this region of extremely shallow wells the static well in the ZnSe well is much more sensitive to the height of the (DMS) barrier, which increases with the field. As the barrier continues to increase, the energy of the state confined in the ZnSe well becomes less and less sensitive to the barrier height and eventually flattens out, approaching the behavior of the non-magnetic quantum well in which that state is confined [4,5].

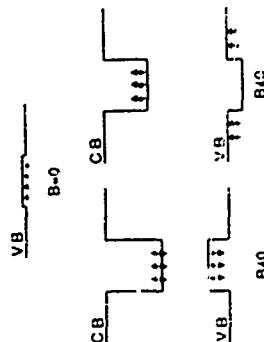
For comparison, we show on the right of Fig. 3 the position of free exciton magnetoabsorption data observed for σ_L and σ_R polarizations in an epilayer grown with the same Mn concentration as the $\text{Zn}_{1-x}\text{Mn}_x\text{Se}$ layers of the SSL. Note that, in contrast with the SSL data, the σ_L and σ_R branches for the epilayer are quite symmetric. The asymmetry seen on the left-hand side is a characteristic signature of spin-separating structures.

B. Magnetic-Field-Induced Type-I \rightarrow Type-II Transition

Systems closely related to the SSL are DMS-based superlattices which exhibit a transition between type-I and type-II band alignment. Consider as an example a DMS/non-DMS superlattice with a type-I band alignment at $B = 0$, consisting of deep conduction band wells and shallow wells in the valence band, both occurring in DMS layers, as shown in Fig. 4 (top). As before, DMS regions are indicated by shade. Consider now what happens when a magnetic field is applied. For our spin orientation (spin-down) this will only enhance the type-I nature of the band alignment (i.e., wells in both bands become deeper). For the other spin state, however, the enormous Zeeman splitting of the valence band will at some field exceed the initial offset of that band, transforming the original valence band well into a barrier, as shown in Fig. 4 for $B \neq 0$.

Conversion from type-I to type-II superlattices is manifested by a dramatic change in optical properties, because in a type-II structure the carriers initially involved in the strongest optical transitions are now physically separated into different layers. The phenomenon of such band-alignment conversion has already been experimentally observed in several systems, e.g., in $\text{Zn}_{1-x}\text{Fe}_x\text{Se}/\text{ZnSe}$ [7] and $\text{Cd}_{1-x}\text{Mn}_x\text{Te}/\text{CdTe}$ [8]. It is important to note that this phenomenon is particularly important in II-VI-based DMS superlattices involving common-anion systems (e.g., $\text{ZnMnSe}/\text{ZnSe}$), since these are typically characterized by very small valence-band offsets. Such small offsets can be easily overcome by the large Zeeman shift of the valence band, thus changing the type of alignment even at moderate magnetic fields. When this is achieved, we automatically obtain spatial separation of spin states similar

Fig. 4



to the spin superlattice discussed earlier, but for one band only. α : in the case of the SSL, such spin separation again leads to the characteristic asymmetry of transition energies already seen in Fig. 3 because of the difference in the values of α and β .

4. MAPPING OF WAVE FUNCTIONS IN SUPERLATTICES

One of the most important properties of semiconductor superlattices is their ability to localize electrons and holes in specific layers. Localization of carriers (as measured by their spatial wave-function distributions) is fairly obvious for low-lying states in deep quantum wells. It is an altogether different matter, however, for states at energies above the barriers: these may be confined in well layers, in barrier layers, or may not be localized at all. Furthermore, below-barrier states with energies close to the top of the barrier (i.e., states in very shallow wells, or high-lying excited states) exhibit significant leakage into the barrier regions. Determination of the degree of leakage in the latter case, and of the region of localization in the case of above-barrier subbands, presents a major challenge.

One can meet this challenge by exploiting the fact that, in superlattices consisting of DMS and non-DMS layers, the Zeeman splitting of a given state will reflect its weighted probability distribution over the two media. In other words, the Zeeman splitting will be determined effectively by how many localized magnetic moments does the electron "see". This has already been alluded to in the case of spin superlattices (the spin-up transitions in the left panel of Fig. 3), and in this section we emphasize the application of this idea further, specifically as a tool for mapping the wave function (or probability) distribution in superlattices and other heterostructures.

Consider first below-barrier states. Figure 5 shows photoluminescence (PL) spectra obtained at several magnetic fields on two superlattices consisting of non-DMS quantum wells ($\text{Zn}_{1-x}\text{Cd}_x\text{Se}$, $x = 0.12$) and DMS barriers ($\text{Zn}_{1-x}\text{Mn}_x\text{Se}$, $x = 0.20$) with different well widths (45 Å and 135 Å) [9]. States in the narrower wells, lying closer to the top of the barrier, should experience a greater degree of penetration into the DMS barrier layers -- and thus a greater Zeeman splitting -- than states in the wider wells. This is clearly seen in Fig. 5 by the amount of σ shift exhibited by PL from the two superlattices when magnetic field is applied. We remark parenthetically that in the PL data in Fig. 5 only the red shift is observed (corresponding to spin down transitions i.e., to the σ_L polarization), since these lower energy transitions become energetically favored as the field increases. In fact there can also be observed a weak blue-shifted line corresponding to the σ_R polarization, but this decreases rapidly in intensity with field, and at fields shown in Fig. 5 is no longer seen on the scale of the figure. The rise of decay of the σ_R component can in fact be used to investigate spin lifetimes [10] -- another important topic in the area of Zeeman-tuning which, however, is outside the scope of the present paper.

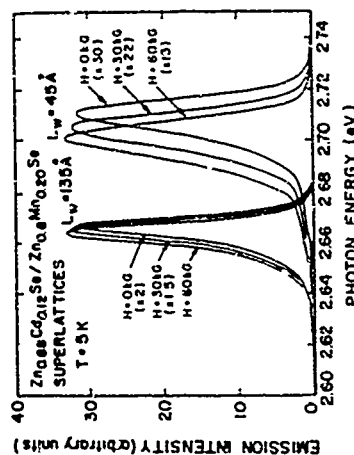


Fig. 5

A more challenging -- and qualitatively different -- aspect of wave function mapping is the distribution of superlattice subbands with energies exceeding the top of the barriers. We will illustrate this by discussing the localization of above-barrier excitons in type-I ZnSe/ZnMnSe superlattices, and of type-II (spatially-direct) excitons in type-II ZnTe/CdMnSe and Zn:MnTe/CdSe superlattices.

A. ZnCdSe/ZnMnSe Type-I Superlattice

The observations of transitions involving above-barrier states in superlattices were first reported several years ago [11,12]. Since then it has become clear that such high-lying subbands participate strongly in optical transitions due to the formation of localized states above the barriers. This has been clearly demonstrated experimentally for type-I ZnCdSe/ZnMnSe superlattices [13], and we will use such a superlattice ($\text{Zn}_{0.8}\text{Cd}_{0.2}\text{Se}/\text{Zn}_{0.8}\text{Mn}_{0.2}\text{Se}$, with well and barrier widths both equal to 75 Å) as an example. The band structure of this system is depicted in the inset of Fig. 6. Since the energy gap of ZnCdSe is considerably smaller than that of ZnMnSe for the Cd and Mn concentrations used here, the wells correspond to the nonmagnetic layers, while the barriers are magnetic.

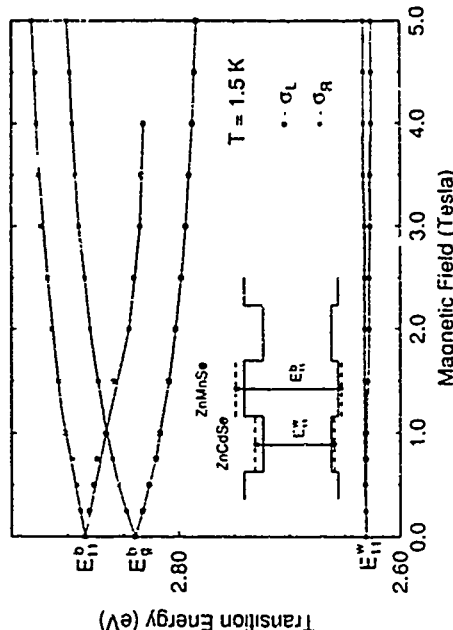


Fig. 6

The structure exhibits several strong excitonic peaks at low temperature. We concentrate on the lowest energy peak labeled E_{11}'' in Fig. 6, which is identified as the free exciton transition between the first heavy-hole ground state and the conduction electron ground state of the superlattice; and peak E_{11}' , which is identified as the transition between the first above-barrier heavy-hole state and the first above-barrier electron state (the lowest-energy above-barrier transition). Note that E_{11}' occurs at a higher energy than the energy gap of the barrier material, the latter determined on an epilayer of $\text{Zn}_{0.8}\text{Mn}_{0.2}\text{Se}$ grown under identical conditions as the barriers and labeled E_g^B in the figure.

When an external magnetic field is applied, the band edges of the ZnMnSe barriers will be Zeeman-split, leading in turn to the splitting of optical transitions in the superlattice. Figure 6 shows the energies of the E_{11}' and E_{11}'' transitions as a function of the applied field. Also shown in the figure is the Zeeman splitting of the exciton line E_{11}'' . The solid lines in the figure are only to

guide the eye. It is significant that the spin splitting of the above-barrier transition E_{11}^{\uparrow} is clearly much larger than that of the below-barrier transition E_{11}^{\downarrow} , and almost (but not quite) as large as that in the ZnMnSe epilayer.

We recall that the structures investigated are type-II superlattices, consisting of nonmagnetic wells and magnetic barriers. The relatively small (but observable) Zeeman splitting of the ground-state exciton transition E_{11}^{\uparrow} (which originates and terminates in the nonmagnetic wells) thus arises from the partial penetration of the wave functions of the initial and final states into the magnetic barriers. By contrast, the much larger Zeeman splitting of E_{11}^{\downarrow} (almost the same as that for the bulk Zn_{0.99}Mn_{0.01}Se material) indicates that the E_{11}^{\downarrow} transition originates and terminates on states localized predominantly in the DMS (i.e., the barrier) regions. The fact that the splitting of E_{11}^{\downarrow} is slightly (about 15%) below that observed for the Zn_{0.99}Mn_{0.01}Se epilayer indicates that a part of the above-barrier wave functions which determine the transition extends into the non-DMS layers. The data shown in Fig. 6 thus provide direct evidence that above-barrier excitons in a type-I superlattice are localized in the barrier layers.

B. CdSe/ZnMnTe and CdMnSe/ZnTe Type-II Superlattices

Using the same techniques, it was also shown that there exist spatially direct type-II-like excitons in type-II superlattices [14,15]. The inset in Fig. 7 shows a schematic diagram of the type-II band alignment for a CdMnSe/ZnTe superlattice. Here the quantum wells for electrons and for holes exist in different (i.e., adjacent) layers. The conduction electrons at energies below the barriers are localized in the CdMnSe layer, while the below-barrier heavy holes are in the ZnTe layers. Excitonic transitions have been considered unimportant in such a system, because wave functions of the electrons and the holes are spatially separated, resulting in weak Coulomb attraction.

As seen in the inset, two types of excitonic transitions are possible in such type-II superlattices. One takes place between electron states localized in CdMnSe wells and hole states in ZnTe wells, as shown by the arrow marked "II" in Fig. 7. This is the well-studied type-II

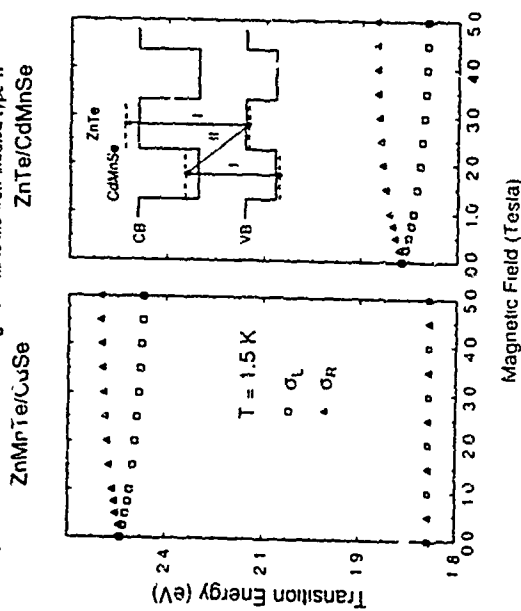


Fig. 7

excitonic transition. The other occurs between electron (or hole) subbands confined in the wells, and hole (or electron) subbands at above-barrier energies, confined in the barriers. In that case both the initial and the final state involved in a given transition are localized in the same layer, as shown by the arrow marked "I" in Fig. 7. We shall refer to these spatially direct processes as type-I excitonic transitions.

To show the existence of type-I excitons in type-II superlattices, and to pin-point their localization, we studied two systems: CdSe/Zn_{0.99}Mn_{0.01}Te, where conduction electrons are localized in a nonmagnetic well, and Cd_{0.99}Mn_{0.01}Se/ZnTe, where electrons are localized in a magnetic well. In these two cases the type-I excitons confined in the nonmagnetic layer will exhibit very different magneto-optical properties from those confined in the DMS layer.

The magneto-optical spectrum measured on CdSe/ZnMnTe superlattices revealed two clear excitonic absorption peaks, whose energies are shown on the left in Fig. 7. The lower energy peak was identified as the type-I (spatially direct) excitonic transition between the lowest electron state confined in the CdSe conduction-band wells and the first above-barrier hole state confined in the CdSe valence-band barrier layers. The higher-energy peak was attributed to a similar type-I transition, between the above-barrier electron state confined in the ZnMnTe barriers and the hole state confined in the ZnMnTe wells.

The difference in the magneto-optical behavior of both transitions is shown in Fig. 7, where energies observed for σ_L and σ_R circular polarizations are plotted as a function of magnetic field. It is quite striking that there is no observable splitting for the lower-energy transition, confirming that this transition indeed takes place between states strongly localized in the nonmagnetic CdSe layers. In contrast, there is a large Zeeman splitting for the higher-energy transition, which clearly indicates that it occurs between states localized in the DMS layer.

On the right of Fig. 7 we also show the Zeeman splitting of the lowest-energy absorption peak observed in the ZnTe/CdMnSe superlattice. This absorption line now exhibits a large Zeeman splitting, indicating that the transition occurs between electron states localized in CdMnSe wells and above-barrier holes localized in the same layers. (The higher-energy line, which now would correspond to states localized in the ZnTe layers, was obscured by the absorption due to the ZnTe buffer on which this structure was grown.) Both panels of Fig. 7 thus clearly establish the existence of type-I excitons in type-II superlattices, and identify their localization.

The unambiguous experimental demonstration of how above-barrier states are distributed in space was accomplished by exploiting the difference in Zeeman splitting in the DMS and the non-DMS regions comprising the superlattices. However, it should be emphasized that the effects discussed here are of course not limited to systems based on the DMSs, but represent general properties of type-I and type-II superlattices. The role of the DMS component is only used as a "marker", in order to bring out these general properties of wave function distribution

5. CONCLUDING COMMENTS

In this relatively brief review we have described several important illustrations of Zeeman tuning effects in DMS/non-DMS superlattices, but the material covered should by no means be considered as exhaustive. We have thus not concerned ourselves with the application of Zeeman tuning as a tool for band offset determination in quantum wells [16], with its possible applications in narrow-gap semiconductors (where the consequences of Zeeman splitting are expected to be especially striking, since it can in those materials be comparable to the gap itself), with the interesting prospect of Zeeman-tunable coupling in double quantum wells separated by DMS barriers [17], with the already mentioned spin lifetime determination [10], or the yet unexplored territory of band-edge tuning relative to impurity levels in modulation-doped structures (magnetic freeze-out and boil-off) [18,19]. With further advances in the preparation of new DMS/non-DMS heterostructure configurations, the number and sophistication of these novel situations can only be expected to increase.

ACKNOWLEDGMENTS

The author wishes to acknowledge invaluable discussions and collaborations with his colleagues M. Dobrowolska, H. Luo, Z. R. Ram-Mohan, N. Dai, and F. Zhang. The work was supported by the U.S. National Science Foundation Grant DMR-920841X.

REFERENCES

1. J. K. Furdyna and J. Kossut, eds., *Diluted Magnetic Semiconductors*, Vol. 25 of *Semiconductors and Semimetals* (Academic, Boston, 1988).
2. J. K. Furdyna, *J. Appl. Phys.* **64**, 829 (1988).
3. J. A. Gaj, P. Planet, and G. Fishman, *Solid State Commun.* **79**, 435 (1979).
4. W. C. Chou, A. Petrou, J. Warnock, and B. T. Jonker, *Phys. Rev. Lett.* **67**, 3820 (1991).
5. N. Dai, H. Luo, F. C. Zhang, N. Samarth, M. Dobrowolska, and J. K. Furdyna, *Phys. Rev. Lett.* **67**, 3824 (1991).
6. A. Twardowski, T. Dietl, and M. Demianiuk, *Solid State Commun.* **48**, 845 (1983).
7. X. Liu, A. Petrou, J. Warnock, B. T. Jonker, G. A. Prinz, and J. J. Krebs, *Phys. Rev. Lett.* **63**, 2280 (1989).
8. E. Defeo, J. M. Bernor, G. Bastard, C. Delalande, J. M. Hong, and L. L. Chang, *Phys. Rev. B* **42**, 5891 (1990).
9. R. G. Alonso, Eunsoo Oh, A. K. Ramdas, H. Luo, N. Samarth, J. K. Furdyna, and L. R. Ram-Mohan, *Phys. Rev. B* **44**, 8009 (1991).
10. B. T. Jonker, L. P. Fu, W. Y. Yu, W. C. Chou, A. Petrou, and J. Warnock, *J. Electronic Materials* **22**, 489 (1993).
11. J. E. Zucker, A. Pinchuk, D. S. Chemla, A. Gossard, and W. Weigman, *Phys. Rev. B* **29**, 7065 (1984).
12. J. J. Song, Y. S. Yoon, A. Feldtowsky, Y. B. Kim, J. N. Schulman, C. W. Tu, D. Huang, and H. M. ... *Phys. Rev. B* **34**, 8938 (1986).
13. F. C. Zhang, N. Dai, H. Luo, N. Samarth, M. Dobrowolska, J. K. Furdyna, and L. R. Ram-Mohan, *Phys. Rev. Lett.* **68**, 3220 (1992).
14. F. C. Zhang, H. Luo, N. Dai, N. Samarth, M. Dobrowolska, and J. K. Furdyna, *Phys. Rev. B* **47**, 3806 (1993).
15. H. Luo, W. C. Chou, N. Samarth, A. Petrou, and J. K. Furdyna, *Solid State Commun.* **85**, 691 (1993).
16. W. J. Walicki, A. V. Nurmikko, N. Samarth, H. Luo, J. K. Furdyna, and N. Otsuka, *Appl. Phys. Lett.* **57**, 466 (1990).
17. J. F. Smyth, D. D. Awschalom, N. Samarth, H. Luo, and J. K. Furdyna, *Phys. Rev. B* **46** (Rapid Comm.), 4340 (1992).
18. S. Datta, J. K. Furdyna, and R. L. Gunshor, *Superlattices and Microstructures* **1**, 327 (1985).
19. J. Kossut and J. K. Furdyna, *Acta Phys. Polon.* **A 73**, 851 (1988).

Novel Magnetic Phase Transition Behavior in Short Period EuTe/PbTe Superlattice

J. J. Chen, Z. H. Wang, M. S. Dresselhaus, G. Dresselhaus
Massachusetts Institute of Technology

G. Springholz and G. Bauer
Johannes Kepler Universität Linz

Abstract

[EuTe]₁₀/[PbTe]₁₀ short period superlattices were grown by MBE along the [111] growth direction with ζ denoting the number of monolayers of EuTe separated by η monolayers of diamagnetic PbTe, and $2 \leq \zeta \leq 5$ alternated with $6 \leq \eta \leq 15$. We find that superlattices with even ζ numbers show antiferromagnetic phase transitions, those with odd ζ show ferromagnetic phase transitions, while bulk EuTe is a simple two-sublattice antiferromagnet. The transition temperatures T_c observed for these short period superlattices are all below or close to the bulk phase transition temperature and T_c increases as ζ increases. An antiferromagnetic interlayer correlation along the direction 1 to the superlattice planes is found for superlattices with $\eta \leq 12$. In the paramagnetic regime, the Curie Weiss law fits well for all superlattices except $\zeta=2$, which has its $M(T)$ proportional to $1/\ln T$ instead of the usual $1/T$ dependence. Positive paramagnetic Curie-Weiss temperatures θ are obtained for superlattices with odd ζ numbers while negative θ are obtained for even ζ .

EuTe have been investigated in detail [1]. Both EuTe and PbTe crystallize in the rock salt structure. Their lattice mismatch is 2.1%. The (111) planes perpendicular to the growth direction contain either Eu or Te ions. Within the (111) planes the Eu ions have ferromagnetic coupling denoted by J_1 and antiferromagnetic coupling between adjacent planes denoted by J_2 , and in the bulk $J_1/J_2 \sim -3.5$. Recently the MBE growth of such (EuTe/PbTe)_n superlattices was studied [2] and x-ray investigations have shown their high structural perfection.

We report here temperature-dependent magnetization results from 2 K to 100 K for short period EuTe/PbTe superlattices. The effects of the number of contiguous EuTe layers in the superlattice and of the spacing between these EuTe layers on the magnetic transition temperatures and on the magnetic correlation along the [111] axis (perpendicular to the superlattice plane), is discussed. The observed phase transitions in the magnetization results are analyzed by mean field theory. The Curie-Weiss law is used to fit the magnetization data in the high temperature regime and paramagnetic Curie-Weiss temperatures are obtained.

[EuTe]₁₀/[PbTe]₁₀ short period SL's were grown by MBE along the [111] growth direction. These superlattices have EuTe thicknesses ζ ranging from 2 to 5 monolayers with intervening PbTe thickness η ranging from 6 to 15 monolayers. Typically 1000 Å of PbTe was first deposited to relieve the substrate film interface strain before the growth of alternating EuTe and PbTe layers [2]. These samples all have lateral dimensions of approximately 3 mm by 4 mm. In each of the superlattice samples, the ratio η/ζ is kept at 3, so that the biaxial in plane strains of $\epsilon_{\text{EuTe}} = -1.52\%$ and $\epsilon_{\text{PbTe}} = 0.55\%$, assuming a free standing SL stack, are the same for all measured samples.

The temperature dependent magnetization of these SL's was measured by SQUID magnetometry with the H field in the plane of the SL. The sample

In this work we show that Molecular Beam Epitaxial (MBE) growth technology allow us to prepare a ferromagnetic or antiferromagnetic superlattice (SL) using the same building blocks by growing magnetic layers of different numbers of monolayers in the superlattice. Namely, if the number ζ of magnetic layers is an even number, then antiferromagnetism should result, but if ζ is odd then ferromagnetism should result. Thus by selecting the number of layers different magnetic behavior is observed with no change in atomic structure or chemical species.

In our study we chose our magnetic material to be EuTe, a Heisenberg antiferromagnet (AFM) type II with the MnO structure and a Neel temperature $T_N = 9.6$ K. Along with other europium chalcogenides (EuO, EuS, EuSe), the magnetic properties of bulk

Figure 1 Temperature dependent magnetization for a bulk EuTe thin film and a superlattice [EuTe(4)/PbTe(12)]₁₀₀. The applied field is in the plane of the film with strengths of 1.000 gauss. A sample and 75 gauss for the superlattice.

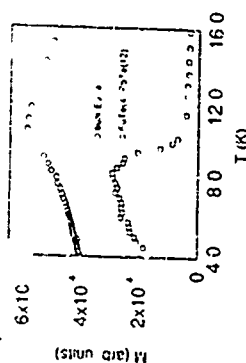


Figure 2 Temperature dependent magnetization measured with the external field $B = 1$ gauss applied parallel to the thin film plane of superlattice [EuTe(3)/PbTe(9)]₁₀₀. The solid line shows a fit to the data using a modified Brillouin function with $T_0 = -0.2$ K. The inset shows the hysteresis loop of same sample taken at 4.7 K.

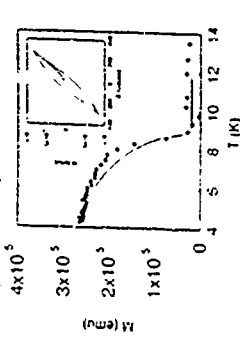


Table 1 Paramagnetic Curie Weiss temperatures θ for short period EuTe/PbTe superlattices

EuTe(4)/PbTe(9)	2/6	3/9	4/12	5/15
θ (K)	3.60	-3.32	0.44	

is held within a transparent plastic drinking straw which is attached to the end of the sample rod of the magnetometer (Quantum Design SQUID system). Magnetization measurements $M(T, H)$ are made after the sample is cooled in zero field to below the transition temperature, and the strengths of the applied field are varied from 10 to 50 gauss. Since the applied field is quite small, the remanent field H_r is monitored by a palladium reference sample, and it is kept below 0.1 gauss by eliminating trapped flux.

First, the temperature-dependent magnetization (Fig. 1) of a MBE-grown EuTe film with a thickness of 3 μm was measured by SQUID magnetometry with $H = 1000$ gauss applied in the plane of the film. A Neel temperature of $T_N = 96$ K was thus found in agreement with that for bulk single crystal EuTe [1]. The magnetization measured by applying an H field perpendicular to the film plane shows no interesting features because the spins are lying in the film plane, and pointing in equivalent $[110]$ directions [2].

The same type of $M(T)$ measurements were then made on short period EuTe SLs with the low H fields applied in the film plane. After the sample was cooled in the zero field, indeed a ferromagnetic transition (Fig. 2) is observed for [EuTe(3)/PbTe(9)]₁₀₀ superlattices with three EuTe monolayers, which has a transition temperature of $T_N = 83$ K (discussed below). This superlattice also shows clear hysteresis effects for magnetization measurements below T_N (in Fig. 2) a manifestation of the formation of long range order. In contrast, we found an antiferromagnetic transition (Fig. 1) in the [EuTe(4)/PbTe(12)]₁₀₀ superlattice with four EuTe monolayers which has a magnetic ordering temperature of $T_N = 94$ K. Furthermore, the [EuTe(5)/PbTe(15)]₁₀₀ superlattice with five EuTe

$$M(T) = \left(\frac{T - T_N}{T_N} \right)^J \quad (1)$$

yielding $J = 0.159$ for the [EuTe(3)/PbTe(9)]₁₀₀ SL and $J = 0.252$ for [EuTe(4)/PbTe(12)]₁₀₀. These J values were found to fall in between $J = 0.125$ and $J = 0.33$ for the 2D and 3D universality classes, consistent with the observed magnetic phase transitions of lower dimension than the phase transitions occurring in bulk samples.

For the $\xi = 2$ and $\xi = 4$ samples antiferromagnetic transitions are observed. Following the convention in determining T_N for bulk EuTe, we obtained $T_N = 4$ K for the $\xi = 2$ sample. For the $\xi = 1$ superlattice it is seen that there is a ferromagnetic transition at 9.3 K, followed by antiferromagnetic behavior at higher temperatures (see Fig. 1). Thus the maximum intensity position of the steepest rise $M(T)$ is determined to be the ordering temperature at 5.4 K. Notice that $M(T)$ is nearly symmetric about T_N for $\xi = 2$ superlattices (see Fig. 1) whereas $M(T)$ is asymmetric about T_N for bulk EuTe. This difference agrees with the prediction of $\chi(T)$ for 2D and 3D antiferromagnetic phase transition [3].

The dependence of the experimental magnetic or

Figure 3 Parallel magnetization versus temperature (denoted by solid circles) measured after superlattice [EuTe(3)/PbTe(9)]₁₀₀ was cooled in zero field (i.e., at 0.7 gauss). Open circles show the parallel $M_p(T)$ measured after the same superlattice was cooled in an external field of 50 gauss. Both measurements were taken with an external field of 50 gauss.

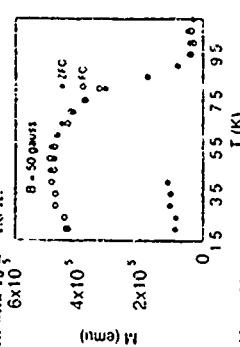


Table 2 The magnetic ordering temperature T_N for various numbers of EuTe layers ξ (for bulk EuTe, $T_N = 96$ K).

# of EuTe monolayers	2	3	4	5
T_N (K)	4.33	8.25	9.4	9.6

ordering temperature T_N on the number of EuTe layers ξ is summarized in Table 2, showing an increase in T_N with an increase in ξ . We note the rapid convergence in T_N to the bulk T_N value with increasing ξ .

We studied the effect of the number of intervening PbTe monolayers n on the magnetic correlation along the $[111]$ axis, the axis perpendicular to the film plane by measuring the temperature dependent magnetization $M(T)$ of a SL [EuTe(5)/PbTe(93)]₁₀₀ and comparing this $M(T)$ to that of [EuTe(5)/PbTe(15)]₁₀₀. The measurements for T_N show little difference between the two samples, thus suggesting the absence of magnetic correlation between two adjacent EuTe blocks separated by an intervening PbTe block of ≥ 15 monolayers, in agreement with elastic neutron scattering experiments on the [EuTe(5)/PbTe(15)]₁₀₀ superlattice which shows almost no magnetic correlation along the $[111]$ axis with $T_N \geq 1.8$ K [6]. On the other hand, for the SL's [EuTe(4)/PbTe(12)]₁₀₀ and [EuTe(3)/PbTe(9)]₁₀₀ strong magnetic correlation along the $[111]$ axis are observed by neutron scattering experiments at 4.2 K in zero external magnetic field [6]. These results imply that an antiferromagnetic interlayer correlation exists along the $[111]$ axis provided that the PbTe layer thickness is no more than 12 monolayers. The interlayer correlation in the [EuTe(3)/PbTe(9)]₁₀₀ SL arises from dipole-dipole interaction between two EuTe layers across the intervening PbTe, which reduces the net magne-

Band Effects and Electronic Structures of $(\text{ZnCdHg})_{1-x}\text{Te}$ Strained Superlattices

Yoshiko Nakayama
Department of Physics, Faculty of Science, Chiba University,
1-33, Inage, Chiba 263 Japan

Abstract
Band effects and electronic structures of various (II-VI) strained superlattices are calculated by the first-principles pseudopotential method in the local density approximation. The differences of band structures under strain between wurtzite and zinc blende crystal structures are first analyzed. The deformation potentials are calculated for all (II-VI) compounds. However, the strain in (II-VI) superlattices is so large that nonlinear variation of energy levels with changing the magnitude of strain appears. There is a chemical trend of effect that energy levels of the heavy hole and the electron states increase as the atomic number of anion and cation atoms increases, respectively. The calculated band offsets drastically vary with changing strain surroundings. The practical usage of the present results is illustrated.

1. Introduction

(II-VI) semiconductor compounds have a high potential to optoelectronic usage, because their band gaps cover the spectral region of visible light. It has become possible by the developments of crystal growth techniques to synthesize (II-VI) strained superlattices (SLs) of good quality. Recent experiments [1-4] showed that (II-VI) widegap SLs such as $\text{Zn}_x\text{Cd}_{1-x}\text{Te}$, $\text{Zn}_x\text{Cd}_{1-x}\text{S}$, $\text{Sb}_x\text{Te}_{1-x}$, $\text{S}_x\text{Te}_{1-x}$ are one of the leading candidates for blue-light emitting devices. However, electronic structures of these systems, especially the band offsets under strain, strain environments have not been understood well. In this view, in order to clarify their fundamental electronic quantities, we have calculated the band structures and band offsets of (II-VI) SLs made of all the combinations of (II-VI) compounds (from ZnS to HgTe) under various strain environments by the first-principles theoretical method. Among various data, the strain effects on the band offsets are concentrated on the difference of the strain effect on band-gap energy between bulk of zinc blende and wurtzite structures, and the variation of band offsets with changing the substrate for the heavy-hole and the electron states of SLs in this paper. This work is the extension of previous works on zinc-compounds SLs [1,2] to all (II-VI) compounds. The present theoretical calculation will help the evaluation of the quality of grown crystals and encourage the challenge to produce new types of devices.

2. Calculational Method

Because of the difference of lattice constant and the presence of substrate, (II-VI) SLs become in general strained systems. In order to determine the crystal structures of SLs, the first-principles elastic theory [5] is employed, the details of which are described elsewhere [6] but the 3-band structure calculation of SLs, we have adopted the plane-wave first-principles pseudopotential method within the local density approximation [1,2]. We use pseudopotentials constructed by Hedin et al. [7] where k points are treated as true electrons.

that is fairly close to the observed transition temperatures. Furthermore, the zero field magnetizations of superlattices $[\text{EuTe}(3)/\text{PbTe}(15)]_{100}$ can be fitted reasonably well by a modified Brillouin function (see Fig. 3), showing that this sample behaves more like 2D magnets than 3D magnets.

In summary, short period EuTe/PbTe SLs show different magnetic behavior depending on the number of EuTe layers N in each period. The T_N values for superlattices with $N \geq 4$ EuTe layers in each period are very close to the bulk EuTe Néel temperature (9.6 K), thus suggesting they may behave more like 3D magnets than 2D magnets. Indeed, a modified Brillouin function provides a good fit to the zero field magnetization data for $[\text{EuTe}(3)/\text{PbTe}(15)]_{100}$. However, $M(T)$ observed for the small period superlattices $[\text{EuTe}(3)/\text{PbTe}(9)]_{100}$ and $[\text{EuTe}(2)/\text{PbTe}(6)]_{100}$ indicate that they are more like 2D magnets. The critical exponent β for $[\text{EuTe}(3)/\text{PbTe}(9)]_{100}$ is 0.129 much closer to 0.125 for the 2D universality class than to 0.33 for the 3D class. Furthermore, in the high temperature regime the magnetization of $[\text{EuTe}(2)/\text{PbTe}(6)]_{100}$ is proportional to $1/\ln T$ instead of $1/T$ is a conspicuous signature of marginal dimension phenomenon. The specific effects that a small number of EuTe monolayers impose on the superexchange and indirect exchange mechanisms going into J_1 and J_2 , respectively, are to be worked out. Such studies are needed to provide a firm theoretical basis for the explanation of the magnetic phases of short period magnetic SLs.

The MIT authors acknowledge NSF grant #DMR-92-05378 for the financial support of this project. The first author acknowledges support from #5440 FWF Vienna.

References

- [1] P. Wachter, in *Handbook on the Physics and Chemistry of Rare Earths*, edited by K. A. Gschneidner Jr. and L. Eyring, North Holland Publishing Company, Amsterdam, 1976, p. 937.
- [2] G. Springer and V. Bauer, *Appl. Phys. Lett.* 62, 2399 (1993).
- [3] R. P. Silbert, *Remote Sensing and Magnetic Properties in Earth and Space*, PhD thesis, Massachusetts Institute of Technology, February 1975.
- [4] D. L. Smith, J. S. Lomax, and D. J. Appl. Phys. 63, 3333 (1991).
- [5] Sheng Hong Ma, *Modern Theory of Crystal Properties*, Freeman, in *Physics Vol. 26*, Addison Wesley Publishing Co., New York, 1962.
- [6] T. Chakraborty, *Phys. Rev. B* 40, 1191 (1989), private communication.

show that both deviations of 2.1 monolayer from the average EuTe layer thickness occur. Typical distances between monolayer steps on the EuTe surface are of the order of 100-200 Å, in comparison to the step distances of the order of 1000 Å for the PbTe surface. Such steps also are expected to reduce the net magnetization of short period SLs.

We postulate that instead of a strict SNSS interface structure, short period EuTe/PbTe SLs can be modeled by an interdiffused spiral structure in the temperature range between 1.7 K to 9.6 K. In this approach the magnetic phase transition temperatures T_N are calculated by mean field theory. The Hamiltonian for the bulk EuTe magnetic interactions is written as

$$H = -J_1 \sum_{i,j} S_i S_j - J_2 \sum_{i,j} S_i S_j \quad (2)$$

where i and j denote nearest neighbor and next nearest neighbor interactions. By a straightforward application of mean-field theory using the Hamiltonian of Eq. 2 we found T_N for the $[\text{EuTe}(3)/\text{PbTe}(6)]_{100}$ SL to be given by

$$T_N = \frac{2S(S+1)(-3J_2 \cos \theta + 5J_1 + 3J_2 \cos \theta)}{3k_B} \quad (3)$$

where θ denotes the angle between the average magnetization of two adjacent EuTe layers. The coupling between sequential EuTe blocks is neglected in the bulk EuTe crystal, $\theta = 180^\circ$, which in turn gives $T_N = 5.99$ K for the SL $[\text{EuTe}(3)/\text{PbTe}(6)]_{100}$ if the bulk $J_1 = 0.01$ K and $J_2 = -0.15$ K values are used [2]. However, the observed T_N value for this $[\text{EuTe}(3)/\text{PbTe}(6)]_{100}$ SL is 4.33 K. Agreement with the measured T_N value is achieved by taking $\theta = 120^\circ$ in Eq. 3. Similarly for the $[\text{EuTe}(3)/\text{PbTe}(9)]_{100}$ spiral lattice mean field theory gives an expression

$$T_N = \frac{2S(S+1)(6J_2 \cos \theta + 5J_1 + 6J_2 \cos \theta)}{3k_B} \quad (4)$$

Observing that for $\theta = 120^\circ$ in Eq. 4 we recover the T_N expression for bulk EuTe crystal which is

$$T_N = \frac{2S(S+1)(-J_2)}{3k_B} \quad (5)$$

and for both $T_N \approx 9.6$ K. For the 3 layer EuTe superlattice the observed transition temperature is again lower than the bulk value at 8.25 K, requiring $\theta = 120^\circ$ in Eq. 4 to yield agreement with experiment. This suggests that the antiferromagnetic spiral structure is suppressed as the number of EuTe layers increases. For SLs with 4 monolayers of EuTe or more within each period, we assume the bulk T_N expression to be valid which gives a 9.6 K transition temperature

and the spin-orbit interaction is not included [13]. The N_v potential with $\alpha=0.7$ is used for the exchange-correlation potential. From the calculated band structures, we evaluate the band offset; the method of which is a standard one in the first-principles scheme [13,8]. Table 1 shows the lattice constants under no strain and the elastic constants of various II-VI compounds, which are used in this work.

3. Results and Discussion

Before going to the calculated results of SLs, two points are discussed. At first, it should be noted that ZnS and CdSe are normally of wurtzite (WZ) structure in bulk, while they show the zinc-blende (ZB) structure when epitaxially grown as SLs. Therefore we have to take into account the difference of electronic structure between WZ and ZB. Figures 1(a) and (b) show the calculated band-gap energy of ZB-CdSe and the difference of the band-gap energy between WZ and ZB, as a function of strains ϵ_{1111} and ϵ_{1122} parallel and perpendicular to the (111) direction. Here the calculated band-gap energy of CdSe is increased constantly by 40.17 eV to correct the values in the local density theory. As seen in Fig. 1(a), the band-gap energy increases as the strain becomes negative; large. This is because the more negative the strain is, the smaller the bond length becomes. As a result, the transfer energy between atoms increases, and the band-gap energy increases. Comparing WZ and ZB structures, WZ has larger band-gap energy than ZB in most strained region in Fig. 1(b). It is generally shown that the difference of band-gap energy originates from the difference of positions of the 1st nearest neighboring atoms between WZ and ZB structures [10] and that all direct-gap semiconductors have larger band-gap energies in WZ forms than in ZB forms [11]. When the lattice constant along (111) decreases, ϵ_{1111} increases in a negative region, the distance to the 1st nearest neighboring atoms in WZ structure becomes so short that the band-gap energy of WZ sharply increases. This fact indicates that the variation of electronic structure of ZB with changing strain surroundings is more moderate than that of WZ.

However, secondly, the lattice constants of II-VI compounds scatter in such a wide region that the strain becomes considerably large (~ 0.1) when II-VI SLs are produced. Therefore, we have to examine the variation of the electronic structure under large strain. Most SLs are produced along (100) and the lattice constant perpendicular to (100) becomes equal to that of the substrate. In this case, only the diagonal components of strain tensor exist [1], which have the following relation in the linear elastic theory,

$$\epsilon_{1111} = -2 \frac{C_{12}}{C_{11}} \epsilon_{1100} \quad (1)$$

Calculating the strained structures of II-VI bulks based on this formula, the band-gap energies and the splitting energy between the light and the heavy-hole states are calculated from the first-principles, which are shown in Figs. 2(a) and (b) respectively, as a function of the lattice constant of the substrate. Here the band gap corresponds to the transition from the heavy-hole state to the lowest conduction-band state at the center of the Brillouin zone. Though the band structure calculation in the local density theory underestimates the band-gap energy, the variation of energy levels with changing strain surroundings is well described by the calculation. Thus the calculated band-gap energies are constantly shifted in order to coincide with observed values [9] only for the unstrained cases, for example, ± 0.106 eV (ZnS) and ± 0.601 eV (ZnTe). Most striking feature seen in Fig. 2(a) is that the band-gap energy of each material has the largest value and the slow variation with changing the substrate, in the region near the unstrained lattice constant. However, far away from this region, though the strain of crystal is treated in the linear theory, the band-gap energy rapidly decreases in a non-linear manner. Similar characteristics are observed in Fig. 2(b) for the splitting energy between the light and the heavy-hole states.

As seen in Figs. 2(a) and (b), though the deformation potential seems to be a well-defined quantity only around the unstrained lattice constant, it becomes the measure of energy-level variation. Without the spin-orbit interaction, the band-gap energy between

the heavy-hole and the lowest conduction-band electron states $E_v = E_{hh}$ and the splitting energy between the light and the heavy-hole states $E_g = E_{hh} - E_{lh}$ are given as follows,

$$E_v = E_{hh} = -0.22 \epsilon_{1100} + 0.1001 \quad (2)$$

$$E_g = E_{hh} - E_{lh} = -0.02 \epsilon_{1100} - 0.1001 \quad (3)$$

Fitting the calculated results to these formulae, we obtain the deformation potential, a and b in Table II.

Then we consider the calculated results of II-VI strained SLs. Most features of electronic structures of various II-VI SLs are similar to those in case of the compounds SLs in previous calculations [9]. Thus, at first, we shortly comment on this. By examining the layer thickness dependence of band-gap energies of SLs and the manner of charge distribution of respective band-edge states in constituent layers, it is concluded that the quantum well picture is well applicable to the states around the fundamental gap in all II-VI strained SLs. This result allows us to define the band offset. Figures 3(a) and (b) show the calculated band offsets at (various II-VI semiconductor)/ZnS interface for the heavy-hole and the lowest conduction-band states, respectively, as a function of the lattice constant of the substrate. As seen in these figures, band offsets drastically vary with changing the substrate, i.e. changing strain strength. These variations are caused by the competition between the energy-level shift by strain and the charge transfer at the interface [3]. There appears a clear trend that the offsets for the heavy-hole state of Te-compounds are large, while those of S-compounds are small. This is because the top of the valence-band states mainly consists of p-orbital of cation atoms, and because the energy of cation p-orbital is higher for Te than for S.

On the other hand, as for the electron state, the energy position is high for Zn-compounds and low for Cd and Hg compounds. This is the reflection from the magnitude of band-gap energies of these materials, and is explained by the fact that the lowest conduction-band state is the center of the Brillouin zone in the zinc-blende state of cation-sublattice. HgSe and HgTe are metals which have negative band-gap energies as shown in Fig. 2(a) even in the strained structures. This is probably the reason why their energy positions are extremely low. In order to clarify the relative position of the band-edge states among II-VI compounds, the band offsets on the ZnS substrate are shown in Fig. 4. From this figure, it is easily concluded, for example, that ZnS/ZnSe and ZnS/CdSe SLs are of type II, which is in good agreement with experimental observation.

Then we compare the calculated offsets with experiment. The ZnS/Zn_{0.95}Cd_{0.05}Se superlattice recently grown on ZnSe [12] is considered for example. Though the spin-orbit interaction is absent in the present first-principles calculation, such an effect can be included a posteriori [3] when we use the observed values of spin-orbit splitting energies as in experiments [9], 0.61 eV and 0.12 eV for ZnS, ZnSe, and CdSe, respectively. The calculated offset for the heavy-hole state of ZnSe/ZnS on ZnSe substrate is evaluated as follows,

$$\Delta E(ZnS/Cd_{0.05}Se/ZnS) = 0.59 + \frac{1}{4} \times (0.12 - 0.061) = 0.80 \text{ eV} \quad (4)$$

Similarly, because the band offset linearly depends on the strain as shown in Fig. 4(a) the offset of Zn_{0.95}Cd_{0.05}Se/ZnS on ZnS is estimated as

$$\begin{aligned} \Delta E(ZnS/Cd_{0.05}Se/ZnS) &= 0.77 + 0.69 + \frac{1}{4} \times (0.12 - 0.061) \\ &+ 0.27 + 0.90 + \frac{1}{4} \times (0.12 - 0.061) = 0.86 \text{ eV} \quad (5) \end{aligned}$$

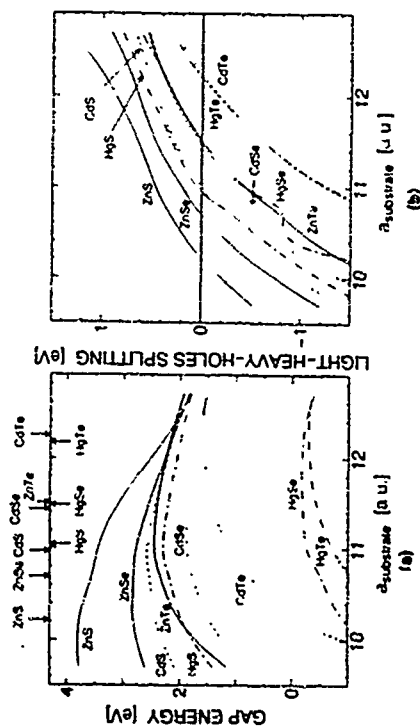


Fig. 2. (a) Calculated band gap energies and (b) spin-orbit splitting energies as a function of the lattice constant of the substrate. Points are of experimental data. Solid lines correspond to the calculated values. Dashed lines correspond to the experimental values.

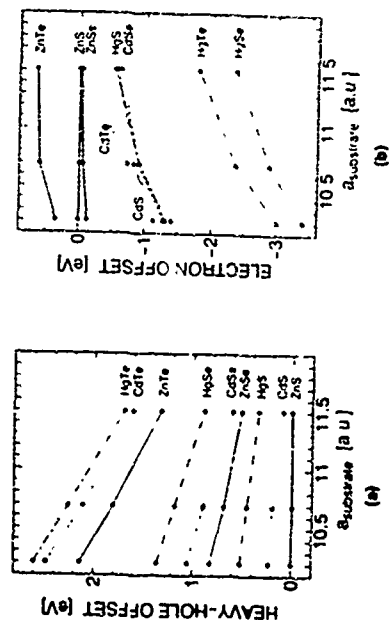


Fig. 3. (a) Calculated band structure for various II-VI compounds as a function of the lattice constant of the substrate. Points are of experimental data. Solid lines correspond to the calculated values. Dashed lines correspond to the experimental values.

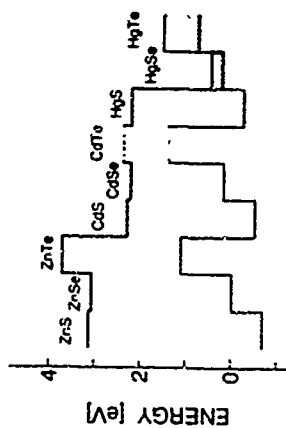


Fig. 4. Calculated band structure for various II-VI compounds as a function of the lattice constant of the substrate. Points are of experimental data. Solid lines correspond to the calculated values. Dashed lines correspond to the experimental values.

ThA4

LIGHT INDUCED INVERSION OF MAGNETIC HYSTERESIS IN $\text{CdTe/Cd}_{0.9}\text{Mn}_{0.1}\text{Te}$ SUPERLATTICES

V. P. Kocherzhenko, I. A. Metel'nikov, G. R. Pozina, and I. N. Ural'tsev
A. F. Ioffe Physico-Technical Institute, Russian Academy of Sciences, 194021 St. Petersburg,
Russia

D. R. Yakovlev*, W. Ossau, A. Waag, and G. Landwehr
Physikalisches Institut der Universität Würzburg, 97074 Würzburg, Federal Republic of
Germany

Circular polarized photoluminescence induced by magnetic fields in Faraday geometry has been used for the study of spin relaxation processes in $\text{CdTe/Cd}_{0.9}\text{Mn}_{0.1}\text{Te}$ short-period superlattices. The spin relaxation has been found to be effective for the free carriers with kinetic energy and to be suppressed for carriers localized at fluctuations of magnetization. The effect of the inversion of sign of the magnetic hysteresis has been observed under excitation by nonpolarized light in the presence of magnetic field. The effect is due to a nonequilibrium magnetization of the Mn-ions which is induced by spin orientation of carriers on Zeeman sublevels in magnetic fields. This magnetization has a long relaxation time of about 10^3 s at temperatures of 1.6 K caused by the "frozen" magnetic moments of spin-glass clusters situated in barrier layers.

1 Introduction

Due to the recent progress in the molecular-beam-epitaxy technology for II-VI semiconductors the growth of high quality quantum well structures and superlattices incorporating layers of semimagnetic semiconductors is feasible. The model semiconductor system for such structures is $\text{CdTe/Cd}_{1-x}\text{Mn}_x\text{Te}$. The specific of semimagnetic semiconductors with strong exchange interaction of carrier spins with spins of magnetic ions has been incorporated into the physics of quantum-confined heterostructures. That made possible the observation of novel effects such as the type I - type II transition of the band alignment induced by external magnetic fields [1,2], the two-dimensional magnetic polarons [3], the modification of magnetic properties of semimagnetic semiconductors in the quasi-two-dimensional layers [4] and at heterointerfaces [5]. In this paper we report a study of the spin relaxation phenomena in semimagnetic superlattices $\text{CdTe/Cd}_{1-x}\text{Mn}_x\text{Te}$. The inversion of sign of the magnetic hysteresis is found and explained in terms of the Overhauser effect.

2 Experimental

We have studied $\text{CdTe/Cd}_{0.9}\text{Mn}_{0.1}\text{Te}$ superlattices (SL) grown by molecular-beam epitaxy on (100)-oriented CdTe substrates after a 0.2- μm thick $\text{Cd}_{0.9}\text{Mn}_{0.1}\text{Te}$ buffer layer. Structures have equal thickness of well and barrier layers and the periods varied from 40 to 120 Å (for details of growth conditions see [6]).

In Fig. 1 photoluminescence (PL) spectrum of a 40-Å-period superlattice taken at 1.6 K is shown by solid curve. PL has been excited by the nonpolarized beam of a He-Ne laser ($E_{\text{exc}} = 1.96$ eV) with low excitation density of 1 W/cm^2 . The PL excitation (PLE) spectrum is represented by the dashed curve and exhibits a strong line with maximum at 1.679 eV and a full width at half maximum of 10 meV. Analyzing the Zeeman pattern [7] we have identified the PLE maximum

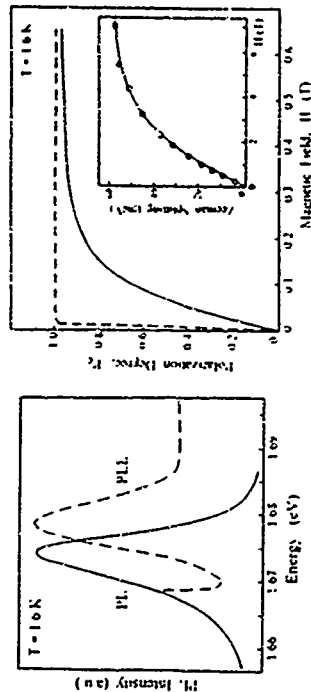


Fig. 1 Photoluminescence (solid line) and PL excitation (dashed line) spectra of a 40-Å-period $\text{CdTe/Cd}_{0.9}\text{Mn}_{0.1}\text{Te}$ superlattice

Fig. 2 Circular polarization degree of PL vs magnetic field for a 40-Å-period $\text{CdTe/Cd}_{0.9}\text{Mn}_{0.1}\text{Te}$ superlattice. Nonpolarized excitation with energy 1.96 eV and density of 1 W/cm^2 has been used. Solid line - experiment, dashed line - results of calculation in the assumption $\tau_s \ll \tau$. The insert shows the Zeeman splitting of the heavy-hole exciton

due to the heavy-hole exciton absorption and have measured a splitting between light-hole and heavy-hole excitons of 4 meV. The low temperature luminescence is dominated by a heavy-hole exciton recombination. The Stokes shift of 45 meV between the maxima of PL and PLE spectra is due to a localization of excitons on fluctuations of SL periods and shows the high structural quality of samples under study. No direct evidences for the exciton magnetic polaron formation have been found by use of the selective excitation technique [3].

3 Magnetic-field-induced polarization of photoluminescence

The circular polarization of photoluminescence induced by magnetic fields in Faraday geometry is due to the thermal population of the Zeeman sublevels [8]. The degree of polarization is determined by $P_c = (I_+ - I_-)/(I_+ + I_-)$, where I_+ and I_- are the intensities of the luminescence with right- and left-handed circular polarization, respectively. These intensities correspond to the population of the upper and lower Zeeman sublevels and depend on the temperature T , the value of the Zeeman splitting $\Delta(H)$ and on the ratio of lifetime τ to spin relaxation time τ_s . In $\text{CdTe/Cd}_{1-x}\text{Mn}_x\text{Te}$ superlattices, where the light-hole states are split off by strain and quantum confinement, the polarization degree is

$$P_c(H) = \frac{\tau(1 + \exp(-\Delta(H)/kT))}{\tau_s + \tau(1 + \exp(-\Delta(H)/kT))} \tanh \frac{\Delta(H)}{2kT} \quad (1)$$

where τ and τ_s could be functions of the magnetic field H . In the case when $\tau_s \ll \tau$ the polarization degree reflects the thermoequilibrium population of the Zeeman sublevels. At $\tau_s \gg \tau$

the carriers recombine before the thermoequilibrium population could be achieved. An analysis of the polarization degree gives an insight into spin relaxation processes.

In Fig 2 the solid line shows the circular polarization degree of a 40-Å-period CdTe/Cd_{0.9}Mn_{0.1}Te superlattice as a function of magnetic field at 1.6 K. Magnetic fields have been applied parallel to the growth axis (Faraday geometry). An inset shows the Zeeman splitting of the heavy-hole exciton taken from reflectivity spectra (for details see [11]). The large value and the Brillouin function like behaviour of the Zeeman splitting is typical for semimagnetic semiconductors where the splitting of spin sublevels in magnetic fields is due to the strong exchange interaction of carrier spins with spins of magnetic ions, namely Mn²⁺ ions for Cd_{0.9}Mn_{0.1}Te [9].

We have put experimental values of the Zeeman splitting in Eq 1 and calculated the polarization degree assuming thermoequilibrium conditions ($\tau_e \ll \tau$). The result of the calculation is shown by the dashed line in Fig 2. A strong disagreement between calculation and experiment in low magnetic fields (≤ 0.3 T) let us conclude that the carrier system is far from the thermodynamic equilibrium with the lattice and the spin relaxation time exceeds the lifetime of the carriers, i.e. $\tau_e > \tau$.

In order to have a detailed insight into the spin relaxation processes we have done an optical orientation experiment [10]. PL in zero magnetic field has been excited by circular polarized light at a laser energy of 1.70 eV and the polarization degree of luminescence has been analyzed. The circular polarized light generates carriers with spin orientation and luminescence will be circular polarized with the degree

$$P_{\omega} = \frac{\tau_e - \tau}{\tau_e + \tau} \quad (2)$$

where P_{ω} is the maximal polarization degree which depends on the structure of electron and hole levels involved in the process. In the considered case, when carriers are photoexcited from light- and heavy-hole subbands but recombination involves the heavy-hole subband only, $P_{\omega} = 0.5$ [10]. In the CdTe/Cd_{0.9}Mn_{0.1}Te superlattice we have found $P_{\omega} = 0$. That means that $\tau_e \ll \tau$, i.e. that free carriers with kinetic energy effectively lose their spin orientation. The considerable value of P_{ω} has been reported for the nonmagnetic QW structures CdTe/Cd_{0.9}Zn_{0.1}Te [11]. We conclude that very fast carrier spin relaxation in the semimagnetic SLs is due to the carrier scattering on the spins of Mn ions.

Summarizing the data of optical orientation experiments, where $\tau_e \ll \tau$ has been found, and of magnetic-field-induced circular polarization of PL, where $\tau_e > \tau$ has been established, we conclude that the spin relaxation is effective for the free carriers with kinetic energy and is considerably suppressed for carriers localized at the extrema of conduction and valence bands. Similar results have been reported for bulk (Cd,Mn)Se and have been explained in terms of a bottleneck in a spin diffusion process [12].

As the next step we have studied the magnetic-field-induced polarization in tilted magnetic fields. Fig 3 shows by solid lines the PL polarization degree as a function of transverse magnetic field H_{\perp} (field is perpendicular to the growth axis) taken at fixed longitudinal field components $H_{\parallel} = 0.08, 0.2$ and 1.4 T. The polarization degree is completely suppressed by transverse magnetic fields when the longitudinal field is small (< 0.1 T). Contrary at the high longitudinal field of 1.4 T there is a very weak influence of the transverse field on the polarization degree. Dashed lines in Fig 3 show the polarization dependences calculated according to the following equation with the assumption that carrier g-factors are isotropic

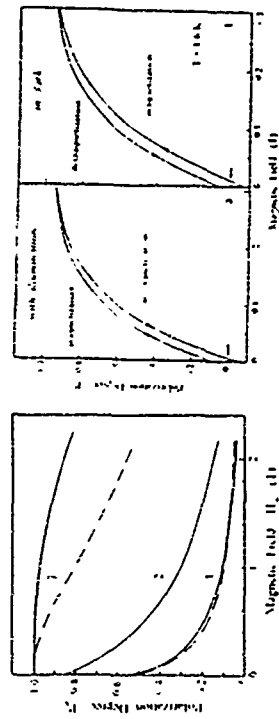


Fig 3 Polarization degree of PL as a function of transverse magnetic field H_{\perp} (Voigt geometry) taken at presence of longitudinal field component $H_{\parallel} = 0.08$ T (1), 0.2 T (2) and 1.4 T (3) for a 40-Å-period CdTe/Cd_{0.9}Mn_{0.1}Te superlattice. $T = 1.6$ K. Solid lines - experiment, dashed lines - calculations with the isotropic g-factor

Fig 4 Hysteresis behaviour of the polarization degree of PL in the remagnetization cycle realized under light illumination (a) and in dark conditions (b) for a 40-Å-period CdTe/Cd_{0.9}Mn_{0.1}Te superlattice

$$P_e(H) = \frac{\tau_e(1 + \exp(-\Delta(H)/kT))}{\tau_e + \tau_e(1 + \exp(-\Delta(H)/kT))} \frac{H_{\parallel}}{H} \frac{\Delta(H)}{2kT}$$

where $H = \sqrt{H_{\parallel}^2 + H_{\perp}^2}$. Experimental data fit well with the calculated dependences at $H_{\parallel} = 0.08$ T and differ considerably at $H_{\parallel} = 1.4$ T. We consider that both electrons and holes are contributing to the polarization degree and the total polarization degree of luminescence is expressed by the equation

$$P_e = (P_e + P_h)/(1 + P_e/P_h) \quad (3)$$

where P_e and P_h are electron and hole polarization degrees, respectively. The electron g-factor is isotropic, whereas the g-factor of heavy-hole in superlattice has a strong anisotropy due to the reduction of the symmetry from T_d in a bulk to D_{2d} in a superlattice. Holes have larger exchange constant and effective mass than electrons and are better localized by the fluctuations of magnetization. As a consequence at low fields the electron system is closer to the thermodynamic equilibrium and provides the dominating contribution to the circular polarization of the luminescence. At stronger longitudinal fields the input of holes to the polarization increases and the polarization anisotropy caused by the anisotropic g-factor of holes became pronounced.

4. Hysteresis phenomena

From the detailed study of the magnetic-field-induced circular polarization we found that the dependence $P_e(H)$ is affected by the history of the sample, i.e. dependent on illumination

and/or magnetic fields applied before the measurement. We have found a magnetic hysteresis loop on $I_s(H)$ and an effect of the inversion of magnetic hysteresis under nonpolarized illumination of the sample at the interband transition energies.

Fig. 4a shows a hysteresis loop observed in a 40-Å-period $\text{CdTe/Cd}_{0.9}\text{Mn}_{0.1}\text{Te}$ superlattice at 1.6 K under the continuous nonpolarized illumination by the light of 1.96 eV photon-energy with excitation density of about 1 W/cm^2 . In Fig. 4b the hysteresis loop taken without illumination is presented. In the latter case the magnetization procedure has been performed in the dark and the structure has been illuminated for a short time of about 10 seconds to register the polarization signal only. We have checked that such short time of exposition gives a negligible contribution in comparison with the continuous illumination.

In both figures (4a and 4b) magnetization and demagnetization branches do not coincide in magnetic fields below 0.3 T, where $I_s(H)$ is below the saturation value. Without illumination the magnetization branch is below that for demagnetization which is typical for magnetization hysteresis effects [12]. The inversion of the ordering of the branches is caused by the illumination. The energy of the spin system of Mn-ions changes in the remagnetization cycle on the value $I_s \sim \int M dH$ (where M is the magnetization), which is the work performed by the external magnetic field and corresponds to the area under the hysteresis loop. In the dark cycle the spin system lowers its energy but under illumination the energy is increased. It is obvious that in the latter case the absorbed energy is taken from the photoexcited carriers. We have found that the amplitude of the inverse hysteresis loop is a function of magnetic field and reaches the saturated value of 0.1 when the field strength exceeds 0.5 T.

The nonequilibrium remanent magnetization of 0.05 in zero magnetic field (see Fig. 4a) has a relaxation time of about 10^3 s at $T=1.6 \text{ K}$. Such long relaxation times are characteristic for systems with a large number of strongly correlated spins [14]. At low temperature applied in the experiment (1.6 K) the correlation in spin clusters is due to the exchange interaction between the spins of Mn-ions located as nearest- and next-nearest-neighbours in a Cd sublattice. The constants of the exchange interaction in the Heisenberg Hamiltonian $J_{nn} = 2/(S_1 S_2)$ are $J_1 \approx -0.526 \text{ meV}$ and $J_2 = -0.095 \text{ meV}$ for nearest and next-nearest neighbour interaction, respectively [15]. Here S_1 and S_2 are spins of Mn-ions. The total energy of the exchange interaction of a nearest-neighbour pair is $14 \text{ J} = -7.9 \text{ meV}$. This energy exceeds significantly the thermal energies $kT \approx 0.1 \text{ meV}$ at $T=1.6 \text{ K}$ and that provides such a long relaxation time of the spin orientation of large spin-glass clusters.

We suggest the following model of the optically induced orientation of spin-glass clusters. Electrons and holes photoexcited by the nonpolarized light relax in energy and populate all spin states with equal probabilities. In magnetic fields the carrier system aims for the equilibrium population of the Zeeman sublevels which is accompanied by the orientation of carrier spins along the field direction. The carriers pass their spin to the system of Mn-ions and turn the Mn spins opposite to the magnetic field direction. If the energy passed by the carriers is large enough, not only paramagnetic spins but high-coercive clusters will be oriented also. As a result of such specific Overhauser effect [16] the magnetic moments of clusters with long spin relaxation times will be oriented against the magnetic field. This orientation will manifest itself in the long-living remanent magnetization and in the inverse hysteresis loop.

The energy which carriers could transfer to Mn ions is equal to the value of the Zeeman splitting and depends strongly on the magnetic field (see insert of Fig. 2). At low fields ($\sim 0.1 \text{ T}$) this energy is not enough to change the orientation of large clusters and no remanent magnetization has been found. At higher fields of about 0.5 T the energy of carriers of 10 meV

gives us the characteristic energies which are required for the reorientation of clusters which are comparable with the energy of the exchange interaction of a nearest-neighbour pair. At these fields the long-living remanent magnetization oriented against the external field direction will be induced by the illumination. This remanent magnetization exhibits the inverse sign of hysteresis loop.

It is worth to note that the suggested model of the effect does not contain any specific feature of SLs with thin layers of semimagnetic semiconductors. However having investigated 2-μm thick epilayers of $\text{Cd}_{0.9}\text{Mn}_{0.1}\text{Te}$ we have not observed the effect of the photoinduced inversion of the hysteresis loop. The usual hysteresis which is analogous to the dark hysteresis in SL has been found only in thin barriers of SL the spin-glass clusters of large sizes modify their structure because their extension in the growth axis direction is limited by the thickness of the barrier layers. The appearance of the thermohysteresis phenomena in thin (520 Å) layers of $\text{CdTe/Cd}_{0.9}\text{Mn}_{0.1}\text{Te}$ has been demonstrated [4]. A modification of the magnetic properties of clusters at the interfaces have been reported recently for $\text{CdTe/Cd}_{0.9}\text{Mn}_{0.1}\text{Te}$ quantum well structures [5].

5. Conclusions

The methods of polarized luminescence have been used for the study of the spin relaxation processes in $\text{CdTe/Cd}_{0.9}\text{Mn}_{0.1}\text{Te}$ semimagnetic superlattices. Very efficient spin relaxation has been found for free carriers whereas localized carriers conserve their spin orientation due to the exchange interaction with the magnetic moments of the spin-glass clusters. Two inputs from electrons and holes into the circular polarization degree of luminescence have been revealed by the application of longitudinal and transverse magnetic fields. The effect of the inversion of sign of the magnetic hysteresis under nonpolarized illumination in magnetic fields has been found. This effect is explained in terms of the Overhauser effect when the magnetic moments of clusters with long spin relaxation times are oriented against the magnetic field via their interaction with the carrier system thermalizing on the Zeeman sublevels.

Acknowledgement The part of this work provided in the Ioffe Institute has been supported by the Soros Foundation Grant awarded by the American Physical Society I A M and V P K acknowledge support of their stay in the University of Wurzburg from NATO grant CRG 921121.

* on leave from A F Ioffe Physico-Technical Institute, St Petersburg, Russia

- 1 E L Ichenko, A V Kuvshinov, V P Kuvshinov, G R Ponomarev, I N Ustinov, D R Yakovlev, R N Bicknell, Tassus, A Waag, and G Landwehr, *Phys Rev B* 46, 7713 (1992)
- 2 N Dai, H Luo, F C Zhang, N Samarth, M Dobrowolska, and J K Furdyna, *Phys Rev Lett* 67, 3824 (1991)
- 3 D R Yakovlev, W Ossau, G Landwehr, R N Bicknell, Tassus, A Waag, S Schneider, and I N Ustinov, *Solid State Commun* 82, 29 (1992)
- 4 D O Anshakov, J M Hong, L L Chang, and G Grinstein, *Phys Rev Lett* 59, 1733 (1987)
- 5 W J Ossau and B Kuhn-Henrich, *Physica B* 184, 422 (1993)
- 6 A Waag, S Schneider, R N Bicknell, Tassus, D R Yakovlev, W Ossau, G Landwehr, and I N Ustinov, *Appl Phys Lett* 61, 2905 (1991)
- 7 B Kuhn-Henrich, M Popp, W Ossau, E Langert, A Waag, and G Landwehr, *Semicond Science and Technology*, in press
- 8 M I Dyakonov and V I Perel, *Sov Phys Solid State* 14, 1245 (1972)

- 9 J A Gaj, R Pizel, and G Fishman, *Solid State Commun* 29, 435 (1978)
- 10 M I Dyakonov and V I Perel, in *Optical Orientation*, Eds F Meier and B P Zaslavskaya (North-Holland, Amsterdam, 1984), p 40
- 11 Y Merle d'Aubigny, L S Dang, F Dalbo, G Lenz, N Maguey, and H Mariette, *Superlattice and Microstructures* 5, 367 (1989)
- 12 D Herman, J Warnock, P A Wolff, R Kershan, D Rudley, K Dwight, and A Wold, *Solid State Commun* 52, 909 (1984)
- 13 K Binder and A P Young, *Rev Mod Phys* 58, 801 (1986)
- 14 S Osoff and P H Keesom, in *Semiconductors and Semimetals* Vol 25, Eds J K Furdyna and J Kossut (Academic Press, London 1989), p 413
- 15 X Wang, D Herman, S Foner, and P Becla, *Phys Rev B* 41, 1155 (1990)
- 16 A W Overhauser, *Phys Rev* 92, 411 (1958)

**Photomodulation Spectroscopy and Cyclotron Resonance
of $\text{Cd}_{1-x}\text{Mn}_x\text{Te/CdTe}$ Semimagnetic and Strained
Multi-Quantum Well Structures**

S.C. Shan*, L.J. Zhang*, W. Lu* and R.M. Richnell†

- * Laboratory for Infrared Physics, Shanghai Institute of Technical Physics, Chinese Academy of Sciences, Shanghai 200083, China
- † Physikalisches Institut der Universität Würzburg Am Hubland, D-8700, Würzburg, F.R.Germany

Abstract

Photomodulation spectroscopy and cyclotron resonance of free carriers of $\text{Cd}_{1-x}\text{Mn}_x\text{Te/CdTe}$ multi-quantum wells are reported for the first time. 5 peaks have been observed in the energy region of 1.55 to 1.80 eV by photoreflectance measurement at low temperature and assigned to excitonic transitions in quantum well. The band-edge alignment and the valence band structure are determined by comparison of experimental transitions to envelope function calculation including strain effect. The cyclotron resonance of electrons in $\text{Cd}_{1-x}\text{Mn}_x\text{Te/CdTe}$ MQW has been observed by use of a modulated cyclotron resonance technique combined with an extra and monochromatic light excitation. The cyclotron mass m_c^* and ω_{res} are determined from fitting the experimental line-shape to the expressions of resonance and to be 0.096 m_0 and around 2 respectively.

1 Introduction

$\text{Cd}_{1-x}\text{Mn}_x\text{Te}$ is a semimagnetic semiconductor or diluted magnetic semiconductor and has been best investigated among this kind of materials during last 20 years [1-8]. With a fraction x of Cd^{2+} ions replaced by magnetic ions Mn^{2+} in II-VI compound CdTe , the mixed crystal $\text{Cd}_{1-x}\text{Mn}_x\text{Te}$ has some novel properties and performances mainly originated from the magnetic exchange interaction between Mn^{2+} ions and movable charge carriers, such as giant Faraday rotations and Voigt effects, large Zeeman splittings of the excitons and g factors of electron, strongly circularly polarized band edge luminescence, large and minus pressure coefficient of interband transition for $\text{Cd}_{1-x}\text{Mn}_x\text{Te}$ with $x > 0.4$, as well as magneto-tunable band-gap and electronic states [1-9]. In addition the materials are also attractive for potential application in optoelectronic devices, such as Faraday rotators, optical isolators and magnetic field sensors.

It is believed that the quantum well structures and superlattices of $\text{Cd}_{1-x}\text{Mn}_x\text{Te/CdTe}$ which combines semimagnetic and usual semiconductor materials, should show a significant enhancement of the electro-optical coefficient with respect to

bulk $\text{Cd}_{1-x}\text{Mn}_x\text{Te}$ materials [10], and be attractive from both academic and practical points of view. Thus a great effort has been made in last few years for preparing the lattice mismatched $\text{Cd}_{1-x}\text{Mn}_x\text{Te}/\text{CdTe}$ multi-quantum wells and superlattices as well as investigating their confined quantum states and related performances by use of photoluminescence excitation, photoluminescence, modulation spectroscopy and other methods [11-19]. K.L. Harper et al [17] have investigated excited confined quantum states in $\text{Cd}_{1-x}\text{Mn}_x\text{Te}/\text{CdTe}$ MQW and superlattices by use of the piezomodulated reflectivity spectroscopy and the interband transitions up to quantum number 5 have been observed at 10 K for the MQW structure with $x=0.13$ and $L_y=L_z=180\text{\AA}$. They also deduced from their data that the valence band offset for $\text{Cd}_{1-x}\text{Mn}_x\text{Te}/\text{CdTe}$ heterostructures might be zero or only a very small part of the total band gap offset. E.g. Alex Hartvit and his coworkers [15] have observed the formation of miniband in the $\text{CdTe}/\text{Cd}_{1-x}\text{Mn}_x\text{Te}$ quantum well system with the decrease of the width of the barriers layer $\text{Cd}_{1-x}\text{Mn}_x\text{Te}$ and the influence of the perpendicular electric field upon the miniband behavior.

But nevertheless there are still lack of impressive experimental results on the confined quantum states, carriers behavior in the wells and related properties, probably due to the difficulty for the preparation of the qualified structures of MQW and superlattice $\text{Cd}_{1-x}\text{Mn}_x\text{Te}/\text{CdTe}$ and doping technology. We have fortunately observed the excitonic transitions up to 33H in this MQW structures by use of photomodulation spectroscopy and the cyclotron resonance of free electrons in the QW by use of the modulation technique of cyclotron resonance combined with an additional and monochromatic light excitation, and report the results here in this paper.

By photomodulation spectroscopy, 5 peaks have been observed in the energy region of 1.55 to 1.80 eV at low temperature and attributed to 11H, 11L, 22H and 33H excitonic transitions for $\text{Cd}_{0.73}\text{Mn}_{0.27}\text{Te}(15\text{nm})/\text{CdTe}(15\text{nm})$, in combination with a modified envelope function calculation. The different temperature dependences for the transition energies of different transitions have been understood in connection with the wavefunction compositions of the sublevels. It has been also demonstrated that the light holes in valence band and the electrons in the conduction band might form second kind of superlattice and exist in different layers for the structures investigated in this paper. The energy splitting for the light and heavy holes at the top of valence band of CdTe layer is determined to be 18 meV.

A sharp peak and a broader band have been observed respectively for $\text{Cd}_{0.79}\text{Mn}_{0.21}\text{Te}(15\text{nm})/\text{CdTe}(15\text{nm})$ MQW by the derivative measurement of the cyclotron resonance absorption caused by a chopped and additional monochromatic excitation light beam with

photon energy larger than (especially resonant to) 11H exciton transition. The measurement with tilted magnetic field has shown that the broader resonant band is corresponding to the resonance of free electrons in QW's. The effective mass and relaxation parameters for the quasi 2D electrons in this semimagnetic and strained QW structures have been extracted from the observation of the cyclotron resonance in this way and with different FIR laser beam with different wavelengths.

II Experimental

The samples used in this investigation were grown by MBE technique. A buffer layer of $\text{Cd}_{1-x}\text{Mn}_x\text{Te}$ or CdTe with thickness of 0.9 μm was grown at first on CdTe substrate oriented along $\langle 100 \rangle$ direction, 50 periods of $\text{Cd}_{1-x}\text{Mn}_x\text{Te}/\text{CdTe}$ with thickness of 150 \AA for both wells and barriers were followed, and a cap layer of CdTe with thickness of 150-300 \AA were grown at last. The x value for the barrier layers of $\text{Cd}_{1-x}\text{Mn}_x\text{Te}$ were experimentally determined from photoluminescence and photomodulation reflectance measurement and to be 0.19 and 0.28 for two different samples used in this investigation.

The photomodulation spectra were measured by a home-made spectrometer. A chopped laser beam of 6328 \AA from He-Ne laser is used as pumping light beam while another swept monochromatic beam from a monochromator is used as probe beam and the Si photodiode or cooled Ge photodiode are used for detectors. The sample is mounted on the cold finger of a He-recycle refrigerator and the sample temperature can be adjusted between 10 to 300 K.

A new and modulated cyclotron resonance technique [20] was tried for the observation of cyclotron resonance of carriers in $\text{Cd}_{1-x}\text{Mn}_x\text{Te}/\text{CdTe}$ MQW since the conventional FIR CR method has failed for a long time for the observation of CR in this system. By the new method, the derivative of the CR absorption induced by a chopped and monochromatic bandedge excitation light beam is recorded while FIR radiation is kept in constant and the samples are mounted in the inner cryostat (1.5 K) of a Oxford superconducting magnet. The monochromatic, chopped and tunable bandedge or interband excitation light beam is come from a monochromator or He-Ne laser and transmitted to the sample by use of a fibre. The power of excitation light beam has been measured at the end of the fibre and was around or below 0.1 mW. Faraday configuration was used for this derivative CR measurement.

III Photomodulation Spectroscopy

We show in Fig.1 the typical photoreflectance spectra for $\text{Cd}_{0.72}\text{Mn}_{0.28}\text{Te}(150\text{\AA})/\text{CdTe}(150\text{\AA})$ MQW at temperature of 300 and 100 K. It is seen from the figure that 5 peaks or spectral

structures can be observed even at room temperature. The peaks and structures become very clear and definite at low temperature due to the big improvement of signal to noise ratio. As an example, 5 peaks located at 1.973, 1.600, 1.626, 1.782 and 1.982 eV respectively can be defined at 100K except two question marks at 1.648 and 1.750eV respectively.

The peak at 1.982eV can be attributed to interband transition in the barrier of $\text{Cd}_{0.79}\text{Mn}_{0.21}\text{Te}$ and $x=0.28$ can be deduced from this transition energy while other peaks and question marks are come from interband transitions in the wells of CdTe . For the accurate determination of the transition energies, a fitting calculation of the experimental spectra to the Aspnas' line shape function has been performed. The transition energies listed above have been corrected via such fitting calculation instead of reading directly from the figures. An envelope function calculation including the effect of lattice mismatch of 0.64% between CdTe and $\text{Cd}_{0.79}\text{Mn}_{0.21}\text{Te}$ has been made for estimation of the sublevel positions in the wells and the transition energies between sublevels of conduction and valence bands. It is found by the calculation that the energy band discontinuity parameter $Q=0.90$ could result in the best agreement of the calculated transition energies to experimental ones. The strain-induced split of the heavy and light holes is calculated to be 18 meV, thus all the light holes are roughly in extended states while there are still confined heavy hole states up to $n=2$ even 3 in CdTe quantum wells. By comparison of the experimental results to calculation, the peaks observed in Fig.1 below 1.8eV can be assigned to transitions of 11H, 11L, 22H and 33H respectively, while the question marks may be connected with some forbidden transitions.

We plot in Fig.2 the energies for above assigned transitions as a function of temperature, as measured from photomodulation spectroscopy. It is worthwhile to mention that the temperature coefficient of transition energy for 33H is -0.48meV/K , while the coefficients for transitions 11H, 11L and 22H are between -0.30 to -0.35meV/K , that is, smaller to that of bulk CdTe . It is known that semimagnetic semiconductor $\text{Cd}_{1-x}\text{Mn}_x\text{Te}$ has much larger temperature coefficient of energy gap (-0.78meV/K as measured in this paper) due to the introduction of Mn^{2+} , the transition 33H in QW CdTe has temperature coefficient much larger than bulk material and QW transitions with low quantum numbers, which implies the stronger interaction and overlapping between the wavefunctions of well and barrier layers for 33H transition.

IV Cyclotron Resonance of Photoexcited Electrons in $\text{Cd}_{0.79}\text{Mn}_{0.21}\text{Te}/\text{CdTe QW}$

We summarize in Fig.3 the CR transmission and its derivative induced by an interband and monochromatic excitation versus the

magnetic field for the sample of $\text{Cd}_{0.79}\text{Mn}_{0.21}\text{Te}(150\text{\AA})/\text{CdTe}(150\text{\AA})$ QW. The vertical coordinate is CR transmission for the conventional FIR CR measurement and the derivative of the CR transmission for the modulated CR measurement. The curve a in Fig.3 is the CR transmission versus magnetic field B as measured with conventional FIR CR technique and without extra-excitation light, it is clear from the curve that one could not observe any trace of CR absorption, though we have tried many times to improve the quality of measurement and increase the signal to noise ratio. The curves b-d are CR derivative or modulation induced by the extra-excitation light beam of 6328\AA line of a pocket type He-Ne laser with a power lower than 0.1mW. The wavelengths of FIR radiation used in the measurements of curve b-d are 96, 104 and 118.8 μm respectively. It is seen from the curve that there are two resonant peaks or structures located in the magnetic field below 3 Tesla and around 10 Tesla respectively. The actual positions of the peaks are dependent on the wavelength of FIR radiation, as an example, they are located at about 3 and 10.7 Tesla respectively for FIR radiation of 96 μm . The curves e and f are CR modulation under magnetic field tilted to the direction of the QW growth with an angle of 15° , which demonstrate that the broad peak at the region of 10 Tesla is corresponding to CR absorption of carriers in QW since its position shifts to higher magnetic field according to the law of $B_{\text{CR}}(\text{tilt}) = B_{\text{CR}}(0)/\cos\theta$, while the peak at 3 Tesla is not influenced by the tilt of the magnetic field and thus demonstrated to be process in barrier layer or substrate material.

The experiment has been performed with monochromatic light excitation with different wavelengths (4-1-10eV) as well as with white light excitation directly from a tungsten halogenide lamp and with a much stronger power than monochromatic excitations. It is found that the monochromatic excitation matched with exciton transition in QW or interband transition in barrier layers will enhance the derivative structure of CR absorption resonantly while the white light excitation can hardly induce the derivative structure of CR absorption in investigated QW structure though the power is much stronger (more than 10^3 times) than that of monochromatic excitation. The 6328\AA line of the He-Ne laser used in this experiment is nearly resonant with the interband transition of barrier layer $\text{Cd}_{0.79}\text{Mn}_{0.21}\text{Te}$ at the experimental temperature of 1.6K.

The cyclotron mass m_c can be determined from the positions of the broad peaks of the curves b to d, or determined together with ω_{res} from the fitting calculation of the lineshape of the resonance to the classical expression $\mu = (1 + (m_c^2/\mu_0^2))^{1/2}$ since we measured actually the cyclotron

resonance of photo-excited electrons in QW. Thus we obtain a cyclotron mass $m_c^* = 0.096m_0$ and $\omega_c = 2$, which means that the cyclotron mass determined from this experiment is in good agreement with the m_c^* values in QW of CdTe as calculated from theory or measured by using other technique, while the scattering time τ_{sc} under magnetic field as well as τ_0 ($1/\tau_{sc} = 0.65 \times (1/\tau_0)$) in the absence of a magnetic field are in the order of 10^{-12} second.

References

- [1] N.B.Brandt and V.V.Noschaltkov, Adv.Phys., **23**, 193(1984)
- [2] R.R.Galazka, Shoichi Nagata and P.H.Keesom, Phys.Rev., **B22**, 3344(1980)
- [3] J.K.Furdyna and J.Kosut, in "Semiconductors and Semimetals", edited by R.K.Willardson and Albert C. Beer (Academic, Boston, 1988), vol.25
- [4] Wei Shan, S.C.Shen and H.R.Zhu, Sov.Sta.Comm., **22**, 472(1985)
- [5] S.C.Shen and S.Jiang, Japan J. Appl. Phys., **22**, suppl. 32-1, 264(1993)
- [6] Z.J.Tian and S.C.Shen, J.Phys. (Cond. Matters), **2**, 6293(1990)
- [7] D.L.Peterson, A.Petron, M.Datta, A.K.Ramas and S.Rodriguez, Sol.Sta.Comm., **41**, 667(1982)
- [8] S.M.Ryabchenko, O.V.Terletska, I.B.Mizetskaya and G.S. Olenik, Sov.Phys.-Semicond., **13**, 1345(1981)
- [9] J.A.Gaj, R.R.Galazka and M.Kawrocki, Sol.Sta.Comm., **23**, 193(1978)
- [10] K.Makamura and H.Makano, Japan J. Phys. Soc., **52**, 1154(1990)
- [11] R.N.Bicknell, N.C.Giles-Taylor, D.K.Blanks, R.W.Yanka, E.L. Duckland and J.F.Schatzina, J.Vac.Sci.Technol., **B3**, 709(1985)
- [12] S.K.Chang, A.V.Nurikho, L.A.Kolodziejski and R.L.Gunshor, Phys.Rev., **B21**, 2589(1986)
- [13] G.M.Williams, A.G.Cullis, C.R.Whitehouse, D.E.Ashenford and B.Lunn, Appl. Phys. Lett., **23**, 1303(1989)
- [14] D.D.Avschalom, J.M.Hong, L.L.Chang and G.Grinstein, Phys. Rev.Lett., **52**, 1731(1987)
- [15] Alex Harvit, C.Hsu, F.Aguilo Raeda and L.L.Chang, Appl.Phys. Lett., **57**, 1789(1990)
- [16] J.J.Dubovskii, A.P.Rott, Z.R.Masilevski and S.J.Rolfe, Appl.Phys.Lett., **52**, 1591(1991)
- [17] R.L.Harper, Jr., R.N.Bicknell, D.K.Blanks, N.C.Giles, J.F. Schatzina, Y.R.Lee and A.K.Ramas, J.Appl Phys., **62**, 624(1989)
- [18] H.Ossau, S.Fischer and R.N.Bicknell, J.Cryst.Growth, **101**, 905(1990)
- [19] R.H.Yenice, W.Williamson, S.A.Lee and J.J.Dubovskii, Bull. Amer. Phys. Soc., **28**, 531(1993)
- [20] S.C.Shen, W.Lu and M.Von Ortenberg, 16th Inter. Conf. on IR and RM Waves, Aug. 26-30, 1991, Lausanne, Switzerland

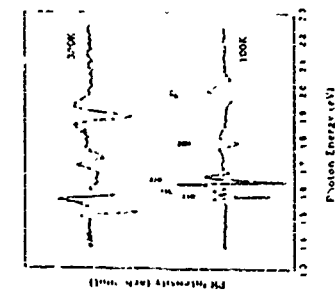


Fig.1 Photoreflectance spectra for $\text{Cd}_{0.72}\text{Mn}_{0.28}\text{Te}(150\text{\AA})/\text{CdTe}(150\text{\AA})$ QW at the temperatures of 100K and 100K.

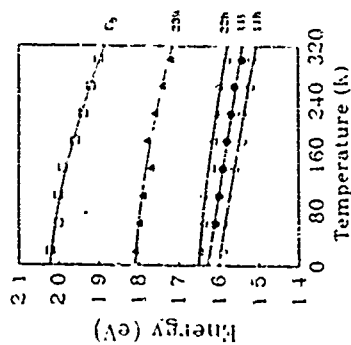


Fig.2 Transition energies of different transitions for $\text{Cd}_{0.72}\text{Mn}_{0.28}\text{Te}(150\text{\AA})/\text{CdTe}(150\text{\AA})$ QW measured by photoreflectance. The points are the experimental results while the curves are the fitting to formula $E(T) = E_0 - \alpha T^2 / (\beta + T)$.

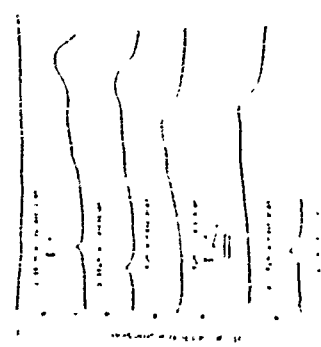


Fig.3 Cyclotron resonance transmission and its derivative to extra excitation power versus magnetic field for $\text{Cd}_{0.70}\text{Mn}_{0.30}\text{Te}/\text{CdTe}$ QW. The detailed elucidation of the curves is described in the text.

ThB1

Optical Properties of Etched GaAs/GaAlAs Quantum Wires and Dots

J.Y. Marzin, A. Izuel and L. Brothau,
France Telecom, CNET PAB, Laboratoire de Bagneux,
F92220 Bagneux, France

Abstract

We show that very narrow wires and dots, exhibiting reduced dimensionality features, can be obtained through etching from a single quantum well structure. The importance of surface cleaning and passivation is emphasized. The low temperature optical data obtained on arrays of wires and dots allow us to estimate quantitatively the size regularity. The peculiar behaviour of the photoluminescence intensity is attributed to huge electrodynamic effects while the predicted intrinsic limitations imposed by slowed down energy relaxation are not evidenced. We finally present experimental photoluminescence and photoluminescence excitation spectra obtained on single wires, as small as $6 \times 25 \times 135 \text{ nm}^3$.

Introduction

The improvement of semiconductor optoelectronic devices obtained in the last two decades in quantum wells based structures, as well as theoretical predictions [1-4] on further potential gain through that of quantum wires and dots, stimulated an active research for fabricating these lower dimensionality objects. Though spectacular effects have already been demonstrated in transport properties, the progress in the field of one and zero dimensional structures for optical applications is much slower. The necessity of confining both electron and holes, together with that of large confinement energies for room temperature operating devices lead to stringent requirements on fabrication processes. Up to now, numerous techniques are used to produce these wires and dots [5], i.e. no ideal technique has been found so far. One may classify these techniques in two main groups: the techniques starting with a quantum well, providing confinement in one direction, and adding confinement in one or the two remaining directions, and those where a single growth step produces the wires or dots. In the first family, a large number of effects have been put to work to obtain the additional confining potentials like etching [6-14], local interdiffusion (either laser induced [15,16], or assisted by ion implantation [17-21]), local strain (either with etched stressors [22,23] or on the lateral surface of a strained quantum well structure [24]). Similarly, the direct growth of wires or dots was obtained on vicinal surfaces (growth of vertical superlattices [25,26] or of inserted grids in quantum wells [27]), on supersteps [28], on high order surfaces with faceted growth [29], on patterned substrates (in V grooves [30, 32], or using localized growth [33,34]).

For most of these techniques, the first demonstration has still to be followed by a careful study of their advantages and drawbacks. In particular, most of them are potentially able to produce very narrow structures (with lateral dimensions of the order or even smaller than 10 nm), so that the key issues concern now more the mastering of size fluctuations in and the understanding of intrinsic limitations such as the slowed down energy relaxation in wires and dots [35,36]. In this paper, we will focus on GaAs/GaAlAs structures fabricated with electron beam lithography reactive ion etching and overgrowth. Low temperature optical data will be presented which underline several key properties of etched wires and dots.



(a)



(b)

Fig 1: Typical SEM micrographs of etched GaAs/GaAlAs wires before (a) and after the anodic oxidation/oxidation step.



(a)



(b)

Fig 2: Typical SEM micrographs of etched GaAs/GaAlAs dots before (a) and after (b) the GaAlAs overgrowth.

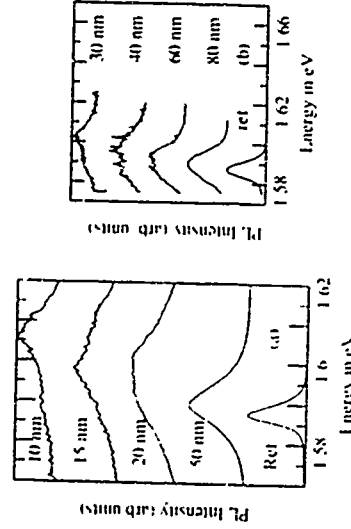


Fig 3: Typical 10 K PL spectra of wires (a) and arrays of dots (b). The spectra are normalized to the maximum and their zeros have been shifted for clarity.

Fabrication

Typical samples on which the optical studies were performed were molecular beam epitaxy grown single GaAs quantum wells (6 nm thick), cladded between 50 to 80 nm Ga_{0.7}Al_{0.3}As barriers, grown on a GaAs (100) substrate and 1500 nm GaAs buffer layer. The choice of the 6 nm thickness for the quantum well locates the low temperature photoluminescence (PL) far enough in energy from the GaAs band gap and avoids that the high energy tail of the buffer layer emission dominates the PL spectra for the narrowest structures. 40x40 μm² gratings of wires or arrays of dots with various pitch (typically 0.5 μm) and lateral dimensions (ranging from less than 20 to 2000 nm) as well as single wires are defined by electron beam lithography using a JEOL 5DIIU machine. A Ni mask is defined through standard lift-off, and used for a SiO₂ Reactive Ion Etching (RIE) procedure (0.3 μm). The following step is the key one for obtaining very narrow structures and consists in an anodic oxidation which enables to remove, by subsequent desoxidation, a surface layer of controlled thickness [37]. This peeling step allows: (i) to remove the surface layer containing most of the RIE induced defects; (ii) to reduce the width of the wires and sizes of the dots by a controlled amount (typically 60 to 70 nm). It is indeed otherwise difficult to define usable metal masks with dimensions smaller than about 30 nm. The beauty of this technique is that it appears to be completely isotropic and that the thickness of the oxide formed during anodic oxidation can be easily controlled with a 5 nm precision. Figure 1 shows the scanning electron micrograph (SEM) of the same wire grating before (a) and after (b) the anodic oxidation and desoxidation steps (such SEM micrographs are used to estimate the quantum wires and dots sizes). Finally, a 0.2 to 0.3 μm Ga_{0.7}Al_{0.3}As layer is overgrown by Metal Organic Chemical Vapour Phase Deposition (MOCVD). Figure 2 shows the SEM micrograph of an array of dots, before (a), and after (b) the GaAs overgrowth in the earliest stages of this work, the overgrowth morphology on wires was very dependent on the orientation of wires [14], whereas it seems to be much less sensitive when it is preceded by anodic oxidation, presumably because of a much cleaner surface. Thanks to that fact, dots could be fabricated recently with this process. This final step is essential to the observation of PL in the narrowest structures because it prevents non radiative recombination on the lateral surfaces [38], yielding an interface recombination velocity that can be lowered by two orders of magnitude as compared to the surface one. Unfortunately, it also appeared to be the limiting step as far as the lateral dimensions are concerned. Mass transport occurring during the 10 min 800°C annealing preceeding the growth itself destroy the narrowest structures (<10 nm).

As we will discuss in more details in the next section, the main drawbacks of this technique lay in the relatively poor homogeneity of sizes [38]. Size fluctuations of ±5 nm are observed on the wires prior to the overgrowth final step. All our studies tend to attribute these fluctuations to the earliest lithography stages of the process, and it seems that the RIE and anodic oxidation just transfer the irregularities on the final object. Several attempts to reduce these fluctuations, among which the use of lower molecular weight PMMA resist failed to reduce these below ±3 nm. With this respect, the use of a chemical etch revealing crystallographic planes which was recently proposed [39], or that of inorganic resists seem very promising. The second severe problem is linked to the use of the overgrowth. The introduction of such a high temperature step in the process is quite delicate and overgrowing a layer with sufficient passivation properties without degrading the optical properties of the starting quantum well is difficult to obtain with a good reproducibility. One must bear in mind that the overgrowth takes place, on the lateral edges of the etched structures, on AlGaAs whose oxides are more stable thermally than those of GaAs. On the

other hand, one would like to minimize the overgrowth temperature to prevent from unwanted intermixing and diffusion of defects created at the overgrown layer interface. This trade off leads to a two steps process: a high temperature annealing (~800 °C) followed by a low temperature (around 700 °C) growth. Let us emphasize that quantum wires and dots issued from a patterned quantum well structure will have anyway to go through overgrowth to obtain a real device. This constitutes perhaps the best argument in favour of (i) fabrication techniques where the wires or dots result from the growth itself. Up to now, we nevertheless lack data to assess precisely and thus compare meaningfully the different fabrication techniques, mainly as far as size and homogeneity control are concerned.

The following section is devoted to the low temperature optical data obtained on the wires and dots produced by the etching plus overgrowth technique.

Optical studies

Photoluminescence

Figure 3 shows typical 10K photoluminescence spectra obtained on gratings of wires (a) and arrays of dots of various sizes (b). The PL is excited by the focused beam (power of the order of 50 μW, spot diameter 2 μm, corresponding to 5-10 wires and 100 dots) of a Sapphire-Ti laser pumped by an Ar⁺ laser. The excitation energy is 1.75 eV, well below the GaAs band gap energy so that carriers are photo-created only in the wires or dots. Even with these low excitation conditions, the PL of the narrowest structures is observed with reasonable signal to noise ratio, showing the efficiency of the anodic oxidation and overgrowth procedures for removing the etching defects and passivating the lateral surfaces, respectively. The spectra of Fig. 3 are normalized and their respective intensities will be discussed in the following. We clearly see a high energy shift of the PL spectrum (up to 20 meV) when the size L_x is decreased, which is attributed to the additional confinement. For the smallest L_x, the peak broadens, i.e. only towards the high energy side. The origin of this broadening is attributed to two effects: part of it is due to the inhomogeneity in the width of the structure while defects migration occurring during the overgrowth step is likely to contribute significantly to the broadening of the PL spectrum for the narrowest wires and dots.

The integrated intensity per unit wire or dot area is the relevant quantity to compare the emission intensities as a function of L_x because the absorption scales as this area, at least when 1D subbands or 0D levels form a quasi-continuum (sizes > 100 nm). This corrected integrated intensity (CII) is plotted in Fig. 4 for wires and dots. Electrodynamic effects [11,40] may play an important role in the observed increase of the CII for intermediate L_x (around 100 nm). Experimentally, the effects are more important in dots (or in single short wires) than in arrays of wires, but no quantitative analysis of the data could be obtained up to now. Another important point is the reduction by only a factor of 2 of the CII between the reference 2D regions and the narrowest wires or dots. This is somewhat in contradiction with the recent theoretical prediction of a dramatic decrease of the radiative efficiency for small dots or wires [36]. The strong reduction of the carrier scattering rates by acoustic phonons, together with the impossibility for electrons in small boxes to emit LO phonons should quench by orders of magnitude the emission intensity of the smallest structures. Though there may be a certain compensation of the predicted decrease in intensity by a better coupling with the incoming laser light through electrodynamic effects, energy relaxation seems still pretty fast in the smallest (~20 nm wide) wires or (~30x30 nm²) dots. Some recent experimental evidence pleads for the existence of additional efficient energy relaxation mechanisms. We have indeed observed short PL rise times through time-

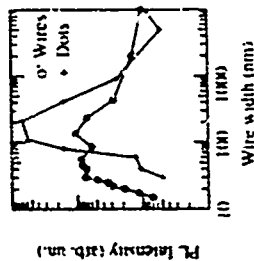


Fig 3: 10 K corrected integrated intensities observed in wires (o) and dots (+). Please note the logarithmic scale.

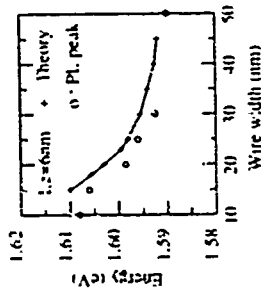


Fig 4: 10 K PLE spectra observed on the reference part of one sample, and on gratings of wires of various width L_x . All the spectra were normalized to their maxima and correspond to the laser parallel (broken line) and perpendicular (full line) to the wire axis.

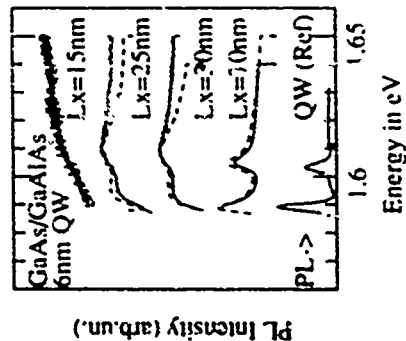


Fig 5: 10 K PLE spectra observed on the reference part of one sample, and on gratings of wires of various width L_x . All the spectra were normalized to their maxima and correspond to the laser parallel (broken line) and perpendicular (full line) to the wire axis.

resolved spectroscopy for the narrowest dots (less than 100 ps). A similar result was obtained in InAs dots embedded in GaAs(41), with shorter times (15 ps). The typical size of these latter dots is $30 \times 30 \times 2 \text{ nm}^3$. In both cases, the carriers were photoexcited in the barrier material. These short times thus include diffusion to the dots and energy relaxation inside them. In the particular case of InAs dots, the surface of the sample is flat and electrodynamic effects do not modify the apparent radiative efficiency. Though recent theoretical estimates show that Auger effects may provide the channels for a quick electron energy relaxation in these moderate size dots(42), additional experiments have still to be performed to deepen the understanding of carrier energy relaxation in these structures.

Finally, Fig 5 shows the good agreement between the experimental maximum energies of the PL spectra and theoretical estimates of the energy of the first excitonic transition, in the case of wires.

Photoluminescence Excitation

The expected signature of 1D effects in the PLE spectra are: i) a shift of the onset of the absorption; ii) polarization effects for laser polarized along or across the wire axis Y; iii) the appearance of transitions between excited 1D electron-hole states.

It should be emphasized that the differences in the TE (E along the wire axis) and TM (H along the wire axis) PLE spectra, obtained with an incoming laser perpendicular to the surface, do not constitute alone a proof of reduced dimensionality effects on the hole band structure. As evidenced in ref. 40, in the TM configuration, due to the non-planarity of the surface, the electric field has a significant component along the growth axis z. This component may change the relative strengths of the transitions in the TE and TM absorption spectra. Fortunately, this effect should be moderate thanks to the parity of E_z which is odd in x (x being the direction transverse to the wire).

Figure 6 shows the 10 K excitation spectra for gratings of wires for various L_x and X and Y polarizations. Whereas the first two criteria are met in those spectra, no 1D excited transitions are observed. The two σ_{HH} and σ_{HY} excitons seen in the reference PLE spectrum broaden progressively instead, and are completely smeared out in the narrowest wires. We attribute this broadening mainly to wire width inhomogeneities, as discussed in the previous section. We nevertheless observe a shift of the onset of the absorption together with clear polarization effects. As far as the differences in the spectra obtained in the two polarizations, please note that all the spectra are normalized to their own maxima, because there is a difference in the collected intensity in the two polarizations due to the electrodynamic effects. Nevertheless, the first transition is always more polarized along the wire axis than that of the second one, in good agreement with the calculated absorption spectra displayed in Fig 7. These spectra were calculated assuming a finite potential in z, an infinite one in x. It takes into account the full hole band structure and neglects the excitonic interaction(43). We furthermore take into account the width fluctuations (38), by calculating the absorption coefficient for a collection of wires with a Gaussian distribution (mean width L_x , standard deviation ΔL_x). Fig 7 (a) shows the evolution of the absorption spectrum for a $L_x = 30 \text{ nm}$ wide wire with the width fluctuation ΔL_x . The spectra of Fig 7(b), calculated for various L_x and $\Delta L_x = 5 \text{ nm}$, show a reasonable agreement with the experimental spectra. SEM top view micrographs of the etched wires, just before the overgrowth step, allow to extract a typical value of $\pm 5 \text{ nm}$ for the width fluctuations, confirming this analysis. Though a satisfactory agreement is found for the PLE experiments when these width inhomogeneities are taken into account, they are not sufficient to yield alone, as mentioned in the previous section, the broadenings that are observed in the PL spectra of Figure 3. The additional broadenings, beyond those due to the size

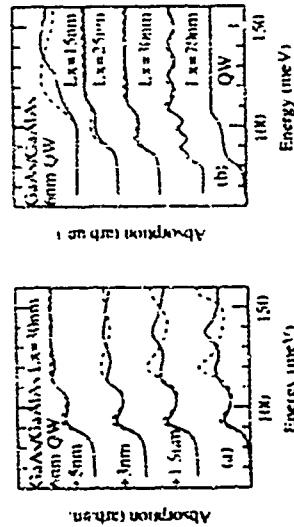


Fig 7: Calculated absorption spectra (neglecting excitonic effects) on excitations of wires with a Gaussian distribution of sizes. of average L_x and standard deviation Δd . in a), $L_x = 30$ nm and $\Delta d = 0, 1.5, 3$ and 5 nm. in b), $L_x = 10-5$ nm and $L_x = 1.5, 2.5, 3.0, 7.0$ nm in both cases. all transistors are broadened by 5 meV.

Fig 8: 10 K PL spectra of a single $6 \times 20 \times 145$ nm³ wire (full line), and of a grating of $6 \times 20 \times 80000$ nm³ wires (dashed line)

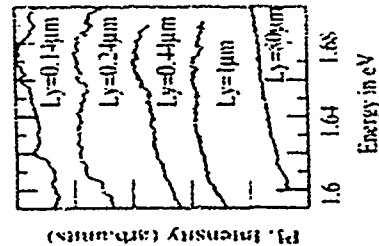
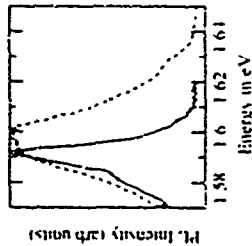


Fig 9: 10 K PL spectra of a grating of 0.25×80000 nm³ wires and of single $6 \times 25 \times L_y$ nm³ wires with various length L_y



inhomogeneities, scale as the lateral surface to volume ratio for wires and boxes, and this suggests strongly that they may be due to defects migration (or intermixing) during the annealing and overgrowth step.

Though there are other possible ways to reduce the effects of inhomogeneities, the simplest one is to study single objects. The results of such studies are presented in the next section.

Single wires

Thanks to the high PL efficiency obtained in the narrowest wires, we could perform PL and PLE spectroscopy on isolated (and over) short wires. Figure 8 shows the 10K PL spectrum of a single $6 \times 20 \times 145$ nm³ wire as compared to that obtained on a grating of wires (5 to 10 wires), with the same excitation conditions. Let us emphasize again that the observation of the PL spectrum of this single short wire (still excited below the GaAs band gap with a $100 \mu W$, $2 \mu m$ diameter spot) shows the efficiency of the process to give narrow quantum structures with a low density of non radiative defects and a good radiative efficiency. The Full Width at Half Maximum (FWHM) of the PL spectrum of the single wire is reduced by a factor of 2, as compared to that of the spectrum obtained on the grating. However, the reduction of the broadening is not symmetric: it is difficult to exclude that this particular single wire is somewhat wider than the average wire width in the grating.

Perhaps more convincing is the evolution of the PLE spectra for single wires with decreasing lengths displayed in Figure 9. Whereas it is featureless for the longest wires, some structures are progressively evidenced in shorter and shorter wires. The detail of the PLE spectrum for single short wires of varying width is shown in figure 10. Though the experiments are difficult on these objects, we could verify that the main features in the spectra are significant. We assign them to transitions between 1D excited electron and hole subbands. Unfortunately, the length of the shortest wires is still large as compared to the typical length where the width is uniform (~ 50 nm); they are still rather disordered objects, for which a quantitative comparison with calculated transition energies is not satisfactory.

In our opinion, the spectroscopy of single shorter wires can be performed which will give us information on the intrinsic properties of 1D and 0D objects, and clarify the energy relaxation problems.

Conclusion

To summarize, we have shown that electron-beam lithography, associated with reactive ion etching, anodic oxidation and overgrowth, is a suitable tool for fabricating quantum wires and dots. The low temperature optical properties show that reasonable efficiencies can be restored even in the narrowest structures, which display reduced dimensionality features. However, the fluctuations of their sizes have still to be reduced (to typically better than 1.5 nm) to meet the drastic requirements needed to improve the characteristics of optoelectronic devices.

Acknowledgement

The authors wish to thank to J.M. Gerard, M. Voos and G. Bastard for many fruitful discussions. This work was partly funded by the ESPRIT Basic Research program of the European Community.

Phys. Lett. 55, 667 (1989)
 29 R. Nitzel, N. N. Ledentsov, L. Dawentz and K. Ploog, Phys. Rev. B 45, 3507 (1992)
 30 E. Kapon, J.P. Harbison, C.P. Yun and N.G. Stoffel, Appl. Phys. Lett. 52, 607 (1988)
 31 E. Kapon, D.W. Hwang, M. Walther, R. Bhat and N.G. Stoffel, Surf. Sci. 287, 593 (1992)
 32 S. Tsukamoto, Y. Nagamune, M. Nishio and Y. Arai, J. Appl. Phys. 71, 533 (1992)
 33 H. Asai, S. Yamada and T. Fukui, Appl. Phys. Lett. 51, 1518 (1987)
 34 Y. Nakamura, S. Tsukamoto, M. Nishio and Y. Arai, Proceedings of the International Conference on Solid State Devices and Materials 1991 (Yokohama, Japan) (1991)
 35 U. Bockelmann and G. Bastard, Phys. Rev. B 42, 8947 (1990)
 36 H. Benisty, C.M. Sotomayor-Torres and C. Weisbuch, Phys. Rev. B 44, 10945 (1991)
 37 A. Izrael, unpublished, patent pending
 38 L. Brocheau, A. Izrael, J.Y. Marzin, R. Azoulay, V. Thierry-Mieg and F.R. Ladan, Appl. Phys. Lett. 3023 (1992)
 39 M. Nishio, M. Nishio and T. Tamamura, Appl. Phys. Lett. 62, 2350 (1993)
 40 U. Bockelmann and G. Bastard, Europhys. Lett. 16, 601 (1991)
 41 J.M. Gerard and B. Sermage, unpublished
 42 U. Bockelmann and T. Egler, Phys. Rev. B 46, 15574 (1992)
 43 U. Bockelmann and G. Bastard, Europhys. Lett. 15, 215 (1991)

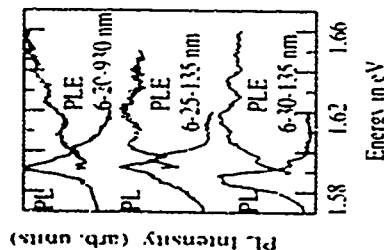


Fig 10: 10 K PLE spectra of single wires, whose characteristics are indicated in the figure (The first figure is the quantum well width, the second Lx and the third Ly)

References
 1. Y. Arakawa, K. Vahala and A. Yariv, Appl. Phys. Lett. 45, 850 (1984)
 2. M. Asada, Y. Miyamoto and Y. Suemitsu, Jpn. J. Appl. Phys. 24, L95 (1985)
 3. C. Weisbuch, in "Applications of Nonequilibrium Wides, Selective Dopant, and Superlattices", Semiconductors and Semimetals Vol. 24, R. Chen (ed.), Academic Press, Boston, 1 (1987)
 4. T. Takahashi and Y. Arakawa, Optoelectron. Dev. and Technol. 3, 155 (1988)
 5. K. Kash, Journal of Luminescence 46, 69 (1990) and references therein.
 6. D. Gerchoni, H. Temun, J. Dittmer, S.N.G. Chu and M.B. Panish, Appl. Phys. Lett. 53, 895 (1988)
 7. M. Watt, C.M. Sotomayor-Torres, R. Cheung, C.D.W. Wilkinson, H.E.G. Auer and S.R. Beaumont, Superlattices and Microstruct. 4, 2124 (1988)
 8. W.E. Leish, C.M. Sotomayor-Torres, D. Lodi, S. Thoma, P. van Daele, C.R. Stanley, P. Demester and S.P. Beaumont, Surf. Sci. 263, 622 (1992)
 9. A. Forchel, B.E. Maile, H. Loh and R. Gernann, Springer Series in Solid State Sciences 83, Physics and Technology of submicron structures (Springer, Berlin, 1994), p. 28.
 10. M. Kohn, D. Heinmann, P. Grambow and K. Ploog, Phys. Rev. Lett. 63, 2124 (1989)
 11. M. Kohn, D. Heinmann, W.W. Rühle, P. Grambow and K. Ploog, Phys. Rev. B 41, 12338 (1990)
 12. R. Cingolani, H. Legg, L. Tiedler, H. Kalt, D. Heinmann and K. Ploog, Phys. Rev. Lett. 67, 651 (1991)
 13. A. Izrael, B. Sermage, J.Y. Marzin, O. Ougazzaden, J. Etard, Appl. Phys. Lett. 56, 830 (1990)
 14. A. Izrael, J.Y. Marzin, B. Sermage, R. Azoulay and V. Thierry-Mieg, Microelectron. Eng. 11, 39 (1990)
 15. K. Brunner, G. Abstreiter, M. Walther, G. Böhm and G. Trankle, Surf. Sci. 267, 218 (1992)
 16. K. Brunner, U. Bockelmann, G. Abstreiter, M. Walther, G. Böhm, G. Trankle and G. Weimann, Phys. Rev. Lett. 69, 3216 (1992)
 17. J. Coert, P.M. Petroff, G.J. Dolan, S.J. Pearson, A.C. Gossard and J.H. English, Appl. Phys. Lett. 49, 1275 (1986)
 18. J. Coert, P.M. Petroff, G.J. Dolan, S.J. Pearson, A.C. Gossard and J.H. English, Superlatt. and Microstruct. 3, 35 (1987)
 19. Y. Hirayama, S. Tanaka, Y. Suzuki and H. Okamoto, Phys. Rev. B37, 2774 (1988)
 20. C. Vieu, M. Schneider, D. Maity, R. Planel, H. Launois, J.Y. Marzin and B. Descouts, J. Appl. Phys. 70, 1444 (1991)
 21. H. Lier, A. Forchel, G. Höcher, J. Hommel, S. Bayer, H. Rühlitz, G. Weimann and W. Schlapp, J. Appl. Phys. 67, 1805 (1990)
 22. K. Kash, J.M. Worlock, M.D. Sturge, P. Grabbe, J.P. Harbison, A. Scherer and P.S.D. Lin, Appl. Phys. Lett. 53, 762 (1988)
 23. K. Kash, B.P. Van der Gaag, Derek D. Mahoney, A.S. Gorkov, L.T. Florez and J.P. Harbison, Phys. Rev. Lett. 67, 1326 (1991)
 24. D. Gerchoni, J.S. Weiner, S.N.G. Chu, G.A. Barati, J.M. Vandenbergh, L.N. Pfeiffer, K. West, R.A. Iqbal and T. Tanbun-Ek, Phys. Rev. Lett. 65 (1990)
 25. P.M. Petroff, A.C. Gossard and W. Wegmann, Appl. Phys. Lett. 45, 620 (1984)
 26. M.S. Miler, C.E. Pior, H. Weman, L.A. Samuska, H. Kroemer and P.M. Petroff, J. of Cryst. Growth 111, 323 (1991)
 27. M. Tanaka and H. Sakaki, Appl. Phys. Lett. 54, 1326 (1989)
 28. E. Colas, E. Kapon, S. Smboriny, H.M. Cox, R. Bhat, K. Kash and P.S. Lin, Appl.

ThB2

Modelle Reconnection in pseudomorphale latissimale Quasium Wires curren in Nucleonoid Substrats

M. Srinivasan^{1,2}, V. Tucci³, J. Cunniff⁴, F. Kuper¹, D. A. Hwang¹, C. (Vocant) R. Hsieh¹, D. Hunkeler¹

1. Define the following terms:

2 Festum der Konstitution, Teilnahme Universität Berlin
 Festum der Konstitution, Teilnahme Universität Berlin

[illegible]

Abstract

The concept of fabricating quantum wires (QWRs) by growing quantum wells (QW) over non planar substrates is introduced in the present work. A system of two QW's is grown as the active region in a new structure between p-doped AlGaAs (100 Å) and n-doped GaAs (200 Å) leading layers on a p-doped GaAs substrate. The different "special" components of the luminescence depending on the AlGaAs barriers, the top quantum well on the ridge in between the grooves, (1.57 eV) which is about half the critical thickness, the side walls, the AlGaAs wire itself can be unambiguously assigned to the respective region using spatially resolved cathodoluminescence (CL) measurements with a peak wavelength of 800 nm (1.54 eV) with a full width of half maximum of 10 nm. This value compares well with earlier results. Experiments for all other resonances (3.0 eV) we find a recombination time constant of 1 ns. The recombination is dominated by radiative processes.

Introduction:

The improvement of properties of mixed semiconductor electronic and photonic devices using charge carriers in reduced dimensions is constantly reported. However, the nanotechnology realization of such structures has still difficult stringent requirements [1] such as small feature size with reproducible dimensions, small lateral size fluctuations and low quantum defects. With respect to these requirements, the concept of fabricating quantum wires (QWRs) with diameters in the nm regime by growing quantum wells on various planar substrates has been successfully implemented in the AlGaAs/GaAs system [2]. Due to the in situ transformation of the containing interfaces in the V-groove during OMVPE (Organometallic Vapor Phase Epitaxy) these structures exhibited high luminescence efficiency [3]. In this paper, we report on the growth of GaAs QWRs on GaAs substrates, etched by hydrogen zinc etch [4], and on the growth of GaAs QWRs on GaAs substrates, etched by hydrogen zinc etch [4], and on the growth of GaAs QWRs on GaAs substrates, etched by hydrogen zinc etch [4].

the incorporation of strain into the active region of the QWR. It is expected that the QWR laser is expected to improve the laser performance due to the modification of the band structure as in the case of conventional QW structures [4]. With biaxial compressive strain the light hole states are shifted from the conduction band and thus their thermal population is reduced resulting higher optical gain and a preference for TE polarization [5]. The lower effective mass of the heavy holes leads to a larger splitting of the heavy hole one dimensional (1D) subbands. Infinitely QWR lasers grown on GaN/AlN on sub-micron pin structures have been studied and operated up to room temperature [6]. Recently, GaN/AlN QWR lasers grown by molecular beam epitaxy (MBE) have also been demonstrated and operated at room temperature with a record low threshold current density as low as 200 A/cm² [7]. Other values reported on MBE growth include 100 A/cm² [8] and 100 A/cm² [9]. On patterned GaN substrates, although the luminescence from the wires was not identified unambiguously in that case [9].

10/10/2013

As a substitute we used a 1 liter water in each with 4 gram pinch was a hexamethyl ethyl 7, 7, 7-trifluorooctanoic acid. Following the growth in an 18 liter flask aseptically bottle the QM is poured in the medium in the 1

structures by growing a 700 nm InGaN (30%) quantum well within a graded InGaAsP (10%) layer structure. The cladding layers are made of undoped Al_{0.3}Ga_{0.7}As with linearly varying composition between 1 and 2 to 100. The lower part of the structure is doped with Si, the upper one with Zn and the InGaAs active layer and graded regions are undoped. Fig. 1 shows the schematic layer sequence. The structure was grown in atmospheric pressure MOCVD at 740°C.

The luminescence from this structure was analysed with a specially constructed cathodoluminescence (CL) A₂ detector as well as a standard photodiode with a sensitive range up to λ_{CL} 1 μm . By using beam blanking we accomplished pulsed excitation with arbitrary pulse length, 1 ns, and repetition rate up to 10 MHz. The total time resolution of 25 ps achieved with a fast photomultiplier was limited to 35 ps by the speed of the 350 kV electron gun.

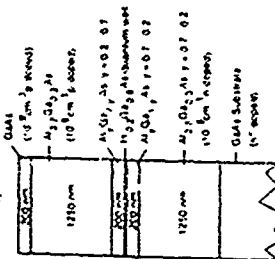


Fig. 1. When the sample view size

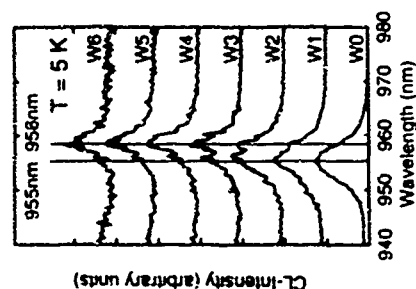


Fig. 2
(15000X 50000X 120000X)
240000X 100000X 100000X

Results and Discussion

The cross-sectional TEM (Transmission Electron Microscopy) image of the butt-joint of two V-grooves (see Fig. 2) shows the crescent-shaped InGaAs QWR in the center. The InGaAs QWR layer grows on the side walls exhibiting quasi-periodic thickness modulation with a pitch of approx. 100 nm, which probably due to strain accumulation with results in three-dimensional growth. Similar periodic structures were reported also by Gruber et al. [11]. The thickness of the QWR in the center is 2.2 nm. The lateral geometrical width W_{lat} of the QWR, which has been confirmed by experimental results [11] and [12], where part of the QWR has a thickness above the critical value $W_{lat} = 1.45 \mu\text{m}$, whereas part is well below $1.45 \mu\text{m}$, where part of the QWR has a thickness above the critical value such a narrow QWR must not exceed the energy required to penetrate the modulation, even though the thickness of a single QWR may be calculated for a planar structure. The electric field in the unstrained (UNSTC) and QWR region is about 4.14 MV/cm. A field of this magnitude is estimated to have a linear effect of a few meV shift in the conduction level [13].

energy level (14). The transverse luminescence properties of the QWR were evaluated by using a reduced wave area of about 10 nm^2 around the wire central core (see in Fig. 3). The luminescence pulse of the QWR (in air under reduced polarization) with the first pulse and a 100 MHz repetition rate is shown in Fig. 5. The transient has an initial time constant of 1 ns with the first 10³ decays. This time constant is longer than 100 ps measured for AlGaInAs QWRs [15]. This is probably due to the larger size of the wire. The luminescence from the top QWL (uncoupled with reduced wave area) for the top of the subject has an initial time constant of 1 ns , a value similar to what has been reported before for GaInAs nanowires [16] and for GaInAs nanowires [17]. The transient of the QWR has a tail with a much larger decay time constant of about 10 ns .



Time delayed TDI spectra allow for identification of the corresponding reconstruction channel. We have set seven time windows: $W10=10$ lines, $W141=1$ line, $W142=1$ line, $W143=1$ line, $W144=1$ line, $W145=1$ line, $W146=1$ line, $W147=1$ line, $W148=1$ line, $W149=1$ line, $W150=1$ line, $W151=1$ line, $W152=1$ line, $W153=1$ line, $W154=1$ line, $W155=1$ line, $W156=1$ line, $W157=1$ line, $W158=1$ line, $W159=1$ line, $W160=1$ line, $W161=1$ line, $W162=1$ line, $W163=1$ line, $W164=1$ line, $W165=1$ line, $W166=1$ line, $W167=1$ line, $W168=1$ line, $W169=1$ line, $W170=1$ line, $W171=1$ line, $W172=1$ line, $W173=1$ line, $W174=1$ line, $W175=1$ line, $W176=1$ line, $W177=1$ line, $W178=1$ line, $W179=1$ line, $W180=1$ line, $W181=1$ line, $W182=1$ line, $W183=1$ line, $W184=1$ line, $W185=1$ line, $W186=1$ line, $W187=1$ line, $W188=1$ line, $W189=1$ line, $W190=1$ line, $W191=1$ line, $W192=1$ line, $W193=1$ line, $W194=1$ line, $W195=1$ line, $W196=1$ line, $W197=1$ line, $W198=1$ line, $W199=1$ line, $W200=1$ line, $W201=1$ line, $W202=1$ line, $W203=1$ line, $W204=1$ line, $W205=1$ line, $W206=1$ line, $W207=1$ line, $W208=1$ line, $W209=1$ line, $W210=1$ line, $W211=1$ line, $W212=1$ line, $W213=1$ line, $W214=1$ line, $W215=1$ line, $W216=1$ line, $W217=1$ line, $W218=1$ line, $W219=1$ line, $W220=1$ line, $W221=1$ line, $W222=1$ line, $W223=1$ line, $W224=1$ line, $W225=1$ line, $W226=1$ line, $W227=1$ line, $W228=1$ line, $W229=1$ line, $W230=1$ line, $W231=1$ line, $W232=1$ line, $W233=1$ line, $W234=1$ line, $W235=1$ line, $W236=1$ line, $W237=1$ line, $W238=1$ line, $W239=1$ line, $W240=1$ line, $W241=1$ line, $W242=1$ line, $W243=1$ line, $W244=1$ line, $W245=1$ line, $W246=1$ line, $W247=1$ line, $W248=1$ line, $W249=1$ line, $W250=1$ line, $W251=1$ line, $W252=1$ line, $W253=1$ line, $W254=1$ line, $W255=1$ line, $W256=1$ line, $W257=1$ line, $W258=1$ line, $W259=1$ line, $W260=1$ line, $W261=1$ line, $W262=1$ line, $W263=1$ line, $W264=1$ line, $W265=1$ line, $W266=1$ line, $W267=1$ line, $W268=1$ line, $W269=1$ line, $W270=1$ line, $W271=1$ line, $W272=1$ line, $W273=1$ line, $W274=1$ line, $W275=1$ line, $W276=1$ line, $W277=1$ line, $W278=1$ line, $W279=1$ line, $W280=1$ line, $W281=1$ line, $W282=1$ line, $W283=1$ line, $W284=1$ line, $W285=1$ line, $W286=1$ line, $W287=1$ line, $W288=1$ line, $W289=1$ line, $W290=1$ line, $W291=1$ line, $W292=1$ line, $W293=1$ line, $W294=1$ line, $W295=1$ line, $W296=1$ line, $W297=1$ line, $W298=1$ line, $W299=1$ line, $W300=1$ line, $W301=1$ line, $W302=1$ line, $W303=1$ line, $W304=1$ line, $W305=1$ line, $W306=1$ line, $W307=1$ line, $W308=1$ line, $W309=1$ line, $W310=1$ line, $W311=1$ line, $W312=1$ line, $W313=1$ line, $W314=1$ line, $W315=1$ line, $W316=1$ line, $W317=1$ line, $W318=1$ line, $W319=1$ line, $W320=1$ line, $W321=1$ line, $W322=1$ line, $W323=1$ line, $W324=1$ line, $W325=1$ line, $W326=1$ line, $W327=1$ line, $W328=1$ line, $W329=1$ line, $W330=1$ line, $W331=1$ line, $W332=1$ line, $W333=1$ line, $W334=1$ line, $W335=1$ line, $W336=1$ line, $W337=1$ line, $W338=1$ line, $W339=1$ line, $W340=1$ line, $W341=1$ line, $W342=1$ line, $W343=1$ line, $W344=1$ line, $W345=1$ line, $W346=1$ line, $W347=1$ line, $W348=1$ line, $W349=1$ line, $W350=1$ line, $W351=1$ line, $W352=1$ line, $W353=1$ line, $W354=1$ line, $W355=1$ line, $W356=1$ line, $W357=1$ line, $W358=1$ line, $W359=1$ line, $W360=1$ line, $W361=1$ line, $W362=1$ line, $W363=1$ line, $W364=1$ line, $W365=1$ line, $W366=1$ line, $W367=1$ line, $W368=1$ line, $W369=1$ line, $W370=1$ line, $W371=1$ line, $W372=1$ line, $W373=1$ line, $W374=1$ line, $W375=1$ line, $W376=1$ line, $W377=1$ line, $W378=1$ line, $W379=1$ line, $W380=1$ line, $W381=1$ line, $W382=1$ line, $W383=1$ line, $W384=1$ line, $W385=1$ line, $W386=1$ line, $W387=1$ line, $W388=1$ line, $W389=1$ line, $W390=1$ line, $W391=1$ line, $W392=1$ line, $W393=1$ line, $W394=1$ line, $W395=1$ line, $W396=1$ line, $W397=1$ line, $W398=1$ line, $W399=1$ line, $W400=1$ line, $W401=1$ line, $W402=1$ line, $W403=1$ line, $W404=1$ line, $W405=1$ line, $W406=1$ line, $W407=1$ line, $W408=1$ line, $W409=1$ line, $W410=1$ line, $W411=1$ line, $W412=1$ line, $W413=1$ line, $W414=1$ line, $W415=1$ line, $W416=1$ line, $W417=1$ line, $W418=1$ line, $W419=1$ line, $W420=1$ line, $W421=1$ line, $W422=1$ line, $W423=1$ line, $W424=1$ line, $W425=1$ line, $W426=1$ line, $W427=1$ line, $W428=1$ line, $W429=1$ line, $W430=1$ line

447544

ing ZnGa₂S₄ quantum wires with high optical quality have been fabricated on V-grooved GaAs substrate. The wires emit at $T=4\text{ K}$ at 455 nm with a 1.1 eV FWHM of line-V. Cathodoluminescence experiments performed on a sample with a yield a recombination time constant of the minority electrons, a component of the time delayed spectroscopy process shows up below the bandgap with orders of magnitude slower decay rates

References

- [1] J. Kapton, H. Walther, J. Christen, M. Grunmann, C. Casadeu, D. M. Huang, L. Cides, R. Bhata, G. H. Nong, D. Bumber, *Superlattices Microstruct.* **12**, 491 (1992).
- [2] I. Kapton, D. M. Huang, R. Bhata, *Phys. Rev. Lett.* **63**, 4301 (1989).
- [3] S. Simbawa, F. Kapon, L. Cides, D. M. Huang, *IEEE Trans. Electron Devices* **39**, 225 (1989).
- [4] J. O'Reilly, *Semiconductor Sci. Technol.* **4**, 121 (1989).
- [5] D. Abo, T. K. Yoo, *Appl. Phys. Lett.* **60**, 348 (1992).
- [6] J. Kapton, C. Casadeu, D. M. Huang, L. M. Schuchman, *Appl. Phys. Lett.* **62**, 2170 (1993).
- [7] H. Walther, J. Kapton, C. Casadeu, D. M. Huang, J. M. Woodall, *IEEE Trans. Electron Devices*, **40**, 3459 (1993).
- [8] R. P. Martin, H. Tang, H. W. Weinm, M. Leonard, T. Yasuda, J. L. Bowers, E. L. Hu, J. Vac. Sci. Technol. **A** **10**, 697 (1992).
- [9] J. Christen, M. Grunmann, D. Bumber, J. Vac. Sci. Technol. **B** **9**, 2358 (1991).
- [10] M. Grunmann, J. Christen, D. Bumber, *Superlattices Microstruct.* **9**, 65 (1991).
- [11] M. Grunmann, J. Christen, J. L. Bowers, J. N. Miller, *Phys. Rev. B* **43**, 10120 (1991).
- [12] G. Grunwald, Y. Zou, J. S. Oshiki, P. D. Dapkin, J. Crystal Growth **107**, 383 (1991).
- [13] J. N. Miller, M. A. Haddad, J. Crystal Growth **27** (1978) 118.
- [14] M. Grunmann, J. Christen, D. Bumber, J. N. Miller, J. Vac. Sci. Technol. **B** **9**, 751 (1991).
- [15] G. Grunwald, J. M. Leonard, J. Chung, *IEEE Trans. Res. B* **28**, 1231 (1988).
- [16] J. Christen, J. Kapton, M. Grunmann, D. M. Huang, M. Josko, D. Bumber, *phys. stat. sol. (b)* **173**, 107 (1992), and references therein.
- [17] J. Christen, M. Grunmann, J. Kapton, L. Cides, D. M. Huang, D. Bumber, *Appl. Phys. Lett.* **61**, 67 (1992).
- [18] M. Grunmann, M. Turek, J. Kapton, J. Christen, D. M. Huang, C. Casadeu, R. Bhata, D. Bumber, *Appl. Phys. Lett.* (1993), unpublished.

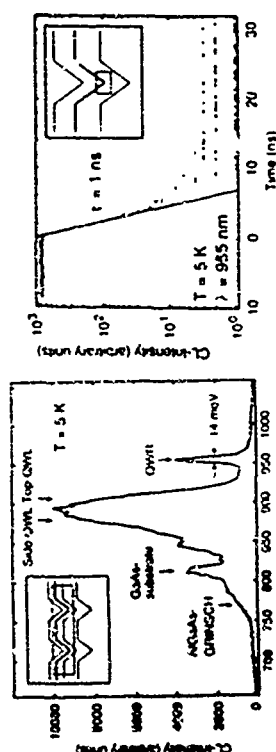


Fig. 6. Treatment of QVRLV infection.

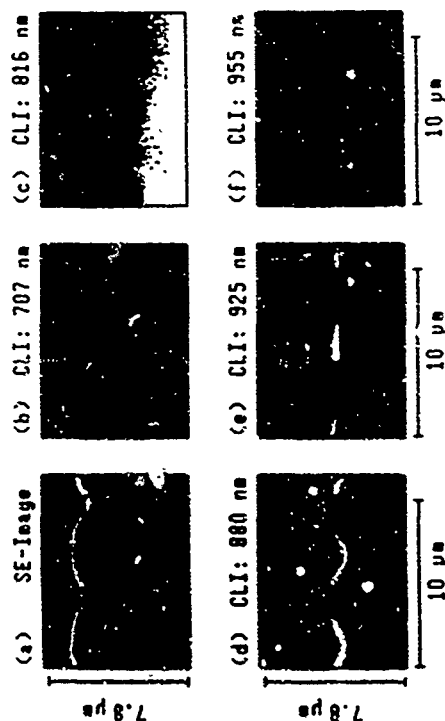


Fig. 4 Secondary electron image of cross section and microhardness (H_v) at different wavelengths

ThB3

Optical characterization of InGaAs/GaAs quantum dots defined by lateral top barrier modulation

A. Schmidt, A. Forciel, F. Faller, I. Idrachov, A. Vasiliev

Technische Physik, Universität Würzburg, Am Hubland, D-97074 Würzburg, Germany
* on leave from Russian Academy of Science, Tchernogolovka, Russia

Abstract. We have produced effectively buried quantum well dots on the basis of InGaAs/GaAs single quantum wells using high resolution electron beam lithography and selective wet etching of the top barrier. The lateral barriers are realized by the difference in quantization energy in quantum wells with a semiconductor top barrier compared to quantum wells with a vacuum potential barrier. Dot structures with widths down to 20 nm have been generated. We observe that the structures maintain high luminescence efficiencies down to the smallest sizes. We also observe a blueshift of up to 12 meV for 10 nm quantum dots which are nonselectively etched. Furthermore we have studied the dependence of the quantization energies for well material with different Indium content.

1. Introduction

Recently, low-dimensional semiconductor structures have been the subject of intense studies. Crystal growth techniques like molecular beam epitaxy (MBE) and metalorganic vapor phase epitaxy (MOVPE) allow to realize quantum well layers exhibiting quantum confinement in one direction. For structures exhibiting quantum confinement in two or even three dimensions like quantum wires or dots, several different approaches are used [1-8]. High resolution electron beam lithography and transfer of the pattern to the semiconductor quantum well substrate e.g. by dry or wet etching, impurity induced disordering processes or selective epitaxy on patterned or high-index substrates are the most commonly used patterning methods. Surface effects and defects due to e.g. etching processes limit the quantum efficiency in luminescence experiments.

In the presently used approach the active removal of the top barrier layer in a wet etching step generates virtually no open sidewalls and leads to a laterally confining potential for electrons and holes in the unetched regions under the remaining cap layer [5]. By the selective wet etch step the GaAs/InGaAs conduction and valence band discontinuities (on the order of 1 eV) are replaced by the substantially higher energy difference of the InGaAs-vacuum transition (electron affinity of about 5 eV). If the quantum wells are appropriately thin, the barrier height controls the quantization energy of electron and hole states in the etched region. The decrease of the confining energy pushes the wavefunctions of electrons and holes in the GaAs barrier layer below the quantum well. This leads to higher energies for the ground state in GaAs/InGaAs-vacuum quantum wells than in GaAs/InGaAs/GaAs quantum wells. The difference in the quantization energies leads to a lateral confinement potential and localizes the carriers beneath the GaAs cap layer in the InGaAs material.

The unetched InGaAs quantum well layer acts both as active quantum dot and barrier material. Virtually no defects are induced by the selective wet chemical etching process in the active regions. In this method effectively buried structures are generated with low surface recombination velocities.

2. Lithography and pattern transfer

The starting material for the patterning process were InGaAs/GaAs single quantum wells with different In content grown by molecular beam epitaxy on undoped, 100° oriented GaAs substrate. The samples were spin coated with a positive tone high resolution electron beam resist. For the exposure a conventional scanning electron microscope equipped with an external pattern generator and scan controller was used. Quadratic dot grids of field size of 100 µm with an area filling factor of 1/16 and dot sizes down to 25 nm in diameter were exposed in the resist. After developing the exposed structures a 15 nm Al mask was thermally evaporated. By a lift off process in an ultrasonic bath Al dot etch masks were obtained. The Al pattern then was transferred in the quantum well using H₂O₂/NH₄OH buffered to pH 7.0.

With this process we generate dots with structure sizes down to 20 nm in diameter with a dot pitch of 90 nm. The dot sizes were measured in an field emission scanning electron microscope. Fig. 1 shows the 45 nm features obtained after mask removal with 1% NaOH solution.



Fig. 1 45 nm dot structures prepared by electron beam lithography and wet chemical etching after mask removal

3. Experimental results and discussion

The samples were characterized by photoluminescence in an He immersion cryostat at 2 K. An Argon laser was used as excitation source. Spectral resolution was accomplished with a 250 nm focal length grating spectrometer with a 1200 line grating. For detection an optical multichannel analyzer with S25 photodiode was used.

Fig. 2 shows several photoluminescence spectra of quantum dots of different dot sizes. All spectra are normalized to their maximum. The fitting factor corrected quantum efficiency was greater than ten percent for all dot sizes down to 20 nm. From this we conclude that we have produced almost defect free quantum structures. We see no abrupt drop in luminescence yield

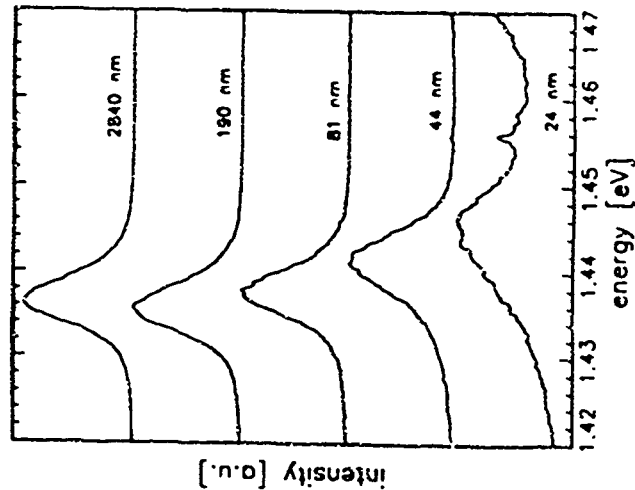


Fig. 2 Photoluminescence spectra for several different dot sizes in a selectively etched quantum well structure. Spectra are normalized to their maximum. The excitation density was approximately 30 W cm^{-2} .

as proposed by other authors for quantum dots [9]. The normalized intensity even exceeds unity by almost a factor of eight. We attribute this to effective carrier capture from the GaAs barrier beneath the InGaAs quantum well. The maximum capture efficiency is reached at dot distances of 1000 nm. This implies an ambipolar diffusion length on the order of 800 nm.

For dot structures below 100 nm in size we observe in Fig. 2 an energetic blue shift. This value is approximately two times the value of the onset of the blueshift in barrier modulated wires. Simultaneously with this blueshift we observe that for small structures an increase of the linewidth up to a value of 14 meV for the smallest structures. From the dependence of the blueshift on the dot size we can estimate the size fluctuations within a dot array to be on the order of $\pm 3 \text{ nm}$.

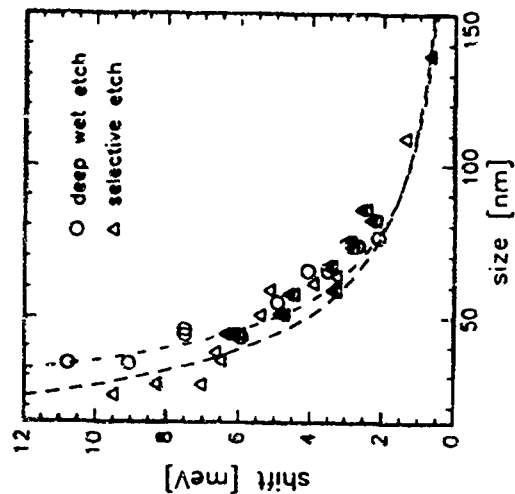


Fig. 3 Energy shift plotted versus dot size for the sample of Fig. 2 (open triangles) and for a sample where the QW material was also etched laterally (open circles). The lines show results of simple model calculations for quantum dots with 25 meV (solid line) and 5 eV (dashed line) lateral potential.

In Fig. 3 the blueshift of the luminescence maximum for two differently processed samples is plotted versus the dot diameter. The triangles denote data taken from a sample from which the top barrier layer has been selectively removed. The circles represent data of quantum dots which have been prepared by deep wet chemical etching. In this case the lateral confinement energy is directly given by the electron work function. The maximum energy shift is 10 meV.

for barrier modulated dots with 23 nm diameter. This is about half the value of the laterally confining potential in the barrier modulated structures (25 meV [10]). The dashed line in the graph represents a model calculation for the shift of the lowest subband edge in a quantum dot structure. This model does not account for the increasing excitonic correlation in a quantum dot structure. This may influence the observed energy shift especially for dots below 40 nm in diameter as shown by Le Goff and Sibbe [11].

The dash-dotted line in Fig. 2 shows a model calculation for the deep etched dots based on a lateral vacuum barrier of five eV due to the semiconductor work function. For dot sizes above 40 nm the lateral quantization induced energy shift of the luminescence in barrier modulated and deep etched structures is similar. As expected, due to the larger confinement potential, we observed slightly stronger quantization effects in small deep etched structures than in barrier modulated dots of comparable size. Fig. 3 indicates that barrier modulated structures are well suited to observe lateral quantization effects in dots with diameters of about 20 nm.

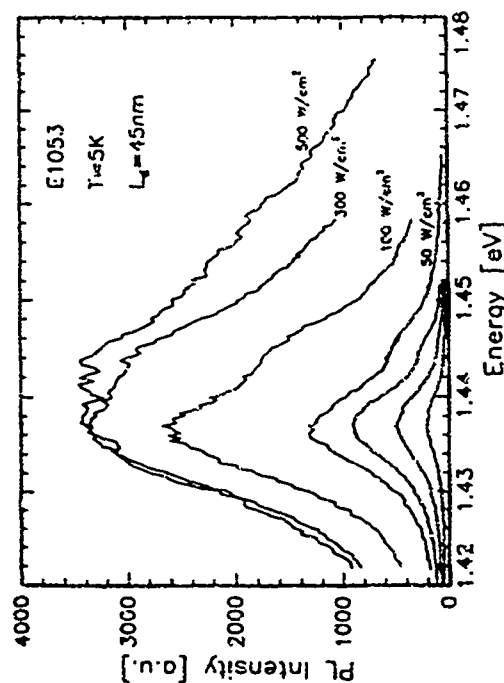


Fig. 4: Low temperature (5K) cw-laser excitation spectra of 45 nm dots taken under different laser excitation. Two peaks separated by 8 meV can be clearly seen.

Furthermore, we have investigated the behavior of small structures under cw-high excitation. The result of this measurement is depicted in Fig. 4 for a dot structure with an average dot diameter of 45 nm. It can be seen that the lowest subband peak increases with increasing laser

excitation and finally saturates at an intensity of 500 W/cm². Already at relatively low excitation powers a second luminescence band in the spectrum, it is located about 8 meV to higher energy from the first peak. Our model predicts a subband separation of about 10 meV which would suggest that we see the second lateral subband luminescence. We may attribute the early onset of the second level luminescence signal peak to the slowed relaxation by reduced phonon scattering rates in quantum dots.

4. Conclusions

We have fabricated high-quality low damage quantum dots by selective wet chemical etching in the InGaAs/GaAs material system. The quantum structures exhibit high normalized luminescence ratios. Furthermore small structures show a strong energetic blueshift correlated with the structure size. From the relationship between blueshift and decrease the broadening of luminescence linewidths can be explained by an inhomogeneous size distribution in the range of 7 nm. High resolution measurements reveal the existence of a second lateral subband in smaller dot structures. The early onset of luminescence from the lateral subband is possibly due to reduced phonon scattering in quantum dots.

5. Acknowledgements
We thank M. Emmertling for the assistance in preparing the quantum well substrate for lithography. The financial support of this work by the Deutsche Forschungsgemeinschaft is gratefully acknowledged.

References

1. B.E. Maile, A. Forchel, R. Gernann, J. Sunka, L. Korte, and C. Thamm, *Appl. Phys. Lett.* **57**, 807 (1990).
2. A. Izrael, B. Sermage, J.Y. Marzin, A. Dugast, R. Azevedy, J. Ertland, V. Thierry-Mieg, and L. Henry, *Appl. Phys. Lett.* **56**, 850, (1990).
3. M. Nocchi, M. Nagasawa, T. Nishida, T. Tamenori, H. Iwamura, S. Nagima, and M. Okamoto, *Appl. Phys. Lett.* **58**, 723 (1991).
4. Y. Naganuma, Y. Arakawa, M. Nishida, S. Sano, and N. Miura, *Phys. Rev. Lett.* **69**, 2936 (1992).
5. Ch. Gruber, L. Buvor, F. Dählinger, A. Forchel, P.A. Knipp, T.L. Reinecke, *Phys. Rev. B* **47**, 7626 (1993).
6. H. Leier, A. Forchel, B.E. Maile, G. Mayer, J. Hommel, G. Weimann, and W. Schlapp, *Appl. Phys. Lett.* **56**, 48 (1990).
7. J.A. Roberts, C.S. Tai, K.J. Vahala, and T.P. Kuech, *Appl. Phys. Lett.* **56**, 2642 (1990).
8. R. Nözel, N.N. Ledentsov, L. Däweritz, K. Ploog, and M. Hohenstein, *Phys. Rev. B* **45**, 3507 (1992).
9. H. Heulay, C.M. Sokomayor-Torres, and C. Weisbuch, *Phys. Rev. B* **44**, 10945 (1991).
10. A. Schmidt, A. Forchel, J. Sunka, I. Gyuro, P. Speiser, and E. Ziehlisch, *J. Vac. Sci. Technol.* **B** **10**, 2896, (1992).
11. S. Le Goff and B. Sibbe, *Phys. Rev. B* **47**, 1383 (1993).

Electron-Phonon Scattering Rates in Quantum Wires

P. A. Knap
Department of Physics and Computer Science
Christopher Newport University
Newport News, VA 23606-2998

and
T. L. Rimechis
Naval Research Laboratory
Washington, D.C. 20373

Electron-phonon scattering rates for quantum wires of arbitrary shapes are calculated rigorously within the dielectric continuum approach for the phonons. An integral equation approach is developed for the interface phonons, and the contribution to the scattering rates from the confined phonon modes are expressed in terms of the interface modes by a simple relation. Detailed results are given for the intrasubband and intersubband transition rates as functions of the electron energy and of the wire width for wires of rectangular cross section. The relative importance of the interface and confined phonons is discussed as a function of wire size. A quantitative appraisal is given of scattering rates obtained using simple separable approximations for the phonons.

Quantum wire systems composed of a wire of one compound semiconductor material within another have attracted considerable interest recently both because of their use in potential device applications as well as for the opportunity of studying novel physical phenomena in these quasi-one-dimensional systems. Electron-phonon interactions and scattering rates have been of particular interest in these systems, particularly in the context of the cooling of excited carriers on the picosecond time scale and room temperature optical properties. They have been a focus of attention in studying the effects of phonon confinement on the optical and transport properties of semiconductor nanostructures.

To date, however, a rigorous, quantitative treatment of electron-phonon scattering rates for wires of the general shapes of interest experimentally has not been given. The principal difficulty in treating electron-phonon interactions in quantum wires is that the equations of motion and boundary conditions for the phonons do not separate in these geometries. Recent work has been reported for the simple case of a cylindrical quantum wire for which the treatments separate into one-dimensional problems [1]. Additional approximations [2] have been used to treat the phonons for rectangular cross sections. The results given here show that such approximations lead to significant errors in the scattering rate.

The scattering rate of an electron from a subband α with wavevector k_α to a subband β with wavevector k_β accompanied by the emission of a phonon of wavevector $q = k_\beta - k_\alpha$ is given by

$$\Gamma_{\alpha\beta} = \frac{2\pi^2}{h} \sum_{\mathbf{q}} N(\omega_{\mathbf{q}}) |\langle \beta | \hat{H}_{\text{ep}} | \alpha \rangle|^2 \delta(E_{\beta} - E_{\alpha} + \hbar\omega_{\mathbf{q}}) \quad (1)$$

The rate for electron scattering due to phonon absorption is similar. Ψ_{α} are the electron wavefunctions, Φ_{ν} are the phonon potentials, and N is the Bose function. E_j and k_j are the electron and phonon energies respectively. The index ν indicates the optical phonon modes of the system including both "confined" or "interface" phonons. The confined modes are localized either in the wire region or in the exterior region.

The intrasubband and intersubband electron scattering rates calculated here due to phonon emission at room temperature are shown as functions of energy in Fig. 1 for a 100 Å x 200 Å wire of GaAs in AlAs. In these calculations a small imaginary part ($\approx 0.25\%$) has been included in the phonon frequencies to represent their finite lifetimes due primarily to anharmonicity. The sharp features arise from the divergent density of electronic states at the bottom of the ground subband. For this wire width the energy difference between the first and second subbands is 34.2 meV. For smaller wires the intrasubband spacing is larger than the phonon energies, and thus for them these sharp features are not present in the intrasubband rates. The electron scattering rates due to phonon emission are shown as functions of wire width in Fig. 2. Results are also given for models of bulk GaAs phonons and bulk AlAs phonons. For large wires the confined modes in the GaAs wires tend to dominate the scattering, and the intrasubband scattering rate approaches that for bulk GaAs phonons. For small wire sizes the AlAs-like interface modes make a large contribution, and the intrasubband scattering rate approaches that for bulk AlAs phonons.

We have used the macroscopic dielectric continuum approach [3] to treat the optical phonons of the quantum wires. This approach gives analytical results for the electron-phonon interaction, and it makes possible the treatment of wires of general size and shape. For quantum well systems this approach gives scattering rates in good agreement with those obtained using lattice dynamics results for the phonons [4]. The principal challenge in treating the phonons of quantum wires within macroscopic approaches is that the problem is not in general separable. For wires with general cross sections we have developed a treatment [5] in which Laplace's equation and the boundary conditions for the interface modes are transformed into an integral equation

$$\oint_{\partial V} dS_j \lambda_j(\mathbf{r}) \phi_j(\mathbf{r}) = \lambda(\mathbf{r}) \phi(\mathbf{r}) \quad (2)$$

where ∂V is the contour around the wire perimeter, and λ is the surface charge density associated with the interface phonon $\lambda(\mathbf{r}) = \epsilon_1(\omega) - \epsilon_2(\omega) / [\epsilon_1(\omega) - \epsilon_2(\omega)]$ where $\epsilon_1(\omega)$ and $\epsilon_2(\omega)$ are the dielectric functions for the wire and the exterior region respectively. Equation (2) can be solved by standard matrix diagonalization

sectional shapes. In this work one of the most interesting features that has arisen is that the interface phonons tend to be localized in regions of large curvature of the wire interface with a degree of localization that increases strongly with the degree of sharpness of the corners. An example of such a corner localized phonon is shown in Fig. 3. In order to study the effects on the electron scattering rates of this corner localization of the interface phonons we have calculated the scattering rates for rectangular wires with varying corner curvatures characterized by a/R where a is the radius of curvature of the corner, and R is the wire width. We find that the scattering rates vary by less than 1% for variations in a/R between 0.2 and 10⁻⁴. Thus although the interface modes are sensitive to the sharpness of the wire corners, the total scattering rates, which involve a sum over the modes, are not.

In the present work we have calculated the electron rates within the effective mass approximation with finite potential barriers using the usual masses and potential offset [6]. The wavefunctions were calculated using a technique that we developed earlier [7] which involves discretizing Schrödinger's equation in the plane perpendicular to the wire and iteratively solving the resulting matrix equation. We have investigated the effects on the

scattering rates of using simple separable approximations for the electron wavefunctions and have found the effects of these approximations to be small for the wire widths studied here (on the order of a few per cent for wire widths of 100 Å).

In recent years there has been some controversy concerning the boundary conditions to be used in calculating the confined phonons in semiconductor nanostructures [8]. For quantum wells it has been found that scattering rates calculated using the simple dielectric continuum model agree quite well with those based on lattice dynamics for the confined phonons [4]. In the dielectric continuum model [3] the electrostatic potential of the confined phonons goes to zero at the interfaces, and the corresponding optic phonon displacements have a maximum there. On the other hand, lattice dynamics calculations indicate that the optic phonon displacements as well as the electrostatic potentials go to zero at the interfaces. Recently we have investigated [9] the effects on the electron-phonon scattering rates of these boundary conditions on the confined phonons in a variety of nanostructures. We have found that provided the confined phonons satisfy Maxwell's equations at the interfaces the additional constraint that the phonon displacement go to zero there has no effect on the scattering rates. We ascribe this result to the fact that the contribution of the confined phonons to the scattering rates involves a sum over a complete set of degenerate phonon states. In general the contribution of the confined phonons to physically measurable quantities such as scattering rates is given by the structure factor

$$\rho(\vec{r}, \vec{r}') = \sum_{\lambda} \frac{\Phi_{\lambda}(\vec{r}) \Phi_{\lambda}^*(\vec{r}')}{\int d^3r |\Phi_{\lambda}(\vec{r})|^2} \quad (3)$$

where the sum over λ is over the confined phonon states. Results for $\rho(\vec{r}, \vec{r}')$ for a cylindrical wire are shown in Fig. 4. From these results and those for other nanostructures given in Ref [9] we see that $\rho(\vec{r}, \vec{r}')$ given by these two sets of boundary conditions are identical.

As a part of this study of the confined phonon modes we have derived a useful expression for the contribution of the confined phonon modes to the scattering rates in nanostructures. It is given by

$$\rho(\vec{r}, \vec{r}') = \frac{1}{4\pi\epsilon_0^2} \frac{\Phi_{\lambda,\lambda}(\vec{r}) \Phi_{\lambda,\lambda}^*(\vec{r}')}{\int d^3r |\Phi_{\lambda,\lambda}(\vec{r})|^2} \quad (4)$$

for \vec{r} and \vec{r}' within the nanostructure. Here $\Phi_{\lambda,\lambda}$ are the potentials associated with the interface modes. Thus the contribution of the confined modes can be written in terms of the interface phonon potentials. This form is convenient for systems of low symmetry, and it has been used in the present calculations to obtain the contributions of the "confined" phonons in the ALAs material outside of the wires. These modes are extended throughout the exterior region, and it is difficult to form a complete set of them as required for the scattering rate by other means.

In order to discuss the electron scattering rates it is useful to look at their dependence on wavevector transfer. This is given by the quantity

$$f_{\lambda}(q) = \frac{|\int d^3r \Psi_{\alpha}(\vec{r}) \Psi_{\beta}^*(\vec{r}) \Phi_{\lambda}(\vec{r})|}{\int d^3r |\Psi_{\alpha}(\vec{r})|^2 |\Psi_{\beta}(\vec{r})|^2} \quad (5)$$

$\Psi_{\alpha}(\vec{r})$ describes the contribution to the scattering rate of the α th phonon mode (interface or confined) evaluated at the wavevector q involved in the scattering process. The sum of the contributions $f_{\lambda}(q)$ from all interface modes and from all confined modes for intrasubband and intersubband processes are shown in Fig. 5. For both interface and confined modes these quantities are decreasing functions of qR . The interface modes make the larger contribution to the scattering rates at small qR , and thus they dominate for small wire size. In addition, when the subband splitting is comparable to the phonon energies small wavevectors are dominant in the intersubband scattering processes. This accounts for the broad maximum in the intersubband rate for $R = 100$ Å in Fig. 2b. It is interesting to note that for small q the sum of the interface modes $f_{\text{IF}}(q)$ diverges as q^{-1} for quantum wells and only as $-\ln(qR)$ for quantum wires. Thus we expect that the approach of the intrasubband rate to that for bulk ALAs should be faster for quantum wells than for quantum wires of comparable size. This appears to be the case in comparing our results in Figs. 2 with those in Ref. 4.

A widely used approximation [2] for the interface modes of rectangular quantum wires involves a separable approximation for the phonon potentials. In Fig. 5 we compare the sum of the interface modes $f_{\text{IF}}(q)$ from the present complete calculations with corresponding results obtained using this separable approximation. The contribution of the interface phonons in this approximation goes to a constant for small qR rather than diverging. This qualitative error is a result of its poor representation of the totally symmetric interface mode. As a result this approximation gives poor results for the intersubband scattering rates, especially for small wire sizes. In addition, this separable approximation gives no contribution at all from the interface modes to the intersubband scattering rate between the first excited electronic subband and the ground subband as a result of the absence of interface modes which are symmetric along one direction and asymmetric along the other.

This work was supported in part by contracts of the U. S. Office of Naval Research (PAK and TLR).

FIGURES

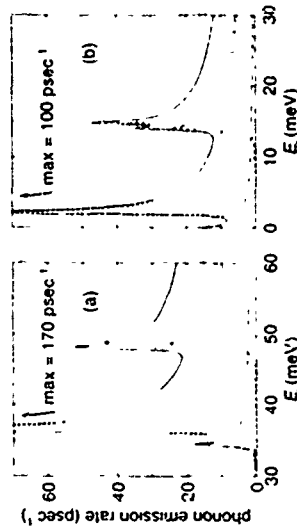


Fig. 1 (a) Intrasubband and (b) intersubband electron scattering rates due to phonon emission as functions of the initial electron energy for quantum wires of size 100 Å x 200 Å.

A. The intersubband splitting for this wire size is 34.2 meV. Energies are measured from the respective subband bottoms, i.e. from the bottom of the lowest subband for the intrasubband rate and from the bottom of the next higher subband for the intersubband rate. The total scattering rates are given by the solid line, the contributions of the confined phonons by the dotted line, the contributions of the AlAs-like interface phonons by the short dashed lines, and the contributions of the GaAs-like interface phonons by the long dashed lines.

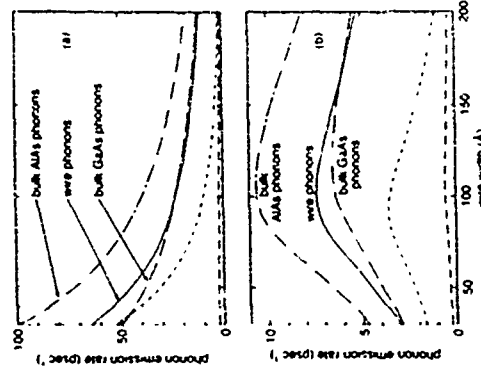


Fig. 2 (a) Intrasubband and (b) intersubband electron scattering rates due to phonon emission as function of wire width R . R is the smaller of the two sides of the cross sections of rectangular wires having aspect ratios of 2:1. The initial electron energy has been chosen to be 60 meV above the respective subband bottoms. The total rate is given by the solid line, and the rates from models of bulk GaAs and bulk AlAs phonons are given by the dot-dashed and long dashed-short dashed lines respectively. The contributions from the confined phonons, the AlAs-like interface phonons, and the GaAs-like interface phonons are given by the dotted, the short dashed, and the long dashed lines respectively.

Fig. 3 Interface phonon potential for a mode with wavevector $kR = 2$ and azimuthal quantum number $m = 0$ for a rectangular quantum wire with aspect ratio 1:2 and corner curvature $\alpha = R/2l$.

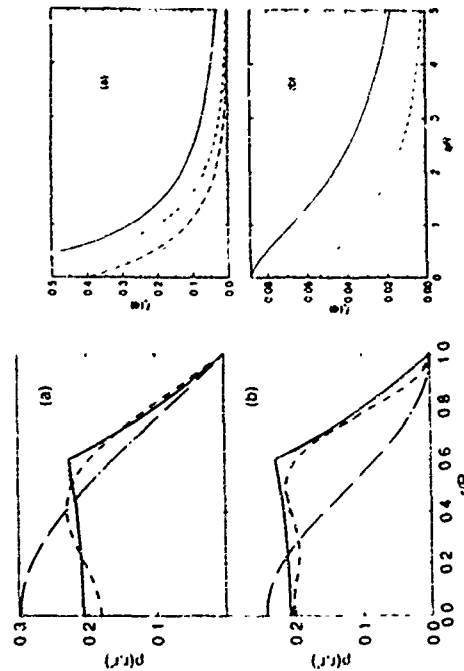


Fig. 4 The contribution to the structure factor defined in Eq. (3) for a cylindrical quantum wire from confined phonon modes which have azimuthal quantum number $m = 0$ and wavevector $kR = 1, 0$. Here R is the cylinder radius, r is the radial distance, and $r' = 0.6R$. (a) is for confined phonons from the dielectric continuum model, and (b) is for phonons whose displacement also is required to go to zero at the interface. The dot-dashed, dashed, dotted and solid lines indicate truncation of the sum in Eq. (3) after 1, 3, 10 and ∞ terms respectively.

Fig. 5 $f(q)$ from Eq. (5) for (a) intrasubband and (b) intersubband scattering as functions of qR where R is the wire width. The total contribution from the confined modes and total from the interface phonons are given by dotted line and the short dashed line respectively, and total from all modes is given by the solid line. The long dashed line in (a) gives the contribution of the interface phonons in the separable approximation of Ref. [2].

REFERENCES

1. P. E. Selbmann and R. Enderlein, *Superlattices and Microstructures* **12**, 219 (1993).
2. K. W. Kim *et al.*, *J. Appl. Physics* **70**, 319 (1991); R. Mücke *et al.*, *Superlattices and Microstructures* **11**, 277 (1992).
3. See e.g. M. V. Klein, *IEEE J. Quantum Electron.* **QE-22**, 1760 (1986).
4. H. Rucke, E. Molinari, and P. Lugli, *Phys. Rev. B* **44**, 3463 (1991); *Phys. Rev. B* **45**, 6747 (1992).

U. Bochtelmann, K. Brunner and G. Abstreiter
 Walter Schottky Institut, Technische Universität München
 Am Coulombwall, D-85748 Garching, Germany

Radiative and non-radiative excitation states of quantum dots with parabolic lateral potentials are calculated in an effective-mass approximation. Energy spectrum, radiative recombination rates and LA phonon scattering rates of the different excitons are discussed in their dependence on the lateral confinement potential. For sufficiently strong lateral potentials the relaxation of excitons by LA phonon emission becomes so weak that several excitonic levels should be observable in a photoluminescence experiment even at low excitation intensity. The theoretical results are compared to microscopic photoluminescence data collected from a series of single GaAs quantum dots fabricated by laser induced local interdiffusion.

In quantum dots or quasi-zero-dimensional (0D) systems the charge carriers are confined in all three spatial directions and therefore the energy spectrum consists of atomic-like, discrete levels. In principle, artificial (0D) structures based on direct gap semiconductors (e.g. the GaAs/GaAlAs system) could be studied in great detail by interband optical spectroscopy, i. e. by photoluminescence (PL) and photoluminescence excitation (PLE) spectroscopy. The interband spectra should reflect the details of the confining potentials as well as exciton and many-body effects. Information on the exciton relaxation dynamics could be deduced from the intensity ratios of the different PL peaks and also from a comparison of PL and PLE spectra [1]. In practice, samples prepared for optical studies often contain a large number of quantum dots supposed to be equal. Differences in composition and size between the individual structures however lead to important inhomogeneous line broadening which usually covers the details of the interband spectra. This problem can be circumvented by local spectroscopy of a single quantum dot. This way, distinct narrow lines have been observed in microscopic PL and PLE spectroscopy on a series of single quantum dots fabricated by focused laser beam induced interdiffusion of GaAs/GaAlAs quantum wells [2].

In this contribution, we present theoretical results on energy states, relaxation and radiative decay of excitons in quantum dots based on GaAs/GaAlAs quantum wells. The theoretical description is well suited for a comparison with the quantum dot samples fabricated by laser induced interdiffusion. We present PL spectra measured at low excitation power from a series of dots of different lateral size and compare them to the theoretical results.

For quantum dots fabricated from quantum wells the confinement induced by the lateral potential is usually weak compared to the confinement along the quantum well growth axis z . We therefore build the near band gap action states of the quantum dot on the electron and heavy-hole ground subbands of the underlying quantum well (envelope functions $\chi_e(z)$ and $\chi_h(z)$, respectively), neglecting heavy-hole light-hole mixing and excited subbands. The envelope function of the quantum dot excitons are of the form.

$$\Psi_{\sigma}(\mathbf{r}_e, \mathbf{r}_h) = \phi(x, y, z_h, z_e) \chi_e(z_e) \chi_h(z_h) \quad (1)$$

The functions ϕ depending on the lateral electron and hole coordinates are the eigensolutions of the Hamiltonian

5. P. A. Knipp and T. L. Reinecke, Phys. B 45, 9091 (1992).
6. The effective masses for electrons in GaAs and AlAs were taken to be 0.0665 and 0.15 respectively, and the conduction band offset was 873 meV.
7. Ch. Jüdel, L. Butov, F. Daiminger, A. Forchel, P. A. Knipp and T. L. Reinecke, Phys. Rev. B 47, 7626 (1993)
8. S. Rudin and T. L. Reinecke, Phys. Rev. B 41, 7713 (1990), Phys. Rev. B 43, 9298 (1991).
9. P. A. Knipp and T. L. Reinecke, Phys. Rev. B (to be published)

$$H = H_0 + H_m$$

$$H_0 = \sum_{l,m} \frac{\hbar^2}{2m} \left(\frac{\partial^2}{\partial r^2} + \frac{\partial^2}{\partial \theta^2} \right) + \frac{1}{2} m \omega_0^2 (x^2 + y^2)$$

$$H_m = - \iint dx dy dz \left[\chi_0(r) \right]^2 \left[\chi_0(r_0) \right]^2 \frac{e^2}{\epsilon_0 |r - r_0|}$$

We describe the lateral confinement by rotational-symmetric, parabolic potentials with different angular frequency for electrons and holes (ω_e and ω_h). The Hamiltonian H is diagonalized numerically by expanding it on the set of analytical eigenfunctions of Ho-Ho describes two-dimensional harmonic oscillations independent for the electrons and holes. The solutions, originally derived by Fock [3], are parametrized by the radial quantum numbers n_r , n_θ (0, 1, 2, ...) and the angular momentum quantum numbers l_r , l_θ (0, 1, 2, ...). The total angular momentum $j = l_r + l_\theta$ is a good quantum number of the Hamiltonian H because of the rotational symmetry of the lateral potential. The expansion on a basis of independent electron hole states has been used in earlier theoretical studies of radiative excitons in quantum dots [4-6]. In an alternative approach, H is written as a function of the center-of-mass (CM) coordinate $R = (m_e r_e + m_h r_h) / (m_e + m_h)$ and the relative coordinate $r = r_e - r_h$ of the exciton. The expansion on a set of functions depending separately on R and r exhibits a faster convergence for weak lateral confinement but has the important disadvantage that the r -dependent basis functions are not analytical [5,6].

Excitons with a non-zero value of j are non-radiative. From the wavefunction of the $j=0$ excitons we determine the radiative lifetimes τ_0 in the dipole approximation:

$$\tau_0^{-1} \propto \iint d\mathbf{r} \psi_0^*(\mathbf{r}, \mathbf{r}) \hat{\mathbf{r}} \psi_0(\mathbf{r}, \mathbf{r})^2 \quad (3)$$

Energies and radiative lifetimes of quantum dot excitons are presented in fig. 1. We consider dots fabricated from a 30 Å wide GaAs/Al_{0.7}Ga_{0.3}As quantum well with a constant ratio ω_h/ω_e to allow for a detailed comparison with our experimental results. Only radiative excitons are included in the figure where the length of the lines is chosen to be proportional to the rate of radiative recombination. At small $\hbar\omega_0$, the spectrum is dominated by a series of equidistant lines. In this limit, the CM coordinate R and the relative coordinate r of the exciton are only weakly coupled. The equidistant lines originate from the quantization of the CM coordinate by the parabolic potential. The additional, weakly radiative excitons appearing at higher energies involve excited states of the relative motion. With increasing $\hbar\omega_0$, the energy levels shift to higher values and the CM and the relative motion become increasingly coupled. The radiative lifetime of excitons originating from the ground state (excited states) of the relative coordinate increase (decrease) with increasing lateral confinement. The Coulomb attraction strongly influences the energy spectrum and radiative lifetimes of the quantum dot. The binding energy of the ground state exciton grows from 7.9 meV to 15.4 meV with $\hbar\omega_0$ increasing from 1 to 10 meV which is in no case small compared to the lateral confinement energies. When the electron hole Coulomb interaction is neglected, the radiative lifetime of the ground state of the $\hbar\omega_0 = 6$ meV dot is 0.3 ns, three times longer than the excitonic lifetime given in fig. 1.

The relation between the electron and hole confinement parameters used in fig. 1, is suggested by a simple model calculation of the process of laser induced thermal interdiffusion

[2]. Fig 2 demonstrates that the lowest exciton energies change only slightly when the ratio ω_h/ω_e is varied. All exciton states (radiative and non-radiative ones) are plotted for fixed $\omega_e = \omega_h$. The total angular momentum of the exciton is indicated by the length of the plotted line. The exciton spectrum becomes increasingly dense with increasing energy separation from the ground-state.

Let us now discuss the relaxation properties of the exciton. At low temperature and carrier density, emission of longitudinal acoustic (LA) phonons represent the dominant relaxation mechanism of excited states of energy below the optical phonon branches. It has been shown theoretically, that in quantum dots the electron LA phonon scattering rates decrease by several orders of magnitude when the separation of the discrete energy levels increases above a threshold value [7]. How do the corresponding results look like for excitons? The rate of a transition from an initial exciton state i to a final state f accompanied by emission of a phonon at zero temperature is given by the Fermi golden rule

$$\tau_{i \rightarrow f}^{-1} = \frac{2\pi}{\hbar} \sum_{\mathbf{q}} \left| \langle \Psi_f | W | \Psi_i \rangle \right|^2 \delta(E_i - E_f - \hbar\omega_{\mathbf{q}}) \quad (4)$$

The sum extends over the wavevector \mathbf{q} of the phonon of energy $\hbar\omega_{\mathbf{q}}$. We consider bulk GaAs LA phonons neglecting confinement effects on the phonon spectrum. An isotropic dispersion relation $\omega_{\mathbf{q}} = c_s q$ is assumed, with $c_s = 3700$ m/s. To derive the exciton-phonon interaction potential W we first determine the strain tensor associated with the phonon. The interaction potential is then given by the sum of the strain induced shift of the electron and hole part of the exciton. The latter is obtained from the diagonal part of the Γ_8 strain Hamiltonian, derived by Pikus and Bir [8]. For heavy holes W takes the form

$$W \propto q^{1/2} \left(D e^{-i\mathbf{q} \cdot \mathbf{r}} + \left[\frac{1+m}{2} \frac{(q_x^2 + q_y^2)}{q^2} + m \frac{q_z^2}{q^2} \right] e^{-i\mathbf{q} \cdot \mathbf{r}_0} \right) \quad (5)$$

where D is the conduction band deformation potential and l, m are valence band deformation potentials.

Fig. 3 shows the relaxation rate τ_i^{-1} of the first excited radiative exciton in comparison to its radiative decay rate τ_0^{-1} . The quantity τ_i^{-1} is defined as the sum over the LA phonon scattering rates to all exciton states below the initial state at zero temperature. We assume that the final states are unoccupied. Scattering between any pair of exciton states is possible. This also means that non-radiative excitons are important for the relaxation dynamics of radiative states. The contribution of a given transition depends strongly on the energy separation of the involved levels which is equal to the phonon energy (energy conservation expressed by the delta function in eq. 4). For small q the exciton phonon matrix element increases with q due to the prefactor $q^{1/2}$ of eq. 5. For q above about $2\pi/\lambda_0$, the matrix element decreases strongly with increasing q (increasing energy). Roughly speaking, when the phonon wavelength becomes small compared to the smallest dimension of the quantum dot (usually the well width L_z) the exciton-phonon coupling becomes weak, in a similar way as in the case of the electron-phonon interaction [7].

The relaxation rate of the first excited $j=0$ state, plotted in fig. 1, is dominated by scattering into the $j=\pm 1$ ground state. Typically, PL spectra of one, two and three dimensional semiconductor structures show only one peak corresponding to the exciton ground state. This is because the relaxation of excited states is more efficient than their radiative decay. From

Fig.3 it appears clearly, that in 0D systems the relaxation rate of excited excitons can be comparable or even smaller than the rate of radiative recombination. From a detailed rate equation analysis based on calculated rates of exciton relaxation and radiative recombination follows that it should be possible to observe strong PL signals from excited quantum dot states even for very low excitation intensity [9].

For the experimental studies a series of single quantum dots of different lateral size has been fabricated by laser-induced thermal interdiffusion of a 30Å wide GaAs/Al_{0.65}Ga_{0.35}As single quantum well [2]. A schematic cross section of the dot structures is given in the inset of Fig.4. The lateral potential is defined by drawing a square frame of size w with a focused Ar⁺ laser beam on the sample surface. Afterwards an area of $6\mu\text{m} \times 6\mu\text{m}$ around the dot is interdiffused by scanning the beam continuously. This procedure gives rise to a lateral modulation of the band-gap as shown schematically in the lower part of the inset. The strongly nonlinear temperature dependence of the interdiffusion allows to realize steep potential barriers for electrons and holes. PL and PLE spectroscopy have been performed with a spatial resolution of about 1.5 μm at liquid helium temperature. Only one quantum dot is measured at a time and consequently there should be no inhomogeneous broadening of the experimental spectra. Details of sample preparation and experimental setup are given in ref.2.

In Fig.4 we present PL spectra of three quantum dots of different lateral size w . Excitation was performed with a HeNe laser of low power density. The PL line-widths have been found to increase with intensity [2]. The energy shift of the lowest PL peak with increasing structure size w is a combined effect of lateral confinement and alloying of the dot center. The effective size of the lateral confinement is given by the interdiffusion profile and not just by the geometrical size w . Decreasing w from large values, the laser induced barriers move closer together which leads to an increasing lateral quantization. Maximum confinement is obtained when the barriers are about to meet at the dot center. We expect this to be realized in the $w=450\text{nm}$ dot where a maximum line splitting of about 10meV is observed. Further decreasing w , the increasing Al content near to the center of the dot leads to a strong blue shift of the PL ground state but the lateral barrier height decreases. For $w>50$, we approach the case of a homogeneously alloyed 2D layer without lateral confinement. Near the dot center, a simple model of the local quantum well interdiffusion gives nearly isotropic x - z parabolic lateral potentials with a similar curvature for electrons and heavy holes. This means $m_e^*w_x^2 = m_h^*w_z^2$ or equivalently $w_x = w_z(m_e^*/m_h^*)^{1/2}$, the relation used above in calculating figures 1 and 3. The PL spectra of the 400nm and 500nm dots are dominated by the lowest energy peak but display clear structures of almost equidistant spacing at higher photon energies. The position of the experimental lines compare quite well with Fig.1 if we consider $\hbar\omega_p = 3\text{meV}$ (2meV) for $w=400\text{nm}$ (500nm). For the 450nm dot the interdiffusion model gives $\hbar\omega_p = 3\text{meV}$. The 10meV separation between the lowest two peaks agrees with Fig.1 but the threefold splitting of the excited state is not born out by the calculation. Fig.2 shows that the fine structure cannot be explained either by varying the ratio w_x/w_z . However, the first excited radiative ($j=0$) state is almost degenerate with the $j=\pm 2$ ground states (Fig.2). A deviation of the lateral potential from the rotational symmetry could mix the three states i.e. the non-radiative excitons would gain oscillator strength. Such a deviation can be due to charged defects introduced by the laser processing in the surrounding area or simply by not perfectly constant interdiffusion conditions during writing the square frame which defines the dot. PLE spectra of the 450nm dot as shown for example in reference 2 display for detection at the lowest luminescence peak small peaks with roughly an equidistant energy separation of about 2meV between the luminescence ground state and first excited state. These weak structures cannot be understood from the calculated exciton energies, even if we assume a much weaker confinement for the holes than for the electrons (see Fig.2). The main features of the experimental PL lines (Fig.4), especially the fact that the excited states are most prominent

in the dot with the largest level splitting are in agreement with a strong decrease of the exciton relaxation rate with increasing lateral confinement.

In conclusion, relaxation and radiative recombination of excitons in quantum dots have been studied theoretically. The calculations show that the radiative lifetimes of one part of the exciton states increase with increasing lateral confinement (in particular the lowest states) but there exist also exciton states that exhibit the opposite dependence. In quantum dots of sufficiently strong lateral confinement the relaxation of excited excitons by emission of LA phonons can be less efficient than their radiative decay. This suggests that excited excitons can be observed in PL, which is in agreement with recent microscopic PL experiments on single quantum dots. The variation of position and intensity of the PL peaks with lateral structure size qualitatively confirms the theoretical results.

This work has been supported in part by the "Deutsche Forschungsgemeinschaft (SFB 348)" the "Bundesministerium für Forschung und Technologie (DFE Verbundprogramm TK363/2)" and by a "PROCOPE" contract.

- [1] G. Bastard, "Wave Mechanics Applied to Semiconductor Heterostructures (Les Editions de Physique, Les Ulis, 1988)
- [2] K. Brunner, U. Bockelmann, G. Abstreiter, M. Wallner, G. Böhm, G. Tränkle and O. Weinmann, Phys. Rev. Lett. 69, 3216 (1992)
- [3] V. Freck, Z. Phys. 47, 446 (1928)
- [4] G. W. Bryant, Phys. Rev. B37, 8763 (1988)
- [5] V. Halonen, T. Chakraborty and P. Pietiläinen, Phys. Rev. B45, 5980 (1992)
- [6] W. Que, Phys. Rev. B45, 11036 (1992)
- [7] U. Bockelmann and G. Bastard, Phys. Rev. B 42, 8947 (1990)
- [8] G. E. Pikus and G. L. Bir, Fiz. Tverd. Tela 1, 1502 (1959) [Sov. Phys. Solid State 1, 1502 (1960)]
- [9] U. Bockelmann, submitted for publication

Fig.1 Energy and inverse radiative lifetime τ_0^{-1} of the radiative excitons as a function of the confinement parameter $\hbar\omega_p$. The value of τ_0^{-1} is given by the length of the lines, in comparison to the double-arrow on the right. Zero-energy corresponds to the bandgap of the underlying quantum well, namely the sum of the bandgap of bulk GaAs and the confinement energies associated with $\chi_e(z)$ and $\chi_h(z)$.

Fig.2

Exciton energy spectra for a ratio w_x/w_z varying from 0.5 to 5 but fixed sum $w_x+w_z=10\text{meV}$ of the electron and hole lateral confinement potentials. The length of the lines indicate the quantum number j of the total angular momentum.

Fig.3

Relaxation rate τ_1^{-1} (solid line) and radiative recombination rate τ_0^{-1} (dashed line) of the first excited radiative exciton as a function of lateral confinement.

Fig.4

PL spectra of single dot structures for three lateral sizes w . Laser excitation was at 1.96eV with a power of 1 μW (125nW for $w=450\text{nm}$) focused to a spot of 1.5 μm diameter. The dot structure fabricated by focused laser beam interdiffusion of a single quantum well is presented schematically in the inset.

ThP1

DETERMINATION OF BAND-EDGE OFFSET BY WEAK FIELD HALL MEASUREMENT ON MBE PbSe/PbEuSe MULTI-QUANTUM WELL STRUCTURES ON KCL

Z. Shi, A. Lambrecht and M. Tacke

Fraunhofer Institute of Physical Measurement Techniques (IPM) Heidenhofstrasse 8, W-7800 Freiburg, Federal Republic of Germany

Weak field Hall effect measurements between 34 and 300K were applied to three PbSe/PbEuSe (Eg(PbEuSe)=440meV at 300K) MQW samples on KCL. By calculating the quasi-Fermi energy levels the temperature dependent band-edge offsets were determined. The valence band offset ΔE_v was found to be 35meV at 34K with a positive temperature coefficient of 0.68 meV/K. Thus $\Delta E_v=43 \pm 0.68T$ (meV) is suggested.

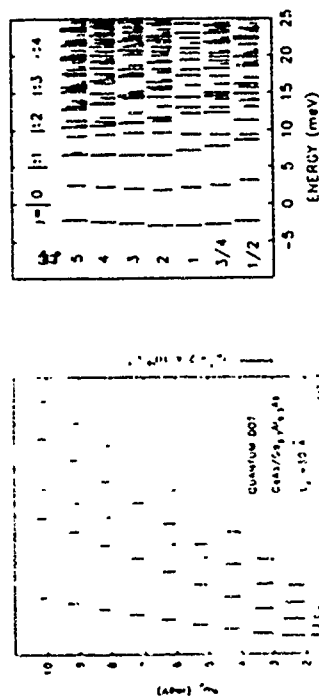


Fig. 2

Fig. 1

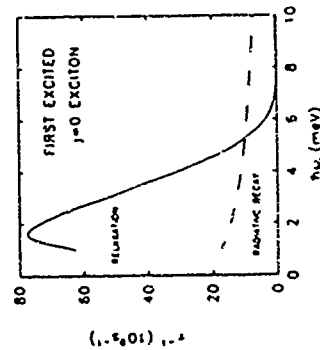


Fig. 3

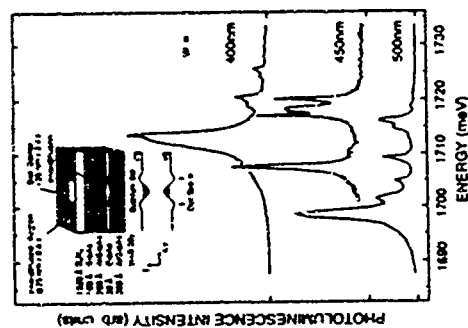


Fig. 4

IV-VI lead salt semiconductors are widely used for lasers and detectors in the wavelength of 3-32 μ m [1,2]. Heterojunctions (HJs) and quantum well structures are used in the devices to provide selective control over carrier transport by means of energy band discontinuity. Former investigations of IV-VI band-edge offset were mainly on PbS/PbTe HJs by two groups [3,4] with different results, obtaining a type I alignment as well as type I'. By Hall measurement of multi-quantum wells (MQW) samples with different barrier thickness, a type I alignment was suggested by Shi et al [5]. Later, Pb ν -PbEuSeTe and PbSe/PbEuSe were also investigated by several methods. Photoluminescence (PL) gave an alternative result of $\Delta E_{c-v} = 0.9$ or 0.1 [6] for PbTe/PbEuSeTe and $\Delta E_{c-v} = 9.8$ was used to interpret the PL result of PbSe/PbEuSe [7]. Problems of PL were also summarized in [7]. By comparing the interband transition energies deduced from the infrared spectroscopy and the calculated energy shifts [8] and Yuan et al [9] found that the band offsets in the PbTe/Pb ν -Eu ν Te system ($\alpha < 5\%$) is quite symmetric. Electron-Beam-Induced current measurements were also applied for the determination of band-edge offset of PbTe/PbEuSeTe and PbSe/PbEuSe heterostructure [10]. Such junction methods of IV-VI materials usually suffer from the following problems: (1) R_{p-A} is low, about three magnitudes lower than that of HgCdTe; (2) There are probably relatively large number of interface states; (3) possible deep traps with high concentrations which are up to now not well investigated; (4) Fermi energy levels are usually obtained on insulating (111) BaF_2 while the junction measurements are on (100) PbTe or PbSe substrates. This may cause estimated errors of several tens of meV.

In this paper a similar method as [5] but with quantitative analysis was applied to a series of p-p PbSe/PbEuSe MQW structures. The valence band, and thus the conduction band discontinuities between 34-180K were determined. Problems 2 to 4 of electrical analysis are expected to be relevant within the frame of this method.

The static dielectric constant in PbSe and Pb ν -Eu ν Se (with low α) is high [20]; and a typical screening length is several thousands \AA . In good approximation one can neglect the band bending effect in the MQW structure when both the well layer and the barrier are narrow enough. The calculated quasi-Fermi levels on both sides should then be

$F_1 = E_F + V_{b1}$ and $F_2 = E_F + V_{b2}$, where E_F is the equilibrium Fermi level measured from the respective band edge, V_{b1} is the built-in PbSe potential of the interface and V_{b2} is the PbSe potential. Thus the energy band-edge effect can be obtained by adding quasi-Fermi levels F_1 and F_2 . By doing so the following advantages are expected: (1) The carrier concentration is very sensitive to the quasi-Fermi level so that the quasi-Fermi level can be determined quite correctly even when there are certain errors in the concentration; (2) Since all deep traps are depleted within the PbSe band gap and fully occupied within PbSe band gap they will not affect the result; (3) Interface states add almost the same amount to the quasi-Fermi levels of both sides and compensate themselves when calculating the band discontinuity so that the influence of the interface states can be neglected.

A series of p-p PbSe/PbEuSe MQW were thus grown for Hall measurements by molecular beam epitaxy (MBE) with alternating Eu growth chamber under Se rich condition. The background vacuum during growth is 3×10^{-8} Torr. The substrates are cleaved KCL (100) and the substrate temperature is 360 °C. The growing rate is 30nm/min. Table 1 gives the related parameters of the samples.

Table 1 Growth parameters of the PbSe/PbEuSe MQW structure.

sample number	buffer layer (PbEuSe)	PbSe-PbEuSe period (nm)	top layer (PbEuSe) thickness	total thickness
1513-1	150nm	20-20nm	68	150nm
1514-3	150nm	20-40nm	48	150nm
1515-3	150nm	20-60nm	35	150nm

The aim of the buffer and the top layer is to avoid any interface and surface potential effects on the Hall data. The use of KCL substrates has the advantage that the subbands from four valleys are equivalent for the (100) surface. The PbEuSe layers have a minimum thickness of 20nm to ensure a quantum well condition under the assumption that holes are confined to the PbSe layer and a maximum thickness of 60nm to make the neglect of band bending still a good approximation. The Hall measurements were performed by Van der Pauw method with gold wires soldered with Indium to edges of the specimen. The energy band gap of PbEuSe at room temperature was measured to be 40meV by infrared transmission spectroscopy. For optimum comparability of the above three samples, they were grown one after another under the same growth condition and substrate pieces were cut from the same block of KCL.

For two layer structures the Hall coefficient can be written as [11]:

$$R_H = (d_1 n_1 \mu_1^2 + d_2 n_2 \mu_2^2) / (d_1 + d_2) / e c (d_1 n_1 \mu_1 + d_2 n_2 \mu_2)^2 \quad (1)$$

Measurements on single PbSe and PbEuSe ($E_g = 440\text{meV}$ at 100K) epitaxial layers showed that the mobility of PbSe on KCL is 10 to 20 times larger than that of PbEuSe between 180K and 34K. The hole concentration in the PbSe layers of a MQW structure is expected to be at least 10 times larger than that in the PbEuSe layers because of the carrier injection from PbEuSe barrier layers. For all samples in this experiment, the PbEuSe layer thicknesses d is at most a factor of 3.1 larger than that of PbSe layer, hence we can approximate equation (1) by neglecting the terms for PbEuSe layers. Fig.1 shows the hole concentration ($1/eR_H$) of the samples. In this paper only the data between 34K and 180K

were used because above 180K the difference of mobility is not big enough for the one layer model approximation. For a QW structure the relation between E_F and the carrier concentration n is given as

$$n(E_F) = n_0 \sum_{i=1}^{\infty} \rho_i(E) f(E) dE \quad (2)$$

where

$$f(E) = \frac{1}{(1 + \exp[(\frac{E - E_F}{kT}])}$$

$$\rho_i(E) = \frac{m_0^2}{\pi \lambda^2} \theta(E - E_i)$$

and [12]

$$E_i = \frac{1}{2} (-E_g + \sqrt{E_g^2 + \frac{2\lambda^2}{m_0^2} (\frac{1}{D})^2 E_g}) \quad (3)$$

$\rho_i(E)$ is the density-of-states, E_i is the subband energy level and E_F is measured from the band edge of the bulk crystal [13]; $m_0 = m_e = m_0^* (2K + 1)/3$, $m_0^* = 3K/(2K + 1)$, m_0^* is the transverse effective mass at the band edge, E_g is the energy gap in bulk crystal, $n_0 = 4$ is the number of valleys, d is the width of well layer and i is the quantum number of subband. The temperature dependence of the PbSe-related parameters were obtained from [14]. The quasi-Fermi energy level and the subband energy level were thus calculated according to equation (2) and (3) under the assumption that equation (2) is also suitable for the quasi-Fermi level. The non-parabolicity of the two dimension density-of-states was not considered in this paper. The results were shown in Fig.2, where E_a , E_b and E_c represent the quasi-Fermi energy levels in the PbSe well layers of samples 1513-1, 1514-3 and 1515-3, respectively.

Equation (3) is based on the assumption that the height of the well potential is sufficiently larger than the Fermi level and that the two band model is applicable in each quantum well. It is noteworthy that a small change of E_i turned out to change the calculated ΔE_v only slightly, so that the change of ΔE_v can be neglected. Therefore, we would not be in the dilemma that we should first know ΔE_v for the evaluation of E_i .

The increase of the hole concentration in the PbSe well layers of samples 1514-3 and 1515-3 compared with 1513-1 is due to the increased thickness of the PbEuSe barrier layer. Holes of the barrier layer will flow into the well layer as long as the increase of barrier width is within $2x_d$, where x_d is the depletion length. In the following expression for convenience the subscript 1 and 2 will be used to represent PbSe and PbEuSe respectively, the superscript a, b, and c stand for the 1513-1, 1514-3 and 1515-3 samples respectively, d represent the thickness of a single well or barrier layer and S the area, and p_0 represent the hole concentration in a PbEuSe single bulk epitaxial layer. With these definitions, the increase of hole concentrations in 1514-3 to 1513-1 can be expressed as following: a PbEuSe layer with a hole concentration of p_0 and a volume of d_2 PbSe injects its holes into the well layer so that its hole concentration become p_2^a and increases p_1^a to $p_1^a + p_2^a$. Because of the conservation of hole numbers, we can write with this reasoning:

$$S \cdot (d_2^b - d_2^a) (p_0 - p_2^b) = S \cdot d_1^b (p_1^b - p_1^a) + S \cdot d_2^a (p_2^b - p_2^a) \quad (4)$$

For the comparison of 1515-3 and 1513-1, we can get in the same way:

$$S^*(6.2 \cdot 10^{-2} \cdot d_2^2) (p_0 \cdot p_2^2) = S^* d_1^2 (p_1^2 \cdot p_2^2) + S^* d_2^2 (p_2^2 \cdot p_2^2) \quad (5)$$

The left hand side gives the difference in the number of holes transferred from the barriers of samples a and b into the well. It neglects deep levels and assumes that the barrier doping is equivalent to the bulk concentration p_0 . The first term on right hand gives the resulting increase of the well carrier concentration. It is corrected by the second term which takes into account the different barrier concentrations of samples a and b that result from the different barrier thickness.

By combining equation (4) and (5) one can get an equation without p_0 . The advantage of using another QW sample instead of a bulk sample as a reference sample is:

(1) If there are deep energy levels in PbEuSe layer, one can not use the p_0 data measured from a single PbEuSe epitaxial layer for equation (4) and (5). The reason is that the deep levels contribute differently to p_0 due to the difference of Fermi levels in PbEuSe barrier layers and a single epitaxial layer.

(2) Since deep levels are all depleted in PbEuSe barrier layer and the difference of Fermi levels in two different MQW samples are small, one can consider a consistent p_0 in all QW samples in this experiment. Thus the effect of deep levels can be neglected. With the definition at thermal equilibrium:

$$E_{F1}^b \cdot E_{F2}^a = E_{F2}^b \cdot E_{F1}^a = \delta E_{F1} \quad (6)$$

$$E_{F1}^c \cdot E_{F2}^a = E_{F2}^c \cdot E_{F1}^a = \delta E_{F2} \quad (7)$$

and the hole concentration for bulk narrow gap semiconductor is given by [15]:

$$p = \frac{2}{\sqrt{\pi}} N_v G(\eta)$$

where $\eta = (E_F - E_V)/kT$ is the reduced Fermi energy and $G(\eta)$ is equal to the generalised Fermi integral $\int_0^\infty \frac{x^2}{1 + \exp(x - \eta)} dx$ [1, p. 50]

$$p_2^b/p_2^a = \exp(\delta E_{F1}/kT) \quad (9)$$

$$p_2^c/p_2^a = \exp(\delta E_{F2}/kT) \quad (10)$$

Since $p_1^a, p_1^b, p_1^c, E_{F1}^a$ and E_{F2}^a can be obtained from Fig. 2, p_2^a, p_2^b, p_2^c and thus the quasi-Fermi energy level $E_{F2}^a, E_{F2}^b, E_{F2}^c$ can then be derived from the combination of equation (4), (10) for these calculation. The effective mass of PbEuSe was assumed to increase proportionally to the increase of the energy band gap. The temperature dependence coefficient of the PbEuSe energy E_{V-P} is assumed to change linearly from that of

PbSe to the Photoluminescence result of [7] and assumed that it can be extended to the situation that Eu composition is slightly larger. By adding the quasi-Fermi energy levels of the PbSe layers and PbEuSe layers of the same sample the valence band-edge offset was obtained and is shown together with the band gap differences in Fig. 3.

As seen in Fig. 3, the valence band discontinuity increases and thus the conduction band discontinuity decreases almost linearly with the increasing temperature. The temperature dependence coefficient for δE_V was thus obtained from Fig. 3 as 0.03 meV/K and for this certain Eu composition $\delta E_V = 43 \pm 0.08$ (meV) is thus suggested. It seems quite possible that PbSe/PbEuSe ($E_g = 460$ meV) will change from type I at lower temperature to a staggered structure at 300K. This will influence the QW laser operation at high temperature, which is waiting to be approved.

There are two possible error sources in our measurements. One lies in the fact that a minimum of three samples have to be used, hence all three relative sample errors enter. The experiments were performed on two independent sets of three samples with the same results, hence we believe that this error can be neglected. Second, the KCL substrate material has a mismatch of the thermal expansion coefficients as compared to the MQW. Hence, our results may be influenced by resulting strains.

In summary, we evaluated the data of the PbSe/PbEuSe band-edge offset by calculating the quasi-Fermi energy levels of both barrier layer and well layer in a proper designed MQW structure. To accomplish this, Hall measurements were performed on a series of MBE PbSe/PbEuSe MQW structures on KCL. The temperature dependence δE_V and δE_C were obtained.

Acknowledgement: The authors acknowledge helpful discussion with their colleagues B. Halford, H. Bötner, J. Xu and K. Sienner. The work was supported in part by an exchange program of the Fraunhofer Gesellschaft and the Chinese Academy of Sciences.

REFERENCES

- [1] D.L. Parlin, IEEE J. Quantum Electron., 24, 1716(1988)
- [2] M. Tachibana, Journal de Physique IV, C7-23 (1991)
- [3] M. Krichbaum, K.E. Ambrosch, E.J. Fainner, H. Clemens, and G. Bauer, Physical Rev., B30, 3394(1984)
- [4] K. Murase, S. Shimomura, S. Takasaka, A. Ishida, and H. Fujiyasu, Superlattices and Microstructures 1, 177(1985)
- [5] Z. Sun, W. Chen, H. Song, H. Yang, Y. Fu, Y. Jin, Chinese J. Infrared Millim. Waves, 9(4), 255(1990)
- [6] W. Goltsos, J. Nakahara, A.V. Nurmikko, and D.L. Parlin, Appl. Phys. Lett., 46, 1174(1985)
- [7] M.V. Valeiko, I.I. Zaslavskii, A.V. Matveenko, B.N. Matsonashvili, and Z.A. Rukhadze, Superlattices and Microstructures, 9(2), 195(1991)
- [8] A. Ishida, S. Matsuura, M. Mizuno, and H. Fujiyasu, Appl. Phys. Lett. 51, 478(1987)
- [9] S. Yuan, H. Krenn, G. Springholz, and G. Bauer, Appl. Phys. Lett. 62, 885(1993)
- [10] H. Heinrich, C. Panhauer, A. Eisenbeis, H. Preier, and Z. Zell., Superlattices and Microstructures, 5(2), 175(1989)
- [11] E.F. Sizov and Darchuk, Phys. Stat. Sol. (a), 113, 107(1989)
- [12] S. Takahashi, T. Okumura and K. Murase, A. Ishida, and H. Fujiyasu, Solid State Communications, 58, 673(1986)
- [13] F. Stern and W.E. Howard, Phys. Rev., 163, 816(1967)
- [14] H. Preier, Appl. Phys., 20, 189(1979)
- [15] G. Nimts and B. Schlöfner, Narrow-Gap Lead Salt, Springer Tracts in Modern Physics, Vol. 98, P. 52, Ed. G. Höbner.

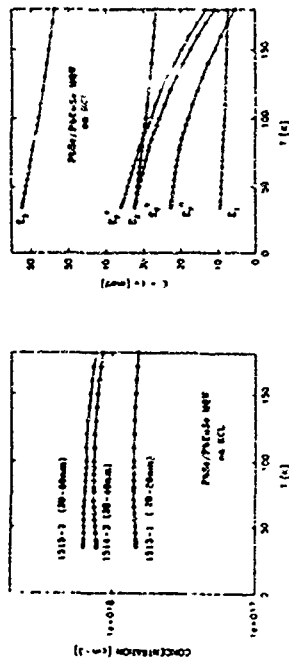


Fig. 1 Temperature dependence of the band effect
carrier concentration of MBE structures

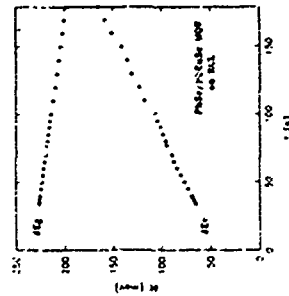


Fig. 2 Subband energy levels and quasi-Fermi energy levels in Pds-InSb heterostructure at different temperatures

Fig. 3 Temperature dependence of voltage band effect and the band gap difference of Pds/InSb MBE and Pds

Static and dynamical properties of the bound magnetic polaron in CdTe/Cd_{1-x}Mn_xTe quantum wells

P. BOUDINET and G. BASTARD

Laboratoire de Physique de la Matière Condensée
Ecole Normale Supérieure, 24 rue Lhomond, F-75005 PARIS

We study the static and dynamical properties of the bound magnetic polaron in CdTe/Cd_{1-x}Mn_xTe quantum wells.

In the case of a heavy hole bound to an acceptor located in the barrier, and for some parameters of the heterostructure, the calculations of the stationary states show the existence of a transition of the B-MP between a magnetic and a non-magnetic state. The relaxation of the B-MP is calculated on the basis of a mechanism of spin exchange between the manganese ions involved in the B-MP and the other ones which are randomly lined up. We show that the B-MP displays a two times dynamics: it has two stable states of opposite polarisation, and reaches one of these states in a short time in a longer time, a complete equilibrium takes place between the two states.

The bound magnetic polaron (B-MP) has been widely studied in the case of bulk materials and the theoretical calculations are in good agreement with the experimental results [1-3]. However, only a few calculations [4-6] have been carried out in the case of B-MPs occurring in heterostructures. Except [7-9], there is to our knowledge no work dealing with the dynamical properties of the B-MP in quantum wells. A model exists for the bulk case [9].

We will firstly present our theory of the static properties of an acceptor bound magnetic polaron in CdTe/Cd_{1-x}Mn_xTe quantum wells and show that qualitative differences with the bulk case can arise. We will subsequently deal with the dynamical properties of the B-MP in quantum wells.

For the static properties, our model of B-MP is the following: in a CdTe/Cd_{1-x}Mn_xTe quantum well, an acceptor lies in the barrier at a distance z_1 from the interface. A heavy hole of effective mass m^* experiences the potential V created for one part by the quantum well and for another part by the coulombic attraction of the acceptor. Let H_0 be its hamiltonian. Since there are also m^* magnetic ions (spin $S_1 = 1/2$) in the barrier, they interact with the hole spin S with the exchange hamiltonian

$$H_{ex} = -J \sum_i S_i S_1 \quad (1)$$

S_1 denotes the spin of a hole located at r_1 . H_0 is responsible for the interaction of a given S_1 also interacts with its closest nearest neighbours with the interaction hamiltonian

$$H_{int} = -J' \sum_j S_1 S_j \quad (2)$$

The interaction is restricted to the nearest neighbours when J' is strong enough to bind the hole. The interaction between S and the S_1 s leads to the formation of a B-MP. The localisation and the binding energy of the hole are determined by the exchange interaction in order to calculate them, we have determined additionally the ground state $\Psi(H_0 + H_{ex})$.

We have assumed that the S_1 s are classical vectors. The vector S due to the hole will be the following firstly on a configuration of (S_1, S_2, \dots, S_N) and the S_1 s one will determine the eigenstates of energy $E(S, S_2, \dots, S_N)$ and eigenfunctions $\Psi(S, S_2, \dots, S_N)$. Secondly, one should calculate the thermodynamical average energy $E_B(\beta) = \langle E(S, S_2, \dots, S_N) \rangle$ by the Boltzmann formula

$$E_B(\beta) = \langle E(S, S_2, \dots, S_N) \rangle = \frac{\sum_{(S, S_2, \dots, S_N)} E(S, S_2, \dots, S_N) \exp(-\beta E(S, S_2, \dots, S_N))}{\sum_{(S, S_2, \dots, S_N)} \exp(-\beta E(S, S_2, \dots, S_N))} \quad (3)$$

where $\beta = 1/k_B T$ is the inverse temperature.

In the same way, one should calculate the localisation of the hole. Since the number of configurations of the multiplet (S_1, S_2, \dots, S_N) rises very quickly with the number N of S_1 s involved in the B-MP, we used rather the following approximate procedure. Firstly, given a fixed wave function $\Psi(r)$, we determined the value of $\langle \Psi | H_{ex} | \Psi \rangle$ and the thermodynamical average value of $\langle \Psi | H_{ex} | \Psi \rangle$. Secondly, we minimised the sum of both the previous terms with respect to Ψ . The minima are identified to $E_B(\beta)$. We have verified that, at the first order in perturbations, the two procedures are equivalent. Differences arises at the second order. We used the following form for $\Psi(r)$

$$\Psi(r) = \chi(z) \exp(-r/a) \quad (4)$$

$\chi(z)$ is the wave function which corresponds to the ground state of the square well potential (growth axis z), and $\exp(-r/a)$ is the wave function of the hole localisation in the acceptor in a bulk problem. The effective Bohr radius a has been our variational parameter. We took Hahn's account in the following way. Since it leads to the localisation of the B-MP, we assumed that for a given S_1 , $\langle \Psi(r) | S_1 | \Psi(r) \rangle$ is greater than a certain Ψ_C^2 , then the S_1 participates to the B-MP without antiferromagnetic interaction. If this is not the case, this S_1 is not involved in the B-MP. Ψ_C is estimated following reference [1]. We have averaged the positional disorder of the S_1 s by calculating the sum of the energies related to each occupable site, and multiplying it by the occupation probability x .

When the ground state of the acceptor is deeper than the well, the hole will always be localised on the acceptor. The result is a polaron effect which is qualitatively the same as in the bulk. Cd_{1-x}Mn_xTe when the depth of the well equals the ground state of the acceptor, qualitative differences arise. Eqs. (1) shows the averaged magnetic energy for two different values of z_1 in the case of $x=0.3$ and $L=86 \text{ \AA}$. When z_1 is large enough, which corresponds to two clearly separated attractive potentials, there exists a certain critical temperature T_C . Below T_C , the hole is located near the acceptor and there is a polaron effect. Above T_C , the hole is located in the well with no polaron effect. When the acceptor is close to the well, there is no such phenomena and the magnetic energy behaves qualitatively like in the bulk case. A physical explanation is the following: the hole localises near the acceptor interacts with the S_1 s and T_C is a B-MP like in the bulk case. The energy E_1 of this system depends on T . On the contrary, the energy E_2 of the system formed by the hole in the square well is almost temperature independent to the extent that the hole wave function is kept almost small in the barrier. T_C is qualitatively defined as $E_1(T_C) = E_2$. When $T < T_C$, $E_1 < E_2$ and there is a polaron effect (the hole prefers to be localised near the acceptor). When $T > T_C$, there is no polaron effect since the hole prefers to be localised in the well. If chemical terms, we have a polarised bond between the well and the acceptor. The localisation is temperature dependent and driven by exchange interaction. Let us now turn to the dynamical properties of the B-MP. We retain a slightly different model for our B-MP system. The potential which localises the hole is assumed to be a square defect rather than an acceptor. This assumption ensures that Ψ is strongly dependent on the temperature as above. We firstly compute and classify the eigenstates of the B-MP. Secondly, we compute the transition probability between the states of the B-MP which leads to its relaxation. The evolution of the B-MP can be solved numerically. However, we shall present a comparison between the numerical and approximate algebraic results. It should be stressed that any relaxation mechanism must be able to transfer spin out of the B-MP in order to allow a relaxation to a new state. We showed that the hamiltonian H_0 which must be used in the sum of the Boltzmann formula is the H_0 and H_{ex} exchange term. We should also consider the interaction between the hole and the nearest neighbours.

hole states, and therefore to allow the free electron gas with wave vector \vec{k} and heavy hole states there would be no hole relaxation within γ HR assumed that the \vec{k} and \vec{k}' are classical vectors.

$$\text{HeI} \rightarrow \begin{array}{cc} \text{B} \cdot \sum_{\mathbf{b}, \mathbf{m}_1 \mathbf{m}_2} & \text{A} \\ \lambda \cdot \sum_{\mathbf{b}, \mathbf{m}_1 \mathbf{m}_2} & \end{array} \quad (5)$$

where $b_1 = (3/2)(\Psi, F_1)^2$. The B_1 and A_1 are fixed by the square of the wave function and the parameters of the lattice perturbation (for details, see [7]) and the m_{12} are the eigenvalues of the S_{12} . Each BRP is characterised by different values of B_1 , B_2 , A_1 , and A_2 for any ℓ . Our numerical investigations correspond to the case of $B_1 = B_2 = B_0$ and $A_1 = A_2 = 0$. We assumed that this case was the generic case or, in another way, that B_0 and B_1 are the averaged values over a large number of BRPs ψ_ℓ of the B_1 , B_2 and B_3 . The averaging operation and the determination of the eigenvalues of H_{eff} would then have been interchanged. Let $\Omega = \sum_{\ell=1}^N m_{12} \psi_\ell$ be the polarisation of the BRP Ω is proportional to the magnetic energy of the BRP in our model (which is the BCS model of superconducting He^3) admits two types of singularities

the higher eigenstates ψ_{m_1, m_2} of the energy,

$$E_{m_1, m_2} = B \cdot (\lambda^2 \Omega^2 b^2)^{1/2} \quad (6)$$

They are related to the situations where the spin S of the hole and the S_1 's are mostly antiparallel.

$$E = (m + \frac{1}{2})\hbar\omega, \quad \omega = \sqrt{\frac{k}{m}}$$

they are related to a situation where the spin S of the particle and the S_z are equal

Fig. 2 shows the curves $\xi_1(\Omega)$ and $\xi_2(\Omega)$ which are calculated in a similar manner to the study of the BP dynamics in the β plane. Thus it is much like its two spin valleys and a stable point.

For the transitions between the spin states, a Heff. due to a perturbation of the BP for an external system which has to be specified during the relaxation of the BP towards the bottom of the spin valleys is given. This relaxation can be done by many units. Only efficient relaxation mechanism is the interaction of the BP with other β states. The spin S_{β} which are not involved in the transition are closer to the S_{β} spin interaction with other β states which are remote from the BP. If it is not lesser to a certain interaction the results of the transition, which are not involved in the BP clear treasury. If a smaller size unit gives rise to the spin relaxation of the BP. This case, it is called to the BP by the following form:

(8) $\sum_{n=0}^{\infty} \frac{(-1)^n}{(n+1)!}$

The involved States: Squares in the triangle, shaded to indicate, although the transition probability between the initial stable configuration (the left) and the final stable configuration (the right) is very low, the energy balance

$W_A C \rightarrow D = 1/2 \pi \hbar \omega / n_A \lambda_A C \hbar \hbar \omega \text{oup}(\text{D}) / 2 \delta E(E-E_i)$ (9)

$$\gamma_n(h) = (1/2\pi\sigma^2)^{-3/2} \exp(-h^2/2\sigma^2) \quad (10)$$

we are then able to calculate the transition probability $\mathbb{P}_{\mathbb{A} \rightarrow \mathbb{B}}$ between the two states \mathbb{A} and \mathbb{B} of the ETP. The selection rules we found are the following: in the E-branch $\mathbb{A} \rightarrow \mathbb{B}$ is the state $1 - m_1 \geq m_2 > m_1 \geq 1$, only the B states which are of the form $1 - m_1 \geq m_2 > m_1 \geq 1$ can be reached. B differs from A in only one of its m_2 which becomes $m_2 \pm 1$. m_1 will in the following denote this m_2 - then of $\mathbb{A} \rightarrow \mathbb{B}$.

are shown in Figure 1. Our results are

$$\|f\|_{\infty} = \sup_{x \in \mathbb{R}^n} |f(x)| = \sup_{x \in \mathbb{R}^n} \left| \sum_{j=1}^n x_j \right| = \sqrt{n}.$$

(c) [redacted] has been advised by the FBI that the information provided by the informant is reliable.

[illegible]

$$I = \frac{1}{2} \int_{-\infty}^{\infty} \psi^* \left(-\frac{\hbar^2}{2m} \frac{\partial^2}{\partial x^2} + V(x) \right) \psi dx$$

typical value of \mathbf{r} is 10^{-4} s (1) allows to study the dynamics of the BRP. Let $\text{Pr}(\mathbf{m}, t)$ be the probability of finding the BRP in the state $(-\mathbf{m}, 1)$ at time t . \mathbf{P} can be seen as a vector with QV components which obeys

$$dp \, q(t) + p$$

S_1 is involved in the first element; the variation arises directly from (1). Let us look at the analogy of (1) as a problem of coupled diffusion in a two-dimensional discrete hypercube with homogeneous boundary conditions. We have previously solved (1) in the case $\gamma = 0.5$ in order to obtain the exact value of the average polarisation $S(t)$ of the first

$$(5) \quad \left| \left(\frac{1}{2} + \frac{1}{2} \sqrt{1 - 4\alpha} \right) \right| \sum_{n=0}^{\infty} n! b_n$$

In our model $\chi(T)$ is directly proportional to the magnetic susceptibility $\chi(T)$ of the Br₂. Results are plotted in **Fig. 1**. $\chi(T)$ exhibits a two times increase in χ in the vicinity of T_c . The results are clearly at low temperatures in a short time τ . $\chi(T)$ reaches a quasi-stationary value χ_0 . Subsequently, it decays slowly to zero following an exponential law $\exp(-T/\tau)$. The part of the function $\chi(T)$ is characterised by T_0 and tends to the initial temperature T_0 of the film. In the case of a smaller T_0 , $\chi(T)$ was observed to be lower. The function $\chi(T)$ is characterised by T_0 and τ . The two values T_0 and τ through the data of $\chi(T)$ at different temperatures T_0 are plotted in **Fig. 2**. It has been shown that T_0 and τ are independent of T_0 and τ are independent of T_0 .

$$D = (1) \cdot \sum_i P_i(m_i) \quad (16)$$

$\Sigma_i (\Sigma_i^-)$ denotes the summation over the states of the positive (negative) spin valley P_+ denotes the probability to find the BRP in the positive spin valley and P_- to find it in the negative spin valley if our conceptions about the long time dynamics of the BRP are right, one should be able to write that for $t \gg \tau_S$

$$\frac{dP_+}{dt} = (1/\tau_1) (P_+ - P_-) \quad (17)$$

Then in a situation where the initial state of the BRP is the bottom of the positive spin valley one should have

$$S(t) \approx S_0 \exp(-t/\tau_1) \quad (18)$$

while if $t \ll \tau_1$

$$P_+ \approx t/\tau_1 \quad (19)$$

we have verified that the slope of P_+ at medium times is the same as the slope of $-2 \log(S(t))$ at long times.

In order to be able to consider a BRP with a parameter V of Si is greater than 1 or 5, we have carried out theoretical calculations, we will present a theoretical evaluation of τ_1 .

One can write again (1) in the following form

$$\frac{d\Pi}{dt} = -\Pi \Pi^T \quad (20)$$

The vector P has been split into the two vectors Π_+ and Π_- . The components of Π_+ (Π_-) are related to the states of the positive (negative) spin valley. Π_1 (Π_2) is related to the intravalley (intervalley) dynamics. μ couples the states which are on both sides of the saddle point. Π admits a null eigenvalue corresponding to the thermodynamical equilibrium and several negative eigenvalues. Let us be the eigenvector of Π related to the vanishing eigenvalue, note that the space of the P 's is not hermitian. At large times there is

$$\exp(\Pi t) \approx \Pi^T \exp(t) \quad (21)$$

if Π is written as $\exp(\Pi t)$, one can write at large times

$$D(P) A_{++} / dt = \Pi_+ \Pi_+^T D(P) A_{++} \quad (22)$$

$$D(P) A_{+-} / dt = \Pi_+ \Pi_-^T D(P) A_{+-} \quad (23)$$

$$D(P) A_{-+} / dt = \Pi_- \Pi_+^T D(P) A_{-+} \quad (24)$$

$$D(P) A_{--} / dt = \Pi_- \Pi_-^T D(P) A_{--} \quad (25)$$

which is a 2x2 scalar system analogous to (1) - we then have

$$D(P) A_{++} / dt = \Pi_+ \Pi_+^T D(P) A_{++} \quad (26)$$

$$D(P) A_{+-} / dt = \Pi_+ \Pi_-^T D(P) A_{+-} \quad (27)$$

$$D(P) A_{-+} / dt = \Pi_- \Pi_+^T D(P) A_{-+} \quad (28)$$

$$D(P) A_{--} / dt = \Pi_- \Pi_-^T D(P) A_{--} \quad (29)$$

$$D(P) A_{++} / dt = \Pi_+ \Pi_+^T D(P) A_{++} \quad (30)$$

$$D(P) A_{+-} / dt = \Pi_+ \Pi_-^T D(P) A_{+-} \quad (31)$$

$$D(P) A_{-+} / dt = \Pi_- \Pi_+^T D(P) A_{-+} \quad (32)$$

$$D(P) A_{--} / dt = \Pi_- \Pi_-^T D(P) A_{--} \quad (33)$$

$$D(P) A_{++} / dt = \Pi_+ \Pi_+^T D(P) A_{++} \quad (34)$$

$$D(P) A_{+-} / dt = \Pi_+ \Pi_-^T D(P) A_{+-} \quad (35)$$

$$D(P) A_{-+} / dt = \Pi_- \Pi_+^T D(P) A_{-+} \quad (36)$$

$$D(P) A_{--} / dt = \Pi_- \Pi_-^T D(P) A_{--} \quad (37)$$

$$D(P) A_{++} / dt = \Pi_+ \Pi_+^T D(P) A_{++} \quad (38)$$

$$D(P) A_{+-} / dt = \Pi_+ \Pi_-^T D(P) A_{+-} \quad (39)$$

$$D(P) A_{-+} / dt = \Pi_- \Pi_+^T D(P) A_{-+} \quad (40)$$

$$D(P) A_{--} / dt = \Pi_- \Pi_-^T D(P) A_{--} \quad (41)$$

$$D(P) A_{++} / dt = \Pi_+ \Pi_+^T D(P) A_{++} \quad (42)$$

$$D(P) A_{+-} / dt = \Pi_+ \Pi_-^T D(P) A_{+-} \quad (43)$$

$$D(P) A_{-+} / dt = \Pi_- \Pi_+^T D(P) A_{-+} \quad (44)$$

$$D(P) A_{--} / dt = \Pi_- \Pi_-^T D(P) A_{--} \quad (45)$$

$$D(P) A_{++} / dt = \Pi_+ \Pi_+^T D(P) A_{++} \quad (46)$$

$$D(P) A_{+-} / dt = \Pi_+ \Pi_-^T D(P) A_{+-} \quad (47)$$

$$D(P) A_{-+} / dt = \Pi_- \Pi_+^T D(P) A_{-+} \quad (48)$$

$$D(P) A_{--} / dt = \Pi_- \Pi_-^T D(P) A_{--} \quad (49)$$

$$D(P) A_{++} / dt = \Pi_+ \Pi_+^T D(P) A_{++} \quad (50)$$

$$D(P) A_{+-} / dt = \Pi_+ \Pi_-^T D(P) A_{+-} \quad (51)$$

$$D(P) A_{-+} / dt = \Pi_- \Pi_+^T D(P) A_{-+} \quad (52)$$

$$D(P) A_{--} / dt = \Pi_- \Pi_-^T D(P) A_{--} \quad (53)$$

2-D.R. Yakovlev, I.N. Ural'tsev, W. Ossau, G. Lindwehr, R.N. Bicknell-Tassius, A. Nag, S. Schneusser, *J. Appl. Sci.* **623** (1992) 285.
 3-E.T. Goncalves Da Silva, *Phys. Rev. B* **32** (1985) 6962.
 4-A. Mauger, N.S. Almeida, D.L. Mills, *Phys. Rev. B* **38** (1988) 1296.
 5-P. Boudinet, G. Bastard, *Europ. Phys. Lett. A* **20** (1992) 149.
 6-P. Boudinet, G. Bastard, To be published in *Semicond. Sci. Technol.*
 7-A.V. Kavokin, *Unpub. sheet* (1993).
 8-D. Scalbert, P. Hawrock, C. Benoit a la Guillaume, J. Cernogora, *Phys. Rev. B* **37** (1988) 4479.
 9-C. Chen-Tannoudji, J. Dupont-Roc, G. Grynberg, *Processus d'interaction entre photons et atomes* Editions/Editions du CNRS (1988).

Table 1 Comparison between the theoretical and numerical values of the activation energy of the BRP for $V = 1, 2, 5$

V	Theoretical	Numerical
1	0.00	0.00
2	0.00	0.00
5	0.00	0.00

Table 2 Comparison between the theoretical and numerical values of τ_1 for $V = 1, 2, 5$ in two different units 1/b) and for reduced units 1/b) and for $V = 1, 2, 5$

V	1/b)	Reduced units
1	0.00	0.00
2	0.00	0.00
5	0.00	0.00

1-A.K. Bhattacharjee, R. Planel, C. Benoit a la Guillaume, *Phys. Rev. B* **37** (1988) 4479.
 2-T. Dietl, J. Spies, *Phys. Rev. Lett.* **48** (1982) 1000.

Time-resolved optical study of vertical transport in $\text{Cd}_{0.82}\text{Mn}_{0.18}\text{Te/CdTe}$ superlattices.Ph. Roussigneol^{a,*}, J. Martinez-Pastor^{a,*}, A. Vinetier^a, C. Delalande^a, and B. Luan^b^(a) Laboratoire de Physique de la Matière Condensée de l'Ecole Normale Supérieure, 24 rue Lhomond-75005 Paris, France.^(b) Laboratorio Europeo di Spettroscopia Non Lineare e Dipartimento di Fisica, Università di Firenze, Largo E. Fermi 2, 50125 Firenze, Italy^(*) Departament de Física Aplicada, Universitat de València, 46100 Burjassot, València, Spain.^(d) Department of Engineering Design and Manufacture, University of Hull, Hull, HU6 7RX, United Kingdom.

Abstract

We have performed cw and time-resolved photoluminescence measurements on a $30/30 \text{ Cd}_{0.82}\text{Mn}_{0.18}\text{Te/CdTe}$ superlattice containing two enlarged wells with different widths. Excitation above the alloy band gap allows to study the Bloch transport along the growth direction of the superlattice. Both ambipolar transport and hopping of carriers are observed in the 4-100K temperature range. At low temperatures (<20K), mobilities of the order of $4 \cdot 10^4 \text{ cm}^2/\text{Vs}$ and $3 \cdot 10^2 \text{ cm}^2/\text{Vs}$ are estimated for the two processes, respectively.

Introduction

In the last few years the improvement in molecular beam epitaxy growth has made possible the observation of vertical transport in superlattices [1]. Experimental evidences of this type of conduction first predicted by Esaki and Tsu [2] have been brought in heterostructures based on III-V semiconductors by using various optical or electric techniques [3-5]. Time-resolved photoluminescence in superlattices containing enlarged wells appeared to be one of the most powerful techniques and allowed an extensive study of the carrier transport in the AlGaAs/GaAs system [6]. In this paper, vertical transport is addressed by the same optical technique, in the case of the less investigated II-VI semiconductor heterostructures.

The sample was grown by molecular beam epitaxy on a InSb substrate. On this substrate are grown in succession, a 1000\AA thick CdTe layer, a 2000\AA $\text{Cd}_{0.82}\text{Mn}_{0.18}\text{Te}$ layer, 40 periods of $30/30 \text{ Cd}_{0.82}\text{Mn}_{0.18}\text{Te/CdTe}$ superlattice (SL) and a 60\AA thick enlarged well (EW). The second EW, 200\AA thick, is separated from the first one by 40 periods of SL, and followed by 160 periods of SL. Finally a 2000\AA thick $\text{Cd}_{0.82}\text{Mn}_{0.18}\text{Te}$ cap layer completes the structure.

The excitation source for the time-resolved measurements was a Nd:YAG synchronously pumped dye laser, providing 5 ps pulses in the range $560\text{--}780 \text{ nm}$ at the repetition rate of 76 MHz. Measurements have been also performed by using, for excitation, the second harmonics of the Nd:YAG laser (80 ps pulse duration at 532 nm). The PL signal was dispersed through a 0.22 m double monochromator (spectral resolution: 1 mV) and detected by a synchronous streak camera, with an overall time resolution of 20 ps. For decay times longer than 1 ns, the PL signal was analyzed by using a time correlated single photon counting system and a cavity dipper was inserted in the dye laser cavity in order to decrease the repetition rate; in this case the overall time resolution was of the order of 200 ps.

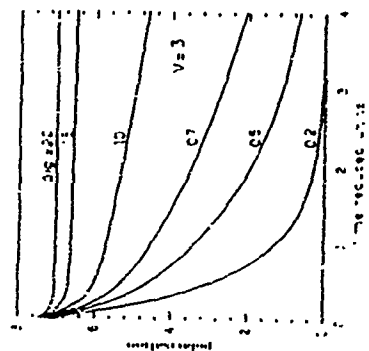


Fig. 3 Calculated time evolution of the averaged polarization $S(t)$ of the BPP for several values of B . g depends the energy unit B .

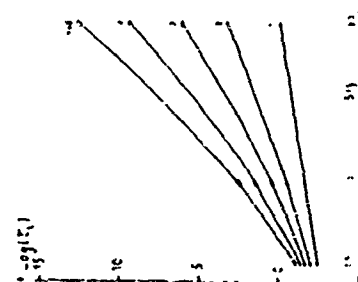


Fig. 4 Temperature evolution of logarithm $\log(I(t))$.

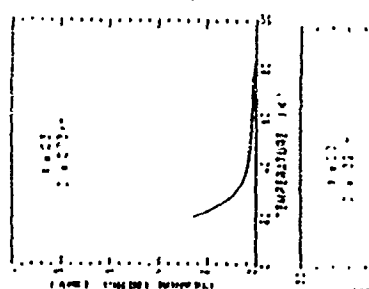


Fig. 1 BPP magnetic energy versus the temperature for 210.33 nm and 1.22 nm .

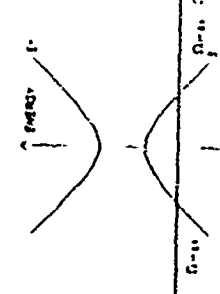


Fig. 2 Energies E_1 of the BPP versus polarization D .

Experimental results

In order to study the Bloch transport over the SL minibands, the structure is excited at 2.33 eV (Nd:YAG second harmonics) or 2.18 eV (dye laser), far above the alloy band gap (1.869 eV at 4K). In this case all the carriers are photo-generated within the 200Å thick CdMnTe cap layer. Typical PL spectra obtained at different temperatures are shown in Fig. 1. At 10K (lower curve in Fig. 1) the main peak at 1.722 eV corresponds to the excitonic recombination in the superlattice. The PL lines observed at 1.595 and 1.645 eV correspond to the excitonic recombination in the 200Å and 60Å EWs, respectively. The PL emission lines on the low energy side of the excitonic peaks are likely related to impurity assisted recombinations (A^0X , eA^0 , ...). As clearly shown in Fig. 1, at low temperatures (4-50K) the main peaks in the PL spectrum of the heterostructure correspond to the recombination in the SL. Excitonic recombination in the two EWs is also observed evidencing the vertical transport. Nevertheless, considering the rather low intensity of the EWs PL peaks, transport along the growth axis of the heterostructure does not seem so efficient: most of the photo-generated carriers get localized and recombine in the superlattice region before reaching the enlarged wells. When the temperature increases the contribution to the PL emission of the EWs increases. However, above 80-90 K the PL line of the 60Å EW tends to disappear. As commonly observed [8], this behaviour is certainly due to a worse quality of the thinner well, which made it more sensitive to non radiative processes. Above those temperatures the luminescence from the 200Å EW is more important than that of the SL and becomes the dominant feature of the PL spectrum of the structure. Indicating that the vertical transport is now more efficient than the localization process. An Arrhenius plot of the PL intensity ratio between the PL from the 200Å EW and that of the SL shows an activated behaviour above 50 K, with an activation energy of about 28 meV.

In the time-resolved measurements excitation powers of 20 - 200 mW were used corresponding roughly to excitation densities of about 10^{17} - 10^{18} cm⁻³. We report in Fig. 2 the PL decay curves of the 200Å EW at 4 and 40K obtained for two different excitation energies. Under resonant excitation of the E1H1 transition the PL decay times shown in Fig. 2a and 2b) is fast with time constants of 20 and 50ps at 4 and 40K, respectively. Such a resonant excitation gives the recombination time of the isolated well. The PL decay of the 200Å EW is strikingly different when all the carriers are photo-generated in the cap layer (continuous lines in Fig. 2a and 2b). The long decay times obtained when exciting the heterostructure above the SL band gap are then characteristic of the vertical transport. In fact, the decay time of the isolated well, being much shorter, influences only the rise time of the measured PL signal as it can be seen in Fig. 2 (the apparent lifetime is always related to the faster mechanism involved in the PL dynamics). A similar behaviour is observed for the 60Å EW.

At low temperatures (4-35K), the PL decay curves of the EWs under non resonant excitation (transport conditions and continuous line of Fig. 2a for the 200Å EW) can be decomposed as a sum of two exponentials with a lifetime corresponding to the decay time of the isolated EW and two decay times characteristic of the transport mechanism which are shown in Fig. 3a for the whole temperature range investigated. In fact, the fast component dominates the PL decay curve: the intensity ratio between the slow and the fast component is of the order of 0.10. Moreover, when increasing the excitation power, this ratio tends to decrease. The two characteristic times of the EWs PL decay seem to be related to two different types of carrier transport, the fastest one being favoured by an increase of the excitation power.

Above 40 K a monoexponential decay is observed as shown in Fig. 2b

The diffusion mobility, μ_D , can be deduced from the transport times according to

$$\mu_D = \frac{eD}{kT} = \frac{e^2 v_D \tau_R}{kT} \quad (1)$$

19)

where D is the diffusion coefficient, τ_R the recombination time along the carrier path and v_D the drift velocity, determined by the path length (L_{SL}), and the diffusion time (τ_D).

The diffusion mobilities reported in Fig. 3b have been estimated using Eq. 1, with $L_{SL} = 9600$ Å and 1.2000 Å (the distance between the cap layer and the EWs 200Å and 60Å, respectively) and $\tau_R = 350$ ps. The PL decay time in the SL exhibits a weak temperature dependence: from 250ps in the 4-100K temperature range. Therefore, this time, although influenced by the transport, can be mainly attributed to excitonic recombination in the SL. A τ_R value of 350ps will give the right order of magnitude for the recombination time of the SL, although somewhat underestimated, in the whole range of temperature.

In the 4-25K temperature range, the fastest transport mechanism gives high diffusion mobilities ranging from 40000 cm²/Vs to 2000 cm²/Vs. Above 30K this mobility drops significantly to reach a value of 40 cm²/Vs at 70K. The slowest mechanism gives much smaller mobilities, of the order of 300 cm²/Vs. However, when the slow component is observable (4-20K) its decay time is not accurately determined (intensity ratio $\sim 10\%$) and this mobility should be considered as an order of magnitude.

Discussion

Let us first consider the low temperature measurements (4-30K). At the large excitation intensities used in our experiments (10^{17} - 10^{18} carriers per cm³) we can reasonably assume that the main contribution to the transport provided by the fast component is due to ambipolar Bloch transport of carriers [10]. Electron-hole pairs are created in the cap layer of the heterostructure and ambipolar band transport takes place. Nevertheless, for these temperatures, as it can be seen in Fig. 1, localization of carriers occurs. Carriers can be captured by ionized acceptors in order to give neutral acceptor or localized on defects before arriving to the large well. Due to the smaller width of the HH miniband, holes are certainly more sensitive to localization than electrons. The long time constant can then be related to an other transport mechanism, hopping through localized states, this mechanism being much slower than Bloch conduction [11].

As a matter of fact, PL spectra of the heterostructure obtained at high cw excitation power (150 mW $\sim 10^{17}$ - 10^{18} carriers/cm³) are dominated by the excitonic recombinations in the SL and EWs; saturation of the finite number of the sites responsible for the localization of the carriers does occur. In time-resolved measurements a similar carrier density is photo-created, so we mainly see the band transport of free carriers. When the carrier concentration becomes sufficiently low, transport due to localized carriers begins to be observable. Moreover, when the excitation power is increased, due to the finite number of trapping sites, the ratio between free and localized carriers increases and the hopping process is less observable, as experimentally seen.

For temperatures higher than 30K we observe a monoexponential decay for the two EWs. Two main reasons make the observation of the slow component impossible. On one hand, as the temperature increases more and more carriers get detrapped from localized tail states of the SL and are thermally activated upwards the extended states [12]. The activation energy of 28 meV found for our heterostructure is consistent with the calculated localization energy on a two monolayers fluctuation (~ 30 meV). On the other hand, carrier scattering by acoustic and optical phonons takes place [13] and produces a large drop of the mobility (Fig. 3b). The transport time becomes longer than the hopping characteristic time and makes difficult the observation of the minor component.

At low temperature the mobilities in our $30\text{Å} \times 200\text{Å} \times 82\text{Å}$ CdTe/Cd_{0.82}Mn_{0.18}Te superlattice depicted in Fig. 3b are of the same order of magnitude as those reported for electrons in the GaAs/AlGaAs system [6, 14]. In fact, the ambipolar diffusion coefficient is expected to be close to the hole diffusion coefficient ($D_{amb} \sim 2 D_h$) [15]. At 10K we estimate a diffusion coefficient of 15 cm²/Vs which is intermediate between electron and hole diffusion coefficient

in a $\text{XV30 GaAs/Alp 15GaAs}$ superlattice (30 cm^2/s and 2 cm^2/s , respectively) [10]. Hole mobility seems then somewhat higher in the II-VI heterostructure. If we consider the small number of data available in the literature for II-VI systems, the estimated value of 4 cm^2/Vs seems also to be intermediate between the electron mobility (5 cm^2/Vs - 10 cm^2/Vs at 100K) and the hole mobility (1.5 cm^2/Vs in a HgTe/CuTe superlattice [17]). At higher temperatures, the ambipolar mobility ($\approx 20 \text{ cm}^2/\text{Vs}$ at 100K) is lower than the values reported for holes in these materials (200 cm^2/Vs in a HgTe/CuTe superlattice [17] and 1200 cm^2/Vs in bulk CuTe [13] at 170K). However hole mobilities are much dependent on the valence band structure and can be hardly compared so directly, especially at high temperature, where acoustic and optical phonons scattering plays a major role and is also much sensitive to the valence band dispersion via the Fröhlich potential.

Conclusion

We have presented experimental results, obtained by means of time-resolved photoluminescence, on carrier transport in a II-VI $\text{Cu}_2\text{O}/\text{MnO}$ 18Te/CuTe superlattice with two CuTe enlarged wells. Excitation above the band gap of the superlattice allows us to excite the sample near its surface. Band transport occurs but cw PL spectra show that localization of carriers plays an important role in this structure. A clear thermally activated behaviour is observed. In the time-resolved measurements two transport mechanisms with different time scales are individuated. The faster one can be assigned to Bloch transport along the growth axis of the heterostructure, the slower one to hopping between localized states. At low temperature, ambipolar mobilities of 40000 cm^2/Vs have been estimated for Bloch transport and 300 cm^2/Vs for hopping. The two orders of magnitude difference between the two mobilities is consistent with calculations in the GaAs/AlGaAs system [11]. These values can be compared and are in reasonable agreement with the values reported in similar systems [13, 16, 17].

References

1. see for example F. Capasso, K. Mohammed and A. Y. Cho, IEEE, J. Quant. Electron. QE-22, 1853 (1986).
2. L. Esaki and R. Tsu, IBM J. Res. Dev. 14, 61 (1970).
3. G. Belle, J. C. Nuan and G. Weinmann, Sol. St. Commun. 56, 65 (1985).
4. R. A. Davies, M. J. Kelly and T. M. Kerr, Phys. Rev. Lett. 55, 1114 (1985).
5. J. F. Palmier, C. Minot, J. F. Lieven, F. Alexandre, J. C. Harmand, J. Dujong, C. Dubon-Chevallier and O. Ankn, Appl. Phys. Lett. 49, 1360 (1986).
6. B. Lambert, F. Clérot, B. Deveaud, A. Chomette, G. Tablaieff and A. Regreny, B. Sermaige, J. Lumin. 44, 277 (1989).
7. A. Golink, J. Guier and J. A. Gaj, J. Phys. C 16, 6073 (1983).
8. M. Gurtoli, A. Vinatier, M. Celozzi, C. Deparis, J. Massies, G. Neu, A. Bosacchi, and S. Franchi, Phys. Rev. B 44, 3115 (1991).
9. P. Kireev, La Physique des Semiconducteurs, Ed. Mir, Moscow (1975).
10. B. Lambert, B. Deveaud, A. Chomette, A. Regreny and B. Sermaige, Semicond. Sci. Technol. 4, 513 (1989).
11. D. Calecki, J. F. Palmier and A. Chomette, J. Phys. C 17, 5017 (1984).
12. A. Chomette, B. Deveaud and A. Regreny, G. Bastard, Phys. Rev. B 31, 1464 (1985).
13. B. Segall, M. R. Lorenz and R. E. Hultved, Phys. Rev. 129, 2371 (1963).
14. B. F. Levine, W. T. Tsang, C. G. Bethea, and F. Capasso, Appl. Phys. Lett. 41, 470 (1982).
15. S. M. Sze, Physics of Semiconductor Devices, J. Wiley & Sons, New York, 1981.
16. S. Hwang, J. F. Schetzina, Properties of II-VI Semiconductors, Ed. F. J. Bartoli, H. F. Schaake and J. F. Schetzina, MRS Symposium Proc. vol. 151, 245 (1989).

17. C. A. Hoffman, J. R. Meyer, and F. J. Bartoli, Properties of II-VI Semiconductors, Ed. F. J. Bartoli, H. F. Schaake and J. F. Schetzina, MRS Symposium Proc. vol. 151, 403 (1989).

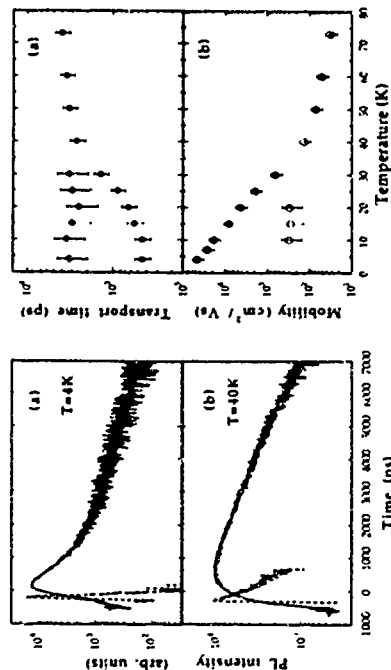
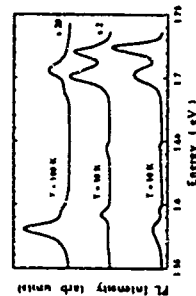


Figure 1 PL spectrum of the heterostructure excited above the SL band gap at different temperatures.

Figure 2 Semilogarithmic plots of the PL decays of the 200 Å enlarged well at 4 K (a) and 40 K (b). The dotted lines correspond to a resonant excitation of the E1H1 transition of the EW, the continuous lines are obtained when the excitation energy is higher than the CdInTe barrier band gap and all the carriers generated in the Cu_2O layer of the heterostructure.

Figure 3 (a) Temperature dependence of the transport times obtained from the slow (○) and the fast (●) component of the PL decay curve of the 200 Å EW (b) Log-log plot of the estimated carrier mobility (as explained in text) in the superlattice as a function of the temperature. Estimation of the hopping mobility is also reported (○).

Electron Subband Structure of HgCdTe Metal-Insulator-Semiconductor Heterostructures

Jinhao Chu¹⁾, R. Sizunano²⁾, Kun Liu¹⁾, I. Nachew³⁾, F. Koch²⁾

1) National Laboratory for Infrared Physics, Shanghai Institute of Technical Physics, Academia Sinica, Shanghai 200083, China

2) Physics Department E-16, T. U. München, 8046 Garching, F. R. Germany

3) Institute of Microelectronics, 1784 Sofia, Bulgaria

Abstract

The doping and pressure dependence of surface layer capacitance has been investigated in this work for $\text{Hg}_{1-x}\text{Cd}_x\text{Te}$ with doping concentration N_A from 3×10^{16} to $1 \times 10^{18} \text{ cm}^{-3}$ and under hydrostatic pressure up to 7.3 kbar at temperature 4.2 K. By using a capacitance-voltage spectroscopy (C-V) fitting model, the subband structures such as the first subband energy E_0 as a function of the energy gap E_g and the variation of E_0 with doping have been determined. The second onset of the inversion in capacitance spectroscopy on HgCdTe MIS structure has been observed. By using an expanded C-V fitting model several quantum parameters relating to the second subband of inversion layer electron can be determined quantitatively.

1. Introduction

The subband structure of n-type inversion layer of p-type HgCdTe metal-insulator-semiconductor (MIS) structures in quantum limit has been determined by a C-V fitting model directly from the capacitance-voltage relation. Recently it becomes more fruitful after conductivity oscillation (3dH) measurements [1]. In order to investigate systematically the subband structures for the inversion layer of p-type $\text{Hg}_{1-x}\text{Cd}_x\text{Te}$ with different doping concentration and under different pressure, we have investigated the doping and pressure dependence of surface layer capacitance for $\text{Hg}_{1-x}\text{Cd}_x\text{Te}$ with doping concentration N_A from 3.6×10^{16} to $1 \times 10^{18} \text{ cm}^{-3}$ and under hydrostatic pressure up to 7.3 kbar at 4.2 K. By using the modified subband model, the subband structures such as the first subband energy E_0 as a function of the energy gap E_g and the variation of E_0 with doping have been determined.

The second onset of the inversion in capacitance spectroscopy on HgCdTe MIS structure has been observed for the first time. Several key points have been presented in this paper in order to expand the C-V fitting model to determine the subband structures with two occupied subbands of n-type inversion layer in p-type HgCdTe MIS structures. By using this expanded C-V fitting model to fit the measured C-V relation, several quantum parameters relating to the second subband of inversion layer electron can be also determined quantitatively.

2. Model

We have presented a physical parameter fitting method to determine quantitatively the subband structure and its dependence on the inversion layer electron concentration in the electric quantum limit [1,2]. The basic idea is as follows: (i) the one-dimensional Poisson's equation is applied to give the relation between electric charge distribution and surface potential; (ii) the ground state energy E_0 is expanded into a series of surface electron concentration N_0 in the ground subband, $E_0 = E_{00} + E_{01}N_0 + E_{02}N_0^2$; (iii) a characteristic parameter $j = Z_{00}/Z_0$ is introduced for describing the wavefunction distribution of subband electrons, thus the electron gas in an inversion layer with depth Z_0 can be regarded on the average as being distributed in the plane that is Z_{00} distant from the surface; (iv) then from the calculations of capacitance-voltage relation of the MIS system to fit the measured C-V curve, and the results of 3dH and CR measurements, the subband structure can be obtained. In the case of existing resonant defect states, several modifications should be done. First, the charge density of chargeable resonant defect states should be involved in the one-dimensional Poisson's equation.

$$\frac{d^2\phi}{dz^2} = -\frac{1}{\epsilon_0} [\rho_i(Z) + \rho_{sp}(Z) + \rho_d(Z)] \quad (1)$$

where $\rho_i(Z)$ is the charge density of subband electrons in the inversion layer, expressed as equation (8) in reference [1], $\rho_{sp}(Z)$ is the charge density in the depletion layer, $\rho_d(Z)$ is the charge density of resonant defect states.

$$\rho_d(Z) = -eN_R \quad (0 < Z < Z_R) \quad (2)$$

where Z_R is the depth of chargeable resonant states. In the region $Z < Z_R$ the resonant level sinks down below the Fermi level. N_R is the density of resonant states. Secondly, semiconductor surface layer capacitance C_s can be redefined by taking account of the contribution of resonant defect states as

$$C_s = \frac{\partial Q_s}{\partial \phi_s} = -e \left(N_A \frac{\partial Z_d}{\partial \phi_s} + N_R \frac{\partial Z_R}{\partial \phi_s} + \frac{\partial N_s}{\partial \phi_s} \right) \cdot A \quad (3)$$

where ϕ_s is the surface potential, Q_s is the surface charge, A is the area of the capacitor; Z_d is the depletion width, N_s is the electron concentration in the inversion layer subband, the term of N_R is the contribution of resonant defect states to the semiconductor surface layer capacitance. Finally, the total induced charge can be separated into three parts: depletion charge, resonant defect state charge, and surface electron charge. Thus the relationship between surface electron concentration and gate voltage is

$$N_s = C_s(V_g - V_{FB})/e - N_A Z_d - N_R Z_R \quad (4)$$

For the heavily doped bulk p-type HgCdTe samples, the influence of resonant defect states on the subband structure should be taken into account in the calculation of subband structures. This is very important to get doping dependence of subband structure.

In the case of two occupied subbands of n-type inversion layer in p-type HgCdTe MIS structures the C-V fitting model should be expanded. The main procedures are as follows.

(i) like the ground state energy E_0 , the first excited state energy E_1 is also expanded into a series of electron concentration N_A in the second subband.

$$E_1 = E_{10} + E_{11}N_A + E_{12}N_A^2 \quad (5)$$

where E_{10} can be obtained from the calculation of one-subband $C-V$ fitting procedure at the second threshold voltage V_{T1} . E_{11} and E_{12} are two adjustable parameters in the two-subband $C-V$ fitting calculation after the second onset. (ii) after the second onset, the total concentration of surface electrons is

$$N_s = N_{s0} + N_A \quad (6)$$

The relation between N_s and the Fermi level E_F is

$$N_s = \int_{E_0}^{E_F} \frac{M_0^*}{\pi \hbar^2} \left[1 + \frac{2(E - j_1 E_0)}{E_s} \right] dE + \int_{E_1}^{E_F} \frac{M_1^*}{\pi \hbar^2} \left[1 + \frac{2(E - j_1 E_1)}{E_s} \right] dE \quad (7)$$

where j and j_1 are wave function distribution parameters for E_0 subband and E_1 subband, respectively. They can be obtained from the Fan-Howard wave function [3] (iii) in the calculation, all the combination and their derivatives change as

$$\begin{cases} N_s Z_0 \rightarrow N_{s0} Z_{00} + N_A Z_{01} \\ N_s \frac{\partial Z_0}{\partial \phi_s} \rightarrow N_{s0} \frac{\partial Z_{00}}{\partial \phi_s} + N_A \frac{\partial Z_{01}}{\partial \phi_s} \\ \frac{\partial N_s}{\partial \phi_s} \rightarrow Z_{00} \frac{\partial N_{s0}}{\partial \phi_s} + Z_{01} \frac{\partial N_{s1}}{\partial \phi_s} \end{cases} \quad (8)$$

where Z_{00} and Z_{01} are depths of the first subband and the second subband, respectively.

By fitting to the measured $C-V$ curve in the voltage region after the second onset we can get the second subband energy E_1 and other quantum parameters versus subband electron concentration

3. Results

In order to investigate the doping dependence of subband structure, we have measured the capacitance spectroscopy, magneto-conductivity oscillation, and cyclotron resonance of subband electrons for p -type $\text{Hg}_{1-x}\text{Cd}_x\text{Te}$ ($x=0.21$) samples with doping concentration N_A from 3.6×10^{16} to $1.1 \times 10^{18} \text{ cm}^{-3}$. The sample preparation and the experimental details have been reported in our previous work [1,4]. By using the modified model described above, the one-subband $C-V$ fitting calculation has been performed for all the measured samples. The subband energy coefficients E_{00} and E_{01} depend on N_A . The subband threshold energy E_{00} varies with doping concentration N_A . From the best fit to the data, an empirical relation of E_{00} can be derived as

$$E_{00} = 4.97 \times 10^{-14} [g(N_A)]^{10} + 1.6 \times 10^{-12} N_A - 7 \times 10^{-26} N_A^2 \quad (\text{eV}) \quad (9)$$

which is applicable to $\text{Hg}_{1-x}\text{Cd}_x\text{Te}$ ($x=0.21$) samples with different doping concentrations from 3.6×10^{16} to $1.1 \times 10^{18} \text{ cm}^{-3}$ for $N_A < 8 \times 10^{17} \text{ cm}^{-3}$. Table 1 shows the comparison of equation (9) with the results from theoretical calculation

Table 1 Comparison of subband energy E_0 in this work with that of theoretical calculation

samples	this work [eq. (9)]	theory
$N_A = 4.0 \times 10^{17} \text{ cm}^{-3}$	0.215	0.220 Ref. [5]
$N_A = 6.3 \times 10^{17} \text{ cm}^{-3}$		
$N_A = 3.2 \times 10^{17} \text{ cm}^{-3}$	0.163	0.170 Ref. [5]
$N_A = 2.0 \times 10^{17} \text{ cm}^{-3}$		
$N_A = 5 \times 10^{16} \text{ cm}^{-3}$	0.126	0.122 Ref. [6]
$N_A = 3 \times 10^{16} \text{ cm}^{-3}$		

The Fermi level and the effective mass of subband electrons at the Fermi level as well as the depths of inversion layer and depletion layer can be also obtained from the $C-V$ fitting calculation. When $N_A = 3 \times 10^{17} \text{ cm}^{-3}$, as the N_A increases from 3×10^{16} to $1.1 \times 10^{18} \text{ cm}^{-3}$, Z_0 decreases from 90 nm to 30 nm, Z_1 decreases slowly from 20 nm to 10 nm.

All of these data including subband energy E_0 , Fermi level E_F , effective mass $M^*(E)$ and the sizes of depletion and inversion layers and their N_A -dependence are necessary for deriving the subband Landau level fan chart and dispersion relation of subband electrons by combining the Kane's model and considering the contribution of k -linear term of spin-orbit interaction, so the obtained Landau level fan chart is in good agreement with the data of magneto-optical resonance of subband electrons [7].

The one-subband $C-V$ fitting model can also be applicable to determine the pressure dependence of subband. The pressure dependence of surface layer capacitance has been measured in this work for $\text{Hg}_{0.9}\text{Cd}_{0.1}\text{Te}$ at hydrostatic pressure up to 7.3 kbar at temperature 4.2 K. Figure 1 shows the capacitance spectroscopy for $\text{Hg}_{0.9}\text{Cd}_{0.1}\text{Te}$ at pressure of 0, 1.9, 2.9, 4.4, 5.8, and 7.3 kbar. It is obviously that the onset of inversion is delayed and the flat band voltage also moves towards the voltage-increasing direction as the pressure increases, i.e., as the energy gap E_g increases. The pressure dependence of energy gap for HgCdTe is $E_g(P) = E_g(0) + (9.5 \text{ meV/kbar}) \cdot P$. From the $C-V$ fitting model we get the subband energy E_0 and other quantities of subband as a function of energy gap E_g . Table 2 shows the related

Table 2 Related quantities of the $C-V$ fitting calculation at different pressure

P (kbar)	C_s (pF)	V_{T0} (Volt)	V_{T1} (Volt)	E_{00} (meV)	E_{01} (meV)	E_{00} (theory) (meV)
0	51.65	-75	0	128	146	151
1.9	54.62	-65.3	11.5	146	148.6	154
2.9	54.61	-62.9	15.3	156	149.2	155.2
4.4	54.596	-59.7	20.5	170	151	156
5.8	54.603	-56	26.2	183	154	158
7.3	54.601	-52	32	197	155	159.4

quantities of the $C-V$ fitting calculation, where the values of $E_0(\text{exp})$ are obtained by the $C-V$ fitting calculation, the values of $E_0(\text{theory})$ are from the self-consistent variation calculation [8,9]. Figure 2 shows the subband threshold energy E_0 versus energy gap E_g and hydrostatic pressure P that was applied to the sample.

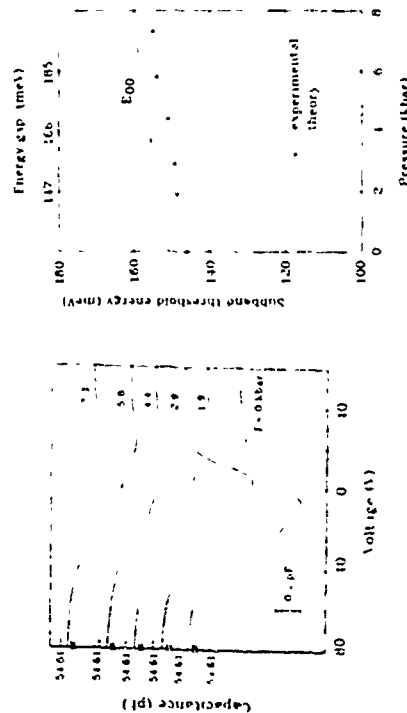


Fig. 1 The measured capacitance spectroscopy for $\text{Hg}_{0.74}\text{Cd}_{0.26}\text{Te}$ at 4.2 K and hydrostatic pressure P for $\text{Hg}_{0.74}\text{Cd}_{0.26}\text{Te}$ at pressure of 0, 1.9, 2.9, 4.4, 5.8 and 7.3 kbar, respectively

Fig. 2 The subband energy E_0 versus energy gap E_g and pressure P for $\text{Hg}_{0.74}\text{Cd}_{0.26}\text{Te}$ at 4.2 K

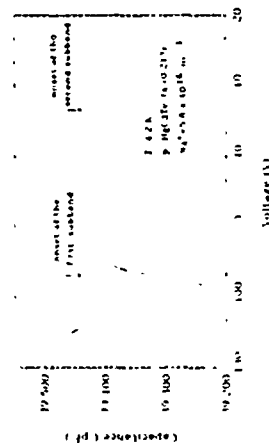


Fig. 3 The measured capacitance spectroscopy with the first and second onset of inversion for $\text{Hg}_{1-x}\text{Cd}_x\text{Te}$ samples with $x = 0.21$ and $N_A = 5.8 \times 10^{16} \text{ cm}^{-3}$

The capacitance spectroscopy can be also used to study higher subband structures. In principle, the variation of C with V above the threshold should give evidence for higher subbands E_1, E_2, \dots , etc. and allows one to determine the density of states in the subbands. However, it is difficult to measure the higher onset of inversion due to the inhomogeneity. For measuring the second onset of inversion, a uniform sample or a relatively small area of gate is necessary. By a careful experiment we have measured the capacitance spectroscopy with the first and second onset of inversion for $\text{Hg}_{1-x}\text{Cd}_x\text{Te}$ samples with $x = 0.213$ and $N_A = 5.8 \times 10^{16} \text{ cm}^{-3}$ at 4.2 K (Fig. 3). In the figure we can see clearly the second onset of inversion. The second inversion threshold is reached when band bending equals an energy of $E_g + E_1$, and electrons start to occupy the bottom of the second subband. By using the $C-V$ fitting model that has been expanded to determine the subband structures with two occupied subbands of n -type inversion layer in p -type HgCdTe MIS structures, the energy E_1 and other quantum parameters relating to the second subband of inversion layer electron can be also determined quantitatively, which will be published elsewhere.

References

- [1] J. H. Chu, Z. Y. Mi, R. Sizmann and F. Koch, *Phys. Rev. B* **44**, 1717 (1991)
- [2] J. H. Chu, Z. Y. Mi, R. Sizmann, F. Koch, R. Wollrab, J. Ziegler and H. Maier, *J. Vac. Sci. Technol. B* **10**(4), 1569 (1992)
- [3] F. F. Fang and W. E. Howard, *Phys. Rev. Lett.* **16**, 797 (1966)
- [4] J. H. Chu, R. Sizmann, R. Wollrab, F. Koch, J. Ziegler, and H. Maier, *Chin. J. IR Res.* **8**, 327 (1989)
- [5] R. Sizmann, Doctor Thesis, T. U. München, (1989) p. 38, p. 50
- [6] I. Nachev, *Semicond. Sci. Technol.* **3**, 29 (1988)
- [7] J. H. Chu, R. Sizmann, Z. Y. Mi, F. Koch, *21st Int'l. Conf. on Phys. of Semicond. Beijing*, Oct. 1992
- [8] K. Liu, J. H. Chu, D. Y. Tang, to be published
- [9] F. Stern, *Phys. Rev.* **B5**, 4891 (1972)

Zeeman studies of $\text{CdTe-Cd}_{1-x}\text{Mn}_x\text{Te}$ multiquantum wells

S. Jackson, S. R. Bell, J. Sirtor, W. F. Hagston,

P. Harrison and J. E. Nicholls

Department of Applied Physics, University of Hull, HU6 7RX, U.K.

28th June 1993

Abstract

Various novel features of the magnetic field splitting associated with the photoluminescence quantum well structures are described. Attention is focused on those aspects of the data which reveal certain novel features of the physics involved. Sometimes these features are associated with observations that are the same for both the Faraday and Voigt configurations (isotropic effects) whereas at other times they involve observations that are decidedly different for these two configurations (anisotropic effects). In this way evidence is presented for the existence of interface potentials together with anisotropic effects resulting from the rotation of the spin quantization axis by an external magnetic field. The latter leading to an admixture of the light and heavy hole states with increasing field in the Voigt configuration.

1 Introduction

Dilute magnetic semiconductors (DMS) such as the $\text{Cd}_{1-x}\text{Mn}_x\text{Te}$ system described here are characterized by large magneto optical effects resulting from the carrier magnetic ion exchange interaction [1]. In the multiquantum well system formed from CdTe wells and $\text{Cd}_{1-x}\text{Mn}_x\text{Te}$ barriers, this interaction gives rise to novel effects in the magnetic field dependence of the photoluminescence (PL) and photoluminescence excitation (PLE) spectra. In the following we describe the manner in which these effects manifest themselves and in particular we distinguish between those features that are similar in both the Faraday and Voigt configurations (isotropic effects) and those that are different (anisotropic effects).

2 Experiment

Since the effects to be described are characteristic of many different quantum well structures, we present detailed results for only one sample. The latter was formed from 15 wells of width z of z of width 72 Å sandwiched between $\text{Cd}_{0.5}\text{Mn}_{0.5}\text{Te}$ barriers of width 176 Å. The sample was grown with a VG Semicon V8000 molecular beam epitaxy (MBE) system on InSb (001) substrate. Layer thicknesses were determined from a calibration of the molecular flux rates and checked by double crystal X-ray diffraction.

The zero field PLE spectra consist of 3 emission bands shown in Figures 1 and 2 for the Faraday and Voigt configurations respectively. Two of these are free excitons at different intra well widths together with their associated donor bound excitons ≈ 3 meV lower in energy. The relative increase in the higher energy component of each pair is a free of bound at elevated temperature is consistent with the assignment to intra well width (as opposed to inter well width) fluctuations. Similarly the energy separation between the free and bound excitons is consistent with the assignment of the latter as an exciton bound to a neutral donor, since once the calculations we have carried out

show that the binding energy of an electron to a donor varies from ~ 20 meV when the donor is in the centre of the well to ~ 5 meV when the donor is in the centre of the barrier. From this it follows that the peak separation ≈ 1 meV is consistent with an exciton binding energy ≈ 0.14 that of the donor electron, and agrees with calculations of this ratio for bulk material [2]. These same calculations also show that the donors are distributed throughout the well and barrier region, since this explains, for the Faraday configuration, the decrease in both the intensity of the bound exciton emission at all values of the applied field (as the latter successively destabilizes bound exciton formation [3]) at donor positions moving from the centre of the barrier in toward the well region) and the change in the emission peak energies as a function of field shown in Figure 1.

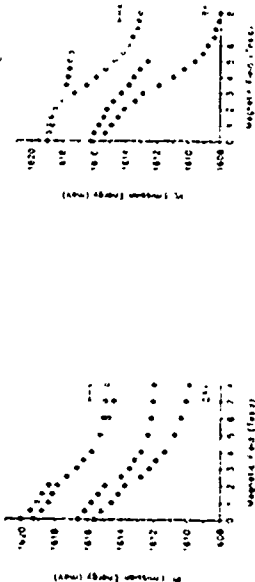


Figure 1 PLE emission energy as a function of magnetic field in Faraday configuration

For this configuration the PLE is associated with pure heavy hole exciton transitions. This is to be contrasted with observations of these lines in the Voigt configuration shown in Figure 2. Here the PLE spectra show, in agreement with the predictions of the theory to be described below, that an anti crossing will occur at ~ 2 Tesla between a light hole and a heavy hole state. Prior to this anti crossing there exists only a small splitting of the heavy hole state. Consequently the emission spectrum consists of two free exciton lines whose energy position is almost independent of the field up to ≈ 2 Tesla. Following the anti crossing, which leads to large energy shifts, only one line is ultimately resolved in the PLE spectrum.

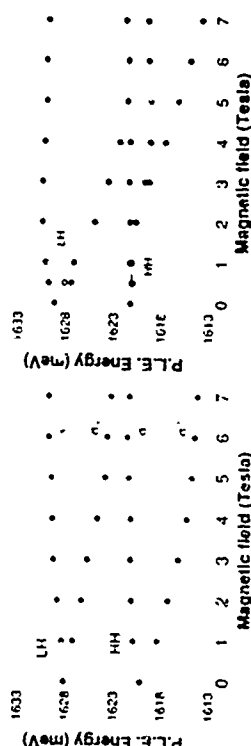


Figure 2 PLE emission energy as a function of magnetic field in Voigt configuration

The PLE spectra are quite complicated partially as a result of the existence of two effective well widths. For clarity we therefore display only those aspects of the data that illustrate novel features.

and/or the asymmetry in the splittings between the Faraday and Voigt configurations. Within this restriction the relevant parts of the P.L.E. data for the Faraday and Voigt configurations are shown in Figures 3 to 5. Some of the important points of these spectra, as regards their discussion, are discussed following. The heavy hole excitation transitions in the barrier, which are almost identical for both configurations, are displayed in Figure 3. There is isotropy with regard to the 'mean' Zeeman splitting of these lines in both the Faraday and Voigt configurations. It is to be noted however that there is an asymmetry in the σ^+ and σ^- splittings of the heavy hole excitation transitions. If the mean of the magnitude of these splittings is fitted to a Brillouin function for both the light and heavy hole states, it is found that the value of λ_{eff} , which characterizes the exchange interaction of the electrons in the conduction band, is typically 20 meV, smaller than the bulk value [1].

With regard to the energy transitions in Faraday configuration in Figure 3, which are associated with excitons in the well region, one characteristic feature is the anomalously large splitting of the light hole excitation states compared with the heavy hole states. Likewise there is a marked anisotropy in the magnetic field splittings between Figure 3 and Figure 1. The heavy hole excitation states hardly split at all in the Voigt configuration until a field ≈ 2 Tesla when the anti-crossing effect referred to earlier produces a significant splitting of these states. As opposed to this the light hole states show appreciable splitting in the magnetic field.

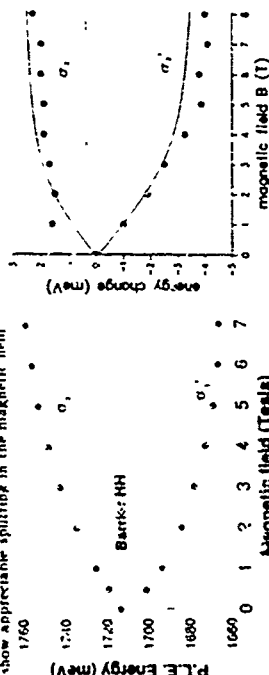


Fig. 3. Barrier heavy hole (HH) transition as a function of magnetic field

3 Discussion

The fact that the magnetic response of the first few monolayers in a magnetic barrier could differ from the rest of the barrier region has been noted by other workers [1]. Similarly the reduction in the value of λ_{eff} has been seen in Faraday rotation experiments [3]. Coupling these features together shows, for example, that in the Faraday configuration the change in the potential profile for the light hole σ^- transition on application of a magnetic field could differ markedly from the normal square quantum well profile [6]. In this manner, by assigning a different Brillouin function response to the first few monolayers of the barrier region we have been able to obtain a theoretical fit to both the heavy hole and the light hole excitation splittings, where the light hole splitting in Faraday configuration together with the theoretical fit without (detached lines) and with interlayer potentials (solid lines) is depicted in Figure 6. It can be seen that the theoretical fit to the light hole splittings is improved by making allowance for the anomalous magnetic response of the first few monolayers of the barrier region where the holes are effectively 'confined'. These same considerations can also account for the asymmetry in the splitting of the heavy hole barrier exciton, since the corresponding deviations in the magnetic response of the first few monolayers

can be treated as a perturbation which effectively renormalizes the band gap of the material (which is why we chose the mean of the magnitude of the splittings earlier).

The theoretical analysis of the line splitting in the Voigt configuration is identical with that already described in the literature [7,8] and hence will not be described in detail here. It leads to results that give good overall agreement with regard to both the number of lines seen and their relative intensity as a function of the field. In particular it predicts the negligible splitting of the heavy hole states at low fields and the anti-crossing of the light and heavy hole states in the field range 2 - 3 Tesla. Although there is good overall agreement with the observed light hole splittings the quantitative agreement is improved (exactly as in the Faraday configuration) by inclusion of interface potentials.

4 Conclusions

The observed asymmetry in the splitting of the barrier excitonic states is consistent with the existence of short range interface potentials resulting from the different magnetic response of the interface region. These same results also show that the magnetic exchange interaction of the conduction band electron with the Mn^{2+} ions is reduced in the finite barriers described here. A combination of both these effects can account for the anomalously large splitting of the light hole state in the Faraday configuration.

The energies and intensities of the bound exciton states are consistent with their being assigned to donors which are themselves distributed across the entire well and barrier region. Similarly the mixed asymmetry in the field splittings in the Faraday and Voigt configuration of the light and heavy hole states associated with the well region is consistent with the rotation of the spin axis of quantization in the latter configuration. This also leads to an anti-crossing of a light and heavy hole state which manifests itself clearly in both the P.L. and P.L.E. data.

Acknowledgements The authors wish to thank the Science and Engineering Research Council (U.K.) for supporting this work. One author (L.S.) would like to thank the University of Hull for the award of a Brammor Jones Scholarship.

References

- [1] Semiconductors and Semimetals, R. K. Willardson and A. C. Beer, Treatise Editors, J. K. Furdyna and J. Kossut, Volume Editors, Academic Press, Boston 1983 Vol. 23.
- [2] Physics and Chemistry of III-V Compounds, ed. J. S. Prener and V. Averb, North Holland Publishing Co. (1969).
- [3] L. J. Gregory, J. F. Nicholls, J. J. Davies, J. O. Williams and A. Maung, Semicond. Technol. 3 1193 (1986).
- [4] D. R. Yakovlev, Festkörperprobleme, Advances in Solid State Physics 32, ed. by L. Rosler (Vieweg, Braunschweig/Wiesbaden 1992) 251.
- [5] M. Kohl, M. R. Freeman, J. M. Hong and D. D. Awschalom, Phys. Rev. B 43 2111 (1991).
- [6] I. Stürmer, P. Harrison, W. I. Hagston and J. P. Gerdien, J. Appl. Phys. 73 5081 (1993).
- [7] L. Z. Kachibovich, Solid State Commun. 80 283 (1991).
- [8] P. Jorda, A. Wasiele, A. Morle, J. Vabre, D. I. Ashenford and B. Lunn, Phys. Rev. B 47 1251 (1993).

ThP6

Time-resolved photoluminescence studies of simulated emission and excitation dynamics in $\text{ZnSe/ZnSn}_{18}\text{S}_{82}$ superlattices

C. J. Stevens, R. A. Taylor & J. E. Ryan
University of Oxford, Department of Physics,
Clarendon Laboratory, Parks Road, Oxford, England OX1 3PU
M. Dalbacci, M. Ferrara, R. Cogoliotti
Department of Physics, Università degli Studi Di Bari, Bari, Italy
Y. Kuroda, J. Suenne
Faculty of Engineering, Hiroshima University, Higashihiroshima 724, Japan

We report measurement of time-resolved photoluminescence from $\text{ZnSe/ZnSn}_{18}\text{S}_{82}$ superlattices. We observe an anomalous fast decay component in the luminescence at an energy corresponding to that at which simulated emission is observed at high pump densities. From consideration of the timescales and spectral position of the fast line, we infer an excitation scattering mechanism to be responsible for fast decay in these samples.

1. Introduction

Recent developments in the growth of II-VI semiconductor heterostructures [1] have led to the fabrication of laser diodes operating at wavelengths in the green and blue [2]. The physical processes which give rise to simulated emission from these materials, particularly in the low threshold layers, are not well understood and make the subject of some controversy. It is photon assisted recombination [1] and exciton mediated scattering [4] have been proposed as possible mechanisms. In this paper we report on time-resolved photoluminescence measurements of simulated emission and excitation dynamics in $\text{ZnSe/ZnSn}_{18}\text{S}_{82}$ superlattices which have been shown to display low threshold lasing [3].

2. Experiment

The sample studied here is a 0.01 period $\text{ZnSe/ZnSn}_{18}\text{S}_{82}$ symmetric superlattice with 10 nm layer widths, grown on a GaAs substrate. The intrinsic confinement for this ternary composition is not strong, the conduction band offset is approximately 100 meV, while the valence band offset is 100 meV [6]. It is not clear yet whether the band alignment is type I or II [7]. The excitation binding energy E_b is roughly 100 meV, yet whether the band alignment is type I or II [7]. The excitation binding energy E_b is roughly 100 meV, yet whether the band alignment is type I or II [7]. The excitation binding energy E_b is roughly 100 meV, yet whether the band alignment is type I or II [7].

Photoluminescence was excited using a frequency doubled, modelocked Ti:sapphire laser which produces a 76 MHz train of 150 fs pulses at 410 nm (1.2 eV) with an average power of 150 mW. Luminescence was detected using a synchronous streak camera and an intensified silicon detector. A subtractive dispersion double spectrometer with a bandwidth of 10 nm (FWHM) was used to select different luminescence wavelengths. The overall time resolution was 20 ps. The maximum carrier density generated in the time-resolved experiments was $\sim 5 \times 10^{18} \text{ cm}^{-3}$, which is somewhat lower than that required for optically pumped lasing. In order to study simulated emission at low time resolution, we used a frequency tripled Nd:YAG laser which produces a full beam of 100 ps pulses at 355 nm (3.5 eV).

The sample had cleaved faces forming a 100 nm optical cavity. Free emission was measured from a cleaved face, the pump beam being focused to a 100 nm diameter spot. Stimulated emission was used to vary the excitation density while keeping the illuminated volume constant. All of the measurements reported here were made with the sample mounted in a He gas flow cryostat with a base temperature of 4 K.

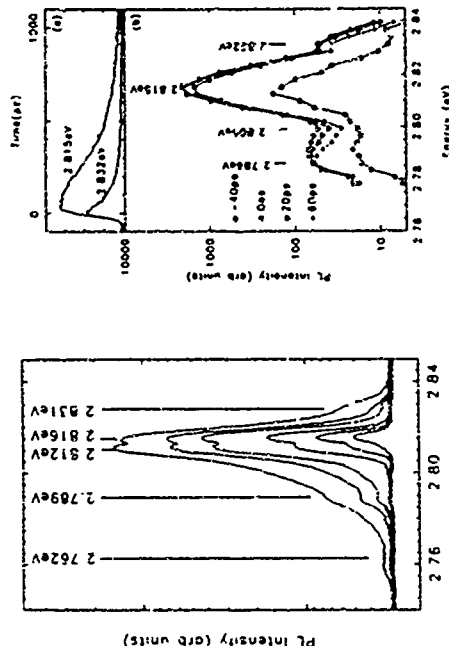
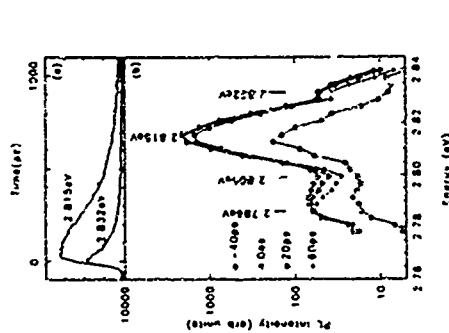


Figure 1. Edge emission spectra at pumping powers of 150, 75, 37.5, 18.75, 9.375, 4.6875, 2.34375, and 1.171875 mW. The inset shows a zoomed-in view of the 2.812 eV peak.



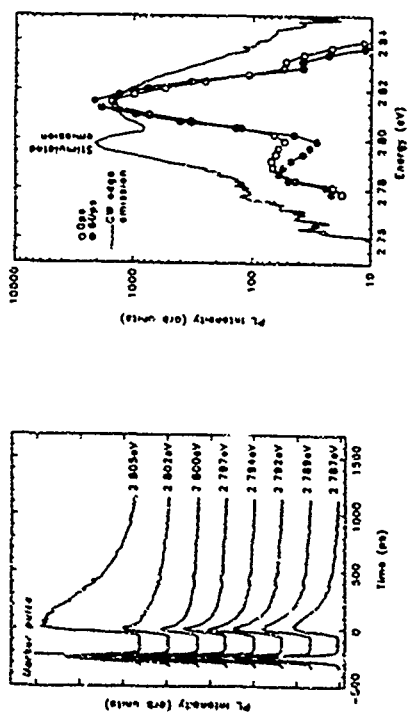


Figure 3 Time evolution of the PL signal in edge emission geometry at energies near the measured simulated emission energy of 2.83 eV

Fig. 3 shows in more detail the time evolution of the signal at different energies in the range 2.787 eV - 2.805 eV where the fast recombination is observed. At the upper and lower extremes the decay time is rather long, roughly equal to that of the 1 line (see Fig. 2(a)). However, close to 2.83 eV there is a very distinct fast component superimposed on the slower bound exciton recombination (the detection bandwidth here is 6 meV). The rapid onset and decay of this component are very similar to that of the free exciton luminescence (see Fig. 2(a)). This observation is strongly suggestive that the recombination in this energy range originates from free excitons.

Simulated emission from the sample was measured under conditions of more intense excitation with long (10 ns) laser pulses (the laser intensity at the sample was $\sim 10^{18} \text{ W cm}^{-2}$, generating an estimated carrier density of 10^{17} cm^{-3}). The time integrated luminescence spectrum presented in Fig. 4 shows the 1 band together with strong simulated emission at 2.83 eV. Also reproduced in the figure are the 1 and 2 band time-resolved spectra obtained at lower excitation densities; the comparison shows quite convincingly that the 1,2 decay and the simulated emission are related.

Discussion

The time-dependence of the 2.83 eV spontaneous emission (Fig. 3) indicates that free excitons are involved since the temporal evolution of both signals are very similar. The free exciton luminescence at 2.83 eV (2.1 meV) lies higher in energy by one LO phonon energy, which suggests that excitation scattering to the lower polariton branch by LO phonon emission is a possible mechanism. However, the heavy hole exciton absorption peak in a similar sample has been measured to be at 2.825 eV [8], which would require that the luminescence involves hot exciton recombination, and that the phonon wavevector is approximately $3.82 \times 10^8 \text{ cm}^{-1}$. The mechanism leading to stimulated emission, however, is not so clear: not only must the optical field be coherent, but so also must the phonons. Since the initial reports by Holmbeck and co-workers [9] of lasing on phonon sidebands of electron-hole plasma recombination in GaAs, it has not been

possible to establish the presence of coherent nonequilibrium phonons, and no lasing mechanism which involves phonon emission have remained in doubt.

The results presented here clearly identify the energy for stimulated emission to be in the low energy wing of the bound exciton luminescence. In addition to the possibility of free exciton phonon emission just mentioned, the obvious mechanisms for lasing involve the recombination of bound excitons, and free exciton-bound exciton scattering. The first of these can most likely be ruled out on the basis of the low density of excited states; furthermore, the rate at which excitons can be trapped at the relevant sites is relatively slow, as we have seen above (Fig. 2), which further dictates against this mechanism. An excitonic scattering mechanism in which the free exciton is removed and the bound exciton recombines is energetically favourable, as the BE emission at 2.816 eV lies approximately one exciton binding energy (19 meV) above the 2.83 eV emission. However, it would seem that this process would saturate at high pump levels, determined by the trap density and exciton trapping kinetics. Consequently, this excitonic mechanism would be expected to give way eventually to plasma formation and stimulated emission in the usual fashion so far as this has not been observed.

Conclusions

We have made time-resolved luminescence measurements of spontaneous emission in a $\text{ZnSe/ZnS}_{0.98}\text{Se}_{0.02}$ symmetric superlattice and found evidence of efficient exciton phonon-assisted recombination. This emission occurs at the same energy as simulated emission of 'trapped' at much higher excitation density, which suggests that the lasing mechanism may involve exciton-phonon interactions.

This work was supported by SERC in the UK and CNR in Italy.

References

- [1] Shahzad K., Olego D. J., Van de Walle C. G. and Cammack D. A. 1990 *J. Lumin.* 46 109
- [2] Nakajima K., Suemura I., Nishio H., Kuroda Y. and Yamashita M. 1990 *Lap-nese Journal of Appl. Phys. Part 2 Letters* 29 7072
- [3] Nakajima K., Suemura I., Fumi Y., Kuroda Y., Yamashita M. 1991 *Appl. Phys. Lett.* 59 1401
- [4] Ding J., Joss H., Nishio H., Hagerott M., Nurmikko A. V. 1992 *Phys. Rev. Lett.* 69 1707
- [5] Shahzad K., Olego D. J., Van de Walle C. G. 1988 *Phys. Rev. B* 38 1417
- [6] Dabbicco M., Lepore M., Cingolani R., Scamarcio G., Ferrara M., Suemura I. 1992 *Semicond. Sci. Technol.* 7 681
- [7] Landolt-Bornstein, Properties of II-VI & I-VII compounds, Semimagnetic Semiconductors p127
- [8] Tommasi R., Lepore M., Neri K., *4th European Quantum Effect Conf.* 1991 (to be published)
- [9] Holmbeck N., Kolbas R. M., Dupuis R. D., Dajkovic P. D. 1980 *IEEE J. Quant. Elect.* QE-16 170

ThP7

STRAIN, CONFINEMENT, CARRIER DYNAMICS, AND HIGH DENSITY EFFECTS IN ZnSe/ZnMnSe-QUANTUM STRUCTURES

F. Kretler, A. Schulgen, F. Henneberger, J. Puls, and U. Stiller

Humboldt-Universität zu Berlin, Fachbereich Physik,
Sitz: Invalidenstr. 110 Unter den Eichen 6, 10099 Berlin (Germany)

ABSTRACT

MBE grown ZnSe/ZnMnSe quantum structures are investigated using various spectroscopic techniques. Conventional photoluminescence and excitation spectroscopy demonstrate an enhanced effective band offset due to tensile strain and a confinement induced shift of the excitonic resonances up to 100 meV. Time-resolved luminescence reveals progressive localization of excitons on the 10 ps-time scale followed by rapid recombination within 100 ps. Optical gain is observed under 400 kW/cm² excitation which is interpreted in terms of an electron-hole plasma.

1. INTRODUCTION

Wide-gap II-VI semiconductor related quantum structures are very promising candidates for electro-optical and photonic devices operating in the blue-green spectral range. Recent progress has occurred in heteroepitaxial and doping techniques, leading to profound improvement in material quality as well as proof-of-concept devices for blue-green light emitters in the ZnSe-based quantum well configuration [1, 2].

In this paper we focus on ZnSe/ZnMnSe quantum well structures. Our aim is to study a binary quantum well with no alloy fluctuations in addition the emission wavelength can be tuned deeper into the blue range as compared with ZnCdSe/ZnSe mostly used until now for laser devices. Early work on ZnSe/ZnMnSe structures was done by the groups of Brown and Pardee [3], but no systematic conclusions were achieved with respect to both growth perfection and optical properties.

The structures of the present study were grown by molecular beam epitaxy on (001) GaAs substrates, on top of which a ZnSe buffer layer was first deposited. Typically, a structure consists of 10 ZnSe quantum wells of the same thickness separated by about 100 nm wide ZnMnSe barrier layers. The well widths studied range from 1 to 10 nm. A composition of 20 to 28 percent results in a total band offset of 0.5 to 1.2 eV. [4] Steady-state photoluminescence (PL) and photoluminescence excitation (PLE) spectra demonstrate the reproducible growth of high quality type I quantum structures. The low temperature PL spectra are dominated by a light hole (lh) emission band accompanied by a more or less distinct low energy shoulder which is typical for all quantum well samples investigated. In the PLE spectra both the light and heavy hole (hh) excitation transitions are observed. The FWHM of the excitonic resonances is on the order of 5 to 10 meV and a Stokes-shift between PL and PLE of 3 to 6 meV is found.

2. STRAIN AND CONFINEMENT

In Fig. 1 the energetic positions of the n=1 lh and hh exciton resonances for different well widths taken from PLE spectra are shown. The data demonstrate the interplay between strain

and confinement. The structures are designed in a way (well width clearly smaller than both critical thickness and barrier width) so that the misfit induced strain is entirely and coherently assimilated by the ZnSe quantum well. As the (001) lattice constant of ZnMnSe is the larger one this strain is tensile and for the present barrier composition (x=0.25) on the order of 5 to 10 %. A characteristic feature of a tensile in-plane strain situation is that the exciton resonances shift to lower energies and that the lh excitons occur energetically below the hh one [5]. As a consequence of this, the exciton structures of the larger wells in Fig. 1 appear below the position of the ZnSe bulk exciton. † Decreasing the well width the influence of the carrier confinement becomes increasingly important. For the 1 nm well a confinement induced high-energy shift of about 100 meV is found for the lh-exciton resonance.

In consistency with the assignment based upon the above strain discussion the hh exciton with the heavier mass exhibits a weaker confinement shift so that the lh and hh structures eventually merge together for wells smaller than 2 nm. A variational calculation of the lh and hh exciton energy using a trial function of the form [6]

$$\Phi_r = \Phi_e(z_r) \Phi_h(z_r) \sqrt{\frac{1}{x^2}} e^{-\frac{z}{x}} \quad (1)$$

(with x as parameter of variation) yields a reasonably good agreement with the experimental data. The fit in Fig. 1 relies on commonly accepted bandstructure parameters of ZnSe ($\chi=4.089$, $\gamma_1=1.404$, $m_e=0.06$, $m_h=0.4$, $F_0=2.822$ eV) and a total band offset of 76 meV

between the unstrained materials taken from [4]. We deduced from the calculation that 40 meV of this total offset stem from the conduction and 30 meV from the valence band. The actual band offsets are enhanced by the strain. The fit yields 5 meV for both electron and hh and 45 meV for lh, respectively. Thus, the effective offset for the lh exciton of 120 meV is considerably larger than predicted without strain. In addition to the offsets the calculation provides exciton parameters. We find a maximum binding energy of 25 meV for $d_w=4.5$ nm.

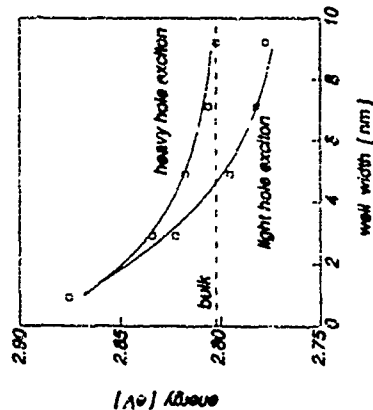


Fig. 1 Energetic positions of the lh and hh exciton resonances deduced from PLE spectra of ZnSe/Zn_{0.25}Mn_{0.75}Se MQWs at 5K □ experimental points, line calculation

† For superlattice structures of equal barrier and well width the exciton resonances occur at higher energies than those of the structures in Fig. 1 with the same well width as an average strain across barrier and well is formed.

3. TIME-RESOLVED PHOTOLUMINESCENCE

The excitation dynamics in the quantum structures are studied by time-resolved PL. Tunable sub-ps pulses in the blue spectral range are used to excite electron-hole pairs resonantly at the transitions of the 1h and 2h excitation as well as in the barrier. Decay curves at different spectral positions across the 1h excitation band are recorded with a synchroscan streak camera yielding an overall time resolution after data deconvolution of 5 ps.

The time behaviour of the 1h excitation PL is practically the same for each of the three excitation wavelengths. Thus, capture of the carriers by the well and subsequent relaxation into the 1h excitation state is completed on a 1 ps time scale. In Fig. 2 the rise and decay times for a sample of intermediate well width deduced from the PL decay curves are shown. For comparison the time-integrated PL measured under the same excitation conditions is given. On the low-energy side of the 1h excitation band a clearly resolved rise of the PL within some 10 ps is found followed by a decay within approximately 100 ps. With increasing photon energy both time constants decrease continuously. At the high-energy edge of the PL band the rise is not further resolved, whereas the decay time comes into the order of the rise time at the low energy tail. We attribute this behavior to progressive localization of the excitons at barrier alloy fluctuations. The interplay between spectral diffusion and rapid recombination leads to a non-thermal carrier distribution and causes the low energy structure in the steady-state PL line shape of the 1h excitation. An exceedingly large radiative rate of the ZnSe quantum well is suggested by the 100 ps decay time. A detailed study of the radiative yield is in progress.

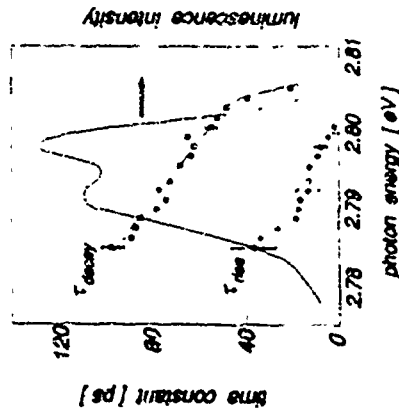


Fig. 2 Left scale: Photon-energy dependence of the PL rise and decay times of a MQW structure consisting of 10 periods of 5 nm ZnSe and 85 nm Zn_{0.4}Mn_{0.6}Se layers. Right scale: Time-integrated PL.

4. HIGH EXCITATION AND GAIN

Intensive sub-ps pulses from a dye laser are used to excite the samples in a quasi-steady state mode. The emission signal is dispersed by a grating monochromator and subsequently detected with a MCP-photomultiplier.

Spontaneous emission spectra were recorded in a backward geometry. The data for the same sample used for the time-resolved measurements presented above are summarized in

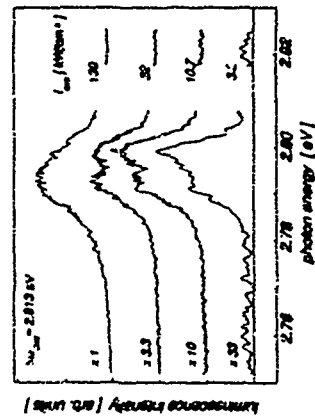


Fig. 3 5K spontaneous emission spectra of the same ZnSe-MQW as in Fig. 2 at various excitation intensities. Excitation is at the 1h excitation resonance.

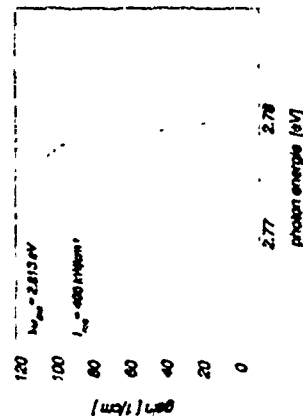


Fig. 4 Gain spectrum of the same ZnSe-MQW sample as in Fig. 3 obtained by the stripe-length method at 5K.

Fig. 3. For excitation intensities below 10 kW/cm² the spontaneous emission is very similar to the low-density (time-integrated) PL spectrum shown in Fig. 2. Further increasing of the excitation intensity yields a growing contribution in the spectral range of the low-energy shoulder. Simultaneously, the width of the structures increase. At 130 kW/cm² only a broad band is seen with a pronounced low-energy tail. For even higher intensities the spectra are distorted by stimulation effects.

For gain measurements the method of stripe-length variation is applied [7]. A rectangularly shaped spot of variable width (30-350 μm) and fixed height (30 μm) is focused onto the sample at a cleaved edge along the natural (110) cleavage plane. A typical unsaturated gain spectrum obtained at an excitation intensity of 400 kW/cm² is presented in Fig. 4. The spectral gain is found to be very sharp with a FWHM of approximately 5 meV and a maximum value of 100 cm⁻¹.

Different processes are known to explain stimulated emission at low temperatures in wide gap II-VI compounds. At intermediate intensities exciton-phonon and exciton-exciton scattering processes dominate, whereas above the Mott-transition the gain is due to the population inversion in the degenerated ch-plasma. Recently, it was shown that also excitons localized at alloy composition fluctuations in ternary quantum wells can give rise to gain at intermediate densities [8]. Taking into account the carrier lifetime of about 100 ps determined above and an absorption coefficient of 10⁴ cm⁻¹ an electron-hole pair density of 3·10¹⁷ cm⁻³ is estimated at the excitation intensity used in the present gain studies. This value is clearly above the Mott-density and a

ThP8

PBSrS MQW LASERS AND THE EFFECT OF QUANTUM WELL ON OPERATION TEMPERATURE

A. Ishida, N. Sakurai*, K. Aikawa, and H. Fujiyasu
Faculty of Engineering, Shizuoka University,
Johoku 3-3-1, Hamamatsu 432, Japan

*Graduate School of Electronic Science & Technology,
Shizuoka University, Johoku 3-3-1, Hamamatsu 432, Japan

Abstract: Very few studies have been performed for IV-VI narrow gap semiconductor quantum well lasers especially for the laser with small well width, probably owing to the large diffusion of the constituents. In narrow gap semiconductor, it is considered that the free carrier absorption strongly affects the laser operation as well as Auger recombination, and that the multiple quantum well structure is very effective in increasing the maximum operation temperature. We prepared PbS_{0.95}/PbS multiple quantum well (MQW) lasers with well width as large as 100 Å using the wet layer epitaxy technique. The laser properties are compared with that of PbS_{0.95}/PbS and PbS_{0.95}/PbS_{0.95} Di lasers. The MQW laser showed small threshold current compared with that of Di laser, and pulsed laser operation was obtained up to 253 K (280 °C). The operation temperature is the highest ever reported for PbS based semiconductor lasers. In this paper, properties of the PbS_{0.95} MQW lasers and effects of the quantum well on the laser properties, especially on the operation temperature, are discussed.

renormalized bandgap of 2.76 eV follows from the theory [9]. The rather well with the low-energy onset of the gain spectrum, which supports the gain in terms of an electron plasma.

In conclusion, the present study has demonstrated that the ZnSe/ZnMnSe system provides high-quality type-I quantum structures with robust confinement. We have observed exciton localization and very rapid recombination within 100 ps. Stimulated emission related to an electron plasma yields gain in 100 cm⁻¹ range.

Acknowledgements: The authors thank N. Hoffmann, J. Griesche, K. Jacobs for cooperation in the MBE growth. This work was partly supported by the Deutsche Forschungsgemeinschaft.

REFERENCES

1. M. A. Haase, J. Qu, J. M. DePuydt and H. Cheng, *Appl. Phys. Lett.* **59**, 1272 (1991)
2. H. Jeon, J. Ding, W. Patterson, A. V. Nurmikko, W. Xie, D. C. Grillo, M. Kobayashi and R. L. Gunshor, *Appl. Phys. Lett.* **59**, 1619 (1991)
3. L. A. Kolodziej, R. L. Gunshor, N. Otsuka, S. Datta, W. M. Becker and A. V. Nurmikko, *IEEE J. Quantum Electronics* **QE-32**, 1666 (1986)
4. R. L. Gunshor, L. A. Kolodziej, N. Otsuka and S. Datta, *Surf. Sci.* **174**, 522 (1986)
5. G. L. Bir and G. E. Pikus, *Symmetry and Strain-Induced Effects in Semiconductors* (Wiley, New York (1974))
6. G. Bastard, *Wave Mechanics Applied to Semiconductor Heterostructures* (Les editions de physique, Les Ulis, France (1988))
7. K. L. Shaklee and R. F. Leheny, *Appl. Phys. Lett.* **18**, 475 (1971)
8. J. Ding, H. Jeon, T. Ishihara, M. Hagerott, A. V. Nurmikko, H. Luo, N. Samarth and J. Furdyna, *Phys. Rev. Lett.* **69**, 1707 (1992)
9. S. Schmitt-Rink, D. S. Chemla and D. A. B. Miller, *Adv. Phys.* **38**, 89 (1989)

1. INTRODUCTION

IV-VI compounds are narrow gap semiconductors with the direct gap at Γ point in the Brillouin zone. Various lasers have been prepared using the IV-VI compounds [1-5]. Band gaps of the PbSe and PbS decrease with the Sn content, and they have been used as lasers of 6-20 μ m range. Operation temperature of these lasers were usually less than 200K, owing to the large Auger recombination probability and strong free carrier absorption in the narrow gap semiconductors and also poor carrier confinement [6]. Recently, PbSe, PbS, and PbSSe lasers have been reported [7-10]. The band gap of the film lasers have been reported 7-10 μ m. The band gap of the film increases very rapidly with the Sn or Se content, and they are very useful for cladding layers of the PbSe, PbS, or PbSSe lasers. These lasers can cover the wavelength range of 2-8 μ m [10-12], and many of the lasers operate above 200 K in pulsed condition owing to the effective carrier confinement and relatively small Auger recombination. However, room temperature operation is difficult owing to some large loss mechanisms of light and carrier in the narrow gap semiconductors. The multiple quantum well structure is considered to be very effective to increase the maximum operation temperature, because relatively small injected carrier density is needed to obtain population inversion and large optical gain, which exceeds strong free carrier absorption in the narrow gap semiconductor. It is obtained by the VQW structure.

In this paper, first we describe and discuss operation condition of the PbS, PbSSe, and VQW lasers, then preparation and properties of the VQW and DB lasers are described and the effect of the quantum well on the operation temperature are discussed.

2. OPERATION CONDITION OF PbS, PbSSe DBL and VQW LASERS

Figure 1 shows the joint density of states $D(h\nu)$ and gain $g(h\nu)$ of the PbS, PbSSe DBL (a) and VQW (b) lasers at 300K. For the joint density of states of the VQW laser conduction band offset was assumed to be equal to that of valence band, and 1 μ m thick optical confinement layer with 10 periods of PbSSe(200Å) / PbS (100Å) VQW active layer was assumed. In the gain calculation all the light was assumed to be confined in the optical confinement layer, so the real gain is somewhat smaller than this value. DBL(b) in the Fig. 1 shows the joint density of states in which corresponding conduction band states are filled with electrons. The integral of the $D(h\nu)$ with respect to the photon energy by represents electron concentration in the conduction band. Hole concentration was assumed to be equal to that of the electron in this gain calculation. In Fig. 1(b), the carrier concentration in the active layer is $6.5 \times 10^{18} \text{ cm}^{-3}$, and the optical gain expected is as high as 300 cm^{-1} . In the narrow gap semiconductor main optical loss is free carrier absorption which can be estimated by the equation below [16]

$$\alpha_{\text{FCA}} = \frac{2}{\pi} \pi^2 \frac{E_g}{\hbar^2} \frac{1}{v} \left(\frac{m_e}{m_0} \right)^{1/2} \frac{n}{p_0} \quad (2)$$

where p_0 and p_n are the mobility of the electron and hole, and the m_e and m_h are the conductivity effective mass of the holes and electrons, respectively. The free carrier absorption is proportional to the carrier concentration and wavelength squared, and inversely proportional to the mobility. Free carrier absorption is calculated to be around 250 cm^{-1} for the electron and hole pairs shown in Fig. 1(a) using the Eq. (1). Real free carrier absorption seems to be somewhat larger than this value, and it is understood that very high concentration carriers are needed obtaining sufficient optical gain. In calculating threshold current of the laser, life time of the carrier should be considered. Life time of the spontaneous emission of the PbS is about $1 \times 10^{-8} \text{ s}$, and real life time of the carrier is much shortened by a carrier loss mechanism such as the Auger recombination, which increases strongly with temperature and carrier concentration. Taking the life time of the carrier as $1 \times 10^{-9} \text{ s}$, and active layer thickness as 1 μ m, the threshold current of the PbS/PbSSe DBL laser becomes as high as 100 kA/cm^2 at room temperature. For the VQW laser, carrier concentration needed to the laser operation is strongly decreased by the two-dimensional density of states as shown in Fig. 1 (b). In the model, band gap difference between PbS quantum well and PbSSe barrier or PbSSe optical confinement layer is assumed to be 170 meV, and optical gain as high as 400 cm^{-1} can be obtained by the carrier concentration of only $2.5 \times 10^{18} \text{ cm}^{-3}$. It should be noted that only $7 \times 10^{18} \text{ cm}^{-3}$ of electrons are in the quantum well and the rest is overflowing to optical confinement layer. The ratio of the overflowing carriers to the carriers in the quantum well increases with the decrease of the number of quantum wells. Maximum gain obtained from one quantum well is as high as 120 cm^{-1} [13], and the gain for the single quantum well laser becomes very small increasing only overflowing current. Thus it is understood that the VQW structure is very effective for the laser with large free carrier absorption, and that the single quantum well laser is not effective for the narrow gap semiconductor laser with the large optical losses.

3. PREPARATION AND PROPERTIES OF PbS/PbSSe LASERS

Figure 2 shows the PbS, PbSSe multiple quantum well laser structure prepared on p-type PbS substrate. PbS layer (2 μ m) and PbSSe (200Å) cladding layer (2 μ m). PbSSe (200Å) layer (0.3 μ m) for optical confinement and VQW active layer (0.3 μ m) which consists of 10 periods of PbSSe(200Å)/PbS(100Å) SL were prepared on the active layer. PbSSe (200Å) layer

(0.35 μm) and $\text{Pb}_{0.97}\text{Sr}_{0.03}$ cladding layer (2 μm) were prepared successively. The room temperature band gap of the PbS is 110 meV. Band gap of the cladding layer is 660 meV, and that of the optical confinement layer is 580 meV. Laser structure prepared is stripe contact laser with stripe width of 50 μm and length of 300-1000 μm . Pulsed laser operation was measured for the laser with 1 ps pulse width and 250 Hz repetition. Figure 3 shows the dependence of the threshold current of the PbS laser (closed circle), $\text{Pb}_{0.97}\text{Sr}_{0.03}/\text{PbS}$ (open circle) and $\text{Pb}_{0.97}\text{Sr}_{0.03}/\text{Pb}_{0.97}\text{Sr}_{0.03}/\text{PbS}$ (square for undoped active layer, and triangle for doped active layer) the $\text{PbS}/\text{PbS}/\text{PbS}$ DI laser has PbS active layer of 0.5 μm and this is the one which showed highest operation temperature [9]. The thickness of the $\text{Pb}_{0.97}\text{Sr}_{0.03}$ active layer of $\text{PbS}/\text{PbS}/\text{PbS}$ DI laser is also 0.5 μm , and doping level of the doped p-type PbS/PbS active layer is the order of 10^{18} cm^{-3} . Threshold current of the laser with PbS/PbS active layer becomes somewhat higher than that of PbS active layer, and significantly increase for the laser with doped active layer. This is considered to be due to the free carrier absorption in the low mobility PbS/PbS active layer. Since the mobility of the carrier strongly decreases with Sr content [11], the free carrier absorption effect becomes also important in the cladding layer of the DI laser and optical confinement layer in the PbS laser. For the PbS laser significant decrease of the threshold current was observed as expected and laser operation was observed up to 253 K, which is the highest operation temperature ever reported for the PbS based lasers.

Figure 3 shows the output photon energy of the PbS and DI lasers. Output photon energy of the $\text{PbS}/\text{PbS}/\text{PbS}$ DI laser is about 20 meV higher than the band gap of unstrained PbS . This is due to the strain caused by the lattice mismatch between PbS/PbS cladding and PbS active layers [12]. At high temperature, difference between heat sink and active layer is somewhat affecting the deviation of the output photon energy. Dashed line in the figure shows the energy between first conduction and valence subbands calculated for the PbS structure without strain. Tensile strain of the PbS quantum well layer is increasing the band gap also. It should be noted that the temperature dependence of the output photon energy for the PbS laser and PbS/PbS laser with doped active layer is somewhat different from the others. Since the threshold current of the PbS/PbS laser with doped active layer is very large, this is considered to be due to the temperature difference between heat sink and the active layer. For the PbS laser, hole and electron effective masses increase with the temperature as the band gap increases. Thus the output photon energy of the PbS laser increases somewhat slowly compared with the band gap increase of the PbS bulk.

In this experiment clear decrease of the threshold current was observed for the PbS laser, and significant increase of the operation temperature is expected for PbS lasers. If optimum laser structure is taken from the threshold current densities of the $\text{PbS}/\text{PbS}/\text{PbS}$ DI and PbS lasers, it is also estimated that the life time of the minority carrier is as high as $5 \times 10^{-8} \text{ s}$.

below 200 K and the lifetime seems to be decreasing rapidly with the temperature above 200 K. Free carrier absorption becomes significant at high temperature, but the absorption only can not explain the rapid increase of the threshold current. Other mechanism such as Auger recombination or recombination through crystal imperfection should be considered combined with the free carrier absorption. In our calculation band offsets of the conduction and valence band edges are assumed to be equal. Real heterojunction may have different band offsets. So effect of the carriers overflowing to the cladding layer may also affecting the threshold current at high temperature.

4. SUMMARY

PbS/PbS PbS laser was prepared by hot wall epitaxy, and pulsed laser operation was obtained up to 253 K (2.80 μm). This laser was compared with that of PbS/PbS and $\text{PbS}/\text{PbS}/\text{PbS}$ DI lasers, and clear decrease of the threshold current was observed in the PbS compound laser. It was shown that the free carrier absorption becomes one of the main loss mechanism, and the PbS laser is useful for the reduction of the threshold current because the PbS structure gives large gain with relatively small carrier concentration injected.

Acknowledgement - We would like to thank Mr. K. Matsushita for preparing PbS single crystal for the laser preparation.

1. H. Preier, M. Delecker, A. Riedel and H. Muter, Appl. Phys., Lett., 28, 669(1976)
2. A. Halpole, A. R. Calawa, T. C. Harman and S. H. Groves, Appl. Phys., Lett., 20, 552(1976).
3. A. Shinkha, Y. Nishijima, H. Ebe, A. Ishida, and H. Fujiyasu, Appl. Phys. Lett., 47, 1184(1985).
4. A. P. Shotoy and Yu. G. Spitsynov, JETP Lett., 15, 3(1987).
5. Y. Nishijima, J. Appl. Phys., 65, 935(1989).
6. W. Anderson, IEEE J. Quantum Electron., QE-13, 532(1977).
7. D. L. Partin, Superlattices and microstructures, 1, 131(1985).
8. B. Spanger, V. Schlegel, A. Ambrecht, H. Hütner, and H. Tacke, Appl. Phys., Lett., 53, 2582(1988).
9. A. Ishida, K. Yamamoto, H. Tanaka, and H. Fujiyasu, Appl. Phys., Lett., 55, 430(1989).
10. H. Tacke, B. Spanger, A. Ambrecht, P. R. Norton and H. Hütner, Appl. Phys., Lett., 53, 2260(1988).
11. D. L. Partin and C. N. Thrush, Appl. Phys., Lett., 15, 193(1981).
12. S. Kohnemann, J. K. Nakano, A. Ishida, and H. Fujiyasu, Jpn. J. Appl. Phys., 32, 1658(1993).
13. A. Ishida, Y. Sase, T. Okamura, H. Fujiyasu, Y. Nishijima, and A. Shinkha, Superlattices and Microstructures, 6, 27(1989).
14. A. Shinkha, K. Yamamoto, K. Ishino, and H. Fujiyasu, Semicond. Sci. Technol., 5, 533(1990).
15. H. Hütner, V. Schlegel, H. Tacke, Superlattices and Microstructures, 7, 97(1990).

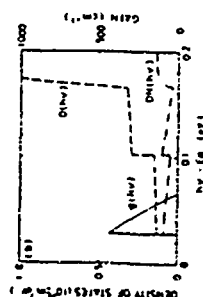
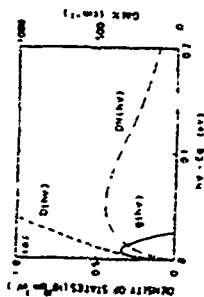
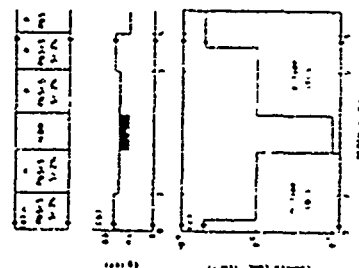


Fig. 1. Joint density of states $\rho(\omega)$ and optical gain $g(\omega)$ of PbInAs and InGaAs layers. The $\rho(\omega)$ in the figure shows joint density of states in which corresponding conduction band states are filled with electrons.



2015
 2014
 2013
 2012
 2011
 2010
 2009
 2008
 2007
 2006
 2005
 2004
 2003
 2002
 2001
 2000
 1999
 1998
 1997
 1996
 1995
 1994
 1993
 1992
 1991
 1990
 1989
 1988
 1987
 1986
 1985
 1984
 1983
 1982
 1981
 1980
 1979
 1978
 1977
 1976
 1975
 1974
 1973
 1972
 1971
 1970
 1969
 1968
 1967
 1966
 1965
 1964
 1963
 1962
 1961
 1960
 1959
 1958
 1957
 1956
 1955
 1954
 1953
 1952
 1951
 1950
 1949
 1948
 1947
 1946
 1945
 1944
 1943
 1942
 1941
 1940
 1939
 1938
 1937
 1936
 1935
 1934
 1933
 1932
 1931
 1930
 1929
 1928
 1927
 1926
 1925
 1924
 1923
 1922
 1921
 1920
 1919
 1918
 1917
 1916
 1915
 1914
 1913
 1912
 1911
 1910
 1909
 1908
 1907
 1906
 1905
 1904
 1903
 1902
 1901
 1900
 1899
 1898
 1897
 1896
 1895
 1894
 1893
 1892
 1891
 1890
 1889
 1888
 1887
 1886
 1885
 1884
 1883
 1882
 1881
 1880
 1879
 1878
 1877
 1876
 1875
 1874
 1873
 1872
 1871
 1870
 1869
 1868
 1867
 1866
 1865
 1864
 1863
 1862
 1861
 1860
 1859
 1858
 1857
 1856
 1855
 1854
 1853
 1852
 1851
 1850
 1849
 1848
 1847
 1846
 1845
 1844
 1843
 1842
 1841
 1840
 1839
 1838
 1837
 1836
 1835
 1834
 1833
 1832
 1831
 1830
 1829
 1828
 1827
 1826
 1825
 1824
 1823
 1822
 1821
 1820
 1819
 1818
 1817
 1816
 1815
 1814
 1813
 1812
 1811
 1810
 1809
 1808
 1807
 1806
 1805
 1804
 1803
 1802
 1801
 1800
 1799
 1798
 1797
 1796
 1795
 1794
 1793
 1792
 1791
 1790
 1789
 1788
 1787
 1786
 1785
 1784
 1783
 1782
 1781
 1780
 1779
 1778
 1777
 1776
 1775
 1774
 1773
 1772
 1771
 1770
 1769
 1768
 1767
 1766
 1765
 1764
 1763
 1762
 1761
 1760
 1759
 1758
 1757
 1756
 1755
 1754
 1753
 1752
 1751
 1750
 1749
 1748
 1747
 1746
 1745
 1744
 1743
 1742
 1741
 1740
 1739
 1738
 1737
 1736
 1735
 1734
 1733
 1732
 1731
 1730
 1729
 1728
 1727
 1726
 1725
 1724
 1723
 1722
 1721
 1720
 1719
 1718
 1717
 1716
 1715
 1714
 1713
 1712
 1711
 1710
 1709
 1708
 1707
 1706
 1705
 1704
 1703
 1702
 1701
 1700
 1699
 1698
 1697
 1696
 1695
 1694
 1693
 1692
 1691
 1690
 1689
 1688
 1687
 1686
 1685
 1684
 1683
 1682
 1681
 1680
 1679
 1678
 1677
 1676
 1675
 1674
 1673
 1672
 1671
 1670
 1669
 1668
 1667
 1666
 1665
 1664
 1663
 1662
 1661
 1660
 1659
 1658
 1657
 1656
 1655
 1654
 1653
 1652
 1651
 1650
 1649
 1648
 1647
 1646
 1645
 1644
 1643
 1642
 1641
 1640
 1639
 1638
 1637
 1636
 1635
 1634
 1633
 1632
 1631
 1630
 1629
 1628
 1627
 1626
 1625
 1624
 1623
 1622
 1621
 1620
 1619
 1618
 1617
 1616
 1615
 1614
 1613
 1612
 1611
 1610
 1609
 1608
 1607
 1606
 1605
 1604
 1603
 1602
 1601
 1600
 1599
 1598
 1597
 1596
 1595
 1594
 1593
 1592
 1591
 1590
 1589
 1588
 1587
 1586
 1585
 1584
 1583
 1582
 1581
 1580
 1579
 1578
 1577
 1576
 1575
 1574
 1573
 1572
 1571
 1570
 1569
 1568
 1567
 1566
 1565
 1564
 1563
 1562
 1561

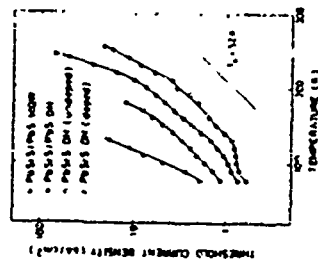


Fig. 2 Threshold current densities of the $\text{Pb}_{0.75}\text{Sn}_{0.25}$ epilayer is found to be 100 A/cm^2 , 150 A/cm^2 , 200 A/cm^2 and 250 A/cm^2 for the $\text{Pb}_{0.75}\text{Sn}_{0.25}$ epilayers with undoped, p-doped, n-doped and p-n-doped active layer (epitaxial) and p-layer (isotype) as a function of temperature.

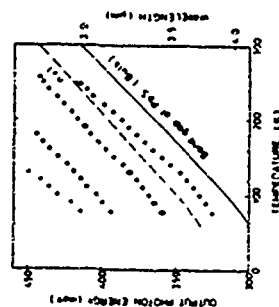


Fig. 4. Dependence of the output energy of the PMS/PMG laser on the temperature of the PMS/PMG with that of the PMS/PMG.

Electronic structure of thin Si layers in CaF_2 : hybridization versus confinement

A. Fasolino, Stefano Ossicini, F. Bernardini
Dipartimento di Fisica, Università di Modena, Via Campi 213/A, 41100 Modena, Italy

ABSTRACT

We present first principle calculations of thin (1-7 double layers) silicon (111) layers in CaF_2 , a system with strong analogies to porous silicon. We show that the Si band gap opening is dominated by the valence band which follows the effective mass confinement picture, while the conduction band is found to flatten and shift very modestly due to hybridization effects between Si and Ca states which lead to bonding-antibonding interface states in the gap. The relevance of these results for Si based low-dimensional structures is discussed.

The observation of bright, visible light emission from porous Si [1] has stimulated experimental [2] and theoretical effort [3-11] to understand both the energy shift and the increased efficiency of luminescence in porous Si, and in general of laterally confined Si structures, with respect to bulk Si. In fact, bulk Si has a 1.1 eV indirect gap resulting in luminescence in the near infrared with very low efficiency.

All theoretical approaches, ranging from the effective mass approach [3] to tight binding [4-5] to ab initio LDA treatments [7-11], give a qualitative account of the shift of the band gap from the near infrared to the visible range as due to confinement and an enhancement of the $\vec{e} \cdot \vec{p}$ matrix element for radiative transitions resulting from the better overlap of confined wavefunctions. However, even assuming the persistence of crystalline order, both the energy spectrum and the dipole matrix elements for radiative transitions strongly depend on the model geometry chosen to represent porous Si. The increase of luminescence efficiency has been attributed to the presence of a dipole allowed direct gap present in the energy spectrum of (100)-oriented wires [7-9]. The very recent observation of phonon assisted transitions in the photoluminescence of porous silicon [12] seems to contradict the hypothesis of a direct gap and of a columnar shape of the crystallites.

The main problem for a quantitative description of porous Si is the still not characterized microscopic structure and shape. This is why we have chosen to address the problem of Si crystallites embedded in CaF_2 , as prototype of a Si-based system with known microscopic structure [13,14]. Moreover, preliminary evidence of visible luminescence from Si layers in CaF_2 has been reported [15].

We show that the energy spectrum of Si layers is affected both, by confinement and by hybridization effects with the saturating agent, be it the Ca atoms in our case and H or O in porous silicon. Our results are compatible with the observation of luminescence in this system, since the band gap energy is found to increase for decreasing slab size. Moreover, hybridization of the Si p-states with the Ca s-d-states leads to a high joint density of states all over the Brillouin zone.

We present first principle calculations, performed by the Linear Muffin Tin Orbital method in the Atomic Sphere Approximation (LMTO-ASA) within the local density approximation (LDA), of the band structure of thin (1-7 double layers (4dL-5dL) Si(111) slabs in CaF_2 . CaF_2 is a good insulator, with a ~ 12.1 eV band gap; crystalline CaF_2 and

Si have similar fcc structures, with a room temperature lattice mismatch of only 0.6%, allowing the growth of high quality epitaxial layers. The LMTO-ASA method has proven to describe correctly the interface properties of this system [13]. Due to the LDA we underestimate the energy gap: we obtain 0.56 eV and 0.96 eV for Si and CaF_2 respectively. We use supercells formed by thin Si layers of variable thickness and by CaF_2 layers large enough to make the central CaF_2 planes exhibit bulk-like properties. As shown in Fig. 1, the first monolayer of CaF_2 loses half of its fluorine atoms leading to a Ca-Si bond at the interface. The interface Ca atoms occupy the T_d sites, the triangular filled sites on top of the second layer Si atoms, while the F atoms are located on the H_3 sites, the triangular hollow sites on top of the fourth layer Si atoms. We use the lattice constant of CaF_2 except for the interfacial Si-Ca distance, which is taken to be 3.15 Å. The experimental Ca-Si bond length is $\sim 3.1 \pm 0.1$ Å [16,17].

In Fig. 2 we show the calculated band structure for 2 and 4 dL's of Si in CaF_2 compared to that of bulk Si. By taking the slab thickness as that between the Ca atoms on the two interfaces, the thicknesses of 2 and 4 dL's are 8.7 and 14.9 Å respectively. We show the bands projected along the Γ -M and Γ -K symmetry directions of the hexagonal two-dimensional Brillouin zone (BZ) of the (111) surface and along the (111) direction perpendicular to the surface BZ. The bulk BZ direction Γ -X, where the minimum of the Si conduction band occurs, is now projected along the Γ -M direction.

Fig. 1 Structural model for the Si- CaF_2 interface; 1 dL is indicated.

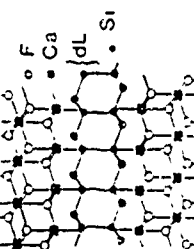
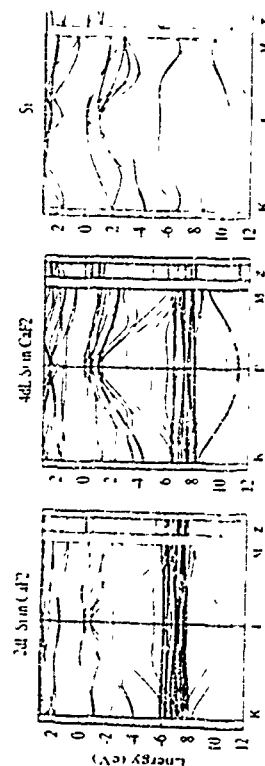


Fig. 2 Band structure projected along two symmetry directions of the hexagonal two-dimensional Brillouin zone (BZ) of the (111) surface (Γ -M and Γ -K reaching out one corner and the middle of one side of the hexagon respectively) and along the (111) direction perpendicular to the surface BZ, indicated as z, for 2 dL Si (4dL Si in CaF_2 and bulk Si respectively. Energies (in eV) are referred to the valence band maximum.



It can be seen that major changes occur in the energy region around the gap, in particular, the band gap increases and the width of the lowest conduction band is largely reduced. Even for thicker slabs, the bulk-like situation is not recovered: in fact interface states appear just below the conduction band at Γ and in the valence band region. The latter becomes the highest energy valence band state at finite wavevectors. These interface states are the bonding-antibonding states resulting from the Ca-Si bonds. In particular, at Γ , the bonding state has an upward curvature, since it results from an hybridization of the s -states of the Ca atoms (which constitute the conduction band of CaF_2) with the valence p -states of Si. It should be noted that the Si-Ca bond at the interface is somewhat intermediate between the covalent Si-Si bond and the ionic Ca-F bond. Therefore, the bonding-antibonding states are not removed from the gap as in the case of H-saturated Si structures. The H-Si bond, being mostly covalent, gives rise instead to a much larger bonding-antibonding energy separation and pushes the interface states inside the Si valence and conduction bands [19]. The Ca-Si bonding-antibonding interface states have a finite dispersion along the (111) growth direction, contrary to those related to the Si valence band which, as expected for confined states, are completely flat. Further evidence of the interface character of these states and of the confined nature of the state related to the bulk valence band comes from the calculated wavefunction along the (111) growth direction shown in Fig. 3.

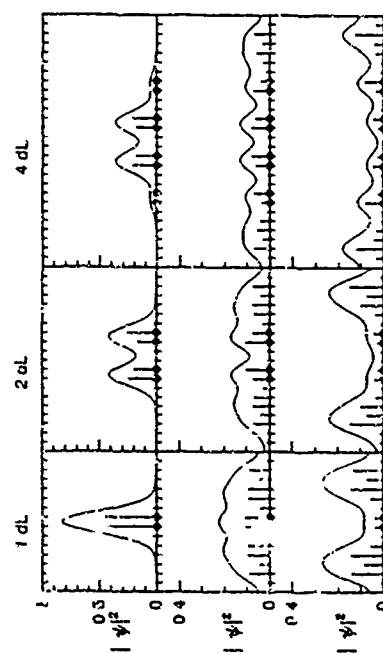


Fig. 3 Squared amplitude of the wavefunction along the (111) growth direction. The dots indicate the position of the Si planes. The envelope is obtained by dressing the squared amplitude of the wavefunction on each plane (indicated by the vertical bars) with a Gaussian two inter plane spacing wide. Top panels: Double degenerate top valence state at Γ for 1, 2, 4 dL's Si in CaF_2 . Note the confined character. Middle panels: same for the upper valence interface state at Γ . This state is spread both over the Si layer and the interface. Lower panels: same for the lowest conduction state at Γ . Note the pronounced interface character.

The previous results show that both hybridization and confinement play a role in the opening of the gap in laterally confined Si slabs. We can distinguish the two contributions by taking advantage of the possibility given by the LMTD method of fixing a single energy scale for all calculations. In Fig. 4, we have aligned the results for the different embedded (1.7 dL's) Si slabs by using the fluorine $2s$ core levels as a zero of energy. It can be seen that the opening of the gap is largely dominated by the Si valence band, which shifts to lower energies for thinner layers. The energy shift with layer thickness compares very well with that calculated within the effective mass theory, by taking the heavy hole mass as 0.281 m_0 for bulk Si, 0.3 m_0 in CaF_2 , and a valence band offset of 0.6 eV, values estimated from LMTD calculations.

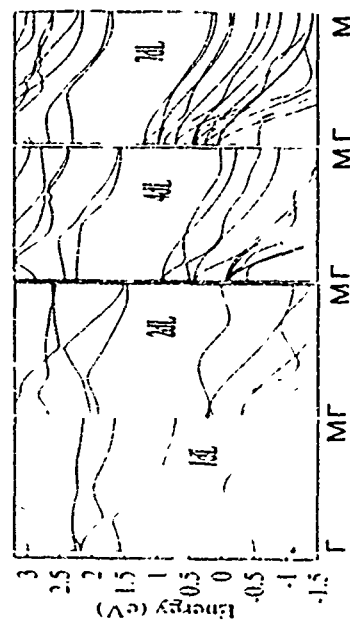


Fig. 4 Band structure along the Γ -M symmetry direction of the two-dimensional hexagonal (111) BZ on a single energy scale (see text) for 1 dL's, 2 dL's, 4 dL's and 7 dL's Si in CaF_2 . The band gap opening is dominated by the confinement induced shift of the valence band of Si evidenced by dots.

Therefore, the quantum confinement picture accounts for the great part of the blue shift of the gap. The lowest conduction band level, instead, is dominated by hybridization effects which affect the dispersion, flattening it out; the symmetry properties, lifting the zone boundary degeneracy, and altering the original character, leading all over the BZ to a mixed s - p - d state with strong matrix element with both the Si valence band edge, and the interface bonding state which emerges, for thinner layers, from the Si valence band to become the highest occupied level.

In conclusion we have calculated the electronic properties of thin Si(111) slabs in CaF_2 , a system which, due to its well characterized structure, is an ideal testing ground for experimental/theoretical comparisons. We have shown that, for laterally confined Si slabs,

COULOMB ATTRACTION IN OPTICAL SPECTRA OF QUANTUM DISCS

B. Adolph, S. Glutsch and F. Bechstedt
Friedrich-Schiller-Universität, Max-Weip-Platz 1, 07743 Jena, Germany

Abstract

We present a theory which describes the influence of the Coulomb interaction on the optical spectra of quantum discs within the envelope function formalism. Starting from a non local Floet formula luminescence is traced back to two particle wave functions and energies. They are solutions of the corresponding Schrodinger equation for an electron hole pair under the influence of the Coulomb attraction and confinement potentials determined by the spatial variation of the band edges of the considered microstructure.

1. Introduction

Novel crystal growth techniques together with nanometer lithographic techniques have made it possible to fabricate various semiconductor microstructures among them quasi 0D quantum dot systems. One interesting preparation technique is the focussed laser-beam induced thermal cation interdiffusion of narrow quantum well structures[1], whereby the form of the written laser lines determines the lateral shape of the resulting flat microstructure.

The spectroscopy of optical interband transitions across the band gap is a powerful tool to study these systems. In particular, photoluminescence spectra are governed by efficient intrinsic radiation of free excitons and exhibit a superior optical performance[2]. Studying the development of the corresponding line spectra one can learn somewhat about the mutual interaction of excited electrons (e) and holes (h) and its interplay with the vertical and lateral confinement potentials.

In this paper flat cylindrical quantum dots are studied. We solve the exciton problem for the ground state as well as excited states completely numerically. The solutions for wave functions and energies are used to calculate the exciton luminescence for flat dots, i.e. discs, which has been observed recently[3]. In Sec. 2 the basic equations are given. The explicit solution of the electron hole problem in single quantum discs is described for different disc confinement potentials. We discuss exciton energies, wave functions and oscillator strengths versus the disc radius. Optical spectra are explicitly calculated in Sec. 3. The

confinement effects dominate the Si band gap opening, while Si-Ca hybridization effects lead to dipole allowed optical transition all over the Brillouin zone. These findings are compatible with the observations of visible luminescence in the Si-CaF₂ system. A more detailed calculation of dipole matrix elements for optical transitions is in progress. We hope that our results will also stimulate further experimental work on this system.

Acknowledgements This work has been carried out within the European projects ESPRIT III n. 7220 EOIDS (S.O. and F.B.) and n. 7260 SOLIDES (A.F.).

- [1] L.T. Canham, Appl. Phys. Lett. **57**, 1046 (1990);
- [2] for a recent review see L.T. Canham in "Optical Properties of Low Dimensional Silicon Structures" ed. by D. Bensahel, L.T. Canham and S. Ossicini, Plenum Press, New York 1993
- [3] M.S. Hybertsen, Mater. Res. Soc. Proc. **236**, 175 (1992)
- [4] J.P. Poot, C. Delaue, and G. Allan, Appl. Phys. Lett. **61**, 1948 (1992)
- [5] S.Y. Ren and J.D. Dow, Phys. Rev. B **45**, 6492 (1992)
- [6] G.D. Sanders and Y.C. Chang, Phys. Rev. B **45**, 9202 (1992)
- [7] A.J. Read, R.J. Needs, K.J. Nash, L.T. Canham, P.D.J. Calcott, and A. Quresh, Phys. Rev. Lett. **69**, 1232 (1992)
- [8] F. Buda, J. Kuhnoff, and M. Parnello Phys. Rev. Lett. **69**, 1272 (1992)
- [9] T. Ohno, K. Shiraishi, and T. Ogawa, Phys. Rev. Lett. **69**, 2400-2403 (1992)
- [10] F. Koch, V. Petrova-Koch, T. Muschik, A. Kux, F. Muller, V. Gavrilenko, F. Moller, Proc. 21st ICI S World Scientific (1993) in press
- [11] C.G. Van de Walle and J.E. Northrup, Phys. Rev. Lett. **70**, 1116, (1993)
- [12] P.D.J. Calcott, K.J. Nash, L.T. Canham, M.J. Kane, and D. Brumhead, J. Phys. Condens. Matter **5**, L91 (1993)
- [13] S. Ossicini, C. Arcangeli and O. Bisi, Phys. Rev. B **43**, 9823 (1991), Surface Sci. **269/270**, 743 (1992)
- [14] J.C. Alvarez, K. Hirano, A. Yu. Kazimirov, M.V. Kovalevich, A. Ya. Kienure, N.S. Sokolov, and N.L. Yakovlev, Semicond. Sci. Technol. **7**, 1432 (1992)
- [15] A.P. Taylor, K. Stokes, P.D. Parsons, L.J. Schowalter, and F.K. Legouez, Proceedings of MRS Conference (1992) Boston (USA), to be published
- [16] R.M. Tromp and M.C. Reuter, Phys. Rev. Lett. **61**, 1756 (1988)
- [17] J. Zegenhagen and J.R. Patel, Phys. Rev. B **41**, 5315 (1990)
- [18] M. Buongiorno Nardelli, F. Finocchi, M. Palummo, R. De Felice, C.M. Bertoni, F. Bernardini, and S. Ossicini, Surface Sci. **269/270**, 879 (1992)

variation of the shape of the spectra with the disc radius is discussed. The results are compared with recent luminescence measurements for discs fabricated by laser induced cation interdiffusion of narrow quantum wells.

2. Theory

For systems, for which the spatial variation of the photon propagator may be neglected, the optical properties can be expressed in terms of a frequency dependent optical susceptibility $\chi(\omega)$. It follows from the corresponding wavefunction by two space integrations. The space dependent optical function can be directly related to the electron hole pair wave functions $\Phi(\mathbf{x}, \mathbf{x}_h)$ and energies E , with α is the complete set of quantum numbers for the two particle problem

$$\chi(\mathbf{x}, \mathbf{x}', \omega) = \frac{2}{\hbar} \text{Im} \left[\sum_{\alpha} \frac{\Phi(\mathbf{x}, \mathbf{x}_h) \Phi^*(\mathbf{x}', \mathbf{x}'_h)}{E - \hbar\omega + i\epsilon} \right] \quad (1)$$

where ϵ denotes the vacuum dielectric constant and \mathbf{x}, \mathbf{x}' denotes a certain damping of the electron hole pairs.

In the framework of the effective mass approximation and masses $m_e(m_h)$ of electrons (holes) the electron hole pairs obey a Schrodinger equation of the form

$$\left\{ E_2 + \sum_{\alpha} H_{\alpha}(\mathbf{x}_\alpha) - \frac{e^2}{1 - \epsilon(\mathbf{x}_\alpha - \mathbf{x}_h)} \right\} \Phi(\mathbf{x}, \mathbf{x}_h) = E \Phi(\mathbf{x}, \mathbf{x}_h) \quad (2)$$

where $H_{\alpha}(\mathbf{x}_\alpha)$ ($\alpha = e, h$) are the single particle Hamiltonians for electron and hole. E_2 denotes the energy of the allowed optical transition in the underlying bulk material and ϵ is the relative static dielectric constant.

Following the preparation method described in Refs. 1 and 2 we can assume strong confinement in growth ($x = z$) direction. Therefore it is sufficient to study only the most interesting spectral region of the first heavy hole to conduction band transition. As a result, the pair equation (2) can be written for systems in the xy plane with the quasi 2D Coulomb potential $V(r) = -e^2/(4\pi\epsilon_0 r)$ with ϵ_0 as the effective width of the underlying quantum well. Using center of mass (\mathbf{r}_m) and relative (\mathbf{r}) coordinates of the electron hole pairs F_2 as the energetical distance of first heavy hole and first electron well subband and a reduced set of quantum numbers f the Schrodinger equation for the pair motion in the xy plane follows from Eq. (2) to be

$$\left\{ \frac{\hbar^2}{2m_e} \nabla_{\mathbf{r}_m}^2 + \frac{\hbar^2}{2m_h} \nabla_{\mathbf{r}}^2 + U_e(\mathbf{r}) + U_h(\mathbf{r}) + \frac{m_e}{M_0} \nabla_{\mathbf{r}_m}^2 + \frac{m_h}{M_0} \nabla_{\mathbf{r}}^2 + V(r) \right\} \Phi(\mathbf{r}, \mathbf{r}_m) = E \Phi(\mathbf{r}, \mathbf{r}_m) \quad (3)$$

With the dipole matrix element $|p|$ the optical susceptibility $\chi(\omega)$ can be written as a sum over oscillators

$$\chi(\omega) = \frac{2}{\hbar} \sum_{\alpha} |p|^2 \frac{f_{\alpha}}{E_{\alpha} - \hbar\omega + i\epsilon} \quad \text{with} \quad f_{\alpha} = \int d\mathbf{r} |\Phi(\mathbf{r}, \mathbf{r}_m)|^2 \quad (4)$$

In the quasi 0D case expression (1) replaces the Elliott formula well known for the 3D and 2D cases.

The excitons are considered to be optically excited in an isolated flat cylindrical quantum dot of characteristic lateral radius r_0 , usually consisting of GaAs and embedded in a semiconductor layer with a higher energy gap usually $\text{Ga}_{1-x}\text{Al}_x\text{As}$, which itself is in an epitaxially grown barrier layer. The Al mole fraction x as a function of the distance from the disc center is responsible for the electron and hole confinement potentials in the xy plane. Two different types of potentials are used. In order to simulate infinite barriers by differentiable expressions we apply a power law

$$U_i(r) = a_i (r/r_0)^v \quad (5)$$

We use typical values $v = 16$ for which convergence in energy eigenvalues is essentially reached with respect to the infinite barrier results. To model the effect of the finite barrier heights we study the potential form

$$U_i(r) = \Delta E_i \left[1 - \exp(-r/r_0) \right] \quad (6)$$

A probable result of such a potential choice is the unique splitting of the electron and hole confinement potentials

$$U_i(r) = U_i(r_h) + U_i(r_e) + U_{int}(R, r, \phi - \varphi) \quad (7)$$

into confining potentials for the center of mass motion, $U_{int}(R)$, as well as the relative motion, $U_{rel}(r)$ and a coupling term of the two motions $U_{int}(R, r, \phi - \varphi)$. Therefore the exact solutions of the equation (6) can be expanded in terms of functions obtained without coupling

$$\Phi(\mathbf{R}, \mathbf{r}) = \sum_{N, n} \sum_{\lambda, \mu} c_{N, n, \lambda, \mu}(\mathbf{r}) \Psi_{N, n}(\mathbf{R}) \chi_{N, n}(\mathbf{r}) \quad (8)$$

where the radial parts with certain radial quantum numbers N and n as well as eigenvalues $E_{N, n}$ and $E_{n, n}$ obey decoupled Schrodinger equations. We solve them by means of a Rungge-Kutta-Galerkin method [1] numerically. That procedure has been already successfully applied to describe the optical properties of flat quantum wires [1]. From the definition (1) of the oscillator strengths

$$f_{\alpha} = \left| \sum_{N, n} c_{N, n}(\mathbf{r}) \chi_{N, n}(\mathbf{r}) \right|^2 \int d\mathbf{R} |\Psi_{N, n}(\mathbf{R})|^2 \quad (9)$$

it follows that only the s states of the two radial equations with zero angular momentum are needed. The unknown coefficients $c_{N, n}(\mathbf{r})$ are derived from a system of algebraic equations which results from Eq. (1) with the ansatz (8).

3. Discussion

Fig. 1 shows the imaginary part of the optical susceptibility (1) near the energy gap E_g between the first electron and first heavy hole subband in the underlying quantum well structure. For numerical reasons a small bias voltage $U = 0.05$ V is assumed.

independent of the certain two particle state. The spectra are plotted for different disc radii r_0 and the confinement potentials in (5). Calculations are done with and without coupling of center of mass and relative motion. For large dots (Fig. 1a) the exciton spectrum of the underlying GaAs quantum well is reproduced. Decreasing the disc radius (Fig. 1b,c) strong quantization effects in the center of mass motion are observed. A series of blue shifted satellites with smaller oscillator strengths and belonging to higher quantum numbers V appear. In addition a fine structure, related to the influence on the disc confinements on the internal motion of the electron-hole pairs, occurs (Fig. 1c). The Coulomb degeneracy is lifted. The coupling of the two motions becomes more and more important for the decreasing dot radii, and for radii close to the Bohr radius (Fig. 1d,e). The disc confinement leads to well separated peaks, which can be interpreted in terms of uncorrelated electrons and holes, i.e. the physical nature of the spectra changes qualitatively. The red shift of the spectrum without coupling in comparison to the correct one indicates that the neglect of the coupling of the two motions effectively acts as a decreasing of the disc confinement.

For very small dots the Coulomb attraction seems to be treated as a small perturbation. To check this assumption optical spectra with and without the Coulomb interaction of electrons and holes are plotted in Fig. 2. It can be seen that for $r_0 \leq a_B$ (a_B - the Bohr radius of the bulk exciton) the peaks mainly arise from uncorrelated electron-hole pairs and are only shifted by the Coulomb attraction. They can be neatly characterized by pairs of single-particle quantum numbers of electrons and holes. On the other hand, the Coulomb correlation strongly increases the oscillator strengths and the Coulomb shift of the peaks does not follow clear rules.

The imaginary part of the optical susceptibility Eq. (4) is plotted in Fig. 3 for different effective dot radii r_0 . To compare with experimental luminescence results some realistic features are introduced in the description. The spectra are cut at the high energy side by $6.32 E_B$ above the lowest excitation peak to model the occupation due to the photoexcitation. The damping parameter Γ depends on the disc radius because of the thickness fluctuations in the underlying quantum well structure[1]. We assume a size dependence in the form $\Gamma = \{E_B[1 - r_0/2a_B]\}$. The extent of the underlying quantum well is chosen as $r_w = 0.12a_B$.

The series of theoretical spectra in Fig. 3 is in qualitative agreement (with respect to the position and the number of peaks) with the luminescence measurements of Brumme et al [1,2]. To compare theoretical curves with experimental results one has to take into account the following facts: (i) Because of the finite height of the fabricated layers spectral lines cannot be observed up to arbitrary high energies. On the other hand, the spectra are truncated by the occupation of electron-hole pairs. (ii) Due to the thermal diffusion band offsets of minor influence on the observed spectra. (iii) Due to the thermally induced profile the dot radii entering the confinement potential differ from the detection of the laser-excitation lines of about 200 nm. (iv) For small dot radii we are faced with a superposition of the diffusion tails from the left and the right side. Thus, the positions of the confinement potentials are shifted and the effective energy gap is increased leading to a blue shift of the spectrum as observed experimentally.

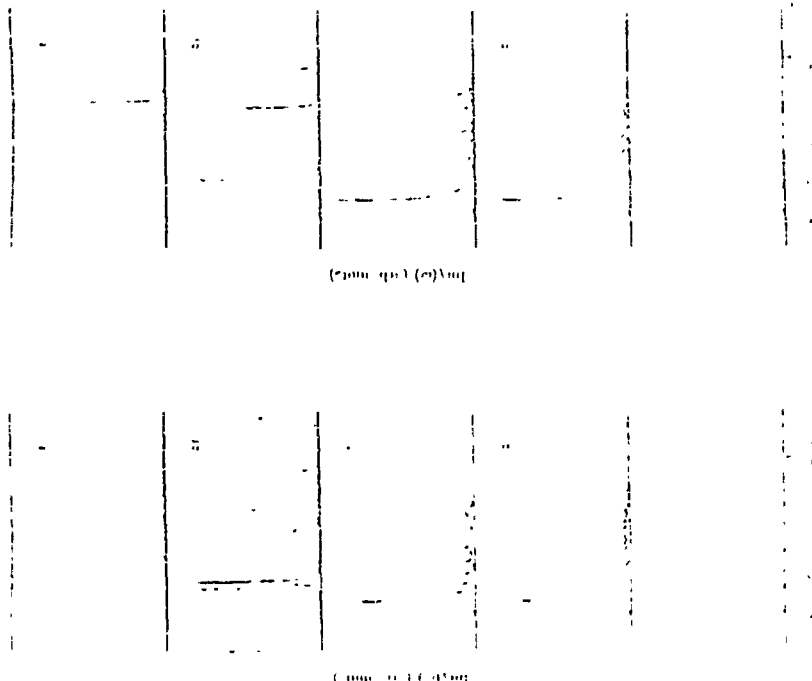


Fig. 1

Imaginary part of the optical susceptibility for different disc radii $r_0 = 100 a_B$, (a), $50 a_B$, (b), $25 a_B$, (c), $10 a_B$, (d), and $5 a_B$, (e). Solid lines represent calculations without inclusion of the Coulomb attraction whereas dashed lines give the spectrum for uncorrelated electron-hole pairs.

Imaginary part of the optical susceptibility for different disc radii $r_0 = 100 a_B$, (a), $50 a_B$, (b), $25 a_B$, (c), $10 a_B$, (d), and $5 a_B$, (e). Solid lines represent calculations without inclusion of the Coulomb attraction whereas dashed lines give the spectrum for uncorrelated electron-hole pairs.

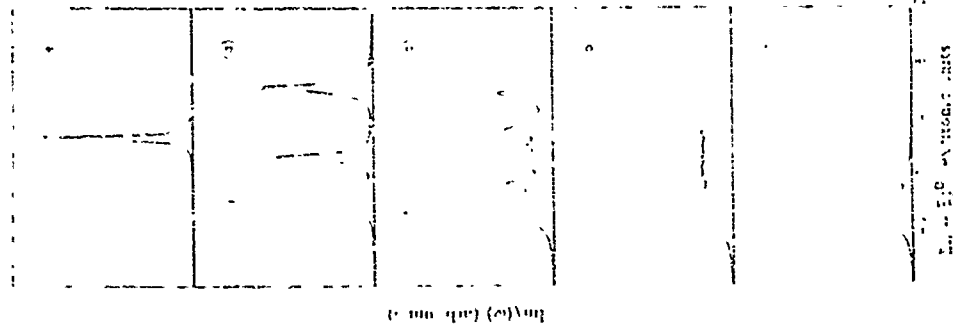


Fig. 3. Imaginary part of the optical susceptibility for different disc radii $r_0 = 100$ (a), $r_0 = 50$ (b), $r_0 = 20$ (c). The solid line represents the susceptibility with a uniform excitation, the dashed line represents the susceptibility with a Gaussian excitation.

Conclusions

In conclusion we have demonstrated the transition from the complete 2D exciton in an extremely narrow quantum well to quasi 0D excitons in well separated quantum discs prepared by laser induced cation interdiffusion. This transition is characterized by the interplay of the center of mass motion of the electron hole pair, its internal motion associated with exciton binding, and the confinement of electron and hole due to the disc potential.

In the case of flat discs with characteristic radii r_0 and high barriers in the disc plane the strengths of the different effects can be discussed comparing r_0 with the exciton Bohr radius a_B . In a wide range of disc sizes, $r_0 \gtrsim a_B$, the coupling of center of mass and internal motion plays a minor role. Only in the limit of strong confinement, $r_0 \ll a_B$, the consideration of this coupling is necessary. When the disc confinement effects overcome the Coulomb effects, i.e. when $r_0 \ll a_B$, the resulting spectra are similar to those obtained without excitonic effects. The Coulomb attraction gives rise to a divergent Coulomb shift $\sim 1/r_0$.

Our results are applied to explain qualitatively recent photoluminescence spectra of single discs with varying size. The development of the photoluminescence near the lowest exciton hole exciton of the underlying quantum well is interpreted in terms of the interplay of excitonic effects and disc confinement. However, a more quantitative analysis of experimental spectra requires the inclusion of matrix element effects, the fluctuations in the vertical and lateral sizes, and, in particular, more realistic confinement potentials which more strongly reflect the interdiffusion profile.

Acknowledgements

We would like to thank G. Abstreiter and K. Brose for helpful discussions and leaving of unpublished photoluminescence spectra.

References

- [1] K. Brunner, G. Abstreiter, M. Wabner, G. Böhm, and G. Frankle, *Surface Sci.* **122**, 218 (1992).
- [2] K. Brunner, V. Beckhmann, G. Abstreiter, M. Wabner, G. Böhm, G. Frankle, and G. Weinmann, *Phys. Rev. Lett.* **69**, 3216 (1992).
- [3] J. Stoer and R. Burckel, *Introduction to Numerical Analysis* (Springer, New York, 1984).
- [4] S. Glusch and J. Bockelmann, *Phys. Rev. B* **41**, 11546 (1990).

ELECTRONIC PROPERTIES AND ELECTRON-PHONON INTERACTION IN AN ARRAY OF ANISOTROPIC PARABOLIC QUANTUM DOTS IN THE PRESENCE OF A MAGNETIC FIELD

R. Haupt and E. Wendler¹⁾¹⁾ Institut für Festkörperelektronik und Theoretische Optik, Friedrich-Schiller-Universität Jena, Max-Müller-Platz 1, D-07743 Jena, Federal Republic of Germany²⁾ Fachbereich Physik, Vordorferstr. 1, Universität Halle, Friedrichmann-Bach-Platz 6, D-06099 Halle, Federal Republic of Germany

ABSTRACT

The electronic properties of a two-dimensional array of anisotropic parabolic quantum dots in the presence of a quantizing magnetic field is investigated in the tight binding approximation. The main bands strongly depend on the superlattice periods. The eccentricity of the anisotropic parabolic quantum dots and the magnetic field. The electron-phonon interaction renormalizes the gap between the main bands, their widths and results in a resonant level splitting.

1. Introduction

In polar semiconductors the motion of an electron is coupled to the well induced polarization field of long wavelength optical phonons to form a quasi particle which is called polaron. Owing to this coupling the free electron properties are changed by (i) a shift in the energy, (ii) a mass renormalization and (iii) a polarization induced nonparabolicity. The most significant investigations can be made in a cyclotron resonance experiment. The applied magnetic field quantizes the electron motion in the plane perpendicular to the magnetic field. With increasing magnetic field the phenomena of level crossing would appear in the absence of electron-phonon interaction. The excited electronic levels can become degenerated with the lowest electronic level plus one optical phonon. Due to the electron-phonon interaction the levels split at each resonance into two non-crossing levels (resonant magnetopolarons). Hence, for strong magnetic fields the lower energy levels are pinned to the lowest level plus one optical phonon. Polarons ($\hbar \neq 0$) and magnetopolarons ($\hbar \neq 0$) have been extensively studied both theoretically and experimentally [1-4].

Advances of lithography and etching techniques make it possible to confine laterally a quasi-two-dimensional (Q2D) electron system into quantum dots (QD) of diameters d which are less than the mean free path of the electrons. QDs have been fabricated by electrostatic confinement and deep-potential etching techniques. The confining potential in such QDs is probably well represented by a parabolic potential. QDs can be viewed as artificial atoms with the atomic Coulomb potential replaced by the confinement potential of the QD. Polarization effects are studied in QD systems [5, 12] and more recently in QD quantum well structures [13]. QD isotropic [11] and anisotropic [13] parabolic QDs. The reduced dimensionality changes the electronic and polaronic properties considerably. In QD and QDQ (for instance it depends on the confinement potential if the resonant magnetopolaron exists or not [13, 14]).

In this paper we investigate the electronic and polaronic properties of a 2D array of anisotropic parabolic QDs. The electronic ground state will be described within the tight binding scheme because in the usual confined states the QDs are well separated. The electron-phonon interaction will be calculated within second order perturbation theory for arbitrary magnetic fields.

2. Electronic Ground-State Properties

The eigenstates of a single electron confined in a xy plane along the z direction in a QD are confined in the lateral direction to the potential of a QD parabolic. $\psi_{\alpha\beta\gamma}$ of anisotropic parabolic QDs in the presence of a quantizing magnetic field is described by the Hamiltonian

$$H_0 = \frac{1}{2m_0} p^2 + \frac{1}{2} \omega_c^2 r^2 + V(r) \quad (1)$$

The parabolic confining potential is assumed to be $V(r) = \frac{1}{2} (x^2 + y^2 + z^2) + \frac{1}{2} (x^2 + y^2 + z^2) + \frac{1}{2} (x^2 + y^2 + z^2)$ where ω_c is the lateral confinement frequency and ω_c is the cyclotron frequency and ω_c is the number of QDs in the considered array. In Eq. (1) we ignore the Zeeman spin splitting, m_0 is the effective electron mass, $\hbar = 1$ and \mathbf{r} is the vector position with $r^2 = x^2 + y^2 + z^2$. For each k we use the symmetric gauge $\mathbf{A} = (-y, x, 0)/2$.

We first consider the single anisotropic QD. The lateral potential of a single anisotropic QD is given by $V(r) = \frac{1}{2} m_0 \omega_c^2 (x^2 + y^2 + z^2)$. The one electron Hamiltonian $H_0^{(1)} = H_0 + V(r)$ can be separated in an isotropic part

$$H_0^{(1)} = \frac{1}{2m_0} p^2 + \frac{1}{2} \omega_c^2 r^2 + \frac{m_0 \omega_c^2}{2} z^2 \quad (2)$$

with $\Omega = \omega_c$ and $r^2 = x^2 + y^2$ and the deviation from it

$$H_1^{(1)} = \frac{m_0 \omega_c^2}{2} z^2 \cos^2 \varphi \quad (3)$$

with $\Omega_z^2 = \omega_c^2 - \Omega^2$ and $z = r \cos \varphi$. The eigenenergies and corresponding single particle wave functions of the isolated isotropic parabolic QD are given by

$$\epsilon_{n,m}^{(0)} = \hbar \omega_c (2n + |\ell| + 1) + \hbar \omega_c m, \quad \ell = 0, \pm 1, 2, \dots, \quad m = 0, \pm 1, \dots \quad (4)$$

and $\psi_{n,m}^{(0)}(r, \varphi) = \psi_{n,m}^{(0)}(r) e^{i\ell\varphi}$ with

$$\psi_{n,m}^{(0)}(r, \varphi) = \psi_{n,m}^{(0)}(r) e^{i\ell\varphi} \left(-\frac{m_0 \omega_c^2}{2} z^2 \right)^{\frac{1}{2}} \quad (5)$$

respectively where $\omega_c = (e\hbar/2m_0) \Omega_z^2$ is the hybrid frequency with $\omega_c = e\hbar/2m_0$ the cyclotron frequency and Ω_z is the constant hyperfine interaction. The normalization constant is

$$N_{n,m} = \left(\frac{1}{\pi} \frac{\omega_c^2}{\omega_c^2} \right)^{1/2} \left(\frac{m_0 \omega_c^2}{\hbar} \right)^{1/2} \quad (6)$$

where N_0 is the radial and in the radial quantum number. According to the strict confinement assumed in 2D direction $\psi_{n,m}^{(0)}(r, \varphi) = \psi_{n,m}^{(0)}(r)$ is valid. To obtain the single particle energies and eigenstates of $H_0^{(1)}$ we express them in the representation of the states of the isotropic parabolic QD

$$\psi_{n,m}^{(1)}(r, \varphi) = \sum_{n',m'} V_{n',m'}(r, \varphi) \psi_{n',m'}^{(0)}(r, \varphi) \quad (7)$$

The eigenenergies are determined from the algebraic system of equations

$$\sum_{n',m'} (E_{n',m'}^{(0)} - E_{n,m}^{(1)}) V_{n',m'} = -\sum_{n',m'} V_{n',m'}^{(1)} V_{n',m'}^{(0)} \quad (8)$$

According to the spatial symmetry of the problem this system of algebraic equations splits into two sectors one for even m and the other for odd m . The eigenenergies can be found [16] to be explicitly

$$E_{n,m} = \hbar \omega_c \left(2n + |\ell| + 1 \right) + \hbar \omega_c \left(2n + |\ell| + 1 \right) \left(1 + \frac{\omega_c^2}{\omega_c^2} \right) \quad (9)$$

$$V_{n,m} = 0 \quad (10)$$

For vanishing inhomogeneity we can identify the quantum numbers $N_0 = 2n + |\ell| + 1$ and $m = N_0 - |\ell|$ as known [17] that $H_0^{(1)}$ is invariant under the unitary group $U(2)$ with the irreducible representation of the dimension $2N_0 + |\ell| + 1$ corresponding to the degeneracy of this case. This situation of symmetry [18] is broken by the anisotropy

For Fig. 1, 2, 3, first order energy levels $E_n^{(1)}$ of the anisotropic parabolic QD are plotted for a GaAs (GaAs) Al heterostructure (GaAs, $m_0 = 0.067 m_0$ is the free electron mass). In Fig. 1a the electron energy levels $E_{n,m}^{(1)}$ of the isotropic parabolic QD are shown. At vanishing magnetic field ($\omega_c = 0$) the energy levels are $(2N_0 + |\ell| + 1)$ fold degenerated. In Fig. 1b the anisotropy, i.e. the z direction of the equivalent lines of $V(r, \varphi)$ from circles is very weak and hence the energy spectrum is very similar to that of the isotropic parabolic potential. It is also seen that the $(2N_0 + |\ell| + 1)$ fold degeneracy of the energy level $E_{n,m}^{(1)}$ of the isotropic QD for vanishing magnetic field is lifted by the anisotropy. In Fig. 1c the equivalent lines are more eccentric ellipses and following the energy spectrum deviates appreciably from that of the isotropic

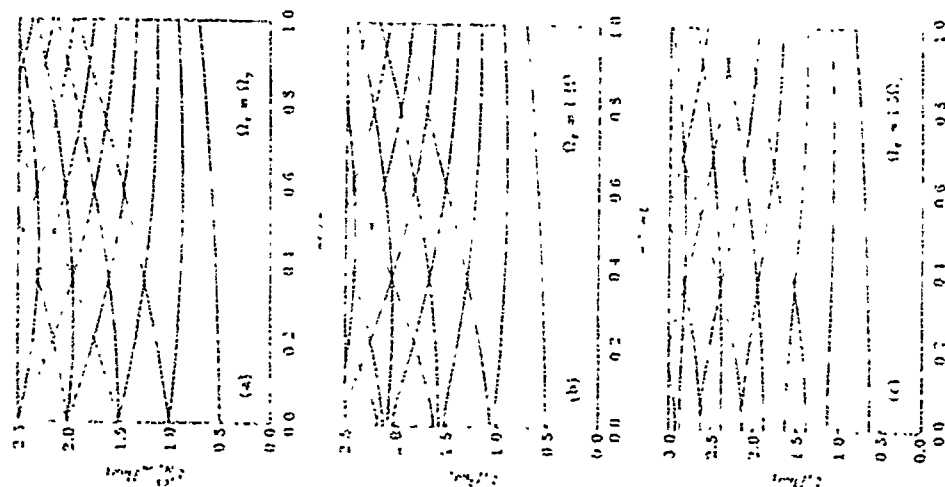


Fig. 1 Energy levels E_n as a function of the magnetic field of an anisotropic parabolic QD with $\Omega_x = 0.5$, $\Omega_y = 0.5$, $\Omega_z = 0.5$, $\Omega_x = 0.5$, $\Omega_y = 0.5$, $\Omega_z = 0.5$.

case. From Figure 1a, it is seen that level crossing at finite magnetic fields occurs as in the case of the isotropic parabolic QD (Fig. 1c).

For the parabolic QD we assume

$$V(x, y, z) = \begin{cases} \frac{1}{2} m \omega_x^2 x^2 + \frac{1}{2} m \omega_y^2 y^2 + \frac{1}{2} m \omega_z^2 z^2 & \text{if } |x| \leq l_x, |y| \leq l_y, |z| \leq l_z \\ \infty & \text{otherwise} \end{cases} \quad (10)$$

The widths of a single QD in the x , y , and z directions are l_x , l_y , and l_z in the x , y , and z directions, where $l_x = 2l_x/2$, $l_y = 2l_y/2$, $l_z = 2l_z/2$. Assuming that the QD is a cell of material, $l_x, l_y, l_z < l_0$, we can use the tight-binding approximation. In this case the single-particle wave function reads

$$\Phi_{n, \mathbf{k}, \mathbf{l}}(\mathbf{r}) = \sum_{\mathbf{r}} c_{\mathbf{r}} \exp(i \mathbf{k} \cdot \mathbf{r}) \exp(i \mathbf{l} \cdot \mathbf{r}) \quad (11)$$

where \mathbf{r} denotes the position vector in the x, y, z plane and $\mathbf{l} = (l_x, l_y, l_z)$ is the wave vector, ranging through the \mathbf{l} values in the first Brillouin zone consistent with the assumed periodic harmonic potential conditions. $\mathbf{l}_0 = (l_x, l_y, l_z)$ is the lattice vector of the 2D Bravais lattice. Applying the Hamiltonian (1) with the potential (10) on the wave function (11) in the Schrödinger equation for an electron in the 2D area of anisotropic QD, the eigenvalue equation system reads

$$\sum_{\mathbf{l}'} [t_{\mathbf{l}, \mathbf{l}'}^x (\delta_{\mathbf{l}, \mathbf{l}'} - \delta_{\mathbf{l}, \mathbf{l}'}^x) + t_{\mathbf{l}, \mathbf{l}'}^y (\delta_{\mathbf{l}, \mathbf{l}'} - \delta_{\mathbf{l}, \mathbf{l}'}^y) + t_{\mathbf{l}, \mathbf{l}'}^z (\delta_{\mathbf{l}, \mathbf{l}'} - \delta_{\mathbf{l}, \mathbf{l}'}^z)] c_{\mathbf{l}'} = E_n c_{\mathbf{l}} \quad (12)$$

where we have assumed for the integral $\int d^3 r \exp(i \mathbf{k} \cdot \mathbf{r}) \exp(i \mathbf{l} \cdot \mathbf{r}) \approx \delta_{\mathbf{k}, \mathbf{l}}$, which specifies the normalization constant of the wave function $\mathbf{l} = \frac{1}{2}$ and we further include only the nearest-neighbor Hamiltonian matrix elements according to

$$t_{\mathbf{l}, \mathbf{l}'} = \int d^3 r \exp(i \mathbf{k} \cdot \mathbf{r}) \exp(i \mathbf{l} \cdot \mathbf{r}) \exp(i \mathbf{l}' \cdot \mathbf{r}) \quad (13)$$

$$t_{\mathbf{l}, \mathbf{l}'} = \int d^3 r \exp(i \mathbf{k} \cdot \mathbf{r}) \exp(i \mathbf{l} \cdot \mathbf{r}) \exp(i \mathbf{l}' \cdot \mathbf{r}) \quad (14)$$

with $\Delta(\mathbf{l}, \mathbf{l}') = \int d^3 r \exp(i \mathbf{k} \cdot \mathbf{r}) \exp(i \mathbf{l} \cdot \mathbf{r}) \exp(i \mathbf{l}' \cdot \mathbf{r})$. In the tight-binding approximation it is assumed that the unit band E_n is very close to the band level E_n . Following (14), (12) is to be solved assuming that for the calculation of the unit-band energy $E_n(\mathbf{l})$ the unit-band energy levels through those dot levels with energies either degenerated with or very close to the corresponding dot level.

Figure 2 shows the three lowest unit-band energies E_n of the 2D area of QD along $\Gamma-X$, $\Gamma-Y$, and $\Gamma-Z$ of the square lattice where Γ , X , and Y are points in the first Brillouin zone that correspond to $(0,0,0)$, $(\frac{1}{2}, 0, 0)$, and $(0, \frac{1}{2}, 0)$, respectively, with $l_x = l_y = l_z = 1$. In Fig. 2b the unit bands are plotted for $\omega_x = 0$ and in Fig. 2c for $\omega_x = 0.25$.

III. Electron-Phonon Interaction

Our interest is directed to QD's generated by nanostructured gate electrodes via the $h\nu$ effect in heterostructures of polar semiconductors. Hence the electrons occupying the unit bands $E_n(\mathbf{k})$ interact with the optical phonons of the system. Neglecting the effects of interface phonons [10], the Hamiltonian of the electron-phonon interaction including only \mathcal{V} bulk longitudinal optical (LO) phonons is the standard Frohlich Hamiltonian and reads [20]

$$H_{EP} = \sum_{\mathbf{k}} \left(\frac{\hbar \omega_{LO}}{2} \right) \left(a_{\mathbf{k}} + a_{-\mathbf{k}}^\dagger \right) \sum_{\mathbf{l}} c_{\mathbf{l}} \exp(i \mathbf{k} \cdot \mathbf{r}) \exp(i \mathbf{l} \cdot \mathbf{r}) \quad (15)$$

with a the dimensionless 3D polar coupling constant ($\omega_{LO} = 0.07$ for the corresponding 3D polariton energy $\hbar \omega_{LO} = 3.98$ meV, $\hbar \omega_{LO} = 3.98$ meV, $\hbar \omega_{LO} = 3.98$ meV) and $\mathbf{l} = (l_x, l_y, l_z)$. The interaction Hamiltonian is given by $H_{EP} = H_{EP} + H_{EP} + H_{EP}$ with $H_{EP} = \sum_{\mathbf{k}} \hbar \omega_{LO} (a_{\mathbf{k}} + a_{-\mathbf{k}}^\dagger) \exp(i \mathbf{k} \cdot \mathbf{r}) \exp(i \mathbf{l} \cdot \mathbf{r})$. The first two terms represent the unperturbed electron and phonon system $H_0 = H_e + H_p$ and the electron-phonon interaction H_{EP} is the perturbation H_1 . The energy levels of an electron in the 2D area of anisotropic parabolic QD's are shifted $\pm \Delta E_n(\mathbf{k})$ by the electron-phonon interaction with the LO phonons to $E_n(\mathbf{k}) \pm \Delta E_n(\mathbf{k})$. In the weak-coupling limit $\Delta E_n(\mathbf{k}) \ll E_n(\mathbf{k})$.

Monte-Carlo Calculation of Few-Electron Systems in Quantum Dots

F. Bollmann
*Institut für Theoretische Physik,
 Universität Regensburg, Germany
 D-93040 Regensburg*

Selected eigenstates are calculated for 1-10 electrons in a quasi-2-dimensional harmonically confined dot as a function of magnetic field. This includes a detailed look at the ground state of three electrons and a more general calculation for 1-10 electrons carried out in the lowest Landau level for different spin configurations. The results provide an outline of the N -electron ground state as a function of magnetic field, enabling a comparison to be made with recent experiments involving capacitance measurements on quantum dots. The calculations are made using the fixed node quantum Monte-Carlo method which can accurately estimate electron correlation and easily extends to large numbers of electrons.

1 Introduction

Basic to our understanding of quantum dots is the ability to calculate spectra in the few-electron regime (0-50) particles. In particular, experimental probes of quantum dots require the calculation of dipole excitations, in the case of optical spectroscopy, and ground state energies in the case of tunnelling experiments. Since the few-particle regime is numerically quite taxing, there have only been a few examples of such spectra calculations [1, 2]. Experimental work on tunnelling, however, has already reached the point where ground state spectra for 0-50 electrons are measurable [3]. Also the possibility of different spin states, although not often considered, remains a relevant effect up to magnetic fields of about 3T in GaAs.

From the theoretical side what is required is a method whose computational difficulty increases gently with respect to the number of electrons N . One such method is the fixed node Monte-Carlo algorithm whose computational effort grows only as N^2 . The basic method is described in detail in the article by Reynolds et al [4] and the modifications appropriate to the present application are discussed in Bollmann [5]. Here we give just a brief outline of the method. Consider a general N -particle Hamiltonian

$$H = -\frac{\hbar^2}{2m} \left(\sum_{i=1}^N \nabla_i^2 \right) + V(\vec{r}) \quad (1)$$

where $V(\vec{r})$ is a general potential which includes any interactions, and $\vec{r} = (r_1, \dots, r_N)$ denotes a many-particle configuration. In the fixed node approximation we consider the propagation of $f(\vec{r}, t) = \Psi_0^*(\vec{r}) \Psi_T(\vec{r})$ in imaginary time t . Here $\Psi_T(\vec{r})$ is a trial function approximation to the solution, and in the limit as $t \rightarrow \infty$ goes to infinity $\Psi_T(\vec{r}) \approx \Psi_0(\vec{r})$ is the sought after solution to H . The advantage in considering the propagation of the product

$f = \Psi_0^* \Psi_T$ is that f remains a positive real function and this is a basic requirement of the quantum Monte-Carlo algorithm. The equation for the propagation of $f(\vec{r}, t)$ in imaginary time is

$$-\frac{\partial f(\vec{r}, t)}{\partial t} = -\frac{\hbar^2}{2m} \left(\sum_{i=1}^N \nabla_i^2 f \right) + (E_L f(\vec{r}) - E_T f) + \frac{\hbar^2}{2m} \sum_{i=1}^N \nabla_i \cdot \left(f \nabla_i(\vec{r}) \right) \quad (2)$$

where $E_L(\vec{r}) = \hbar \Psi_T \nabla^2 \Psi_T$ defines the local energy and the gradient $E_T(\vec{r}) = 2 \nabla \Psi_T \nabla \Psi_T$ introduces a drift term to the equation (see [1, 3]). The constant E_T is a parameter which is adjusted during the run until the distribution $f(\vec{r})$ becomes stable — neither growing nor shrinking in imaginary time. This procedure finds the lowest energy eigenstate of the Hamiltonian H which is consistent with the total structure of the trial function Ψ_T . With a suitable choice of trial function we can find the eigenenergies of fermionic states and even excited states. The use of a trial function only partly restricts the solution as it is seen by considering the nature of the constraints. The solution Ψ is constrained to vanish on the same nodal surfaces and maintain the same complex phase as Ψ_T . Within these constraints, however, the Hamiltonian is solved exactly, including the effects of electron correlation.

The model considered here is that of a quasi-two-dimensional quantum dot so that only degrees of freedom in the plane of the dot are considered. The problem is solved in the effective mass approximation with effective mass m^* and in a cylindrically symmetric harmonic confinement $\frac{1}{2} m^* \omega_0^2 r^2$. The Hamiltonian considered is thus

$$H_0 = -\frac{\hbar^2}{2m^*} \sum_{i=1}^N \nabla_i^2 + \frac{1}{2} m^* \omega_0^2 \sum_{i=1}^N r_i^2 + \frac{\hbar^2}{2} \sum_{i=1}^N L_{i,z} + \frac{1}{4\pi\epsilon_0} \sum_{i,j=1}^N \frac{1}{r_{ij}} \quad (3)$$

where a magnetic field B enters via the hybrid oscillator strength $\omega^2 = \omega_0^2 - (\omega_c/2)^2$, with $\omega_c = eB/m^*$ and $L_{i,z}$ is the z -component of orbital angular momentum. The introduction of a magnetic field into the model Hamiltonian does not cause any great difficulties for the Monte-Carlo procedure. Our trial functions Ψ_T now have to be complex but, as noted above, this can be accommodated in the algorithm [2]. The only significant alteration to H is the addition of the angular momentum term. Since the total angular momentum is conserved under the Hamiltonian, this term evaluates to just a constant.

In the next three sections we take a detailed look at the ground state of a three particle system and then look at selected eigenstates of between one and ten electrons. A possible comparison of these results with capacitance experiments is indicated in section 4.

2 Three-Particle Problem

For the special case of three particles we are able to compute a rather complete spectrum of the Hamiltonian H . There is available in this case a particularly convenient coordinate system (see [1, 3]) and we restrict our attention here to states in the lowest Landau level. For three particles the relative motion can be specified with the complex coordinates

$$\begin{aligned} \rho_0 &= z_1^2 + z_2^2 + z_3^2 + z_1 z_2 z_3 \\ \rho_1 &= z_1^2 + z_2^2 + z_3^2 + z_1 z_2 z_3 \end{aligned} \quad (4)$$

the absolute energies. Solid curves are drawn to mark the lowest calculated eigenenergy in each case for systems of 1-10 electrons. For example the upper group of six states

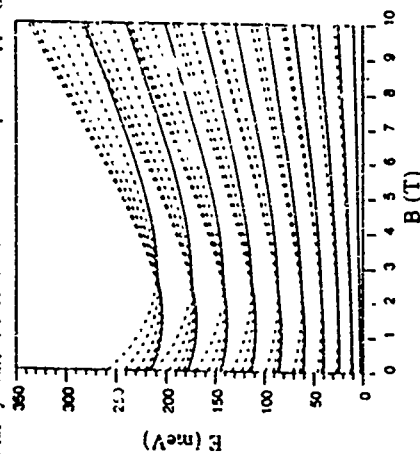


Figure 2 The energy levels given by the trial functions of equation (7) are plotted for 1-10 electrons with a solid line indicating the lowest N -electron energy in each case. Parameters are for GaAs with confinement $\hbar\omega_c = 3\text{meV}$ and zero Zeeman splitting

is composed of eigenstates of ten electrons with total spin $S = 0$. Clearly, as the spectra are incomplete, we cannot infer that the lowest of the calculated energies correspond to the ground state for all values of the magnetic field B . However, these eigenstates provide us with a skeleton of the lowest Landau level in each case. It is also a reasonable assumption that for zero magnetic field the lowest N -electron eigenenergy thus calculated is indeed that of the ground state since the corresponding trial function is chosen to have minimal kinetic energy.

To facilitate comparison with capacitance experiments we have plotted in fig. 3 the energy required to add electrons to the dot as a function of magnetic field. The lowest curve shows the energy required to add the first electron, the next curve the second electron and so on. The curves in fig. 3 thus show effective "single particle" energy levels and are calculated simply by taking the differences between successive N -particle ground states in fig. 2. It is interesting to compare these results with the experiments of Ashouri et al [6] in their capacitance experiments they measured a similar sequence of N -electron ground states as a function of magnetic field. Our choice of confinement strength of $\hbar\omega_c = 3\text{meV}$ differs from the value of $\hbar\omega_c = 5\text{meV}$ suggested in [6] as a fit to a two dimensional confinement potential. In their paper it is not indicated that allowance has been made for the contribution from confinement in the growth direction. Therefore we suppose that the confinement energy of 5meV consists partly of a contribution from confinement in the

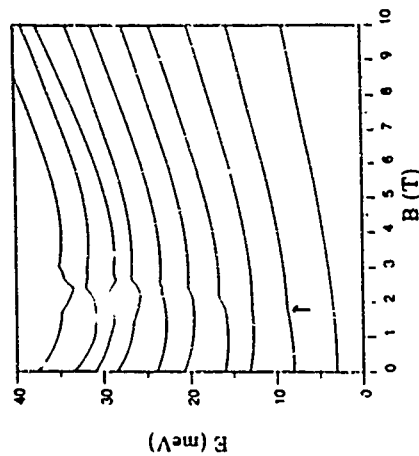


Figure 3 This graph shows the effective "single-electron" energy levels derived by plotting the differences between successive N -electron ground states in fig. 2 as a function of magnetic field. The arrow indicates the position of the spin singlet-triplet crossover in the two particle ground state.

z -direction. We have preferred to use the spectrum of two electrons as a guide to choosing $\hbar\omega_c$ since the two electron system is theoretically very well understood (see Merkt et al [10]). The appearance of a slope discontinuity in the two-particle ground state can be taken as a clear sign of the first spin-triplet crossing [11]. Thus we have chosen $\hbar\omega_c$ so that this slope discontinuity occurs in approximately the same place in our fig. 3 as in fig. 2(a) of [6]. Comparing theory and experiment more closely now we observe a similar spacing of energies at $B = 0$ for the first four levels. The most interesting feature of fig. 3 is the sequence of irregular humps occurring in different levels over the range 1.5T to 3T. Their resemblance to the features highlighted in [6] is striking and the two may turn out to be related. However there are some significant differences between the calculations and experiment. In fig. 3 the energies for $N > 4$ show a distinct drop as the magnetic field increases from zero whereas the energy levels in [6] remain nearly constant over the same range of B . Also the range of energies at $B = 0$ spans roughly 0 to 35meV in fig. 2 compared with 0 to 30meV in [6]. These discrepancies might be explicable as being due to mixing of the even states with higher quantum well subbands (an effect not considered in the model). The relatively broad well width of 175Å makes this a likely factor.

5 Conclusion

Results have been presented of ground state spectra calculated using a quantum Monte Carlo algorithm. We have been able to make a tentative comparison with ca-

peculiar measurements of N -electron ground states. The limitations to this comparison probably stem from the quasi-two dimensional nature of the model. Finally these calculations show that the fixed node Monte-Carlo method has the potential to be a flexible and accurate tool in the calculation of few-electron spectra in quantum dots.

Acknowledgements: The author wishes to thank U. Rösby for helpful discussions and his critical reading of the manuscript. Support is gratefully acknowledged from the Deutsche Forschungsgemeinschaft, SFB348.

References

- [1] R. B. Laughlin, *Phys. Rev. B* **27**, 3383, (1983)
- [2] S. M. Girvin and T. Jach, *Phys. Rev. B* **28**, 4506, (1983).
- [3] P. A. Mahaym and T. Chakraborty, *Phys. Rev. Lett.* **65**, 108, (1990)
- [4] A. Kumar, S. E. Laux and F. Stern, *Phys. Rev. B* **42**, 5166, (1990)
- [5] P. Hawrylak and D. Pfannkuche, *Phys. Rev. Lett.* **70**, 483, (1993)
- [6] R. C. Ashoori, H. L. Stormer, J. S. Weiner, L. N. Pfeiffer, K. W. Baldwin and K. W. West (to be published in *Phys. Rev. Lett.*)
- [7] F. J. Reynolds, D. M. Ceperley, D. J. Alder and W. A. Lester Jr., *J. Chem. Phys.* **77**, 5520, (1982)
- [8] F. Balton (to be published).
- [9] S. M. Girvin and T. Jach, *Phys. Rev. B* **29**, 5617, (1984)
- [10] U. Merkt, J. Huer and M. Wagner, *Phys. Rev. B* **43**, 7320, (1991)
- [11] M. Wagner, U. Merkt and A. V. Chaplik, *Phys. Rev. B* **45**, 1951 (1992)

Spectral luminescence enhancement in three-dimensional optical microcavities formed by GaAs microcrystals

S. JÜHN, K. F. LAMPRECHT, R. RÖDERER, R. A. HÖPTEL
Institute of Experimental Physics, University of Innsbruck, Technikerstr. 25/A, A-6020 Innsbruck, AUSTRIA.

Abstract

The photoluminescence of GaAs microcrystallites with average sizes in the range of 0.35 μm to 1.3 μm has been studied experimentally. The observed spectral blue-shift and line-broadening of the luminescence are explained by spectral enhancement and inhibition of spontaneous emission due to a modified photonic density-of-states in the dielectrically confined microcrystallites. The emission spectra calculated for rectangular particles via their photonic density-of-states agree well with the experimental results. Theoretical emission spectra obtained from Mie theory for spherical GaAs microcrystals yield similar results. Furthermore, the internal and surface fields of GaAs microcrystals calculated via Mie theory reveal field enhancement factors of up to 20 for optical excitation at resonance frequencies of the microcavity.

1. INTRODUCTION

Recently, there has been a strong interest in the control of spontaneous emission in microscopic resonators [1-7]. In these structures the coupling between electronic states and the radiation field is restricted to a small number of electromagnetic field modes. Resonant coupling enhances the spontaneous emission rate and ultimately allows zero-threshold laser action by the spatial and spectral overlap of a single field mode with the gain medium [2]. Increased light emission efficiencies and spectral alterations were demonstrated in one- and two-dimensional semiconductor microcavities based on III-V quantum well structures [3-7]. Theoretical calculations predict a drastic reduction of the threshold current for microcavity surface emitting lasers with sub-micron lateral dimensions [8].

In this paper we report on anomalies in the photoluminescence spectra of size-selectively fabricated sub-micron GaAs crystallites. The microcrystals are strongly dielectrically confined due to a change in the index of refraction of $\Delta n = 2.4$ at their surface. The observed spectral characteristics are shown to be consistent with the expected light emission from a three-dimensional optical microcavity. The emission spectra are calculated for rectangular GaAs microcrystals via the photonic density-of-states of these microresonators. For comparison, the emission spectra are calculated on the basis of Mie theory by estimating the absorption efficiency of spherical GaAs crystals. Finally, numerical results for the internal field distribution of GaAs microspheres are presented.

2. PHOTOLUMINESCENCE EXPERIMENTS

The GaAs microcrystallites investigated in the photoluminescence experiments were fabricated and characterized as reported previously by pulverization of monocrystalline bulk GaAs, particle separation by sedimentation techniques, and sample deposition on Si-substrates

[9, 10]. The average microcrystallite diameters and standard deviations are (a) $D_A = 0.35 \mu\text{m}$ ($\pm 0.12 \mu\text{m}$) (sample (A)), (b) $D_B = 0.55 \mu\text{m}$ ($\pm 0.19 \mu\text{m}$) (sample (B)), and (c) $D_C = 1.3 \mu\text{m}$ ($\pm 0.48 \mu\text{m}$) (sample (C)). The luminescence spectra were measured from microcrystals adhered on polished Si-substrates (immersed in liquid nitrogen) using a He-Ne laser (632.8 nm) and a Ti:Sapphire laser for cw-excitation with a maximum power density of 200 W/cm^2 and a CCD detection system with a spectral resolution of 1.4 meV .

Fig. 1 shows photoluminescence spectra from the smallest GaAs crystallites (sample (A)) at a temperature of 77 K . The spectra represent the integrated emission of roughly 20 (± 10) particles and were recorded from two different excitation areas to demonstrate the inhomogeneity of the emission spectrum within one sample. The luminescence spectra in Fig. 1 and, similarly, that of samples (B) and (C), are broadened and their maxima are shifted to higher energies as compared to the reference GaAs spectrum. The luminescence linewidth $\Delta E_{1/2}$ and the blue-shift of the luminescence maximum ΔE_m are smaller for samples (B) and (C), i.e. $\Delta E_{1/2}$ and ΔE_m decrease with increasing average crystal size. The photoluminescence intensity scales with the square of the excitation power density for all samples, indicating bimolecular band-to-band recombination. The spectral position and shape of the luminescence is independent of the excitation power density.

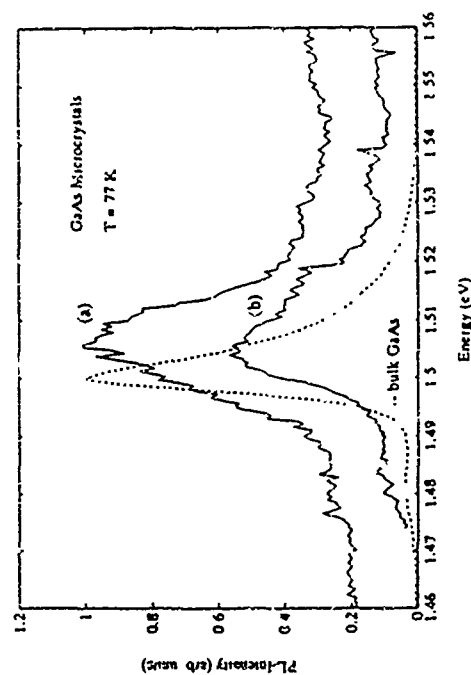


Fig. 1: Experimental photoluminescence spectra from GaAs crystallites with an average diameter of $0.35 \mu\text{m}$ (sample (A)) at a temperature of 77 K . Spectra (a) and (b) were recorded from two different excitation areas within the same sample. Dashed curve: bulk GaAs photoluminescence spectrum.

Fig. 2 summarizes the experimental results for samples (A), (B), and (C). The observed spectral blue-shift ΔE_m and the luminescence linewidth $\Delta E_{1/2}$ are plotted as a function of the microcrystallite size. The theoretical results plotted in Fig. 2 (open circles) are described below.

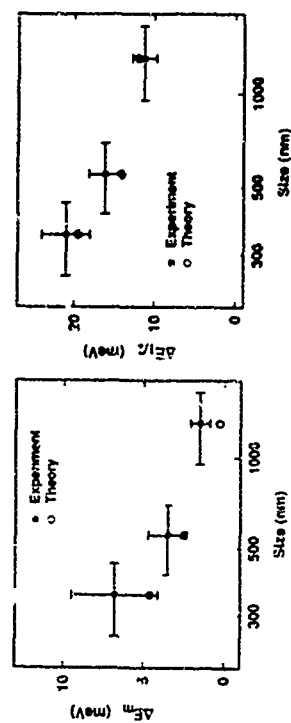


Fig. 2: Experimental results for the spectral blue-shift ΔE_m and the luminescence linewidth $\Delta E_{1/2}$ as a function of the microcrystallite size for samples (A), (B) and (C) (filled circles). Theoretical results from the microcavity model are plotted as open circles.

3. MICROCAVITY MODEL

In the following, we use the concept of the photonic density-of-states, i.e. the optical mode density, to describe the light emission from semiconductor microcrystals. The spontaneous emission rate per unit volume and unit energy is given by [11]

$$\gamma_{sp}(h\nu) = \frac{c}{n} \rho_c(h\nu) \alpha_s(h\nu) / f_{ph} \quad (1)$$

where c is the vacuum velocity of light, n is the real part of the refraction index, ρ_c is the local photonic density-of-states (i.e. the number of optical modes at $h\nu$ per unit energy and unit volume), α_s is the absorption coefficient of the unexcited bulk semiconductor, f_{ph} is the electron occupation probability in the excited state (conduction band), and f_{ph} is the hole occupation probability in the ground state (valence band) at the corresponding transition energy. Due to the strong dielectric confinement of the GaAs microcrystals (change of its index of refraction $\Delta n = 2.4$, critical angle of reflection $\phi_c = 17^\circ$) most of the internally generated light is totally reflected and redistributed to allowed modes determined by the geometry.

Fig. 3 illustrates the effect of a modified local photonic density-of-states in a microcavity on the emission spectrum. The dashed line shows the band-to-band luminescence spectrum from bulk GaAs with the continuum photonic density-of-states $\rho_0(V) = 8\pi \cdot n^3/c^3$ (dotted line). The thick solid line represents the emission spectrum for an oscillating mode density ρ_c (thin solid line). The radiative decay rate is increased ('enhanced'), if $\rho_c > \rho_0$, and decreased ('inhibited') in the opposite case.

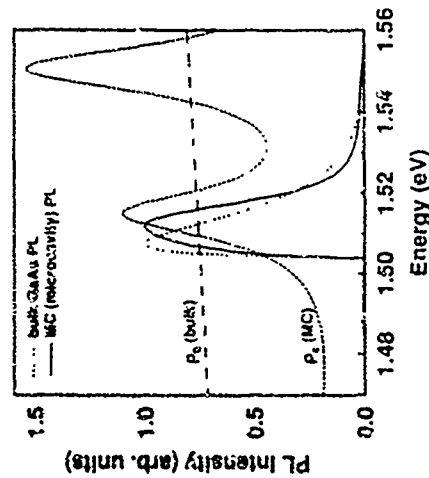


Fig. 3: Dotted line band-to-band luminescence spectrum from bulk GaAs with the continuum photonic density of states P_0 (dashed line). Thick solid line band-to-band luminescence spectrum caused by an oscillating photonic density of states P_0 (thin solid line). The radiative decay rate is increased (enhanced), if $P_0 > P_0$, and decreased (inhibited), if $P_0 < P_0$.

The photonic density of states of a square box microcavity can be approximated by [10],

$$\rho_c(\nu) \approx \frac{1}{8L^3} \sum_{\mu} \frac{\Gamma_{\mu l}/2}{(\nu - \nu_{\mu l})^2 + (\Gamma_{\mu l}/2)^2} \quad (2)$$

$$\Gamma_{\mu l} = \frac{c}{2\pi n} (\alpha_0(\nu) + \alpha_s - \frac{1}{L} \ln R_{\mu l}) \quad (3)$$

where L is the length of the cube, $\nu_{\mu l}$ is the resonance frequency of mode (μ, l) , and losses $\Gamma_{\mu l}$ are determined by the bulk material absorption coefficient $\alpha_0(\nu)$, scattering losses α_s due to surface roughness, and propagating modes (subscript n for propagating modes with $R_{\mu l} = 0.32$, subscript l for total internal reflection with $R_{\mu l} = 1$).

The photonic density of states and the luminescence spectrum were calculated from Eqs (1)-(3) for GaAs microboxes with box lengths (A) $L = 0.35 \mu\text{m}$, (B) $L = 0.55 \mu\text{m}$, and (C) $L = 1.0 \mu\text{m}$. The output coupling from individual modes in Eq (2) was taken into account by multiplying them with the corresponding average transmission coefficient (including losses due to surface roughness) [10]. The estimated luminescence linewidths and blue-shifts of the emission maximum are plotted in Fig. 2 (open circles).

4. MIE THEORY

The photonic density of states given by Eq (2) does not take into account the spatial mode distribution inside the microcrystal. The microscopic photonic density of states has been

calculated in Ref. [11] for spherical particles and is related to the efficiency factors for scattering and absorption defined in Mie theory [14]. Starting from Mie theory, analytical expressions were derived for the internal and scattered electromagnetic fields of spherical particles [14]. Furthermore, the angle-averaged external emission rate per unit energy is given by

$$r_s(h\nu) = c\rho_s(h\nu)/8\pi(h\nu)Q_{abs}(h\nu)h\nu^2 \quad (4)$$

for a spherical particle with radius a and the absorption efficiency Q_{abs} defined as the ratio of the absorption cross section to the geometrical cross section [14]. Eq (4) was derived for thermal equilibrium of the particle with a radiation field described by the Bose-Einstein distribution function f_{BE} and the free space photonic density of states ρ_1 . The absorption efficiency of a sphere with radius a is given by

$$Q_{abs} = 2 \left(\frac{\lambda}{2\pi a} \right)^2 \sum_{n=1}^{\infty} (2n+1) \left[\text{Re} \{ a_n + b_n \} - |a_n|^2 - |b_n|^2 \right] \quad (5)$$

where λ is the wavelength in the surrounding medium, and a_n and b_n are the complex scattering coefficients [14].

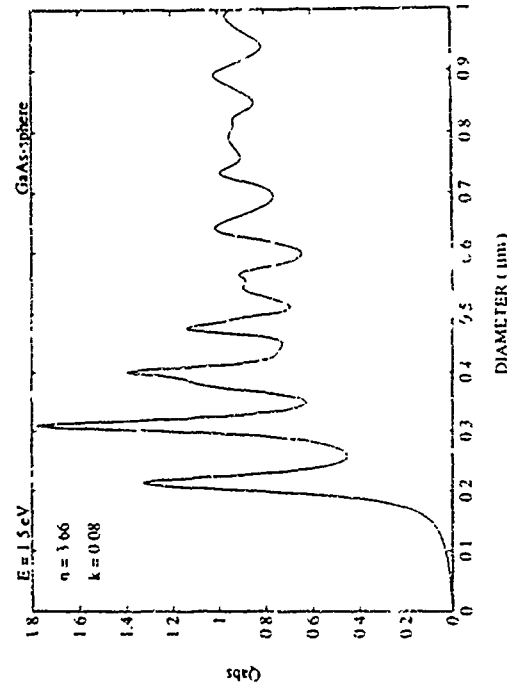


Fig. 4: Calculated absorption efficiency Q_{abs} of a spherical GaAs microcrystal as a function of the sphere diameter for optical excitation at the bandgap energy (index of refraction for bulk GaAs $n_1 = 3.66 + i0.08$ for $E = 1.5 \text{ eV}$ ($T = 77 \text{ K}$), surrounding medium $n = 1.2 + i0.0$).

In Fig. 4 the calculated absorption efficiency Q_{abs} of spherical GaAs microcrystals is plotted as a function of the sphere diameter for optical excitation at the bandgap energy. The calculation was performed after Ref. [14]. The curve shows an oscillatory behavior with several size ranges where the absorption efficiency exceeds unity, leading to an increased emission rate according to Eq. (4). Since Q_{abs} scales with the ratio of sphere diameter to wavelength, the energy dependence of Q_{abs} for a given particle size is qualitatively similar to the size dependence at a given wavelength [14].

Fig. 5 shows the emission spectra from GaAs microcrystals calculated from Eq. (4) as a function of energy at a temperature of 77 K. The spectra were estimated for the sphere diameters 400 nm, 550 nm, and 900 nm, where Q_{abs}/E_{gap} reaches a maximum, respectively (see Fig. 4). The dashed curve in Fig. 5 shows the bulk GaAs luminescence spectrum for comparison. The microsphere luminescence spectra reveal a size- and energy-dependent enhancement that leads to a spectral blue-shift of the luminescence maximum and a line-broadening.

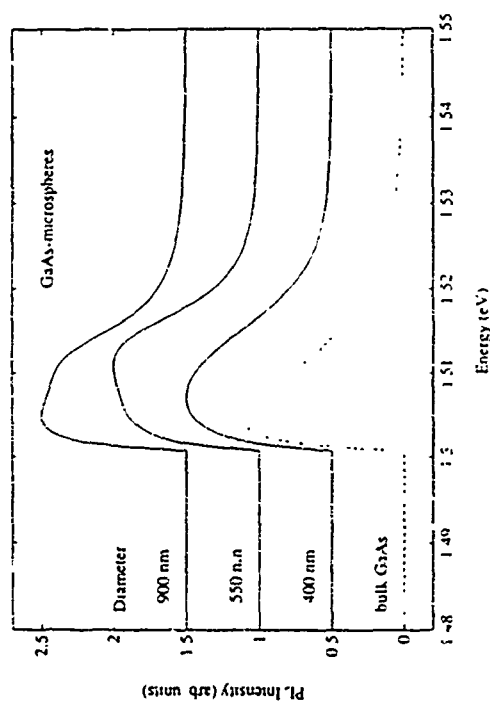


Fig. 5: Calculated luminescence spectra from GaAs microcrystals as a function of energy at a temperature of 77 K. The spectra were estimated for the sphere diameters 400 nm, 550 nm, and 900 nm, where Q_{abs}/E_{gap} reaches a maximum, respectively (see Fig. 4). Dashed curve: bulk GaAs luminescence spectrum.

The internal electric field of GaAs microcrystals was calculated after Ref. [15] for optical excitation at the bandgap ($E = 1.5$ eV at 77 K) by a plane wave with a field amplitude E_0 . Fig. 6 shows the normalized angle-averaged electric field $\langle E \rangle / E_0$ as a function of the normalized radius r/a for different sphere diameters $2a$. The values for the radii were chosen from Fig. 4 at

'resonant' ($Q_{abs} > 1$) and 'nonresonant' ($Q_{abs} < 1$) positions. At resonant sizes ($2a = 0.214$ μm , 0.31 μm , and 0.89 μm) the averaged internal field is enhanced up to $\langle E \rangle / E_0 \sim 20$ near the surface, whereas at nonresonant sizes (e.g. $2a = 0.26$ μm) the field maximum occurs at the sphere center and is less pronounced. Similarly, an estimation of the surface field following the treatment in Ref. [16] revealed resonant enhancement of the radial field component at the surface [17].

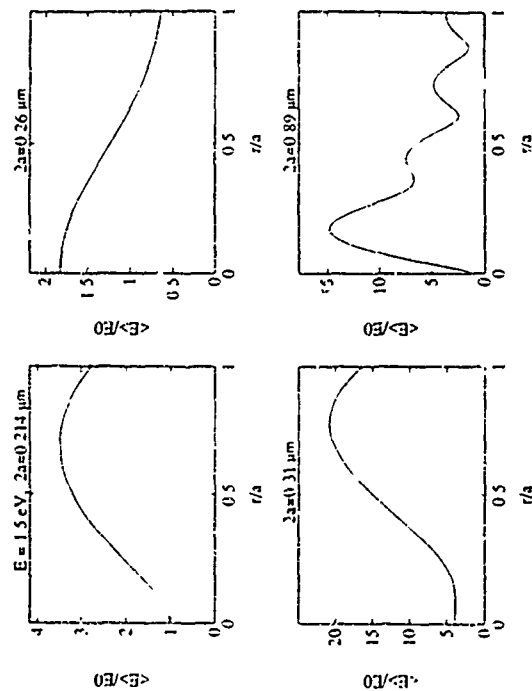


Fig. 6: Calculated angle-averaged electric field $\langle E \rangle / E_0$ in GaAs microcrystals (laser excitation at the bandgap with a field amplitude E_0) as a function of the normalized radius r/a for different sphere diameters $2a$ (given in micrometers). The values for the radii were chosen from Fig. 4 at 'resonant' ($Q_{abs} > 1$) and 'nonresonant' ($Q_{abs} < 1$) positions.

5. DISCUSSION

The experimentally observed photoluminescence spectra from GaAs microcrystallites exhibit a line broadening and a blue-shift of the luminescence maximum which both increase with decreasing average crystal size (Fig. 2). This anomalous behavior is consistent with the calculated effects due to dielectric light confinement in semiconductor microcrystals.

The theoretical results for a three-dimensional optical microcavity show that a resonance in the photonic density-of-states above the band gap energy enhances the emission rate and thus

modifies the shape of the luminescence spectrum. Due to the asymmetry of the luminescence spectra and the statistical size distribution of the crystals, a blue-shift of the total luminescence maximum is expected, and the spectral changes get more pronounced with decreasing crystal size, i.e. increasing mode spacing [10]. The optical excitation process of the microcrystals and the interaction with the Si-substrate are not included in our model. However, the results from similar experiments show only a minor effect of different substrates (insulator or metal) on the emission spectrum [18]. In these experiments structural resonances were observed in the luminescence spectra of dye-doped dielectric microspheres [18].

Similar theoretical results for the luminescence spectra are obtained from an analysis based on Mie theory for GaAs microspheres. The emission spectrum is determined by the absorption efficiency, which is implicitly related to the photonic density-of-states [19]. Since the absorption efficiency is resonantly enhanced as a function of both the sphere size (Fig. 4) and the excitation wavelength, size-selective excitation is expected. Therefore, the relative luminescence intensity from spheres with different sizes (Fig. 5) depends on the absorption efficiency both at the excitation and the emission wavelength.

The strength of the internal field enhancement (Fig. 6) reaches remarkable values of up to a factor of 20 at resonant excitation. This field enhancement near the surface corresponds to the 'whispering gallery' modes that have been reported in disklike semiconductor structures [6]. The resonant field enhancement on the microcrystal surface should lead to surface-enhanced Raman scattering as already observed on GaP microcrystallites [20]. The internal field enhancement depends strongly on the imaginary part of the index of refraction and reaches several orders of magnitude below the bandgap of GaAs. Therefore, strong optical nonlinearity or even intrinsic optical bistability might be feasible at spectrally narrow optical transitions below the bandgap or at indirect transitions in different materials.

The agreement of the calculated spectral characteristics in Fig. 2 and Fig. 5 with the experimental results in Fig. 3 leads us to the conclusion, that the observed photoluminescence spectra result from *spectral enhancement and inhibition of spontaneous emission in dielectrically confined GaAs microcrystallites*.

6. CONCLUSION

Spectral alterations in the photoluminescence of GaAs microcrystallites have been investigated experimentally. The observed behavior is in agreement with the calculated effects of dielectric light confinement in three dimensional semiconductor microcavities. The consequences of enhanced spontaneous emission in this kind of microcavity are promising for applications in nonlinear optics and optoelectronics.

This work has been supported by the Fonds zur Förderung der Wissenschaftlichen Forschung (FWF), Austria, under projects number P7558 and P8704.

REFERENCES

1. E. Yablonovitch, *Phys Rev Lett* **58**, 2059 (1987).
2. F. De Martini, G. Innocenti, G. R. Jacobovitz, P. Mariani, *Phys Rev Lett* **59**, 2955 (1987).
3. Y. Yamamoto, S. Machida, K. Igeta, G. Bjelt, in *Coherence Amplification and Quantum Effects in Semiconductor Lasers*, edited by Y. Yamamoto (Wiley, New York, 1991).
4. T. J. Rogers, D. G. Deppe, B. G. Strzemecki, *Appl Phys Lett* **57**, 1855 (1990).

5. T. Yamauchi, Y. Arakawa, M. Nishio, *Appl Phys Lett* **58**, 2339 (1991).
6. S. L. McCall, A. F. J. Levi, R. E. Slusher, S. J. Pearton, R. A. Logan, *Appl. Phys. Lett.* **60**, 289 (1992).
7. E. F. Schubert, Y.-H. Wang, A. Y. Cho, L.-W. Tu, G. J. Zydzik, *Appl Phys Lett* **60**, 921 (1992).
8. T. Bzba, T. Hamano, F. Koyama, K. Iga, *IEEE J Quantum Electron* **28**, 1310 (1992).
9. S. Juen, K. Ueberbacher, J. Baldaut, K. F. Lamprocht, R. Tossadi, R. Lackner, R. A. Hopfel, *Superlattices and Microstructures* **11**, 181 (1992).
10. S. Juen, K. Ueberbacher, J. Baldaut, K. F. Lamprocht, R. A. Hopfel, *Appl Phys Lett* **62**, 1958 (1993).
11. H. B. Bebb, E. W. Williams, in *Semiconductors and Semimetals*, Vol. 8, ed. by R. K. Willardson and A. C. Beer (Academic Press, 1981).
12. D. P. O'Brien, P. Meystre, H. Walther, in *Advances in Atomic and Molecular Physics*, Vol. 21, ed. by D. Bates and B. Bederson (Academic Press, Orlando, 1985).
13. S. C. Ching, H. M. Lai, K. Young, *J Opt Soc Am B* **4**, 1995 (1987).
14. C. F. Bohren, D. S. Huffman, *Absorption and Scattering of Light by Small Particles* (John Wiley, New York, 1983).
15. P. R. Conwell, P. W. Barber, C. K. Ruthford, *J Opt Soc Am A* **1**, 52 (1984).
16. B. J. Messinger, K. U. von Raben, R. K. Chang, P. W. Barber, *Phys Rev B* **24**, 649 (1981).
17. S. Juen, K. F. Lamprocht, R. Rodriguez, R. A. Hopfel, unpublished.
18. S. C. Hill, R. E. Benner, C. K. Ruthford, P. R. Conwell, *Appl. Opt.* **23**, 1680 (1984).
19. A. J. Campillo, J. D. Eversole, H.-B. Lin, *Phys Rev Lett* **67**, 437 (1991).
20. S. Hayashi, R. Koh, Y. Ichiyama, K. Yamamoto, *Phys Rev Lett* **60**, 1085 (1988).

ThP14

Efficiency of the carrier capture efficiency of a quantum well

France Telecom, CNET/PAB, 196 av. Henri Ravera, 92225 Nanterre Cedex FRANCE
J.M. Gerard
and
B. Deveaud
France Telecom, CNET/LAB, 22401 Nanterre FRANCE

Abstract:

A GaAs quantum well (QW) placed in an AlGaAs barrier layer of linearly graded composition has been studied by photoluminescence, so as to evaluate experimentally the carrier capture efficiency of a QW in an electric field. The capture probability can be drastically enhanced or reduced by introducing a slight compositional asymmetry (3 to 5% Al) between both sides of the QW. This tuning is efficient for temperatures as high as 77K. Our experimental results, supported by a quantum mechanical calculation of the capture probability, suggest novel routes for optimizing QW infrared photodetectors and QW lasers.

The efficiency of carrier capture processes often define the ultimate performance of quantum well (QW) based devices. For instance, the capture of photoexcited carriers by subsequent QWs limits the optical gain, and therefore the responsivity and detectivity of QW infrared photodetectors (QWIPs) [1]. Hence, the capture time of electrons in the optical cavity by the QW limits the modulation bandwidth of separate confinement QW lasers [2]. The capture efficiency of a quantum well (QW) markedly depends on its design. For instance, the oscillatory dependence of the capture time as a function of the QW thickness, predicted theoretically some years ago [3], has found recently a clear experimental confirmation from time resolved photoluminescence (PL) studies [4, 5]. It is therefore necessary (and possible) to take into account capture processes in a global attempt to optimize optoelectronic QW devices. Up to now, only a minimization of the electron capture time in undoped separate confinement multi QW heterostructures has been considered [6]. It appears now more generally (highly desirable) to study the capture efficiency of a QW for electrons diffused by an electric field (which is the relevant situation for vertical transport optoelectronic devices such as QWIPs or electrically pumped lasers). 2) We are able to adjust independently such electronic properties of the structure as its operating wavelength and the QW capture efficiency.

We show for the first time that the capture probability p_c of a diffused electron to be captured by a QW can be tuned very efficiently by introducing a slight asymmetry of the barrier heights of the QW. For moderate electric fields, the dominant capture mechanism presumably relies on LO phonon scattering in absence of electric field. In order to avoid the capture of a carrier (e.g. an electron), we can raise the upstream barrier height h_1 with respect to the downstream barrier height h_2 by typically $h_{ph} \approx 30$ meV, even after emission of a single LO phonon (the electron still occupies relaxed quantum state and can be diffused by the electric field). Electron capture then requires multiple phonon emission, and is therefore drastically less probable. On the other hand, the capture probability p_c can also be drastically enhanced by raising h_2 with respect to h_1 . If the barrier height difference $\Delta h = h_2 - h_1$ is larger than the typical kinetic energy of incoming electrons, the capture probability will become close to unity.

Since time resolved PL experiments cannot be easily conducted for QWs under electric field, we used a direct approach which permits an optical investigation by e.w. PL of the influence of the QW barrier asymmetry on p_c . We mimic the presence of an electric field by inserting the QW whose capture efficiency is studied in a barrier of linearly graded composition. The PL intensity of the QW under continuous excitation of the upstream barrier is then proportional to the probability for injected electrons to be captured by the QW. We describe hereafter two series of experiments which highlight the efficient tuning of p_c resulting from a slight asymmetry in the QW composition profile.

Our GaAs/AlGaAs test structures have been grown by molecular beam epitaxy (MBE) on GaAs (001) substrates. Their design is plotted in the insets of figures 1 and 2 for the first and second series of experiments respectively. Each sample comprises: from surface to buffer layer, a thick surface absorbing GaAs cap layer (0.4 μ m), the upstream Ga_{0.9}Al_{0.1}As graded

barrier (width = 1 μ m), the GaAs QW (C), whose capture efficiency is studied, the "downstream" Ga_{0.9}Al_{0.1}As graded barrier (width = 1 μ m), and a broad GaAs QW (T). A low MBE growth rate (0.3 μ m/s) has been implemented in order to ensure a perfect control of the composition profile. Finally, the structure is entirely Be-doped low n -type (1.5×10^{18} cm⁻³).

Our e.w. PL experiment is performed at 8K under excitation with the blue 476.5 nm lines of an argon-ion laser. For this wavelength the absorption coefficient in the cap layer A is $\alpha \approx 6000$ cm⁻¹, so that we have no significant direct excitation of QWs T and C. The generated electron-hole pairs diffuse in layer A, and the electrons are drifted in the apparent electric field of the graded barrier layer. The valence band configuration of this p -type heterostructure is essentially flat in our power density range (typically 500 W cm⁻²), so that this apparent electric field is close to 15 kV/cm in the graded layers, i.e. in the useful range for QWIPs. On the other hand, majority holes move nearly freely throughout the structure. A fraction p_c of the injected electrons is captured by QW C, whereas transformed electrons are collected in QW T. At such a low temperature (8K), thermoemission of electrons out of QW C can be neglected, since GaAs/GaAlAs structures have furthermore a radiative efficiency close to unity at low temperature. The PL intensity of QWs C and T respectively reflect the proportions of incoming electrons which have been captured or not by QW C, i.e. p_c and $1-p_c$.

We study in a first experiment a 65 Å thick Ga_{0.9}Al_{0.1}As QW. In our reference sample R_1 , the downstream barrier of QW C has a 0.7% lower Al composition than the upstream barrier, in order to mimic the potential drop across the QW for a 1.5 kV/m electric field. In a series of "modified" samples, the Al composition of the upstream barrier has been uniformly lowered (or raised) by a variable Δx . The PL spectra obtained at 8K for these samples ($\Delta x = 0.005$ and -0.005) are shown in figure 1. We observe for each sample two PL peaks, easily attributed to the thin QW C and to the large QW T. The relative intensity of these peaks is drastically affected by the introduction of a small barrier ($\Delta x = 0.005$) or a small "jump" ($\Delta x = 0.005$) for the diffused electrons: the PL intensity of QW T is reduced by a factor of 10 in the first case, and enhanced by a factor of 2.5 in the second case, which reveals a similar change for the proportion $1-p_c$ of the transmitted electrons.

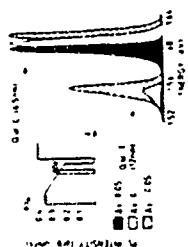


Fig. 1 Normalized 8K PL spectra for the reference sample R_1 ($\Delta x = 0$), and for two modified samples, for which the electron capture by QW C is enhanced ($\Delta x = 0.005$) or inhibited ($\Delta x = -0.005$). The Al composition profile of these GaAs/GaAlAs heterostructures is sketched in insert by solid and dashed lines respectively.

This efficient tuning of $1-p_c$ is obtained for a moderate change of the composition profile ($\Delta x = 0.005$ corresponds to 45 meV change of the upstream barrier height, i.e. in the energy range of the (higher energy) AlAs-type LO phonons in the GaAlAs barrier (≈ 47 meV). In this experiment however, the capture efficiency of QW C is always very large (p_c equal to 0.85 for the reference sample, remains larger than 0.5 for all samples). The comparison with our second experiment will indicate that this large capture probability is essentially related to the presence of a high barrier on the substrate side of QW T in the vicinity of QW C (distance: 37 nm). A second series of samples, which mimics more closely the conduction band configuration in QWIPs, has also been grown. Their structure sketched in figure 2, differs of the first series in that: 1) the high barrier on the substrate side of QW T has been suppressed, 2) the width of the downstream barrier has been enlarged up to 100 nm, 3) our reference QW C is now a 5 nm thick Ga_{0.9}Al_{0.1}As QW. Furthermore, the "modified" samples are now obtained by changing the height of the downstream barrier.

The PL spectra obtained for the reference sample R_2 ($\Delta x = 0$) and two modified samples ($\Delta x = 0.005$ and -0.005) are displayed in figure 2. The capture probability p_c for the reference sample

is now 0.4. Here again a drastic modification of the intensity ratio of QWs, C and T emissions is observed when a slight QW asymmetry is introduced. It is worth being emphasized that the total PL intensity remains, as expected, essentially constant p_c becomes close to 0.85 when the composition of the Al composition of the downstream barrier is raised by 0.03, whereas capture probabilities as low as 0.15 and 0.10 are observed when it is lowered by 0.03 and 0.06 respectively. On the other hand, the PL peak energy of QW C is essentially unaffected for the "modified" samples: capture characteristics and other electronic properties of QWs can be optimized independently by using this technique.

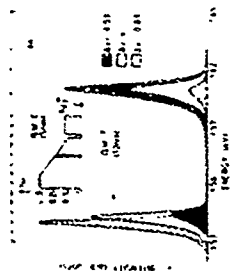


fig. 2. Same as fig. 1, for the reference sample R_1 ($\Delta x = 0$), and two modified samples ($\Delta x = 0.03$ and 0.06). The Al composition profile of these GaAs/GaAlAs heterostructures is sketched in insert, by solid and dashed lines respectively. The PL intensity scale is the same for all samples.

As required for any practical application to QWIPs, this effect is also observed at 77K; we obtain $p_c = 0.20, 0.45$ and 0.70 respectively for $\Delta x = 0.03, 0$ and 0.06 . Thermoemission of electrons from QW C totally blurs the data obtained at 300K (by simply enhancing the PL intensity of QW T), and presumably accounts for the slight differences observed between 8K and 77K results.

No quantum mechanical calculation of p_c has been conducted up to now for carriers drifted in an electric field. We propose here a model approach, which gives, despite its roughness, a good estimate of p_c in QWIPs and describes satisfactorily the influence of Δx on p_c . Two major problems are the difficulty to describe the overall relaxation of the electrons in the graded layer and the fact we need to take into account the finite electron mean free path of the electron wave function when calculating p_c . To overcome these difficulties, we consider an electron "just arriving" at QW C, we attribute to this electron a wave packet ψ , which typical extension is defined by the electron mean free path. We then compute the bound states k_z of this heterostructure comprising both QWs, the graded layer and a semi-infinite barrier on the substrate's side of QW T, and the scattering rate W_{ph} for single LE phonon emission processes for all possible initial and final electron minibands, by using Fermi's golden rule and a Fröhlich matrix element. Retaining the dominant energy relaxation processes only, we estimate p_c as

$$|V\rangle = \sum_k |k\rangle \quad p_c = \frac{\sum_k |V_k|^2}{\sum_k |V_k|^2 + \sum_k |V_{\text{ph}}|^2}$$

where V labels the miniband originating from the simple bound state k_z at QW C. Figure 3 displays for both series of samples the influence of Δx on the calculated capture probability, for a 20 nm broad rectangular wave packet (this size corresponds to the typical mean free path of the electron for a 1.5×10^6 V/m electric field and a $\mu_e = 2000 \text{ cm}^2/\text{Vs}$ electron mobility in GaAs/AlAs [6]). For the reference samples R_1 and R_2 , we respectively estimate p_c to be 0.195 and 0.1 (for a lower quality barrier material, p_c is somewhat larger, e.g. $p_c \approx 0.1$ and 0.15 for a 15 nm broad wave packet). On the one hand, this clear difference confirms the drastic influence of the proximity of a high barrier on the capture efficiency of QW C, already observed experimentally. On the other one, our theoretical estimate for p_c in sample R_1 is in correct agreement with previous measurements of p_c ($p_c \approx 0.1$) by admittance spectroscopy [7] and ac, 20 mHz, particularly well for the $p_c \approx 0.19$ average estimate, which has been extracted from

the measurement of the optical gain of numerous QWIPs [8]. Though rather crude, our model is therefore very likely to describe accurately the influence of a QW asymmetry on p_c . The theoretical dependence of p_c on Δx is plotted on figure 3. For the second series of samples (as well as QWIPs), a small Δx ($\Delta x \leq 0.05$) allows to reduce by a factor of three (down to 0.03) or enhance p_c up to 0.85.



fig. 3. The experimental and theoretical values of p_c are plotted as a function of Δx for both kind of heterostructures, whose composition profiles are sketched in the inserts of fig. 1 and 2 respectively.

Though the experimental relative dependence of p_c on Δx is well described for both series of samples, differences are observed between experimental and calculated values of p_c . This effect is presumably related to the ambipolar character of the transport and capture in our samples. At the initial stage of the illumination, the capture probability by QW C is much larger for the holes than for the electrons. A photoinduced electric field E_{ph} appears between QW C and QW T under steady state illumination [9], in order to favor the transport of holes across the structure toward QW T. Consequently, the capture probability of the incoming electrons by QW C is enhanced (E_{ph} is such that electron and hole currents flowing from QW C to QW T are equal, as such, E_{ph} and the capture probability of electrons are independent of the extraction power). We therefore do not expect our experiment on the reference sample to give a quantitative estimate for p_c in conventional QWIPs, but reflect only qualitatively the dependence of p_c on Δx . The determination becomes however quantitative when p_c is large, since nearly all photo-created electron-hole pairs then recombine in QW C.

To conclude, the introduction of a slight compositional asymmetry for QW barriers allows to tune very efficiently the probability for electrons, drifted by an electric field, to be captured by this QW. This opens the way to an independent optimization of capture characteristics and optical properties of numerous QW based optoelectronic devices.

The authors gratefully acknowledge J.Y. Marzin, G. Bastard, J.F. Palmer, A. Regreny, B. Lumbert, F. Clément, D. Morin, M. Voss and M. Quilès for stimulating discussions.

References

- [1] *Interband Transport in Quantum Wells*, edited by E. Rosencher, B. Vinter and D.F. Lequeux (Reims, London 1992).
- [2] P.W.M. Blom, J.E.M. Haverkort and J.H. Wolter, *Appl. Phys. Lett.* **58**, 2762 (1991).
- [3] J.A. Brun and G. Bastard, *Phys. Rev. B* **33**, 1420 (1985).
- [4] B. Deveaud, A. Chomette, D. Jorini and A. Regreny, *Solid State Comm.* **85**, 367 (1993).
- [5] P.W.M. Blom, C. Smir, J.E.M. Haverkort and J.H. Wolter, *Phys. Rev. B* **47**, 2072 (1993).
- [6] Stringfellow G.B., *J. Appl. Phys.* **50**, 4178 (1979).
- [7] F. Lau, E. Rosencher and B. Vinter, *Appl. Phys. Lett.* **62**, 1143 (1993).
- [8] H.C. Liu, *Appl. Phys. Lett.* **60**, 1707 (1992).
- [9] C.T. Lin, J.M. Liu, P.A. Galtburka, S. Luryi, D.I. Sisco and A.Y. Cho, *Phys. Rev. Lett.* **67**, 2231 (1991).

Stark-Wannier states in nanostructures

E.A.M. Fagotto, P.A. Schulz and J.A. Brum
 INSTITUTO DE FÍSICA, UNICAMP, Cx. 6153, 13081 - Campinas (SP) - Brazil

Abstract

We study the effects of a longitudinal external electric field on the electronic properties of an open-quantum-dot superlattice. These structures present the formation of two different gaps, one associated with the periodicity of the structure imposed upon the 1D mode and the other associated to the destructive interference between the 1D mode and the quantum-dot states. The transmission coefficients between two quasi-two dimensional reservoirs through these structures are calculated. The electric field presents different regimes at weak fields the transmission peaks associated to the tunneling through the confined dot states show an energy shift and a progressive decline of the transmission. At moderate fields the transmission bands become sharp and the transmission peaks to one. As the electric field increases the anti-resonance gaps widen. Finally, at large electric fields, the Wannier-Stark levels are completely formed and the transmission is characterized by a series of relatively equally spaced peaks.

Nanoscopic systems have been intensively studied in the recent years [1]. With the improvement of nano-scale fabrication techniques, it has been possible to design a whole new kind of structures based on the high-mobility two-dimensional (2D) electron gas formed in GaAs (GaAlAs hetero) junctions. The physics behind these systems is based on the lateral confinement which binds the carriers in one or two additional dimensions besides the epitaxial one. Recently, the interplay between one- and zero-dimensional levels has been considered. Particularly, an open-quantum-dot superlattice was built and transmission gaps were observed [2]. The existence of carrier confinement in open cavities was first discussed by van der Marel [3] and Peeters [4]. More et al [5] discussed for the first time the effects of a periodic quantum-dot structure superimposed on a one-dimensional channel. Brum [6] discussed the effects of the interplay between the cavity confined states and the superlattice states. More recently, other structures based on the same principles have been considered [7,8]. The effects of a longitudinal external electric field, F , in a single constriction and quantum chains have been studied by Castano et al [9]. Their emphasis was on the nonlinear transport characteristics in these nanostructures.

An electric field superimposed on a periodic potential leads to the replacement of the band structure by a ladder of spatially localized states (Wannier-Stark states) equally spaced in energy by eFd , where d is the periodicity of the structure [10]. Recently, these states have been observed in one-dimensional semiconductor superlattices [11,12]. The coupling among Wannier-Stark levels originated from different subbands has also been considered [13,14].

In this work, we discuss the effects of an external electric field, applied along an asymmetric multiple-open-quantum-dot structure (AMQDS). Our main interest is on their electronic properties. They will be probed by the transmission coefficient through the structure employed by two quasi-two-dimensional reservoirs. On structure is similar to the one discussed previously by one of us [6]. A laterally patterned GaAs/(Ga,Al)As heterojunction is considered. We assume a strong confinement along the z -direction so that the system is in the Electric Quantum Limit with

respect to quantization of motion in this direction. The lateral confinement is sketched in Figure 1. Two structures are studied: one with a single quantum dot and the other with three quantum dots. We perform a multi-mode transmission calculation following the same lines as in previous work [6]. We approximate the electric field effects by considering only the potential drop from one layer respective to the other. Inside each layer, a flat band is assumed. Our calculations for a large number of dots have shown that three dots are already enough to reflect the non-superlattice effects. Basically, they are formed by periodic interference superimposed on one side of a one-dimensional (1D) channel. The carriers are assumed to be ballistic in its transport. They are linked to the two wide leads which behave as quasi-two dimensional reservoirs. The calculations give origin to a zero-dimensional confinement potential. At least one zero-dimensional state is energetically below the first 1D mode. The excited dot states will then be resonant with the 1D modes.

In the absence of electric field, the transmission probability is rich in structures [4]. At energies below the first 1D mode, it shows a narrow band of energy with unitary transmission. This is associated with the tunneling through the confined-quantum-dot level. At energies above the first 1D mode, transmission gaps are superimposed on the transmission-step quantization. These gaps have two different origins: one is associated to the superlattice gaps, due to the periodicity introduced in the 1D channel. The other comes from the destructive interference between the 1D mode and the quantum-dot levels. The latter can also be seen as the anti crossing between two bands: a wide band, the 1D mode, and a narrow band, formed by the small overlap among the quantum-dot levels. Due to the one-dimensionality of the transmission channel, the anti crossing creates a gap in the transmission, associated with the anti resonance gap on the band structure [6]. The character of the 1D mode levels is well illustrated with the wave-functions. Fig. 3(a) shows the wave-function probabilities for an open-quantum-dot structure for an energy at the second transmission maximum in the absence of electric field. Fig. 5(a) and Fig. 6(a) show the wave-function probabilities for a three-open-quantum-dot structure, for an energy at the third peak of the first transmission band maximum and at the second peak of the second transmission band maximum, respectively, in the absence of the electric field. Figures 3(a) and 6(a) show maxima of probability of finding the electron at the narrow constrictions characterizing the states as 1D mode-like. On the other hand, the third peak of the first transmission band maximum, Figure 5(a), shows the maximum of the wave-function probability at the wide constriction, i.e., at the quantum dot.

In the presence of an electric field applied along the AQDS the two bands present a qualitative different behavior. This is reflected at the gaps formed in its transmission probability. On one side, the Wannier-Stark states are evenly spaced in energy in both leads. This implies that the narrow band will largely widen with the electric field in comparison to the wide band in order to accommodate the Wannier-Stark levels. At the same time, the coupling of these bands is responsible for the anti resonance gap. These effects may be separated in three ranges of values for the electric field showing qualitative different behavior. In the following, we compare the effects for the one dot and the three dot case for the different electric fields.

Figures 2 (a-i) shows the transmission probability for the one-dot case as a function of the electron incoming energy for several values of electric field. At weak electric fields, we clearly observe a linear shift in energy of the first transmission peak. The peak is associated with the tunneling through the fundamental quantum-dot state below the first 1D mode. The anti resonance gap, associated to the second dot state, shows an identical shift, as it is expected. For

the same range of electric field, the transmission maxima fall to values lower than one. This is a consequence of the break of symmetry in the barriers through which the electron has to tunnel [15]. As the electric field increases, the first peak is suppressed since it shifts to energy values below the smaller minimum.

At intermediate fields, we observe the evolution of the transmission band towards a sharp peak. Originally, this band is associated with the first 1D mode. The electric field breaks the degeneracy between the modes from the two narrow constrictions. The first 1D mode hybridizes with the dot state given origin to a sharp transmission. When these states are resonant one with the other, the hybridization is maximum and the transmission reaches the unitary value. As the electric field further increases, the dot state falls below the energy of the 1D mode. The transmission is then due to the tunneling through a confined state, in a similar behavior as the fundamental dot state at the zero electric field. The difference to the latter case is that now, the confined state is a hybrid one. This is illustrated in Figures 3(a) and 3(b) where the wave-function probability for the second transmission maximum is plotted for zero electric field and for $F=0.53$ kV/cm. We clearly observe its evolution from a 1D mode toward a 1D-0D hybrid state. As a consequence of this hybridization, the energy shift of this maximum has a weaker dependence with the electric field than the dot levels. Its position gets close to the anti resonance gap and their wave-function probabilities are quite similar.

For higher electric fields (not shown here), the above behavior repeats in a quite similar way for the higher dot levels.

Figure 4 (a-i) shows the three-dots structure transmission probability as a function of the electron incoming energy for several electric fields. The three-dots case presents a quite different behavior. As mentioned before, the superlattice effects are already present. The first series of maxima in the transmission are associated to the narrow band formed by the confined fundamental dot states. The second transmission band is associated with the 1D mode. After that we observe a strong reduction in the transmission probability which is related to the gap formed by the periodicity of the structure. The next gap is due to the anti crossing between the 1D mode and the dot bands. This gap is strongly marked even for a small number of periods [6].

At weak electric fields, the first band shows a similar behavior as the single dot case: a linear energy shift is observed accompanied by the fall of the transmission probability. At higher electric fields ($F > 0.02$ kV/cm) the transmission peaks again for a single level, reaching the unitary value for the last level of the band. The other levels have practically disappeared. This behavior is similar to the transmission band associated to the first 1D mode in the single dot case and it is a common characteristic to the transmissions through a set of levels. Here, due to the discreteness of the states, the sharpening of the band is replaced by the peak at a single level. The same behavior can be observed for the other bands, with the sharpening of the transmissions and remaining at unitary value at $k_z = \pi$ for one level. Only at higher electric fields ($F > 0.04$ kV/cm) these transmissions start to fall below one. In Figures 5 (a) and (b) we plot the wave-function probabilities for the third peak at the first transmission band for $F=0$ kV/cm and $F=0.06$ kV/cm, respectively. We clearly observe the extended state to localize into a discrete state, typical of a Wannier-Stark level. Figures 6 (a) and (b) show the wave-function probabilities for the second peak at the second transmission band at the same values of electric field as in Figures 5. As in Figures 3, we clearly observe the 1D mode and the dot level hybridization.

We also observe in Figures 4 (a-i) a different behavior for the transmission gaps. The superlattice gap practically does not change. This is not surprising since the electric field splits the wide 1D mode bands into discrete levels. For the electric fields considered here, the band width can accommodate the Wannier-Stark levels without modifying the gap width. At the higher fields shown here, we observe a slight narrowing of the superlattice gap. This reflects the limit of the 1D mode band to accommodate the Wannier-Stark levels within its energy width. A complete different behavior is shown by the anti resonance gap. Here, the gap is formed by the anti crossing of the narrow dot band with the wide 1D band. As the Wannier-Stark levels are formed, they further contribute to prevent the transmission. At intermediate electric fields ($F = 0.04$ kV/cm), the transmission gap broadens significantly. This is due to the increasing separation in energy of the dot levels. They are, however, close enough to each other in order to prevent almost entirely the transmission in this energy range due to the anti resonance effect. At higher fields, the Wannier-Stark levels are too separated in energy and some transmission is possible for the energy between two different levels. Actually, for these and higher values of electric field, the concepts of gap and band start to break down.

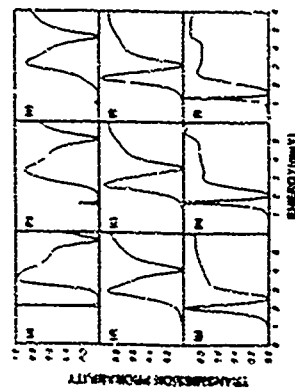
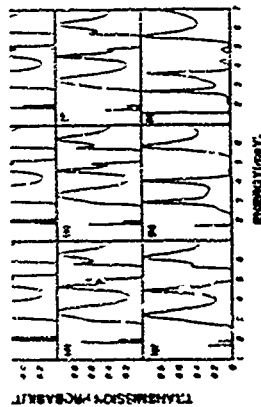
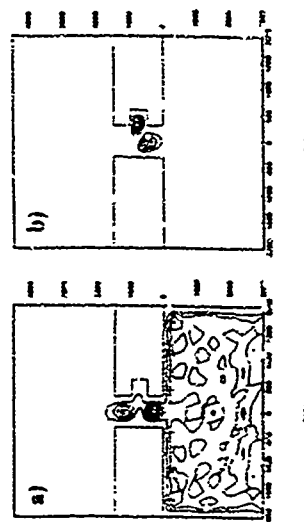
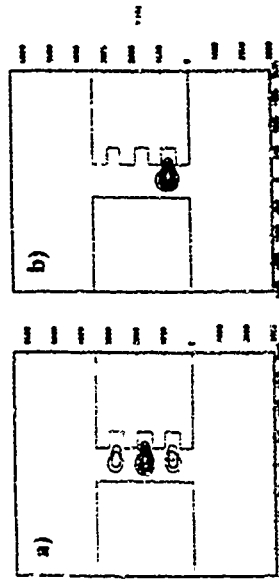
A direct observation of the above effects depends on several additional effects. Conductance measurements have been one of the most powerful experimental tools to probe similar effects [1,2]. However, some aspects remain to be cleared: charge effects, such as Coulomb blockade, may hamper their observation for the state-of-art of the mesoscopic systems. Another difficulty is in the connection among transmission probabilities and conductance measurements, particularly in the presence of nonlinear effects. A complete solution of the transport problem in these systems is beyond the scope of this work. Nevertheless, we believe that the effects discussed here should be reflected in the electronic properties of actual systems and should be considered whenever confined cavity states are coupled to 1D modes.

Acknowledgments: E.A.M.F. is supported by the Brazilian Agency CAPES, P.A.S. and J.A.B. are partially supported by the National Council for Research and Development (CNPq, Brazil).

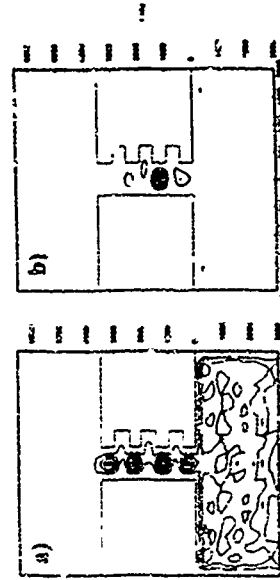
1. For a review see Beenakker and van Houten, *Quantum Transport in Semiconductor Nanostructures*, in *Solid State Physics*, p. 1, edited by H. Ehrenreich and D. Turnbull, Academic Press, New York, 1991.
2. L.P. Kouwenhoven, and W.J. Hekking, B.J. van Wees, C.J.P.M. Harman, C.E. Timmering, and C.T. Foxon, *Phys Rev Lett* **65**, 361 (1990).
3. D. van der Marel, in *Nanostructures Physics and Fabrication*, 1989, (College Station, Texas, p. 149, ed by M.J. Reed and W.P. Kirk, Academic Press, New York, 1990).
4. S.M. Peters, *Science and Engineering of Low-Dimensional Semiconductor Structures*, p. 107, ed by S.P. Beaumont and C.M. Sotomayor Torres (Plenum, New York, 1990).
5. E. Ufeda, E. Castaño, and G. Kirczenov, *Phys Rev B* **41**, 12350 (1990).
6. J.A. Brum, *Phys Rev Lett* **64**, 12082 (1990).
7. K. Nakazawa and R.J. Blakie, *J. Phys. Condens. Matter* **3**, 5723 (1991).
8. H.W. and D.W.L. Syung, *Phys Rev B* **47**, 1502 (1993) and H.W. and D.W.L. Syung, and J. Manurall, *J. Phys. D: Appl. Phys.* **26**, 798 (1993).
9. E. Castaño, G. Kirczenov and S.F. Ufeda, *Phys Rev B* **42**, 3753 (1990).
10. G.H. Wannier, *Rev Mod Phys* **34**, 6.5 (1962).
11. E.E. Mendez, F. Agullo-Rueda, and J.N. Hong, *Phys Rev Lett* **60**, 2426 (1988).

-

between the district of the respondents and the district of the respondent's mother. Table 1. - By

[illegible][illegible]

Also 1 - 4 from 1941, 1942 - 44, 1946 - 47
- 2 World War II only possibly on evidence about top of every field marking 1941, 1942



$\text{Slope} = \frac{5400 - 22,400}{19 - 1}$
 $= - 975$

Multi-phonon Relaxation of Electrons
in a Semiconductor Quantum Dot

T. Inoshita and H. Sakaki

Quantum Wave Project, JNDC

1-1-1 R2 Komaba, Akiba-ku

Tokyo 153, Japan

Intra-band electron relaxation via phonon emission is an important process that governs the light emission efficiency of semiconductor lasers. Using a perturbation theory, electron relaxation rate in a GaAs quantum dot is calculated to the second order in electron-phonon interaction. If first order processes only are included, rapid relaxation, as a small (~ 1000 Å) dot is impossible unless the interlevel separation is exactly tuned to the LO phonon energy. Two-phonon (LO+LA) processes efficiently alleviate the tuning condition by creating a window of rapid (subpicosecond) relaxation around the LO phonon energy. Based on this finding, prescriptions are given for the achievement of highly efficient quantum dot lasers.

1. Introduction

It was predicted a decade ago that the use of 1D (quantum wire) and, in particular, 0D (quantum dot) structures will produce semiconductor lasers with high efficiency due to their highly peaked (1D) or δ -function-like (0D) density of states [1]. This prediction has given considerable impetus to the research of these low-dimensional systems and seems to have been generally accepted. Experiments, however, have so far shown evidence of photoluminescence degradation, rather than enhancement, for dot size below ~ 1000 Å [2]. Damage introduced during the fabrication process has been suspected as the cause of this degradation.

A different and intrinsic mechanism was recently put forward by Benisty, Soumry, and Taves and We, which [3]. Its main points can be summarized as follows. In the usual process of light emission in a laser, electrons and holes, first created in higher energy continuum, relax down to the ground level in cascade emitting phonons and finally recombine to emit light. Thus, the relaxation rate is an important factor dominating emission efficiency. In a quantum dot, strong radiative-optical (LO) phonon emission, which is by far the most efficient relaxation mechanism in higher dimensional systems, is forbidden due to the very discrete nature of the levels, unless the level separation equals the zone-center LO phonon energy, $\hbar\omega_{LO}$. Deformation potential interaction with longitudinal-acoustic (LA) phonons, which is already weak in the bulk, weakens further as the dot size is reduced, due to decreasing form factor [3-4]. Hence carriers are unable to reach the ground level and compelled to stay in excited levels, where radiative lifetime is long (due to orthogonality between electron and hole levels) with different level index [3].

Although the above argument is convincing, one would still like to ask, "Is this the whole story?" Is there no way out of this dilemma which can point the way to achievement of efficient light emission? In an effort to answer this question, we have calculated the electron relaxation rate with both one- and two-phonon processes included [5].

2. Method of calculation

We take a GaAs dot and consider the relaxation of a single electron. (Hole relaxation should be much faster due to smaller level separation ω_n .) The electron is assumed to be confined in the dot by a parabolic potential $V(r) = \frac{1}{2} m^* \omega_n^2 r^2$ (it should be stressed that this parabolic model is used here only to facilitate the calculation of matrix elements). The energy of electrons in this potential is of the harmonic oscillators form $E_n = \hbar\omega_n(n + \frac{1}{2})$, where $m^* = 0.067$. The transition rate between the lowest two electronic levels, $1/2 \rightarrow 1/2$, is $(1.0/0.0)$, with energy separation of E_2 is calculated by the standard perturbation theory. (First and second order)

for the phonons, we take into account bulk LA and LO phonons of GaAs [6], which interact with electrons via deformation potential and Fröhlich interactions, respectively.

This bulk approximation for the phonons may need some explanation. Although no detailed study of the phonon modes in quantum dot structures has been made yet, phonon modes in GaAs/AlAs multi-layer structures are well understood by now [7,8]. The LA modes are delocalized and can be treated as bulk modes. The LO modes, in contrast, are well localized and are classified into confined LO (CLO) modes and interface LO (ILO) modes. In spite of the localized nature of these modes, the relaxation rate calculated in the simple bulk approximation agrees fairly well with that obtained in a fully microscopic calculation [8]. Thus, the bulk approximation is valid for both the LA and LO modes. We will assume that the same is true of our quantum dot structure.

Our calculation was carried out for a total of five processes: LO and LA (one-phonon), and LO+LA and 2LA (two-phonon), where \pm denotes emission (absorption). The result indicates that LO and LO+LA are the most important. Thus, we will confine our discussion hereafter to these three processes. (For the discussion of LA and 2LA processes, see [5].)

Since an electron-phonon matrix element is proportional to the form factor $\langle \psi_f | \hat{H}_{ep} | \psi_i \rangle$, which decays rapidly to zero as q goes beyond $Q = \pi/L$ (where L is the dot diameter and hence $Q \propto 1/L$), only long-wavelength phonons are important. Combining this with energy conservation ($\hbar\omega_f = \hbar\omega_i \pm \hbar\omega_L$ or $\hbar\omega_i = \hbar\omega_f \pm \hbar\omega_L$), we can deduce that rapid relaxation by the LO and LO+LA processes is possible only when E_0 is in the vicinity of $\hbar\omega_{LO} \approx 35$ meV.

3. Results

The calculated relaxation rate $1/\tau$ at $T = 0$ K is shown in Fig. 1 as a function of level separation E_0 . As expected, relaxation rate due to the LO (one-phonon) process is sharply peaked immediately below $\hbar\omega_{LO}$. The peak value is as large as $10^{15} s^{-1}$ (independent of temperature for $kT \ll \hbar\omega_{LO}$) but the peak is so sharp that $1/\tau$ drops to only $10^6 s^{-1}$ for a slight detuning of $\Delta E_0 = -0.05$ meV. (Note that we have taken into account the dispersion of the LO mode.) Thus one cannot take advantage of the large peak value unless E_0 is precisely tuned to $\hbar\omega_{LO}$, far more precise than is possible with today's microfabrication technology.

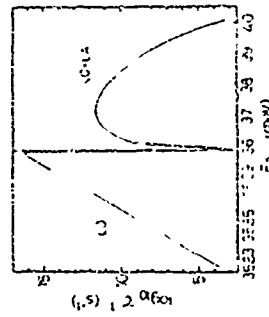


Fig. 1. Calculated electron relaxation rate $1/\tau$ at $T=0$ K. Note that the peak in abscissa is different above and below $\hbar\omega_{LO}/2$, which is indicated by the vertical dotted line.

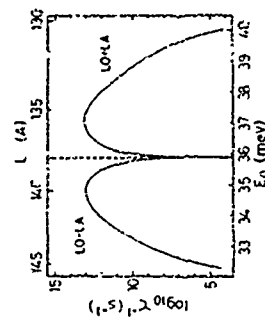


Fig. 2. Calculated electron relaxation rate $1/\tau$ at $T=300$ K. The diameter L , corresponding to different E_0 is shown across the upper part. Note the uniform scale in the abscissa.

The inclusion of the second-order LO-LA process drastically improves the situation. As seen from Fig. 1, LO-LA produces a rather broad peak on the high energy side of $\hbar\omega_{LO}$ with the peak value exceeding 10^{11} s^{-1} (corresponding to $\tau \approx 10 \text{ ps}$). This peak, although smaller than the LO peak, is large enough for our purpose of achieving efficient light emission. (The radiative recombination lifetime of electrons and holes in their ground levels is estimated by the golden rule to be on the order of 1 ns. Hence $\tau \ll 1 \text{ ns}$ is required for efficient luminescence.) Moreover, the large peak width considerably alleviates the tuning condition. For example, $\tau \ll 1 \text{ ns}$ is in a broad window of $56.1 \text{ meV} < E_0 < 38.8 \text{ meV}$. The tuning condition is further alleviated at higher temperatures. Figure 2 illustrates calculated $1/\tau$ at $T = 300\text{K}$. Now the LO-LA process, which is usually absent at $T=0\text{K}$, contributes another broad peak on the low energy side of $\hbar\omega_{LO}$. Also, the LO-LA peak is enhanced by a factor of 10^4 compared to $T=0\text{K}$. This is due to the enhanced Bose distribution function of LA phonons. Thus, at finite temperatures, the enhanced Bose function and the emergence of the LO-LA peak act to increase detuning tolerances. For τ to satisfy $\tau \ll 1 \text{ ns}$, the tolerable range of E_0 is now $33 \text{ meV} < E_0 < 39.1 \text{ meV}$. (The narrow dip in $1/\tau$ on the immediate high-energy side of $\hbar\omega_{LO}$ should be smeared out by phonon broadening, which is neglected in our calculation.) The LO peak is not shown in Fig. 2 since it is essentially the same as in Fig. 1 in this logarithmic scale.

The level separation E_0 can be translated into dot diameter L by the relation

$$L = 2\sqrt{\frac{\hbar^2 E_0}{2m^*}} \quad (2)$$

where m^* denotes the ground state wavefunction. The L thus determined is shown in Fig. 2 across the top. (Due to the parabolic confinement, this definition of L is rather arbitrary.) It is seen that L must be on the order of 100 \AA to achieve rapid relaxation

4. Discussion

In our calculation, we have simulated the real LO mode (CLO and ILO modes) in our structure by a single 'bulk' LO mode. By doing so, we have implicitly assumed that CLO and ILO have the same energy. If we take account of the energy difference between CLO and ILO, there are two windows of rapid relaxation (corresponding to CLO-LA and ILO-LA processes) centered around CLO and ILO energies, respectively. Now the level spacings are required to fall into either of these two energy windows.

We can further increase the number of windows by using a mixed-crystal of multi-LO-mode type, such as $\text{Al}_x\text{Ga}_{1-x}\text{As}$, as barrier material. There are now two types of ILO modes (GaAs-like and AlAs-like) that differ in energy by over 10 meV . We can alternatively use such a mixed crystal as dot material, which results in two CLO modes.

Although the introduction of more than one relaxation window considerably eases level tuning, additional level tuning may be required to fully adjust the level separations to these windows. This can be accomplished by introducing a localized (i.e., with extent smaller than the dot size) potential into the dot. Placing a small domain of a different semiconductor material serves this purpose [9,10]. How this affects the energies of various

levels depends on the position and sign of the localized potential. For example, if the dot has an inversion symmetry and this domain is located at the center of the dot, then electron levels of even parity are pushed up (if the localized potential is positive) or down (negative), the change being largest for the ground state (Fig. 3). Odd-parity states, in contrast, remain unchanged, since the wavefunction vanishes at the localized potential.

In our calculation, many-body correlation between carriers such as exciton and Auger effects was totally neglected. It is possible that these effects further enhance relaxation. In fact, Brockelmann and Egerter [11] recently calculated electron relaxation rate via the Auger effect in the random-phase approximation, and concluded that it strongly enhances relaxation at high optical excitation. More study seems necessary to fully clarify the role of many-body effects in carrier relaxation in a dot.

5. Conclusion

We have studied the effects of multi-phonon processes on electron relaxation in a GaAs dot. The results indicate that, in spite of the general slowing down of relaxation, efficient light emission is still possible by adjusting the level separations to the windows of rapid relaxation created by LO-LA processes. To be able to do this, there should not be more than several bound states. Hence the barrier height should not grossly exceed 100 meV .

References

- [1] Y. Arakawa and H. Sakaki, *Appl. Phys. Lett.* **24**, 195 (1982).
- [2] See, for example, M. Notomi, M. Naganuma, T. Nishida, T. Yamamura, H. Iwamura, S. Niyima and M. Okamoto, *Appl. Phys. Lett.* **58**, 720 (1991).
- [3] H. Benisty, C. M. Sotomayor-Torres and C. Weibuch, *Phys. Rev. B* **44**, 10945 (1991).
- [4] U. Brockelmann and G. Bastard, *Phys. Rev. B* **42**, 8947 (1990).
- [5] T. Inoshita and H. Sakaki, *Phys. Rev. B* **46**, 7200 (1992).
- [6] K. C. Rustagi and W. Weber, *Solid State Commun.* **18**, 673 (1976).
- [7] M. V. Klein, *IEEE J. Quantum Electron.* **QE-22**, 1760 (1986).
- [8] H. Pucker, E. Molnar, and P. Lugli, *Phys. Rev. B* **45**, 6747 (1992).
- [9] W. Trzciaskowski and B. D. McCombe, *Appl. Phys. Lett.* **55**, 851 (1989).
- [10] J. M. Gerard and J. Y. Marzin, *Phys. Rev. B* **40**, 6450 (1989).
- [11] U. Brockelmann and T. Egerter, *Phys. Rev. B* **46**, 15574 (1992).

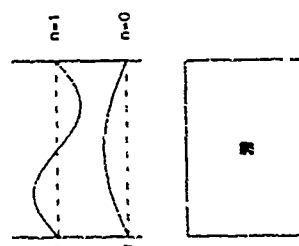


Fig. 3 Introduction of a localized potential in a dot (grey rectangle) by means of a small domain of a different semiconductor material (shaded area) placed at the center of the dot. The upper part shows unperturbed wavefunctions. The ground state ($n=0$) has a finite amplitude at the potential and is perturbed, whereas the first excited state ($n=1$) vanishes there and is unaffected.

Ground state properties of interacting electrons in semiconductor quantum dots: Exact and Unrestricted Hartree-Fock results

Instituto de Ciencias de Matemáticas (I.C.M.), Universidad Nacional de Madrid (España) 28002, Madrid, Spain

J. J. Pilsbry and C. Taylor
 Department of Zoology, University of California, Berkeley, California
 November 1922

6) Chappin and P. Lewis
 Oportunitades de la zona agrícola de Huante Apurimac y zonas limítrofes
 (July 9 1981)

The ghosted elite perception of ap in intersecting elections continued to weigh upon later voters as they faced a stark disjunction of the left flankists. The behavior with the negative field is isolated as well as its possible implications on the unenlightened proportion of said source. In such a competition with an international flatter-out ap-
 know it reveals the latter one to be an excellent candidate to go beyond the low elections

Properties of spin and data QDs have been extensively studied in the last couple of years, both as potential and theoretical [1]. Measurements have been performed mainly on the transport properties of some small, self-assembled, as well as on the capacitance of such systems [2]. In both cases, it has been shown that the invention of QD are greatly altered by adding or removing a single electron. The calculations have been performed in the literature on the properties of such systems can be classified in two groups: large number of electrons and small number of electrons in the QD. In the first case, the approximation of representing the electron-electron interaction by a classical capacitive term has proved to be qualitatively satisfactory [3]. In the *one-electron* based, when the number of electrons is small and correlations at strong, this model is expected to fail. This has been shown in exact calculations performed in this regime considering the full electron-electron interaction, for small number of electrons ($N \leq 5$) in one-dimensional QDs [4] and in two-dimensional (2D) QDs with high symmetry in the confining potential [e.g. 5]. Two quantities related to the electron dot are of special interest: due to their relevance to measurable properties such as the conductance, the energy and the spectral weights [6, 10].

$$\{(-1)^{i_1} \phi_1^{\dagger} \phi_1, \phi_1^{\dagger} \phi_1\} \{(-1)^{i_2} \phi_2^{\dagger} \phi_2, \phi_2^{\dagger} \phi_2\} = (-1)^{i_1 i_2} \{(-1)^{i_2} \phi_2^{\dagger} \phi_2, (-1)^{i_1} \phi_1^{\dagger} \phi_1\}$$

where i, j index one electron eigenstates ϕ_i, ϕ_j under many-body eigenstates at fixed λ and $d_i(u_i^2)$ is the annihilations (creation) operators for the one electron eigenstate i .

The purpose of this paper is twofold: (i) to show the changes that a perpendicular magnetic field induces on the electronic properties (Fermi level, E_F , and energy gap, E_g) of the Cu_2S and (ii) to show that the T-intersected Hartevoog-Lock (THL) approach can be used as an accurate way to calculate properties of Cu_2S , especially in the intermediate- and high- N regime. We present exact calculations for N up to 5, i.e., different magnetic moments, and compare these exact results with the ones obtained with the THL approach and, given the good agreement is found, we extend the study to higher N .

These results are extended to a 2D square box, under the influence of a periodicity vector \mathbf{H} (it was represented by a column vector \mathbf{h} in the previous section) and a periodicity vector \mathbf{K} (represented by a column vector \mathbf{k} in the previous section), which has to satisfy the condition $\mathbf{K} \cdot \mathbf{H} = 0$. The vector \mathbf{K} is associated with the periodicity of the system. In order to obtain eigenvalues and eigenfunctions, the Hamiltonian H is expressed in a second quantization basis by the boson b and b^\dagger creation and annihilation operators. The calculation of the eigenvalues and eigenfunctions of the Hamiltonian H is performed by using a truncated basis. The truncation is done by neglecting the states with a number of particles greater than a fixed value. The results are compared with those obtained by using a truncated basis. The results are compared with those obtained by using a truncated basis. The results are compared with those obtained by using a truncated basis.

$$H_{0111} = \sum_{i,j,k,l} \dots$$

$$\begin{aligned}
& + \sum_{i,j=1}^n \sum_{k=1}^n v_{i,j,k}(d_i^k, d_j, d_k, \omega) \left(d_i^k - \frac{1}{2}(d_i^k, d_j, d_k, \omega) \right) + \\
& + \sum_{i,j=1}^n \sum_{k=1}^n v_{i,j,k}(d_j^k, d_i, d_k, \omega) \left(d_j^k - \frac{1}{2}(d_j^k, d_i, d_k, \omega) \right) - \\
& - \sum_{i,j=1}^n \sum_{k=1}^n v_{i,j,k}(d_i^k, d_j, d_k, \omega) - \frac{1}{2}(d_i^k, d_j, d_k, \omega) \left(d_i^k, d_j, d_k, \omega \right) - \\
& - \sum_{i,j=1}^n \sum_{k=1}^n v_{i,j,k}(d_j^k, d_i, d_k, \omega) - \frac{1}{2}(d_j^k, d_i, d_k, \omega) \left(d_j^k, d_i, d_k, \omega \right)
\end{aligned} \quad (2)$$

where σ labels the electron spin, ϵ_{σ} are the eigenenergies for noninteracting electrons, $\mathbf{1}$ are the matrix elements of the Coulomb interaction in the one-electron basis set and the expectation values, and therefore the Hamiltonian, have to be recalculated in each iteration until convergence is reached.

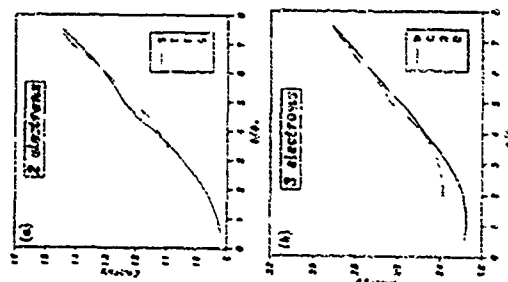


Fig. 3. First four of twenty many-body wave functions for a square quantum dot as a function of the magnetic flux through the dot for (a) two electrons in the dot in 'singlet' and (b) triplet and (c) other electrons in the dot (1) 'doublet and' (2) 'singlet', for the dot, numbered (1) to (12) the unit, $\varphi = \pi/2$, $\varphi = \pi$ and $\varphi = 3\pi/2$ is over.

$A^{(1)}$ parameters, as deuterium content and effective mass, are taken to have the values in the $2D_1$ electron gas formed in $3HeT_2$ at $T_2 = 4.2$ K. The results presented in this paper are for a *single* set of area $A = 1$ mupm. Figure 1 shows the calculated eigenvalues as a function of the magnetic flux ϕ through the dot for h ranging from 1 to 100. This corresponds to a perpendicular magnetic field $B = 0.56(\phi/\text{mupm})$ T, with $\phi_0 = h/e$. The dashed line marks the $2D_1$ conduction band and the electron charge for $(\phi, \lambda) = 1, 12$ over the entire range was functions of 12 mupm long) were used throughout the calculations. In both figures these *conduction bands* and *antiresonances* (resonances) were *coupled* between eigenvalues corresponding to the levels with ϕ and λ equal (as the $2D_1$ conduction bands have been taken into account in the determination of the eigenvalues). While antiresonances occur between levels with the same value of

spin, and are reminiscent of the transitions between states with different angular momentum that have been found in parabolic 2D QD. Both after a crossing or anticrossing between the two lowest lying eigenstates, the character of the ground state wave function changes abruptly. As we show later on, this abrupt change is going to be reflected on the values of spectral weights.

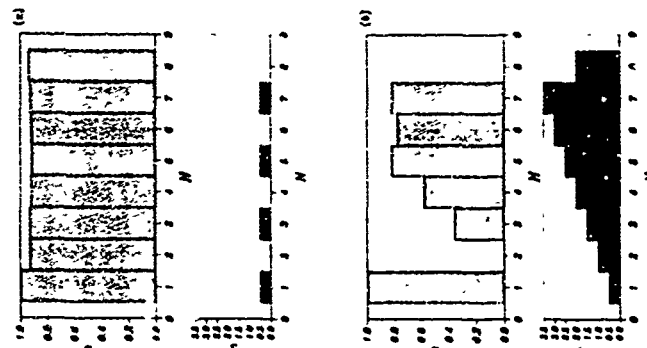


FIG. 2. Spectral weight $\Delta(N)$ and total spin $S(N)$ for (a) $\phi = 1/2$ and (b) $\phi = 1/4$ for a square quantum dot calculated from the exact many-body ground state wave functions.

Figure 2 shows $\Delta(N)$ and the spin total $S(N)$ up to $N = 8$ for two different magnetic fluxes: (a) $\phi = 1/2$ and (b) $\phi = 1/4$ ($\phi = h/e^2 R$ being the flux constant and e the electron charge) which are typical representatives of the low- and high-magnetic field regimes respectively. In the low H case the ground state eigenfunctions have minimum total spin that is $S(N) = 0$ for N even and $S(N) = 1/2$ for N odd. In this case $\Delta(N)$ is a very smooth, although not monotonous, function of N . For high H , the ground state eigenfunctions are spin polarized, for small N even when, in order to obtain the results shown in Fig. 2(b), the electron-electron interaction has been fully taken into account, this may be understood so as to minimize the exchange energy. The relevance of the kinetic energy contribution to the total energy decreases with H as a consequence of the complication of our electron energy levels

into Landau levels. Spectral weights change rapidly as a function of N for N small, in this regime. For example, while $\Delta(1) = 1$ always, $\Delta(2)$ decreases as g increases, reflecting the fact that the occupancy of the first one-electron eigenstate decreases (for $g > 3.904$ i.e., after the first crossing between the ground and the first excited state). The reason for this is that the charge is more spread out when occupying one-electron edge states than when occupying the first one-electron state which is localized on the center of the QD. Eventually, for large enough N , all the first one-electron levels are occupied and after that, $\Delta(N)$ seems to tend to 1 for large N . Notice that Kumar *et al.* [9] predict a quenching of $\Delta(N)$ in a different situation: they calculated $\Delta(N)$ for states such that the filling factor remains constant, and these are not necessarily the ground states of the many-body system. It is also worth mentioning the disappearance of $\Delta(N)$ due to the change of N for $N = 8$ electrons (in comparison with $N = 7$) by more than 1/2.

Our LHF calculations produce an excellent approximation to the ground state energy as well as to the wave function as shown in Table I. The LHF ground state energy approximates better than 2% the exact ground state energy, and it is always in between the energies of the ground state and the first excited state in the exact many-body calculation. The excellent agreement found for the LHF calculations leads us to extend the calculation of both the many-body energies and spectral weights to large N . The $\Delta(N)$ and $S(N)$ calculated from the LHF wave functions are shown in Fig. 3 for $\phi = 1/2$ and $1/4$. It is worth reflecting qualitatively all the features found in the exact calculations and the agreement between them is quantitatively rather good for $\Delta(N)$ when $N \geq 3$. LHF calculation supports the idea that $\Delta(N)$ tends to 1 for large N for the dot considered, while showing a clear parabolic trend of the ground state. An observation that deserves a more detailed investigation in the future is that the overlap between the exact and the LHF ground state wave functions remain above 0.9 in all cases except close to the fractional filling factors ν considered (defining $\nu = N/g$) suggesting a very correlated groundstate for these cases. A more detailed description of these effects for different geometries and of the intermediate H regime where $\Delta(N)$ presents abrupt changes as a function of H will be published elsewhere.

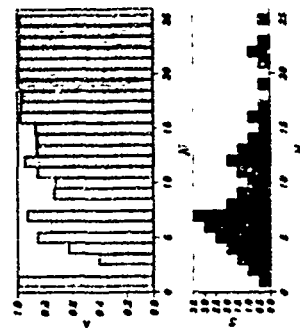


FIG. 3. $\Delta(N)$ and $S(N)$ for $\phi = 1/2$ and $1/4$ calculated from the exact many-body ground state wave functions obtained from the unrestricted Hartree-Fock method and extended to 25 electrons.

In conclusion, we have calculated the many-body lowest lying eigenenergies and their corresponding eigenstates in a square 2D QD for up to 25 electrons and different magnetic fields. While for small H the spectral weights are a smooth function of N , for high H they are strongly modulated. A similar effect is expected to appear in the conductance through these systems at low temperatures. Finally, it has been shown that Hartree-Fock is an excellent approximation for the calculation of properties on a periodic dot.

Strong lateral quantization effects in the luminescence of InGaAs/InP quantum wires

P. Ils, M. Michel, A. Forchel
Technische Physik, Universität Würzburg, Am Hubland,
97074 Würzburg, Germany;

I Gyuro, M. Klenk, E. Zielinski
Alcatel SEL AG Research Center, Lorenzstr. 40, 70435 Stuttgart, Germany

Abstract

We have fabricated $\text{In}_{0.5}\text{Ga}_{0.47}\text{As}/\text{InP}$ quantum wires with lateral widths down to 8 nm by high voltage electron beam lithography and deep wet chemical etching. The wires were studied by photoluminescence spectroscopy at room temperature and at 2K. We observe only a weak decrease of the luminescence yield with decreasing wire width, which indicates that no significant damage has been induced at the sidewalls of the wires during the fabrication process. For wires with widths smaller than about 60 nm an increasing blue shift of the photoluminescence energy up to about 75 meV (for 8 nm wide wires) is observed indicating a strong lateral quantization. The photoluminescence emission of the wires is strongly polarized parallel to the wire orientation with increasing polarization degree for decreasing wire width.

Introduction

One- and zero dimensional structures have been raised considerable interest in the last years regarding novel physical properties as well as the potential for applications in optoelectronic devices [1-4]. A number of techniques involving different physical mechanisms have been used recently to obtain structures with lateral confinement and to study their specific physical properties [5-9].

A strong lateral carrier confinement requires the observation of a one-dimensional system, i.e., energetic splitting between the lateral subbands should be significantly larger than the characteristic energy describing the carrier distribution (e.g., thermal energy or Fermi energy). The analysis of the experimental results should be based on well-defined sample quantities like semiconductor parameters and geometrical data. Damage free fabrication processes are required to avoid the formation of optically inactive regions.

In the present work we report on the results obtained from photoluminescence studies of ultranarrow In_{0.53}Ga_{0.47}As/InP quantum wires with lateral dimensions down to 8 nm, which were fabricated by the combination of high resolution electron beam lithography at 200 kV and wet chemical etching. Down to the smallest widths obtained the In_{0.53}Ga_{0.47}As/InP wires show a good luminescence yield even at room temperature due to the absence of damage in our fabrication processes. The photoluminescence emission of wires with widths down to 8 nm shows a energy shift up to more than 70 meV indicating the strong lateral carrier quantization in our wire structures. Furthermore the photoluminescence emission is strongly polarized parallel to the wire orientation.

TABLE I. Ground state energies in meV (β first and $1/\beta$ last) \backslash electrons in a square box of 0.5 μm of side with no transverse magnetic flux in the words of the first quotation in *ibid.* The discrepancy between the exact and LHF wavefunction results also given. 12 mono-electronic wave functions are included in the sub-diagonal (including spin). The German contribution has been neglected.

α/cm	Energy (eV)	1	2	3	4	5	6	7	8	9	10
1	Energy (1 sec)	5.416	11.11	22.95	35.29	48.55	61.81	75.07	88.33	101.58	114.84
	$< \Phi_{\text{photon}} >$	0.919	1.872	0.959	0.966	0.959	0.954	0.941	0.918	0.918	0.918
15	Energy (1 sec)	12.081	22.83	35.22	50.73	63.19	75.65	88.11	100.57	113.03	125.49
	$< \Phi_{\text{photon}} >$	1.251	2.256	1.194	0.945	0.945	0.945	0.918	0.918	0.918	0.918
	$< \Phi_{\text{photon}} >$	0.736	0.237	0.994	0.621	0.621	0.611	0.611	0.611	0.611	0.611

- [7] M. A. Kuznetsov, *Phys. Today*, January 1991, p. 25, and references therein.
- [8] R. P. Akhiezer et al., *Phys. Rev.* **161**, 68 (1968).
- [9] T. W. J. Donnelly, *Phys. Rep.* **14**, 44 (1971).
- [10] F. Alfaro et al., *Phys. Rev. Lett.* **68**, 1926 (1992).
- [11] S. Haeder, *II. Jahresber. d. Max-Planck-Ges.* **85**, 135 (1992).
- [12] G. P. Mikhailov and I. V. Sokolovski, *Phys. Rev. Lett.* **65**, 104 (1991).
- [13] P. H. Alkati, J. Hauer, and M. Wagner, *Phys. Rev. B* **42**, 129 (1990); M. Wagner, P. H. Alkati, and M. Wagner, *Phys. Rev. B* **42**, 1312 (1990).
- [14] D. Pfannkuche and R. Gerhardt, *Phys. Rev. B* **44**, 11112 (1991).
- [15] M. Minari et al., *Phys. Rev. B* **43**, 1099 (1992); doi: 10.1103/PhysRevB.43.1099 (1992).
- [16] J. Peltonen, L. Martin-Moreno, and J. Sanchez-Solano, *Nature*, in press.

Technology

The starting material for the wire fabrication are metal organic vapor phase epitaxy grown $\text{In}_{0.53}\text{Ga}_{0.47}\text{As}/\text{InP}$ single quantum well layers with a 200 nm InP buffer layer, a 5 nm $\text{In}_{0.53}\text{Ga}_{0.47}\text{As}$ layer and an InP cap layer with a thickness of 8 nm. The samples are coated with a 100 nm thick layer of polymethylmethacrylate (PMMA) electron beam resist. The high resolution electron beam exposure is performed with a transmission electron microscope at an acceleration voltage of 200 kV in order to reduce the proximity effect [10]. Using a lift-off process gold wires with lateral widths down to about 15 nm are obtained, which serve as a mask for deep wet chemical etching with a $\text{Br}_2/\text{HBr}/\text{H}_2\text{O}$ etchant. Fig. 1 shows a scanning electron micrograph of wet etched $\text{In}_{0.53}\text{Ga}_{0.47}\text{As}/\text{InP}$ wires delineated parallel to the [011] direction after the removal of the gold mask. Here the lateral width of the $\text{In}_{0.53}\text{Ga}_{0.47}\text{As}$ layer in the wires, which is located below the 8 nm thick InP cap layer, is about 15 nm.

As a result of the lithography process we have obtained wet etched $\text{In}_{0.53}\text{Ga}_{0.47}\text{As}/\text{InP}$ wires with SEM measured lateral widths of the $\text{In}_{0.53}\text{Ga}_{0.47}\text{As}$ layer down to 8 nm. The wire width fluctuations arising from the roughness of the gold masks and the roughness caused by the etching process amounts to about ± 5 nm. The lateral dimensions realized in our structures are in general comparable to the thickness of typical quantum well layers. Therefore strong lateral confinement effects should be observable in our structures.

Optical Studies

The wires were investigated by photoluminescence spectroscopy at temperatures of 300 K and 2 K. The experiments were carried out on wire arrays of $50 \times 50 \mu\text{m}^2$ size. Beside these wire arrays some mesa structures of the same size were placed on the samples serving as two-dimensional references. The distance between the different arrays was about 200 μm . For the excitation the 314 nm line of an argon ion laser was used at normal incidence. The laser beam was focused to a diameter of about 40 μm to obtain a sufficiently high spatial resolution. The photoluminescence signal was detected by a liquid nitrogen cooled germanium detector and lock-in technique.

The $\text{In}_{0.53}\text{Ga}_{0.47}\text{As}/\text{InP}$ quantum wires show a good photoluminescence yield down to the smallest wire widths even at room temperature. This demonstrates the high quality of our wire structures. Fig. 2 displays photoluminescence spectra for different lateral wire widths taken at room temperature. The wire widths indicated in the figure have been determined by a high resolution scanning electron microscope. The relative intensities are normalized. The position of the photoluminescence peak remains unchanged down to geometrical wire widths about 60 nm. For wire widths smaller than 60 nm an increasing blue shift of the photoluminescence signal is observed, which amounts to about 60 meV for this 11 nm wide wires displaying a strong lateral quantization.

Both, the absence of a shift for wire widths above 60 nm and the strong emission energy shifts observed in narrower structures indicate thus a steep lateral confinement potential is obtained by the $\text{In}_{0.53}\text{Ga}_{0.47}\text{As}/\text{vacuum}$ transition at the etched surfaces leading to one-dimensional quantum effects for wire widths smaller than 60 nm. The observed photoluminescence energy shift fits well theoretical calculations for the lateral quantization E_{yd} of the geometrical wire widths [11]. This indicates that in contrast to dry-etched wires [12] there exist no pronounced dead layers at the sidewalls of the wires. The increase of the spectral halfwidth of the photoluminescence signal with decreasing wire width is predominantly due to wire width fluctuations and is consistent with the lateral quantization itself. From the measured increase of the spectral halfwidth as a function of wire width a typical wire width fluctuation ΔL_x of about ± 3 nm is estimated, consistent with the value determined from the SEM micrographs.

The wire width dependence of the photoluminescence intensity at room temperature is shown in Fig. 3. Here the integrated intensities of the wire spectra, corrected by the area filling factor

and normalized with respect to the quasi-two-dimensional mesa reference are displayed as a function of the measured wire width. The wire widths were obtained from high resolution scanning electron micrographs. The error in the determination of the geometrical wire width is about 5 nm. Taking the nonradiative surface recombination into account the wire structures show good quantum efficiencies for wire widths down to 8 nm. The 200 nm wide wires show nearly the same luminescence yield as the two-dimensional reference, for 20 nm wide wires it amounts to about 5 % of the 2D value. At room temperature the 8 nm wide wires still have a quantum efficiency of about 0.6 %.

Compared to dry-etched wire structures the decrease in quantum efficiency with decreasing wire width is clearly weaker [8]. In particular the photoluminescence does not vanish abruptly for wire widths smaller than 60 nm. This strong decay of the quantum efficiency in narrow dry-etched wires has been attributed to the formation of optically inactive ('dead') layers at the dry-etched sidewalls [8,12]. A dead layer of 20 nm as observed in these dry-etched structures would lead to vanishing quantum efficiency at a wire width of about 40 nm in clear disagreement with our data. Quantum efficiencies greater than 1 observed for wire widths greater than 100 nm are due to efficient carrier capture from the InP barriers. Carriers excited by the laser in the InP layers can diffuse into the $\text{In}_{0.53}\text{Ga}_{0.47}\text{As}$ layer in the wires and thus contribute to the photoluminescence signal of the $\text{In}_{0.53}\text{Ga}_{0.47}\text{As}$ wires.

The photoluminescence emission of the $\text{In}_{0.53}\text{Ga}_{0.47}\text{As}$ wire structures at a temperature of 2 K was also studied for different polarization directions. As shown in Fig. 4 the luminescence signal is preferentially polarized parallel to the wire direction. The polarization degree increases significantly with decreasing wire width and amounts to about (60 \pm 5) % for wire widths of about 10 nm, which is roughly comparable to theoretical expectations [13]. The polarization dependence of absorption and photoluminescence emission is determined by the heavy-hole and light-hole character of the one-dimensional valence subbands. The strong mixing of heavy-hole and light-hole states in one-dimensional structures reflects itself in the anisotropy of the optical transitions involved. This anisotropy increases with decreasing wire width due to the increasing mixing of heavy-hole and light-hole states [13].

Additionally to this intrinsic anisotropy based on the electronic band structure a further electrodynamic effect may play an important role. As our experiments are performed on arrays of wires, these periodic configurations of deep etched wires act as grating structures. Due to the lateral modulation of the dielectric constant in these wire gratings the magnitude of the local electric field induced by the incoming electromagnetic wave is different for different polarizations [14]. This may be the reason for the fact that we observe a strong polarization of the photoluminescence parallel to the wire orientation already for relatively wide wires with widths in the region between 1000 nm down to about 80 nm, where the electronic effect on the polarization of the $e_{11}-hh_1$ transition due to the band mixing of heavy-hole and light-hole states can practically be neglected [11].

Conclusions

By means of high voltage electron beam lithography and deep wet chemical etching we have developed $\text{In}_{0.53}\text{Ga}_{0.47}\text{As}/\text{InP}$ quantum wires with pronounced lateral quantization effects. $\text{In}_{0.53}\text{Ga}_{0.47}\text{As}/\text{InP}$ quantum wires with widths down to 8 nm have been fabricated. The wires show strong optical emission at $T=2$ K and at room temperature even without having been overgrown. The photoluminescence signal from the $\text{In}_{0.53}\text{Ga}_{0.47}\text{As}$ wires is polarized parallel to the wire orientation with significantly increasing polarization degree for decreasing wire width. In contrast to previous studies on dry-etched structures we found no indications for the existence of an optically inactive 'dead' layer at the sidewalls of the wires, which clearly demonstrates the advantage of the damage free wet etching process. The photoluminescence energy of the $\text{In}_{0.53}\text{Ga}_{0.47}\text{As}$ wires is independent of the wire dimensions down to widths of about 60 nm. For the narrowest structures the energetic blue shift of the photoluminescence peak amounts to about 70 meV. Our results indicate that by electron beam lithography and wet

chemical etching of quantum well layers quantum wires with comparable quantization in the vertical and lateral direction can be obtained

We are grateful to S. Kuhn for expert technical assistance and to A. Wolf for preparing the SEM micrographs. The financial support of the Volkswagen Stiftung is gratefully acknowledged

References

- [1] Y. Arakawa and P. Sakaki, *Appl. Phys. Lett.* **40**, 939 (1982).
- [2] Y. Arakawa, K. Vahala, and A. Yaniv, *Appl. Phys. Lett.* **45**, 950 (1984).
- [3] M. Asada, Y. Miyamoto, and Y. Suematsu, *Jap. Jour. Appl. Phys.* **24**, L95 (1988).
- [4] S. Schmitt-Rink, D. A. H. Miller, D. S. Chemla, *Phys. Rev. B* **35**, 8113 (1987).
- [5] M. Nozomi, M. Nagatsuma, T. Nishida, T. Tanamura, H. Iwamura, S. Nojima, and M. Okamoto, *Appl. Phys. Lett.* **58**, 720 (1991).
- [6] A. Israel, J. Y. Marzin, P. Sernage, L. Brotheau, D. Roben, R. Azoulay, J. L. Benchimol, L. Henry, V. Thierry-Mieg, F. R. Ladan, and L. Taylor, *Jap Jour. Appl. Phys.* **30**, 3256 (1991).
- [7] Y. Nagatsuma, Y. Arakawa, S. Tsukamoto, M. Nishioke, S. Sasaki, and N. Miura, *Phys. Rev. Lett.* **69**, 2963 (1992).
- [8] B. E. Maile, A. Forchel, R. Germann, D. Grützmacher, H. P. Meier, and J. P. Reithmaier, *J. Vac. Sci. Technol.* **B7**, 2030 (1989).
- [9] Ch. Greus, L. Bülow, F. Damminger, A. Forchel, P. A. Knapp, and T. L. Rennecke, *Phys. Rev. B* **47**, 7626 (1993).
- [10] P. Ili, M. Michel, A. Forchel, I. Gyuro, P. Speier, and E. Zielinski, *Mat. Res. Soc. Symp. Proc. Vol. 283*, 777 (1993).
- [11] P. Ili, M. Michel, A. Forchel, I. Gyuro, M. Klenk, and E. Zielinski, is to be published.
- [12] E. M. Clausen Jr., H. G. Craighead, J. M. Worlock, J. P. Harbison, L. M. Schiavone, L. Filzer, and B. Van der Gaag, *Appl. Phys. Lett.* **55**, 1427 (1989).
- [13] U. Bockelmann and G. Bastard, *Phys. Rev. B* **45**, 1688 (1992).
- [14] U. Bockelmann, *Europhys. Lett.* **16**, 601 (1991).

Figure Captions

Fig. 1 SEM micrograph of wet etched $\text{In}_{0.53}\text{Ga}_{0.47}\text{As}/\text{InP}$ wires delineated parallel to the [011] direction after mask removal. The optically active $\text{In}_{0.53}\text{Ga}_{0.47}\text{As}$ layer (thickness 5 nm) is located 8 nm below the top of the semiconductor structures. The lateral width of the $\text{In}_{0.53}\text{Ga}_{0.47}\text{As}$ layer is about 15 nm

Fig. 2 Photoluminescence (PL) spectra of the $\text{In}_{0.53}\text{Ga}_{0.47}\text{As}/\text{InP}$ wires for different lateral wire widths taken at room temperature (laser power 2 mW)

Fig. 3 Wire width dependence of the photoluminescence (PL) intensity of the $\text{In}_{0.53}\text{Ga}_{0.47}\text{As}/\text{InP}$ wire structures at room temperature. Here the integrated intensities of the photoluminescence signal, corrected by the area filling factor and normalized with respect to the quasi two dimensional mesa reference are displayed as a function of the geometrical wire width as obtained from SEM micrographs.

Fig. 4 Wire width dependence of the polarization degree of the photoluminescence emission parallel to the wire orientation at a temperature of 2 K

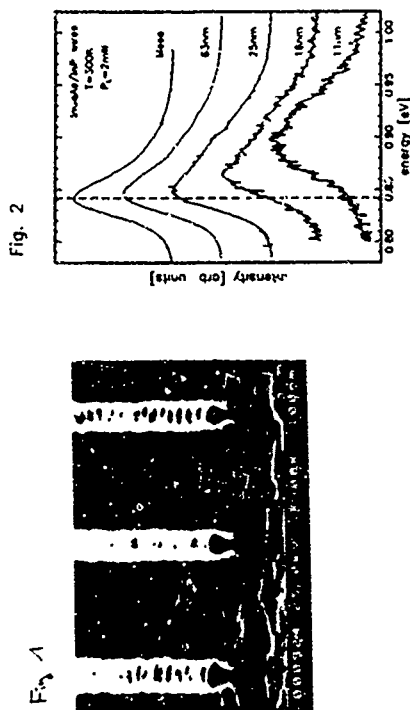


Fig. 2

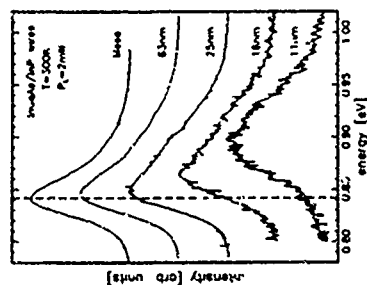


Fig. 3

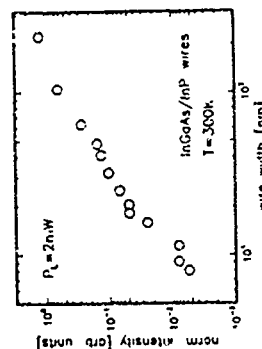
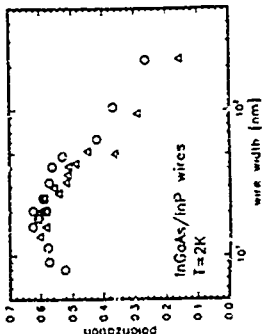


Fig. 4



GaAs/AlGaAs Quantum Well Infrared Photodetectors

J. Miyazaki, S. Honohata, I. Ezaki, P. Kubo, N. Mori,
K. Umegaki and C. Hanaguchi
Department of Electronic Engineering Faculty of Engineering
Osaka University, Suita City, 565, Japan

Abstract

We fabricated GaAs (Si-doped, 10^{19} Al_{0.35}Ga_{0.65}As (undoped, 500 Å) multi-quantum well infrared photodetectors to realize a high efficiency. The detector is based on the intersubband transition from a bound state in the GaAs quantum well to extended continuum states above the AlGaAs barrier so that the excited electrons can flow easily. In order to improve the detectivity the incident surface is polished at 45° off the quantum well layers, to provide multireflection of the light in the device. The photocurrent was observed at $T = 77$ K in the incident photon wavelength region of $8 \sim 10 \mu\text{m}$ with peak photocurrent at $8.5 \mu\text{m}$. Since the operation mechanism is based on the photocurrent carried by the electrons in the extended continuum states excited from the bound state in the GaAs wells, the band width is expected to be broader than the devices which utilize the transition between the bound states in the well. We calculated also a coefficient of photocon by using the energy band structures obtained from *Kronig-Penney model* and photoconcurrent with a simplified model. The results well explain the band width of the detectivity and also a weak structure (weak peaks) in the photocurrent.

Introduction

In recent years, a lot of interests have been placed on intersubband absorption in GaAs/AlGaAs quantum wells [1, 2]. For example, infrared detection using intersubband absorption in doped quantum wells has been a subject of much current interest. Up to now, many studies on GaAs/AlGaAs multi-quantum well (MQW) infrared (IR) photodetectors with high performance have been reported [3, 10].

Conventional IR photodetectors for the long wavelength of $5 \sim 10 \mu\text{m}$ have been fabricated using narrow band gap semiconductor materials such as HgCdTe. However, with the use of an internal band process rather than an interband process, it is possible to fabricate an IR detector of wide band gap materials such as GaAs/AlGaAs MQWs instead of narrow gap materials. The major advantage of GaAs/AlGaAs MQW IR photodetectors with respect to HgCdTe devices is that the range of detection wavelength can be controlled with the GaAs quantum well width L_z , the AlGaAs barrier width L_b , or the Al alloy composition x [9, 11].

The GaAs/AlGaAs MQW IR photodetector we discuss here is based on an electron transition between the localized bound state and the extended continuum states. In such quantum well photodetectors, two dimensional electron gas is in the bound state at thermal equilibrium. Under IR illumination, electrons in the bound state are excited to the extended continuum states, and photo-excited electrons are mobile in the conduction band and contribute to the photocurrent. Therefore, such a photodetector is expected to have a higher detectivity as compared with photodetectors based on bound state absorption in quantum wells [8, 12, 13]. In addition, the AlGaAs barrier width L_b can be increased without affecting the sensitivity of the photodetector, resulting in the significant reduction of an undesirable dark tunneling current [8, 12, 13].

In the present work, we fabricate GaAs/AlGaAs MQW IR photodetectors as described above. Photocurrent measurement of the photodetectors is carried out and the photocurrent spectrum is calculated with a simplified model. By comparing both results, we clarify the mechanism of IR detection.

Experimental Results and Discussions

The MQW device for structure is grown on a semi-insulating GaAs substrate by molecular beam epitaxy, consisting of 50 periods with 40 Å wells of GaAs (Si-doped, $N_D = 1.0 \times 10^{18} \text{ cm}^{-3}$) and 500 Å barriers of Al_{0.35}Ga_{0.65}As. The MQW layers are sandwiched between a 0.5 μm top and 1 μm bottom contact layers of GaAs with donors $N_D = 1.0 \times 10^{18} \text{ cm}^{-3}$. The thickness of the GaAs quantum well and AlGaAs barrier layers and Al alloy composition are measured by the X-ray rocking curve method. Subband energy levels are calculated for this structure by solving the Schrödinger equation and the Poisson equation self-consistently. In this analysis, exchange interaction and depolarization effects are ignored for simplicity. For exchange

interaction and depolarization effects are very important in a device with very high doping density but not so important in our samples with low doping concentrations of $1.0 \times 10^{18} \text{ cm}^{-3}$. The effective mass of 0.067 m_0 is used both in the GaAs quantum wells and in the Al_{0.35}Ga_{0.65}As barriers. The other physical parameters used in the present calculation are as follows [17]: the static dielectric constant of GaAs of 12.9, the difference of the band gap between GaAs and Al_{0.35}Ga_{0.65}As of 312 meV and the quantum well barrier height of 208 meV appropriate to $x = 0.35$. We confirmed that the GaAs/Al_{0.35}Ga_{0.65}As MQW has only one bound state in the well from the result of the calculations. The bound state is formed at 95 meV above the GaAs conduction band minimum. The first excited state, which lies in the continuum states is located just above the edge of the Al_{0.35}Ga_{0.65}As barrier. The energy difference between the bound state and the first excited state is 115 meV, corresponding to the wavelength $\lambda = 10.8 \mu\text{m}$.

Figure 1 shows a GaAs/AlGaAs MQW IR photodetector used for photocurrent measurement. The sample was partly etched off to the bottom contact layer and formed an electric field component of the incident light perpendicular to the quantum wells and to make the optical coupling in the VQWs more efficient [4, 6, 16]. As a final step in the processing, ohmic contacts were made to the top and bottom contact layers.

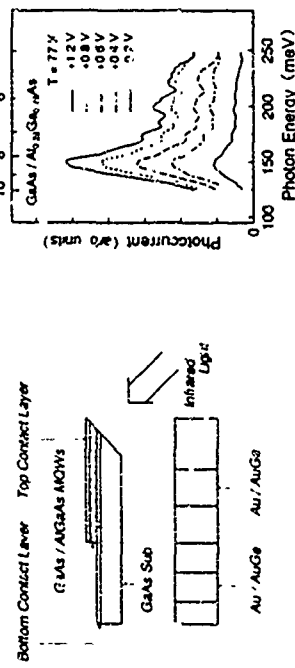


Figure 1 Schematic illustration of the GaAs/AlGaAs VQW IR photodetector

Figure 2 Photocurrent spectra at 77 K measured at applied bias voltages from +0.2 to +1.2 V with respect to the bottom contact layer

The photocurrent is measured using an infrared radiation source and a single grating monochromator with a standard lock-in technique. The measurement is performed at 77 K with the sample mounted on a cold finger in the liquid nitrogen-cooled stage. Figure 2 shows the photocurrent spectra versus the incident IR photon energy, where the photocurrent was normalized by the light intensity spectrum of the infrared radiation source. The electric field of unpolarized incident IR light is parallel to the 45° polished facet. The bias voltages applied to the sample are changed from +0.2 to +1.2 V with respect to the bottom contact layer. The spectra demonstrate that all the photocurrent curves have a peak at $8.5 \mu\text{m}$ regardless of the applied voltage and the photocurrent increases with the applied bias voltage. We found, however, that the minimum excited states above the barrier are located in the well region in the presence of such a high electric field.

We calculate absorption spectra of IR radiation and induced photocurrent in a GaAs/AlGaAs MQW structure to clarify the origin of the peaks in the photocurrent spectra. Electronic states in the structure are calculated by the *Kronig-Penney model* since the band folding due to doped Si is found to be negligibly small in our samples from the self-consistent calculation. The effective mass of the electrons is assumed to be equal to 0.067 m_0 as usual. We find a good agreement of the lower two energy levels between the self-consistent calculation and the result of the *Kronig-Penney model*.

Only the ground state is occupied in the thermal equilibrium and thus the absorption coefficient α is expressed by the transition probability W_{if} of electrons in the ground state by absorbing photons of $\omega = \omega_{if}$

$$\alpha = h\nu W_{if} / I_0(F) \quad (1)$$

ThP20

New type of photoconductivity induced by continuum-confined states in intersubband transitions

Carla Sirtori, Jerome Fusti, Federico Capasso, Deborah L. Sivo and Alfred Cho

AT&T Bell Laboratories,
Murray Hill, NJ 07974 (908) 582 2731

Bound states above the barrier height confined by Bragg reflectors have been recently detected via intersubband transitions^{1,2}. A new asymmetric structure, where the confinement in the classical continuum arises from a Bragg reflector on one side and a field-induced barrier on the other, has been investigated by means of photocurrent spectroscopy. Our AlInAs/GaInAs sample consists of 40 periods, each period comprises a GaInAs quantum well (32 Å, n-type doped $1.5 \times 10^{18} \text{ cm}^{-3}$) sandwiched between an AlInAs barrier (280 Å) and an AlInAs/GaInAs electron quarter wave stack. A strong narrowing of the photocurrent spectra demonstrates the effect of confinement. For small electric fields however a unique feature has been observed: the photocurrent changes polarity as a function of the photon energy. We can understand this result considering that in the range of energies where the quarter-wave stack act as an electron reflector, quasi-bound states at energies higher than the barrier height extend above the doped well plus thick barrier combined. For small electric fields the centroids of these states is located above the thick barrier. The electrons which are photoexcited from the ground state to one of these quasi-bound states can either scatter back into the center well and therefore do not contribute to the transport or scatter in the next $\lambda/4$ stack and give rise to a current against the direction of the electric field. Transitions at energies above the continuum-confined states will instead generate a photocurrent in the direction of the electric field and therefore produce a change of sign in the photocurrent spectra

1; F. Capasso, C. Sirtori, J. Fusti, D. L. Sivo, A. Y. Cho, Nature 358, 565 (1992)

-903-

ThP21

Landau Levels of Bragg Confined Electrons and Holes

M. Zahler, E. Cohen, J. Salzman and E. Linder

Solid State Institute
Technion-Israel Institute of Technology, Haifa 32000, Israel
and L.N. Pfeiffer
AT&T Bell Laboratories, Murray Hill, NJ 07971, U.S.A.

Abstract

We report on the observation of the electronic Landau level splitting in Bragg confining structures (BCS) under an applied magnetic field at $T \approx 2\text{K}$. The BCS consists of finite GaAs/Al_{0.37}Ga_{0.63}As superlattice (SL) sections that clad Al_{0.37}Ga_{0.63}As spacer layers. The SL sections act as Bragg reflectors that give rise to confined electron and hole states in the spacer layers (en, hh_B and lh_B). The Landau levels are observed in the photocurrent resonance excitation spectra in the Faraday configuration. The electron and hole cyclotron frequencies correspond to a two-dimensional motion in the Bragg confining barrier. We use the magnetic field dependence in order to determine the $e_B - hh_B$ and $e_B - lh_B$ band gaps and from there we find the Bragg confined exciton binding energy.

In semiconductor Bragg confining structures (BCS) the carriers are confined in the quantum barrier [1,2], or in the well with an energy higher than that of the barrier [3,4]. The confinement mechanism is then based on two requirements: a. The carrier wavefunction must be coherent over a long distance in the confinement direction, that is, the growth direction (z) of the structures discussed below; b. The carrier de Broglie wavelength along the confinement direction must fulfill a certain Bragg reflection condition [5,6], so that its wavefunction amplitude outside the barriers is greatly reduced. In such BCS, properly designed superlattice (SL) sections act as Bragg reflectors [6]. This results in a discrete energy level, corresponding to the barrier confined state that falls within the first SL mini-stop-band.

Undoped BCS have been studied by photoluminescence (PL) and its excitation (PLE) spectroscopy [1], as well as by LO-phonon resonant Raman scattering [7] in doped BCS were studied by intersubband absorption [3]. In this paper we present a study of the Landau level splitting of the Bragg confined electrons and holes in undoped BCS under a magnetic field applied along the z direction.

The BCS studied here was grown by molecular beam epitaxy on (001) oriented GaAs substrates. It consists of SL sections, each one has 5 periods of 6 monolayers (ml's) of GaAs wells and 22 ml's of Al_{0.37}Ga_{0.63}As barriers. Between these SL sections there are Al_{0.37}Ga_{0.63}As spacers, 66 ml's thick. The 'unit cell' of this BCS is schematically shown in Fig. 1. In the band gap variation of the constituent materials along the growth direction (it is repeated 66 times) the band offset is taken as $V_c/V_v \approx 6/1$. The

-904-

calculated Bragg confined energy levels (e_g , hh_g and lh_g). They are shown together with their associated envelope functions.

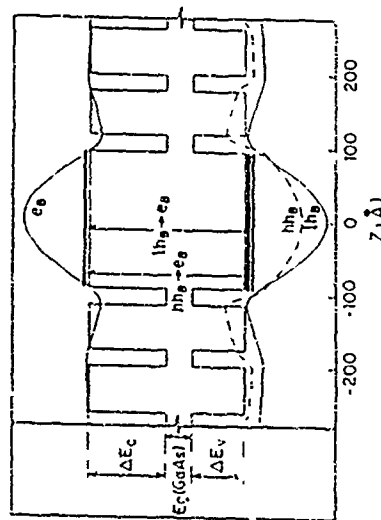


Fig. 1: A schematic description of the "unit cell" of the Bragg confining structure studied here. e_g , hh_g and lh_g are the Bragg confined electron, heavy hole and light hole states, respectively. They are represented by the energy levels (heavy horizontal bars) and envelope functions.

For the spectroscopic measurements, the sample was placed in an immersion type dewar (at $T=2K$), in the bore of a superconducting magnet (Faraday configuration). It was excited by cw dye lasers pumped with an Ar^{+} laser. The dye laser linewidth was $0.1 meV$ and the intensity at the sample surface was varied in the range of $0.1-5 W/cm^2$. A backscattering geometry was used, and the scattered radiation was dispersed by a double monochromator (resolution of $0.05 meV$).

The PL spectrum of the BCS, at $B=0$, is shown in Fig. 2a. The two PL bands with peaks at $1.981 eV$ and $1.991 eV$ are identified as the $(e_g, hh_g)LS$ and $(e_g, lh_g)LS$ excitonic transitions. The PLE spectra (Figs. 2b-e) are monitored in the $(e_g, hh_g)LS$ excitonic transition of the SL sections (at $1.75 eV$, not shown here). The PLE spectrum, for $B=0$, shows the same Bragg confined exciton transitions as observed in PL, but blue-shifted by $\sim 3 meV$. This shift is probably due to exciton dynamics within its inhomogeneously broadened band, as in other alloy semiconductors. The PL band at $2.02 eV$ is shifted by $\sim 35 meV$ from the $(e_g, hh_g)LS$ band. This is the energy of the

GdAs-like LO phonon in $Al_{0.32}Ga_{0.68}As$. It is thus assigned to a phonon sideband of the (e_g, hh_g) excitonic transition.

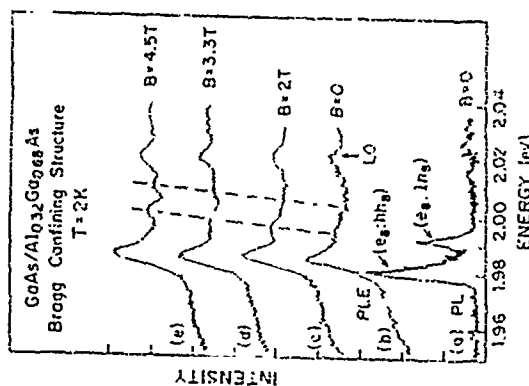


Fig. 2: The photoluminescence (a), under a cw excitation at $2.1 eV$, and the magnetic field dependent photoluminescence excitation spectra (b-e), of the Bragg confining structure depicted in Fig. 1. The emission (in the PLE spectra) was monitored at $1.75 eV$, at the $(e_g, hh_g)LS$ excitonic transition of the superlattice sections. The band denoted LO, in the PLE spectra, is the GdAs-like LO phonon sideband of the $(e_g, hh_g)LS$ exciton band.

Under a magnetic field ($B=5T$), applied along the direction perpendicular to the BCS plane, the PL spectrum does not change. Nor do the $(e_g, hh_g)LS$ band (at $1.981 eV$) and its LO phonon sideband, observed in the PLE spectra (Figs. 2b-e). This is expected, since the LS exciton shows only a diamagnetic shift that is much smaller than its inhomogeneous width. The PLE spectra show two bands that shift linearly to higher

energies with increasing magnetic field, according to:

$$E_n = E_n^0 + \frac{1}{2} \hbar \omega_c \quad (1.2)$$

E_{01} and E_{02} are the extrapolated (to $B \rightarrow 0$) energies of the two field dependent bands. We identify these two bands as the transitions between the lowest electron Landau level ($N_{eh} = 0$) and the highest heavy and light hole Landau levels ($N_{lh} = N_{lh}^0 + 0$), which are $B^{-1/2}$ enhanced. Therefore, E_{01} and E_{02} correspond to the $e_h - hh_h$ and $e_h - hh_l$ band gaps, respectively. The difference between these energies and the energy measured by P.E. of the 35 exciton bands yields the exciton binding energies, $Ry(e_h - hh_h)$ and $Ry(e_h - hh_l)$. The cyclotron frequency, ω_c , is given by

$$\omega_c = \frac{2\pi e B}{\hbar(m_e^* m_0)} \quad (2)$$

where μ_B is the free electron Bohr magneton, m^0 is the free electron mass and m_e^* is the reduced electron-hole in plane effective mass

$$\frac{1}{m_e^*} = \frac{1}{m_e} + \frac{1}{m_h} \quad (3)$$

The reduced masses are determined from the dependence of the respective cyclotron frequencies on the magnetic field, i.e., from the field dependent slopes of E_{01} and E_{02} (as shown in Fig. 2)

In Table 1 we compare the calculated values of the $e_h - hh_h$ and the $e_h - hh_l$ band gaps (1), effective in-plane masses [9][10] and exciton binding energies (11), with the measured quantities. As one can see, there is an excellent agreement between theory and experiment for both the band gaps and the exciton binding energies. For the calculated reduced effective masses, the in-plane values, $m_{eh} = 0.07m^0$, $m_{eh}^* = 0.15m^0$, and $m_{hl} = 0.23m^0$ are taken from Refs. [9] and [10]. The agreement with the measured values is lower. This may be due to both experimental errors and inaccuracy of the assumption of uncoupled hole states [8].

Table 1: Calculated and experimental DC transition energies, in-plane masses and exciton binding energies

	calculated	experimental
$e_h - hh_h$	band gap (E_{01})	1.995 eV
	m_e^*/m_0	0.048
	$Ry(e_h - hh_h)$	9 meV
$e_h - hh_l$	band gap (E_{02})	2.003 eV
	m_e^*/m_0	0.053
	$Ry(e_h - hh_l)$	9 meV

See Refs. [9, 10] and [11]

The observation of the Landau levels proves that the Bragg confined electrons and holes are free to move in the $Al_{0.55}Ga_{0.45}As$ spacer layers (parabolic motion). The high values of the Bragg confined exciton binding energies confirm its two dimensional character, as was recently deduced from the LO-phonon RRS profiles [7] and predicted theoretically by Grundmann and Bimberg [11].

Acknowledgments: The research at the Technion was supported by the U.S. Israel Binational Science Foundation (BSF), Jerusalem, Israel, and was done in the Center for Advanced Opto-Electronics. E. Linder acknowledges the support of the Center for Absorption in Science, Ministry of Immigrant Absorption, State of Israel.

References

- [1]: M. Zahler, I. Brener, G. Lenz, J. Salzman and E. Cohen, Appl. Phys. Lett. 61, 949 (1992)
- [2]: F. C. Zhang, N. Dai, H. Luo, N. Samarth, M. Dobrowolska, J. K. Furdyna and L. H. Rein, Phys. Rev. Lett. 68, 3220 (1992)
- [3]: C. Sirtori, F. Capasso, J. Faist, D. L. Sivco, S. N. G. Chu and A. Y. Cho, Appl. Phys. Lett. 61, 1798 (1992)
- [4]: F. Capasso, C. Sirtori, J. Faist, D. L. Sivco, S. N. G. Chu and A. Y. Cho, Nature 358, 565 (1992)
- [5]: F. H. Stillinger, Physica B 85, 270 (1977)
- [6]: G. Lenz and J. Salzman, Appl. Phys. Lett. 56, 871 (1990)
- [7]: M. Zahler, E. Cohen, J. Salzman and E. Linder, to be published in Phys. Rev. Lett.
- [8]: D. Heim, in The spectroscopy of Semiconductors V23, Ed. by D. J. Scilla, C. L. Lütler (Academic Press, New York (1992)), p. 16-18
- [9]: T. Datta, Modular Series on Solid State Devices, Vol. 13, Quantum Phenomena, Ed. by R. F. Pierret and G. W. Neudeck, (Addison-Wesley Publishing Company, 1990), p. 200
- [10]: L. C. Andreani and A. Pasquarello, Phys. Rev. B 42, 8928 (1991), L. C. Andreani, Ph.D. thesis (Scuola Normale Superiore, Pisa, 1989), p. 11-15
- [11]: M. Grundmann and D. Bimberg, Phys. Rev. B 38, 13486 (1988)

ThP22

Long Lived Photoexcited Electron-Hole Pairs in Modulation Doped GaAs/AlGaAs Quantum Wells Studied by Intersubband Spectroscopy

Y. Garmi,^a E. Ehrenfreund,^a E. Cohen,^a and Arza Ron^b
Solid State Institute Technion Israel Institute of Technology, Haifa 32000, Israel
(^a Department of Physics, ^b Department of Chemistry)

K. K. Law, J. L. Metz and A. D. Gossard
Center for Quantum Electronic Structures (QUEST)
University of California, Santa Barbara, CA 93106, U.S.A

Abstract

We present a study of the $e1-e2$ intersubband absorption in modulation doped GaAs/Al_{0.3}Ga_{0.7}As MQW's that are photoexcited by interband radiation. A comprehensive study of the photoinduced absorption (PIA) strength as a function of exciting (laser) intensity and modulation frequency indicates that only a subgroup of the photoexcited electrons contribute to the PIA. These electrons are long lived in MQW's with a 2DEG density in the range of $1-3 \times 10^{10} \text{ cm}^{-2}$. The existence of long lived electrons is explained by a model based on localized, photoexcited holes, that have a reduced radiative recombination rate with the 2DEG. We calculate this recombination rate and show that it is much longer than that of free electrons and holes.

Introduction

The optical properties of doped quantum wells (QW's) strongly depend on the interaction of the photoexcited electron-hole pairs with the two dimensional electron gas (2DEG) [1, 2]. This is mainly due to phase space filling and screening [3, 4]. Most of the experimental work aimed at studying photoexcitation of doped QW's is based on interband transitions [5, 6]. However, the intensity, spectral shape and decay time of the interband transitions vary gradually with n_0 (the electron area density) in the low 2DEG density range, and therefore, they are not sensitive enough to small variations in n_0 . In this work we report on a study of the $e1-e2$ intersubband absorption in modulation doped GaAs/Al_{0.3}Ga_{0.7}As QW's, under interband photoexcitation. We show that the photoinduced intersubband absorption (PIA) is strongly dependent on both n_0 and the density of photoexcited $e-h$ pairs. These observations are compared with the dependence of the photoluminescence (PL) on the excitation intensity. The results are analyzed in terms of a model based on the existence of long lived electrons in the photoexcited 2DEG. These are due to localized holes that have a small recombination probability with the electrons.

Experimental

Several GaAs/Al_{0.3}Ga_{0.7}As modulation doped MQW's with different n_0 were studied. They were grown by molecular beam epitaxy on (601) oriented GaAs substrates. Each MQW consists of 50 GaAs wells of 50 Å nominal thickness, separated by ~100 Å thick barrier. Each barrier is Si doped in the middle 40 Å and the densities were in the range of $n_0 = 1 \times 10^{10} - 1 \times 10^{12} \text{ cm}^{-2}$ (in each well). The samples were cut and polished

at 45° to the QW plane. This 'waveguide configuration' provided a finite electric field of the infrared radiation along the normal to the QW plane (z direction). Most studies were done in the range of 2-100 K, by placing the samples in an immersion-type dewar. The infrared beam passed through a Bruker IFS-66V Fourier transform infrared spectrometer. It was modified in order to record small changes in the absorption, which were induced by excitation with an Ar⁺ laser or a Pyridine 2 dye laser. The intersubband transitions were measured with a spectral resolution of 2 meV. The PIA spectra were obtained by measuring $(-\Delta T/T)$, where T is the sample transmission and ΔT is its photoinduced change. The sensitivity in measuring the PIA was better than 10^{-4} . The exciting laser beam was chopped with an acoustic optic modulator in the range of $10^2 - 10^4 \text{ Hz}$. For the PL measurements we used a double grating monochromator with a resolution better than 0.1 meV.

The PL spectrum of the MQW with $n_0 = 1 \times 10^{10} \text{ cm}^{-2}$ is shown in Fig. 1a. The measured integrated intensity of this PL band as a function of exciting laser intensity, in the intensity range of $I_L = 0.01 - 1 \text{ W/cm}^2$ is found to be linear. However, the band shape varies slightly with increasing excitation intensity. In order to study this effect we obtained the differential PL (DPL) spectra by first normalizing each spectrum by its integrated intensity. Then we subtract the normalized spectra taken under two excitation intensities. Figs. 1b-d show three such DPL spectra. $(I_1 - I_0)/I_0$ denotes the spectrum obtained by subtracting the normalized spectrum for $I_L = 0.03 \text{ W/cm}^2$ from that of $I_L = 1 \text{ W/cm}^2$. Fig. 2 shows the absorbance and PIA spectra for two MQW's with $n_0 = 1 \times 10^{10}$ and $7 \times 10^{10} \text{ cm}^{-2}$. The observed absorption band is due to the $e1-e2$ intersubband transition [8, 9]. Its integrated intensity is proportional to the doping level and to the optical path of the infrared beam in the sample. The PIA spectra were observed under interband excitation energy of 2.41 eV and intensity of 0.64 W/cm^2 (at the sample surface). It is clearly seen that while the PIA is relatively strong ($[-\Delta T/T]_{\text{max}} \approx 6 \times 10^{-3}$) for $n_0 = 1 \times 10^{10} \text{ cm}^{-2}$, it is unobservable for $n_0 = 7 \times 10^{10} \text{ cm}^{-2}$. No PIA signal could be observed for the MQW's with higher doping levels. It should be noted that the direct absorption and PIA of the same MQW have the same spectral shape, and are polarized along the growth direction. Fig. 3 shows the dependence of the integrated PIA intensity, $I_A \approx \int (-\Delta T/T) d\epsilon$, on the exciting laser intensity, for two MQW's, with $n_0 = 1 \times 10^{10}$ and $3 \times 10^{10} \text{ cm}^{-2}$.

Analysis

The PIA spectrum (observed only for the lightly doped samples, $n_0 < 3 \times 10^{10} \text{ cm}^{-2}$) has the same shape as that of the absorption spectrum. Therefore, the PIA is due to electrons added to the 2DEG with the same energy distribution. The fact that the integrated PL intensity dependence on exciting laser intensity is linear, means that the total density of photoexcited electron-hole pairs depends linearly on the laser intensity. On the other hand, the PIA saturates with increasing laser intensity (Fig. 3). We thus conclude that the electrons contributing to the PIA are only a finite subset of the total photoexcited electron population. We have measured the dependence of I_A on the exciting laser modulation frequency [10] and found that the lifetime of these electrons is of the order of a few μsec . We also found that while the PIA intensity depends very strongly on both n_0 and I_L , the DPL intensity (Fig. 1b-d) varies very weakly with I_L (for a given n_0). This supports the conclusion that only a subgroup of photoexcited electrons contributes to the intersubband absorption, while all these electrons contribute to the interband PL.

This suggestion can be tested by fitting the PIA intensity on I_L using a phenomenological approach. Following Ref. 1, we propose that the generation rate of the electrons contributing to the PIA (with a density $\sim N_{PIA}$) is given by $g(1 - N_{PIA}/N_A)$. Here g is the photogeneration rate ($g \propto I_L$) and N_A is the saturation density of the electrons contributing to the PIA. If we further assume that these electrons have a lifetime τ , then the rate equation is:

$$\frac{dN_{PIA}}{dt} = g(1 - N_{PIA}/N_A) - \frac{N_{PIA}}{\tau} \quad (1)$$

Its steady state solution is

$$N_{PIA} = \frac{g\tau N_A}{g\tau + 1} \quad (2)$$

The experimentally measured I_A is directly proportional to N_{PIA} : $I_A = I_0 N_{PIA}/N_A$, where I_0 contains various constants including the infrared optical path in the sample. The fit of this model to the data of Fig. 3 is shown by the solid lines. The parameters obtained by this fit are: $N_A \approx 1.2$ and $0.36 \times 10^{16} \text{ cm}^{-3}$ and $\tau \approx 12$ and $1.6 \text{ } \mu\text{sec}$ for the $n_0 = 1$ and $3 \times 10^{16} \text{ cm}^{-3}$ MQW's, respectively. For comparison, we show in Fig. 3 the linear dependence of I_A on laser intensity, as measured for undoped MQW's. It is clear that the PIA in the doped MQW's is due to a different mechanism than the undoped MQW's (long lived electrons vs short lived excitons). In order to account for the existence of long lived photoexcited electrons in doped MQW's with $1 \times 10^{16} \leq n_0 < 7 \times 10^{16} \text{ cm}^{-3}$, we propose the following model: a subgroup of the photoexcited hole population consists of localized holes, whose wavefunction weakly overlaps with the 2DEG wavefunctions. It is assumed that the hole localizing centers do not localize electrons. It is conceivable that such hole localization can occur due to interface roughness together with a random distribution of the Si dopant atoms (which are located only $40 \text{ } \text{\AA}$ from the interfaces). A finite density of such hole localizing sites results in a sizeable density of long lived photoexcited electrons, because the localized holes will have a reduced recombination rate with the 2DEG. We estimate this rate by the following calculation. The x -dependent part of the electron wavefunction is obtained by self-consistently solving the Schrödinger and Poisson equations, for a given n_0 . Using the resulting electrostatic potential, the z dependent part of the hole wavefunction, $\psi_h(z)$, is obtained. Then, following Bastard [11], we assume a cylindrical localization potential on the interface and set the Schrödinger equation for the in-plane hole wave function $\{\psi_h(r)\}$

$$\left[\frac{p_z^2 + p_r^2}{2m^*} - V_A \Theta(a-r) \right] \psi_h(r) = (E - E_v) \psi_h(r) \quad (3)$$

where p_z, p_r are the in-plane momentum operator components, m^* is the hole effective mass in the well, $\Theta(a-r)$ is a step function that defines a cylindrical well with radius a and a potential of V_A . P_h is the probability of finding the hole on the interface. E_v is the lowest confined hole energy level and E is the localized hole energy level. Assuming $f(r) = 1/\sqrt{2} e^{-r/a}$, $n_0 = 1 \times 10^{16} \text{ cm}^{-3}$, a valence band offset of $V_A = 0.17 \text{ eV}$ and $a = 200 \text{ } \text{\AA}$, we obtain $E = 3.5 \text{ meV}$ and $\lambda = 100 \text{ } \text{\AA}$ for the binding energy and the wavefunction extension radius, respectively. The extension radius and the density of localizing sites that we have found are in reasonable agreement with other works done on interface roughness [12, 13]

Now, assuming that the electrons in the 2DEG have a 2D free particle wavefunction, we can calculate the recombination rate (in comparison to that of a free electron recombining with a free hole) by using Fermi's golden rule (Fig. 4). The result (which is approximated for the case where $\hbar\omega_A^2 > 1$) is: $\tau_f/\tau_h \approx n_0 \lambda^2$, where τ_h is the radiative recombination rate of a free electron with a localized hole and τ_f that of a free e and h . Taking $n_0 = 1 \times 10^{16} \text{ cm}^{-3}$ and the parameters quoted above we had:

$$\frac{\tau_f}{\tau_h} \sim 500 \quad (4)$$

This result leads to a lifetime of the localized holes and corresponding excess electrons in the order of $0.5 \text{ } \mu\text{sec}$. Moreover, since $n \propto 1/n_0$, the density of electrons contributing to the PIA will be greatly reduced with increasing n_0 , resulting in a very weak PIA spectrum (as observed).

Summary

We find that the (el-e2) PIA is strongly dependent on the density of the 2DEG and on the exciting (laser) intensity. This absorption is only observed for $1 \times 10^{16} \leq n_0 < 7 \times 10^{16} \text{ cm}^{-3}$, and is non-linearly dependent on I_L . The intensity of the interband PIA on the other hand is linearly dependent on I_L , with very small variations in its slope. We show that these results are well explained by a model based on the existence of a subgroup of long-lived photoexcited holes. We present a model of hole localization centers that are due to interface potential fluctuations. The calculated hole wavefunction leads to a radiative recombination rate with the 2DEG, that is much smaller than that of a free hole. Our study shows that the in-v-l band spectroscopy of low density 2DEG is a much more sensitive tool than interband spectroscopy.

Acknowledgments The work at the Technion was supported by the US-Israel Binational Science Foundation (BSF), Jerusalem, Israel, and was carried out in the Center for Advanced Micro-electronics. The work at UCSB was supported by the National Science Foundation Science and Technology Center, QULEST.

References

- [1] S. Schmitt-Rink, D. S. Chemla and D. A. B. Miller, *Adv. Phys.* **36**, 89 (1995).
- [2] G. D. Sanders and Y. C. Chang, *Phys. Rev. B* **35**, 3305 (1987).
- [3] G. Livescu, D. A. B. Miller, D. S. Chemla, M. Ramaswamy, T. Y. Chang, N. Saver, A. C. Gossard and J. H. English, *IEEE Journal of Quantum Electronics*, **24**, 1677 (1988).
- [4] D. Huang, H. Y. Chu, Y. C. Chang, R. Roudre and H. Morkoc, *Phys. Rev. B* **38**, 1246 (1988).
- [5] L. A. Kleinman, *Phys. Rev. B* **32**, 3766 (1985).
- [6] H. W. Lin, C. Delalande, G. Bastard, M. Voos, G. Peter, R. Fischer, E. O. Gobel, J. A. Brum, G. Weimann and W. Schlapp, *Phys. Rev. B* **45**, 8469 (1992).

- [7] C.D. Delalande, G. Bastard, J. Orgonas, J.A. Brum, H.W. Liu, M. Voos, G. Weimann and W. Schlapp, *Phys. Rev. Lett.* **59**, 2690 (1987).
- [8] L.C. West, S.J. Eglash, *Appl. Phys. Lett.* **46**, 1156 (1985).
- [9] Y. Gani, M. Olshaker, E. Cohen, E. Ehrenfreund, Arza Ron, K.K. Law, J.L. Mers and A.C. Gossard, *Superlattices and Microstructures* **7**, 287 (1990).
- [10] Y. Gani, E. Ehrenfreund, E. Cohen, Arza Ron, K.K. Law, J.L. Mers and A.C. Gossard, *Phys. Rev. B* **48** (Aug. 1993).
- [11] G. Bastard, "Wave Mechanics Applied to Semiconductor Heterostructures", (Les editions de physique, Les Ulis, 1988), Chap. 4.
- [12] J. Christen and D. Bimberg, *Phys. Rev. B* **42**, 7212 (1990).
- [13] C.A. Warwick, R.F. Kopf, *Appl. Phys. Lett.* **60**, 386 (1992).

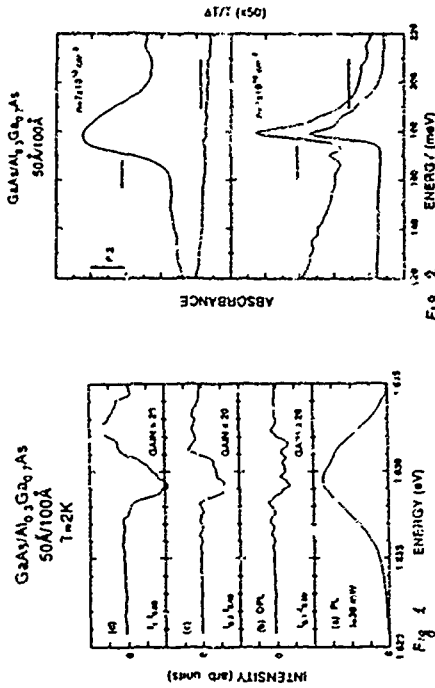


Figure Captions
Fig. 1 : a. The photoluminescence (PL) spectrum of the MQW with $n_0 = 1 \times 10^{18} \text{ cm}^{-3}$. b. The differential photoluminescence (DPL) spectrum obtained by subtracting the (area-normalized) PL spectrum for excitation intensity of $I_{\text{exc}} = 303 \text{ W/cm}^2$ from that excited by $I_{\text{exc}} = 0.1 \text{ W/cm}^2$. (c), (d) are the same as (b) but with different excitation intensities.

Fig. 2 : The absorbance and photo-induced absorption ($-\Delta T/T$) of two MQWs with the indicated areal electron densities, observed at liquid He temperature.

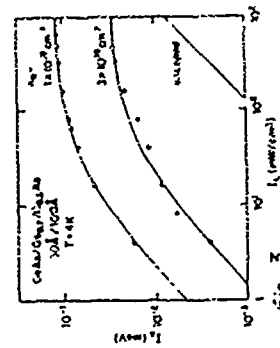


Fig. 3 : The integrated photoluminescence (PL) spectra of two MQWs as a function of excitation intensity. Also shown is the measured photo-induced absorption strength of an undoped MQW.

Fig. 4 : A schematic description of the localized hole-free electron recombination model (see text).

ThP23

Electron Transport in $\text{InAs/Ga}_{1-x}\text{In}_x\text{Sb}$ Superlattices

C. A. Hoffman, J. R. Meyer, E. R. Youngdale, and F. J. Bartoli
Code 5813, Naval Research Lab, Washington, D.C. 20375

R. H. Miles

Hughes Research Laboratories, Malibu, CA 90265

L. R. Ram-Mohan

Worcester Polytechnic Institute, Worcester, MA 01609

We will discuss a magneto-transport and quantum transport investigation of $\text{InAs-Ga}_{1-x}\text{In}_x\text{Sb}$ strained layer superlattices, which are of great current interest as a potentially more producible alternative to $\text{Hg}_{1-x}\text{Cd}_x\text{Te}$ in infrared detector applications. Despite a crucial role in photovoltaic device operation, the transport properties of electrons and holes in this system have received almost no previous attention. The present data will be correlated with theoretical band structures from an 8-band $k \cdot p$ calculation.

Temperature-dependent electron mobilities have been determined for a series of n-type superlattices with constant $\text{Ga}_{1-x}\text{In}_x\text{Sb}$ barrier thickness ($d_2 = 25 \text{ \AA}$) but a range of InAs well thicknesses ($d_1 = 25\text{-}80 \text{ \AA}$). Interface roughness scattering is found to dominate in all samples and most temperatures up to ambient ($T \leq 300 \text{ K}$). However, the dependence on d_1 is found to be much weaker than the d_1^{-6} relation observed in other heterostructure systems with larger d_2 . This is, in fact, consistent with the theoretical prediction of a weaker sensitivity of the energy levels to monolayer fluctuations in the well width. Theory also predicts that the low-temperature mobility should abruptly drop when d_1 is increased to the point where the energy gap vanishes and the superlattice becomes a semiconductor. Not only is this confirmed experimentally, but the observed decrease in μ_n is much larger than that predicted. The calculations show that when d_2 is thin, the E1 and E1' bands strongly repel one another. Semimetallic $\text{InAs-Ga}_{1-x}\text{In}_x\text{Sb}$ thus has much more in common with semimetallic HgTe-CdTe superlattices than with semimetallic InAs-GaSb (for thick d_2). The experimental observation of two coexistent electron species whose relative populations shift with T is a predicted consequence. All of the samples in the series display quantum oscillations in both the diagonal and Hall conductivities. Since the system has a strongly 3D rather than 2D character, it is surprising that in several superlattices the oscillations in σ_{xx} are considerably stronger than those in σ_{xy} .

-915-

ThP24

Comparison of Far-Infrared- and DC-Conductivity of Electron-Systems Laterally Patterned by Low-Energy Ion Beam Exposure

C. Lettau(a), M. Wendt(a), A. Schmeidler(a), W. Hassenfeldt, J. P. Kothaus(a), G. Böhm(b), G. Weimann(b), and M. Hölzl(c)

(a) Sektion Physik, Ludwig-Maximilians-Universität München, D-80539 München
(b) Walter-Schottky Institut, TU München, D-85748 Garching
(c) DEEE, University of Glasgow, GB-Glasgow G12 8QQ

We investigate the electronic properties of quantum wires that are prepared in AlGaAs-GaAs heterojunctions with a low energy ion beam irradiation technique. Magneto-transport measurements on single wire structures reveal that diffuse scattering at the lateral boundaries is enhanced in these structures compared to wires prepared by split gates or etching techniques. Furthermore, the lateral depletion width is relatively small, i.e., the electronic width is only 40 nm smaller than the width of the lithographically defined mask. In addition we study the far-infrared conductivity of these quantum wires. We find that the boundary roughness scattering has a dramatic impact on the resonance linewidth in low magnetic fields. The 1D intersubband plasmon is found to be much more affected than the 1D intrasubband plasmon reflecting highly anisotropic scattering.

Low-dimensional electron systems such as quantum wires and quantum dots are preferably prepared by lateral patterning of a two-dimensional electron system (2DES) in semiconductor heterostructures. Different patterning techniques have been employed of which the most widely used are etching into the sample surface or patterned field effect electrodes [1]. The properties of wires generated with these methods are thus intensively investigated and it is found that, generally, the external charges that define the electrostatic binding in lateral direction are separated from the electron system by relatively large depletion widths. This leads to smooth potential walls, i.e., channel boundaries with roughness that can be characterized by a correlation length comparable to the depletion width. A less thoroughly characterized technique is the lateral patterning by low energy ion beam irradiation although existing experiments show intriguing results. [2,3] In particular, these results indicate that the depletion widths in ion beam defined quantum wires are considerably smaller than in field effect defined samples and that the boundary scattering is considerably more diffuse reflecting more roughness. Here we focus on the impact of enhanced diffuse boundary scattering on the dynamic conductivity in ion beam defined quasi-one-dimensional (1D) electron systems.

Two conventional HEMT-structures are used for the preparation in which the hetero-interfaces are 70 nm and 50 nm below the sample surface. At $T = 4 \text{ K}$ the 2DESs have electron densities of $n_s = 4 \cdot 10^{15} \text{ m}^{-2}$ and $5 \cdot 10^{15} \text{ m}^{-2}$ and mobilities of $17 \text{ m}^2/\text{Vs}$ and $50 \text{ m}^2/\text{Vs}$, respectively. The ion beam irradiation results in a depletion of mobile electrons except from those areas that are protected by mask. As irradiation mask a resist pattern defined by optical or electron beam lithography was used.

For DC magneto transport measurements we have prepared single quantum wires by electron beam lithography. The geometries of the Ni-AuGe ohmic contacts are defined with PNMA positive resist whereas the ion beam irradiation masks are made of 100 nm thick negative resist (Fluorist AZ PN 114) stripes connecting the previously prepared ohmic contacts. Quantum wires with resist stripe widths between 100 nm to 1000 nm have been fabricated. Three pairs of voltage probes for measurements of the Hall resistance are arranged along the wires with 7.5 μm separation between each pair. The samples for (FIR) transmission measurements are multiple quantum wire arrays defined with a holographically exposed positive photoresist layer

-916-

(Shipley AZ1805) of 140nm thickness. Periods of the wire arrays range from 300nm to 700nm. The widths of the photoresist stripes are typically less than half the period, e.g. 300nm for a sample with period 700nm.

The ion beam exposure is performed in a commercial ion-milling-machine modified to use low ion dose rates (typically $5-6 \mu\text{C}/\text{cm}^2$) with low acceleration voltages (200-300V). The use of low energy Ne ions results in low sputtering rates when irradiating the sample surface. This is verified with an atomic force microscope with which a material removal of 2-3nm height has been measured after irradiating the sample with a typical dose ($3.5 \text{mC}/\text{cm}^2$) necessary to pattern the electron system. Detailed investigations concerning the confinement mechanism in these ion beam defined wires will be published elsewhere [6]. We note that the small surface corrugation makes the ion beam irradiation technique very advantageous for combination with additional patterning techniques like, e.g., additional metal gates on the sample surface. Thus, as described later, a metal grating coupler for the investigation of 1D plasmons can easily be fabricated on top of the sample after the ion beam exposure. The irradiation effect on the 2DEG is monitored during the ion beam exposure by measuring the increase of the resistance between two ohmic contacts during ion beam exposure. Additionally, in the single wires the vanishing of the low temperature resistance measured at $B=0$ in Hall geometry serves as an independent test for the successful isolation of the unmasked regions. On the other hand in the wire arrays for FIR transmission measurements the successful isolation of the wires can be judged from the frequency of the dimensional resonance as described below.

The inset of Fig. 1 shows typical traces of the longitudinal DC resistance in ion beam defined quantum wires as function of the magnetic field applied perpendicular to the sample surface for various wire widths. At low fields a pronounced maximum of the longitudinal resistance is observed, with a position that depends on the electronic widths of the quantum wires. This maximum arises from diffuse scattering at the boundaries of the 1D channels on the longitudinal magneto-resistance. [3] At zero magnetic field the channel resistance is dominantly determined by electron trajectories that reflect from the channel boundaries under glancing angles. A small magnetic field bends the trajectories towards the boundaries and thus intensifies contact to the channel boundaries. Diffuse scattering processes then lead to an enlarged resistance. At higher fields the opposing channel boundaries become decoupled, i.e. an electron trajectory is either bound to one of the boundaries or in the sample center. The magneto-resistance decreases accordingly at high magnetic fields. The strength of the magneto-resistance anomaly indicates the importance of boundary roughness in our samples.

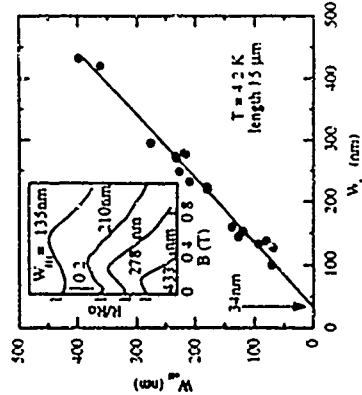


Fig. 1. Effective widths of electron wires defined by ion beam exposure plotted vs. the lithographic width of the mask. W_{eff} is calculated as explained in the text. Inset: Longitudinal magneto-resistance of those wires at small magnetic fields, showing the resistance anomaly that arises from diffuse boundary scattering.

The magnetic field position B_{max} of the resistance maximum can be used to determine an effective width of the electron wire. [3] A numerical model for description of the magneto-resistance anomaly [7,8] relates the classical cyclotron radius $R_c = \hbar k_F / e B_{\text{max}}$ to the effective width W_{eff} of the 1D electron system according to: $W_{\text{eff}} = 0.55 R_c$. In Fig. 1 the effective widths determined from the resistance anomaly are plotted as a function of the lithographic width of the mask as determined from SEM-pictures. The straight line is a least square fit to the data. The intercept with the abscissa reflects twice the depletion width, i.e. the amount by which the effective widths of the electron channels are smaller than the lithographic width of the mask. We thus have a lateral depletion length smaller than 20nm, a very low value compared to those found with other patterning techniques. The slope of the line is close to one as expected if the depletion width does not depend on the lithographic width.

The thus determined effective width W_{eff} together with the electron density determined from the high field quantum oscillations of the magneto-resistance are used to determine an electron mobility from the longitudinal resistance at $B=0$. In Fig. 2 the mobility is depicted vs. the effective wire width. We consider the modification of the phase space for scattering processes arising from the reduced dimensionality in our quantum wires as unimportant. If scattering is 100% specular the as-grown mobility represents an upper limit for the electron mobility in the 1D channels as indicated by the upper solid line. The lower solid line is calculated with a model

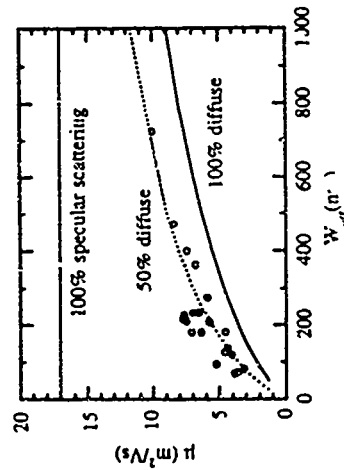


Fig. 2. Electron mobilities in ion beam defined quantum wires determined from the zero field resistance as function of the effective wire width. Solid lines are calculated for 100% specular and 100% diffuse scattering, respectively (see text).

of Beenaker et al. [9] assuming 100% a diffuse scattering. The dashed line demonstrates that the mobilities found in our ion beam defined quantum wires are best described assuming about 50% diffuse boundary scattering.

The FIR-transmission-spectra are measured with a rapid scan Fourier-transform-spectrometer at $T=2\text{K}$. We first discuss measurements on wire arrays that have periods of 700nm, 500nm and 300nm and no additional grating coupler on the sample surface. With the FIR radiation polarized perpendicular to the wires we excite the intersubband plasmon at wave vector $q=0$, the so-called dimensional resonance. Dimensional resonances of a wire array with 700nm period recorded at different magnetic fields are shown in Fig. 3 along with the resonance linewidths as function of magnetic field (inset). Whereas the linewidth is low at high magnetic fields it strongly increases with decreasing magnetic field. The resonance oscillator strength remains roughly constant. The magnetic field dependent broadening is even more drastic in samples

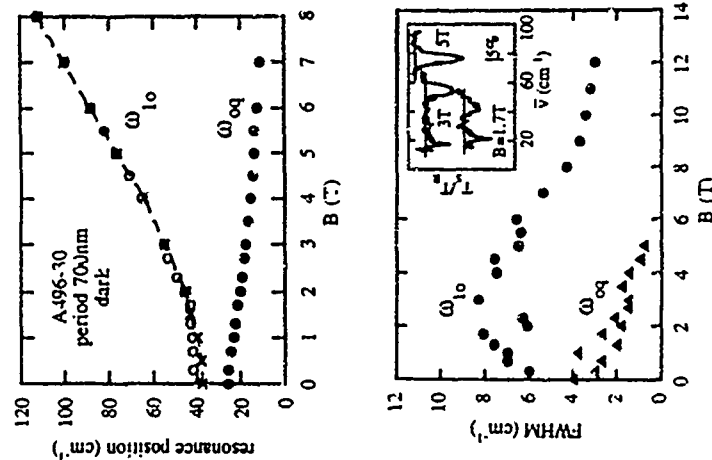


Fig. 4: (a) resonance positions of intersubband plasmons $\omega_{1,0}$ and intrasubband plasmons $\omega_{0,q}$ of the sample in Fig. 3 as a function of the magnetic field. The dashed line is calculated as described in the text. Crosses denote resonance positions measured before the grating coupler was prepared on the sample surface. Circles are measured with a grating coupler consisting of stripes oriented perpendicular to the electron wires and period $b=1\mu\text{m}$. (b) Resonance linewidth of the $\omega_{0,q}$ (triangles) and $\omega_{1,0}$ mode. The inset shows three typical FIR transmission spectra

lower frequency. The magnetic field dependence of the resonance positions are shown in Fig. 4a together with the resonance positions of the dimensional resonance in this sample before fabrication of the grating coupler. The resonance position of the intersubband plasmon is only slightly shifted with respect to the dimensional resonance measured without grating coupler.

The negative magnetic field dispersion of the low frequency mode unambiguously identifies this mode as the intrasubband plasmon. [10,11] In the experimental spectra the FWHM of the intrasubband plasmon is remarkably small compared to the linewidths of the intersubband plasmon as demonstrated by the data in Fig. 4b and the spectra in the inset of the same figure. This behaviour can be understood with the assumption that the effectivity of the diffuse boundary scattering process is anisotropic with respect to the angle between channel boundary and direction of electron motion. Since at $B=0$ the electron motion associated with the intrasubband plasmon is along the channel the small resonance linewidth suggests that glancing angle wave-

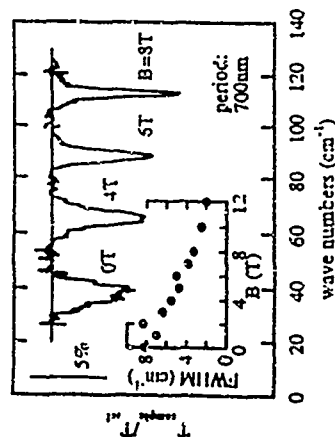


Fig. 3: Dimensional resonances of an ion beam defined wire array with period 700nm. The inset shows the FWHM of the resonances vs. magnetic field.

with 500nm period and different from line widths of dimensional resonances in wire arrays fabricated with more conventional techniques. Here the linewidth increases with decreasing magnetic field so strongly that at $B=0$ no dimensional resonance can be resolved. The resonance position follows the $\omega_{1,0}$ magnetic field dispersion $\omega_{1,0}^2 = \omega_{0,q}^2 + \omega_c^2$ as shown by the crosses in Fig. 4a. [1] The dashed line is calculated according to this formula. Since ω_0 is an additional measure of lateral confinement we can use the ω_0 extracted from the measured resonance positions as another indicator for successful ion beam patterning. In wire arrays with 500nm and 700nm resist gratings the resonance shifts by about 15cm^{-1} at $B=3\text{T}$ after ion beam exposure. In samples with a resist mask of 300nm period and exposed to a successively increasing ion dose to meet this criterion at $B=3\text{T}$ it was found that the resonance vanishes before a significant shift of the resonance position could be resolved.

A small increase of the resonance linewidth is often also observed in field effect defined wire arrays. This, generally, is discussed in terms of fluctuations of the wire width and an associated inhomogeneous broadening of the resonance position. In our experiments on field effect defined quantum wires [1] we used the same fabrication process for the resist masks as is used here. Thus in both cases the roughness of the resist masks should be comparable. The drastic increase of the resonance FWHM in ion beam defined wires at small magnetic fields can be understood in terms of boundary roughness created by the ion beam exposure. This is in agreement with the enhanced boundary roughness found in above DC transport experiments. A simple argument considering the classical electron trajectories connected with the dimensional resonance shows that diffuse scattering can effectively smear the dimensional resonance. At $B=0$ the dimensional resonance is associated with electron motion perpendicular to the channel boundaries and thus can be broadened by diffuse boundary scattering. In a magnetic field this situation changes since the magnetic field localizes the electron wave function within the channel. In the classical picture the majority of the classical electron trajectories have reduced boundary contact. Accordingly, the FWHM decreases with increasing magnetic field.

After successful investigation of wire arrays with 700nm period a grating coupler was prepared on the sample surface. The grating coupler consists of an gold grid of period $b=1\mu\text{m}$. The gold strips have 35nm thickness and a width of approximately 700nm. With unpolarized FIR radiation we now observe in addition to the dimensional resonance an intrasubband plasmon at

ThP25

NOVEL TUNABLE FAR INFRARED DETECTOR BASED ON A QUANTUM BALLISTIC CHANNEL

L. Fedichkin, V. Ryzhii* and V. V'yurkov*

*Institute of Physics and Technology,
25A Krasikov Str., Moscow, 117218, Russia
** University of Aizu, Tsuruga, Ikkimachi,
Aizu-Wake-atsuta-City, 965 JAPAN

Abstract

A new tunable far infrared detector based on a quantum ballistic channel in the asymmetric split-gate structure is proposed and considered theoretically. The asymmetric split-gate provides a long constant width channel with a rather sharp asymmetric narrowing at its end. It is supposed that only the lowest subband in a wide channel is occupied by electrons. There is a thick barrier for these electrons in the narrow channel, so the dark current reduces almost to zero. Due to the asymmetric variation of the channel width the electrons can pass the narrow region of the channel under illumination with the photon energy close to subband separation.

The aperture-lattice responsibility of the photovoltaic detector under is evaluated. The advantage of the proposed detector is a possibility of tuning by a gate voltage and the small response time.

The detection mechanism of the detector with a constant F...
The energy variation of the detector is not uniform for infrared detector
applied. The detector is not uniform in its response time due
to the conservation of the electron energy. The detection of the electron
energy factor is not uniform in the current through the

ring processes much less effectively damp the resonances in contrast to the large angle scattering processes associated with the intersubband resonance. We note that the direction of electron motion probed in DC transport experiments again is preferentially along the channel as in the case of intrasubband plasmons.

In conclusion, we investigate the DC as well as FIR conductivity of quantum wires defined by low-energy ion beam exposure. DC transport measurements demonstrate that diffuse boundary scattering processes are important in such wires. The resonance linewidth of the FIR conductivity reflects the high anisotropy of these scattering processes.

Acknowledgements: We like to thank A. Wisforth and A. Huber for valuable discussions and gratefully acknowledge financial funding by the Deutsche Forschungsgemeinschaft.

References

1. W. Hansen, U. Merkt, and J. P. Kouhaas, in *Semiconductors and Semimetals*, ed. R. K. Willardson, A. C. Beer, E. R. Weber, Vol. 35, ed. M. Reed, (Academic Press, San Diego 1992) p. 279.
2. M. L. Roukes, A. Scherer, S. J. Allen, Jr., H. G. Craighead, R. M. Ruthen, E. D. Beebe, and J. P. Harbison, *Phys. Rev. Lett.* **59**, 3011 (1987).
3. T. J. Thornton, M. L. Roukes, A. Scherer, and B. P. Van de Gaag, *Phys. Rev. Lett.* **63**, 2128 (1989).
4. M. L. Roukes, A. Scherer, and P. Van der Gaag, *Phys. Rev. Lett.* **64**, 1154 (1990).
5. T. J. Thornton, M. L. Roukes, A. Scherer, and B. van der Gaag, in *Science and Engineering of 1- and 0-Dimensional Semiconductors*, ed. S. P. Beaumont and C. M. Sotomayor-Torres (Plenum).
6. C. Lettau, M. Wendel, A. Schmeller, W. Hansen, J. P. Kouhaas, G. Bühm, G. Weimann, and M. Holland, to be published.
7. E. Diefen and J. Lohse, *Philos. Mag.* **14**, 759 (1966).
8. A. B. Pippard, *Magnetoresistance in Metals*, (Cambridge University Press, Cambridge 1989).
9. C. W. J. Beenakker and H. van Houten, *Phys. Rev. B* **38**, 3232 (1988).
10. G. Eliazon, J.-W. Wu, P. Hawrylak, and J. J. Quinn, *Solid State Commun.* **60**, 41 (1986).
11. T. Demel, D. Heitmann, P. Grambow, and K. Ploog, *Phys. Rev. Lett.* **66**, 2657 (1991).

ballistic channel under illumination is almost the same as in darkness. We offer the split-gate structure like that in Fig. 1. The essential feature of the electrode shape is that it provides a long constant width channel with a rather sharp asymmetric narrowing at its end so that the subband bottom vs longitudinal coordinate diagram is alike to that in Fig. 2.

The main idea is the following. Suppose that only lowest 1st subband in a wide channel is occupied by electrons, i.e. 1st subband is under the Fermi level in a two-dimensional electron gas (2DEG) reservoir. There is a thick barrier for these electrons in a narrow channel; so the dark current reduces almost to zero. A dark current caused by a thermal activation or tunneling is very small. When a photon has an energy $\hbar\omega$ close to subband separation $\hbar\omega_0$ in the wide channel and is polarized perpendicular to the channel axis an electron can absorb a photon and be excited to the 2nd subband. When the channel width variation is rather sharp and asymmetric the transition to the 1st subband is possible. In this way the electron can pass the narrow channel if its energy surmounts the 1st subband barrier height E_b . It occurs at least when E_b is higher than Fermi energy E_F and lower than subband separation $\hbar\omega_0$. In reality there is a simultaneous photon assisted transition rather than two sequential processes of absorption and transition. To evaluate the responsibility of the structure we have used a common perturbation theory for electron-photon interaction in a long wave limit because we assumed the wave length (about 50-150 μ) to be much greater than all geometrical parameters of the structure. Practically gate electrodes are semitransparent for wave length

50-150 μ . As usual the constrictive potential caused by split-gate is supposed to be parabolic [1]

$$U(x,y) = \frac{m}{2} \Omega^2(x)(y_c(x)-y)^2, \quad (1)$$

where x-axis is directed along the channel, y-axis lies in a plane of the structure, y_c is a channel center coordinate. In the wide part of the channel $\Omega(x) = \omega_0 = \text{const}$, so the subband energy spectrum has oscillatory equidistant form. x-dependence of Ω and y_c describes respectively narrowing and bending of the channel.

The probability of a transit, from a state (n,k) with a subband number n and a wave number k in x-direction to a state (n',k') was calculated. It differs from zero only for transitions to adjacent subband with conservation of a wave number k and only for y-polarization of incident light.

Provided there is an asymmetric narrowing in the channel an excited electron can transform into another subband electron, pass the channel and contribute to a photocurrent. To evaluate the transformation efficiency $T_{nn'}$ from n -th to n' -th subband we have used a weak bent channel model which assumed that $(kR)^{-1} \gg 1$ where kR is a longitudinal momentum and R is a radius of channel bending. For the 2nd to 1st subband transformation efficiency T_{21} a simple estimation is valid when the electron energy $\frac{\hbar^2 k^2}{2m}$ is not too small compared with subband separation $\hbar\omega$:

$$T_{21} \approx \frac{\hbar}{m\omega p}, \quad (2)$$

When the narrow split (Fig. 1) is more than twice or so less than the wide split the bending radius R is about half average split width. The transformation efficiency, according to (2) attains a value about 0.1 for $\hbar\omega = 5 \text{ meV}$ and split width 0.1 μ . Really for this conditions the transformation efficiency can be

much greater (about unity as in (2)).

For the low temperature limit responsivity R_A was obtained

$$R_A = \frac{4\pi L e^3}{h^2 S \omega_0 n_0} v_f T_{av} \delta(\omega - \omega_0) \quad (3)$$

where L is a channel length, S is a structure area, v_f is the Fermi velocity, T_{av} - averaged transfer coefficient. For real channels a broadening $\Delta\omega$ should be taken into account. So the δ -function in (3) should be replaced by the Lorentz function

$$f_L(\omega - \omega_0) = \frac{1}{\pi} \frac{\Delta\omega}{\Delta\omega^2 + (\omega - \omega_0)^2} \quad (4)$$

A finite channel length L leads to a broadening $\frac{\Delta\omega}{2\pi}$ about a reciprocal transit time $\tau = \frac{L}{v_f}$. In this way a simple expression for the peak sensitivity of the detector was obtained

$$R_A = \frac{2}{\pi n_0} \frac{e^2}{\hbar \omega_0} \frac{L^2}{S} T_{av} \quad (5)$$

Supposing $S = L^2$, $\omega_0 = 5$ meV and T_{av} about unity this expression gives R_A about 0.2 A/W which is close to that achieved previously [3]. However the advantage of the proposed detector is a convenient tuning by a gate voltage. The response time is limited by a transit time τ . The sensitivity peak can be operated by a gate voltage. The detector is photovoltaic and rather fast.

References

1. F. Stern, S.E. Laux, D.J. Frank. *Surface Science*, 196, 101 (1988)
2. J.C. Wu, M.N. Hybourne, W. Yindeepol, A. Weisshaar, S.M. Goodnick, *Appl. Phys. Lett.*, 59, 102 (1991)
3. E. Diöbel, G. Müller, D. Weiss, K. von Klitzing, K. Ploog, R. Losch, H. Nickel, W. Schlapp, *Appl. Phys. Lett.*, 58, 2231 (1991)

ThP26

Cyclotron FIR Emission from Hot Electrons in
GaAs-GaAlAs Heterostructures

W. Zawadzki, C. Chevalier, D. Dur, W. Knap, and A. Raymond
Groupe d'Etudes des Semiconducteurs
Université Montpellier II
34095 Montpellier, France

We study far infrared emission from GaAs-GaAlAs heterostructures, induced by electric pulses in the presence of a magnetic field and a hydrostatic pressure. Cyclotron masses are measured as functions of 2D electron density in the strong electron heating regime at pressures $P=0$ and $P=7\text{ kbar}$ and its detection energy of 4.43 meV . The results are described by an effective two-level $\tilde{k} \cdot \tilde{p}$ theory, which takes consistently into account the effect of band nonparabolicity in GaAs on electric and magnetic quantization. It is shown that the observed emission spectrum is due to eight transitions between Landau levels (populated up to the optic phonon energy), since under the strong heating conditions the 2D electron gas is nondegenerate. This is independently confirmed by magnetotransport measurements. Very good theoretical description of emission experiments at pressures $P=0$ and $P=7\text{ kbar}$ is achieved with the use of bulk GaAs parameters. Theoretical estimations of the heating conditions in crossed magnetic and electric fields indicate that the electric field in our GaAs-GaAlAs structures is highly inhomogeneous.

ThP27

Resonant Magneto-Polarons in Strongly-Coupled Superlattices

F.M. Peeters*, J.M. Shi†, J.T. Devreese‡, J.P. Cheng*, B. McCombe*
and W. Schaffl

* Department of Atomkernfysica, Universiteit Antwerpen (UVA), B-2610 Antwerpen, Belgium;
† Department of Physics and Astronomy, SUNY at Buffalo, NY 14260, USA
‡ Presently at Francis Bitter National Magnet Laboratory, MIT, Cambridge, MA 02139
§ Cornell University, Ithaca, NY 14853, USA

Abstract

Inquiry bound magneto polarons are studied experimentally and theoretically in a strongly coupled Ga 1-x Al x As superlattice. The $1s \rightarrow 2p_z$ transition of well center donors is tuned through resonance with the GaAs optical phonon mode. An anti level crossing behavior and three different peaks are clearly observed at the LO phonon energy. The theoretical analysis shows that the size of the magneto polaron effects: 1) are very close to those for the bulk system, and 2) no direct evidence is found for non bulk LO phonon interaction.

1 Introduction

High magnetic field cyclotron resonance experiments are a sensitive probe to investigate: 1) the coupling strength between electrons and optical phonon modes, and 2) the frequency of the relevant optical phonons which are involved in the coupling. We use such experiments to investigate the polaron coupling in confined structures and in particular in strongly-coupled superlattices.

Recently, there has been considerable interest in polaron effects in confined structures. One of the key questions is whether or not coupling of electrons to different phonon modes like bulk phonons, confined phonons, interface phonons, etc., are observable. In previous work [1] on cyclotron resonance of free electrons in GaAs heterostructures no such coupling had to be introduced in order to explain the available experimental results. But in those experiments polaron effects were considerably weakened by many body effects like screening and the occupation effect [2]. In the case of low density impurity bound polarons no such complications are present and the system is effectively a one-particle problem.

In the present work, which is partly experimental and partly theoretical, thin-barrier superlattices are investigated. Such strongly coupled superlattices are different from the earlier quantum well system in the sense that: 1) the electron wavefunction is much extended, 2) propagating phonon modes exist when the AlGaAs barriers are thinner than about 2 nm [3], 3) large interface effects may be present, and 4) zone folding of LO phonons should occur [4].

We have carried out a far infrared photoconductivity spectroscopic study of impurity bound magnetic polarons in a $\text{GaAs}/\text{AlGaAs}$ superlattice consisting of 80Å wide wells and 9Å wide barriers and Si donors planarly doped at the center of each well. The $1s \rightarrow 2p_z$ transition was tuned through the resonant interaction region with GaAs optical phonons by magnetic fields up to 21T. An anti level crossing behavior has been clearly observed at the energy of the GaAs LO phonon. Several different peaks are identified in the spectrum. This is the first study of a $\text{GaAs}/\text{AlGaAs}$ superlattice in which the lower branch can be traced into the reststrahlen band, in contrast to the case of isolated quantum wells (QWs), where the transition vanishes at much lower energies.

A detailed theoretical analysis is made of the experimental results. Effects like 1) tunneling of the bound electron into the adjacent wells, 2) band non-parabolicity, and 3) the coupling of the electron with bulk LO phonon modes are included in the calculation. Good agreement is obtained with the experimental results.

2 Experiment

The sample used was a $\text{GaAs}/\text{AlGaAs}$ superlattice grown by molecular beam epitaxy (MBE). It consists of 40 periods of 80Å GaAs wells separated by 9Å AlGaAs barriers. The wells were planar doped with Si donors at the center with a concentration of 10^{19}cm^{-3} . The superlattice structure was sandwiched between two thick ($\sim 2000\text{Å}$) AlGaAs cladding layers, and the whole structure was grown on a GaAs buffer layer on top of a semi-insulating GaAs substrate and capped by a $\sim 100\text{Å}$ thick GaAs layer.

A capacitively coupled photoconductivity technique was used to enhance the signal to ratio and to reduce the dielectric effects near the reststrahlen band region in comparison to normal transmission measurements. In this technique two semitransparent chromium electrodes separated by a small gap were evaporated on the top surface of the sample. A low frequency ($\sim 100\text{Hz}$) ac voltage was applied to the two electrodes coupled capacitively to the resistively conducting superlattice planes, and the ac current through the sample was detected with a current sensitive preamplifier / lock in amplifier. Far infrared magnetic optical spectra were obtained in a 9T superconducting magnet (Boulder or a 21T Bruker magnet) from the latter National Magnet Laboratory using Fourier transform spectrometers. All data presented in this paper were taken at liquid helium temperatures in the Faraday geometry (magnetic field parallel to the propagation direction of FIR light and normal to the sample surface).

Results. Photoconductance spectra of the impurity $1s \rightarrow 2p_z$ transition are shown in Fig. 1 near the resonant polariton region for several magnetic fields. At low magnetic fields the $1s \rightarrow 2p_z$ transition is a sharp anti-symmetric line, and it moves to higher energies with increasing magnetic field. At about 15T a new line appears around the GaAs LO phonon energy ($\sim 29\text{meV}$ at low temperatures) which is the upper branch of the resonant process. It increases in relative intensity and moves to higher energies as the field increases. Meanwhile the lower branch loses intensity and nearly disappears as it approaches the GaAs LO phonon (25meV at $x=0$ see the 19T spectrum). At slightly higher fields it reappears inside the reststrahlen band and finally vanishes at the highest magnetic fields. In the highest field region an additional transition at about $110 \rightarrow 120\text{meV}$ growing in intensity with increasing magnetic field is clearly visible. This line is attributed to the mixing of the $2p_z$ state with the virtual $(2p_z + \text{one LO phonon})$ state through the electron LO phonon

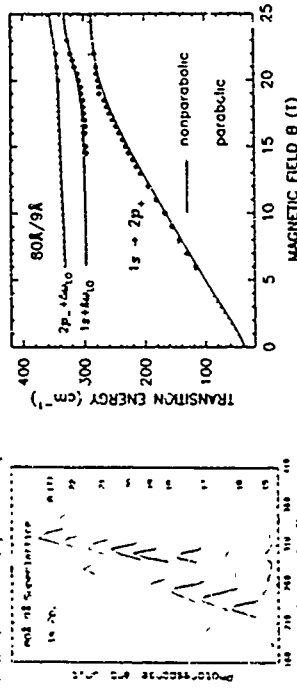


FIG. 1. Photoconductivity spectra at several magnetic fields.

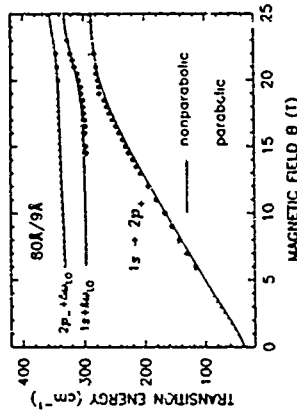


FIG. 2. Transition energy as function of magnetic field. The solid dots are experimental data and the curves are the results from a variational calculation of magnetic polaron effects for shallow impurities with (solid curves) and without (dotted curves) inclusion of band nonparabolicity.

interaction.

In Fig. 2 we display the magnetic field dependence of the impurity transition energy (dots), and compare the results with the theoretical calculations (curves). In the non-resonant field region, (low fields), the $1s \rightarrow 2p_z$ transition for this sample shows a slightly smaller slope (hence larger CR mass) as a function of magnetic field as compared to bulk GaAs [5] or MQW structures [6] due to the finite probability of the electrons being inside the barrier [7]. In the resonant magnetic field region the lower branch shows a clear sublinear behavior as it approaches the resonance condition, $E(2p_z) = E(1s) + \hbar\omega_{LO}$, and it can be traced into the reststrahlen band, in contrast to the case of isolated QWs [6], where the transition vanishes at much lower energies. Typical anti-level crossing behavior has been observed in this field region with three branches separated by two resonant interaction gaps involving the $2p_z$ state interacting with the $(1s + \text{one-phonon})$ state (the so-called two-level resonance) and the $(2p_z + \text{one-phonon})$ state (three-level resonance), respectively.

3 Theory

In the present system of a strongly coupled superlattice it is no longer possible to approximate the system by a single quantum well [8]. In previous work we found that even for relative thick barriers (e.g. a 100 Å AlGaAs superlattice) the corrections due to the tunneling of the electron to the barrier walls leads to observable corrections in the transition energies. The first step in our calculation is to find the energies of the lowest lying electron states of a hollow donor at the center of the quantum well. It is strongly interacting superlattice placed in a magnetic field directed perpendicular to the interface. This system is described by the Hamiltonian

$$H = \frac{p^2}{2m} + V(r) + \frac{1}{2} \mu_B B^2 + \frac{1}{2} \mu_B B^2 + \dots \quad (1)$$

where we exploited the cylindrical symmetry of the problem by using the polar coordinates (ρ, ϕ, z) , with the z direction chosen along the magnetic field. We use the following units: 1) the effective Bohr radius $a_B^* \equiv \hbar^2/m_e^*e^2 \approx 100 \text{ \AA}$ for the length with $m_e^* \approx 12.75$ the static dielectric constant and $m_e^*/m \approx 0.067$ the electron band mass of GaAs; 2) the electron charge and m , the electron mass in vacuum; 3) the effective Rydberg $R^* \equiv e^2/2a_B^* \approx 15.24 \text{ meV}$ for the energy and 4) $\gamma \equiv \hbar\omega/2m_e^*e^2 \approx 0.151/\hbar$ is a dimensionless measure for the strength of the magnetic field $L = -i\hbar\partial/\partial\phi$ is the component of the angular momentum operator in units of \hbar which is still a good quantum number in the present system. The superlattice potential is modelled by a series of square well potentials of height V_0 with barrier width b and well width a . The barriers are made out of the material $\text{Al}_x\text{Ga}_{1-x}\text{As}$ which has $V_0 = 0.691x \times 0.22 \text{ eV}$ (in eV) and $m_e^* = 0.067 + 0.081x$. The Schrödinger equation corresponding to the Hamiltonian (1) cannot be solved exactly and therefore we relied on a variational calculation of the donor states with the trial wave functions given by

$$\psi_{\pm} = \psi_0 \exp(-\zeta_0 \rho) \exp(\pm i\gamma\phi) \exp(-\zeta_z z) \quad (2)$$

where ψ_0 is the lowest energy solution in the absence of the magnetic field and the Coulomb potential ζ_0, γ are two variational parameters which are chosen in such a way that they minimize the unperturbed energy of the s state of the donor $E_s^0 = \langle \psi_0 | H^0 | \psi_0 \rangle$.

The results of such a calculation are given in Table I for the binding energy in units of R^* of the $1s$ and $2p$ states and the $1s \rightarrow 2p$ transition energy at $B = 0$. We compare the results of the present system under study (80-9A) of a strongly coupled superlattice, 2) a weakly coupled superlattice (100-100A), 3) a broad multi quantum well structure (150/125A), and 4) the bulk system. Notice that the results of the present system are very close to those of the bulk, while the two other cases have an appreciable larger Coulomb energy which is a result of the strongly confinement of the donor states to quasi two dimensions.

TABLE I Binding energy of a shallow donor for a parabolic band at $B = 0$ and in the absence of electron-phonon interaction

state	80A/9A	100A/100A	450A/125A	30
1s	1.0521	1.1111	1.2312	1.01946
2p	0.2551	0.3596	0.4257	0.25603
$1s \rightarrow 2p$	0.7970	1.1581	0.9656	0.7500

Since GaAs is a weakly polar material, the polaron correction to the energy of the s state of the donor can be calculated within second order perturbation theory

$$\Delta E = - \sum_{\vec{k}} \sum_{\vec{q}} \frac{1}{\hbar\omega_{\vec{k}}} \frac{1}{\hbar\omega_{\vec{q}}} \frac{1}{\hbar\omega_{\vec{k}+\vec{q}}} \frac{1}{\hbar\omega_{\vec{k}}} \frac{1}{\hbar\omega_{\vec{q}}} \frac{1}{\hbar\omega_{\vec{k}+\vec{q}}} \quad (3)$$

where $H_{\vec{k}\vec{q}}^0$ is the Frohlich electron-LO phonon interaction Hamiltonian given by

$$H_{\vec{k}\vec{q}}^0 = \sum_{\vec{r}} \left(\frac{1}{\hbar\omega_{\vec{k}}} \frac{1}{\hbar\omega_{\vec{q}}} \frac{1}{\hbar\omega_{\vec{k}+\vec{q}}} \frac{1}{\hbar\omega_{\vec{k}}} \frac{1}{\hbar\omega_{\vec{q}}} \frac{1}{\hbar\omega_{\vec{k}+\vec{q}}} \right) \quad (4)$$

where $H_{\vec{k}\vec{q}}^0$ is the creation (annihilation) operator of a LO phonon with wave vector \vec{q} and frequency $\omega_{\vec{q}}$. Ω is the volume of the system, $n \approx 0.067$ the dimensionless electron-phonon coupling constant. In the calculation only the 1D LO phonon modes of GaAs are included $\hbar\omega_{\vec{q}} \approx \hbar\omega_{1D} \approx 296 \text{ cm}^{-1} \approx 46.7 \text{ meV}$. In Eq (6) $\Delta E = 0$ for the non resonant states and $\Delta E_s \approx \Delta E_{2p} - \Delta E_1$ for the $2p$ state. Away from the magneto-polaron resonant region the sum over the donor states in Eq (6) converges very slowly and the incorporation of only the lowest few states is insufficient. Therefore we relied on a different method, which is described in detail in [2], in which all intermediate donor states are included in an approximate way. One outcome of such a calculation is that it is possible to prove that in the case of $m_e^* \approx m$ the polaron correction satisfies $\Delta E_s/\hbar\omega_{1D} \leq -0.1$.

The results of such a calculation are given in Fig. 3a where we depict the polaron correction to the $1s$ and the $2p$ states for the present system (solid curves) and compare them with the results for the 3D system. Notice that the polaron correction to the $1s$ state is slightly larger for the strongly coupled superlattice while the one for the $2p$ state is almost the same as for the bulk case. The resulting polaron correction to the transition energy is given in Fig. 3b. Notice that for small magnetic fields ($B < 10-15 \text{ T}$) the polaron correction is very small and slightly positive, i.e. it increases the transition energy. Near the resonance region ($15 < B < 150 \text{ T}$) the amplitude of the polaron correction decreases appreciably the transition energy. Notice that for the strongly coupled superlattice the result for the polaron correction to the transition energy is very close to the one for the bulk case. Only for the weakly coupled superlattice (100/100A) we find that the polaron correction is appreciable different from the 3D situation.

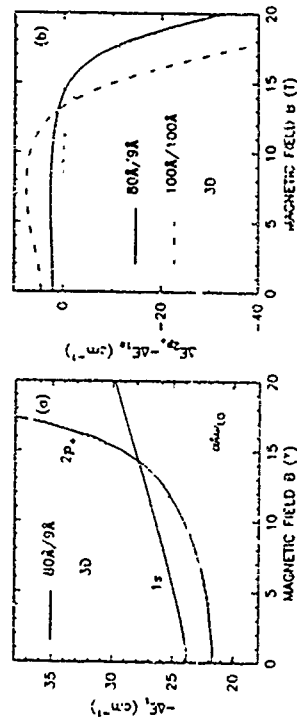


FIG. 3 Polaron correction (eV) to the $1s$ and $2p$ states and (b) to the transition energy $1s \rightarrow 2p$ for different systems.

Before we are able to compare our theoretical results with experiments we must include another correction: band nonparabolicity. We use the standard Kane model, which was successfully applied to GaAs, the nonparabolicity in GaAs: $E_c = E_g/2[1 - 1 - \sqrt{1 + 4(E_c - E_g)/E_g}]$ where E_c and E_g are the band energies with and without the effect of band nonparabolicity is respectively. $E_g = 1.52 \text{ eV}$ is the energy gap of GaAs.

4 Comparison and conclusions

In Fig. 2 the present theoretical results for the $1s \rightarrow 2p_x$ transition (solid curves) are compared to the present experimental results (solid dots) for donors located at the center of the wells of a $(GaAs/Alb)$ superlattice with $w = 80 \text{ \AA}$ and $b = 9 \text{ \AA}$. The dotted curves are the theoretical results where the effect of band nonparabolicity is excluded. Near resonance the polarization correction and the correction due to band nonparabolicity are largest. There the energy difference $E_{1s} - E_{2p_x}$ is relevant, which is appreciably large and this implies that the two different corrections to the energy of the $1s$ and to the $2p_x$ state are different and thus do not cancel.

The agreement between experiment and theory is very good. Nevertheless there are two small discrepancies: 1) below the LO phonon energy the experimental results are between the results with (solid curve) and without (dotted curve) band nonparabolicity. This may indicate that the effect of band nonparabolicity is slightly overestimated; 2) the gap at the anti-crossing point is theoretically slightly overestimated as compared to experiment. Nevertheless one should keep in mind that in this energy region one is in the reststrahlen band of $GaAs$ and that radiation is strongly absorbed by the lattice.

Acknowledgments: The high magnetic field measurements were carried out at the Francis Bitter National Magnet Laboratory; we thank all staff, especially B. Brant and L. Rubin for assistance.

JPC and BDM thank the Office of Naval Research for support under Grant No. N00014-89-J-1671. One of us (FMP) is supported by the Belgian National Science Foundation and part of the theoretical work is supported by "Dienst van de Programmatie van het Wetenschappelijk" under contract No. IT/SC/21.

References

1. F.M. Peeters, N.G. Wu, J.T. Devreese, C.J.G.M. Langerak, J. Singleton, D.J. Barnes and R.J. Nicholas, *Phys. Rev. B* **45**, 4296 (1992).
2. J.M. Shi, F.M. Peeters and J.T. Devreese, *Phys. Rev. B* **45**, 1303 (1992).
3. D.-S. Kim, V. Bouhalkha, J.M. Jacob, J.F. Zhou, J.J. Song, and J.F. Klem, *Phys. Rev. Lett.* **68**, 1002 (1992).
4. A.K. Sood, J. Menéndez, and M. Cardona, *Phys. Rev. Lett.* **54**, 2115 (1985).
5. J.-P. Cheng, B.D. McCumber, and G. Rozak, *Phys. Rev. B* **43**, 9124 (1991), and *Surf. Science* **267**, 185 (1992).
6. J.-P. Cheng, B.D. McCumber, J.M. Shi, F.M. Peeters, and J.T. Devreese, *Phys. Rev. B* **48** (1993).
7. G. Rozak et al., *Phys. Rev. Lett.* **64**, 471 (1990); M.J. Yang et al., *Phys. Rev. B* **47**, 1691 (1993).
8. M. Helmi, F.M. Peeters, F. DeRosa, E. Colan, J.P. Harbison, and L.T. Fiza, *Phys. Rev. B* **43**, 1584 (1991), *Surf. Sci.* **238**, 518 (1992).

Far infrared response of quantum dots: from few electron excitations to magnetoplasmons

D. Pfannkuche¹, Vidar Gudmundsson², P. Hawrylak³, R.B. Gerhardt¹

¹ Max-Planck-Institut für Festkörperforschung, Heisenbergstr.1, 70568 Stuttgart 40, Germany.

² Science Institute, University of Iceland, Dunhaga 3, IS-107 Reykjavik, Iceland.

³ Institute for Microstructural Sciences, National Research Council of Canada, Ottawa, K1A 0R6, Canada

(July 1, 1993)

We study the far infrared (FIR) response of quantum dots with a variable number N_e of electrons and a non-parabolic confinement in a magnetic field B . For few electrons we compare the results of a Hartree (HF) and a Hartree-Fock (HF) approach with those obtained by an exact diagonalization of the few-particle Hamiltonian. A good qualitative agreement is found between the HF approximation and the exact calculation. The resonance spectra are fingerprints of the ground state of the electron system and depend therefore strongly on N_e and B . With an increasing number of electrons, the HF- and the HF-calculations show new features evolving in the FIR spectra. These features resemble the non-local mode coupling effects observed in the magnetoplasmon dispersion of two- and one-dimensional systems marking the transition to a quasi-classical hydrodynamic behaviour.

1. INTRODUCTION

The experimental study of quantum dots is proceeding rapidly [1-5], often producing FIR spectra differing from the simple spectrum predicted by Kohn's theorem for harmonically confined electrons [6-9]. The simple spectrum for parabolically confined electrons can be obtained analytically due to the decoupling of the center of mass (CM) and relative motion (RM). In order to understand the more complex spectra it is therefore important to have reliable methods to calculate the properties of electrons in quantum dots where the CM and RM excitations couple and simple analytical calculations cannot be performed. Recently, for few electrons, an 'exact' numerical diagonalization [6,10-15] has been performed and for many electrons a H-approximation has been used [7,16,17]. A comparison between the results of an exact numerical diagonalization and those of a H- and a HF-approximation has established that exchange and correlation effects are of great importance for the ground state properties when the electrons are not spin polarized [18].

In the present work the FIR spectra obtained in the HF-approximation are compared to the spectra from the exact diagonalization and the H-approximation. In the light of the good qualitative agreement between the models, the HF- and H-approximation are used to investigate the evolution of the spectra with increasing number of electrons.

II. MODELS

N_e Electrons in a quantum dot are described by the Hamiltonian

$$H = \sum_{i=1}^{N_e} \left[\frac{1}{2m^*} \left(\vec{p}_i + \frac{e}{c} \vec{A}(\vec{r}_i) \right)^2 + V_{cm}(\vec{r}_i) + \frac{e^2 \mu_B}{\hbar} \vec{B} \cdot \vec{S}_i \right] + \sum_{i < j} \frac{e^2}{4\pi\epsilon_0 |\vec{r}_i - \vec{r}_j|}$$

$$= \sum_{i=1}^N H(i) + \sum_{i,j} \frac{q^2}{r_{ij}} \quad (1)$$

The confining potential $V_{conf}(r)$ is composed of a harmonic part and an anharmonic one proportional to r^4 , $V_{conf}(r) = \frac{1}{2} m \Omega^2 r^2 + b r^4$, and we assume the electrons to be strictly confined to the plane perpendicular to the magnetic field B . The Coulomb interaction between the electrons is modified by the dielectric constant ϵ of the material, m^* and g^* denote the bulk effective mass and g factor, respectively. The vector potential \vec{A} is chosen in the symmetric gauge, $\vec{A} = \frac{1}{2} \vec{B} \times \vec{r}$. According to the rotational symmetry the eigenfunctions $|\Theta\rangle$ of the system

$$H(\Theta) = \epsilon_z |\Theta\rangle. \quad (2)$$

can be classified by the total angular momentum $L = \hbar M = \hbar \sum_i m_i$, the total spin S , the spin component parallel to the magnetic field, S_z , and an energy quantum number which labels the eigenstates so for given M , S , and S_z in ascending order, i.e. the ground state for fixed M , S , and S_z is labeled by $(\Theta) = (M, S, S_z; 0)$.

FIR radiation incident on a quantum dot (in the regime where linear response holds) induces transitions between the ground state and excited states, if the FIR frequency corresponds to the energy difference between those states. The oscillator strength f_{Θ} , given by

$$f_{\Theta} = \frac{2m^*}{\hbar} (\epsilon_0 - \epsilon_\infty) |\langle \Theta | H^{int} | \epsilon_\infty | \Theta \rangle|^2, \quad (3)$$

is a measure for the likelihood of this transition. (In this equation $|\Theta\rangle$ denotes the ground state and H^{int} is the interaction Hamiltonian of the FIR field \vec{E}^{int} with the electron system.)

For two and three electrons we calculated the few-particle energy spectra and wave functions by diagonalizing the Hamiltonian matrix numerically [12,13,19]. Due to the small size of the quantum dots (< 300 nm) the FIR radiation field is spatially constant throughout a single dot. Therefore, it only couples to the center-of-mass (CM) motion of the electrons,

$$H^{int} = \sum_{i=1}^N e \vec{E}^{int} \cdot \vec{r}_{i,CM} = e N_e \vec{E}^{int} \cdot \vec{r}_{CM}, \quad (4)$$

where \vec{r}_{CM} is the CM coordinate.

Out of the rich spectrum only those transitions are excited which occur between states with non-vanishing overlap of the internal (relative) wave functions. In a strictly parabolic quantum dot (where the wave functions factorize into the CM part and the relative wavefunction [10,20,21]) only two transitions are allowed. The corresponding resonance frequencies are given by $\omega_0 = \sqrt{4\Omega^2 + \omega_c^2} \pm \omega_c/2$, regardless of the number of electrons in the dot and their mutual interaction (Kohn's theorem). ω_c is the cyclotron resonance frequency. However, even a small anharmonicity allows the coupling to the internal degrees of freedom and additional resonances can be observed [13].

In the HF approximation the interacting many-body problem is reduced to a problem of non-interacting particles subjected to an effective external potential. The HF single particle states $|\alpha\rangle$ together with their eigenenergies ϵ_α are found by iterating the HF equations [18] in the basis of the non-interacting states $|\alpha\rangle$ (the eigenstates of H in (1)). The total energy of the system E can then be found by summing up the single electron contributions and carefully counting the interaction energy of each electron pair only once [18].

The FIR absorption of the system is calculated as a self-consistent linear response to an external potential ϕ^{ext} . In this so-called time-dependent HF approximation the change of the density matrix due to an adiabatically switched total electrostatic potential ϕ^{tot} is calculated within a linear approximation. The total potential consists of the external potential and the induced potential $\phi^{ind} = \phi^H + \phi^P$ due to the direct and the exchange interaction of the electrons. The induced potential in turn depends on the density matrix, thus closing the circle and allowing for a self-consistent evaluation of the total potential together with an expression for the frequency dependent dielectric tensor $\epsilon_{\alpha\beta\gamma}(\omega)$. The power absorption is then calculated from the Joule heating of the system due to ϕ^{tot}

$$P(\omega) = e E^{ext} \sum_{\alpha\beta} \frac{(\vec{E}_\alpha - \vec{E}_\beta)}{\hbar} \langle \beta | \vec{r} | \alpha \rangle 2 \pi \delta \epsilon_{\alpha\beta}(\omega) \ln \left\{ \frac{\Gamma^0(\omega) |\alpha\rangle \langle \alpha| (-e \phi^{ext}) | \beta \rangle}{\Gamma^0(\omega) |\beta\rangle \langle \beta| (-e \phi^{ext}) | \alpha \rangle} \right\}, \quad (5)$$

where E^{ext} is the strength of the external field and

$$\Gamma^0(\omega) = \frac{1}{\hbar} \left\{ \frac{\Gamma_0 - \beta}{\omega + (\omega_0 - \omega) + i\eta} \right\} \quad (6)$$

with the Fermi distribution Γ^0 , $N_e = \pm 1$ corresponds to left or right circular polarization ω_0 , β . The HF calculations are done for the temperature $T = 1.0$ K, but since the ratio of the thermal and the confinement energy is very small the results can be compared with the exact calculations for $T = 0$ K.

III. FIR RESPONSE OF FEW ELECTRONS

For quantum dots with two and three electrons we calculated the FIR response within the diagonalization approach as well as in the HF approximation. The results for quantum dot helium are shown in Fig. 1. Lines mark the Hartree and HF results, and symbols mark those obtained by the 'exact' method. Within the shown magnetic field range, the ground state changes from the spin-singlet state $|0, 0, 0\rangle$ for low magnetic fields ($B < 2.6$ T) to the spin-triplet state $|1, 1, 1; 0\rangle$ for higher magnetic fields. The figure shows the FIR resonances from both initial states within the whole magnetic field range. The upper resonance in the spin-triplet state is split due to the non-parabolicity [13]. The HF approximation reproduces this line splitting as well as the resonance position to a very high accuracy. This is in accordance with the good agreement between the HF and the exact ground state in the spin-triplet state for two electrons [18]. More remarkable is the coincidence of the results for the spin-singlet state. Here the HF ground state deviates strongly from the exact one [18] due to correlations which are important in this state. Nevertheless, the FIR resonances agree very well in both approaches. The two models predict different values for the magnetic field where the spin-singlet spin-triplet transition occurs. Accordingly, the HF approximation predicts the splitting of the upper resonance for $B > 0.67$ instead of $B > 2.6$ T.

The resonances calculated in the Hartree approximation do not show the line splitting of the upper many-body level. However, they are blueshifted with respect to the spin-singlet resonance. A similar blueshift appears for the lower spin-triplet mode with respect to the spin-singlet resonance. This is a consequence of the larger spatial extent of the spin-triplet states which leads to a stronger influence of the r^{-4} potential. Accounting for this blueshift by an effective confining frequency Ω , which depends on the strength of the confining frequency as well as the actual ground state

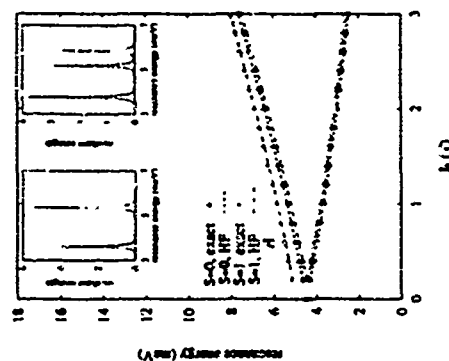


FIG. 1. FIR resonances as function of the magnetic field for a dot occupied by two electrons. Resonances are shown for the spin-singlet state $[0,0,0;0]$ (which is the ground state for $0T < B < 2.6T$) and the spin-triplet state $[-1,1,1;0]$. Symbols and solid lines mark results of the diagonalization approach. HF results are shown as dashed ($S=0$) and dash-dotted ($S=1$) lines, and dotted lines refer to Hartree results. Left inset: oscillator strength of the spin-singlet transition. The exact and HF results are nearly indistinguishable. Right inset: oscillator strength of spin-triplet transitions. Parameters: $M_0 = 3.37\text{meV}$, $\delta = 2.5 \times 10^{-10}\text{meV/\AA}^4$, GaAs bulk parameters: $m^* = 0.069m_0$, $\epsilon = 12.4$, $g^* = -0.44$.

wave function, the resonances can even in the presence of the anharmonicity be well described by $2\omega_{1,0} = \sqrt{6\Omega^2 + \omega_0^2} \pm \omega_0$, i.e., Ω replaces the bare confining frequency Ω_0 .

The resonance patterns for three electrons (Fig. 2 and Fig. 3) show even more clearly that the FIR excitation spectra for few electrons are fingerprints of the actual ground state of the quantum dot. The resonances of the spin-doublet ground state $[-1, \frac{1}{2}, \frac{1}{2}; 0]$ (Fig. 2) resemble those of the 2-electron triplet state $[-1, 1, 1; 0]$. The HF approximation yields a single lower mode and two upper modes with nearly the same oscillator strength. As for two electrons, the ω_0 resonance splits due to the coupling of the CM excitation to a R3F excitation which in the harmonic potential has the same energy. This line splitting which is due to an internal symmetry of the system is equally well described in the HF and the 'exact' treatment. The exact approach shows a weak additional resonance below these modes, which also appears in the H-approximation. This additional mode is due to ground state contributions (linear combinations of Slater determinants) which are not allowed in the HF ansatz. This witness the existence of ground state correlations which are strong

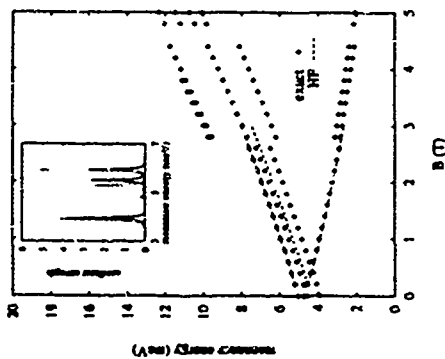


FIG. 2. FIR resonances as function of the magnetic field for a dot occupied by three electrons. Resonances are shown for spin-doublet transitions from $[-1, \frac{1}{2}, \frac{1}{2}; 0]$ ($B < 2.6T$) and $[-2, \frac{1}{2}, \frac{1}{2}; 0]$. Inset: corresponding oscillator strengths in exact (solid line), HF (dashed), and H approach (dotted). Parameters as in Fig. 1.

in the non-spin polarized states.

At $B = 2.6T$ the ground state changes to the spin-doublet $[-2, \frac{1}{2}, \frac{1}{2}; 0]$ which cannot be found in the HF approximation. Here, a small splitting of the lower mode appears, while the upper one is single. The upper resonance shows very weak satellites. These additional resonances occur due to the mixing of CM and relative wave functions in the r^4 -potential. It becomes the more important the more the electrons feel the steeper (than harmonic) confining potential in states with higher angular momentum.

For even higher magnetic fields ($B > 3.5T$) the 3-particle ground state is the spin-quartet state $[-3, \frac{3}{2}, \frac{3}{2}; 0]$ (Fig. 3). It clearly shows two upper resonances which in the HF approximation have similar oscillator strengths. The origin of these two modes is not a line splitting, but the strong mixing of different CM and internal wave functions in the ground state. These distinct contributions are differently affected by the r^4 -potential giving rise to distinct frequencies Ω . Due to correlations effects the different contributions to the ground (and excited states) have different weight in the diagonalization and HF results. This is most obvious from the differences in the oscillator strengths of the corresponding resonances which are much more sensitive to the actual wavefunctions involved than the resonance positions

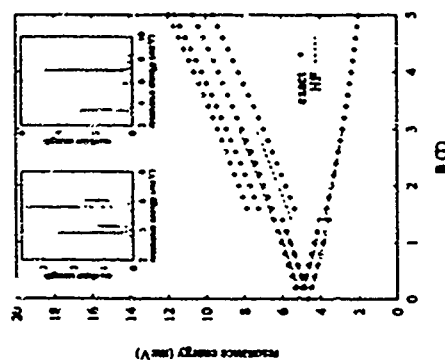


FIG. 3. FIR resonances as a function of the magnetic field for a dot occupied by three electrons. Resonances are shown for spin-quartet transitions from $|0, \frac{3}{2}, \frac{3}{2}, 0\rangle$ ($B < 1.6$ T) and $|1, -3, \frac{3}{2}, 0\rangle$ ($B > 1.6$ T). Left inset: oscillator strength at $B = 1$ T ($M = 0$), right inset: oscillator strength at $B = 2$ T ($M = -3$).

IV. FIR RESPONSE OF MANY ELECTRONS

In 2D electron systems, quantum wires [22], and dots [23] a splitting of the plasmon dispersion curve (or the upper excitation branch, $\omega_+(B)$ in quantum dots) has often been observed when the frequency $\omega_+(B) < \Delta$, i.e., $2\omega_+$ -splitting. In contrast to the anticrossing caused by deviations from circular symmetry [23], this line splitting is independent of the form of the dots. Instead it shows a strong dependence on the number of electrons in the system, becoming clearer the more electrons occupy the dot. It has not been observed in small dots with few electrons ($N_e \sim 1-10$). Theoretically, the coupling to the second harmonic of the cyclotron frequency has been predicted for a 2DEG when the interaction between the electrons and the electromagnetic field is considered to a higher order than in the dipole approximation, thus being called a non-local correction [24]. The $2\omega_+$ -splitting has also been found in a Hartree-calculation (H-calculation) for many electrons in a quantum dot [17], where the confinement of the 2DEG causes modes with different wave vectors to be mixed and the ω_+ -oscillation from the parabolic confinement makes these mode crossings visible.

Since this mode coupling appears only for a high number of electrons and in larger systems, it can best be described in terms of magnetoplasmons rather than by excitations of a specific quantum dot atom. Therefore, this spectral feature is expected to be adequately treated by a mean field

theory such as the H and the HF approximation, especially since even for few-particle systems the time-dependent HF-method qualitatively well reproduces the main FIR resonances. Accordingly, the H and HF calculations show no $2\omega_+$ -splitting (for the used confinement of $\Omega_0 = 3.37$ meV) for less than ten electrons, but the first sign of it develops for $N_e = 10$ and the splitting is almost complete for $N_e = 16$ as is seen in Fig. 4. This is accompanied by the density of electrons $n_e(r)$

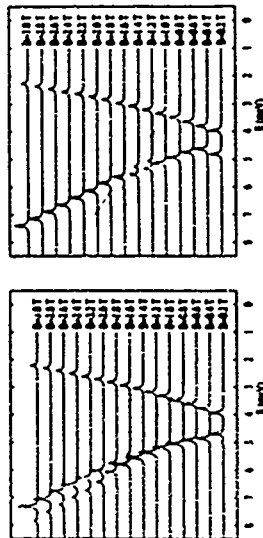


FIG. 4. The absorption $P(h\nu)$ as a function of the magnetic field B in the H-approximation with $N_e = 16$ (left figure), and in the HF-approximation with $N_e = 20$ (right figure). The dashed lines represent the energy $2h\nu_+$. $\hbar\Omega_0 = 3.37$ meV, $\phi = 30 \times 10^{-13}$ meV/Å², $m^* = 0.067m_0$, $\epsilon = 12.4$, $\eta^* = -0.44$, $\eta = 0.01A\Omega_0$, and $V = 1.0$ K.

becoming homogeneous within a region larger than the effective magnetic length $[16] \lambda$ inside the dot. We, therefore, believe the splitting to indicate a transition from a 0DEG to a confined 2DEG. In contrast to the infinite 2DEG, where the mode coupling to the second harmonic of the cyclotron resonance is due to deviations from a constant external electric field, in the confined 2DEG it is caused by the anharmonicity of the confining potential. For few electrons a region with homogeneous density can never develop as the dot diameter is of the order of λ , thus inhibiting the pronounced occurrence of the $2\omega_+$ -splitting. Nevertheless, we found a precursor of this feature in a wide dot with a strongly anharmonic confinement occupied by three electrons only.

An analysis of the participating single electron transitions for the two peaks occurring for $N_e = 16$ at $B = 1.6$ T shows that the lower one represents the normal stiff oscillations of the mass center predicted by Kohn's theorem, while the upper peak includes only transitions of electrons in states with high values of M . This reflects the characteristics of a radial mode which affects only the relative coordinates of the electrons (breathing mode). The mutual Coulomb interaction of the electrons is essential for the occurrence of the $2\omega_+$ splitting. Without the interaction the $2\omega_+$ -anharmonicity causes the $\omega_+(B)$ branches to be split into many parallel lying modes without any crossings. Changes in the ground state can be observed when $\omega = 2\omega_+$, as well as for other values of the magnetic field. These changes manifest themselves as a change in the number of parallel resonance lines.

A careful evaluation of the H-approximation for different strengths of the anharmonic part

of the confinement shows that the occurrence of the splitting can deviate slightly from the field where $\omega_1(B) = 2\omega_2$, just as has been observed in experiments. The $2\omega_2$ splitting is independent of the exact form of the deviation from the parabolic confinement, it occurs for ρ^2 as well as for ρ^4 deviations over a wide range of strength of the anharmonicity.

The HF calculation also shows this $2\omega_2$ splitting when N_2 increases, however, since $\omega_1(r)$ does never develop a totally flat region, but maintains small modulations, the splitting is never as clear as in the II approximation (see Fig. 1).

V. SUMMARY

Anharmonicities in the confinement potential introduce features in the FIR resonance spectra of quantum dots which cannot be explained by pure excitations of the CM of the electron system, i.e. deviations from Kohn's theorem arise. While the magnetodispersion $\omega(B)$ of the modes can still be described by a formula of the type $\omega(B) = (\sqrt{10})^2 + \omega^2 \approx \omega^2/2$, the effective confining frequency Ω_c is no longer given by the bare confining frequency, but strongly depends on the number of particles, the Coulomb interaction, and the strength of the anharmonicity. Moreover, beside the pure CM excitations, which are the only ones to occur in parabolically confined quantum dots, additional modes appear: due to a mode coupling between the CM excitations and those of the internal (relative) degrees of freedom.

The few particle spectra not only differ for dots occupied by different numbers of electrons, but are also fingerprints of the actual ground state which changes with increasing magnetic field. We compared the few particle resonances obtained by diagonalizing the Hamiltonian matrix and by a time-dependent HF approach. Even though the ground states calculated by both methods differ considerably, the FIR resonance positions agree very well. Differences, of course, appear in the results for the oscillator strength of the resonances, since this quantity is much more sensitive to the features of the initial and final wave functions.

For quantum dots with many particles (more than 10) the fine structure of the resonance spectra, reflecting transitions which are unique for the actual quantum dot atom, vanishes. Simultaneously, the anticrossing of the upper CM resonance, ω_+ , with another non-dipole active mode appears, when $\omega_+ \approx 2\omega_2$. The crossing mode is an excitation of the internal degrees of freedom only (breathing mode). Its occurrence is coupled to the existence of a mesoscopic region with homogeneous particle density inside the dot. Since the mode coupling does not occur for a non-interacting electron system, we consider this mode to be the dot-analogue of the non local resonance in pure two-dimensional systems.

ACKNOWLEDGMENTS

We would like to thank D. Hellmann, P. Grambow, E. Vasiladon, and B. Meurer for fruitful discussions about experimentally observed FIR spectra on various quantum dots. Two of us (D.P. and V.G.) very much appreciate the intense and instructive discussions with A.H. MacDonald about the origin of the $2\omega_2$ mode.

This research was supported in part by the Icelandic Natural Science Foundation and the Bundesministerium für Forschung und Technologie under contract number FK0373/2 as well as a NATO Collaborative Research Grant (RG921201).

- [1] C. Sikorski and U. Merkt, Phys. Rev. Lett. **62**, 2164 (1989).
- [2] T. Demel, D. Hellmann, P. Grambow, and K. Ploog, Phys. Rev. Lett. **64**, 788 (1990).
- [3] A. Lori, J. Koithaus, and K. Ploog, Phys. Rev. Lett. **64**, 2339 (1990).
- [4] B. Meurer, D. Hellmann, and K. Ploog, Phys. Rev. Lett. **68**, 1371 (1992).
- [5] J. Altmeyer, E. Datz, and J. Koithaus, Phys. Rev. B **41**, 1639 (1990).
- [6] P. Makym and T. Chakraborty, Phys. Rev. Lett. **66**, 108 (1990).
- [7] D. Brodjo, K. Kempa, and P. Bakshi, Phys. Rev. B **42**, 11400 (1990).
- [8] L. Brev, N. Johnson, and B. Halperin, Phys. Rev. B **40**, 10617 (1989).
- [9] W. Kohn, Phys. Rev. **123**, 1212 (1961).
- [10] U. Merkt, J. Huser, and M. Wagner, Phys. Rev. B **43**, 7320 (1991).
- [11] Q. Li et al., Phys. Rev. B **43**, 5151 (1991).
- [12] T. Chakraborty, V. Halonen, and P. Pietiläinen, Phys. Rev. B **43**, 11289 (1991).
- [13] D. Pfannkuche and R. Gerhardt, Phys. Rev. B **44**, 13132 (1991).
- [14] M. Wagner, U. Merkt, and A. Chaplik, Phys. Rev. B **46**, 1951 (1992).
- [15] P. Makym and T. Chakraborty, Phys. Rev. B **45**, 1947 (1992).
- [16] A. Kumar, S. Laux, and F. Stern, Phys. Rev. B **42**, 5166 (1990).
- [17] V. Gudmundsson and R. Gerhardt, Phys. Rev. B **43**, 12098 (1991).
- [18] D. Pfannkuche, V. Gudmundsson, and P. Makym, Phys. Rev. B **47**, 2244 (1993).
- [19] P. Bakshi, D. Brodjo, and K. Kempa, Phys. Rev. B **42**, 7410 (1990).
- [20] P. Bakshi, D. Brodjo, and K. Kempa, Phys. Rev. B **42**, 7410 (1990).
- [21] N. Johnson and M. Payne, Phys. Rev. Lett. **67**, 1157 (1991).
- [22] H. Dreier et al., Phys. Rev. Lett. to be published (1993).
- [23] B. Meurer, Ph.D. thesis, Universität Stuttgart, 1992.
- [24] N. Horing and M. Yildiz, Annals of Physics **97**, 216 (1976).

Cyclotron and intersubband resonance studies in [001] and piezoelectric [111] InAs/(Ga,In)Sb superlattices

M. Lakrimi, T.A. Vaughan, R.J. Nicholas, D.M. Symons, N.J. Mason, and P.J. Walker
*Jarrendon Laboratory, The Department of Physics, The University of Oxford, Parks Road,
 Oxford OX1 3pu, U.K.*

Abstract

Cyclotron resonance and inter subband excitation experiments have been performed on superlattices of the semimetallic, strained type II system InAs/InGaInSb . We observe simultaneously one cyclotron resonance from the 2D electrons located in the InAs and two resonances from the 2D holes in the (Ga)InSb layers. The two hole resonances originate from the $M_1 = 1/2 \uparrow$ state. We have found a strong crystallographic anisotropy in the hole masses between structures grown along [001] and [111A] orientations attributed to strain decoupling of the heavy and light hole levels in the (Ga)-InSb valence band. In addition, we demonstrate for the first time that intersubband resonances can be directly seen for the electrons at large tilt angles.

1. Introduction:

The InAs/GaSb combination is a type-II crossed gap system, characterized by a semiconductor-semimetal transition when the InAs layer thickness exceeds 45 Å [1] and a small lattice mismatch of ~0.6%. In the semimetallic regime, the system contains both two-dimensional electrons in the InAs and holes in the GaSb. Further interest has arisen from growth in directions different to the conventional $\langle 001 \rangle$. Due to the lack of inversion symmetry and non-zero off-diagonal tensor strain components, [111]-oriented layered structures contain a strain-induced piezoelectric field which modifies the optical and electronic properties [2]. This has led to the observation of novel phenomena [3], such as enhanced carrier densities and optical absorption.

cyclotron resonance (CR) and resonant subband Landau level coupling (RSLLC) have been extensively studied in single carrier type systems. CR has mainly been used for the determination of the effective mass and its dependence on energy with infra red light and magnetic field applied parallel to the growth direction. RSLLC, however, is a convenient way of determining the effective subband energy separation ([4] when resonant coupling between the cyclotron and the cyclotron motion is induced by, tilting the sample with respect to the direction of the magnetic field.

Previous far infrared studies on the InAl_{0.5}Ga_{0.5}Sb system concentrated mainly on the cyclotron resonance [see Ref. [5] for a review]. While recently Sudarshan and co-workers [5] observed both the electron and hole resonances, Afsar et al. [6] mostly observed electron and interband transitions between the electrons and hole subbands along with two π - π^* transitions from two electron subbands. Tilted field experiments were initially performed by Afsar and co-workers [7]. Recently, CR studies have been extended to pulsed magnetic fields [8], thus bridging the semimetallic-semiconducting regimes.

We report on cyclotron resonance experiments performed on nine 20 period $\text{InAs}/(\text{Ga}_{0.5}\text{In}_{0.5})\text{Sb}$ superlattices grown along $[001]$ and $[111]$ orientations. First, we compare the effective masses of the carriers and then tilt the samples at large angle with respect to the direction of the magnetic field to determine the energy separation between subbands.

2. Experimental details:

The superlattices were not intentionally doped and are unintentionally grown on (001), [111]A, and [111]B oriented GaAs substrates, put side by side, at atmospheric pressure in an MOVPE reactor [9]. The indium content was varied from 0 to 10%. Thick GaSb buffer layers (at

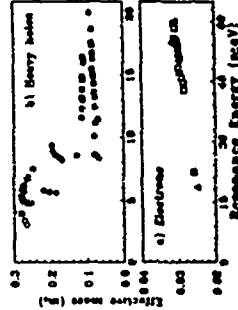


Fig. 1: Electron and hole effective masses for $[001]$ (empty symbols) and $[111]A$ (filled symbols) orientations for sample 1263 (summarized growth parameters to 1266)

states [10]. x^2-y^2 predicts that in-plane heavy hole masses in a strained quantum well, in the limit where there is a strong decoupling between the light and heavy hole bands, to be given by $m_0^2(1 + \gamma_2)^{-1}$ and $m_0^2\gamma_1 + \gamma_2)^{-1}$ for [001] and [111] orientations, respectively [11]. Conversely, the bulk in-plane heavy hole masses are given by $m_0^2(1 - \gamma_2)^{-1}$ and $m_0^2(1 - \gamma_2\gamma_1)^{-1}$ for [001] and [111], respectively [11].

[illegible]

Table 1: Measured effective masses and calculated electron (E_g) and heavy hole energy (HLL) levels along with the sample parameters for three superlattices. The superlattice period is given with the InAs thickness first. The carrier densities listed in magnetotransport data are given in units of 10^{11} cm^{-2} .

For GaSb, the Landinger parameters γ_1 , γ_2 , and γ_3 are 11.3, 3.3, and 6.5, respectively [12], giving quantum well bulk in plane masses of 0.0310, 0.2710, and 0.0310, 0.2710, for [001] and [111] orientations, respectively. In practice, such low values for the hole masses are only seen for the lowest Landau level, due to the rapid onset of level interactions with higher states. This probably leads to the dominance of the relatively heavy hole mass which is seen in the samples with higher hole densities, due to their high Fermi energy levels. It is clear, however, that the [111] oriented samples show consistently lower values for the in-plane mass. Such a difference has also been observed recently in p-type GaSb/(Ga,In)As strained quantum wells [13]. Our GaSb/(Ga,In)As structures of Ref. [13].

One further significant factor which may influence the observation of lighter hole resonances in the case of [111] is the significantly enhanced band overlap which has recently been reported for this orientation. Symons *et al* [14] have found that [111] structures have a band overlap of over 40 meV larger than [001] structures and this may lead to an enhanced decoupling.

Another complicating factor is the possible influence of magnetoplasmon effects. Das Sarma and Quinn [15] have derived an expression for the collective mode excitations for an electron-hole system. In the limit of $qL \ll 1$, where L is the period of the superlattice and q the wavevector, the coupled magnetoplasmons, of frequency ω , are given by:

$$\frac{\omega_p^2}{\omega^2 - \omega_c^2} + \frac{\omega_p^2}{\omega^2 - \omega_h^2} = 1 \quad (1)$$

where the plasmon and cyclotron frequencies are $\omega_p = \sqrt{N e^2 / (m^* \epsilon_0 \epsilon_r)}$ and $\omega_c = eB/m^*$, respectively. The index i refers to electrons or holes. We have calculated the magnetoplasmon resonances with the electron mass and with the light heavy hole mass and the heavy mass separately and these plasmon branches are plotted in figure 3. It is clear that the observed electron transitions at least are not associated with plasmons and by inference this is also true for the holes.

4. Resonant subband Landau level coupling:

We have used tilted field experiments to study the resonant subband Landau level coupling (RSLC). Given that the energy range between 230 and 320 cm^{-1} is inaccessible due to the GaAs and GaSb transition bands, sample 1266 (for samples with similar growth parameters) was best suited for the RSLC experiment. This sample and others were measured at a tilt angle of 0, 10, 30, and 60 degrees with respect to the magnetic field and light propagation directions. Figure 2 shows typical experimental spectra at 60 degrees.

Figure 3 shows the data for sample 1266 for both orientations at 0, 10, and 60 degrees plotted against the perpendicular component of the magnetic field. There are two groups of different resonances: three low energy resonances following a $B \cos \theta$ dependence and high energy resonances at around 100 cm^{-1} which become stronger on tilting.

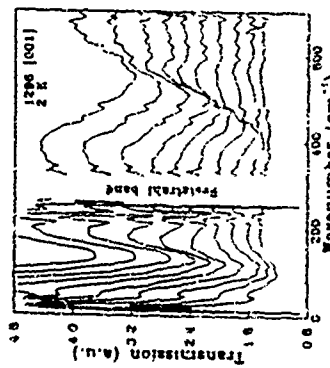


Fig. 3: Transmission spectra for sample 1266 [001] oriented against the zero field spectrum at a tilt angle of 60 degrees. The magnetic field is decreased in 1 T steps from 11 T (top trace).

The three resonances that are shown to obey the well-established $B \cos \theta$ dependence for two-dimensional systems at low energies originate from the low energy branches of the CB: one from the 2D electrons and the other two from the 2D holes. As the tilt angle increases they show increasingly strong subband coupling, pushing the lower branch of the electron resonance down in energy.

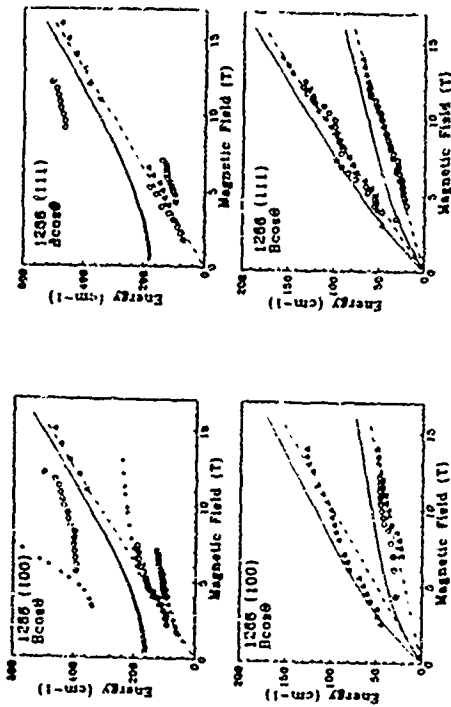


Fig. 3: Plot of the observed resonances at 0 (Δ), 30 (○), and 60 (□) degree angles for both 1266 [001] and [111]A. The dashed lines represent the bare cyclotron resonances for the electrons and holes whilst the solid lines correspond to the plasmon coupled resonances. Calculations for the [001] orientation at 30 and 60 degree tilts are shown by * and + respectively.

The highest energy resonances, extrapolating at zero magnetic field to about 400 cm^{-1} for both orientations, are attributed to the upper branch of the resonant subband Landau level coupling from the electrons. To interpret these tilted sample experiments, we solve the Schrödinger equation in the presence of a magnetic field for any arbitrary angle with respect to the growth direction. The calculation is performed self-consistently taking into account the band bending due to charge transfer and the experimentally determined electron to hole density ratio (but not the actual densities). However, electron to hole and hole to hole band mixing have been neglected. To a first order, the agreement between theory and experiment is rather good. For example, the theoretically calculated electron and hole densities are within 5% of values obtained by fitting the magnetotransport traces. Table 1 lists the superlattice parameters and the electron and hole confined energy levels. The energies are given with respect to the lowest point in the InAs conduction band and the change of band overlap between [100] and [111]A has been included in the calculation.

Assuming that transitions take place between a filled and a partially filled or empty level, we expect to see RSLC for the [001] superlattice 1266 at 400 and 237 cm^{-1} corresponding to E_1-L_1 and H_1-H_2 transitions, respectively. Similarly, the RSLC is expected to occur in the [111]A superlattice 1266 at 496 and 205 cm^{-1} corresponding to E_1-L_0 and H_0-H_1 transitions, respectively.

Figure 3 demonstrates excellent agreement with theory for the lower electron branch at both 30 and 60 degrees, and quite good agreement for the upper branches. Considerable non-parabolicity effects occur at the higher energies, and we expect that mixing of the electron and hole bands should also be taken into account for the theory to agree quantitatively with experiment. By 60 degrees the two branches of the resonance observed for the electrons at high field have moved to $1.26 \pm 0.1550 \text{ cm}^{-1}$, as shown in figure 2. In contrast to the electron behavior, we see no evidence of significant hole subband coupling in the data at 30 degrees, and by 60 degrees the hole resonances are very difficult to resolve underneath the lower electron branch. This result is rather surprising, since we expect stronger subband coupling for holes [6], due to the anisotropic nature of the valence band, although the field range used does not fully approach the coupling condition $\hbar\omega_c = \hbar\omega_v - \hbar\omega_c$ even for the lighter of the two hole resonances.

5. Conclusion:

In summary we have measured the electron and heavy hole masses for both [001] and [111] orientations. We find that the heavy hole masses are anisotropic. The light heavy hole resonance is attributed to the strain and quantisation induced decoupling of the valence band. Large angle tilt allowed us to determine the electron subband energy separation: the agreement between experiment and theory was very good.

6. Acknowledgement:

We gratefully acknowledge Drs. F.Y. Seong and G.R. Hooker for transmission electron microscopy studies and the Science and Engineering Research Council (UK) for continued financial support. One of us (TAV) would like to acknowledge the National Science Foundation for financial support.

References

- [1] L.L. Chang, *J. Phys. Soc. Jpn* **49**, 997 (1980).
- [2] D.L. Smith and C. Mailhot, *Rev. Mod. Phys.* **62**, 173 (1990).
- [3] M. Lakrimi, R.W. Martin, C. Lopez, D.M. Symons, F.T.R. Chidley, R.J. Nicholas, N.J. Mason, and P.J. Walker, *Semicond. Sci. Technol.* **8** S167 (1993) and references therein.
- [4] G.L.J.A. Bikken, H. Sigg, C.J.G.M. Langerak, H.W. Myron, J.A. A.J. Perekboom, and G. Weinmann, *Phys. Rev. B* **34**, 5598 (1986).
- [5] C.M. Sundaram, R.J. Warburton, R.J. Nicholas, N.J. Mason, and P.J. Walker, *Semicond. Sci. Technol.* **7** 985 (1992) and references therein.
- [6] J.C. Maan, Ch. Uhlir, L.L. Chang, and L. Esaki, *Sol. St. Commun.* **44**, 653 (1982); Y. Guldner, J.P. Viret, P. Votin, M. Voos, J.C. Maan, L.L. Chang, and L. Esaki, *Sol. St. Commun.* **41**, 755 (1982).
- [7] J.C. Maan, M. Altarelli, H. Sigg, P. Wyder, L.L. Chang, and L. Esaki, *Surf. Sci.* **113**, 317 (1982); H. Bluyssen, J.C. Maan, P. Wyder, L.L. Chang, L. Esaki, *Phys. Rev. B* **25**, 5364 (1982).
- [8] R.J. Nicholas, K.S.H. Dalton, M. Lakrimi, C. Lopez, H.W. Myron, N.J. Mason, G.M. Summerson, G.M. Sundaram, D.M. Symons, P.J. Walker, R.J. Warburton, M.I. Erements, D.J. Barnes, N. Miura, L. van Hockstad, R. Hopcroft, and F. Herlach, *Physica B* **184** 268 (1993).
- [9] D.J. Barnes, R.J. Nicholas, N. Miura, R.J. Warburton, N.J. Mason, P.J. Walker, *Physica B* **184** 268 (1993).
- [10] M. Lakrimi, R.W. Martin, N.J. Mason, R.J. Nicholas, and P.J. Walker, *J. Cryst. Growth* **124** 395 (1992).

- [10] R.W. Martin, R.J. Nicholas, G.J. Rees, S.K. Haywood, N.J. Mason, and P.J. Walker, *Phys. Rev. B* **42** 9237 (1990).
- [11] For a review see C. Wierbuch and B. Vinter, *Quantum semiconductor structures: physics and applications*, Academic Press 1991, pp135-171.
- [12] A.P. Roth and E. Fortin, *Can. J. Phys.* **56**, 1168 (1978).
- [13] R.J. Warburton, R.A. Lewis, R.J. Nicholas, N.J. Mason, and P.J. Walker, *Physica B* **184** 151 (1993).
- [14] D.M. Symons, M. Lakrimi, R.J. Warburton, R.J. Nicholas, N.J. Mason, P.J. Walker, and M.I. Erements, *to be published* (1993).
- [15] S. Das Sarma and J.J. Quinn, *Phys. Rev. B* **25**, 7603 (1982).
- [16] A.D. Wieck, F. Thiele, U. Merkt, K. Ploog, G.L.J.A. Bikken, H. Sigg, C.J.G.M. Langerak, H.W. G. Weinmann, and W. Schlapp, *Phys. Rev. B* **32**, 3785 (1985).

MAGNETIC FIELD TUNED TRANSITION OF AHARONOV-BOHM OSCILLATIONS FROM $h^2/4$ TO $h^2/2e$ PERIODICITY IN THE ARRAY OF $\text{AlGaAs}/\text{GaAs}$ RINGS.

G. M. Gusev, P. Basunijic, D. L. Dubashev,
Instituto de Física e Química de São Carlos,
Universidade de São Paulo, SP, Brasil

J. C. Portal
Service National des Champs Intenses, Centre National
de la Recherche Scientifique, F-13012, Grenoble
and INSA-Toulouse, 31077, France

L. V. Litvin, Yu. V. Nastashkevich and A. I. Toropov
Institute of Semiconductor Physics, Russian Academy of Sciences,
Siberian Branch, Novosibirsk, Russia

Abstract.

The variation of Aharonov-Bohm oscillation periodicity and persistent magnetoresistance have been observed in the array of $\text{AlGaAs}/\text{GaAs}$ rings with diameter of 0.3 μm . Magnetic field tuned impurity levels were suggested to be responsible for this behavior. It can be a result of the local electron density variation due to the influence of the weak magnetic field on the interference effect in mesoscopic samples.

Magnetoresistance oscillations in the normal metal ring with small diameter due to the Aharonov-Bohm effect is one of the remarkable phenomena that demonstrated the quantum behavior of an electron in solids. These Aharonov-Bohm (AB) oscillations are very sensitive to impurities, because defects introduce the additional shift to the electron wave function phase and, consequently, to magnetoresistance oscillations of a small single ring at zero magnetic field [1,2]. In small samples, whose size are comparable to the phase coherence length L_ϕ , the conductance fluctuations are random because of the interference among all possible trajectories. The results of interference are not averaged, but rather depend on the specific arrangement of the scattered centers in the given samples [3]. The change in the configuration of the random potential in microstructures gives rise to variation of the mesoscopic fluctuation pattern in a specific sample. This configuration can be changed as a result of spontaneous switching [1,3] under the interband irradiation [6,7] and after application of a strong electric field pulse [5,6]. Magnetic field also can influence the impurity level, and change in the switching time of a single impurity with in electric field was observed [8]. However, it is difficult to see the influence of magnetic field on the conductance fluctuations because of their random pattern. Another situation exists in the single submicron ring. In this case AB oscillations with the periodicity given by the flux quantum $\Phi_0 = h^2/4e$ are dominant. Introduction of an additional shift in the magnetic field can change an apparent periodicity of AB oscillations.

In this paper we report the variation from $h^2/4$ to $h^2/2e$ AB oscillation periodicity in the array of rings tuned by magnetic field. We suggested that the impurities are responsible for this behavior. We directly observed also nonmonotonic behavior of the impurity energy which can be connected to a mechanism based on the influence of the electron local density on the defect [9].

The test samples were Hall bridges based on $\text{AlGaAs}/\text{GaAs}$ heterostructures with 2D electron gas. In the initial heterostructures the electron density was $n_s = 1 \times 10^{11} \text{ cm}^{-2}$ and electron mobility $\mu = 2 \times 10^4 \text{ cm}^2/\text{Vs}$. The samples with area $500 \times 200 \text{ nm}^2$ were split off, and in the middle part between the potential contacts the square bridge was formed with size $2 \times 2 \text{ nm}^2$. In this bridge a periodic lattice of holes (antidots) was

patterned using electron lithography. The lattice period d was 0.3 μm , lithography antiod size $e = 0.15 \text{ nm}$. Next, the lithography samples were etched using reactive plasma etching, which was stopped before the AlGaAs spacer. The antiod size was larger than the geometric diameter because of the depletion region around the antidots, therefore we have $n = 2 + \epsilon$, where ϵ is the width of this depletion region. Thus, our system is different from other antidot lattices, which have been studied previously and for which $d/a \gg 1$ [10]. Also our samples have a small size $L = 1$, where L - mean free path in the initial heterostructures, therefore the electron transport was quasi-ballistic. The geometry of our array is closer to the geometry of the coupled rings with diameter 0.3 μm . The magnetoresistance was measured by the four probe method at frequencies 70-700 Hz in a magnetic field up to 0.5 T at temperature 1.7-4.2 K. We measured two samples with identical parameters.

We found the magnetoresistance oscillations which can be connected most clearly with AB effect, however their behavior was unusual. The typical curves of this magnetoresistance are shown in fig. 1a. Fig. 1b shows the periodicity of AB oscillations. The periodicity is varied from $\Phi_0/5$ to $\Phi_0/25$, where $\Phi_0 = h^2/4e$ is the flux quantum with diameter d . The envelope of the magnetoresistance curve, correlated with periodicity variation is observed. After several sweepings of B the oscillation picture is slightly changed; in particular, the second minimum of the resistivity moves to the higher magnetic field (curves 3). At oscillations with periodicity $h^2/4e$ move to the higher B too. We swept B 10-20 times and found that the sample begins to reveal hysteresis behavior. The same situation was observed when we swept B up with low velocity (0.3 T/min) and switched off B after the approach of base with high velocity (2 T/min). Fig. 2 shows some typical magnetoresistance curves when the magnetic field was swept up and down. We observed two features differ from AB oscillations in a single $\text{AlGaAs}/\text{GaAs}$ ring: decrease of the periodicity and hysteresis of the magnetoresistance oscillations. For curves 1, 2 the resistivity did not return to the initial state when B was turned off. The sample resistivity was relaxed to this state during 10 s. The magnetic field B was swept up and down 10 times, and magnetoresistance curves were slightly transformed into the curves 1, 1' which also reveal hysteresis. For these curves after 40-100 s at zero magnetic field the sample returned to the first state. This behavior was repeated several times. Oscillation periodicity for curves 3, 1 is changed from $h^2/5$ to $h^2/25$ (fig. 2). Maximum amplitude of the conductance oscillation was found to be $0.5 \text{ mV}/h$.

As follows, that the impurities are responsible for this behavior. For the dynamic study of this effect we measured the resistance as a function of time during a sweeping of the magnetic field. Fig. 3 shows the resistance as a function of time for these oscillations. At zero magnetic field the sample state was stable during expectation time 10 min. Next we swept the magnetic field up and down. As can be seen in fig. 3 the oscillation with hysteresis was observed, and when the magnetic field was swept down, the sample resistance was found to be higher, than for the initial state. The relaxation of the resistivity to the initial state was observed. The relaxation time was found to be 10 s. We did not see any spontaneous switching of impurities during the record of the magnetoresistance curves (magnetoresistances), which can change the oscillation picture. Thus, all results give evidence, that the magnetic field influences the impurity level, and changes AB oscillations.

In mesoscopic samples telegraph noise connected to switching of the two level impurity state has been observed [11]. This switching is related to tunneling in a double well energy potential with slight asymmetry or activation over this internal barrier [11], and thus, with the motion of the scatterer from one place to another. In this case the telegraph noise pattern can be affected by this motion [1]. If defect hopping is activated by the temperature, we believe that this mechanism is dominant in our case; activation energy is not possible for the switching time. When the activation energy is larger than the temperature, the impurity spends all time in the lower state. The proposed mechanism of the impurity switching influence on the AB oscillations is illustrated

in fig. 1. When the magnetic field increases, impurities hop to the other state (fig. 1b). Configuration of the random potential is changed, therefore the new phase shift to AB oscillations is introduced. In our case magnetic field changes the state of many impurities (a long relaxation time tail was observed). Therefore AB oscillation phase is not changed abruptly, but smooth transition is observed (fig. 1c). As magnetic field increases further, impurities can hop back to the initial state (fig. 1c) or defects with higher hopping barrier bright switch to the second state. As a result of the change in the configuration of the random potential AB oscillations periodicity is slightly randomized - it is varied between $h/2e$ and $h/2e$. We also believe, that the envelope of magnetoresistance oscillations on fig. 1 can be connected with impurity hops to the other state. In this case it is a new kind of magnetoresistance due to the changing in the configuration of the random potential. We see also this magnetoresistance for curve 1 (fig. 2), however because the oscillations are smeared, analysis of their periodicity is difficult. For the two level system the living time t_1 and t_2 spent in up and down states can be introduced. For the system with a barrier when the activation mechanism is dominant $t_1/t_2 \approx \exp(E_a/kT)$, where E_a - activation energy. In our case at $B \approx 0$ $t_1 \gg t_2$ and $E_a \gg kT$, in a magnetic field this situation is reversed $t_1 \ll t_2$, i.e. E_a decreases and changes the sign. The magnetic field influence on the telegraph noise in a mesoscopic sample was observed in ref. [8], however the mechanism of this effect was not clear. It is well known that the activation energy increases with B for the conduction band T valleys. Also it is necessary to apply high magnetic field (> 1 T) to shift the impurity energy to the χ dir-k1 due to the Zeeman splitting, if g-factor is equal 2, and magnetic moment is different for these two levels in a double well defect. Another mechanism has been proposed by Af'stuhler and Spivak [9]. Interference of the electron waves is responsible for the local electron density. Magnetic field influences the interference due to AB effect, and thus, electron local density is changed, therefore the energy of the nearby located impurity is varied too. The Af'stuhler Spivak mechanism should lead to a random fluctuation of the local impurity energy, because of the random pattern of the electron density in the disordered scattering potential. The autocorrelation function of the impurity energy is equal [9]

$$\langle I(t)I(0) \rangle \approx (h\omega)^2 \quad (1)$$

for $I \approx I_0$ - cyclotron frequency. In the array of rings the electron interference is determined by the ring geometry and not by the specific impurity configuration as in mesoscopic samples. Therefore the impurity energy should oscillate with periodicity Φ_0 , and the amplitude of this oscillation should increase linearly with magnetic field. As can be seen from fig. 1, 2 transition of AB periodicity is observed at $B \approx 0.2$ T, therefore $E_a \approx h\omega \approx 0.35$ meV. It is comparable to temperature, therefore $t_1 \approx t_2$. As we mentioned above, when the magnetic field was swept down with high velocity, the sample resistance hopped to the other state. A similar effect exists in a heavily doped GaAs and AlGaAs alloy system after illumination of the sample by light at low temperature - persistent photoconductivity [12]. In our case impurity switching time lies in the interval $1-30$ ns, therefore when the magnetic field is turned off at a high rate, some defects were staying in the metastable state due to the barrier. The sample was switched to the state with another resistivity in a zero magnetic field, and we observed persistent magnetoresistivity and hysteresis behavior (fig. 1, 2, 3). This persistent magnetoresistivity can be positive (fig. 2) or negative (fig. 3). We also see the long tail of the impurity relaxation arising from the different switching time in the ensemble of impurities. Some defects have a longer relaxation time, therefore the picture of the magnetoresistances differs from the initial. However, after irradiation by light or heating of the sample up to room temperature, we turned off the device to the initial state. These experiments were carried out during two months, and all time we observed the impurity switching induced by the weak magnetic field.

It should be noted that recently new magnetoresistances with periodicity $h/2e^2$ have been observed in samples which contain 10^{19} antedots [13, 14]. As was suggested in

[14], it is not due to AB effect, and quantization of the orbital orbits (QPO) is responsible for these oscillations. The next difference in our experiments can be emphasized: QPO oscillations appear only at $B > 0.5$ T and $T < 1.5$ K in contrast to AB oscillations which are seen at smaller magnetic field and at $T \approx 1.2$ K. The thermal broadening of energy levels, which depends on the magnetic field value, is responsible for the behavior of QPO oscillations.

In summary, we have observed the influence of the weak magnetic field on the impurity state in the system with an array of submicron rings. Novel magnetoresistance appeared because of the changing in the configuration of the random potential by magnetic field. Metastability of these states is responsible for the hysteresis of the magnetoresistance and persistent magnetoresistivity. A more delicate effect connected with sensitivity of the AB oscillation periodicity to the impurity state has been found: variation of periodicity between $h/2e$ to $h/2e$. The Af'stuhler Spivak mechanism because of the change in the local electron density which leads to the impurity energy shift is responsible for this behavior.

Two of us (G.M.G. and D.L.L.) are supported by CNPq (Brazil). This work is supported by funds CNPq and FAPESP.

*Permanent address: Institute of Semiconductors Physics, Russian Academy of Sciences, Siberian Branch, Novosibirsk, Russia

REFERENCES

- [1] S. Washburn, R. A. Webb, Rep. Prog. Phys. **55**, 1311 (1992)
- [2] A. D. Benoit, S. Washburn, C. P. Umbach, R. B. Landowitch, R. A. Webb, Phys. Rev. Lett. **57**, 1765 (1986)
- [3] B. L. Af'stuhler, B. Z. Spivak, JETP Lett., **42**, 117 (1985)
- [4] M. I. Koton, M. J. Uren, Adv. Phys., **38**, 467 (1989); R. S. Balla, R. A. Bulman, Phys. Rev. Lett., **60**, 2111 (1988); D. L. Benoit, T. J. Moeslein, N. Giordano, Phys. Rev. Lett., **58**, 1210 (1987)
- [5] G. M. Gusev, Z. D. Kvon, E. B. Ol'shanetskii, V. Sh. Aliev, A. M. Kudryashov, S. V. Paleyev, J. Phys.: Cond. Matter, **36**, 6307 (1989)
- [6] G. M. Gusev, Z. D. Kvon, I. B. Ol'shanetskii, Sov. Phys. JETP **74**, 715 (1992)
- [7] S. J. Kippelen, O. Mello, M. W. Keller, D. I. Puder, R. N. Sacks, Phys. Rev. B, **44**, 8189 (1991)
- [8] N. M. Zimmerman, B. Galdung, W. M. Hammecke, Phys. Rev. Lett., **67**, 1322 (1991)
- [9] B. L. Af'stuhler, B. Z. Spivak, JETP Lett., **49**, 671 (1989)
- [10] K. Enslin, P. Petroff, Phys. Rev. B, **41**, 12107 (1990); G. M. Gusev, V. I. Dolgoplos, Z. D. Kvon, A. V. Shashkin, A. M. Kudryashov, L. V. Litvin, Yu. V. Nastashiev, JETP Lett., **54**, 461 (1991); A. Lorke, P. Kothlars, K. Ploog, Phys. Rev. B, **44**, 1117 (1991)
- [11] C. J. Rogers, R. A. Bulman, Phys. Rev. Lett., **55**, 879 (1985)
- [12] D. V. Lang, R. A. Logan, Phys. Rev. Lett., **39**, 615 (1977)
- [13] I. Ahls, K. Nakamura, Physica B, **181**, 198 (1991)
- [14] D. Weiss, K. Richter, J. Vashithan, G. L. Loring, Proc. 19th Int. Conf. on LP2DS, New York, 26 (1991)

Figure captions

Fig 1 a) Magnetoresistance as a function of magnetic field $T = 1.2$ K. Insert: Schematic view of the sample

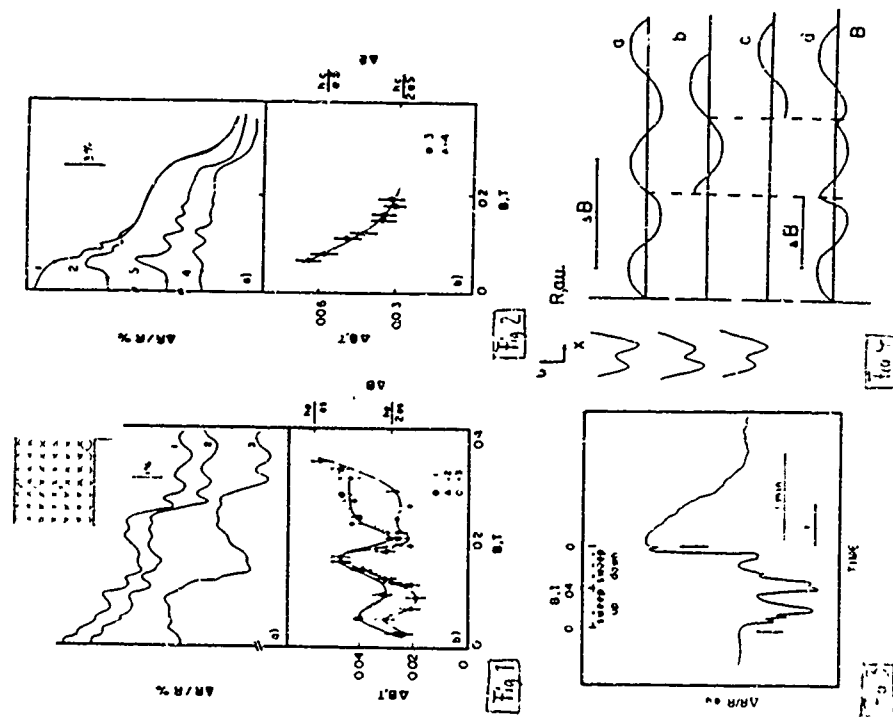
b) Periodicity of oscillations for the different magnetoresistance curves

Fig 2 a) Magnetoresistance with hysteresis as a function of B $T = 1.3$ K sweep up, 2.4 K sweep down

b) Periodicity of AB oscillations for curves 1,4

Fig 3 Resistivity as a function of time during a magnetic field sweeping and following relaxation

Fig 4 Schematic illustration of the AB periodicity variation due to the changing in the impurity state. Insert left: impurity potential at different magnetic field



ThP31

Negative Conductance at THz Frequencies in Multi-well Structures

W. S. Truscott

Department of Electrical Engineering and Electronics, University of Manchester Institute of Science and Technology, PO Box 38, Manchester, M60 1QD, UK

Abstract

An algorithm by which the exact first order ac response of quantum electronic devices, including tunnelling structures, may be calculated rapidly is described. Pinet multi-well tunnelling structures with negative conductance maxima at 1.4×10^{12} Hz (1.4 THz) and 14 THz at temperatures of 80 K and 300 K respectively are presented. Devices of this sort are expected to operate as power sources, mixers and amplifiers between 0.5 and 20 THz. The effects of bias and departures from the ideal geometry are discussed as are the factors which indicate that such devices are realisable in practice.

Three new aspects of the response at extremely high frequencies of electronic transport structures, particularly tunnelling and other quantum devices, are presented in this paper: first, an algorithm to calculate both the terminal currents and the internal carrier displacement currents that are induced when an external ac potential is applied to a structure; second, a novel device structure which may operate as a power source or amplifier at frequencies in the range $0.5 - 20$ THz ($5 \times 10^{11} - 2 \times 10^{13}$ Hz); and, third, experimental and theoretical considerations related to the practical production and utilisation of these devices.

This work is based on exact solutions to Schrodinger's equation for systems in uniform time dependent fields [1]. The solutions are inherently self-consistent, i.e. where one of these solutions applies, the additional time dependence caused by the ac field is independent of the carrier-carrier interactions. Full details of, and justification for, their use in the calculation of the ac response of semiconductor devices will be reported later; here the method is outlined. The response of a wave function to a time dependent field is close to the motion of a classical particle in that field, in addition there is a time-dependent phase modulation. As a specific example, $\text{Aexp}(ikx)$ is a wave function for a particle of mass m in a region of constant potential, when the potential $-F\cos(\omega t)$ is added an exact wave function is:

$$\text{Aexp}\left\{ikx + \frac{F\cos(\omega t)}{m\omega^2}\right\} - \frac{iE}{h} \cdot \frac{iF\sin(\omega t)}{h\omega} - \frac{iF^2(2\omega t - \sin(\omega t))}{2h\omega^2} \quad (1)$$

Exact solutions also exist for regions in which the potential is a linear or parabolic function of distance. A semiconductor device subject to an ac bias may be divided into regions within each of which there are many time dependent wave functions that will be exact solutions of Schrodinger's equation; however, most of these will not satisfy the continuity equations at regional boundaries since the adjoining wave functions will have different time dependencies for their amplitudes and phases. For the above example, this will always occur if either F or k changes at a boundary. In a seminal paper concerned with a transit time for tunnelling which has acted as a major stimulus to this work, Buttiker and Landauer have given a solution [2]; for any wave function with energy E this describes the device with a static potential, there is a related one for the structure subject to an additional sinusoidal time dependent field of period $2\pi/\omega$ which has a similar wave function at energy E together with a series of functions with time dependencies which differ from it by $\exp(in\omega t)$ where n is any

integer. The latter are wave functions for the local potential with energies $E + n\hbar\omega$ selected so that their sum satisfies the continuity equations and the boundary conditions at all times. The first order response is associated solely with the components identified with $\exp(\pm i\omega t)$; a total of three functions in any region are sufficient to describe the linear behaviour of a device.

To first order, the time dependent continuity equations at any boundary divide into two parts separating the effects of the ac field in adjacent regions. The algorithm used for this paper calculates the effect of the ac field on each region of the potential having an exact solution; with this approach the waves generated at the two boundaries of a region tend to cancel outside it. First order forms for the amplitude and spatial derivative of the wave function of equation (1) for a boundary at $x=a$ may be found by multiplying the

$$\text{function } \text{Aexp}\left\{ikx - \frac{iE}{h} \cdot \frac{iF\sin(\omega t)}{h\omega}\right\} \text{ by } \left[1 + \frac{i\hbar F}{m\omega^2} \cos(\omega t)\right] \text{ and}$$

$\left[ik - \frac{k^2}{2} \cos(\omega t) + \frac{i\hbar}{k} \sin(\omega t)\right]$ respectively. If the ac potential is continuous then the original function will also be continuous at $x=a$ and it is only the time dependence associated with the multipliers that has to be counterbalanced by wave functions at energies $E \pm \hbar\omega$; waves of the required amplitude and derivative are added at one side of the boundary with respect to the other. They propagate through the region to the second boundary at $x=b$ where a similar set of functions describe the amplitude and derivative. For small values of ω the latter at $E \pm \hbar\omega$ will almost exactly cancel those required for the boundary at $x=a$; the residual sum of the waves satisfying the boundary conditions at $x=a$ and at $x=b$ propagates into the rest of the structure and gives rise to the time dependent terminal current. The carrier displacement current in any region of the structure is found by summing the net current due to all other regions, the current associated with the initial time dependent wave function and that associated with the waves within the region generated at its boundaries.

The results in this paper are from a computer programme which uses the above algorithm. This programme can analyse any structure which is composed of a sequence of regions of constant potential separated by abrupt steps in potential. There are many advantages in restricting the structures in this way: all the functions within the algorithm are analytical and any result may be checked (in simple structures) by an independent calculation; because the functions involved are either exponential or trigonometrical the calculation is much faster than it would be if the functions had to be numerically integrated; the programme is simple and has been checked and verified over a long period of time, the probability of error in these results is very small. This algorithm is readily extended to include regions with a linear or parabolic variation of potential and programmes have been developed to analyse structures including such regions: the results from these are not different in kind from those presented here. The modulation of the current, emerging from a double barrier resonant tunnelling diode structure (DBRTS) calculated using this programme is consistent with results published elsewhere [3],[4],[5]; the overall response is that of a system with a single resonance for which a characteristic time, τ , is defined by the ratio of Planck's constant to the half width of the transmission peak.

The limitations on the frequency response intrinsic to the DBRTS are overcome in structures with two or more quasi-bound levels which have spacings corresponding to the operating frequency. The algorithm has allowed the behaviour of many different structures

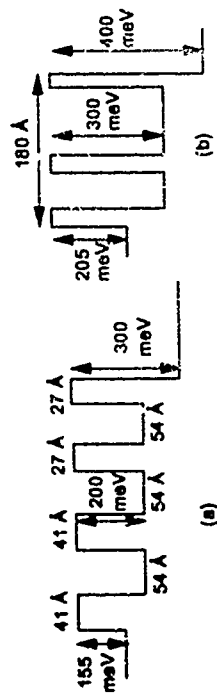


Figure 1: Conduction band energy diagrams of two structures exhibiting negative conductance. They are optimised for 1.4 THz (a) and 14 THz (b) respectively.

to be investigated; the overall pattern of phase and amplitude variation is characteristic of spatially distinct states whose coupling through an external potential is characterised by a resonant response. The argument that this resonant modulation of a unidirectional particle flux by an external field is a novel quantum effect will be given in a later paper; this is concerned with the practical implications of the effect. The pattern of the results that have been obtained allows optimised device structures to be evolved; examples of the conduction band diagram of two of these are shown in Figures 1(a) and 1(b). The key features of these are the wider barriers on either side of the left hand well and the nearly uniform spacing in energy of the three lowest quasi-bound levels when the device is biased at the optimum operating point. The wider barriers cause the tunnelling transmission to be dominated by the quasi-bound state at energy $E2$ associated with the left hand well. There will be a significant accumulation of carriers in this well when a tunnelling current flows. The rest of the structure is designed so that the energies of two other levels, $E1$ and $E3$ satisfy $E3 - E1 = 2\hbar\omega$. The calculated response to an applied field when $E2 = \frac{1}{2}(E1 + E3)$ is very small because the effects of the coupling to levels 1 and 3 are equal and opposite. This is shown by Figure 2 which illustrates for electrons with energies corresponding to the transmission window at $E2$, the reactive and conductive parts of the terminal current as a function of the energy $E \pm \hbar\omega$ of the state to which the tunnelling electrons are coupled by the ac field. The reactive currents are opposite in sign for coupling to the states at $E1$ and $E3$, as are the conductive currents for a given modulation frequency if $E2 < \frac{1}{2}(E1 + E3)$; these two parts always vary with energy in accordance with expectations based on the Kramers-Kronig relationships. However if $E2 > \frac{1}{2}(E1 + E3)$, the case shown in Figure 2, the coupling between levels 2 and 3 occurs at lower frequencies than that between 2 and 1; it is the overlap between the two responses which gives the large negative terminal conductance which is constant over a substantial bandwidth. Figures 3(a) and 3(b) show the frequency dependence of the real and imaginary parts of the admittance of the structures in Figures 1(a) and 1(b) respectively when bias is applied so that $E2 > \frac{1}{2}(E1 + E3)$.

The quantities plotted in Figure 3(a) are the real and imaginary components of the ac

terminal current produced by unit field across the device structure for an incident electron spectrum at the left hand side of Figure 1(a) that is characterised by a temperature of 80 K, while those plotted in Figure 3(b) are the identical quantities for the structure of Figure 1(b) with an incident electron temperature of 300 K; in both cases an effective mass one-third the electron mass has been assumed. The algorithm described above is used to calculate at a fixed frequency and incident electron energy the magnitude and phase of the modulation of the tunnelling current produced by the ac field. The observed admittance at that frequency is found by integrating the modulation weighted by the transmission probability over the electron spectrum; this integration extends over the range of incident energies that cover the transmission peak, $E1$, $E2$ and $E3$. For some structures and frequencies there is significant cancellation between the response of the electrons with the highest energies in the central transmission peak and those with the lowest energies. The structure shown in Figure 1(a) minimises this with barrier widths designed so that the major transmission peak at $\omega = 2\pi E2$ is about half the width of those at energies $E1$ and $E3$, in which case the phase of the modulation produced by the ac field does not vary significantly over the transmission peak at $E2$.

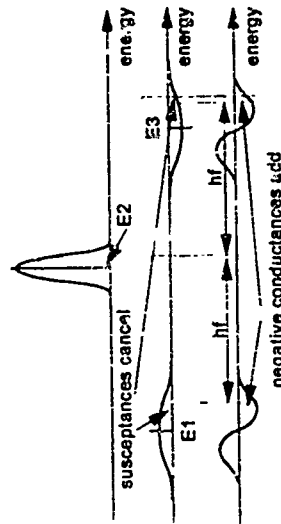


Figure 2: An explanation of the calculated admittance frequency curves of Figure 3. The upper curve shows the transmission peak at energy $E2$. The lower curves are sketches of the susceptance and conductance for any electron with energy close to $E2$ coupled to energies close to $E1$ or $E3$ by the applied ac field at a frequency f .

The total current flowing through any device similar to those shown in Figure 1 is composed of two parts, first, the tunnelling current which passes through the right hand barrier into the contact and second, the displacement current associated with the electrical polarisation of the material and carriers within the structure. The dielectric polarisation is a fixed function of the device geometry, the barrier polarisation normally adds to this, increasing the overall structural capacitance. In these devices however, the negative

resistance is the result of the reduction in the density of carriers adjacent to the final barrier when the ac field is directed towards it; the carrier displacement within the device under optimum operating conditions is therefore inductive. These two devices therefore exhibit an effect of great importance in THz applications, namely that the capacitance of the device is reduced below its structural value by the carrier displacement currents within the active region of the device. Calculation of the combined structural and carrier capacitance is possible using the above theory but, since this effect is of the same order as the variation in the applied field over the device due to carrier accumulation, such a calculation will only be valid in a model which includes these effects.

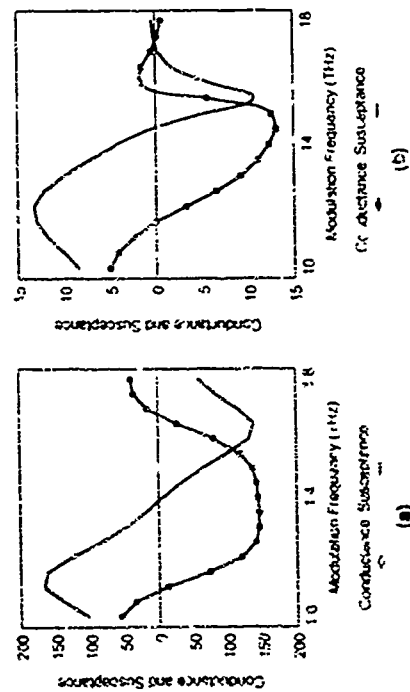


Figure 3: The calculated conductance and susceptance (arbitrary scales) as a function of frequency for the two device structures of Figure 1

Devices using this new concept can only be realised experimentally and exploited commercially if the range of parameters such as structural width, barrier height and device bias over which the effect is exhibited covers the probable range of deviations that may occur in the normal manufacturing processes and operating conditions for such structures. The effect on the negative conductance characteristic of changing the energy offset between the barriers and the wells for the structure in Figure 1(a) by 5% is shown in Figure 4(a), as is the effect of changing the overall width scale by 2%. It can be seen that, as a result of the bandwidth over which the device has a constant negative conductance, devices with either of these departures from the designed structure would still perform as oscillators or amplifiers at the design frequency of 1.4 THz. Since these variations are in excess of the degree of control which can be achieved in MBE growth, normal structural variations will not restrict the performance of these devices. Figure 4(b) shows the negative resistance characteristic with three different values of forward bias, the effect of reducing the bias by

a few mV over the active region of the device to the condition that $E2 < 1/2(E1 + E3)$ is to switch the sign of both the conductance and susceptance at the operating frequency. This device may therefore be used as a modulator. Changing the bias by a similar amount in the opposite direction splits the feature in the device response associated with the coupling between $E2$ and $E3$ from that between $E2$ and $E1$ giving a reduced magnitude for the negative conductance, but an increased bandwidth and a correspondingly less rapid change of susceptance with frequency. A single device may therefore be used in high gain narrow bandwidth and low gain wide bandwidth applications depending on the applied bias.

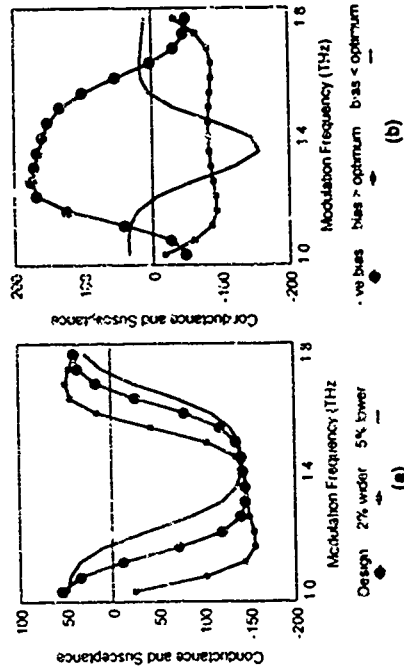


Figure 4: Variation of the conductance for the device in Figure 1(a) with (a) device geometry decrease in barrier height and a 2% increase in geometrical widths, and curves are presented for forward biases which are larger and smaller than the optimum bias and also for a small negative bias.

The band structure diagrams shown in Figure 1 are significantly different from those for real devices fabricated in GaAs/AlGaAs, a material system which minimises the broadening of the quasi-bound levels, subject to a dc bias prompting an electron flow. The bias will cause an electric field over the whole structure; in addition the accumulation of carriers, particularly in the left hand well, will make this field vary over the active region. The problem of designing a structure which has the required energies for the three quasi-bound levels when a forward bias is applied is considerable and must be overcome before the negative conductance can be demonstrated. This design process needs to combine theoretical modelling with experimental assessment as a means of empirical optimisation of the model. Although it might seem a very difficult task to produce a structure with three energy levels whose relative energies are correct within 0.5 meV, there are two factors that are a considerable assistance for structures similar to that of Figure 1(a): first, levels $E1$ and

Perpendicular Transport Through Rough Interfaces in the Metallic Regime

Arne Bratans [*] and Gerrit E.W. Bauer
Faculty of Applied Physics and DIMES, Delft University of Technology
Lorentzweg 1, 2628 CJ Delft, The Netherlands

June 28, 1993

Abstract

Perpendicular transport through an interface in the metallic regime is considered. The semiclassical theory presented is based on the Landauer-Büttiker formalism, it generalises previous work by taking into account an effective mass mismatch at the interface and a non-zero average of random scattering potentials. The transmission probability for a given mode is found in terms of the effective mass and the conduction band profile to the left and to the right of the interface. The Fermi energy, the self-energy of the electron, and the transverse wave vector of the electron. The diffuse and specular contributions to the interface roughness scattering are shown to be equally important in the weak scattering limit. Predictions for the transport properties of interfaces with a low concentration of strongly scattering defects should be accessible to verification by experiments. The theory is applied to the spin-valve effect in magnetic multilayers.

The importance of interface scattering in many areas of metal and semiconductor physics is reflected by numerous papers since the seminal work by Fuchs [1]. The overwhelming majority of the work is concerned with transport parallel to an impenetrable rough interface, e.g. in the two-dimensional electron gas [2]. Here, a theory of interface scattering based on the Landauer-Büttiker formalism [3] is presented which is concerned with transport normal to the interfaces in the metallic regime. The relation between diffuse and specular scattering at an interface is usually described by introducing a factor p which is determined empirically or derived from a microscopic model of the interface roughness [1, 4]. We will show that diffuse scattering is uniquely connected to the so-called vertex correction. Our approach gives a simple relation between the specular and diffuse part of the transmitted wave and a simple formula for the specularly parameter. The conductance for a system of multiple interfaces can be found by a semiclassical concatenation of a single interface. The theory is applied to find the magnetoresistance in magnetic multilayers, where spin-dependent interface scattering is generally believed to be responsible for the "giant" magnetoresistance or spin valve effect [5, 6, 7, 8, 9, 10, 11, 12]. The

E_3 are associated with the mixed states of right hand wells; the minimum value of E_3-E_1 as the bias is varied is determined only by the barrier between these wells, and it changes slowly with this field about this condition because of the mixing. There will therefore be a useful range of applied bias over which the E_3-E_1 will be close to $2\hbar\omega_c$. Second, the position of E_2 with respect to E_1 and E_3 is controlled by the bias, a suitable value can always bring their energies into the correct relation to show negative conductance at some frequency. Because E_3-E_1 varies slowly over a certain range of applied bias, the design requirements reduce to establishing an appropriate barrier thickness between the right hand wells and choosing the widths of these wells so as to ensure that the bias is which E_2 is in the correct relative position is close to that at which E_3-E_1 reaches its minimum value.

An important factor determining the practical applications of these devices is temperature at which they can be operated. The negative conductances shown in Figures 3(a) and 3(b) have been calculated for electrons at 80 K and 300 K; the structures therefore have the potential to operate at practical temperatures. The other factor which will determine the maximum operating temperature is the broadening of the quasi-bound levels by phonon scattering. Rostko et al. [6] have reported the observation of up to 15 cycles of radiation at a frequency of 1.5 THz caused by coherent electron oscillations in an optically excited double well structure at a temperature of 10 K. The basis for this phenomenon is closely related to that giving rise to the negative conductance; this observation strongly suggests that the high frequency negative conductance will be observed in suitable structures at practical temperatures as does the observation at temperatures up to 185 K of maxima in the tunnelling current - voltage curve associated with a 38 meV miniband spacing in a multi-well structure [7].

The author wishes to thank his colleagues for the stimulating environment which has led to this work. It has been supported solely by research element of the Higher Education Funding Council for England recurrent grant to UMIST. The author believes that the future exploitation of these ideas is a fruitful area for international collaboration.

1. W.S. Truscott, Phys. Rev. Lett. 70, 1900, (1993).
2. M. Büttiker and R. Landauer, Phys. Rev. Lett. 49, 170 (1982).
3. W.R. Frenley, Appl. Phys. Lett. 51, 448 (1987).
4. H.C. Liu, Appl. Phys. Lett. 52, 453 (1988).
5. V. Kislov and A. Kamenov, Appl. Phys. Lett. 59, 1500 (1991).
6. H.G. Rostko, M.C. Nuss, J. Shah, K. Leo, D.A.B. Miller, A.M. Fox, S. Schmitt-Rink and K. Köhler, Phys. Rev. Lett. 68, 2216 (1992).
7. P.C. Harness, Ph.D. Thesis, "Resonant-Tunnelling Structures incorporating Finite Superlattice Energy Filters", Faculty of Technology, University of Manchester, UK pp. 170 - 177, (1992).

Let us first consider scattering at a single interface. The interface roughness is modeled by short-range scatterers that are randomly distributed over the interface with density ρ . The incoming and outgoing electron states are taken to be Bloch waves and are approximated by plane waves. Heterostructures are described by means of spin-dependent potential steps and effective masses. The wave function at an energy E is determined by the Schrödinger equation

$$\left\{ -\frac{\hbar^2}{2} \nabla^2 - \frac{1}{r} + U(x, y, z) \right\} \psi(x, y, z) = E \psi(x, y, z). \quad (1)$$

The conduction band profile, $U_c(x)$, and the effective mass of the electron $m^*(x)$, are simply step functions at $x = 0$. The interface roughness given, relative to the potential $V(x, y, z)$, by integrating out the transverse coordinates (y and z), a one-dimensional equation is obtained [14]. We assume that the particles are incident from the left with transverse momentum k_y . To the left of the interface the longitudinal part of the wave function consists of the incoming and reflected waves and to the right side of the interface there are only transmitted right-going waves. For propagating modes, the longitudinal wave

$$c_p(x) = \begin{cases} \sqrt{\frac{2}{\pi}} c_p \beta_p^{-1/2} e^{-\sqrt{\frac{2}{\pi}} x / \beta_p} & x \leq 0 \\ \sqrt{\frac{2}{\pi}} c_p \beta_p^{-1/2} e^{-\sqrt{\frac{2}{\pi}} x / \beta_p} & x \geq 0 \end{cases} \quad (2)$$

where S_y and k_z are the transverse and longitudinal components of the wave vector and $k_z^2 = \frac{1}{2}(\mathbf{k}^2 - k_\perp^2)$; $k_\perp^2 = \frac{1}{2}(\mathbf{k}^2 - k_z^2)$. Note that we have normalised the longitudinal parts of the wave function, $\psi_z(z)$, so that they carry unit flux. The transmission (reflection) coefficient from state i to state j (T_{ji} (R_{ji})). Excrescent modes correspond to complex longitudinal wave-vectors, which should be treated as in Ref. [13]. For low temperatures, the conductivity can now be found from the Landauer-Büttiker formalism [3].

$$C = \frac{1}{K} \sum_{i,j} |c_{ij}|^2. \quad (3)$$

where the summation is over propagating modes. In matrix notation the transmission coefficients are determined by the equation $\{t\}(1 + \Gamma)^{-1} = \delta$, $t_i, \Gamma_i = \sqrt{k_1 k_2}/k_1$ and

$$\Gamma_2 = \sum_2 \frac{m_{21} \sqrt{A_2} e^{i\phi_2}}{k_1} \frac{1}{\sqrt{A}} \frac{k_1}{\sqrt{A}} e^{-i\phi_2} \quad (2)$$

with $m^* = \sqrt{m_1^2 m_2}$ and $k_1 = (m_1^2 L^2 + \eta_1^2 L^2)/2m^*$. This result generalises Eq. (4) in Ref. [13] for the case of different effective mass to the left and to the right of the interface. Current conservation and the continuity of the wave function relate the transmission probabilities and the transmission coefficients as

$$\sum_{\nu=0}^{\infty} \frac{k_{\nu}}{k_0} |c_{\nu}|^2 = \sqrt{\frac{k_0}{k_1} \operatorname{Re}(c_1^2 c_0^*)}. \quad (5)$$

which has the same form as Eq. (5) in Ref. [13].

The transmission probabilities of present interest are given by the ensemble average of all impurity configurations, which cannot be treated exactly. We have chosen a perturbation approach. The relevant perturbation series are obtained by inverting the matrix relation for t , expanding $(1 + t)^{-1}$ as a power series in t and by taking the configurational average. Green functions can be introduced to identify the terms in the expansion and as a tool to understand the nature of the approximations ([13] and references therein). The diagrams contributing to the transmission probability can be classified as crossing or non-crossing. The crossing diagrams describe phase coherence and are g -responsible for weak (Anderson) localisation of the wave function [16]. Neglecting crossing diagrams, i.e. phase coherent scattering between different defects, it is possible to find the transmission probability in terms of the irreducible self-energy Σ [13].

$$(9) \quad \frac{\frac{1}{2} \left[\frac{1}{2} \left(\frac{1}{2} + 1 \right) \right]}{1/4} \frac{\frac{1}{2} \left[\frac{1}{2} \left(\frac{1}{2} + 1 \right) \right]}{1/4} - \frac{\frac{1}{2} \left[\frac{1}{2} \left(\frac{1}{2} + 1 \right) \right]}{1/4} \frac{\frac{1}{2} \left[\frac{1}{2} \left(\frac{1}{2} + 1 \right) \right]}{1/4} + \frac{\frac{1}{2} \left[\frac{1}{2} \left(\frac{1}{2} + 1 \right) \right]}{1/4} \frac{\frac{1}{2} \left[\frac{1}{2} \left(\frac{1}{2} + 1 \right) \right]}{1/4} = \left(\frac{1}{2} \right)^2 \left(\frac{1}{2} \right)^2$$

Quantum interference between different scattering centers is neglected. The approximation therefore be labeled as semiclassical and breaks down when the distance between dephasing inelastic collisions becomes larger than the average separation between scatterers. Electrons are scattered specularly at the interface if the transverse component of the wave vector is conserved, which is the first term on the right hand side of Eq. (6). The second term clearly represents the diffuse scattering contribution, which vanishes if the vertex correction is not taken into account.

correction is not taken into account. In the following we set $\Delta C = 0$ and $\Delta m^* = 0$, which considerably simplifies the analytical treatment. It is interesting to make contact with the traditional treatment of interface roughness in terms of the specularly factor p . The factor p , defined as the fraction of electrons transmitted specularly is found to be

$$p_1(\theta) = \frac{\cos(\theta)}{\sin + \cos(\theta)}. \quad (7)$$

where $\eta_H = -m^2 \text{Im}(\chi)/k^2 k_F$ is a scattering parameter and θ is the angle of incidence of an electron wave vector measured from the surface normal. This expression is exact for

semiclassical transport and the specular factor is independent of the real part of the self energy. Diffuse scattering increases for larger incident angles as shown in Fig. (1). Electrons with wave vector perpendicular to the interface $s = \pi$ scattered purely specularly, and electrons with wave vector parallel to the interface plane $s = 0$ will be completely diffused. A similar relation can be derived for reflected electrons.

To lowest order in the self-energy $m^* \gamma / \hbar^2 k_F$ the conductance is

$$G = \frac{2e^2 A k_F^2}{\hbar} \left(1 - \frac{m^* \gamma}{\hbar^2 k_F} \right) \quad (8)$$

and is independent of the real part of the self energy. The first term is the Sharvin conductance which is proportional to the sample cross section A . The second term reduces the conductance due to specular scattering. The third, diffuse term increases the conductance by opening additional channels for electron transport.

The self-energy is

$$\Sigma^B = n/n^* - i \frac{m^* \gamma}{\hbar^2} \left(\frac{1}{\tau} - k_F \right) \left(1 - \sqrt{1 - \gamma^2} \right) \quad (9)$$

in the Born approximation, where the average scattering strength $\gamma = \sum_s \gamma_s / n/n^*$ and the mean square value of the scattering strength $\gamma^2 = \sum_s \gamma_s^2 / n/n^*$ are introduced. Here a ultraviolet divergence in the summation over intermediate evanescent states has been cut-off at a wave-vector αk_F to account for the finite range of the potential, $\alpha \geq 1$, but not much larger than unity for magnetic multilayers, since the range can not be shorter than a d orbital radius. The Born approximation is valid if the weak scattering limit $|m^* \Sigma^B / \hbar^2 k_F| \ll 1$ and $m^* \gamma / \hbar^2 k_F \ll 1$, which means that the probability of strong scattering by a single impurity is small. The scattering parameter is in this approximation $n/n^* = n/n^* \gamma / \alpha$. The specular factor is not affected by the non-zero average of the scatterers. In the weak scattering limit, the non-zero average of scatterers has also no effect on the conductance.

We will now study the situation where all scatterers have equal magnitude of strength, such that $|\gamma_s| = \gamma$. The self-energy is calculated in the single-site approximation, i.e., using the exact cross-section for isolated defects but neglecting crossed diagrams which stand for quantum interference between different defects

$$\Sigma^B = \frac{n/n^*}{1 + \frac{m^* \gamma}{\hbar^2} \left(\frac{1}{\tau} - k_F \right) \left(1 - \sqrt{1 - \gamma^2} \right)} \quad (10)$$

This result reduces to the Born result in the weak scattering limit ($m^* \gamma / \hbar^2 k_F \ll 1$). For strong scattering ($m^* \gamma / \hbar^2 k_F \gg 1$), but to lowest order in n/n^* , we obtain the interesting result that

$$G = \frac{e^2 A k_F^2}{\hbar} \left(1 - \frac{n/n^*}{\alpha} \right) \quad (11)$$

Here $|m^* \gamma k_F / \hbar^2| \ll (m^* \gamma k_F / \hbar^2)^2$ in the present regime has been used. The conductance is reduced by a factor proportional to the number of defects, $n/n^* \propto \Delta n/n$. Each scatterer

effectively blocks one channel and the conductance becomes independent on the scattering strength. This blocking is somewhat reduced by a factor $1/\alpha^2$ via a "leak" of evanescent states. An experiment is proposed to test this expression: insert a layer (or a multilayer, see below) with strong short-range scatterers between two perfect leads. By measuring the conductance and the number of impurities the theory can be checked and the "leaking factor" α can be determined which provides information about the scattering potential. A non-zero average of scatterers has no effect on the conductance.

Results for a single interface can be generalized to a multilayer situation where interface scattering and bulk impurity scattering is taken into account. Semiclassical concatenation of transmission probabilities [14] is consistent with the neglect of crossing diagrams in the single interface scattering. The transmission properties do not change with the distance between the interfaces in this approximation. By allowing the interfaces to be infinitesimally close to each other, one can convince oneself that the relation between the transmission probabilities and the transmission coefficient, Eq. (3), still holds for the N -interface configuration. Concatenation of the diagonal transmission coefficient, is straightforward and the conductance for transport through N interfaces is

$$\frac{G^{(N)}}{G} = 1 - 2(N\eta/n^*) + 2(N\eta/n^*)^2 \ln(1 + \frac{1}{N\eta/n^*}) \quad (12)$$

This equation has been verified by comparison with numerical results for the concatenated total transmission probabilities Eq. (6). The conductance obtained by neglecting the diffuse scattering in Eq. (6) gives a similar result, but the scattering parameter is increased by a factor 2. The diffuse contribution due to the vertex correction is therefore important. The conductance calculated with and without the diffuse part is shown in Fig. (2). A bulk system is modeled by N interfaces with an interface scattering parameter η/n^* . Letting $N \rightarrow \infty$ and $\eta/n^* \rightarrow 0$ but keeping $N\eta/n^* = L\eta/n$, where L is the length of the bulk material and η/n is the scattering parameter for the bulk system. The conductance for a multilayer is

$$\frac{G^{(N)}}{G} = 1 - 2\left(\frac{N}{N}\right) + 2\left(\frac{N}{N}\right)^2 \ln(1 + \frac{N}{N}) \quad (13)$$

where N is the mean free number of traversed interfaces given by $N = (n/n^* + L\eta/n)^{-1}$. This relation agrees with Eq. (11) in Ref. [9] for $\Delta U_C = 0$. In the large N limit a Drude-like (Ohm's law) expression is obtained for the conductivity of a thick multilayer

$$\sigma = \frac{e^2}{4\pi} \lim_{N \rightarrow \infty} N L G^{(N)} / A = \frac{2e^2}{3\pi} \frac{1}{\alpha} \frac{1}{L} \quad (14)$$

which agrees with the results of Zhang and Levy [8]. The Drude result is approached rather slowly.

For a magnetic multilayer it is now straightforward to find the conductance by including spin-dependent interface scattering and bulk scattering. The difference in mean free number of traversed interfaces between both spin channels is ΔN and the spin-averaged result is N . The relative magnetoresistance of an antiferromagnetically coupled multilayer $\Delta G/G$ is shown in Fig. (3), where $\Delta G = G^F - G^A$ and $G = (G^F + G^A)/2$.

The relative magnetoconductance depends on the ratios $\Delta R/R$ and N/Q . The spin-valve effect increases with the number of bilayers and saturates at the Drude limit for $N \gg R$ as given by Zhang and Levy [8]. In this limit of a magnetic superlattice the relative magnetoconductance is $(\Delta G/G)_{D=0} = (\Delta N/2N)^2$.

The effect of the potential steps and different effective masses in the materials on the conductance can be found by concatenation of Eq. (6). This should be done numerically since the expression for the N-layer conductance is very complicated.

In summary, we have derived semiclassical expressions for perpendicular transport through disordered interfaces which are exact for the present model. The effect of a different effective mass to the right and to the left of the interface is included in the formalism. In the weak scattering limit the effect of a non-zero average of the random potential on the conductance is found to be of a higher order in the concentration of scatterers n/a and can be neglected in most cases. An experiment to check the theory is proposed which might lead to a deeper understanding of the scattering process and the microscopic structure of disordered interfaces. A simple, semiclassical formula for the giant magnetoconductance of antiferromagnetically coupled magnetic multilayers in terms of the mean free number of traversed interfaces for the majority and minority spins is derived.

This work is part of the research programme of the "Stichting voor Fundamenteel Onderzoek der Materie (FOM)", which is financially supported by the "Nederlandse Organisatie voor Wetenschappelijk Onderzoek (NWO)".

References

- [1] Permanent address: University of Trondheim, The Norwegian Institute of Technology, Faculty of Physics and Mathematics, Division of Physics, N-7034 Trondheim.
- [2] K. Fuchs, *Proc. Philos. Camb. Soc.* **34**, 103 (1938).
- [3] T. Ando, A. B. Fowler, and F. Stern, *Rev. Mod. Phys.* **54**, 437 (1982).
- [4] R. Landauer, *Z. Phys.* **B 86**, 217 (1987).
- [5] S. B. Soffer, *J. Appl. Phys.* **36**, 1710 (1967).
- [6] M. N. Baibich, J. M. Broto, A. Fert, F. Nguyen van Dau, and F. Petroff, *Phys. Rev. Lett.* **21**, 2172 (1983); G. Binasch, P. Grünberg, F. Saurenbach, and W. Zinn, *Phys. Rev. B* **39**, 4828 (1989). For a recent review see R. Coefourn, *Europe Physics News* **24**, 45 (1993).
- [7] W. P. Pratt, S. F. Lee, R. Lolee, P. A. Schroeder and J. Bass, *Phys. Rev. Lett.* **66**, 3060 (1991).
- [8] M. A. M. Gijs, S. L. J. Lenczowski and J. B. Giesbers, preprint.

- [9] S. Zhang and P. M. Levy, *J. Appl. Phys.* **69**, 4786 (1991); S. Zhang and P. M. Levy, *Phys. Rev.* **45**, 8559 (1992); H. E. Camblong, S. Zhang, and P. M. Levy, *Phys. Rev. B* **46**, 4735 (1992).
- [10] G. E. W. Bauer, *Phys. Rev. Lett.* **69**, 1676 (1992). The Erratum **70**, 1733 (1993) is superseded by the present results.
- [11] R. Q. Hood and L. M. Falicov, *Phys. Rev. B* **46**, 8287 (1992).
- [12] T. Valet and A. Fert, preprint.
- [13] Y. Asano, A. Oguri and S. Maekawa, preprint.
- [14] A. Brataas and G. E. W. Bauer, preprint.
- [15] M. Cahay, M. McLennan and S. Datta, *Phys. Rev. B* **37**, 10125 (1988).
- [16] P. H. Bagwell, *Phys. Rev. B* **41**, 10354 (1990).
- [17] P. A. Lee and T. V. Ramakrishnan, *Rev. Mod. Phys.* **57**, 2 (1985).
- [18] J. Inoue, A. Oguri, and S. Maekawa, *J. Phys. Soc. Jpn.* **60**, 376 (1990).

A. G. Markelz, E.G. Gwinn, M. S. Sherwin
Center for Free Electron User Studies, University of California, Santa Barbara
C. Nguyen and H. Kneumer
Electrical and Computer Engineering, University of California, Santa Barbara

[illegible]

Recently, high quality In_{0.5}As_{0.5} wells have been grown with 3D electron densities as high as $\sim 10^{19}$ cm⁻³ in the InAs wells.⁴ The density-, mass-, and frequency-dependence of the free-carrier, third-order susceptibility $\chi^{(3)}$ due to non-parabolicity in narrow-gap semiconductors leads one to expect that these wells should be strongly nonlinear materials at far-infrared frequencies. For degenerate, bulk material, $\chi^{(3)}$ is

$$\chi'(\omega, \omega, \omega) = \frac{\kappa^2}{m^2} \frac{l}{(\omega - \frac{1}{2}l)(\omega - \frac{1}{2}l + \frac{1}{2}E_0)} \frac{l + \frac{1}{2}E_0}{5E_0} \quad (1)$$

where τ is the momentum relaxation time [4, 5]. This relation, which is derived assuming a perturbative fundamental field, has been confirmed experimentally in *bulk*, n-type InAs [6]. However we find that the density dependence of $\chi^{(3)}$ for InAs quantum wells cannot be described solely by a nonparabolicity as in Eq. 1, and that $\chi^{(3)}$ depends on the incident intensity, indicating non-perturbative response.

The sketch on the left side of Fig. 1 shows the structure of the MBE-grown, 150 Å-wide InAs quantum wells studied here. The 1.35 eV conduction-band offset between the InAs and the AlGa barrier allows large sheet densities. Samples with $n_s = 2.5 \times 10^{12} \text{ cm}^{-2}$ and $n_s = 4 \times 10^{12} \text{ cm}^{-2}$ are δ -doped by Fe sheets set back 500 Å from the top side of the wells. For the $n_s = 8 \times 10^{12} \text{ cm}^{-2}$ sample, the Fe sheets are set back by 100 Å from each side of the well. Table 1 gives the effective mass at the Fermi energy and the 300 K mobility. Mobilities and n_s were measured in a Van-der-Pauw geometry. The effective masses for two of the samples were determined from 4.2 K cyclotron resonance measurements, and in both cases agreed well with the Kane model [28]. Because n_s is nearly independent of temperature, we extract these masses

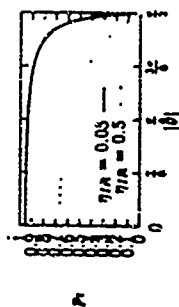


Figure 1: Fraction of electrons transmitted specularly as a function of incoming angle to the normal of the interface. The specularity factor is shown for $\eta_R = 0.35$ at $\eta_R = 0.5$ (dotted line).

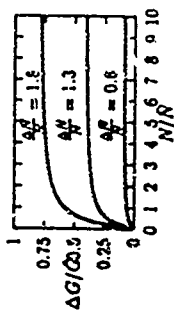


Figure 2: Conductance for a metallic multilayer. The dotted line is the conductance where only specular scattering is considered. The solid line shows the conductance where diffuse scattering is included.

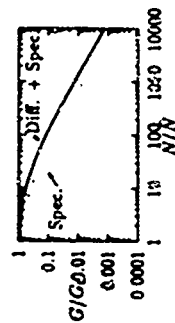


Figure 3: Magnetoresistance for an antiferromagnetically coupled magnetic multilayer. The curves illustrate the effect of spin dependent mean free number of traversed interfaces

to apply to our 300 K experiments. The effective mass for the lowest density sample was calculated using the Kane model [8].

The right side of Fig. 1 shows the optical set-up. After a small fraction of the power in the incident beam is split off to a reference detector, the radiation is focused at normal incidence on the sample. We vary the power by inserting polarizing attenuators before the beam splitter.

The radiation from the sample is collimated over a short section, and focused onto a cooled bolometer through a high-reflection, low-pass waveguide filter, which prevents the fundamental radiation from reaching the bolometer. A Fabry-Pérot etalon in the collimated beam

Table 1. Parameters of the tested wells.

n_s (10^{12} cm^{-2})	2.5	4.0	8
m^*	0.051	0.0421	0.057
μ ($10^4 \text{ cm}^2/\text{Vs}$)	1.9	2.2	1.9
Effective mass calculated from Kane model for this sample only			

is used to measure the frequency content of the radiation from the sample.

In preliminary experiments, we used a CO_2 TEA-pumped methyl fluoride molecular gas laser (MGL) at 29.5 cm^{-1} . The MGL provides short pulses with peak power to several MW/cm². For the $n_s = 8 \times 10^{12} \text{ cm}^{-2}$ sample, Fabry-Pérot scans showed that the sample emitted odd harmonics up to the 7th order [9]. To our knowledge, this is the highest order harmonic generation seen from a semiconductor sample. Because our MGL has complex, erratic pulse structure, it is unsuitable for quantitative measurements of nonlinear susceptibilities. To

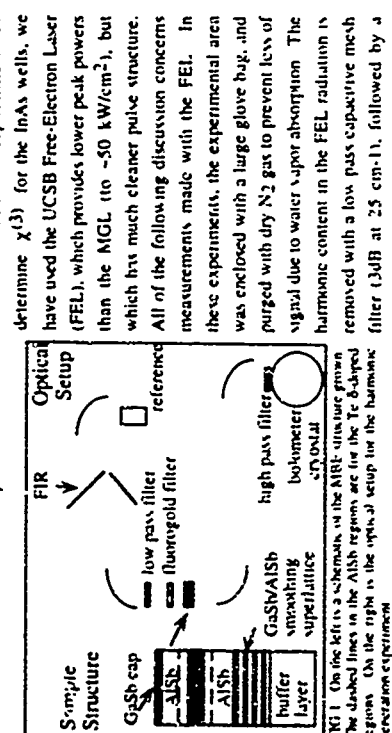


FIG 1. On the left is a schematic of the MBE structure grown. The dashed lines in the AISh regions are for the Te-doped regions. On the right is the optical setup for the harmonic generation experiment.

detect only third harmonic radiation from the electron gas in the InAs wells, improved FEL peak power may make observable the higher-order harmonics found with the MGL.

For all of the samples studied, and for all frequencies investigated (from 19 cm^{-1} to 23 cm^{-1}), we find that the intensity of the third harmonic emitted by the samples, $I(3\omega)$, has a sub-cubic dependence on the fundamental intensity, $I(\omega)$, to the lowest $I(\omega)$ that produces a detectable signal. In the most commonly studied regime of nonlinear response, the fundamental field can be treated perturbatively, and the intensity of the n th harmonic scales as the n th power of the fundamental: $I(n\omega) \propto I(\omega)^n$. Thus, the observed sub-cubic dependence of $I(3\omega)$ on $I(\omega)$ may indicate that our wells are in a non-perturbative regime. Mayer and Keilmann have also shown sub-cubic power dependence in experiments on free-carrier third harmonic generation from n-GaAs [1], at the much higher peak powers provided by a MGL. They ascribed this behavior to intervalley scattering from the Γ valley to the L valley, where $\chi^{(3)}$ should be much smaller. For InAs, the Γ to L valley energy difference is 1.17 eV , compared to $\sim 0.3 \text{ eV}$ in GaAs. Thus, it is not likely that intervalley scattering can explain the power dependence that we observe.

To compare our results on InAs quantum wells to earlier results on bulk InAs [6], we have made an absolute determination of $\chi^{(3)}$, which is proportional to $[I(3\omega)/I(\omega)^3]^{1/2}$. Reference materials with known $\chi^{(3)}$ are unavailable at the frequencies used here. The fundamental intensity incident on the sample is found from the spot size measured at the sample plane, and from the incident power, which is measured with an electrically-calibrated photo-acoustic detector (Thomson Keating). The collected third harmonic intensity is calibrated by tuning the FEL to 3ω and measuring the bolometer response through the high pass filter, relative to the response of the photo-acoustic detector.

We find a bulk $\chi^{(3)}$ by treating the InAs well as a bulk slab with $n_D = n/150 \text{ \AA}$. To account for etalon and phase matching effects, we use Bethune's method for calculating the harmonic field for a multilayer system [10]. This gives a calculated linear transmission that agrees well with the transmission measured with an FTIR. $\chi^{(3)}$ is calculated as:

$$\chi^{(3)} = \frac{I(3\omega)}{I(\omega)^3} \frac{1}{\sqrt{(n_D)^2 I(\omega)^2}} \quad (2)$$

where $|E_{\text{FEL}}|^2$ is a factor that corrects for phase-matching and standing-wave effects [9].

Figure 2 shows the dependence of $\chi^{(3)}$ on the fundamental field at the plane of the electron gas, for all three samples, at 22 cm^{-1} . The incident polarization is along (110). The decrease in $\chi^{(3)}$ with increasing fundamental field reflects the sub-cubic behavior discussed above. The dependence of $\chi^{(3)}$ on carrier density shown in Fig. 2 does not agree with Eq. 1; the sample with the middle charge density has the largest $\chi^{(3)}$. However, for the low test density

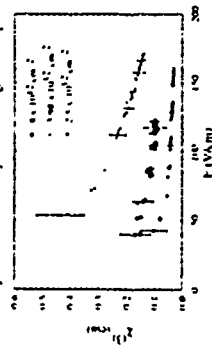


FIG 2. $\chi^{(3)}$ measured at 22 cm^{-1} for the three samples with field at the well.

Enhancement of Free-to-bound Transitions due to Resonant Electron Capture in Be-doped AlGaAs/GaAs Quantum Wells

K. Muraki, Y. Takahashi*, A. Fujiiwara, S. Fukatsu, and Y. Shiraki

Research Center for Advanced Science and Technology (RCAST),

The University of Tokyo,

4-6-1 Komaba, Meguro-ku, Tokyo 153, Japan

*IBM Research, Tokyo Research Laboratory, 1623-14,

Shimo-Ogino, Yamato, Kanagawa 242, Japan

We report a new phenomenon concerning the photoluminescence from $\text{Al}_x\text{Ga}_{1-x}\text{As}/\text{GaAs}$ quantum wells with Be-doping at the well center. For excitation photon energy larger than the barrier band gap, the relative intensity of the free-to-bound and the excitonic transitions was found to display a strong oscillation as a function of the well width. For "resonant" well widths, the free-to-bound transition was observed to be 2 times as strong as the excitonic transition. We correlate this phenomenon with the electron capture efficiency from the barrier into the well, which also exhibits a similar oscillation as a function of the well width.

Photoluminescence (PL) spectra of undoped quantum wells are usually dominated by intrinsic, i.e., free exciton transitions even at very low temperatures. This makes a sharp contrast to bulk material, in which extrinsic luminescence dominates the low-temperature spectra even in samples of highest purity. This difference has been attributed to the enhanced radiative transition rate of free excitons in quantum wells which results from the increased binding energy and the broken translational symmetry along the quantization axis, i.e., the lack of polarization effect [1]. Thus, in undoped quantum wells most of the photo-generated carriers recombine as free excitons before they are captured by residual impurities. To this end, studies of impurity-related luminescence in quantum wells have been done mainly on intentionally doped samples. Various spectral features originating from heavy-hole excitons bound to neutral and ionized donors [2-4] and acceptor acceptors [5] have been identified. Free-to-bound transitions, however, are usually very weak or absent even in doped samples [5]. Holitz et al. have reported that the resonant excitation at the heavy- or light-hole exciton energy enhances the free-to-bound transition in Be-doped quantum wells [6]. For acceptor-doped quantum wells, however, they have reported that the free-to-bound transition was not observed for Be-doping concentrations of $5 \times 10^{18} \text{ cm}^{-3}$ per well.

In this paper, we report a new phenomenon concerning the photoluminescence from $\text{Al}_x\text{Ga}_{1-x}\text{As}/\text{GaAs}$ quantum wells with Be-doping at the well center ($[\text{Be}] = 10^{18} \text{ cm}^{-3}$). Under excitation by light with photon energy larger than the barrier band gap, we have observed a significant enhancement of the free-to-bound transition for particular well widths. Furthermore, the relative intensity of the free-to-bound and the excitonic transitions displayed a strong oscillation as a function of the well width, featuring a series of resonance peaks appearing periodically. For these "resonant" well widths, the free-to-bound transition was observed to be 2 times as strong as the excitonic transitions. We correlate this phenomenon with the electron capture efficiency from the barrier into the well, which also exhibits a similar oscillation as a function of the well width [7,9].

Samples are $\text{Al}_x\text{Ga}_{1-x}\text{As}/\text{GaAs}$ ($x = 0.3$) quantum well structures grown at 580°C on semi-insulating GaAs (100) substrates in a molecular beam epitaxy reactor (VG semiconductor). Each sample contained several GaAs quantum wells separated by 30-nm AlGaAs barriers. Be was delta-doped at the well center at an areal density of 10^{18} per well. Delta-doping was employed to minimize the spectral broadening due to the variation of the bound exciton energy with the doping position [10]. Photoluminescence was measured at $6.8 \pm 0.17 \text{ K}$ using an Ar^+ ion laser as the excitation light source. The excitation power density was about 0.3 W/cm^2 .

sample, the magnitude of $\chi^{(3)}$ is comparable to that expected from scaling the bulk susceptibility calculated by Jha and Bloembergen for bulk InAs [3] to our frequencies and mobilities. We calculate a bulk $\chi^{(3)}$ of 0.06 e.u. for $n_0 = 1 \times 10^{18} \text{ cm}^{-3}$, which corresponds to a sheet density $n_s = 1.5 \times 10^{12} \text{ cm}^{-2}$ for a 150 \AA slab. This reasonable agreement with the range of $\chi^{(3)}$ observed for our lowest density sample may be fortuitous, due to the apparent non-perturbative response, and the unusual density-dependence of $\chi^{(3)}$.

Finally, we show that the measured anisotropy in $\chi^{(3)}$ is consistent with the crystal symmetry of InAs. Figure 4 shows the dependence of $\chi^{(3)}$ at fixed incident intensity on the polarization of the incident field, for the $n_s = 2.5 \times 10^{12} \text{ cm}^{-2}$ sample. The maxima in $\chi^{(3)}$ occur when the polarization is aligned with the (110) axis, and $\chi^{(3)}$ has the expected 90 degree periodicity. A cosine-squared fit to the data gives an anisotropy of 1.18 ± 0.03 , comparable to the measured value for GaAs at 25 cm^{-1} [1]. All samples and all frequencies measured give comparable anisotropy.

In conclusion, we have found that electrons in single, remotely-doped InAs wells produce large, 300 K $\chi^{(3)}$ ($\sim 1 \text{ e.u.}$, relative to a GaAs $\chi^{(3)} \sim 10^{-4} \text{ e.u.}$) and non-polyacetylene ($\chi^{(3)} \sim 10^{-7} \text{ e.u.}$) [2]. It may be that a useful device can be fabricated from a superlattice of InAs wells. Future work requires extending our sensitivity to lower powers, at which we expect to recover a cubic power dependence, and cooling the sample to help elucidate the scattering contribution to $\chi^{(3)}$.

The authors would like to thank S. J. Allen Jr., J. Heyman, N. G. Astar, and K. C. Chang for many useful discussions, and Matt Sundaram for providing us with the results of his cyclotron resonance experiments. In addition, we are grateful for the assistance of the staff at the Center for Free Electron Laser Studies. Work at the Center for Free Electron Laser Studies was supported by the Office of Naval Research (N00014-92-1-1452). Clean room use was supported by the NSF Center for Quantum Electronics, Stanford, Grant No. DMR88-11410.

- [1] A. Mayer and F. Kernmann, Phys. Rev. B 33, 6962 (1986).
- [2] C. Halvorsen, D. Moxey, F. W. Hapler, Y. Cao, A. H. Heeger, Syn. Met. 49-50, 49 (1992).
- [3] C. Nguyen, B. Bar, C. R. Bolognesi, J. J. Pekarik, H. Kroemer, J. H. English, J. Elec. Mat. 22, 255 (1993).
- [4] S. S. Jha and N. Bloembergen, Phys. Rev. 171, 891 (1968).
- [5] P. A. Wolff and G. A. Pearson, Phys. Rev. Lett. 17, 1015 (1966).
- [6] J. J. Wynne, Phys. Rev. 178, 1295 (1969).
- [7] M. Sundaram, S. J. Allen Jr., C. Nguyen, H. Kroemer, to be published.
- [8] E. O. Kane, J. Phys. Chem. Solids 1, 239 (1957).
- [9] A. G. Markel et al., to be published.
- [10] D. S. Bethune, J. Opt. Soc. Am. B 6, 910 (1989).

Figure 1 shows the 17 K photoluminescence spectra of a sample containing four quantum wells with various well widths. Peaks labeled FE and BE are due to the radiative decay of free excitons and excitons bound to neutral acceptors, respectively. The energy separation between FE and BE, i.e., the binding energy of an exciton to a neutral acceptor, is 4.1 and 4.3 meV for the 9.0- and 6.3-nm wells, respectively. These values compare favorably with the reported value [5]. For narrower two wells, FE and BE are not resolved because of the increased inhomogeneous broadening. The peaks at 1.329 and 1.397 eV, labeled F-B, are assigned to the free-to-bound transitions associated with the 9.0- and 4.5-nm wells, respectively, in which electrons in the $n = 1$ conduction subband recombine with holes bound to neutral acceptors. It is surprising that such narrow peaks are observed for the free-to-bound transition in quantum wells with low doping concentrations. More interesting is that the free-to-bound transition is absent for the 6.3- and 3.2-nm wells through the doping concentration is the same. These observations lead us to speculate that the relative intensity of the free-to-bound and the excitonic transitions is a strong function of the well width.

In order to investigate the well-width dependence in more detail, we adopted the following procedure: in the molecular beam epitaxy of the samples the substrate rotation was deliberately interrupted during the growth of the quantum well layer, thereby allowing the well width to vary across the wafer due to inhomogeneous Ga beam flux. Thus, by scanning the laser spot on the sample, we can systematically investigate the PL spectrum as a function of the well width. In Fig. 2 photoluminescence spectra taken at 6 K are shown for various well widths. The well width was calculated from the transition energy of the $n = 1$ band-to-hole free exciton. It is seen that the relative intensity of the free-to-bound transition and the excitonic transition drastically changes with the well width. Meanwhile the total intensity remains the same.

In Fig. 3 the PL intensity ratio of the free-to-bound transition to the excitonic (free exciton plus bound exciton) transition is plotted as a function of the well width. The PL intensity ratio exhibits a strong oscillation as a function of the well width. Up to five peaks labeled M_n ($n = 2-6$) are clearly observed, accompanied by subsidiary peaks labeled L_n ($n = 2-5$). (The peaks L_5 and M_6 are overlapped.) It is noteworthy that the M_n peaks appear almost periodically with a period of about 3.7 nm.

We have further carried out the PL mapping experiments with various excitation photon energies from below and above the barrier band gap using an Ar⁺ ion laser pumped dye (DCM) laser and a Ti:sapphire laser. The results were almost the same as that in Fig. 3 when the excitation photon energy is larger than the barrier band gap. In contrast, the oscillation is not observed for the below-barrier excitation [11]. These results strongly suggest that the capture of carriers from the barrier into the well is the controlling process causing the oscillation. According to the effective-mass calculation taking the conduction band nonparabolicity [12] into account, the position of the M_n peak corresponds to the well width for which the energy of the n -th conduction subband in the quantum well coincides with the conduction band-edge of the barrier. And that of the L_n peak compares favorably with the well width for which the energy of the n -th conduction subband lies near the L₂-photon energy (36 meV) below the barrier band-edge. Brum and Bastard [7] have calculated the capture time of carriers as a function of the well width, and predicted that for such well widths the electron capture efficiency is remarkably enhanced. The experimental evidence for this, the resonant electron capture, has been first given by Fujiwara et al. using cv-photoluminescence [18]. And recently, the resonant electron capture time has been successfully measured by Blum and co-workers using subpicosecond luminescence technique [9]. Therefore, it is reasonable to consider that the free-to-bound transition is enhanced when the electron capture efficiency is high.

We explain this by considering the charge build-up in the quantum well induced by the different capture time of electrons and holes. Photogenerated excitons as equal number of electrons and holes in the barrier, however, one of these two types of carriers can be captured preferentially depending on their capture time. In the steady-state, the number of electrons and holes captured per unit time must be equal. It should be noted, however, that the number of electrons and holes present in the well can be different even in the steady-state. Thus, the negative charge will build-

up in the quantum well if the capture time of an electron is shorter than that of a hole. In the usual off-resonant conditions, the capture time is shorter for holes due to the larger density of states in the valence band [7]. In this hole-rich condition the excess holes will intrinsically neutralize the ionized acceptors, if present. Thus, all the acceptors remain neutral at low temperatures. Since the radiative lifetime of the free-to-bound transition is much longer than that of the excitonic [13], most of the carriers recombine as excitons in this case. In the resonant condition, on the other hand, the capture efficiency becomes larger for electrons. In this electron-rich condition the excess electrons, which can not participate in exciton formation, will recombine with holes bound to acceptors, thereby creating ionized acceptors. These ionized acceptors are subsequently neutralized by trapping free holes, which decreases the number of holes available for the exciton formation. As a result, the exciton formation is quenched and excess electrons are left in the conduction subband. These electrons recombine with holes bound to neutral acceptors as in the first step. Since this consecutive-like chain reaction, only a slight excess of electrons can lead to a drastic enhancement of the free-to-bound transition. This qualitatively explains the correlation between the enhancement of the free-to-bound transition and the electron capture efficiency.

In summary, we have reported a new phenomenon concerning the photoluminescence from quantum wells doped with Be. For above-barrier excitation, a strong oscillation of the relative intensity of the free-to-bound and the excitonic transition was observed as a function of the well width. This phenomenon has been tentatively attributed to the charge build-up in the quantum well induced by the resonant capture of electrons, and the resultant ionization of the acceptors. These ionized acceptors quench the exciton formation by trapping free holes out of the photogenerated electron-hole pairs and enhance the free-to-bound transition. Since this charge build-up is not specific to Be-doped quantum wells and considered to occur generally in quantum well structures, we expect that it might shed light on some aspects of the carrier-dynamics in intrinsic quantum wells. However, further investigation is required to confirm this assertion.

One of the authors (K.M.) was supported by Fellowships for Japanese Junior Scientists (JSPS). The authors thank to S. Ohake for technical assistance.

References

1. J. Feldmann, G. Peter, E. O. Gobel, P. Dawson, K. Mawer, C. Fritton, and R. J. Elliott, *Phys. Rev. Lett.* **59**, 2337 (1987).
2. Y. Nimura, K. Shirozaki, and M. Ichi, *J. Appl. Phys.* **58**, 1864 (1985).
3. X. Liu, A. Petrou, B. D. McCombe, J. Rajan, and G. Wicks, *Phys. Rev. B* **38**, 4522 (1988).
4. D. C. Reynolds, C. E. Leak, K. K. Bajaj, C. E. Stutz, R. L. Jones, K. R. Evans, P. W. Yu, and W. M. Theiss, *Phys. Rev. B* **40**, 6210 (1989).
5. P. O. Holtz, M. Sundaram, K. Doughty, J. L. Merr, Jr., A. C. Gossard, *Phys. Rev. B* **49**, 12338 (1989).
6. P. O. Holtz, M. Sundaram, J. L. Merr, Jr., and A. C. Gossard, *Phys. Rev. B* **41**, 1489 (1990).
7. J. A. Brum, and G. Bastard, *Phys. Rev. B* **33**, 1420 (1986).
8. A. Fujiwara, S. Fukatsu, Y. Shiraki, and R. Ito, *Surf. Sci.* **243**, 642 (1992).
9. P. W. M. Blum, C. Smut, J. E. M. Haverkort, and J. H. Winkler, *Phys. Rev. B* **47**, 2172 (1993).
10. G. C. Rine, P. O. Holtz, M. Sundaram, J. L. Merr, Jr., A. C. Gossard, and B. Mawer, *Phys. Rev. B* **44**, 4010 (1991).
11. For below-barrier excitation, the PL intensity ratio depends on the excitation photon energy rather than the well width, which is far beyond the scope of this study and will be published elsewhere.
12. T. Rul and M. Cardona, *Phys. Rev. B* **41**, 11747 (1990).
13. We have performed time-resolved measurements and observed the radiative decay time of the free-to-bound transition as long as 34 ns, which will be published in the future.

Constructive Superposition of Field- and Carrier Induced Absorption Changes in Hetero-n-i-p-i Structures

M. Kneissl, K.H. Guldén, P. Kiesel, A. Lützel, S. Malzer, G.H. Döhler
Institut für Technische Physik, Universität Erlangen,
Erwin-Rommel-Str. 1, 91058 Erlangen, Germany

X. Wu and J.S. Smith
University of California at Berkeley, Berkeley, CA 94720, USA

By applying a voltage U_{on} to hetero-n-i-p-i structures with n- and p-contacts, both the internal fields in the intrinsic layers and the carrier concentrations in the quantum wells are changed. Therefore, large changes of the absorption coefficient can be achieved simultaneously by field effects and phase space filling. In this paper we demonstrate that a constructive superposition can be achieved by shifting the bandfilling contribution to lower photon energies in type-I hetero-n-i-p-i crystals. A 25 period InGaAs/GaAs hetero-n-i-p-i structure with 10 nm pseudomorphic $\text{In}_{0.07}\text{Ga}_{0.93}\text{As}$ quantum wells was grown by "shadow mask MBE" in order to obtain selective contacts to the n- and p-layers. At room temperature a relative transmission change of more than 2:1 at photon energies of 1.39 eV with a voltage swing from -2.5 V to +0.8 V could be demonstrated. This corresponds to a total change of the absorption coefficient of about 2000 cm^{-1} referred to the total sample thickness of 3.55 μm . These large absorption changes ($\Delta\alpha$) are a consequence of the constructive superposition of the Franz-Keldysh effect in the intrinsic layers and phase space filling in the InGaAs quantum wells. Comparing our experimental results with theory we deduce a maximum $\Delta\alpha$ of more than 10000 cm^{-1} (referred to the total quantum well thickness) by bandfilling, whereas the Franz-Keldysh effect contributes a $\Delta\alpha$ of about 1450 cm^{-1} (referred to the total intrinsic layer thickness).

1. Introduction

Recently much effort has been devoted to the study of electro-optic effects in semiconductor crystals for applications in modulators and switches [1,2]. The absorption changes are based either on field effects or on carrier induced phase space filling [3] in n-i-p-i

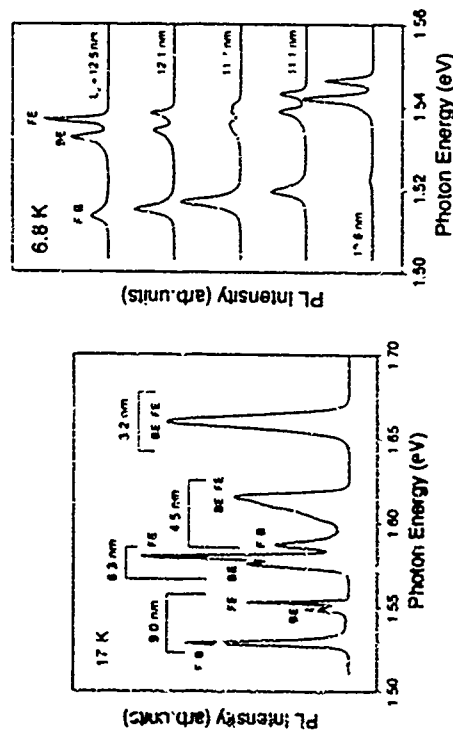


Figure 1
17-K PL spectra of an $\text{Al}_x(\text{Ga}_{1-x})\text{As}$ quantum well structure with various well widths. Each well is doped with Be to an areal density of 10^{10} cm^{-2} .

Figure 2
69-K PL spectra of Be-doped $\text{Al}_x(\text{Ga}_{1-x})\text{As}$ quantum wells with various well widths

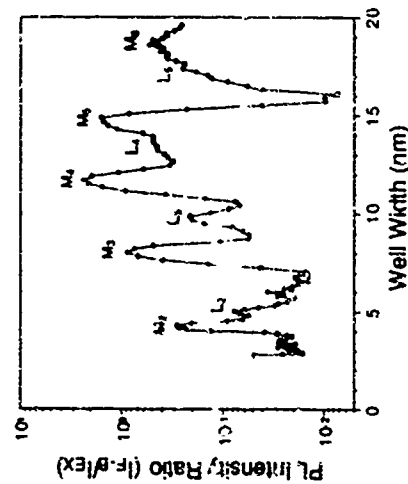


Figure 3
PL intensity ratio of the free to-bound transition to the electronic free exciton plus bound exciton transition as a function of the well width

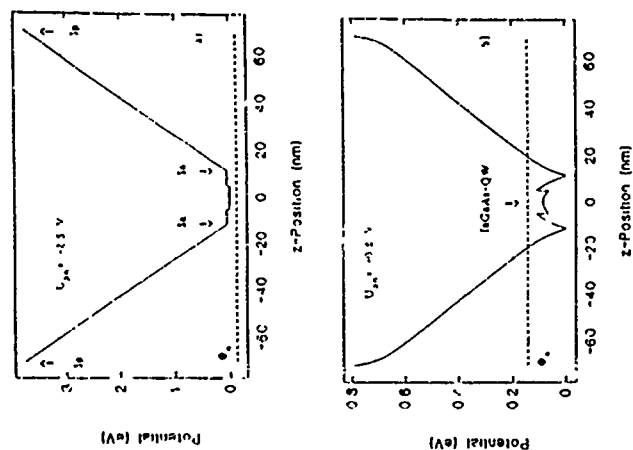


Figure 1. Calculated real space conduction band diagram for the investigated hetero n-i-p-i structure. a) At the threshold voltage $U_{pn} = -2.5$ V, the case where the QW's in the n-region are completely depleted. b) At a forward bias of $U_{pn} = +0.8$ V with $J_{ph} = 2.5 \cdot 10^{12} \text{ cm}^{-2}$, the case where the QW's have different energy levels in part a) and b).

$1.3 \cdot 10^{15} \text{ V/cm}$ and at the same time the carrier concentration in the InGaAs quantum wells rises to $7.4 \cdot 10^{12} \text{ cm}^{-2}$ (see Fig. 1b). This leads simultaneously to a reduction of the absorption coefficient in the intrinsic GaAs layers, due to the Franz-Keldysh effect and also in the QW's, due to phase space filling. By using a suitable sample design we succeeded in shifting the bandfilling contribution to lower photon energies, so that a constructive superposition of field and carrier induced absorption changes is achieved.

crystals both effects are present [4]. Strong changes of the absorption coefficient up to 8000 cm^{-1} have been achieved by bandfilling in hetero-n-i-p-i structures [5,6]. However, the active region in such structures is very small, which limits the performance of modulator devices. In homo-n-i-p-i doping superlattices field induced changes of the absorption coefficient due to the Franz-Keldysh effect of about 2000 cm^{-1} have been demonstrated [7]. The active region in these structures can extend over almost the whole sample thickness especially in δ -doped n-i-p-i devices. Both phenomena, field and bandfilling effects, contribute simultaneously to the absorption changes in n-i-p-i structures. However, in homo-n-i-p-i crystals a significant contribution of both effects occurs just above the bandgap where the two effects have opposite signs. Therefore, a reduction of the pure Franz-Keldysh induced absorption changes above the bandgap is observed as a result of the destructive superposition of these two effects. On the other hand the maximum field and bandfilling induced absorption changes in hetero-n-i-p-i devices so far occur at different photon energies. In this paper we demonstrate that in a type-I-hetero-n-i-p-i structure the bandfilling contributions can be shifted to lower photon energies, so that a constructive superposition of the two effects is achieved.

II. Experiment

The investigated InGaAs/GaAs-hetero n-i-p-i crystal consists of 25 pseudomorphic $\text{In}_{0.07}\text{Ga}_{0.93}\text{As}$ quantum wells imbedded in a GaAs δ -doped n-i-p-i structure. The 10 nm wide QW's are modulation doped on both sides with $\delta n(2) = 4.5 \cdot 10^{12} \text{ cm}^{-2}$ and 7 nm thick GaAs spacer layers. The width of the intrinsic GaAs layer is 59 nm, the $\delta p(2)$ doping is $1.1 \cdot 10^{12} \text{ cm}^{-2}$. The total sample thickness is 355 μm . The n-i-p-i crystal was grown by a new epitaxial "shadow mask MBE" technique which allows the *in situ* lateral structuring of the doping profile on a μm scale. This enables the fabrication of n-i-p-i doping superlattices with built-in high selective and ohmic contacts [8,9]. By applying an external voltage U_{pn} to the n- and p-layers, the electric field in the intrinsic GaAs region and the carrier density in the InGaAs quantum wells is tuned simultaneously. Figure 1 shows the calculated real space conduction band diagram for the investigated sample. At a certain threshold voltage, in this case $U_{pn} = -2.5$ V, the quantum wells in the n-layers are completely depleted. Therefore, the absorption coefficient of the InGaAs-QW's is expected to be very high for photon energies near and above the lowest QW electronic transition. At the same time the electric field in the intrinsic GaAs layer reaches its maximum value of $6.3 \cdot 10^5 \text{ V/cm}$. At such high fields, the absorption coefficient below the GaAs bandgap which is due to the Franz-Keldysh effect, is also very large (see Fig. 1a). By applying a forward bias of $U_{pn} = +0.8$ V the electric field decreases to

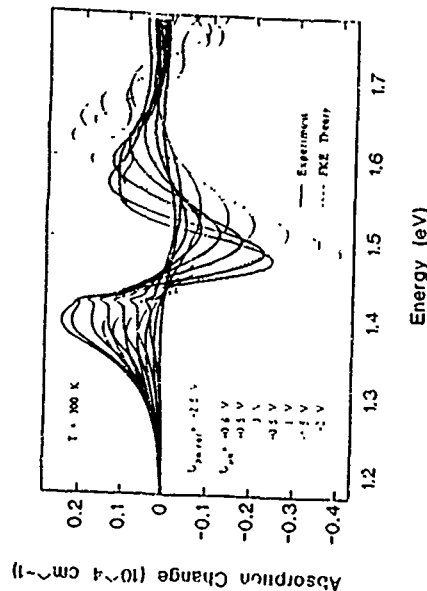


Figure 3: The solid curves show the absorption changes for different voltage swings derived from the transmission measurements in Fig. 1. The dotted lines exhibit the calculated absorption changes due to the Franz-Keldysh effect for the corresponding different electric fields in the intrinsic GaAs region. All curves are related to the total intrinsic layer thickness of $2.75 \mu\text{m}$. Below the GaAs bandgap ($E_{\text{gap}} = 1.42 \text{ eV}$) the bandfilling and the field contributions superpose constructively. This leads to an enhancement of the absorption changes for photon energies below the bandgap. Above the GaAs bandgap both effects superpose destructively and therefore the absorption changes are reduced.

have opposite signs. Therefore, the observed absorption changes for photon energies above the bandgap are reduced, compared to the Franz-Keldysh changes. Figure 4 shows the difference spectra between the measured and the calculated Franz-Keldysh-absorption changes related to the total QW thickness of $d_{\text{QW}} = 250 \text{ nm}$. The resulting curves should only contain the absorption changes due to phase space filling, providing that the non-uniformity of the field in the intrinsic GaAs layers and its influence on the Franz-Keldysh-absorption can be neglected. For photon energies below the GaAs bandgap maximum absorption changes of almost 15000 cm^{-1} due to phase space filling are deduced. As can be seen in Fig. 1 b) bandfilling does not only occur in the InGaAs-QW's but also in the adjacent GaAs region, which also leads to large absorption changes above the GaAs bandgap. In this energy region, however, the Franz-Keldysh and the bandfilling induced absorption changes have opposite signs which results in a destructive superposition of the two effects.

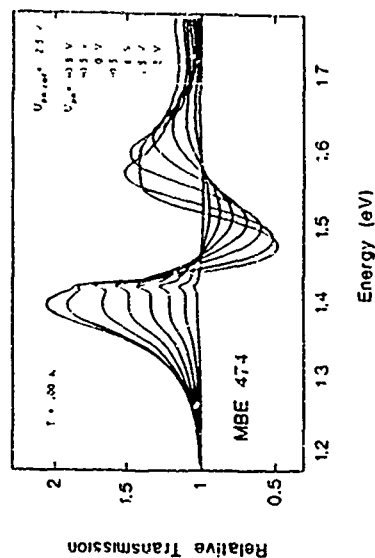


Figure 2: Measured relative transmission spectra for 25 periods of a superlattice structure $\text{In}_{0.53}\text{Ga}_{0.47}\text{As}/\text{GaAs}$ type I nitride $\text{n}^+\text{-p}^+\text{-n}^+$ structure. The Quantum wells ($E_{\text{QW}} = 10 \text{ meV}$) are modulation doped on both sides with $2 \times 10^{18} \text{ cm}^{-3}$ ($E_{\text{QW}} = 10 \text{ meV}$). The width of the intrinsic region is 50 nm the $\text{In}_{0.53}\text{Ga}_{0.47}\text{As}$ layer is $1.1 \times 10^{17} \text{ cm}^{-3}$. The total sample thickness is $3.35 \mu\text{m}$.

Fig. 2 shows the measured relative transmission spectra for the investigated $\text{n}^+\text{-p}^+\text{-n}^+$ structure. At room temperature a maximum relative transmission change of more than 2.1 around photon energies of 1.37 eV with a voltage swing from -2.5 V to $+0.8 \text{ V}$ is observed. Note that the contrast ratio remains larger than 2.1 over an energy range of more than 26 meV , implying very good stability against temperature variations or wavelength detuning, which is important for device applications. The low switching bias of only 3.2 V is also an attractive feature for applications in integrated optics. The large transmission changes correspond to an absolute change of the absorption coefficient of more than 2000 cm^{-1} referred to the total sample thickness of $3.35 \mu\text{m}$. Figure 3 shows the measured absorption changes (solid lines) and the corresponding calculated $\Delta\alpha$ due to the Franz-Keldysh effect in the intrinsic GaAs layers (dotted lines). All curves are related to the total intrinsic layer thickness of $d_{\text{QW}} = 2.75 \mu\text{m}$. Comparing our results with the calculated Franz-Keldysh data, these large absorption changes can only be explained by the superposition of field effects in the intrinsic regions and phase space filling in the InGaAs-QW's. At photon energies below the GaAs bandgap ($E_{\text{gap}} = 1.42 \text{ eV}$) the superposition is constructive as the field induced absorption changes are enhanced due to the bandfilling contributions of the quantum wells. Above the GaAs bandgap the field and bandfilling absorption changes

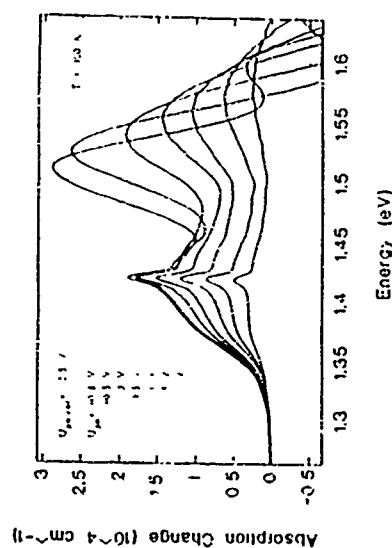


Figure 2: Measured absorption changes $\Delta\alpha$ vs the bandfilling contributions related to the total quantum well thickness (100 nm) for different voltage swings. The carrier concentration in the quantum wells is varied by the external bias U_{bias} from 0 V to 10 V ($U_{\text{bias}} = 0.5 \text{ V}$ up to 0.5 V in 0.5 V steps).

III. Summary

In summary, we have reported on a novel electro-optic modulator device based on the constructive superposition of field and bandfilling absorption changes. A type-II InGaAs/GaAs hetero-n-i-p-i structure was grown by a new shadow mask MBE technique in order to obtain built-in high selective contacts. By applying a voltage U_{bias} to the n-i-p-i crystal, both the fields in the intrinsic GaAs regions and the carrier concentration in the InGaAs quantum wells are varied simultaneously. At room temperature a relative transmission change of more than 2% at photon energies of 1.39 eV with a voltage swing from -2.5 V to +0.8 V has been demonstrated. Comparing our experimental results with theory these large absorption changes are the consequence of the constructive superposition of the absorption changes due to field effects of 1500 cm^{-1} (related to the total intrinsic layer thickness) and bandfilling contributions of the InGaAs-QWs of more than 10000 cm^{-1} (referring to the total QW thickness). By optimizing the design of the hetero-n-i-p-i structure it will be possible to improve on the performance of the modulator device furthermore.

This work was partly supported by the Volkswagen-Stiftung under contract number I/68 042

References

- 1 B.S. Rybin, Phys. Stat. Sol. (b), 150, 567 (1988)
- 2 D.A.B. Miller, D.S. Chemla, T.C. Damen, A.C. Goswami, W. Wiegmann, T.H. Wood, and C.A. Burrus, Phys. Rev. B 32, 1023 (1985)
- 3 M. Wegener, J.E. Zucker, T.Y. Yang, N.J. Sauer, K.L. Jones and D.S. Chemla, Phys. Rev. B 41, 309, (1990)
- 4 S. Malzer, N. Linder, K.H. Guldien, A. Höfner, P. Kiesel, M. Kneissl, X. Wu, J.S. Smith, and G.H. Döhler, Phys. Stat. Sol. (b) 171, 459 (1992)
- 5 A. Larson and J. Materjani, Appl. Phys. Lett. 58, 1946 (1991)
- 6 X. Wu, K.H. Guldien, J. Thomas, J.S. Smith and J.R. Whinnery, S. Malzer, P. Kiesel, M. Kneissl, and G.H. Döhler, Appl. Phys. Lett. 62, 152 (1993)
- 7 P. Kiesel, K.H. Guldien, A. Höfner, M. Kneissl, B. Knäuper, N. Linder, P. Riel, X. Wu, J.S. Smith and G.H. Döhler, Appl. Phys. Lett. 62, 25, (1993)
- 8 G.H. Döhler, G. Hühner, and J.N. Miller, Appl. Phys. Lett. 49, 704 (1986)
- 9 K.H. Guldien, X. Wu, J.S. Smith, P. Kiesel, A. Höfner, M. Kneissl, P. Riel and G.H. Döhler, Appl. Phys. Lett. 62, (1993)

POLARIZATION OF THE SPONTANEOUS EMISSION
OF STRESSED LASER HETEROSTRUCTURESA.A. Ptashchenko, M.V. Doych, N.V. Hironchenko, F.A. Ptashchenko
Odessa University

ul. Petra Velikogo 2, 270100 Odessa, Ukraine

Abstract-measurement system with a polaroid was constructed allowing to detect the degree of the light polarization (ρ) of $0.15 \cdot \rho$ as a function of driving current (I) and axial stress (σ) was studied for spontaneous output of the AlGaAs lasers at low pumping levels. It was found that in the range of sufficiently small currents ρ linearly depends on I and σ . When extrapolated to $I=0$, the ρ depends not only on σ , but also on the light amplification parameters of the individual laser structure. These observations must be taken into account when one attempts to estimate the strain in the active layer of a diode laser through the polarization measurements. The Cassidy's one-dimensional model of the polarization effects in diode lasers was modified to include modulation of the optical absorption by the stimulated emission in the active region at very low pumping intensities.

Introduction

Axial stress in the active region of the semiconductor lasers essentially affects the spectra of the spontaneous and stimulated emission, modifies the threshold current value [1,2]. Mechanical stress in heterostructures enhances degradation processes in diode lasers [3]. The most sensitive method of detecting the anisotropic deformation in semiconductor structures is based on the polarization-resolved measuring of the recombination radiation [4,5]. Polarization technique was successfully used for estimating the strain in the active layer of semiconductor lasers [6,7]. The degree of polarization of the sub-threshold emission from the active region, defined as

$$\rho = (L_1 - L_2) / (L_1 + L_2), \quad (1)$$

where L_1 and L_2 are the light intensities with transverse electric (TE) and transverse magnetic (TM) polarization, was shown to depend on the difference in reflectivity ΔR at the facet mirror as well as on the variation in the single-pass gain for the TE and TM modes [6]. This dependence generally is nonlinear, making difficulties in its using for detecting the strain in semiconductor lasers.

In [6] was postulated that in the range of pumping current $I < I_{th}$, where I_{th} corresponded to the lasing threshold, ρ was approximately independent of current. This assumption allowed the authors [6] to estimate the proportionality coefficient between the ρ and the axial stress σ and, using the nonlinear part of the dependence $\rho(I)$, to obtain the difference in reflectivity ΔR for the TE and TM modes. But the degree of polarization of the spontaneous emission in the range of low pumping levels was not detailed studied. The minimal magnitude of ρ ,

detected with the accuracy of $\pm 20\%$, was 0.01 [4-6]. The purpose of this work was detailed study of the spontaneous light polarization of diode lasers at low pumping levels in order to prove the technique [3] of stress detecting. For this purpose the sensitive polarization measurement system was constructed; the dependences $\rho(I)$ and $\rho(\sigma)$, where ρ denotes external pressure, were studied; the one-dimensional laser model [6] was more detailed analyzed for the case of low driving levels.

Our measurements were performed on the AlGaAs double-heterostructure lasers with stripe geometry. We found that at low pumping intensities the degree of polarization of the spontaneous output of diode lasers was not constant, but linearly depended on the driving current. And the rate of change in ρ with I depended on the individual parameters of a laser. And finally, the proportionality coefficient between $\rho(I)$, extrapolated to $I=0$, and σ was observed to depend on the amplification properties of the individual laser structure.

2. Measurement system

The measurement system is schematically depicted in Fig. 1. Laser diode LD was mounted on the massive copper cooler and pumped by the current source S_1 . Axial stress in the perpendicular plane, pressed to the upper metallized surface of the heterostructure. The pressure was hydraulically regulated. The light output of the laser was collimated with a lens, passed through the polaroid P, rotating with a fixed frequency, and detected by photodiode PD₁. The dc component of the photodiode signal V_1 was proportional to the averaged light intensity $\langle I_{LD} \rangle / 2$. The ac component of the signal V_2 , being proportional to $\rho \cdot \langle I_{LD} \rangle$, was detected by the selective amplifying system light $L_1 - L_2$, was determined as $q \cdot V_2 \cdot \Omega / V_1$, where q was a calibrating coefficient. In order to determine the sign of ρ , the additional optical circuit was used. The output of the light-emitting diode LED was passed through the modulator M, coupled to the rotating polaroid P, and then directed on the photodiode PD₂. The phases of the signals from the photodiodes PD₁ and PD₂ were compared by the phase analyzer PA, giving the sign of ρ . The constructed experimental system allowed measuring the degree of polarization of 0.001 (with the error less than 20%).

3. Experimental results

Fig. 2 represents the degree of polarization of the spontaneous emission ρ , measured under various external pressures correspond to the diode laser DL N°481 with $q > 0$, and the lower curves were measured on the DL N°484 with $q < 0$. One can see that ρ is not constant at low biasing currents. It means that estimation the mechanical stress in the active region of a laser, as basing on the spontaneous emission polarization measurements, is more delicate problem than it was supposed in [6], assuming $\rho = \text{const}$. It is also seen that the axial pressure in the perpendicular direction to the active layer shifts all the curves $\rho(I)$ down in the both cases of positive and negative signs of q . It confirms the conclusion of [1,2,6] that the

compressive strain in this direction increases the intensity of the TM mode and reduces the TE mode. Comparison of the data, presented in Fig. 2, shows that the external pressure decreases the derivative $d\rho_0/dI$. In the most interesting for this work range of low currents, the curves of the Fig. 2 can be approximated by

$$\rho_0 = \rho_0^0 + \beta_1 I, \quad (2)$$

where ρ_0^0 and β_1 are independent of current, but are different for the individual samples. Both the coefficients ρ_0^0 and β_1 decrease with the axial pressure.

Fig. 2 represents the degree of polarization of the spontaneous emission from a facet mirror of the laser DL 451, measured

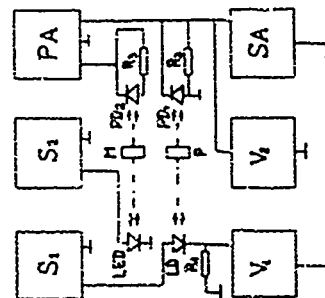


Fig. 1. Schematic diagram of the measurement system.
Fig. 2. Degree of polarization of the lasers as a function of I.

at various driving current as a function of the external pressure. The presented data show that this dependence $\rho_0(I)$ generally is nonlinear, in agreement with the results [5]. In the range of driving current $I < 0.1$ A, where I is threshold current, the curves $\rho_0(I)$ were practically linear for all the investigated laser diodes. Deviations from the linear dependence $\rho_0(I)$ in this range of I were less than 10%. These observations corroborate the conclusion of Cassidy et al. [6] that the range of small pumping currents is most suitable for estimating the strain with the help of the polarization measurements.

4. Comparison with the model [6]

In analysing the obtained experimental data we used the one-dimensional laser model [6]. This model gives for the intensity of the spontaneous emission, partly amplified in the active region,

$$L = \frac{B L (1-R)(G-1)}{\ln G (1-GR)}, \quad (3)$$

where B is the radiative recombination rate in the active layer of the length of L; R is the reflectivity at the facet mirrors; G is single-pass gain

$$G = \exp(\alpha L), \quad (4)$$

α denotes the gain coefficient. For the most interest (in respect to measuring the strain in the active layer) $\alpha \ll \beta$ assuming that the axial stress produces the difference $\Delta\beta$ and $\Delta\alpha$ in values of β and α between the TE and TM modes, and that $\Delta\alpha/\alpha \approx \Delta\beta/\beta \approx \Delta\epsilon/B$ and supposing that difference in ref-

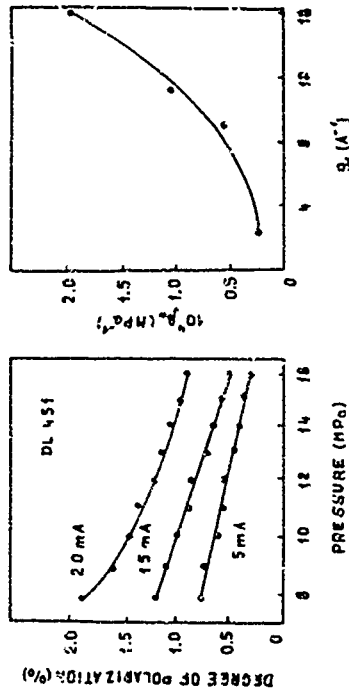


Fig. 3. Plot of the degree of polarization vs. external pressure. The driving currents are given at the curves.

Fig. 4. Correlation between the pressure-sensitivity of the polarization ρ_0 and the value α_1 , defined Eq. (6). Rectivity between the TE and TM modes $\Delta R \ll R$ for $q_1 \ll 1$ one can obtain

$$\rho_0 = 0.5 \alpha_1 \cdot \Delta R / (1-R^2) q_1, \quad (5)$$

where

$$q_1 = q_1 / I \quad (6)$$

is fixed parameter for a given sample. Eq. (5) predicts a linear dependence of ρ_0 on I in the range of very small pumping intensities, which agrees with the empirical form (2) describing the experimental curves $\rho_0(I)$ in the range of small I. Analysing the experimental data on $\rho_0(I)$,

measured on the lasers under various external pressures, we can obtain $\delta(P)$ and ΔR in Eq. (5). The magnitude of δ_1 as well as the ratio δ/δ_0 can be estimated; analyzing the experimental curve $L(I)$ with the help of Eq. (5). Such analysis, made for all the studied diode lasers assuming $\delta \sim \delta_0$, where δ_0 is the axial stress in the active region, yielded δ in the $2 \cdot 10^2$ to $2 \cdot 10^3$ Pa range. ΔR was found to be practically independent on I and lying in the interval 0.04-0.06. Independence of ΔR of I indicates that the guiding properties of the active layer in the double heterostructure lasers remain at very low pumping currents below threshold.

Our data indicated that the stress-sensitivity of polarization, as defined by

$$\rho_0 = d\rho_0 / d\delta, \quad (7)$$

where ρ_0 was the degree of the laser output polarization, extrapolated to $I=0$, varied in the range of one order of the magnitude among the studied samples. Fig. 4 plots the magnitudes of ρ_0 , obtained in the above described manner, versus δ_1 defined Eq. (6) and estimated on the same lasers. The presented data show that there is a definite correlation between these values. Laser, having δ_1 , i.e. larger gain coefficient at the fixed current, revealed stronger sensitivity of ρ_0 to the axial stress. On the other hand, the difference in the spontaneous light intensity among the studied lasers at a current $I \ll I_{th}$ was much less than the variation in δ_1 . The pressure-sensitivity of ρ_0 was higher for those samples which revealed larger ratio δ_1/δ_0 .

5. Modification of the model [5]

The most probable origin of the variation in the gain coefficient g among lasers, having approximately the same quantum yield of the spontaneous emission, are [8]: a) difference in the doping level; b) variation in the thickness of the active layer. This factor leads to a difference in the pumping density among lasers at the same driving current; c) difference in the absorption coefficient λ .

In order to study the effect of the doping level on ρ_0 we measured the spectrum shift of the spontaneous emission with current. No correlation was found between the individual values of the rate of this shift, depending on the doping level [3], and ρ_0 . Absorption of the spontaneous emission in the active region of a laser can be taken into account, using the expression for the total gain coefficient [5]

$$g_t = g_0(I - I_0) - \lambda, \quad (8)$$

where λ is the absorption coefficient, δ_0 and I_0 are parameters, depending on the active layer thickness and the doping level in a given laser. It means that quantum amplification in the active layer begins not from $I=0$, but from

$$I_1 = I_0 + \lambda/q_0. \quad (9)$$

At $I \ll I_0$ there are no quantum amplification effects, so that $g_t = -\lambda$ in the range $I \ll I_0$, resonant light is not amplified in the active region, but the total absorption coefficient ($-\delta_0$) is modulated by the pumping current, according to Eq. (3). This modified model gives for the degree of the polarization in the range $I \ll I_0$

$$\rho = \frac{\delta_0}{2\delta} - \frac{1-\delta}{2(I-R)(I-R_0)} \Delta R, \quad (10)$$

where $G = \delta_0(I-R_0)/\lambda < 1$. Eq. (10) indicates that, contrary to the authors [5], the degree of polarization of the spontaneous output must depend on ΔR at very small pumping currents.

In the range $I \ll I_0$, when $G \ll 1$, Eqs. (1), (2) and (3), supposing after [6] $\delta_0 \Delta R/B = \delta_0 \delta_0/\delta_0$, lead to

$$\rho = \frac{1}{2} \left(\frac{\Delta R_0}{\delta_0} - \frac{\Delta}{\lambda} \right) \frac{\lambda}{\lambda - g_0(I - I_0)} - \frac{\Delta R}{I - R}, \quad (11)$$

where δ_0/δ_0 and Δ/λ are the relative differences in δ_0 and axial stress. The magnitude of the stress-sensitivity of polarization, as defined by Eq. (7), can vary among lasers because differences in λ , δ_0 and I_0 . More effective lasers, having higher δ_0 and lower λ and I_0 , must reveal higher polarization-sensitivity to the stress.

Conclusions

Detailed study of the degree of polarization (ρ) of the spontaneous emission of AlGaAs double-heterostructure lasers as a function of current (I) and axial pressure (P) in the range of low driving intensities showed that using these measurements for the estimation of the mechanical stress in the laser active region is more delicate problem than it seemed previously [5]. The ρ is not constant at low pumping currents, but linearly depends on I . This dependence, when extrapolated to $I=0$, gives ρ_0 which can be used as a measure of the stress (δ) in the active layer. The magnitude of ρ_0 depends not only on the δ , but also on the difference ΔR in the reflectivities at the facet mirrors between the TE and TM polarized photons, as well as on the g_0 , the proportionality coefficient between the gain coefficient and I . The last effect takes place in the range of low I , where the spontaneous emission is partly absorbed in the active region, but the absorption coefficient is modulated by the stimulated emission. In this case the axial stress causes not only the difference ΔR between the rates of the radiative recombination, producing TE and TM polarized photons, but additionally modulates (differently for the TE and TM modes) the effective length of the portion of the active layer supplying the registered output photons. Therefore, in order to applying the polarization measurements for the estimation of the value of the strain in the laser active region, one must study the influence of the laser structure on the difference in reflectivities ΔR

BISTABILITY EFFECT IN LASER-TRANSISTOR
RESONANT-TUNNELING STRUCTURE

V. R. Zhil and I. Khayrova
The University of Aizu,
1-1 Suruga, Aizu-nachi, Aizu-Wakamatsu-City,
Fukushima Prefecture, 965 JAPAN

Abstract

We report laser-bipolar transistor incorporating a resonant-tunneling structure (RTLBT) operation. An analytical model of RTLBT is proposed and used. It is shown that RTLBT can exhibit bistable operation, so in a certain range of collector voltage ($V_C < V_C^*$) the collector and the base currents, and the stimulated photon emission intensity, are double-valued. The physical nature of the bistability effect is associated with a mobile electron space charge in the collector that influences the electron transparency of the resonant-tunneling structure and the pumping conditions of the laser active region.

Introduction

Modulated semiconductor heterostructures have recently attracted considerable attention as important components for optical preprocessing and photonic switching functions (see, for example [1,2]). In this paper we report a laser-bipolar transistor incorporating resonant-tunneling structure (RTLBT) as an optoelectronic switching device. The RTLBT has electrical and optical switching characteristics exhibiting a bistable operation in a certain range of the collector voltage. The band structures of the RTLBT in both the on and off states are shown in fig. 1. The narrow-gap p-layer plays the role of the laser active region and the transistor base simultaneously. The double-barrier resonant-tunneling (RT) structure placed between the base and the collector plays the role of the electron filter controlled by the electric field which is created by the mobile electron space charge in the collector region. The origin of the bistability effect in the RTLBT under consideration is associated with the mobile electron space charge being accumulated in the collector layer behind the RT-structure. The variation of the electron concentration in the base (laser active region) because of different electron transparency of the RT-structure admits control of the stimulated radiative recombination and photon emission in the base. In the closed state the collector current (J_C) and the electron space charge in the collector (Q) are negligible ($J_C=0$, $Q=0$) and the base electron concentration exceeds the laser generation threshold concentration. In this case the intensity of emitting light $H_0 \neq 0$. In the opened state the electron leakage through the RT-structure ($J_C \neq 0$, $Q \neq 0$) suppresses the stimulated emission ($H_0 = 0$). In order to switch

between the "S" and "M" modes, as well as the influence of the quantum amplification parameters of the actual lasers on g .

Acknowledgments

The authors gratefully acknowledge Prof. P. G. Eliseev and Prof. R. P. Chavich for the presentation of the reprint and preprints of their works. We would like to thank Dr. J. A. Filipchuk and M. I. Kordov for supplying the heterostructures and L. P. Prukhnovich for the assistance in assembling of the measurement system.

REFERENCES

1. P. G. Eliseev, M. Sverdlov, I. L. Malilov, and N. Shokudzhayev, Sov. J. Quantum Electron., 15, 1046 (1986).
2. P. G. Eliseev, M. Sverdlov, I. L. Malilov, and N. Shokudzhayev, Sov. J. Quantum Electron., 16, 1051 (1986).
3. R. J. Nelson, A. K. Dutta, J. Appl. Phys., 64, 2923 (1987).
4. S. L. Vekua, R. I. Dzhalov, B. F. Zakharov, L. L. Ivchenko, and V. G. Fleyshef, Sov. Solid State Physics, 17, 1096 (1975).
5. M. S. Sverdlov, A. T. Gorenok, and I. S. Tarasov, Sov. J. Phys.-Solid State Technol. of Semiconductors, 17, 1927 (1983).
6. D. R. Cassidy and C. S. Adams, IEEE J. Quantum Electron., 25, 1156 (1989).
7. P. A. Peters, D. K. Cassady, Applied Optics, 23, 3744 (1984).
8. O. V. Bogdankevich, S. A. Parinok, and P. G. Eliseev, Poluprovodnikovye laseri, P. 415. Nauka, Moscow (1975).

on the collector current and switch off the stimulated light emission it is necessary to store the mobile electron space charge which opens the RT structure by reducing the applied collector voltage to a value lower than a certain threshold value (V_{th}).

If current flows through the RT structure and collector region and thereby creates the mobile electron space charge in this region, to switch off the current and to switch on the stimulated light emission, it is necessary to increase the collector voltage over another threshold value (V_{th}). Since $V_{th} > V_{th}$, this results in double-valued current-voltage and intensity voltage (Watt-voltage) characteristics. Recently the smaller bistability effect in the resonant-tunneling bipolar transistor (operating only as an electronic device) was predicted and discussed by one of the authors and J. Khrenov in [3].

Model

A simple one-dimensional model of RTLET was utilized to evaluate its performances. This model includes the following assumptions:

- (i) There is a single RT level in the double-barrier collector structure. The RT level energy shift is proportional to the electric field within the double-barrier structure (E_r).
- (ii) The base (laser active region) is equipotential due to a significant hole concentration; the electron density is uniform within the base.
- (iii) The electron nonradiative recombination in the base is linear, so the recombination time (τ_R) may be introduced.
- (iv) Spontaneous light emission is negligible. Spatial distribution of the light is not essential; the photon life time (τ_U) approximation is valid.

With these assumptions one can write down the following equations for the electron concentration in the base (n) and the photon density (N_U)

$$\frac{dn}{dt} = \frac{j_E - C}{eV_B} - \frac{n}{\tau_R} - G(n) N_U \quad (1)$$

$$\frac{dN_U}{dt} = G(n) N_U - \frac{N_U}{\tau_U} \quad (2)$$

Here j_E and j_C are the emitter and collector current densities, V_B is the base (laser active region) width, τ_R is the electron recombination time, τ_U is the photon life time, $G(n)$ is the stimulated emission function which can be expressed usually as $G = K(n - n_{th})$, if $n \geq n_{th}$ and $G = 0$, if $n < n_{th}$, where n_{th} is the threshold electron density, K is the coefficient. The emitter current density j_E depends on the applied base-emitter voltage and it is treated as a given value. The collector current density j_C may be represented as

$$j_C = ev_T n \left(\tau_p \exp(-c_r/T) \theta(c_r) + \tau_n \exp(-c_n/T) \right) \quad (3)$$

where v_T is the thermal electron velocity, e is the electron charge, c_r is the energy of the RT level with the respect to the emitter conduction band edge, c_n is the height of the double barrier, τ_r and τ_n are the coefficients characterizing the electron transport via RT level (resonant part of the collector current) and electron transport over the barriers (thermionic part of the collector current), respectively. ($\tau_r, \tau_n < 1$), $\theta(x)$ is the step-like function. In the simplest case it can be taken as follows.

$\theta(x) = 1$, if $x > 0$ and $\theta(x) = 0$, if $x < 0$.
Naturally, $c_r < c_n$. For appropriate RT structure with high peak-to-valley ratio the following inequality is valid

$$\frac{\tau_r}{\tau_n} \exp((c_n - c_r)/T) \gg 1$$

According to the accepted assumptions one can use the following expression

$$c_r = c_0 - eE_r w,$$

where c_0 is the RT level energy in the absence of electric field ($E_r = 0$). Taking into account the electron space charge $Q = \frac{j_C}{v_s}$ in the collector region and its drift nature one can rewrite (see [5]) the last formula as

$$c_r = c_0 - \frac{eV}{W_C} (V_C + V_{bl}) + \frac{2\pi e W_C}{\kappa V_s} j_C \quad (4)$$

Here w is the effective width of the double barrier RT structure, W_C is the width of the collector region (in reality $w \approx W_C$), V_C and V_{bl} are the applied collector voltage and the collector built-in voltage, v_s is the electron saturation velocity, κ is the dielectric constant of the collector material.

Stationary Characteristics

For the stationary states of the RTLET one can get from eq. (1) and (2) the following expressions

$$N_U = 0, \quad n = \frac{\tau_p}{eW_B} (j_E - j_C), \quad (5)$$

if $j_E < j_C + j_{th}$, and

$$N_U = \frac{\tau_U}{eW_B} (j_E - j_C - j_{th}), \quad n = n_{th} + \frac{j}{K\tau_U} \quad (6)$$

if $j_E \geq j_C + j_{th}$, where $j_{th} = \frac{eW_B}{\tau_R} (n_{th} + \frac{j}{K\tau_U})$.

Substituting expressions (5) and (6) into formula (3) and using

formula (4) one can obtain

$$j_c = \frac{v_{tr}}{W_B} \left[\frac{1}{1 + \frac{v_{tr}}{W_B} \left(\frac{1}{j_c} \exp(-\frac{1}{j_c}) \right) + \frac{1}{j_c} \exp(-\frac{1}{j_c})} \right] \quad (7)$$

if $j_E < j_{th} + j_C$.

and

$$j_C = \frac{v_{tr}}{W_B} \left[\frac{1}{1 + \frac{v_{tr}}{W_B} \left(\frac{1}{j_C} \exp(-\frac{1}{j_C}) \right) + \frac{1}{j_C} \exp(-\frac{1}{j_C})} \right] \quad (8)$$

if $j_E = j_{th} + j_C$.

$$\text{Here } j_T = \frac{K V_B}{2 n W_B} T, \quad j = \frac{K V_B}{2 n W_B} (V_C - V_{bi}).$$

where $V_{bi} = \frac{e}{k} \frac{W_C}{W_B} - V_{bi}$.

By introducing dimensionless variables and parameters such as

$$n = \frac{W_B}{W_C}, \quad i_C = \frac{j_C}{j_T}, \quad i_E = \frac{j_E}{j_T}, \quad u_C = \frac{e V_C}{k T},$$

$$\text{and } i_{th} = \frac{j_{th}}{j_T}, \quad u_C = \frac{e V_C}{k T}, \quad a = \frac{V_{tr}}{W_B} \tau,$$

one can rewrite equations (7) and (8) in the form

(9)

$$i_C = i_E \frac{1 + a \exp(u_C - u_C - i_C) \theta(u_C - u_C + i_C) + \beta}{1 + a \exp(u_C - u_C - i_C) \theta(u_C - u_C + i_C) + \beta}$$

for $i_E < i_{th} + i_C$, and

$$i_C = i_E \frac{1 + a \exp(u_C - u_C - i_C) \theta(u_C - u_C + i_C) + \beta}{1 + a \exp(u_C - u_C - i_C) \theta(u_C - u_C + i_C) + \beta} \quad (10)$$

$$i_C = i_{th} \frac{1 + a \exp(u_C - u_C - i_C) \theta(u_C - u_C + i_C) + \beta}{1 + a \exp(u_C - u_C - i_C) \theta(u_C - u_C + i_C) + \beta}$$

for $i_E = i_{th} + i_C$.

Here $\beta = \frac{v_{tr}}{W_B} \tau \exp(-\frac{1}{j_c})$.

This set of equations gives rise to dependencies of the dimensionless collector current i_C and dimensionless photon density n via dimensionless applied voltage u_C under a given value of the dimensionless emitter current i_E . The quantity $u_C = \frac{e(V_C - V_{bi})}{k T}$ is defined by the RTLBT material and structure

parameters (c_{or} , V_{bi} , v and W_C), and the temperature. Typical current-voltage (i_C , u_C) and $i_B = i_E - i_C = i_B(u_C)$ and

photon-density-voltage ($n = n(u_C)$) characteristics are shown in fig.2. In many cases the dependencies of the values α and β upon u_C can be considered as weak. Neglecting these dependencies one can obtain the analytical expressions for critical points $i_C(A, B, C, D)$ and $n(A, B, C, D)$ (see fig.2). There are three different modes of the RTLBT operation:

(a) If $i_E < i_{th}(1 + \beta)$ the RTLBT operates as a bistable transistor. Thus only the current-voltage characteristic exhibits the bistability (see fig.2a), so $n = 0$. In this case

$$i_{th} = \frac{u_C + i_E}{1 + \beta}, \quad i_C = \frac{u_C + i_E}{1 + \beta}, \quad i_D = \frac{u_C + i_E}{1 + \beta}, \quad i_B = \frac{u_C + i_E}{1 + \beta}.$$

The value $i(A)$ may be determined from a transcendental equation

$$as \quad i_C = \frac{1 + a \exp(-i_C + \beta)}{1 + a \exp(-i_C + \beta)}, \quad so \quad i_C = i_C(A).$$

(b) In the case $i_{th}(1 + \beta) < i_E < i_{th}(1 + \alpha + \beta)$ the RTLBT operates as a transistor and a laser simultaneously exhibiting the bistability in a certain range of collector voltages ($u_{th} < u_C < u_{th}$). Moreover the laser generation arises if $u_C > u_C$ (fig.2b).

Provided the emitter current densities satisfy the above inequalities one can obtain from eqs.(9) and (10):

$$i_{th} = \frac{u_C + i_E}{1 + \beta}, \quad u_C = \frac{u_C + i_E}{1 + \beta}, \quad i_D = \frac{u_C + i_E}{1 + \beta}, \quad i_B = \frac{u_C + i_E}{1 + \beta}.$$

In this case

$$n(D) = n(C) = i_E - i_{th}(1 + \beta) \text{ and } n(A) = n(B) = 0.$$

(c) Finally, if $i_E > i_{th}(1 + \alpha + \beta)$ the RTLBT can operate in both the transistor and laser modes under all collector voltages being considered. Moreover in the range $u_{th} < u_C < u_{th}$ it exhibits the bistable characteristics (see fig.2c). As for critical points they are $i_C(D) = i_C = i_{th}(1 + \beta) < i_C(A) < i_{th}(1 + \alpha + \beta)$.

$$n(B) = i_E - i_{th}(1 + \alpha + \beta) < n(A) < n(D) = n(C) = i_E - i_{th}.$$

In this case $u_{th} = u_C + i_{th} \beta$, $u_{th} = u + i_{th}(\alpha + \beta)$.

Discussion

It is seen in fig.2 that both collector current and photon density are double valued functions of the collector voltage. Thus the RTLBT can be considered as an electronic and photonic

device simultaneously. The bistability effect of this type appears if $i_E > i_{th}$. The difference between "on" and "off" voltages $\bar{u}_{th} - \bar{u}_{ch}$ (and certainly $\bar{u}_{th} - \bar{u}_{ch}$) is proportional to the emitter current density (for cases (a) and (b) in fig. 2) and to the value j_{th} (for case (c) in fig. 2). Returning to the dimensional variables we get

$$\Delta V_{ch} = \bar{u}_{th} - \bar{u}_{ch} = \frac{2\pi}{\kappa} \frac{W_C^2}{V_S} \frac{\alpha}{(1+\alpha\beta)(1+\beta)} j_E \quad (11)$$

if $i_E < i_{th}(1 + \alpha + \beta)$, and

$$\Delta V_{th} = \frac{2\pi}{\kappa} \frac{W_C^2}{V_S} \alpha j_{th} \quad (12)$$

if $i_E > i_{th}(1 + \alpha + \beta)$.

In the most interesting case ($\beta < 1$, $\alpha > 1$) formulae (11), (12) can be rewritten as $\Delta V_{th} = \frac{2\pi}{\kappa} \frac{W_C^2}{V_S} j_E$ and $\Delta V_{ch} = \frac{2\pi}{\kappa} \frac{V_T}{V_S} W_C^2 i_R i_T j_{th}$.

If $\kappa = 12$, $V_S = 10^7$ cm/s, $W_C = 5 \cdot 10^{-5}$ cm, $j_E = 10^4$ A/cm² one can obtain from above formula $\Delta V_{th} = 1$ V.

1. G.W. Taylor and P.W. Cooke. IEEE Trans. Electron Dev., 39, 2529 (1992).
2. M. Mestraspasqua, S. Luryi, F. Capasso, A.I. Hatchinson, D.L. Sivco and A.Y. Cho. IEEE Trans. Electron Dev., 40, 250 (1993).
3. V. Ryzhii and G. Khranov. Semiconductor Sci. and Techn., 7, 1178, (1992).

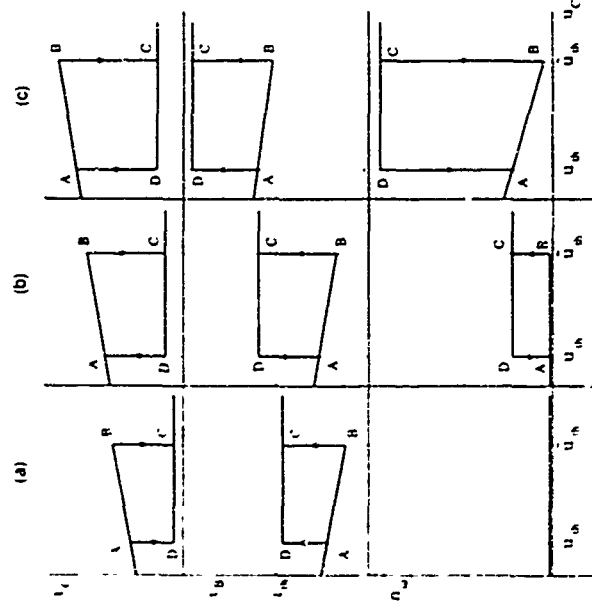


Fig. 2 Qualitative view of current-voltage and photon density voltage characteristics under different emitter current densities

(a) $i_E < i_{th}(1+\alpha+\beta)$, (b) $i_E < i_{th}(1+\alpha+\beta)$, (c) $i_E > i_{th}(1+\alpha+\beta)$

Optoelectronic Properties of (001) and (111) Lattice-Matched and Strained Quantum Wire Lasers - Comparison with Quantum Well Lasers

Igor Vurgaftman and Jasprit Singh
Solid State Electronics Laboratory,

Department of Electrical Engineering and Computer Science,
The University of Michigan, Ann Arbor, MI 48109-2122

June 18, 1993

Abstract

We investigate the optoelectronic properties of GaAs wires along the [001] and [111] directions for a range of cross sections and compare these with the corresponding parameters for optimized quantum wells. The relative benefits of built-in strain in quantum wire and quantum well systems are also studied. We find that the threshold current density in the $150\text{\AA} \times 50\text{\AA}$ wire is 80 A/cm^2 compared with 560 A/cm^2 in a 50\AA GaAs well. The differential gain in quantum wires is increased by an order of magnitude in comparison with quantum wells, and can be as high as 10^{-13} cm^2 . The narrow gain spectrum is calculated for quantum wire lasers ensuring high mode selectivity and strong damping of relaxation oscillations. We also consider the issue of carrier relaxation in quantum-confined structures, which may impose an upper limit on the laser modulation frequency. Performing a Monte Carlo simulation of the relaxation process, we find that the electron relaxation time in quantum wires is increased to above 100 ps in comparison with $\approx 10\text{ ps}$ in quantum wells. Within our model, this unusually slow relaxation process may limit the small signal modulation frequency of quantum wires to several GHz. Since modulation frequencies of over 20 GHz have been achieved in quantum wells, we conclude that although quantum wires possess superior optoelectronic properties as compared with those of quantum wells, the degraded small-signal response can make the use of quantum wire lasers for high speed applications undesirable.

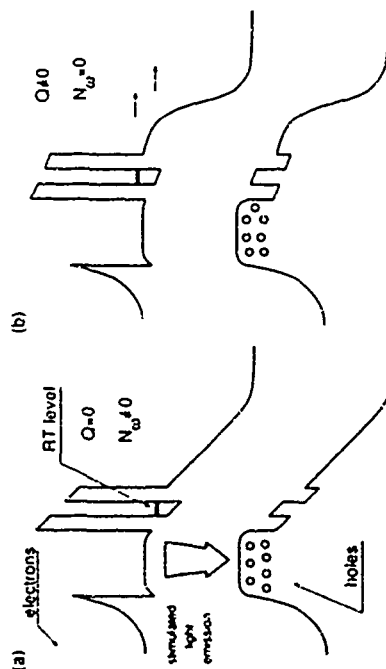


Fig 1 Band diagrams of the RTLT in closed collector state (a) and open collector state (b)

1 Introduction

The rapid development of the quantum well laser technology is the direct consequence of the advantages that the 2D density of states offers over the 3D density of states in the conventional double heterostructure laser [1] [3]. However, the 2D density of states is not ideal in terms of laser applications. What is desired is the highest possible concentration of available states near the band-edge, which will result in the lowest necessary injection level to overcome the cavity losses. While quantum wire fabrication presents many more difficulties than the fabrication of quantum wells [4] [5], there also purely theoretical concerns that may reduce the expectations for quantum wire speed and efficiency. Non-parabolicities in the bandstructure and heavy-light hole mixing may affect negatively the threshold current and modulation speed. The efficiency of the carrier capture and relaxation mechanisms in quantum wells has been a matter of some concern [6] [7]. The situation in quantum wires is even less optimistic, since the absence of intrasubband electron-electron scattering may lead to bottlenecks in the relaxation process due to lack of thermalization in the electron gas which loses energy primarily by emitting monoenergetic LO phonons [8]. In both cases, a detailed numerical simulation is the only solution taking into account the complexity of the underlying mechanisms and the number of interacting particles.

In this paper, we present the results of a detailed theoretical analysis of the optoelectronic properties of the (001) and (111) strained and lattice-matched quantum wire lasers as well as the relaxation characteristics for electrons injected in a thermal distribution at the potential well edge and carry out a thorough comparison of these with similar properties in the quantum well structures. In Section 2, we examine the considerations affecting primarily laser efficiency as quantified by the notion of the threshold current, and in Section 3, we cover the properties which influence high speed modulation in quantum wire lasers. We summarize the results and offer our conclusions in Section 4. The list of symbols used in this work and their numerical quantities, where appropriate, is given in Table 1.

2 Optoelectronic Properties

The optoelectronic properties of GaAs quantum well and quantum wire lasers can be studied directly on the basis of the bandstructure. The conduction band structure can be computed quite accurately in the effective mass approximation by solving the one-band Schrödinger equation for s-type states, while the procedure for solving for the valence band structure is to diagonalize the Kohn-Luttinger four band Hamiltonian. Both problems can be solved by the finite difference method in which the appropriate derivative terms in the differential equations are approximated as difference terms on a mesh in the wire or well region. The resulting matrix equation is then solved by the standard eigenvalue technique. In Fig. 1 we show the bandstructure and the density of states for the valence band in a $100\text{\AA} \times 100\text{\AA}$ wire. Although the conduction band structure is approximately parabolic, the valence band structure is much more complex owing to the non-parabolicities and

heavy light hole mixing. The effect of the non-parabolicities on the density states is to broaden or smear the sharp peak at the bandedge which may be expected from the parabolic dispersion relation analysis. The strain is incorporated into our formalism by calculating the splitting between the heavy and light holes by the method found in Ref. [9]. Compressive strain is obtained by adding ϵ into the well region, and the lattice mismatch ϵ is related to the In mole fraction by $\epsilon = -(0.07)x$. Tensile strain is obtained by adding ϵ into the well region. The resulting bandstructure for the $100\text{\AA} \times 100\text{\AA}$ $\text{In}_{0.3}\text{Ga}_{0.7}\text{As}$ wire is shown in Fig. 2.

The material gain can be calculated from the Fermi Golden Rule yielding (in Gaussian units)

$$g(\hbar\omega) = \frac{4\pi^2 e^2 \hbar}{n_0 m_0^2 \omega} \frac{1}{2\pi} \int d\mathbf{k}_\parallel \sum_{\mathbf{k}_\perp} |\hat{P}_{nm}(\mathbf{k}_\perp)|^2 \delta(E_n^-(\mathbf{k}_\perp) - E_m^-(\mathbf{k}_\perp) - \hbar\omega) [f^-(E_n^-) - f^-(E_m^-)] \quad (1)$$

where $f^-(E_n^-)$ and $f^-(E_m^-)$ are the electron and hole quasi-Fermi functions respectively. The light experiences optical gain only in the well region, therefore, we characterize the laser optical gain by multiplying the material gain by an optical confinement factor $\Gamma = \gamma W$, where γ is the optical confinement per unit width and W is the width of the quantum wire in the direction of the current flow.

The differential gain is given as the partial derivative of the material gain with respect to the carrier concentration. The recombination rate is also necessary in order to determine the threshold current and is given by the dipole transition rate for carrier-confined states

$$R_{sp} = \int d(\hbar\omega) \frac{4\pi^2 n_0 \hbar \omega}{3m_0^2 c^2 \hbar} \frac{2}{2\pi} \int d\mathbf{k}_\parallel \sum_{\mathbf{k}_\perp} |\hat{P}_{nm}(\mathbf{k}_\perp)|^2 \delta(E_n^-(\mathbf{k}_\perp) - E_m^-(\mathbf{k}_\perp) - \hbar\omega) [f^-(E_n^-) (1 - f^-(E_m^-))] \quad (2)$$

Note that the above expressions are applicable to quantum wires. The formalism for quantum wells can be found in Ref. [3]. In order to provide a theoretical estimate of the threshold carrier density we set up the optical loop gain for the cavity losses, resulting in the transparency condition

$$\Gamma g(n_A, E_{pss}) = \frac{1}{L_c} \ln \frac{1}{R} + \alpha_i \quad (3)$$

where $g(n_A, E_{pss})$ is the material gain at the peak mode E_{pss} , L_c is the length of the cavity, R is the reflectivity of the mirrors, and α_i is the intrinsic cavity loss. We assume a total loss of 48 cm^{-1} for the Fabry-Pérot laser cavity. Below threshold, the current is completely due to spontaneous recombination, and the threshold current density is given by

$$J_A = e R_{sp}(n_A) \quad (4)$$

The transparency carrier density and maximum differential gain are shown for a number of lattice-matched and strained wires in Table 2. The same parameters are shown in Table 3 for a variety of quantum well structures. Reduction in the transparency density

can be achieved by built-in strain compressive as well as tensile, or orienting the wire axis along the [111] direction. Growth along [111] offers a more than 50% decrease in the transparency (density due to the greater separation between the subbands resulting in a more nearly parabolic dispersion relation). The effect of strain is similar, but less pronounced (see Fig. 2). The transparency densities in quantum wells are 30-40% greater than those in quantum wires for optimized wire and well sizes. A lower transparency density normally corresponds to a lower threshold current for identical optical cavities provided the recombination rates are comparable for different structures. We have calculated a threshold current density of 80 A/cm² for the 100 Å × 100 Å GaAs wire, and that of 30 A/cm² for the In_{0.3}Ga_{0.7}As wire of the same cross section. This corresponds to a threshold density of 560 A/cm² for the 50 Å GaAs well and 150 A/cm² for the 50 Å In_{0.3}Ga_{0.7}As well. While the threshold currents are found to be much smaller in quantum wires than in quantum wells, we note that the reduction achieved by incorporation of strain is not as drastic.

The gain spectrum found as a result of our calculations is much more narrow than that calculated for quantum well lasers explicable by the sharpness and narrowness in the density of states function in a quantum wire. The narrow gain spectrum not only insures excellent mode selectivity and ease of single mode operation at low injected currents, but also provides substantial damping of the relaxation oscillations observed as the response to a step in the driving current since the resonant power is very low. Also shown in Tables 2 and 3 is the maximum differential gain achievable in each structure. The differential gain is an important parameter for high speed modulation of semiconductor lasers. It is clear that quantum wire lasers are capable of significantly higher differential gains than quantum wells, in some cases of the order of 10⁻¹⁵ cm². Higher differential gains may lead to a much lower linewidth of emission in quantum wires. However, high speed modulation in quantum wires may be degraded by the extremely slow relaxation processes as discussed in the following section.

3 Relaxation Processes

The modulation speed for a semiconductor laser is normally calculated with the assumption of a quasi-Fermi distribution for both electrons and holes. This assumption is excellent for bulk lasers, in which the intraband relaxation times are of the order of one picosecond. In quantum wells, however, the relaxation time increases by as much as an order of magnitude due to the reduction in the momentum space and difficulty in coupling of the extended states in the barrier to the confined states in the well. While the capture time in quantum wells depends on the width [7] and structure, the relaxation time for electrons injected into the well is of the order of picoseconds. The relaxation time for holes is expected to be much lower than that for electrons primarily due to the higher density of states and a greater number of subband levels in the valence band.

In quasi one-dimensional systems, the only intrasubband electron-electron scattering process allowed by the requirement of simultaneous conservation of energy and momentum

is the exchange of states by the colliding electrons. The main mechanism for energy loss in quantum wires is expected to be emission of polar optical phonons whose energy is nearly constant near the zone center. The lack of randomization by electron-electron scattering may result in bottlenecks in the relaxation process, in which the temperature of the electron distribution significantly exceeds that of the lattice up to time scales of 100 ps. The bottlenecks are eventually overcome owing to the small, yet finite, inelasticity of the acoustic phonons, but the relaxation times may range, depending on the wire size, from 100 ps to 1 ns [9]. With such long relaxation times, the assumption of the Fermi-Dirac distribution for electrons in the small-signal analysis is no longer correct. In fact, laser modulation with frequencies exceeding the reciprocal of the relaxation time is problematic. In this sense, we say that electron relaxation sets the upper limit on the laser modulation frequency.

We calculate the electron relaxation times for a number of quantum wire cross sections by an ensemble Monte Carlo simulation. A large number of electrons (5,000-10,000) are injected in a thermal distribution at the edge of the potential well formed by the barrier region. They are allowed to interact with the reservoir of acoustic and polar optical phonons, as well as between themselves, and their progress is recorded as a function of time. The scattering rates are calculated in the Born approximation as follows:

$$W_{n,n'} = \frac{2\pi}{\hbar} \sum_q |M_{n,n'}(q)|^2 \delta(E_{n'} - E_n \pm \hbar\omega), \quad (5)$$

where the upper sign corresponds to absorption and the lower sign to emission of a phonon. Since we consider quantum wires of cross sections from 100 Å × 100 Å up, we assume that the coupling between the confined electronic states and localized electronic states is significantly smaller than that between electrons and confined bulklike phonons, and perform our calculations only for the latter interaction. The Fröhlich coupling between polar optical phonons and electrons is much stronger than the deformation-potential coupling between acoustic phonons, the POP scattering rates are on the order of 10¹² s⁻¹ with sharp peaks corresponding to the peaks in the density of states, while the AP scattering rates are smaller by an order of magnitude. The effect of screening is incorporated using the Thomas-Fermi theory. The details of the formalism are presented elsewhere [10].

In Fig. 3, we plot the electron relaxation times for two electron concentrations for the 100 Å × 100 Å quantum wire. At a high screening carrier density characteristic of laser operation, the relaxation time ranges from 120 ps for the 100 Å × 100 Å wire to 30 ps for the 200 Å × 200 Å wire (Fig. 4). However, for large wire sizes, the threshold current approaches that in quantum wells, therefore, we must conclude that based on the model described above, the relaxation times in quantum wires exceed those in quantum wells by at least an order of magnitude. The theoretical limit on the modulation frequency for 100 Å × 100 Å quantum wire laser is thus calculated to be less than 10 GHz. That is well below the highest modulation frequencies obtained for some quantum well lasers.

4 Conclusions

We have made a comparative analysis of the optoelectronic properties in lattice-matched and strained quantum well and quantum wire systems. We have found that in quantum wires the transparency carrier density is reduced considerably in comparison with quantum wells, which leads to significantly lower threshold currents. The maximum differential gain is increased in quantum wires by an order of magnitude in comparison with quantum wells, which may lead to a lower linewidth for emission. However, a consideration of the relaxation processes with the inclusion of electron-phonon and electron-electron interaction leads us to believe that the electron relaxation time in quantum wires may be increased to over 100 ps and may constitute the upper limit on the modulation frequency. Therefore, although the quantum wire laser requires a significantly lower threshold current than a comparable quantum well laser, high speed operation in quantum wire lasers may be degraded in comparison with quantum wells due to exceedingly slow carrier relaxation processes.

References

1. Y. Arakawa and A. Yariv, *IEEE J. Quant. Electron.* **22**, 1887 (1986).
2. J.P. Loch and J. Singh, *IEEE J. Quant. Electron.* **27**, 708 (1991).
3. Y. Lam, J.P. Loch and J. Singh, *IEEE J. Quant. Electron.* **28**, 1218 (1992).
4. P.M. Petroff, A.C. Gossard, R.A. Logan and W. Wiegman, *Appl. Phys. Lett.* **41**, 635 (1982).
5. M. Tsuchiya, J.M. Gaines, R.H. Yan, R.J. Sines, P.O. Holtz, L.A. Colden and P.M. Petroff, *Phys. Rev. Lett.* **62**, 466 (1989).
6. S.M. Goodnick and P. Lugh, *Phys. Rev. B* **37**, 2578 (1988).
7. J.A. Brum and G. Bastard, *Phys. Rev. B* **33**, 1420 (1986).
8. J.P. Leburton, *Phys. Rev. B* **45**, 11022 (1992).
9. I. Vurgaftman and J. Singh, *Appl. Phys. Lett.* **62**, 2251 (1993).
10. I. Vurgaftman and J. Singh, submitted for publication.

List of Figures

- Fig. 1 The valence band structure (a) and density of states (b) for the $100\text{\AA} \times 100\text{\AA}$ GaAs/Al_{0.3}Ga_{0.7}As quantum wire.
- Fig. 2 The valence band structure (a) and density of states (b) for the $100\text{\AA} \times 100\text{\AA}$ In_{0.3}Ga_{0.7}As/Al_{0.3}Ga_{0.7}As quantum wire.
- Fig. 3 The energy averaged over a large number of electrons as a function of time after injection for a $100\text{\AA} \times 100\text{\AA}$ GaAs quantum wire for low and high injected carrier concentrations. The horizontal line corresponds to the expectation value of the energy for the equilibrium Fermi distribution.
- Fig. 4 The electron relaxation time as a function of the wire cross section. A square cross section is considered, the length of the side is given for carrier concentrations of 10^{16} cm^{-3} and 10^{18} cm^{-3} .

Symbol	Physical Meaning	Numerical Quantity
ϵ	Lattice Mismatch	$\sim 10\%$ for In _{0.3} Ga _{0.7} As
n_0	Refractive Index	3.6 in GaAs
$\hbar\omega$	Photon Energy	
A	Wire Cross-Sectional Area	
\vec{p}	Light Polarization	
P_{ex}	Momentum Matrix Element	$\frac{1}{2} \langle \sigma p_x \sigma \rangle = 23.7\text{ eV}$
$f(E)/f(E_F)$	Electron and Hole Quasi Fermi Functions	
γ	Optical Confinement per Unit Width	0.0025 1/Å
W	Width in Direction of Current Flow	
L_z	Cavity Length	500 μm
R	Mirror Reflectivity	0.32
α	Internal Cavity Loss	10 cm ⁻¹
β_{ex}	Scattering Rate between States n and n'	
M_{ex}	Overlap Matrix Element between n and n'	

Table 1 The list of symbols with numerical quantities used in calculations (where appropriate)

Structure	Transparency Density	Differential Gain
GaAs (001)	$1.10 \times 10^{18}\text{ cm}^{-3}$	$3.0 \times 10^{-13}\text{ cm}^2$
100Å GaAs (001)	$1.25 \times 10^{18}\text{ cm}^{-3}$	$2.0 \times 10^{-13}\text{ cm}^2$
50Å GaAs (001)	$0.90 \times 10^{18}\text{ cm}^{-3}$	$5.0 \times 10^{-13}\text{ cm}^2$
100Å InGaAs (001)	$1.00 \times 10^{18}\text{ cm}^{-3}$	$1.2 \times 10^{-13}\text{ cm}^2$
50Å InGaAs (001)	$0.85 \times 10^{18}\text{ cm}^{-3}$	$4.2 \times 10^{-13}\text{ cm}^2$
100Å GaAs (111)	$1.05 \times 10^{18}\text{ cm}^{-3}$	$1.2 \times 10^{-13}\text{ cm}^2$
50Å GaAs (111)	$0.90 \times 10^{18}\text{ cm}^{-3}$	$7.0 \times 10^{-13}\text{ cm}^2$
100Å GaAs (111)	$0.60 \times 10^{18}\text{ cm}^{-3}$	$4.3 \times 10^{-13}\text{ cm}^2$

Table 2 The transparency carrier density and the maximum differential gain for a number of quantum wire structures

Structure	Transparency Density	Differential Gain
50Å GaAs (001)	$1.80 \times 10^{18}\text{ cm}^{-3}$	$3.0 \times 10^{-13}\text{ cm}^2$
50Å InGaAs (001)	$1.25 \times 10^{18}\text{ cm}^{-3}$	$1.0 \times 10^{-13}\text{ cm}^2$
50Å GaAs (111)	$0.75 \times 10^{18}\text{ cm}^{-3}$	$2.0 \times 10^{-13}\text{ cm}^2$

Table 3 The transparency carrier density and the maximum differential gain for a number of quantum well structures

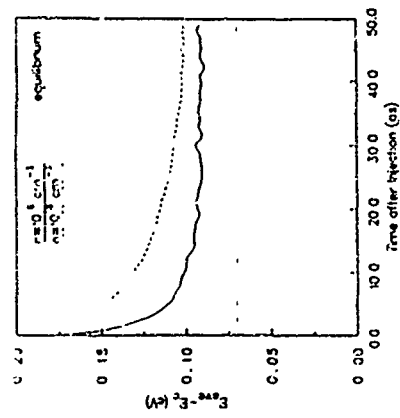


Figure 3.

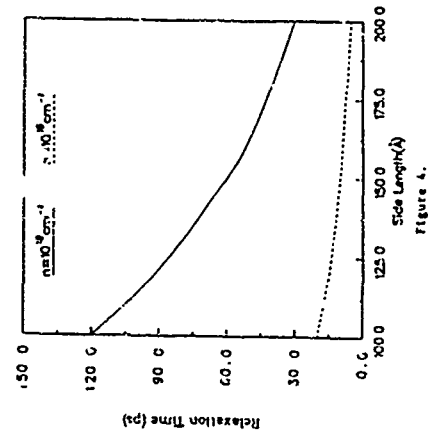


Figure 4.

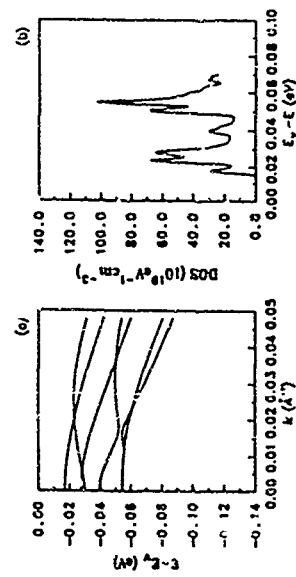


Figure 1.

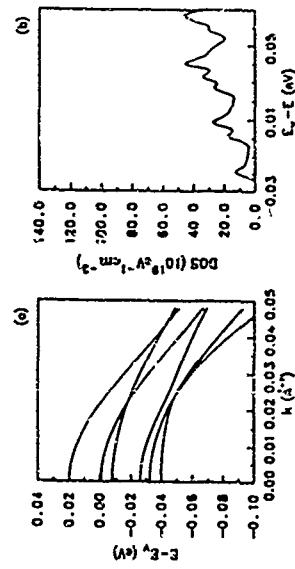
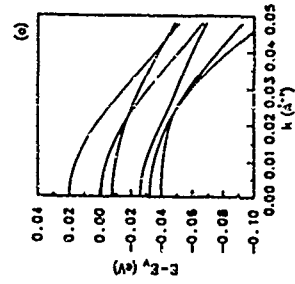
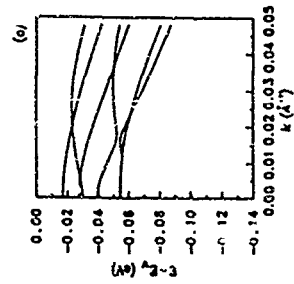


Figure 2.



Photomodulation Spectroscopy of Narrow Minibands in the Continuum of Multi Quantum Wells

J. Oiknine-Schlesinger, E. Ehrenfreund, D. Gerahoni and D. Rütter
Solid State Institute, Technion-Israel Institute of Technology,
Haifa 32000, Israel

R.A. Hamm, J.M. Vandenberg and S.N.G. Chu
AT&T Bell Laboratories, Murray Hill, NJ 07974, USA

Abstract

Photomodulation technique is utilized to spectroscopically resolve minibands structure in the energy "continuum" above the barriers of a InGaAs/InP multi quantum-well structure. Above-bandgap radiation is used to continuously pump electrons into the first electronic level, which is confined in each well. Infrared radiation is used to probe the optical transitions of these electrons to higher subband levels. The transition to the second electronic level, which is also confined, is observed together with higher order transitions to extended states. By comparison between the experimental observations to calculations based on the $\vec{k} \cdot \vec{p}$ model, we account for the energy, the line shape and temperature dependence of the newly observed minibands.

Introduction

A discrete set of energy levels characterizes the energy spectrum of a quantum-well (QW) below its barrier's energy. The wavefunctions associated with these levels are confined to the well. Above the barrier, the energy spectrum evolves into a continuum of levels with extended wavefunctions which are no longer confined to the well. Right above the barrier, however, the continuum is not uniform and the variations in the density of states still resemble the discrete-spectrum at lower energies. In a multi quantum-well (MQW) structure, at energies lower than the energy of the barriers, the spectrum is discrete and is similar to that of a single QW, since wavefunctions of neighboring wells do not interact. However, right above the barriers, minibands of finite width, separated by forbidden minigaps, where the density of states vanishes, are formed. The wavefunctions associated with these minibands are not confined to an individual well, and they extend over the whole structure (similar to a superlattice (SL)). At yet higher energy above the barrier, the forbidden gaps between the minibands diminish, and a continuum of states is restored. Interband absorption in MQWs and superlattices (SLs) has been intensively studied in recent years, following the pioneering work of West and Fegloh [1]. Most of the works reported interband absorption between the first two confined states ($n=1$ to $n=2$) in a MQW structure [1-4]. The characteristic width of the absorption line at low temperatures,

due to this optical transition was found to be 10-20 meV. This width was attributed to inhomogeneous broadening caused by interface roughness and structural fluctuations of the samples studied. Considerably broader absorption lines were found in narrow MQW structures, where only one confined state exists in each QW. In these structures the second level is pushed above the barrier, and a miniband of extended states is formed. The spectral width of the absorption line in these structures reflects the finite width of this second ($n=2$) miniband [5, 6]. These latter structures are used as efficient infrared (IR) detectors [6]. Recently, confined electronic states above the barrier were reported in special structures where a "Bragg reflector" was used to confine carriers to the barrier region [7, 8].

In this work we study the continuum minibands that correspond to truly propagating states in MQW structures. We focus our attention here to intersubband transitions studied by the photomodulated absorption (PIA) technique. This is a two beam method, in which we continuously pump electrons into the lowest $n=1$ level, using interband excitation, while probing the changes in intersubband absorption by weak IR radiation [9]. Using this technique, we have observed transitions between the $n=1$ and $n=2$ confined levels [10], and between the $n=1$ confined level and the continuum minibands. We analyze our experimental results by means of an eight band $\vec{k} \cdot \vec{p}$ theoretical model [11], which is used to calculate the electronic band structure and wavefunctions of the MQWs. The matrix elements for optical transitions between the various states are calculated by the dipole approximation using the calculated wavefunctions [12]. The absorption is then calculated by summing over all the allowed optical transitions from occupied to unoccupied states. The distribution of carriers within our one-electron band structure is calculated using the estimated carrier concentration, and assuming thermal equilibrium [12].

Experimental

The optical measurements were performed on a sample of InGaAs quantum well lattice matched to InP . The sample was grown by metal organic molecular beam epitaxy (MOMBE) as described elsewhere [13]. It consists of 15 periods of nominally undoped 65 \AA $\text{In}_{0.53}\text{Ga}_{0.47}\text{As}$ ternary wells separated by 367 \AA InP binary barriers. The sample dimensions were determined by high resolution x-ray diffraction and transmission electron microscopy [13]. Carrier concentration is estimated from Hall measurements performed on thick ($> 1 \mu\text{m}$) ternary layers grown under the same conditions. The estimated unintentional n-doping concentration in our sample is $< 1 \times 10^{16} \text{ cm}^{-3}$. To allow for an IR electric field component parallel to the MQW axis the sample was fabricated as a multipass waveguide by polishing a 45° angle on both edges. The changes, ΔT , in the IR transmission, T , through the waveguide due to above-bandgap optical excitation of the sample surface were measured using a lock-in technique and a step-scan Fourier transform IR spectrometer. The photoinduced changes in the absorbance of the whole waveguide is then equal to $-\Delta T/T$. An all-lens Ar^+ laser was used for the pump and incandescent Nernst glowbar source for the probe. The sample was placed in a Helium immersion cryostat, with variable temperature capability.

Results

The PIA results are presented as $\Delta\alpha$, the average change in the absorption coefficient per period. $\Delta\alpha$ is obtained from the measured $-\Delta T/T$ by taking into account the number of passes the IR beam makes inside the waveguide, the number of wells, the direction of the IR beam and the period of the MQW. The solid (dashed) line in Fig. 1a is the photoinduced absorption spectrum, $\Delta\alpha$, for IR light polarized parallel (perpendicular) to

the growth direction. The lowest optical band centered at 0.155 eV, is identified as the ϵ_1 - ϵ_2 transition [10]. It is polarized along the growth direction. Its shape is distinguishably asymmetric. It can be described as composed of two components: a relatively narrow line of 7 meV full width at half maximum, characteristic of intersubband absorption between two confined states, and a broad shoulder in the high energy side. Three additional bands, around energies of 0.18, 0.20 and 0.22 eV, respectively, are clearly resolved (solid line). Since the barrier in this sample is estimated to be at energy of 0.165 eV above the $n=1$ level, there additional absorption bands are due to optical transitions between the $n=1$ confined state to states above the barrier. This conclusion is in perfect agreement with our model calculations as displayed in Fig. 1b. The absorption spectra in Fig. 1b are calculated for a uniform background electron concentration of $\sim 2 \times 10^{18} \text{ cm}^{-3}$ per period. The intensity of the laser pump in these experiments was 1 Watt/cm^2 , for which we estimate the steady state photoexcited electron density as $\sim 6 \times 10^{17} \text{ cm}^{-3}$ per period [14]. In addition to the background electron density. Since we have found that the absorption spectrum is nearly linear with the electron density, we have calculated the changes in the absorption due to laser beam, $\Delta\alpha$, by dividing the absorption calculated for the actual background density by a factor of 15. The solid line is the calculated changes in the absorption for the nominal width of the well, 65 Å. Apart from the strong ϵ_1 - ϵ_2 transition (at 0.15 eV), there appear several distinct weaker bands, at 0.17, 0.18, 0.20 and 0.22 eV, which we identify as the ϵ_1 - ϵ_3 , ϵ_1 - ϵ_4 , ϵ_1 - ϵ_5 and ϵ_1 - ϵ_6 transitions, respectively. The bands are identified by the optical transition which contribute the most to their oscillator strength. From the agreement between the measured and calculated spectra both in spectral positions and relative intensities we conclude that the observed spectral bands at energies above the ϵ_1 - ϵ_2 transition, are due to optical transitions into the continuum minibands. Moreover, the typical asymmetric shape of the absorption lines can be understood by monolayer fluctuations in the QW widths. In order to show this, we have plotted the absorption spectra for identical samples having 62 and 68 Å well width and the same periodicity (broken lines, Fig. 1b). The sharp rise at low energies and the slower fall at the high energy side, can be reproduced by averaging over the three spectra shown in Fig. 1b.

In Fig. 2a we show the experimental PIA spectrum at various temperatures in the range 3-200 K. Since the experimental spectra are polarized along the growth direction (see Fig. 1), these experimental spectra were taken with unpolarized IR radiation in order to increase the signal to noise ratio. Two features are apparent in the evolution of the PIA spectra as the temperature increases: (a) There is additional absorption in the low energy side of the ϵ_1 - ϵ_2 transition, which makes this line more symmetric in shape. (b) The "continuum" minibands become weaker relative to the ϵ_1 - ϵ_2 band and are barely observable above 130 K.

Discussion

In order to discuss our results, it is instructive to consider the conduction subband structure relevant to our sample. Fig. 3a shows the calculated subbands energies ϵ_n in the plane wavevector, k_x [11]. In addition to the two discrete confined levels ϵ_1 and ϵ_2 , there are also very narrow minibands at energies above the barrier. The widths of these minibands result from the finite overlap between wavefunctions of neighboring periods. The overlap becomes more significant for higher subbands and at high enough energies a continuum of states is formed. Thus, it is only the spectral region in the close vicinity to the barrier which distinguishes between the MQW and the single QW case. The absorption spectra shown in

Figs. 1b and 2b, were all calculated using the band structure and wavefunctions (not shown) of Fig. 3a. Fig. 3b shows the population density of the ϵ_1 level in thermal equilibrium, $n(E)$, as a function of the energy E . It is seen that, as the temperature increases, a larger portion of the Brillouin zone is occupied by electrons. This, in turn, gives rise to lower energy optical ϵ_1 - ϵ_2 transitions due to the difference in curvature (effective mass) between the two subbands. This qualitatively explains the evolution of the low energy tail of the ϵ_1 - ϵ_2 transition as the temperature increases. A more quantitative description is given in Fig. 2b, where the intersubband absorption spectra are calculated for various sample temperatures.

The relative decrease of the observed ϵ_1 to minibands absorption as a function of temperature, can only be partially accounted for by our model. In the temperature range, 3-90 K, the reduction in the relative intensity of the measured minibands absorption is somewhat larger than what we calculate (see Fig. 2). We believe that this discrepancy, has to do with important extrinsic contributions to the PIA signal. These contributions explain also the saturation of the PIA at large laser intensities [15]. Since our model does not take any extrinsic effects into account, it cannot explain all the experimental details.

Finally, we have also studied these intersubband transitions in n-doped samples by measuring their dark absorption (without interband excitation). Under these conditions there could not be any effect of photoexcited holes on the intersubband absorption. Detailed account of this study is reported separately [16].

Summary

We have studied, by means of phot induced absorption spectroscopy, optical transitions between confined electronic states of a MQW to minibands in its continuum. By comparison with a theoretical model we identify all the observed transitions, explain their strength, spectral shape, polarization selection rules, and temperature dependence.

Acknowledgments The work was carried out in the Center for Advanced Optoelectronics, and was supported by the Technion Vice President Fund-the Sydney Goldstein Research Fund and by the Basic Research Foundation Administered by the Israel Academy of Sciences and Humanities, Jerusalem, Israel.

References

- [1] L.C. West and S.J. Eglash, Appl. Phys. Lett. 48, 1156 (1985).
- [2] B.F. Levine, R.J. Malik, J. Walker, K.K. Chou, C.G. Bethea, D.A. Kleinman and J.M. Vandenberg, Appl. Phys. Lett. 50, 273 (1987).
- [3] A. Seilmeier, H. J. Hubner, G. Abstreiter, G. Weimann and W. Schlapp, Phys. Rev. Lett. 59, 1345 (1987).
- [4] H. Asai and Y. Kawamura, Phys. Rev. B 43, 4748 (1991).
- [5] G. Abstreiter, T. Egeler, S. Breck, A. Seilmeier, H.J. Hubner, G. Weimann and W. Schlapp, Surface Science 100, 613 (1988).

- [6] S.D. Gunapala, B.F. Levine, R.J. Logan, T. Tanbun-Ek and D.A. Humphrey, *Appl. Phys. Lett.* **57**, 1802 (1990).
- [7] M. Zacher, J. Bruner, G. Lenz, J. Salzman, E. Cohen and I. Pfeiffer, *Appl. Phys. Lett.* **61**, 945 (1992).
- [8] F. Capasso, C. Sirtori, J. Faist, U.L. Sivco, S.N.G. Chu and A.Y. Cho, *Nature* **358**, 565 (1992).
- [9] M. Ohzaki, E. Ehrenfreund, E. Cohen, J. Bajaj, and G.J. Sullivan, *Phys. Rev. Lett.* **62**, 2907 (1989).
- [10] J. Oshroon-Schlesinger, D. Ehrenfreund, D. Gershoni, D. Ritter, M.B. Panish and R.A. Hamm, *Appl. Phys. Lett.* **59**, 970 (1991).
- [11] G.A. Baraff and D. Gershoni, *Phys. Rev. B* **43**, 4011 (1991).
- [12] D. Gershoni, C.M. Henry and G.A. Baraff, *IEEE Journal of Quantum Electronics* (in press, 1993).
- [13] D. Ritter, R.A. Hamm, M.B. Panish, J.M. Vardenberg, D. Gershoni, E.D. Gunapala and B.F. Levine, *Appl. Phys. Lett.* **59**, 552 (1991).
- [14] J. Bruner, D. Gershoni, D. Ritter, M.B. Panish and R.A. Hamm, *Appl. Phys. Lett.* **58**, 965 (1991).
- [15] E. Ehrenfreund, J. Oshroon-Schlesinger, D. Gershoni, D. Ritter, M.B. Panish and R.A. Hamm, *Surface Science* **237**, 461 (1992).
- [16] D. Gershoni, J. Oshroon-Schlesinger, E. Ehrenfreund, D. Ritter, R.A. Hamm and M.B. Panish, submitted for publication.

Figure Captions

Fig. 1 (a) The photoluminescence absorption Δn , per well for infrared light polarized along the growth direction (solid line) and perpendicular to it (dashed line). (b) The calculated Δn , for light polarized along the growth direction. Solid line - nominal well width thickness of 25 monolayers. Dashed (dotted) line - well width of 23 (21) monolayers.

Fig. 2 Measured (a) and calculated (b) Δn for various temperatures. The spectra are vertically displaced for clarity. The calculated spectra are averaged over ± 1 monolayer fluctuations.

Fig. 3 (a) Calculated conduction subband structure plotted as energy vs. the in-plane wavevector, k_x . The energy is measured from the top of the InGaAs QW valence band. (b) The calculated electron occupation density $n(E)$, in thermal equilibrium, for $T=3$ and 200 K.

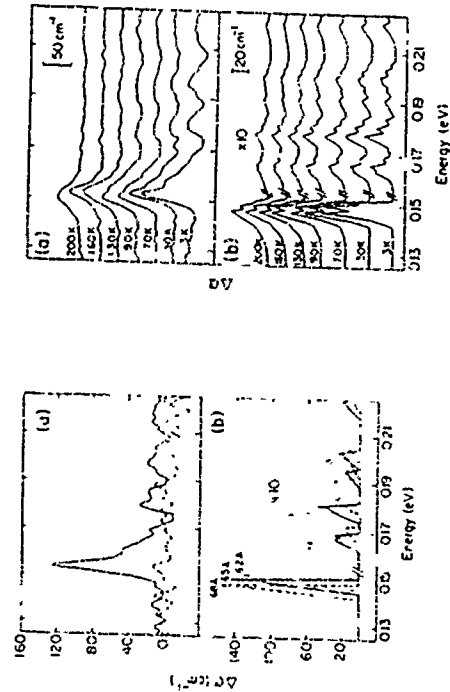


Fig. 1

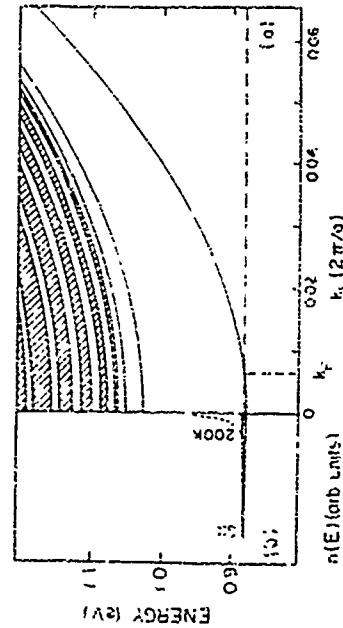


Fig. 2

ThC1

Inter-subband lifetime in quantum wells with transition energies above and below the optical phonon energy

Josune F. Jari, Federico Capasso, Carlo Sirtori, Deborah L. Sivo, Alfred Y. Cho, Loren Pfeiffer and Ken West

AT&T Bell Laboratories, Murray Hill, NJ 07974 (908) 582 2336

A new measurement of the intersubband lifetime is presented. In a first set of experiments, electrons are pumped from the ground state to the first excited state of a n -type quantum well using a CO_2 laser. A Fourier transform infrared spectrometer beam splitter the absorption cross-section between the first and second excited state, measuring the population of optically excited electrons. From this cross-section, we find a lifetime equal to $\tau_1 = 0.65 \pm 0.15$ ps for a 85 \AA GaP's quantum well and $\tau_2 = 0.8 \pm 0.2$ ps for a 100 \AA Ga_{0.37}In_{0.63}As quantum well, in good agreement with the theoretical predictions of Ferreira and Barraud. In a second set of experiment we investigate a asymmetric modulation-doped GaAs/AlGaAs coupled quantum well in which the spacing between the ground and first excited state $E_{01} = 16 \text{ meV}$ is below the optical phonon energy. Electrons are optically pumped on the short-lived second excited state ($E_{02} = 115 \text{ meV}$) and some of them, cascading down, are trapped on the first excited state. A measurement of the differential absorption between the first and second excited state proves the existence of a bottleneck effect and we estimate an electron lifetime of about $\tau_2 = 300$ ps. The extremely narrow (FWHM = 2.6 meV) luminescence line of the (0-2) transition corresponds to a time $\tau = 0.5$ ps, very close to the lifetime (0.65 ps) measured in the first experiment. This is a clear indication that we are able to observe the ultimate broadening mechanism of intersubband transitions: lifetime broadening.

ThC2

MINIBAND DISPERSION, CRITICAL POINTS, AND IMPURITY BANDS IN SUPERLATTICES: A MINITRAP ABSORPTION STUDY

M. Klein, W. Hübner, T. Frommer, Institut für Halbleitertechnik, Universität Linz, A 4040 Linz, Austria

F. M. Doster, Department of Physics, University of Arkansas (USA), B 2410 Wilshire, Belgium

K. Alavi, R. N. Pothol, Center for Advanced Electron Devices and Systems, Department of Electrical Engineering, The University of Texas at Arlington, Arlington, TX 76019

ABSTRACT

Infrared absorption is employed to study the structure of the minibands in GaAs/AlGaAs superlattices. The miniband dispersion is directly revealed through two absorption maxima, related to the singularities of the density of states at the center and the edge of the mini-Bellouin zone. The total intensity is strongly asymmetric and can be quantitatively explained, when the k_z -dependent transition matrix elements are taken into account. It is argued that the asymmetric follows from the oscillator strength. When the doping is low, so that the Fermi energy lies in the first miniband, the k_z - $\pi/2$ peak can be suppressed at low temperature due to thermal depopulation, which reflects the curvature of the lowest miniband. At low temperature another absorption line is observed, identified as $1s-2p_2$ impurity transition. The existence of this transition implies that the impurity band has not merged with the conduction band despite the metallic behavior.

1. INTRODUCTION

Despite the impressive recent progress in the physics of semiconductor superlattices, as is evidenced by the observation of the Wannier-Stark ladder [1] and of Bloch oscillations [2], the number of experiments directly revealing the curvature of the minibands is rather scarce. In transport experiments, the measured current-voltage characteristics has to be simulated with a complicated model [3], and in optical experiments [4] one has to deal with holes in addition to the electrons, and also with excitons [5].

In the present paper we show that infrared absorption between minibands is a way of directly probing the miniband dispersion. Since all minibands within the conduction band have the same in-plane curvature (neglecting nonparabolicity aside), the joint density of states has one-dimensional character and shows 6 features like singularities. This is in contrast to interband transitions, where the joint density of states contains electronic and hole states and is much less divergent due to their different curvatures. In the here reported experiment the miniband dispersion is directly evidenced through strong absorption maxima resulting from the critical points at the mini-zone edges [6]. A strong asymmetry is observed and can be explained, if the k_z -dependent transition matrix elements are taken into account. At low temperature thermal depopulation of the first miniband is reflected in the absorption spectrum through the appearance of the k_z - $\pi/2$ peak. Furthermore an impurity transition ($1s-2p_2$) contributes to the absorption at low temperature.

2. EXPERIMENTAL DETAILS

Two GaAs/Al_{0.37}Ga_{0.63}As superlattices with different doping concentrations were studied. They were grown by molecular beam epitaxy on semi-insulating GaAs (100) substrates and a 2000 \AA

wide, undoped GaAs buffer. It both cases the nominal width of the GaAs quantum wells was 75 Å and the width of the AlGaAs barriers 25 Å, corresponding to a superlattice period of 100 Å. Superlattice No. 1 was heterogeneously doped n-type, to give an electron concentration of $6 \times 10^{17} \text{ cm}^{-3}$, with a total thickness of 2 μm (200 periods). Superlattice No. 2 was doped to $n = 6 \times 10^{16} \text{ cm}^{-3}$ and had a thickness of 5 μm (500 periods). Due to the homogeneous doping, band bending can be assumed to be rather small. Sample characterization was performed by X-ray diffraction and Hall measurements, yielding a period of 96.5 Å for both superlattices and a peak mobility of $3000 \text{ cm}^2/\text{Vs}$ (at 100 K) for sample No. 1 and $6000 \text{ cm}^2/\text{Vs}$ (at 100 K) for No. 2, respectively.

Infrared absorption measurements were performed with a Bruker IFS 113v spectrometer. Further transform spectrometer. The samples were mounted in a liquid helium flow cryostat, where the sample temperature could be varied between 5 K and 100 K. In order to achieve an active polarization for the intersubband absorption (electric field perpendicular to the layers), the samples were prepared in a multi-pass waferguide geometry [17]. Then the ratio of active and inactive polarization was measured for the superlattices and a reference substrate in the same geometry. In order to obtain data which were completely free of any system artifacts, a relative rate $(I/I_0)/\Delta\omega$ was determined on the waferguide samples and was used to modulate the electron density in the top section of the sample.

3. THEORY

Fig. 1 shows the band structure for the nominal parameters of the superlattices, calculated within the one-band effective mass approximation. For sample No. 1 the Fermi energy at low temperature is calculated to be 67 meV, that is between the first and second miniband, and for sample No. 2 at 41 meV, which is approximately in the middle of the first miniband (for both effects neglected). In addition, the 1s and 2p_z donor states are shown schematically. Although the binding energy of impurities in superlattices depends on the position of the impurity atom, its dimension is smaller than 3 meV in the present case, and can therefore be neglected compared to the other energies involved. Moreover, since the doping level is well above the metal-insulator transition ($n = 1.5 \times 10^{16} \text{ cm}^{-3}$ for both GaAs), the donors will form impurity bands rather than isolated energy levels. These two donor states can be regarded as bands for band widths of 25 meV, sitting at the bottom of or midgap below each miniband.

Within a single-particle approximation the absorption coefficient for transitions between the two lowest minibands can be expressed as

$$\alpha = \frac{4\pi^2 e^2 \hbar^{-1}}{c_0 m^* \hbar^2 \omega} \int_0^{\pi/d} dk \frac{d}{dk} \left(\frac{E_2(k_2) - E_1(k_1)}{E_2(k_2) - E_1(k_1)} \right) \left(\frac{E_2(k_2) - E_1(k_1)}{E_2(k_2) - E_1(k_1)} \right) \left(\frac{E_2(k_2) - E_1(k_1)}{E_2(k_2) - E_1(k_1)} \right) \quad (1)$$

where ϵ_0 is the dielectric constant and \hbar is the reduced Planck constant. The other quantities have their usual meaning. The dispersion of the first and second minibands $E_1(k_1)$ and $E_2(k_2)$ as well as the momentum matrix elements (also k_2 -dependent) are calculated within the above model. Note that for miniband systems, the k_1 and k_2 dependence has to be used for the electron velocity, whereas the effective electron mass is to be used for the wavefunction. The wavefunction does not vanish in the barriers [18]. The Fermi energy E_F has to be determined from the electron concentration n at low temperature. It is assumed that each transition at wave vector k_2 is accompanied in a localized fashion with the backscattering parameter Γ . There are basically three factors determining the absorption coefficient. The joint density of states, the Fermi Dirac distribution (already integrated over k_1 and k_2) and the squared momentum matrix element. The latter can be expressed through the oscillator strength

by $f_{12} = (2/m^* \hbar \omega_{12}) \langle 1 | p_x | 2 \rangle \langle 2 | p_x | 1 \rangle$. The joint density of states for the present superlattices is shown in Fig. 2 (dashed line). The slight asymmetry stems from the fact that Kohn-Sharvany-like bands have a weaker curvature at their bottom edges than at their top edges. For tight-binding bands the shape would be exactly symmetric [8]. The second contribution to α , the thermal occupation factor, has the opposite effect, since at $k_2 = 0$ there are more occupied states with finite in-plane wavevectors than at $k_2 = \pi/d$, the high frequency peak is enhanced. The third, and most important contribution to α is the oscillator strength. For the present system we calculate $f_{12} = 0.3$ at the zone center ($k_2 = 0$) and $f_{12} = 2.3$ at the zone edge ($k_2 = \pi/d$), which is a variation by a factor of 7.5 (the physical reason for this will be discussed later). This behavior strongly enhances the low frequency peak. The resulting absorption coefficient (for sample 1 at T=5K) is also shown in Fig. 2 (solid line).

4. EXPERIMENTAL RESULTS AND DISCUSSION

In Fig. 3 the measured absorption spectrum for the highly doped sample (No. 1) is shown for $T = 5 \text{ K}$ and $T = 300 \text{ K}$. The line shape remains essentially the same at both temperatures, since the thermal smearing of the distribution function occurs well above the top of the first miniband. Contributions from both critical points in the Brillouin zone are clearly resolved, a peak at 106 meV (at 5K, 101 meV at 300K) and a shoulder at about 180 meV. Comparison with the calculated absorption (Fig. 2) shows that the shape of the absorption, in particular the relative strength of the two peaks is predicted surprisingly well without adjustable parameters.

In the lower-doped sample the situation is more complex. Absorption spectra for five different temperatures between 5 and 300 K are shown in Fig. 4. At high temperatures, when kT is larger than the width of the lowest miniband, the absorption is similar to the one of the highly doped sample. On decreasing the temperature, the peak at 106 meV disappears, because the top of the miniband at $k_2 = \pi/d$ becomes thermally depopulated. This demonstrates clearly the well-developed curvature of the first miniband. In addition, a new peak at 126 meV occurs at low temperature, which can readily be identified as the 1s-2p_z donor transition [9]. Since the 1s and 2p_z levels are pinned to the bottom of the first and second miniband respectively, the spectral position of the 1s-2p_z transition can be used to determine the individual widths of the first and second miniband (and not only the sum of both) in the following way: $\Delta_1 = E_1(k_2) - E_1(k_1)$ (bottom) = $E(1s-2p_2)$ and similarly $\Delta_2 = E_2(k_1) - E_2(k_2)$ (top) = $E_2(k_1) - E_1(k_2)$. This gives $\Delta_1 = 17 \text{ meV}$ and $\Delta_2 = 54 \text{ meV}$. Whereas Δ_1 agrees well with the theoretical value (18 meV), Δ_2 is predicted to be 74 meV. This is however not surprising, since our above calculation does not include nonparabolic effects, which are definitely important at energies of $\sim 200 \text{ meV}$. If, introducing an energy dependent effective mass and fitting the Al content in Al-barrier (initial Al content = 35%) we can get a good agreement of both the miniband widths and the absolute energy positions.

The occurrence of the impurity transition at low temperature is remarkable in itself, since our sample is doped four times higher than the critical density for the AlGaAs insulator transition. We have also checked the metal-like nature of the sample by low temperature transport measurements. Our observations imply that (1) the Fermi energy is located in the first miniband (since the $k_2 = 0$ min band peak remains visible), but (2) the impurity band has $n \sim 10^{16} \text{ cm}^{-3}$ completely with the absorption band (since the impurity peak is visible).

Finally we want to make a few remarks on the variation of the oscillator strength along the superlattice Brillouin zone. It is well known that the oscillator strength obeys the so-called f-sum rule which for a superlattice can be expressed as [19]

$$\sum_n \frac{2}{\omega_n} f_{n0} = \frac{\hbar^2}{m^*} \quad (2)$$

Here, n ($n=1$ and k_2 ($k_2=1$)) are the initial (final) miniband index and wavevector along the superlattice axis, respectively. For absorptive transitions f is positive, for emission it is negative. The sum has to be performed over all possible final states, even if this involves non-direct transitions ($k_2 \neq k_1$), where the momentum transfer is provided by phonons or impurities. If $k_2 = k_1$, such transitions correspond to $n=1$ miniband absorption (2-photon-like one-dimensional free-carrier absorption [11]). Now ($n=1$, $k_2=1$) is the ground state of the system from which only absorptive processes are possible. Therefore, in order to fulfill Eq. (2), all individual terms of the sum have to be smaller than unity, including the most important term ($f_{12}(k_2=k_1=1)$). In contrast, at $k_2 \neq k_1$ direct intra-miniband excitation processes are possible, which cannot require in Eq. (2). Therefore the intra-miniband oscillator strength at the low edge has to be greater than unity, $f_{12}(k_2=k_1 \neq 1) > 1$. This tendency becomes more substantial for larger miniband widths. Besides the asymmetry α of the absorption spectrum there is second manifestation of this effect. As can be seen in Fig. 4 the area under the absorption curve is not constant, but increases at low temperature. Following the above arguments, the "missing" area is contained in the intra-miniband absorption at very low frequency (< 10 meV, not measured in the present experiment). At high temperature, when the whole miniband is populated, this absorption vanishes as has been demonstrated recently [11]. Thus, the asymmetry of the miniband absorption spectrum is a generic feature which follows from fundamental physical reasons.

5 SUMMARY

We have demonstrated that infrared spectroscopy is a powerful tool to study the electronic structure of superlattices, and more specific, the nature of the minibands. The critical points at the mini-zone edges manifest themselves as strong absorption maxima. The asymmetry between the two maxima is an intrinsic feature which follows from an as basic principle as the oscillator sum rule. The dispersion of the lowest miniband is further evidenced through thermal depopulation of the zone edge. Finally, the impurity-band transition enables determination of the individual widths of the two lowest minibands. The same techniques can be applied to investigate the metal-insulator transition in superlattices, which will be attempted in future experiments.

ACKNOWLEDGMENT

This work has been supported by the "Fonds zur Förderung der wissenschaftlichen Forschung" (Venus), by the Texas Advanced Technology Program (Nos. 033656-141, 033656-062), and Texas Advanced Research Program (No. 033656-102). One of us (J.M.P.) acknowledges support by the German National Science Foundation.

REFERENCES

1. E. E. Mendez, F. Aguilera-Ruiz, and J. M. Hwang, *Phys. Rev. Lett.* **60**, 2428 (1988); P. Vossni, J. Blase, C. Burck, S. Galland, C. Allibert, and A. Reggiani, *Phys. Rev. Lett.* **61**, 1619 (1988).
2. Ch. Wenzel, H. G. Ruck, R. Schneider, K. Loh, H. Kurz, and K. Köhler, *Phys. Rev. Lett.* **70**, 3317 (1993), and H. G. Ruck et al., this volume.
3. P. England, J. R. Hayes, E. Collas, and M. Helm, *Phys. Rev. Lett.* **64**, 52 (1990).
4. F. Palmier, H. Warz, and F. Alkhalil, *Phys. Rev. Lett.* **64**, 52 (1990).
5. B. Deward, J. Shah, T. C. Damen, B. Lambert, and A. Reggiani, *Phys. Rev. Lett.* **64**, 575 (1990), 11 T (1990); H. Schneider, K. von Klitzing, and K. Köhler, *Phys. Rev. Lett.* **64**, 1294 (1990).
6. J. J. Song et al., *Phys. Rev. B* **40**, 5562 (1989); B. Deward et al., *ibid.* **40**, 5502 (1989); K. Mauer, M. Helm, W. Hülber, T. Fromherz, F. M. Peters, N. Alavi, and R. N. Pathak, *Phys. Rev. B* **48**, 1517 (1993).

7. H. Hülber, G. Schubert, E. Cornik, G. Abstreiter, and F. Schöllner, *Appl. Phys. Lett.* **57**, 2777 (1991).
8. A. Lane and K. L. Greene, *Phys. Rev. B* **33**, 5071 (1986).
9. M. Helm, E. M. Peters, F. DePaul, E. Collas, J. F. Hartmann, and L. T. Florez, *Surface Sci.* **263**, 518 (1992).
10. F. M. Peters, M. Matsuda, M. Helm, T. Fromherz, J. W. Hwang, submitted to publication.
11. G. Ruck, M. Helm, F. DePaul, C. H. Ferry, M. Koz, A. Bost, and S. J. Allen, Jr., *Phys. Rev. Lett.* **64**, 3163 (1990).

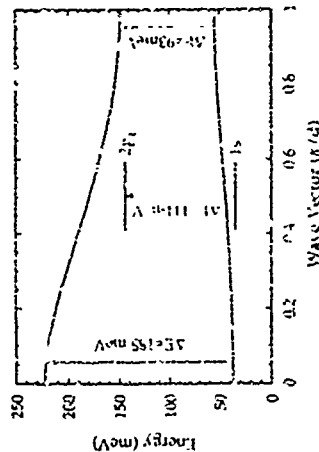


Fig. 1 The calculated dispersion of the two lowest minibands. The 1s and 2p2 impurity states are included schematically. The transition energies at the center and the edge of the Mini-Brillouin zone as well as the impurity transition energy are indicated.

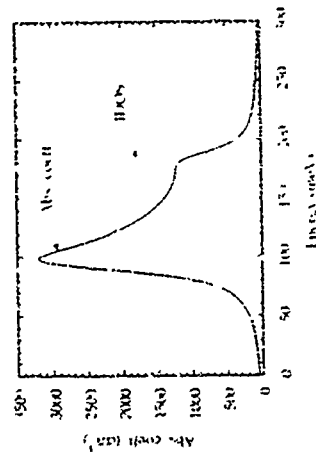


Fig. 2 One-dimensional joint density of states (dashed line) and absorption coefficient according to Eq. (2) for $f = 10$ meV, $n_{ph} = 10^{17} \text{ cm}^{-3}$, and $T = 5\text{K}$ (solid line) for the minibands of Fig. 1. The units of the joint density of states are arbitrary.

ThC3

Inelastic Light Scattering by Electrons in GaAs Quantum Wires: Spin-Density, Charge-Density and Single-Particle Excitations.

A. Schmeier*, A.R. Goh†, A. Pinczuk, J.S. Weiner, J.M. Calleja‡, B.S. Dennis, L.N. Pfeiffer and K.W. West.

AT&T Bell Laboratories, Murray Hill, New Jersey, USA

In inelastic light scattering experiments we observe for the first time clearly resolved one-dimensional (1D) intersubband spin-density excitations. Together with new structure at energies close to the 2D intersubband transitions, these observations display the formation of 1D subbands. The depolarization shift (W_{dep}) and the excitonic shift (W_{xc}) can be deduced approximately from our experiments. These shifts are of special interest because they are related to the direct and exchange-correlation terms of the electron-electron interaction. We find ratios of the shifts (W_{xc}/W_{dep}) of up to 55 %.

Since the first observation of one-dimensional intersubband plasmons (charge-density excitations, CDEs) in far infrared (FIR) transmission experiments by Hansen et al. [1] there has been an enormous body of work devoted to the study of collective excitations in low-dimensional electron systems (IDES or quantum wires) [2,3]. Most of this work was done by FIR transmission. The study of manybody effects by this technique, however, is hampered by three inherent limitations. Firstly, due to the generalized Kohn's theorem [4] only the lowest intersubband CDE couples to the far infrared light for a parabolic bare potential and only recently it was possible to realise IDES structures with a sufficiently non parabolic confinement to observe higher intersubband plasmons in FIR transmission [5]. Secondly, a different experiment, usually magneto transport measurements [6,7], has to be performed to compare the observed collective CDE energy to the single particle spectrum. Thirdly a different kind of collective excitation involving changes in spin-density (spin-density excitations, SDE) can not be observed. These excitations are of special interest, because, unlike the CDE, they are only affected by the exchange and correlation part of the electron-electron interactions (excitonic shift) and therefore their observation allows separation of contributions of direct and exchange-correlation interactions [8].

These limitations are overcome by measuring the light scattered inelastically by the electrons. Charge-density and spin-density excitations of two-dimensional (2D) electron systems have been observed and identified by simple polarization selection rules [8]. Besides the collective excitations, light scattering also allows the direct observation of single-particle excitations (SPE), which are not affected by many-body corrections [9].

present addresses:

* Sektion Physik, Universität München, München, GERMANY.
† Max-Planck-Institut für Festkörperforschung, Stuttgart, GERMANY.
‡ Universidad Autónoma, Madrid, SPAIN.

-1021-

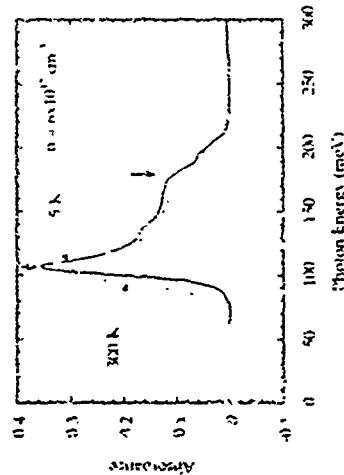


Fig. 3 Experimental absorption spectrum of superlattice No. 2 ($n=6 \times 10^{17} \text{ cm}^{-3}$) at T=5K and T=300K. The peaks resulting from the critical points at $k_x = 0$ and $k_y = \pi/d$ are indicated. (Absorbance $\propto \text{Re}[\epsilon(\omega)]$)

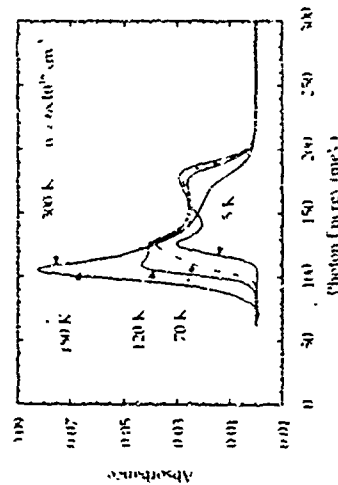


Fig. 4 Experimental absorption spectrum of superlattice No. 2 ($n=6 \times 10^{17} \text{ cm}^{-3}$) at different temperatures as indicated.

-1022-

Inelastic light scattering was only recently applied to 1DES [3,10-13]. The results of Egeler et al. [13] obtained in a system with many occupied one-dimensional subbands could be explained in a semi-classical effectively two dimensional picture of confined plasmons. The work by Gohi et al. [3,10] revealed the characteristic near dispersion of the one-dimensional intrasubband plasmon. They also found indications for an enhancement of the excitonic shift that could be evidence of stronger correlations in one dimension. However separate SDEs were not observed leaving uncertainties in the contributions of exchange and correlation.

Here we report the first observation of one-dimensional intersubband spin-density excitations in GaAs quantum wires. These excitations as well as intersubband CDE are identified by clear polarization selection rules. Transitions from the occupied states of the 1D-subbands to the first excited 2D-subband (quasi-2D transitions) also give an indication of the 1D-subband spacing. As the Fermi wave vector of our system can be inferred from the wave vector dispersion of intrasubband spin-density excitations, we achieve a complete characterization of the sample parameters and the basic electron excitations. Our experiments show that the contributions of exchange electron-electron interactions are comparable to the ones of direct electron-electron interactions.

One-dimensional structures were fabricated from a modulation doped, 250Å wide GaAs/AlGaAs single quantum well (SQW) grown by MBE. The top barrier was silicon-delta-doped. The mobility and carrier density of the as-grown SQW at 4.2 K was $2.4 \times 10^6 \text{ cm}^2/\text{Vs}$ and $3.12 \times 10^{11} \text{ cm}^{-2}$. 700Å wide lines with 2000Å period patterned into PMMA by electron beam lithography served as mask for the subsequent etching in an Plasmatherm SL700 electron cyclotron resonance reactive ion etcher (ECR-RIE). The $\text{BCl}_3\text{-Ar}$ mixture was found to give good etching characteristics, low damage and a well reproducible etching rate of about 170 Å/minute under the selected operating conditions [14]. Therefore the etching



Figure 1: SEM photograph of the cleaved edge of a sample

time could be chosen to remove the Si dopant in the gaps between the lines. This confines the carriers in the SQW electrostatically into a type II lateral superlattice. Figure 1 shows an SEM photograph of the cleaved edge of the quantum well.

Figure 2 compares photoluminescence spectra of asgrown and patterned regions on a quantum wire sample. Figure 2a shows the well-known features of a SQW containing electrons: The signal peaks at the fundamental edge and displays a long high energy tail with a cutoff at the Fermi energy. The formation of quantum wires strongly changes the light emission as shown in figure 2b. The photoluminescence peak becomes broad, rather symmetric and red shifted. Its energetic position now depends on the intensity of the exciting laser light. This effect is well known from nipi structures [15] and has also been seen in shallow etched quantum wire samples [16,17]. It is due to spatially indirect electron-hole recombination in the type II superlattice. Photo induced carriers tend to screen the confinement potential and therefore cause a shift of the PL peak as a function of incident light intensity. The energy difference between the Fermi edge in the unstructured regions and the peak position of the structured regions gives an indication of the lateral potential modulation, because the indirect recombination is most likely to occur from the Fermi edge of the quantum wires due to the

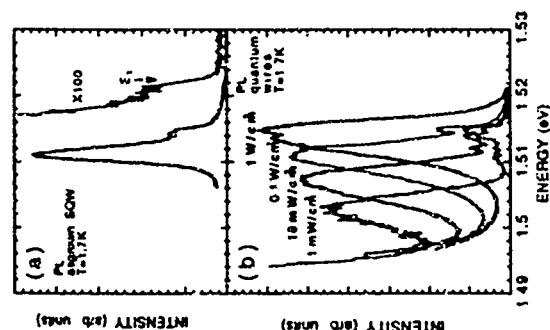


Figure 2: (a) PL spectrum taken in an unpatterned region of the sample showing the light emission from the asgrown SQW. The part containing the cutoff at the Fermi energy is enlarged by a factor of 100. (b) PL spectra taken in the quantum wire region. Parameter is the power density of the incident laser light.

enhanced electron hole overlap. We find a modulation of approximately 10 meV even under az illumination of 1 W/cm^2 , which was the power density used in the light scattering experiments. The quantum wire Fermi energy was deduced from the wave vector dispersion of intrasubband spin-density excitations to be 5.0 ± 0.2 meV. Together with a subband spacing of 2.5 ± 0.5 meV this results in two occupied subbands ($n_0 = 6.1 \pm 0.1 \cdot 10^5 \text{ cm}^{-1}$, $n_1 = 4.3 \pm 0.4 \cdot 10^5 \text{ cm}^{-1}$).

Figure 3 shows the effect of the quantum wire formation on intersubband transitions between subbands due to confinement in growth direction. The upper panel displays spectra taken in an unstructured region. Polarized and depolarized spectra, i.e. spectra taken with the polarization of incident and scattered light parallel or crossed, show strong peaks of charge- and spin-density excitations, respectively (labelled CDE and SDE). A peak due to single particle excitations (SPE) is apparent in both spectra [9]. In the quantum wire region we also observe main peaks at energies similar (but not identical) to the spectra of the as grown SQW. These peaks labelled CDE_{0,1} and SDE_{0,1} in the polarized and depolarized spectrum, respectively, are assigned to charge-density and spin-density excitations associated with the transition between the lowest 1D subband and the first excited 2D subband. The small peak on the high energy side of the SDE_{0,1} energetically coincident with the low-energy shoulder of the CDE_{0,1} peak is assigned to the corresponding single-particle transition (SPE_{0,1}). Furthermore new features appear at energies below 20 meV in both spectra labelled CDE_{0,1} and SDE_{0,1}. They are assigned to charge-density and spin-density excitations corresponding to transitions between the first excited 1D subband and the first excited 2D subband. From these observations it is possible

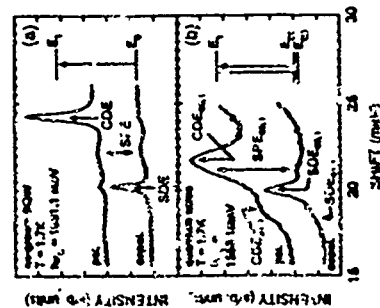


Figure 3: Inelastic light scattering spectra taken in an unstructured (a) and quantum wire (b) region. The insets show the transitions schematically.

to deduce the 1D subband spacing to be larger than 2 meV, assuming that the difference of the single-particle excitation energies is given by the splitting of the 1D subbands (inset of fig. 3b). Given a Fermi energy of ~ 5 meV we conclude to have at least 3 well confined 1D subbands of which two are occupied with electrons. There are two 1D intersubband transitions with a change in subband index of one ($\Delta n = 1$) and one transition with a change of two ($\Delta n = 2$).

The 1D intersubband excitations are also observed. Figure 4 shows depolarized and polarized low energy spectra for different incident photon energies. Observations of the electronic excitations of the IDEs are possible due to strong

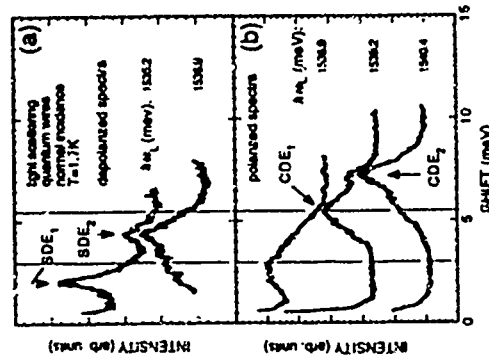


Figure 4: Depolarized (a) and polarized (b) inelastic light scattering spectra showing 1D intersubband excitations. Parameter is the incident light energy.

resonant enhancements, if the energy of the scattered light matches an excitonic transition of the sample (outgoing resonance) [18]. The polarized spectra (fig. 4b) exhibit a strong peak at 7.4 meV and weaker features at around 5.5 meV and 3 meV. The weak features occur at energies expected for single particle transitions according to the 2D-like spectra (fig. 3b) and the assumption of nearly equally spaced 1D electron levels. The sharp peak at 7.4 meV is most likely to be a collective charge-density excitation. Being the highest energetic feature we assign it to the $\Delta n = 2$ CDE (labelled CDE₂). We believe that the $\Delta n = 1$ CDEs are not as pronounced and merge with the $\Delta n = 2$ SPE in the 5.5 meV feature. One possible reason might be parity conservation, because for a symmetric potential a

two photon process such as inelastic light scattering is only sensitive to even transitions ($\Delta n=2, 4, \dots$).

Figure 4a shows depolarized spectra in the same energy range. We observe two well defined peaks at 2.0 and 4.4 meV which are assigned to the SDEs with $\Delta n=1$ and $\Delta n=2$ (labelled SDE₁ and SDE₂). The clear polarization selection rule identifies these peaks as spin-density excitations. This is the first observation of intersubband SDEs in a IDES. However the approximate parity selection rule seen for CDEs seems to be absent for the ϵ^*Es intersubband SPEs are on the contrary not clearly resolved in figures 4a. Nevertheless, changes in line shape of the spectra as a function of incident laser wavelength again suggests additional features around 3 meV and 5.5 meV (indicated by vertical lines).

The energies of the collective modes can be connected to the single-particle energy (\bar{E}_{SPE}) and the depolarization (W_{dep}) and excitonic (W_{xc}) shifts by writing $(ECDE)^2 = (\bar{E}_{SPE})^2 + (W_{dep})^2 + (W_{xc})^2$ and $(ESDE)^2 = (\bar{E}_{SPE})^2 - (W_{xc})^2$ [3]. This leads to ratios of the shifts (W_{xc}/W_{dep}) of up to 55 % in the case of the $\Delta n=2$ transition ($ESDE \approx 4.4$ meV, $\bar{E}_{SPE} = 5.5$ meV, $ECDE = 7.4$ meV), a value close to the ratio of 68% deduced from the 2D intersubband excitations of figure 3a. However due to experimental uncertainties the exact number can not yet be deduced from our experiments.

In conclusion we have investigated the transition from a 2D to a 1D system in light emission and light scattering experiments. The spatially indirect nature of the electron-hole recombination is apparent in the emission line shape and a shift of the emission peak energy with incident light intensity. The formation of 1D subbands produces new structure in light scattering spectra in the energy range of transitions to the first excited 2D subband. Our light scattering data show the first measurements of 1D intersubband spin-density excitations. Consequently, it is possible to observe the basic excitations of a IDES by inelastic light scattering. The energetic position of the intersubband SDEs is shifted from the SPEs by a correction due to exchange and correlation electron-electron interactions (excitonic shift). Similar to the two-dimensional case this shift appears to be comparable to the depolarization shift in one-dimensional electron systems in GaAs.

One of us (A.S.) would like to thank H.Drexler and W.Hansen for many important discussions. He also acknowledges financial support by the Deutsche Forschungsgemeinschaft.

References

- [1] W.Hansen, M.Horst, J.P.Koithaus, U.Merkel, C.Sigorski and J.Ploog, Phys. Rev. Lett. 58, 2586 (1987)
- [2] W.Hansen, J.P.Koithaus and U.Merkel in *Semiconductors and Semimetals*, Vol. 35 (1992), edited by R.K.Willarkson and A.C.Beier

- [3] A.R.Godli et al. in *Phonons in Semiconductor Nanostructures*, edited by J.P.Leburton, J.Pascual and C.M.Stonmayer-Torres (Kluwer, New York, 1993), to be published.
- [4] S.K.Yip Phys. Rev. B 43, 1707 (1991), and references therein.
- [5] H.Drexler, W.Hansen, J.P.Koithaus, M.Holland and S.P.Beaumont Phys. Rev. B 46, 12849 (1992).
- [6] F.Brinkop, W.Hansen, J.P.Koithaus and K.Ploog, Phys. Rev. B 37, 6547 (1987)
- [7] T.Demel, D.Heimann, P.Granbow and K.Ploog, Phys. Rev. B 38, 12732 (1988).
- [8] A.Pinczuk and G.Absreiter in *Light Scattering in Solids V*, edited by M.Cardona and G.Günterodt (Springer, Berlin 1989) p. 153.
- [9] A.Pinczuk, S.Schmitt-Rink, G.Danan, J.P.Valladares, L.N.Pfeiffer and K.W.West, Phys. Rev. Lett. 63, 1633 (1989).
- [10] J.S.Weiner, G.Danan, A.Pinczuk, J.Valladares, L.N.Pfeiffer and K.W.West Phys. Rev. Lett. 65, 1641 (1989).
- [11] A.R.Godli, A.Pinczuk, J.S.Weiner, J.M.Calleja, B.S.Dennis, L.N.Pfeiffer and K.W.West, Phys. Rev. Lett. 67, 3298 (1991).
- [12] A.R.Godli, A.Pinczuk, J.S.Weiner, B.S.Dennis, L.N.Pfeiffer and K.W.West, Phys. Rev. Lett. 70, 1151 (1993).
- [13] T.Egler, G.Absreiter, G.Weimann, T.Demel, D.Hellmann, P.Granbow and W.Schlapp, Phys. Rev. Lett. 65, 1804 (1990).
- [14] J.S.Weiner, J.M.Calleja, A.Pinczuk, A.Schmeller, B.S.Dennis, A.R.Godli, L.N.Pfeiffer and K.W.West, submitted to APL.
- [15] G.H.Döhler, H.Künzel, D.Olego, K.Ploog, P.Ruden, H.J.Solz and G.Absreiter, Phys. Rev. Lett. 47, 864 (1981).
- [16] F.Hirler, R.Küchler, R.Surenz, G.Absreiter, G.Böhm, J.Smoliner, G.Trabale and G.Weimann Surf. Sci. 263, 536 (1992).
- [17] M.Fritze, A.V.Nurmikko and P.Hawrylak in *Proceedings of the tenth International Conference on Electronic Properties of 2-Dimensional Systems (EP2DS-10)*, Newport, USA 1993 (in press).
- [18] G.Danan, A.Pinczuk, J.P.Valladares, L.N.Pfeiffer, K.W.West and C.W.Tu Phys. Rev. B 39, 5512 (1989).

Tunable far infrared absorption in logarithmically graded quantum wells

P. P. Hoyle, (1) M. Scudlark, (2) G. L. Campman, (1) G. Belloni, (1) E. L. York, (2)
S. J. Allen, Jr., (1) and A. C. Gossard, (1)
(1) Motorola Dynamics and Diagnostics of Electrical and Computer Engineering
(2) Quantum Institute, University of California, Santa Barbara, CA 93106

Compositional grading in the growth direction z is used to simulate a potential well of the form $V(z) = e^2/(4\pi\epsilon_0) + \alpha z$, where α and ϵ_0 are constants. Using both a front gate and an epitaxially grown back gate, we observe a gradual shift from 35 cm⁻¹ to 125 cm⁻¹ in the collective electronic resonant frequency by moving the electron gas through the asymmetric well.

In this paper, we present the first experimental evidence of compositionally tunable far infrared (FIR) absorption in wide graded quantum wells in zero magnetic field. The wide quantum confinement in a logarithmically graded well (100 Å), compositionally graded, GaAs/Al_{0.3}Ga_{0.7}As quantum wells leads to collective electronic excitations at FIR frequencies (0.4 THz ≈ 3.3 THz) [1-4]. With scattering of carriers already induced by remote doping, the FIR resonances in these wells are sharp (see Fig. 1) and strong at the low temperature studied ($T < 10$ K). In contrast to the low temperature pseudomorphic confinement structures with near perfect parabolic confinement and in zero magnetic field, optical excitation resonances at only a single frequency ω_{FIR} corresponding to the electronic harmonic oscillator frequency [1,3]. To study additional FIR collective modes in wide graded wells, periodic patterning of the back gate [4] and grating coupling [5] have been added to periodic wells and heterostructure wells have been added [6,7]. In the present work, following concepts presented in references 8, we have fabricated wide graded well structures with a specific goal of a tunable far infrared response at zero magnetic field. By using both a front gate and an epitaxially grown back gate, we controllably position the electron gas in a "logarithmic" well, we observe a shift that thus tunes the electronic resonances over a frequency range of more than 350% (from 35 cm⁻¹ to 125 cm⁻¹). By coopting previous work on narrower (~100 Å) asymmetric wells that yielded much weaker shifts in the frequency of the interband optical absorption [9, 10].

We study a bare well potential $V(z)$ in which the harmonic oscillator frequency ω_{FIR} at the potential maximum varies linearly with applied electric field $E(z) = E$ across the well:

$$\omega_{\text{FIR}}(z_{\text{max}}) = \alpha \left[\frac{1}{m^*} \left(\frac{\partial^2 V_T(z_{\text{max}})}{\partial z^2} \right) \right]^{1/2} = \frac{\alpha}{\sqrt{m^*}} (\alpha E + b) \quad (1)$$

where α and b are constants, α is the electronic charge, $V_T(z) = V(z) + eEz$ is the total potential in the well, $V(z)$ is the well potential in the absence of electric field, and the second derivative is evaluated in the maximum point of $V_T(z)$. A solution of Eq. (1) is the bare well potential $V(z) = -2\epsilon_0(\alpha E + b)/z$. In this paper, we study such a "logarithmic" well design in which $\alpha = 0.0751$ (meV)/Å, $b = 0.0263$ (meV)/Å^{1/2}, $\epsilon = 450$ Å and $z = 1005$ Å are the well edges, and the empty well tunability $\Delta\omega_{\text{FIR}}/\Delta E$ is 2.0 cm⁻¹/kV/cm.

To investigate the theoretical absorption properties of this well filled with electrons, we followed the example of Birn et al. [3] and first calculated the ground state energies and wavefunctions by self-consistently solving Poisson and Schrödinger equations [7] for the well, including exchange-correlation in the local density functional approximation (LDA). The calculations were done for zero temperature, assumed a constant mass $m^* = 0.07$ and relative dielectric constant $\epsilon = 13$, added an infinite potential barrier at the well edges, and included an electric field by adding the potential eEz to the bare well potential. The next to Fig. 1 shows the charge density $n(z)$ and total self-consistent potential $V_T(z) = V(z) + eEz + V_A(z) + V_{\text{exch}}(z)$, where $V_A(z)$ is the electrostatic potential of the electron gas and $V_{\text{exch}}(z)$ is the exchange-correlation potential [3], for $n_0 = 1 \times 10^{11}$ cm⁻² and for an applied electric

field of $+13.5$ kV/cm. The net applied electric field is V_0/eW , where $V_0 = V_T(z) - V_T(z) = 1005$ Å is the potential drop across the well of width $W = 1455$ Å.

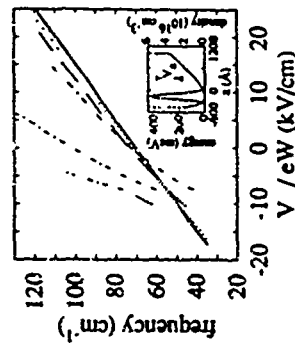


FIG. 1. Calculated absorption peak frequencies for a logarithmic well versus applied field V_0/eW for a series of electron fillings: $n_0 = 1 \times 10^{10}$ cm⁻² (solid line), 5×10^{10} cm⁻² (dashed line), 1×10^{11} cm⁻² (dotted line). Inset: self-consistent potential $V_T(z)$ and electron density $n(z)$ for the case $n_0 = 1 \times 10^{11}$ cm⁻² and $V_0/eW = 13.5$ kV/cm.

The optical absorption was calculated using the time-dependent LDA [3,11]. Fig. 1 shows the calculated absorption peaks for the logarithmic well as a function of V_0/eW . The peak frequencies are shown for four fillings of the well, $n_0 = 0.1, 0.5, 1$, and 2×10^{11} cm⁻². For $n_0 = 1 \times 10^{10}$ cm⁻², the calculated peak frequencies agree with Eq. (1) within the limits used. For small n_0 , the well region occupied by the narrow electron gas is essentially parabolic, and the absorption frequency is to a good approximation given by Eq. (1) [11]. For larger n_0 , the wider electron gas occupies a well region which contains substantial nonparabolicity. In this case, the frequency of the center-of-mass mode shifts from Eq. (1) and additional peaks are clearly seen [3]. For these higher densities, the center-of-mass of the electron gas $\bar{z} = n_0^{-1} \int n(z) dz$ shifts noticeably from the well minimum. Using Eq. (1) to decrease ω_{FIR} , qualitatively explains the peak shift. Increasing the electron gas width as fixed n_0 by applying a more negative voltage V_0/e can similarly result in multiple observed peaks in the absorption. Calculated spectra for $n_0 = 1 \times 10^{11}$ cm⁻² and 2×10^{11} cm⁻² at large negative fields show complicated

peak structure, and these frequencies were not plotted.

The sample presented in this paper is one of a series of samples grown by molecular beam epitaxy on semi-insulating GaAs (100) substrates. To simulate the potential $V(z)$ studied above, a 1455 Å well was constructed from a 15 Å period digital alloy superlattice [12] of GaAs and Al_{0.3}Ga_{0.7}As with the average Al composition a per period varied so that:

$$x(z) = (\Delta E_c / z) \left[\frac{1}{2} \ln(\alpha E + 1) + \frac{1}{2} \right] + 0.01; \quad -450 \text{ Å} \leq z \leq 1005 \text{ Å} \quad (2)$$

where we have assumed that the Al_{0.3}Ga_{0.7}As/GaAs conduction band offset ΔE_c is constant and equal to 877 meV, and α and b are given above. Electronic for the well comes from Si δ-doped Al_{0.3}Ga_{0.7}As barrier regions located at $z = -1065$ Å and $z = +1205$ Å. A highly doped ($N_D = 2 \times 10^{18}$ cm⁻³) 150 Å quantum well was grown at $z = -3.5$ μm below the asymmetric well to serve as a back gate electrode. Included in the 3.5 μm barrier was a 5000 Å low temperature grown ($T_{\text{growth}} = 230$ °C) GaAs layer. After etching a mesa, AuGeNi and In ohmic contacts were annealed to separately contact the 1455 Å well and the 150 Å well, respectively. In addition, a 4 mm dia. 50 Å/500 Å Ti/Au front gate was sputtered and evaporated onto the sample surface, ~2700 Å above the 1455 Å well.

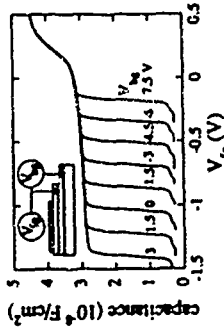


FIG. 2. Front gate to electron gas small-signal capacitance data for a series of DC back gate voltages V_0 with the sample cooled in the dark at $T = 4.2$ K.

In Fig. 2 we demonstrate complex modulation of the electron filling n_0 in the logarithmic well with either the front gate or the back gate. Plotted is the front gate to electron gas capacitance-voltage (CV) data for the sample while immersed in liquid helium at 4.2 K in the dark. A DC gate voltage (V_0) and small (10 mV peak-peak) 400 Hz AC signal were

applied between the front gate and the ohmic contacts to the electron gas, at a series of different DC voltages applied between the back gate and the electron gas ($-7.5 \text{ V} \leq V_g \leq +3.0 \text{ V}$). The CV data show a monotonic decrease in the capacitance with decreasing V_g as the depletion edge is moved down from the top doping layer through the asymmetric well and to the back gate. Likewise, the front gate depletion voltage V_d increases almost linearly as V_g is decreased, indicating that the back gate depletion edge is sweeping up through the well. Integrating each capacitance curve from V_d to V_g gives $n_s(V_g, V_d)$, so that the carrier density in the well is known for each combination of gate voltages.

Far-infrared absorption measurements were made using a Fourier transform infrared spectrometer (FTIR), with the sample and bolometer detector cooled to 4.2 K under illumination. A series of scans was taken. Absorption data were collected for 2 separate coadditions of the sample to provide a 3-polarized electric field. FTIR scans were taken at a series of different V_g values, with V_d fixed. After each FTIR scan at V_g , a scan at $V_g = -2.5 \text{ V}$ was taken to normalize the data. After the scan at the V_g then was completed, the back gate voltage was changed, a CV measurement was made (analogous to a single curve in Fig. 2), and a new series of scans was taken. Absorption data were collected for 2 separate coadditions of the sample. A series of V_g CV curves similar to Fig. 2 were found on both coadditions, although the corresponding values of V_d had shifted.

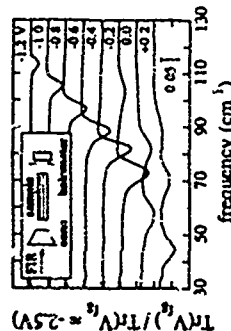


FIG. 3. $T = 4.2 \text{ K}$ normalized transmittance spectra for $V_d = 0 \text{ V}$ and several V_g values. Basic experimental setup for the absorption measurements.

The large tunable absorption in the logarithmic well is demonstrated in Fig. 3, which shows a typical set of spectra for $V_d = 0 \text{ V}$ and several V_g values. From the CV data we determined the well density $n_s = 1.0 \times 10^{11} \text{ cm}^{-2}$ at $V_g = 0 \text{ V}$. Plotted versus frequency is the normalized transmittance $\text{Tr}(V_g)/\text{Tr}(V_g = -2.5 \text{ V})$. A dip in the transmittance

corresponds to a peak in the absorption by the electrons in the well. With large negative V_g , there are electrons only in the higher curvature part of the well, and the observed absorption frequency is high. As V_g increases, the electron gas extends into well regions with lower curvature, decreasing the observed frequency. In addition, n_s increases and so the integrated absorption strength increases (3). Absorption peaks are clearly observed for $V_g \geq -0.1 \text{ V}$.

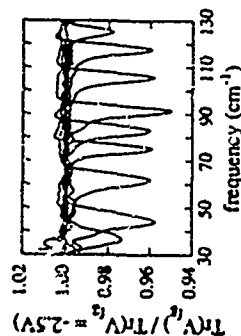


FIG. 4. $T = 4.2 \text{ K}$ normalized transmittance spectra for combinations of gate voltages in which the density in the well was approximately the same $n_s(V_g, V_d) = 1.2 \pm 0.1 \times 10^{11} \text{ cm}^{-2}$. The corresponding gas blues and CV derived n_s for each absorption peak are listed in Table I.

Although the three terminal device allows great flexibility in adjusting n_s and the well tilt on either side of the electron gas, it is difficult to determine the exact V_g and V_d to apply a uniform Stark tilt, as in the calculations of Fig. 1. Instead, we proceed in Fig. 4 a compiled series of scans (over the 2 coadditions) in which the density in the well was approximately the same $n_s(V_g, V_d) = 1.2 \pm 0.1 \times 10^{11} \text{ cm}^{-2}$. The corresponding gas blues and CV derived n_s for each absorption peak are listed in Table I. In this device it is possible to Stark shift the single sharp absorption peak from 35 cm^{-1} to 125 cm^{-1} by moving the electron gas through the logarithmic well. From Table I we estimate $d^2 \ln \text{Tr}(V_g)/d(V_g - V_d)^2 = 1.9 \pm 0.4 \text{ cm}^{-1}/\text{V}^2$ where $d = 3.9 \text{ nm}$ is the distance between the front and back gates. This rough estimate of the usability of the well is close to the theoretical empty well value of $2.0 \text{ cm}^{-1}/\text{V}^2$.

In conclusion, we have used linear FIR spectroscopy to study the collective electronic excitations of remotely doped, wide, logarithmically graded quantum wells. We observe a giant Stark shift of the resonances in these slowly varying potential wells. Harmonic generation and other nonlinear properties of these inhomogeneous potentials

G. L. Snider, and A. Wulforth for useful discussions. We thank N. G. Amar for use of the Princeton S. J. Muller program. This work was supported by the Air Force Office of Scientific Research under grant AFOSR-91-0214, by the NSF Science and Technology Center for Quantum Electronic Structures (QUEST) DMR-91-20007, by the NSF DMR-90-02491, and the ONR N00014-92-1-0152.

could also be studied, using high intensity FIR excitation. Similar graded well structures have been proposed as tunable, narrow band, FIR solid state oscillators, which do not require the application of magnetic fields [8,13].

We thank J. Maruyama for proposing the concept of tunable emitters based on wells with graded curvature [8]. We also thank K. Enslin, E. G. Gwinn, J. Ibbettson, P. R. Pihlu, A. J. Aronson, G. Robinson,

TABLE I. Gate voltages and calculated densities n_s for spectra in Fig. 4.

Peak frequency (cm^{-1})	36.5	44.1	61.7	75.1	82.9	91.3	106	118	124
V_g (V)	0.2	0.0	-0.2	-0.5	-0.7	-0.8	-1.0	-1.4	-1.4
V_d (V)	-14	-12	-10	-8	-6	-2	0	+2	+6
n_s (10^{11} cm^{-2})	4.9	4.3	4.8	4.3	4.7	5.8	6.1	5.0	4.1
coaddition #	2	2	2	2	2	1	1	1	1

References:

1. L. Brey, N. F. Johnson, and B. I. Halperin, Phys. Rev. B40, 10647 (1989).
2. K. Karim, X. Ying, H. D. Drew, M. Santos, M. Shayegan, Phys. Rev. B40, 12020 (1989); A. Wulforth, M. Sundaram, J. H. English, and A. C. Gossard, The Physics of Semiconductors, ed. by E. M. Anastassakis and J. D. Joannopoulos (World Scientific, 1990), Vol. II, p. 1703.
3. L. Brey, J. D. Joannopoulos, and B. I. Halperin, Phys. Rev. B42, 1260 (1990).
4. K. Karim, X. Ying, H. D. Drew, M. Santos, M. Shayegan, R. E. Tang, and A. H. MacDonald, Phys. Rev. Lett. 67 (1991) 3421.
5. R. P. G. Smeets, J. G. Gossard, J. H. English, and A. C. Gossard, Phys. Rev. B46, 7234 (1992); A. Wulforth, M. Sundaram, M. Sundaram, and A. C. Gossard, Sol. Stat. Comm. 84, 861 (1992).
6. N. F. Johnson and J. E. Velasco, Appl. Phys. Lett. 61, 627 (1993).
7. N. G. Amar and E. G. Gwinn, Phys. Rev. B46, 4752 (1992).
8. J. Maruyama and A. C. Gossard, "Tunable quantum well submillimeter-wave oscillators", Tech. Briefs 14, 7 (July 1990).
9. E. Mariani, F. Liu, E. Knechtel, Ph. Bole, and R. P. G. Smeets, Appl. Phys. Lett. 60, 895 (1992).
10. R. P. G. Smeets, Y. J. Ma, K. L. Wang, Appl. Phys. Lett. 58, 1986 (1990).
11. A. G. Zil'berman, Phys. Rev. Lett. 51, 1907 (1983); W. L. Schaich, Phys. Rev. 5, 37, 6711 (1980); for the calculations, a model (200 cm^{-1}) in-plane wavevector was used.
12. M. Sundaram, A. Wulforth, A. Wulforth, R. S. Gell, A. C. Gossard, and J. J. English, J. Vac. Sci. Technol. B 9, 1524 (1991).
13. M. Helim, E. Colas, P. England, F. DeRosa, and S. J. Allen, Jr., Appl. Phys. Lett. 53, 1714 (1988).

Widely Tunable Quantum Wire Arrays in MISFET-type Heterojunctions with a Stacked Gate

G. Hertz(a), H. Drexler(a), W. Hansen(a), A. Schmelzer(a), J.P. Kotthaus(a),
M. Holland(b), and S.P. Beauregard(b)
(a) Sektion Physik, Ludwig-Maximilians-Universität München, D-80539 München
(b) DEEE, University of Glasgow, GB-Glasgow G128QQ

A stacked gate technique is applied to study electronic excitations in electron quantum wires, quantum dot and antidot arrays in GaAs/AlAs MISFET-type heterojunctions at far-infrared frequencies. The gate configuration consists of a finely (period 222.5nm) patterned bottom electrode on the surface of the heterostructure, a dielectric spacer and a homogeneous top gate. An electron grating is induced at the heterostructure interface either beneath the strips or beneath the gaps of the grating gate. With the fields induced by the top gate the confining potential can be controlled nearly in dependence of the electron density in quantum wires below the bottom gate. This is demonstrated by far-infrared studies of the dimensional resonances in Ga wires. In a perpendicular magnetic field we observe a very pronounced splitting of the dimensional resonance. We study this behaviour as a function of wire separation and potential form and find this splitting to reflect the anharmonicity of the confining potential.

Currently the investigation of laterally microstructured electron systems attracts much interest. Suitable metal oxide semiconductor (MOS) structures and heterostructures are very good systems to study the properties of electron wires and dots. On MOS structures it was demonstrated that the transition between electron systems of different topology and dimensionality can be studied by using a stacked gate technique to generate the superlattice potential [1-3]. Here we have succeeded in developing such a stacked gate configuration on GaAs/AlAs heterostructures. Thereby we obtain a nearly independent control of the electron density and the confining potential in quantum wires and dots.

The collective excitations of electron systems with lateral dimensions of about 100nm are in the far-infrared (FIR) spectral region. If the so-called bare confining potential of the electron system is parabolic the FIR response of a quantum wire has only one resonance according to the generalized Kohn theorem [4] corresponding to the center-of-mass motion of all electrons in the bare potential. Here the bare potential is understood to be generated by all external charges, e.g. charges on the gates or charged surface states, excluding the electrons that occupy the low-dimensional electron system. Then the resonance energy solely depends on the bare potential and the applied magnetic field. It was found that in many of the experimentally realized electron wires or dots the assumptions of the generalized Kohn theorem are valid in good approximation. Here we focus on the FIR conductivity if the Kohn theorem becomes invalid. This is the case if e.g. there are non-harmonic terms in the bare confining potential or there is a strong mutual influence of adjacent electron systems. In previous experiments by Drexler et al [5] strong deviations from the predictions of the Kohn theorem were observed in electron wire arrays prepared in a novel type of MISFET (metal-insulator-semiconductor-field-effect-transistor) heterojunctions. There the fundamental resonance shows a pronounced splitting at a magnetic field at which the cyclotron resonance energy $\hbar\omega_c$ becomes equal to the energy of the dimensional resonance at $B=0$. In these previous experiments the electron wires were field-effectively induced by a metal grid on the sample surface. Here we use more elaborate gate configurations to study the dependence of this splitting on the wire separation as well as the form of the confining potential.

Like in the previous experiments [5,6] we use MISFET heterojunctions that consist of an undoped AlAs/GaAs superlattice barrier grown by molecular beam epitaxy on an undoped GaAs

substrate. A highly conducting layer buried about 1.5µm beneath the heterojunction interface serves as back electrode with respect to which the gate voltage is applied. A grating gate of parallel strips or a mesh-type gate with period 222.5nm are fabricated on the surface of the heterojunction crystal. The metal grid is lithographically defined either by optical holography or by e-beam exposure. In latter case we can easily fabricate gratings that have a rather large aspect ratio of gate width to period.

Furthermore, in order to gain additional control over the potential in the gaps of the bottom gate we use a so-called stacked gate configuration. A second homogeneous top gate is evaporated onto a dielectric spacer deposited on top of the bottom gate. Similar stacked gates were previously realized on silicon MOS structures [7].

As illustrated in the inset of Fig. 1 the stacked gate configuration allows to induce electron systems in two different modes. In the so-called sub-grating mode a positive voltage is applied between the bottom gate and back electrode and electrons are induced beneath the bottom gate. The top gate bias controls the lateral barriers between the electron wires. In the sub-gap mode the two gates are biased such that the electron system now resides beneath the gaps of the bottom gate. Then the bottom gate biased below threshold voltage controls the barriers between the electron systems. The data in Fig. 1 depict the resonance frequency of the dimensional resonance as function of the magnetic field in a sample that is operated in either the sub-gap (circles) or sub-grating (rhombi) mode with corresponding gate voltages as indicated in the figure. The bottom gate consists of metal strips of width $w=200$ nm arranged in an array of period $a=800$ nm. The FIR transmission of the sample was also studied before the preparation of the top gate. Squares in Fig. 1 denote the positions of the dimensional resonance without top gate. In all three cases resonances of about equal oscillator strength are observed at different resonance frequencies, demonstrating that with the stacked gate configuration it is possible to induce electron wires in the sub-gap as well as in the sub-grating mode.

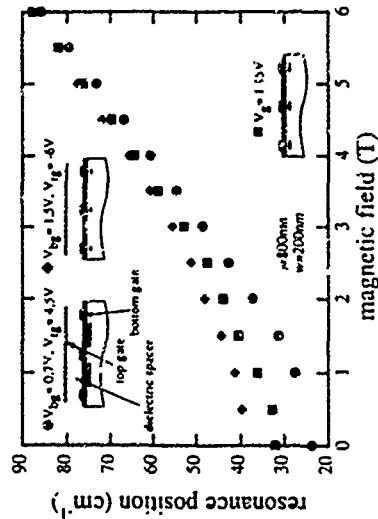


Fig. 1 Positions of the dimensional resonance in a MISFET heterojunction with stacked gate as function of a perpendicular magnetic field. As indicated in the insets the three sets of data are recorded before preparation of the top gate (squares), in the sub-grating mode (rhombi) and in the sub-gap mode (circles).

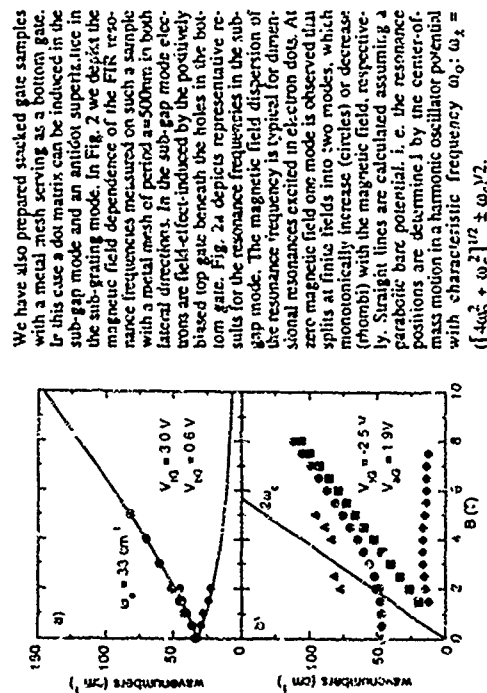


Fig. 2: Resonance positions measured on a MISFET heterojunction with stacked gate. The bottom gate is a metal mesh with period of 500nm. The gates are biased in the (a) sub-gap mode and (b) sub-gap mode, respectively.

ence of the modes as compared to the dot case is the absence of a mode with negative magnetic field dispersion at low magnetic fields ($B < 3$ T) in the case of Fig. 2b). Instead, at low magnetic fields below the cyclotron resonance frequencies (squares) a strong resonance occurs with positive magnetic field dispersion. The positive dispersion saturates at higher fields exhibits a maximum at about 3.5 T and then decreases with increasing fields beyond 4 T. At the same time the oscillator strength is gradually transferred to the high frequency mode (dots). A very similar behaviour has been observed on etched antidots in InGaAs [8] it has been suggested [8] that at high magnetic fields the low frequency mode corresponds to classical motion of electrons around a single antidot. Correspondingly, the mode becomes an edge magneto-plasmon at high magnetic fields with frequency $\omega_{\text{gap}} \propto 1/R$ determined by an effective antidot radius R . Such edge modes in an antidot superlattice are difficult to observe on etched GaAs structures. In such structure the antidot size usually is considerably enlarged by the depletion length and therefore the absorption frequency lies below the spectral region easily accessible to Fourier spectroscopy. The stacked gate allows us to vary the size of the antidots and thus to observe the edge mode by FIR spectroscopy.

The fundamental dimensional resonance in the electron wire arrays of Fig. 1 shifts in a perpendicular magnetic field and at low electron densities as predicted by the generalized Kohin theorem $\omega_{\text{gap}} = \omega_c + \omega_0$. However, a very pronounced splitting of the fundamental mode into several branches is observed at higher electron densities [5,9] Here we study this behaviour as function

of wire separation and shape of the confining potential. In order to investigate the influence of the inter-wire interaction on the splitting, we have employed electron beam lithography to fabricate samples with large aspect ratios ($l \gg w$) between grating period l and width w of the metal stripes. In Fig. 3 the resonance frequencies of a wire array in the sub-gap mode with an aspect ratio $l \approx 10$ are shown as function of the magnetic field. The sample has a grating gate of period $l = 1.5 \mu\text{m}$ and width $w = 150 \text{ nm}$ so that the wire separation is very large as compared to the wire width. A clear splitting is observed implying that inter-wire interaction is not responsible for the splitting. Furthermore, we note that here three branches appear in the magnetic field region ($\omega_c \approx \omega_0$) where the splitting occurs, whereas in previous experiments [5] only two modes have been resolved.

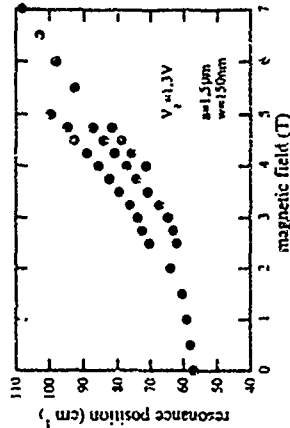


Fig. 3: Resonance positions vs. magnetic field of the dimensional resonance measured on a sample with large aspect ratio $l \approx w$ between array period $l = 1.5 \mu\text{m}$ and gate width $w = 150 \text{ nm}$.

The stacked gate technique enables us to modify the shape of the potential in the electron wires. This is demonstrated in Fig. 4 where the frequency of the dimensional resonance in a sample with a stacked gate is plotted vs. the magnetic field for three different gate voltage configurations. These are chosen so that the electrons are induced beneath the bottom gate and the oscillation lengths of the resonances are about equal. The bottom gate of the sample has a period of $l = 400 \text{ nm}$ and aspect ratio $l \approx 2$. The B=0T resonance position (ω_0) shifts clearly from 25 cm^{-1} to 45 cm^{-1} with decreasing top gate voltage. The dashed lines in Fig. 4 indicate the magnetic field at which the cyclotron frequency equals the B=0T resonance frequency in the wire array ($\omega_c = \omega_0$). The magnetic field region at which the splitting occurs increases systematically with the strength of the bare confining potential and is roughly at the field where $\omega_c = \omega_0$.

To extract more information on the bare lateral potential as function of the voltages applied at bottom and top gate we have calculated the potential distribution from the Poisson equation, assuming that no electrons occupy the potential minima. If Kohin's theorem is valid the second derivative V'' at the potential minima reflects the resonance frequency according to $\omega_{\text{gap}}^2 \propto V''/m^*$. Here we neglect image charges that result from the polarization of the surrounding material by the charge in the electron wires. If we compare the potential form with the experimental resonance positions with the assumption that no surface charges occupy the gaps in the bottom gate, we find that the calculated resonance frequencies are always significantly lower. They are roughly described by above calculations if we assume that an additional negative areal charge density of $5 \cdot 10^{11} \text{ cm}^{-2}$ resides in the gap areas of the bottom gate. A further indication for importance of surface charges in the gap regions is found if the samples are illuminated. After illumination with band gap radiation the potential modulation is found to be reduced in strongly that the frequency of the dimensional resonances do not deviate from the cyclotron resonance frequency of a homogeneous two-dimensional electron system. Surface charges may also be responsible for the fact that in some of our samples no splitting is observed in the whole gate voltage regime investigated.

Acknowledgements: We gratefully acknowledge financial support of the Deutsche Forschungsgemeinschaft.

References

1. A. C. Warren, D. A. Antoniadis, and H. I. Smith, *Phys. Rev. Lett.* **56**, 1858 (1986).
2. J. Alsmeyer in "High Magnetic Fields in Semiconductor Physics III", Ed. G. Landwehr (Springer, Berlin, 1992) p. 614.
3. A. Lorke, I. Jajina, and J. P. Kotthaus, *Phys. Rev. B* **46**, 12845 (1992).
4. L. Brey, N. F. Johnson, and B. I. Halperin, *Phys. Rev. B* **40**, 10647 (1989).
5. H. Drexler, W. Hansen, J. P. Kotthaus, M. Holland, and S. P. Beaumont, *Phys. Rev. B* **46**, 12849 (1992).
6. H. Drexler, W. Hansen, J. P. Kotthaus, M. Holland, and S. P. Beaumont, *Semicond. Sci. Technol.* **7**, 1008 (1992).
7. J. Alsmeyer, E. Batke, and J. P. Kotthaus, *Phys. Rev. B* **40**, 12 574 (1989).
8. K. Kern, D. Heilmann, P. Grambow, Y. H. Zhang, and K. Ploog, *Phys. Rev. Lett.* **66**, 1618 (1991).
9. W. Hansen, H. Drexler, J. P. Kotthaus, M. Holland, and S. P. Beaumont, *Proc. 21st Int. Conf. "Physics of Semiconductors"* (Beijing, 1992), in press.
10. J. Dempsey and B. I. Halperin, *Phys. Rev. B* **47**, 4674 (1993).

The lateral potential distribution as derived from the Poisson equation contains in addition to parabolic terms also considerable terms with 4th and 6th power. Our finding that the splitting becomes stronger at higher electron densities might be explained by the fact that the non-parabolic terms become more effective at higher densities. Dempsey and Halperin calculated the FIR absorption spectrum of an electron system in a two dimensional parabolic well, that is truncated at both sides by steep potential walls, and compare it to the spectrum of a perfect parabolic well [10]. The calculations show a fundamental mode according to the generalized Kohn theorem for a well with perfect parabolicity. A splitting of the fundamental mode similar to ours appears in calculations for the truncated well at sufficiently high electron densities so that the electrons in the well sense the steep potential walls. Similarly to our experimental data on one dimensional electron channels, the oscillator strength of the splitting shift, with increasing magnetic field from the upper to the lower branch. The oscillator strengths are about equal in the region $\omega_0 \approx \omega_c$.

The similarity of the results obtained by Dempsey and Halperin with our experimental data as well as of the Voigt geometry in a two-dimensional parabolic well with a one-dimensional wire in a perpendicular magnetic field suggests that a corresponding calculation for our wires will explain our data. Indeed, power spectra that numerically average over classical trajectories [5] indicate already that the behaviour of the oscillator strength at $\omega_0 \approx \omega_c$ can be caused by a change in the character of the combined density of states in this magnetic field region. The FIR excitations in the region $\omega_0 < \omega_c$ ($\omega_{\text{res}} > \sqrt{2}\omega_c$) are mainly determined by the electrostatic confinement potential of the electron channel, whereas the magnetic field is dominant in the region $\omega_0 > \omega_c$ ($\omega_{\text{res}} < \sqrt{2}\omega_c$). With increasing magnetic field the electrons become more and more localized in the wire center, i.e. the number of electron trajectories influenced by the wire wall decreases. Therefore the importance of the non-harmonic terms of the confinement potential decreases with increasing field and the transitions become cyclotron-resonance-like. A detailed calculation of the influence of non-harmonic terms in the bare potential on the dimensional resonances in one dimensional electron wires still needs to be done.

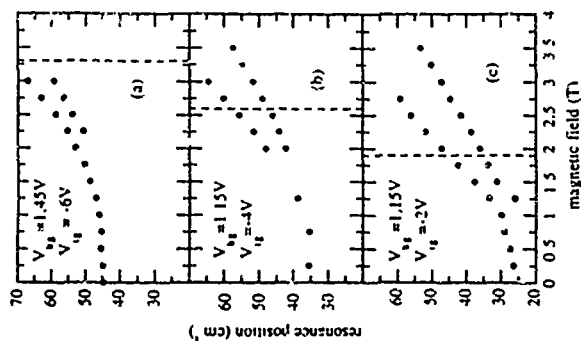


Fig. 4: Resonance positions vs. magnetic field of a MISFET heterojunction with stacked gate. The bottom gate is an array of metal stripes with period $a=500\text{nm}$ and aspect ratio $t=2$. In (a) - (c) different gate voltages are applied at the top and bottom gate. The dashed lines indicate the magnetic fields where the cyclotron frequency is equal to the $B=0$ resonance frequency.

lator strength at $\omega_0 \approx \omega_c$ can be caused by a change in the character of the combined density of states in this magnetic field region. The FIR excitations in the region $\omega_0 < \omega_c$ ($\omega_{\text{res}} > \sqrt{2}\omega_c$) are mainly determined by the electrostatic confinement potential of the electron channel, whereas the magnetic field is dominant in the region $\omega_0 > \omega_c$ ($\omega_{\text{res}} < \sqrt{2}\omega_c$). With increasing magnetic field the electrons become more and more localized in the wire center, i.e. the number of electron trajectories influenced by the wire wall decreases. Therefore the importance of the non-harmonic terms of the confinement potential decreases with increasing field and the transitions become cyclotron-resonance-like. A detailed calculation of the influence of non-harmonic terms in the bare potential on the dimensional resonances in one dimensional electron wires still needs to be done.

ThC6

Infrared Spectroscopy of Lateral-Density-Modulated 2DES in InAs/AlSb Quantum Wells

M. Sindaram and S. J. Allen, Jr.

Quantum Institute, University of California, Santa Barbara, CA 93106, USA

&
C. Nguyen, B. Bar, V. Jayaraman, and H. Kroemer

Dept. of Electrical & Computer Eng., University of California, Santa Barbara, CA 93106, USA

In infrared transmission experiments through a two-dimensional electron system with substantial lateral density modulation in an InAs quantum well, we directly observe plasmon absorption without the mediating help of a surface metallic grating. The plasmon frequency is determined by the average density, and its strength by the amplitude of the density modulation. It disperses in a magnetic field in predicted fashion.

We have observed plasmon absorption in lateral-density-modulated two-dimensional electron systems (2DES) in InAs quantum wells in far infrared spectroscopy. Its location and strength agree well with the dynamic conductivity $\sigma(q, \omega)$ that we explicitly derive for such a system. The dispersion of the plasmon frequency ω_p in a magnetic field agrees well with existing theory.

Far infrared plasmon experiments on 2DES have traditionally relied on the fabrication of a surface metallic grating (of period a) to couple to plasmons with fixed wave vectors $q = n\pi/a$ ($n = 1, 2, \dots$) [1] in 2DES residing as inversion layers in Si MOSFETs or as accumulation layers in GaAs/AlGaAs heterojunctions and quantum wells [1, 2]. Such measurements have shown the position, width, and strength of the plasmon resonance, and also its dispersion in a magnetic field B to agree with theory in detail. Non-local effects have manifested themselves in the plasmon B field dispersion via a coupling between the magnetoplasmon and the second harmonic of the cyclotron frequency $2\omega_c$ [3]. Most of these experiments have been on 2DES with lateral uniformity. Measurements on 2DES with electron density laterally modulated with submicron spatial periodicity in both the Si

MOSFET [4] and the GaAs/AlGaAs [3] systems reveal the resultant creation of minibands in the plasmon dispersion, manifested as a splitting of the plasmon peak. Increase of the periodicity to micron levels appears to shift the plasmon to higher frequencies and cause the splitting to vanish [5]. Density modulation was achieved with modulated oxide thickness in the former material system [4]; it was a side-effect of a surface metallic grating [3] enhanced by illumination [5] in the latter system.

The InAs/AlSb system offers certain unique advantages in the study of laterally modulated 2DES. The electron density n_s in an InAs quantum well sandwiched between AlSb barriers is extremely sensitive to both the composition of the cap layer and its separation from it [6]. Firstly, its 1.35 eV depth allows deep donors in the barriers and surface to drain electrons into it resulting in typical n_s values of 10^{12} cm^{-2} . Secondly, the absence of a surface depletion layer allows the quantum well to be located closer to the surface than in the GaAs/AlGaAs system, resulting in substantially more sensitivity to it. Thirdly, the selection of a cap layer, either InAs or GaSb, can result in a difference of n_s in excess of 100% by virtue of the difference in the surface Fermi level pinning in each cap [6]. Growing and laterally patterning a bilayer InAs/GaSb cap [7] and thereby modulating the surface Fermi level suggests itself as a logical means of impressing large lateral modulation on the 2DES residing in the quantum well a short distance below (Fig. 1)

The sample for this experiment had the following epilayer sequence: on a semi-insulating (100) GaAs substrate were grown a GaAs buffer, AlAs and AlSb nucleation layers, a 1 μm AlSb buffer, a $10 \times (2.5 \text{ nm GaSb} + 2.5 \text{ nm AlSb})$ short-period smoothing superlattice, a 20 nm AlSb bottom barrier, followed by the 15 nm InAs quantum well, a 15 nm AlSb top barrier, a 5 nm GaSb cap, a 10 nm AlSb cap separator, and a 3 nm InAs cap (sufficiently thin that it contains no electrons, due to the large quantization of the ground state). The sample was not intentionally doped. More details on the growth procedure for this material system can be found elsewhere [8]. The periodic patterns of alternating InAs and GaSb cap layers were fabricated by conventional photolithography and selective etching. For the two samples investigated here, the period a is 4 μm , and the duty cycle ϕ/a (ϕ = opening in InAs cap) 0.5 and 0.75 (Fig. 1)

The samples were characterized by low-temperature (4.2K) magnetotransport on conventional Hall bars both before and after the lateral patterning. The as-grown sample with the InAs cap had a 2DES with density $n_s = 5.2 \times 10^{11} \text{ cm}^{-2}$ and mobility $\mu = 170,000 \text{ cm}^2/\text{Vs}$. Stripping this cap and exposing the GaSb cap caused these values to rise to $9.2 \times 10^{11} \text{ cm}^{-2}$ and $250,000 \text{ cm}^2/\text{Vs}$, respectively. For the sample with $\phi/a = 0.5$, the low-field Hall resistance both along and across the lateral superlattice (LSL) gave an electron density $n_s = 7.2 \times 10^{11} \text{ cm}^{-2}$, exactly the average of the two unpatterned values. The mobilities dropped to $80,000 \text{ cm}^2/\text{Vs}$ across the LSL and $160,000 \text{ cm}^2/\text{Vs}$ along it. The

high-field magnetotransport differed drastically in the two directions. From these measurements the amplitude of the lateral potential modulation is calculated to be 30 meV [7].

Transmission measurements were performed with a conventional rapid-scan Fourier transform spectrometer with the radiation light-piped through the sample immersed in a cryostat at 4.2 K. The transmission T(B) was measured with a resolution of 1 cm⁻¹ at various magnetic fields B up to 8 Tesla in steps of 0.2 Tesla.

Several absorption features are observed in a T(B)/T(0) trace. The 2D plasmon (B = 0) is observed only when the radiation is polarized perpendicular to the LSL (Fig. 2). Cyclotron resonances with identical line shapes are observed in both polarizations; so also are the magnetoplasmons (since the B field mixes polarizations). The fractional change in transmission $-\Delta T/T = 1 - T(B)/T(0)$ for both samples show the high-frequency Drude tails with plasmon absorptions at $\omega_p = 49$ cm⁻¹ and $\omega_p = 52.5$ cm⁻¹ for the samples with $U_A = 0.5$ and 0.75, respectively (Figs. 3). The peak absorption is ~ 10% for the former sample, ~ 4% for the latter. The polarization-dependence and the fit in theory (developed below) leave no doubt about the identification of these peaks as 2D plasmon resonances.

$-\Delta T/T$ directly measures the real part of the dynamic conductivity of a 2DES [9]

$$-\Delta T/T = 2 \operatorname{Re} \sigma(\omega) / (Y_0 + Y_1) \quad (1)$$

where Y_0 and Y_1 are the wave admittances of free space and the host semiconductor, respectively. For a 2DES with lateral density modulation $n_s = n_0 + \Delta n_0 \cos(qy)$, where $q = 2\pi/\lambda$, on the surface of a semiconductor with dielectric constant ϵ_s , we derive $\sigma(\omega)$ explicitly as

$$\sigma(\omega) = \frac{\sigma_0}{1 + i\omega\tau} = \frac{\Delta n_0 \Delta n_0^2}{2 \left[(\omega_p^2 - 2\omega^2) + \frac{\Delta n_0 \Delta n_0^2}{\tau} + \omega^2 (\omega_p^2 - \omega^2)^2 \right]} \quad (2)$$

where

$$\omega_p = \sqrt{\frac{n_0 e^2 q}{m^* (\epsilon_0 + \epsilon_s)}}, \quad \Delta \omega_p = \sqrt{\frac{\Delta n_0 e^2 q}{m^* (\epsilon_0 + \epsilon_s)}} \quad (3)$$

where ω_p is the plasmon frequency, m^* the electron effective mass, τ the relaxation time, $\sigma_0 = en_0 q \lambda_0$ is the dc ($\omega = 0$) conductivity, $\Delta \sigma_0 = e \Delta n_0 q \lambda_0$, and μ_0 is the dc electron

mobility. The first part on the right-hand side of (2) is the Drude part and is determined solely by the average electron conductivity, the second part is the plasmon part: its pole determines the plasmon frequency to be ω_p , given by the classic expression (3) for a 2DES with uniform density n_0 [10] and its strength and shape are determined by Δn_0 and τ respectively. From (1) and (2) for $\omega \gg 1/\tau$, the peak absorption at ω_p simplifies to

$$-\frac{\Delta T}{T}(\omega = \omega_p) = \frac{e \Delta n_0 q \lambda_0 \Delta n_0}{Y_0 + Y_1 n_0} \quad (4)$$

and is seen to be directly fixed by the size of the density modulation. As expected, it also vanishes as the density modulation is tuned to zero.

For a rectangular density modulation of period a and duty cycle U_A with low and high (in the region 1) density values of n_{A1} and n_{A2} , the average density $n_0 = n_{A1}(1-U_A) + n_{A2}U_A$, and the amplitude of the first Fourier component, $\Delta n_0 = (2/\pi)(n_{A2} - n_{A1}) \sin(\pi U_A)$. Using the values of n_{A1} , n_{A2} , and U_A measured above, an effective mass $m^* = 0.037 m_0$ (from the cyclotron resonance), and $\epsilon_s = 10.5 \epsilon_0$ for the thick AISb cladding layer, we calculate ω_p to be 49 cm⁻¹ and 52.5 cm⁻¹ for U_A values of 0.5 and 0.75, in exact agreement with measurements. Furthermore, the peak absorption strengths from (4) are respectively 10% and 5% for the two cases, again in close agreement with experiment. The detailed absorptions from (1) and (2) are plotted along with the measured spectra in Figs. 3. There are no adjustable parameters in the calculated trace in Fig. 3a. For Fig. 3b, the calculated trace assumes the dc mobility along the LSL to be 100,000 cm²/Vs to get a better fit to the Drude tail.

The positions of all resonances for the sample with $U_A = 0.5$ are plotted as a function of magnetic field up to 8 Tesla in Fig. 4. From the cyclotron resonance frequencies we calculate an electron mass $m^* = 0.037 m_0$. The magnetoplasmon resonances obey the relation [11]

$$\omega_{hp}^2 = \omega_c^2 + \omega_p^2 \quad (5)$$

very well, as indicated (Fig. 4). No evidence is seen in these samples for the coupling of the magnetoplasmon resonance with harmonics of the cyclotron resonance. Measurements on LSLs with two-dimensional modulation yielded results identical to the 1D LSLs.

In summary, we observe the absorption of 2D plasmons in one-dimensional and two-dimensional lateral density-modulated 2DES in an InAs quantum well sandwiched between AISb barriers. The density modulation is achieved by lateral modulation of the surface

Fermi level with a periodic alternation of the composition of the cap layer between InAs and GaSb. In a LSL with 4 μm period we observe up to 10% peak absorption at 49 cm^{-1} . Both the location and strength of the plasmon absorption, as well as the dependence of these quantities on the duty cycle, agree well with theory. Sub-micron periodicities achieved with holographic lithography should lift the plasmon absorption to higher frequencies, and make possible the observation of non-local effects, which, in first order, are proportional to a^2q , where a^2 is the Bohr radius. The higher Bohr radius for a 2DES in InAs together with a higher q should make this interaction appear in far infrared transmission measurements on such samples. These investigations will be reported elsewhere.

It is a pleasure to thank P. Pitsukanjana, A. Lorke, and A. Wixforth for many illuminating discussions. This work was supported in part by the Office of Naval Research (ONR grant #N000 15-92-J-1452) through the Quantum Institute, and by the National Science Foundation (NSF grant #DMR-91-10430) through QUEST, a National Science and Technology Center, at the University of California, Santa Barbara.

1. S. J. Allen, Jr., D. C. Tsui, and R. A. Logan, *Phys. Rev. Lett.* **38**, 980 (1977).
2. D. Heinmann, *Surf. Sci.* **170**, 332 (1986), and references therein.
3. E. Batke, D. Heinmann, J. P. Kotthaus, and K. Ploog, *Phys. Rev. Lett.* **54**, 2367 (1985).
4. U. Mackens, D. Heinmann, I. Prager, J. P. Kotthaus, and W. Beinvogl, *Phys. Rev. Lett.* **53**, 1485 (1984).
5. P. Pitsukanjana, E. L. Yuh, E. G. Gwlan, M. Sundaram, P. F. Hopkins, and A. C. Gossard, to be published.
6. C. Nguyen, B. Brar, and H. Kroemer, to be published.
7. C. Nguyen, B. Brar, V. Jayaraman, A. Lorke, and H. Kroemer, to be published.
8. C. Nguyen, B. Brar, C. B. Bolognesi, J. J. Pekarik, H. Kroemer, and J. H. English, *J. Electron. Mater.* **22**, 255 (1993).
9. S. J. Allen, Jr., D. C. Tsui, and F. DeRosa, *Phys. Rev. Lett.* **35**, 1359 (1975).
10. For a comprehensive review on electronic properties of a 2DES, see: T. Ando, A. B. Fowler, and F. Stern, *Rev. Mod. Phys.* **54**, 437 (1982).
11. F. Stern, *Phys. Rev. Lett.* **18**, 546 (1967).

Figure Captions

- Fig. 1. Lateral composition modulation of the cap layer can result in substantial lateral density modulation in an InAs quantum well. U_A is the duty cycle. Figure not to scale.
- Fig. 2. Relative transmission spectra at $B = 5.6$ Tesla for the lateral superlattice with $U_A = 0.75$ for both polarizations. The lower trace has been vertically offset for clarity.
- Fig. 3. Relative transmission for the sample with $U_A = 0.5$ (a) and for the sample with $U_A = 0.75$ (b). Dashed curves are obtained from Eq. (2). The reference spectrum is $T(B = 8.4\text{ Tesla})$.
- Fig. 4. Absorption frequencies at different magnetic fields, for the sample with $U_A = 0.5$. Closed circles denote cyclotron resonance, open ones the 2D plasmon resonance. The dashed line fit for the CR line assumes $m^* = 0.037m_0$. Dashed curve for the plasmon dispersion is calculated from Eq. (3).

Middle Infrared ($\lambda=2-5 \mu\text{m}$) High Quantum Efficiency Luminescence in GaSb/InAs II-type Multi-Quantum Well Structures.

S V Ivanov, B K Kurikova, N M Ledentsov, B Ya Melner, A A Monakhov, A A Rogachev, S V Shapovalov, and P S Kop'ev

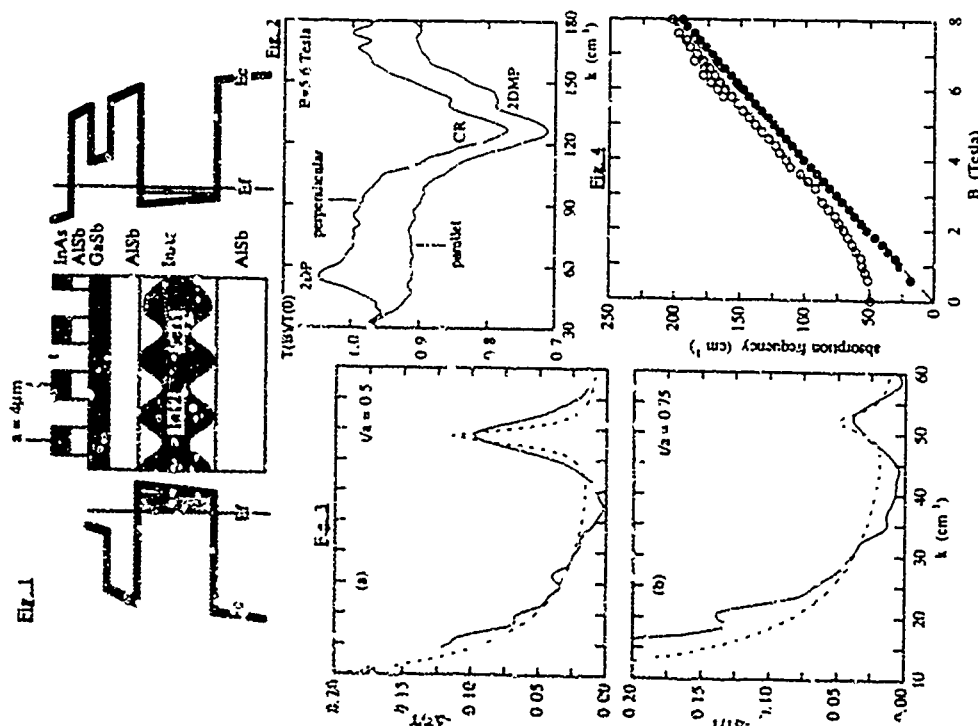
A F Ioffe Physico-Technical Inst., Academy of Sciences of Russia, Pulkovskoye Shosse, St. Petersburg 19021, Russia

The paper reports for the first time a high radiative recombination yield within the range of $2-5 \mu\text{m}$ in II-type GaSb/InAs multi-quantum well (MQW) structures grown by molecular beam epitaxy (MBE) on lattice matched (100)GaSb substrates. Earlier these superlattices were developed by L. Esaki et al [1].

The investigated structures include the buffer layer sequence, consisting of $0.2 \mu\text{m}$ -GaSb layer followed by ten period 50\AA -AlSb/ 50\AA -GaSb superlattice and a top $0.3 \mu\text{m}$ -GaSb layer, and GaSb/InAs MQW structure. The GaSb barrier thickness was always constant of 100\AA , while the InAs QW thickness varied from 10 to 30\AA . The details of substrate preparation, growth regimes have been reported elsewhere [2,3]. The growth temperature was chosen of 520°C . Special care was taken in forming the GaSb/InAs interface [4].

The double crystal differential x-ray diffraction (XRD) and transmission electron microscopy (TEM) data indicate very high structural quality of the structures. Their luminescence spectra are dominated up to room temperature by the very intensive line which is assigned to be associated with the recombination of electrons and holes in InAs/GaSb II-type MQW because of the pronounced red shift of luminescence band maxima position with the InAs QW thickness increase. The 300K to 77K integral luminescence intensity ratio was observed to be $3-4$ at $3 \mu\text{m}$ (17\AA QW) and ~ 2.5 at $5 \mu\text{m}$ (25\AA QW) at $1\text{W}/\text{cm}^2$ excitation density. These structures seem to be very promising for optoelectronic applications.

- [1] L. Esaki and L. L. Chang, Thin Solid Films 36 (1976) 285
- [2] S. V. Ivanov et al., Semicond. Sci. Technol. 8 (1992) 247
- [3] P. S. Kop'ev et al., Sem. Phys. Semicond. 24 (1990) 450
- [4] G. Tuttle et al., J. Appl. Phys. 67 (1990) 3032



-1048-

-1047-

Friday, August 27

FrA Optical Properties - Lasers

FrB Ultrafast Processes - New Optical Phenomena

A. F. J. Levi
Department of Electrical Engineering and Electrophysics
University of Southern California
Los Angeles, CA 90089-1112, USA

Abstract

InGaAs/InGaAsP quantum well microdisk lasers 0.8 μm in radius and 0.18 μm thick with emission at $\lambda = 1.542 \mu\text{m}$ can be fabricated and operated at room temperature. Optical mode spacing in such structures is so large that a significant fraction (~20%) of spontaneous emission feeds into the lasing line resulting in superlinear output over a wide pump range.

Introduction

A conventional laser diode consists of an electrically driven semiconductor optical gain medium such as InGaAs placed within a resonant optical cavity. A Fabry-Pérot cavity, defined by the presence of two parallel mirror faces, results in definite longitudinal optical resonances called cavity modes. Figure 1(a) shows the geometry of such an edge emitting laser. The optically active gain medium is typically 300-500 μm in long, approximately 1 μm wide, and 0.1 μm thick. When electrically pumped, the number of electrons (holes) injected into the conduction (valence) band of a direct band gap semiconductor may be large enough to result in optical gain over a small spectral region near the band edge. Optical gain will approach total optical loss first for the high Q (low ν_{sp}) Fabry-Pérot cavity mode nearest the peak in the gain spectrum. Lasing emission should occur predominantly into this cavity mode because the cavity resonance ensures optical losses are low. However, due to their relatively large size, these devices tend to be power hungry with threshold current for lasing greater than 10 mA. One way to reduce threshold current is to decrease the size of the device and increase the Q of the optical cavity. To some extent the advent of semiconductor microlasers was inspired by such goals.

15 years ago Iga and co-workers at the Tokyo Institute of Technology invented the Vertical Cavity Surface Emitting Laser (VCSEL) [1]. Since then designs have been refined [2] so that today dielectric mirror stacks of the order one micrometer thick above and below a quantum well active region form the high-Q resonant cavity with lasing light emission possible from the surface of the semiconductor substrate. Figure 1(b) shows a schematic diagram of a VCSEL. The optically active gain medium typically consists of one or more approximately 100 Å thick quantum wells placed at an anti-node of the cavity resonance. Small lateral dimensions in the range 3-20 μm give a potentially superior optical beam profile for launching into optic fiber as well as low threshold currents in the range of 1 mA. Threshold currents would be even lower if more of the optical field were more tightly confined to the gain medium. Nevertheless, while many practical issues still need to be addressed such as the high series resistance for current flowing through the minor stacks, initial results are encouraging enough that some companies are considering developing VCSEL arrays for use in high speed parallel optical data links.

Recently very small laser diodes have been fabricated using a different type of resonant cavity in which light is very tightly confined to the gain region and emission is in the plane of the semiconductor substrate [3, 4]. The device consists of an InGaAs/InGaAsP multiple quantum well structure formed into a 1.5-10 μm diameter disk approximately 0.1 μm

thick. Electrical current and mechanical support is provided by n- and p-type InP structures above and below the disk. Figure 1(c) shows a schematic diagram of this type of laser and figure 2 shows a scanning electron micrograph of such a microdisk laser. Total internal reflection for photons traveling around the perimeter of the semiconductor disk result in high Q whispering-gallery resonances. The term "whispering-gallery" is taken from Lord Rayleigh's explanation of sound propagation in the dome of St. Paul's Cathedral, London [5]. In the microdisk laser, the low optical losses associated with high Q whispering-gallery modes allow room temperature lasing action with a measured submilliwatt threshold current [4]. Improved designs should result in threshold currents as low as a few tens of microamps. Of course, a consequence of using very high Q resonators is that not much lasing light radiates out into free space. However, it is possible to use light output couplers which slightly spoil the Q and yet allow the emitted light to be increased and redirected in or out of the substrate plane [6]. Other structures which make use of whispering gallery modes, such as the "trenchy" under laser laser diode [7], are also being investigated.

Submicron radius disk laser

It is natural to consider how small a microdisk can be made and still function as a laser. In this context it is useful to focus on the microdisk laser since very small gain volumes and high Q cavities may be simultaneously achieved using this geometry. Figure 3 shows a scanning electron micrograph of a very small optically pumped InGaAs/InGaAsP quantum well microdisk of radius $R = 0.8 \pm 0.05 \mu\text{m}$ and thickness $L = 0.18 \mu\text{m}$. The disk is composed of six 120 Å thick quantum wells of InGaAs material lattice matched to InP. Five barriers 120 Å thick of InGaAsP separate the quantum wells, and InGaAsP layers 240 Å thick enclose the quantum well-barrier structure. The InGaAsP material has a band-edge corresponding to 1 μm wavelength radiation. After post growth fabrication the device is measured with the sample maintained at room temperature. Optical pump power from a diode laser with emission at wavelength $\lambda = 0.83 \mu\text{m}$ is focused onto the disk laser top surface using a 0.5 numerical aperture (N.A.) lens, so that at best only about 80% of total incident pump light is intercepted by the $R = 0.8 \mu\text{m}$ radius disk. The total incident pump power, P_{in} , is delivered during an 8 ns period at a repetition period of 100 ns. It is observed that heating becomes significant for pulse widths of 30 ns (30% duty cycle) or greater as evidenced by a decrease of both laser and waal light output. The radiation emitted by the microdisk is collected by the same 0.5 N.A. lens, and directed to a spectrometer. The lens collects lasing light scattered by disk imperfections into the vertical direction. The spectra shown in figure 4 were obtained with 5 nm resolution. The figure shows a luminescent background, a lasing line at $\lambda = 1.542 \mu\text{m}$, and a resonance at $\lambda = 1.690 \mu\text{m}$.

The power in the lasing line versus total incident pump power, P_{in} , is shown in figure 5. It is clear from this data that output lasing power is superlinear with input. This is in accord with simple models for very small semiconductor lasers and is most readily explained by considering the steady state intensity, S , in the lasing mode, $S = r_{\text{sp}} / (R - g_{\text{net}})$ where r_{sp} is the spontaneous emission rate into the lasing mode, R is the optical loss rate in the cavity and g_{net} is the modal gain. For S to reach a given threshold intensity S_{th} when r_{sp} is small requires a much smaller value of $(R - g_{\text{net}})$ than when r_{sp} is relatively large. Hence, superlinear behavior extends over a larger range of pump power for r_{sp} large, because the rate of change in S with P_{in} around S_{th} is larger when r_{sp} is small.

Mode counting

It is possible to construct a straight-forward mode counting argument to calculate the fraction, β , of total spontaneous emission that feeds into the lasing mode. For an ideal disk the whispering mode frequencies ω_m may be calculated to an accuracy of a few percent by solving the equation $2\pi m a_0(\omega)R = x_{0,p}c$, where c is the speed of light in vacuum, $n_d(\omega)$ is the (two-dimensional) effective refractive index, and $x_{0,p}$ is the smallest positive root of $J_p(x) = 0$, where J_p is the usual Bessel function with integer index M . Larger roots are denoted by $x_{0,p}'$. The effective refractive index is found from

$$\text{Im}(\omega) \sqrt{\epsilon - n_{\text{eff}}^2} / \lambda = \sqrt{(n_{\text{eff}}^2 - 1) / (\epsilon - n_{\text{eff}}^2)}$$

where ϵ is the real part of the semiconductor dielectric constant. The small discrepancy between the calculated $\lambda_1 = 1.480 \mu\text{m}$ and $\lambda_2 = 1.634 \mu\text{m}$ and experimentally measured ($\lambda_1 = 1.542 \mu\text{m}$, $\lambda_2 = 1.690 \mu\text{m}$) values of λ_0 is in part due to uncertainties in the exact physical dimensions of the disk.

The spontaneous emission rate into a mode may be expressed as

$$r_{\text{sp}}^{\omega} = \int r_{\text{sp}}(\omega) \Gamma(\omega) d\omega$$

where

$$\Gamma(\omega) = \frac{\gamma(\omega) / \pi}{(\omega - \omega_c(\omega))^2 + \gamma(\omega)^2}$$

is the cavity function and $\gamma(\omega)$ describes the frequency dependent line shape of the resonance centered at $\omega_c(\omega)$. For simplicity we consider the case where both ω_c and γ are independent of ω . Clearly, if γ is small, it follows that Γ is a δ -function and so $r_{\text{sp}}^{\omega} = r_{\text{sp}}(\omega_c)$. Even though the cavity line width γ may be small and the spontaneous emission into the mode originates from the frequency interval $\omega_c \pm \gamma$, such emission is enhanced by $1/\gamma$ so that the principle of mode partition is preserved. However, when γ becomes larger than the luminescence width, r_{sp}^{ω} is usually reduced below $r_{\text{sp}}(\omega_c)$ by an overlap factor

Spontaneous emission within a dielectric slab of the disk's thickness ($0.4 \times \lambda$ in the material) and composition is about 75% into trapped transverse electric modes (evanescent above and below the dielectric), 10% transverse magnetic modes and about 15% into free modes propagating outside the dielectric [Ref. 8]. Very little goes into trapped transverse magnetic modes because most of the corresponding modal energies are outside the dielectric. If one assumes these properties of dielectric slab also apply to disks then about 75% of spontaneous emission is into two-dimensional disk modes of transverse electric character describable by scalar forms $J_p(n_d \rho \omega / c) e^{i p \theta}$, where θ is the polar coordinate angle and ρ is the radial coordinate. There are four roots $x_{0,p}$ of Bessel functions J_p

between $x_{0,1} = 9.936$ and $x_{0,2} = 7.588$, namely $x_{0,1}' = 8.771$ (corresponding to the $M = 5$ whispering-gallery mode lasing emission measured at $\lambda_1 = 1.542 \mu\text{m}$), $x_{0,2}' = 8.654$, $x_{0,3}' = 8.417$, and $x_{0,4}' = 9.761$. Thus, in this region, there are about $(2 + 2.5)$ modes in an interval centered on the $M = 5$ whispering mode and with endpoints halfway to the adjacent whispering modes. The factor 2.5 is from counting half of the 5 modes corresponding to $x_{0,1}'$, $x_{0,2}'$, and $x_{0,3}'$, taking into account the degeneracy factor of two for $M > 0$. The factor 2 is from $x_{0,4}'$ and its degeneracy of two. The separation of the $M = 4$ and $M = 5$ whispering modes is about 350 nm and the measured spectral width of luminescence (full-width half-maximum) is about 220 nm for $P_{\text{in}} = 1 \text{ mW}$. Including the 75% factor mentioned above, one may therefore estimate that the fraction of spontaneous emission which goes into one of the $M = 5$ whispering gallery modes is $\beta(P_{\text{in}} = 1 \text{ mW}) = (150 \times 0.75) / (220 \times 4.5) = 0.106$, or 0.212 into both $M = 5$ whispering modes.

This result for β appears to be inconsistent with the measured emission shown in figure 4. However, it should be noted that in an ideal disk geometry, radiation from whispering modes is emitted into directions near the plane of the disk, not towards the vertical direction and into the detection apparatus. In addition, the measured smooth luminescence background has a substantial and perhaps dominant contribution from free modes. Furthermore, below transparency, light emitted into whispering modes is substantially absorbed before it escapes the laser structure and is detected. Overall, these effects reduce the apparent β value as determined by casual inspection of the vertically emitted emission spectrum. It is worth mentioning that disk modes other than whispering gallery modes are expected to have relatively low Q values. If a mode width exceeds the luminescence width, the amount of spontaneous emission into such a mode is reduced by an overlap factor. In that case, low Q modes with central frequencies outside the luminescence region experience some spontaneous emission. Nevertheless, the sum of modes times their overlap factor should still give the fraction, β , calculated above.

Device physics

The above results and discussion are representative of present knowledge of microlaser operation. In fact, it is remarkable that while very small laser diodes have been fabricated, our understanding of how such devices work is manifestly inadequate. Much of what is interesting about microlasers cannot be modeled with the commonly used rate equations for carrier and photon density in the device. In fact, efforts to parameterize microlaser effects with such an unjustifiably simplistic approach are somewhat pointless and bound to fail. The weakness of such modeling motivated the use of mode counting (described above) to establish a value for β . Clearly, it is necessary to examine every relevant aspect of the physics governing device operation before developing a new model for microlasers.

The spacing between the mirrors of a standard Fabry-Pérot laser is relatively large so that several hundred longitudinal cavity modes overlap the optical gain spectrum. It follows that only a small fraction ($\beta = 10^{-4}$ - 10^{-5}) of spontaneous photon emission feeds into the longitudinal lasing mode. This combined with the large difference between stimulated and spontaneous recombination rates gives rise to an abrupt increase in lasing light output with increasing drive current above threshold. However, below threshold there exists between a intensity in cavity modes. In fact, the formal mathematical analogy which exists between a nonequilibrium Landau-Ginzburg phase transition and photon field statistics around

threshold allows us to describe all photons in cavity modes below threshold as (unsustainable) fluctuations [Ref. 9].

In a very small resonant cavity, such as those used in microcavity lasers, it is possible that only one optical mode overlaps the semiconductor's gain and spontaneous emission spectrum. In such a situation every spontaneous emission event fluctuates into the lasing mode and there is no abrupt increase in average lasing level with which to define a laser threshold. Similarly, it is no longer possible to define a threshold by considering moments of the statistical distribution in photon number [Ref. 10]. Apparently, the concept of a laser threshold along with the implicitly mean-field language of Landau-Ginzburg phase transitions is no longer useful and a full quantum mechanical description may become necessary [Ref. 11].

It is also worth mentioning that fluctuations in photon number may also be driven directly by fluctuations in electron number. This may become important in microlasers which are so small they operate using only a few thousand electrons. In such a situation the influence of variations in electron chemical potential can be modified depending on whether the laser is driven by an external voltage or current source.

Of course, the above relates to only one aspect of the problem which, unfortunately, is overshadowed by the more fundamental concern of optical gain in a resonant cavity. Even after several decades of effort, physicists have failed to develop a satisfactory quantitative model of optical absorption and gain in bulk, intrinsic semiconductors. Such a poor state of affairs is perhaps understandable when one begins to consider the complexity of the problem [Ref. 12]. If one specializes to the case of electron distributions in thermal equilibrium with the semiconductor lattice, then, under low drive current conditions, the semiconductor's band-edge absorption spectrum shows strong conduction-valence band many-electron interaction effects in the form of spectrally sharp excitation features. Under high drive current the semiconductor may contain on order 10^{18} cm^{-3} excess electrons and display optical gain over a small spectral range near the band-edge and absorption elsewhere. Electron interaction effects redistribute and broaden the spectral weight in the excitation features and a significant band tail develops in the semiconductor's renormalized band gap. Even if many-electron interaction effects could be evaluated beyond the mean field (random phase) approximation and a satisfactory quantitative explanation of band tails be established we would still be limited to the case of thermal equilibrium. It seems unlikely, however, that the electron distribution in a microlaser is, in fact, at thermal equilibrium with the semiconductor lattice. The reason for this is that the calculated time scales for various optical and electronic relaxation processes in microlasers are comparable. For example, a microlaser of radius $R = 1 \mu\text{m}$ with emission wavelength $\lambda = 1.5 \mu\text{m}$ has a calculated cavity round trip time of 40 fs, a cavity photon lifetime of 150 fs, and an electron-electron scattering rate in the range of 100 fs. In these circumstances one is tempted to speculate that lasing photons remove electrons from the system at such a fast rate that the electron distribution is unable to equilibrate. The resulting spectral hole burning [Ref. 13] in the electron distribution reduces the spontaneous emission into the lasing mode modifying both the intensity and spectral purity of the microlaser output characteristics. In practice however, except for devices with disk radius less than $1 \mu\text{m}$ this situation is somewhat masked by spatial diffusion of charge carriers from regions of low photon field intensity in the microstructure.

The short and comparable characteristic time scales for cavity round trip time, photon lifetime, and electron scattering rate in microcavity lasers raises the interesting issue of distinguishing between optical and electronic processes on short time scales. One is tempted to speculate that, since electron scattering is mediated via emission and absorption

of a photon on very short time scales one ultimately cannot distinguish between optical and electronic phenomena.

Conclusion

In summary, room temperature lasing action in a very small InGaAs/InGaAsP quantum well microlaser of radius $R = 0.8 \mu\text{m}$ and thickness $L = 0.18 \mu\text{m}$ has been demonstrated. It is estimated that, for this device, approximately 20% of the spontaneous emission feeds into the $M = 5$ whispering gallery modes at wavelength $\lambda = 1.542 \mu\text{m}$. Although it should be possible to fabricate even smaller structures which lase into the $M = 4$ whispering gallery mode, there is still much to be understood about the physics of microlaser operation.

REFERENCES

1. H. Sasa, K. Iga, C. Kitahara, and Y. Suenatsu, *Japn. J. Appl. Phys.* **18**, 2129 (1979), and K. Iga, S. Kinoshita, and F. Koyama, *Electron. Lett.* **23**, 134 (1987).
2. For a review, see J. L. Jewell, editor of special issue *Microresonator devices*, *Quantum Electronics* **24** (1992).
3. S. L. McCall, A. F. J. Levi, R. E. Slusher, S. J. Pearton, and R. A. Logan, *Appl. Phys. Lett.* **60**, 289 (1992).
4. A. F. J. Levi, R. E. Slusher, S. L. McCall, T. Tanbun Ek, D. L. Coblenz, and S. J. Pearton, *Electron. Lett.* **28**, 1010 (1992).
5. Lord Rayleigh, *Scientific Papers*, p. 617, Cambridge University, Cambridge, England (1912).
6. A. F. J. Levi, R. E. Slusher, S. L. McCall, J. L. Glass, S. J. Pearton, and R. A. Logan, *Appl. Phys. Lett.* **62**, 561 (1993).
7. A. F. J. Levi, R. E. Slusher, S. L. McCall, S. J. Pearton, and W. S. Hobson, *Appl. Phys. Lett.* **62**, 2021 (1993).
8. S. J. Ho, S. L. McCall, and R. E. Slusher, *Quant. Electron. Laser Sci. Tech. Dig.* **11**, 53 (1991).
9. This discussion is discussed by H. Haken, *Licht*, Vol. 2, *Laser Light Dynamics*, North Holland, Amsterdam (1986), also see V. De Giorgio and M. O. Scully, *Phys. Rev. A*, **22**, 1170 (1970), R. Graham and H. Haken, *Z. Physik*, **273**, 3; (1970), S. Guenzburg and P. H. Richter, *J. Phys.*, **242**, 458 (1971), M. Conti and V. De Giorgio, *Phys. Rev. Lett.* **36**, 1173 (1976).
10. H. J. Channin, *Lasers and Quantum Optics*, editors L. M. Narducci, P. J. Quel, and J. R. Tredence, World Scientific, Singapore (1991).
11. M. Lax, *1966 Rhoades University Summer Institute of Theoretical Physics*, vol. II, editors M. Chretien, L. P. Gross, and S. Deser, Gordon and Breach, New York (1968), also V. Korenman, *Annals of Physics*, **39**, 72 (1966).

- 12 For an overview see: *Quantum theory of the optical and electronic properties of semiconductors*, H. Haug and S. W. Koch, World Scientific, Singapore, (1990)
- 13 For a recent discussion on spectral hole burning see K. Henneberger, P. Herzog, S. W. Koch, R. Binder, A. L. Paul, and D. Scott, *Phys. Rev. A* **45**, 1853 (1992)

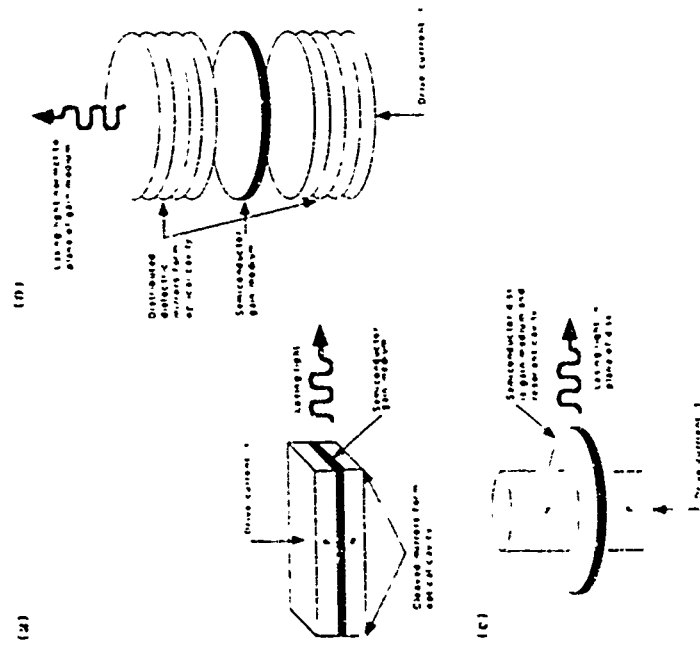


Fig. 1 Schematic diagram of (a) an edge emitting Fabry-Pérot laser diode, (b) a VCSEL, and (c) a microdisk laser. Drive current is indicated.

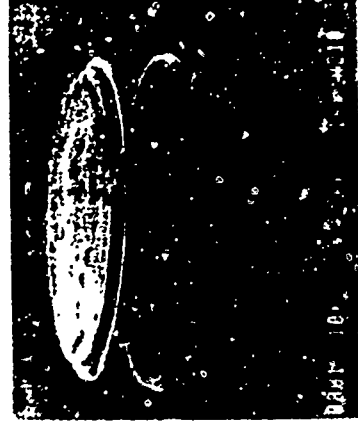


Fig. 2 Scanning electron micrograph of an approximately 10 μm diameter microdisk laser diode similar to the device discussed in Ref. 4

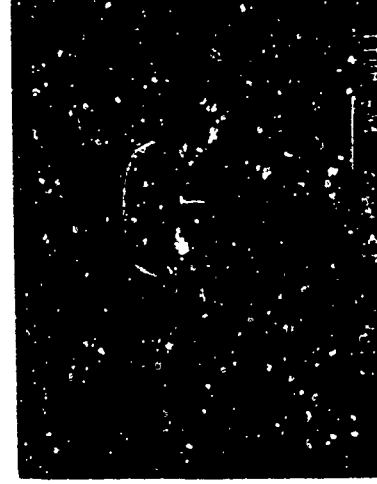


Fig. 3 Scanning electron micrograph of an InGaAs/InGaAsP multiple quantum well microdisk laser with $R \approx 0.8 \mu\text{m}$ and $L \approx 0.18 \mu\text{m}$. The 1 μm bar provides a scale

FrA2

GaAs-AlAs and Si-SiGe Quantum Well Structures For Applications in Nonlinear Optics.

M.J. Shaw, K.B. Wong, and M. Jaros

Physics Department, The University, Newcastle upon Tyne, England, NE1 7RU.

Both, GaAs-AlAs and Si-SiGe quantum well structures have been considered for applications as infrared detectors, modulators and switching devices. The miniband structure in these systems covers a wide range of energies (e.g. 1-200 meV) and offers an opportunity to design optical devices that would operate in the far infrared range of wavelengths. An external electric field and triangular wells have been used to modify the structure of confined states. This enhances optical nonlinearities (e.g. the second order susceptibility). In this paper we present the first full scale evaluation of GaAs-AlAs and Si-SiGe quantum well structures in which the nonlinearity arises due to virtual optical transitions between valence minibands. We aim at structures which could operate in the 10-15 micrometer range. We present both the magnitude and the frequency dependence of the second order susceptibility. We show that the valence band structure offers several advantages compared to the conduction band. We find that - contrary to commonly held views - the strongest contributions to the second order response originate from regions in momentum space lying farther from the zone centre. Also, the frequency of the peak response does not correspond to that expected from simple models.

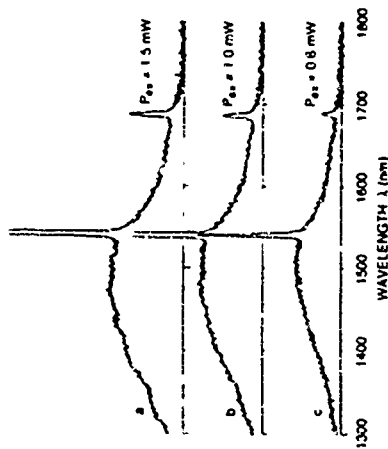


Fig 4 Room temperature photoluminescence spectra of a $R = 0.8 \mu\text{m}$ radius microdisk laser. Excitation is by a pulsed AlGaAs/GaAs laser diode emitting at $\lambda = 0.85 \mu\text{m}$. Pump power incident on the device is P_{in} .

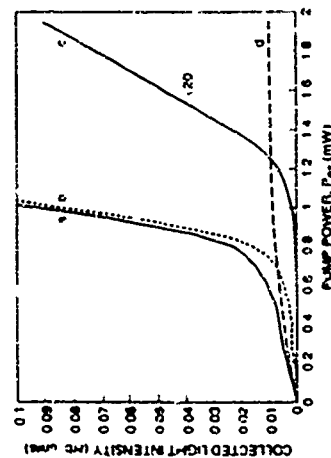


Fig 5 Room temperature power at the lasing wavelength versus incident pump power. P_{in} for the $R = 0.8 \mu\text{m}$ microdisk laser of Fig 3 and 4. (b) Power in the lasing line versus pump power. (c) Power at the lasing wavelength versus pump power. Vertical scale is divided by 20. (d) Power in the spontaneous emission background at the lasing wavelength versus pump power. Resolution is 5 nm.

FrA3

Charge Transfer and Electrosorption in an Electric Field Tunable Double Quantum Well Structure

K. Bernhard, A. Zrenner, G. Böhm, G. Trökle and G. Weimann
Walter Schottky Institut, Technische Universität München,
85748 Garching, Germany

Abstract

An optical modulator based on electric field induced charge transfer in a double quantum well structure is introduced. The modulator is configured as n-i-n diode for waveguide applications at a wavelength of $\sim 1 \mu\text{m}$. Dark currents caused by thermionic emission are suppressed by introducing specially designed InGaAs/AlGaAs hetero barriers. Room temperature operation with negligible dark current up to internal electric fields of $1.7 \times 10^5 \text{ V/cm}$ is demonstrated. Electric field tunable absorption is obtained by both band filling and Stark effect in a GaAs/InGaAs double quantum well unit which has been repeated five times in the i-region of the n-i-n structure. Absorption spectroscopy is performed in waveguide geometry and applications as optical modulators are demonstrated.

The introduction of III/V quantum well (QW) structures opened a variety of new perspectives in semiconductor optoelectronics. Deliberate control over individual layer composition and thickness allows the construction of highly optimised optoelectronic devices. In this contribution we describe an optical modulator based on charge transfer [1,2] and quantum confined Stark effect [3] in a pseudomorphic GaAs/InGaAs double QW structure. The present structure is configured as an electric field tunable n-i-n hetero diode for optical waveguide applications. In contrast to the related InP-based BRACQWET device [1,2] our structure is designed for a wavelength in the range of $1 \mu\text{m}$ to match to the emission lines of strained layer InGaAs QW lasers.

The overall band diagram of our layer sequence is shown in Fig. 1. The electro-optically active parts of the structure are the double QW (DQW) units in the centre of the AlGaAs i-region. Five DQW units have been introduced into the i-region to obtain sufficient electroabsorption and optical confinement on one hand and to avoid problems with the overall critical layer thickness of the strained layer InGaAs system on the other hand. The layer sequence of a single unit is indicated in the left bottom part of Fig. 1. The modulator is operated near the fundamental band gap of the 80 Å i-InGaAs 15%GaAs QW. This optically active QW is separated on one side by a 10 Å GaAs interface layer and a 150 Å i-Al_{0.45}Al_{0.55} barrier from a 120 Å n-doped GaAs QW, which acts as a charge reservoir. On the other side a 102 Å p-Al_{0.45}Al_{0.55} layer is separated by a 10 Å GaAs interface layer and a 100 Å i-Al_{0.45}Al_{0.55} spacer. The basic purpose of this layer sequence is twofold: The charge reservoir first of all has been designed to provide electrons for an electric field induced transfer over the AlGaAs barrier into the InGaAs QW. The p-AlGaAs layer on the other hand has been introduced to increase the effective barrier height in order to minimise thermionic emission of electrons out of the DQW region. Without loss due to thermionic emission and tunnelling each single unit is by itself

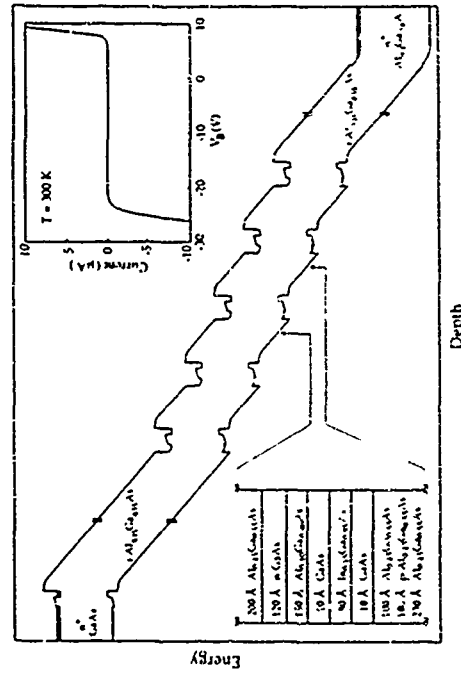


Fig. 1: Calculated band diagram of the n-i-n double QW modulator structure. The layer sequence of one out of the five active double QW units is shown on the left. The insert on the right shows the room temperature I-V characteristic of the structure as measured on a $200 \mu\text{m} \times 300 \mu\text{m}$ mesa diode.

neutral. The net number of free electrons N_e in each unit is given by $N_e = N_D - N_A = 1 \times 10^{12} \text{ cm}^{-2}$, where N_D (N_A) is the doping concentration of the n-layer (p-layer) and d_p (d_n) the corresponding layer thickness. As shown in Fig. 1 the additional dipole field between the n- and p-doping layer leads to a saw-tooth like potential drop throughout the structure. Although thermionic emission currents are suppressed by the presence of the p-doped AlGaAs barriers and by the introduction of the InGaAs/AlGaAs hetero interface, additional care has been taken to avoid the depletion of individual units even on a long time scale. If electron depletion happens in a given unit, the electric field on the right hand side of the unit is reduced, while the field on the left hand side is increased (for the bias conditions shown in Fig. 1). This in turn has an influence on the thermionic depletion of the neighbouring units. A homogeneous potential drop throughout the structure as indicated in Fig. 1 can only be obtained if the effective barrier heights of all built-in hetero barriers are identical. The first hetero barrier on the top left part of Fig. 1 (n-i junction) has therefore been chosen to be identical to those used in the optically active DQW units. From these considerations it is also quite obvious, that a unipolar charge transfer device as described here can only be implemented as n-i-n structure. Attempts to introduce the active DQW units in the intrinsic region of a p-i-n structure would result in a depletion of the active units and in an inhomogeneous potential drop throughout the structure.

The room temperature I-V characteristic of a $200 \mu\text{m} \times 300 \mu\text{m}$ mesa diode processed from our n-i-n layer sequence is shown in the insert of Fig. 1. The introduction of the InGaAs/AlGaAs hetero interface and the p-type doping layer in the AlGaAs barrier results in a maximum bias voltage V_b of

about 25V with negligible dark current. This means that electric fields up to 1.7×10^5 V/cm can be controlled without significant current flow.

Such a tuning range is sufficiently high to cause an appreciable electric field induced charge transfer within the DQW units. The individual layer width and composition of the DQW units have been calculated to allow for a transfer of 5×10^{11} cm⁻² electrons from the GaAs into the InGaAs QW within the available tuning range of the electric field. With our design parameters and tuning range the interwell charge transfer is expected to happen on a picosecond time scale⁴. For realistic applications the modulation bandwidth of our structures will be therefore RC-limited. The band diagrams and charge distributions as calculated with a self-consistent model calculation for room temperature are shown in Fig. 2 for two different bias conditions. The results in Fig. 2 have been obtained by treating the DQW unit as a coupled QW system. Only the relevant subband levels are indicated. All subbands are shown with their probability distribution. Levels with significant electron occupancy are shown in gray and are scaled proportionally to the individual electron occupancy in order to visualize the field induced charge transfer.

At $V_g = 3V$ all electrons are confined in the doped GaAs QW. The InGaAs QW is empty and biased by the electric field which builds up between the doped GaAs QW and the p-type doping layer in the Al_{0.3}Ga_{0.7}As barrier. At $V_g = 20V$ half of the original charge in the GaAs reservoir has transferred into the now unbiased InGaAs QW. What the optically active InGaAs QW is concerned, both the changes in electric field in terms of the QCSE and the changes in charge accumulation (band filling) lead to a blue-shift in the absorption spectrum of the lowest spatially direct transition in the InGaAs QW as V_g is decreased from 3V ($E_g \rightarrow E_{g0}$) to -20V ($E_g \rightarrow E_{g0}^*$).⁵

All optical investigations on our structure have been performed in waveguide geometry for TE polarization. The optical transmission as a function of wavelength is shown in Fig. 3 for different bias conditions. The spectra have been recorded with a stabilized Ti:sapphire laser and a Si p-i-n detector diode. Both facets of the waveguide remained uncoated. The dimensions of the electric field tunable waveguide structure are shown in the insert of Fig. 3. The high frequency Fabry-Pérot oscillations caused by the internal reflections at the facets have been removed for clarity by a numerical filtering process. The data clearly confirms the predicted blue-shift of the absorption which appears here as a blue-shift of the transmission for decreasing V_g (7V \rightarrow -20V). The observed blue-shift is considerably stronger in the regime of the band QCSE ($V_g > 3V$) as compared to the regime of band filling ($V_g < 0V$), where part of the blue shift is compensated by the red shift which originates from band gap

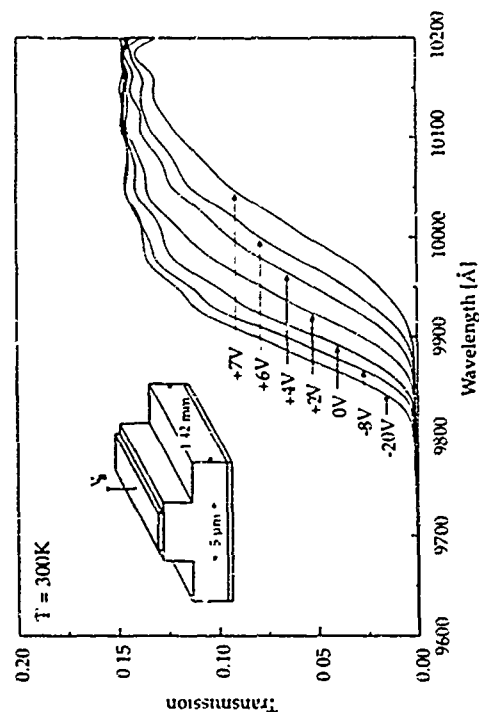


Fig. 3: Optical transmission in waveguide geometry as a function of wavelength for different V_g . The dimensions of the optical waveguide are indicated.

recombination^{6,7}. From the displayed data it is difficult to clearly separate the regime of band filling and QCSE. In the transition region between those two regimes an interesting enhancement of the blue-shift is observed (compare data for 0, 2, 4 and 6V). From the QCSE alone a monotonic blue-shift of the incremental blue-shift with decreasing V_g would be expected, as observed for $V_g = 7, 6$ and 4V. Between $V_g = 4$ and 2V however again an increase of the incremental blue-shift is observed, just before the regime of band filling at $V_g < 0V$. We tentatively attribute this behaviour to the appearance of an excitonic regime which is quenched by the QCSE on one side and by the transition to a charged plasma due to band filling on the other side.⁸

The electric field induced changes of the absorption spectrum can be directly applied in a modulator which is operated in the electro-absorptive mode in the region around 9900Å. The on/off ratio for this operation mode is shown in Fig. 4 as a function of wave-length. The bias voltage V_g was switched between a fixed reference voltage of 7V and the indicated values. The set of data demonstrates that the electro-absorptive straight waveguide version of this n-i-s structure can be directly used for device applications at room temperature. The propagation loss for $V_g = 20$ at the operation wavelength of 9900Å is only 2dB as shown in the insert of Fig. 4. If a lower on/off ratio can be tolerated in a system design, also high speed operation with reduced voltage swing is possible (for example 0V \rightarrow 2V). This reduces the requirements of the digital driver circuit. The RC time constant (50Ω system without parasitic capacitance) of the investigated waveguide structure is only 20ps.

FRA4

Strained InAs/Ga_{0.7}In_{0.3}As quantum-well heterostructures grown by molecular-beam epitaxy for long-wavelength laser applications

I. Journeai, P. Grunberg, C. Foullant, A. Baranov, A. Loullie, and K. H. Ploog

Max Planck Institut für Festkörperforschung D-70506 Stuttgart (Germany)
LM2 URA CNRS 192 Université de Montpellier II F-34095 Montpellier (France)
Paul Drude Institut für Festkörperelektronik D-10117 Berlin (Germany)

Abstract

Strained InAs single quantum wells (SQWs) embedded in a Ga_{0.7}In_{0.3}As matrix are studied by photoluminescence spectroscopy. Spontaneous emission is obtained up to 2.1 μm at 100 K, which is the longest wavelength achieved so far with QWs grown on InP substrates. Laser diodes based on a 10 ML wide InAs SQW confined by Ga_{0.7}In_{0.3}As layers are characterized. At 80 K, the emission spectrum of broad area diodes is centered at 1.56 μm and the threshold current density is 175 A/cm². Continuous wave operation is achieved with narrow stripe devices but at shorter wavelength due to increased losses and filling of the QW energy levels.

Introduction

The study of strained layer heterostructures (SLHs) attracts currently much attention because they exhibit unique physical properties [1] which find applications in microwave as well as optoelectronic devices. One of the most remarkable benefits of SLHs manifests itself in the quantum-well (QW) laser field where the peculiar valence band configuration of compressively strained layers [2, 3] results in superior laser performances as compared to lattice matched devices [4]. Strained InAs QWs confined by Al_{0.4}In_{0.6}As lattice matched to InP have been previously been credited a high potential for laser emission near 1.5 μm [5]. Substituting the Al_{0.4}In_{0.6}As confining layer by a Ga_{0.7}In_{0.3}As layer, which has a much narrower band gap energy (0.75 eV versus 1.15 eV at 300 K), should in principle allow emission to be obtained at longer wavelengths, where a number of interesting applications exist. However, stimulated emission has not yet been reported in these materials systems because the high strain (1.2%) experienced by InAs renders the epitaxy of high quality structures very difficult. In this work we demonstrate that the InAs/Ga_{0.7}In_{0.3}As QW materials system is suited for emission above 1.6 μm and we report the first operation of laser diodes made from this system.

Growth Procedure

The samples under investigation are InAs SQWs embedded in a Ga_{0.7}In_{0.3}As matrix which are grown on n⁺ (100) oriented InP substrates by solid source MBE in a Riber 12P system. The detailed growth procedure can be found in Ref. [6]. The key point is that the InAs SQWs are grown under virtual surfactant conditions [6] which allow superior quality QWs to be obtained and enhance the critical thickness before defect generation [7]. The InAs SQW with lies between 2 and 23 ML in different samples. High resolution double-crystal x-ray diffraction (HRXRD) was used to check the structural properties of the samples and to demonstrate that the epitaxial structures are actually pseudomorphic.

Present address: Paul Drude Institut für Festkörperelektronik, Bussestrasse 7, D-10117 Berlin (Germany)

-1064-

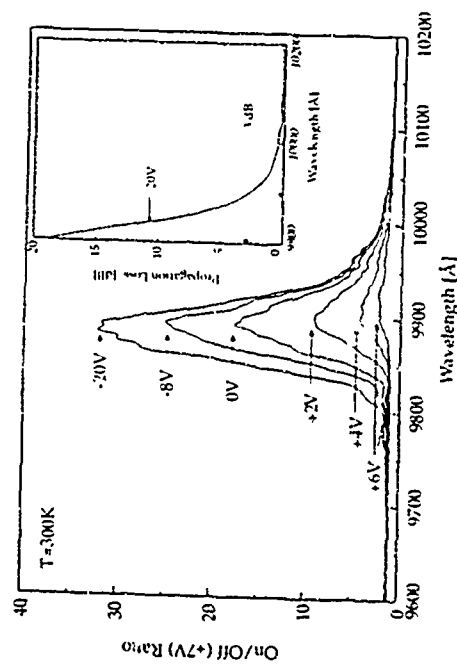


Fig. 4: On/Off ratio of the transmitted light intensity as a function of wavelength for various Vb. The reference bias voltage for all the data is 7V. The propagation loss is shown in the inset.

In conclusion we have introduced an optical modulator based on electric field induced charge transfer and QCSE in a DQW unit. The modulator is configured as a n-i-n type tunable waveguide structure for applications at wavelength around 1 μm . Thermooptic emission at room temperature is controlled by introducing InGaAs/AlGaAs hetero interfaces. Electric field tunable absorption is obtained by both band filling and Stark effect in a GaAs/InGaAs double quantum well unit. Absorption spectroscopy is performed in waveguide geometry and the application as optical modulator is demonstrated. This work has been supported by the BMEFT Photonics project.

References:

- [1] M. Wegner, J. E. Zucker, T. Y. Chang, N. J. Sauer, K. L. Jones and D. S. Chemla, *Phys. Rev. B* **41**, 3097 (1990)
- [2] J. E. Zucker, M. Wegner, K. L. Jones, T. Y. Chang, N. Sauer and D. S. Chemla, *Appl. Phys. Lett.* **56**, 1951 (1990)
- [3] D. A. B. Miller, D. S. Chemla, T. C. Damen, A. C. Gossard, W. Wiegmann, T. H. Wood and C. A. Burus, *Phys. Rev. Lett.* **53**, 2173 (1984)
- [4] J. Wang and J. P. Leburton, *Appl. Phys. Lett.* **59**, 2709 (1991)
- [5] The indicated transitions are the energetically lowest transitions in the InGaAs QW. Both transitions are dipole allowed.
- [6] H. Sakaki, H. Yoshinaka, and T. Matsunae, *J. Appl. Phys. Japan* **16**, L1104 (1987)
- [7] A. Pinczuk, J. Shah, R. C. Miller, A. C. Gossard and W. Wiegmann, *Solid State Commun.* **50**, 735 (1984)

-1063-

Photoluminescence Spectroscopy

For the PL experiments, the excitation source was the 0.17- μm line of a Kr^+ laser and the emitted signal was detected by a cooled InSb detector. We have plotted in Fig. 1 the PL spectra taken at low temperature (6 K) from representative SQWs. Note that they span the 1.4 to $2.2\text{ }\mu\text{m}$ wavelength range. The vertical arrows indicate the positions of the transitions from the confined electron state e_1 and the confined heavy-hole state hh_1 , calculated with the envelope function model.³¹ Assuming fully strained InAs QWs and using the parameters given in Ref. 16, excellent agreement between calculated and experimental values is obtained except for the thinnest wells which are more sensitive to any interface fluctuation. However, when increasing the SQW width above 15 ML , the PL line broadens and becomes less intense. This result is indicative of a slight structural deterioration as also observed by HRXRD. Nevertheless, the excellent agreement between experimental and calculated positions indicates that even the widest SQWs are elastically strained as also confirmed by transmission electron microscopy.²¹ It has to be noted that we have measured the narrowest PL lines ever reported for InAs QWs grown on InP substrates [10], which reveals the superior quality of our samples.

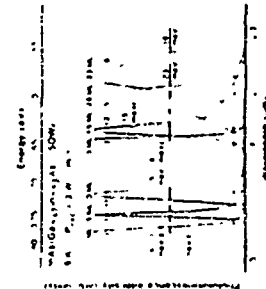


Fig. 1. PL spectra taken at 6 K from (a) pure $\text{PbO} \cdot \frac{1}{2} \text{Pb}$ spectrum taken at 600 K from the same sample $\text{PbO} \cdot \frac{1}{2} \text{Pb}$; (b) $\text{PbO} \cdot \frac{1}{2} \text{Pb}$ and $\text{PbO} \cdot \frac{1}{2} \text{CaO} \cdot \frac{1}{2} \text{PbO} \cdot \frac{1}{2} \text{CaO}$; (c) $\text{PbO} \cdot \frac{1}{2} \text{Pb}$ and $\text{PbO} \cdot \frac{1}{2} \text{CaO} \cdot \frac{1}{2} \text{PbO} \cdot \frac{1}{2} \text{CaO}$.

To further evaluate the potential of the $\text{In}_x\text{As}_{1-x}/\text{GaAs}$ QW materials system for light emitter application we have studied the emission as a function of the temperature. PL could be obtained up to 400 K from all samples investigated in this study. As an example we show in Fig. 2 the PL spectrum taken from the widest (2.2 nm) InAs/GaAs QW structure. Although the QW line is rather broad, its peak position (2.2 eV) is very well with the calculated value indicated by the vertical arrow. Any structural relaxation of this QW would give a red shift by as much as 0.2 eV. This wavelength (620 nm) is our knowledge the longest wavelength achieved up to now with QW's grown on InP substrates.

Laser diode characteristics

layer diodes were fabricated from a 10 M Ω InAs/GaSb film. As shown in Fig. 1, the output power versus current for a typical broad-area (200 μm \times 500 μm) diode under pulsed current injection is as large as 1 mW at 1.4 μm emission wavelength. The broad-band current density is

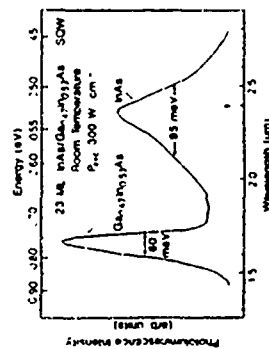
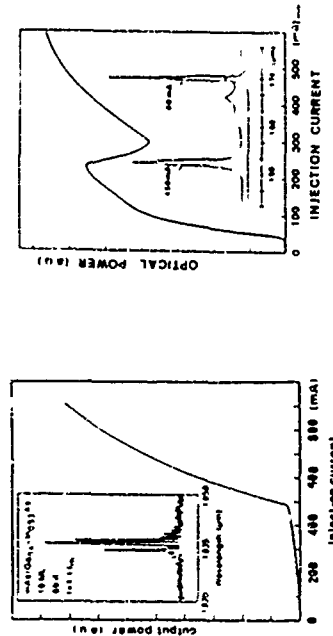


Fig. 1. PL spectra taken at 6 K from (a) pure $\text{PbO} \cdot \frac{1}{2} \text{Pb}$ spectrum taken at 600 K from the same sample $\text{PbO} \cdot \frac{1}{2} \text{Pb}$; (b) $\text{PbO} \cdot \frac{1}{2} \text{Pb}$ and $\text{PbO} \cdot \frac{1}{2} \text{CaO} \cdot \frac{1}{2} \text{PbO} \cdot \frac{1}{2} \text{CaO}$; (c) $\text{PbO} \cdot \frac{1}{2} \text{Pb}$ and $\text{PbO} \cdot \frac{1}{2} \text{CaO} \cdot \frac{1}{2} \text{PbO} \cdot \frac{1}{2} \text{CaO}$.

The lasing characteristics of the p-n junction diodes strongly depend on the stripe width. The laser output current versus voltage (I - V) curves at different temperatures are shown in Fig. 6. It can be seen from Fig. 6 that the forward bias voltages required for the onset of lasing decrease as the temperature increases. The threshold current density increases with increasing temperature according to the law $J_{th} \propto T^{-1}$, which is typical of semiconductor lasers (see, e.g., [7]). Figure 7 shows the output power versus current (P - I) curves at different temperatures. As can be seen from Fig. 7, the maximum output power decreases as the temperature increases. Two spectra taken under pulsed current injection of 60 mV and 150 mV are displayed in the inset of Fig. 1. Several features have to be noted. First, under low injection (60 mV), the spectrum is centered at 1.74 μm . Instead of the 1.81 μm obtained with a broad area device (Fig. 1) although both devices were made from the same epitaxial wafer. Second, under high injection the main laser emission occurs at a shorter wavelength of 1.72 μm at the 600 K-InAs barrier wavelength. Finally, we have also noted that when increasing the temperature above 80 K, the threshold current density increases exponentially with a low characteristic temperature of $T \approx 40$ K for the broad area diode and $T \approx 35-40$ K for the narrow stripe devices. Above 110 K, the main layer mode in the InGaInSb barrier corresponds to the Ga_{0.9}In_{0.1}Sb barrier. To understand such a priori puzzling findings, one has to consider the band structure of the 10 ML In_{0.9}Ga_{0.1}In_{0.9}Sb displayed in Fig. 5. The well is rather shallow; the heavy hole and electron levels lie respectively 42 meV and 80 meV below the barrier band edges, respectively. In addition, it has



I_{in} vs. I_{out}: Output power versus drive current measured at 40 k from a narrow stripe diode (7 μm × 50 μm). The inset shows I_{out} vs. I_{in} taken under 40 k and 530 mV current densities respectively.

(5) $\lambda_{\text{em}} = 1.50 \mu\text{m}$: the inset in Fig. 3 shows a spectrum taken from the same diode at $I = 1.1 I_{\text{th}}$. It is centered at $1.50 \mu\text{m}$ with about ten clearly resolvable longitudinal modes. This is the first observation of laser emission from InAs QWs grown on InP substrates. The peak position well fits the value of the e_1 – hh_1 transition calculated for a 30 ML InAs/GaAs SQW (1.515 μm). Planar narrow stripe devices ($5 \mu\text{m} \times 850 \mu\text{m}$) were also fabricated from the same epitaxial wafer. In this case the threshold current density at 80 K is $10 \text{ mA}/I_{\text{th}} = 1.2 \text{ A}/\text{cm}^2$, which allows continuous wave (cw) operation to be achieved. Quantitative measurements of the light emitted in cw operation under 100 mV current injection yield an output power of 5 mW and a differential quantum efficiency of $\approx 1\%$, both per uncoated facet.

active region consisting of two $40\text{-}\text{\AA}$ GaAs wells and an $11\text{-}\text{\AA}$ $(\text{Ga}_{0.5}\text{In}_{0.5})\text{As}$ barrier a tunability of over 7 nm can be achieved at room temperature.

Figure 1(a) shows the band diagram and the electron and heavy hole squared wave functions of the lowest subbands under flat-band condition in a symmetric QW laser structure consisting of two coupled quantum wells separated by a thin barrier layer. When carriers are pumped and lasing occurs, the optical transition between these two subbands is dominant, since the transition probability between them is the largest of the possible transitions. When an electric field perpendicular to the wells is applied, the energy levels are modified and the wave functions are increasingly localized in separate wells, as sketched in Fig. 1(b). The energy of the lowest transition decreases as the field increases, which tunes the lasing wavelength. The transition, indicated by the arrow on Fig. 1(b), can be considered as spatially indirect, since the electron wave function is mostly localized in one well while the hole wave function is fully confined in another one. The degree of localization depends on the field strength.

There are several possible aspects which would limit the tuning characteristics of this device. First, the gain coefficient would decrease as the field increases because it strongly depends on the overlap integral between the electron and hole wave functions. Second, the wave-length tunability would be limited by the effect of field screening due to the pumped carriers in the wells. The concentration of pumped carriers decreases the effective strength of the applied external field, reducing the shift of the quantized levels, and correspondingly the tunability of the device. Third, at room temperature, carriers can exist in subbands higher than the lowest subbands. The population of carriers in higher states would contribute to the spatially direct transition. Consequently, a larger number of carrier is needed to exceed the threshold gain for stimulated optical transition between the lowest subbands. Fourth, at high fields pumped carrier in the wells can tunnel out, which would increase the screening effect since the tunneling rates of electrons and holes are different due to the difference in the masses.

Considering these important aspects, we have simulated the feasibility of the operation of QW laser diodes (LDs) at room temperature mainly from the standpoint of the gain coefficient.

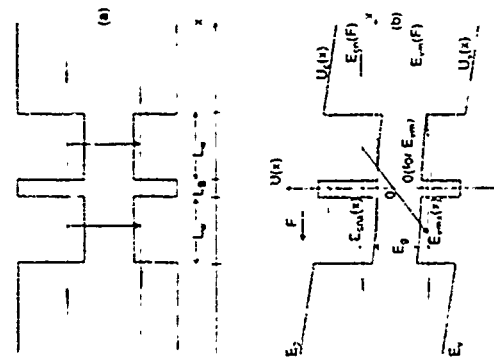


Fig. 1. Schematics of potential profile and electron and heavy hole squared wave functions for a QW laser structure under flat band conditions and (b) for application of an external electric field. Figure 1(b) also shows the definitions and relations of physical quantities used in the text. The arrows show the lowest optical transitions dominant in emission.

The linear gain g in a QW LD structure depends on applied fields through the dipole moment μ_{nm} formed by the field-induced separation of electrons in subband n and holes in subband m . We consider the magnitude of the dipole moment for the TE mode oscillation, since in this structure it is much larger than that for the TM mode. If we choose the z -axis along the direction of quantization, and the y -axis along the direction of light propagation, the unit polarization vector lies along the z -axis. Then the magnitude of the matrix element of the dipole moment is written as

$$|\mu_{nm}|^2 = \frac{|R|^2}{2} \left\{ \left| \int_{-\infty}^{\infty} \Psi_n^*(x) \Psi_m(x) \cos \theta(x) dx \right|^2 + \left| \int_{-\infty}^{\infty} \Psi_n^*(x) \Psi_m(x) dx \right|^2 \right\} \quad (\text{TE } c \rightarrow hh), \quad (1)$$

where $\Psi_n(x)$ and $\Psi_m(x)$ are the envelope functions of the n -th subband in the conduction band and the m -th subband in the valence band, respectively and θ is the angle between k and k_y -axis. The magnitude of the optical matrix element $|R|$ in this equation is given by

$$|R|^2 \approx \frac{q^2}{4\omega_{nm}^2} \left[\frac{E_g(E_g + \Delta_0)}{E_g + 2\Delta_0/3m_0^*} \right], \quad (2)$$

where Δ_0 is the spin-orbit splitting energy and m_0^* is the conduction edge effective mass. In previous reports [6], [7], the dipole moment was averaged over all possible directions since no external field was applied. On the other hand, in the present theory, we have taken into account the effect of the external field on the dipole moment. We obtain the relationship between the transition energy $E_{nm} = \hbar\omega_{nm}$ and the angle θ using the parabolic-band approximation and the k -selection rule as

$$\begin{aligned} \cos \theta(x) &= \frac{k_x}{k} = \sqrt{\frac{E_{nm}(x)}{E_{nm}(x) + E_g}}, \\ \sin \theta(x) &= \frac{k_y}{k} = \sqrt{\frac{E_{nm}(x)}{E_{nm}(x) + E_g}}, \end{aligned} \quad (3)$$

where $E_{nm}(x)$ is the total energy of subband n in the conduction band, $E_{nm}(x)$ the quantized energy, and E_g is the energy perpendicular to the x -direction given by

$$\begin{aligned} E_{nm}(x) &= E_{nm}(x) + E_g, \\ E_{nm}(x) &= \frac{m_0^*}{m_0^*} [E_{nm}(x) - E_g(F) - U_{nm}(x)], \end{aligned} \quad (4)$$

where $U_{nm}(x)$ is the energy of the conduction band, and m_0^* is the reduced mass defined by

$$m_0^* = (m_0^{-1} + m_{hh}^{-1})^{-1}. \quad (5)$$

The gain coefficient g of a QWLD subjected to electric fields is then similarly calculated as developed for QW lasers [6, 7] and conventional lasers [8] and given by

$$g = \frac{\mu_0 \omega_{nm}}{\sqrt{\epsilon_0 \hbar n_r} \pi \hbar^2 L_w} \sum_{n,m} \int_{E_{nm}(x)}^{\infty} \frac{1}{L_{nm}(x)} \frac{1}{(E_{nm}(x) - E_g)^2} \frac{1}{\hbar \omega_{nm}} \frac{1}{\lambda^2} dE_{nm}. \quad (6)$$

where μ_0 and ϵ_0 are the permeability and dielectric constant of air, respectively, ω the angular frequency of light, n , the refractive index of the material, L_W the total width of the coupled wells ($= 2L_w + L_B$), and T_1 the intra band relaxation time. E_{tr} is the transition energy between the electron E_{en} and hole E_{ho} energies given by $E_{tr} = E_{en} - E_{ho}$. MAY is the number of levels relevant to the optical transition, and f_c and f_v are the Fermi-Dirac distribution functions. The origin of energy is at the cross point of the center of the QW structure and the bottom of the GaAs conduction band minimum. For holes, E_{ho} is measured from the cross point of the center of the QW structure and the top of the GaAs valence band down into the valence band (Fig. 1(b)). The quasi Fermi levels E_{en} and E_{ho} are related to the injected surface carrier density N_s into the wells as

$$N_s = \frac{m_0^* k_B T}{4\pi} \sum_{i=1}^{MAY} \ln \left[1 + \exp \left(\frac{E_{tr} - E_{en}(F)}{k_B T} \right) \right] \quad (7)$$

$$N_s = \frac{m_0^* k_B T}{4\pi} \sum_{i=1}^{MAY} \ln \left[1 + \exp \left(\frac{E_{tr} - E_{ho}(F)}{k_B T} \right) \right] \quad (8)$$

Here we have neglected the contribution from the light hole band, since the density of states in this band is much smaller than that of the heavy hole band.

In the calculation of the gain coefficient, subband energies E_{en} and E_{ho} and the wave functions ψ_{en} and ψ_{ho} are obtained by solving Schrödinger's and Poisson's equations self-consistently taking into account the spatial dependence of such parameters as the effective masses and permittivity.

We have finally obtained the gain coefficient of a QWELL, where the effect of the external electric field on the dipole moment, and the screening effect are taken into account through eqs. (1) and (4). When the electric field is set to zero and eqs. (1) and (6) are averaged over all possible directions of θ , the results coincide with those in the literature G_{00} .

We have applied the calculation to two hetero structures with different material parameters. Structure A consisting of two 50 Å GaAs wells and a 20 Å $\text{Ga}_{0.7}\text{Al}_{0.3}\text{As}$ barrier, which is identical to that used in Ref. 4 and structure B consisting of two 40 Å GaAs wells and an 11 Å $\text{Ga}_{0.7}\text{Al}_{0.3}\text{As}$ barrier. We have used standard band parameters for the calculation by In Figs. 2(a) and (b), we show the low temperature ($T = 5$ K) gain spectra of structures A and B, respectively, at various applied fields for an injected surface carrier density $N_s = 4 \times 10^{11} \text{ cm}^{-2}$. The threshold gain, indicated by a dashed line in each figure, is estimated as 146 cm^{-1} for an optical confinement factor of 0.021 and a cavity loss of 4.5 cm^{-1} . These parameters are typical for a laser structure with high reflection coating (99%) on its facets whose length is 300 μm and core width is 2000 Å.

As seen in Fig. 2(a) and (b), under flat band condition ($F = 0 \text{ kV/cm}$) even for a relatively low injection of carriers, the gain far exceeds lasing threshold. This is because at low temperature most carriers reside on the lowest subbands and the overlap between the lowest electron and hole states is maximum under flat-band condition. As the electric field increases, the gain peak shows red shift, which corresponds to the tunable operation, simultaneously, the gain decreases, eventually dropping below threshold. From the peak shift, the tunability can be estimated for each laser structure. Figure 2(c) shows the dependence of the oscillation wavelength (tunability) and the gain coefficient on applied fields in each structure. Structure A shows a tuning range of 7 nm, which is comparable to the tunability in the reported experiment (4) when a high reflection coating (99%) on the facets was used. On the other hand, with structure B a tunability of more than 20 nm can be achieved, if we can apply an electric field up to 110 kV/cm.

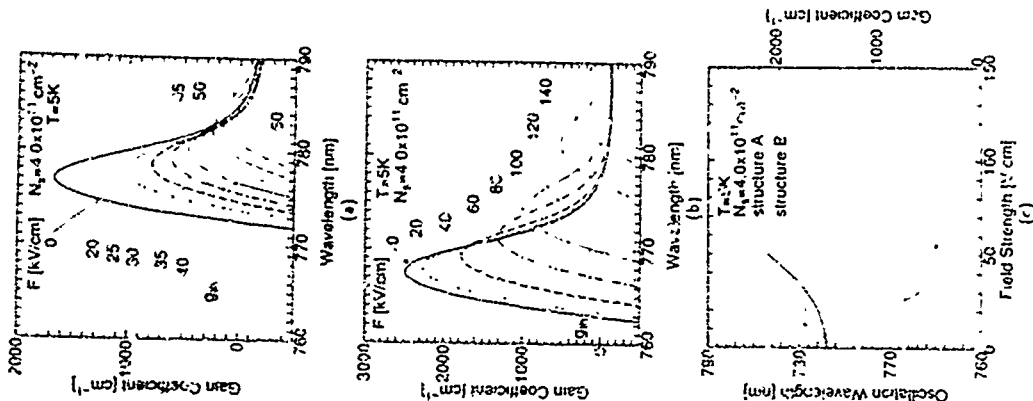


Fig. 2 Linear gain spectra of QW laser structures at 5 K as a function of the external field F calculated for (a) structure A with two 50 Å GaAs wells and a 20 Å $\text{Ga}_{0.7}\text{Al}_{0.3}\text{As}$ barrier and (b) structure B with two 40 Å GaAs wells and an 11 Å $\text{Ga}_{0.7}\text{Al}_{0.3}\text{As}$ barrier. The injected surface carrier concentration $N_s = 4.0 \times 10^{11} \text{ cm}^{-2}$ and the intraband relaxation time T_1 of $1 \times 10^{-11} \text{ sec}$ are assumed in the calculation. The threshold gain is indicated by the dashed line in each figure. (c) Field dependence of the tunability and the peak gain coefficient in each structure.

As seen in Fig. 2(c), structure A loses its gain more drastically than structure B with increasing electric field. This is due to the fact that with the field the electron and hole wave functions are well localized in opposite wells and this localization is much enhanced in structure A as the field becomes stronger, since the barrier width L_B is larger than in structure B. At low temperature, the magnitude of the overlap between the wave functions of the lowest electron and hole subbands is so sensitive to the field that the gain curves show a drastic decrease with an increase of the field. This explains the saturation of the red shift and the drastic decrease of the gain beyond a certain bias voltage in the experiment of Ref. 4.

At low temperatures, a relatively low density of carriers is enough to surpass the threshold gain. However, at room temperatures, carriers can exist in subbands other than the lowest ones, and a large number of carriers is needed to exceed the threshold gain. For structure A, a carrier density of at least $2.8 \times 10^{12} \text{ cm}^{-2}$ is needed for lasing at 300 K, but in this case the field screening effect would prevent any significant tunability. At lower densities, lasing would not occur. These results are consistent with the absence of stimulated emission at 300 K in the experimental device of Ref. 4.

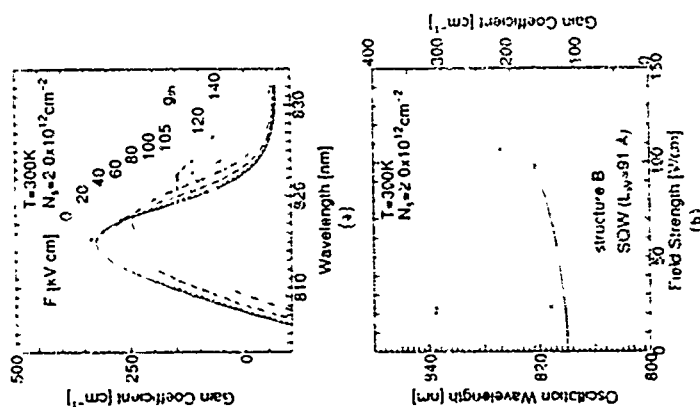


Fig. 3 (a) Calculated linear gain spectra at 300 K of structure A with $V_g = 2.0 \times 10^{13} \text{ cm}^{-2}$. (b) Comparison of tunability and gain coefficient between structure B and a single quantum well (SQW) laser structure with the well width of 91 Å. In the SQW structure the electric field is applicable only up to 100 kV/cm where the lowest subband in the valence band disappears. The injected surface carrier density is assumed to be as in Fig. 3(a).

On the other hand, as shown in Fig. 3 (a), in structure B, gain above threshold can be maintained for a density of $2.0 \times 10^{13} \text{ cm}^{-2}$ and tunability is possible. In this structure, the gain coefficient is mainly from the contribution of the transition between the lowest subbands of σ_z , spatially indirect transition. In this structure tunability of up to 7 nm would be possible if a field of 105 kV/cm were applicable. Our calculation has not taken into account the likely tunneling of carriers through barriers at such a high field, but such a limitation could be overcome by incorporating multi-quantum barriers [10] on both sides of the CQW.

For comparison we have also calculated the gain spectra for a single quantum well laser diode whose well width is 91 Å. This structure corresponds to the case where the barrier E_B is removed from structure A, keeping constant the total width of the CQW. The results are shown in Fig. 3(b). This figure shows slightly higher gain coefficient than that of structure B. However, this structure shows a reduction of tunability, to 4 nm, since the lowest subband in the valence band disappears at fields higher than $F \approx 100 \text{ kV/cm}$, thus preventing the transition between the lowest subbands. Therefore, the CQW structure B is a more favorable structure than either structure A or a single quantum well for the successful room-temperature operation of the tunable LDs using Stark effect. A systematic study of CQWs with various well and barrier widths around the parameters of structure B should yield the optimum design point.

In summary, we have simulated the operation of the CQW LDs from the standpoint of gain coefficient and shown that a CQW LD whose active region consists of two 40 Å GaAs wells, separated by an 11 Å $\text{In}_{0.2}\text{Al}_{0.8}\text{As}$ potential barrier is favorable to laser at room temperature and is tunable over a wavelength range of 7 nm.

One of the authors (M. Ogawa) would like to acknowledge Prof. T. Sugawara of Kyoto University for his continuous encouragement. He also would like to acknowledge the staff of IBM Research Division for their hospitality and thank IBM Japan for financial support. This work has been partially supported by the Army Research Office.

References

- [1] E. E. Mendez, G. Bastard, L. L. Chang, and L. Esaki, *Phys. Rev. B* **26**, 7101 (1982).
- [2] M. Yamamoto, and I. Suemune, *Jpn. J. Appl. Phys.* **22**, L22 (1983).
- [3] Y. Kan, M. Yamamoto, M. Okuda, K. Nakayama, T. Ohnishi, M. Kawamoto, and I. Suemune, *Appl. Phys. Lett.* **55**, 1119 (1989).
- [4] L. Y. Lu, E. E. Mendez, and H. Merer, *Appl. Phys. Lett.* **60**, 2971 (1992).
- [5] E. O. Kane, *J. Phys. Chem. Solids* **1**, 219 (1957).
- [6] M. Asada, A. Kameyama, and Y. Suematsu, *IEEE J. Quantum Electronics* **QE-20**, 745 (1984).
- [7] M. Yamamoto, and I. Suemune, *Japan J. Appl. Phys.* **23**, L35 (1984).
- [8] W. E. Lamb, Jr., *Phys. Rev.* **134**, A1429 (1961).
- [9] We have used the following values throughout the text for GaAs: $0.067m_0$ (m_0 is the free electron mass) for the conduction edge effective mass, $0.34m_0$ for the heavy-hole effective mass, 1.424 eV for the energy gap at 300 K, 1.519 eV at 5 K, 13.1 for the dielectric constant, and 0.34 eV for the spin splitting of the valence band, for $\text{Ga}_{0.77}\text{Al}_{0.23}\text{As}$, $0.086m_0$ for the conduction edge effective mass, $0.355m_0$ for the heavy-hole effective mass, 1.71 eV for the energy gap at 300 K, 1.81 eV at 5 K, 12.4 for the dielectric constant, for $\text{Ga}_{0.7}\text{Al}_{0.3}\text{As}$, $0.092m_0$ for the conduction edge effective mass, $0.36m_0$ for the heavy-hole effective mass, 1.80 eV for the energy gap at 300 K, 1.69 eV at 5 K, 12.2 for the dielectric constant. They are taken from the literatures: H. C. Casey, Jr., and M. B. Panish, *Heterostructure Lasers*, Part A, Chap. 4, Academic Press, New York (1978) and V. Butty, U. Ekenberg, A. Chui, and E. P. O'Reilly, *Semicond. Sci. Technol.* **4**, 901 (1989).
- [10] K. Iya, H. Uenohara, and F. Koyama, *Electron. Lett.* **22**, 1008 (1986).

Detection of Bloch Oscillations in a Semiconductor Superlattice by Time-Resolved Terahertz Spectroscopy and Degenerate Four-Wave Mixing

Christoph Waser, Patrick Leisching, Peter Haring, Robert Hall-Scheller, Frank Bruggemann, Martin G. Bock, Karl-Ludwig Bohnert, and Rüdiger W. Heilmann, Institut für Halbleitertechnik II, Rheinisch-Westfälische Technische Hochschule Aachen, D-52074 Aachen, Germany

Manuscript received for Topical Review 11/11/93; revised manuscript received 1/11/94

We have studied the spatial dynamics of coherent excited wave packets of charge carriers in a semiconductor superlattice of width 10 nm by time-resolved THz spectroscopy and degenerate four-wave mixing. In the Wannier-Stark ladder regime, we observe a clear Bloch oscillation with a frequency that depends linearly on the electric field and can be linked to a few hundred cells and 5 THz.

1. Introduction

In the last few years four-wave mixing (FWM) and THz wave spectroscopy have been established as powerful means to study the dynamics of wave packets in semiconductors. Recent interest in Bloch oscillations in superlattices (SLs) stems from the observation of coherent wave packet propagation in a wave packet of charge carriers in a semiconductor superlattice of width 10 nm by time-resolved THz spectroscopy and degenerate four-wave mixing (DFWM).

Recently, these spectroscopic techniques have revealed the first observation of Bloch oscillations (BO) in a semiconductor superlattice of width 10 nm [1]. In this experiment, the observation of coherent wave packet propagation in a semiconductor superlattice was achieved by the observation of coherent wave packet propagation in a semiconductor superlattice of width 10 nm [1]. In this experiment, the observation of coherent wave packet propagation in a semiconductor superlattice was achieved by the observation of coherent wave packet propagation in a semiconductor superlattice of width 10 nm [1].

2. Experimental setup

The superlattice structure used for both types of experiment is a GaAs/AlGaAs superlattice of width 10 nm [1]. In this experiment, the observation of coherent wave packet propagation in a semiconductor superlattice was achieved by the observation of coherent wave packet propagation in a semiconductor superlattice of width 10 nm [1].

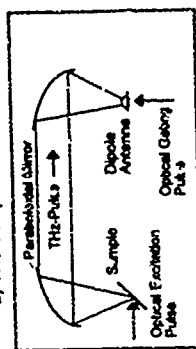
is the signature of superlattices [13-15]. In 1990, observation of negative differential velocity (NDV) of electrons in superlattices was reported [16]. This phenomenon is closely related to BO because, in k space, both rely on reaching the upper part of the miniband where the real space velocity decreases with field. Later, the simultaneous observation of NDV and WS localization finally confirmed the analogy between WS states in frequency space and BO in the time domain [16].

For the direct observation of BO in Ref. [3-7], it turned out to be important that optical excitation and detection of BO are decoupled from the resonant circuit of the superlattice. Hence, unlike in all electrical transport measurements, no sophisticated ultrafast frequency circuitry is needed for the generation and observation of BO. Furthermore, DFWM and THz wave emission spectroscopy are only sensitive to coherent transport processes in the structure. Incoherent processes do not make a background signal.

In this paper, we summarize our main results related to the observation of BO in a GaAs/AlGaAs superlattice structure. We demonstrate THz wave emission by BO from 100 GHz to more than 2 THz and demonstrate by DFWM that oscillations at frequencies as high as 5 THz can be generated.

undoped Al_{0.15}Ga_{0.85}As buffer on top. A reverse bias field can be applied between the doped substrate and a transparent I^2V or I^2N Schottky contact on the sample surface. For the DFWM transmission measurement, a substrate window is etched into the sample to enable experiments in transmission geometry.

a) The Setup



b) Four-Wave Mixing Setup

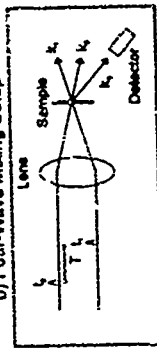


FIG. 1. Experimental setup for a) THz emission spectroscopy, b) DFWM.

In both experiments, we use a self-amplified THz signal from a free-running oscillator (see Fig. 1a). The duration of the optical pulse is about 100 fs with a full width at half maximum (FWHM) band width of 20 meV. We tune the center wavelength of the laser to 800 nm, close to the heavy-hole excitation transition in flatband.

The experimental setup for the time-resolved THz emission spectroscopy is shown schematically in Fig. 1a [3]. The laser beam is split into two parts. One part excites the superlattice sample mounted in a closed cycle cryostat cooled down to temperatures as low as 10 K. Corresponding to the generated THz signal, a 1 THz wave is emitted in a direction nearly collinear with the incident optical beam. The THz pulse is collected by a horn antenna and focused with a parabolic mirror onto a 30 μm wide second detector. The output of the detector is amplified by a low-noise amplifier and the signal is recorded by a lock-in amplifier. The phase of the electric field is measured by a phase-locked loop (PLL) circuit.

tions at a density of $1 \times 10^{18} \text{ cm}^{-2}$ per quantum well (average laser power 18 mW, diameter of the illuminated spot 350 μm). The dipole moment associated with the optically excited charge oscillations is directed normal to the surface allowing THz-wave emission only in directions off the surface normal. In this experiment, we have chosen an excitation and emission angle of 45° .

Figure 1b shows the experimental setup used for DFWM measurements [14]. The laser beam is split into two copolarized beams of equal intensity (average laser power 1.3 mW per beam). The first pulse is focused onto the sample (100 μm spot diameter) inducing a microscopic polarization that is probed by the second time-delayed pulse in a self-diffraction geometry. The time-integrated nonlinear DFWM signal is measured by a lock-in amplifier. The delay time τ between the two pump pulses is varied by a motor-driven delay line.

III. Wannier-Stark ladder formation

At low reverse bias, close to flatband ($\pm 0.6 \text{ V}$) strong inter-well coupling leads to delocalization of the wave functions over many periods of the superlattice [17]. The eigenstates of the superlattice overlap and form minibands. For our superlattice structure, we calculate a width of 19 meV (2 meV) for the lowest electron (heavy-hole) miniband using a Kronig-Penney model. Increasing the bias voltage reduces the coupling between the wells and leads to a strong localization of the wave functions [13, 14, 17]. The minibands split into a series of discrete levels, the WS ladder. To lowest order, the energy separation between ladder states increases linearly with the bias voltage (for a more precise description taking into account excitonic effects see Ref. [18]).

Figure 2 shows low-excitation photocurrent spectra of our structure at $T = 4 \text{ K}$ for different bias voltages. An increase of the voltage by 10 V raises the internal electric field by 10 kV/cm. Close to flatband in the miniband bias regime, the spectra are weakly structured revealing three excitation transitions. We assign them to the fundamental heavy-hole (hh) exciton, the light-hole (lh) exciton, and excited hh excitons (hh2) at the onset of the miniband [19]. Increasing the reverse bias voltage above 4.5 V results in a break up of the minibands into WS ladders. In Fig. 2, we have marked the predominant transitions for the hh ladder. We assume that the low-lying hh excitons are completely localized even at low internal fields [11, 17]. The indicated excitation lines involve transitions originating from localized hh states into conduction band states with parabolic dispersion. Wave functions of hh states are localized in a conduction band state with the highest probability density in the same well (with well transitions) and hh exciton transitions to conduction band states with wave functions peaked in adjacent wells.

Figure 1 is a 3D surface plot showing the relationship between External Bias (mV), Time Delay (μ s), and Forward Current (mA). The vertical axis represents Forward Current (mA), ranging from 0 to 400. The horizontal axis represents External Bias (mV), ranging from 0 to 1200. The depth axis represents Time Delay (μ s), ranging from 0 to 2. The surface shows a sharp peak in current at low bias and low delay, which decreases as bias and delay increase.

The overall decay time of the DFM signals is on the order of 1 ns and rather independent of the electric field in the low range measured here. The relative field independence is an indication that tunneling processes to higher minibands (the present sample has a second miniband in this field range) are rather unimportant in this field range. It is indeed a prerequisite for the observation of HQ that such tunneling processes are slow compared to the HQ frequencies.

comparing the 1 Hz emission and the DMM results, we find general agreement to within 10%. In the fundamental regime we observe with both techniques a signal around 1 MHz that we associate with half-quantum beats in the transition regime from the fundamental to the WS regime; this signal disappears in the WS regime, both experiments find strong signals with both tunable for

there are likewise some differences in the data of the two experiments. The 10 Hz resonance means (averages) reveal a signal at 300 GHz in the minibus data, but this signal is not found in the DFWM data. At present, the origin of this signal is speculative. The higher frequency of the 10 Hz data does not support the idea that the 300 GHz data has low time resolution. The 100 GHz signal results from quantum beats of minibus states π of similar origin as the RQ in the WS regime. We can rule out that the signal is caused by quantum beats between free and bound excitons or involves fluctuations, because the signal has the same dependence on sample temperature as the RQ in the WS regime. It is not clear at the moment why the signal is not visible in the DFWM data. It may well be that DFWM measurements with long gate time delay have detected a feature around 300 GHz.

We finally discuss results obtained for different sample temperatures. Increase of the temperature leads to a reduction of the peak amplitude of both the ILL reflectivity and the modulated DPMV signal. At 60 K, the amplitude of the ILL wave is about a third of that on 10 K. The DPMV amplitude decreases to 20% when the temperature is raised from 10 K to 20 K. Together with the signal amplitude, the dephasing time of the signals decreases with rising temperature.

-1079-

IX. Conclusion

-1080-

- [1] K. Leo, E. O. Göbel, T. C. Damen, J. Shah, S. Schmitt, R. W. Schlögl, J. F. Müller, N. Köhler, and P. Giamber, *Phys. Rev. B* **44**, 525 (1991).
- [2] K. Leo, J. Shah, F. O. Göbel, T. C. Damen, S. Schmitt, R. W. Schlögl, J. F. Müller, N. Köhler, *Phys. Rev. Lett.* **66**, 201 (1991).
- [3] J. F. Redman, K. Leo, J. Shah, D. A. B. Miller, J. E. Cunningham, T. Wier, G. von Platen, A. Schulz, P. Thomas, and S. Schmitt-Rink, *Phys. Rev. B* **40**, 7252 (1989).
- [4] K. Leo, P. Haring-Bolivar, F. Brügmann, R. Schwedler, and N. Köhler, *Solid State Commun.* **84**, 913 (1992).
- [5] H. G. Rübner, M. C. Nuss, J. Shah, K. Leo, D. A. B. Miller, A. M. Jos, S. Schmitt Rink, and N. Köhler, *Phys. Rev. Lett.* **68**, 2216 (1992).
- [6] M. C. Nuss, M. C. Nuss, J. Brueser, K. W. Goossen, M. C. Leo, S. L. Chuang, and L. Pfeiffer, *Phys. Rev. Lett.* **69**, 3000 (1992).
- [7] C. H. Winkle, H. G. Rübner, R. S. Swedler, K. Leo, H. Kurz, and N. Köhler, *Phys. Rev. Lett.* **70**, 3119 (1993).
- [8] B. Krieger and G. J. Iafrate, *Phys. Rev. B* **33**, 5194 (1986).
- [9] G. Hatala and R. Fiesens, in *Spectroscopy of Semiconductors* (Materials Research Society, NATO ASI Series (Physics, Vol. 190), 1991), p. 111.
- [10] F. Bock, *Z. Phys.* **52**, 553 (1929).
- [11] *Trans. Faraday Soc. London Ser. A* **168**, 322 (1941).
- [12] J. E. Eakins and R. E. IBM J. Res. Dev. **14**, 61 (1970).
- [13] J. Hwang, G. J. Staud, and P. Yoon, *Phys. Rev. Lett.* **60**, 220 (1988).
- [14] J. F. Meier, J. A. Rueda, and J. M. Hong, *Phys. Rev. Lett.* **60**, 2148 (1988).
- [15] J. A. Rueda, J. F. Palmer, H. Wang, and F. Meier, *Phys. Rev. Lett.* **64**, 52 (1990).
- [16] J. A. Rueda, J. F. Palmer, and F. Meier, *Appl. Phys. Lett.* **60**, 317 (1992).
- [17] J. A. Rueda, L. E. Meier, and J. M. Hong, *Phys. Rev. Lett.* **60**, 1337 (1988).
- [18] M. M. Hsueh and J. L. Site, *Phys. Rev. B* **43**, 4037 (1991).
- [19] J. A. Rueda, J. A. Rueda, and F. Meier, and J. M. Hong, *Phys. Rev. B* **43**, 3626 (1991).
- [20] J. E. Eakins and R. E. Winkler, et al. in preparation.
- [21] J. E. Eakins and R. E. Winkler, et al. in preparation.

Femtosecond Degenerate Four-Wave-Mixing on unstrained (InGa)As/InP Multiple-Quantum-Wells Using an Optical Parametric Oscillator

T. F. Albrecht, J. H. H. Sandmann, S. T. Cundiff, J. Feldmann, W. Stolz and E. O. Göbel
*Fachbereich Physik und Wissenschaftliches Zentrum für Materialwissenschaften,
 Philipps-Universität Marburg Renthof 3, D-35032 Marburg, Germany*

Abstract

We have constructed a femtosecond optical parametric oscillator in order to perform transient four wave mixing experiments on (InGa)As/InP quantum well superlattice structures in the 1160 - 1300 nm wavelength region. The dependence of the low temperature excitation dephasing rate on sample parameters and temperature is investigated. The observed temperature dependence indicates disorder induced localization of excitons, which is consistent with inhomogeneous broadening of the exciton emission and absorption lines. In addition, we observe quantum beats in the FWM decay and attribute them to localized and bound excitons.

Semiconductor heterostructures based on the Ga-In-As-P material system have gained considerable interest recently due to their potential for optoelectronic applications, especially in fiber communications [1]. The effective bandgap of (InGa)As quantum wells (QW) lattice matched to InP can be tuned from 1.2 eV to 0.75 eV by varying only the QW thickness. For many device applications high quality of the interfaces and the ternary well material is essential. However, standard characterization methods like photoluminescence (PL), absorption or x-ray diffraction techniques often do not provide sufficient information to fully determine the properties of these structures. Transient four-wave mixing (FWM) experiments on (AlGa)As/GaAs [2,3] and In/VI compounds [4,5] have been used to study interface and alloy disorder via its contribution to exciton dephasing. FWM experiments allow a distinction to be made between the different contributions to the dephasing of excitonic excitations in semiconductors and semiconductor quantum wells, which includes, interface, alloy, phonon and exciton-exciton scattering [6].

Measurement of exciton dephasing by FWM requires resonant excitation with picosecond (ps) or femtosecond (fs) laser pulses. While such lasers are currently available for GaAs based heterostructures, no tunable, high repetition rate fs pulse sources were available for experiments on (InGa)As/InP QWs. Recently, femtosecond optical parametric oscillators (fs-OPOs) synchronously pumped by a fs-Ti:sapphire laser have been developed [7-9]. They can be continuously tuned through the visible energy range of the (InGa)As/InP QW system. In this paper we present the first FWM experiments carried out with such a fs-OPO.

The dephasing of the exciton is sensitive to interactions between the exciton and its environment, including interaction with excitations such as phonons or other excitons and interaction with static disorder. The broadening of the excitonic resonance in the linear optical spectra for these samples indicates the presence of strong disorder, which we attribute to

a combination of interface roughness and alloy fluctuations. The temperature dependence of the exciton dephasing rate displays the functional form associated with thermal activation of disorder localized excitons, consistent with the interpretation of the linear spectra. The dephasing rate is observed to increase sharply with decreasing barrier width, in agreement with the broadening of the exciton resonances due to miniband formation. One of the samples displays quantum beats in the FWM signal, which are attributed to the simultaneous excitation of disorder localized excitons and defect bound excitons.

We used an OPO based on that reported in Ref. [9] and described in more detail elsewhere [10]. The OPO is synchronously pumped by 110 fs pulses from a commercial, Kerr-lens modelocked Ti:sapphire laser (Coherent Mira 900). Because the OPO spectrum is extremely sensitive to length changes of only a few 100 nm, the length of the resonator is actively stabilized. The OPO uses a 2 mm thick, antireflection coated KTP crystal cut for type II ($e \rightarrow e$) anisotropic phase matching in the xy-plane ($\phi = 0^\circ$, $\theta = 90^\circ$). This enables a collinear pump-geometry resulting in high conversion efficiency and relatively easy alignment and operation, compared to non-collinear pumped OPOs [7,8]. The emission wavelength is tuned via the pump wavelength and small adjustments of the OPO resonator length. Under optimized operating conditions transform limited pulses of 160 fs (FWHM) duration with more than 1 nJ pulse energy are generated. An energy conversion efficiency into the signal beam of 30% was achieved for non-transform limited pulses. Currently this is the highest value reported for a fs-OPO. The experimentally determined tuning range is from 1060 nm to 1330 nm using two mirror sets. Additional mirror sets should extend OPO operation to 1640 nm with the Ti:sapphire laser as the pump source [11]. The FWM experiments described below represent the first application of a fs-OPO and demonstrate its potential for time resolved spectroscopy in a spectral regime which has been difficult to access.

The unstrained (InGa)As/InP multiple quantum well (MQW) samples were fabricated by standard low pressure metal organic vapour phase epitaxy [12] in commercial equipment (Aix 200, Aixtron Corp.). The semi-insulating InP substrates were Fe doped and exactly (100) oriented. They were prepared for growth as described in Ref. [13]. The growth temperature was 640°C, the pressure was 20 mbar and the gas velocity in the reactor was approximately 1.8 m/s. A growth interruption of 5 s under PH_3 was used during switching from InP to (InGa)As-growth. At the As terminated interfaces growth was not interrupted. The growth rates were 3.3 Å/s and 6 Å/s for the InP and (InGa)As layers, respectively.

We have grown a set of MQWs with thin wells (1.6 nm and 3.0 nm) and several barrier widths between 40 nm and 5 nm. This allows us to study phenomena related to the transition from a MQW to a superlattice (SL), i.e., phenomena due to the delocalization of the electronic wavefunctions and the formation of minibands. The samples were characterized by low temperature photoluminescence (PL), absorption spectroscopy and high resolution x-ray diffraction (HRXRD). All samples consisted of a 390 nm thick InP buffer layer, a MQW and a 525 nm thick (InGa)As caplayer. The caplayer was used to calibrate the (InGa)As-composition through the HRXRD spectra, which cannot be unambiguously determined from the MQW itself. It was removed by selective etching prior to the optical experiments.

The HRXRD measurements (not shown here) exhibit sharp peaks for both zero order and satellite reflections of the MQW for all samples, indicating high quality epilayers. Details of the structural sample properties and the analysis of the HRXRD spectra will be reported elsewhere [14]. The absorption and PL spectra of two typical MQWs with well widths of 1.6 nm and 3.0 nm are shown in Fig. 1

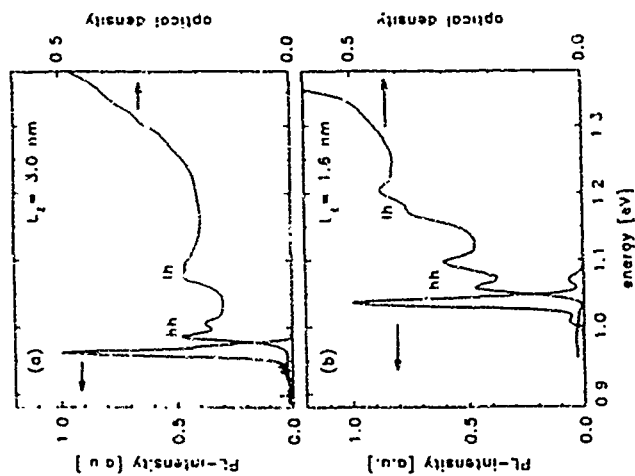


FIG. 1 Absorption and photoluminescence spectra of two MQWs with $L_z = 1.6$ nm and $L_z = 3.0$ nm. Both absorption spectra show ML splitting of the heavy hole (hh) and light hole (lh) resonances. The luminescence spectra are Stokes shifted by approximately the value of the inhomogeneous broadening. ML splitting is resolved only in the PL of the 1.6 nm well.

Both samples consist of 50 periods with a barrier thickness of approximately 40 nm. The absorption and PL spectra are inhomogeneously broadened and exhibit a Stokes shift on the order of 20 meV. This can be partly ascribed to the high quantization of the electronic levels in connection with interface roughness, but also reflects the presence of alloy fluctuations. Therefore, we expect that the excitons will be localized. A monolayer (ML) splitting of the heavy and the light hole exciton resonances is observed in the absorption spectra of both samples and in the luminescence spectrum of the thinner well. For the thicker well, the splitting is smaller and not clearly resolved in luminescence. The FWM experiments use the degenerate two-pulse self-diffraction technique [15]. The sample is excited by two laser pulses with wave vectors k_1 and k_2 with a time delay Δt . The Δk -dependent diffracted FWM signal

is detected in the phase matched direction $2k_1 - k_2$ using a slow germanium photodiode. If a single resonance is excited, the signal decays with a time constant τ . This allows the determination of the dephasing time T_2 and thus the homogeneous linewidth $\Gamma_h = 2\hbar/T_2$ irrespective of inhomogeneous broadening effects. For inhomogeneously broadened transitions the dephasing time is $T_2 = 4\tau$ [15].

All FWM experiments were done with parallel polarized beams and photon energies corresponding to the low energy side of the lowest energy heavy hole absorption peak of the respective sample. For higher energies the diffracted signal becomes very weak and its decay time approaches our time resolution. Although we estimate carrier sheet densities in the order of 10^{10} cm^{-2} , the density dependence of the measured dephasing times is very weak. We attribute this to the strong inhibition of exciton-exciton scattering due to their localization. For all experiments shown here, the exciton-exciton scattering contribution to the dephasing rate is less than 10%.

Localization modifies the exciton-phonon interaction and hence the temperature dependence of the homogeneous linewidth. The homogeneous linewidth, as determined from the FWM measurements, is plotted as a function of temperature, T , in Fig. 2. This data is for the heavy hole exciton resonance in the sample for which the linear spectra are shown in Fig. 1.

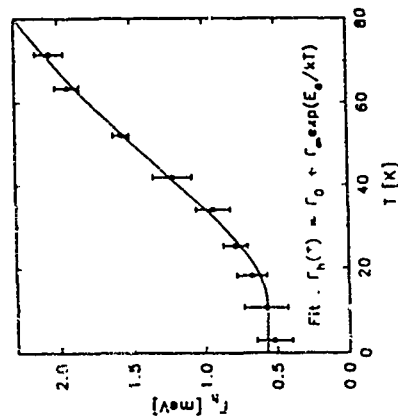


FIG. 2 Temperature dependence of the homogeneous linewidth of the 3 nm well MQW for which the spectra are shown in Fig. 1. The photon energy was 2.3 meV below the absorption peak. The fit is discussed in the text.

The homogeneous linewidth, Γ_h , clearly does not exhibit the linear temperature dependence expected for single phonon scattering of free excitons. The data is well fit by the functional form expected for thermal activation [2],

$$\Gamma_h(T) = \Gamma_0 + \Gamma_0 \exp(-E_0/kT)$$

where Γ_{ph} is the high temperature limit for dephasing due to activated behavior, E_a is the activation energy, k is Boltzmann's constant and Γ_0 is additional dephasing due to non-activated processes. Γ_{ph} includes possible contributions due to exciton-exciton interactions and tunneling or hopping relaxation channels. Although relaxation due to tunneling or hopping is temperature dependent [16], the dependence is relatively weak and so determination of the pertinent processes is not possible. The fit yields an activation energy of (7.3 ± 0.5) meV, where the activated behavior was attributed to a mobility edge. However, the similarity of the activation energy to the exciton binding energy suggests that acoustic phonon relaxation of the exciton may contribute due to a lifting of the crystal momentum conservation selection rules because of exciton localization. The large activation energy, compared to the inhomogeneous width, is consistent with earlier observations in (InGa)As MQW that all optically active excitons are localized [17].

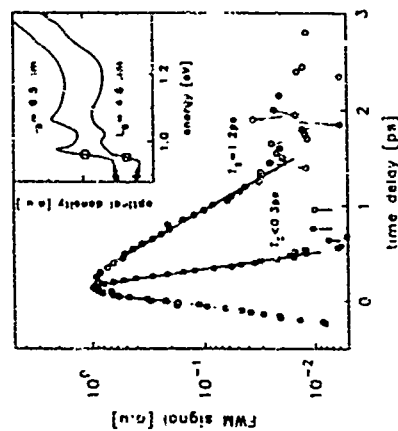


FIG. 1 FWM traces for samples with $L_B = 9.5$ nm (circles) and $L_B = 4.6$ nm (squares) with the fitted decays. The inset shows the corresponding absorption spectra and the respective spectral positions for these measurements (1.046 eV and 1.054 eV).

When the barrier thickness L_B is decreased so that the quantum wells become strongly coupled and as the electronic levels are broadened to minibands a drastic change in dephasing time is observed. The inset of Fig. 3 shows absorption spectra of two samples with 100 periods, $L_B = 3.6$ nm and barrier widths of 9.5 nm and 4.6 nm. The calculated widths of the minibands are 3.7 meV and 3.9 meV, respectively, for the electrons and below 0.1 meV for the heavy holes, i.e. the holes remain localized in these samples. These values agree well with the observed broadening of the prominent absorption structures. To compare the dephasing of the two samples, the measurements must be carried out at equivalent spectral positions. We have chosen the half maximum points of the absorption edges as the excitation photon energy in both cases, as indicated in the inset. The measurements were carried out

under the conditions described above. Fig. 3 shows the FWM signal as a function of delay time. While $T_2 = 1.2$ ps for the sample with nearly uncoupled wells ($L_B = 9.5$ nm), which is the same value as for samples with thicker wells, T_2 of the $L_B = 4.6$ nm SL is considerably shorter and actually below our time resolution ($T_2 < 0.3$ ps).

There are several phenomena which should modify the excitonic dephasing rate as the transition from a QW to a superlattice is made. While the delocalization of the wavefunctions increases the probability density of the exciton at the interface, resulting in an increased scattering, this is counteracted by the increased probability density within the barriers, which should reduce the alloy scattering within the well regions. Probably the most important effect is the modification of the exciton wavefunction itself. The exciton binding energy is reduced [18] as is the electron-hole overlap [19]. The exact contributions of these competing effects are difficult to distinguish and require further, more extensive investigation.

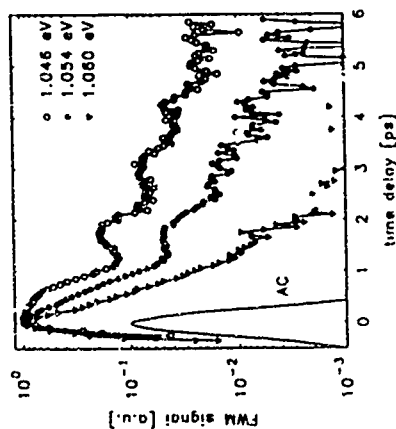


FIG. 1 FWM traces of a MQW sample with 1.6 nm wells and 20.5 nm barriers for photon energies of 1.046 eV (circles), 1.054 eV (squares), and 1.060 eV (triangles). The inset shows the typical autocorrelation curve for the 1.060 eV curve. The beating period is 1.2 ps.

In one particular sample with 1.6 nm well width and 20.5 nm thick barriers we have observed quantum beats [20] at a temperature of 4 K. Fig. 4 shows three transient FWM signals for different photon energies along with an autocorrelation curve. The beating phenomenon is only observed for energies lower than 1.058 eV. The beating period is 1.3 ps corresponding to an energy splitting of $\Delta E = 3.2$ meV between the interfering quantum mechanical states. This energy spacing is considerably smaller than any structure resolved in the absorption or luminescence spectra. Yet, as mentioned before, FWM is able to resolve transitions which are obscured in the linear spectra by the considerable inhomogeneous broadening. We attribute the beating to the simultaneous excitation of excitons localized in alloy or well width fluctuations and excitons that are bound to an impurity or defect [21, 22]. A

definite identification of the state involved is not possible on the basis of the present results. The beats are absent or very faint in the other samples, suggesting that this defect might be related to the particular epitaxial run.

The dephasing times obtained from the transient FWM traces shown in Fig. 4 drop from about 6 ps at 1.060 eV to 1.2 ps at 1.046 eV. This result is in qualitative agreement with similar investigations on inhomogeneously broadened exciton lines in other structures [3,5]. It reflects the decrease of the exciton hopping rate at lower energy due to the decrease in density of states and thus larger separation of sites with lower energy.

In conclusion we have investigated the dependence of the dephasing times of excitons in unstrained (InGa)As/InP MQWs on energy, temperature and barrier thickness. The temperature dependence of the dephasing could be explained with a model for localized excitons that dephase via thermal activation with an activation energy of $E_a = 7.3$ meV. We furthermore demonstrate that the transition from a MQW to a SL by lowering the barrier width results in the drastic reduction of T_2 by more than a factor of 4. In one sample pronounced quantum beats were found that are attributed to the coherent excitation of localized and bound excitons. The binding energy of this bound exciton is 3.2 meV, yet its identification is still open. Altogether our experiments have demonstrated the great potential of a fs-OPO operating in the near IR-spectral regime for time resolved, nonlinear spectroscopy.

We thank A. Nebel, C. Fallnich and R. Beigang for support with the construction of the OPO and making available to us their results prior to publication. We are grateful to T. Marschner for help with the sample characterization, G. von Plessen, U. Lemmer and M. Koch for stimulating discussions and M. Preis and T. Ochs for expert technical support. This work has been supported by the Deutsche Forschungsgemeinschaft.

REFERENCES

- [1] e.g. N. Pits, *J. Cryst. Growth* **107**, 806 (1991) and references therein
- [2] see e.g. Hegarty and M.D. Sturge, *J. Opt. Soc. Am. B*, **2**, 1143 (1985) and references therein.
- [3] M.D. Webb, S.T. Cundiff, and D.G. Steel, *Phys. Rev. B* **43**, 12858 (1991).
- [4] G. Noll, U. Siegner, E.O. Göbel, and S. Shevel, *Phys. Rev. Lett.* **64**, 792 (1990).
- [5] U. Siegner, D. Weber, E.O. Göbel, D. Benhardt, V. Henkeroth, R. Saleh, S. Barascschi, P. Thomas, H. Schwab, C. Klüngshirn, J.M. Hvam, and V.G. Lyssenko, *Phys. Rev. B* **46**, 4564, (1992).
- [6] J. Kuhl, A. Honold, L. Schultheis, and C.W. Tu in: *Festkörperprobleme / Advances in Solid State Physics*, Vol. 29, ed. by U. Rössler, (Vieweg, Braunschweig 1989), p. 157 and references therein.
- [7] Q. Fu, G. Nak, and H.M. van Driel, *Opt. Lett.* **17**, 1006 (1992).
- [8] W.S. Feltch, P.E. Powers, and C.L. Tang, *Opt. Lett.*, **17**, 1070 (1992).
- [9] A. Nebel, U. Socha, R. Beigang, in *Ultrafast Phenomena 8*, ed. by J.-L. Martin, A. Migus, G.A. Mourou, A.H. Zewail, Springer Verlag (1993), p.187.
- [10] A. Nebel, C. Fallnich, R. Beigang, R. Wallenstein, accepted for publication in *J. Opt. Soc. Am. B*, spec. issue on optical parametric oscillators and amplifiers.
- [11] T.F. Albrecht, J.H.H. Sandmann, J. Feldmann, W. Stolz, E.O. Göbel, A. Nebel, C. Fallnich and R. Beigang, submitted to *Appl. Phys. Lett.*
- [12] The idler pulse that is simultaneously produced with the signal pulse provides even longer wavelengths between 2.15 μm and 3.3 μm .
- [13] M.J. Ludowise, *J. Appl. Phys.* **58**, R31 (1985) and references therein.
- [14] Y. Nishitani, T. Kotani, *J. Electrochem. Soc.: Solid-State Sc and Techn.* **126**, 2269 (1979).
- [15] T.F. Albrecht, T. Marschner, W. Stolz, E.O. Göbel unpublished.
- [16] T. Yajima, Y. Tera, *J. Phys. Soc. Jpn* **47**, 1620 (1979).
- [17] T. Takagahara, *Phys. Rev. B* **32**, 7013 (1985).
- [18] J. Hegarty, K. Tai, W.T. Tsang, *Phys. Rev. B* **38**, 7843 (1988).
- [19] M.M. Dignam and J.E. Sipe, *Phys. Rev. B* **43**, 4097 (1991).
- [20] G. Peter, Ph.D. thesis, Marburg (1990).
- [21] see e.g.: K. Leo, E.O. Göbel, T.C. Damen, J. Shah, S. Schmitt-Rink, W. Schäfer, J.F. Müller, K. Köhler, P. Ganser, *Phys. Rev. B* **44**, 5726 (1991).
- [22] K. Leo, T.C. Damen, J. Shah, K. Köhler, *Phys. Rev. B* **42**, 11359 (1990).
- [23] M. Koch, D. Weber, J. Feldmann, E.O. Göbel, T. Meier, A. Schulte, P. Thomas, S. Schmitt-Rink, and K. Ploog, *Phys. Rev. B* **47**, 1532 (1993).

Time-Resolved Spectroscopy of Electron Decay in Coupled Quantum Wells: Observation of Relaxation Induced Slow-Down

I. Bar-Joseph⁽¹⁾, G. Cohen⁽¹⁾, B. Devaud⁽²⁾, P. Bergman⁽¹⁾ and A. Regreny⁽¹⁾

(1) Department of Physics, The Weizmann Institute of Science, Rehovot 76100 Israel
(2) Ecole Polytechnique, CNRS, 91120 Palaiseau, France

Abstract

Electron decay from symmetric coupled quantum wells through a potential barrier to a continuum is studied using time-resolved optical spectroscopy. We find that at the limit of a thin barrier the decay rate decreases with decreasing barrier thickness and the energy splitting between the electron levels disappears. We show that this behavior is general for systems where resonant tunneling is coupled to a relaxation channel.

Introduction

Optical spectroscopy was successfully implemented in recent years in studying the resonant tunneling process of electrons and holes in coupled quantum wells (CQW) [1-6]. The system on which these studies were performed is asymmetric CQW, consisting of a narrow and a wide well. A theoretical analysis of the electron decay process in these structures has revealed that it is affected by quantum interference phenomena in an unexpected way [7]. It was shown that when a CQW system is in contact with a relaxation channel, the electron decay rate through this channel can be sometimes slowed down with increasing relaxation rate. In fact, it was suggested that the extremely long decay time, which was measured for resonant tunneling of holes in CQW, is due to elastic relaxation processes which suppress the decay rate [8].

Unfortunately, it is rather difficult if not impossible to experimentally vary the coupling to phonons and study the dependence of the decay process on V_0 , the relaxation rate. An alternative system, which exhibits a similar behavior, is symmetric CQW, where one of the wells is coupled via a thin barrier to a continuum. It was shown in Ref. [7] that the asymmetric CQW, where the decay is through phonon emission, and the symmetric CQW, which decays by tunneling, are described by the same effective Schrödinger type equation, with V_0 being the relaxation rate due to coupling to phonons or to the continuum states, respectively. The advantage of such a system as a model for experimentally studying the coupling between quantum tunneling and relaxation is obviously the ability to change the relaxation parameter in a controlled manner.

In this paper we experimentally investigate the symmetric CQW system. Using time-resolved photoluminescence (PL) and differential transmission (DT) spectroscopy, we monitor the decay rate of photo-excited electrons in these structures. We investigate samples, each having a different thickness of the outer barrier which separates the CQW from the continuum, while all the other parameters are kept constant. We show that the decay rate varies in a non-monotonic way as a function of outer barrier width such that the decay rate from the sample with the medium barrier width is the fastest. Solving the spectral line shape we find a splitting of the electron levels only in the wide barrier sample and explain the collapse of the splitting at the other samples as representing a transition from an oscillatory to a two exponential decay.

Samples and experimental set-up

Three samples have been grown by molecular beam epitaxy. Their structure consists of 10 repetitions of the following structure: Two 80 Å quantum wells with a 30 Å $\text{Al}_0.5\text{Ga}_{0.5}\text{As}$ barrier between them (designated by L_1), which on one side are coupled to a continuum (800 Å wide GaAs layer) by a thin $\text{Al}_0.5\text{Ga}_{0.5}\text{As}$ outer barrier of thickness L_2 , while on their other side there is a thick (200 Å) $\text{Al}_0.5\text{Ga}_{0.5}\text{As}$ barrier. The values of L_2 in the three samples are 50, 20, and 10 Å. Hereafter the samples will be labelled by the width of their outer barrier.

Two complementary experimental techniques were used in this work, time-resolved PL and DT spectroscopy. In the first, the system is excited at an energy which is larger than the gap and the recombination rate of the photo-excited free electron and holes is monitored using non-linear optical gating in the up conversion mode. In the DT measurement the sample is excited at the energy of the lowest exciton and the photo induced changes in the absorption spectrum are measured. The experimental system is a conventional pump probe set-up. The measurements were conducted at relatively low densities, $5 \times 10^{16} \text{ cm}^{-2}$, at liquid helium temperature, with a time resolution of 0.6 ps.

Results

A typical PL spectrum taken at a constant delay is shown in Fig. 1a. The decay time of the large peak at 1.52 eV is relatively slow, of the order of 1 ns, while the decay of the small peak at 1.57 eV, corresponding to the CQW, is much faster in all 3 samples. Fig. 1b shows the temporal evolution of the CQW luminescence in the three samples. It is seen that the decay time is very short, and depends on the thickness of L_2 . The measured decay time decreases from 11 ps in the 50 Å sample to 3 ps in the 20 Å sample and then increases to 5 ps in the 10 Å sample. These results show very clearly that the decay rate varies non-monotonically with the coupling strength, and demonstrate the anomalous decay behavior of the system.

To get a deeper insight into the behavior of the system and to determine the influence of extrinsic processes, such as hole tunneling and possible energy mismatch between the symmetric wells, we shall examine now the DT measurements. The DT signal is generally composed of two components. The first is associated with the electrons escape from the CQW and lasts a few picoseconds. The second component is related to the holes and is much slower. The tunneling time of the holes from the inner well is very long, and is comparable with the time elapsing between two consecutive pulses (11 ns). Consequently, there is a persistent contribution to the DT signal, which does not appear in the PL measurements, and is seen in all three samples as an early time signal. In the following we shall concentrate on the fast component.

Fig. 2a displays a typical DT measurement of the 50 Å sample. In this measurement the probe pulse is kept at a constant time delay with respect to the pump pulse and the excitation energy is scanned. This scan is performed for a set of time delays, between 0 to 11 ps. Two spectral features, 1 meV apart, are clearly observed: a high energy peak, centered at 1.570 eV, and a lower one, centered at 1.566 eV. A similar line splitting is seen at the cw PL of this sample. These two features are associated with the splitting of the electronic levels in CQW. It is seen that the two features decay in magnitude as time elapses at different rates. Just after the excitation by the pump (dashed line) the two are of similar height. However, 10 ps later

(dotted dashed line) the low energy peak has strongly decayed while the high energy peak only slightly decreased in magnitude. The corresponding decay times of the low and high energy components are 7 and 16 ps, respectively. This line splitting is not observed in the D1 and cw PL measurements of the other two samples. We shall later show that the absence of the splitting in these two samples is well explained by the theory.

Turning to the 20 Å sample two decay times are observed throughout the excitation line, a very fast one of 3 ps and a slower one of 15 ps (Fig. 2b). Since only the fast component is found in the PL measurement we can attribute it to the electrons escape from the CQW and conclude that the slow component is due to holes escape from the outer well. This conclusion is further supported by the fact that the measured time constant of 15 ps for the slow component agrees with the computed time for tunneling of holes through a 20 Å barrier.

Figure 2b gives also the results of the temporal measurement for the 10 Å sample. A single component of 6 ps decay time is measured throughout the excitonic line. As found in the PL measurement, the observed decay time is longer than that of the 20 Å sample. The holes that are created in the outer well escape through the 10 Å barrier very fast, and are not apparent in the PL signal.

Discussion

Let us turn now to a quantitative analysis of the results. Following Ref. [7] the electron wave function in the CQW is given by the solution of an effective Schrödinger equation of the form

$$\frac{d}{dt} \begin{pmatrix} \psi_1(t) \\ \psi_2(t) \end{pmatrix} = \begin{pmatrix} E_1 & 0 \\ 0 & E_2 + \Delta_0 - i\frac{\delta}{2} \end{pmatrix} \times \begin{pmatrix} \psi_1(t) \\ \psi_2(t) \end{pmatrix} \quad (1)$$

where $|\psi_i(t)|^2$ is the probability of finding the system in the i -th well with an energy E_i , Δ_0 and δ are the level shift and width due to coupling to the continuum, respectively, and δ is the energy splitting due to tunneling between the levels of the different wells. The two eigenvalues of the matrix are

$$\lambda_{1,2} = E_1 + \frac{\Delta_0}{2} \pm \frac{1}{2} \sqrt{\Delta^2 + \delta^2} - \left(\frac{1}{2} \right)^2 + i\Delta\lambda_0 \quad (2)$$

where $\Delta = \Delta_0 + \delta$, $\epsilon = E_2 - E_1$. Let us assume for the moment that $\Delta \neq 0$. It can easily be seen that when $\Gamma_0/2 < \delta$ (weak relaxation) we get two non-degenerate levels, with an energy splitting which is equal to $\sqrt{\delta^2 - (\Gamma_0/2)^2}$. In the opposite case of $\Gamma_0/2 \geq \delta$ (strong relaxation), we get two degenerate energy levels and the energy splitting disappears. Further insight into the behavior of the system is obtained by inspecting the imaginary part of the eigenvalues, which represents the decay time. In the weak relaxation regime we get approximately the same value $\Gamma_0/2$ for both energy levels. In the strong relaxation regime, however, the imaginary part of the eigenvalues bear two different values, $\Gamma_0/2$ and $\epsilon^2/2\Delta_0$, representing a fast and a slow decay, respectively. Thus, in the strong relaxation regime the overall time evolution of the system is a two exponential decay. Including of a finite Δ_0 would obviously change the situation, and there will be an energy splitting also in the strong relaxation

regime. However, since $\Delta_0 \ll \epsilon$, the splitting, which is $\sim \sqrt{\Gamma_0\Delta_0}/2$, is much smaller than the width of the broad resonant $\Gamma_0/2$, and is therefore not very significant.

Let us turn now to a quantitative comparison of the system behavior with theory. Examining the parameters of the three samples we find that in the 30 Å sample, where $\Gamma_0/2 \approx L_1$, the condition $\Gamma_0/2 \ll \delta$ is satisfied, and we are in the weak relaxation regime. The 20 Å sample is chosen to be at the transition between the weak to strong relaxation, where $\Gamma_0/2 \approx \delta$. In the 10 Å sample, where $\Gamma_0/2 > L_1/2$, we are in the regime of strong relaxation, where $\Gamma_0/2 \gg \delta$. Thus the observed collapse of the energy splitting in the 20 and 10 Å is well explained by the theory. Our temporal resolution does not enable us to resolve the fast component of the two exponential decay, which in the 10 Å sample is 10 fs. We therefore measure the time evolution of the slower component only. Since the decay time of this component scales like $1/\Gamma_0$, it is clear that in the 10 Å sample the measured time for the depletion of the system is expected to be longer than in the 20 Å sample.

There are, however, some discrepancies between the observed decay times and the calculated ones are observed. Most noticeable is the existence of different decay rates for the two electron levels at the 20 Å sample (7 and 16 ps), whereas theory predicts that there should be a single decay rate for both levels. We could exclude well width fluctuations and level misalignment (due to the coupling to the continuum) as the possible source of the different decay rates. A possible explanation is that in steady state the holes density is larger in the outer well due to Coulomb attraction to the electrons in the continuum. This results in lowering the electron energy level in the outer well and consequently in a slower decay time of the higher energy component. It should be emphasized, however, that the shortest measured decay time (7 ps) is shorter than the one that should have been measured in an ideal case with a zero energy mismatch, and is, therefore, a low limit for it.

In conclusion, we have shown that decay rate of CQW to continuum depends in a non trivial way on the coupling strength between the two. In the weak relaxation limit the decay rate increases with increasing the coupling strength. However, in the strong relaxation limit it decreases with increasing the coupling strength. This result is applicable to any system in which resonant tunneling is coupled to a relaxation channel.

This work was supported by the Minerva foundation, Munich, Germany.

References

1. D. Y. Olsch et al. Phys. Rev. B 40, 1028 (1989)
2. M. G. W. Alexander et al. Phys. Rev. B 41, 12295 (1990)
3. I. Matsuzaki et al. Phys. Rev. B 42, 5519 (1990)
4. K. Lee et al. Phys. Rev. B 42, 7665 (1990)
5. A. P. Heibich, W. W. Rohde, C. Koller, Phys. Stat. Sol. B 173, 881 (1992)
6. B. Deveaud et al. Phys. Rev. B 42, 7021 (1990)
7. S. A. Gurvitz, I. Ben Joseph and B. Deveaud, Phys. Rev. B 43, 11701 (1991)

Modulation of Wannier-Stark Transitions by Miniband Franz-Keldysh Oscillations in Strongly Coupled GaAs-AlAs Superlattices

Karl-Heinz W. Godello-Glatz, A. Lindner, G.H. Dohler
Institut für Polymerphysik, Physik-Universität Flensburg, Sankt-Annen-Route 1
D-24603 Flensburg, Germany

Ulrich Gerdahn & Ploeg

II. Schlusssatz
 Einmaliges Instrukt. zur Vermeidung von Verwirrungen (illustriert) 10-15 min

[illegible]

1991-1992

In type I semiconductors the well-known Wannier-Stark WS scattering formula (1) predicts the field dependence of absorption $\propto \exp(-\alpha_0 E)$. At high applied electric fields the electric field-induced hole wave functions are strongly localized. The therefore only spatially direct transitions are allowed. The two direct \rightarrow conduction band transitions are reflected in a step-like absorption coefficient. With decreasing electric field E the delocalization of the wave functions increases. Due to the different effective mass the heavy hole remains localized even at rather weak applied fields while the \rightarrow conduction wave function size a extends over several wells. Thus the heavy hole wave function acts as a detector for the \rightarrow conduction band indirect transitions. WS transitions appear in the absorption spectra (Fig. 1). These transitions shift linearly towards the center of mass position E_0 according to

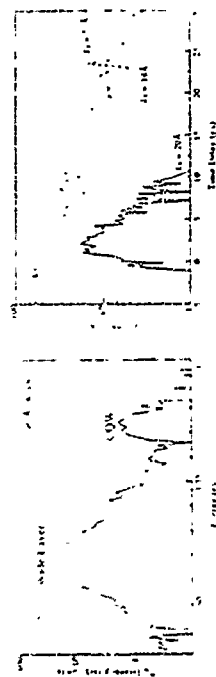


Fig. 1. (a) Fluorescence spectrum of the 30 Å sample at a delay time of 10 ps. (b) Decay behavior of the CQW luminescence in the 3 samples.



Figure 1 illustrates the relationship between the number of nodes in the network and the number of nodes in the network. The number of nodes in the network is denoted by N and the number of nodes in the network is denoted by N . The number of nodes in the network is denoted by N and the number of nodes in the network is denoted by N .

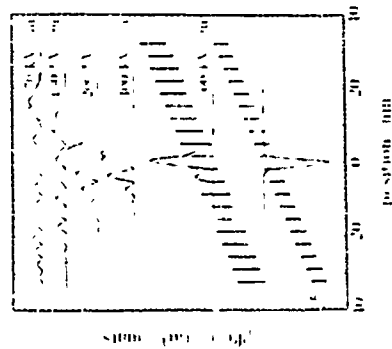


Fig. 1 Field dependent behavior of the squared electron wavefunction. The lower part of the figure shows the aperture potential and the heavy hole wavefunction at 500 kV/cm.

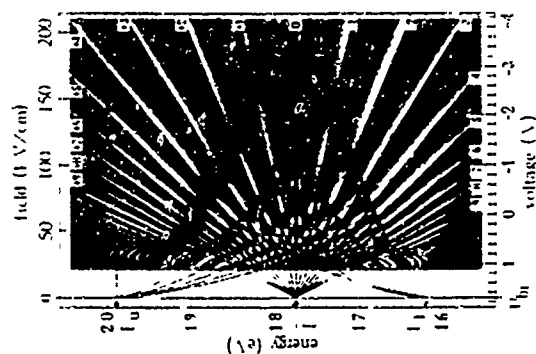
$$f_{\text{max}} = f_{\text{min}} + \frac{1}{2} \left(\frac{f_{\text{max}} + f_{\text{min}}}{2} \right) \left(\frac{f_{\text{max}} - f_{\text{min}}}{2} \right)$$

If there is no field applied all wavefunctions are completely delocalized. The resonant subbands split into minibands with a three-dimensional combined density of states and three-dimensional critical points \mathcal{N}_d at each minimum edge in the superlattice structure. The field-dependent absorption of a three-dimensional system is described by the well-known Franz-Haas effect (cf. Fig. 1). It is characterized by oscillations inside the band region from the negative field according to

$$f_{\infty} = f_0 + f_1 + f_2 + \dots + f_{n-1} + f_n$$

[illegible]

In this paper we report about theoretical and experimental investigations of the induced transition from the three-dimensional manifold system to the WS regime with its one-dimensional character which is reflected in steps of the WS ladder in the superlattice absorption along different photon-polarization steps (DPRS) at a special wavelength. At the same time we are able to resolve a symmetric WS fan up to an index of 2.9. At the same time FK oscillations appear at the laser and even at the upper miniband edge. Shifting towards the center of the manifold with the frequency, oscillations are riding to $l \approx 2$. Our theory details this competition of the new WS fan with the non-linear fan of the theory.



of FFETs: 2. Calculated wavelength derivative of the longitudinal change of the refractive index as a function of λ , $d n(\lambda)/d\lambda = 0.92$ Å⁻¹, depicted in Fig. 10. The refractive index of the substrate is taken as a grey scale, therefore, small amplitude values are highlighted. The wave number of the waveguide amplitude is fixed up to Fig. 10. The linear FETs fan (black numbers) is evaluated with $\omega_{\text{FET}} = 1.772 \times 10^{15}$ s⁻¹ and $\omega_{\text{FET}} = 1.772 \times 10^{15}$ s⁻¹ is compared to Eq. 1 ($\omega_{\text{FET}} = 1.772 \times 10^{15}$ s⁻¹), as depicted in Fig. 11. The linear FET fan (black numbers) is compared to Eq. 1 ($\omega_{\text{FET}} = 1.772 \times 10^{15}$ s⁻¹), as depicted in Fig. 11. The non-linear FET fan (blue numbers) is calculated according to Eq. 2 ($\omega_{\text{FET}} = 1.016 \times 10^{15}$ s⁻¹) and $\omega_{\text{FET}} = 0.085 \times 10^{15}$ s⁻¹ is compared to Eq. 1 ($\omega_{\text{FET}} = 1.772 \times 10^{15}$ s⁻¹), as depicted in Fig. 12.

1. The first step is to identify the problem or question that needs to be answered. This involves understanding the context and the specific requirements of the task.

THEORY

In our calculations (Fig. 1) we used the Kane formalism which gives a crystal momentum representation of the wavefunction (ψ , s). The theoretically investigated superlattice is composed of 11 monolayer ($\text{In}_{1-x}\text{Ga}_x$) wells and one monolayer AlAs barriers. The average combined width of the lowest electron and heavy hole manifold is 380 meV. The conduction dispersion is determined by the Kronig-Penney model. Because of the strong coupling between the wells the tight-binding model is not appropriate for our theoretical considerations. In particular the unimodal dispersion is strongly asymmetric with respect to the lower and upper miniband edges. The field depends on superlattice absorption is given by the average of the electron and heavy hole wavefunction. Due to a three times smaller oscillator strength and a larger delocalization of the wavefunction light hole transitions are negligible.

and a two-dimensional theory. In order to compare our theory with our experimental data we do not calculate simple absorption spectra but the wavelength derivative of the field induced change of the absorption $\partial\alpha/\partial\omega$. Fig. 2 shows ladder transitions (labelled by black numbers) are clearly observed at the lower and upper miniband edges the non-linear FK fans modulate the intensity, if the WS levels while the oscillations move towards Γ with the period proportional to $f \pm 2\gamma$ (see Fig. 1).

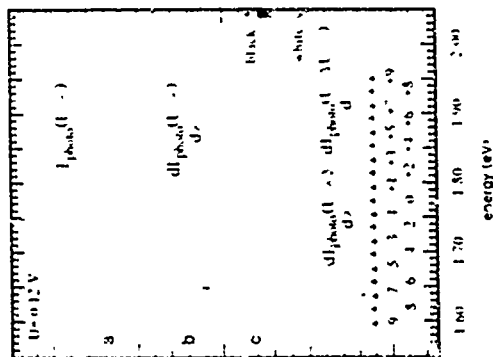


Fig. 1. Comparison between Pt (100) DPQ and DDPT spectra ($\Delta E = 0.02$ eV). The lower part of Fig. 1 shows the calculated WS transition energies according to Eq. 1.

Due to the asymmetric miniband dispersion the field dependence of the FK oscillations at the lower miniband edge marked by thick dots and white numbers is much better described by the effective mass δ^* criterion with the Lorentz-Penney model in contrast to the upper edge. The small lines, which describe the field dependent shift of the FK oscillations at the upper miniband edge, are calculated with Eq. 2 using a fitted effective mass $m_{\text{penney}}^* = 0.02 m_0$, $E_g = 2.034$ eV. Therefore, these lines are only guide lines for the eyes. Due to a large effective mass the FK oscillation period is smaller at the lower miniband edge compared to the upper one (cf. Eq. 2). In the low field limit the energetic distance ef_d between adjacent WS states is too small to be resolved and the WS features add only a fine structure to the FK oscillations. At intermediate fields the WS structure becomes increasingly coarse. The competition of the WS and FK features presents a checkered pattern in Fig. 2. For higher fields when the first FK absorption maxima corresponds to the lower and upper miniband edges, the extreme WS regime, where the spontaneous direct transition becomes more and more dominant while all other levels of the WS ladder gradually disappear [1, 3].

III. EXPERIMENT

In our experiments we have studied λ -GaAs/ λ -AlAs superlattices which were grown on a GaAs n^+ -substrate with molecular beam epitaxy. The superlattice consists of 50 periods of 11 monolayer GaAs wells and only one monolayer AlAs barriers. The superlattice was etched between 8 to 10 μm wide Al_{0.3}Ga_{0.7}As n^+ and p^+ -shape regions followed by a 0.2 μm n^+ -doped

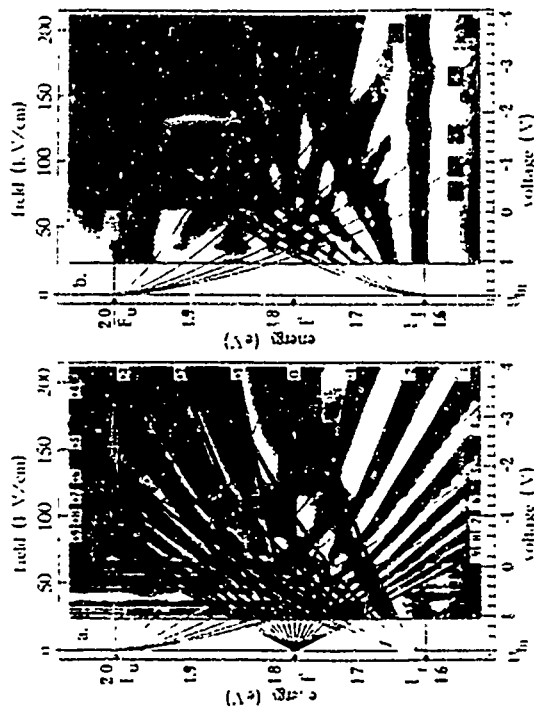


Fig. 2. Experimentally observed wavelength derivative of the field induced change of the Pt (100) DPQ spectra at $\Delta E = 0.02$ eV and is the experimental counterpart to Fig. 1. The WS and FK features are identical. In part (b) DPQ spectra at higher fields are related to the DPQ spectrum measured in the very low field limit, $dI_{\text{DPQ}}(1.2 \text{ V})/dV = dI_{\text{FK}}(1.2 \text{ V})/dV$. The lower and upper miniband edge (E_L and E_U) and FK oscillations (dashed lines) and 1 to 6 dominate in the spectra.

GaAs on the n^+ -side and 400 λ Be-doped GaAs layers on the p^+ -side of the sample. We used DPQ, a new wavelength modulation technique [10], which is much more sensitive compared to normal photoluminescence spectroscopy. Fig. 3a shows the photoluminescence spectrum measured at 77 K and an applied voltage of 0.12 V. Only the lower combined heavy hole miniband edge and wide field independent Fabry-Pérot oscillations above the fundamental gap energy lying on top of a huge background signal are clearly observable. In the wavelength derivative of the photoluminescence (Fig. 3b) a sharp peak at the lower miniband edge and narrow Fabry-Pérot oscillations appear. However, in contrast to Fig. 3a the large background signal is suppressed by the first derivative character and a small fine structure becomes visible caused by field dependent WS ladder transitions. To remove the field independent structure it is useful to study the difference of two DPQ spectra measured at different applied fields (Fig. 3c). The investigation of the field induced change of the photoluminescence allows a detailed and very sensitive study of the field dependent superlattice absorption (Fig. 3c, d).

J. M. Gerard, V. Izuel, J. Y. Marzin and R. P. Rajen
France Telecom/NTT-PDA, 196 av. Henri Ravera, F-92220 Bagneux, FRANCE
and R. Ladan
Laboratoire de Microstructures et Microelectronique CNRS, 196 av. Henri Ravera, F-92220
Bagneux, FRANCE

ՀԱՅԿԻ

The existence of an absolute photonic bandgap in the near infrared for two dimensional periodic dielectric structures is discussed for photons propagating in the plane of such 2D crystals. A special emphasis is put on the influence of the shape and size of the filling pattern on the absolute bandgap formation. Very large absolute photonic bandgaps are predicted for 2D crystals formed by etching in a semiconductor slab periodic arrays of large vertical cylindrical voids of circular cross section arranged in a triangular lattice. The technological feasibility of such epitaxially grown 2D crystals by standard processing techniques (electron beam lithography and reactive ion etching) is demonstrated.

Tailoring the spontaneous emission of a semiconductor active medium is particularly challenging, for fundamental reasons, as well as in the view of a further optimisation of optoelectronic devices. The insertion of the emitting center in a microstructured material with three-dimensional (3D) periodicity potentially allows to inhibit optical transitions within the photonic bandgap (PBG) covering range of this material, to couple the emission to a single, or a few, selected modes.¹⁻⁴ If, though, optiumum 3D antiresonator crystals are very attractive due to their large theoretical PBG in the near infrared, it is presently very difficult to process such structures. In this respect, it seems presently easier to fabricate antiresonator crystals with 2D periodicity. After this, owing potential applications of such crystals, we will present the results of a large scale study of the influence of the shape, symmetry and size of the pattern on the existence of a photonic bandgap. Among those which have been considered, a simple class of structures (large circular holes on a triangular lattice) allows to get a large PBG, common for both polarisations. Preliminary results concerning the microfabrication of such crystals are presented.

Two-dimensional air-semiconductor crystals, formed by a periodic array of cylindrical vertical semiconductor rods or of vertical cylindrical holes in a semiconductor matrix, can in principle be produced by standard processing techniques. Due to the strong periodic modulation of the dielectric constant in this material, large PBGs appear in the photonic dispersion curves as soon as the direction propagation of the photons is different of the direction of the rods (or holes). It is important to note however that these PBGs appear generally in different energy ranges for the rods and holes case. Two classes of interesting applications are opened for such a material.

In a guided wave geometry, as is the case for most optoelectronic devices and integrated circuits, a 2D crystal displaying a PHG for photons propagating in its plane (χ) can be used, as a low loss depolarization dependent mirror, allowing no cut off in angle (angle-unlike Bragg mirrors). The application to photon recycling in laser is particularly attractive. Since for appropriate patterns a large PHG exists, which is common to all directions of propagation in or close to the χ plane, a full control of optical transitions could be obtained by operating a slab of this anisotropic material between two Bragg mirrors, or by orienting preferentially the optical transition dipole in a direction that is the case for strained quantum wells, under strong biaxial tension. The full control of spontaneous emission is here clearly the main challenge.

We will essentially discuss hereafter the results of our calculations in terms of a maximization of the width W of the PHG of the crystal for photons propagating in the xy plane. It is some our attention on the second class of applications, indeed we see that a PHG wider than W is always out of the question.

Dephasing is more important in the ch_{11} type than in ch_{12} WSIs, since the ch_{11} and ch_{12} band edge structures (Fig. 4b) dominate in such double-diffraction of photon current spectra (IDDPDPS). In Fig. 4a WS transitions from ψ_{up} to ψ_{down} are clearly visible. Their intensities are modulated by FK oscillations which is in very good agreement with our theory (e.g. Fig. 2), although evanescent effects are not included in our calculations. The small deviations at high fields can be explained by the quantum confinement Stark effect which is not included in our calculated spectra. In order to see the FK oscillations and the miniband edges more clearly it is advantageous to relate DPC spectra measured at higher fields to a DPC spectrum taken in the very low field limit (Fig. 6b). Now FK oscillations appear at the lower and upper miniband edge reflecting the field-dependence of Eq. 2. All difference spectra exhibit a field independent band edge structure caused by the zero field limit spectrum with characteristic nearest peak at each miniband edge. The experimentally observed upper miniband edge energy is slightly smaller than expected from theory. This deviation can be explained by conduction band non parabolicities. At higher fields WS levels are not again

11-11-12

We have studied the transition from the miniband to the WS regime, i.e. from a three-dimensional resonant density of states to a two-dimensional one. The difference of two DPC spectra measured at different applied fields shows a symmetric WS line up to an index of 2.9 and for the first time FK oscillations across the whole lowest miniband have been observed. In our experiments as well as in our theoretical results a modulation of the WS transitions by FK oscillations is clearly visible. In conclusion there is no sharp transition from a three-dimensional system to a two-dimensional one but rather a coexistence of the two and the WS regime over a wider field range.

510, 1811, 183

- [1] P. Vasani, *Superlattices Microstruct.* **8**, 123 (1990).
- [2] F. E. Meier, J. Agallo-Rueda and J. M. Hwang, *Phys. Rev. Lett.* **60**, 2126 (1988).
- [3] J. Bleuse, C. Bastard and P. Vasani, *Phys. Rev. Lett.* **60**, 229 (1988).
- [4] D. E. Aspnes, *Handbook on Semiconductor*, edited by J. S. Moss, Vol. 2, Ch. 1A, 109.
- [5] H. Schneider, A. Fischer and K. Ploog, *Phys. Rev. B* **45**, 6129 (1992).
- [6] C. Corrao, D. Campi, C. Cacciatore, C. Abbate, S. Galliani, B. Lander, and A. Reguly, *Ferrophys. Lett.* **10**, 591 (1991).
- [7] E. O. Kane, *J. Phys. Chem. Solids* **12**, 181 (1959).
- [8] M. Satoh, *J. Phys. C: Solid State Phys.* **5**, 915 (1972).
- [9] F. E. Meier, and F. Agallo-Rueda, *J. Lum.* **14**, 221 (1990).
- [10] K. Schumacher, A. D'Intino, N. Under, M. Ima, G. H. Dohler, H. I. Gradien, K. Kawasumi, and K. Furusawa, *Superlattices Microstruct.* **12**, 181 (1992).

It has already been shown that 2D arrays of circular rods, for holes in a triangular lattice exhibit, for appropriate parameters, a large PBG for either E or H polarizations (i.e. electric or magnetic field parallel to z) [4]. Up to now, however, the fundamental question of whether the PBGs for E and H polarizations overlap (i.e. the existence of an 'absolute' PBG) has not been addressed to our knowledge.

2D crystals obtained for a circular pattern and a triangular lattice are particularly favorable to the appearance of a large PBG. Such a crystal (and therefore its photonic band structure) retains the full symmetry of the triangular Bravais lattice, which makes easier the overlap, all around the edge of the first Brillouin zone, of the photonic gaps relevant for each direction of propagation. We plot for instance in figure 1 the calculated photonic band structure of a crystal formed by large circular vertical holes in a $G_{1.5}$ matrix (dielectric constants $\epsilon_{\text{rod}} = 1$, $\epsilon_{\text{matrix}} = 1.5$). The filling factor f defined as the fraction of the xy plane which is covered by the cross section of the circular cylinders is here 0.78. Details of the calculation, based on a plane wave expansion of the solutions of Maxwell's equations, have been presented elsewhere [4, 5]. Since the band structure scales with the lattice parameter a of the crystal, we plot here $\omega a / 2\pi c$ (to photon polarizations E and H) as a function of the Bloch vector k . Numerous band degeneracies occur at high symmetry points of the Brillouin zone, so that only two large PBGs exist for the lower energy bands: H and E . (We refer from now on to H and E in order to design the PBG, if any, between the E and the H bands in H/E polarization) Interestingly, E and H PBGs widely overlap for this set of parameters, which will be shown hereafter to be an exceptional feature for 2D crystals. The absolute PBG is for instance, 280 meV large if centered near the 1.12 eV electronic gap of GaAs at room temperature, which will in principle be the case for $a = 0.4 \mu\text{m}$. Note that for this lattice parameter and a 0.78 filling factor, nearest neighbour holes are separated by a semiconductor wall as thin as 300 Å.

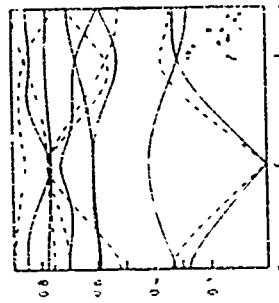


Fig. 1. Photonic band structure for a $G_{1.5}$ crystal with circular holes (solid line) and H (dashed line) polarizations. The filling factor f is here 0.78. The first Brillouin zone of the 2D crystal and the $\sqrt{3} \times \sqrt{3}$ path along which the dispersion curves have been calculated are shown in the insert.

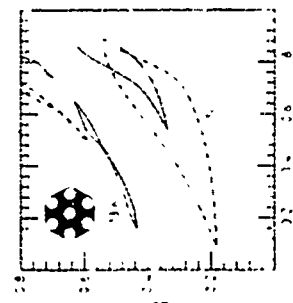


Fig. 2. Plot of the energy range of all PBGs existing for the first seven bands in E and H polarization for a 2D crystal with triangular Bravais lattice, formed by an array of vertical circular holes in GaAs as a function of the fraction f of the medium occupied by the holes.

In an attempt to optimize both H and the technological feasibility of the crystal, we have investigated the photonic band structure for various patterns conforming to the crystal the full symmetry of the triangular Bravais lattice. All bandgaps appearing for the nine lower energy bands have been plotted for all possible values of the filling factor (0.525-0.86) for an array of circular holes in GaAs (figure 2); or of GaAs circular rods in air (figure 3). For holes, the only possible significant PBGs are H and E . E opens only for $f > 0.6$, so that a large absolute PBG is observed only when f is close to the maximum filling factor of a plane by disks ($f = 0.86$). As in the previous example, neighbour rods are separated by a very thin dielectric sheet, which makes the microprocessing of such crystals somewhat delicate, even in the state of the art etching techniques. It is more generally easier to etch semiconductor rods rather than drill holes in a semiconductor slab. Considering figure 3, however, we see that arrays of circular GaAs rods on a triangular lattice never display an absolute PBG. Though large E PBGs exist for most values of f , H the single PBG observed in H polarization, never overlaps one of these.

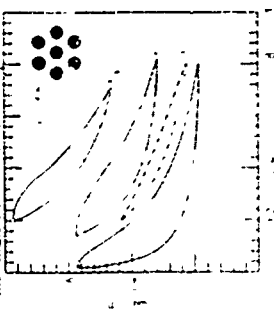


Fig. 3. Same as figure 2, for an array of GaAs vertical rods with circular cross section f in air. Here the fraction of the medium occupied by the rods.

The various ways to lower the symmetry of the crystal have been systematically investigated in an attempt to lift some symmetry induced degeneracies, and open novel gaps [5]. When actually achieved, this result is generally obtained at the expense of a reduction of the E or H PBGs observed for circular patterns for the same filling factor. Furthermore, these novel gaps generally have a small width, so that no interesting absolute PBG can be obtained. To understand this result, one should keep in mind that large PBGs are the more likely to appear in a medium which is as close to in plane isotropy as possible: arrays of circular rods or holes in a triangular lattice are optimum in this respect. Similarly, the marked anisotropy of 2D crystals between E and H directions is the minimum reason why E -gaps and H -gaps so rarely overlap. For optimum 3D crystals (16 cm^{-1}) with face centered cubic lattices, E and H polarizations play rather similar roles, and an absolute PBG results from the overlap of E and H PBGs. For 2D crystals on the opposite, E and H polarizations intrinsically play very different roles. Coupling coefficients in the eigenvalue problem being systematically smaller for the H than for the E polarization [1, 5], the H band is, for instance, at a much lower energy for f than for H , in particular $f = 0.5$, and H bands both open never overlap.

Finally, the calculation has also been conducted for an array of holes with hexagonal cross section, this pattern being the more orientation as the Wigner-Seitz unit cell at the first order. The interest is here twofold. Firstly, it is possible to test to some extent the sensitivity of the absolute PBG of arrays of circular holes to deviations of the pattern for an ideal circular shape. Secondly, it is possible for such a pattern to study the photonic band structure for the whole range of filling factors ($0 < f < 1$). The energy location of the E and H PBGs is plotted as a function of f in figure 4, which should be compared to figure 2, relevant for circular holes. No more PBGs exist for this hexagonal pattern, since both corresponding 2D crystals exhibit the same symmetry. As expected also, all gaps pinch off to $f = 0$ for $f = 1$, i.e. at the limit of a perfect medium. The location and width of the PBGs are remarkably similar for both crystals for the smaller filling factors ($f < 0.5$). The photonic band structure is indeed hardly modified (for a given f) as long as pattern modifications occur at a scale much smaller than the correlation length of the electromagnetic waves in the medium ($a/5$ to $a/10$). When f approaches

the critical filling factor for which circular holes get in touch how, yet, the repartition of the dielectric material becomes very different for circular and hexagonal holes. We observe a drastic shrinking of the PBG f_c for an hexagonal pattern. Whereas f_c is essentially unaffected. As a result, this crystal has a very small absolute PBG. For regular polygons with a higher number n of sides, we recover the limit of circular holes rather quickly ($n = 8$ or 10) in good approximation the width and position of PBG f_c is the same within 10 per cent).

Fig. 1 Same as figure 2 for an array of vertical voids in GaAs with hexagonal cross-section. f_c is here the fraction of the medium occupied by the voids.

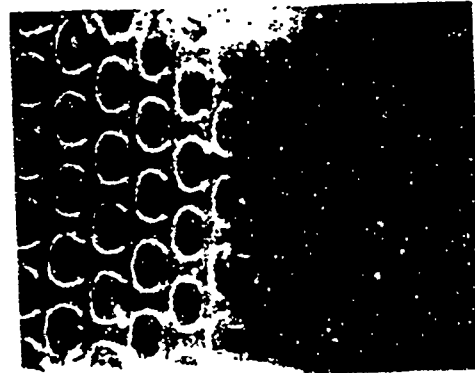
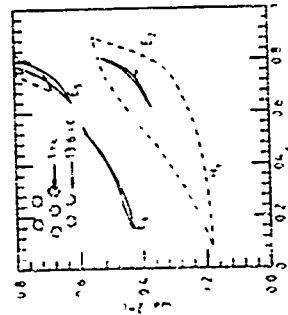


Fig. 5 Scanning electron micrograph obtained for a view with 45° incidence of the cleared edge of a 2D air GaAs crystal. Note the

Etching deep holes with submicronic diameter and vertical walls is still a major technological challenge. Preliminary experiments have been conducted so as to demonstrate the feasibility of optimum 2D air GaAs crystals and test their degree of perfection. Our test structures are arrays of circular holes in GaAs arranged on a triangular lattice of submicronic parameter ($a \approx 0.6 \mu\text{m}$). For this lattice parameter, the absolute PBG is theoretically centered near 1.4 eV for optimum structures ($0.7 < f < 0.8$). Various crystals have been processed, for hole diameters in the $0.25 \mu\text{m}$ ($f \approx 0.47$) to $0.7 \mu\text{m}$ ($f \approx 0.72$) range. The holes are drilled by SiCl_4 reactive ion etching (RIE), under conditions which optimize the verticality of the etched walls. For that purpose, we use a Ni mask defined by electron beam lithography in a JEOL SDHU machine. Figure 5 displays a typical scanning electron micrograph obtained on the cleared edge of a 2D air GaAs crystal after $f \approx 0.6$ after $0.6 \mu\text{m}$ deep holes have been etched. The shape and depth of the holes seem pretty homogeneous. It is important to note that their bottom (essentially flat) do not exhibit the round shape typical of an inefficient etching process. Etching deeper holes with a good verticality seems therefore realistic, at least up to a $0.8 \mu\text{m}$ deep (which would be enough for most applications). Finally, the cross-section of the holes at the surface is close to a perfect disk. This is the combined result of a careful definition of the circular pattern at the lithography step, and also of the intrinsic tendency of resist patterns to smooth at the revelation step.

To conclude, the photonic band structure of some 2D air-semiconductor crystals has been studied as a function of the shape and size of the same simple crystal patterns. A detailed review of the performance of some simple 2D PBG crystals highlights some design rules for obtaining large absolute PBGs. A wide absolute PBG has only been obtained for arrays of large voids etched in the semiconductor matrix. Circular voids lead (for $0.75 \leq f \leq 0.8$) typically to the largest absolute PBG attainable, resulting tunable in the 3D case from the overlap of H_z and E_z PBGs. Any deviation from this perfectly symmetric pattern reduces the width of the absolute PBG. Elongated shapes (rectangles for instance) are particularly detrimental in this respect. This kind of design rule qualitatively indicates that the medium must be as isotropic as possible for the crystal to have a large absolute PBG. Finally, we have shown that state of the art lithography and etching techniques allow to produce such 2D air/GaAs crystals which theoretically display a large absolute PBG in the near infrared. An optimization of the etching procedure, so as to obtain deeper vertical holes, and the spin, if study of the photonic band structure have still to be performed.

References

- [1] Y. Abramowitz, Phys. Rev. Lett. **58**, 2950 (1987).
- [2] S. John, Phys. Rev. Lett. **58**, 3186 (1987).
- [3] Y. Abramowitz, T. J. Gmitter, R. D. Meade, A. M. Rappe, K. D. Brommer, J. D. Joannopoulos, Phys. Rev. Lett. **67**, 3380 (1991).
- [4] M. Pihlal, A. Shambrook, A. A. Maradudin and P. Sheng, Opt. Communications **80**, 199 (1991).
- [5] M. Pihlal, A. Shambrook, A. A. Maradudin, Phys. Rev. B **44**, 8568 (1991).
- [6] R. P. J. P. J. M. G. and J. Y. Marzari, to be published in the Review of Modern Optics Special issue on photonic bandgap.
- [7] K. M. Ho, C. T. Chan and C. M. Soukoulis, Phys. Rev. Lett. **65**, 3152 (1990).
- [8] Y. Abramowitz, T. J. Gmitter and K. M. Soukoulis, Phys. Rev. Lett. **67**, 2295 (1991).

Author Index

Abstetter, G	MoC7	319	Berchstedt, F	ThP10	846	Butov, L V	MoP40	275	Devraud, B	ThP14	875
	TuP22	559	Bedel, E	MoP12	54	Bykov, A A	MoP37	261	Devresse, J T	ThP27	928
	TuP24	572	Behr, D	MoP11	110	Calleja, J M	ThC3	1022	Deych, M	ThP36	985
Adachi, A	ThB5	790	Belticky, V I	MoP12	119	Campbell, P M	MoP6	80	Dietrich, B	TuP23	565
Adolph, B	MoP9	102	Belloni, G	ThC4	1029	Campman, K L	ThC4	1029	Diesche, W	MoP31	228
Agullo-Rueda, J	ThP10	846	Bending, S J	TuP39	652	Caneau, C	ThB2	773	Dilger, M	MoA3	13
Aihara, K	TuC4	424	Bennett, B R	MoC2	290	Capasso, F	ThC1	1015	Diniz, R	TuB2	377
Alkawa, K	MoP35	248	Bergman, P	FrB3	1089	Capizzi, M	ThP20	903	Dmowski, L H	MoP28	208
Akiyama, H	ThP8	874	Bernardini, F	ThP9	841	Cardona, M	MoP19	157	Dohler, G H	TuC4	424
Alavi, K	MoC1	281	Bernhard, K A	FrA3	1059	Carmona, H	MoP12	119		ThP35	978
Albrecht T F	ThC2	1016	Berrout, J M	MoP22	175	De Carr, L	MoC6	314	Dotling, R	FrB4	1094
	TuP13	515	Betton, P H	TuP25	576	Cerva, H	TuP38	645	Dresselhaus, G	MoP30	220
Albrekisen, O	FrB2	1081	Bhat, R	MoP8	94	Chang, K H	MoC5	307	Dresselhaus, M S	ThA2	736
Allen Jr, S J	TuP13	712	Bicknell, R N	TuP30	605	Chang, Y H	WeB1	700	Drexler, H	ThA2	738
	WeB2	1029	Bimberg, D	TuP28	593	Chaubet, C	MoP27	200	Dur, D	ThC5	1033
	ThC4	1039	Bird, J P	ThB2	773	Cheeks, T L	ThP26	927		ThP26	927
Alperovich, V L	TuA5	360	Birotheau, L	ThA5	756	Chen, J J	WeA3	680	Dutarte, D	TuP25	576
Andersson, T G	MoP23	181	Bloch, J	ThB2	773	Chen, J J	ThA2	738	Dutisseul, E	MoP33	238
André, J P	WeA5	694	Bockelmann, U	MoA2	9	Cheng, J P	MoP27	200	Dzyubenko, A B	TuP14	522
André, J P	MoP18	151	Bogaerts, R	ThB1	763	Choi, A Y	ThP27	928	Eaves, L	TuP23	593
Aoyagi, Y	MoP36	252	Bohm, G	MoA2	9	Chou, D H	TuP11	502		TuC6	435
Apetz, R	TuP26	581	Bois, P	ThB5	790	Chou, S N G	ThP17	889	Eberl, K	TuP30	605
Arakawa, Y	MoP5	73	Bologna, C	TuA5	360	Christen, J	ThP20	903	Ehrenfreund, E	TuP27	585
	MoA1	1	Bolton, F	ThP24	916	Chu, J	ThC1	1015		MoP39	268
Aristone, F	TuP40	688	Boudinet, P	MoP28	206	Chu, S N G	ThB2	73		MoP31	228
Aschauer, M	TuP24	572	Brar, B	FrA3	1059	Cingolani, P	ThP4	1009		MoA3	13
Asmat, N G	MoP32	234	Brataas, A	TuA2	338	Cockburn, J W	MoP22	175		ThP39	1009
Almani, H	MoP2	54	Brehmer, D	MoP4	68	Cohen, E	ThP39	1009	Eisele, J	ThP22	909
Badoz, P A	TuP31	613	Brill, B	ThP12	859	Cohen, G	ThP6	825	Ekenberg, U	TuP29	600
Baldwin, K W	TuP25	576	Brown, C V	ThP2	803	Cundiff, S T	ThP35	634	Engelhardt, C M	MoP24	182
Bar-Joseph, I	MoB2	23	Bruggermann, F	ThC6	1039	Dabbico, M	ThP21	904	Engslin, K	TuP24	572
Baranov, A	FrB3	1089	Brum, J A	MoP22	175	David, J P R	ThP22	909	Evans, H B	MoP39	268
Baratov, P G	FrA4	1064	Bruni, M R	ThP12	962	Davis, J L	FrB3	1089	Ezaki, T	ThP19	899
Bardorf, S R	TuP15	523	Brunner, K	TuA5	360	Dawentz, L	MoP22	175	Fagotto, F A M	ThP15	879
Barnes, D J	ThP5	821	Buckley, P D	MoB1	21	De Boeck, J	FrB2	1081	Fam, G	TuP33	625
Bartoli, F J	WeA2	675	Buhmann, H	TuP18	645	DeLalande, C	TuC4	424	Faust, J	ThC1	1015
Basmaji, P	ThP23	915	Bungaro, C	FrB1	1075	Dennis, B S	ThP6	825		TuP20	903
Bass, S J	ThP30	949		TuP37	640	De Rosa, F	MoP20	165		ThB3	777
Bastard, G	TuC2	411		TuB2	377	Deveaud, B	MoC2	165	Fischer, A	TuB3	777
	TuP2	411		MoP22	175		MoC2	290		TuP34	629
	TuP2	411		ThP15	879		MoP11	110		ThP9	841
	TuP3	454		MoP19	157		TuA4	354		ThP25	922
Bauer, G	ThP2	803		ThB5	790		WeA3	80		FrB2	1081
	TuP22	559		TuP35	634		ThP3	810		ThP6	825
	MoP17	144		MoP39	268		ThC3	1022		TuP2	446
	ThA2	738		TuP30	605		TuA5	160		TuP3	454
Bauer, G E W	ThP32	962		MoC8	324		FrB3	1089		TuP6	471
Beaumont, S P	ThC5	1033									

Fischer, A	MoC5	307	Goldoni, G	TuP34	629	Haug, R. J	TuP36	635	Ikoma, T	MoC4	302
Fisher, T A	MoP20	165	Gohi, A R	ThC3	1022	Haupt, R	ThP11	853	Ilg, M	MoC3	298
	MoP39	266	Gorezyca, J	MoP28	206	Hawrylak, P	ThP28	934	Ils, P.	ThP18	894
Fontaine, C	TuC2	411	Gornik E.	TuP24	572	Heath, M.	TuP30	605	Inata, T	TuB4	389
Forchel, A	MoP2	54		TuC5	431	Heberle, A	MoC3	298	Inoshita, T	MoC1	281
	ThB3	777		TuB2	377		TuP18	541	Inoue, K.	ThP16	885
Forster, A	ThP18	894		ThC2	206	Heblum, M	MoB1	21		MoP9	102
Forster, T. J	TuP38	377	Gossard, A C	ThC3	909	Heime, K	MoP7	88		MoB4	35
	TuP28	593		ThC4	1029	Heimann, D	MoA3	13	Ishibashi, K.	MoP36	252
Foullant, C	FrA4	1064	Grahn, H T	TuC4	424	Helm, M	TuP22	559	Ishida, A	ThP8	834
Frankenfeld, H	TuP23	565		FrB4	1094		ThC2	1016	Ishikawa, T	MoP1	46
From'ertz, T	TuP22	559	Grambow, P	MoA3	13	Hemmi, M	TuC6	435	Ito, R.	MoP16	527
	ThC2	1016	Grey, R	MoP20	165		TuP30	605	Ito, T.	MoP10	104
Frosz, J E F	TuP1	365		TuP35	634		TuP28	593	Iskevich, I E	ThB3	777
Frova, A	MoP19	157	Grimmuss, H G	TuP23	565	Henneberger, F	MoP39	268	Ivanov, S V	MoP40	275
Fu, Y	MoP5	396	Grundberg, P	FrA4	1064	Herlach, F	ThP7	829	Ivchenko, E L	ThC7	1046
Fujiwara, A	ThP34	974	Guasch, C	ThB2	773	Hertel, G	TuA5	360	Izrael, A.	TuB5	396
Fujiwara, K	TuP1	442	Gudmundsson, V	MoP2	54	Hessman, D	ThC5	1033		ThB1	763
	TuP4	460	Gulden, K H	ThP28	934	Hey, R	TuP12	509	Jackson, S	FrB5	1100
	TuP10	496	Guldner, Y.	ThP35	978		MoP11	110	Jaros, M.	ThP5	821
Fujiyasu, H	ThP8	834	Gusev, G M	ThP30	949	Hilbel, W	TuA4	354	Jaroshevich, A S	FrA2	1058
Fukatsu, S	MoA4	17	Gwinn, E G	ThP33	970	Hill, G	ThC2	1016	Jayaraman, V	MoP23	181
	TuP20	553	Gyuro, J	ThP18	541		TuC6	435	Jayaraman, M B	ThC6	1039
	ThP34	403	Haacke, S	ThP5	821		TuP31	613	Johnson, M D	WeB2	712
Furdyna, J K	ThA1	729	Hagston, W E	TuC5	431		MoP20	165	Jones, G A C	WeB3	714
Gadaleta, C	MoP16	199	Hamaguchi, C	TuP19	899	Hiyamizu, S	TuP15	634	Joullie, A	TuB1	365
Garni, Y	ThP22	909	Hamberger, P	MoP17	144	Hoffman, C A	MoP9	102	Juen, S	FrA4	1064
Geim, A K	TuP38	645	Hamm, R. A	ThP39	1009	Hofmann, D M	ThP23	915	Jungk, G	MoP11	110
	TuP39	652		MoP22	175	Hogg, R A	MoP26	192	Kamal-Saadi, M	MoP25	188
Geibelbrecht, W	TuP28	593	Han, H-X	ThP9	492	Hohenstein, M.	MoP20	165	Kang, W	MoB2	23
Gerard, J M	FrB4	1094	Hansen, W	ThP24	916	Holland, M	ThP24	916	Kapon, E	ThB2	773
	ThP14	875		ThC5	1033		ThC5	1033	Kasper, E	MoC7	319
Gerhards, R R	ThP28	934	Hara, K	MoP21	170	Holy, V	MoP17	144	Kawashima, K	MoP17	144
	MoP29	213	Harbison, J P	WeA3	680	Hopfel, R A	ThP13	866		TuP1	442
Gershoni, D.	ThP39	1009	Haring Bolivar, P	FrB1	1075	Hopkins, P F	ThC1	1029	Kelly, M J	TuP4	460
de Groncoli, S	MoC7	319	Hazle, V	MoP26	192		MoP32	234	Kersmidas, V G	TuB1	365
	MoP15	131	Harmand, J C	MoP33	238	Herrick, M	TuA4	354	De Keyser, A	WeA3	680
Glutsch, S	ThP10	846	Harriot, L R	MoP22	175	Horiata, S	ThP19	899	Khan-Cheema, U M	TuA5	360
Gmachl, C	TuC5	431	Harris, J J	TuP39	652	Hosoda, M	TuP1	442	Khmyrova, I	TuP31	613
Gmezilov, V P	MoP14	124	Harrison, P A	ThP5	821	Hu, E L	WeA1	665	Kibbel, H	ThP37	992
Gobel, E O	MoP8	94	Hartmann, A	MoP39	268	Huang, Y-S	TuP11	502		MoC7	319
	TuP13	515	Hartmann, T C	TuP26	581	Hugues, O H	MoP39	268	Kiesel, P	MoP17	144
	FrB2	1081	Haseberg, T C	TuP32	617	Hunt, A W	WeB3	714	Kiselev, A A	ThP35	978
Goiran, M	MoP.	54	Hashimoto, Y	MoC4	302	Hwang, D M	ThB2	773	Klamura, J	TuB5	396
						Ichinose, H	MoC1	281		MoP21	170

Kunke, W	TuP29	600	Lamprecht, K F	ThP13	866	Majer, M	WeA4	687	Mironchenko, N V	ThP36	985
Klein, B	TuP29	600	Landschtr, G	ThA4	749	Maile, B E	TuP37	640	Miura, N	WeA2	675
Klenk, M	ThP18	894	Langheinrich, W	MoP7	8	Main, P C	TuP38	645		TuC2	411
Klipstein, P C	TuP31	413	Laruelle, F	MoA2	9		TuP28	593	Miyatake, T	ThP19	899
von Kitzing, K	MoP31	228		TuP33	625	Malzer, S	ThP35	978	Miyutani, T	MoP35	248
	MoA3	11	Lavallard, P	TuP15	523	Mansouri, L	TuP30	605	Molenskamp, L W	MoB3	29
	TuP36	635	Law, K-K	ThP22	909	Mansurov, V G	MoP37	261	Mollari, E	MoC7	319
Knap, W	MoP25	186	Law, V J	TuB1	365	Maracas, G N	TuP11	502		MoC8	324
	ThP26	927	Le Person, H	MoP33	238	Markelz, A G	ThP33	970		TuP40	131
Krauss, M	ThP35	978	Leadbeater, M I	ThC7	1046	Marschner, T	MoP32	234	Mollet, F	TuP40	658
Knapp, P A	ThB4	783	Ledentsov, N N	MoP27	200	Martelli, F	TuP13	515	Monakhov, A A	ThC7	1046
Knot, R	MoP31	228	Lee, C	MoA3	13	Martin, A D	MoP19	157	Mori, N	ThP19	895
Kobbi, F	MoP25	186	Lehmann, A	FrB1	1075	Martin, P M	TuP27	595	Morifuji, M	TuC5	431
Koch, F	ThP4	815	Leisching, P	FrB1	1075	Martín-Moreno, L	MoP39	268	Mori, A	MoP21	170
	TuP37	640	Leo, K	FrB1	1075		ThP17	889	Moschenko, S P	MoP37	261
Kocherskko, V P	ThA4	749	Lerch, M I F	TuP27	585	Martinez-Pastor, J	TuB1	365	Mosser, V	MoP25	188
Koenraad, P	WeB2	712	Leroux, G	MoP33	238	Marzin, J Y	ThP3	810	Motolusa, J	MoP3	60
Koldi, P	WeA4	687	Leuthner, C	ThP24	916	Mashkov, I V	FrB5	1100	Mowbray, D J	MoP20	165
Kop'ev, P S	ThC7	1046	Lew, A F J	TuP26	581	Mason, N J	TuP15	523	Muggelberg, C	TuA4	354
Koppensteiner, E	TuP22	559	Li, G-H	FrA1	1049		TuP31	613	Muraki, K	TuP7	479
	MoP17	144	Linder, E	TuP9	492		WeA2	675	Murase, K	ThP34	974
Koshida, S	MoC1	281	Lindt, J	ThP21	904		ThP29	943	Muto, S	ThP4	815
	MoP3	60	Lindwin, L V	FrB4	1094	Mathine, D L	TuP11	502	Nachew, I	TuB4	389
Kostal, H	TuA4	354	Litvin-Siszevskaya, E	TuP29	600	Matsuyama, I	MoP1	48	Nagamune, Y	ThP5	73
Kotthaus, J P	ThP24	916	Liu, K	ThP30	949	Mau, D K	TuC6	435	Nakamura, Y	MoC1	281
	ThC5	1033	Liu, X	MoP37	261	McCombe, B	TuP40	658	Nakata, S	MoP3	60
	MoP4	68	Liu, Z-X	MoP25	188	McMarr, P J	ThP27	928	Nakayama, M	MoP35	248
Kowalski, B	MoP26	192	Lockwood, D J	ThP4	815	Mehr, W	MoP6	80	Nakayama, T	TuP4	430
Kreller, F	ThP7	829	Lomsadze, A V	TuP9	492	Meners, U	TuP23	565	Nash, K J	ThA3	742
Kroemer, H	MoP4	68	Loe, R	MoP14	124		TuP37	640	Nastaushev, Yu V	TuC2	411
	ThC6	1039	Lopez, M	MoP40	275	Mellser, B Ya	TuB2	377		MoP37	261
	ThP33	970	Lorke, A	TuP26	581	Mendez, E E	ThC7	1046		ThP30	949
	WeA1	665	Lous, E	MoP1	48		FrA5	1068	Nayak, D K	ThP20	553
Kuba, H	TuC5	431	Lu, W	MoB5	44	Merikulov, I A	TuA3	347	Newbury, R	TuP1	365
	ThP19	899	Luc, F	ThP17	889	Merz, J L	ThA4	749	Nguyen, C	MoP4	68
	TuC6	435	Luczak, A	ThA5	756		ThP22	533	Nicholas, R J	ThC6	1039
Kuhn, O	MoP21	170	Lugagne-Delpon, E	TuP30	949	Mestres, N	TuP17	479		ThP33	970
Kukimato, H	MoP40	275	Lugak, A	TuA2	338	Meyer, B K	MoP26	192		WeA1	665
Kulakovskii, V D	TuP29	600	Lugh, P	MoP18	151	Meyer, J R	TuP23	915		WeA2	675
Kulik, L V	ThC7	1046	Lugue, P	MoC8	324	Michel, M	ThP18	894		TuC3	416
Kunze, U	ThP6	825	Lunn, B	ThP3	810	Nichols, J G	TuC3	416		ThP29	943
Kurinkiev, B K	MoA3	13	Luigen, S	TuP13	515	Nigal, V P	MoP37	261	Nicholls, J E	ThP5	821
Kuroda, Y	FrB1	1075	Luth, H	TuB2	377	Milekhin, A	MoP13	123	Nicholls, J T	TuB1	365
Kurtenbach, A	MoP37	261	Maam, J C	TuP26	581	Miles, R H	ThP23	915	Nishida, A	MoB4	35
Kurz, H	TuP28	593		TuP17	533	Mine, T	MoA4	17	Nishimura, H	TuP4	460
Kvon, Z D	ThP29	943		TuP18	541	Miot, C	MoP13	238	Nishuoka, M	MoP5	73
La Scala Jr, N	ThP1	796									
Laktimi, M											
Lamprrecht, A											

Nocera, J.	TuA3	347	Pinczuk, A	ThC3	1022	Robert, J. L.	MoP25	188	Schneller, A	ThP24	916
Noge, H.	MoC1	281	Pistol, M-E	TuP12	509	Robson, P. N	MoP20	165		ThC5	1033
	MoP3	60	Ploog, K	TuP15	523	Rocher, A	MoP2	54	Schmidt, A	ThB3	777
Nomuta, Y	MoP1	48		MoP12	119	Rodrigues, R	ThP13	866	Schmidt, G.	MoP7	88
Nöitzel, R.	MoC6	314		MoC6	314	Rodriguez, F. J	TuP5	466	Schmidt, K. H	TuC4	424
	MoC5	307		TuP6	471	Rogachev, A. A	ThC7	1046		FrB4	1094
Nützel, J. F.	TuP24	572		TuP8	485	Romanov, N. G	TuP15	523	Schmitz, J	WeA4	687
	TuP22	559		TuC4	424	Ron, A.	ThP22	909	Schneider, H	TuP6	471
Oakeshott, R. B. S.	TuP38	645		TuP39	652	Rosencher, E	TuA2	338		TuP8	485
Ogawa, M.	FrA5	1068		MoP31	228	Roskos, H. G.	FrB1	1075	Scholl, E.	FrB4	1094
Ohmon, Y.	MoP16	199		TuP10	496	Rossi, F.	MoC8	324	Scholz, F.	MoP30	220
Ohno, T.	MoP10	104		MoP16	199	Rota, L.	MoC8	324	Schorer, R.	MoP26	192
Okimura-Schlesinger, J.	ThP39	1009		TuP17	533	Roussignol, Ph	ThP3	810	Schulman, J. N	MoC7	319
Okamoto, H.	MoP16	199		MoP34	244	Rucker, H	TuP23	565	Schulz, P. A	TuP32	617
Onling, P.	MoP26	192		TuP36	635	Ruf, T.	MoP12	119	Schulzgen, A	ThP15	879
Onabe, K.	TuP16	527		FrB4	1094		MoC6	314	Schwedler, R	ThP7	829
Orr, B. G.	WeB1	714		MoC5	307	Ruhle, W. W	TuB1	389	Seidel, W	FrB1	1075
Ossau, W.	ThA4	749		MoC3	298		TuP18	541	Seifert, W	WeA5	694
Ossicini, S.	ThP9	841		FrA4	1064	Ryon, J. F	ThP6	825	Selbmann, P. E	TuP12	509
Osten, H. J.	TuP23	565	Polato, W. H. M	TuP21	558	Ryzhu, V. I	ThP37	992	Shanabrook, B. V	MoP38	262
Ota, K.	TuP16	527	Polimeni, A	MoP19	157		ThP25	922	Shaposhnikov, S. V	MoC2	290
Ozanyan, K. B.	MoP19	157	Pollak, F. H.	TuP11	502	Sagnes, J	TuP25	576	Shaw, M. J	ThC7	1046
Pabla, A. S.	MoP20	165	Popovic, Z. V	MoC6	314	Saito, T	MoC4	302	Shen, S. C.	FrA2	1058
Paden, R.	FrB5	1100	Portal, J. C	ThP30	949	Sakai, J. W.	TuP28	583	Sherwin, M. S	ThA5	756
Palacios, J. J.	ThP17	889		TuC6	435	Sakaki, H.	MoC1	281	Sheu, Y. M	ThP35	970
Palmer, J. F.	TuP40	658		TuP40	658		MoP3	60	Shi, J. M	MoP27	200
	MoP33	238	Potemski, M	TuP17	533	Saker, M. K	ThP16	885	Shi, Z.	ThP27	928
Palmstrom, C. J.	TuA5	360	Pothner, H	TuP18	541	Sakurai, N.	TuC2	411	Shimizu, A	ThP1	796
Panish, M. B.	MoP22	175	Pozina, G. R	TuP36	635	Salemink, H. W. M	ThP8	834	Shimomura, S	MoC1	281
Pale, M.	TuC6	435	Presting, H.	ThA4	749	Salzman, J	WeB2	712	Shirashi, K	MoP9	102
	MoP20	165	Ptashchenko, A. A	MoP17	144	Samuelson, L	ThP21	904	Shiraki, Y	MoP10	104
	TuP35	634	Ptashchenko, F. A	ThP36	985	Sanchez-Rojas, J. L	TuP12	509		TuP16	527
	TuP28	593	Puls, J	ThP36	985	Sandmann, J. H. H	MoP20	165		MoA4	17
	ThC2	1016	Pusep, Y.	ThP7	829	Sands, T	FrB2	1081		TuP20	553
	TuP39	652	Qiang, H.	MoP13	123	Sano, N	WeA3	680	Shtrikman, H	ThP34	974
	ThP27	928	Ralsion, J. D	TuP11	502	Sapega, V. F	MoP9	102	Shubin, W	MoB1	21
	ThC2	1016	Ram-Mohan, L. R	WeA4	687	Sasaki, S	MoP12	119	Sibani, H.	MoP40	275
	TuA5	360	Ramstein, M	ThP23	915	Scamarcio, G	TuC7	411	Sibille, A	MoP25	188
	TuC2	411	Raymond, A	MoP11	110	Schaff, W	MoP16	199	Simeone, M. G	TuP40	658
	MoB5	44	Rees, G. J	MoP25	188	Schaffner, F	ThP27	928	Simmonds, P. E	MoP19	157
Peggs, D. W.	TuB1	365	Reinecke, T. L.	ThP26	927	Schapers, T.	TuP24	572	Singh, J	TuP27	585
Pepper, M.	MoB5	44	Reichue, D. A	MoP20	165	Schubler, H. F	TuA1	333	Sirton, C	ThP38	1000
Petroff, P. M.	TuC3	416	Ritter, D	FrB3	1089	Schley, P	TuP26	581		ThC1	1015
Peyla, P.	MoP2	54		ThB4	783	Schmalz, K	MoP23	181	Sivachenko, A. Yu	ThP20	903
Peyrade, J. P.	ThP28	934		TuP6	471	Schmeller, A	TuP23	565	Sizmann, R	TuP14	522
Plannkuche, D.	ThC1	1015		MoP24	182		MoP4	68		ThC1	1015
Pfaffner, L. N.	ThC3	1022		TuB1	365		TuP23	565		ThP20	903
	ThP21	904		ThP39	1009		ThC3	1022		ThP4	815
	MoB2	23									

Skarbiszewski, C	MoP25	188	Tamguchi, K	ThP16	899	Wada, K	MoC1	281	Woodhead, J	MoP20	165
Skolnick, M S	MoP20	165	Tapier, L	MoP16	199	Wagner, J	TuP6	471	Worren, T	MoP19	157
	TuP35	624	Taylor, R A	MoC5	307		WeA4	687	Wu, X	ThP35	978
	MoP39	268	Taylor, C	ThP6	825		MoP11	110	Yaguchi, H	TuP16	527
	TuP3	411		TuP5	466		TuP8	485	Yakovlev, D R	TuA4	749
	TuP35	634		ThP17	889	Wagner, R J	MoC2	290	Yamaguchi, M	TuC5	431
	TuP31	613	Temkin, H	MoP22	175	Walker, P J	TuP31	613	Yamamoto, M	MoP35	248
	TuP35	978	Terekhov, A S	MoP23	181		WeA2	675	Yamamoto, T	TuP10	496
	TuC2	411	Tewordt, M	TuB1	365		ThP29	943		MoP9	102
	MoP28	206	Theodorou, G	TuP19	548	Wang, C C	MoP27	200	Yang, C H	TuB3	383
	MoP6	80	Thibaut, I	TuA2	338	Wang, H	MoP33	233	Yassievich, I N	TuP23	565
	MoC1	281	Tikhov, A	WeA5	694	Wang, J	TuP30	605	Yasuda, T	MoP21	170
	MoP8	94	Tobben, D	TuP24	572	Wang, W I	TuP7	479	Yeh, J J	MoP27	200
	MoP12	119	Tominaga, K	TuP1	442		TuA3	347	Yoh, K	MoB4	35
	MoC6	314	Toropov, A I	MoP13	123	Wang, Z P	TuP9	492	Yoshino, J	MoP21	170
	ThA2	738	Tourne, E	ThP30	949	Wang, Z H	ThA2	738	YOUNGDALE, E R	ThP23	915
	MoP22	175	Trankle, G	FrA4	1064	Warburton, R J	WeA2	675	Yuh, E L	ThC4	1029
	ThP6	825	Truscutt, W S	FrA3	1059		TuC3	416	Zahler, M	ThP21	904
	ThP5	821	Tserbak, C	ThP31	955	Warren, P	TuP25	576	Zastrow, U	TuP26	581
	TuP39	652	Tsukawa, M	TuP19	548	Waschke, C	FrB1	1075	Zawadzki, W	ThP26	927
	MoP8	94	Tsukamoto, S	MoP3	60	Waterman, T	MoP9	102	Zekentes, K	MoP25	188
	TuP13	515	Tuerck, V	MoP5	73	Webb, J B	MoC2	290	Zhang, L J	ThA5	756
	FrB2	1081	Turner, T S	ThB2	773	Wegscheider, W	MoP14	124	Zhang, Y H	TuP17	533
	MoB2	23	Turner, M E	MoP39	268	Weimann, G	MoB2	23	Zielinski, E	ThP18	894
	TuB4	389	Uraltsev, I N	MoC2	290		ThP24	916	Zrenner, A	FrA3	1059
	ThP7	829	Usami, N	ThA4	749		TuP18	541			
	WeB3	714		MoA4	17		MoP28	206			
	ThP6	825	Uzmeier, T	TuP20	553	Weiner, J S	FrA3	1059			
	MoP36	252	V'yurkov, V V	MoP4	68	Weis, J	ThC3	1022			
	MoP38	262	Vandenbergh, J M	ThP25	922	Wendel, M	TuP36	635			
	TuP22	553	Vasiliev, A	ThP30	1009	Wendler, L	ThP24	916			
	ThC4	1029	Vaughan, T A	ThB3	777	West, K W	ThP11	853			
	TuC6	1039	Vep, E	ThP29	943		ThC1	1015			
	TuB2	377	Vescan, L	TuP38	645		ThC3	1022			
	MoP28	206	Vieren, I P	TuP26	581	Wetzel, C	MoB2	23			
	ThP29	943	Vin, L	TuP25	576	Whittaker, D M	MoP26	192			
	TuP36	645	Vinathra, A	TuP7	479		MoP20	165			
	ThP1	796	Vinot, B	ThP3	810		TuP35	634			
	TuB4	389	Voulet, F	TuA2	338		MoP39	268			
	MoP16	199	Vousin, P	MoP2	54	Wick, A D	TuC2	411			
	MoC3	367		TuP3	454	Willander, M	MoP34	244			
	ThP34	974		WeA5	694	Willcox, A R K	TuB5	396			
	MoP21	170		MoP18	151	Wilson, R A	MoP20	165			
	TuP4	460		WeA5	694	Wisniewski, P	TuB3	383			
	WeA3	686		TuP25	576	Wolk, C	MoP28	206			
	MoP9	102	de Vries, D K	MoP34	244	Wong, K B	TuP37	640			
	MoP1	48	Vurgattman, I	ThP38	1000	Woodbridge, K	FrA2	1058			
	TuC5	431	Waag, A	ThA4	749		TuC3	416			

END
10-94

-1116-

-1115-